

FRACTURE MECHANICS

*Proceedings of the
Eleventh National Symposium
on Fracture Mechanics:
Part I*

C. W. Smith, editor

ASTM STP 677

**AMERICAN SOCIETY FOR
TESTING AND MATERIALS**

FRACTURE MECHANICS

Proceedings of the
Eleventh National Symposium
on Fracture Mechanics: Part I

A symposium sponsored by
ASTM Committee E-24 on
Fracture Testing of Metals
AMERICAN SOCIETY FOR
TESTING AND MATERIALS
Virginia Polytechnic Institute
and State University
Blacksburg, Va., 12-14 June 1978

ASTM SPECIAL TECHNICAL PUBLICATION 677
C. W. Smith, Virginia Polytechnic
Institute and State University,
editor

List price \$60.00
04-677000-30



AMERICAN SOCIETY FOR TESTING AND MATERIALS
1916 Race Street, Philadelphia, Pa. 19103

Copyright© AMERICAN SOCIETY FOR TESTING AND MATERIALS 1979
Library of Congress Catalog Card Number: 78-74567

NOTE

The Society is not responsible, as a body,
for the statements and opinions
advanced in this publication.

Printed in Baltimore, Md.
August 1979

Foreword

This publication, *Fracture Mechanics*, contains papers presented at the Eleventh National Symposium on Fracture Mechanics which was held 12–14 June 1978 at Virginia Polytechnic Institute and State University, Blacksburg, Va. The American Society for Testing and Materials' Committee E-24 on Fracture Testing of Metals sponsored the symposium. C. W. Smith, Virginia Polytechnic Institute and State University, served as editor of this publication.

The proceedings have been divided into two volumes: Part I—*Fracture Mechanics* and Part II—*Fracture Mechanics Applied to Brittle Materials*.

Related ASTM Publications

Developments in Fracture Mechanics Test Methods Standardization, STP 632 (1977), \$24.75, 04-632000-30

Fractography—Microscopic Cracking Process, STP 600 (1976), \$27.50, 04-600000-30

Mechanics of Crack Growth, STP 590 (1976), \$45.25, 04-590000-30

A Note of Appreciation to Reviewers

This publication is made possible by the authors and, also, the unheralded efforts of the reviewers. This body of technical experts whose dedication, sacrifice of time and effort, and collective wisdom in reviewing the papers must be acknowledged. The quality level of ASTM publications is a direct function of their respected opinions. On behalf of ASTM we acknowledge with appreciation their contribution.

ASTM Committee on Publications

Editorial Staff

Jane B. Wheeler, *Managing Editor*
Helen M. Hoersch, *Associate Editor*
Ellen J. McGlinchey, *Senior Assistant Editor*
Helen Mahy, *Assistant Editor*

Contents

Introduction	1
FATIGUE CRACK GROWTH STUDIES	
Effect of Biaxial Stresses on Crack Growth—A. F. LIU, J. E. ALLISON, D. F. DITTMER, AND J. R. YAMANE	5
Fatigue Crack Growth Threshold in Mild Steel Under Combined Loading—L. P. POOK AND A. F. GREENAN	23
Sequence Effects on Fatigue Crack Propagation; Mechanical and Microstructural Contributions—H. NOWACK, K. H. TRAUTMANN, K. SCHULTE, AND G. LÜTJERING	36
Variations in Crack Growth Rate Behavior—M. E. ARTLEY, J. P. GALLAGHER, AND H. D. STALNAKER	54
Application of Fracture Mechanics to Damage Accumulation in High Temperature Fatigue—M. J. DOUGLAS AND A. PLUMTREE	68
Cryogenic Effects on the Fracture Mechanics Parameters of Ferritic Nickel Alloy Steels—R. L. TOBLER, R. P. MIKESSELL, AND R. P. REED	85
Evaluation of Temperature Effects on Crack Growth in Aluminum Sheet Material—D. E. PETTIT AND J. M. VAN ORDEN	106
Effects of Temperature and Frequency on the Fatigue Crack Growth Rate Properties of a 1950 Vintage CrMoV Rotor Material—T. T. SHIH AND G. A. CLARKE	125
Structural Memory of Cracked Components Under Irregular Loading—H. FÜHRING AND T. SEEGER	144
Effect of the Active Plastic Zone on Fatigue Crack Growth Rates—GUNTER MARCI	168
A Comparative Experimental Study on the Fatigue Crack Closure Behavior Under Cyclic Loading for Steels and Aluminum Alloys—J. A. VAZQUEZ, AUGUSTO MORRONE, AND J. C. GASCO	187
Effect of Residual Stresses on Fatigue Crack Growth in Steel Weldments Under Constant and Variable Amplitude Loads—GRZEGORZ GLINKA	198
Role of Crack-Tip Stress Relaxation in Fatigue Crack Growth—A. SAXENA AND S. J. HUDAK, JR.	215
Crack Closure During Fatigue Crack Propagation—W. J. D. SHAW AND I. LE MAY	233

Fatigue at Notches and the Local Strain and Fracture Mechanics Approaches— N. E. DOWLING	247
A Strain Based Intensity Factor Solution for Short Fatigue Cracks Initiating from Notches— M. H. EL HADDAD, K. N. SMITH, AND T. H. TOPPER	274
Crack Initiation in a High-Strength Low-Alloy Steel— B. L. BRAGLIA, R. W. HERTZBERG, AND RICHARD ROBERTS	290
Effect of Spherical Discontinuities on Fatigue Crack Growth Rate Per- formance— W. G. CLARK, JR.	303
Prediction of Fatigue Crack Growth Under Spectrum Loads— A. E. GEMMA AND D. W. SNOW	320

SURFACE FLAWS

Semi-Elliptical Cracks in a Cylinder Subjected to Stress Gradients— J. HELIOT, R. C. LABBENS, AND A. PELLISSIER-TANON	341
Stress Intensity Factor Solutions for Internal Longitudinal Semi-Elliptical Surface Flaws in a Cylinder Under Arbitrary Loadings— J. J. MCGOWAN AND M. RAYMUND	365
Theoretical and Experimental Analysis of Semi-Elliptical Surface Cracks Subject to Thermal Shock— G. YAGAWA, M. ICHIMIYA, AND Y. ANDO	381
Growth of Part-Through Cracks— L. HODULAK, H. KORDISCH, S. KUNZEL- MANN, AND E. SOMMER	399
Stress Intensity Factors for Two Symmetric Corner Cracks— I. S. RAJU AND J. C. NEWMAN, JR.	411
Influence of Flaw Geometries on Hole-Crack Stress Intensities— C. W. SMITH, W. H. PETERS, AND S. F. GOU	431

EXPERIMENTAL FRACTURE MECHANICS— K_{Ic} , J_{Ic} , SPECIMEN GEOMETRY EFFECTS, AND EXPERIMENTAL TECHNIQUES

Variation of Fracture Toughness with Specimen Geometry and Loading Conditions in Welded Low Alloy Steels— A. PENELON, M. N. BASSIM, AND J. M. DORLOT	449
J_{Ic} Results and Methods with Bend Specimens— J. H. UNDERWOOD	463
Investigation of Specimen Geometry Modifications to Determine the Con- servative, J_I-R Curve Tearing Modulus Using the HY-130 Steel System— J. P. GUDAS, J. A. JOYCE, AND D. A. DAVIS	474
An Experimental Study of the Crack Length/Specimen Width (a/W) Ratio Dependence of the Crack Opening Displacement (COD) Test Using Small-Scale Specimens— P. M. S. T. DE CASTRO, J. SPURRIER, AND P. HANCOCK	486

Dynamic Photoelastic and Dynamic Finite Element Analyses of Polycarbonate Dynamic Tear Test Specimens—S. MALL, A. S. KOBAYASHI, AND Y. URABE	498
Effect of Specimen Geometry on Crack Growth Resistance—S. J. GARWOOD	511
Single-Edge-Cracked Crack Growth Gage—J. A. ORI AND A. F. GRANDT, JR.	533
Measurement of Crack-Tip Stress Distributions by X-Ray Diffraction—J. E. ALLISON	550
Correlations Between Ultrasonic and Fracture Toughness Factors in Metallic Materials—ALEX VARY	563

SPECIAL TOPICS

Analysis of Load-Displacement Relationships to Determine J-R Curve and Tearing Instability Material Properties—HUGO ERNST, P. C. PARIS, MARK ROSSOW, AND J. W. HUTCHINSON	581
Path Dependence of J in Three Numerical Examples—M. E. KARABIN, JR., AND J. L. SWEDLOW	600
Description of Stable and Unstable Crack Growth in the Elastic Plastic Regime in Terms of J, Resistance Curves—C. E. TURNER	614
Strain Energy Release Rate Method for Predicting Failure Modes in Composite Materials—R. S. WILLIAMS AND K. L. REIFSNIDER	629
An Analysis of Tapered Double-Cantilever-Beam Fracture Toughness Test for Adhesive Joints—S. S. WANG	651
Analytical Modeling and ND Monitoring of Interlaminar Defects in Fiber-Reinforced Composites—R. L. RAMKUMAR, S. V. KULKARNI, R. B. PIPES, AND S. N. CHATTERJEE	668
Stress Intensity Factors for a Circular Ring with Uniform Array of Radial Cracks Using Cubic Isoparametric Singular Elements—S. L. PU AND M. A. HUSSAIN	685
Interpretations of Crack Surface Topologies for Poly(Vinyl Chloride)—E. M. SMOLEY	700

ENGINEERING APPLICATIONS

Experimental Determination of K_I for Hollow Rectangular Tubes Containing Corner Cracks—M. E. MCDERMOTT AND R. I. STEPHENS	719
Fracture Analysis of a Pneumatically Burst Seamless-Steel Compressed Gas Container—B. W. CHRIST, J. H. SMITH, AND G. E. HICHO	734
Crack Growth in Externally Flawed, Autofrettaged Thick-Walled Cylinders and Rings—J. A. KAPP AND R. EISENSTADT	746
Estimating Fatigue Crack Propagation Lives at the Test Site—D. R. GALLIART	757
On the Cup and Cone Fracture of Tensile Bars—B. KONG AND P. C. PARIS	770

SUMMARY

Summary

783

Index

789

Introduction

Developments in the field of fracture mechanics have exerted a strong influence upon the advancement of structural technology during the past decade. Papers which chronicle an important part of these developments have been published in various ASTM special technical publications (STP). This volume consists of the Proceedings of the Eleventh National Symposium on Fracture Mechanics which is sponsored by ASTM Committee E-24 on Fracture Testing. The main body of the proceedings, consisting solely of contributed papers, presents an overview of the current state of analytical and experimental research as viewed by those members of the international technical community who participated in the Symposium. A separate publication on Brittle Fracture, ASTM STP 678, consisting solely of solicited papers, has recorded the proceedings of those special sessions of the Symposium. This publication delineates frontiers of research in the several areas of fracture mechanics which are addressed herein and should be of interest to scientists and engineers wishing to keep abreast of such developments.

Specifically, this volume documents progress in research in several areas; the area of greatest activity being that of fatigue crack growth. Papers which study the influence upon fatigue crack growth of combined fields, nonperiodic load spectra, temperature effects, crack closure and residual stresses, notches, and other effects are included. Both analytical and experimental studies on stress intensity distributions and shapes of surface flaws involving finite element, boundary integral-weight function, photoelastic, and overload marking techniques are included. Research on experimental techniques and the analysis of specimens is reported together with new results on K_{Ic} - J_{Ic} determination and elastic-plastic fracture analysis. Three papers are included which deal with the fracture of composite materials. Finally, a series of papers dealing with topics outside of the above areas which were designated as special topics are included along with a group of papers illustrating the application of fracture mechanics to problems of current and future technological importance.

A feature of the Eleventh National Symposium was the announcement by Committee E-24 Chairman J. G. Kaufman of the establishment of the George Rankin Irwin Medal to be awarded annually to the outstanding young researcher in the field of Fracture Mechanics. The first medal was presented to Dr. Irwin at the Symposium.

The value of the Eleventh National Symposium on Fracture Mechanics is evidenced by the contents of this volume and *ASTM STP 678*. The contributions of the symposium organizing committee, the authors, reviewers, referees, J. J. Palmer and J. B. Wheeler of the ASTM and their staffs, together with the participation and support of P. E. Torgersen, Dan Frederick and J. D. Wilson of Virginia Polytechnic Institute and State University are gratefully acknowledged.

C. W. Smith

Department of Engineering Science and
Mechanics, Virginia Polytechnic Institute
and State University, Blacksburg, Va.,
24061; symposium chairman and editor.

Fatigue Crack Growth Studies

A. F. Liu,¹ J. E. Allison,² D. F. Dittmer,¹
and J. R. Yamane¹

Effect of Biaxial Stresses on Crack Growth

REFERENCE: Liu, A. F., Allison, J. E., Dittmer, D. F., and Yamane, J. R., "Effect of Biaxial Stresses on Crack Growth," *Fracture Mechanics, ASTM STP 677*, C. W. Smith, Ed., American Society for Testing and Materials, 1979, pp. 5-22.

ABSTRACT: This paper presents the results of a systematic evaluation of biaxial loading on fatigue crack propagation behavior using experimental techniques, and determines the accuracy with which a current advanced state-of-the-art analytical approach can predict this behavior. These results provide data for evaluating biaxial loading effects on crack propagation.

The effects of both biaxial stress ratio and applied stress level have been evaluated by conducting crack propagation tests on cruciform specimens made of 7075-T7351 and 2024-T351 aluminum alloys. Tests were conducted at various biaxial stress ratios ($-1.5 \leq \sigma_x/\sigma_y \leq 1.75$). The magnitudes of the applied stress were from 20 to 60 percent of the material tensile yield strength. Test results indicate that biaxial stress states contribute a negligible effect on fatigue crack propagation rate as compared to data developed from uniaxial loading conditions.

KEY WORDS: biaxial loading, crack propagation, fracture mechanics, metals, structures, fatigue (materials)

Nomenclature^a

- a One half of the total crack length, or the distance between a point on the X -axis to the center of the cruciform specimen, mm (in.)
- a_x Projected length of " a ", perpendicular to σ_x , mm (in.)
- a_y Projected length of " a ", perpendicular to σ_y , mm (in.)
- f Cyclic frequency (Hz)
- F_{ty} Material uniaxial tensile yield strength, kPa (ksi)
- K_{max} Stress intensity corresponding to σ_{max} , $MN(M)^{3/2}$ (ksi $\sqrt{in.}$)

¹ Senior technical specialist and senior engineers, respectively, Northrop Corp., Aircraft Group, Hawthorne, Calif. 90250.

² Graduate student, Carnegie-Mellon University, Pittsburgh, Pa. 15213, formerly Captain, United States Air Force.

K_{\min}	Stress intensity corresponding to σ_{\min} , $MN(M)^{3/2}$ (ksi $\sqrt{\text{in.}}$)
P_x	Load applied to X-axis of a cruciform specimen, always parallel to the crack, N (kip)
P_y	Load applied to Y-axis of a cruciform specimen, always perpendicular to the crack, N (kip)
W_c	Width of a center cracked specimen, mm (in.)
ΔK	$K_{\max} - K_{\min}$, $MN(M)^{3/2}$ (ksi $\sqrt{\text{in.}}$)
σ_x	Stress parallel to the crack, tension or compression, kPa (ksi)
σ_y	Stress perpendicular to the crack, always in tension, kPa (ksi)

^a Original measurements are in English units.

Fracture mechanics techniques currently are being used to perform safe life analysis on aircraft and many other types of structural components. Because the problems of multiaxial loading are common in aircraft airframe and engine components, it is important to evaluate and quantify multiaxial effects in order to improve the crack propagation prediction capability for design purposes.

Consider that a plate, containing a through-the-thickness crack, is subjected to a biaxial stress field. One of the stress components is acting perpendicular to the crack and another component parallel to the crack. For problems that are solved using purely elastic formulations [1,2],³ the crack tip stress intensity, K_1 , in the opening mode, theoretically is not affected by the lateral stress component. On the other hand, it can be shown by elastic-plastic analysis, for example, [2-6], that the size of a crack tip plastic zone varies with biaxial loading conditions. Therefore, one may speculate that the crack tip stress intensity (K) as well as the crack growth rate (da/dN) will also be influenced by the presence of the lateral stress component. Experimental data concerning the biaxial loading effect on cyclic crack growth rate, residual strength, and the direction of crack growth, are available [7-14]. However, the results of these few investigations have been inconsistent, and none of them contained enough data to offer conclusive evidence to support, or to correlate with, the existing theories.

The objective of the present investigation is to evaluate systematically the effect of the biaxial stress field on cyclic crack growth rate behavior. An analytical/experimental study program has been designed to answer the following questions:

1. Do biaxial stresses affect crack tip stress intensity, cyclic crack growth rate, or crack tip plastic zone size?
2. Is an elastic - K adequate for correlating the biaxial da/dN data?

³ The italic numbers in brackets refer to the list of references appended to this paper.

3. Is the crack tip plastic zone important in the mechanics of constant amplitude crack growth?

The scope of the program includes the following:

1. Determination of the load-stress relationship on a selected specimen geometry.
2. Determination of the elastic crack tip stress intensity factors for a crack in that geometry.
3. Analytical determination of the crack tip plastic zone sizes.
4. Development of experimental data and evaluation of the effects of biaxial stress ratio and applied stress level on the cyclic crack growth rate behavior of 7075-T7351 and 2024-T351 aluminum alloys.

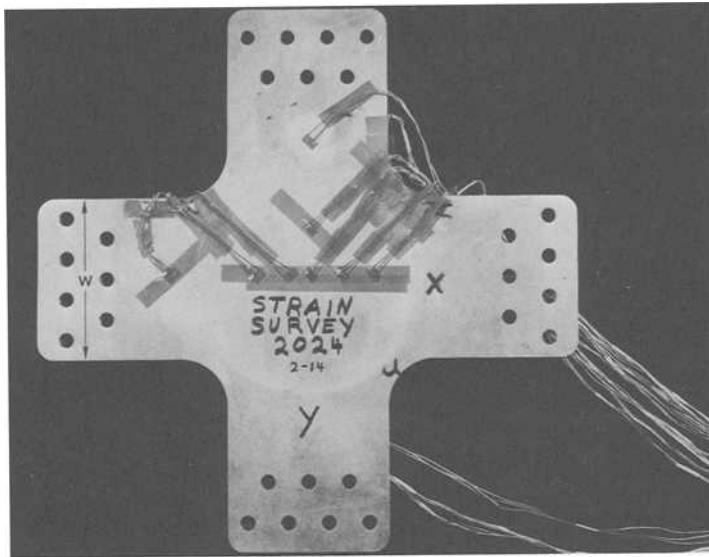
Specimen Configuration

There are many types of specimens that can be used to accomplish a biaxial loading condition. For example, Pook and Holmes [11] used a flat cruciform specimen containing longitudinal slots in the loading arms; Beck [7] used a very large square sheet and loaded the sheet through many little straps attached around the sheet edges. The criteria for designing a specimen configuration to fulfill all the objectives in the present study are:

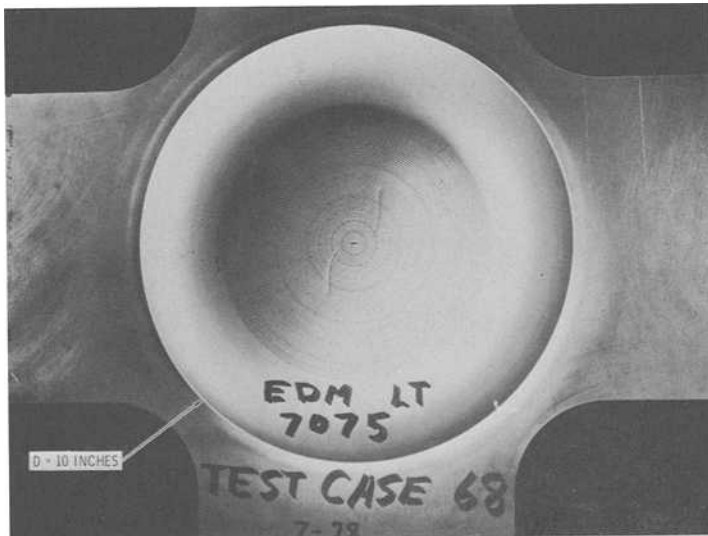
1. The specimen should be capable of taking compression load.
2. The specimen should be designed to avoid fatigue damage at the grip or in any area other than that containing the crack.
3. The size of the specimen should be large enough to minimize boundary effects on crack tip stress intensity; but it should not be too large, so that the required load levels can be kept within the capacity of the testing machine.
4. The stress distribution across the specimen width should be fairly uniform.
5. The specimen configuration should be simple in order to minimize machining costs.

A cruciform specimen configuration has been selected for generating biaxially loaded crack growth rate data. Generally, the specimen has an overall length of 597 mm (23.5 in.) including grip areas at each end of the loading arms. It also has a thinner region, 6 in. in diameter, in the center of the specimen. An overall view of the specimen is shown in Fig. 1(a). Figure 1(b) is a closeup photograph of the center section. Loading conditions and dimensions of the specimen are shown in Fig. 2.

It has been considered that the thickness of the center region (t_1) and the thickness and width of the loading arms (t_2 and W) were the three primary variables affecting the stress distribution. A 17.7-mm (0.5-in.) thick loading arm was selected for t_2 to eliminate one of the three variables



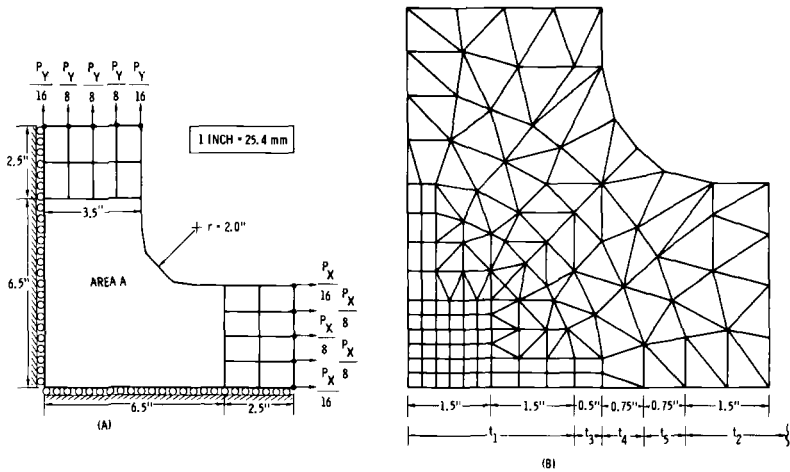
(a)



(b)

- (a) An overall view.
- (b) Closeup of the center portion (containing a curved crack).

FIG. 1—Cruciform specimen.



(a) Boundary conditions.
 (b) Details of Area A.

FIG. 2—Finite element model for one quarter of a cruciform specimen.

and also to minimize material and machining costs. The t_1 and W dimensions have been optimized by conducting stress analysis on a dummy panel configuration (without crack). Stress distributions across the thin section were determined by using the NASTRAN computer program. Figure 2 shows the finite element model representing one quarter of the cruciform specimen. Here $t_1 = 4.57$ mm (0.18 in.), $W = 17.78$ cm (7 in.) and $t_2 = 17.7$ mm (0.5 in.). Also shown in Fig. 2 are three rings of triangular elements of different intermediate thicknesses (t_3 , t_4 and t_5) to simulate the curvature connecting t_1 and t_2 .

The analytical results are presented by the curves of Figs. 3 and 4. In Fig. 3, the load and stress relationship at the center of the specimen is presented; the magnitude of σ_y and σ_x (per (1000 lb) of P_y) are plotted as functions of P_x to P_y ratio. The load and stress relationship (the NASTRAN lines in Fig. 3) can be represented by:

$$\sigma_y = \frac{P_y}{12} [6.55 - 1.73 (P_x/P_y)] \tag{1}$$

$$\sigma_x = \frac{P_y}{12} [6.57 (P_x/P_y) - 1.75] \tag{2}$$

For an actual test, the required P_x and P_y values corresponding to any desirable σ_x and σ_y combinations can be determined by solving Eqs 1 and 2.

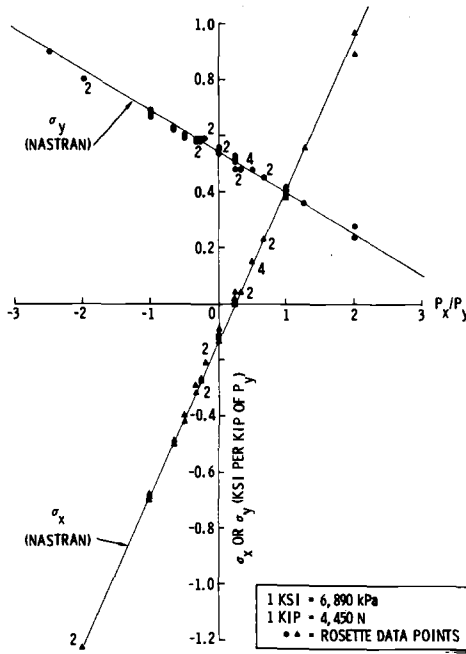
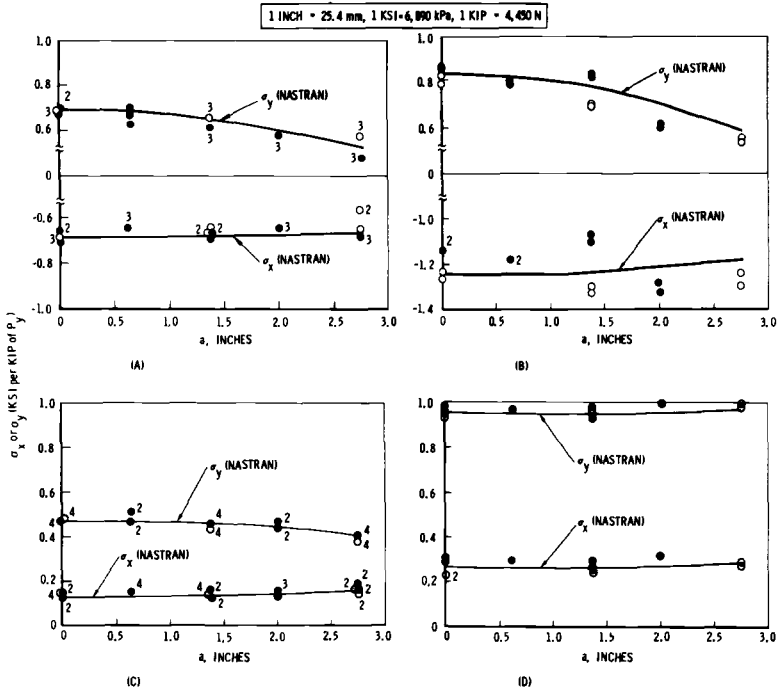


FIG. 3—Load-stress relationship at the center point of a cruciform specimen.

In Fig. 4, stress distributions along the X -axis of the cruciform specimen are presented. Since the specimen is symmetrical about its center lines, the magnitudes of σ_x and σ_y are plotted as functions of a . The stress distributions corresponding to many P_x/P_y ratios were determined; however, only four typical examples are shown here.

Stress Survey

One cruciform specimen of each material was instrumented with rectangular rosettes along X -axis of the specimen. The specimens (without crack or cut, or elox) were loaded in the horizontal biaxial loading machine under various biaxial load ratios (for example, $0, \pm 0.5, \pm 1.0, \pm 2.0$, etc.). The biaxial test unit is composed of three pairs of actuators and load cells. Two 224 750 N (55 kip) capacity actuators are mounted opposing each other; these are commanded in such a manner as to provide a fixed specimen center point location so that the third actuator (342 650 N, or 77 kip, capacity), mounted perpendicular to the other two, will always be in proper alignment. The three load cells monitor the actual loads applied by each actuator. Loads are supplied by hydraulic pumps and monitored by a central electronic control unit. Stress distributions along the X -axis of the specimen were determined by strain measurements at five locations (one



(a) $P_x = -P_y$, 7075-T7351 specimen.
 (b) $P_x = 2P_y$, 2024-T351 specimen.
 (c) $P_x = P_y/2$, 7075-T7351 specimen.
 (d) $P_x = 2P_y$, 2024-T351 specimen.

FIG. 4—Stress gradient along the X-axis of a cruciform specimen.

pair of back to back rosettes at the center of the specimen and two rosettes on each side of the center covering 69.85-mm (2.75-in.) radius, two of the side locations also had back-to-back rosettes). A guide was used to prevent out-of-plane buckling under compression loads.

At each loading condition, up to four load levels were applied and two readings were taken at each load level. The specimen was placed in the machine at two orientations. One set of the strain gage data was taken while the Y-axis of the specimen was lined up with the 244 750 N (55 kip) load cells and another set of strain gage data was taken while the Y-axis of the specimen was lined up with the 342 650 N (77 kip) load cells (that is, the specimen was rotated 90 deg). Typical experimental data are plotted on Figs. 3 and 4, and it is observed in these figures that the correlations between strain gage results and the NASTRAN finite element analysis results are very good. Note that in these figures, each data point represents an average of two readings. Occasionally, there is a number

adjacent to a data point indicating that more than one data point was superimposed on another; for example, the number 4 implies that the data point represents an average of eight measurements (four load levels and two readings per each load level). The solid and open symbols in Fig. 4 indicate the results from back-to-back gages. Since the results for the back-to-back gages are almost identical, only one side of the results are presented in Fig. 3. It is significant to note that experimental data (although not all of them are presented here) have shown that the load response characteristics of the cruciform specimen were not affected by the position of the specimen, that is, whether the Y -axis of the specimen was placed in line with the 342 650 N (77 kip) or the 244 750 N (55 kip) load cells, the strain gage results were identical.

Stress Intensity Factors

In the theory of linear elastic fracture mechanics, crack tip stress intensity can be expressed as

$$K = \sigma_y \sqrt{\pi a} \cdot F(a) \quad (3)$$

where σ_y is the gross area stress normal to the crack. In case of a center cracked specimen (CCT), σ_y will be the far field uniform stress and $F(a)$ accounts for the boundary conditions. According to [15]

$$F(a) = \left[1 - .025 \left(\frac{2a}{W_c} \right)^2 + 0.06 \left(\frac{2a}{W_c} \right)^4 \right] \cdot \sqrt{\sec \left(\frac{\pi a}{W_c} \right)} \quad (4)$$

In case of a cruciform specimen, for a given ratio of biaxial loads, there is a pair of stress components, σ_x and σ_y , at every point along a predetermined crack plane. In this case, the crack plane will be the X -axis in Fig. 2. As postulated in Ref 1, the elastic K value for a given crack length in a biaxial state of stress should be the same as in the uniaxial loading condition. In other words, the K -expression of Eq 3 is applicable to the cruciform specimen except that σ_y would be the (reference) stress in the center of the uncracked specimen and $F(a)$ would be a function of the boundary conditions and the stress gradient of σ_y along the X -axis.

Finite element analysis of the cruciform specimen with cracks has been conducted. The finite element model of Fig. 2 was used to determine elastic K values. A special "crack tip" element, originally developed by Tong et al [16] has been incorporated into the NASTRAN. In each case analyzed, for example, each crack length, a special element was placed in the general finite element model occupying a region representative of the predetermined crack tip location, and the elements representing the crack were freed from the boundary restrictions. Eight specimens with crack lengths ($a = 6.35$ to 69.85 mm) were loaded to various biaxial loading

ratios with $\sigma_y = 12$ ksi. The results are graphed in Fig. 5. Several K values calculated from Eq 3 with $F(a) = 1.0$ are also plotted in Fig. 5 for comparison. It is seen that the effects of loading conditions on elastic K values is negligible and that the cracked cruciform specimen behaves actually like an infinite sheet especially at positive biaxial loading conditions. It is even more important to note that the apparent deviations in K , for $a > 38.1$ mm (1.5 in.), were mainly due to the effect of specimen geometry rather than the effect of biaxial loading ratios. The hypothesis is substantiated by the fact that the K values for long cracks under negative σ_x loads were actually lower than those under positive σ_x loads. Comparing Figs. 4(a) and 4(b) to Figures 4(c) and 4(d) it is evident that the tension-compression loading cases exhibited more reductions in the σ_y stresses in the area near the rim.

It has been demonstrated by elastic analysis [17] that a crack will grow straight (stay on its initial path) under tension-compression biaxial stresses, but the crack will turn away from its initial path if the biaxial stress ratio is larger than unity, that is, if $\sigma_x > \sigma_y$ in tension. For a curved crack in a biaxial stress field, an approximate method used by Leever et al [12] can be used to compute K . Since their method of analysis primarily deals with an inclined crack (with respect to either σ_y or σ_x), it would be necessary to compute both the opening mode stress intensity K_1 , and the sliding mode crack tip stress intensity, K_2 . Therefore, their equation has been written as

$$K_1 = F_{1y}\sigma_y\sqrt{\pi a_y} + F_{1x}\sigma_x\sqrt{\pi a_x} \tag{5}$$

1 KSI $\sqrt{\text{INCH}} = 1.0988 \text{ MN(MI)}^{3/2}$, 1 INCH = 25.4 mm, 1 KSI = 6,890 kPa

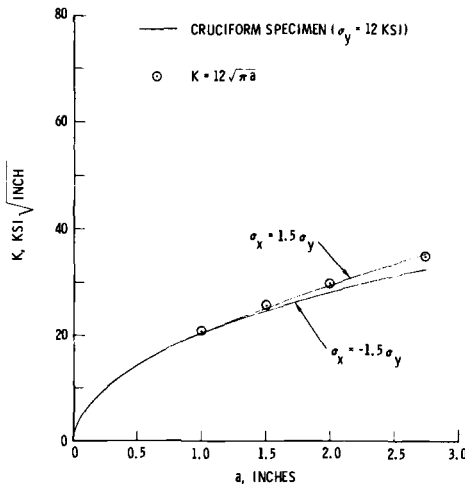


FIG. 5—Stress intensities for center through cracks in a cruciform specimen.

$$K_2 = F_{2y}\sigma_y\sqrt{\pi a_y} + F_{2x}\sigma_x\sqrt{\pi a_x} \quad (6)$$

where the factors F_{1y} , F_{1x} , F_{2y} and F_{2x} are given in the literature (Eqs 12 through 15 of Ref 12).

When Eqs 5 and 6 are used to correlate crack growth rate or residual strength test data, or both, it is necessary to adopt a failure criterion (or an equivalent K value) accounting for the combined effects of K_1 and K_2 at the crack tip. There are numerous failure criteria available in the literature, for example Refs 18, 19, and 20. In the present study, the following possibilities have been evaluated:

$$K = (K_1^2 + K_2^2)^{1/2} \quad (7)$$

based on Irwin's theory of fracture [18]; and

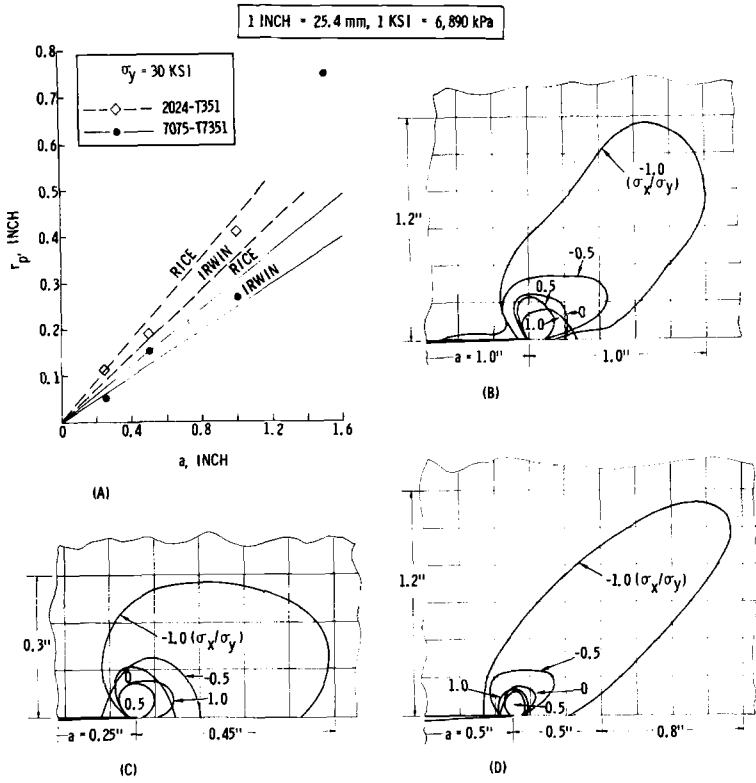
$$K = K_1 + K_2 \quad (8)$$

derived from experimental data on fracture testing of aluminum alloys and 4300 steel [8,21].

Crack Tip Plastic Zone Sizes

Using the NASTRAN computer program, elastic-plastic finite element analyses have been conducted to determine the crack tip plastic zone sizes in a biaxially loaded cruciform specimen. Finite element models similar to those shown in Fig. 2 were used. Plastic elements (not cracked) were placed around the crack. The crack tip elements were much smaller than those used in Fig. 2 having an area as small as 2.54 mm (0.1 in.) long by 0.9525 mm (0.0375 in.) tall of an isosceles triangle, depending on the crack size.

Plastic zone sizes for five loading cases ($\sigma_x/\sigma_y = 0, \pm 0.5$ and ± 1.0) at $\sigma_y = 206\ 700$ kPa (30 ksi) for both 7075-T7351 and 2024-T351 materials, at seven crack lengths ($a = 6.35, 17.7, 25.4$ and 38.1 mm for the 7075-T7351 and $a = 6.35, 17.7$ and 25.4 mm for the 2024-T351 specimens) have been determined. Typical results are shown in Fig. 6. The dimension for r_p is the largest distance between the crack tip and the border of the plastic zone. Also in Fig. 6(a) are the plastic zone sizes computed by using Eqs 9 and 31a of Ref 22; that is, $r_p = (K_{\max}/F_{ty})^2/\pi$ and $r_p = \pi (K_{\max}/F_{ty})^2/8$, respectively. These theoretical values are included here to provide some indication of the relative sizes of the crack tip plastic zone in the cruciform specimen.



(a) Plastic zone sizes for $\sigma_x = 0$.
 (b) 7075-T7351, $a = 1.0$ in.
 (c) 2024-T351, $a = 0.25$ in.
 (d) 2024-T351, $a = 0.5$ in.

FIG. 6—Crack tip plastic zone at 30 ksi.

Facts that can be observed from all the analytic plastic zone contour maps (including those not shown in Fig. 6) are listed in the following:

1. The plastic zone sizes for biaxial ratios of 0.5 and 1.0 are approximately the same and are insignificantly smaller than those for the uniaxial tension.
2. The plastic zone sizes for tension-compression biaxial ratios are significantly larger than those for the uniaxial and tension-tension biaxial conditions, the higher the tension-compression ratio, the larger plastic zone size.
3. Since the finite element value of r_p for 7075-T7351 at $a = 38.1$ mm (1.5 in.) is significantly larger than the theoretical value, it seems to indicate that the crack tip plastic zone size in the cruciform specimen is a nonlinear function of the crack length.

Experiments

A group of tests has been conducted to investigate the effects of biaxial stress ratio (σ_x/σ_y) and applied stress level (σ_y/F_{1y}) on fatigue crack growth rate behavior of 7075-T7351 and 2024-T351 aluminum alloys.

Tension coupons, center cracked panels (CCT), and cruciform specimens (CF) were fabricated from ten sheets of 7075-T351 and four sheets of 2024-T351 plate stocks. All the sheets of each material were from the same heat. The size of these commercial aluminum plates was 121.92 cm (4 ft) wide by 365.76 cm (12 ft) long by 17.7 mm (0.5 in.) thick. The specimens were cut from randomly selected areas in these aluminum plates. The testing conditions for the CCT specimens and the cruciform specimens are listed in Table 1. Descriptions of experimental procedures for each test type are given in the following.

Tension Tests

Thirty-six tension test coupons were machined from all 14 sheets of aluminum alloys. Specimen configuration was those specified in ASTM Tension Testing of Metallic Materials (E8-77a), with specimen thickness equal to 4.572 mm (0.18 in.). A 178 000 N (40 kip) MTS machine was used for conducting the tension tests.

Baseline Crack Growth Rate Tests

Both the CCT and the cruciform specimens were used to develop crack growth rate data for uniaxial loading conditions ($\sigma_x = 0$). All but two of the CCT specimens were tested in a 356 000 N (80 kip) MTS machine.⁴ The last two CCT specimens and the cruciform specimens were tested in the biaxial loading frame to ensure that compatible crack growth rate data will be developed from both the CCT and the cruciform specimens and to check out the loading characteristics of the newly built biaxial test unit through testing of the CCT specimens in both testing machines.

The size of the CCT specimens was 17.78 mm (7 in.) wide by 40.64 cm (16 in.) long, having the central portion tapered down from 17.7 mm (0.5 in.) to 4.572 mm (0.18 in.). The cruciform specimen configuration has been discussed in the previous section.

Since in some biaxial loading cases the crack might not grow perpendicular to the principal loading direction, it was desirable to measure the crack in both magnitude and direction. A photographic polar grid such as that shown in Fig. 1(b) was printed onto the very finely polished cruciform specimen surface. Tick marks were placed at every 15 deg around the circumferential grid line, and the spacing between grid lines was 1.27 mm (0.05 in.).

⁴ Manufactured by Material Testing Systems, Inc., Minneapolis, Minn.

TABLE 1—Test matrix.^a

Material	Test Case	σ_y , max	σ_y , min	σ_x , max	σ_x , min	f	Specimen Type	Grain Direction
7075-T7351	24	12	1.2	12.0	1.2	5	CF	LT
	26	12	1.2	-1.2	-12.0	5	CF	LT
	28	12	1.2	6.0	0.6	8	CF	LT
	29	12	1.2	-0.6	-6.0	5	CF	LT
	30	12	1.2	-0.6	-6.0	10	CF	LT
	141	12	1.2	15.0	1.5	5	CF	LT
	68	12	1.2	18.0	1.8	5	CF	LT
	142	12	1.2	21.0	2.1	5	CF	LT
	70	12	1.2	-1.8	-18.0	8	CF	LT
	133	18	1.8	18.0	1.8	5	CF	LT
	57	18	1.8	9.0	0.9	5	CF	LT
	58	18	1.8	-0.9	-9.0	5	CF	LT
	135	18	1.8	-0.9	-9.0	2	CF	LT
	139	30	3.0	15.0	1.5	2	CF	LT
	64	30	3.0	-1.5	-15.0	2	CF	LT
	1	6.0	0.6	0	0	5	CCT	LT
	2	10.0	1.0	0	0	5	CCT	LT
	123	4.8	0.48	0	0	10 ^c	CCT	LT
	7	12.0	1.2	0	0	5	CF	LT
	8	12.0	1.2	0	0	10	CF	LT
125	4.8	0.48	0	0	10 ^c	CCT	TL	
131 ^b	20.0	2.0	0	0	5	CCT	TL	
5	7.0	0.7	0	0	5	CCT	TL	
13	12.0	1.2	0	0	5	CF	TL	

TABLE I—Continued.

Material	Test Case	σ_p , max	σ_p , min	σ_x , max	σ_x , min	f	Specimen Type	Grain Direction	
2024-T351	134	10	1.0	10.0	1.0	5	CF	LT	
	34	10	1.0	-1.0	-10.0	5	CF	LT	
	35	10	1.0	5.0	0.5	10	CF	LT	
	36	10	1.0	5.0	0.5	5	CF	LT	
	37	10	1.0	-0.5	-5.0	10	CF	LT	
	38	10	1.0	-0.5	-5.0	5	CF	LT	
	32	12	1.2	12.0	1.2	5	CF	LT	
	136	15	1.5	7.5	0.75	2	CF	LT	
	61	15	1.5	7.5	0.75	5	CF	LT	
	62	15	1.5	-0.75	-7.5	5	CF	LT	
	65	25	2.5	12.5	1.25	2	CF	LT	
	140	25	2.5	-1.25	-12.5	2	CF	LT	
	138	30	3.0	15.0	1.5	2	CF	LT	
	137	30	3.0	-1.5	-15.0	2	CF	LT	
	3	10	1.0	1.0	0	0	5	CCT	LT
	4	6	0.6	0.6	0	0	5	CCT	LT
	9	10	1.0	1.0	0	0	5	CF	LT
10	10	1.0	1.0	0	0	10	CF	LT	
6	6	0.6	0.6	0	0	5	CCT	TL	
132 ^b	8	0.8	0.8	0	0	5	CCT	TL	
14	10	1.0	1.0	0	0	5	CF	TL	

^a All stress units are in ksi (1 ksi = 6890 kPa).

^b Tested in the biaxial loading machine.

^c 20 Hz for $da/dN < 10^{-6}$ in./cycle (0.0254 $\mu\text{m}/\text{cycle}$).

Both the CCT and the cruciform specimens were precracked from an initial electro discharge machining (EDM) slot, at the center of the specimen, to the desired initial flaw size (approximately 3.81 mm in total length). All specimens were precracked at test maximum load level by applying tension-tension load cycles normal to the EDM slot using the MTS machine or the biaxial loading frame, whichever is convenient. Crack length measurements were made at very small increments to obtain an adequate understanding of the crack growth behavior. For the cruciform specimens, testing was terminated when the crack growth rate was faster than $2.54 \mu\text{m}/\text{cycle}$ ($10^{-4} \text{ in.}/\text{cycle}$) or the crack had reached the border of the flat area.

The effect of cyclic frequencies was not the primary interest of this investigation. However, due to the nature of the biaxial loading tests, lower frequencies had to be used for testing at higher applied loads, whereas higher frequencies could be applied to lower load test cases. Therefore, as shown in Table 1, some test cases consisted of several replications, and each of them was run at a different cyclic frequency to ensure that test results would be consistent with the range of frequencies being applied.

Biaxial Crack Growth Rate Tests

Fifteen 7075-T7351 specimens and fourteen 2024-T351 specimens have been tested under various biaxial loading conditions ($-1.5 \leq \sigma_x/\sigma_y \leq 1.75$) at various applied stress levels ($0.2 \leq \sigma_y/F_{ty} \leq 0.6$).

A buckling guide was used in all the tension-compression biaxial ratio tests. The apparatus for preventing specimen buckling consisted of two square-shaped aluminum plates and two circular steel plates. The steel plates were inserted into the circular hole in the center of the aluminum plate. The test specimen was sandwiched in between the aluminum plates. The crack could be seen from an open slot 19.05 mm (0.75 in.) wide and 12.7 cm (5 in.) long in the center of the circular plate. The circular plate could be rotated to follow the crack growth direction.

The precracking and the crack growth rate recording procedures are the same as those described in the preceding paragraph.

Test Results

The average tensile yield strength (the 0.2 percent offset value) for the 7075-T7351 alloy was 412 022 kPa (59.8 ksi) for both the LT and TL directions. The average tensile yield strength for the 2024-T351 alloy was 367 237 kPa (53.3 ksi) for the LT direction and 319 007 kPa (46.3 ksi) for the TL direction. Engineering stress-strain curves were also obtained from each tensile test. One typical curve was selected from each alloy and it was used for conducting the elastic-plastic finite element analyses.

Stress intensities for cracks in the CCT specimens have been computed using Eqs 3 and 4. The crack growth rate versus ΔK plots for both aluminum alloys are presented in Fig. 7.

For the cruciform specimens, the test results indicated that the crack grew straight in all the tests with $\sigma_x \leq \sigma_y$. However, when σ_x exceeded σ_y , the crack turned away from its initial plane and finally ended up propagating in a direction perpendicular to σ_x (see the example shown in Fig. 1(b) for $\sigma_x = 1.5 \sigma_y$). Stress intensity values presented in Fig. 5 (adjusted by the actual σ_y in each test) were used to correlate the da/dN data for the straight cracks. The da/dN data for the curved cracks have been analyzed by using Eqs 7 and 8. Comparing the results, it was revealed that Eq 8, which defines the effective crack tip stress intensity as being the sum of the K values of Eqs 5 and 6, fits better with the experimental data.

Typical da/dN versus ΔK curves for the cruciform specimen tests are presented in Fig. 7. Examination of all the test results (including those not shown in Fig. 7) has revealed that all the crack growth rate curves are almost identical; that is, for the same material and cyclic stress amplitude, there is no effect on fatigue crack growth rate due to differing biaxial stress ratios. It is significant to note that the da/dN curves in Figs 7(c) and 7(f), for biaxial ratios of -0.5 and $+0.5$, respectively, are the composites of many sets of test data and each set of those data had been generated from different combinations of stress levels and cyclic frequencies. Five test technicians were involved at different times in collecting the crack length versus cycles records for all 45 tests. Even so, it is very evident that the crack growth rate behavior for all the tests has remained consistent.

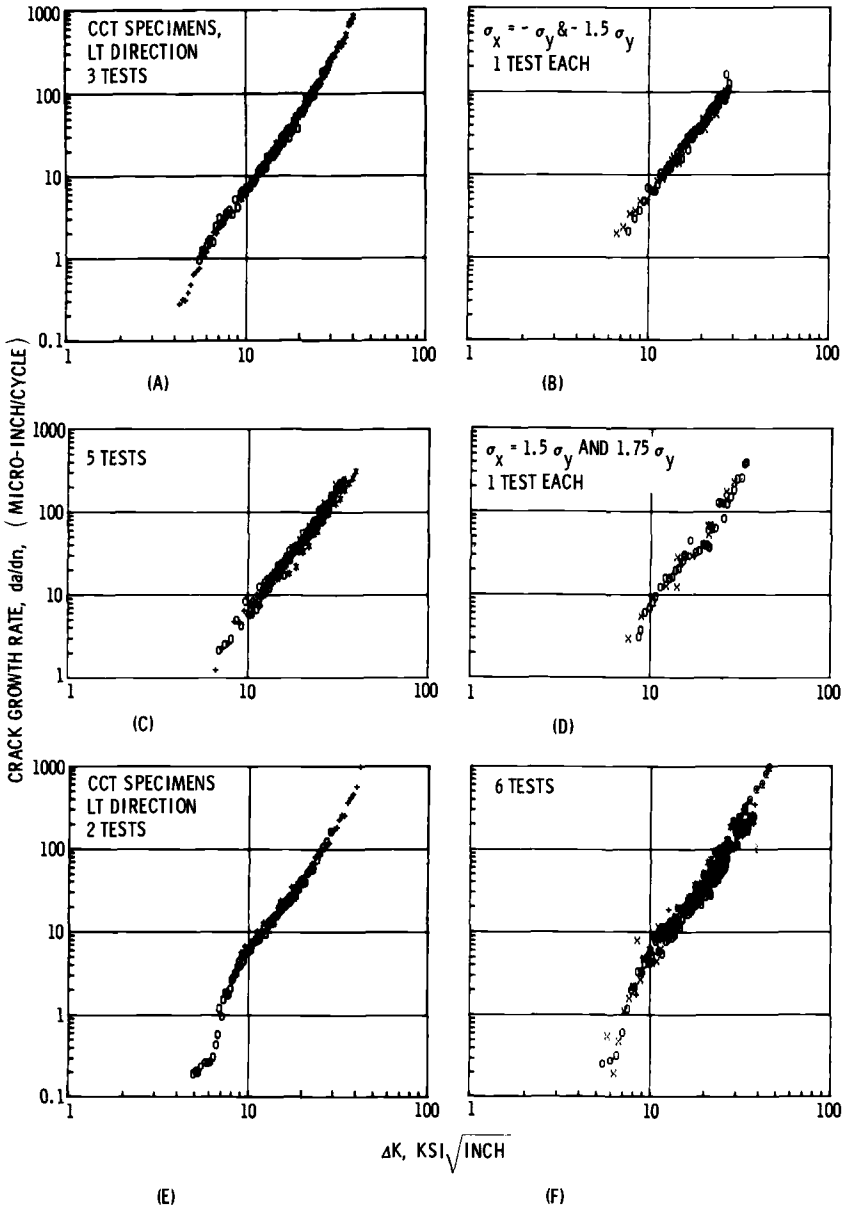
Summary

A series of experiments and analyses has been carried out on the cyclic crack growth behavior of center-cracked cruciform specimens under biaxial loading. The results may be summarized as follows:

1. For cracks perpendicular to σ_y , the effect of σ_x on constant amplitude crack growth rate is negligible.
2. Cracks will grow straight except for $\sigma_x > \sigma_y$.
3. Elastic K factors are obtainable for both straight and curved cracks and are adequate for correlating the biaxial da/dN data.
4. Analytical estimates of crack tip plastic zone size varies with biaxial ratio but experimentally this appeared to have no effect on constant amplitude crack growth rate.

Acknowledgment

This work was performed under contract to the United States Air Force Flight Dynamics Laboratory, Contract F33615-76-C-3121.



$$1 \text{ KSI} \sqrt{\text{INCH}} = 1.0988 \text{ MN(M)}^{3/2}, 1 \mu\text{-INCH} = 0.0254 \mu\text{m}$$

- (a) 7075-T7351, $\sigma_x = 0$
- (b) 7075-T7351, $\sigma_x \leq -\sigma_y$
- (c) 7075-T7351, $\sigma_x = -\sigma_y/2$
- (d) 7075-T7351, $\sigma_x > \sigma_y$
- (e) 2024-T351, $\sigma_x = 0$
- (f) 2024-T351, $\sigma_x = \sigma_y/2$

FIG. 7—Cyclic crack growth rate behavior of 7075-T7351 and 2024-T351 aluminum alloys.

References

- [1] Paris, P. C. and Sih, G. C. in *Fracture Toughness Testing and Its Applications*, ASTM STP 381, American Society for Testing and Materials, 1965, pp. 30–83.
- [2] Miller, K. J. and Kfoury, A. P. *International Journal of Fracture*, Vol. 10, No. 3, Sept. 1974, pp. 393–404.
- [3] Kfoury, A. P. and Miller, K. J., Paper No. MS294, 4th International Conference on Fracture, Waterloo, Canada, 19–24 June 1977.
- [4] Hilton, P. D., *International Journal of Fracture*, Vol. 9, No. 2, June 1973, pp. 149–156.
- [5] Smith, S. H. in *Prospects of Fracture Mechanics*, G. C. Sih, H. C. VanElst, and D. Broek, Eds., Noordhoff International Publishing, Leyden, The Netherlands, 1974, pp. 367–388.
- [6] Adams, N. J. I., *Engineering Fracture Mechanics*, Vol. 5, 1973, pp. 983–991.
- [7] Beck, E. J., "Fatigue Flaw Growth Behavior in Stiffened and Unstiffened Panels Loaded in Biaxial Tension," NASA Report CR-128904, National Aeronautics and Space Administration, Washington, D.C., Feb. 1973.
- [8] Liu, A. F., *AIAA Journal*, Vol. 12, No. 2, American Institute of Aeronautics and Astronautics, Feb. 1974, pp. 180–185.
- [9] Roberts, R. and Potheraj, S., Paper No. L8/3, 2nd International Conference on Structural Mechanics in Reactor Technology, Berlin, Germany, 10–14 Sept. 1973.
- [10] Kibler, J. J. and Roberts, R., *Journal of Engineering for Industry; Transactions*, American Society of Mechanical Engineers, Series B, Nov. 1970, pp. 727–734.
- [11] Pook, L. and Holmes, P., International Conference on Fatigue Testing and Design, London, England, 5–9 April 1976.
- [12] LeEVERS, P. S., Radon, J. C., and Culver, L. E., *Journal of Mechanics and Physics of Solids*, Vol. 24, 1976, pp. 381–395.
- [13] Radon, J. C., LeEVERS, P. S., and Culver, L. E., Paper No. MS47, 4th International Conference on Fracture, Waterloo, Canada, 19–24 June 1977.
- [14] Radon, J. C., LeEVERS, P. S., and Culver, L. E., *Experimental Mechanics*, Vol. 17, 1977, pp. 228–232.
- [15] Tada, H., Paris, P. C., and Irwin, G. R., *The Stress Analysis of Cracks Handbook*, Del Research Corporation, Hellertown, Pa., 1973, p. 2.2.
- [16] Tong, P., Pian, T. H. H., and Lasry, S., *International Journal of Numerical Mathematics in Engineering*, Vol. 7, 1973, pp. 297–308.
- [17] Cotterell, B., *International Journal of Fracture Mechanics*, Vol. 2, 1966, pp. 526–533.
- [18] Irwin, G. R. in *Treatise on Adhesives and Adhesion*, R. L. Patrick, Ed., Marcel Dekker, New York, 1966, pp. 233–267.
- [19] Erdogan, F. and Sih, G. C., *Journal of Basic Engineering; Transactions*, American Society of Mechanical Engineers, Series D, Vol. 85, 1963, pp. 519–527.
- [20] Sih, G. C. in *Mechanics of Fracture*, Volume 1, Methods of Analysis and Solutions of Crack Problems, G. C. Sih, Ed., Noordhoff International Publishing, Leyden, The Netherlands, 1973, pp. XXI–XLV (Introductory Chapter).
- [21] Shah, R. C. in *Fracture Analysis*, ASTM STP 560, American Society for Testing and Materials, 1974, pp. 29–52.
- [22] Rice, J. R. in *Fatigue Crack Propagation*, ASTM STP 415, American Society for Testing and Materials, 1967, pp. 247–311.

Fatigue Crack Growth Threshold in Mild Steel Under Combined Loading

REFERENCE: Pook, L. P. and Greenan, A. F., "Fatigue Crack Growth Threshold in Mild Steel Under Combined Loading," *Fracture Mechanics, ASTM STP 677*, C. W. Smith, Ed., American Society for Testing and Materials, 1979, pp. 23–35.

ABSTRACT: Conventional specimens used to determine fatigue crack growth behavior have the initial crack oriented in such a way that only Mode I displacements are present. The fatigue-crack growth threshold behavior of mild steel in the presence of Mode II displacements was investigated by considering the fatigue behavior of spot-welded joints, where both Modes I and II are present at the point of failure, and by some experiments using specimens designed to give pure Mode II displacements.

It was found that the threshold behavior is controlled by the ease with which a Mode I branch crack forms at the tip of the initial crack. If such a branch forms easily, threshold behavior is controlled by ΔK_I for the branch crack, whereas, if branch formation is difficult, threshold behavior is controlled by ΔK_I for the initial crack. Branch crack formation seems to be facilitated by the unwanted Mode III displacements which appear when the initial crack tip is curved. For the special case of nominally pure Mode II displacements, failure takes place away from the initial crack front if this is straight, and threshold behavior is determined by other factors.

KEY WORDS: fatigue (materials), stress cycling, fatigue tests, mild steel, crack propagation, crack initiation, combined loading

Nomenclature

- a' Uncracked ligament (Fig. 4)
- a_0 Pre-crack length
- E Young's modulus
- K Stress intensity factor, subscripts I, II, and III denote mode
- K_{I*} Maximum value of K_I for branch crack
- ΔK Range of K in fatigue cycle, subscripts, I, II, and III denote mode
- ΔK_{Ic} Critical value of ΔK_I for fatigue crack growth

¹ Senior principal scientific officer and higher scientific officer, respectively, National Engineering Laboratory, Glasgow, Scotland.

- ΔK_{IIc} Critical value of ΔK_{II} for fatigue crack growth
 P Load (Figs. 4 and 7)
 r Distance from crack tip
 u Crack surface displacement
 W Specimen width (Fig. 4)
 θ Angle between branch crack direction and main crack direction
 σ Stress

Fatigue cracks grow perpendicular to the maximum principal applied tensile stress, or put more precisely into fracture mechanics terms, in the opening mode (Mode I, Fig. 1). Like most generalizations this one has its exceptions [1-3],² but it does mean [1-5] that fatigue-crack growth data can be analyzed conveniently in terms of the range of Mode I stress intensity factor, ΔK_I . A threshold value of ΔK_I , ΔK_{Ic} must be exceeded before a crack will grow [1,3-5].

Various techniques can be used to determine ΔK_{Ic} ; usually they all give essentially the same result [6]. However, as with the plain specimen fatigue limit, a threshold is not necessarily defined clearly, so the precise formal definition employed can affect the numerical values obtained. National Engineering Laboratory (NEL) practice is to determine an S/N curve for cracked specimens, with endurance plotted against the initial values of ΔK_I , and to take the threshold as the fatigue limit of this S/N curve. This method does not always give values of ΔK_{Ic} which are independent of initial crack size. For some materials low values are obtained at very short initial crack sizes [5]. However, provided the initial crack is sufficiently long, an "upper shelf" value is obtained; this upper shelf value is discussed in detail in Ref 3.

Conventional specimens used to determine fatigue-crack growth behavior have the initial crack oriented perpendicular to the applied stress. A crack-like flaw from which a fatigue failure originates will not be so oriented necessarily, and crack growth, in general, will not be in the plane of the initial crack. Definition of threshold behavior in terms of the fatigue limit of cracked specimens extends naturally to such combined mode situations; for example, ΔK_{IIc} may be defined as the critical value of ΔK_{II} , the range of the edge sliding Mode (Mode II, Fig. 1) stress intensity factor, K_{II} , necessary to cause crack growth which leads to failure, even though crack growth is not in the plane of the initial crack. It has been pointed out recently [7] that, for nominally pure Mode II loading, fatigue crack growth threshold behavior depends on the ease with which a Mode I branch crack forms at the tip of the initial crack. This paper gives the experimental evidence on which this conclusion was based, together with the results of some further tests designed to test its validity. Threshold

² The italic numbers in brackets refer to the list of references appended to this paper.

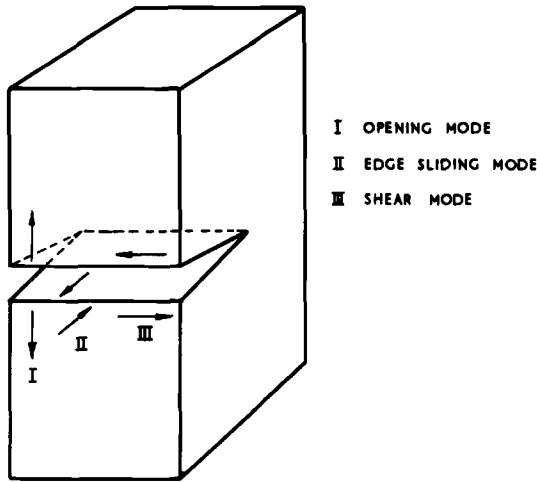


FIG. 1—Basic modes of crack surface displacement.

behavior for combined Mode I/II loading is examined by considering the fatigue behavior of spot-welded joints, and discussed in the light of some recently published Mode I/II threshold data for mild steel [8]. Attention is confined to cases where behavior is essentially elastic, that is, the average net section stress is less than 80 percent of the yield stress [5].

Theoretical Background

In the absence of Mode III deformations there are two plausible approaches to the estimation of combined mode threshold behavior; experimental data can be found to support either. The simpler approach is to assume that the value of ΔK_{II} can have no effect on the value of ΔK_{Ic} on the grounds that Mode II fatigue-crack growth cannot occur [9] by the accepted mechanism for fatigue-crack growth, and also because elastic theory indicates [3] that the addition of Mode II displacement has no effect on the profile of a Mode I crack, although it does displace the profile within the cracked body. This approach implies that a pure Mode II crack cannot cause fatigue failure: in other words, there is no Mode II threshold.

The alternative approach is to postulate that a branch forms at the tip of the initial (main) crack in the direction so that K_{II} for the branch crack has its maximum value of K_I^* and $K_{II} \rightarrow 0$. A number of criteria have been suggested for the determination of this direction; a recent survey [10] pointed out the preferred direction is not well defined. Some information [11] suggests that this initial direction is given approximately by

$$K_I \sin \theta = K_{II} (3 \cos \theta - 1) \quad (1)$$

where θ is measured from the original crack direction. Negative values of K_I are not permitted and the root required lies in the range of ± 70.5 deg If Mode III displacements are present, the problem becomes three-dimensional and is further complicated because a preferred plane of crack growth will, in general, only intersect the initial crack front at one point.

This approach implies that threshold behavior is controlled then by the value of K_I^* , so predictions require values of K_I and K_{II} for the main crack in terms of K_I^* . Figure 2 shows values based on numerical data for small but finite branch cracks presented graphically in Ref. 12; this is interpreted most usefully as a failure envelope for branch crack growth under combined Mode I/Mode II loading. For pure Mode II, K_I^* is about 25 percent greater than K_{II} for the main crack, implying that ΔK_{IIc} should be about $0.8\Delta K_{Ic}$. For $K_I = K_{II}$, K_I for the main crack is only about 55 percent of K_I^* , which implies that ΔK_{Ic} should be reduced similarly.

One problem that affects any form of combined mode testing is that, in Mode I, variations from the ideal initial crack shape lead merely to some uncertainty in the value of K_I , whereas in the combined mode situation such variations can introduce unwanted deformation modes. For example, in a specimen intended to give pure Mode II, crack front curvature

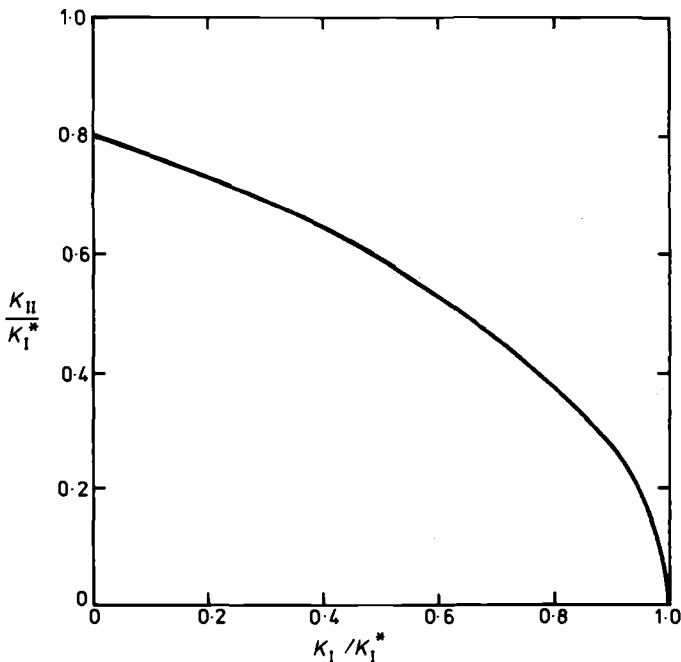
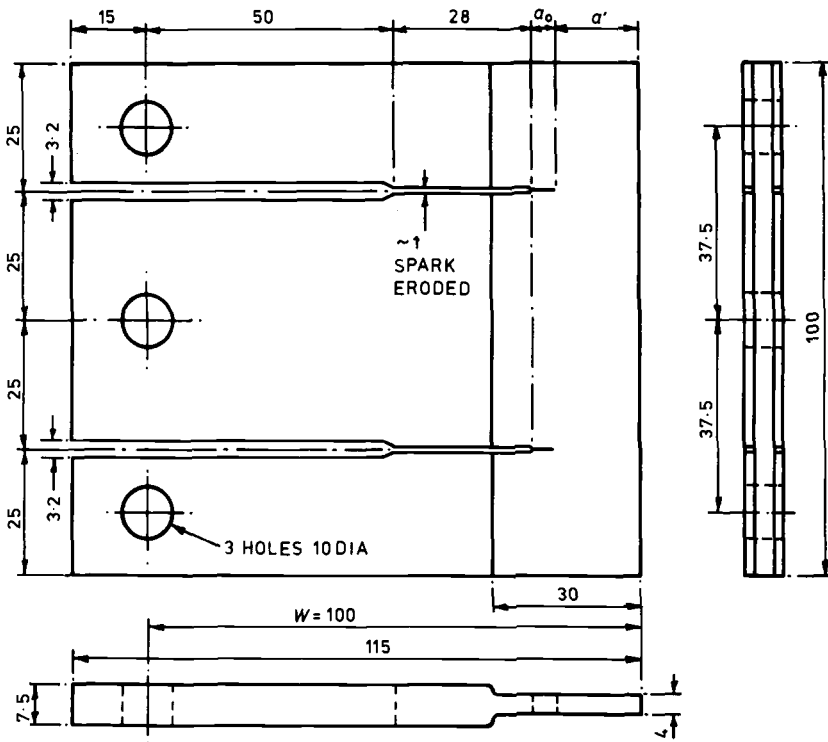


FIG. 2.—Failure envelope for branch crack growth under combined Mode I/II loading.

introduces unwanted Mode III displacements. Because of the complicated three-dimensional situation, it usually is not practicable to obtain accurate numerical values for the stress intensity factors involved.

Determination of Mode II Threshold Using Precracked Specimens

The tests were carried out on mild steel at room temperature in air. The mechanical properties of the En 3 mild steel used (test mark MFLW) had a tensile strength of 465 MN/m² and a 0.2 percent proof stress of 330 MN/m². The specimen design used, based on that developed by Jones and Chisholm [13] and shown in Fig. 3, is similar to that used previously [3] but with the thickness away from the crack tips increased to improve transverse stiffness and prevent loading hole failure. The slits were spark-eroded, with a width of about 1 mm. The test technique was similar to that previously used at NEL to determine threshold data [1,3-5], and fuller details are given in Ref 14. Cracks were grown in Mode I from each initial slit by loading in tension between the central hole and an outer hole. After stress relief in vacuum for 1 h at 650°C, the precracked plates were



ALL DIMENSIONS IN mm

FIG. 3—Mode II test specimen.

tested at various load levels, with a mean to alternating load ratio of about 1.1 (the same as in Ref 3), using the loading method shown in Fig. 4. The results obtained are shown in Table 1.

Values of ΔK_{II} were calculated from the data [3] shown in Fig. 4. Specimens failed only at the precrack having the shorter uncracked ligament, a' , and hence higher ΔK_{II} . Specimens which were unbroken after a large number of cycles were retested at a higher load; data given refer to the precrack at which failure eventually took place. To ensure that conditions were essentially elastic, the average shear stress on the uncracked ligament, at maximum load, was checked and was found to be less than 80 percent of the shear yield stress, which was taken as half the 0.2 percent proof stress.

The asymmetrical situation during precracking tended to cause the precrack to deviate from the desired path; deviation was not necessarily the same on both sides of a specimen, leading to a twisted precrack. The two angles quoted in Table 1 are for opposite sides of the specimen, are conventionally positive when deviation is towards the outer edge, and were taken in the vicinity of the precrack tip. Deviations quoted [3] for the previous tests were for an average over the precrack length. The precrack fronts were all curved to some extent; the two distances shown under curvature in Table 1 are the amounts by which the precrack front trailed at the two specimen surfaces.

The majority of the specimens failed at the precrack tip (tip failure); the remainder failed at the end of the spark-eroded slit (slit failure). The specimens for the earlier tests generally had longer precracks, and many failures were caused by fretting fatigue 2 or 3 mm away from the precrack tip. The test results for the two series are combined in Fig. 5.

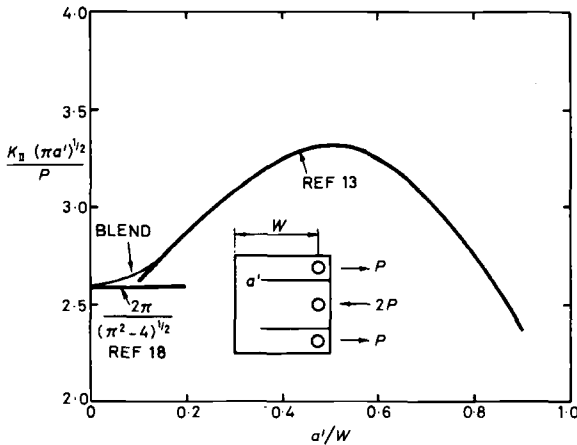


FIG. 4—Stress intensity factors for Mode II test specimen.

TABLE 1—Test results, precracked specimens.

Specimen No.	Precrack Length a_0 , mm	Uncracked Ligament a , mm	Precrack curvature (See Text), mm	Precrack deviation (See Text), deg	ΔK_{II} , MN/m ^{3/2}	Endurance, cycles	Failure Site	Crack Growth Angle θ , deg
MFLW 3 ^a	2.9	14.1	0.4	-5	16.5	3.74×10^5	end of slit	III defined
8 ^b	2.8	14.2	0.25	-1	16.3	1.34×10^6	end of slit	III defined
12	4.4	12.3	0.1	1	14.9	9.20×10^5	precrack tip	77
2	3.1	13.7	0.25	4	13.2	2.54×10^6	end of slit	III defined
8 ^a	2.8	14.2	0.25	-1	13.0	1.83×10^7 U ^c
1	5.5	11.4	0.1	0	12.8	2.89×10^6	precrack tip corner	72
11	4.8	12.3	0.4	1	11.6	1.96×10^6	precrack tip corner	73
3	2.9	14.1	0.4	-5	10.8	8.36×10^7 U ^c
2	3.1	13.7	0.25	4	10.3	8.48×10^7 U ^c
5	2.4	14.6	0.25	0	10.1	2.19×10^6	end of slit	III defined
10	3.3	13.4	0.35	2	9.3	1.30×10^6	precrack tip	70
15 ^a	2.5	14.5	0.1	3	9.1	3.62×10^6	end of slit	80
13	2.3	14.7	0.6	1	9.1	1.16×10^6	precrack tip	III defined
7	3.1	14.2	0.2	0	9.1	2.01×10^6	precrack tip	75
8	2.8	15.2	0.25	-1	8.7	9.50×10^7 U ^c
9	3.1	14.4	0.4	5	8.2	2.26×10^7	precrack tip	70
14	2.5	14.9	0.2	3	8.1	3.56×10^6	precrack tip	III defined
4	2.9	14.7	0.95	10	7.3	1.00×10^8 U ^c
15	2.5	14.5	0.1	3	6.8	4.32×10^7 U ^c

^a Previously tested at lower load.

^b Previously tested at two lower loads.

^c U = unbroken

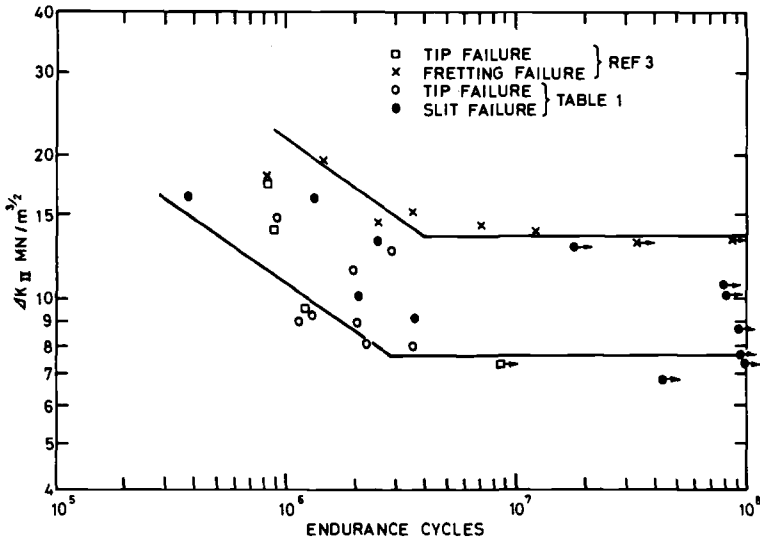


FIG. 5—Test results, precracked specimens.

Symbols for specimens which did not fail and were retested at higher load refer to the eventual failure type. Results are plotted in terms of the initial value of ΔK_{II} for the precrack where failure took place.

The results show that precrack tip failure usually requires the lowest level of ΔK_{II} and is therefore the expected type of failure. These failures define a threshold, ΔK_{IIc} , of about $7.6 \text{ MN/m}^{3/2}$, which is a little higher than the corresponding value [3] of ΔK_{Ic} ($6.6 \text{ MN/m}^{3/2}$). Other types of failure require higher load levels, and therefore only occur if for some reason tip failure is suppressed. For the present tests the alternative is slit failure; not surprisingly there is considerable scatter, both because the slit tip shape was not controlled and there are variations in precrack length. For the previous similar tests [3] the precrack length was generally much greater, so the slit tips were in a less highly stressed region and fretting failures occurred at still higher load levels. The fretting failure results define an apparent threshold of about $13.6 \text{ MN/m}^{3/2}$.

In all cases crack growth was at an angle of roughly 70 deg to the precrack, as predicted by Eq 1, which is consistent with the view that crack growth was in Mode I, although scatter is too great for firm conclusions to be drawn. The curved precrack fronts meant that crack growth was initially on a curved plane, which made it difficult to define the subsequent crack direction.

A straightforward explanation would be that tip failure occurs when a Mode I branch crack forms easily. However, ΔK_{IIc} is somewhat higher

than the predicted value of $0.8\Delta K_{Ic}$, possibly because the curved precrack fronts mean that K_I^* is overestimated by the two-dimensional theory used.

Discussion

Examination of the precrack front-shape data (Table 1) suggests that there is a broad correlation between precrack front shape and failure type. Tip failure only occurs when precrack curvature, defined as the difference between maximum and minimum crack length divided by specimen thickness, is about 0.1 or greater. Curvature introduces unwanted Mode III displacements, which suggests that these are needed for tip failure to occur. Precrack twist and deviation, which introduce unwanted Mode I displacements, have comparatively little effect. The most likely explanation for the effect of precrack curvature is that a Mode I branch crack forms when the ratio $\Delta K_{III}/K_{II}$ exceeds some critical value, which is equivalent to crack curvature exceeding a critical value.

The precrack tip curvature in the previous Mode II tests [3] was around 0.1 for all specimens, but it is suspected that other factors, possibly inadequate stress relief after precracking, controlled the failure type. The mechanism of the fretting failures is obscure. The average stress was far too low to cause fretting fatigue so it is pertinent to investigate stresses and displacements in regions where failure occurred, typically 2 to 3 mm from the precrack tip. From elastic theory [15] the tensile stress along the crack face is given by

$$\sigma = K_{II} (2/\pi r)^{\frac{1}{2}} \quad (2)$$

where r is distance from the crack tip, and the displacement is given by

$$u = \frac{2K_{II}}{E} \left(\frac{2r}{\pi} \right)^{\frac{1}{2}} \quad (3)$$

where E is Young's modulus. Mode II is antisymmetric, so the signs of σ and u are reversed on the opposite face. In practice, crack tip plasticity will modify the values of σ and u . However, substituting $K_{II} = 13.6 \text{ MN/m}^{3/2}$, $r = 2.5 \text{ mm}$, and $E = 2 \times 10^5 \text{ MN/m}^2$ gives $\sigma = 217 \text{ MN/m}^2$ and relative displacement (slip amplitude) $2u = 0.01 \text{ mm}$. This slip amplitude is about the optimum [1] to produce the lowest fretting fatigue strength, which would explain why failure took place around 2 to 3 mm from the precrack tip, and a stress range of 217 MN/m^2 is of the right order for the fretting fatigue limit of mild steel [1]. Crack tip plasticity effects make these calculations suggestive rather than conclusive.

It is evident, at least for some situations, that combined mode fatigue-

crack growth threshold behavior depends on two separate factors—first, whether or not a Mode I branch crack forms at or near the precrack tip under the loading being applied, and, second, whether the loading is sufficient to cause continued crack growth from the branch. The existence of two separate criteria accounts for the apparently contradictory experimental results. High precrack tip curvature, which introduces unwanted Mode III deformations, appears to facilitate the formation of a branch crack at a low value of ΔK_{II} . As the curvature is reduced, higher values of ΔK_{II} are needed for branch crack formation, and, if the curvature is below a critical amount, the site of failure moves away from the crack tip, scatter increases, and high apparent ΔK_{IIc} values may be observed.

Tests on Uncracked Mode II Specimens

In an attempt to verify the aforementioned explanation, some further tests were carried out using the specimen design shown in Fig. 3. Instead of precracking (the test technique was otherwise exactly as before), the 1 mm wide spark-eroded slits were terminated with a 20 deg included angle, with a tip radius of approximately 0.02 mm. Therefore, they could be regarded as equivalent to a crack as far as the calculation of stress intensity factors is concerned. The nominal remaining ligament size was 17 mm, and specimens were stress relieved prior to testing. It was argued that because spark erosion introduces randomly oriented cracks, these specimens could be regarded as containing Mode I branch cracks at the main "crack" tips, and would therefore be expected to behave as specimens in which a Mode I branch forms very easily.

The results obtained are shown in Table 2 and Fig. 6. Specimens failed

TABLE 2—Test results, uncracked specimens.

Specimen No.	Remaining Ligament, a' , mm	ΔK_{II} , MN/m ^{3/2}	Endurance, cycles	Crack Growth Angle θ , deg
MFLW 20 ^a	16.8	11.0	7.70×10^5	78
23 ^a	17.0	9.9	1.02×10^6	80
27 ^a	16.8	8.3	1.45×10^6	79
26	16.9	8.2	2.42×10^6	78
25	16.8	8.0	2.04×10^6	78
22	16.9	7.3	1.81×10^6	78
20	16.8	7.1	4.62×10^7 U ^b	...
23	17.0	7.1	6.47×10^7 U ^b	...
28	16.9	6.9	2.16×10^6	75
27	16.8	6.2	6.15×10^7 U ^b	...

^a Previously tested at lower load.

^b U = unbroken

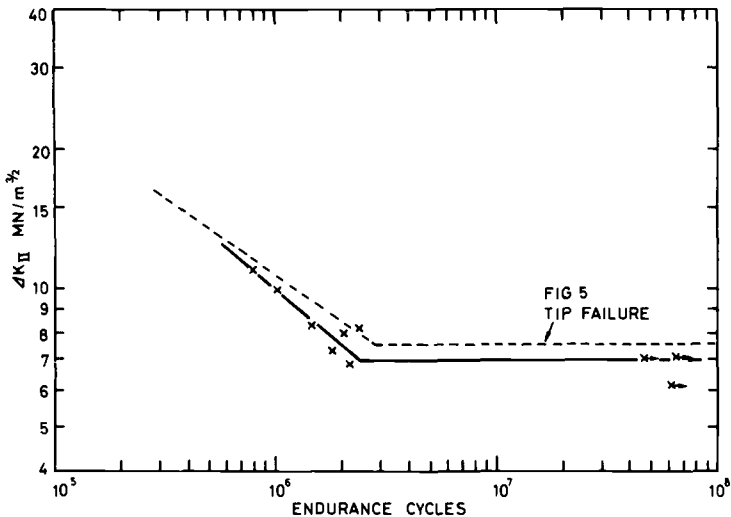


FIG. 6—Test results, uncracked specimens.

consistently at the same side of the test machine, indicating that there must have been some slight misalignment, despite the care taken in manufacture and alignment of the fixture used. It is possible that some of the scatter in the results for the precracked specimens, which failed consistently at the side having the shorter uncracked ligament, could have been due to this slight misalignment.

The results obtained are consistent with the arguments; they indicate a ΔK_{IIc} of 7.0 MN/m^{3/2}, close to the value of ΔK_{Ic} , slightly lower than the value obtained from the precracked tip failure specimens, but still above the theoretical value of $0.8\Delta K_{Ic}$. However, although the spark-eroded slit has a straight front so that two-dimensional theory can be used, the randomly occurring crack at which growth occurs may not be oriented ideally, and growth is from a tip with a finite radius rather than a sharp crack so that ΔK_1^* may have been overestimated again.

Threshold Behavior Under Combined Mode I/II Loading

As already pointed out a flaw from which a fatigue failure originates will not necessarily be perpendicular to the applied stress. It may be oriented such that Mode II or Mode III displacements, or both, are present. For practical calculations involving the fatigue-crack growth threshold, it has been NEL practice [3] to take the resolved stress perpendicular to the flaw for internal flaws and the resolved length perpendicular to the surface for surface flaws; this gives a reasonable estimate of K_1 for flaws inclined such that Mode I and II displacements are present. In either case it was

implicitly assumed that ΔK_I alone controlled threshold behavior. This assumption was without experimental justification, although it did not cause difficulties in practice.

For example, re-analysis [16] of some fatigue results under zero to tension loading, for steel spot-welded joints, where $\Delta K_I \approx \Delta K_{II}$ at the failure site (A in Fig. 7), showed that ΔK_I at the fatigue limit was equal to ΔK_{Ic} for the material. However, for a spot-weld, there are no Mode III deformations at the failure site [17]; there is therefore no mechanism by which a Mode I branch crack can form, so that it is not surprising that threshold behavior, and hence the fatigue limit, was controlled by ΔK_I .

By contrast, Otsuka, Mori, and Miyata [8] obtained a failure envelope similar to that in Fig. 2 by using an equivalent criterion, and supported it by an extensive series of tests on mild steel. As predicted, Mode II displacements had a substantial effect on the threshold (defined as complete failure), and in particular $\Delta K_{IIc} \approx \Delta K_{Ic}$. They did not give details of precrack front shape of their specimens, but they did obtain fractographic evidence of limited amounts of fatigue-crack growth at stress intensity factor values well below those needed for continued crack growth. The implication is that their precrack fronts were curved sufficiently for the critical value of ΔK_{III} for branch crack formation to be exceeded.

Conclusions

The fatigue-crack growth threshold behavior of mild steel in the presence of Mode II deformations depends on the ease with which a Mode I branch forms at the tip of the main crack. If such a branch forms easily, or is already present, threshold behavior is controlled by ΔK_I for the

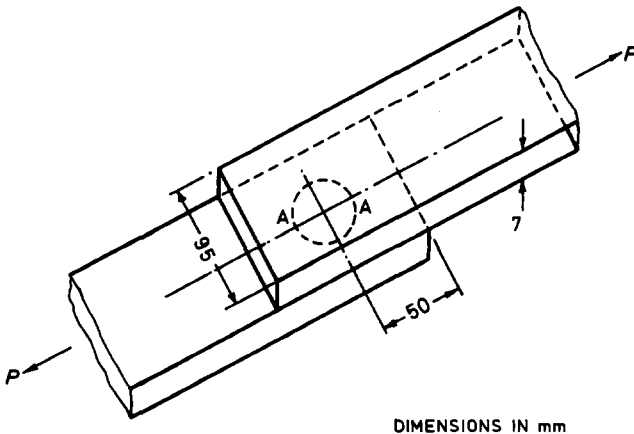


FIG. 7—Typical spot weld.

branch crack. If branch crack formation is suppressed, higher apparent threshold values are obtained and threshold behavior is controlled by ΔK_I for the main crack; for pure Mode II displacements, failure takes place away from the main crack tip.

Branch crack formation appears to be facilitated by the presence of Mode III displacements. Such displacements can occur in nominally Mode I and II combined loading, and nominally pure Mode II loading, if the main crack front is curved. For nominally pure Mode II displacements, it was found that threshold behavior could be correlated with the curvature of the main crack front.

Acknowledgment

This paper is presented by permission of the Director, National Engineering Laboratory, Department of Industry. It is British Crown copyright reserved.

References

- [1] Frost, N. E., Marsh, K. J., and Pook, L. P., *Metal Fatigue*, Clarendon Press, Oxford, England, 1974.
- [2] Pook, L. P., *Metal Science*, Vol. 10, No. 9, 1976, pp. 334–335.
- [3] Pook, L. P. and Greenan, A. F., in *Proceedings, Fatigue Testing and Design Conference*, Society of Environmental Engineers, London, Vol. 2, 1976, pp. 30.1–30.3.
- [4] Pook, L. P., *Journal of Strain Analysis*, Vol. 10, No. 4, 1975, pp. 242–250, 264.
- [5] Frost, N. E., Pook, L. P., and Denton, K. in *Engineering Fracture Mechanics*, Vol. 3, No. 2, 1971, pp. 109–126.
- [6] Jerram, K. and Priddle, E. K., *Journal of Mechanical Engineering Science*, Vol. 15, No. 4, 1973, pp. 271–273.
- [7] Pook, L. P., *International Journal of Fracture*, Vol. 13, No. 6, 1977, pp. 867–869.
- [8] Otsuka, A., Mori, K., and Miyata, T. in *Engineering Fracture Mechanics*, Vol. 7, No. 3, 1975, pp. 429–439.
- [9] Pook, L. P. and Frost, N. E., *International Journal of Fracture*, Vol. 9, No. 1, 1973, pp. 53–61.
- [10] Swedlow, J. L. in *Cracks and Fracture, ASTM STP 601*, American Society for Testing and Materials, 1976, pp. 506–521.
- [11] Sih, G. C. and Cha, B. C. K. in *Engineering Fracture Mechanics*, Vol. 6, No. 4, 1976, pp. 699–723.
- [12] Chatterjee, S. N., *International Journal of Solids and Structures*, Vol. 11, No. 5, 1975, pp. 521–538.
- [13] Jones, D. L. and Chisholm, D. B. in *Engineering Fracture Mechanics*, Vol. 7, No. 2, 1975, pp. 261–276.
- [14] Pook, L. P. and Greenan, A. F., “The Mode II Fatigue-Crack Growth Threshold in Mild Steel,” NEL Report No. 654, National Engineering Laboratory, Glasgow, 1978.
- [15] Paris, P. C. and Sih, G. C. in *Fracture Toughness Testing, ASTM STP 381*, American Society for Testing and Materials, 1965, pp. 30–83.
- [16] Pook, L. P., *International Journal of Fracture*, Vol. 11, No. 1, 1975, pp. 173–176.
- [17] Pook, L. P., “Approximate Stress Intensity Factors for Spot and Similar Welds,” NEL Report No. 588, National Engineering Laboratory, Glasgow, 1975.
- [18] Tada, H., Paris, P. C., and Irwin, G. R., *The Stress Analysis of Cracks Handbook*, Del Research Corporation, Hellertown, Pa., 1973.

H. Nowack¹, K. H. Trautmann¹, K. Schulte¹, and
G. Lütjering²

Sequence Effects on Fatigue Crack Propagation; Mechanical and Microstructural Contributions

REFERENCE: Nowack, H., Trautmann, K. H., Schulte, K., and Lütjering, G., "Sequence Effects on Fatigue Crack Propagation; Mechanical and Microstructural Contributions," *Fracture Mechanics, ASTM STP 677*, C. W. Smith, Ed., American Society for Testing and Materials, 1979, pp. 36–53.

ABSTRACT: The fatigue crack propagation of high strength aluminum alloys subjected to variable amplitude loading is strongly influenced by sequence effects. For a reliable evaluation of the sequence effects, an exact knowledge of the changes in the mechanical and physical conditions of the material surrounding the crack becomes necessary. To allow greater understanding of these processes, two aspects which are based on recent crack propagation investigations are considered in the present study.

First, a verification of a new detailed stress and displacement analysis based on continuum mechanics is attempted by displacement measurements using a special grid technique. The experimental results coincide well with the analysis predictions. That means, that the mechanical processes are a predominant cause of the sequence effects.

Secondly, a systematic variation of the microstructural crack propagation mechanism of aluminum alloys is used for an evaluation of the influence of the microstructural mechanisms on the sequence effects. The results show that there is an essential influence, which can lead to significant deviations in the crack propagation behavior from that as predicted by continuum mechanics.

KEY WORDS: fatigue (materials), crack propagation, sequence effects, displacements (deformations), crack closure, microstructural crack propagation mechanism, aluminum alloys

¹ Department head and research fellows, respectively, Deutsche Forschungs-und Versuchsanstalt für Luft- und Raumfahrt, DFVLR, Institut für Werkstoff-Forschung, Köln, West Germany.

² Professor, Ruhr-Universität Bochum, Institute for Materials, Bochum, West Germany.

Nomenclature

a	Instantaneous crack length
a^*	Crack length, where sequence effects occur (see Fig. 11)
Δa_i	Crack growth per cycle
da/dN	Crack propagation rate
$(da/dN)_{\min}$	Minimum crack propagation rate
C	Constant
E	Young's modulus
k	Exponent
K_{\max}	Maximum stress intensity in a cycle
K_{\min}	Minimum stress intensity in a cycle
ΔK	Stress intensity range in a cycle ($\Delta K = K_{\max} - K_{\min}$)
l_y	Grid spacing, deformed
l_{oy}	Spacing of the completely undeformed grid
N	Cycle number
N_D	Number of cycles with retardation
R	Stress ratio
$r_{K_{\max}}$	Extension of the K_{\max} plastic zone on the x -axis
$r_{\Delta K}$	Extension of the reversed plastic zone
t	Time
v	Displacement in the Y -direction
Δv_i	Variation of displacement per cycle
v_o	Displacements along the crack line (see Fig. 3b)
W	Stretched zone width due to an increase in load
x	X -direction
y	Y -direction
ϵ_F	True fracture strain
ϵ_y	Deformation in the Y -direction
ϵ_{ys}	Yield strain
σ_F	True fracture stress
σ_{ys}	Yield strength

Until now predictions of the crack extension under random loading are performed mainly using linear cumulative damage hypotheses or empirical factors. The application of these prediction methods can only provide satisfactory degrees in reliability if their range in application is already known from previous investigations with the same or quite similar specimens and loading histories. Realistic crack growth predictions still remain difficult because development of the essential mechanisms and the

influencing factors of the cycle by cycle crack extension under variable amplitude loading is still incomplete, although much research work has been done, especially during the past decade [1].³

To allow greater insight into the crack propagation mechanisms and the sequence effects under variable amplitude loading, two new aspects are considered which trace back on the results of quite recent investigations:

- Führung and Seeger recently published a continuum mechanics analysis based on the Dugdale-Barenblatt-Model [2,3], which overcomes several limitations of previous proposals [4,5]. Since this analysis gives a detailed insight into the stress and displacement variations for every consecutive half-cycle, it is not only well suited to the general understanding of the mechanical influences on crack propagation, but also it serves as a suitable basis for quantitative crack propagation predictions for engineering purposes. The experimental verification of the analysis in the present study shows the capability of this treatment, but also—in more general terms—the possibilities offered by continuum mechanics analyses to evaluate sequence effects.
- An evaluation of the influences of the microscopical crack propagation mechanism on the da/dN rates after load variations is possible, if high strength aluminum alloys of the 2000 type (technical alloy 2024-T3) and of the 7000 series (technical alloys 7075, 7475, and the laboratory alloy X-7075) are used [6]. Due to special heat treatments, different but well defined crack propagation mechanisms can be achieved. In this study the loading conditions in the tests were varied in such a way that changes in the crack propagation mechanism could occur.

An essential basis for systematic crack propagation investigations with variable amplitude loading is the choice of suitable loading histories so that no complicated superposition of crack accelerating or decelerating sequence effects occurs [7]. In the present study three types of loading histories were chosen: constant amplitude loading with an increase in mean stress, with a decrease in mean stress, and with a single peak overload inserted.

The crack propagation measurements were made by light microscopy (magnification $\times 100$) with an accuracy of one hundredth of a millimetre. In order to minimize possible errors due to a curvature of the crack front, specimens of 1 mm thickness were chosen. Striation measurements on the fracture surfaces were performed by scanning electron microscopy (SEM) to verify the surface measurements. The standard width of the center cracked specimens was 80 mm. In order to enable more accurate displacement analyses the specimen width was increased to 320 mm for these test series.

³ The italic numbers in brackets refer to the list of references appended to this paper.

Figure 1 shows the crack propagation behavior of different 2024-T3 aluminum specimens for the different loading histories (inserts) used in this study. The crack rates da/dN were plotted versus the crack length a , because this gives an illustrative impression of the variations in crack growth due to sequence effects. In Fig. 1c the crack growth predictions of some convenient models [8-11] are shown additionally. The deviations from the actual crack extension behavior clearly indicate the lack in the

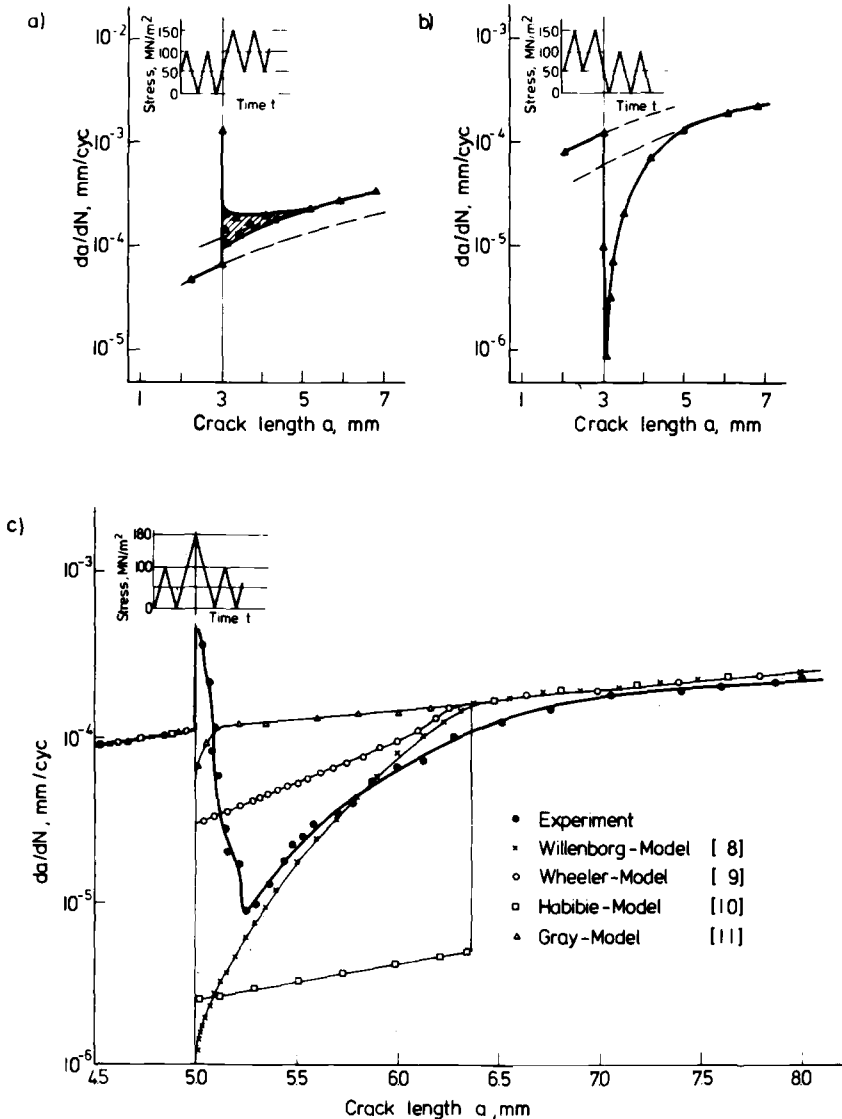


FIG. 1—Crack propagation behavior of 2024-T3 under typical load variations.

physical basis of these models and the necessity of further systematic investigations.

Displacements Around and Behind the Crack Tip

In previous investigations, where the displacements in the crack tip area were measured using a special extensometer [12,13] two essential observations were made: the closure of cracks during a load cycle and a close correlation between the variations in the displacements per cycle (Δv_i) measured in the crack tip plastic zone area and the crack propagation behavior under variable amplitude loading.

Based on the latter observations the following expression was suggested for the crack growth per cycle (Δa_i) for arbitrary loading histories

$$\Delta a_i = C \cdot \Delta v_i^k \quad (1)$$

where C and k are constants, depending on the material. For practical applications of this equation it is desirable that the amounts of Δv_i per cycle can be determined quantitatively by numerical routines. Besides that, the stress distributions along the crack line are important. Figure 2a shows a schematical representation of the stress and strain distributions along the crack line and within the plastic zones both for the maximum A and the minimum load B in a cycle, assuming an approximately ideal elastic-plastic material behavior.

Figure 2b shows the stress distribution along the crack line as predicted by the continuum mechanics analysis by Führung and Seeger [4,5]. The model presumes a two-dimensional stress field and also an ideal elastic-plastic material behavior.

During the crack growth increment in each cycle the new crack surface is formed along with high tensile plastic deformations. Parts of these deformations remain back when the crack propagates in a manner as shown in the lower part of Fig. 2b by the dashed areas. When the crack is fully open, the deformations increase linearly and show their maximum at the crack tip.

For a verification of the numerical analysis predictions by experimental displacement measurements, a procedure similar to that applied in Ref 14 was used. A fine grid was engraved on the specimen surface. The line spacing was 0.1 mm. The deformations around the crack tip were determined as follows: one photograph of the completely undeformed grid was taken before the beginning of the test. In the course of the test at those instances which were of special interest, another photograph of the deformed grid was made. From a comparison of the line spacings of the undeformed grid at the beginning of the test, and of the deformed grid the

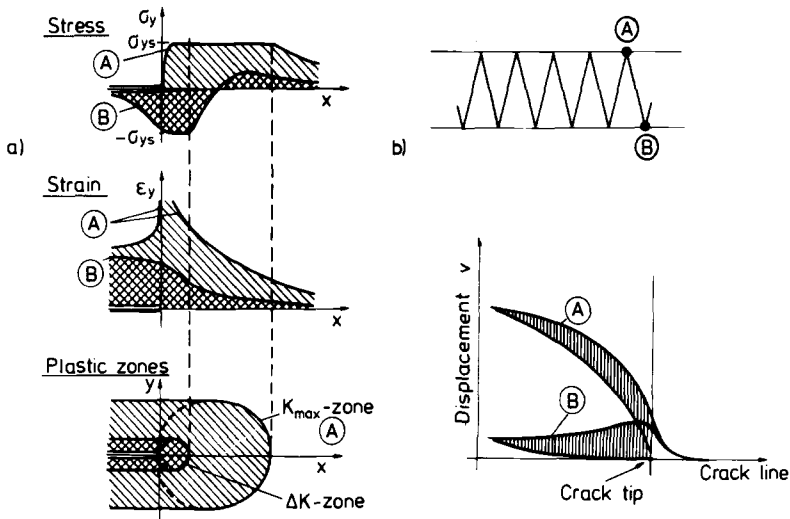


FIG. 2—Stresses, deformations, and displacements along the crack line [7,5].

instantaneous absolute magnitude of the elastic-plastic deformation could be evaluated at all points of interest in the area surrounding the crack tip.

In Figure 3a the experimentally determined K_{max} -zone is shown. Within that area the experimentally determined deformations in the y -direction were equal or larger than 0.5 percent, approximately the observed monotonic elastic yield strain of the material investigated.

For the determination of the area with reversed plasticity in a cycle, denoted as ΔK -zone (see Fig. 3a), the amount of the deformations at maximum load in the cycle (determined by applying the grid technique as previously described) and the amount of the deformations at the minimum load in the cycle (again determined with the grid technique) had to be compared in the surrounding of the crack tip. All those points, where the amounts of the deformations differ more than about 1 percent between maximum and minimum load in the cycle fall within the ΔK -zone, because 1 percent is the approximate maximum range of deformation that the material investigated could deform elastically between yield stress in the tension and yield stress in the compression direction. From Fig. 3a it can be seen that the ΔK -zone is—as a consequence of the crack closure behavior—significantly smaller than one-fourth of the K_{max} -zone area. This result of the experimental deformation analysis coincides with the predictions based on continuum mechanics.

The displacements along the crack, v_o , were also determined experimentally. Although a basis of about 0.2 mm across the crack had to be taken for the displacement evaluations as indicated in the upper half of

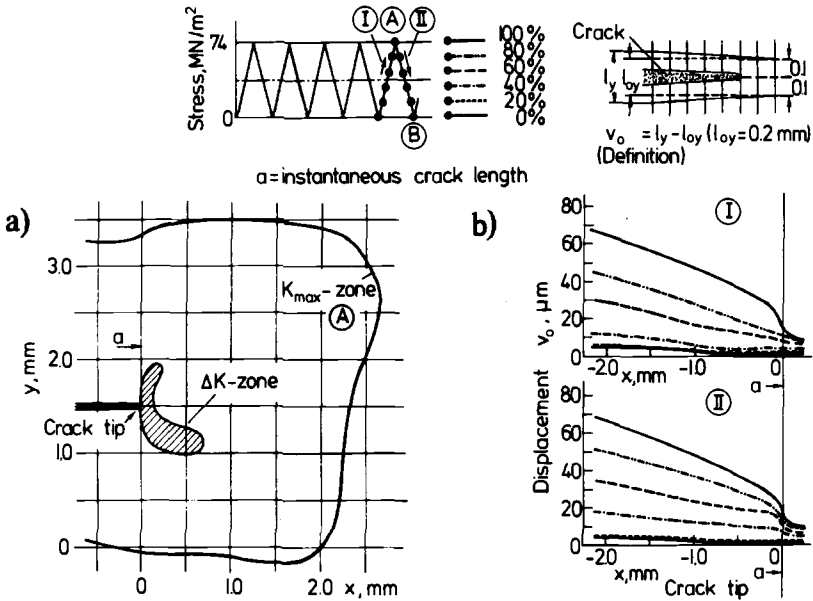


FIG. 3—Experimentally determined plastic zones and displacements under constant amplitude loading.

Fig. 3b, which causes an integrating effect, the measurements showed a very good detailed agreement with the continuum mechanics analysis (see Fig. 2b). From the experimental results in Fig. 3b it can further be seen that the crack completely opens at about 40 percent of the total load variation during loading in a cycle and closes at a lower value upon unloading. The tensile plastic deformations which are generated especially before the crack tip during the loading portion of the cycle lead to the lowest v_o values, not immediately at the crack tip but at some distance behind the crack tip at unloading.

Low-High Loading

Figure 4a shows the predicted stress distributions and displacements along the crack line when a high load (C) is applied during constant amplitude loading. At the first increase in load a large K_{max} -zone is generated with considerably higher tensile plastic deformations than under the preceding constant amplitude loading conditions. The large tensile plastic deformations in the K_{max} -zone area are the reason the crack remains open or closes only a little upon unloading. The absence or the strong reduction of areas where crack surface contact and load transfer can occur at unloading leads to the formation of a larger ΔK -zone as compared to the preceding constant amplitude loading conditions.

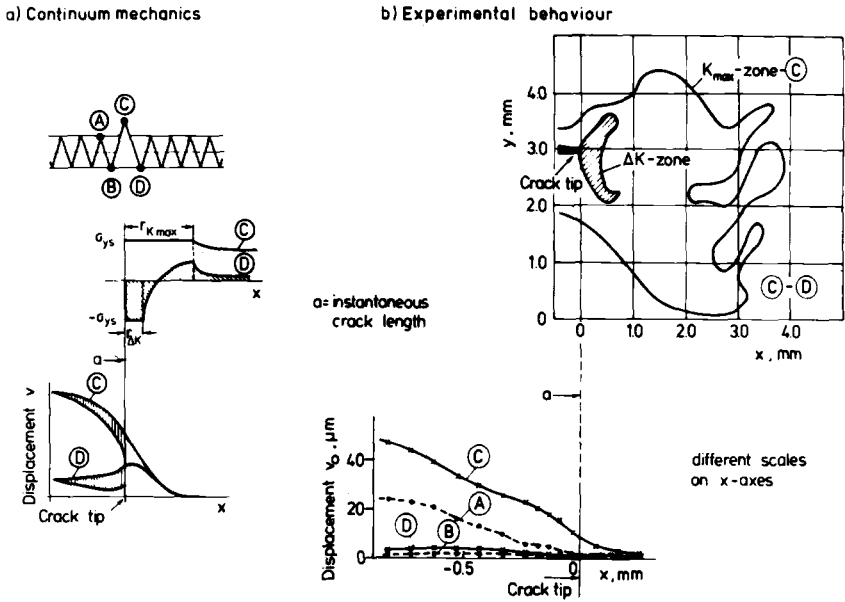


FIG. 4—Stresses, displacements, and plastic zones due to an overload.

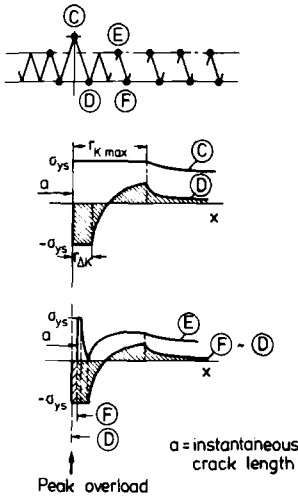
Figure 4b shows the K_{max} - and ΔK -zones and in the lower part of the figure the measured $v_o = f(x)$ behavior. There is a good agreement with the continuum mechanics analysis predictions. The fact that the crack surfaces come into contact in the experiments upon unloading indicates that the peak load C was not high enough to hinder any larger crack surface contact.

High-Low Loading

After a single or multiple high loads or after a program sequence with a high loading level, the crack growth behavior shows a considerable retardation accompanied by several variations in the da/dN rates (see Fig. 1).

Figure 5a shows the stress distributions as predicted by the continuum mechanics analysis at maximum and at minimum load in a cycle after some cycles at the low loading level after the peak load have been applied. The loading on to the maximum load in a cycle leads to the formation of a very small zone, where reversed plasticity occurs. This zone lies within the ΔK -zone which was generated during the unloading from the high peak load (C to D). Figure 5b shows the experimentally determined plastic zone behavior. The small zones with reversed plasticity in a cycle become clearly visible.

a) Continuum mechanics



b) Experimental behaviour

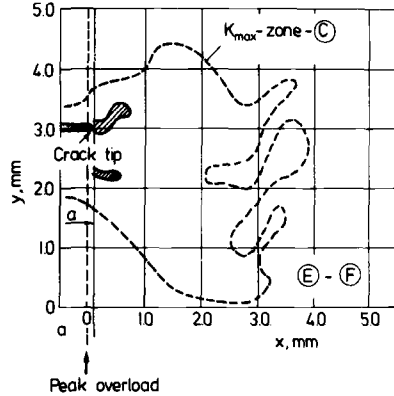


FIG. 5—Plastic zones and stress distributions in the loading period after an overload.

As the crack propagates the continuum mechanics analysis predicts stress distributions at maximum load and at minimum load in a cycle as shown in Fig. 6. Considerable changes in the behavior take place, when the boundary of the zone with reversed plasticity per cycle reaches—due to the crack extension—the boundary of the ΔK -zone, which was formed previously during unloading from the peak overload (C to D).

During the following cycling the new K_{max} -zone and ΔK -zone conditions for the low loading period begin to develop. Another essential feature is the formation of the stress hump on the fracture surfaces as the crack propagates. The hump builds up at that range of crack lengths where the K_{max} -zone due to the high load (C) occurred (Fig. 7).

Figure 7a shows the results of the experimental deformation analysis for the cycle I to J. At that instant, where the displacement measurements were made, the development of the new K_{max} -zone has just started.

Figure 7b shows the experimentally determined $v_0 = f(x)$ -behavior at different amounts of crack propagation. The displacement measurements clearly indicate that the residual deformations along the crack contour really exist, which lead to the stress hump as it was predicted by the continuum mechanics analysis (see Fig. 6).

The comparative considerations in this section could only deal with some typical loading situations. Displacement analyses for other loading histories can reveal further details.

From the present considerations the conclusion can be drawn that the

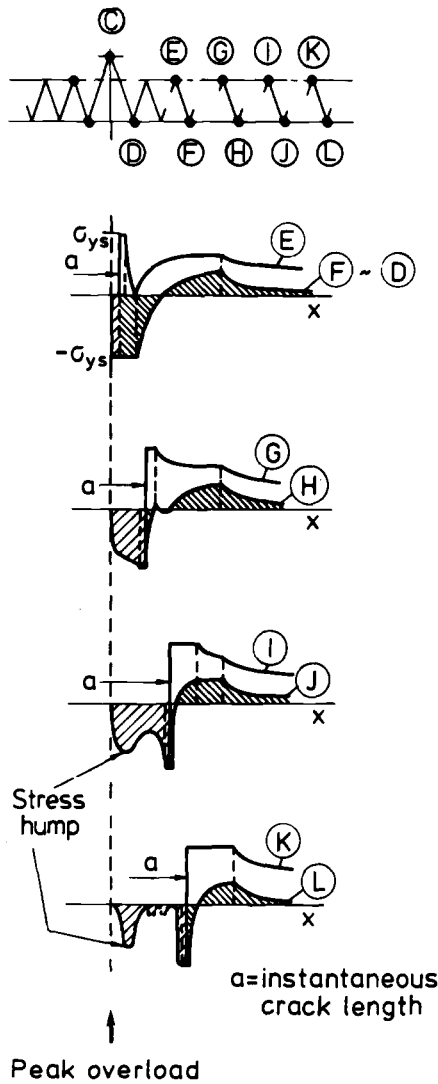


FIG. 6—Stress distributions in the loading period after the high load (continuum mechanics analysis).

continuum mechanics analysis by Führung and Seeger enables suitable predictions of the stresses and displacements around the crack tip. The fact that even details of the processes around the propagating crack are predicted realistically indicates that the stresses and the deformations and their treatment following the principles of continuum mechanics analyses are of predominant importance for the evaluation of sequence effects.

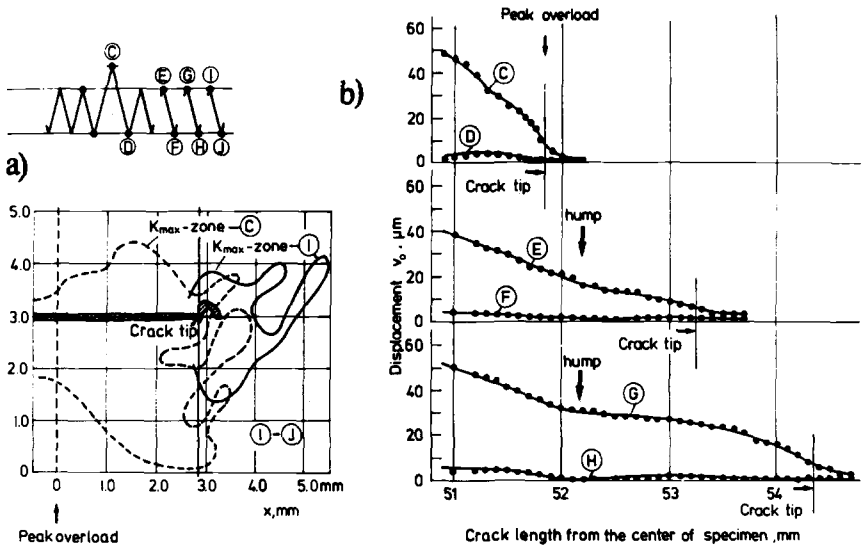


FIG. 7—Experimentally determined plastic zones and displacements at several amounts of crack propagation after the high load.

Influence of Microstructure and Material Properties on the Sequence Effects

Complementary to the displacement analyses in the previous sections, considerations of the microstructural crack propagation behavior can give more information about the mechanisms that control the crack propagation during each consecutive load cycle, and the sequence effects. As already mentioned earlier, a test program with different high strength aluminum alloys which show a different microstructural crack propagation behavior was performed. Table 1 gives a survey of the alloys investigated, the tensile properties and the aging treatments. While the technical alloys Al 2024, Al 7075, and Al 7475 were investigated only in the underaged condition the X-7075 alloy was used in the underaged as

TABLE 1—Aging treatments and tensile properties of the materials investigated.

Alloy	Aging Treatment	E , MN/m ²	σ_{YS} , MN/m ²	σ_P , MN/m ²	ϵ_F
2024	T3	74 000	340	716	0.4
7075	24 h 100° C	72 000	415	776	0.33
7475	24 h 100° C	70 000	420	810	0.36
X-7075	24 h 100° C	72 000	430	730	0.37
X-7075	48 h 180° C	72 000	390	560	0.36

well as in the overaged condition. In contrast to the technical alloys the laboratory alloy X-7075 does not contain any chromium, iron, or silicon.

Figure 8 shows the da/dN behavior and the microstructural crack propagation mechanism of the aluminum alloy under constant amplitude loading conditions. From previous investigations [15,16] it is known that all these alloys show a crack propagation along slip bands (SB) at low ΔK values and low crack propagation rates. With increasing ΔK values, a change from the SB fracture to a dimple type crack extension (D) takes place for the technical alloys, because of the manganese-rich inclusions in the 2024 alloy and the chromium-rich inclusions in the 7075 and the 7475 alloys. The laboratory alloy X-7075 in the underaged condition shows no change in the crack propagation mode as a function of da/dN and ΔK . A SB-fracture type is present over the entire range. The X-7075 alloy in the overaged condition shows a change to a crack extension along grain boundaries (GB) because of the precipitate free zones at the grain boundaries.

Crack Propagation Under Variable Loading Conditions

In the tests the loading conditions and crack lengths were chosen such that a change in the microstructural crack propagation mechanisms could occur. The load variations were performed at constant stress ranges in the cycles and with changes in the stress ratios from $R = 0$ to $R = 0.33$.

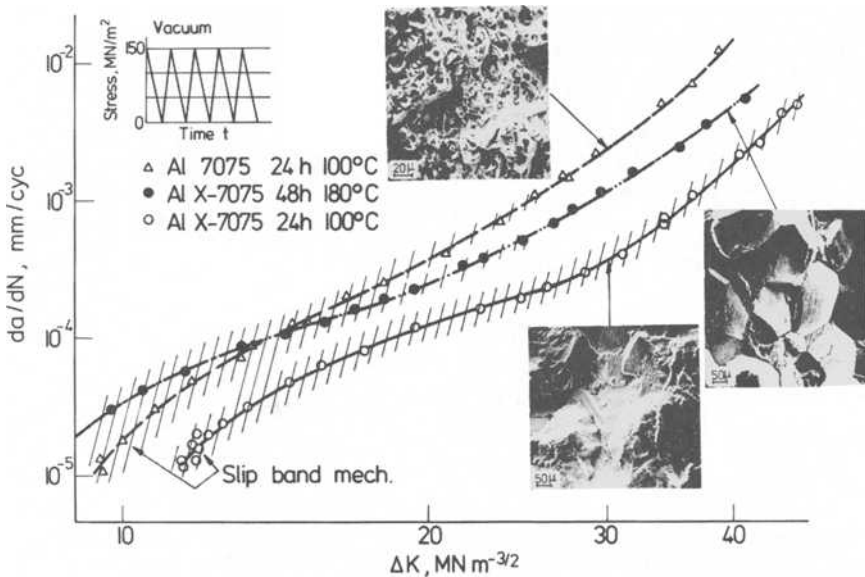


FIG. 8—Crack propagation behavior and microscopical crack propagation mechanisms under constant amplitude loading.

Crack Propagation Under Low-High Loading

Figure 9 shows the observed crack propagation behavior under low-high loading. Because of the difficulties in exactly determining the crack extension by surface measurements the crack propagation was determined by SEM-analyses of the fracture surfaces (see Fig. 9). During the first increase in load on the high level the formation of a stretched zone was observed in all cases. The measured widths of the stretched zones W are also shown in Fig. 9.

The interpretation of the subsequent fatigue crack growth behavior was more difficult. That is mainly because several influencing factors become active: the instantaneous crack closure level, the cyclic strain hardening condition of the crack tip material and the strain hardening profile along the plastic zones, blunting of the crack tip, incompatible crack front orientation, etc. These all become simultaneously active. The observed scatter band in the da/dN versus values shown in Fig. 9 (dashed area) is a visible manifestation of the complicated physical background. The da/dN scatter band did not change its character, when the crack propagation mechanism remained the same (a SB-type) after the transition to the high loading level or when it changed from the SB- to the D- or GB-mechanism.

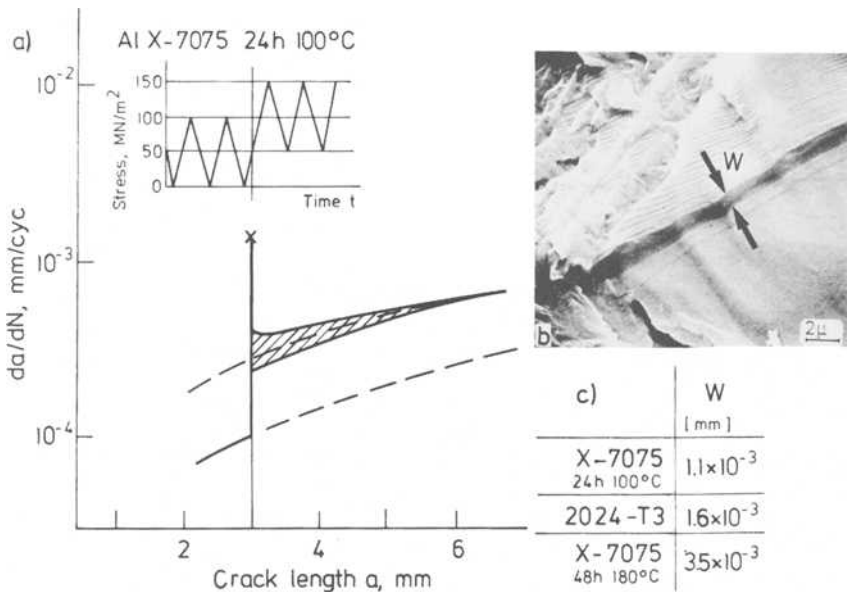


FIG. 9—Crack propagation under a low-high loading sequence.

Crack Propagation Behavior Under High-Low Loading

Figure 10 shows the experimentally determined da/dN versus a behavior for crack lengths of 8 and 12 mm. The decrease in da/dN was so pronounced in all cases that a SB-mechanism occurred.

From the observed behavior the following general trends could be outlined:

1. All materials show a similar overall retardation behavior, which coincides qualitatively with the prediction of continuum mechanics.
2. A quantitative comparison of the $da/dN = f(a)$ -behavior at a crack length of 8 mm shows that:
 - The affected crack length where retardation occurs (see Fig. 11), is significantly larger for the 2024-alloy than for the alloys of the 7000 series. This coincides again with continuum mechanics analyses, which suggest that the retarded crack length is proportional to the inverse of σ_{ys}^2 of the material [5].
 - The N_D values, which are used commonly in literature for the characterization of the crack retardation (see Fig. 11), and which are of special importance for an engineering characterization of the sequence effects are significantly larger for the 2024 alloy than for the alloys of the 7000 series. Among the alloys of the 7000 series the X-7075 alloy in the overaged condition shows the lowest retardation.

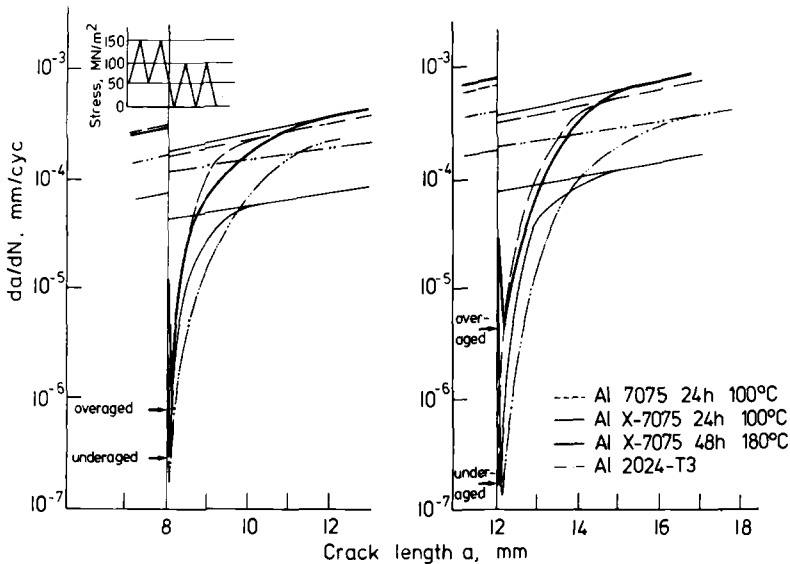
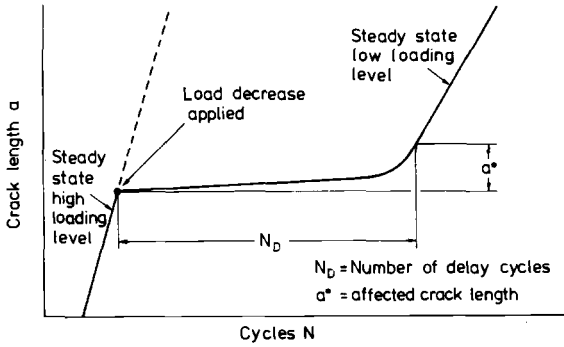


FIG. 10—Crack propagation behavior under a high-low loading sequence at two different crack lengths.



Alloy	N_D	N_D
	Crack length 8mm	Crack length 12mm
7075 24 h 100°C	133 000	182 000
X-7075 24 h 100°C	100 000	141 000
X-7075 48 h 180°C	110 000	67 000
2024-T3	950 000	1050 000

FIG. 11—Crack delay under high-low loading.

3. When the da/dN versus a -behavior at 8 mm is compared to that at 12 mm crack length the qualitative behavior remains the same. However, quantitatively there are some differences:

- The X-7075 alloy in the underaged condition and also the technical alloys showed an increase in the N_D values as the crack length where the load variation occurred increased.
- The overaged X-7075 alloy, however, showed a decrease in the N_D value.

In order to find possible explanations of the observed behavior SEM investigations of the fracture surfaces were performed. In Table 2 the observed crack extension mechanisms are given. The X-7075 alloy in the overaged condition is the only one where a change from a predominantly GB-mechanism at the high loading level to a SB-mechanism in the low loading level occurred. Furtheron, the portion of GB-mechanism increased as the crack length at the high loading level was increased. All other aluminum alloys showed different types of crack propagation mechanisms before the decrease in load occurred.

These observations indicate that the crack propagation mechanism influences the retardation behavior.

One possible explanation for the observed behavior is the interrelation between the specific crack propagation mechanisms and the crack closure

TABLE 2—Crack propagation mechanisms under high-low loading.

	High Load Period	Low Load Period
2024-T3	<i>dimple mechanism</i> ^a + slip band mechanism	slip band mechanism
7075 / 7475 24 h 100° C X-7075	<i>dimple mechanism</i> ^a + slip band mechanism	slip band mechanism
48 h 180° C (overaged) X-7075	<i>grain boundary</i> ^a + slip band mechanism	slip band mechanism
24 h 100° C (underaged)	<i>slip band mechanism</i>	slip band mechanism

^a Predominant mechanism, increasing portion on the fracture surfaces with increasing crack length.

process. In the case of the GB-mechanism of the X-7075 alloy in the overaged condition large flat grain boundary interfaces remain on the crack surface (see Fig. 12a). When the crack closes during the unloading portion of the cycles an intermeshing of the crack surfaces is favored which leads to a low crack closure stress level. This level is lower than that which can occur when a SB- or a D-mechanism are present with

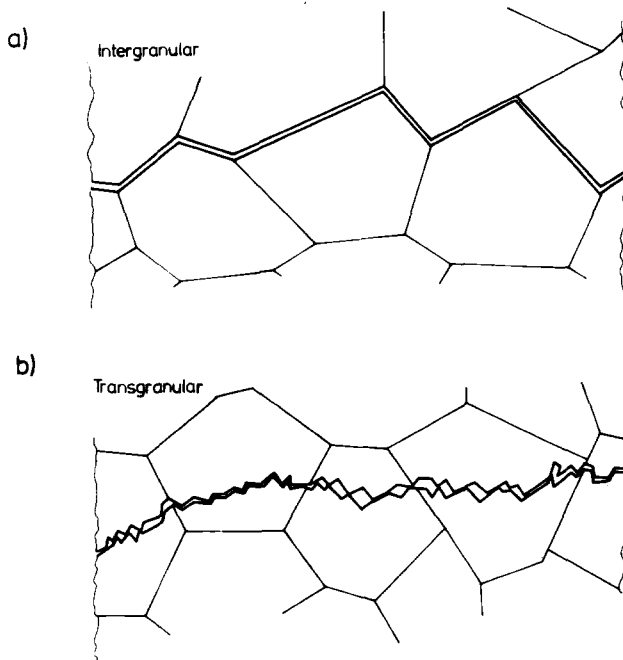


FIG. 12—Different types of microscopic crack extension.

many small sized randomly distributed contact faces during unloading as it can be seen in Fig. 12*b* for the 7075 alloy as an example. The lower crack closure stress level in the high load level period for the overaged condition remains effective when the load level is decreased and reduces the retardation. This explanation is further substantiated by the fact that the retardation is reduced further if the grain boundary structure of the fracture surfaces is more pronounced as is it the case when the crack length increases from 8 to 12 mm.

Although these considerations of the geometrical shape of the fracture surfaces offer a reasonable explanation of the observed differences in the retardation behavior, other contributions—like differences in the strain hardening behavior and differences in the strain distributions at the crack tip—might also be important.

Conclusions

In the present study two new aspects of recent crack propagation investigations are considered regarding their significance for the evaluation of sequence effects: a recently published continuum mechanics analysis by Führung and Seeger [4,5] and the systematical variation of the microstructural crack propagation mechanisms.

An experimental displacement analysis where a special grid technique was applied showed that the measurement results coincide well with the predictions of the stresses and displacements by continuum mechanics. That means that continuum mechanics analyses offer an essential basis for the evaluation of the crack propagation under variable amplitude loading.

The influence of microstructure on crack propagation under variable amplitude loading was investigated systematically on aluminum alloys of the 7000 series. Due to different heat treatments specific but well defined crack propagation mechanisms were achieved.

For a low-high loading sequence the formation of a pronounced stretched zone at the first increase of load was observed.

The crack propagation behavior under a high-low loading sequence was influenced significantly by the microscopic crack propagation mechanism. When the crack propagated along grain boundaries before the load was decreased, the retardation was less, whereas the SB- and D-mechanisms favored the crack delay.

Acknowledgments

The financial support of this work by the Deutsche Forschungsgemeinschaft (DFG) is gratefully acknowledged. The authors wish to thank J. Strunck for the displacement measurement evaluations.

References

- [1] *Fatigue Crack Growth Under Spectrum Loads*, ASTM STP 595, American Society for Testing and Materials, 1976.
- [2] Dugdale, D. S., *Journal of Mechanics and Physics of Solids*, Vol. 8, 1960, pp. 100–104.
- [3] Barenblatt, G. I., *PMM*, Vol. 23, No. 3, 1959, pp. 434–444.
- [4] Führung, H. and Seeger, T., "Remarks on Load-Interaction Effects Based on Fatigue Fracture Mechanics Calculations," Symposium of the 9th International Committee on Aeronautical Fatigue, Darmstadt, Germany, May 1977.
- [5] Führung, H., "Berechnung von elastisch-plastischen Beanspruchungsabläufen in Dugdale-Riss-Scheiben mit Rissuferkontakt auf der Grundlage nichtlinearer Schwingbruchmechanik," Veröffentlichung des Instituts für Statik und Stahlbau der TH Darmstadt No. 30, Darmstadt, Germany, 1977.
- [6] Schulte, K., Nowack, H., and Lütjering, G., "Rasterelektronenmikroskopische Analyse der Bruchflächen hochfester Aluminiumlegierungen bei systematisch veränderter Schwingbeanspruchung," Tagungsberichte, 8. Sitzung des DVM-Arbeitskreises "Rasterelektronenmikroskopie," Berlin, Deutscher Verband für Materialprüfung, Ed., Oct. 1977, pp. 175–183.
- [7] Jacoby, G., Nowack, H., and van Lipzig, H. T. M. in *Fatigue Crack Growth Under Spectrum Loads*, ASTM STP 595, American Society for Testing and Materials, 1976, pp. 172–183.
- [8] Willenborg, J. D., Engle, R. M., and Wood, H. A., "A Crack Growth Retardation Model Using an Effective Stress Concept," AFFDL-TM-71-1-FBR, Air Force Flight Dynamics Laboratory, 1970.
- [9] Wheeler, O. E., *Transactions*, American Society of Mechanical Engineers, *Journal of Basic Engineering*, Vol. 94, 1972, pp. 181–186.
- [10] Gray, T. D. and Gallagher, J. P. in *Mechanics of Crack Growth*, ASTM STP 590, American Society for Testing and Materials, 1976, pp. 331–344.
- [11] Habibie, B. J., "On the Integration Method of Crack Propagation in Elasto-Plastic Material Under Operational Loads and Plane Stresses," 3rd International Conference on Fracture, München, April 1973.
- [12] Elber, W. in *Damage Tolerance in Aircraft Structures*, ASTM STP 486, American Society for Testing and Materials, 1971, pp. 230–242.
- [13] Nowack, H., "Ein Beitrag zur Untersuchung der Schadensakkumulation auf der Grundlage biharmonischer Belastungsabläufe," *DLR Forschungsbericht 71-23*, Abteilung Wissenschaftliches Berichtswesen der DFVLR, Ed., Köln-Porz (Germany), 1971.
- [14] Broek, D., *Elementary Engineering Fracture Mechanics*, Noordhoff International Publishing, 1974, p. 260.
- [15] Albrecht, J., Martin, J. W. R., Lütjering, G., and Martin, J. W., "Influence of Micromechanisms on Fatigue Crack Propagation Rate of Al-Alloys," *Proceedings*, 4th International Conference on the Strength of Metals and Alloys, Nancy, France, Vol. 2, 1976, pp. 463–467.
- [16] Albrecht, J. and Lütjering, G., "Einfluss der Mikrostruktur auf die Ermüdungsrissausbreitung in Aluminium-Legierungen," *DLR Forschungsbericht 77-07*, Abteilung Wissenschaftliches Berichtswesen der DFVLR, Ed., Köln-Porz (Germany), 1977.

M. E. Artley¹, J. P. Gallagher², and H. D. Stalnaker¹

Variations in Crack Growth Rate Behavior

REFERENCE: Artley, M. E., Gallagher, J. P., and Stalnaker, H. D., "Variations in Crack Growth Rate Behavior," *Fracture Mechanics, ASTM STP 677*, C. W. Smith, Ed., American Society for Testing and Materials, 1979, pp. 54-67.

ABSTRACT: Three variable amplitude stress histories based on a single repeating flight of a bomber aircraft are applied to two 610 mm wide, 4.6 mm thick, center-crack panels of 7075-T6 aluminum. The stresses in each stress history are controlled so that the stress intensity factor coefficient (K/σ) is maintained constant as the crack grows. The resulting fatigue crack growth (FCG) data are utilized to show that the derived variable amplitude fatigue crack growth rate (FCGR) behavior is controlled by a stress intensity factor parameter. These FCG data are also used to evaluate the influence that differentiation method, crack length measurement interval, and stress history have on the FCGR behavior and its variability. Within the limits spelled out in the text, the value of the (statistical) mean FCGR is shown to be independent of differentiation method and of crack length measurement interval. The choice of stress history is shown to affect the mean FCGR value as would be expected.

The variability in FCGR behavior, as characterized by the coefficient of variation, is affected by all the parameters studied. As the crack length measurement interval increases, the FCGR variability associated with the secant method of differentiation is shown to decrease toward the almost constant level of FCGR variability exhibited by the seven-point incremental polynomial method. Also, the coefficient of variation, while significantly affected by crack length measurement interval for a given stress history, is shown to be independent of stress history when the FCGR data for the three stress histories are derived using similar crack length measurement intervals.

KEY WORDS: fatigue (materials), crack growth, statistical methods, stress intensity factor, variable amplitude loading, crack propagation

An accurate assessment of fatigue crack growth (FCG) behavior is important to the structural design of fracture critical aerospace components. The analysis is accomplished using a fracture mechanics approach that is based on derived fatigue crack growth rate (FCGR) data [1,2].³

¹ Aerospace engineers, Structural Mechanics Division, Air Force Flight Laboratory, Wright-Patterson Air Force Base, Ohio 45433.

² Group leader, Service Life Management, University of Dayton Research Institute, Dayton, Ohio 45469.

³ The italic numbers in brackets refer to the list of references appended to this paper.

Currently, the analysis approach is a deterministic approach wherein single valued functional relationships are established between stress intensity factor parameters and the FCGR behavior. The single valued functional relationships are based normally on mean FCGR behavior; sometimes however, they are based on "upper bound" FCGR behavior in order to be "conservative." When upper bound behavior is utilized, not much consideration is given to how the variability in a given FCGR data set relates to the variability in the fatigue crack life. When the designer is basing calculations on FCGR data, he is interested in the crack life variability due to material effects. However, the variability in FCGR data not only results from variability in material behavior but also from (a) crack length measurement errors, (b) imprecise control of load, and (c) method of numerical differentiation as applied to the experimental FCG data [3,4]. Measurement, load, and differentiation discrepancies can be minimized by standardizing test procedures. The American Society for Testing and Materials (ASTM) is in the process of developing such a test method (ASTM Test for Constant-Load-Amplitude Fatigue Crack Growth Rates Above 10^{-8} m/cycle (E 646-78 T)). Paragraphs 8.1, 8.4, 8.5, 8.6, and 9.2 of Method E 646 address such areas as the number of tests required, test equipment, differentiation process, specimen geometry, and a general test procedure.

This paper addresses the variability of FCGR data and some of the factors that influence this variability in order to establish a data base for relating the variability in FCGR data to the variability in fatigue crack life behavior. The FCG data utilized in this study were generated using three repeating-block, variable amplitude load histories applied to center-crack panels of 7075-T6 aluminum alloy. The choice of using variable amplitude histories (versus constant amplitude history) was dictated by a general desire to study and characterize FCG behavior induced by variable amplitude loading histories. As the paper will demonstrate, the particular loading histories studied result in FCGR behavior that is similar to that exhibited under constant amplitude loading conditions.

Test Methods and Procedures

Basic Load History

The basic variable amplitude load history used in this investigation is shown in Fig. 1. The Fig. 1 history represents a single mission derived from the 135 000 cycle (per lifetime) bomber design load history described in Refs 5 and 6. There are 57 separate load levels and 123 cycles of load in the stress history given in Fig. 1. The load levels are given in percent of the largest level experienced in the design load history; note that the largest level in the repeating flight is 88 percent of the largest level in the design

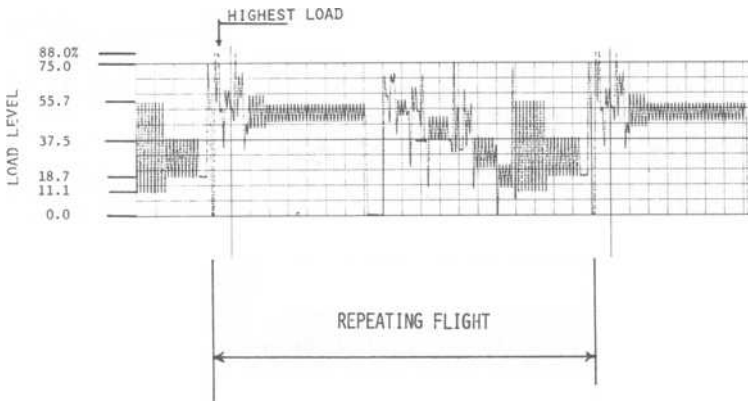


FIG. 1—Load history based on bomber design stress history.

load history. Since it was desired to conduct the tests in this study without any stiffening devices, all the negative loads in the bomber mission were truncated to a zero load level as described by Fig. 1.

Material, Specimen Geometry and Test Equipment

Two 610 mm (24 in.)⁴ wide center-cracked panels manufactured from 4.6 mm (0.182 in.) thick 7075-T6 aluminum alloy were used. The machined central notch for the first panel was 41.1 mm (1.620 in.) in length, the second was 42.2 mm (1.663 in.). An overview of the testing equipment with a center-cracked panel in place is shown in Fig. 2. This equipment includes a 2.2 MN (500 kip) static, 1.1 MN (250 kip) dynamic capacity load frame under closed-loop servocontrol used to apply the variable amplitude load history. The load levels and cycle shape were stored in a 4096 byte memory digital programmer and then fed to the load servocontrollers.

The applied test loads were monitored through an independent data system, and were maintained within one percent of the programmed value. The overloads were applied manually.

Stress Intensity Factor (SIF) Control Procedures

The level of loading for this study was controlled so that the stress intensity factor (SIF) coefficient (K/σ) was maintained constant. Specifically, the load levels were reduced proportionally, as the crack length increased, using the SIF finite-width secant formula suggested by Fedderson [8]:

⁴ All measurements and testing were performed in U.S. customary units (in parenthesis).

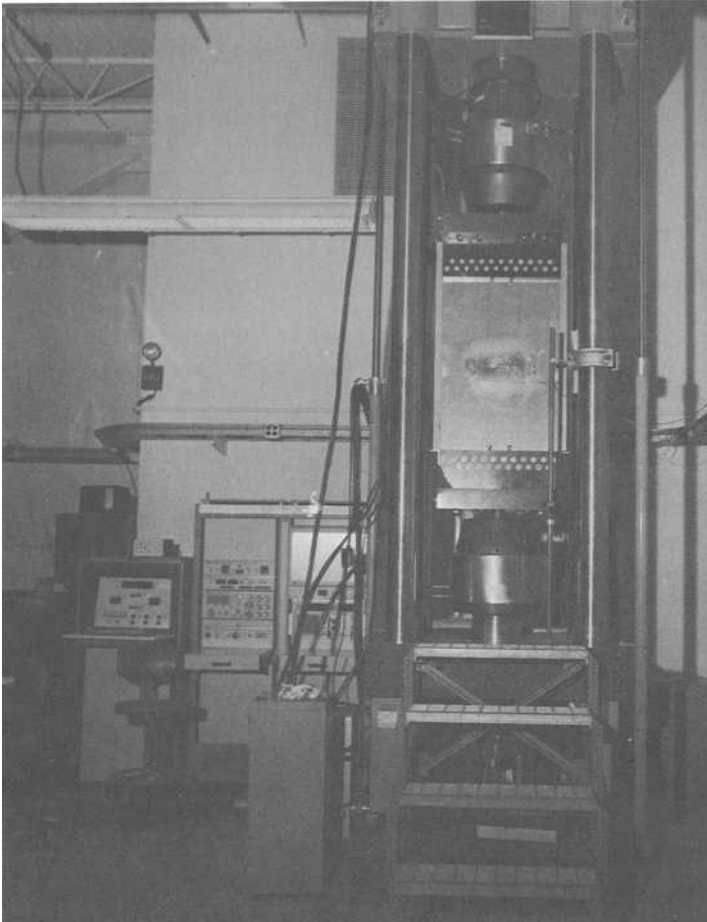


FIG. 2—Description of test specimen and equipment.

$$K = \sigma \left[\pi a \secant \frac{\pi a}{W} \right]^{\frac{1}{2}} \quad (1)$$

where W = specimen width and a = half crack length. The stress (σ) used to describe the specific stress (load) magnification factor applied in test to provide a constant stress intensity factor control condition is the 100 percent stress (load) level associated with the Fig. 1 stress (load) history. Thus, the reported maximum stress intensity factors (K_{\max}) values were calculated based on the 100 percent level of stress. The level of SIF was controlled to within 1 percent of the desired conditions by ensuring that the total crack growth increment ($\Delta 2a$) did not exceed 1.27 mm (0.050 in.) prior to reducing the load level.

By keeping the SIF level constant, FCGR data are generated under conditions in which the normal crack growth driving parameter is fixed. By controlling the SIF, it was possible to accumulate the desired quantities of FCG data necessary to perform statistical studies. These FCG data thus provided the data base to study the variability in FCGR data resulting from loading conditions, measurement interval size, and differentiation method.

Stress Intensity Factor (SIF) Histories

The FCG data were generated using three similar SIF histories based on the Fig. 1 defined set of variable amplitude loads. The three histories are:

(1) The basic history based on a maximum stress intensity factor of $33 \text{ MPa}/\sqrt{\text{m}}$ ($30 \text{ ksi } \sqrt{\text{in.}}$). This history will be referred to subsequently as the Type I history.

(2) The basic history based on a maximum stress intensity factor of $27.5 \text{ MPa}/\sqrt{\text{m}}$ ($25 \text{ ksi } \sqrt{\text{in.}}$), the Type II history.

(3) The basic history with (a) a maximum stress intensity factor of $33 \text{ MPa}/\sqrt{\text{m}}$ ($30 \text{ ksi } \sqrt{\text{in.}}$) and (b) a single $37.6 \text{ MPa}/\sqrt{\text{m}}$ ($34.3 \text{ ksi } \sqrt{\text{in.}}$) cycle before every block of 15 flights, the Type III history. Note that the single load cycle is applied at a 114 percent load level which is equivalent to a 30 percent overload based on the highest load in the repeating flight.

Crack Growth Measurement

For all test histories, the crack length was measured each time a block of 15 flights had been applied. A binocular zoom microscope with a maximum magnification of $40\times$ was used to make the measurement in conjunction with a mylar scale calibrated in 0.125 mm (0.005 in.) increments attached to the specimen. The crack was measured on both sides of the notch, a total crack length ($2a$) was calculated, and the half crack length (a) versus flights (F) data were tabulated.

Methods of Differentiation

Two methods of differentiation were used to process the FCG data generated from the basic history. These were: (1) the secant method, and (2) the seven-point incremental polynomial method; both were proposed in the ASTM Method E 646. Comparisons of the two methods of differentiation were made based on the resulting scatter. Only the secant method of differentiation was used to evaluate and compare the FCGR behavior resulting from all three SIF histories.

Results and Discussion

Preliminary Analysis

A typical segment of the fatigue crack growth (FCG) data generated under the Type I load history is shown in Fig. 3. The FCG data from the Type I loading were tabulated and processed using a statistical analysis computer program (SACP) developed at Purdue University under AFOSR Grant 76-1038 [8,9]. When the four distribution functions (normal, log normal, three parameter log normal, and Weibull) contained within SACP were fit to the FCGR data, it was found that all four distributions appeared to adequately describe the central tendency of the FCGR data [10].

For the segment of crack length shown in Fig. 3, the FCGR data shown in Fig. 4 were generated using the secant method of differentiation. The solid points shown in Fig. 4 define the values of crack length measured immediately after the load reduction. These points were defined to emphasize that the variability in the FCGR determination seems to be due to factors other than the load reduction, as can be seen by the randomness of those data. Overall, the data are seen to be scattered around a mean FCGR. The following statistical study was conducted in order to investigate and describe the variability associated with FCGR determination as

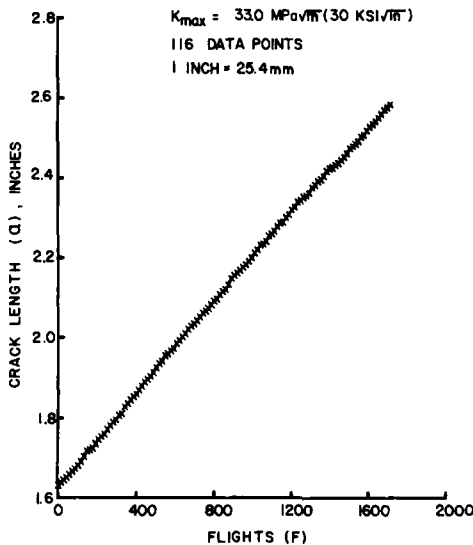


FIG. 3—Fatigue crack growth (FCG) behavior observed under constant stress intensity factor coefficient control for Type I histories.

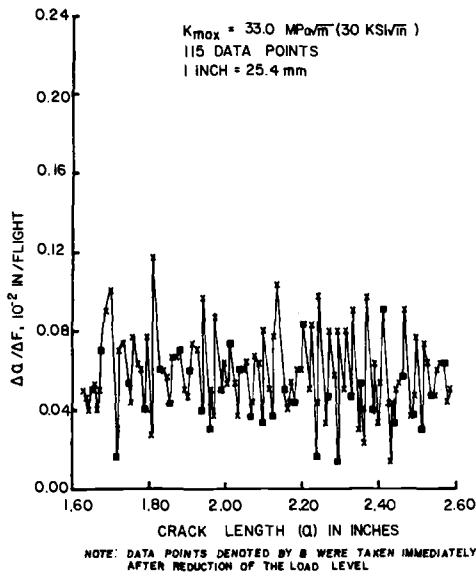


FIG. 4—Fatigue crack growth rate (FCGR) data generated from Fig. 3 data using the secant method of differentiation.

related to load history levels, measurement interval size, and differentiation method.

Determination of Steady State Behavior

To determine if the stress intensity factor control condition led to crack length independent behavior, the FCGR data generated under Type I loading in the first test panel were segregated into four crack length intervals, each having a length of approximately 12.7 mm (0.50 in.). The sample means and standard deviations of these segregated FCGR data are shown in Fig. 5 to remain constant as the crack progressed. The means were indistinguishable from each other using a Student's *t* test at a 95 percent confidence level. The fact that the sample means are indistinguishable from a statistical viewpoint shows that no stress intensity factor gradient effect exists as the crack advances, and thus, the FCGR behavior can be classified as steady state behavior [6,11]. In essence, steady state behavior implies that FCGR behavior can be described as a function of a stress intensity factor parameter. The characteristics of steady state FCGR behavior are similar to that exhibited by constant amplitude behavior. Because the repeating stress history generated steady state FCGR behavior, the segregated FCG data described in Fig. 5 can be

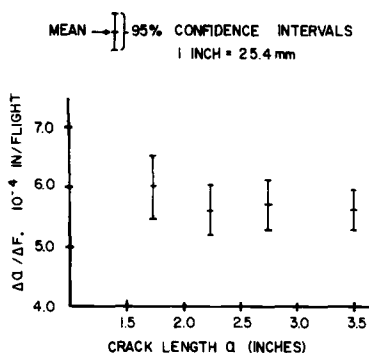


FIG. 5—Mean FCGR data (with 95 percent confidence bands) associated with four crack length segments. Data shown were generated under Type I history.

considered individually or collected together for evaluation of statistical distribution functions.

Effect of Crack Increment and Differentiation Method

A study of the effect of crack growth increment size and of numerical differentiation technique on FCGR variability was conducted. The crack growth increment size was controlled by selectively omitting FCG data points. First, every other FCG data point was considered, thereby doubling the crack size increment. Next, only every third point was considered which essentially tripled the crack size increment. The process of omitting FCG data was continued until only every fifth point was considered.

The two methods of differentiation considered for evaluation were the secant method ($\Delta a / \Delta F$), and the incremental polynomial method. The secant method used successive data points. The polynomial method involved fitting a quadratic equation in a least squares sense to consecutive sets of seven successive FCG data points prior to differentiation, as described in ASTM Method E 646.

The sample means and standard deviations for this comparative study of FCGR behavior based on the set of 116 FCG data points shown in Fig. 3 are presented in Table 1. Results of considering all FCG points from that set, as well as the effect of omitting points, are presented for the two differentiation methods. From Table 1, it can be seen that the method of differentiation does not affect the mean crack growth rates. The standard deviations obtained using the incremental polynomial method were significantly less than those obtained using the secant method of differentiation.

In the process of omitting points, the variability associated with the secant method of differentiation decreased as the measurement interval

TABLE 1—Sample means and variances of FCGR data for successively removing FCGR data points from Fig. 3 data set.

FCG Points in Set	Effective Measurement Frequency (ΔF) Flights	Mean Crack Growth Increment (Δa), in.	FCGR Data for Method of Differentiation				Coefficient of Variation ^a , v	
			Secant Method		Incremental Polynomial			
			Mean FCGR 10^{-4} in./Flight	Standard Deviation 10^{-4} in./Flight	Coefficient of Variation ^a , v	Mean FCGR 10^{-4} in./Flight		Standard Deviation 10^{-4} in./Flight
116	15	0.008	5.7	2.04	0.36	5.7	0.50	0.09
58	30	0.017	5.7	1.44	0.25	5.6	0.42	0.08
38	45	0.026	5.7	0.90	0.16	5.7	0.30	0.05
29	60	0.034	5.6	0.66	0.12	5.6	0.35	0.06
23	75	0.042	5.6	0.79	0.14	5.5	0.36	0.06

^a Coefficient of Variation = $\frac{\text{standard deviation}}{\text{mean}}$

1 inch = 25.4 mm

size was increased. The standard deviation for the secant method initially was observed to decrease approximately as a function of the square root of the number of intervals added. It also appears that the variability (coefficient of variation) observed in the secant differentiated FCGR data approaches that of the polynomial differentiated FCGR data as the measurement interval size is increased as shown in Fig. 6. For this variable amplitude load history applied to the 7075-T6 aluminum alloy center-cracked panels, the coefficient of variation appears to approach 8 percent for both differentiation methods. Virkler et al [9] reported similar variability in crack growth lives under constant amplitude, constant load using 2024-T3 aluminum alloy center cracked panels. This value would then appear to be an indication of the true material variability for these two similar types of aluminum alloys. Larger values of reported variability would indicate that a second look at the test procedure and data processing technique would be in order.

ASTM has attempted to standardize the FCGR test procedure which should help to maintain uniformity in reported variability. One such guideline involves a requirement for the size of the crack length measurement interval. The proposed minimum value for Δa is the greater of 0.25 mm (0.01 in.) or ten times the crack length measurement precision (ASTM Method E 646). The crack length measurement precision (ϵ) is defined as "the standard deviation on the mean value of crack length determined for a set of replicate measurements" (ASTM Method E 646).

The crack length measurement precision (ϵ) for this study, as determined by a set of ten replicate measurements was determined to be 0.038 mm (0.0015 in.). To keep the coefficient of variation below twenty percent, a minimum Δa should be 15 times the measurement precision as

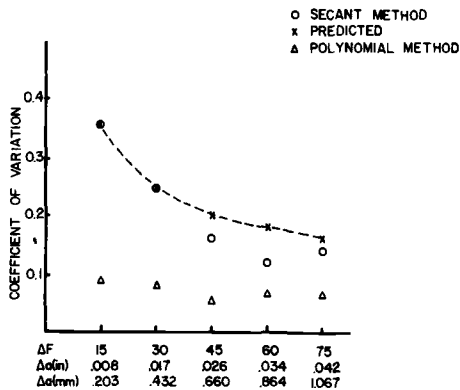


FIG. 6—Variation in FCGR coefficients of variation (v) as a function of crack length measurement interval size.

indicated by the data in Fig. 6 when using the secant method of differentiation. When using the polynomial method of differentiation, the minimum Δa is not as important. If design is to be based on an "upper bound" approach, it is essential that a potentially overly conservative determination of the FCGR be avoided by limiting the reported variability.

Effect of Loading History

In this part of the study, the effect of loading history on the mean FCGR and its variability was investigated. The FCG data from the three types of loading used in this study are shown in Fig. 7. Because the stress intensity factor coefficient (K/σ) was the control condition, different test histories could be run in any combination on a particular panel. Crack growth behavior that could be interpreted easily as transient behavior resulting from a change in stress intensity factor history was excluded from consideration in this study. For presentation purposes, FCG data generated using the three load histories were normalized to the same initial crack length for zero flights of loading as described in Fig. 7. The Type I FCG data described in Fig. 7 were taken from a different crack length segment than the data reported in Fig. 3. The FCG data described in Fig. 7 were differentiated using the secant method to obtain the FCGR data summarized in Table 2.

Table 2 shows that as the maximum stress intensity factor is lowered by a factor of 1.2 (Type I to Type II), the mean FCGR is lowered by a factor

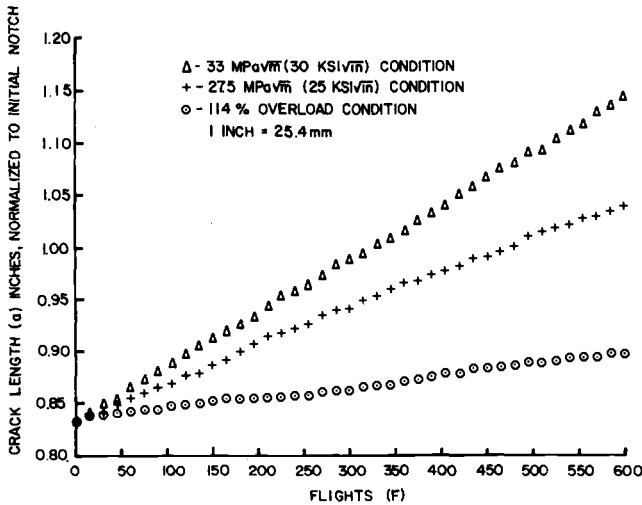


FIG. 7—Fatigue crack growth (FCG) behavior observed under constant stress intensity factor coefficient control for Type I, Type II, and Type III histories.

TABLE 2—Effect of stress intensity factor history on FCGR behavior.

History	ΔF	Mean $\Delta a/\Delta F$ (10^{-4} in./Flight)	Standard Deviation (10^{-4} in./Flight)	Mean Δa , in.
Type I	15	5.6	1.6	0.008
Type II	15	3.5	1.3	0.005
Type III	15	1.2	0.82	0.0018

1 in. = 25.4 mm

of 1.5. Applying the periodic overload to the basic history (Type III) lowered the FCGR by a factor of about five. As the mean decreased, the ratio of the standard deviation to mean, which is the coefficient of variation, increased substantially, for the constant ΔF measurement interval shown. The mean change in crack length (Δa) for 15 flights is shown in Table 2 for the three loading conditions.

The comparison between the coefficients of variation, ν , for the three loading conditions are shown in Table 3. The mean Δa for 15 flights, along with the coefficients of variation for the three types of load histories are given in the first row of the table. The coefficient of variation increased as the change in crack length decreased. In the last two rows of Table 3, coefficients of variation are comparable for similar amounts of growth, as indicated by the mean Δa . This comparison was made possible by omitting points before differentiating the FCG data. The comparison was only possible for crack length intervals resulting from multiples of 15 flights. As in the extensive study of the Type I condition, the coefficient of variation was seen to decrease as the measurement interval size was increased for all three test conditions. For Δa approximately equal to 0.584 mm (0.023 in.) the

TABLE 3—Comparison between coefficients of variation (ν) and crack growth measurement intervals (Δa) for three stress intensity factor histories.

	Type I History			Type II History			Type III History		
	ΔF	mean Δa , in.	ν^a	ΔF	mean Δa , in.	ν^a	ΔF	mean Δa , in.	ν^a
Variable	15	0.008	0.28	15	0.005	0.37	15	0.0018	0.68
~ 0.008	15	0.008	0.28	30	0.010	0.24	75	0.0075	0.24
~ 0.023	45	0.023	0.15	75	0.025	0.14	195	0.022	0.12

^a Coefficient of Variation = $\frac{\text{standard deviation}}{\text{mean}}$

1 inch = 25.4 mm

measurement precision ratio as defined as the crack length measurement interval divided by the crack length measurement precision (ϵ) is 15. The coefficients of variation for this increment size are also below 20 percent for all test conditions, irrespective of the mean FCGR.

Effect of Load Variations

Since the only difference between the Type I and Type II SIF histories was in the magnitude of the SIF, the mean FCGR data for these two histories were used to establish the coefficients of a power law equation written in the following form [6,11]:

$$\frac{da}{dF} = C (K_{\max})^p \quad (1)$$

The power law exponent (p) was determined to be 2.58. This exponent value is quite similar to that (2.65) derived using least squares procedures applied to FCGR data generated over the same interval of K_{\max} using a slightly more complicated type of stress history [6]. The loadings were held constant for the Ref 6 tests, that is, K_{\max} increased with crack length.

To sense the impact of small variations in stress history control, on FCGR behavior, Eq 1 was employed. A 2 percent variation in stress (or SIF) level would change the rate of FCGR by about 5 percent. Since in this investigation, stress (or load) levels in the test histories were controlled to within ± 1 percent of desired levels, it would appear that the variation in loading contributed only a small fraction to the total variability in FCGR data. Less accurate stress control will result in corresponding greater variability in FCGR data; and, if biased will affect the mean FCGR behavior as described by Eq 1.

Conclusions

As a result of this investigation, in which the measurement precision ratio was defined as the crack length measurement interval (Δa) divided by the crack length measurement precision (ϵ), the following conclusions were derived from an analysis of fatigue crack growth data collected under stress intensity factor control conditions.

1. The coefficient of variation for FCGR data obtained using the seven-point incremental polynomial method is independent of the measurement precision ratios for ratios greater than five. The coefficient of variation for FCGR data generated herein by this numerical differentiation method was about 8 percent.

2. As the measurement precision ratio increases, the coefficient of variation for FCGR data obtained using the secant method of differentia-

tion decreases toward the level of the FCGR coefficient of variation associated with the seven-point incremental polynomial method.

3. To achieve coefficients of variation in FCGR data generated via the secant method at levels below 20 percent, it is necessary to have a measurement precision ratio ($\Delta a/\epsilon$) greater than 15.

4. The coefficient of variation in FCGR data obtained using the secant method is independent of stress intensity factor history when the measurement precision ratio is controlled at a fixed level.

5. One of the most dangerous experimental variables that must be controlled during a test is the level of loading because small differences in load control can affect the mean as well as the variability of the FCGR data. The other variables investigated do not appear to introduce systematic errors in the FCGR data.

References

- [1] Paris, P. C. in *Proceedings*, 10th Sagamore Army Materials Research Conference, Syracuse University Press, 1964, pp. 107-132.
- [2] Wood, H. A., Gallagher, J. P., and Engle, R. M., *The Mechanics of Fracture*, American Society of Mechanical Engineers, Vol. 19, 1976, pp. 171-190.
- [3] Clark, W. G., Jr. and Hudak, S. J., Jr., *Journal of Testing and Evaluation*, Vol. 3, No. 6, 1975, pp. 454-476.
- [4] Wei, R. P., Wei, W., and Miller, G. A., "Considerations of Measurement Precision and Data Processing Procedures for Fatigue Crack Growth Testing and Analysis," submitted to *ASTM Journal of Testing and Evaluation*, for review, 1978.
- [5] Potter, J. M., "An Experimental and Analytical Study of Spectrum Truncation Effects," AFFDL-TR-73-117, Air Force Flight Dynamics Laboratory, Wright-Patterson Air Force Base, Ohio, Feb. 1974.
- [6] Gallagher, J. P. and Stalnaker, H. D., *Journal of Aircraft*, Vol. 15, No. 2, Feb. 1978, pp. 114-120.
- [7] Feddersen, C. E., discussion in *Plane Strain Crack Toughness Testing of Metallic Materials*, ASTM STP 410, American Society for Testing and Materials, 1969, pp. 77-79.
- [8] Virkler, D. A., Hillberry, B. M., and Goel, P. K., "An Investigation of Statistical Distribution of Fatigue Crack Propagation Data," presented at American Society for Testing and Materials Committee Meeting E-24.04, Norfolk, Va., 24 May 1977.
- [9] Virkler, D. A., "The Statistical Nature of Fatigue Crack Propagation," M.S. thesis, Purdue University, Lafayette, Ind., 1978.
- [10] Artley, M. E. and Stalnaker, H. D., "Variability in Flight-by-Flight Crack Growth Rate Behavior," AFFDL-TM-78-9, Air Force Flight Dynamics Laboratory, Wright-Patterson Air Force Base, Ohio, Jan. 1978.
- [11] Gallagher, J. P., *Experimental Mechanics*, Vol. 16, No. 11, Nov. 1976, pp. 486-494.

Application of Fracture Mechanics to Damage Accumulation in High Temperature Fatigue

REFERENCE: Douglas, M. J. and Plumtree, A., "Application of Fracture Mechanics to Damage Accumulation in High Temperature Fatigue," *Fracture Mechanics, ASTM STP 677*, C. W. Smith, Ed., American Society for Testing and Materials, 1979, pp. 68-84.

ABSTRACT: A unified theory for life predictions based upon damage accumulation has been applied to high-temperature, high-frequency, low-cycle fatigue tests of austenitic iron-nickel-chromium alloys (similar to Alloy 800). Damage may be related to the formation of cracks and its accumulation is shown to be a function of the fatigue crack growth rate. Damage accumulation data are reported for small axially loaded smooth specimens for varying strain levels. This in turn may be correlated to an elastic-plastic fracture mechanics analysis through the concept of the J-integral (the J-values being estimated from stress-strain data). It is suggested that relating standard fracture-mechanics concepts to damage accumulation in small specimens will be useful in obtaining a better understanding of the fatigue process.

KEY WORDS: damage accumulation, high temperature fatigue, fatigue crack growth rate, J-integral, Alloy 800, fatigue (materials), crack propagation.

The application of damage concepts in the field of rupture has proved to be very useful in failure prediction at high temperatures [1-7].³ Such applications must deal with the complex problem of creep-fatigue interaction.

Life prediction methods commonly employed for high-temperature fatigue may be separated into four main areas. These include modifications of low-temperature relationships [8,9], ductility exhaustion [10], strain-range partitioning [11], and linear summation of time and cycle

¹ Project engineer, Procter and Gamble, Hamilton, Ontario, Canada.

² Professor, Department of Mechanical Engineering, University of Waterloo, Waterloo, Ontario, Canada.

³ The italic numbers in brackets refer to the list of references appended to this paper.

ratios [12,13]. Although damage theory first introduced by Kachanov [14] was used for prediction of pure creep rupture, the theory has been modified to the point where a unified model exists for fatigue-creep interaction based upon nonlinear accumulation [2].

Since the present work deals only with pure fatigue damage accumulation at high temperature, the interaction aspects will not be dealt with here although the authors will concern themselves with that problem at a later date.

The differential equation of damage evolution during strain controlled fatigue is given by

$$\frac{\delta D}{\delta N} = \frac{f(D)}{(p+1)N_F} \quad (1)$$

where

$$\begin{aligned} D &= \text{damage,} \\ N &= \text{number of cycles,} \\ N_F &= \text{number of cycles to failure at a given strain range, and} \\ f(D) &= [1-D]^{-p}. \end{aligned}$$

The constant p is material and temperature dependent, which may be obtained from a relation between damage and cyclic plastic behavior. Using boundary conditions such that $D = 0$ when $N = 0$ and $D = 1$ at $N = N_F$, integration of Eq 1 for the evolution of fatigue damage at constant strain amplitude yields

$$D = 1 - \left\{ 1 - \frac{N}{N_F} \right\}^{\frac{1}{p+1}} \quad (2)$$

The background and derivation of Eqs. 1-3 are given in Appendix I, which also includes the derivation of equations for creep and fatigue damage under stress control. The application of damage theory to high temperature fatigue has yielded predictions within 60 percent [15].

In applying damage concepts, the problem is to define the term, "damage." In this case, as in Refs 1 and 2, damage is regarded as the formation and growth of a dominant crack. If indeed this hypothesis is correct, it should be possible to establish a direct relationship between the damage accumulation rate (dD/dN) during cycling and the fatigue crack growth rate (da/dN). This latter parameter generally is expressed using fracture mechanics methods.

It is the purpose of this study to establish a relationship between damage and crack size, and show that the damage accumulation rate is proportional to the fatigue crack growth rate. Subsequently, the damage

accumulation rate will be correlated with the J-integral through an elastic-plastic analysis.

Experimental Procedure

Material and Specimens

The material tested was an austenitic iron-nickel-chromium alloy Sanicro 31 (trade name of Sandvik AB) containing 0.043 percent carbon, 21.7 percent chromium, 33.2 percent nickel, 0.33 percent titanium, 0.20 percent aluminum. This is a high temperature alloy, similar to (Incoloy) Alloy 800, which is used where corrosion resistance and strength are required at elevated temperatures.

The fatigue specimens were machined with threaded ends for gripping and a reduced diameter cylindrical test section, 7.5 mm long and 4.85 mm in diameter. These specimens were identical to those used for earlier damage prediction studies [1,2].

Procedure

All tests were conducted on a closed loop electrohydraulic servocontrolled testing system. The tests were carried out under strain control and the testing procedure used for controlling strain was similar to that described in Ref 16. The testing variable was strain range with the cyclic deformation rate and temperature being held constant at $2.4 \times 10^{-1} \text{ s}^{-1}$ and 600° C respectively. Under these conditions the deformation of this material was found to be entirely time independent, so that time dependent damage (oxidation or creep) may be neglected [17]. The stress response was monitored continuously throughout the test in order to determine the amount of damage according to

$$D = 1 - \frac{\Delta\sigma}{\Delta\sigma^*} \quad (3)$$

where $\Delta\sigma$ is the stress range response at any particular number of cycles, N , and $\Delta\sigma^*$ is the stress range at saturation. The derivation of Eq 3 is included in Appendix I. Once the various values of D were determined for given numbers of cycles, then it was possible to evaluate the exponent p in Eq 2.

Several tests were conducted in order to establish a relationship between damage accumulation and crack growth rate. This required that a suitable procedure be found for detection and size evaluation of the cracks. The technique developed involved the use of a dye penetrant and ultraviolet light. This technique is used extensively in the power industry where the detection of very fine hair-line cracks in turbine blades

is essential. Due to the nature of the conditions required for examination (that is, cooling and reheating) none of the specimens was interrupted more than three times before failure, and in general each specimen was interrupted only once before failure took place.

Surface crack lengths and crack depths were measured using an optical microscope equipped with a measuring eyepiece; measurement was achieved in the following manner: on removal of the specimen from the testing machine, the threaded ends were masked with tape and the reduced test section was treated with a penetrating dye sensitive to ultraviolet light. Sufficient time was allowed (approximately $\frac{1}{2}$ h) for the dye to penetrate all surface defects and then excess dye was removed with alcohol and a lint free cloth. At this time a developer was applied to the test section which drew out any dye trapped in the surface defects resulting in a visual observation of a yellow dye on a white background outlining the surface defects. The developer then was removed leaving behind a residue which was clearly visible. Alternatively, the specimen could be examined directly under the ultraviolet light without a developer being applied. Surface crack lengths then were measured under the ultraviolet light using a low powered optical microscope equipped with a measuring eyepiece. Crack depths were measured upon fracture. The dye penetrant had the effect of discoloring the oxide on the fracture surface. When the test was stopped and dye applied, the extent of crack penetration was defined clearly. This procedure was verified by stopping a test followed by sectioning the specimen in order to show that the crack size corresponded with that determined using the dye penetrant. It should be noted that in general only one dominant crack developed after half life had elapsed.

The crack profile always was curved slightly, neither semicircular nor parabolic, and since no correction factor was available for this geometry, it was decided that it could best be represented as a planar surface crack, where the stress intensity factor ΔK , is expressed using the formula

$$\Delta K = 1.12 \Delta\sigma \sqrt{\pi a} \quad (4)$$

where a is the crack depth. However, rather than using ΔK , it was decided to use ΔJ [18], since the crack tip plastic zone could not be regarded as being negligibly small.

The J-integral has been shown to be a promising correlation factor for fatigue crack growth under plastic conditions [19, 20, 21]. The interpretation of J for the elastic-plastic case is that it gives a measure of the crack tip strain field. For the present study, the derivation of J is similar to that used by Dowling [19]. The final result of the analysis is given in Appendix II, which yields

$$\Delta J = 7.88 a \Delta W_e + 7.60 a \Delta W_p \quad (5)$$

where ΔW_e and ΔW_p are the elastic and plastic strain energies.

Results and Discussion

Damage evolution for constant strain conditions is given in Eq 2 [see also Appendix I]. However, the exponent, p , is required. This may be determined by monitoring the stiffness change as a crack forms and grows through the specimen [Appendix I]. More simply, the change of load (or stress amplitude) for a given displacement (or strain) will also yield the change in stiffness. Hence, by following the stress response of four tests carried out at total strain ranges of 1.54 and 2.2 percent at 600° C, it was possible to derive the damage evolution. Under steady-state conditions the stress response, $\Delta\sigma^*$, was monitored and once the stiffness of the specimen decreased due to the presence of a crack, the stress response, $\Delta\sigma$, at the corresponding number of cycles was recorded allowing the amount of damage to be determined according to Eq 3. Using the relation

$D = 1 - \{1 - N/N_F\}^{\frac{1}{p+1}}$ [that is, Eq 2] the log-log plot of $(1 - D)$ [from Eq 3] versus $\{1 - N/N_F\}$ yielded the value of p for the given strain range: for $\Delta\epsilon_T = 2.2$ percent, $p = 17$ and for $\Delta\epsilon_T = 1.54$ percent, $p = 27$. Damage versus the cycle ratio for both strain rates is plotted in Fig. 1 using these exponents. This plot shows that for a given life ratio the accumulated damage is dependent upon strain level.

Provided that it is possible to derive a relationship between damage and crack size, then it follows that the crack size for a given life ratio should be dependent upon strain level. The results of measuring the surface crack length, ℓ , against the crack depth, a , for various life ratios at the two strain levels are given in Table 1 and shown in Fig. 2. It is apparent that a critical crack length, ℓ^* , exists below which the crack size or depth, a , is very small and more importantly does not increase significantly with

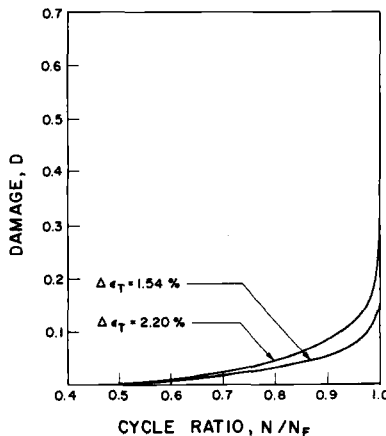


FIG. 1—Damage curves for $\Delta\epsilon_T=1.54$ percent ($N_F=2700$) and $\Delta\epsilon_T=2.2$ percent ($N_F=900$).

TABLE 1—Crack sizes for given life ratios.

Test No.	$\Delta\epsilon_T$, %	Cycle Ratio at Measurement	ℓ	a	Cracked Area, mm ²
			Surface Crack Length, mm	Crack Depth Max, mm	
T4-C	1.54	0.50	<0.76	0.00	0
		0.52	0.76	<0.03	0
		0.96	5.46	1.50	62
		0.99	8.89	3.25	210
T1-C	1.54	0.83	2.92	0.56	19
T3-C	1.54	0.88	3.12	0.74	25
Section-1	1.54	0.95	4.45	1.07	60
T2-C	1.54	0.99	8.00	2.64	170
T5-C	2.2	0.51	<0.76	0.00	0
		0.99	8.13	2.84	184
T9-C	2.2	0.85	3.18	0.71	30
T7-C	2.2	0.90	3.81	0.99	48
T6-C	2.2	0.93	5.33	1.42	68
T8-C	2.2	0.96	5.56	1.98	101
		0.99	9.4	3.51	239

an increase in ℓ . At life ratios of $N/N_F < 0.5$ the cracks or damaged areas were extremely small and highly localized. For $N/N_F \geq 0.5$ these localized cracks began to link together and form one common crack front which then penetrated into the specimen. Stopping the test prior to 0.5 N_F resulted in extreme difficulty in repropagating the small cracks associated with the damaged regions.

It is suggested that a critical amount of damage or a specific incubation period in high-frequency cycling (corresponding to a critical number of cycles, N^*) is required for propagation. In this case the critical amount of damage, or crack size, corresponded to approximately half life, that is,

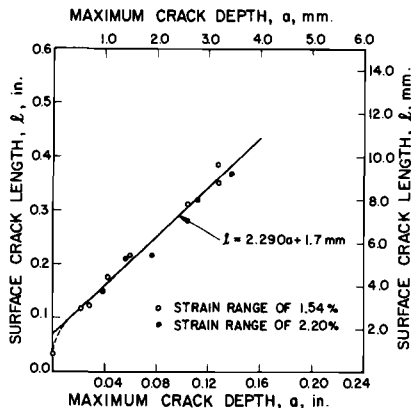


FIG. 2—Relationship between surface crack length and maximum crack depth.

$N^* = 0.5 N_F$. Results of work conducted by Kunio and Yamada [22], indicated that many small nonpropagating cracks existed below a critical crack size. Exceeding this level resulted in propagation of a single catastrophic crack.

The plot of crack depth against life ratio for $\Delta\epsilon_T = 1.54$ and 2.2 percent is shown in Fig. 3, and it appears that the crack depth for a given life ratio is dependent upon strain level. The difference between the present data and that obtained by Dowling [19], using a similar technique at room temperature, may be explained by the fact that when the exponent in Eq 2 becomes large ($p \geq 15$) the damage curves for the two different strain ranges approach each other, and that the scatter band obtained in Ref 19 is large enough that it could possibly represent separate damage curves. A close observation of the data presented in Ref 19, suggests that for a given life ratio the crack size increases with strain.

In order to clarify the hypothesis of damage being related to crack size it was necessary to determine whether a relationship existed between the damage accumulation rate (dD/dN) and the fatigue crack growth rate (da/dN). This required that the two parameters be correlated using an elastic-plastic fracture mechanics analysis. As mentioned previously, it was decided to use ΔJ [18,23], since the crack tip plastic zone could not be considered as being negligibly small.

Crack growth data were obtained from Fig. 3 (a versus N/N_F) by the difference method. These data were then correlated with the J-integral. The plot of $\log(da/dN$ or dD/dN) versus ΔJ shown in Fig. 4 indicates that a typical Paris type relationship is obeyed such that,

$$da/dN = C(\Delta J)^n \quad (6)$$

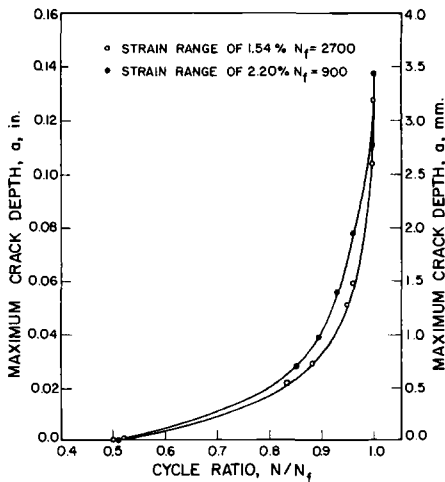


FIG. 3—Variation in crack depth with strain level for different life fractions.

where C and n are material constants which are dependent upon the environment. For this present study the values of C and n are given in Fig. 4. It follows from the preceding discussion that given $D = f(a)$ and using the difference method to obtain the slope of the damage curve for a given number of cycles (Fig. 1), then the damage accumulation rate dD/dN must be dependent upon the fatigue crack growth rate. This is shown to be the case in Fig. 4. Hence for a given amount of damage or given cycle ratio it should be possible to determine the surface crack length, ℓ , and crack depth, a .

A simple empirical relationship between crack size and damage was found for the specimens tested. By determining the cracked area, which is dependent upon crack size a , and dividing by twice the original cross-sectional area, it was possible to establish a relationship between this parameter and the damage, as shown in Fig. 5 for the two strain levels of 1.54 and 2.2 percent. The data points obtained from the crack size measurements fall very close to the damage evolution curve derived from the stress response (or stiffness) measurements which has been replotted from Fig. 1. Both the stress response (or stiffness) and crack size measurements indicated that below a critical number of cycles ($N^* = 0.5 N_F$), the amount of damage was extremely small. In fact, it would appear that

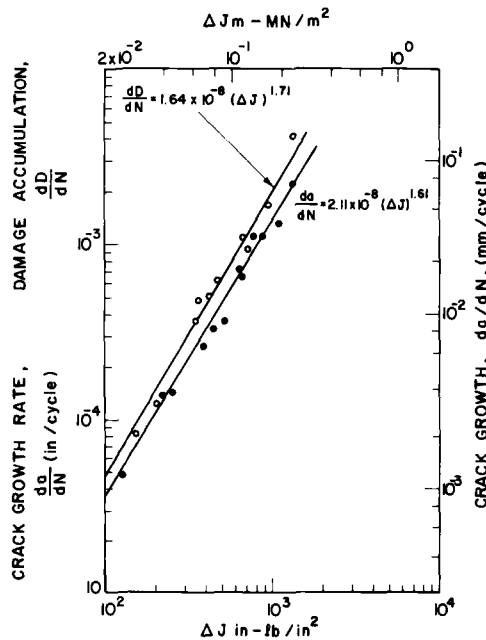


FIG.4—Relationship between crack growth rate (da/dN), damage accumulation rate (dD/dN) and ΔJ .

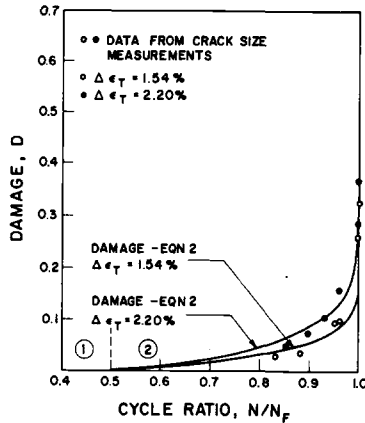


FIG. 5—Plot of damage obtained from crack size measurements at two strain levels for different life fractions superimposed on damage curve of Fig. 1.

significant damage evolution starts only after the critical number of cycles. This has been verified independently by Douglas [24] and Plumtree and Persson [17]. Creep or low frequency cycles ($\nu \sim 0.005$ Hz) was preceded by varying numbers of cycles in fatigue at 600°C and in each case a complete and unaffected creep life or life under low frequency cycling conditions was observed when the amount of prior fatigue was less than or equal to $0.5 N_F$.

It is suggested then that the damage curve for this present work may be divided into two regimes as indicated in Fig. 5. Regime 1 ($N/N_F < 0.5$) corresponds to the development of several small and localized cracks or damaged areas with surface lengths from about 0.5 to 0.8 mm. Regime 2 corresponds to the formation and growth of a common crack front when $N \geq N^*$. The smaller cracks link together and the resulting main crack penetrates into the specimen eventually causing failure.

Conclusions

1. A relationship between crack size measurements and damage obtained by using the concepts of nonlinear damage accumulation has been established for the fatigue crack growth behavior of Sanicro 31 (similar to Alloy 800) at 600°C .

2. The fatigue damage accumulation rates under elastic-plastic conditions have been found to be related to the J-integral through the empirical equation $dD/dN = C(\Delta J)^n$.

3. The crack size for a given life fraction appears to vary with strain level. This effect substantiates predictions derived from the damage model.

4. A critical number of cycles, N^* , has been identified for these high-temperature fatigue tests. When $N < N^*$, several small localized cracks were present. On exceeding N^* , the cracks joined together to form a common front and a single crack propagated to failure. For the present work, this critical number of cycles occurs at approximately half life.

Acknowledgments

The authors would like to thank N-G. Persson, Sandvik AB, Sweden, for providing the Sanicro 31 specimens and for many valuable discussions. One of the authors (A. Plumtree) wishes to acknowledge the National Sciences and Engineering Research Council of Canada for providing financial assistance through Grant A-2770. The authors would like to express their thanks to Linda McIntosh for typing the manuscript.

APPENDIX I

Application of Damage Concepts

In 1958 Kachanov [14] proposed a theory of brittle rupture based on a concept of what he called the "continuity," D , of the material; as time passes damage accumulates which changes the proportion of material available to carry load. If the load is constant, the average stress is increased according to the amount of damage until, eventually, continuity is destroyed and rupture occurs.

If the specimen of initial cross-sectional area A_0 is subjected to a load P the initial stress is

$$\sigma = \frac{P}{A_0}$$

After time t , during which the specimen is damaged, the cross-sectional area is reduced according to

$$A_t = A_0(1 - D) \quad (7)$$

so that the stress at time t is

$$\sigma_t = \frac{P}{A_t} = \frac{\sigma}{(1 - D)} \quad (8)$$

To enable the variation of damage with time to be calculated, Kachanov assumed a power relationship between the continuity and stress which has since been modified for ductile materials. Considering intergranular creep, the evolution of damage may be expressed by the modified Kachanov equation

$$\frac{dD}{dt} = \left\{ \frac{|\sigma|}{C(1-D)} \right\}^r [1-D]^{-q} \quad (9)$$

which becomes important during the tertiary creep stages. Obviously, the amount of damage is regarded as being very small during the primary and secondary stages of a pure creep test. Assuming that the Norton creep equation applies, then for

$$\text{Secondary creep: } \sigma = K \dot{\epsilon}_p^* \frac{1}{W} \quad (10)$$

and for

$$\text{Tertiary creep: } \frac{\sigma}{1-D} = K \dot{\epsilon}_p \frac{1}{W} \quad (11)$$

where

$\dot{\epsilon}_p$ = plastic strain rate,
 $\dot{\epsilon}_p^*$ = steady-state plastic strain rate, and
 K and W = material constants.

The damage evolution can then be obtained from Eqs 10 and 11 such that

$$D = 1 - \left(\frac{\dot{\epsilon}_p^*}{\dot{\epsilon}_p} \right)^{\frac{1}{W}} \quad (12)$$

Knowing this evolution from a creep test, $(r + q)$ is calculated by identification with the integrated damage Eq 9 for constant stress, that is

$$D = 1 - \left\{ 1 - \frac{t}{t_c} \right\}^{\frac{1}{r+q+1}} \quad (13)$$

t_c being the time to rupture and the solution of the damage equation for $D = 1$ when $t = t_c$, gives

$$t_c = \frac{1}{r + q + 1} \left[\frac{\sigma}{C} \right]^{-r} \quad (14)$$

which allows the possibility of determining r from isothermal curves $\sigma(t_c)$.

The differential equation of evolution of transgranular cracks during fatigue is of the same type as the creep damage Eq 9, in this case

$$\frac{\delta D}{\delta N} = \left\{ \frac{\sigma_M - \bar{\sigma}}{B(\bar{\sigma}) [1 - D]} \right\}^\beta f(D) \quad (15)$$

where

N = number of cycles

σ_M = maximum stress during the cycle, and

$\bar{\sigma}$ = mean stress, also

$$f(D) = [1 - D]^{-p}$$

B , β , p are temperature dependent material characteristics which may be obtained from the relation of cyclic plastic behavior coupled with damage. Assuming that pure fatigue (no effect of time) corresponds to plastic behavior between stress range $\Delta\sigma$ and strain range $\Delta\epsilon_p$, then for negligible damage under stabilized conditions

$$\Delta\sigma = K \Delta\epsilon_p^* \frac{1}{M} \quad (16)$$

and applying Eq 8 to cyclic conditions with damage present after stabilization

$$\frac{\Delta\sigma}{1 - D} = K \Delta\epsilon_p^* \frac{1}{M} \quad (17)$$

where K and M are material characteristics under plastic conditions. Then from stress controlled fatigue tests

$$D = 1 - \left(\frac{\Delta\epsilon_p^*}{\Delta\epsilon_p} \right)^{\frac{1}{M}} \quad (18)$$

The thermodynamic approach using damage as an internal variable directly leads to differential equations of evolution with stress being the controlling variable. However, in practice many tests and applications are

conducted under strain control, hence prediction using damage equations written in terms of strain must be considered. These equations may be deduced from the earlier equations using stress-strain relationships.

Pure fatigue at high frequencies results in strain behavior which is purely plastic, having neither frequency nor wave shape effect. Given the stress-strain range Eq 17, the strain dependent fatigue damage equation can be obtained by simple substitution of

$$\frac{\sigma_M - \bar{\sigma}}{1 - D} = \frac{\Delta\sigma}{2[1 - D]} = \frac{K}{2} \Delta\epsilon_p^{\frac{1}{M}} \quad (19)$$

in Eq 15 giving

$$\frac{\delta D}{\delta N} = \left[\frac{K}{2B} \right]^\beta \Delta\epsilon_p^{\frac{\beta}{M}} [1 - D]^{-p} \quad (20)$$

The number of cycles to failure N_F for a constant amplitude $\Delta\epsilon_p$ in pure fatigue is obtained by integration using the conditions:

$$N = 0 \rightarrow D = 0 \text{ and } N = N_F \leftarrow D = 1$$

$$N_F = \frac{1}{[p + 1] \left[\frac{K}{2B} \right]^\beta \Delta\epsilon_p^{\frac{\beta}{M}}} \quad (21)$$

This function $N_F(\Delta\epsilon)$ is considered as characteristic for the material and

$$\frac{\delta D}{\delta N} = \frac{[1 - D]^{-p}}{[p + 1]N_F(\Delta\epsilon)} \quad (22)$$

and the evolution of damage at constant strain amplitude is

$$D = 1 - \left\{ 1 - \frac{N}{N_F} \right\}^{\frac{1}{p+1}} \quad (23)$$

Fatigue failure criteria are completely defined by the temperature dependent functions: $N_F(\Delta\epsilon)$ and $p(\Delta\epsilon)$. To obtain numerical values, reference tests must be conducted and the results applied to the mathematical models.

The basic function $N_F(\Delta\epsilon)$ is obtained by carrying out very high-frequency tests ($\nu \geq 5$ Hz) at constant strain amplitude. About five to ten tests are needed to characterize the material and β/M is obtained from the slope of a log-log plot of $N_F(\Delta\epsilon_T)$.

To obtain p , the evolution of damage is required. Among different methods [25,26], the simplest is to record the change of stress amplitude during the five or ten different tests and to derive the damage evolution from the stress-strain Eq 17 which can be arranged to give

$$\Delta\sigma = [1 - D] K \Delta\epsilon_p^{\frac{1}{M}} \quad (24)$$

If $\Delta\sigma^*$ is the value of $\Delta\sigma$ at steady state or stabilized conditions when the damage is negligible then

$$\Delta\sigma^* = K \Delta\epsilon_p^{\frac{1}{M}} \quad (25)$$

Then under constant strain conditions

$$D = 1 \approx \frac{\Delta\sigma}{\Delta\sigma^*} \quad (26)$$

Using the relation $D = 1 - \{1 - N/N_F\}^{1/(p+1)}$ the log-log plot of $(1 - D) [= (\Delta\sigma/\Delta\sigma^*)]$ from one test versus $(1 - N/N_F)$ gives the slope $1/p + 1$ from which the value of p is known for the strain range considered.

To avoid any confusion with cyclic hardening or softening effects, it may be preferable to evaluate D by considering the stiffness of the part with and without the presence of cracks, or more correctly, the modulus of elasticity measured during the reversal of a hysteresis stress-strain loop. Hence when damage is negligible

$$\sigma = E^* \epsilon \quad (27)$$

with a crack present

$$\sigma_t = E \epsilon \quad (28)$$

Substituting Eq 8 into Eq 28 then

$$\frac{\sigma}{1 - D} = E \epsilon \quad (29)$$

Hence for a constant strain

$$D = 1 - E/E^* \quad (30)$$

Considering the stiffness, then

$$D = 1 - \frac{R}{R^*} \quad (31)$$

where R is the stiffness of the specimen when a crack is present and R^* is the stiffness in a crack-free or damage-free specimen.

APPENDIX II

Determination of ΔJ

The method for determining ΔJ is similar to that which is outlined in Ref 19.

The crack extension force or energy release rate (G) is not affected by the plastic deformation at the crack tip when the crack tip plasticity is small. In this case G follows from the elastic stress field

$$\Delta G = \Delta J_{\text{elastic}} = \frac{\Delta K^2}{E} = \frac{\Delta \sigma^2 \pi a}{E} \tag{32}$$

where E is Young's modulus.

From Fig. 6, which is an idealized stress-strain relationship, the elastic strain energy may be derived

$$\Delta W_e = \Delta \sigma^2 / 2E \tag{33}$$

For a linear surface crack, the stress intensity is given as $\Delta K = 1.12 \sigma \sqrt{\pi a}$ and for an embedded crack

$$\Delta K = 1.12 \sigma \sqrt{\pi a} F \tag{34}$$

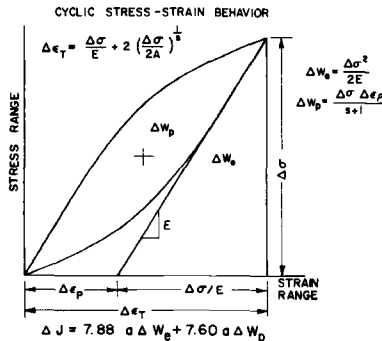


FIG. 6—Estimation of ΔJ and corresponding stress-strain data.

Where F is the crack shape factor. In the present work, the crack profile was constant for nearly the whole of the fatigue life, remaining slightly curved, neither semicircular nor parabolic. Since the value of F is not available, it was decided to represent the crack by the planar surface crack shape factor ($F=1$). Although the absolute values of $\Delta J_{\text{elastic}}$ and $\Delta J_{\text{plastic}}$ will be affected, this will not influence the comparison of dD/dN and da/dN using a common ΔJ scale since the latter is multiplied by F^2 . Hence the crack shape factor is a scale factor once $\Delta J_{\text{elastic}}$ and $\Delta J_{\text{plastic}}$ are added.

Substituting Eq 33 in Eq 32 and correcting for crack geometry (Eq 34), then

$$\Delta J_{\text{elastic}} = 7.88 a \Delta W_e \quad (35)$$

An estimate for the plastic solution of ΔJ has been made by Shih and Hutchinson [27] for a center cracked strip in plane stress

$$\Delta J_{\text{plastic}} = 2\pi f(s) a \Delta W_p \quad (36)$$

where $f(s)$ is a function of the strain hardening exponent and ΔW_p is the plastic strain energy. Accompanying work on the same alloy at 600° C [24] was used to determine the cyclic work hardening exponent, $s = 0.38$. Following the work of Shih and Hutchinson [27] the function of the strain hardening exponent $f(s)$ was estimated to be 1.12 for $s=0.38$. An approximation for ΔW_p , the plastic strain energy is given in Fig. 6,

$$\Delta W_p = \frac{\Delta\sigma \Delta\epsilon_p}{s + 1} \quad (37)$$

Assuming that the combined surface and crack shape correction factors used for the linear elastic case are also applicable to the plastic case, then Eq 36 is modified to give,

$$\Delta J_{\text{plastic}} = 7.6 a \Delta W_p \quad (38)$$

Shih and Hutchinson [27] suggest that J solutions may be approximated by adding the two elastic and plastic solutions. Following this, the summation of Eqs 35 and 38 gives

$$\Delta J = 7.88 a \Delta W_e + 7.6 a \Delta W_p \quad (39)$$

which was used in the present work.

References

- [1] Plumtree, A., "Creep/Fatigue Interaction in Type 304 Stainless Steel at Elevated Temperatures," *Fatigue 1977*, Cambridge, March 1977; also *Metal Science*, Vol. 11, 1977, p. 425.
- [2] Lemaitre, J. and Plumtree, A., "Application of Damage Concepts to Predict Creep Fatigue Failure," Pressure Vessel Conference, American Society of Mechanical Engineers, Montreal, 1978.
- [3] Hayhurst, D. R., *International Journal of Mechanical Sciences*, Vol. 18, 1976, pp. 75-83.
- [4] Leckie, F. A. and Wojewodzki, W., *Journal of Mechanics and Physics of Solids*, Vol. 24, 1976, pp. 239-250.
- [5] Hult, J. and Broberg, H., 2nd National Bulgarian Congress on Theoretical and Applied Mechanics, Vol. 2, Varna, 1976, pp. 263-272.
- [6] Chrzanowski, M., *Swedish Solid Mechanics Reports*, Gothenburg, 1973.
- [7] Chrzanowski, M., *International Journal of Mechanical Science*, Vol. 18, 1976, pp. 69-73.
- [8] Manson, S. S., *International Journal of Fracture Mechanics*, Vol. 2, 1966, p. 327.
- [9] Coffin, L. F., Jr., *Proceedings*, Air Force Conference on Fatigue and Fracture of Aircraft Structure and Materials, AFFDL 70-144, Air Development Laboratory, 1970, p. 301.
- [10] Polhemus, J. F., Spaeth, C. E., and Vogel, W. H. in *Fatigue at Elevated Temperatures*, ASTM STP 520, American Society for Testing and Materials, 1973, p. 625.
- [11] Manson, S. S., in *Fatigue at Elevated Temperatures*, ASTM STP 520, American Society for Testing and Materials, 1973, p. 744.
- [12] Taira, S., *Creep in Structures*, N. J. Hoff, Ed., Springer-Verlag, Berlin, 1962, p. 96.
- [13] Spera, D. A., in *Fatigue at Elevated Temperatures*, ASTM STP 520, American Society for Testing and Materials, 1973, p. 648.
- [14] Kachanov, L. M., in *Problems of Continuum Mechanics*, Society for Industrial and Applied Mathematics, Philadelphia, 1961, pp. 202-218.
- [15] Plumtree, A., *Canadian Metallurgical Quarterly*, in press.
- [16] Abdel-Raouf, H., Plumtree, A., and Topper, T. H., in *Cyclic Stress-Strain Behavior—Analysis, Experimentation and Failure Prediction*, ASTM STP 519, American Society for Testing and Materials, 1973, pp. 28-57.
- [17] Plumtree, A. and Persson, N. G., "Creep-Fatigue Interaction in an Austenitic Fe-Ni-Cr Alloy at 600° C," 4th International Conference on Fracture, Vol. 2, Waterloo, Canada, 1977, p. 821.
- [18] Rice, J. R., *Journal of Applied Mechanics; Transactions*, American Society of Mechanical Engineers, Vol. 35, June 1968, pp. 379-386.
- [19] Dowling, N. E., "Crack Growth During Low Cycle Fatigue of Smooth Axial Specimens," Scientific Paper 76-1E7-PALFA-P2, Mechanics Department, 16 June 1976.
- [20] Dowling, N. E., and Begley, J. A. in *Mechanics of Crack Growth*, ASTM STP 590, American Society for Testing and Materials, 1976, pp. 82-103.
- [21] Dowling, N. E., in *Cracks and Fracture*, ASTM STP 601, American Society for Testing and Materials, 1976, pp. 19-32.
- [22] Kunio, T. and Yamada, K., "Microstructural Aspects of the Threshold Condition of Non-Propagating Fatigue Cracks in Martensitic Ferritic Structure," presented at ASTM-NBS-NSF Symposium on Fatigue Mechanisms, Kansas City, May 1978.
- [23] Paris, P., in *Flow Growth and Fracture*, ASTM STP 631, American Society for Testing and Materials, 1977, pp. 3-27.
- [24] Douglas, M. J., "Damage Accumulation in a High Temperature Austenitic Iron-Nickel-Chromium Alloy," M.A. Sc. thesis, Department of Mechanical Engineering, University of Waterloo, 1978.
- [25] Lemaitre, J. and Duffailly, J., "Models and Identification of Plastic Damage in Metals," 3rd French Congress of Mechanics, Grenoble, 1977.
- [26] Jaliniere, J. M., Baudalet, B., and Argemi, R., *Journal of Material Sciences*, Vol. 13, 1978, pp. 1142-1145.
- [27] Shih, C. F. and Hutchinson, W. J., "Fully Plastic Solutions and Large Scale Yielding Estimates for Plane Stress Crack Problems," Report No. DEAP-S-14, Division of Engineering and Applied Physics, Harvard University, Cambridge, Mass., 1975.

R. L. Tobler,¹ R. P. Mikesell,¹ and R. P. Reed¹

Cryogenic Effects on the Fracture Mechanics Parameters of Ferritic Nickel Alloy Steels

REFERENCE: Tobler, R. L., Mikesell, R. P., and Reed, R. P., "Cryogenic Effects on the Fracture Mechanics Parameters of Ferritic Nickel Alloy Steels," *Fracture Mechanics, ASTM STP 677*, C. W. Smith, Ed., American Society for Testing and Materials, 1979, pp. 85-105.

ABSTRACT: Fracture toughness (K_{Ic} , J_{Ic}) and fatigue-crack growth (da/dN) data for quenched and tempered low-carbon ferritic 3.5Ni and 9Ni steels were measured at temperatures between 295 and 4 K. The tests were performed using 25- and 31-mm-thick compact specimens having fracture planes parallel to the rolling direction (TL orientation). The fracture toughness results for both steels showed qualitatively similar trends: at decreasing temperatures below 295 K, J_{Ic} increased by about 20 percent prior to the onset of classical ductile-to-brittle transitions involving cleavage. The transitions occurred between 172 and 100 K for 3.5Ni steel, and between 76 and 4 K for 9Ni steel. Transitional behavior also was evident in the fatigue crack growth behavior. The room-temperature fatigue crack growth rates for these nickel steels are typical of ferritic steels, but the rates at subtransition temperatures are accelerated drastically, in association with cleavage and other brittle cracking modes. Data comparisons between the 3.5Ni and 9Ni steels tested here and other nickel alloy steels are included.

KEY WORDS: fatigue (materials), fracture (materials), low temperature tests, mechanical properties, nickel alloys, steels

The ferritic nickel alloy steels were developed to provide economic alternatives to the heavily alloyed austenitic stainless steels which are too expensive for use in large-tonnage cryogenic structural applications. Since 1947, the effects of nickel on the mechanical properties of the ferritic steels have been studied and reviewed [1-3],² one major finding being that increased nickel content leads to progressively lower ductile-to-brittle transition temperatures. Construction costs are minimized by selecting the appropriate nickel content for the intended service tempera-

¹ Metallurgist, Metallurgist, and Division Chief respectively, Fracture and Deformation Division, National Measurements Laboratory, Boulder, Colo. 80302.

² The italic numbers in brackets refer to the list of references appended to this paper.

ture range. For example, normalized 3.5Ni steel (ASTM Specification for Pressure Vessel Plates, Alloy Steel, Nickel (A 203 – 74a), grade E) has a minimum use temperature of 172 K and is used for liquid acetylene, ethylene, and propane tankage. Quenched and tempered 9Ni steel (ASTM Specification Pressure Vessel Plates, Alloy Steel, Quenched and Tempered Eight and Nine Percent Nickel, (A 553 – 74), grade A) is used for liquefied natural gas and nitrogen tankage at temperatures as low as 76 K.

The tensile and impact properties of these steels are well researched, but additional data are required to apply the modern techniques of fracture mechanics analysis. The fracture parameters currently needed for fail safe design are: K_{Ic} , the critical plane-strain stress intensity factor; J_{Ic} , the critical value of the J-integral; and da/dN , the fatigue-crack growth rate where a is crack length and N is fatigue cycles. The parameters K_{Ic} and J_{Ic} characterize the magnitude of crack-tip elastic stresses or plastic strains during monotonic loading, while da/dN describes subcritical flaw growth due to cyclic loading.

This paper describes the temperature dependence of these parameters for quenched and tempered 3.5Ni and 9Ni steels. The quenched and tempered condition was chosen because it may confer superior low temperature fracture resistance compared to the alternative normalizing treatments [3,4]. This work supplements a previous study on 5Ni, 6Ni, and 9Ni steels [5], and the combined results are used to support generalizations regarding cryogenic temperature effects on fracture behavior.

Materials and Specimens

A 2.54-cm thick plate of 3.5Ni steel (a reprocessed ASTM Specification A 203 grade E alloy) and a 3.2-cm thick plate of 9Ni steel (ASTM Specification A 553 grade A Type I) were obtained from commercial sources. Both steels were received and tested in the quenched and tempered conditions. The 3.5Ni steel had been reprocessed from its original normalized condition; it was heated at 1172 K for 1 h, and water quenched, then tempered at 896 K for 1 h, and water quenched. The 9Ni steel was heated at 1064 K for 1.5 h, and water quenched, then tempered at 877 K for 1.25 h and air-cooled. The mill chemical analyses for both steels are listed in Table 1. Selected uniaxial tensile properties are listed in Table 2.

TABLE 1—Mill chemical analyses of test materials, weight percent.

Material	Fe	Ni	C	Mn	P	S	Si
3.5Ni steel ^a	balance	3.62	0.10	0.46	0.015	0.013	0.20
quenched and tempered 9Ni steel (ASTM A 553-A)	balance	8.99	0.08	0.62	0.010	0.010	0.19
quenched and tempered							

^a Reprocessed ASTM Specification A 203, E grade.

TABLE 2.—Tensile properties of test materials.

Material	Temperature, K	0.2 Percent Yield Strength ^a , MPa	Ultimate Tensile Strength ^a , MPa	Elongation in 2.54 cm gage ^a , percent	Reduction of Area ^a , percent	Young's Modulus ^b , GPa	Poisson's Ratio ^b
3.5Ni steel quenched and tempered	295	488.2	549.5	33.6	71.8	204	0.288
	194	564.6	659.8	36.2	69.4	209	0.285
	111	776.7	867.7	NA ^c	NA	214	0.283
	76	900.8	911.1	35.1	57.8	214	0.282
9Ni steel quenched and tempered	295	740.5	788.7	24	64.1	192	0.292
	111	913.5	1075.2	NA	NA	200	0.287
	76	1028.7	1202	NA	NA	201	0.286
	4	1329.3	1381.7	NA	NA	202	0.286

^a Average values from duplicate tests.^b Data from Weston, Naumon, and Ledbetter [8].^c NA = not available.

Compact specimens for fatigue and fracture tests were machined in the TL orientation, having planar dimensions proportional to specimen width, W , in accordance with ASTM Method Test for Plane-Strain Fracture Toughness of Metallic Materials (E 399 – 74). The 3.5Ni steel specimens were 2.5 cm thick, with a width-to-thickness ratio, W/B , of 2.0. The 9Ni steel specimens (diagrammed elsewhere [5]) were 3.1 cm thick, with $W/B = 2.4$. Attached to knife edges at the loadline was a double-cantilever beam-type clip gage meeting the ASTM Method E 399 linearity requirements at each test temperature.

Procedures

The test environments were room temperature air at 295 K, nitrogen vapor at 111 or 172 K, liquid nitrogen at 76 K, and liquid helium at 4 K. Two 3.5Ni steel fatigue tests were also performed in an alcohol/dry ice bath at 195 K. The low temperature apparatus included a 100 kN servohydraulic test machine and cryostat previously described [5,6].

Fracture Toughness

Direct K_{Ic} measurements for nickel alloy steels are rarely valid because the thickness criterion for linear-elastic tests is difficult to satisfy. The thickness criterion requires that

$$B \geq 2.5 \left(\frac{K_{Ic}}{\sigma_y} \right)^2 \quad (1)$$

where σ_y is the yield strength of the material. In this study, J-integral and ASTM Method E 399 tests were used alternatively, depending on the type of load-deflection behavior encountered. Typical load-deflection records for 9Ni steel specimens are shown in Fig. 1.

Nonlinear, Plastic Fractures

Where ductile fractures by stable tearing occurred (9Ni steel at 295 and 111 K; 3.5Ni steel at 295 and 172 K), J -resistance curves were determined based on Landes and Begley's method [7]. J as a function of crack extension was determined by experiments in which a series of precracked specimens at each material/temperature combination were loaded to cause crack extensions of between zero and 0.49 cm. After unloading, the specimens were heat-tinted and then completely fractured. Crack extension was measured to the nearest 0.001 cm at three thickness locations, and averaged. J values were calculated from the approximation

$$J = \frac{2A}{B(W - a)} \quad (2)$$

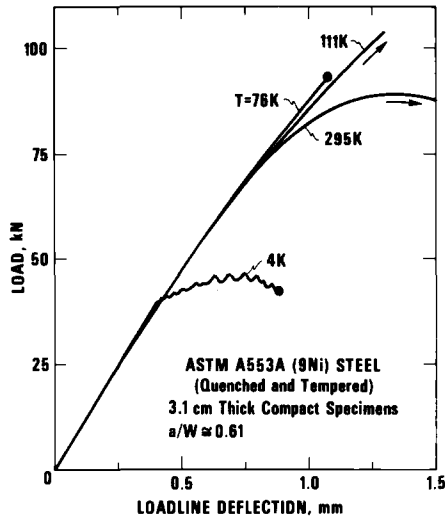


FIG. 1—Load versus loadline deflection curves for 9Ni steel.

where A is the total area (energy) under the test record. J_{Ic} then was obtained by extrapolating the J -versus- Δa plots back to the critical point of material separation, Δa_c . (Crack extensions less than Δa_c are apparent extensions, due only to plastic deformation or blunting.) Estimates of K_{Ic} denoted $K_{Ic}(J)$ were derived from the relation

$$K_{Ic}^2(J) = \frac{EJ_{Ic}}{(1-\nu^2)} \quad (3)$$

The values of Young's modulus (E) and Poisson's ratio (ν) for these steels were reported by Weston, Naimon, and Ledbetter [8].

Linear-Elastic or Unstable Fractures

Where fast fracture occurred (9Ni steel at 76 and 4 K; 3.5Ni steel at 111, 76, and 4 K), the conditional fracture toughness values denoted K_Q were calculated. Some of these K_Q results nearly qualified as K_{Ic} determinations, but none were valid according to a strict interpretation of ASTM Method E 399.

In the case of 3.5Ni steel at 76 and 4 K, excessive crack front curvature proved unavoidable when the precracking stress intensity factor was maintained at levels lower than $0.6 K_{Ic}$. For 3.5Ni steel at 111 K, Eq 1 was not satisfied, and the K_Q data were far from valid. For 9Ni steel at 76 K, Eq 1 was not satisfied, but the test record was sufficiently linear that J_{Ic} could be calculated at maximum load, assuming subcritical crack growth

was negligible. At 4 K, the 9Ni steel test records exhibit a unique saw-toothed appearance, as shown in Fig. 1, presumably due to multiple popins (unstable crack advances) and arrests. The P_{\max}/P_Q ratios at 4 K exceeded 1.10, but the heat-tinting technique indicated that the nonlinearity was due to cracking, not plasticity.

Fatigue Crack Growth Rates

Fatigue crack growth was monitored using the compliance method [5,6]. Rates at stress intensity factors, K_f , as high as $50 \text{ MPa}\cdot\text{m}^{1/2}$ were measured during the precracking stages of fracture specimen preparation, while rates at higher stress intensities were measured with specimens not used for fracture toughness tests. Between two and six specimens were tested per temperature.

All fatigue tests used a sinusoidal load cycle at 20 Hz, and a R ratio (P_{\min}/P_{\max}) of 0.1. The a -versus- N curves were fitted with third-order polynomials and differentiated by computer to obtain da/dN . The da/dN data were plotted as a function of the stress intensity factor ranges, ΔK , which were calculated using the ASTM Method E 399 solutions for K and $f(a/W)$

$$\Delta K = K_{\max} - K_{\min} = \frac{(P_{\max} - P_{\min})}{BW^{1/2}} [f(a/W)] \quad (4)$$

The 9Ni steel of this study showed only slight crack front curvature effects, as compared to pronounced curvatures for 3.5Ni steel and other nickel steels [5]. As an indicator of crack curvature, edge-to-average crack length ratios, a_e/a , are tabulated in the results. These curvature variations should not greatly affect the da/dN comparisons since the compliance method is sensitive to through-the-thickness crack length variations.

Results

Fracture Toughness

Table 3 lists the fracture toughness results for 3.5Ni steel at 295, 172, 111, 76, and 4 K. The J -resistance curves, as shown in Fig. 2, yielded J_{1c} values of 163 kJm^{-2} at 295 K and 193 kJm^{-2} at 172 K. The $K_{1c}(J)$ estimates at these temperatures are $190 \text{ MPa}\cdot\text{m}^{1/2}$ and $219 \text{ MPa}\cdot\text{m}^{1/2}$, respectively. ASTM Method E 399 results for this steel at lower temperatures are invalid, due primarily to excessive crack-front curvature, but it appears that K_{1c} approaches 30 to $50 \text{ MPa}\cdot\text{m}^{1/2}$ near absolute zero.

The fracture toughness results for 9Ni steel at 295, 111, 76, and 4 K are listed in Table 4. The J -resistance curves for this steel (Fig. 3) yielded J_{1c}

TABLE 3—Fracture results for quenched and tempered 3.5Ni steel (specimen thickness = 2.54 cm).

Temperature, K	Specimen	K_{Ic} , MPa·m ^{1/2}	a_c/a	a/W	$\frac{P_{max}}{P_q}$	K_{Ic} , MPa·m ^{1/2}	J , kJm ⁻²	Δa , cm	J_{Ic} , kJm ⁻²	$(J), K_{Ic}^0$, MPa·m ^{1/2}	K_{Ic} , MPa·m ^{1/2}
295	20	48	0.96	0.542	1.7	66	240	0.493			NA
	21	46	0.92	0.546	NA	65	124	0.064			NA
	22	50	0.90	0.552	1.5	69	317	0.838	163 ± 10 percent	190 ± 5 percent	NA
	24	48	0.94	0.544	1.6	67	174	0.135			NA
	27	50	0.93	0.552	1.7	60	254	0.457			NA
	27	50	0.93	0.552	1.7	60	254	0.457			NA
	25	61	0.92	0.571	1.4	86	256	0.363			NA
172	26	52	0.95	0.565	1.4	88	332	0.452			NA
	28	53	0.93	0.569	NA	82	70	0.000	193 ± 10 percent	219 ± 5 percent	NA
	29	67	0.94	0.585	1.4	89	214	0.150			NA
	29	75	0.93	0.596	1.4	90	231	0.321			NA
	2	40	0.98	0.557	1.0	74.8	NA	NA	NA	NA	invalid ^b
	31	45	0.85	0.530	1.4	81.0	NA	NA	NA	NA	invalid ^{b,c,d}
76	10	34	0.90	0.582	1.0	63.4	NA	NA	NA	NA	invalid ^e
	15	31	0.93	0.498	1.0	48.0	NA	NA	NA	NA	invalid ^e
	3	50	0.85	0.475	1.0	60.2	NA	NA	NA	NA	invalid ^{d,e,h}
4	23	44	0.88	0.545	1.0	49.9	NA	NA	NA	NA	invalid ^{d,e,h}
	33	32	0.76	0.523	1.0	53.9	NA	NA	NA	NA	invalid ^d
	36	29	0.75	0.530	1.0	32.2	NA	NA	NA	NA	invalid ^{d,e,f}

^a Calculated using Eq. 3.^b Insufficient specimen thickness.^c Excessive P_{max}/P_q ratio.^d Excessive edge-crack-to-average crack length ratio, a_c/a .^e Excessive precracking stress intensity factor, K_{Ic} .^f Precracked at 76 K.^g Precracked at 195 K.^h Precracked at 295 K.

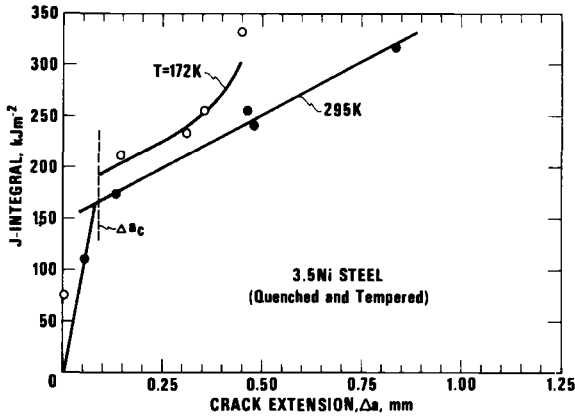


FIG. 2—*J* resistance curves for 3.5Ni steel tested at 295 and 172 K.

values of 117 kJm⁻² at 295 K and 140 kJm⁻² at 111 K. The $K_{Ic}(J)$ estimates at these temperatures are 156 MPa·m^{1/2} and 174 MPa·m^{1/2}, respectively. Between 111 and 76 K, $K_{Ic}(J)$ decreases slightly to 167 MPa·m^{1/2}. Thereafter, the fracture toughness rapidly decreases until, at 4 K, nearly all of ASTM Method E 399 criteria for K_{Ic} measurements are satisfied. However, the *a/W* ratios of about 0.6 slightly exceed the preferred range of 0.45 to 0.55. The statement “ $K_Q \approx K_{Ic}$ ” in Table 4 indicates that the 4 K data for 9Ni steel are believed to be nearly accurate K_{Ic} results.

The temperature effects on K_{Ic} estimates for the 3.5Ni and 9Ni steels are plotted in Fig. 4, along with results for a 5Ni steel [5]. Using 31 mm

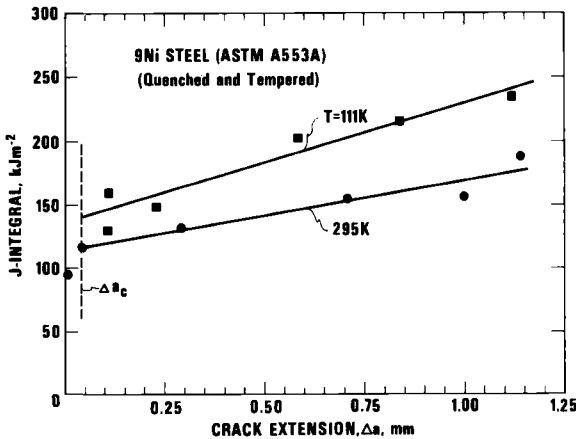


FIG. 3—*J* resistance curves for 9Ni steel at room temperature (295 K) and liquefied natural gas temperature (111 K).

TABLE 4—Fracture results for quenched and tempered 9Ni steel (specimen thickness = 3.1 cm).

Temperature, K	Specimen	K_{Ic} , MPa·m ^{1/2}	a_c/a	a/W	$\frac{P_{max}}{P_Q}$	K_{ϕ} , MPa·m ^{1/2}	J , kJm ⁻²	Δa , cm	J_{Ic} , kJm ⁻²	$K_{Ic}^c(J)$, MPa·m ^{1/2}	K_{Ic} , MPa·m ^{1/2}
295	3	43	0.96	0.615	1.2	124	188	0.117			NA
	7	43	0.95	0.606	>1.17	120	116	0.043			NA
	11	41	0.94	0.611	NA	115	95	0.0	117 ± 10 percent	156 ± 5 percent	NA
	22	41	0.96	0.608	>1.2	113	155	0.100			NA
	23	43	0.96	0.608	>1.3	119	130	0.020			NA
	24	42	0.97	0.609	>1.3	110	153	0.071			NA
111	4	46	0.97	0.617	>1.28	119	130	0.011			NA
	6	48	0.95	0.616	>1.17	142	148	0.023			NA
	9	45	0.95	0.648	>1.25	144	218	0.084			NA
	15	41	0.97	0.607	>1.12	137	162	0.010	140 ± 15 percent	174 ± 8 percent	NA
	16	42	0.96	0.618	>1.19	136	232	0.114			NA
	18	45	0.96	0.606	>1.36	116	203	0.006			NA
	21	40	0.95	0.613	1.07	147	99	NA	99	170	$K_{Ic} \neq K_{Ic}^b$
	20	33	0.96	0.612	1.07	145	92	NA	92	164	$K_{Ic} \neq K_{Ic}^b$
76	17	37	0.97	0.611	1.09	144	97	NA	97	169	$K_{Ic} \neq K_{Ic}^b$
	14 ^c	41	0.97	0.606	1.11	80.5	NA	NA	NA	NA	$K_{Ic} = K_{Ic}^b$
	12 ^c	33	0.98	0.608	1.15	67.3	NA	NA	NA	NA	$K_{Ic} = K_{Ic}^b$
4	5	43	0.98	0.617	1.09	78.2	NA	NA	NA	NA	$K_{Ic} = K_{Ic}^b$

^a Calculated using Eq 3.^b Insufficient thickness.^c Precracked at 76 K.

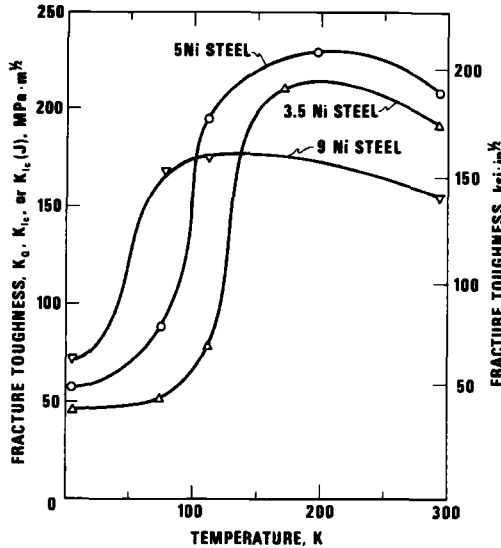
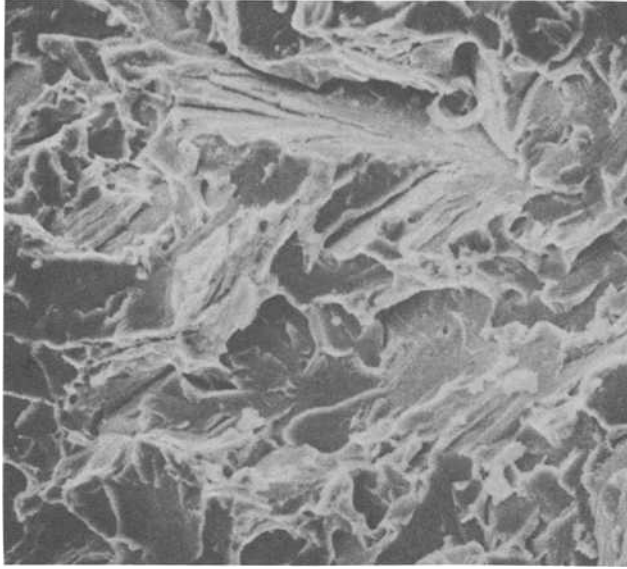


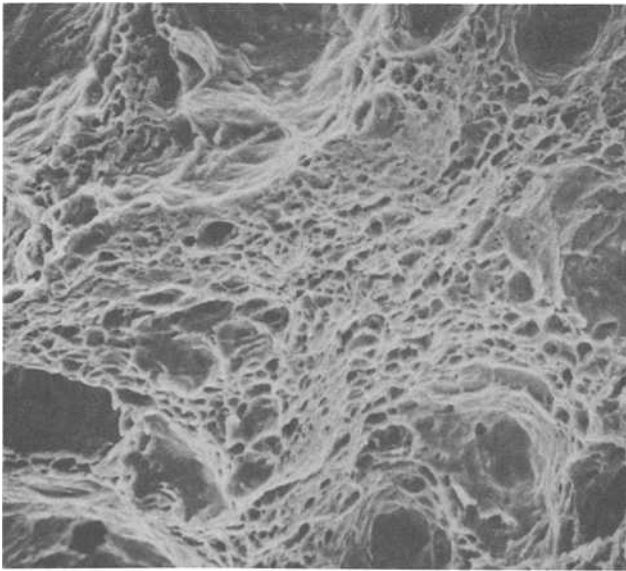
FIG. 4—Temperature dependence of K_{IC} estimates for the quenched and tempered 3.5Ni and 9Ni steels for this study and the austenitized, tempered, and reversion annealed 5Ni steel previously tested (Ref 5).

thick compact specimens and similar procedures, the 5Ni steel was tested in the austenitized, tempered, and reversion annealed condition, which tends to decrease the transition temperature slightly compared to the quenched and tempered condition [9]. In the range 295 to 4 K, these three ferritic steels behave similarly in that they each exhibit: (1) an “upper shelf” temperature region showing an initial enhancement of fracture resistance at decreasing temperatures, (2) a transition range of abruptly decreasing toughness, and (3) a temperature-insensitive sub-transition range. As shown in Fig. 5 for 3.5Ni steel, the transitions are associated with classical fracture mode changes from dimpled rupture at the higher temperatures to cleavage at the lower temperatures. Note also that each steel exhibits a maximum in the fracture toughness-versus-temperature plots, prior to transition. A 6Ni steel also showed this type of behavior between 295 and 76 K [5]. For these steels, the peak $K_{IC}(J)$ value is about 10 to 15 percent higher than the value at room temperature, and up to five times greater than the values near absolute zero.

Nickel's contributions to improved fracture resistance in the transition and subtransition regions are attributed to favorable effects on the deformation characteristics and cleavage resistance of iron, combined with a tendency to promote the formation of retained austenite in some alloys [3,9,10]. As indicated in Fig. 4, the transition temperature intervals decrease with nickel content, lying approximately in the ranges



3.5 Ni steel, fractured at 76 K



3.5 Ni steel, fractured at 295 K

FIG. 5.—SEM fractographs of 3.5Ni steel fracture toughness test specimens, showing dimpled rupture at 295 K and cleavage at 76 K ($\times 1000$). Similar fractographic features were observed for 9Ni steel tested at 295 and 4 K.

$$\begin{aligned}
 &4 \text{ K} < T < 76 \text{ K for 9Ni steel} \\
 &\sim 60 \text{ K} < T < 111 \text{ K for 5Ni steel, and} \\
 &\sim 100 \text{ K} < T < 172 \text{ K for 3.5Ni steel.}
 \end{aligned}$$

The fracture toughness at subtransition temperatures also correlates with nickel content. For example, at 4 K (a subtransition temperature for each steel) the K_{Ic} values increase from 30 $\text{MPa}\cdot\text{m}^{1/2}$ for 3.5Ni steel to 75 $\text{MPa}\cdot\text{m}^{1/2}$ for 9Ni steel. On the other hand, there is no simple correlation between nickel content and toughness in the upper shelf region. The upper shelf toughness values are apparently more sensitive to heat treatment and metallurgical factors other than nickel content. The 5Ni steel exhibits the highest room temperature fracture toughness, perhaps due to the uniform distribution of carbides and other benefits associated with austenitizing, tempering, and reversion annealing [9].

Fatigue Crack Growth Rates

Over the range of stress intensity factors investigated (20 to 80 $\text{MPa}\cdot\text{m}^{1/2}$) the fatigue crack growth rates for the 3.5Ni and 9Ni steels conform to power-law equations of the type

$$\frac{da}{dN} = C(\Delta K)^n \quad (5)$$

where the n and C parameters are material and temperature dependent. Log-log plots of da/dN -versus- ΔK were constructed to reveal linear trends from which the n and C values were determined as the slopes and ordinate intercepts at $\Delta K = 1$, respectively. Table 5 lists the n and C values for all material/temperature combinations investigated.

The room temperature results are compared in Fig. 6. Here, line approximations for the 3.5Ni and 9Ni steel data of this study and the 5Ni, 6Ni, and 9Ni steel data of a previous study [5] are superimposed on a scatterband for commercial structural steels where nickel is not a major alloying element [11-15]. Most of the data for nonnickel steels were obtained from crack length measurements at the specimen edge. If those measurements had been corrected for crack length curvature, agreement with the present results would be further improved. As shown, the data spread for the nickel alloy steels is nearly equivalent to that for the nonnickel steels. The fatigue crack growth rate variations for the nickel steels approach a factor of 4; however, judging from the data for the two quenched and tempered 9Ni steel alloys, heat-to-heat variability can account for variations of at least a factor of two or three. It appears that the fatigue crack growth resistances of nickel alloy steels at room temperature are typical of ferritic steels in general, and there is no simple

TABLE 5—Comparison of Paris equation parameters for nickel alloy steels (da/dN in millimetres per cycle).

Material	Temperature, K	C	n	ΔK Region MPa·m ^{1/2}
3.5Ni Steel (this study)	295	1.3×10^{-8}	3.2	18 to 60
	195	1.3×10^{-8}	3.2	30 to 70
	172	1.0×10^{-9}	3.2	30 to 60
	76	1.6×10^{-14}	7.6	20 to 30
5Ni steel [5] (ASTM A 645)	295	1.1×10^{-8}	2.7	25 to 90
	111	1.1×10^{-8}	2.7	25 to 60
	76	2.0×10^{-10}	4.0	27 to 80
5.5Ni steel [5] (N-TUF Cr-196)	295	3.7×10^{-9}	3.0	22 to 85
	111	3.7×10^{-9}	3.0	22 to 85
	76	4.2×10^{-9}	3.2	25 to 75
9Ni steel [5] (ASTM A 553-A)	295	$\sim 2.3 \times 10^{-7}$	~ 2.0	27 to 100
	76	3.1×10^{-9}	3.3	27 to 100
9Ni steel (ASTM A 553-A) (this study)	295	2.0×10^{-8}	2.7	16 to 70
	111	1.0×10^{-9}	3.4	17 to 80
	76	4.8×10^{-11}	4.4	17 to 64
	4	1.4×10^{-11}	5.3	25 to 35

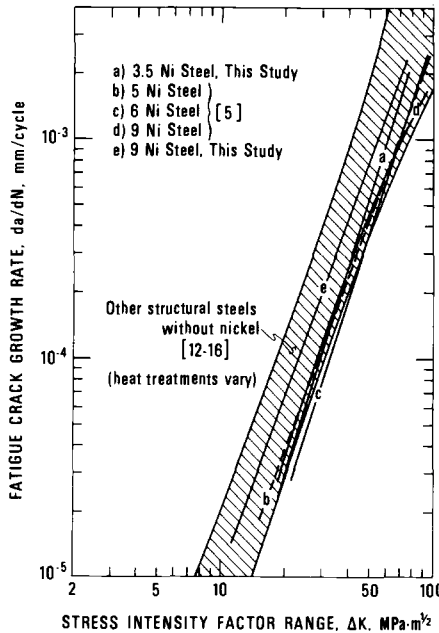


FIG. 6—Room temperature fatigue crack growth data for nickel steels compared with data for other ferritic structural steels.

correlation between fatigue crack growth rates and nickel content at this temperature.

Figure 7 reveals no dramatic temperature effects on the fatigue crack growth resistance of 3.5Ni steel, as long as the temperature remains within the upper shelf region identified by the J_{Ic} tests. The fatigue crack growth rates at 195 and 172 K are nearly equivalent or slightly improved compared to the rates for this steel at room temperature. On the other hand, further temperature reductions to 76 K greatly accelerate the rates to values well above those at room temperature. The crack growth rate equation exponents also increase sharply from $n = 3.2$ at 295 K to $n = 7.6$ at 76 K. As indicated earlier, 76 K is a subtransition temperature for this steel. Scanning electron fractographs such as shown in Fig. 8 indicate that inferior fatigue crack growth rates and irregular a versus N curves at this temperature were both associated with the onset of cleavage-type cracking modes, which become more prominent at higher ΔK values. Another feature observable in Fig. 8 is the decreased tendency to secondary cracking at 76 K. Also, the fatigue surfaces show markings aligned predominantly transverse to the crack propagation direction at 76 K, but not at 295 K.

The fatigue crack growth behavior of 9Ni steel is analogous to that of 3.5Ni steel in that low temperature effects are moderate until the subtransition range is approached. Data for the 9Ni steel at 295, 111, 76,

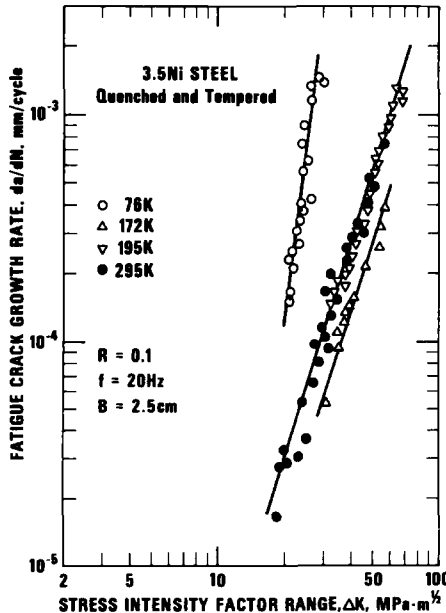
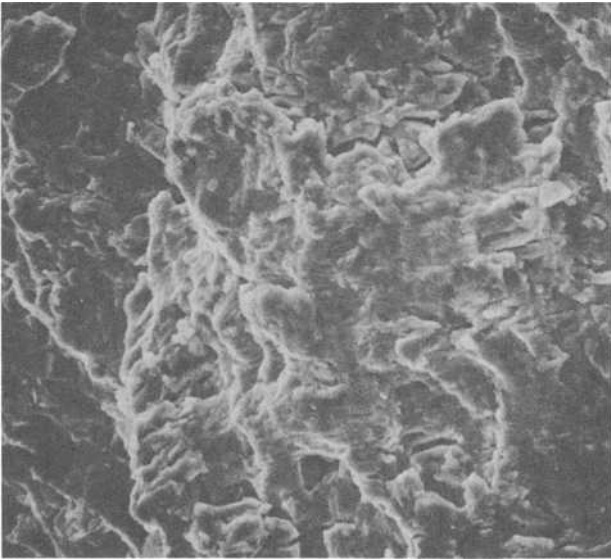
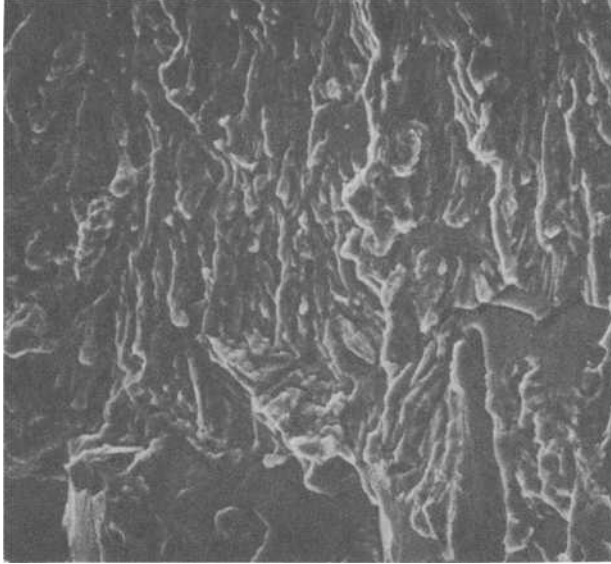


FIG. 7—Fatigue crack growth rates for 3.5Ni steel at room and cryogenic temperatures.



3.5 Ni steel, fatigued at 295 K
 $\Delta K \approx 30 \text{ MPa} \cdot \text{m}^{1/2}$



3.5 Ni steel, fatigued at 76 K
 $\Delta K \approx 27 \text{ MPa} \cdot \text{m}^{1/2}$

FIG. 8—SEM fractographs of fatigue surfaces produced in da/dN tests of 3.5Ni steel specimens at 295 and 76 K ($\times 1000$).

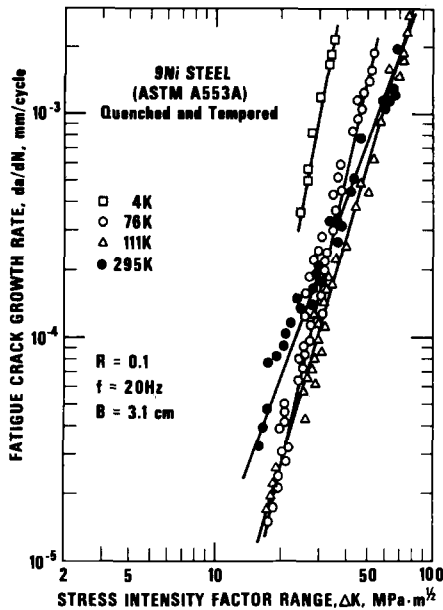


FIG. 9—Fatigue crack growth rates for 9Ni steel at room and cryogenic temperatures.

and 4 K are shown in Fig. 9. The rates decrease as temperature is lowered between 295 and 111 K, but a reversal occurs between 111 and 76 K. Thus, for ΔK greater than $40 \text{ MPa}\cdot\text{m}^{1/2}$, the rates at 76 K exceed those at 295 K. Another quenched and tempered 9Ni steel also exhibited higher rates at 76 K than at 295 K [5]. At more extreme cryogenic temperatures, the present results at 4 K show that fatigue crack propagation resistance continues to deteriorate while the a -versus- N curves show more scatter. The inferior performance at 4 K is associated with brittle cracking modes similar to those shown in Fig. 8 for the 3.5Ni steel tested at 76 K. Thus, for the ΔK ranges investigated, the fatigue crack growth resistance of 9Ni steel is at its maximum near 111 K, the same temperature at which a peak in the static fracture toughness was observed.

Discussion

Usually, strain-rate, section thickness, and notch severity are three major factors that influence the toughness transition temperatures of ferritic steels, but recent reports indicate the fracture toughness of 5Ni and 9Ni steels to be unimpaired by high strain rates [3]. Therefore, the relatively thick and sharply cracked compact specimens used for static fracture tests of these alloys may provide a more severe test of crack tolerance than traditional approaches based on Charpy impact measurements.

Any comparison between the data of this report and the literature must carefully take into account the differences in measurement procedures. Standard K_{Ic} measurements provide the most reliable comparisons, but valid K_{Ic} data are rare. Most authors have reported “ K_c ” or “ K_{max} ” values instead [3]. Usually, these nonstandard parameters are calculated based on the maximum load point, using a variety of data reduction schemes. In the present study, the J-integral at initiation of crack extension is reported, rather than a K value calculated at the maximum load point. In the following discussion, only data obtained by similar procedures are compared.

For 3.5Ni steel in the quenched and tempered condition, Huettich, Pense, and Stout [4] reported K_{Ic} values of 43 and 84 $\text{MPa}\cdot\text{m}^{1/2}$ at 89 K (-300°F) and 102 K (-275°F), respectively. The data trend in Fig. 4 for the present study indicates 30 percent higher toughness at 89 K and 25 percent lower toughness at 102 K. These differences may be due partly to test procedure, since the present cryogenic data are not strictly valid. Furthermore, Huettich, Pense, and Stout precracked their specimens at room temperature.

Huettich et al also tested normalized 3.5Ni steel, obtaining K_{Ic} values of 51 $\text{MPa}\cdot\text{m}^{1/2}$ at 116 K (-250°F) and 75 $\text{MPa}\cdot\text{m}^{1/2}$ at 144 K (-200°F). Our results for quenched and tempered 3.5Ni steel (Fig. 4) indicate at least 50 percent higher toughness at similar temperatures. This confirms the findings of Huettich, Pense, Stout, that the quenched and tempered condition is superior to the conventional normalizing treatment. Note, however, that the quenched and tempered 3.5Ni steels tested in these studies were actually heat treated twice, having been reprocessed from their original normalized conditions.

Syn, Jin, and Morris [16] reported a K_{Ic} value of 78 $\text{MPa}\cdot\text{m}^{1/2}$ for a double-normalized and tempered 9Ni steel tested at 6 K. This nearly agrees with the present result of 75 $\text{MPa}\cdot\text{m}^{1/2}$ for quenched and tempered 9Ni steel at 4 K. The effect of heat treatment on the fracture resistance of 9Ni steels at other test temperatures cannot be evaluated at this time because standard K_{Ic} data and comparable J_{Ic} data for double-normalized and tempered grades are lacking. However, the present $K_{Ic}(J)$ results for quenched and tempered 9Ni steel are up to 16 percent lower than results for a second heat of quenched and tempered 9Ni steel tested at 295 and 76 K [5]. Other differences between the two heats are noted in Fig. 10. These dissimilarities probably arise from variations in composition and processing. The present steel contains less nickel than the previous steel (8.99 versus 9.25 weight percent), as well as higher carbon (0.08 versus 0.06 weight percent), phosphorus (0.010 versus 0.007 weight percent) and sulfur (0.010 versus 0.003 weight percent). All of these compositional variations should tend to lower the toughness of the steel used in the present study.

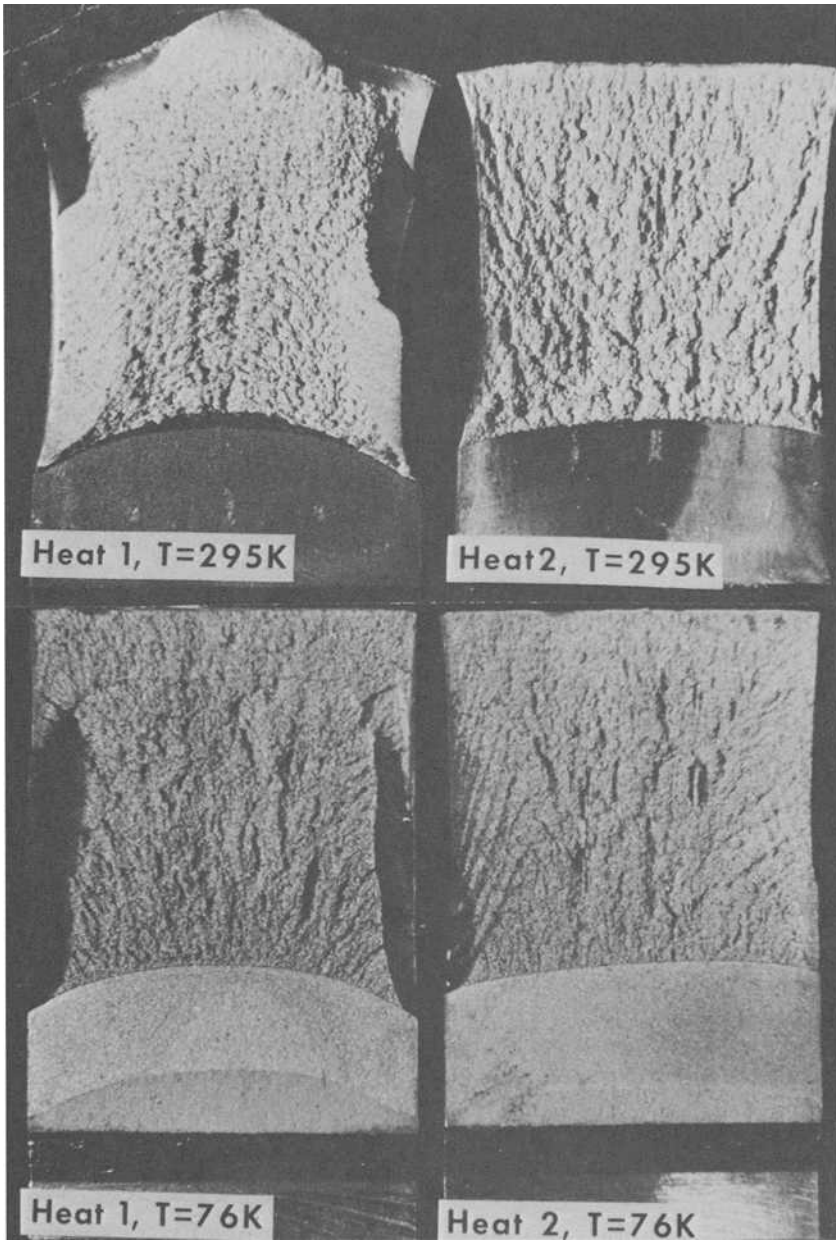


FIG. 10—A comparison of the fracture surfaces of two different heats of quenched and tempered 9Ni steel fractured at 295 and 76 K, showing heat-to-heat variability. The 9Ni steel previously tested (Heat 1, Ref 5) displays a greater proportion of shear fracture at specimen edges, as well as a more pronounced crack-front curvature.

As indicated in Table 5, the Paris equation exponents for nickel steels at room temperature are nearly 3.0, which is expected for ferritic steels, based on Barsom's findings [11]. The exponents tend to increase, depending on the severity of the temperature reduction. For example, the 9Ni steel shows a change from $n = 2.7$ at room temperature to $n = 5.3$ at 4 K. However, the rates for 9Ni steel at 111 and 76 K deviate from their room temperature rates by margins not greater than the range of scatter observed in the comparison for various steels at 295 K (Fig. 6). This suggests that variations in fatigue crack growth resistance due to temperature effects in the upper shelf ranges are similar in magnitude to variations induced by metallurgical effects at room temperature. Extremely high fatigue crack growth rates and n values are observed in conjunction with the low K_{Ic} values at subtransition temperatures. Similarly, for steels at room temperature, Knott and Ritchie correlated high n values with low fracture toughness values, indicating that n is likely to exceed 4.0 if K_{Ic} is 80 MPa·m^{1/2} or lower [17]. Lindley and Richards also associate high n values with brittle crack propagation modes such as occur in static fracture tests [18].

Summary and Conclusions

Our J-integral fracture and fatigue crack growth rate tests on quenched and tempered 3.5Ni and 9Ni steels at temperatures between 295 and 4 K illustrate trends that are believed to be representative, qualitatively, of ferritic steels in general. The results are summarized as follows:

Fracture Toughness—at decreasing temperatures below 295 K, the fracture toughness parameter J_{Ic} increases gradually at first, reaching a maximum prior to the ductile-to-brittle transition. The transition for 3.5Ni steel lies approximately between 172 and 110 K, and the transition for 9Ni steel lies approximately between 76 and 4 K. As estimated from J-integral tests, the maximum K_{Ic} values are between 2.5 and 5 times greater than the K_{Ic} values near absolute zero. The abrupt reduction in fracture toughness is a consequence of the classical transition from dimpled rupture at higher temperatures to cleavage at cryogenic temperatures. Also, it was confirmed that if a normalized 3.5Ni steel is reprocessed to the quenched and tempered condition, improved low temperature fracture resistance is obtained.

Fatigue Crack Growth Resistance—The fatigue crack growth rates for the nickel alloy steels at room temperature are typical of other ferritic steels, and the rates are not measurably influenced by nickel content. Moderate temperature reductions tend to improve the fatigue crack growth resistance slightly, but at subtransition temperatures defined by J tests the fatigue crack growth rates are accelerated drastically. The rates at subtransition temperatures may exceed the rates at higher temperatures

by an order of magnitude. Brittle cracking modes at cryogenic temperatures account for this transitional behavior.

In conclusion, the fracture mechanics parameters reported here for cryostructural nickel steels are directly applicable to design. The findings support current engineering practice which limits the applicability of these ferritic steels to service temperatures not lower than 172 K for 3.5Ni steel and 76 K for 9Ni steel. As long as the service temperatures for these steels remain in the upper shelf regions defined by J_{Ic} tests, both the fatigue crack growth rates at intermediate ΔK values and the fracture toughness values remain at useful levels.

Acknowledgments

This program was sponsored by the National Maritime Administration and the Advanced Research Projects Agency of the U.S. Department of Defense. Test materials were donated by the Lukens Steel and Armco Steel Corporations. Scanning electron microscopy was performed by J. Yaker and C. Miglionico of the Technology and Analysis Division, Air Force Weapons Laboratory, Kirtland Air Force Base. The assistance of R. L. Durcholz of the National Bureau of Standards in conducting the tension tests is also gratefully acknowledged.

References

- [1] Yeo, R. B. G. and Miller, O. O., "A History of Nickel Steels from Meteorites to Maraging," Sorby Centennial Symposium on History of Metallurgy, American Society for Metals, Cleveland, Ohio, 21-23 October, 1963.
- [2] Johnson, R. J., *Metals Engineering Quarterly*, Vol. 15, 1975, p. 1.
- [3] Pense, A. W. and Stout, R. D., "Fracture Toughness and Related Characteristics of the Cryogenic Nickel Steels," WRC Bulletin No. 205, Welding Research Council, 1975, p. 1.
- [4] Huettich, N. J., Pense, A. W., and Stout, R. D., "The Toughness of 2¼ and 3½ Percent Nickel Steels at Cryogenic Temperatures," WRC Bulletin No. 165, Welding Research Council, 1974, p. 1.
- [5] Tobler, R. L., Mikesell, R. P., Durcholz, R. L., and Reed, R. P. in *Properties of Materials for Liquefied Natural Gas Tankage*, ASTM STP 579, American Society for Testing and Materials, 1975, p. 261.
- [6] Fowlkes, C. W. and Tobler, R. L., *Engineering Fracture Mechanics*, Vol. 8, 1976, p. 487.
- [7] Landes, J. D. and Begley, J. A. in *Fracture Analyses*, ASTM STP 560, American Society for Testing and Materials, 1973, p. 231.
- [8] Weston, W. F., Naimon, E. R., and Ledbetter, H. M. in *Properties of Materials for Liquefied Natural Gas Tankage*, ASTM STP 579, American Society for Testing and Materials, 1975, p. 397.
- [9] Sarno, D. A., Havens, F. E., and Bowley, D. L., "Transformations Involved in Developing Notch Toughness in a New 5 Percent Nickel Steel for Cryogenic Purposes," Technical Report No. C70-39-2, American Society for Metals, 1970.
- [10] Floreen, S., Hayden, H. W., and Devine, T. M., *Metallurgical Transactions*, Vol. 2, 1971, p. 1403.
- [11] Barsom, J. M., *Transactions*, American Society of Mechanical Engineers; *Journal of Engineering Industry*, 1971, p. 1190.

- [12] Barsom, J. M., Imhof, E. J., and Rolfe, S. T., *Engineering Fracture Mechanics*, Vol. 2, 1971, p. 301.
- [13] Wei, R. P., Talda, P. M., and Che-Yu Li in *Fatigue Crack Propagation*, ASTM STP 415, American Society for Testing and Materials, 1967, p. 460.
- [14] Brothers, A. J. and Yukawa, S., *Transactions*, American Society of Mechanical Engineers; *Journal of Basic Engineering*, Vol. 89, 1967, p. 19.
- [15] Miller, G. A., *Transactions*, American Society for Metals, Vol. 61, 1968, p. 442.
- [16] Syn, C. K., Jin, S., and Morris, J. W., Jr., "Cryogenic Fracture Toughness of 9 Percent Ni Steel Enhanced Through Grain Refinement," submitted for publication to *Metallurgical Transactions*.
- [17] Ritchie, R. O. and Knott, J. F., *Acta Metallurgica*, Vol. 21, 1973, p. 639.
- [18] Richards, C. E. and Lindley, T. C. in *Engineering Fracture Mechanics*, Vol. 4, 1972, p. 951.

D. E. Pettit¹ and J. M. Van Orden¹

Evaluation of Temperature Effects on Crack Growth in Aluminum Sheet Material

REFERENCE: Pettit, D. E. and Van Orden, J. M., "Evaluation of Temperature Effects on Crack Growth in Aluminum Sheet Material," *Fracture Mechanics, ASTM STP 677*, C. W. Smith, Ed., American Society for Testing and Materials, 1979, pp. 106–124.

ABSTRACT: Tests were conducted initially on 0.305-m (12-in.) wide center-cracked panels at room temperature to evaluate the effect of six different buckling guide configurations and three crack opening displacement (COD) measuring systems on the COD behavior of the panels. The final test configuration was selected and a series of fracture tests conducted on 1.9-mm (0.075-in.) 2024-T3 clad sheet, 1.9-mm (0.075 in.) 7475-T761 clad sheet, 4.8-mm (0.19-in.) 7075-T76 bare sheet. Full R-curves and fatigue crack propagation curves were developed for each material over a temperature range 22 to -54°C (72 to -65°F). The results show a marked drop in the apparent fracture toughness of both the 7000 series alloys with decreasing temperature while the 2024-T3 shows no apparent degradation. The entire R-curves are found to shift to lower K levels at a given Δc as the temperature decreased. Fractographic results show a change in the fracture mode of the 7000 series alloys from ductile rupture to a "quasi-cleavage" mixed with ductile rupture at temperatures of -7°C (20°F) and lower. Metallographic results indicated the "quasi-cleavage" features were due to an increased tendency for grain boundary cracking and generally reduced plastic deformation capability of the matrix at lower temperatures. An increase in the fatigue crack propagation rate also was observed at low temperature at stress intensity levels above $\Delta k \sim 22 \text{ MPa} \cdot \text{m}^{1/2}$ ($20 \text{ ksi} \sqrt{\text{in.}}$). The R-curve and fatigue crack propagation results are discussed in terms of the fracture mode over the temperature range.

KEY WORDS: aluminum alloys, temperature, fracture toughness, R-curve, fatigue (materials), crack propagation, fracture mode

One of the major uses of aluminum sheet in aircraft structures is for skin material in skin/stringer design. The major design parameters for this application include static strength, modulus, fatigue and damage tolerance.

¹ Research scientist senior and research scientist, respectively, Rye Canyon Research Laboratory, Lockheed-California Company, Valencia, Calif. 91520.

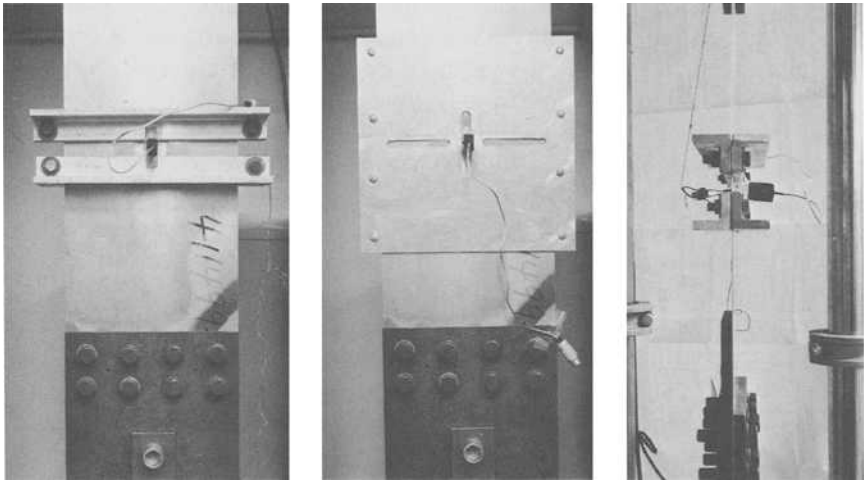
Previous data [1,2]² have indicated that 7475 aluminum alloy sheet and the currently used 2024 alloy have comparable fracture toughness, the 7475 alloy being a significantly stronger material, providing 434 to 469 Pa (63 to 68 ksi) versus 386 Pa (56 ksi) typical tensile yield strength for the 2024 alloy with comparable fatigue behavior. However, no data were available on the effect of test temperature to allow a comparison of properties at typical aircraft operating temperatures to permit a more meaningful comparison of the two alloys. The current program was undertaken (1) to provide quantitative data on the influence of buckling guide variables on the measured thin sheet fracture values, (2) to provide fatigue crack propagation and fracture toughness R-curve data for the normal range of aircraft operating temperature for 1.90 mm (0.075 in.) 2024-T3 clad, 1.90 mm (0.075 in.) 7475-T761 clad, and 4.82 mm (0.190 in.) 7075-T76 bare sheet material, and (3) to evaluate the results in terms of general material behavior in the range of aircraft operating temperatures.

Test Procedure Verification

Twelve-inch wide center-cracked tension specimens were examined first to determine the effect of various types of buckling constraints and attachment methods on the compliance gage output. The study consisted of saw cutting a 1.90 mm (0.075 in.) 7475-T761 12-in. wide panel to crack lengths from 0.05 to 0.28 m (2 to 11 in.) in 6.4-mm (¼-in.) increments and measuring COD versus load on loading and unloading. A second panel was fatigue precracked at low stress to produce the same range of crack lengths. Compliance readings were obtained from an MTS clip gage on the surface of the specimen and a hole gage (of the type described in Ref 3) for six buckling guide configurations: (1) 0.305 by 0.305 m (12 by 12 in.) full surface TFE-fluorocarbon covered face plates 6.4 mm (¼ in.) thick and tightened finger tight; (2) full surface TFE-fluorocarbon coated face plates torqued to 1.5 J (25 in.·lb); (3) TFE-fluorocarbon coated angle bars parallel to the crack with a 25.4-mm (1-in.) spacing from crack line, finger tight; (4) TFE-fluorocarbon coated angle bars, 25.4-mm (1-in.) spacing, torqued to 1.5 J (25 in.·lb); (5) TFE-fluorocarbon coated angle bars, 7.6-mm (0.3-in.) spacing, finger tight; (6) TFE-fluorocarbon coated angle bars, 7.6-mm (0.3-in.) spacing, torqued to 1.5 J (25 in.·lb). Typical test set-ups are shown in Fig. 1.

Plots of load versus COD for each set of conditions were examined and the shape characteristics of the loading and unloading plot noted. Slopes of the load versus COD curves were measured for both the loading and unloading portion of the cycle and the results tabulated along with the degree of linearity observed. Slope values then were reduced to the compliance parameter, *CEB*, as a function of $2c/W$ and the data compared

²The italic numbers in brackets refer to the list of references appended to this paper.



(a) Angle Bar Guides (b) Full Face Plates (c) Side View Showing Hole Gage and Clip Gage

FIG. 1—Test setup for evaluation of buckling guide configuration.

with the Irwin-Westergaard expression [4] with the Liebowitz width correction [5] for an infinite width panel under axial loading.

$$\frac{E \text{ COD}}{\sigma W} = CEB = \left[\frac{\pi c}{W} / \sin \frac{\pi c}{W} \right]^{1/2}$$

$$\left\{ \frac{2Y}{W} \left\langle \frac{2W}{\pi Y} \cosh^{-1} \left(\frac{\cosh \frac{\pi Y}{W}}{\cos \frac{\pi c}{w}} \right) - \frac{1 + \mu}{\left[1 + \left(\frac{\sin \frac{\pi c}{W}}{\sinh \frac{\pi Y}{W}} \right)^2 \right]^{1/2}} + \mu \right\rangle \right\}$$

Two basic questions were addressed in this phase of the study; (1) what set of experimental test conditions provides the most reproducible data with the least indication of buckling? (2) does this set of “best” test condition data correlate with the theoretical compliance calibration curves?

A summary of the number of linear curves observed for each set of

conditions is shown in Table 1. Examination of the data shows the following trends:

1. Results with the full face plate show reasonably good results when finger tight, but become very poor when torqued to 1.5 J (25 in. · lb). This appears to be due to a slight bowing of the face plate as the clamping force at the edge increases, thus pulling the plate away from the specimen at the center and clamping only on the edges.

2. Results with the angle bars show good results with the clip gage, with the results improving slightly as the angles are torqued. Observations indicate this may be due to the lightly torqued clamping action removing any slight curvatures in the sheet specimens.

3. The clip gage results are generally more consistent and reliable than the hole gage results. The hole gage tends to exhibit consistently linear curves on loading which also show a major change in slope on unloading. This marked slope variation (10 to 20 percent) is believed due to a "rocking" of the gage in the hole resulting from mechanical instability produced by (a) no locking location for the gage arms, (b) the gage weight hanging far from the specimen, and (c) relatively low spring factor in the gage arms.

4. Optimum conditions appear to be the following: (a) MTS clip gage, (b) angle bar buckling guides, (c) a light torque of 1.5 J (25 in. · lb) on the guides, (d) 7.6-mm (0.3-in.) spacing from the crack path to the buckling guides. For these conditions linear curves indicating no buckling are obtained for the range of crack lengths and types of cracks.

Compliance values based on the measured load versus COD slope on loading were computed for the 7475-T761 saw cut and 2024-T3 fatigue cracked results using the optimum test conditions and compared with the classical theoretical Irwin-Westergaard solution with the Liebowitz width correction factor as shown in Fig. 2. Also shown in Fig. 2 are recent finite element solutions for the CCT specimen conducted by Shaw [6] and Boundary Collocation results of Newman [7]. The test results agree well with the theoretical values which have been included recently in the revised ASTM Recommended Practice for R-Curve Determination (E 561 - 76 T).

Results from the saw-cut 7475-T761 panel using the full face plates and hole gage are of interest since they are similar to the conditions of previously reported work [8]. Figure 3 shows a comparison of the hole gage results based on the loading slope for these test conditions. Surprisingly the "finger tight" results correlate reasonably well with the original Irwin-Westergaard solution, the same results reported previously in Ref 8. When the types of curves included in these data were reviewed it was noted that the type of curve for the "finger tight" conditions is linear on loading and unloading, but that the two slopes are different by up to 20 percent.

TABLE 1—Summary of linear load versus COD curves observed as a function of gage type and buckling constraint.

Gage Type	Total Number Analyzed	Curve	Face Plate		Angle, 1.0-in. Spacing		Angle, 0.3-in. Spacing	
			Finger Tight	Torqued	Finger Tight	Torqued	Finger Tight	Torqued
7475-T761 SAW-CUT RESULTS								
Clip	18	A ^a	15	7	11	15	11	15
		AB ^b	3	5	5	3	7	3
		C ^c	0	6	2	0	0	0
Hole	18	A	1	6	2	14	0	14
		AB	2	7	5	4	3	4
		C	15	5	11	0	15	0
2024-T81 FATIGUE CRACKED RESULTS								
Clip	13	A	6	1	7	8	5	11
		AB	5	7	6	5	7	2
		C	2	5	0	0	1	0
Hole	13	A	8	2	1	4	2	6
		AB	4	5	2	4	9	5
		C	1	6	10	5	2	2

^a Linear on loading and unloading retracing a single line.^b Linear on loading and unloading with slight deviations (< 3%) between the loading and unloading slopes.^c Non Linear.

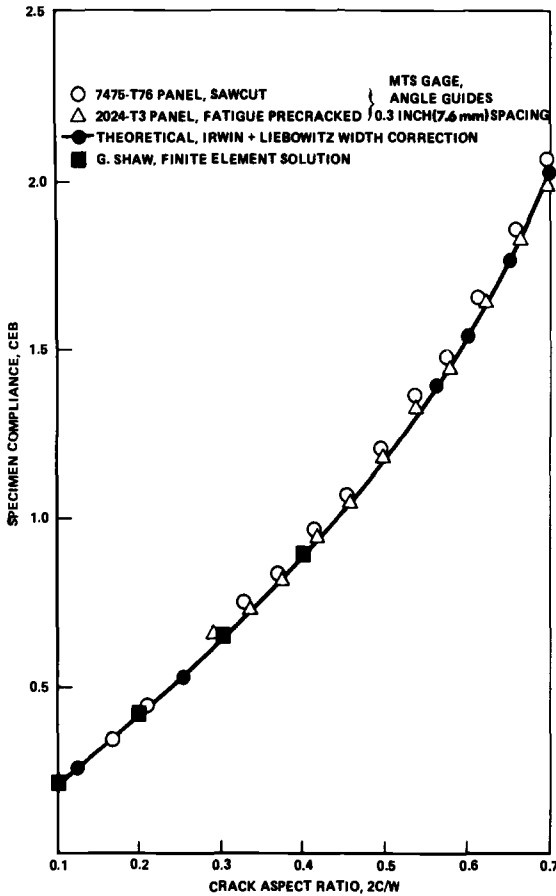


FIG. 2—Comparison of optimum test condition data with theoretical solution.

Based on the results of this study, the following recommendations appear to be warranted:

1. Major variations in the shape of the load versus COD curve and the measured slope of the curve can be produced by the use of inappropriate sheet buckling constraints.
2. The “hole” gage is mechanically unstable with its current mounting system and may not always give reliable results. The commercial MTS clip gage is mechanically stable and gives consistent results.
3. Good buckling constraint can be obtained with lightly torqued 1.5 J (25 in.·lb) lateral braces such as angle bars parallel to the plane of the crack and located from 7.6 to 38.1 mm (0.3 to 1.5 in.) from the crack path, both above and below the crack.
4. The use of two MTS gages, one on each surface of the panel, will also provide a “real time” method of evaluating sheet buckling without

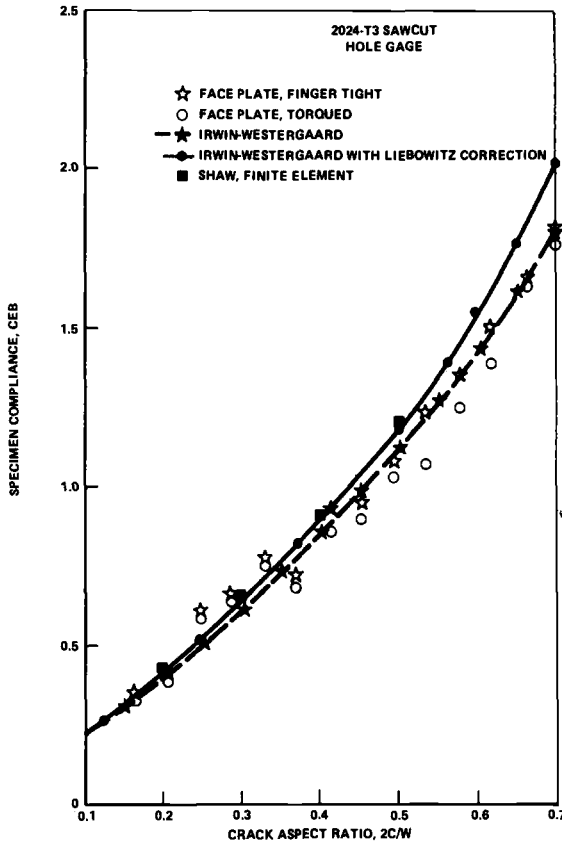


FIG. 3—Comparison of hole gage data for test conditions similar to Ref 8.

the need to partially unload the specimen. A full presentation of results of this phase of the study is presented in Ref 9.

Experimental Results

Tensile Results

The effect of test temperature on the tensile properties of the three materials is shown in Table 2. All three materials show a slight increase in strength with decreasing temperature while no significant variation is noted in the percent elongation or percent reduction of area.

Fracture Results

Based on the previous results, lightly torqued lateral angle bar braces were used with dual MTS clip gages (front and back of sheet) in the test

TABLE 2—Effect of test temperature on tensile properties.

Material	Test Temperature		Ultimate Tensile Strength, σ_u		Yield Strength, σ_y		Elongation, percent	Reduction in Area, percent
	°F	°C	ksi	Pa	ksi	Pa		
7475-T761 clad	+72	+22	73.8	509	64.1	442	12	17
	+72	+22	69.4	478	60.5	417	11	22
	+20	-7	75.7	522	67.1	463	13	21
	-20	-29	76.5	527	66.8	460	11	19
	-65	-54	78.3	540	68.3	471	12	23
	-65	-54	77.8	536	68.1	469	11	16
2024-T3 clad	+72	+22	66.6	459	43.3	299	19	25
	+72	+22	66.1	456	42.2	291	22	25
	-65	-54	68.6	473	44.2	305	24	29
	-65	-54	68.1	469	44.4	306	24	27
7075-T76 bare	+72	+22	80.3	554	72.1	497	11	16
	+72	+22	80.1	552	72.2	498	11	14
	-65	-54	83.9	578	75.4	520	12	21
	-65	-54	83.1	573	75.1	518	11	17

program. Both gages and the load cell were monitored continuously using the Rye Canyon Data Central Computer. All data reduction and other test procedures conformed to ASTM Recommended Practice E 561. The apparent fracture toughness based on the maximum load and initial crack length for the three materials is presented in Fig. 4 as a function of test temperature. The results show a major decrease in the apparent fracture toughness of the two 7000 series materials but no degradation in the toughness of the 2024-T3.

R-curves for the three materials are shown in Figs. 5 through 7. The 2024-T3 clad sheet R-curve behavior is unaffected by a change in temperature from 22 to -54°C (72°F to -65°F). However, the 7475-T761 clad sheet shows a significant decrease in the stress intensity value required to produce a given amount of crack extension with decreasing

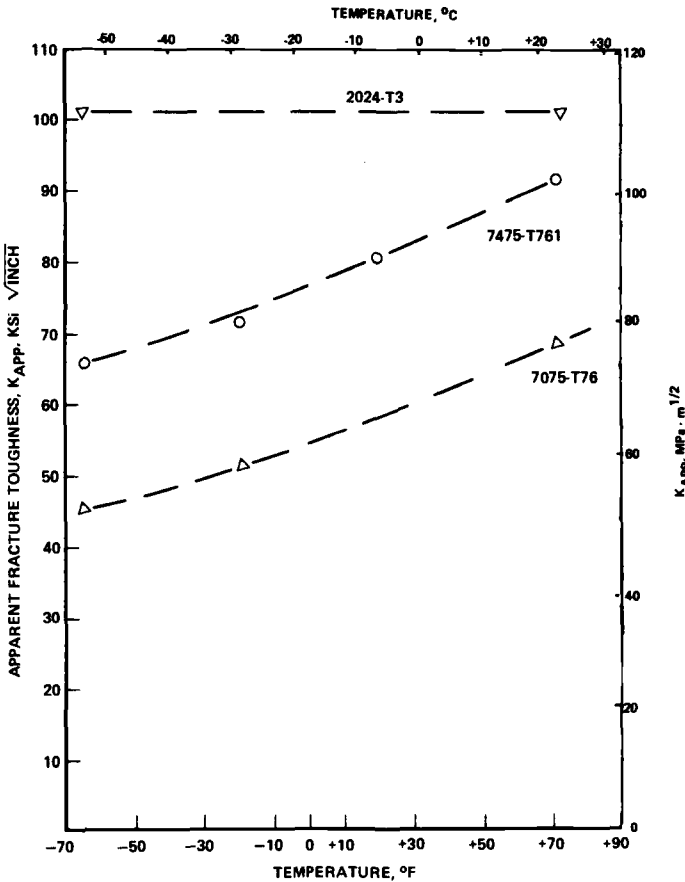


FIG. 4—Effect of test temperature on the apparent fracture toughness of three aluminum alloys.

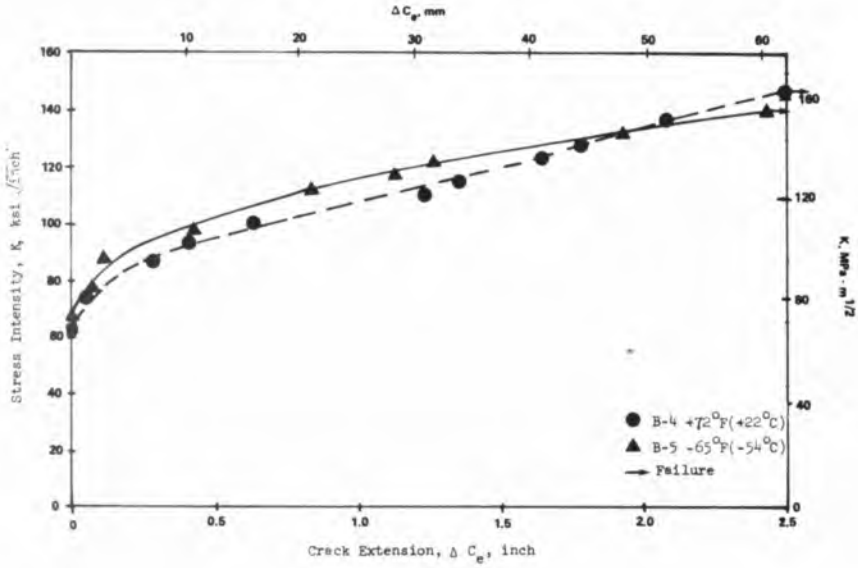


FIG. 5—Effect of temperature on the R-curve behavior of 2024-T3 clad sheet.

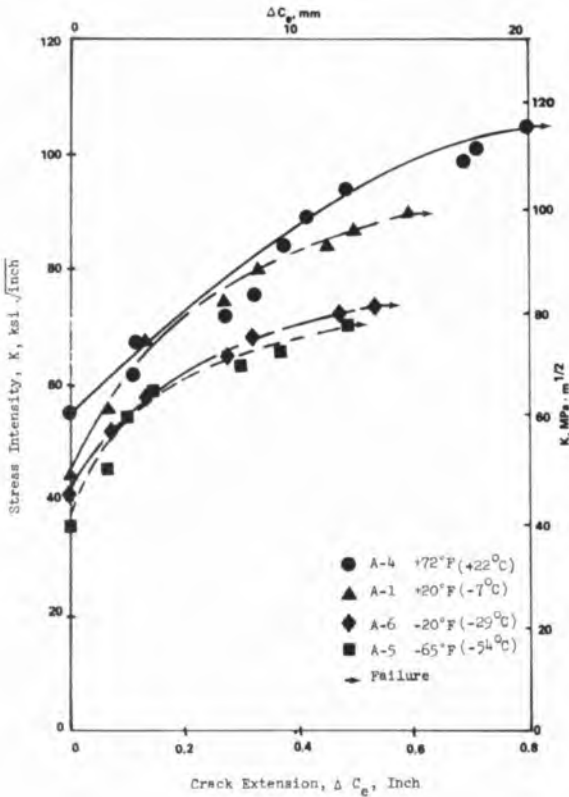


FIG. 6—Effect of temperature on the R-curve behavior of 7475-T761 clad sheet.

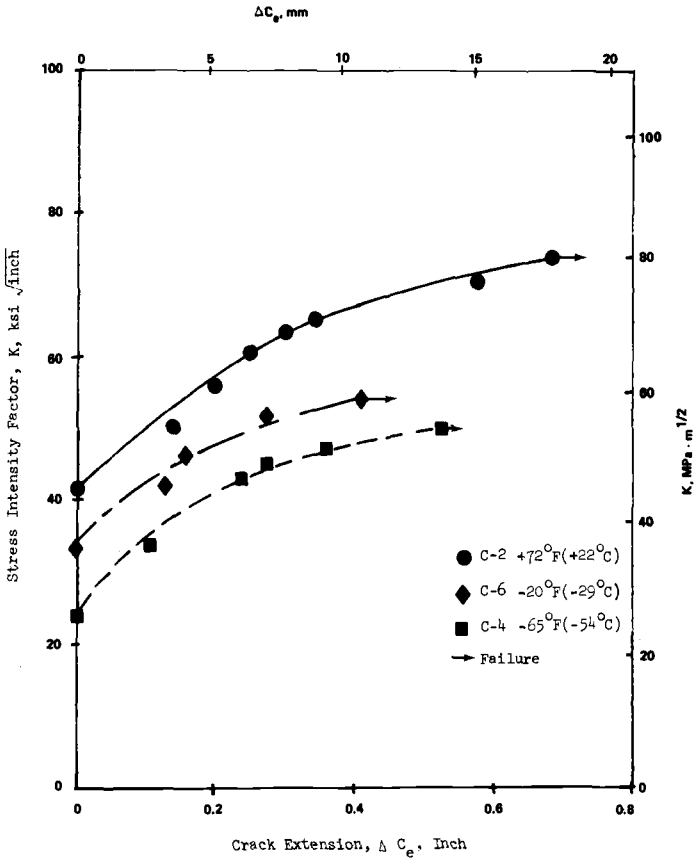


FIG. 7—Effect of test temperature on the R-curve behavior of 7075-T76 bare sheet.

temperature. In addition, the maximum amount of stable crack extension prior to instability and the stress intensity value at which crack extension begins also decreases with temperature. Similar behavior also is observed in the 7075-T76 sheet material.

Fatigue Crack Propagation Results

All fatigue crack propagation testing was done in a 150 kip closed loop electrohydraulic test machine using the same temperature controlled test chamber used in the R-curve tests. Temperature was controlled to $\pm 1^\circ\text{C}$ (2°F) throughout the test. Crack lengths were measured through a window in the chamber using a traversing microscope. Full details are presented in Ref 9.

Fatigue crack propagation data ($R = +0.1$) were generated at 22 and -54°C (72 and -65°F) for both the 2024-T3 and 7475-T761 clad materials

over the full range of fatigue crack propagation rates. Results for 2024-T3 showed no effect of temperature over the entire range of data. For the 7475-T761, however, an increasingly significant acceleration of the crack propagation rate is observed at -54°C (-65°F) relative to the 22°C (72°F) data above a value of $\Delta K \sim 22 \text{ MPa} \cdot \text{m}^{1/2}$ ($20 \text{ ksi} \sqrt{\text{in.}}$), as shown in Fig. 8. Below this value no effect of temperature is observed in the Fig. 8 data.

Fractography Results

Fractographic features of the tension and R-curve specimens were determined with a CWIK-Scan scanning electron microscope (SEM). Typical SEM fractographs of the 7475-T761 tension specimens are shown in Figs. 9, 10, and 11. The results show a major change in the fracture

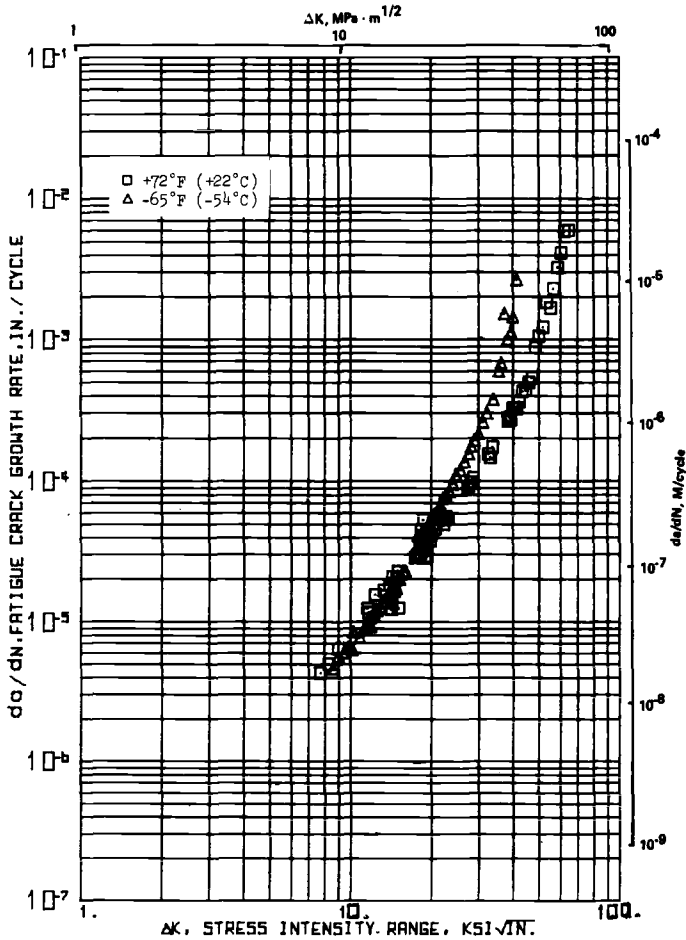
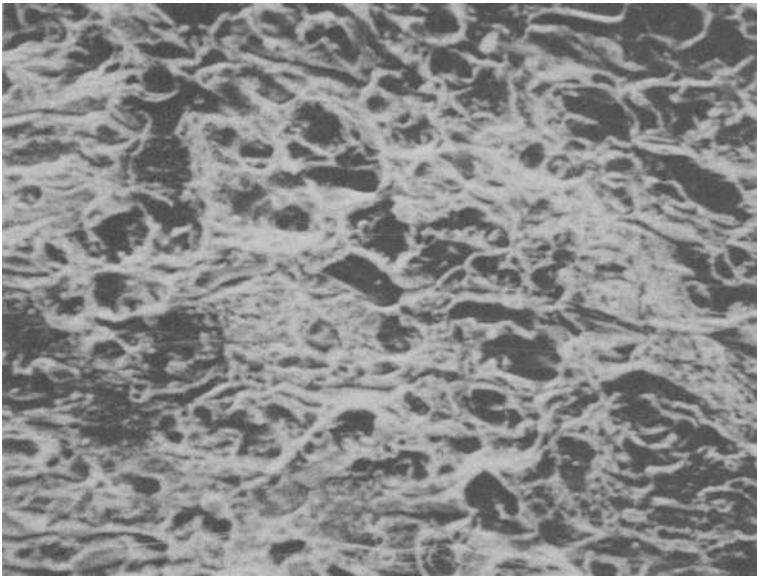
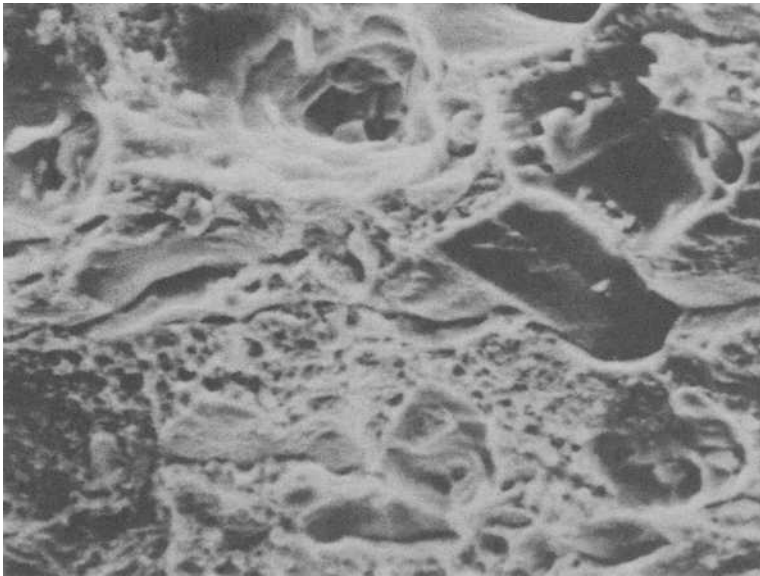


FIG. 8—Effect of temperature on the fatigue crack growth behavior of 7475-T761.

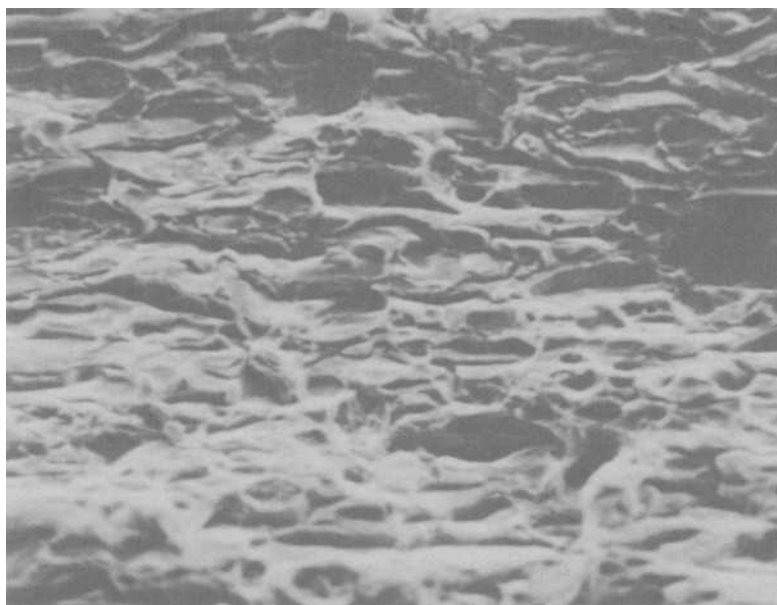


(a)

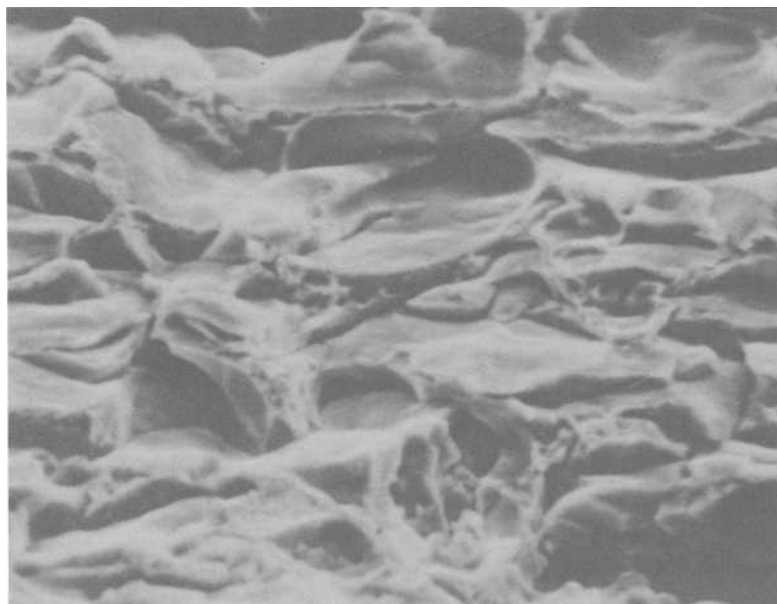


(b)

FIG. 9—SEM fractograph of tension specimen A1, 7475-T761 sheet tested at 22°C (72°F). Magnification (a) $\times 500$, (b) $\times 1500$.

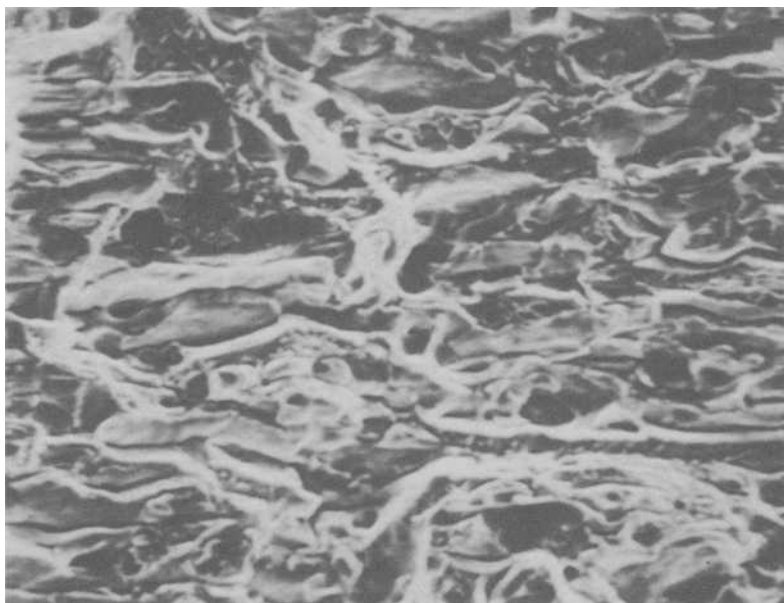


(a)

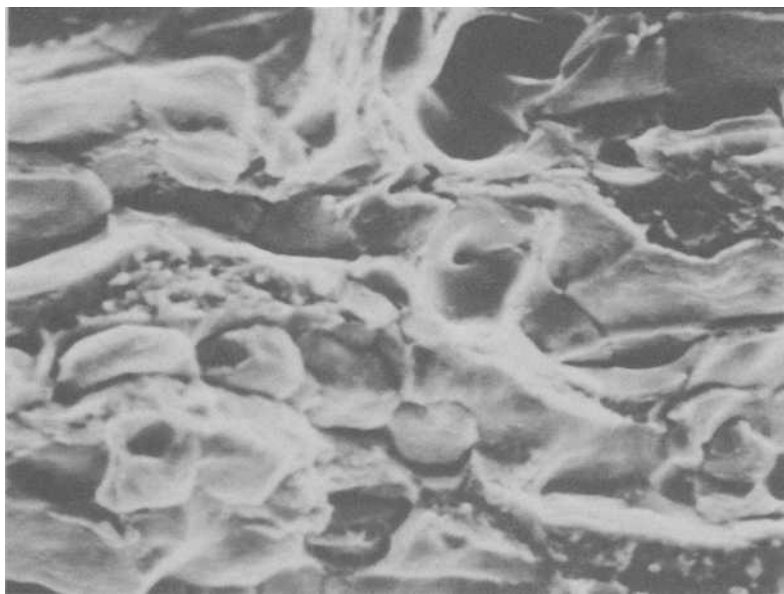


(b)

FIG. 10—SEM fractograph of tension specimen A3, 7475-T761 sheet tested at -7°C (20°F). Magnification (a) $\times 500$, (b) $\times 1500$.



(a)



(b)

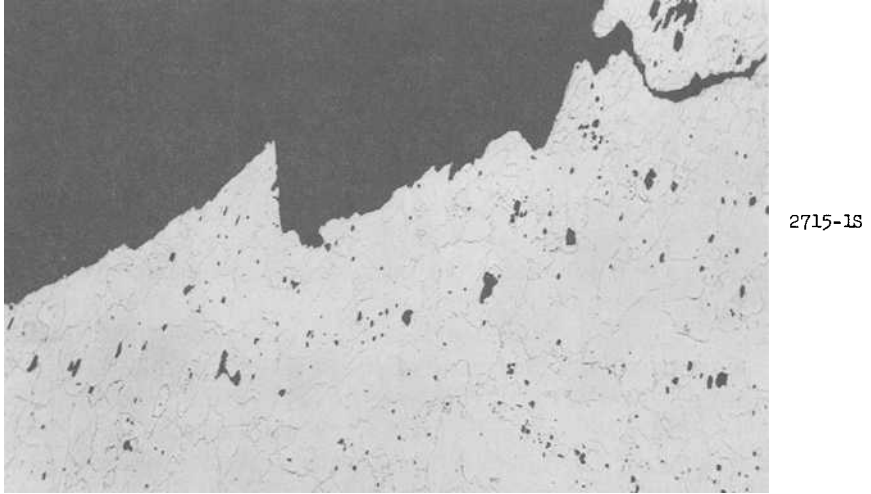
FIG. 11—SEM fractograph of tension specimen A5, 7475-T761 sheet tested at -54°C (-65°F). Magnification (a) $\times 500$, (b) $\times 1500$.

mode of both 7000 series alloys as the temperature decreased from 22 to -54°C (72 to -65°F). At room temperature the fracture surfaces reveal primarily ductile dimple rupture with some local cleavage associated with inclusions. However, as the temperature decreases, the amount of the ductile dimple features formed decreased markedly and a low energy, flat quasi-cleavage type fracture feature was observed. This change is apparent at a temperature of -7° (20°F) and continues to be observed at all test temperatures below this value. The R-curve specimens showed a similar change in fracture mode for both the 7475-T761 and 7075-T76 materials. For more detailed fractographic results, see Ref 9. No change was observed in any of the 2024-T3 specimens with temperature, the fracture mode remaining that of micro-void coalescence and growth (that is, ductile dimple fracture) for all conditions.

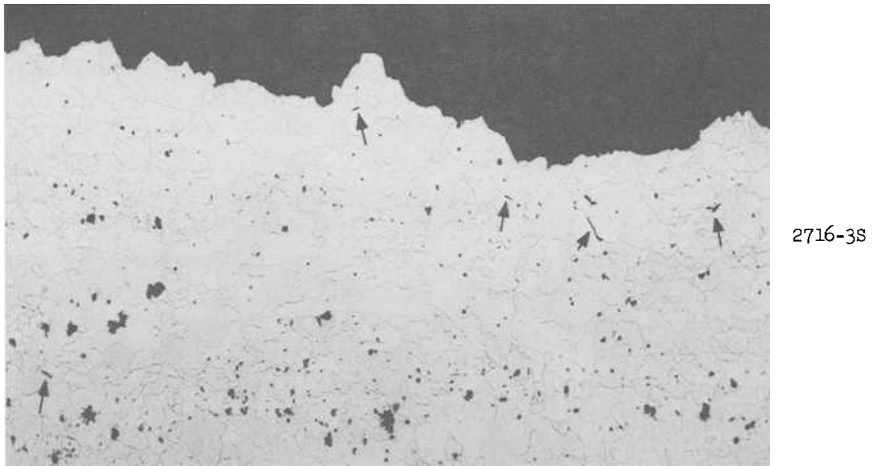
Standard metallographic sections were taken subsequently through the fracture region parallel to the plane of the sheet in the 7475-T761 and 7075-T76 alloys. Typical results, shown in Fig. 12 for the 7475-T761 material, show what appears to be grain boundary cracking (see arrows) at the lower temperature. Based on these results it is believed that the low energy SEM fracture surface features are due to the onset of grain boundary cracking at temperatures of -7°C (20°F) and below.

Discussion of Results

The need for aircraft structural materials that combine light weight, high tensile and fatigue properties, and good fracture toughness and fatigue crack growth characteristics has led to the development of the new generation of advanced 7000 series aluminum alloys. However, most of the property comparisons have been made at room temperature and not at the lower temperatures representative of inflight aircraft operating temperatures. In this study it has been shown that while the new 7475-T761 alloy has fracture values similar to 2024-T3 at room temperature, a major decrease in the fracture toughness is observed as the temperature is decreased to the range -7 to -54°C (20 to -65°F) while no change is observed in 2024-T3. A comparison of the 7475-T761 low temperature fracture behavior with that of 7075-T76 shows a decrease similar to that reported by Wang [10] for 7075-T6. This is of particular interest since the 7475-T761 is representative of the "clean" alloy variations of the basic 7075 material, the aim of the "clean" alloys being to reduce the inclusion content while maintaining the high strength of the 7075 material. This change was aimed at eliminating cracking at inclusions as has been observed previously [11,12]. However, the results at temperatures at or below -7°C (20°F) indicate the increasing dominance of a low energy intergranular failure mode. Intergranular fracture features have been observed previously [11,12,13,14] in alloys such as 7075-T76 at room



(a) A-1, +72°F (+22°C)



(b) A-5, -65°F (-54°C)

FIG. 12—Metallographic sectioning results for 7475-T761 sheet tension specimens. Magnification $\times 1000$.

temperature as the thickness has increased, (that is, increasing constraint), but previously had been observed to occur as "steps" lying parallel to the loading direction. At the lower temperatures examined here, the intergranular cracking occurs in the plane of the crack, that is, more perpendicular to the load path. Thus the decrease in the fracture toughness of the 7475-T761 and 7075-T76 is believed to be due to the increasing tendency to intergranular cracking at lower temperatures.

It is interesting to note that the standard tensile properties show no degradation of the normally reported tensile yield strength, percent elongation or percent reduction of area even though the fracture mode change can be seen fractographically. The fact that the R-curve fracture behavior is affected markedly by this fracture mode change with decreasing temperature indicates that the slight increase in the yield strength observed at low temperatures may be sufficient or at least contributory to an increased state of triaxiality at the crack tip region (that is, in the high strain region) which could result in the onset of the intergranular failure mode.

On balance, the 7475-T761 material does possess good tensile properties and a fracture toughness that is higher than that of the normally used 7075-T76 over the range of aircraft operating temperatures. However, the effect of temperature on the fracture and fatigue crack propagation behavior of all 7000 series alloys must be taken into consideration for any aircraft damage tolerance analysis.

Acknowledgments

This work was performed during 1977 as part of the Lockheed-California Company Independent Research Program. Additional thanks given to W. E. Krupp, E. K. Walker, and G. Wald for their valuable discussions and contributions to this program. D. Black, F. Pickel and D. Diggs were responsible for the laboratory testing for which additional recognition should be given.

References

- [1] Van Orden, J. M., Pettit, D. E., and Chiu, S. T., "Advanced Aluminum Alloys—Fatigue and Fracture of 7475 and 2024 Sheet," Report LR 26284, Lockheed-California Company, Dec. 1973.
- [2] Brownhill, D. J. and Kaufman, J. G., "The Mechanical Properties, Including Fracture Toughness and Fatigue of Some Alcoa 467 Process Bare and Alclad X7475-T761 and T61 Sheet," Alcoa Report No. 9-70-19, June 1970.
- [3] Sullivan, A. M., Freed, C. N., and Stoop, J. in *Fracture Toughness Evaluation by R-Curve Methods*, ASTM STP 527, American Society for Testing and Materials, 1973, pp. 85-104.
- [4] Irwin, G. R., "Fracture Testing of High Strength Sheet Materials Under Conditions Appropriate for Stress Analysis," NRL Report 5486, NRLRA, July 1960.
- [5] Eftis, J. and Liebowitz, H., *International Journal of Fracture Mechanics*, Vol. 8, No. 4, Dec. 1972.

- [6] Shaw, G. T., letter to D. E. Pettit, dated 25 Nov. 1975.
- [7] Newman, J. C., Jr., "Crack-Opening Displacements in Center-Crack Compact, and Crack-Line Wedge-Loaded Specimens," NASA TN D 8268, National Aeronautics and Space Administration, 1976.
- [8] Sullivan, A. M. and Freed, C. N., "The Influence of Geometric Variables on K_c Values for Two Thin Sheet Aluminum Alloys," NRL Report 7270, 17 June 1972.
- [9] Pettit, D. E. and Pickel, F. M., "Crack Growth Resistance Test Methods," Report LR 26290, Lockheed-California Company, May 1975.
- [10] Wang, D. Y. in *Progress in Flow Growth and Fracture Toughness Testing*, ASTM STP 536, American Society for Testing and Materials, 1972, pp. 334-349.
- [11] Tanaka, J. P., Pampillo, C. A., and Low, J. R., Jr. in *Review of Developments in Plane Strain Fracture Toughness Testing*, ASTM STP 463, American Society for Testing and Materials, 1970, p. 191.
- [12] Pettit, D. E. and Hoepfner, D. W., "The Interaction of Material and Geometric Aspects in the Fracture of Aluminum Alloys," *Proceedings*, International Conference on Mechanical Behavior of Materials, Koyoto, Japan, 15-20 Aug. 1971.
- [13] Zinkham, R. E., *Engineering Fracture Mechanics*, Vol. 1, 1968, p. 275.
- [14] Hunter, M. S. and McMillan, J. C. in *Electron Fractography*, ASTM STP 436, American Society for Testing and Materials, 1968, p. 196.

T. T. Shih¹ and G. A. Clarke¹

Effects of Temperature and Frequency on the Fatigue Crack Growth Rate Properties of a 1950 Vintage CrMoV Rotor Material

REFERENCE: Shih, T. T. and Clarke, G. A., "Effects of Temperature and Frequency on the Fatigue Crack Growth Rate Properties of a 1950 Vintage CrMoV Rotor Material," *Fracture Mechanics, ASTM STP 677*, C. W. Smith, Ed., American Society for Testing and Materials, 1979, pp. 125-143.

ABSTRACT: Air environment fatigue crack growth rate data were developed for a 1950 vintage (air cast) chromium-molybdenum-vanadium (CrMoV) rotor steel at temperatures of 24, 121, 260, and 427°C (75, 250, 500, and 850°F) and loading frequencies of 0.0017, 0.017, 0.1, and 1.0 Hz. Results show that the room-temperature fatigue crack growth rate in the 1950 vintage material is on the order of two to eight times faster than that encountered in a more modern vacuum cast forging depending upon the ΔK level of interest. Results also show that the effect of frequency on the fatigue crack growth rate varies with differing test temperatures. At room temperature as well as at 260 and 427°C (500 and 800°F), the rate of crack growth increases with decreasing frequency. At 121° (250°F), there is little effect of loading frequency on fatigue crack growth rate. This temperature dependent frequency effect is attributed to the different mechanisms interacted with fatigue at various temperatures. The effect of temperature on crack growth rates was also found to be frequency dependent with more pronounced temperature effects observed at lower frequencies. However, the general trend is the same for all values of frequency, that the rate of fatigue crack growth initially decreases before increasing at higher temperatures. The fact that fatigue crack growth rates do not increase monotonically with increasing temperature is attributed to the decrease in relative humidity of the test environment with increasing temperature.

KEY WORDS: fatigue (materials), frequency, crack propagation, temperature, rotors, steel-CrMoV

On June 19, 1974 at the Gallatin Station of the Tennessee Valley Authority, the intermediate pressure-low pressure rotor of the No. 2 turbine failed in a catastrophic brittle mode [1,2].² Although steam turbine rotor failures are somewhat a rare occurrence, the potential destructive

¹ Senior engineer and senior engineer respectively, Westinghouse Research and Development Center, Pittsburgh, Pa. 15235.

² The italic numbers in brackets refer to the list of references appended to this paper.

force of a turbine rotor with a running speed of 3600 rpm is considerable. To ensure against such failures occurring in the future, the Electric Power Research Institute (EPRI) has sponsored research to develop lifetime prediction techniques for the evaluation of turbine rotors already in service.

This life prediction program is to be based upon the growth of an estimated or "equivalent" flaw (as determined by nondestructive examination methods) to some critical size. Flaw growth is nominally expected to occur by a fatigue mechanism. Accordingly, cyclic crack growth rate data expressed in terms of the stress intensity factor range for the appropriate mean stress, frequency, and temperature are identified as key material parameters. As part of this research program, Westinghouse Electric is responsible for the generation of fatigue crack growth rate data as input to the life prediction program being developed by Southwest Research Institute, while Battelle-Columbus Laboratories are responsible for defect characterization using nondestructive techniques.

One important aspect of this program is its focus on developing consistent fracture mechanics data for a single group of turbine rotors. The 1950 vintage air melted CrMoV rotors were selected due to the availability of retired rotors, the high likelihood of defect observations, the current interest in predictions of remaining life in these rotors, and because the failed Gallatin No. 2 rotor belongs in this category.

Experimental Work

Material and Specimens

The material studied was taken from a low pressure steam turbine rotor that was retired from the Joppa Station by Electric Energy, Inc. The tensile properties, Charpy energy, and fracture toughness at various temperatures are presented in Figs. 1, 2, and 3, respectively [3].

All fatigue crack growth rate testing was conducted with 25.4-mm (1-in.) thick compact type (1T-CT) specimens with $H/W = 0.486$, as shown in Fig. 4. Grooves 1.27 mm (0.05 in.) deep were machined on each side of the specimen to ensure crack propagation along a plane perpendicular to the loading direction. The specimens were oriented in the C-R direction, that is, the crack propagated in the radial direction of the rotor. All the specimens were fatigue precracked at a stress ratio R of 0.1 ($R = \text{minimum load}/\text{maximum load}$) through a sequence of loads that reduced the maximum stress intensity, K_{\max} , to a level that was equal to or less than the selected starting K_{\max} level for the actual experiments. Fatigue cracks of at least 2 mm (0.08 in.) in length from the end of the starter notch were provided to ensure that subsequent crack growth would be through material that had not been altered by the notch

preparation procedures and would be unaffected by the starter notch geometry.

The stress intensity factor, K_I , for this compact type specimen was computed from Eq 1 [4].

$$K_I = \frac{P(2 + a/w)}{(BB_N)^{1/2} W^{1/2} (1 - a/w)^{3/2}} \{ [0.8072 + 8.858(a/w) - 30.23(a/w)^2 + 41.088(a/w)^3 - 24.15(a/w)^4 + 4.951(a/w)^{1/5}] \} \quad (1)$$

where

- P = applied load,
- B = specimen thickness,
- B_N = net thickness at groove,
- W = specimen width, and
- a = crack length.

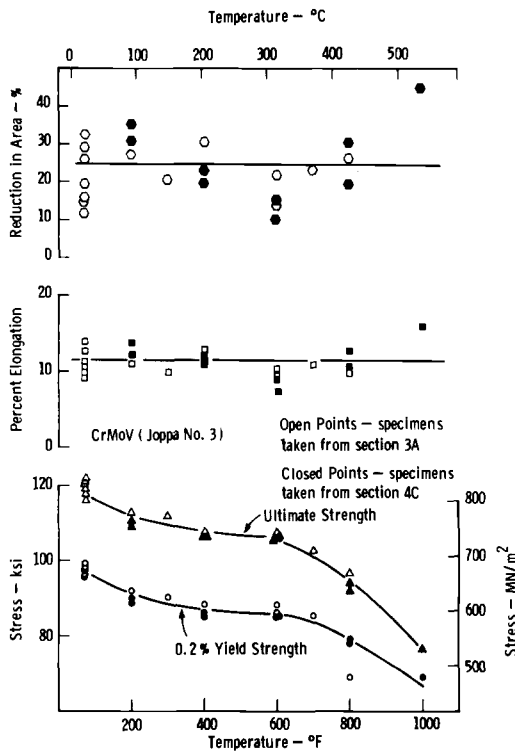


FIG. 1—Tensile properties of CrMoV taken from sections 3A and 4C at various temperatures.

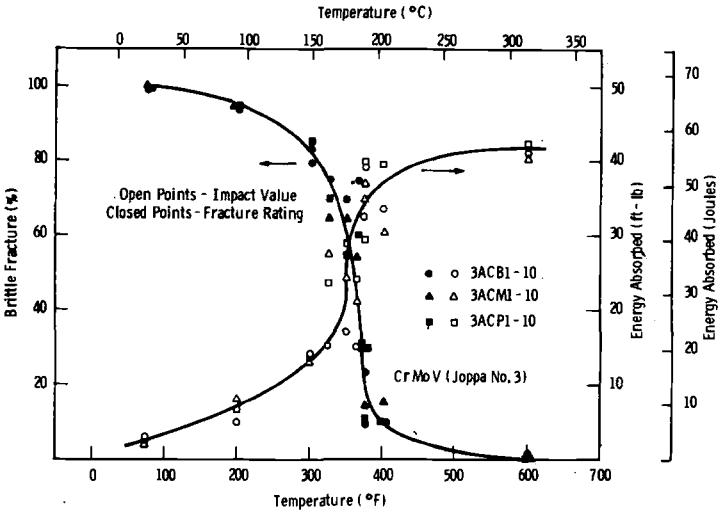


FIG. 2—Charpy V-notch impact properties of CrMoV steel taken from Joppa No. 3.

Both specimen width and crack length were measured from the line of loading, as shown in Fig. 4. The term $(BB_N)^{1/2}$ is used here to account for the effect of side grooves [5].

Testing Procedures

The test matrix given in Table 1 was used to evaluate the effect of frequency and temperature on fatigue crack growth rate behavior of this

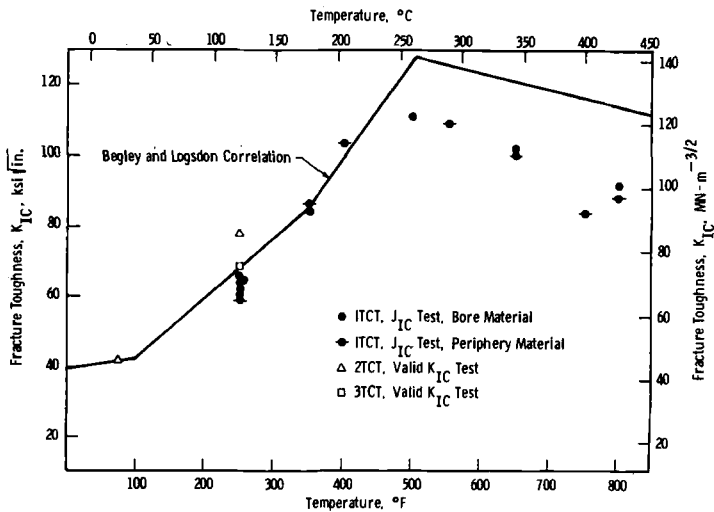


FIG. 3—Fracture toughness properties of CrMoV steel taken from Joppa No. 3.

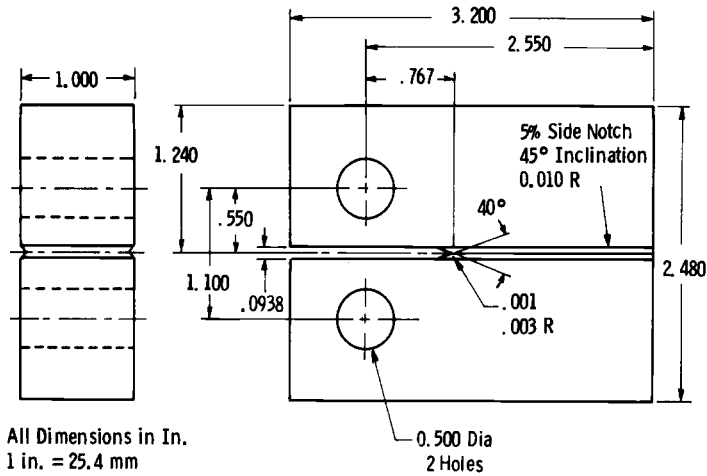


FIG. 4—Compact tension fatigue crack growth specimen.

rotor material. All the tests were carried out in laboratory air under tension-tension (triangular wave) loading in a MTS closed-loop electrohydraulic testing machine operated in load control. Load was controlled within an accuracy of less than ± 1 percent. The desired temperature was achieved by using electrical resistance heating tapes. The temperature was monitored continuously during the tests by means of thermocouples. Temperature stability was kept better than $\pm 3^{\circ}\text{C}$ ($\pm 5^{\circ}\text{F}$) during the test by using fiberglass insulation.

For those tests with a frequency other than 0.0017 Hz, cracks were extended by constant load-amplitude fatigue with a stress ratio $R = 0.1$, cycling at a given frequency. Visual crack length measurements were made without interrupting the test by using a $10\times$ traveling microscopy. The number of cycles was recorded while the crack length measurement was made for approximately each 0.6-mm (0.025-in.) crack extension. A seven point polynomial technique [6] was used to obtain the crack growth

TABLE 1—Test matrix.

Frequency	Temperature	24°C	121°C	260°C	427°C
		(75°F)	(250°F)	(500°F)	(800°F)
1 Hz (1 cps)		X	X	X	X
0.1 Hz (0.1 cps)		X	X	X	X
0.017 Hz (1 cpm)		X	X	X	X
0.0017 Hz (0.1 cpm)			X	X	X

rate from the raw a versus N data; while the stress intensity range was calculated by using Eq 1 with ΔP replacing P .

For 0.0017-Hz tests, a test method similar to the method used by Brothers [7] and Ohmura et al [8] was used to reduce the testing time and is described as follows. For tests conducted at 427°C (800°F) and 260°C (500°F), a given number of test cycles were applied to the specimen at the desired temperature and ΔK level, after which, the frequency was increased to 10 Hz and the temperature decreased to 121°C (250°F). Once a predetermined amount of crack extension was obtained at this frequency and temperature, the original frequency and temperature were resumed and testing continued. This procedure of alternating test frequency and temperature was repeated several times during the test and resulted in a well-defined change in the macroscopic appearance of the fatigue fracture surfaces, as shown in Figs. 5 and 6. The fatigue crack growth rate was determined simply by dividing the width of the crack growth band by the number of cycles elapsed. This test method was modified slightly to accommodate the test conducted at 121°C (250°F). Under this circumstance, crack growth marks were produced by alternating testing frequency along with stress ratio instead of temperature. To ensure that fatigue crack growth marks were produced, periodic heat tint at 427°C (800°F) was made prior to the application of testing cycles.

Results and Discussions

Fatigue crack growth rate data generated in this program are presented, in terms of $\log da/dN$ versus $\log \Delta K$, in Figs. 7 to 11. For the crack growth rate range studied, the rotor steel generally exhibits a linear relationship between $\log da/dN$ versus $\log \Delta K$. Consequently, these data can be expressed readily in terms of the Paris equation, $da/dN = A(\Delta K)^n$ [9]. Here n is the slope of the $\log da/dN$ versus $\log \Delta K$ curve and A is the value of da/dN at $\Delta K = 1 \text{ ksi}\sqrt{\text{in}}$. It was found that a slope of 2.7 is appropriate for most of the data generated in this program. The Paris equation with appropriate empirical constants are noted on the respective crack growth curves.

Since the vacuum degassing technique was not practiced until 1957, the 1950 vintage rotor steel is expected to contain many more discontinuities (both defects and inclusions) than the modern vacuum cast rotor steels. Therefore, a limited effort was made to characterize the effect of these discontinuities prior to the evaluation of the effect of temperature and frequency. Figure 7 presents room-temperature laboratory air fatigue crack growth data generated at 20 Hz from an ultrasonically clean specimen and from a specimen with reported ultrasonic indications, the size of the largest discontinuity is 4.19 mm^2 (0.0064 in.^2). These data clearly show that dispersed small discontinuities, as reported by ul-

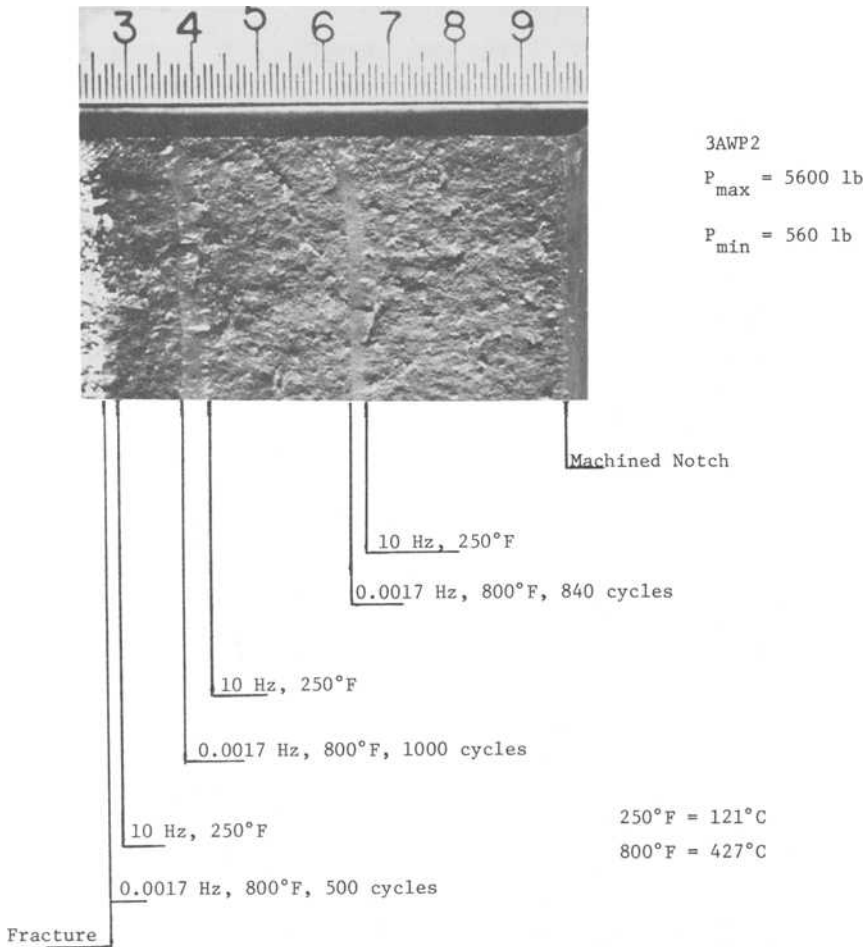


FIG. 5—Macroscopic fractograph of a specimen subjected to alternating temperature and frequency loading.

trasonic procedures, have little effect on fatigue crack growth rates. This is consistent with the report on a T1 steel [10] and with the report on Gallatin No. 2 rotor steel [11]. On the other hand, inclusion segregates were found to accelerate the crack growth rate locally on a NiMoV rotor steel [12]. This discrepancy could be attributed to the difference in the morphology and distribution of discontinuities in the various materials studied.

The effect of frequency on fatigue crack growth rates at various temperatures is presented in Figs. 8 to 11. Figure 8 shows that, at room

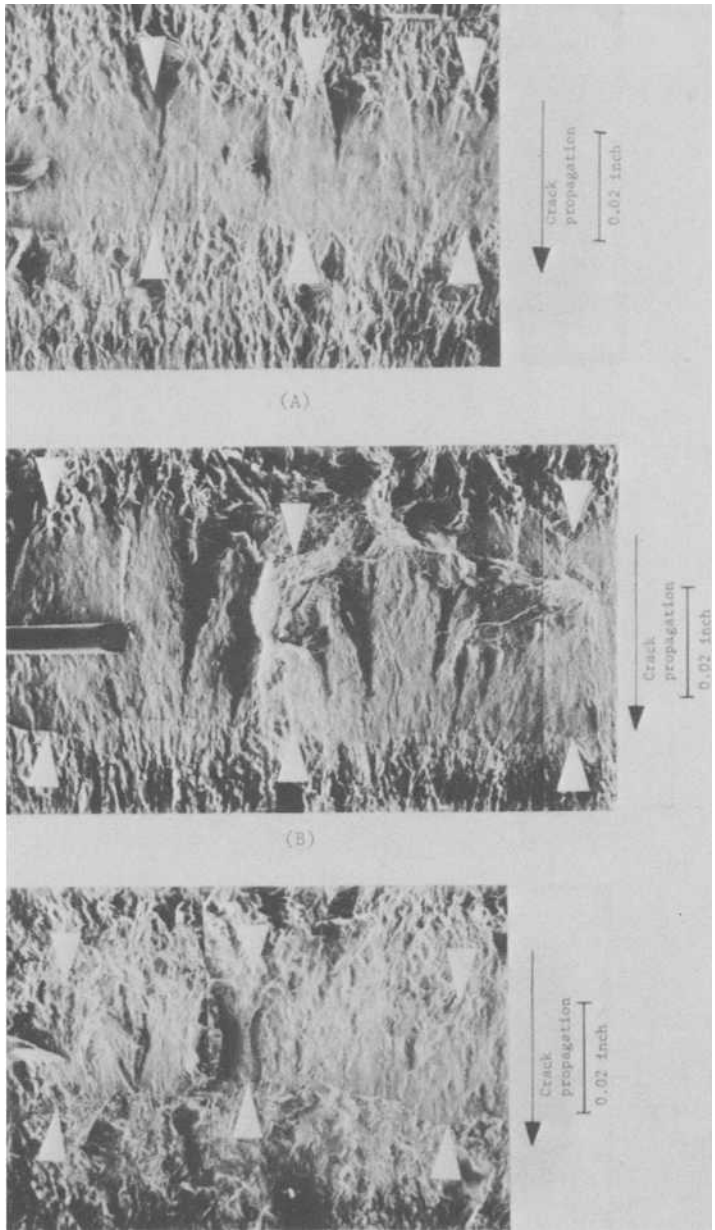


FIG. 6—SEM of fracture surface at $\times 50$ showing fatigue crack growth band for CrMoV at 427°C (800°F), 0.0017 Hz : (a) 840 cycles at $\Delta K = 32\text{ MN/m}^{3/2}$ ($29.5\text{ ksi}\sqrt{\text{in.}}$); (b) 1010 cycles at $\Delta K = 41\text{ MN/m}^{-3/2}$ ($37.5\text{ ksi}\sqrt{\text{in.}}$); (c) 500 cycles at $\Delta K = 48\text{ MN/m}^{-3/2}$ ($44.0\text{ ksi}\sqrt{\text{in.}}$).

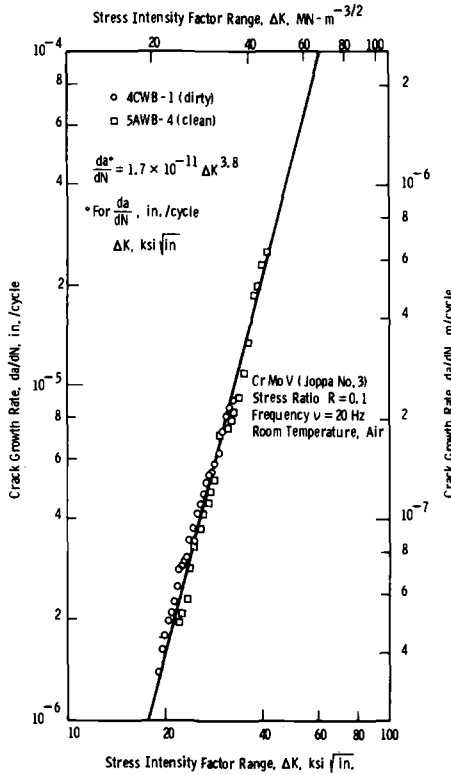


FIG. 7—Room temperature fatigue crack growth rate of CrMoV steel tested at 20 Hz.

temperature in air, the rate of fatigue crack growth increases with decreasing frequency. Fatigue crack growth rates at 0.017 Hz are approximately two times faster than that encountered at 1 Hz. On the other hand, Fig. 9 shows that at 121°C (250°F), the testing frequency has little effect on fatigue crack growth rates. At 260°C (500°F) and 427°C (800°F), fatigue crack growth rates were again found to increase with decreasing frequency, as shown in Figs. 10 and 11, respectively. Fatigue crack growth rates at 0.0017 Hz are approximately 3.5 times and 4.5 times faster than those encountered at 1.0 Hz for 260°C (500°F) and 427°C (800°F), respectively.

To show the effect of temperature on fatigue crack growth rates at different frequencies, the fatigue crack growth data presented from Figs. 8 to 11 were cross plotted and are presented from Figs. 12 to 15. Figure 12 shows that at a cyclic frequency of 1 Hz, there is barely any change in fatigue crack growth rates for this rotor steel as the temperature was raised from 24 to 121°C (75 to 250°F). As the temperature was further increased to 260°C (500°F), fatigue crack growth rates were found to decrease slightly.

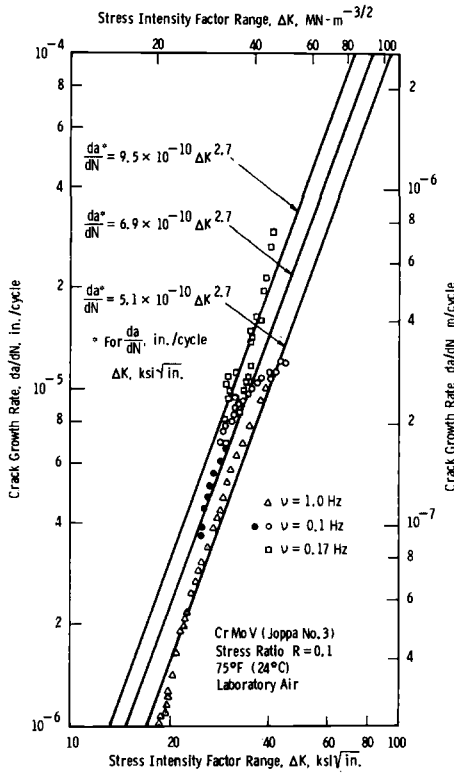


FIG. 8—Effect of frequency on fatigue crack growth rate of CrMoV steel tested at 24°C (75°F).

However, fatigue crack growth rates were increased by a factor of two as temperature was raised from 260 to 427°C (500 to 800°F). At a cyclic frequency of 0.1 Hz, Fig. 13, fatigue crack growth rates decrease slightly as temperature increased from 24 to 121°C (75 to 250°F) and remained similar as temperature is further increased to 260°C (500°F). Figure 13 shows that fatigue crack growth rates at 427°C (800°F) are two times faster than that encountered at 121 and 260°C (250 and 500°F). Figure 14 shows that, at a cyclic frequency of 0.017 Hz, fatigue crack growth rates increase in the following order of temperature: 121, 260, 24, and 427°C (250, 500, 75, and 800°F). At this frequency, fatigue crack growth rates at 427°C (800°F) are approximately three times faster than those encountered at 121°C (250°F). At a cyclic frequency of 0.0017 Hz, Fig. 15 shows that fatigue crack growth rates increase monotonically with increasing temperature from 121°C (250°F) up to 427°C (800°F). Fatigue crack growth rates at 427°C (800°F) are approximately four times higher than those encountered at 121°C (250°F).

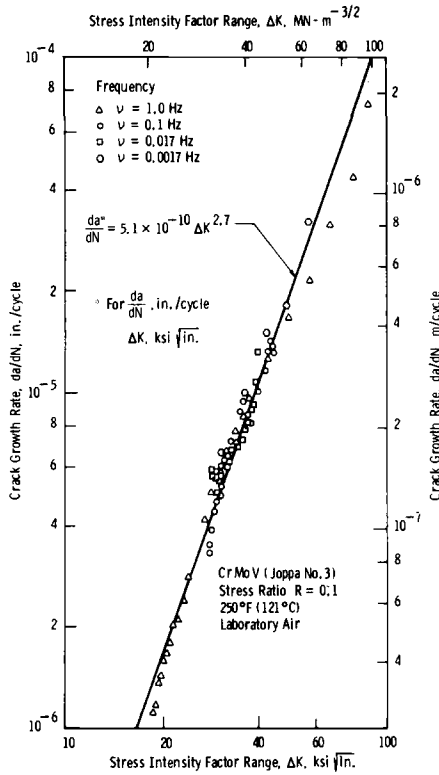


FIG. 9—Effect of frequency on fatigue crack growth rate of CrMoV steel tested at 121°C (250°F).

As described in the previous paragraphs, the effect of frequency and temperature on fatigue crack growth rates is complex and anomalous. The whole picture can best be seen from a surface in the $\log (da/dN) - \log \nu - T$ space as illustrated schematically in Fig. 16. It is known that water vapor in air could increase fatigue crack growth rates of several steels and that fatigue crack growth rates in hostile environments increase with decreasing frequency [13]. Therefore, the increasing crack growth rates with decreasing frequency at room temperature can be related to corrosion fatigue behavior. On the other hand, the increasing crack growth rates with decreasing frequency at 260 and 427°C (500 and 800°F) is consistent with reported results on an A517-F carbon steel at 260 and 510°C (500 and 950°F) [14] and on a HS-188 alloy at 600, 760, and 871°C (1112, 1400, and 1600°F) [8]. This effect of frequency on crack growth rates at elevated temperature was attributed to creep-fatigue interaction effects or oxidation damage or both. This interaction decreases with decreasing temperature and, most probably, does not exist at

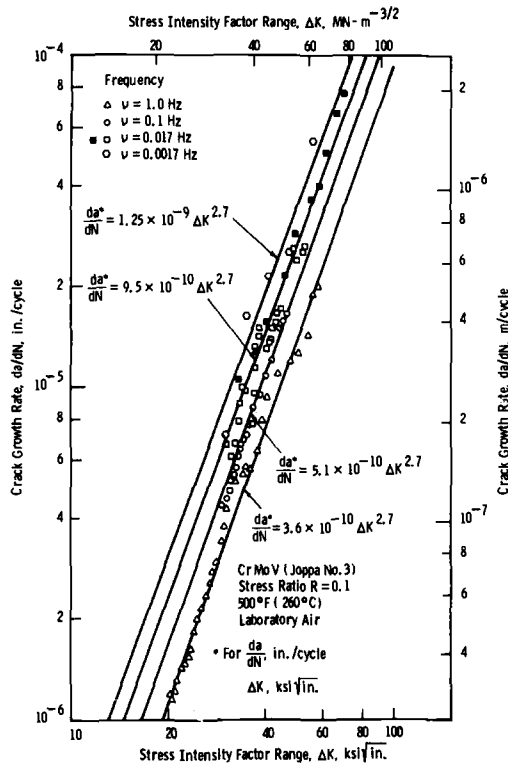


FIG. 10—Effect of frequency on fatigue crack growth rate of CrMoV steel tested at 260°C (500°F).

121°C (250°F). At this temperature, the relative humidity is at such a level that its effect on crack growth rates is very low and is insensitive to the frequency. As a result, fatigue crack growth rates at this temperature are frequency independent.

From Fig. 16, it can be seen that the effect of temperature on fatigue crack growth rates is more significant at lower frequency. This may be attributed to the fact that both corrosion fatigue and creep-fatigue interactions or oxidation damage, or both, are time dependent processes. Nevertheless, for all frequencies tested, the general trend is shown to be that the fatigue crack growth rates will initially decrease before increasing as the temperature increases.³ This initial decreasing of fatigue crack growth rates with increasing temperature can be attributed to the decrease in relative humidity, since it was shown that water vapor enhanced fatigue

³ By extrapolating room temperature fatigue crack growth data from 1.0 Hz, 0.017 Hz down to 0.0017 Hz, room-temperature fatigue crack growth rates at 0.0017 Hz are expected to be higher than those encountered at 121°C (250°F).

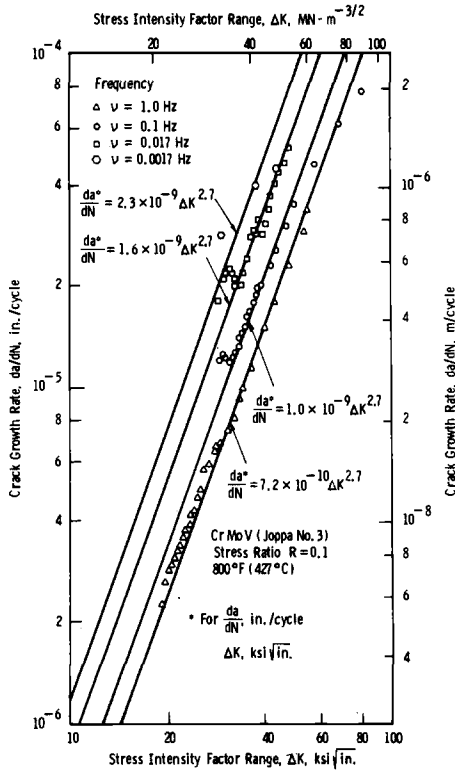


FIG. 11—Effect of frequency on fatigue crack growth rate of CrMoV steel tested at 427°C (800°C).

crack growth rates decrease with decreasing humidity [13]. A similar influence of test temperature on fatigue crack growth rates at 10 Hz was reported on an A533-B steel for temperature of 24, 121, 204, and 288°C (75, 250, 400, and 550°F) [15]. On the other hand, a consistent increase in fatigue crack growth rates with temperature was reported on an A212-B steel at temperatures of 24, 252, and 363°C (75, 485, and 685°F) [7] and also at 24, 260, 343, and 427°C (75, 500, 650, and 800°F) [14] and on an A517-F steel with temperatures at 24, 260, 427, and 510°C (75, 500, 800, and 950°F) [14]. This discrepancy may be caused by the wider temperature increments used in these studies than in the present study.

Comparisons of room temperature fatigue crack growth data of this Joppa No. 3 CrMoV rotor steel with other CrMoV rotor steels are shown in Fig. 17. This comparison shows that fatigue crack growth rate varies only slightly among the Joppa No. 3 material and Gallatin No. 2 material [16]. The rate of crack growth of these 1950 vintage rotor steels,

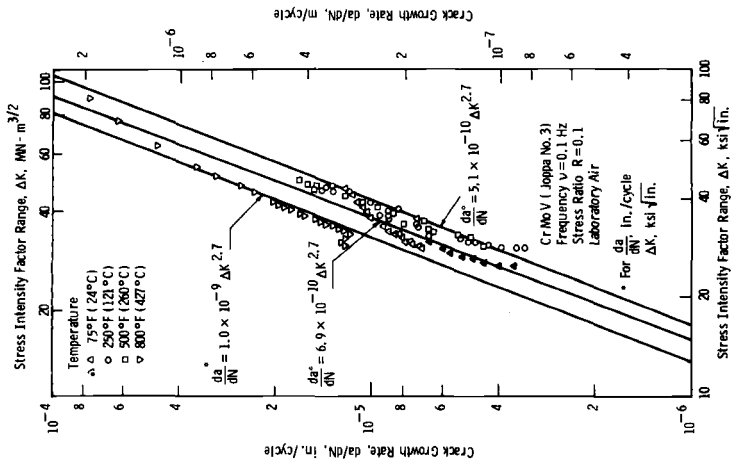


FIG. 13—Effect of temperature on fatigue crack growth rate of CrMoV steel tested at 0.1 Hz.

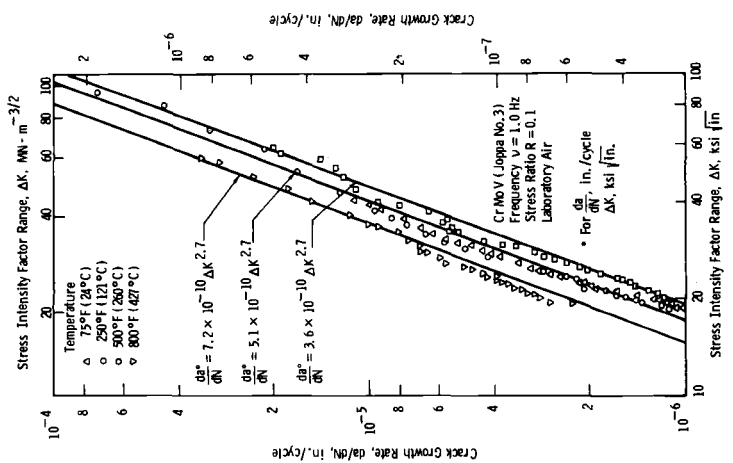


FIG. 12—Effect of temperature on fatigue crack growth rate of CrMoV steel tested at 1.0 Hz.

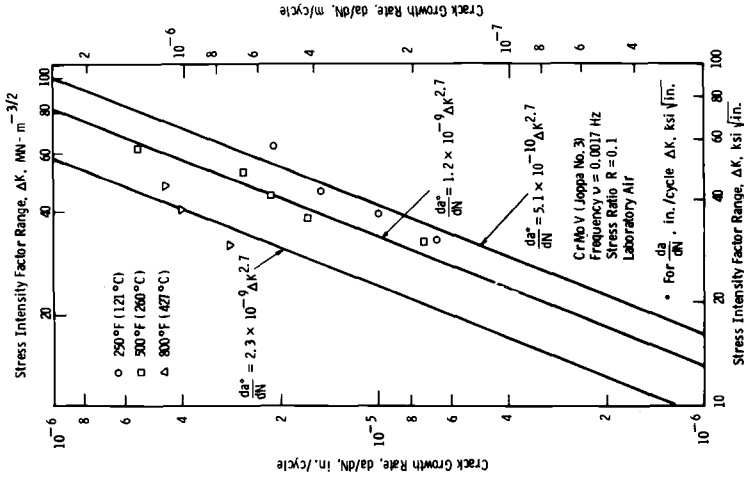


FIG. 15—Effect of temperature on fatigue crack growth rate of CrMoV steel tested at 0.0017 Hz.

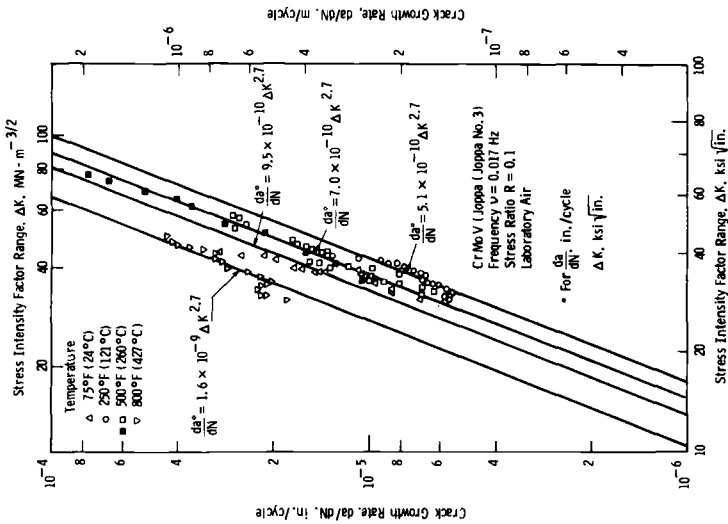


FIG. 14—Effect of temperature on fatigue crack growth rate of CrMoV steel tested at 0.017 Hz.

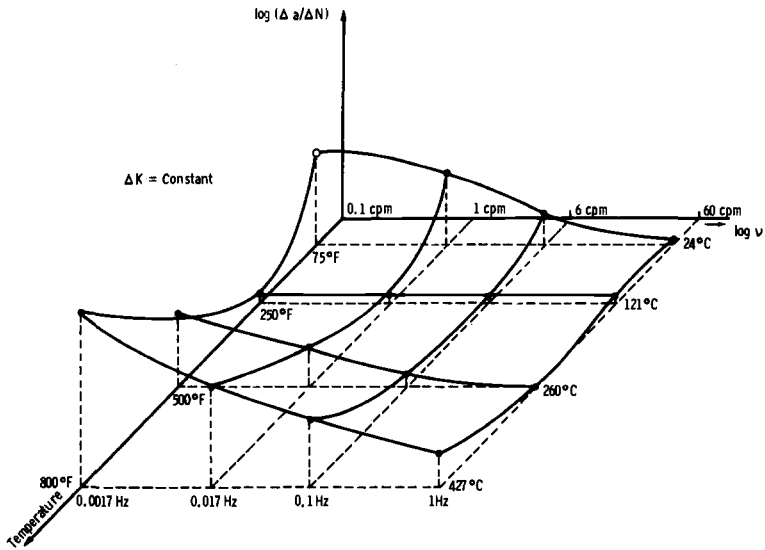


FIG. 16—Three-dimensional representation of effects of frequency and temperature on fatigue crack growth rate in air.

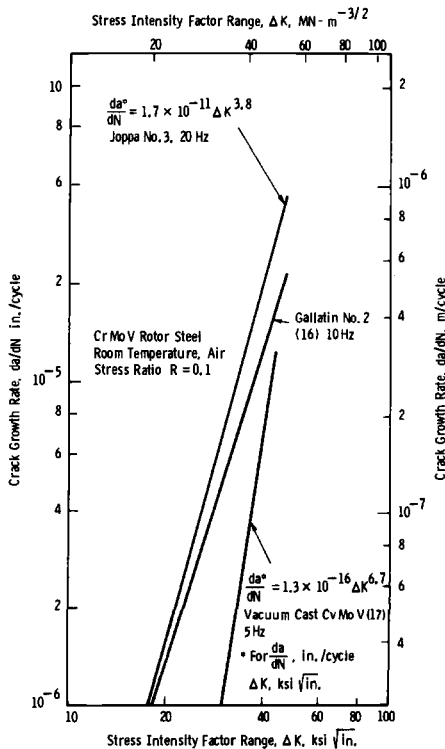


FIG. 17—Fatigue crack growth rate of CrMoV rotor steels at room temperature in air.

however, range between 2 and 8 times that of a rejected vacuum cast rotor steel [17] depending upon the ΔK level. The observed difference in fatigue crack growth rates could be attributed to heat-to-heat variance or to different forging techniques used in the manufacture techniques. Other possibilities are temper or strain-aging embrittlement resulting from the long time exposure at elevated-temperature service conditions experienced by these retired rotors. Further investigation is needed to identify the cause.

Figure 18 shows the fatigue crack growth properties of both Joppa No. 3 material and Gallatin No. 2 material at 427°C (800°F) in laboratory air [3]. At this temperature, crack growth rates of Gallatin rotor steel at 1 Hz are 30 to 100 percent higher than those encountered by Joppa No. 3, while room temperature fatigue crack growth rates of Gallatin rotor steel are slightly less than those encountered by Joppa No. 3 rotor steel.

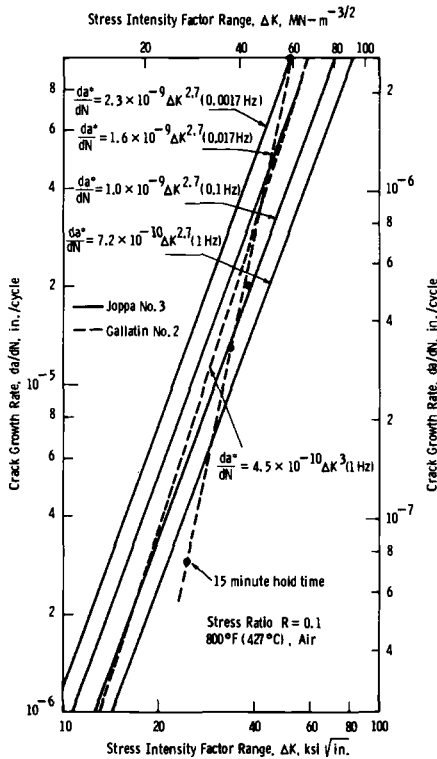


FIG. 18—Fatigue crack growth rate of Joppa No. 3 and Gallatin No. 2 rotor steels at 427°C (800°F) in air.

Summary and Conclusions

A summary of results from this study and pertinent conclusions are as follows:

1. Dispersed discontinuities of small ultrasonically detectable size have little effect on room temperature fatigue crack growth rates of this 1950 vintage CrMoV rotor steel.

2. Room temperature fatigue crack growth rates vary slightly between two air cast CrMoV rotor forgings, Joppa No. 3 and Gallatin No. 6.

3. The rate of fatigue crack growth of these retired air cast rotor materials is two to eight times higher than that encountered in a rejected more modern vacuum cast forging.

4. At room temperature, crack growth rates were found to increase with decreasing frequency, while crack growth rates are frequency independent at 121°C (250°F). This frequency effect on crack growth rates at these temperatures is attributed to corrosion fatigue behavior.

5. At 260 and 427°C (500 and 800°F), crack growth rates were found to increase with decreasing frequency. This frequency effect on crack growth rate is more significant at 427°C (800°F) than at 260°C (500°F) and is attributed to creep-fatigue interaction or oxidation damage, or both.

6. At the same cyclic frequency, crack growth rates initially decrease before increasing at higher temperature. This anomalous behavior of initially decreasing crack growth rates with increasing temperature is attributed to the decrease of humidity with increasing temperatures. The temperature dependence of crack growth rate was also found to be more significant at lower frequency.

Acknowledgment

Support of this work by the Electric Power Research Institute under Contract No. RP 502-4 is gratefully acknowledged. The critical review of W. G. Clark, Jr. and S. J. Hudak, Jr. are highly appreciated. Appreciation is also extended to A. Madeyski for his work on electron-microscope, to W. H. Pryle for help in specimen preparation and to technicians, too many to be named, who carefully conducted the experimental work.

References

- [1] Schmerling, J. M. and Hammon, J. C., "Investigation of the Tennessee Valley Authority, Gallatin Unit No. 2 Turbine Rotor Burst," American Power Conference, Chicago, Ill., 20-22 April 1976.
- [2] Kramer, L. D. and Randolph, D., "Analysis of the Tennessee Valley Authority Gallatin No. 2 Unit Turbine Rotor Burst Part I—Metallurgical Considerations," Symposium on Creep-Fatigue Interactions, New York, N.Y., 6-10 Dec. 1976.
- [3] Clarke, G. A., Shih, T. T., and Kramer, L. D., "Reliability of Steam Turbine Rotors," Semi-Annual Report No. 3, Westinghouse Electric Corporation Research and Development Center, Contract No. RP 502-4, Sept. 1977.

- [4] Saxena, A. and Hudak, S. J., Jr., "Review and Extension of Compliance Information for Common Crack Growth Specimens," Scientific Paper 77-9E7-AFCGR-P1, Westinghouse Electric Corporation, May 1977.
- [5] Freed, C. N. and Kraft, J. M., *Journal of Materials*, Vol. 1, No. 4, 1966, p. 770.
- [6] Clark, W. G., Jr., and Hudak, S. J., Jr., *Journal of Testing and Evaluation*, Vol. 3, No. 6, 1975, pp. 454-476.
- [7] Brothers, A. J., "Fatigue Crack Growth in Nuclear Reactor Piping Steels," Research and Development Report GEAP-5067, U.S. Atomic Energy Commission, March 1968.
- [8] Ohmura, T., Pelloux, R. M., and Grant, N. J., *Engineering Fracture Mechanics*, Vol. 5, No. 4, 1973, pp. 909-922.
- [9] Paris, P. C., "The Fracture Mechanics Approach to Fatigue," *Proceedings, 10th Sagamore Army Materials Research Conference*, Aug. 1963, Syracuse University Press, 1964.
- [10] Bucci, R. J., Clark, W. G., Jr., and Paris, P. C., in *Stress Analysis and Growth of Cracks, ASTM STP 513*, American Society for Testing and Materials, 1972, pp. 125-140.
- [11] Clarke, G. A., "Reliability of Steam Turbine Rotors—Material Mechanical Property Measurements," 11th through 14th Monthly Letter Report, Contract No. RP 502-4, Westinghouse Electric Corporation.
- [12] Brothers, A. J. and Yukuwa, S., *Journal of Basic Engineering*, March 1967, pp. 19-27.
- [13] Wei, R. P., *Engineering Fracture Mechanics*, Vol. 1, No. 4, 1970, pp. 633-652.
- [14] McHenry, H. I. and Pense, A. W., in *Fatigue at Elevated Temperatures, ASTM STP 520*, American Society for Testing and Materials, pp. 345-354.
- [15] Clark, W. G., Jr., *Journal of Materials*, Vol. 6, No. 1, 1971, pp. 134-149.
- [16] Clarke, G. A., Kramer, L. D., and Tu, L. K., "Reliability of Steam Turbine Rotors," Semi-Annual Report No. 1, Contract No. RP 502-4, Westinghouse Electric Corporation.
- [17] Clark, W. G., Jr., *Engineering Fracture Mechanics*, Vol. 2, No. 4, 1971, pp. 287-300.

Structural Memory of Cracked Components Under Irregular Loading

REFERENCE: Führung, H. and Seeger, T., "Structural Memory of Cracked Components Under Irregular Loading," *Fracture Mechanics, ASTM STP 677*, C. W. Smith, Ed., American Society for Testing and Materials, 1979, pp. 144–167.

ABSTRACT: The small scale yielding (SSY) relationships for stationary cracks cannot describe the local elastic-plastic behavior at a crack tip when irregular loading is considered. As a consequence, linear models for crack growth prediction fail. Nonlinear crack growth behavior (retardation, acceleration) is due mainly to load interaction effects which are governed by memory rules. As to stationary cracks, memory which is based on the local behavior (closed hysteresis loops) can be described by reaching certain load levels. Extended to crack growth problems, the "structural memory" criterion is described by striking elastic-plastic boundaries. This points up the central role that the development of plastic zone sizes as a function of crack length and load history plays. The concern of the paper is with those structural analysis aspects under the assumption of perfectly plastic material properties. SSY plastic zone formulae are derived for the peak overload/underload case which are shown to be of central importance for describing the nonlinear effects due to any irregular loading history. It is demonstrated, in principle, how crack closure can be taken into account.

KEY WORDS: fracture mechanics, cyclic loads, plasticity, strain concentration, plastic zone, residual stress, closure, material memory, fatigue (materials), crack propagation, overload, underload

Nomenclature

- a Crack tip distance from x origin
- a_s Crack length at overload application
- $\Delta a = a - a_s$ Increment of crack growth after overload application
- Δa_{AB} Crack growth increment where the curves ω_B^t and ω_A^t intersect each other
- $a_M = a_s + \Delta a_{AB}$ Crack tip location when $\omega^t = \text{minimum } \omega^t$
- Δa_{tc} Crack growth increment where $\omega^c = \omega^t$ holds

¹ Scientific research engineer, Laboratorium für Betriebsfestigkeit, Darmstadt, Germany (formerly with Technical University of Darmstadt).

² Professor, Institut für Statik und Stahlbau, Technical University of Darmstadt, Germany.

- δ Measure of the distance between two fictitious crack tips
- E' Young's modulus (dependent upon stress state)
- F_K, F_v, F_σ Green's functions according to Eqs 33 through 35
- K Stress intensity factor (SIF)
- K_3 SIF of single peak overload S_3
- ΔK Cyclic SIF (SIF range, variational SIF)
- ΔK_4 $K_3 - K_4$
- ΔK_5 $K_5 - K_4$
- ΔK_{eff} $K_{\text{max}} - K_{\text{op}}$ effective cyclic SIF
- ΔK_{MB} Cyclic SIF, if $\Delta K \geq \Delta K_{MB}$ the memory according to memory element I_B is terminated
- ΔK_{MA} Cyclic SIF, if $\Delta K \geq \Delta K_{MA}$ the memory according to memory element I_A is terminated
- λ Extent on the contact zone
- ν Poisson's ratio
- $P = \frac{\Delta K_4}{\Delta K_5}$ Peak cycle ratio
- p_i Applied stresses on the fictitiously extended crack surface
- Δp Variational applied stresses associated with ΔS_i
- p_k Function of contact stresses acting on the crack surface
- $Q = \frac{K_3}{K_5}$ Overload ratio
- $R = S_{\text{min}}/S_{\text{max}}$ Load ratio
- \tilde{r}_i Local coordinate with origin at the fictitious crack tip associated with load reversal point i
- \bar{r}_i Local coordinate with origin at the fictitious crack tip associated with load reversal point i (for localization of the stress and displacement state)
- S_i Load at reversal point i
- $\Delta S_i = S_i - S_{i-1}$ Cyclic load (load range, variational load)
- S_{min} Load at lower reversal points of constant amplitude (CA) loading
- S_{max} Load at upper reversal points of CA loading
- σ_i Elastic stress function at load reversal point i
- $\Delta \sigma_i$ Variational stress function associated with ΔS_i
- σ_Y Yield strength
- v_a Crack tip opening displacement (CTOD) used synonymously for the plastic deformation of the crack tip element (see Fig. 5)
- Δv_a CTOD range
- v_i Displacement function of the fictitious crack surface at reversal point i

- Δv_i Variational displacement under load range ΔS_i
- ω_i Plastic zone size associated with load reversal point i
- ω^t Tensile plastic zone size (associated with upper load reversal points)
- ω^c Compressive plastic zone size (associated with lower load reversal points)
- x Crack axis coordinate
- I_A, I_B Memory elements of the loop with order number 1

The value of the ΔK approach to fatigue crack growth prediction needs no emphasis. Nonetheless, this approach has some limitations even in case of constant amplitude (CA) loading. For example, the mean load dependence of crack growth rates cannot be explained on the basis of the linear elastic fracture mechanics approach. Since Elber's experimental work on crack closure [1],³ some fatigue phenomena are better understood. It can be stated that the cyclic stress intensity factor (SIF), ΔK , describes the local failure process with CA loading at a given R -value fairly well because of proportionality to the effective SIF, ΔK_{eff} . Further on, as a result of our own theoretical studies [2], it was found that ΔK_{eff} is a power function of the crack tip opening displacement (CTOD) range, Δv_a (as a first order approximation, at least).

This fundamental relationship between ΔK and the local behavior is valid no longer when dealing with nonCA loading. From pilot experiments [3,4] in the early sixties and a lot of variable amplitude results obtained since then, it is a well-known fact that crack growth is not a linear process, as implicitly underlying the ΔK approach, but can even be highly nonlinear due to the so-called load sequence effects. It was substantiated [2,5] that the nonlinear mechanics of load interaction yields the most important reasons for such effects. Nonetheless, the ΔK approach is in general use for crack growth prediction under nonCA loading conditions, as well. To account for crack growth retardation effects it is common to apply a modification of the ΔK approach, for example the empirically derived Wheeler correction [6].

The term "structural memory" as introduced here shall describe a more general view on the influences of previous load and crack configurations on any later state of stress and displacement and on damage as well. It is meant as an extension to the memory effect which is well known through the concept of local behavior at notches. All memory effects base on the pure material property, being characteristic for most technical materials, that the stress-strain path after unloading and reloading joins the respective path prior to load reversal at the point where it was left. The main concern of the paper is with structural analysis aspects to

³ The italic numbers in brackets refer to the list of references appended to this paper.

answer the question: what are the basic equations for the elastic-plastic behavior at a crack tip under structural memory conditions? In order to enable closed solutions and to enlarge the range of ΔK application, the present consideration builds upon the Dugdale [7] model solution for small scale yielding (SSY) conditions and perfectly plastic uniaxial material response. In case of monotonic or regular cyclic loading, the expressions for the characteristics quantities of stationary cracks are known from Ref 8. They are the plastic zone size, ω , and the CTOD, v_a , see Appendix I. Similar relationships for load sequence problems are desired. How to derive them is demonstrated in the sequel.

Memory Rules

Crack extension depends upon the behavior of stresses and strains in the crack tip region. According to results of fatigue studies on smooth specimen the crack growth rate da/dN is assumed to be a power function of the plastic strain range [9,10]. In terms of the Dugdale method

$$da/dN \sim \Delta v_a^m \quad (1)$$

Δv_a characterizes the strain range of the material element just ahead of the crack tip. The question arises how to apply the relationship (1) to irregular loading. The answer is, Ref 2: use the $v_a(S_i)$ curves for evaluation with respect to closed hysteresis loops and update the cyclewise obtained Δa (Δv_a) increments to get crack length as a function of loading. In principle, this is the counting method of Ref 11 which resembles the rain-flow counting method [12]. However, contrary to the elastic quantity ΔK or the load range itself in the quoted methods, it is a local elastic-plastic quantity to which damage is related.

Memory with Stationary Cracks

The disadvantage of the local damage concept as demonstrated previously is that relationships for Δv_a as a function of load and crack configuration history do not exist at present. To prepare the subsequent derivations we start with basic memory reflections without considering any history in kinds of preceding loads and crack size alterations. The CTOD development under loads 1 to 7 is depicted in Fig. 1a. For simplicity, all unloading steps are regarded to be contact-free. Loop 1–2 just closes as the increasing load ΔS_3 reaches the S_1 level. Then the CTOD-load path follows the monotonic one. Loop 3–4 is not closed at the following load reversal point 5 where the next loop starts. Loop 3–4 is called to be of the order “I.” The current loop 5–6 being of the order “II” only enters the memory when it is not closed prior to or at the subsequent reversal point. As to the example, the memory consists of two memory

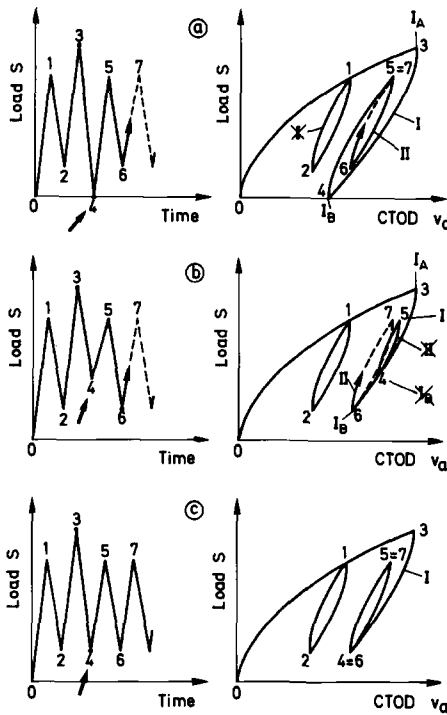


FIG. 1—Examples for memory with stationary cracks, varying the reversal load at point 4 (crossed italic numbers mean cancelled memory elements).

elements which are characterized by a load and a crack size: $I_A(S_3, a)$ and $I_B(\Delta S_4, a)$. All following states of stress and displacement, up to a certain limiting state given by memory rules, depend upon the load history 3–4. Those states, indeed, do not depend on previous loading 1–2, the memory of which was cancelled.

As an alternate case, the example in Fig. 1b shows a loop of order “II” opened at 4 and closed before the lower reversal point 6 is reached. Hence, loop 4–5 yields no memory elements. In view of memory effects on subsequent states with extended crack example, 1b is identical to example 1c which itself is a special version of example 1a. The stress distributions at reversal points 3 to 6 of the examples 1a and 1c are depicted in Fig. 2. At the locations $x_i = a + \omega_i$ of former elastic-plastic boundaries, all following elastic stress profiles show knee-points. The number of knee-points is identical to the number of memory elements. Concerning the real structural behavior, only vague suppositions [13] but no accurate model solutions exist up to now, aside from Ref 2 where the problem is solved numerically under certain assumptions.

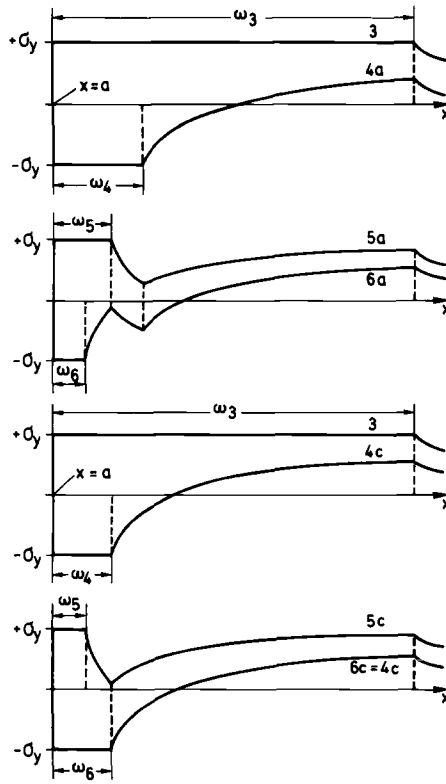


FIG. 2—Elastic-plastic stress distributions according to the Dugdale model for examples a and c in Fig. 1.

Structural Memory

Figure 3 shows a load sequence that occurs with the descending loads of any "incremental step test." There is not a single loop that closes before the loads ascend again. The example is characterized by open loops to the third order and by six memory elements. What is the effect of this particular load history on states after crack extension? It can be stated factually that the particular $v_a(S)$ loops never close, since the material element to which v_a is attributed breaks. Thus, any new branch of a $v_a(S)$ curve reflects the behavior of a material element at an altered location. This is the reason why the usual memory criterion (loop closure defined by reaching a certain load level) must be given up in case of configuration change such as crack growth. Obviously memory rules with stationary crack problems [11] as well as stress concentration problems [12] are but special rules from a more general structural memory theory.

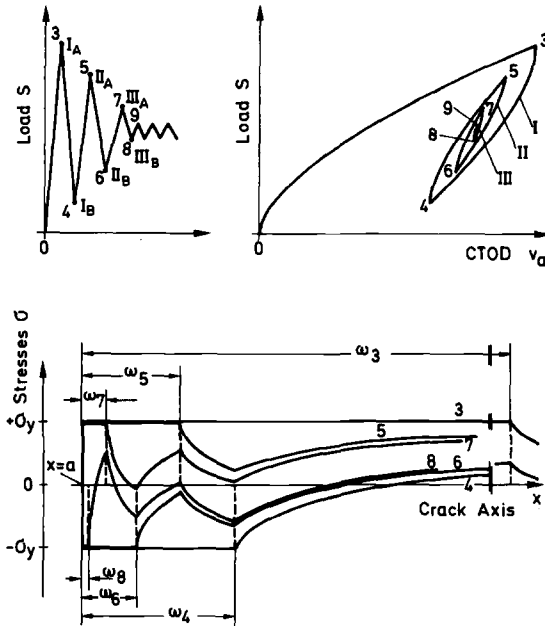


FIG. 3—Load sequence with higher order number of open hysteresis loops (six memory elements).

The desired more general memory criterion can be formulated as follows: The effect of a previous loading state on subsequent loading states ceases not before the elastic-plastic boundary of the previous loading state is reached or is left behind by the boundary of the current plastic zone.

The significance of the elastic-plastic boundaries for the memory phenomenon can be substantiated by means of the stress distributions, Figs. 2 and 3. The loss of the memory of a certain previous loading state occurs just when the whole initially plasticized region has yielded. Since the bearing capacity of all material elements within this region is reached, further load increase or diminishing of the net section leads to stable equilibrium only if the plastic frontier moves ahead. In Ref 14 it is demonstrated for CA loading that the plastic zone size “jumps” in the very moment that memory occurs, that is, when the maximum load level is reached. If crack configuration altered during loading the stress redistribution process would be a continuous one. From the arguments given, it is obvious that the development of local elastic-plastic quantities with configuration change is governed by the shape of the preexisting stress profile.

As a consequence, the habitual representation of local behavior under

load variation according to Fig. 1 must be abandoned when crack extension is taken into account. By simply introducing crack length as a third parameter to the $v_a(S)$ plot, the problem cannot be solved because the dependence of the crack tip displacement on history and current crack length is unknown. In the sequel, the plastic zone size as a function of crack length is favored for best representation of the current local state. The plastic zone size is the basic quantity for describing structural memory effects since it governs the memory criterion as well as stress and displacement functions. The derivation of expressions for v_a and Δv_a is left out in this paper because it would disturb the logical flow of the text. They can be derived according to the scheme described below.

Plastic Zone Development with Crack Extension

Crack Growth Simulation Procedure

Simulation of crack growth usually is based on the assumption that the crack extends under fixed load conditions just at an upper reversal point. For each lower reversal point the crack length is assumed the same as for the preceding upper reversal point [2,14]. The stresses released over an increment Δa come to be redistributed accompanied by simultaneous forward movement of the elastic-plastic boundary, Fig. 4. For convenience, but not necessarily, the Δa increment is chosen smaller than the current plastic zone size ω_1 . Stress redistribution leads to the K -balance at the new fictitious crack tip (see Appendix I, factor $\sqrt{2/\pi}$ cancelled)

$$-\sigma_y \int_{\omega}^{\omega + \Delta a} F_k dr + \int_0^{\delta_1} (\sigma_y - \sigma_1(r_1)) F_k dr = 0 \quad (2)$$

where F_k is the Green's function of Eq 33 and

$$\int_{r_b}^{r_a} F_k dr \cong \int_{r_b}^{r_a} \frac{1}{\sqrt{r}} dr = 2(\sqrt{r_a} - \sqrt{r_b}) \quad (3)$$

The first term in Eq 2 represents the SIF due to the released stress parcel $\sigma_y \Delta a$, the last term represents the SIF due to the stress reserve over the unknown distance δ_1 between the new and the old fictitious crack tip. An alternate way to set up the K -balance is to replace all former stresses in the region $\delta_1 + \omega_1 \geq r \geq 0$ by the new stress distribution in the region $\omega \geq r \geq 0$, thus

$$-\sigma_y \int_{\delta_1}^{\omega_1 + \delta_1} \frac{dr}{\sqrt{r}} - \int_0^{\delta_1} \sigma_1(r_1) \cdot \frac{dr}{\sqrt{r}} + \sigma_y \int_0^{\omega} \frac{dr}{\sqrt{r}} = 0 \quad (4)$$

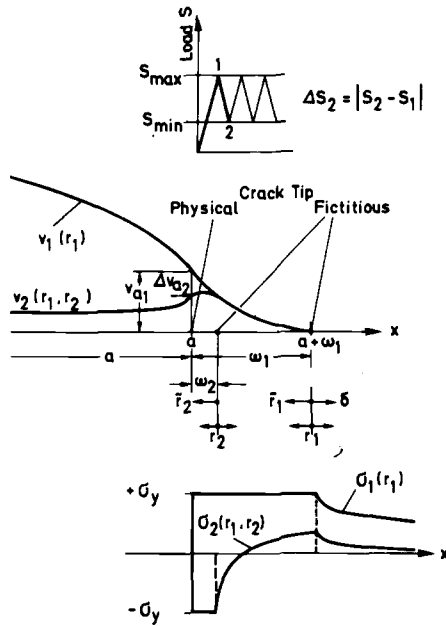


FIG. 5—Definitions and basic functions of the Dugdale model for stationary cracks.

$$2\sigma_y \int_{\delta_2}^{\omega_2 + \delta_2} \frac{dr}{\sqrt{r}} + \int_0^{\delta_2} \Delta\sigma_2(r_2) \cdot \frac{dr}{\sqrt{r}} = \sqrt{\frac{\pi}{2}} \Delta K_2(a + \omega) \quad (8)$$

where

$$\omega_2 + \delta_2 = \omega + \Delta a \quad (9)$$

The meaning of Eqs 7 and 8 is that the combined terms in Eq 4 with the integral over the elastic stress function of a previous loading state can be replaced by the respective value of the SIF related to the new fictitious crack tip. Assuming the new plastic zone size ω small compared to the crack size, the SIF in Eqs 7 and 8 only depends on the new crack length $a = a_1 + \Delta a$.

In the sequel, the described procedure finds its main application to crack growth with nonCA loading history.

Tensile Plastic Zones

Under consideration is the history of a single peak overload followed by a peak underload, see Fig. 1a. The respective crack length at peak load application, called a_s , shall be unchanged between points 1 and 5. With

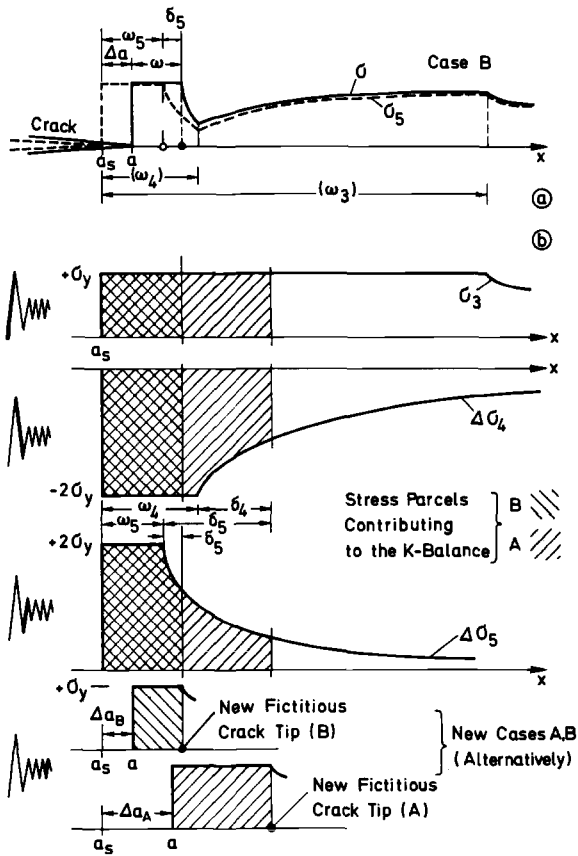


FIG. 6—(a) Crack growth simulation procedure applied to peak overload history, and (b) decomposition scheme for K-balance set-up, alternatively. Case B: the crack is grown by an increment Δa_B so that the actual elastic-plastic boundary lies inside the former plastic zone ω_4 . Case A: the crack is grown by an increment Δa_A so that the actual elastic-plastic boundary lies outside the former plastic zone ω_4 .

peak unloading ΔS_4 it is assumed that crack closure does not occur.⁴ This assumption is approximately valid if the peak underload is greater than or equal to zero [2]. Hence, the compressive plastic zone size ω_4 is given by Eq 44 while the tensile plastic zone size ω_3 is given by Eq 37. The subscript number referring to the reversal points denotes the respective history events causing the memory elements l_B and l_A , see Fig. 1. By means of the described crack growth simulation procedure, crack extension at maximum load in point 5 yields the relationship (see Fig. 6a)

⁴ We additionally assume that the boundary of the plastic zone due to unloading from the peak load will not be cancelled by other advancing boundaries during subsequent crack growth.

$$-\sigma_y \int_{\omega}^{\omega + \Delta a} \frac{dr}{\sqrt{r}} + \int_0^{\delta_5} [\sigma_y - \sigma_5(r_5)] \cdot \frac{dr}{\sqrt{r}} = 0 \quad (10)$$

Since σ_5 is the stress distribution superposed according to Eq 45 by three former loading states

$$\sigma_5(r_3, r_4, r_5) = \sigma_3(r_3) - \Delta\sigma_4(r_4) + \Delta\sigma_5(r_5) \quad (11)$$

the influence of those states on stress redistribution can be readily seen.

When writing Eq 10, the current plastic frontier was assumed to advance not beyond $x = a_s + \omega_4$. At the knee-point in the σ_5 stress profile the $\Delta\sigma_4$ function in Eq 11 is altered. It shows that the function $\omega'(a)$ must be divided into as many branches as memory elements are active. In the present case, there exist two $\omega'(a)$ branches. The validity range of the first branch is given by $a + \omega' \leq a_s + \omega_4$, or

$$\Delta a \leq \omega_4 - \omega'(a) \quad (12)$$

where $\omega'(a)$ denotes the current tensile plastic zone size. In the sequel, the alternate scheme according to Eq 4 as depicted in Fig. 6b is used to formulate the K -balance equations. Hence, Eq 10 is equivalent to

$$-\sigma_y \int_0^{\omega + \Delta a} \frac{dr}{\sqrt{r}} + 2\sigma_y \int_0^{\omega + \Delta a} \frac{dr}{\sqrt{r}} - \left[2\sigma_y \int_{\delta_5}^{\omega + \Delta a} \frac{dr}{\sqrt{r}} + \int_0^{\delta_5} \Delta\sigma_5 \cdot \frac{dr}{\sqrt{r}} \right] + \sigma_y \int_0^{\omega} \frac{dr}{\sqrt{r}} = 0 \quad (13)$$

Within the brackets stands the expression for $\sqrt{\frac{\pi}{2}} \Delta K_5$, according to Eq 8. After combining the various terms, use of Eq 3 leads to

$$2\sigma_y (\sqrt{\omega} + \sqrt{\omega + \Delta a}) = \sqrt{\frac{\pi}{2}} \Delta K_5 \quad (14)$$

Solving Eq 14 with respect to the unknown quantity $\omega \hat{=} \omega_B'(a)$ at a given crack growth increment $\Delta a = a - a_s$, it follows the expression for the first branch

$$\omega_B'(a) = \frac{\left[\frac{\pi}{8} \left(\frac{\Delta K_5}{\sigma_y} \right)^2 - \Delta a \right]^2}{\frac{\pi}{2} \left(\frac{\Delta K_5}{\sigma_y} \right)^2} \quad (15)$$

The subscript ‘‘B’’ was selected to refer to the memory element $I_B(\Delta S_4, a_s)$ which marks the range of validity of Eq 15 as given by inequality 12.

The upper limit of the second $\omega'(a)$ -branch is defined by (see Fig. 6)

$$\Delta a = \omega_3 - \omega'(a) \tag{16}$$

The sum of SIF due to removed stress parcels from preceding loading states 3-4-5 and SIF due to yield stress along the new fictitious extent of the crack according to Fig. 6b yields

$$\begin{aligned}
 & -\sigma_y \int_0^{\omega + \Delta a} \frac{dr}{\sqrt{r}} + \left[2\sigma_y \int_{\delta_4}^{\omega + \Delta a} \frac{dr}{\sqrt{r}} + \int_0^{\delta_4} \Delta\sigma_4 \cdot \frac{dr}{\sqrt{r}} \right] \\
 & - \left[2\sigma_y \int_{\delta_5}^{\omega + \Delta a} \frac{dr}{\sqrt{r}} + \int_0^{\delta_5} \Delta\sigma_5 \cdot \frac{dr}{\sqrt{r}} \right] + \sigma_y \int_0^{\omega} \frac{dr}{\sqrt{r}} = 0 \tag{17}
 \end{aligned}$$

Equation 17 results in

$$2\sigma_y(\sqrt{\omega + \Delta a} - \sqrt{\omega}) = \sqrt{\frac{\pi}{2}} (\Delta K_4 - \Delta K_5) \tag{18}$$

which leads to the expression for the second branch

$$\omega_A'(a) = \frac{\left[\Delta a - \frac{\pi}{8} \left(\frac{\Delta K_4 - \Delta K_5}{\sigma_y} \right)^2 \right]^2}{\frac{\pi}{2} \left(\frac{\Delta K_4 - \Delta K_5}{\sigma_y} \right)^2} \tag{19}$$

Compressive Plastic Zones

For a general load sequence the stress and displacement state at any reversal point depends upon the state at all preceding reversal points (that is, upon load history). The reason why this fact had not been taken into account with the tensile yield zones in the last section is that, in the special case of cycling under constant maximum load, all upper states are contact free and identical to the previous upper state if crack length is assumed unchanged during that cycle. The consideration of compressive plastic zones at lower reversal points, however, makes it necessary to take crack closure into account. Since we are not interested in complicated crack closure calculations, we suggest as a simple assumption

$$\begin{aligned}
 p_k &= \sigma_y = \text{constant} \\
 \lambda &= \Delta a = a - a_s
 \end{aligned}
 \tag{20}$$

where λ denotes the extent of the contact zone.

Equation 20, which means that compressive yield stresses are always present between the former and the current crack tip location (see Fig. 7), is supported by extensive numerical studies with the Dugdale method [2]. As a good approximation the assumption is valid at least in the range where Δa satisfies inequality Eq 12. Before applying the following formulae, the validity of Eq 20 must be controlled strictly. The contact-free $\omega^c(a)$ solution is given in Appendix II.

Depending upon $S_{\min} > S_4$ or $S_{\min} = S_4$, the number of knee-points of stress curve 6a and 6c in Fig. 2 varies. Regarding the case that $S_{\min} > S_4$, that is, $\Delta S_6 < S_5$, the compressive is smaller than the tensile plastic zone. Memory elements induced by S_3 and ΔS_4 do not affect the quantity $\omega^c(a)$ because the respective knee-points in the elastic stress profile vanish through the motion of the tensile plastic frontier ahead of the compressive one. Hence, Eq 41 is valid and through the use of Eq 20 yields

$$\begin{aligned}
 2\sigma_y (\sqrt{\omega} + \sqrt{\omega + \Delta a}) &= \sqrt{\frac{\pi}{2}} \Delta K_6 \\
 \omega^c(a) &= \frac{\left[\frac{\pi}{8} \left(\frac{\Delta K_6}{\sigma_y} \right)^2 - \Delta a \right]^2}{\frac{\pi}{2} \left(\frac{\Delta K_6}{\sigma_y} \right)^2}
 \end{aligned}
 \tag{21}$$

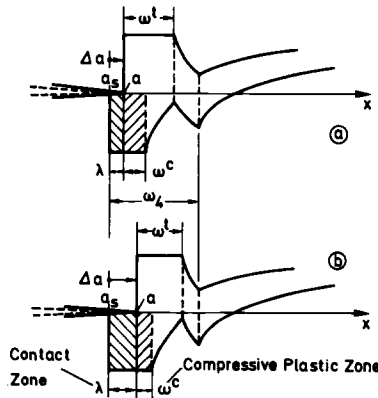


FIG. 7—Special type of contact stresses due to crack closure after overloads.

With respect to the case that $S_{\min} = S_4$ the K -balance reads as

$$-\sigma_y \int_0^{\omega+\Delta a} \frac{dr}{\sqrt{r}} + \sqrt{\frac{\pi}{2}} (\Delta K_4 - \Delta K_5 + \Delta K_6) - \sigma_y \int_0^{\omega} \frac{dr}{\sqrt{r}} - \int_{\omega}^{\omega+\lambda} p_k \cdot \frac{dr}{\sqrt{r}} = 0 \quad (22)$$

Because of $\Delta K_5 = \Delta K_6$, using Eqs 3 and 20, integration yields

$$2\sigma_y (\sqrt{\omega + \Delta a} + \sqrt{\omega} + \sqrt{\omega + \Delta a} - \sqrt{\omega}) = \sqrt{\frac{\pi}{2}} \Delta K_4$$

$$\omega^c(a) = \frac{\pi}{32} \left(\frac{\Delta K_4}{\sigma_y} \right)^2 - \Delta a \quad (23)$$

The relationship in Eq 23 holds as long as the compressive plastic zone size is larger than the tensile one, the latter according to Eqs 15 and 19, respectively.

Discussion

When inserting the appropriate SIF in Eqs 15, 19, 21 and 23, the load sequence effect of a single peak overload on the plastic zone size can be calculated readily. Since the stress intensity factor is a function of the crack length, it is not possible to give an explicit solution to the problem where the transition from the first to the second $\omega^i(a)$ branch takes place. Such a solution would be of interest, because the magnitude of the retardation effect due to peak loading is supposed to be governed by the local behavior in this range [15]. To overcome this deficiency and get simple approximation formulae it is assumed that Δa is small compared to the crack length a_s . Therefore, besides the common SSY assumption (Eq 36), the following assumption is used for the discussion

$$K(a_s + \Delta a) = K(a_s) = \text{constant} \quad (24)$$

From Eq 12 it follows

$$\Delta a_{AB} = \omega_4 - \omega'_B(a)$$

Inserting Eq 15 and the ω_4 expression analogous to Eq 44 leads to

$$\Delta a_{AB} = \frac{\pi \left(\frac{\Delta K_4}{\sigma_y} \right)^2}{32} - \frac{\left[\frac{\pi \left(\frac{\Delta K_5}{\sigma_y} \right)^2}{8} - \Delta a_{AB} \right]^2}{\frac{\pi \left(\frac{\Delta K_5}{\sigma_y} \right)^2}{2}} \quad (25)$$

By use of Eq 24, Eq 25 can be solved with respect to Δa_{AB}

$$\Delta a_{AB} = \frac{\pi \left(\frac{\Delta K_5}{\sigma_y} \right)^2 \left(\frac{\Delta K_4}{\Delta K_5} - 1 \right)}{8} \quad (26)$$

The identical result is obtained when setting equal Eqs 15 and 19. After Δa_{AB} -crack extension the tensile plastic zone size reaches a minimum, Fig. 8,

$$\min \omega^t \triangleq \omega^t(\Delta a_{AB}) = \frac{\pi \left(\frac{\Delta K_5}{\sigma_y} \right)^2 \left(2 - \frac{\Delta K_4}{\Delta K_5} \right)^2}{32} \quad (27)$$

In Eqs 26 and 27 the ratio $\Delta K_4/\Delta K_5$ occurs which should be called the "peak cycle ratio P ." This ratio is considered the predominant parameter for describing the retardation effect due to a single peak overload. P is more significant than the overload ratio $Q = K_{OL}/K_{max} = K_3/K_5$ as used elsewhere in literature. Apart from the specific case of $R = 0$ and $K_4 = 0$ where $Q = P$, the P parameter is able to describe the effect of diminished retardation when the peak underload decreases. Furthermore, by means of Eq 26, the location of the minimum crack growth rate can be estimated dependent on the peak cycle ratio. The value of Eqs 26 and 27 for test result interpretation, is demonstrated in Ref 15.

To answer the question where load interaction finishes with respect to the compressive plastic zone size, the condition

$$\omega^c(a) = \omega^t(a)$$

is used combined with Eqs 19 and 23. The result is

$$\Delta a_{tc} = \frac{\pi}{8} \cdot \left(\frac{\Delta K_5}{\sigma_y} \right)^2 \cdot (P - 1) \quad (28)$$

which means $\Delta a_{tc} = \Delta a_{AB}$ in case of $S_4 = S_{min}$. With Eq 24, Eq 23 represents a straight line on the $\omega(a)$ plot, Fig. 8.

Another question of interest should be: What value must an increasing load have, at arbitrary location of the moving crack tip, in order to meet the memory condition? This question can be answered by means of the

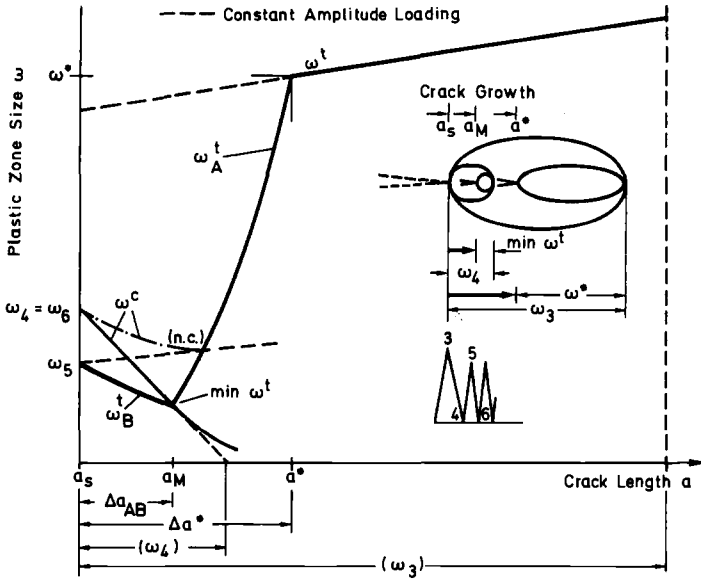


FIG. 8—Plastic zone size development typical with crack growth after a single peak overload. ω^t—tensile plastic zone size according to Eqs 15 and 19. ω^c—compressive plastic zone size according to Eq. 23 nc—no contact, ω^e according to Eq 47.

approximative Eq 26 if ΔK₅ is taken to be the dependent variable due to the desired load and Δa_{AB} the independent variable. Hence,

$$\Delta a = \frac{\pi}{8} \frac{\Delta K_{MB} \cdot (\Delta K_4 - \Delta K_{MB})}{\sigma_y^2} \tag{29}$$

$$\Delta K_{MB} = \frac{\Delta K_4}{2} + \left(\frac{\Delta K_4^2}{4} - \frac{8}{\pi} \sigma_y^2 \cdot \Delta a \right)^{1/2} \tag{30}$$

The subscript capitals denote that Eq 30 is the memory condition for increasing load if Δa is within the validity of Eq 12, governed by memory element I_B (ΔS₄, a_s). The value of the associated maximum stress intensity factor K_{MB} follows from the relationship K_{MB} = K₃ - ΔK₄ + ΔK_{MB}. As to the second branch where Eq 16 holds, the constitutive equation corresponding to Eq 29 reads as

$$\Delta a = \frac{\pi}{8} \frac{K_3^2 - K_{MA}^2}{\sigma_y^2}$$

thus

$$K_{MA} = \left(K_3^2 - \frac{8}{\pi} \cdot \sigma_y^2 \cdot \Delta a \right)^{1/2} \tag{31}$$

In Fig. 3 an example with six memory elements was given. They are $I_A(S_3, a_3)$, $I_B(\Delta S_4, a_3)$, $II_A(S_5, a_3)$, $II_B(\Delta S_6, a_3)$, $III_A(S_7, a_3)$, and $III_B(\Delta S_8, a_3)$. If crack growth is supposed to start beyond point 9, the development of the tensile plastic zone looks like in Fig. 9. The memory of the load history is successively lost beginning with the memory element of highest order number, namely III. To each couple of memory elements with the same order number a couple of $\omega'(a)$ -branches according to Eqs 15 and 19 is attributed. The range of validity of each couple of $\omega(a)$ curves is given by the point of intersection of adjacent A- and B-branches of different order number (see Fig. 9). Hence, the significance of the plastic zone formulae for a more general use is demonstrated. They can also be applied in case the history events do not occur at the same crack length which shall increase as $a_I < a_{II} < a_{III}$. Thus the memory elements are $I_A(S_3, a_I)$, $I_B(\Delta S_4, a_I)$, $II_A(S_5, a_{II})$ etc. When treating this particular structural memory behavior the Δa -term in the ω -formulae (Eqs 15, 19, 21 and 23) must be inserted as

$$\Delta a_i = a - a_i \quad i = I, II, III, \dots \tag{32}$$

The effect of crack growth between peaks is depicted in Fig. 9.

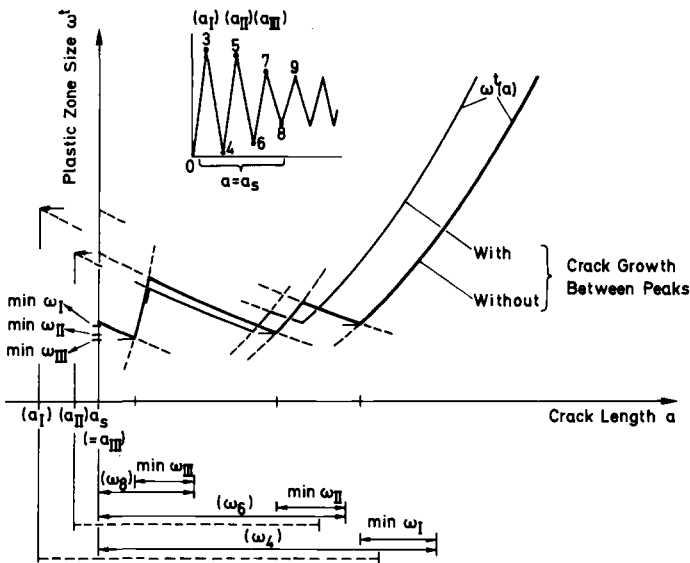


FIG. 9—Plastic zone size development typical with crack growth after more general irregular loading.

Conclusion and Outlook

Following the presented procedure the way on which to go forth in direction of crack growth prediction for irregular loading has become clearer. The solution of the problem as a whole, however, is still in an initial stage.

At the end, there remain at least three central questions open for answer. The answers, given in the sequel, are tentative. First, what is the influence of real material properties on memory? The aforementioned view of the memory effect provides a ground to assume the proposed memory criterion approximately valid in case of non-perfectly plastic material, as well, since the increase of stresses in the plastic zone due to strain hardening can be considered not as significant as the decrease of elastic stresses just in front of the elastic-plastic boundary. Because of that, the main part of the stress redistribution takes place as described in this paper.

Second, what is the optimum damage parameter from the point of view of physical relevance, economy, and applicability as well as prediction accuracy? Possibly, it is not necessary to use the CTOD range according to Eq 1 but to correlate damage directly to the size of the plastic zone, for example. This would mean no restriction of the procedure because the result of structural analysis must be adjusted to experimental constant amplitude growth rate data one time, at any rate.

Third, how does the fatigue crack closure mechanism really affect the local behavior at the crack tip, say crack growth behavior? Some accurate Dugdale solutions to the closure effect are already obtained by means of a numerical program (Dugdale cyclic) [2]. They are needed to find simple approximations in the aforementioned sense. Strictly speaking, the memory criterion formulated in the second section represents but a good approximation. Memory effects are found beyond the point where the criteria is met. They result from crack closure at the hump of residual displacements with overloads, (see Refs 2 and 5).

Remember that in this paper contact was assumed not to occur before the crack extends. If partial crack closure occurred even with peak unloading, it would be significant for the subsequent development of the characteristic elastic-plastic quantities. To treat such special aspects, however, is beyond the scope of this paper which was intended to introduce into structural memory by means of the ΔK approach.

Acknowledgment

The support given by the Laboratorium für Betriebsfestigkeit is gratefully acknowledged. The authors wish to thank Hanne Führung for unselfish help with the English manuscript.

APPENDIX I

Small Scale Yielding Dugdale Model Solution to Stationary Cracks

The central idea of the Dugdale method [7,8] is to extend the crack fictitiously by the amount of the plastic zones and apply internal stresses over the plastic zones which satisfy the material law. From this follows that the model only accounts for the contribution of a strip to the stress and strain redistribution process of elastoplasticity and neglects all other contributions outside the strip [14]. For simplicity, the strip material law is assumed rigid-perfectly plastic. The unknown size of the plastic zone is obtained by satisfying equilibrium which leads to the balance equation for stress intensity factors of the different load cases $\sum K_i = 0$ at the fictitious crack tip.

In case of the plastic zone being small compared to the crack length (or other plane dimensions), that is, in the so-called SSY case, the elastic field solution for the single crack tip in an infinite sheet can be used. Considering monotonic loading the following basic relationships hold (Fig. 5),

$$K_1(a + \omega) - \underbrace{\sqrt{\frac{2}{\pi}} \int_0^{\omega_1} p(\tilde{r}_1) \cdot \frac{1}{\sqrt{\tilde{r}_1}} d\tilde{r}_1}_{F_K} = 0 \tag{33}$$

$$\frac{E'}{2} v_1(r_1) = K_1 \cdot \sqrt{2r_1/\pi} - \underbrace{\int_0^{\omega_1} p(\tilde{r}_1) \cdot \frac{1}{\pi} \ln \frac{\sqrt{r_1} + \sqrt{\tilde{r}_1}}{\sqrt{r_1} - \sqrt{\tilde{r}_1}} d\tilde{r}_1}_{F_r} \tag{34}$$

$$\sigma_1(r_1) = K_1/\sqrt{2\pi r_1} - \underbrace{\int_0^{\omega_1} p(\tilde{r}_1) \cdot \frac{1}{\pi} \frac{1}{r_1 + \tilde{r}_1} \sqrt{\frac{\tilde{r}_1}{r_1}} d\tilde{r}_1}_{F_\sigma} \tag{35}$$

where

$E' = E$ in plane stress, and
 $E' = E/(1 - \nu^2)$ in plane strain.

Solving the equations under the SSY assumption

$$K(a + \omega) = K(a) \hat{=} K \tag{36}$$

leads to the well-known expressions [8] ($p = \sigma_y$, yield stress)

$$\omega_1 = \frac{\pi}{8} \left(\frac{K_1}{\sigma_y} \right)^2 \tag{37}$$

$$\frac{E'}{2} v_1(r_1) = \frac{\omega}{\pi} \sigma_y \cdot \left(2\sqrt{\frac{r_1}{\omega_1}} - \left(1 - \frac{r_1}{\omega_1}\right) \ln \left| \frac{1 + \sqrt{\frac{r_1}{\omega_1}}}{1 - \sqrt{\frac{r_1}{\omega_1}}} \right| \right) \quad (38)$$

$$\sigma_1(r_1) = \frac{2}{\pi} \sigma_y \cdot \text{arc tg } \sqrt{\frac{\omega_1}{r_1}} \quad (39)$$

$$v_{a1} \hat{=} v_1(r_1 = \omega_1) = \frac{K_1^2}{2E'\sigma_y} \quad (40)$$

With unloading to an arbitrary level S_2 , the new fictitious crack tip is located at $x = a + \omega_2$. ω_2 is the compressive plastic zone size (usually called $\Delta\omega$). In the relationships comparable with Eqs 33 to 35 there are to find now two terms for internal loading. One is accounting for crack closure stresses p_k .

$$\sqrt{\frac{\pi}{2}} \Delta K_2 - \int_0^{\omega_2} \Delta p(\tilde{r}_2) \cdot F_K(\tilde{r}_2) d\tilde{r}_2 - \int_{\omega_2}^{\omega_2 + \lambda_2} p_K(\tilde{r}_2) \cdot F_K(\tilde{r}_2) d\tilde{r}_2 = 0 \quad (41)$$

$$\begin{aligned} \frac{E'}{2} \Delta v_2(r_2) = \Delta K_2 \cdot \sqrt{2r_2/\pi} - \int_0^{\omega_2} \Delta p(\tilde{r}_2) \cdot F_v(r_2, \tilde{r}_2) d\tilde{r}_2 \\ - \int_{\omega_2}^{\omega_2 + \lambda_2} p_K(\tilde{r}_2) \cdot F_v(r_2, \tilde{r}_2) d\tilde{r}_2 \end{aligned} \quad (42)$$

$$\begin{aligned} \Delta \sigma_2(r_2) = \Delta K_2 / \sqrt{2\pi r_2} - \int_0^{\omega_2} \Delta p(\tilde{r}_2) \cdot F_\sigma(r_2, \tilde{r}_2) d\tilde{r}_2 \\ - \int_{\omega_2}^{\omega_2 + \lambda_2} p_K(\tilde{r}_2) \cdot F_\delta(r_2, \tilde{r}_2) d\tilde{r}_2 \end{aligned} \quad (43)$$

(Green's functions F_K , F_v , F_σ : cf. Eqs 33 to 35).

In case of a stationary crack and $R = S_2/S_1 \geq 0$ the contact term does not exist [14]. Since $\Delta p = 2\sigma_y$ over the whole fictitious extension of the crack, Eqs 41 to 43 result in similar expressions as Eqs 37 to 40 if each σ_y is replaced by $2\sigma_y$. For instance

$$\omega_2 = \frac{\pi}{32} \left(\frac{\Delta K_2}{\sigma_y} \right)^2 \quad \Delta v_{a2} = \frac{\Delta K_2^2}{4E'\sigma_y} \quad (44)$$

Superposition of stresses and displacements yields the state at minimum load $S_2 = S_1 - \Delta S_2$, see the contact-free case in Fig. 5.

$$\begin{aligned} v_2(r_1, r_2) &= v_1(r_1) - \Delta v_2(r_2) \\ \sigma_2(r_1, r_2) &= \sigma_1(r_1) - \Delta \sigma_2(r_2) \end{aligned} \quad (45)$$

where r_1 and r_2 are related by $r_2 = r_1 \pm (\omega_1 - \omega_2)$, positive sign for elastic stresses, negative sign for displacements. The stress range Δp that the material elements bear with unloading must not necessarily be $\Delta p = 2\sigma_y$. In the main part of the paper it is demonstrated that the validity of this relationship yielding the familiar ΔK formulae is limited to special problems such as CA loading. Definitely, the relationship $\Delta p = 2\sigma_y$ does not hold in any case of structural memory. That is why the ΔK approach for the description of local elastic-plastic behavior at the crack tip must be extended.

APPENDIX II

Compressive Plastic Zone Size with No Contact

As to the contact solution Eq 21, the size of the compressive plastic zone decreases with increasing crack length. Therefore, the compressive plastic frontier never strikes the tensile one and memory of a lower order does not occur. The contact-free case under consideration is different because the compressive plastic zone size initially increases with crack extension (or is constant when applying Eq 24). There are two $\omega^c(a)$ -branches. As to the first branch which only exists in case of $S_{\min} > S_4$,

$$\omega^c(a) \leq \omega^t(a)$$

the K -balance according to Eq 13, Fig. 6b, reads as

$$\begin{aligned}
 -\sigma_y \int_0^{\omega+\Delta a} \frac{dr}{\sqrt{r}} + \sigma_y \int_{\omega}^{\omega+\Delta a} \frac{dr}{\sqrt{r}} + \sqrt{\frac{\pi}{2}} \Delta K_6 \\
 - \sigma_y \int_0^{\omega} \frac{dr}{\sqrt{r}} - \int_{\omega}^{\omega+\lambda} p_K \frac{dr}{\sqrt{r}} = 0
 \end{aligned}$$

The second integral stands for the contribution of released stresses due to crack growth, the last integral vanishes in case of no contact (otherwise it follows Eq 35). Integration yields

$$\begin{aligned}
 2\sigma_y(-\sqrt{\omega} - \sqrt{\omega}) &= -\sqrt{\frac{\pi}{2}} \Delta K_6 \\
 \omega^c(a) &= \frac{\pi}{32} \left(\frac{\Delta K_6}{\sigma_y} \right)^2
 \end{aligned} \tag{46}$$

which is the expression for the cyclic plastic zone size $\omega_2 \triangleq \Delta\omega$, see Eq 44.

The K -balance equation of the second branch where $\omega^c(a) \geq \omega^t(a)$ is that of Eq 22 when the last term is cancelled. Integration leads to

$$2\sigma_y(-\sqrt{\omega + \Delta a} - \sqrt{\omega}) = -\sqrt{\frac{\pi}{2}}(\Delta K_4 - \Delta K_5 + \Delta K_6)$$

$$\omega^c(a) = \frac{\left[\frac{\pi}{8} \left(\frac{\Delta K_4 - \Delta K_5 + \Delta K_6}{\sigma_y} \right)^2 - \Delta a \right]^2}{\frac{\pi}{2} \left(\frac{\Delta K_4 - \Delta K_5 + \Delta K_6}{\sigma_y} \right)^2} \quad (47)$$

At the point of intersection of curves according to Eqs 46 and 28 which by use of approximation Eq 24 comes to be

$$\Delta a_{tc_b} = \frac{\pi}{8} \frac{\Delta K_5(\Delta K_5 - \Delta K_6)}{\sigma_y^2} \quad (48)$$

the $\omega^c(a)$ - curve jumps up to the second branch. In case of $S_{\min} = S_4$, Eq 47 where $\Delta K_5 = \Delta K_6$ may be introduced, is valid from the beginning of crack extension. The second point of intersection is obtained by setting $\omega^c(a) = \omega'_4(a)$ of Eqs 47 and 19. The result for all cases $S_{\min} \geq S_4$ is

$$\Delta a_{tc_A} = \frac{\pi}{8} \frac{(\Delta K_4 - \Delta K_5)(\Delta K_4 - \Delta K_5 + \Delta K_6)}{\sigma_y^2} \quad (49)$$

At this value of crack growth the single peak overload effect on the compressive plastic zone size ceases and Eq 46 holds further on. The situation of contact-free compressive plastic zones is depicted in Fig. 8.

References

- [1] Elber, W. in *Damage Tolerance in Aircraft Structures*, ASTM STP 486, American Society for Testing and Materials, 1971, pp. 230-242.
- [2] Führung, H., "Berechnung von elastisch-plastischen Beanspruchungsabläufen in Dugdale-Risscheiben mit Rissuferkontakt auf der Grundlage nichtlinearer Schwingbruchmechanik," Report No. 30, Institut für Statik und Stahlbau, TH Darmstadt, 1977.
- [3] Schijve, J., "Fatigue Crack Propagation in Light Alloy Sheet Material and Structures," *NLR MP 195*, Amsterdam 1960.
- [4] Hudson, C. M. and Hardrath, H. F., "Effects of Changing Stress Amplitude on the Rate of Fatigue Crack Propagation in Two Aluminum Alloys," Report No. TN D-960, National Aeronautics and Space Administration, Washington, 1961.
- [5] Führung, H. and Seeger, T. in *Proceedings*, 2nd International Conference on Mechanical Behavior of Materials, Boston, 1976, pp. 721-725.
- [6] Wheeler, O. E., *Transactions*, American Society of Mechanical Engineers; *Journal of Basic Engineering*, 1972, pp. 181-186.
- [7] Dugdale, D. S., *Journal of Mechanics and Physics of Solids*, Vol. 8, 1960, pp. 100-104.
- [8] Rice, J. R. in *Proceedings*, 1st International Conference on Fracture, Sendai, 1965, pp. 283-308.
- [9] Klöppel, K. and Seeger, T., "Experimentelle und Theoretische Beiträge zum Schädigungsverhalten dauerbeanspruchter Vollstäbe und Kerbstäbe aus St 37 und St 52," Report No. 3, Institut für Statik und Stahlbau, TH Darmstadt, 1967.
- [10] Liu, H. W., *International Journal of Fracture Mechanics*, Vol. 2, 1966, pp. 393-399.
- [11] McCartney, L. N., *International Journal of Fracture*, Vol. 12, 1976, pp. 273-288.

- [12] Matsuishi, M. and Endo, T., "Fatigue of Metals Subjected to Varying Stress," Japan Society of Mechanical Engineers, Fukuoka, 1968.
- [13] Matsuoka, S., Tanaka, K., and Kawahara, M., *Engineering Fracture Mechanics*, Vol. 8, 1976, pp. 507-523.
- [14] Führung, H. and Seeger, T. in *Engineering Fracture Mechanics*, Vol. M, 1979, pp. 99-122.
- [15] Führung, H. and Seeger T., "Sequence Effects in Fatigue Crack Growth Described on a Continuum Mechanics Basis," 2nd European Colloquium on Fracture, Darmstadt, 1978.

Effect of the Active Plastic Zone on Fatigue Crack Growth Rates

REFERENCE: Marci, Gunter, "Effect of the Active Plastic Zone on Fatigue Crack Growth Rates," *Fracture Mechanics, ASTM STP 677*, C. W. Smith, Ed., American Society for Testing and Materials, 1979, pp. 168–186.

ABSTRACT: The stress intensity range ΔK is divided according to the sign of the plastic strain excursion. The parameter K_I^G is the stress intensity factor at which the transition from compressive to tensile strain occurs. K_I^G was determined for the alloy 2024-T3 to be $0.5 K_{I\max}$. It is shown that loading conditions which produce only excursions in compressive stresses and strain in the crack tip region do not produce "stage II" fatigue crack growth. Furthermore, it is found that excursions in tensile stresses and strains have to exceed a certain range ΔK^T before fatigue crack growth occurs. ΔK^T so defined is denoted as threshold stress intensity range. The conclusion is reached that the following three elements have to be included in equations predicting "stage II" fatigue crack growth rates:

$$\frac{(K_I^G - K_{I\min})}{\Delta K^T} [(K_{I\max} - K_I^G) - \Delta K^T]$$

An equation is proposed, containing the three elements, which predicts the observed fatigue behavior and growth rates quite well.

KEY WORDS: stage II, fatigue (materials), closure, stress ratio, tensile-compressive strains, threshold, growth rate equation, crack propagation

Nomenclature

$K_{I\max}$	Maximum stress intensity factor
$K_{I\min}$	Minimum stress intensity factor
K_I^{LL}	Lower limit of ΔK transmitted to the active plastic zone
ΔK_{eff}	Elber effective stress intensity range
K_{cl}	Closure stress intensity factor
K_I^G	Limit value of the true stress intensity range
ΔK^T	Threshold stress intensity range
R	$K_{I\min} / K_{I\max}$

¹ Project engineer, fracture mechanics, Babcock-Brown Boveri, Reactor GmbH, Mannheim, West Germany.

- e Total equivalent plastic strain
- $\Delta\epsilon_c$ Effective compressive strain range
- $\Delta\epsilon_T$ Effective tensile strain range
- $\Delta\sigma_c$ Effective compressive stress range
- $\Delta\sigma_T$ Effective tensile stress range

The phenomena generally called closure has been divided into the plastic wake zone behind the crack front and in the active plastic zone ahead of the crack front [1].² The plastic wake zone, which is the trace of the previously active plastic zones, causes a reduction of the calculated stress intensity range with R -ratios smaller than 0.35. Contact between the crack faces occurs only in the plane stress region of the plastic wake zone, that is, in the surface region of the specimen [1,2]. This contact between the crack faces is responsible for the thickness dependence of "stage II" fatigue crack growth rates (FCGR) as well as the observed increase in FCGRs after transition from flat to slant fracture in thin specimen [3].

Yet, the primary interest in closure is motivated by the desire to explain the overload effects and crack arrest. None of these phenomena can be explained by the effects of the plastic wake zone, that is, by the reduction of the calculated stress intensity range actually transmitted to the active plastic zone. Therefore, one has to investigate the effects of the active plastic zone. It seems logical to correlate the transmitted stress intensity range with the stresses and strains resulting in the active plastic zone. The work to be presented tries to divide the transmitted stress intensity range according to the sign of the stresses and strains occurring in the near region of the crack front under its action. It is hoped that this partitioning of the transmitted stress intensity range furnishes the elements which have to enter equations predicting the observed "stage II" fatigue behavior.

Preliminaries

The investigation to follow is restricted to "stage II" fatigue crack growth (FCG). The reason for that restriction is that there is no evidence suggesting that ductile tearing (dimple fracture as might occur in "stage III" FCG) and FCG along crystallographic planes is governed by the same continuum parameters as is the growth mechanism in "stage II" which produces the striation. The evidence, gathered with measurements of the active plastic zone size by an optical interference technique [4], suggests that the size of the active plastic zone under tension cycling depends only on the $K_{I\max}$ loading. It is not affected by the magnitude of

² The italic numbers in brackets refer to the list of references appended to this paper.

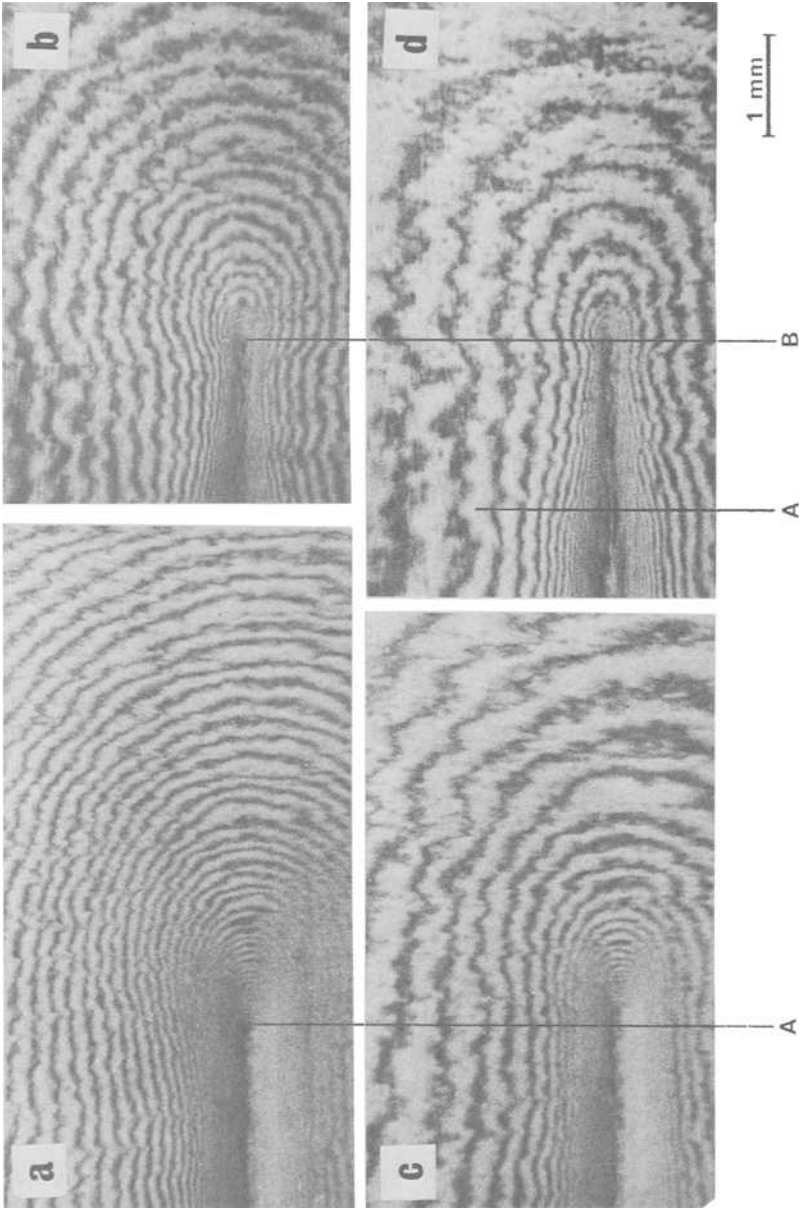


FIG. 1—Interference fringe pattern of the transverse displacement associated with a propagating fatigue crack.

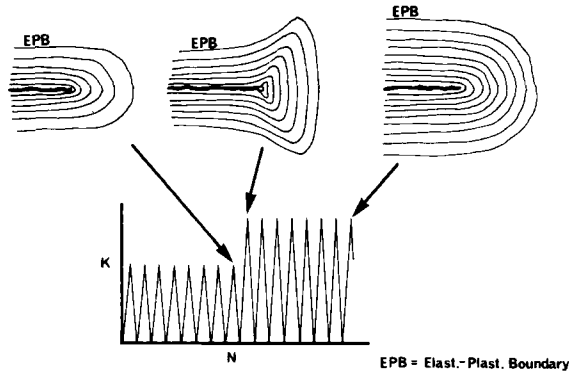


FIG. 2—Change of the fringe pattern due to a step-wise increase of $K_{I_{max}}$ (schematically).

$K_{I_{min}}$. If there is an influence of $K_{I_{min}}$, its effect is secondary and can be neglected for the present.

Figures 1a through 1d show the transverse displacement associated with a propagating fatigue crack. The displacement was made visible by an optical interference technique; each fringe is a line of constant displacement. Details of the experimental procedures are found in Refs 1 and 5. The fatigue crack was produced in 2024-T3 compact specimen with 6.2 mm thickness and 50 mm ligament width. The crack was grown with constant $K_{I_{max}} = 8.8 \text{ MPa}\sqrt{\text{m}}$ (8 ksi $\sqrt{\text{in.}}$) to a crack length of 34.5 mm (position A in Fig. 1). Then $K_{I_{max}}$ was reduced to $5.5 \text{ MPa}\sqrt{\text{m}}$ (5 ksi $\sqrt{\text{in.}}$) and the crack extended to 36.2 mm (position B in Fig. 1). Figures 1a and 1b correspond to $K_{I_{max}}$ loading while Figs. 1c and 1d correspond to $K_{I_{min}} \approx 0$. A reduction in $K_{I_{max}}$ requires the crack to grow out of the plastic zone of the previous $K_{I_{max}}$ loading condition to establish the new plastic zone size. This behavior is clearly visible between positions A and B in Fig. 1.

Figure 2 shows the transverse displacement under increasing $K_{I_{max}}$ schematically as fringe pattern. It is difficult to photograph this type of fringe pattern with low magnification and still obtain reasonable resolution. A single overload cannot produce the same plastic zone size as constant amplitude fatigue cycling with the same $K_{I_{max}}$. With further cycling under overload condition, the size of the plastic zone approaches the size characteristic of that loading condition. The response of the active plastic zone size to a change in $K_{I_{max}}$, as shown in Fig. 1 and 2, and its independence of $K_{I_{min}}$ for tension cycling leads to the following hypothesis:

Constant $K_{I_{max}}$ fatiguing with $R \geq 0$ is hypothesized to be the equilibrium fatigue condition with respect to the size of the active plastic zone and the variation in stresses and strains occurring in it.

While the meaning with respect to active plastic zone size is evident, the meaning of equilibrium with respect to stresses and strains needs to be explained further. Consider the elastic-plastic boundary connected to the crack tip by a straight line in such a way that the line lies in the macroscopic fracture plane. A material element lying on the line experiences stresses and strains under $K_{I\max}$ loading which correspond to a point on the cyclic stress-strain curve of the same material. Such a cyclic stress-strain curve is shown schematically as curve A in Fig. 3; the curve is characteristic for the cyclic behavior of the subject material and the cyclic conditions imposed by the subject $K_{I\max}$ loading conditions. For $K_{I\min} = 0$, the stresses and strains at the elastic-plastic boundary have to stay always in the tensile range, while at the crack tip region they can be compressive. The continuity requirement suggests that the stresses and strains these material elements experience under $K_{I\min}$ loading should correspond to a point on a cyclic stress-strain curve similar to the curves B shown in Fig. 3. The important point is that the curves B are dependent on curve A, that is, the stresses and strains occurring in the active plastic zone under loading conditions between $K_{I\min}$ and $K_{I\max}$ are uniquely dependent upon the $K_{I\max}$ loading. No matter how $K_{I\min}$ is varied from cycle to cycle, the stresses and strains in the active plastic zone under $K_{I\min}$ loading have always had a unique dependence on $K_{I\max}$.

If the aforementioned hypothesis is correct, then under constant $K_{I\max}$ fatigue cycling one should be able to identify the stress intensity factor at which the plastic zone becomes free of compressive stresses for the first time during the loading part of a cycle. In Fig. 3, curve B_3 corresponds to

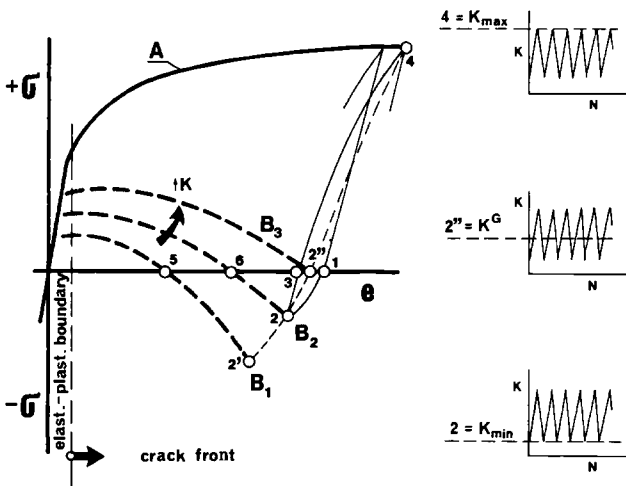


FIG. 3—Stress and strain condition in the active plastic zone.

such a condition. The stress intensity factor, at which the transition from compressive to tensile stresses or vice versa occurs in the region close to the crack tip, divides the transmitted stress intensity range in two parts. During one part of the stress intensity range the near crack-tip region of the plastic zone experiences only excursions of tensile stresses and strains; during the other part of the stress intensity range only compressive stresses and strain excursions occur in that region. This is shown schematically in Fig. 3 by the hysteresis loop. It has to be realized that the width of the hysteresis loop is greatly exaggerated. In reality, the total plastic strain during unloading and reloading (positions 1 and 3 in Fig. 3) would differ only by an incremental amount.

Low cycle fatigue behavior (Manson-Coffin equation [6,7]) suggests that the total plastic strain e (e = equivalent strain), as shown in Fig. 3, is not very influential with respect to fatigue damage. The excursion of strains and the respective stresses should be more important. But the excursion of strains in the near region of the crack tip is exactly what is characterized by the division of the transmitted stress intensity range previously suggested. For clarification, the excursion of the strains and the respective stresses are defined as

$$\begin{aligned}\Delta\epsilon_c &= \text{effective compressive strain range (position 1 to 2)} \\ \Delta\sigma_c &= \text{effective compressive stress range (position 1 to 2)} \\ \Delta\epsilon_T &= \text{effective tensile strain range (position 3 to 4)} \\ \Delta\sigma_T &= \text{effective tensile stress range (position 3 to 4)}\end{aligned}$$

The preceding positions relate to Fig. 3. Accordingly, equations predicting "stage II" FCGRs should contain at least the two elements $\Delta\epsilon_c$ and $\Delta\epsilon_T$.

$$\frac{da}{dN} = f(\Delta\epsilon_c, \Delta\epsilon_T) \quad (1)$$

or equivalently

$$\frac{da}{dN} = g(\Delta K_1, \Delta K_2) \quad (2)$$

where $\Delta K_1 + \Delta K_2 = K_{\text{max}} - K_{\text{min}}$ and g and f are some functions.

Limit Value of the True Stress Intensity Range

One can talk about a stress intensity factor under mode I loading only if tensile stresses and strains in the near crack-tip region are produced by the external loading conditions. Therefore, the stress intensity factor at

which the transition from effective compressive stresses and strains to effective tensile stresses and strains occurs is defined as the "limit value" of the true stress intensity range transmitted to the active plastic zone. This "limit value" is denoted at K_1^G . The effective compressive and effective tensile strain range can now be expressed in fracture mechanics terminology

$$\Delta\epsilon_c \approx K_1^G - K_{\text{imin}} \quad (3)$$

$$\Delta\epsilon_T \approx K_{\text{imax}} - K_1^G \quad (4)$$

and Eq 2 becomes

$$\frac{da}{dN} = g [(K_1^G - K_{\text{imin}}), (K_{\text{imax}} - K_1^G)] \quad (5)$$

The next task is to show that the hypothesis leading to the definition of K_1^G is true, that is, K_1^G is independent of K_{imin} under constant K_{imax} tension cycling, and to measure its magnitude.

Empirical Determination of K_1^G

Elber [8] developed the following equations for the prediction of FCGRs

$$\frac{da}{dN} = C^* (K_{\text{imax}} - K_{cl})^{n^*} \quad (6a)$$

$$= C^* (\Delta K_{\text{eff}})^{n^*} \quad (6b)$$

where C^* and n^* can be considered fitting parameters. The conceptual interpretation of Eq 6a is identical to

$$\frac{da}{dN} = C^* (K_{\text{imax}} - K_1^G)^{n^*} \quad (7)$$

since, as long as the crack faces are in contact (exerting compressive stresses on each other) the material element ahead of the crack front is experiencing compressive stresses, too.

It is a well known fact that R -ratios affect FCGRs, particularly for low R -ratios. The parameters C^* and n^* in Eqs 6 and 7 must incorporate the effect of the compressive strain range $\Delta\epsilon_c$ when $R = 0$. If Eqs 6 and 7 are correct for $R = 0$, then for $R > 0$ ($K_{\text{imax}} - K_{cl}$) or equivalently ($K_{\text{imax}} - K_1^G$) have to be modified. Consider the two fatigue cycles

Case 1: $R = 0 \quad (K_{\text{Imax}}^1 - 0) = \Delta K$

Case 2: $R > 0 \quad (K_{\text{Imax}}^2 - K_{\text{Imin}}^2) = \Delta K$

For Case 1, Eqs 6 and 7 apply directly

$$\Delta K_{\text{eff}} = K_{\text{Imax}} - K_I^G = \alpha \Delta K \tag{8}$$

For Case 2 there is the possibility to choose between two reference stress intensity ranges for the modification

$$K_{\text{Imax}}^1 - 0 = \Delta K \tag{9a}$$

$$K_{\text{Imax}}^2 - 0 = \overline{\Delta K} \tag{9b}$$

and for obvious reasons Elber has chosen the reference stress intensity range given by Eq 9a and modified it.

$$\Delta K = K_{\text{Imax}}^2 - K_{\text{Imin}}^2 = K_{\text{Imax}}^1 - 0 \tag{10a}$$

$$\Delta K_{\text{eff}} = \alpha(K_{\text{Imax}}^1 - 0) + \beta R(K_{\text{Imax}}^1 - 0) \tag{10b}$$

$$= (\alpha + \beta R) \cdot (K_{\text{Imax}}^1 - 0) \tag{10c}$$

The term βR modifies the reference stress intensity range because of the larger effective tensile strain range $\Delta\epsilon_r$ and the smaller effective compressive strain range $\Delta\epsilon_c$ of the ΔK with $R > 0$. That the modification term turns out to be positive indicates the dominating influence of the effective tensile strain range $\Delta\epsilon_r$. Elber determined $U = \alpha + \beta R$ empirically from FCGRs in 2024-T3 aluminum alloy and obtained

$$U = 0.5 + 0.4 R \tag{11}$$

Based on Eqs 6a, 7, and 8 and on the results obtained by Elber for Eq 11 related to 2024-T3 ($\alpha = 0.5$) it can be concluded that

$$K_I^G = 0.5 K_{\text{Imax}} \text{ for 2024-T3 aluminum}$$

Determination of K_I^G by Means of Transverse Displacement Measurement

The typical transverse displacement associated with a propagating fatigue crack is shown by the fringe pattern of Fig. 1. Let this transverse displacement be eliminated by grinding and polishing of the specimen

surface. Then upon reloading the specimen, a new fringe pattern develops which characterizes the removal of compressive contact stresses between the crack faces (for details see Ref 1). If the fatigue crack was propagated under constant $K_{I\max}$ fatiguing the compressive contact stresses between the crack faces increase from a point of last contact toward the crack tip. The transverse displacement due to removal of compressive contact stresses as a function of increasing load is shown schematically in Figs. 4a through 4e by its respective fringe pattern. The line RS indicates the position of the crack tip. It is to be noted that the transverse displacement progresses from the point of last contact toward the crack tip under increasing load. At an incremental distance to either side of the line RS , the plastic stretch and consequently the compressive stresses are identical. Therefore the transverse displacement is identical at both positions. This means that the fringe lines have to be nearly parallel as long as compressive stresses are acting in the crack-tip region.

If the compressive contact stresses are removed, then the crack-tip singularity should govern the distribution of stresses and the resulting transverse displacement, that is, the transverse displacement should obey the radial and angular dependence imposed by the crack-tip singularity. Therefore, one can identify the stress intensity factor K_I^G as the one at which radial expansion of the fringe pattern around the crack tip just begins under increasing load. This is shown schematically in Figs. 4f and 4g. Figure 5 shows such a sequence of fringe patterns for 0.4, 0.5 and 0.6

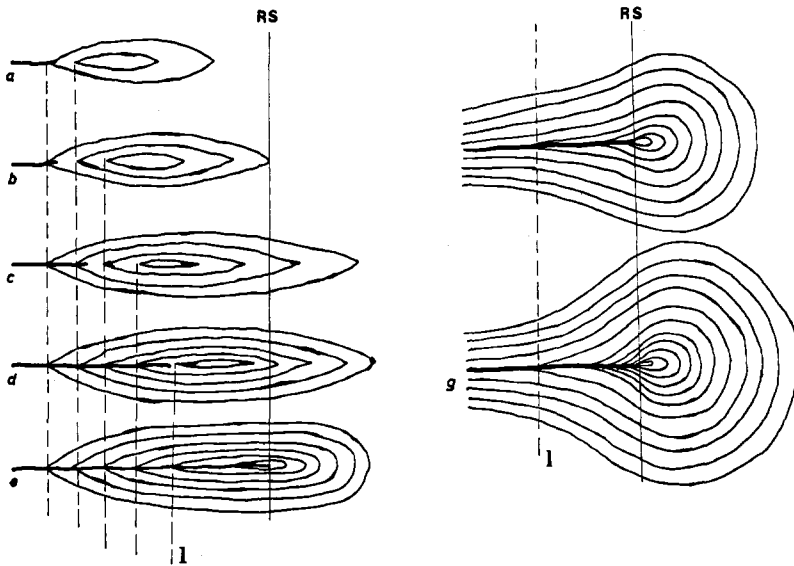


FIG. 4—Change in fringe pattern due to the transition from closure stresses to stresses resulting from the crack tip singularity (schematically).

K_{Imax} . The photographs in Fig. 5 were obtained from a 2024-T3 CT-specimen with 76 mm ligament width and 12.4 mm thickness; the crack length was 32 mm. The arrows inserted in Fig. 5 indicate the position of the crack tip. The specimen had been fatigued under constant $K_{\text{Imax}} = 15.4 \text{ MPa}\sqrt{\text{m}}$ (14 $\text{ksi}\sqrt{\text{in.}}$) with $R \approx 0$.

From Fig. 5 and similar sequences of fringe pattern for different K_{Imax} , different R -ratios and different crack length in the alloy 2024-T3 lead to the conclusion that K_1^G had to be close to $0.5 K_{\text{Imax}}$.

Determination of K_1^G by Means of Load Displacement Curves

It can be shown with the help of Elber's second derivative analysis [8] and the geometric nature of contact between the crack faces [1,2] that load displacement curves usually indicate the macroscopic opening of the crack as lowest point of their linear portion. This is true if the gage, measuring the displacement, is a distance several times the active plastic zone dimensions behind the crack tip and spans approximately the width of the plastic zone. In order to determine K_1^G from load displacement curves the gage position must be right behind the crack tip and should not span more than the width of the plastic wake zone [9]. Then K_1^G can be identified as the lowest point of the upper, linear part of the load displacement curve. In this position and with this gage length the apparent separation of the crack faces due to the removal of the compressive contact stresses would be measured first (lower linear part). But if the compressive contact stresses are eliminated, the crack-tip singularity takes over. This switch takes place within a small loading increment and results in a well-defined transition of the slope between the two linear portions of the load displacement curve. Elber used a gage length of 1.5 mm at 2 mm behind the crack tip and obtained values for the lowest point of the respective linear portion of approximately $0.5 K_{\text{Imax}}$ with the alloy 2024-T3.

Three independent means to determine K_1^G resulted in values for K_1^G of $0.5 K_{\text{Imax}}$ in the alloy 2024-T3. These values seemed not to be affected by the R -ratios for constant K_{Imax} fatigue experiments. Therefore, it is concluded that the previously made hypothesis is correct and K_1^G can be considered a material parameter.

Conditions For Stage II Fatigue Crack Growth

It is the generally held opinion, which is substantiated by the models of striation formation, that Stage II FCG can only occur under excursions of tensile stresses. In the terminology developed in the foregoing section this means that the excursions in load have to produce some excursions of the effective tensile stress range $\Delta\epsilon_T$ or in fracture mechanics terms

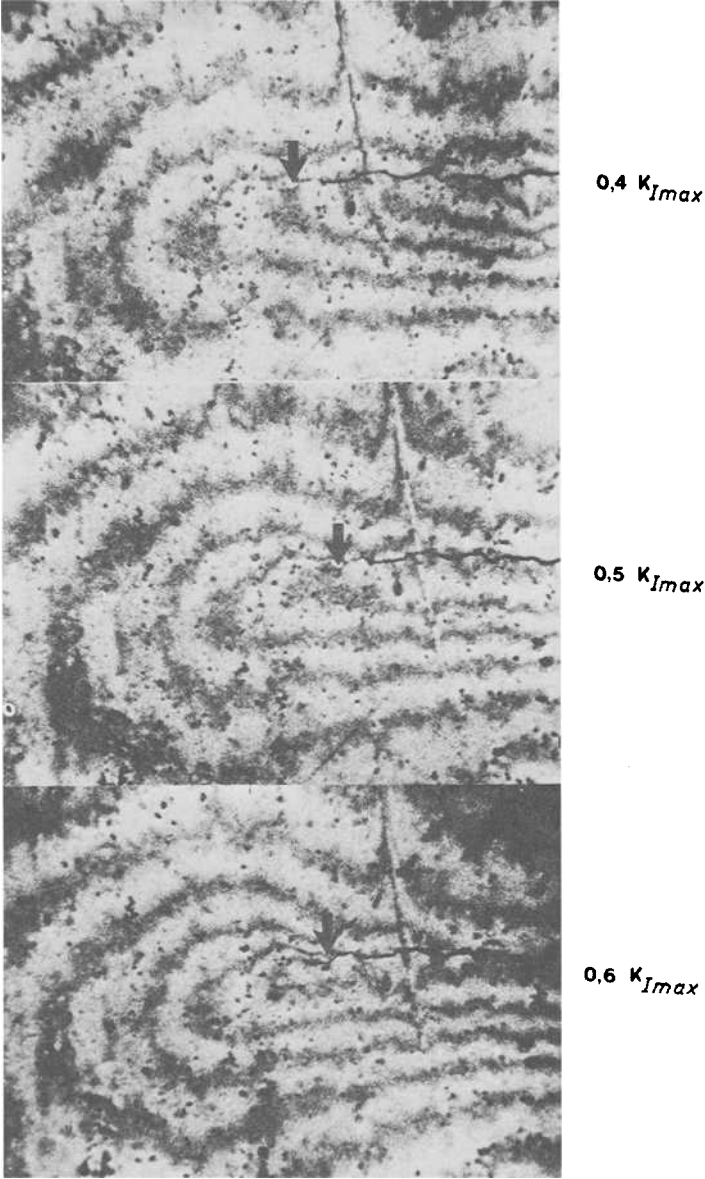


FIG. 5—Fringe patterns showing the beginning of the radial expansion of fringes due to the crack tip singularity.

$$K_{I\max} - K_I^G > 0 \tag{12}$$

To check this, the following experiment was devised. A crack was grown in 2024-T3 aluminum under constant $K_{I\max} = K_I^P$ and $K_{I\min}$ close to zero for 5 mm. It could be assumed that the active plastic zone had established its equilibrium condition. By reducing $K_{I\max}$ to $0.5 K_I^P$, keeping $K_{I\min}$ the same, the cyclic loading produces only excursions of the effective compressive stresses and strains in the near crack-tip region of the active plastic zone. This type of loading should not produce Stage II FCG.

Fatiguing with 4.5×10^5 cycles and frequency of 3 cycles/s did not produce FCG under these loading conditions. The results are shown graphically in Fig. 6, where K_I^P (K_I^P produced the active plastic zone) is plotted along the abscissa and the cyclic loading ($K_I^G - K_{I\min}$) is plotted along the ordinate. These experiments confirm that the crack-tip region has to experience effective tensile stresses and strains for Stage II FCG to occur. The highest stress intensity range ($K_I^G - K_{I\min}$) applied during this test series was $\Delta K = 14.3 \text{ MPa}\sqrt{\text{m}}$ (13 $\text{ksi}\sqrt{\text{in.}}$) which is far above any threshold range.

Since excursions in effective compressive stresses do not produce Stage II FCG, it makes no sense to define a threshold stress intensity range which includes a part or the total of the effective compressive stress range. Therefore, if a threshold stress intensity range exists, it has to characterize a certain excursion in the effective tensile stress range $\Delta\sigma_T$ which does not produce Stage II FCG. The threshold stress intensity range so defined is denoted as ΔK^T .

ΔK^T was determined under constant $K_{I\max} = K_I^P$ fatigue cycling and

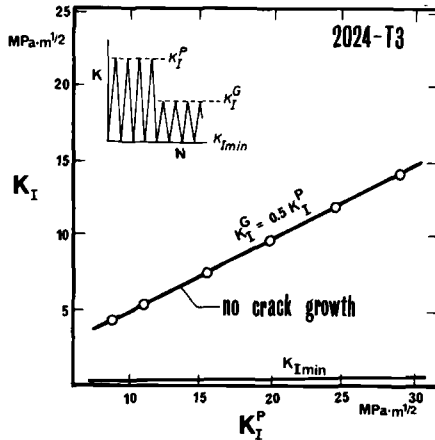


FIG. 6—No fatigue crack growth under loading conditions producing only excursions in effective compressive stresses $\Delta\sigma_c$.

K_{Imin} raised till no FCG was observed after 3×10^3 cycles. The crack length was measured with a traveling microscope with $\times 50$ magnification and the optical interference equipment attached to the specimen. Any change in crack-tip position on the order of 0.05 mm can be detected easily. Similarly, a fatigue crack was grown under constant $K_{\text{Imax}} = K_I^P$ until equilibrium conditions in the active plastic zone were established. Then K_{Imax} was reduced to a value somewhat higher than $K_I^G = 0.5 K_I^P$ and cycling continued for 3×10^3 cycles. If no crack growth was observed, K_{Imax} was increased slightly and cycling continued for another 3×10^3 cycles. This procedure was repeated till crack growth was observed. The K_{Imax} of the previous loading condition (K_{Imax}^3) was used to determine $\Delta K^T = K_{\text{Imax}} - 0.5 K_I^P$.³ The results of the ΔK^T measurements are shown graphically in Fig. 7 for the alloy 2024-T3; the measured value for ΔK^T is $2.5 \text{ MPa}\sqrt{\text{m}}$ ($2.3 \text{ ksi}\sqrt{\text{in.}}$).³

Fatigue Crack Growth Rate Equation

The findings concerning the threshold stress intensity range ΔK^T require that the FCGR-Eq 5 has to be modified. Since excursions of effective tensile stresses and strains have to exceed a range equivalent to ΔK^T before any Stage II FCG occurs, ΔK^T has to be subtracted out of the total effective tensile stress and strain range, that is

$$(K_{\text{Imax}} - K_I^G) - \Delta K^T \quad (13)$$

and Eq 5 is modified to

$$\frac{da}{dN} = h [(K_I^G - K_{\text{Imin}}), \Delta K^T, (K_{\text{Imax}} - K_I^G) - \Delta K^T] \quad (14)$$

where h is some function. The three elements contained in Eq 14 should enter any FCGR-equation explicitly.

The similarity of the concept developed here with that of Elber suggests that the general form of the Paris-Erdogan equation might still be valid. Considering that R -ratios below 0.5 cause a shift in FCGRs in 2024-T3 [10], this would require that the effective compressive stress and strain range has to enter the FCGR-equation in a linear fashion. A threshold stress intensity range had been subtracted out of the leading ΔK term in quite a few equations characterizing FCGRs without entering it explicitly in other terms. This indicates that ΔK^T effects FCGRs in a constant

³ The model of FCG presented in this paper is based on a unique dependence of FCGRs on the loading conditions of each individual cycle. If the FCGR is not any more uniquely related to a loading cycle, as it must be for FCGRs smaller than $3 \times 10^{-10} \text{m/cycle}$, then the model ceases to apply; the same is true for ΔK^T (as defined here). Therefore, the ΔK^T is substantiated if it is shown that the FCGR is smaller than $3 \times 10^{-10} \text{m/cycle}$.

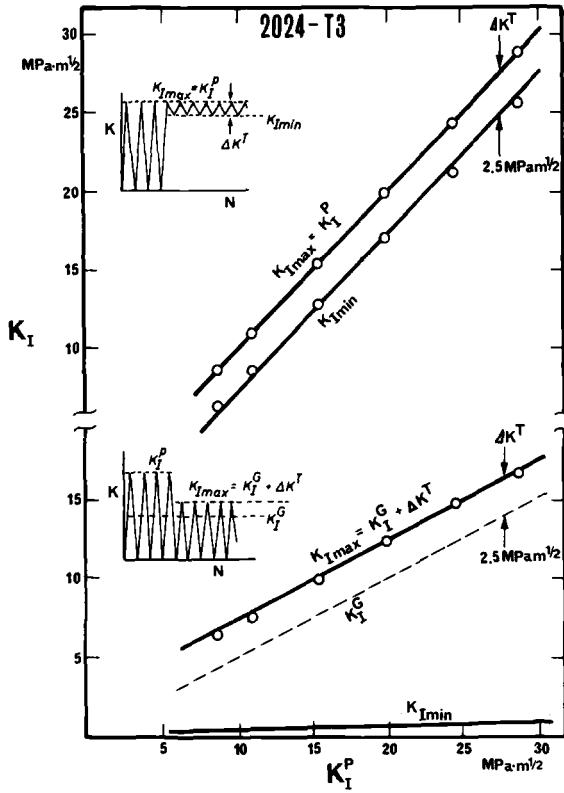


FIG. 7—Conditions and results of the threshold stress intensity range ΔK^T determination.

manner. Due to the lack of better knowledge, it is assumed that ΔK^T has approximately the same effect on FCG as have the effective compressive stresses and strains. Therefore, the following equation is proposed

$$\frac{da}{dN} = C [(K_I^G - K_{Imin}) + (\Delta K^T)^m] \cdot [(K_{Imax} - K_I^G) - \Delta K^T]^n \quad (15)$$

It has to be realized that for $K_{Imin} \geq K_I^G$ Eq 15 becomes

$$\frac{da}{dN} = C (\Delta K^T)^m \cdot [(K_{Imax} - K_{Imin}) - \Delta K^T]^n \quad (16)$$

Equation 15 had been used to calculate the FCGRs for several materials and for different R -ratios. The fatigue parameters were determined based on measured FCGRs [11-14] and are shown in Table 1. The markings in Figs. 8 to 12 are the experimentally measured FCGRs while the lines are

TABLE 1—Fatigue crack growth parameters used to predict the growth rates shown in Figs. 8 to 12.

Material	K_I^G	ΔK^T	m	n	C
2219-T851	$0.5 K_{max}$	2.0	1	2	7×10^{-8}
RA Ti-6Al-4V	$0.6 K_{max}$	4.0	1	2	1.43×10^{-8}
Annealed inconel 600	$0.5 K_{max}$	4.5	1	2	4.4×10^{-9}
Hastelloy X-280	$0.5 K_{max}$	3.5	1	2	1.2×10^{-8}
304 stainless steel	$0.5 K_{max}$	3.0	1	2	1.36×10^{-8}

^a ksi $\sqrt{\text{in.}}$. $da/dN \triangleq \text{in./cycle}$

the theoretical predictions. The agreement seems to be quite good. As can be seen in Table 1, the exponent m was determined to be 1.0 which means that the threshold stress intensity range ΔK^T has the same effect on FCG as has the effective compressive stress and strain range ($K_I^G - K_{Imin}$). The value of 2.0 for the exponent n seems to indicate that the fatigue damage is a function of the linear extent of the active plastic zone. Under the assumption that the findings $n = 2$ and $m = 1$ can be generalized, Eq 15 can be written

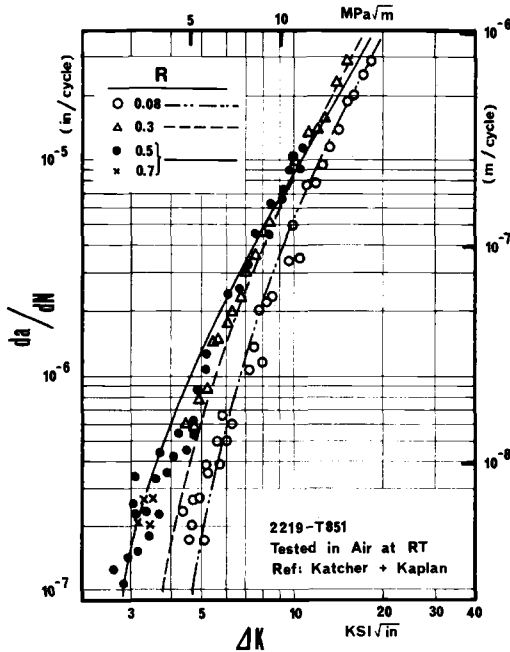


FIG. 8—Experimental results and their prediction by the proposed equation for 2219-T851 aluminum alloy.

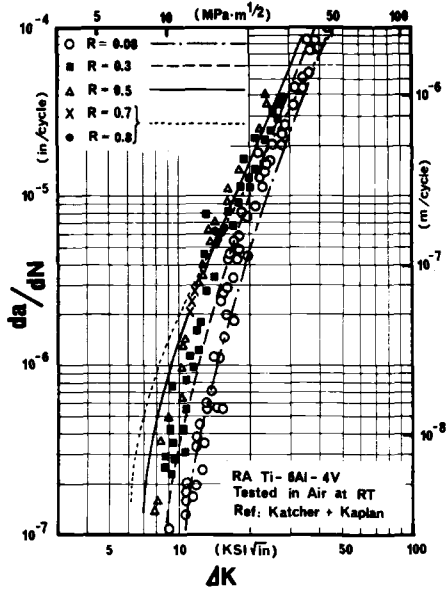


FIG. 9—Experimental results and their prediction by the proposed equation for RA Ti-6Al-4V.

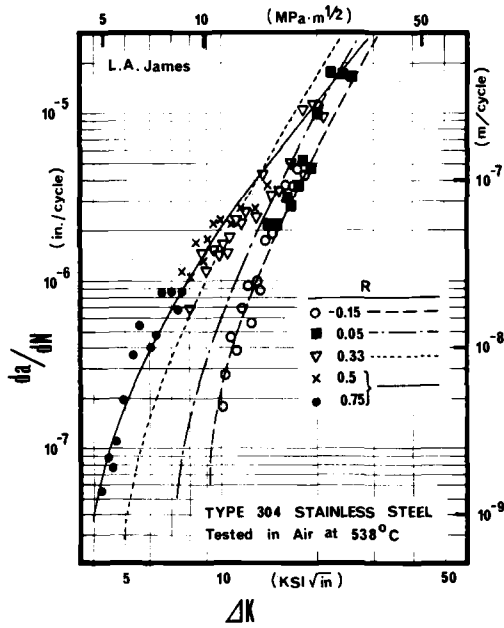


FIG. 10—Experimental results and their prediction by the proposed equation for 304 stainless steel at 538°C.

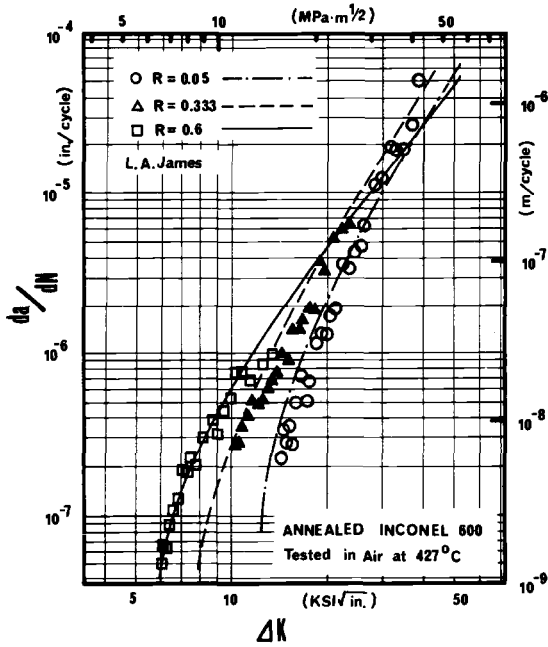


FIG. 11—Experimental results and their prediction by the proposed equation for Inconel 600 at 427°C.

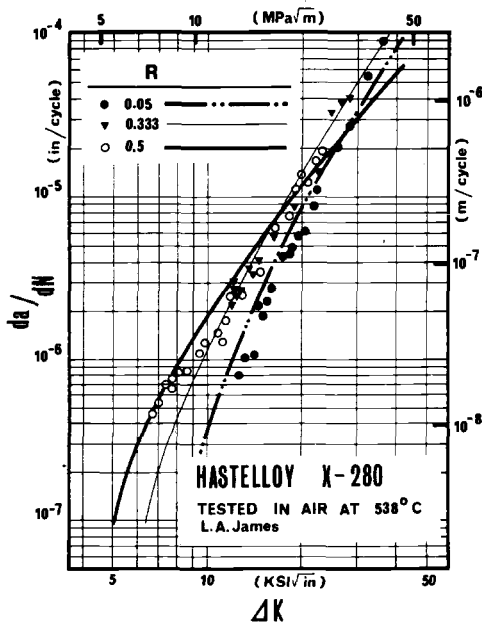


FIG. 12—Experimental results and the predicted R-ratio effect for Hastelloy X-280 at 538°C.

$$\frac{da}{dN} = C [(K_I^G - K_{Imin}) + \Delta K^T] \cdot [(K_{Imax} - K_I^G) - \Delta K^T]^2 \quad (17)$$

Figures 10, 11, and 12 show that the predictive capability of Eq 17 is maintained even for fatigue at elevated temperatures. Further investigations into the temperature dependence of the fatigue parameters are in progress.

The thickness dependence of FCGRs observed with *R*-ratios below 0.35 can be incorporated into Eq 17 by replacing K_{Imin} by its modified value K_I^{LL} which is the lower limit of the stress intensity range actually transmitted to the active plastic zone³. Equation 17 then becomes

$$\frac{da}{dN} = C [(K_I^G - K_I^{LL}) + \Delta K^T] \cdot [(K_{Imax} - K_I^G) - \Delta K^T]^2 \quad (18)$$

Conclusions

For tension fatiguing under constant K_{Imax} amplitude there exists a unique relation between K_{Imax} and the limit-value of the true stress intensity range K_I^G at which the active plastic zone is free of compressive stresses. For the aluminum alloy 2024-T3 K_I^G had been determined to be $0.5 K_{Imax}$.

K_I^G divides the transmitted stress intensity range according to the sign of the excursions in effective stresses and strains.

Stage II FCG can occur only if the excursions in effective tensile stresses and strains exceed a certain range which is characterized in fracture mechanics terms by the threshold stress intensity range ΔK^T .

Fracture mechanics equations predicting Stage II FCGRs must contain the three elements

$$\begin{aligned} & [(K_{Imax} - K_I^G) - \Delta K^T] \\ & \Delta K^T \\ & (K_I^G - K_{Imin}) \text{ or } (K_I^G - K_I^{LL}) \end{aligned}$$

An equation is proposed, containing the three elements, which predicts the experimentally observed fatigue crack growth behavior even at elevated temperatures.

References

[1] Marci, G. and Packman, P. F., *Materialprüfung*, Vol. 18, No. 8, 1976, pp. 260-265.
 [2] Lindley, T. C. and Richards, C. E., *Materials Science and Engineering*, Vol. 14, 1974, pp. 281-293.

- [3] Marci, G. and Packman, P. F., *Materialprüfung*, Vol. 18, No. 11, 1976, pp. 416–421.
- [4] Marci, G., Packman, P. F., and Jones, J. W. in *Proceedings*, 2nd International Conference on Mechanical Behavior of Materials, Boston, 16–20 August 1976, pp. 583–589.
- [5] Marci, G., Ph.D. thesis, Vanderbilt University, Nashville, Tenn., 1976.
- [6] Manson, S. S., "Behavior of Materials Under Conditions of Thermal Stresses," NACA Technical Note 2933, 1954.
- [7] Coffin, L. F., Jr., *Transactions*, American Society of Mechanical Engineers, 1956, p. 527.
- [8] Elber, W., in *Damage Tolerance in Aircraft Structures*, ASTM STP 486, American Society for Testing and Materials, 1971, pp. 230–242.
- [9] Marci, G. and Bazant, E., *Materialprüfung*, Vol. 19, No. 11, 1977, pp. 455–462.
- [10] Schijve, J. in *Fatigue Crack Propagation*, ASTM STP 415, American Society for Testing and Materials, 1967, p. 415.
- [11] Katcher, M. and Kaplan, M. in *Fracture Toughness and Slow-Stable Cracking*, ASTM STP 559, American Society for Testing and Materials, 1974, pp. 264–284.
- [12] James, L. A., *Nuclear Technology*, Vol. 14, No. 2, 1972, pp. 163–170.
- [13] James, L. A., *International Journal of Pressure Vessels and Piping*, Vol. 5, No. 4, Oct. 1977, pp. 241–259.
- [14] James, L. A., "The Effect of Temperature upon the Fatigue Crack Propagation Behavior of Hastelloy X-280," HEDL-TME 76–40.

J. A. Vazquez,¹ Augusto Morrone,² and J. C. Gasco²

A Comparative Experimental Study on the Fatigue Crack Closure Behavior Under Cyclic Loading for Steels and Aluminum Alloys

REFERENCE: Vazquez, J. A., Morrone, Augusto, and Gasco, J. C., “A Comparative Experimental Study on the Fatigue Crack Closure Behavior Under Cyclic Loading for Steels and Aluminum Alloys,” *Fracture Mechanics, ASTM STP 677*, C. W. Smith, Ed., American Society for Testing and Materials, 1979, pp. 187–197.

ABSTRACT: Experimental data on fatigue crack closure for two steels which present different mechanical properties are presented. The data are compared with experimental results obtained under similar test conditions on aluminum alloys. On the basis of such a comparison, an attempt is made to identify the most suitable engineering parameters to describe the fatigue crack closure behavior. As a result, it is shown how fatigue crack closure can be related to several basic features of fatigue crack growth.

KEY WORDS: fatigue (materials), crack propagation, aluminum alloys

Recently, experimental data on fatigue crack closure for two aluminum alloys displaying different tensile properties and tested under tension-tension constant amplitude sinusoidal loading [1]³ have been reported. These data indicated that the fatigue crack closure behavior is controlled primarily by the maximum cyclic value of the stress intensity factor, K_{\max} . Specifically, it was found that, at least for the aluminum alloys tested, K_{\max} can successfully correlate crack opening stress intensity values. In Ref 1 such a correlation is suggested to consider a “master” curve which represents the values of the effective stress intensity range, ΔK_{eff} , as a function of K_{\max} . Using this curve, it was possible to rationalize several

¹ Technical director, Institute of Naval Technology, Research and Development Service of the Argentine Navy, Estados Unidos 25, Capital Federal, Buenos Aires, Argentina.

² Research assistant and former research assistant, respectively, Division of Mechanics of Solids, Institute of Naval Technology, Research and Development Service of the Argentine Navy, Estados Unidos 25, Capital Federal, Buenos Aires, Argentina.

³ The italic numbers in brackets refer to the list of references appended to this paper.

basic features of the fatigue crack propagation behavior. An interesting result emerging from the data reported in Ref 1 is that the ratio, $R = (K_{\min}/K_{\max})$, has a very minor influence in the relationship between ΔK_{eff} and K_{\max} . This would imply that the fatigue crack closure behavior of a material can be investigated from the data obtained for a single value of R . If so, a significant saving of effort and time in collecting experimental information could be achieved. Therefore, there is interest in exploring to what extent the dependence of ΔK_{eff} on K_{\max} , as found in Ref 1 for aluminum alloys, can be considered as characteristic of the fatigue crack closure behavior. The primary aim of the present investigation was to explore further the relationship between ΔK_{eff} and K_{\max} for other alloys systems than that tested in Ref 1. In particular, two steels which present quite different tensile properties were chosen. The results obtained in this work are compared with the data reported in Ref 1.

Materials, Specimens, and Test Procedures

The certified chemical compositions of the steels investigated in this program are listed in Table 1. The tensile properties are recorded in Table 2.

Compact tension type specimens ($H/W = 0.60$, $W = 68.00$ mm thickness, $B = 4.00$ mm) were cut from different bars in the long transverse direction.

Reference 1 gives a detailed description of the testing equipment and procedures used for collecting the present data. Briefly, all experiments were conducted in a MTS servohydraulic testing machine at room temperature. The load amplitude and R -ratio were maintained constant for each specimen. The opening loads, P_{op} , were determined following the procedure described in Ref 1. The frequency of the cyclic load ranged between 10 and 70 Hz.

TABLE 1—Chemical composition of the steels investigated.

	SM1 Steel	1010 Steel
Carbon	0.59	0.08–0.13
Manganese	...	0.30–0.60
Nickel	2.47	...
Phosphorus	...	0.040
Chromium	0.86	...
Sulfur	...	0.050
Molybdenum	0.27	...
Vanadium	0.18	...
Iron	remainder	remainder

TABLE 2—Average mechanical properties of the steels investigated.^a

1010 Steel	
Elastic limit, (MN: m ²)	196
Tensile strength, (MN: m ²)	357
Elongation, percent	11

^a The tensile characteristics of the SM1 steel were not measured except its hardness = 30 Rc.

Experimental Results

Fatigue Crack Growth Rates—The correlation between (da/dN) and ΔK , obtained for 1010 and SM1 steels, for different values of R is shown in Figs. 1 and 2, respectively.

K_{op}/K_{max} versus K_{max} Curves—Figures 3 and 4 show for 1010 and SM1 steels, respectively, the values of the ratio K_{op}/K_{max} (K_{op} , as being defined by Elber [2]), as a function of the maximum cyclic stress intensity value, K_{max} , for different values of the ratio R .

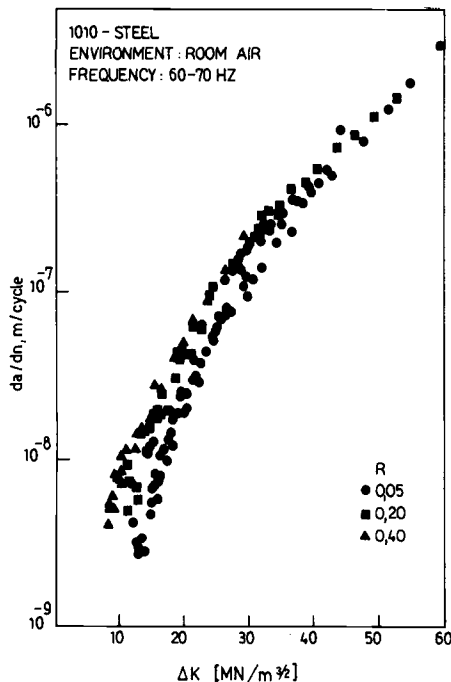


FIG. 1—Fatigue crack growth rate for 1010-steel in room air.

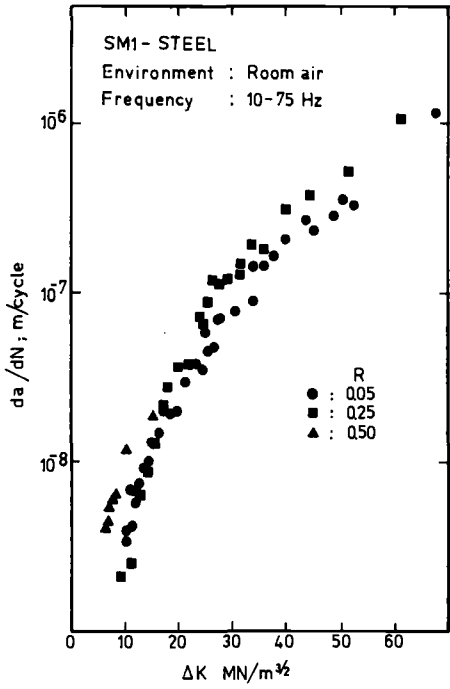


FIG. 2—Fatigue crack growth rate for SMI-steel in room air.

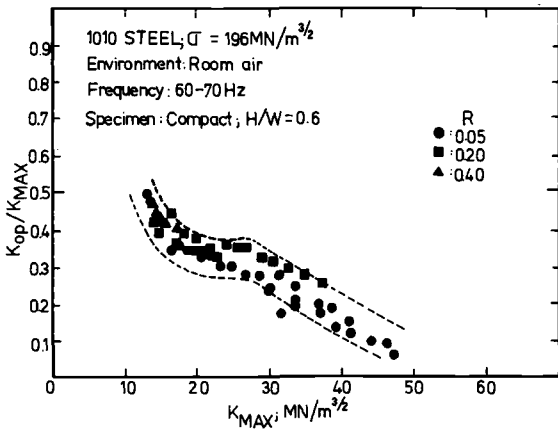


FIG. 3— K_{op}/K_{max} plotted against K_{max} for 1010-steel.

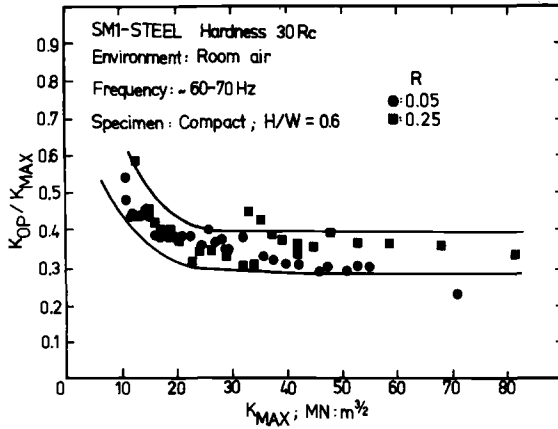


FIG. 4— K_{op}/K_{max} plotted against K_{max} for SMI-steel.

ΔK_{eff} versus K_{max} Curves—Figures 5 and 6 show for 1010 and SMI steels, respectively, the values of the effective stress intensity amplitude, ΔK_{eff} , as a function of K_{max} , for different values of R . In these figures the straight lines given by $(\Delta K_{eff} = (1 - R) K_{max})$ have been drawn. As discussed in Ref 1, the intersection of the $(\Delta K_{eff}$ versus $K_{max})$ curves with such straight lines provides the values of K_{max} (or ΔK) above which the fatigue crack is open during the whole fatigue cycle.

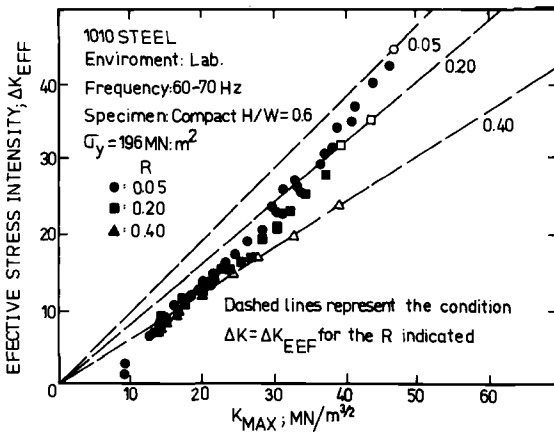


FIG. 5—Effective stress intensity range, ΔK_{eff} , plotted against maximum stress intensity, K_{max} , for 1010-steel. The straight lines represent the condition $\Delta K_{eff} = \Delta K$ for the R indicated. Open symbols indicate K_{op} values less than K_{min} . Environment: room air. Frequency: 60 to 70 Hz.

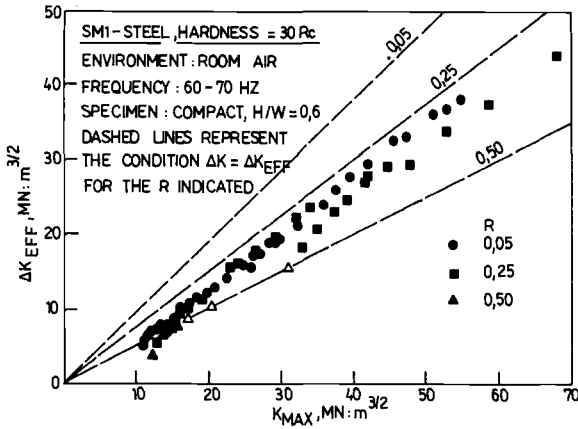


FIG 6—Effective stress intensity range, ΔK_{eff} , plotted against maximum stress intensity, K_{max} , for SMI-steel. The straight lines represent the condition $\Delta K_{eff} = \Delta K$ for the R indicated. Open symbols indicate K_{op} values less than K_{min} . Environment: room air. Frequency: 60 to 70 Hz.

Discussion

The excellent correlation between K_{max} and ΔK_{eff} found for the two steels investigated, as shown in Figs. 5 and 6, offers further proof that K_{max} is the most suitable parameter for an engineering approach to the fatigue crack closure phenomenon.

The general trend of ΔK_{eff} as a function of K_{max} found on the basis of the data generated in this work and that reported in Ref 1, is shown in Fig. 7. By inspecting this figure one is tempted to conclude that the strong

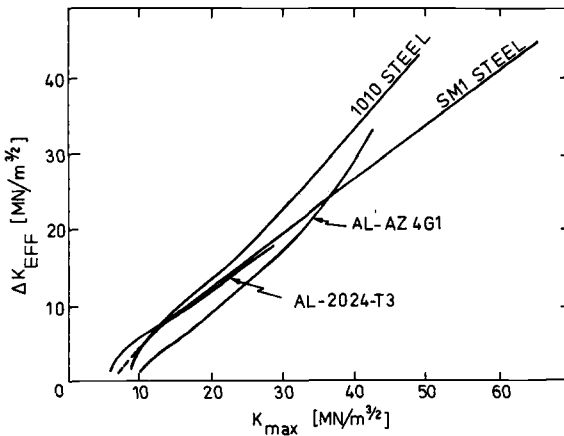


FIG. 7—General trend of ΔK_{eff} as a function of K_{max} for steel and aluminum alloys.

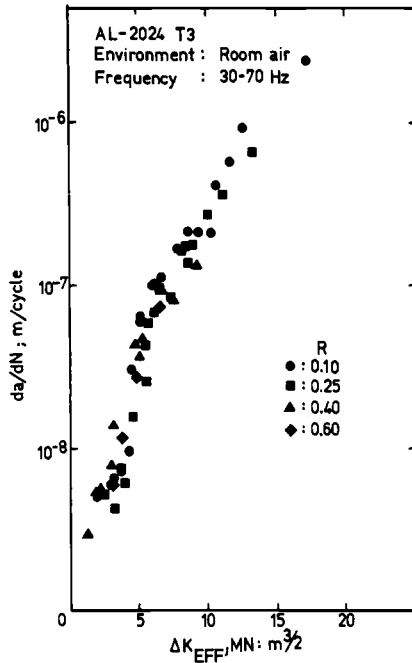


FIG. 8—Growth rate versus effective stress intensity range for 1010-steel.

correlation between ΔK_{eff} and K_{max} is a basic feature of the fatigue crack closure behavior. Of course, a general discussion of the exact dependence of ΔK_{eff} on K_{max} should await the development of more extensive experimental data. However, it is felt that, at present, it is far more important to determine the appropriate parameter to use. In this connection, the data discussed in this work indicate that K_{max} offers the most promise.

In considering the fatigue crack growth behavior, the data presented in this work and in Ref 1 reveal that the effective stress intensity range, ΔK_{eff} , is a powerful unifying parameter to correlate fatigue crack growth rates (Figs. 8 and 9). As was noted first by Elber, ΔK_{eff} depends on R in such a way that R has a negligible influence on the fatigue crack rates when ΔK_{eff} is used as a correlating parameter. This result is more than informative. In fact, it seems to be the key in the attempt to derive a rather general approach to fatigue crack propagation based on continuum mechanics concepts. As it was pointed up in Ref 1, the fact that ΔK_{eff} correlates fatigue crack growth rates for different mean stress intensities seems to offer a definite proof of the validity of the basic hypothesis advanced by Paris in 1962 [3]: "If the instantaneous time histories of the stress intensity factors at two crack tips are the same in a given material,

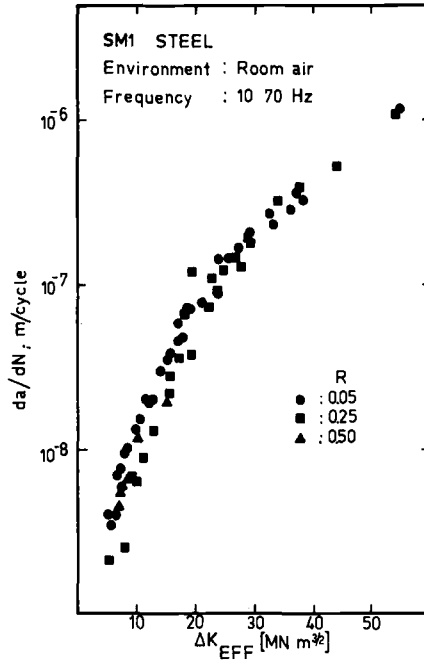


FIG. 9—Growth rate versus effective stress intensity range for SMI-steel.

then the crack propagation rates will be the same.” As is well known, this hypothesis does not meet the experimental results when ΔK is used as the local stress field parameter. However, the same hypothesis is in full agreement with the data when the instantaneous time-history of the local stresses surrounding the tip of the fatigue crack is described by ΔK_{eff} . Since the physical meaning of ΔK_{eff} as a local stress field parameter for a partially closed fatigue crack is the same as ΔK for a fully open fatigue crack, the soundness of Paris’ hypothesis is now apparent.

An interesting result obtained in this work is that, for the two steels tested, ΔK_{eff} approaches zero as K_{max} approaches a certain value which seems to be characteristic of the material and independent of the ratio- R (see Figs. 5, 6, and 7). On the other hand, the data in Figs. 1 and 2 indicate that as ΔK_{eff} approaches zero, K_{max} approaches the value associated with the fatigue crack propagation threshold of the material. It is significant to note that similar results also were obtained for constant amplitude fatigue in two aluminum alloys [1]. Though more experimental data are necessary on this topic, the aforementioned results would indicate the validity of the hypothesis according to which, at threshold level, the fatigue crack should be fully closed [4].

It is also interesting to note that, from the relationship between ΔK_{eff} and K_{max} obtained for the four alloys studied in this work and in Ref 1,

one may conclude that, for a given material and ratio R , there is a value of K_{max} above which the fatigue crack remains open during the complete loading cycle. For a given R , this value of K_{max} is given by the intersection between the "master" curve (K_{max} versus ΔK_{eff}) and the straight line ($\Delta K_{eff} = (1 - R)K_{max}$). Obviously, as K_{max} exceeds such a level, the effective stress intensity amplitude, ΔK_{eff} , equals the "applied" stress intensity range, ΔK . Since it is assumed that ΔK_{eff} controls fatigue crack rates, it is reasonable to expect that the ratio, R , should have no significant effect on fatigue crack growth rates when K_{max} exceeds the level for which $\Delta K_{eff} = \Delta K$. That is, the type of correlation between K_{max} and ΔK_{eff} observed in this study and in Ref 1, explains why, in a plot of (da/dN) versus ΔK , increasing values of R do not produce a continuous shift in fatigue crack rates. Moreover, in such a kind of plot, one should expect that fatigue crack growth rates corresponding to different ratios, R , should fall into a narrow band as soon as $\Delta K = \Delta K_{eff}$. This is, precisely, the fatigue crack growth behavior displayed in Figs. 1 and 2.

Let us consider now the relationship between K_{op} and K_{max} (Figs. 3 and 4). The reasons by which the ratio (K_{op}/K_{max}) sweeps upward at low levels of K_{max} are not evident at present. However, the data discussed in this work indicate that such behavior is characteristic of the fatigue crack closure phenomenon and, therefore, a general approach to the problem should be able to describe it. The same data also seem to indicate that the ratio (K_{op}/K_{max}) is affected by the state of stress at the fatigue crack tip. In this connection we can consider, first, the data for the high-strength alloys, that is, A1-2024-T3 and the SM1 Steel. Figure 10 shows, for these materials, the values of (K_{op}/K_{max}) as a function of K_{max} . From this figure it can be noted that (K_{op}/K_{max}) remains nearly constant for values of K_{max}

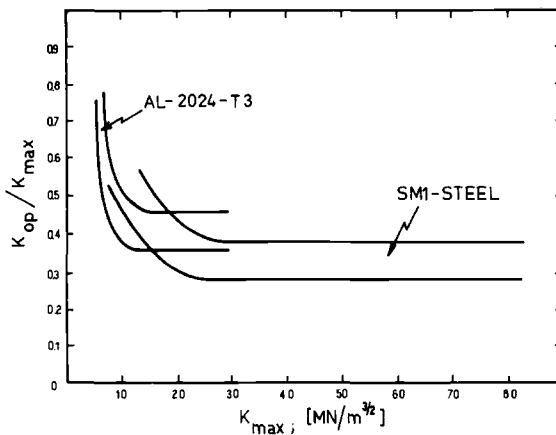


FIG. 10—General trend of (K_{op}/K_{max}) versus K_{max} for high strength materials.

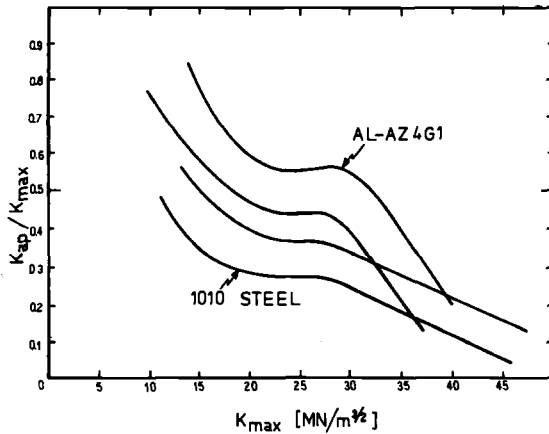


FIG. 11—General trend of (K_{op}/K_{max}) versus K_{max} for low strength materials.

located to the right of the zone in which (K_{op}/K_{max}) sweeps upward as K_{max} approaches threshold conditions. This result is in good agreement with the results of Paris' first order analysis based on concepts of dislocation mechanics [5]. In fact, such an analysis predicts that (K_{op}/K_{max}) should be nearly material independent with a value ranging between 0.33 and 0.52.

Consider now the data shown in Fig. 11 for the low-strength alloys, that is, Al-AZ4G1 and 1010 steel, which present about the same yield strength ($\sim 200 \text{ MN/m}^2$). From this figure it can be noted that (K_{op}/K_{max}) decreases as soon as K_{max} exceeds a certain level which is about $28 \text{ MN/m}^{3/2}$ for both of the alloys. In order to explore this rather unexpected behavior, monotonic traction tests on fatigue precracked compact tension specimens were performed. These tests revealed that, for both alloys, the value of K_{max} for which (K_{op}/K_{max}) begins to decrease is also about the value of K_{max} associated with the beginning of a nonlinear behavior in the load-displacement curve. Therefore, it seems reasonable to conclude that the decrease of (K_{op}/K_{max}) as a function of K_{max} , observed in the case of the low-strength alloys, can be attributed to the presence of rather gross plasticity at the crack tip. As a matter of fact, it can be verified easily that the plastic zone size [computed by $(K_{max}^2/2\pi\sigma_0^2)$] becomes quite similar to the specimen thickness when (K_{op}/K_{max}) begins to decrease. So, it is quite possible that the additional tests on these low-strength alloys using thicker specimens would indicate the existence of a wider range of K_{max} in which (K_{op}/K_{max}) would remain nearly constant.

Conclusions

The analysis and comparison of the data obtained in this investigation and that from Ref 1 reveal several interesting features of the fatigue crack

closure phenomenon, which seem to be useful for an engineering approach to the problem. These features may be summarized as follows:

1. From an engineering point of view, the maximum cyclic value of the stress intensity factor, K_{\max} , is the most suitable unifying parameter to correlate the fatigue crack closure behavior.

2. At least for constant amplitude fatigue, the relationship between K_{\max} and ΔK_{eff} seems to be characteristic of the material. Such a correlation allows the rationalization of several basic features of the fatigue crack growth behavior: the existence of a threshold for fatigue crack propagation and the shift behavior in crack growth rates, as a function of ΔK , for increasing ratios, R .

3. The data obtained for the four alloys studied show that the ratio (K_{op}/K_{\max}) sweeps upward as K_{\max} approaches threshold conditions. This behavior should be considered as typical of the fatigue crack closure phenomenon.

4. As K_{\max} moves away from the threshold region, the ratio (K_{op}/K_{\max}) yields to a value which, for practical purposes, may be considered as nearly constant and ranging between 0.3 and 0.5. These figures are in good agreement with the results of Paris' first order approach to fatigue crack closure.

5. The ratio (K_{op}/K_{\max}) decreases for values of K_{\max} associated with the presence of rather gross plasticity at the crack tip.

Acknowledgment

The authors would like to thank Research and Development Service of the Argentine Navy for financial support under Contract No. 20077. They are also indebted to P. C. Paris for stimulating discussion on the subject. The authors also would like to thank the Argentine CONICET and the U.S. National Science Foundation for their support through a cooperative research project with the Center for Fracture Mechanics of Washington University.

References

- [1] Vázquez, J. A., Morrone, A. and Ernst, H., "Experimental Results on Fatigue Crack Closure for Two Aluminum Alloys," to be published in *Engineering Fracture Mechanics*.
- [2] Elber, W., in *Damage Tolerance in Aircraft Structures, ASTM STP 486*, American Society for Testing and Materials, 1971, p. 230.
- [3] Paris, P. C., "Crack Growth Due to Variation in Load," Ph.D. thesis, Lehigh University, 1962.
- [4] Schmidt, R. A. and Paris, P. C. in *Progress in Flaw Growth and Fracture Toughness Testing, ASTM STP 536*, American Society for Testing and Materials, 1973, p. 79.
- [5] Paris, P. C., private communication.

Effect of Residual Stresses on Fatigue Crack Growth in Steel Weldments Under Constant and Variable Amplitude Loads

REFERENCE: Glinka, Grzegorz, "Effect of Residual Stresses on Fatigue Crack Growth in Steel Weldments Under Constant and Variable Amplitude Loads," *Fracture Mechanics, ASTM STP 677*, C. W. Smith, Ed., American Society for Testing and Materials, 1979, pp. 198–214.

ABSTRACT: The research deals with the effect of welding residual stresses on fatigue crack growth in medium strength low alloy steel weldments. Three kinds of flat specimens have been used—unwelded specimens, specimens with butt perpendicular welds, and specimens with butt longitudinal welds. Residual stress distributions were others in both kinds of welded specimens. All specimens were tested under constant and variable amplitude load with stress ratios $R > 0$. Forman's equation and Wheeler's model of crack retardation were used for theoretical analysis of fatigue crack growth under constant and variable amplitude load, respectively. The theoretical results were more realistic when effective stress ratio R_{eff} and effective stress intensity range ΔK_{eff} , which compensated for residual stresses, were used. It was found that the tensile residual stresses increased the fatigue crack growth rate and compressive stresses reduced it. The lower the applied load, the higher the residual stress effect. This paper presents both experimental results and an analytical method of fatigue crack growth prediction in steel weldments on the basis of results obtained from parent material properties.

KEY WORDS: fatigue (materials), crack propagation, residual stresses

Nomenclature

- a Half crack length, mm
- a_c Critical half crack length, mm
- a_i Current half crack length, mm
- a_p Half crack length with included plastic zone produced by previous higher stress level, mm
- a_o Initial half crack length, mm

¹ Research engineer, Institute of Cranes and Building Machinery, Warsaw Technical University, Warsaw, Poland.

C	Crack growth rate coefficient
C_{pi}	Crack growth retardation factor
$\frac{da}{dN}$	Crack growth rate, mm/cycle
K	Applied stress intensity factor, $\text{MPa}\sqrt{\text{m}}$
K_c	Critical stress intensity factor, $\text{MPa}\sqrt{\text{m}}$
K_{\max}	Applied maximum stress intensity factor, $\text{MPa}\sqrt{\text{m}}$
K_{\min}	Applied minimum stress intensity factor, $\text{MPa}\sqrt{\text{m}}$
$K_{\max,\text{eff}}$	Effective maximum stress intensity factor, $\text{MPa}\sqrt{\text{m}}$
$K_{\min,\text{eff}}$	Effective minimum stress intensity factor, $\text{MPa}\sqrt{\text{m}}$
K_r	Residual stress intensity factor, $\text{MPa}\sqrt{\text{m}}$
ΔK	Applied stress intensity range, $\text{MPa}\sqrt{\text{m}}$
ΔK_{eff}	Effective stress intensity range, $\text{MPa}\sqrt{\text{m}}$
L	Specimen with butt longitudinal weld
m	Shaping factor of Wheeler's model
n	Crack growth rate exponent
P	Specimen with butt perpendicular weld
R	Stress ratio = $\sigma_{\min}/\sigma_{\max} = K_{\min}/K_{\max}$
R_{eff}	Effective stress ratio = $K_{\min,\text{eff}}/K_{\max,\text{eff}}$
U	Unwelded specimen
Y	Finite width factor
σ	Applied stress, MPa
σ_a	Amplitude of applied stress, MPa
σ_{\max}	Applied maximum stress, MPa
σ_{\min}	Applied minimum stress, MPa
σ_m	Applied mean stress, MPa
σ_r	Residual tensile strength, MPa
σ_Y	Yield strength, MPa

Understanding fatigue crack growth is essential in predicting the service lives of many structures subjected to fatigue loading. This is particularly true for welded structures wherein subcritical flaws may be introduced during fabrication. It is widely known that weldments are more susceptible to fatigue failure than the base material because of problems related to the presence of inclusions, incomplete fusion, changes in microstructure, and the introduction of residual stresses.

Studies [1,2]² of fatigue crack growth in steel weldments produced by various welding processes have shown generally that residual stresses are primarily responsible for higher or lower fatigue crack growth rates in comparison with base material. It has been shown that the crack growth rate in the heat-affected zone (HAZ) as well as in the weld metal is similar

² The italic numbers in brackets refer to the list of references appended to this paper.

to the rate in the base material [3–5]. Therefore, residual stresses should be included in calculations of weldment fatigue crack growth rates.

Fatigue crack growth rate usually is analyzed in terms of fracture mechanics by using stress intensity factors [6]. Popular expressions are the Paris equation[7].

$$\frac{da}{dN} = C(\Delta K)^n \quad (1)$$

and the Forman equation, respectively [8]

$$\frac{da}{dN} = \frac{C(\Delta K)^n}{(1 - R)K_c - \Delta K} \quad (2)$$

where

C and n = material constants obtained from unwelded specimens tested under constant amplitude load,

a = half crack length,

N = number of load cycles,

ΔK = range of stress intensity factor, and

K_c = critical stress intensity factor.

Both equations are used in the present study. There were three kinds of plane specimens investigated: unwelded ones, U , those with butt perpendicular welds, P , and others with butt longitudinal welds, L . An attempt to predict fatigue crack growth rates under the influence of weld induced residual stresses is presented.

Materials, Specimens, and Experiments

All specimens (Fig. 1) were made of one metal sheet 4 mm thick. It was low alloy hot-rolled and normalized medium strength steel 18G2AV. The mechanical properties are shown in Table 1. Specimens were cut out parallel to the rolling direction. In order to produce similar residual stress distributions in each particular welded specimen, the specimens were welded after complete preparation of separate details. Welding was the last operation in the specimen fabrication. A manual-coated electrode arc welding was used. The approximate welding speed and current intensity were 120 mm/min and 90 A, respectively. A stress riser (Fig. 1) with a notch length of 14 mm was cut out in the center of each specimen before gripping it in the test machine. In the case of specimens P the stress risers were cut out in the heat-affected zone (HAZ) about 1.5 mm from the fusion line. Experiments were carried out on a mechanical fatigue machine designed and fabricated at the Institute of Cranes and Building

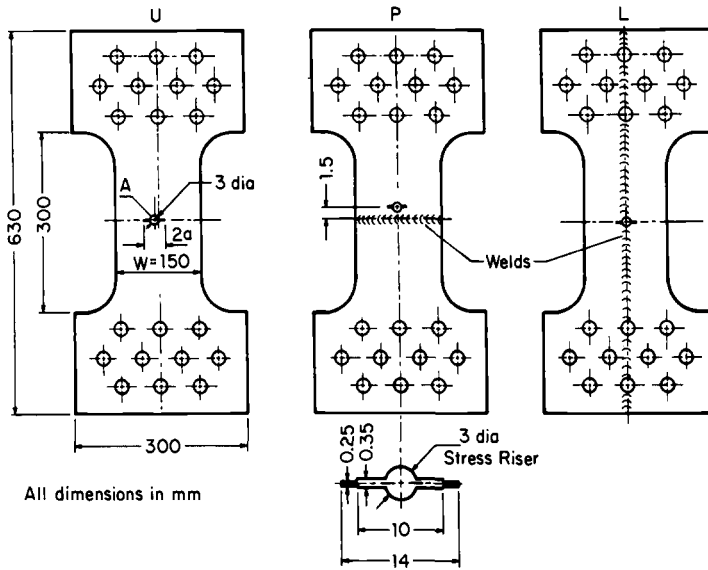


FIG. 1—Specimens shape and dimensions.

Machinery of Warsaw Technical University [9]. Crack lengths were measured using a microscope with $\times 50$ magnification. It was possible to measure 0.05 mm crack extensions. The number of load cycles was monitored by using an electronic cycle counter.

Fatigue crack growth rates were calculated following Smith's method [10]. The rates were computed for cracks with $2a \geq 16$ mm lengths only. The previous crack growth up to length $2a = 16$ mm was assumed as a fatigue crack initiation period.

The stress intensity factor was calculated using Eq 3 for finite width plates [11].

$$K = \sigma\sqrt{aY} = \sigma\sqrt{a} \left[1.77 + 0.227 \left(\frac{2a}{W} \right) - 0.51 \left(\frac{2a}{W} \right)^2 + 2.7 \left(\frac{2a}{W} \right)^3 \right] \quad (3)$$

where

- σ = applied gross section stress,
- a = half crack length, and
- W = specimen width.

The residual stress distributions (Fig. 2) were evaluated on the basis of two randomly selected *P* and *L* specimens, respectively. Residual strains

TABLE 1—Chemical composition by percent weight Steel 18G2AV.

Carbon	Manganese	Silicon	Phosphorus	Sulfur	Chromium	Niobium	Copper	Vanadium	Nitrogen
0.2	1.4	0.4	0.06	0.06	0.3	0.3	0.3	0.12	0.015
Mechanical Properties									
					$\sigma_u = 625 \text{ Mpa}$				
					$\sigma_{UTS} = 784 \text{ MPa}$				

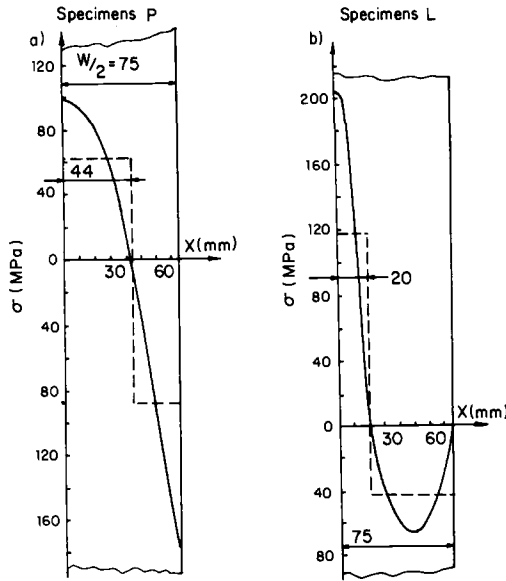


FIG. 2—Residual stresses distributions in the plane of fatigue crack growth.

were measured with a sectioning method using strain gages [12]. Details of the residual strain measurements and residual stress calculations are described in Ref 13. Due to symmetry only half of the stress distributions perpendicular to the crack plane have been shown (Fig. 2).

Theoretical Analysis

The main reason for fatigue crack growth studies is to gather information for fatigue life predictions. However, one must know a proper crack growth relation. In the case of steel 18G2AV, Forman's Eq 2 can be used for constant amplitude testing. However, in the case of welded specimens it was necessary to incorporate residual stresses into Eq 2. A superposition method was used assuming that the effective intensity factor K_{eff} can be computed as a sum of the residual stress intensity factor $K_r = f(\sigma_r)$ and the applied stress intensity factor $K = f(\sigma)$. It was assumed that residual stresses do not diminish under fatigue loading. This assumption overestimates the residual stress effect, but is reasonable from the practical point of view. Having in mind the aforementioned assumptions, the maximum $K_{\text{max, eff}}$ and minimum $K_{\text{min, eff}}$ values of the effective stress intensity factor could be calculated.

Then effective range of stress intensity factor ΔK_{eff} and effective stress ratio R_{eff} were calculated, respectively.

The applied maximum K_{max} and minimum K_{min} stress intensity factors

were calculated on the basis of Eq 3. For calculating the residual stress intensity factor K_r , Kanazawa's [14] formula was used, that is,

$$K_r = \int_{-a}^a \sigma_r(x) \left[\frac{2 \sin \frac{\pi(a+x)}{W}}{W \cdot \sin \frac{2\pi a}{W} \cdot \sin \frac{\pi(a-x)}{W}} \right]^{1/2} dx \quad (4)$$

In order to make the calculations easier, the real residual stress distributions (Fig. 3) were replaced by simplified rectangular distributions drawn with dashed lines.

The final form of Forman's equation used for calculations is

$$\frac{d(2a)}{dN} = \frac{C(\Delta K_{eff})^n}{(1 - R_{eff})K_c - \Delta K_{eff}} \quad (5)$$

In order to calculate fatigue lives, Eq 5 was integrated with a computer. The method and the computer program used for fatigue life calculations under constant and variable amplitude load are described in Ref 15.

The total fatigue life was calculated as a sum of initiation and propagation periods respectively.

$$N_t = N_i + \int_{2a_0}^{2a_c} \frac{(1 - R_{eff})K_c - K_{eff}}{C(\Delta K_{eff})^n} da \quad (6)$$

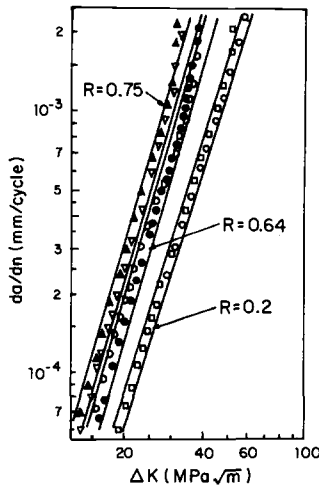


FIG. 3—Effect of stress ratio on fatigue crack growth rate in base material.

where

- N_t = total fatigue life,
- N_i = number of load cycles within initiation period related to crack length $2a = 16$ mm,
- $2a_0 = 16$ mm—assumed initial crack length,
- $2a_c = 80$ mm—assumed critical crack length, and
- C, n, K_c = the same as in Eq 5.

A more complex problem involves the analysis of fatigue crack growth under variable amplitude loads. Particularly difficult is the theoretical prediction of fatigue crack growth retardation. A few simplified models [16] of fatigue crack growth retardation exist but none of them explain the phenomenon completely. However, it has been shown that they can be used for rough predictions of fatigue crack growth retardation. The model applied in this study was proposed by Wheeler [17]. It was assumed in the model that after a sudden reduction of load amplitude the fatigue crack growth rate is decreased by a C_{pi} factor in comparison to the constant amplitude fatigue crack growth rate. In the case of Forman's equation Wheeler's model is written

$$\frac{d(2a)}{dN} = C_{pi} \frac{C(\Delta K)^n}{(1-R)K_c - \Delta K} \quad (7)$$

where

$$C_{pi} = \left(\frac{R_{yi}}{a_p - a_i} \right)^m \text{ for } a_i + R_{yi} < a_p,$$

$$C_{pi} = 1 \text{ for } a_i + R_{yi} \geq a_p,$$

R_{yi} = extent of current yield zone,
 $a_p + a_i$ = distance from tip of current crack to elastic plastic interface,
 and
 m = shaping exponent.

The extent of the yield zone was computed following the formula proposed by Rice [20] for plane stress state

$$R_y = \frac{1}{\pi} \left(\frac{K_{\max}}{\sigma_y} \right)^2 \quad (8)$$

The shape factor m was determined by fitting the theoretical results obtained from Eq 9 to the theoretical data obtained from unwelded specimens, U

$$2a = 2a_0 + \int_{N_i}^{N_f} \frac{C_{pi} \cdot C \cdot (\Delta K_{eff})^n}{(1 - R_{eff})K_c - \Delta K_{eff}} dN \quad (9)$$

Fatigue Crack Growth Under Constant Amplitude Load

Experimental results of $\log d(2a)/dN$ versus $\log (\Delta K)$ are shown in Figs. 3 and 4. Widths of scatter bands were evaluated for probability $p = 95$ percent. The unwelded U specimens were studied under different stress ratios from $R = 0.2$ to 0.75 . It appeared that fatigue crack growth rates in steel 18G2AV depend upon stress ratio, and the higher the stress ratio R , the higher the crack growth rate $d(2a)/dN$. There was little or no effect of stress ratio in the range $R = 0.2$ to 0.5 (Fig. 4a).

It is evident that for a given constant stress ratio R , Eq 1 properly describes the fatigue crack growth behavior. But coefficients n and especially C depend on stress ratio. Therefore, Eq 2 has been used for further studies. The constants C , n , and K_c in Eq 2 were evaluated on the basis of the same data obtained from unwelded specimens U1 to U8 and they are 1.69×10^{-6} , 2.54 , and $108.5 \text{ mPa}\sqrt{\text{m}}$, respectively. All of them

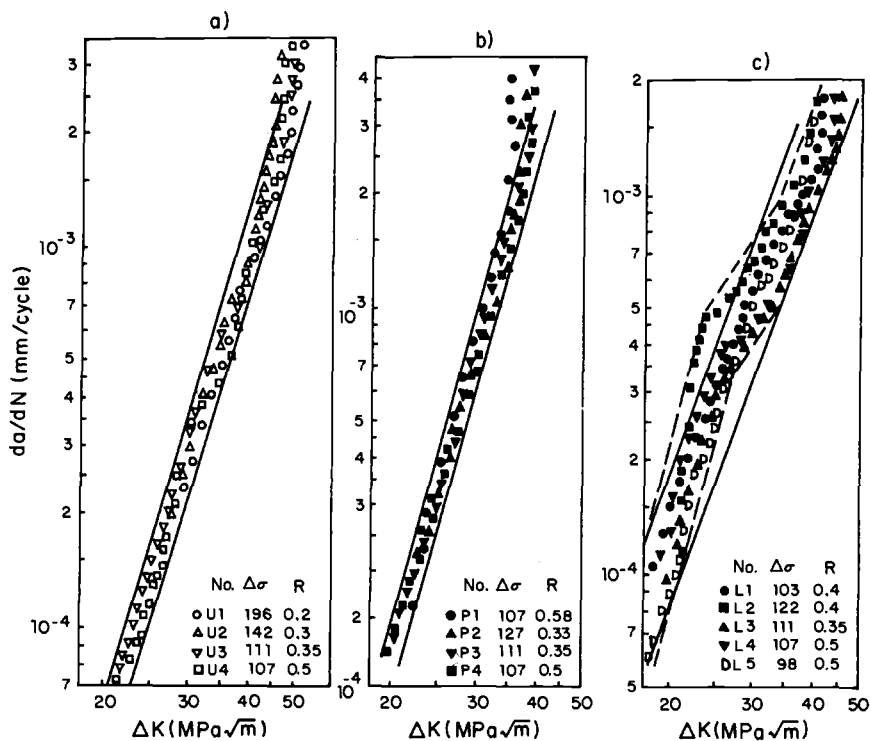


FIG. 4—Scatter bands of experimentally obtained fatigue crack growth rates: (a) in unwelded specimens U, (b) in specimens with perpendicular weld P, and (c) in specimens with longitudinal weld L.

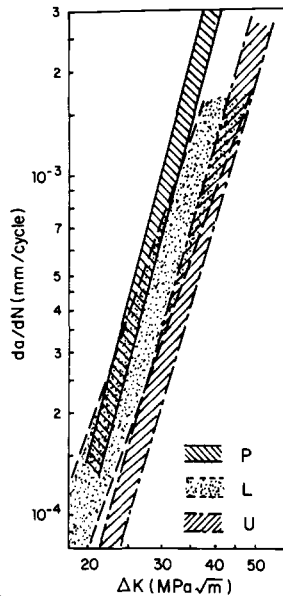


FIG. 5—Comparison of fatigue crack growth rates in different kinds of specimens.

were determined by means of a least squares method [13] for probability $p = 50$ percent.

Results obtained from welded P and L specimens are shown in Figs. 4b and 4c, respectively. Welded specimens were tested under similar load conditions as the unwelded ones, U1 to U4, shown in Fig. 4a. Paris' Eq 1 constants C and n were determined for each group of results shown in Fig. 4. There was a slight difference between constants obtained from specimens U and P . The widths of scatter bands shown in Figs. 4a and 4b are almost the same, too. An essential difference in fatigue crack growth behavior was discovered in the case of L specimens. There were different constants C and n and a wider scatter band of experimental results (Fig. 4c) in comparison to specimens U and P . The experimental results obtained from L specimens do not follow Paris' equation because they lay along a broken line rather than a straight one. It was characteristic that the first discontinuity of the $\log d(2a)/dN - \log(\Delta K)$ curve appeared in the region of residual stress sign change, that is, for cracks of length $2a = 35$ to 40 mm. The wider scatter band in the case of L specimens evidently resulted from crack growth behavior and not from the difference in specimen preparation.

Comparison of the aforementioned three scatter bands is shown in Fig. 5. It is apparent that the highest and the lowest fatigue crack rates were in P and U specimens, respectively. The P scatter band is almost parallel to

the analogous one obtained from specimens *U*. Such a parallel shift of the scatter band was obtained in the case of *U* specimens (Fig. 3) by increasing the stress ratio *R*.

With *L* specimens fatigue crack growth behavior depended strongly on crack length. Fatigue growth rate for crack lengths $2a \leq 40$ mm was usually higher than the rate obtained in the same load conditions from specimens *U*. But longer cracks grew in specimens *L* almost as fast as in unwelded *U* ones. It should be noted that in the case of *L* specimens the fatigue crack tips were out of the HAZ during the whole propagation period. The only reason for such fatigue crack growth behavior (Fig. 4c) in *L* specimens could be residual stress effects. The comparatively low fatigue crack growth rates in specimens *L* with long cracks $2a > 40$ mm were caused by compressive residual stresses. Shorter crack lengths $2a < 40$ mm were completely inside the tensile residual stress zone and therefore they grew faster.

With specimens *P*, fatigue cracks were growing inside the tensile residual stress zone during the whole propagation period. Therefore, the *P* scatter band (Fig. 4b) has no discontinuities and is parallel to the scatter band obtained from specimens *U* (Fig. 5).

The differences between fatigue crack growth rates in the three different specimens *U*, *P*, and *L* are clearly shown on Fig. 6. It is apparent

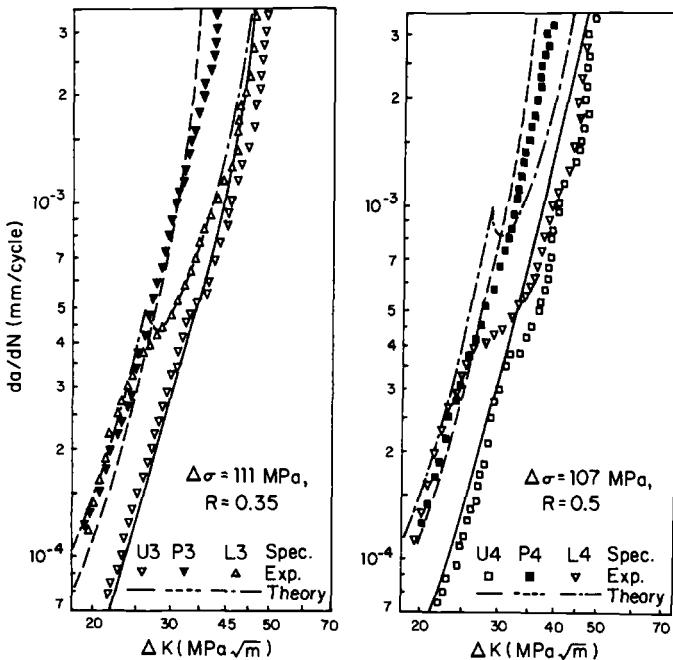


FIG. 6—Constant amplitude fatigue crack growth rates in specimens *U*, *P*, and *L*.

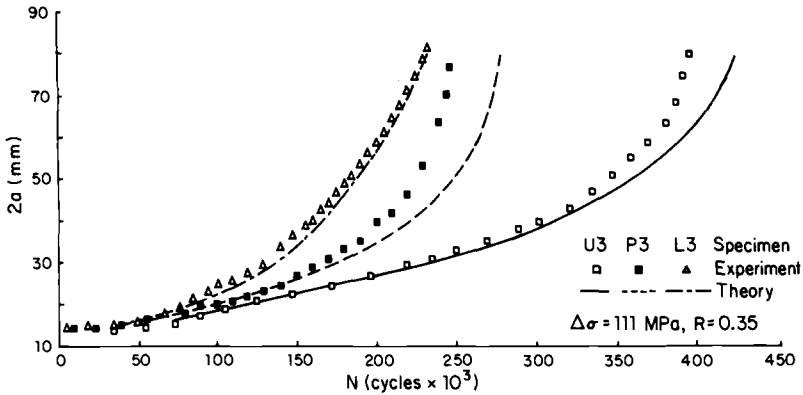


FIG. 7—Fatigue crack growth behavior of specimens U, P, and L with applied stress ratio $R = 0.35$.

that under low stress intensity ranges $\Delta K < 25 \text{ MPa}\sqrt{\text{m}}$, that is, for short cracks, fatigue crack growth rates in *P* and *L* specimens are almost the same and a few times higher than in specimens *U*. But for stress intensity ranges $\Delta K > 35 \text{ MPa}\sqrt{\text{m}}$, fatigue crack growth rates in specimens *L* were almost the same as in specimens *U* and a few times lower than in specimens *P*.

Results presented on Figs. 7 and 8 show the effect of residual stresses on fatigue life. The shortest lives were obtained in the case of specimen *L*, which had both the shortest initiation and propagation periods. Actually,

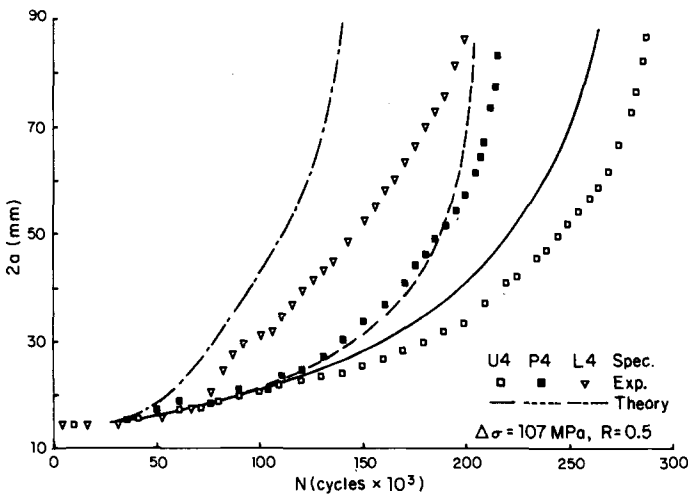


FIG. 8—Fatigue crack growth behavior of specimens U, P, and L with applied stress ratio $R = 0.5$.

the initiation periods in specimens *L* and *P* were almost the same. In the case of specimens *L4*, *P4*, and *U4* (Fig. 8) the crack initiation periods were 10 000, 13 000 and 50 000 cycles while the propagation periods were 185 000, 202 000, and 245 000 cycles, respectively. It is interesting that the shortest lives were obtained in the case of specimens *L* although cracks lengths $2a > 40$ mm grew slower than those in specimens *P*. The reason is that the shorter cracks ($2a < 40$ mm) in specimens *L* grew slightly faster (Fig. 6) than those in the *P* specimens. On the other hand, it is known that fatigue life depends strongly on the initial period of crack growth when cracks are short. Therefore, the highest benefits from the point of view of fatigue life could be reached by decreasing the initial fatigue crack growth rates.

Growth of Fatigue Cracks Under Variable Amplitude Load

Most machine parts and structures are subjected to variable amplitude loads. One of the very popular variable amplitude test methods is using stepped ascending-descending (Lo-Hi-Lo) stress blocks [19].

Two different stress blocks representative of cranes were used (Figs. 9 and 10). Details of the stress block formulation are described in Ref 9. In general, block No. 2 has higher σ_a values and is shorter. In both blocks, σ_m was always equal to 144 MPa. The stress blocks were applied during the test from stress level No. 1 to No. 13 and then the same block was repeated to specimen failure.

Results obtained from specimens tested under stress block No. 1 are shown in Fig. 9 in the diagram form $2a = f(N)$. The tests showed that, in spite of the same stress block, the crack extensions caused by stress

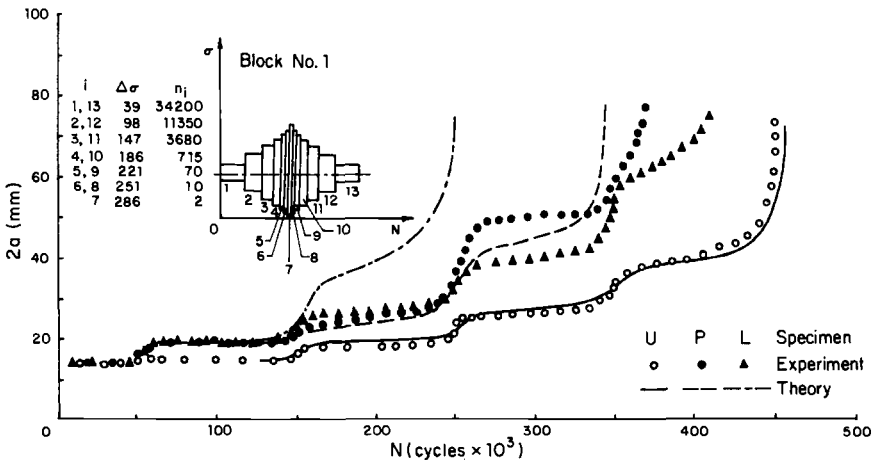


FIG. 9—Fatigue crack growth behavior of specimens U, P, and L with stress block No. 1.

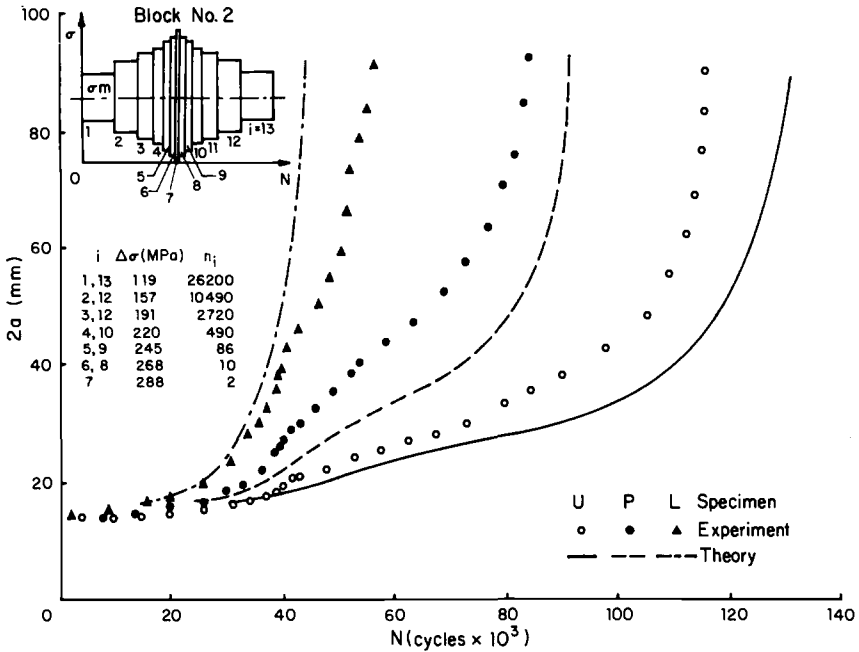


FIG. 10—Fatigue crack growth behavior of specimens U, P, and L with stress block No. 2.

levels of the descending block part were shorter than in the case of the ascending one. It was especially distinct in specimens *U*. The stress levels No. 2 and No. 3 in the ascending block part caused about two times longer crack extensions than analogous stress levels No. 11 and No. 12 of the descending block part. During application of No. 13 stress levels the fatigue crack stopped completely several times. The slower fatigue crack growth under the descending part of the stress block was due to the phenomenon called fatigue crack retardation [16,20]. Similar phenomena have been noticed in the case of welded specimens *L* and *P* (Fig. 9).

The total fatigue lives of the welded specimens were shorter than those of unwelded ones. This was due to short crack initiation periods in welded specimens since the propagation periods (from $2a = 16$ mm to $2a = 80$ mm) were almost equal in all specimens. It shows from the point of view of fatigue life that the early period of fatigue crack growth is just as important as it was under constant amplitude load.

Different results were obtained from specimens tested (Fig. 10) under stress block No. 2. Fatigue lives of the specimens were shorter and the effect of residual stresses on fatigue crack propagation more distinct. The crack propagation periods and total life were shorter in specimens *L* and *P* than in unwelded *U* specimens. The main reason for this was the higher

crack growth rate in welded specimens at short cracks in the early period of their growth. Because of short crack initiation periods, the effect of residual stresses on the crack propagation period was higher in comparison to welded specimens cycled under stress block No. 1.

The considerably shorter fatigue lives of specimens cycled under stress block No. 2 resulted from little or no crack growth retardation. The differences between successive stress levels were too small (Fig. 10) to cause a visible fatigue crack growth retardation.

The tests cycled under both stress blocks were duplicated, but for easier comparison only single specimen behavior is shown on Figs. 9 and 10.

Analysis of Theoretical Results

The theoretical prediction results are shown in previously discussed Figs. 6 to 10. Curves of $\log d(2a)/dN$ versus $\log(\Delta K)$ determined on the basis of Eq 5 are shown in Fig. 6. The curves drawn with solid lines were determined without including residual stresses. The dashed and dot-dashed curves were calculated on the basis of effective stress ratio R_{eff} and effective stress intensity range, ΔK_{eff} .

The curves $2a = f(N)$ shown in Figs. 7 and 8 were determined on the basis of Eq 6. It is evident that inclusion of residual stresses to Eq 6 (dashed and dot-dashed lines) gives more realistic fatigue life prediction for welded specimens. Neglecting them could give overly optimistic results in the case of welded joints.

The theoretical curves (dashed and dot-dashed lines) shown in Fig. 6 suggest that including the residual stresses in Forman's equation makes it possible to predict fatigue crack growth rates in welded specimens on the basis of the data obtained from the base material. Discontinuities of the theoretical dot-dashed curves relating to specimens *L3* and *L4* (Fig. 6) resulted because of rectangular residual stress distributions assumed for the calculation. In the case of welded specimens *L* and *P*, the predicted fatigue crack growth rates of long cracks ($\Delta K > 35 \text{ MPa}\sqrt{\text{m}}$) were usually higher than the rates obtained during experiments. The reason is the diminishing of residual stresses which were assumed to be constant during tests.

Good agreement between theoretical curves $2a = f(N)$ and experiments (Figs. 9 and 10) was reached for $m = 0.6$ and $m = 0$ in case of stress blocks No. 1 and No. 2, respectively. This means that there was no visible crack growth retardation for specimens cycled under stress block No. 2.

The results of integration of Eq 9 are shown in Figs. 9 and 10. The solid lines represent unwelded specimens, *U*, which were fitted to experimental results to obtain the m values. The dashed and dot-dashed lines were determined including the residual stresses. A significant difference between theory and experiments existed in the case of specimens *L* cycled

under stress block No. 1 only (Fig. 9). This probably resulted because of neglecting the diminishing of residual stresses during the test. The best theoretical predictions were obtained for specimens *P*. However, generally, it can be concluded that neglecting the residual stresses gives overly optimistic fatigue life predictions.

Conclusions

Fatigue crack growth rate has an effect on weldment fatigue life. One of the factors affecting the fatigue crack growth rate is represented by the residual stresses. A stress intensity factor approach makes it possible to take into account the magnitude and distribution shape of residual stresses, respectively. The size of the tensile residual stress zone and the crack orientation are especially important. The effect of residual stresses on fatigue crack growth rate depends on the magnitude of the applied load. The lower the applied load, the higher the residual stress effect. Higher applied loads cause greater residual stress relaxation. But generally, as the aforementioned results have shown, the residual stresses can significantly affect the fatigue crack growth rate and weldment fatigue life.

The inclusion of residual stresses in the theoretical analysis permits more realistic predictions and makes it possible to predict fatigue life of weldments more accurately on the basis of data obtained from base material only.

References

- [1] James, L. A., *Journal of Testing and Evaluation*, Vol. 1, No. 1, American Society for Testing and Materials, 1973, pp. 52-57.
- [2] Kapadia, B. M. and Imhof, E. J. in *Flaw Growth and Fracture*, ASTM STP 631, 1977, pp. 159-172.
- [3] Maddox, S. J., "Fatigue Crack Propagation Data Obtained from Parent Plate, Weld Metal and HAZ in Structural Steel," Research Report E/48/72. The Welding Institute, Sept. 1972.
- [4] Parry, M., Nordberg, H., and Hertzberg, R. W., *Welding Journal*, Oct. 1972, pp. 485-490.
- [5] Socie, D. F. and Antolovich, S. D., *Welding Journal*, June 1974, pp. 267-271.
- [6] Irwin, G. R. in *Proceedings*, 1st Symposium on Naval Structural Mechanics, Calif. 1958, pp. 557-592.
- [7] Paris, P. C. and Erdogan, F., *Transactions*, American Society of Mechanical Engineers; *Journal of Basic Engineering*, Series D, No. 3, 1963, pp. 528-534.
- [8] Forman, R. G., Kearney, V. E., and Engle, R. M., *Transactions*, American Society of Mechanical Engineers; *Journal of Basic Engineering*, No. 3, 1967, pp. 459-464.
- [9] Glinka, G. and Sobczykiewicz, W., *Archives of Mechanical Engineering*, to be published (in Polish).
- [10] Smith, R. A., *International Journal of Fracture*, No. 4, 1973, pp. 352-355.
- [11] Brown, W. F. and Srawley, J. E. in *Plain Strain Crack Toughness Testing of High Strength Metallic Materials*, ASTM STP 410, 1967, pp. 1-66.
- [12] Rappe, H. A., *Schweissen und Schneiden*, No. 2, 1974, pp. 45-50, (in German).
- [13] Glinka, G., "An Effect of Load Spectrum on Fatigue Crack Propagation Rate in High

- Strength Steels and Weldments," Philosophical Dissertation, Warsaw Technical University, 1976, (in Polish).
- [14] Kanazawa, T., Oba, H., and Machida, S., *Society of Naval Architects of Japan Journal*, No. 109, 1961, pp. 359-369, (in Japanese).
- [15] Glinka, G. and Lubowicz, J., *Przegląd Mechaniczny*, No. 17, 1976, pp. 581-584, (in Polish).
- [16] Nelson, D. V., *Experimental Mechanics*, No. 2, 1977, pp. 41-49.
- [17] Wheeler, O. E., *Transactions, American Society of Mechanical Engineers; Journal of Basic Engineering*, No. 1, 1972, pp. 181-186.
- [18] Rice, J. R. in *Fatigue Crack Propagation, ASTM STP 415*, 1967, pp. 247-309.
- [19] Gassner, E., Griese, F. W., and Haibach, E., *Archiv für das Eisenhüttenwesen*, No. 3, 1964, (in German).
- [20] Stephens, R. I., *Mechanika Teoretyczna i Stosowana*, Vol. 16, No. 2, 1978, pp. 123-150.

A. Saxena¹ and S. J. Hudak, Jr.¹

Role of Crack-Tip Stress Relaxation in Fatigue Crack Growth

REFERENCE: Saxena, A. and Hudak, S. J., Jr., "Role of Crack-Tip Stress Relaxation in Fatigue Crack Growth," *Fracture Mechanics, ASTM STP 677*, C. W. Smith, Ed., American Society for Testing and Materials, 1979, pp. 215-232.

ABSTRACT: This study constitutes an effort to identify underlying processes which contribute to load ratio (R) effects in fatigue crack growth. Approximate analytical expressions are developed for crack-tip strains during steady-state cyclic loading. Using these expressions, the strain history of an element of material which is being approached by the tip of a fatigue crack—growing at a constant rate of either 2.5×10^{-9} or 2.5×10^{-7} m/cycle (10^{-7} or 10^{-5} in./cycle) was calculated for load ratios of 0 and 0.8. Applying these strain histories to smooth axial fatigue specimens of 10Ni steel and 2219-T851 aluminum simulated the material's mean stress relaxation behavior at the crack tip. The number of cycles to failure correlated with the simulated growth rates. Also, mean stress relaxation characteristics in the crack-tip region qualitatively explain the load ratio effects on da/dN . This information is likely to be important to alloy development and material selection for fatigue resistance as well as for proper modeling of fatigue crack growth data at several load ratios.

KEY WORDS: stress intensity, fatigue (materials), crack growth, aluminums, steels, load ratio, stress relaxation, crack closure, crack propagation

The fracture mechanics approach to the characterization of the rate of growth of preexisting, sharp defects in engineering metals subjected to fatigue loading is used widely. As identified by Paris and Erdogan [1],² the primary parameter controlling the rate of fatigue crack growth, (da/dN), is the stress intensity range, ΔK , which characterizes the elastic stress and strain range in the vicinity of the crack tip. Another loading variable which can influence the fatigue crack growth rate is the load ratio ($R = \text{minimum load}/\text{maximum load}$) [2].

In a recent study [3], the influence of load ratio was fully characterized in a 2219-T851 aluminum alloy and a 10Ni steel for positive R values, Figs.

¹ Senior engineers, Structural Behavior of Materials, Westinghouse Research and Development Center, Pittsburgh, Pa. 15235.

² The italic numbers in brackets refer to the list of references appended to this paper.

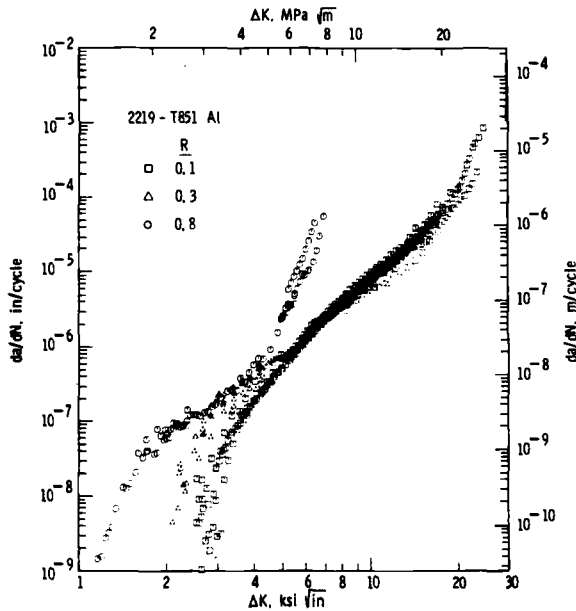


FIG. 1—Wide range fatigue crack growth rate behavior of 2219-T851 aluminum alloy at various load ratios (Ref 3).

1 and 2. The wide range growth rates for which data were obtained, included the full three region behavior for the aluminum alloy and the first two regions for the steel. This sigmoidal shape is characterized by increases in slopes of the log (da/dN) versus log (ΔK) plot in the low (Region I) and high (Region III) growth rates compared to the intermediate growth rates (Region II). The main conclusions of this previous study can be summarized as follows: (a) in Region I, the load ratio is an important loading variable in both materials, (b) in Region II, the aluminum alloy shows a significant effect of R , although not to the extent observed in Region I, (c) in 10Ni steel the influence of load ratio on da/dN in Region II could not be distinguished from the general scatter in the data, and (d) in Region III, (behavior influenced by the onset of static mode fracture—examined here only for the aluminum alloy), the load ratio was again an important factor. These trends are in agreement with observations noted by Ritchie [4] on a 300M steel. Such results demonstrate that the influence of load ratio on fatigue crack growth rate is dependent on both material type and the growth rate regime being considered.

Attempts have been made to rationalize the effect of load ratio on da/dN by using the phenomenon of crack closure proposed by Elber [5]. This phenomenon, attributed to a zone of residual deformation left in the

wake of a growing fatigue crack, assumes the crack surface to be closed even during a portion of the tensile loading cycle. It is postulated that the portion of the loading cycle during which the crack remains closed is ineffective in propagating the crack. If crack closure is a dominant factor in load ratio effects, then measuring the closure load as a function of R and accounting for the reduced load range in terms of an "effective ΔK " should normalize data generated at different load ratios. Despite some degree of normalization that has been demonstrated [5-8], the extent to which crack closure influences fatigue crack growth remains a controversial subject [9].

The intent of this paper is to focus attention on alternative or supplementary crack-tip plasticity phenomena which are likely to influence fatigue crack growth. The individual and combined effects of these underlying phenomena need to be addressed in order to formulate a more complete understanding of the fatigue crack growth process and ultimately aid in material selection and alloy development for preventing fatigue failures.

The specific objectives of this study were to (1) estimate how cyclic plasticity at the crack tip dictates the magnitude of mean stress ahead of a growing fatigue crack, using analysis and measurements on a 10Ni steel and a 2219-T851 aluminum alloy, and (2) relate these mean stress

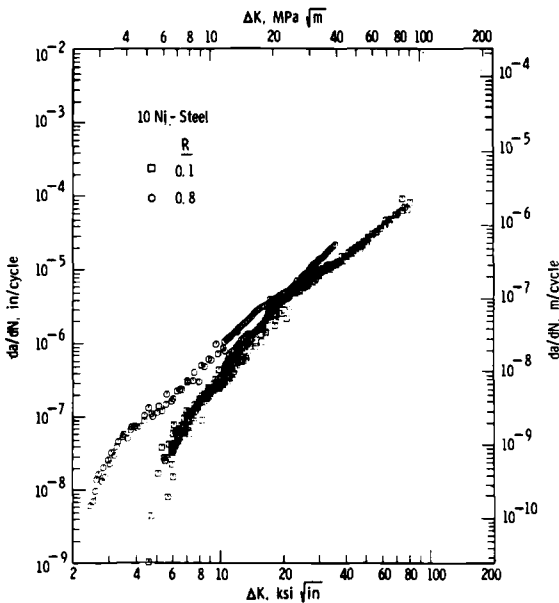


FIG. 2—Wide range fatigue crack growth rate behavior of 10Ni steel at various load ratios (Ref 3).

characteristics to measured load ratio effects on da/dN in these same materials.

Crack-Tip Stresses and Strains

In this section a simple analysis to estimate the maximum and minimum strains in the plastic zone ahead of a fatigue crack growing at a constant rate and given load ratio is described. Similar equations have been used previously in attempts to correlate strain-life data obtained on smooth specimens to fatigue crack growth rate as a function of ΔK [10,11] obtained on precracked fracture mechanics specimens. The strain history thus obtained can be applied to smooth axial fatigue specimens and corresponding stress response recorded as described in the next section. From the combination of the aforementioned analysis and experiment a complete stress-strain characterization of an element of material being approached by a propagating fatigue crack can be obtained. Consider a cracked body loaded with a remote fatigue stress, ΔS , which is applied normal to the plane of crack as shown in Fig. 3. ΔS results in a crack tip stress intensity range, ΔK , and a crack growth rate, da/dN . Figure 4 shows a schematic of the stress-strain behavior experienced by an infinitesimal element, dx (such as shown in Fig. 3), which is located at a distance x from the crack tip. The element locations chosen for illustration are: (a) beyond the monotonic plastic zone, $x > 2r_Y$, (b) between the monotonic and cyclic plastic zones, $2r_Y^c < x < 2r_Y$, (c) at the cyclic plastic zone boundary, $x = 2r_Y^c$; and (d) within the cyclic plastic zone, $x < 2r_Y^c$.

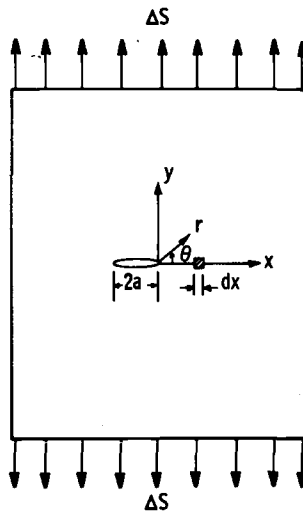


FIG. 3—Semi-infinite cracked body loaded with a remote fatigue stress, ΔS .

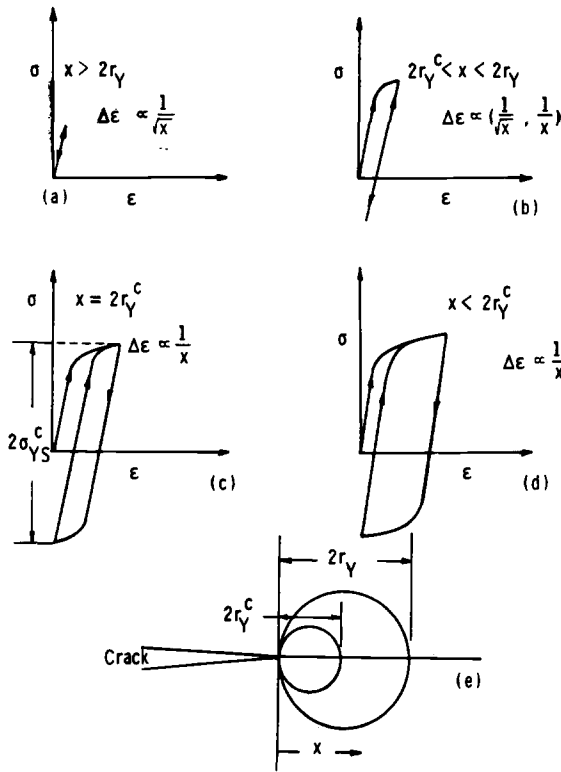


FIG. 4—Stress-strain history of an element approaching the tip of a propagating fatigue crack.

The “elastic” stress distribution along the x axis is analogous to the sustained loading case solved by Irwin [12].

$$\Delta\sigma_y = \Delta\sigma_x \propto \frac{\Delta K}{x^{\frac{1}{2}}} \tag{1a}$$

$$\Delta\tau_{xy} = 0 \tag{1b}$$

Since considerable plasticity occurs at the crack tip, the elastic stress field, Eq 1, must be modified. This modification can be estimated simply using Neuber’s rule [13] as follows

$$k_t = (k_\sigma \cdot k_\epsilon)^{\frac{1}{2}} \tag{2}$$

where

- k_t = elastic stress concentration factor,
- k_σ = stress concentration factor, and
- k_ϵ = strain concentration factor.

Combining the aforementioned definitions and Eq 1a, we have

$$k_t = \frac{\Delta\sigma_y}{\Delta S} \propto \frac{1}{\Delta S} \frac{\Delta K}{(x)^{\frac{1}{2}}} \quad (3a)$$

$$k_\sigma = \frac{\Delta\sigma}{\Delta S} \quad (3b)$$

$$\text{and } k_\epsilon = \frac{\Delta\epsilon \cdot E}{\Delta S} \quad (3c)$$

where $\Delta\sigma$ and $\Delta\epsilon$ are the actual stress and strain ranges in the crack-tip region. From Eqs 2 and 3 it can easily be shown that

$$\Delta\sigma \cdot \Delta\epsilon = c \frac{(\Delta K)^2}{x \cdot E} \text{ for } x < 2r_y \quad (4)$$

c is a constant of proportionality which will be determined later. The $1/x$ -type singularity predicted for the product of stress and strain ranges in Eq 4 is similar to that suggested in the work of Hutchinson [14], Rice and Rosengren [15], and McClintock [16] who have related crack-tip stresses and strains to the path-independent line integral, J , for sustained loading conditions beyond nominal yield. An alternate form of Eq 4 for nonhardening materials is as follows

$$\epsilon_{\max} = \frac{c (K_{\max})^2}{x \cdot E \cdot \sigma_{YS}} \quad (5)$$

where σ_{\max} and ϵ_{\max} are maximum crack tip stresses and strains corresponding to the maximum stress intensity factor, K_{\max} .

The constant c is obtained from the monotonic plastic zone boundary conditions

$$\epsilon_{\max} = \frac{\sigma_{YS}}{E}$$

when

$$x = \frac{1}{\pi} \left(\frac{K_{\max}}{\sigma_{YS}} \right)^2$$

The preceding equation when substituted into Eq 5 gives

$$c = \frac{1}{\pi}$$

Thus, the final set of equations describing the estimated maximum, minimum, and range of crack-tip strains as a function of distance from the crack tip are given by

$$\epsilon_{\max} = \frac{(K_{\max})^2}{\pi \sigma_{YS} \cdot E \cdot x} \tag{6a}$$

$$\epsilon_{\min} = \frac{(K_{\min})^2}{\pi \sigma_{YS} \cdot E \cdot x} \tag{6b}$$

$$\Delta\epsilon = \frac{(1+R)}{1-R} \frac{(\Delta K)^2}{\pi \sigma_{YS} \cdot E \cdot x} \tag{6c}$$

for $R > 0$ and $x < 2r_y$

Simulating the Strain History of a Crack-Tip Element

The strain versus distance relationship defined by Eq 6 can be used to specify a test history in terms of strain versus fatigue cycles. This strain history, when applied to an axial fatigue specimen, can be considered to simulate the cyclic deformation behavior experienced by an element of material being approached by a fatigue crack. The strain versus cycles behavior is obtained by recognizing that the strain history of a material element, dx , located at a distance x from the crack tip, being approached by a fatigue crack growing at a constant rate, da/dN , is equivalent to that of an element moving towards a stationary crack tip at a rate, $-dx/dN$. That is

$$-\frac{dx}{dN} = \frac{da}{dN} \tag{7a}$$

and

$$-\int_{2r_y}^x \frac{dx}{(da/dN)} = \int_0^N dN \tag{7b}$$

Note that, Eq 7b is written for an element which is initially located at the monotonic plastic zone boundary; in other words, $x = 2r_y$ when $N = 0$; thus carrying out the integration in Eq 7b we get

$$x = 2r_y - N \left(\frac{da}{dN} \right) \tag{7c}$$

Substituting Eq 7c into Eqs 6a and 6b we get

$$\epsilon_{\max} = \frac{K^2_{\max}}{\pi \sigma_{YS} \cdot E [2r_Y - N(da/dN)]} \tag{8a}$$

$$\text{and } \epsilon_{\min} = \frac{K^2_{\min}}{\pi \sigma_{YS} \cdot E [2r_Y - N(da/dN)]} \tag{8b}$$

Using Eq 8, strain histories were calculated for growth rates of 2.5×10^{-9} and 2.5×10^{-7} m/cycle (10^{-7} and 10^{-5} in./cycle) for load ratios of 0 and 0.8 for both materials investigated in this study. Figure 5 shows a schematic of such a strain history. The preceding strain histories were each applied to smooth axial fatigue specimens while the mean stress relaxation behavior was observed using procedures described in the next section.

Experimental Procedure

Material Characterization

The materials investigated in this program were a 10Ni steel and a 2219-T851 aluminum alloy. An extensive characterization of wide range fatigue crack growth rates as a function of stress intensity range for several load ratios is available for these materials from an earlier study [3], Figs. 1 and 2. The steel and aluminum was obtained in the form of 25.4-mm (1-in.) and 76.1-mm (3-in.) thick plates, respectively. The chemical composition of these materials is given in Table 1. Both materials exhibited uniformity in conventional tensile properties with respect to location as well as orientation, Table 2.

Cyclic stress-strain properties of the two materials, as described by Eq 10, were characterized using the incremental step test. The strain-life curve, Eq 11, was estimated by Dowling [17] using a modification of the

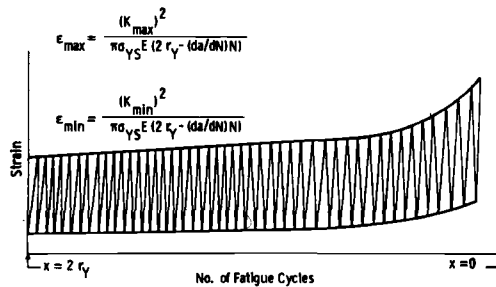


FIG. 5—Schematic of the strain history of an infinitesimal material element being approached by the tip of a crack propagating at a constant rate, da/dN .

TABLE 1—Chemical composition of test materials (weight percent).

Material	C	Si	Mn	Mg	S	P	Cr	Zn	Ti	Co	Cu	Ni	Mo	Al	Fe
10Ni steel	0.12	0.07	0.28	...	0.006	0.008	2.03	8.07	...	10.29	1.03	...	balance
2219-T851 Al	...	0.088	0.25	0.003	<.0001	0.025	0.051	...	6.28	balance
															0.25

TABLE 2—Room temperature mechanical properties of test materials.^a

Material	Orientation	0.2 percent σ_{YS}		σ_{ULT}		Elongation (50 mm gage length), percent	Reduction in Area, percent
		ksi	MPa	ksi	MPa		
10Ni steel	longitudinal	190.0	1309.1	197.0	1357.3	6.9	17.0
	transverse	190.0	1309.1	196.0	1350.4	6.9	17.0
2219-T851 Al	longitudinal	52.0	358.3	66.0	454.7	8.5	19.0
	transverse	51.0	351.4	66.0	454.7	8.2	19.0

^a Steel results: average of 8 tests from 4 locations. Aluminum results: average of 6 tests from 2 locations.

procedures suggested by Landgraf [18] and Morrow [19]. These properties are represented as follows

$$\Delta\sigma/2 = A(\Delta\epsilon_p/2) \quad (10)$$

$$\Delta\epsilon/2 = \frac{\sigma'_f}{E} (2N_f)^b + \epsilon'_f (2N_f)^c \quad (11)$$

where A , n' , σ'_f , ϵ'_f , b and c are fitting constants and $\Delta\epsilon_p/2$ = plastic strain amplitude. Table 3 lists the values of the aforementioned fitting constants for 2219-T851 Al and 10Ni steel.

Simulation Tests

A cylindrical specimen, 6.2 mm (0.25 in.) in diameter and 12.7 mm (0.5 in.) in gage length was used for the simulation tests. Table 4 summarizes the growth rates, load ratios, and the corresponding ΔK values for which the strain histories were simulated. The maximum and minimum strain on the smooth specimen was increased as a function of the number of cycles according to a schedule determined by Eq 8 using step increments of 0.5 percent on maximum strain. Standard MTS servohydraulic equipment was used for these tests. Stress-strain hysteresis loops were recorded periodically to measure the mean stress relaxation behavior. The number of cycles to failure were also recorded.

Results and Discussion

Prior to interpreting mean stress relaxation results obtained from the crack-tip simulation tests, an experimental justification of the strain history developed in an earlier section is perhaps in order. The intent of the simulation tests was to duplicate the strain history of an element that is initially at the monotonic plastic zone boundary and is subsequently approached by the tip of a fatigue crack growing at a constant rate. If the aforementioned strain history is in fact a good approximation, the number of cycles it takes for the smooth specimen to fail should ideally be equal to the number of cycles required for the crack to extend one monotonic plastic zone size in a crack growth test. Alternatively, the monotonic plastic zone size divided by the number of cycles to failure on the corresponding simulation smooth specimen should be equal to the simulated rate of fatigue crack growth. These data are tabulated in Table 4 and demonstrate the suitability of the estimated strain histories.

Mean Stress Relaxation Behavior

In a constant amplitude, strain controlled test, when the strain ratio ($\epsilon_{\min}/\epsilon_{\max}$) is other than -1 , the mean stress during fatigue cycling is

TABLE 3—Fitting constants defining the cyclic stress-strain and strain-life properties of the test materials.

Material	A		σ'_f		b	ϵ'_f	c	σ'_{YS}^a	
	ksi	MPa	ksi	MPa				ksi	MPa
10Ni steel	316	2 177.2	293.0	2 018.8	-0.08	0.54	-0.647	160.5	1 105.8
2219-T851 Al	103	709.7	89.0	613.2	-0.0756	0.35	-0.55	48.5	334.1

^a σ'_{YS} = cyclic yield strength.

TABLE 4—Comparison of targeted growth rates (da/dN) with those estimated from the cyclic life of simulation tests ($2r_y/N_f$).

Material	R	ΔK_c , MPa \sqrt{m}	da/dN, m/cycle	$2r_y^a$, mm	N_f^b	$2r_y$	
						N_f	m/cycle
10Ni steel	0	35.2	2.5×10^{-7}	0.28	1 006	2.72×10^{-7}	
10Ni steel	0	8.8	2.5×10^{-9}	0.0143	4 576	3×10^{-9}	
10Ni steel	0.8	34.1	2.5×10^{-7}	5.38	20 138	2.62×10^{-7}	
10Ni steel	0.8	4.6	2.5×10^{-9}	0.102	37 380	2.67×10^{-9}	
2219-T851 Al	0	11.5	2.5×10^{-7}	0.33	1 165	2.75×10^{-7}	
2219-T851 Al	0	3.85	2.5×10^{-9}	0.046	12 476	3.5×10^{-9}	
2219-T851 Al	0.8	6.65	2.5×10^{-7}	2.79	10 383	2.65×10^{-7}	
2219-T851 Al	0.8	2.25	2.5×10^{-9}	0.32	110 951	2.75×10^{-9}	

NOTE—1 in./cycle = 2.54×10^{-2} m/cycle.

$$^a 2r_y = \frac{1}{\pi} \left(\frac{K_{max}}{\sigma'_{YS}} \right)^2$$

^b N_f = number of cycles to failure.

initially nonzero. In the low-cycle-fatigue regime, which is associated with considerable cyclic plasticity, the initial nonzero mean stress relaxes and quickly attains a value nearly equal to zero. However, in the high cycle fatigue regime which does not involve cyclic plasticity the mean stress remains approximately constant. The presence of a tensile mean stress is associated with a significant decrease in fatigue life [20]. It thus appears rational to characterize the mean stress behavior in the crack tip region by means of simulation tests for various growth rates and load ratios and then attempt to correlate these results with trends observed in the response da/dN to load ratio, R .

Figures 6 and 7 show the residual mean stress, σ_o (normalized with respect to the 0.2 percent yield strength) plotted as a function of number of fatigue cycles, N (normalized with respect to the cycles to failure, N_f) for tests simulating various growth rates and R values for 2219-T851 Al and 10Ni steel, respectively. The same mean stress data can be plotted alternatively against percent fatigue damage. This representation is more realistic because a large number of total fatigue cycles in each of the simulative tests were accumulated at low strain ranges, and thus do not account for a substantial fraction of the damage as may wrongly be interpreted from Figs. 6 and 7.

Fatigue damage was calculated by using Miner's linear damage summation rule [21] given by

$$\sum_{i=1}^N \frac{\Delta N_i}{N_{fi}} = D \tag{12}$$

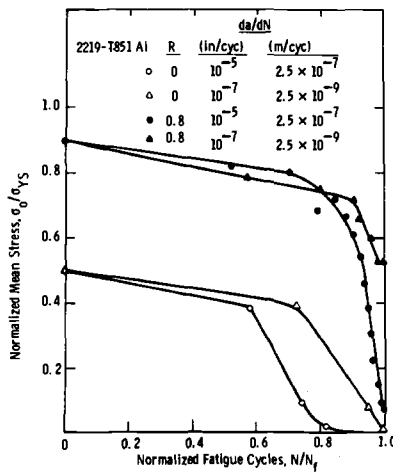


FIG. 6—Normalized mean stress as a function of applied fatigue cycles in 2219-T851 aluminum alloy tests which simulate crack-tip strain histories at various growth rates and load ratios.

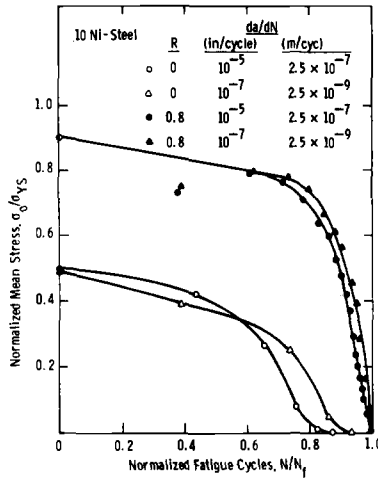


FIG. 7—Normalized mean stress as a function of applied fatigue cycles in 10Ni steel tests which simulate the crack-tip strain history at various growth rates and load ratios.

where

D = damage,

N_i = number of fatigue cycles at a given strain range $\Delta\epsilon_i$, and

N_{fi} = number of fatigue cycles to failure at a constant strain range $\Delta\epsilon_i$.

For a particular strain range, N_{fi} was obtained from a modified form of Eq 11 which accounts for the influence of mean stress (σ_o) [22] on the cyclic life of smooth axial fatigue specimen.

$$\frac{\Delta\epsilon_i}{2} = \frac{\sigma'_f - \sigma_o}{2} (2N_{fi})^b + c'_f (2N_{fi})^c \tag{13}$$

Percent fatigue damage was calculated subsequently using the following equation

$$\text{Percent Damage} = \left(\sum_{i=1}^N \frac{\Delta N_i}{N_{fi}} \right) / \left(\sum_{i=1}^N \frac{\Delta N_i}{N_{fi}} \times 100 \right) \tag{14}$$

Figures 8 and 9 present the normalized mean stress as a function of percent fatigue damage for 2219-T851 Al and 10Ni steel, respectively. The following observations are made from the figures: (a) a high level of mean stress is present for a substantial fraction of the fatigue life, (b) the level of mean stress is strongly dependent on R value, (c) at equivalent R values, the mean stress relaxes more readily in tests simulating growth rates of 2.5×10^{-7} m/cycle (10^{-5} in./cycle) as compared to those corresponding to a

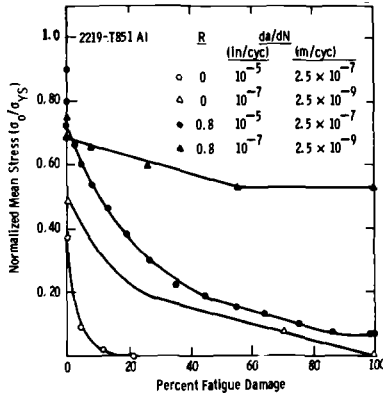


FIG. 8—Normalized mean stress as a function of percent fatigue damage in 2219-T851 aluminum alloy tests which simulate crack-tip strain histories at various growth rates and load ratios.

growth rate of 2.5×10^{-9} m/cycle (10^{-7} in./cycle), and (d) in general, the 10Ni steel specimens were able to relax mean stress more readily as compared to the 2219-T851 aluminum specimens at equivalent growth rate levels and R values.

To further illustrate the last two observations, the difference in the normalized mean stresses at R values of 0.8 and 0, that is $(\sigma_0/\sigma_{YS})_{R=0.8} - (\sigma_0/\sigma_{YS})_{R=0}$, were plotted as a function of percent fatigue damage for the two materials at the two growth rate levels investigated, Fig. 10. For both materials, it is observed that the change in normalized mean stress levels due to an increase in load ratio is significantly larger for growth rates of 2.5×10^{-9} m/cycle (10^{-7} in./cycle) than for growth rate of 2.5×10^{-7} m/cycle

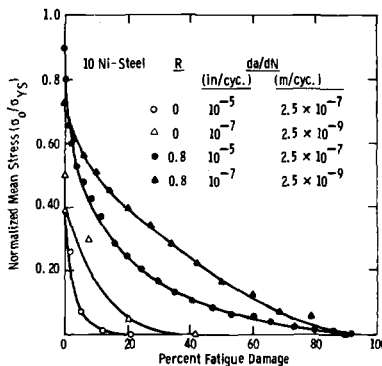


FIG. 9—Normalized mean stress as a function of percent fatigue damage in 10Ni steel tests which simulate crack-tip strain histories at various growth rates and load ratios.

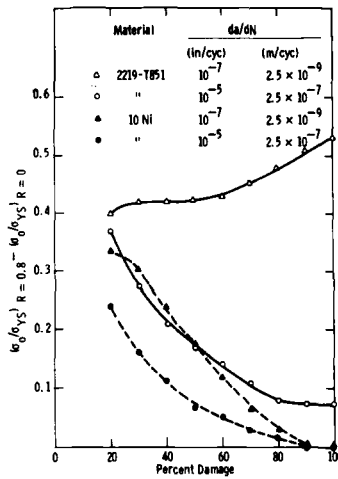


FIG. 10—Comparison between the stress relaxation behavior at $R = 0$ versus $R = 0.8$ in 2219-T851 aluminum alloy and 10Ni steel at various growth rates.

(10^{-5} in./cycle). Also, the change in mean stress level due to an increase in stress ratio for 10Ni steel was significantly less than for 2219-T851 aluminum at both growth rates investigated. Based on the aforementioned observations it is postulated that the load ratio effects in fatigue crack growth are linked directly to the extent of mean stress relaxation in the crack tip region. In Region II of the da/dN versus ΔK relationship the strain histories in the crack-tip regions consist of a high degree of cyclic plasticity and thus, the potential for relaxing mean stresses is also high. Hence, fatigue crack growth rates are not expected to be very sensitive to load ratio. On the contrary, in Region I the extent of cyclic plasticity is limited, thus causing high mean stresses to be retained and consequently the fatigue crack growth rates are very sensitive to load ratios.

It has been demonstrated here in that the ability to relax mean stresses is specific to material type. These differences are more significant in Region II of da/dN versus ΔK relationship which is associated with considerable cyclic plasticity. The 10Ni steel was shown to be more capable of relaxing mean stresses than 2219-T851 aluminum; hence, it would be expected to exhibit smaller changes in growth rates as a function of R in Region II. The differences in the behavior of the aluminum alloy and steel investigated can be linked to the slip character of the two materials. High strength aluminum alloys generally possess a planar slip character [23], while ferritic steels are expected to exhibit a wavy slip mode associated with extensive cross-slip on secondary planes. During fatigue loading, deformation is localized in intense slip bands in planar slip materials and is relatively dispersed and homogeneous in wavy slip materials. During strain controlled cycling, the

wavy slip materials tend to stabilize stresses more readily compared to planar slip materials [11,23,24] and thus would be expected to possess a higher capability to relax mean stresses in the crack tip region during fatigue crack growth. Additional work with different types of materials, including substructure characterization of the fatigued specimens, is needed to confirm this point.

All of the preceding observations are consistent with data on load ratio effects on da/dN in Regions I and II [3,4].³ Additional research is necessary to quantify further the importance of crack-tip residual stresses for a better understanding of the mechanisms of fatigue crack growth. Although, this relaxation behavior and other local crack-tip phenomena such as crack closure, are all related to the plasticity that occurs at the crack tip, the unique contribution of each must be considered in formulating realistic physical models of fatigue crack growth.

Summary and Conclusions

Approximate analytical relationships for crack-tip stresses and strains within the monotonic and fatigue plastic zones were developed for cyclic loading. The strain histories thus derived as a function of the number of fatigue cycles were imposed on smooth axial specimens of 10Ni steel and 2219-T851 aluminum to study the relaxation of mean stress as a function of fatigue damage. The following conclusions were derived from these results.

(1) It was demonstrated, from the fatigue life data obtained on the simulation tests, that the applied strain versus elapsed fatigue cycles are good approximations.

(2) Load ratio effects commonly observed in fatigue crack growth rate data are related directly to the extent of mean stress relaxation behavior at the crack tip.

(3) The extent of mean stress relaxation at given R value depends on the fatigue crack growth regime. Mean stresses were observed to relax more readily in tests simulating growth rates of 2.4×10^{-7} m/cycle (10^{-5} in./cycle) compared to growth rates of 2.5×10^{-9} m/cycle (10^{-7} in./cycle) thus explaining why load ratio effects are stronger at the lower growth rate.

(4) 10Ni steel was shown to be more capable of relaxing mean stresses in the crack tip region as opposed to 2219-T851 aluminum. This trend was linked to differences in slip character of the two materials.

(5) Further work is needed to quantify the crack-tip residual stresses to develop a better understanding of fatigue mechanisms. Ultimately this can

³ As discussed in Ref 4, load ratio effects on Region III are likely to be determined by the presence of an additional mode of cracking as critical stress intensity for instability is approached.

also be used in developing more realistic models for fatigue crack growth and would be valuable information for material selection and alloy development leading to improved materials for fatigue resistance.

Acknowledgments

Gratitude is expressed to N. E. Dowling for helpful discussions during the course of this study. The fatigue crack growth data used in this paper were developed under the sponsorship of the U.S. Air Force, AFML Contract F33615-75-C-5064, project FY-1457-75-02110/7381. The efforts of L. W. Burtner and R. B. Hewlett in conducting the simulation tests are also gratefully acknowledged.

References

- [1] Paris, P. C. and Erdogan, F., *Transactions, American Society of Mechanical Engineers, Series D; Journal of Basic Engineering*, Vol. 85, 1963, p. 528.
- [2] Hudson, C. M., "Effect of Stress Ratio on Fatigue Crack Growth in 7075-T6 and 2024-T3 Aluminum-Alloy Specimens," NASA-TN-D-5390, National Aeronautics and Space Administration, Langley Research Center, Aug. 1969.
- [3] Hudak, S. J., Saxena, A., Bucci, R. J., and Malcolm, R. C., "Development of Standard Methods of Testing and Analyzing Fatigue Crack Growth Rate Data—Final Contract Report," AFML-TR78-4D, Wright Patterson Air Force Base, Ohio, May 1978.
- [4] Ritchie, R. O. in *Metallurgical Transactions, Series A*, Vol. 8A, 1977, p. 1131.
- [5] Elber, W. in *Damage Tolerance in Aircraft Structures, ASTM STP 486*, American Society for Testing and Materials, 1971, p. 230.
- [6] Schmidt, R. A. and Paris, P. C. in *Progress in Flow Growth and Fracture Toughness Testing, ASTM STP 536*, American Society for Testing and Materials, 1973, p. 79.
- [7] Kikukawa, M., Jono, M., and Tanaka, K., "Fatigue Crack Closure Behavior at Low Stress Intensity Level," *Proceedings, 2nd International Conference on Mechanical Behavior of Materials*, Boston, Aug. 1976.
- [8] Lindley, T. C. and Richards, C. E., "The Relevance of Crack Closure to Fatigue," *Proceedings, Mechanics and Mechanisms of Crack Growth*, Cambridge, 1973.
- [9] Uganst, K. T., Shih, T. T., and Wei, R. P., *Engineering Fracture Mechanics*, Vol. 9, 1977.
- [10] Antolovich, S. D., Saxena, A., and Chanani, G. R. in *Engineering Fracture Mechanics*, Vol. 7, 1975, p. 649.
- [11] Saxena, A. and Antolovich, S. D. in *Metallurgical Transactions, Series A*, Vol. 6A, 1975, p. 1809.
- [12] Irwin, G. R., *Transactions, American Society of Mechanical Engineers; Journal of Applied Mechanics*, 1957.
- [13] Neuber, H., *Journal of Applied Mechanics; Transactions, American Society of Mechanical Engineers*, Vol. 28, Dec. 1961, p. 544.
- [14] Hutchinson, J. W., *Journal of Mechanics and Physics of Solids*, Vol. 16, 1968, p. 13.
- [15] Rice, J. R. and Rosengren, G. F., *Journal of Mechanics and Physics of Solids*, Vol. 16, 1968, p. 1.
- [16] McClintock, F. A. in *Fracture*, H. Leibowitz, Ed., Vol. 3, Academic Press, New York, 1971, p. 47.
- [17] Dowling, N. E., unpublished research, Westinghouse Research and Development Center, 1977.
- [18] Landgraf, R. W. in *Achievement of High Fatigue Resistance in Metals and Alloys, ASTM STP 467*, American Society for Testing and Materials, 1970, p. 3.
- [19] Morrow, J. in *Internal Friction, Damping and Cyclic Plasticity, ASTM STP 378*, American Society for Testing and Materials, 1965, p. 45.

- [20] Dubuc, J., Vanasse, J. R., Biron, A., and Bazergin, A., *Transactions; American Society of Mechanical Engineers, Journal of Engineering for Industry*, Paper 69-PVP-1, 1969.
- [21] Miner, M. A., *Transactions, American Society of Mechanical Engineers, Journal of Applied Mechanics*, Vol. 12, 1945, p. A-159.
- [22] Morrow, J., "Fatigue Properties of Metals," *Fatigue Design Handbook*, Section 3.2, Society of Automotive Engineers, 1968.
- [23] Calabrese, C. and Laird, C., *Metallurgical Transactions*, Vol. 5, Aug. 1974, p. 1785.
- [24] Feltner, C. E. and Laird, C., *Acta Metallurgica*, Vol. 15, Oct. 1967, pp. 1621-1632, and Part 2, pp. 1633-1653.

W. J. D. Shaw¹ and I. Le May²

Crack Closure During Fatigue Crack Propagation

REFERENCE: Shaw, W. J. D. and Le May, I., "Crack Closure During Fatigue Crack Propagation," *Fracture Mechanics, ASTM STP 677*, C. W. Smith, Ed., American Society for Testing and Materials, 1979, pp. 233–246.

ABSTRACT: Crack closure in single edge notched fatigue specimens of AISI 4140 steel was studied and it was determined that crack closure occurs at the edges of the specimen in the area of slant mode fracture while the center portion remains open. It was demonstrated that errors arise in the determination of crack opening and crack closure loads if the displacement measurements are not taken an adequate distance from the crack tip. Following careful evaluation of the loads for complete crack opening and complete crack closure, it has been demonstrated that in the equation for correlation or prediction of fatigue crack propagation, improved correlation results when an effective value of ΔK is taken based on the range of stress intensity factor to maximum load from complete crack closure rather than from complete crack opening or minimum load.

KEY WORDS: fatigue (materials), crack propagation, stress intensity factor, steel, closure, correlation

A considerable amount of work has been done on crack closure during fatigue crack propagation, but there is still debate concerning the concept as presented originally by Elber [1,2]³ as to whether crack closure and hence the effective range of stress intensity factor, ΔK_{eff} , rather than the nominal one, ΔK , should be considered in order to provide a more relevant and accurate parameter with which to correlate fatigue crack propagation data using the Paris law [3]. The only direct hard evidence of crack closure is that provided by Chang and Brunner [4] and Lindley and Richards [5], although various techniques for estimating crack closure

¹ President, Shaw Engineering and Research Corp., Saskatoon, Canada (formerly, Department of Mechanical Engineering, University of Saskatchewan, Saskatoon, Canada, S7N 0W0).

² Professor, Department of Mechanical Engineering, University of Saskatchewan, Saskatoon, Canada S7N 0W0.

³ The italic numbers in brackets refer to the list of references appended to this paper.

have been employed including surface measurements by displacement gages [1,2,6-9], enlarged photographs of surface displacements [10], strain gages placed across the crack surfaces [11,12], ultrasonic methods [13], direct optical methods [14], potential measurements [5,15-18], photoelastic techniques [4], and elastic compliance measurements during unloading [19]. The variation in technique employed stems largely from the argument that surface measurements may not reflect inner crack closure in the bulk of the material [19].

Correlation of fatigue crack propagation rate, da/dN , where a is the crack length and N the number of load cycles, with ΔK_{eff} has been examined by a number of workers [2,18,20] with mixed results. Disagreement also exists between measured values of crack closure load for the same material [2,7,11,15,16] and on the variation of closure and closure load with the maximum value of stress intensity factor, K_{max} [2,6-9,16,19]. These contradictory results are due largely to the different methods employed in measuring crack closure [6], although errors may also be due to notch effects [21], environmental effects and mode of crack propagation [17,22], frequency effects [12], as well as material scatter [23]. Hopefully, much of the existing confusion will disappear once the basic concepts and mechanics of crack closure have been examined more systematically and established firmly, and it is hoped that the present work may provide some information in this regard by providing direct evidence of crack closure and on the effect of crack length, and hence K_{max} , on this, by examining the relationship between the position of the gage with respect to the crack tip and the measurement of crack closure, and by evaluating the effect of correcting the operative range of stress intensity factor on the prediction of the fatigue crack growth curve.

Experimental Procedures

Single edge notched fracture mechanics specimens of AISI 4140 steel were used in all tests. The specimens had a thickness of 4.8 mm, a breadth of 76.2 mm, and a length of 305 mm, the material properties being given in Table 1.

Fatigue crack propagation data were obtained from specimens tested under load control in tension-tension loading (0.222 to 18.015 kN) at a frequency of 5 Hz and under constant environmental conditions of 40 percent relative humidity and 22.2°C. Crack growth was measured by means of a traveling metallurgical microscope.

Two specimens were tested extensively for crack closure during fatigue crack propagation, the analysis obtained from these tests being applied in the analysis of 14 other fatigue crack propagation specimens tested under identical conditions.

TABLE 1—Mechanical properties of AISI 4140 steel, quenched and tempered at 300°C.

Hardness, HRC	0.2 Percent Yield Strength, MPa	Ultimate Tensile Strength, MPa	Reduction of Area, Percent	Elastic Modulus, GPa	Fracture Toughness K_{Ic} , MPa·m ^{1/2}
52	1677	1915	25	202	49.0

Crack opening was monitored by means of a surface displacement gage and a crack opening displacement gage. In addition, two-stage plastic-carbon replicas were taken from the specimen surfaces along the length of the entire fatigue crack while the specimen was held at constant load. Surface replicas were obtained for crack opening corresponding to loads from 0 to 16.25 kN in steps of 2.5 kN. The replicas were examined subsequently in a transmission electron microscope after being shadowed at 90 deg from both sides of the crack opening plane. Four recordings of gage displacement across the crack were taken at a number of positions behind the crack tip for each 2.5-mm increment in fatigue crack length. All readings were analyzed statistically to avoid bias.

The crack opening load, P_{op} is defined as the load at which the crack tip is fully open or the point at which the crack tip is on the verge of closing. The crack closing load, P_{cl} , is defined as the load when the entire length of the crack no longer experiences any further closure with reduction of applied load: this parameter is not a measure of crack-tip closure but rather of natural closure of the entire crack behind the tip. These points are defined by the transitions from linear to nonlinear behavior in the curve of load versus crack opening displacement. It was found that their values were unrelated to the direction of loading, that is, loading or unloading.

Results and Analysis

The effect of crack closure can be seen on the fracture surfaces of the fatigue specimens after failure through the presence of rubbed regions as shown in Fig. 1. Figure 1a is taken from the slant mode fatigue failure region along the edge of a specimen and indicates that complete closure has occurred between the two surfaces, with the fracture facets being distorted or rubbed. The sharp demarcation between the open central portion of the crack, where no rubbing marks are evident, and the closed region along the edge is illustrated in Fig. 1b, indicating that closure is an edge or slant mode related phenomenon in agreement with the observations of Lindley and Richards [5]. It is also seen that the crack tip does not close in the interior of the specimen at any time for the specimen configuration used.

A direct comparison between measurements of crack opening from surface replicas and from a displacement gage is shown in Fig. 2. The replica measurements correlated fairly well with the indirect displacement gage measurements, the variation averaging 27 percent, and ranging from 44 percent at low loads to 11 percent at high loads. These observations suggest that the record of crack opening displacement versus applied load is reliable in measuring crack openings and that the nonlinear region is indeed due to the effect of crack opening.

Both the opening and closing load ratios (the ratios of opening or closing load to maximum load, P_{max}) were found to depend on the

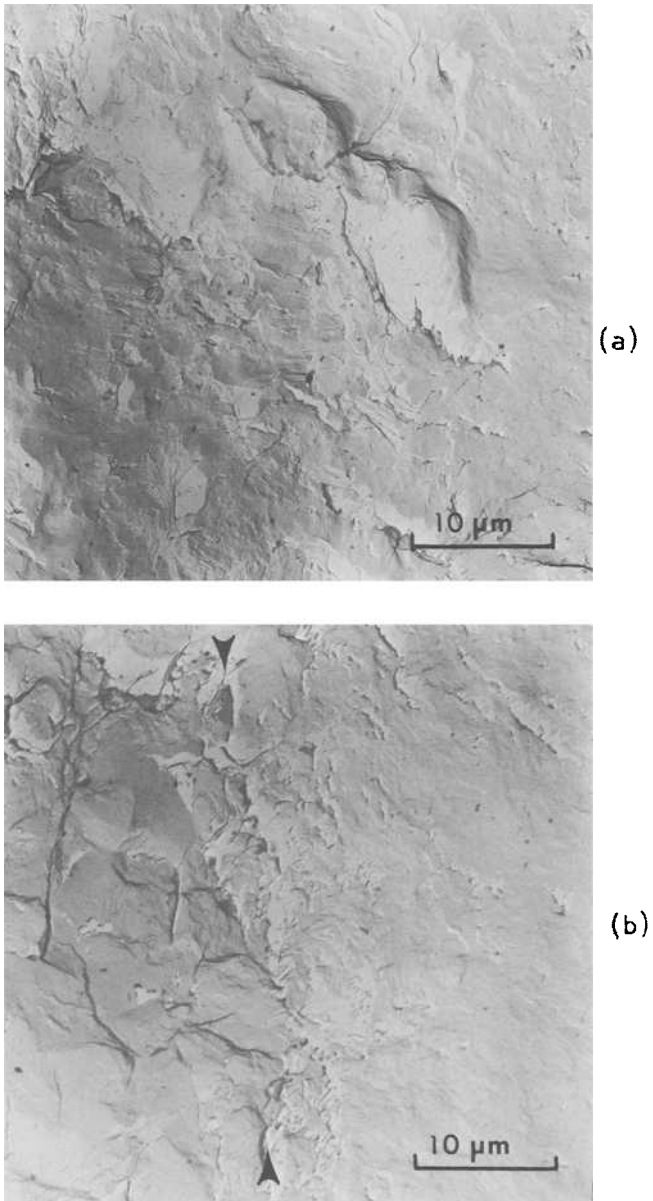


FIG. 1—Fractographic evidence of crack closure: (a) rubbed surface along edge of specimen, (b) transition from rubbed portion at edge to undamaged region in middle of specimen.

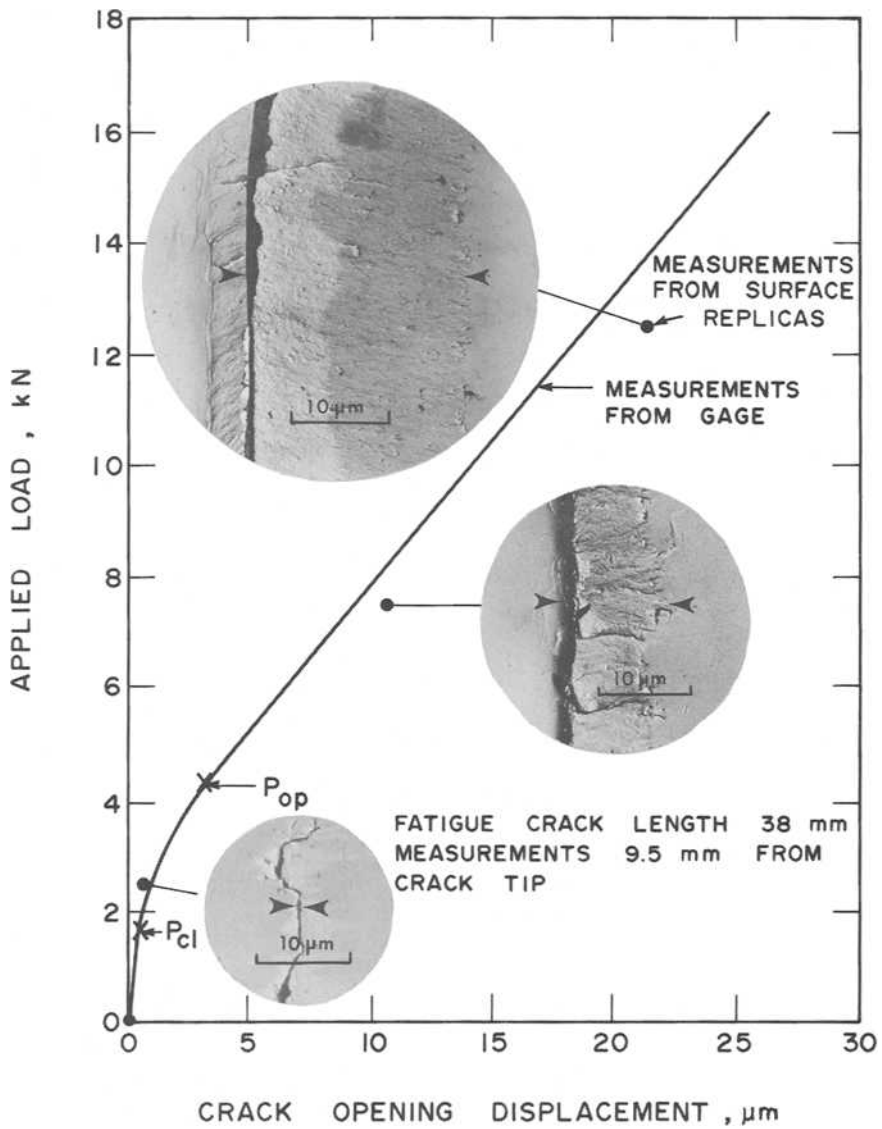


FIG. 2—Comparison between crack opening displacements measured using gage and as determined from replicas at the specimen surface.

distance from the crack tip at which crack opening displacements were measured, as shown in Fig. 3. This figure is drawn up for the opening load ratio and the values are averages for two specimens taken over the entire process of crack growth, the load ratios being independent of crack length as discussed later. It may be seen from Fig. 3 that the load ratios become greater for measurements near to the crack tip, while they are constant when taken more than about 5 mm from it. In order to resolve the reasons for this variation, the finite element method (FEM) was employed to determine the surface strains behind the crack tip (along the crack) due to the specimen loading. The indicated gage displacement will be the sum of the displacement due to crack opening and that due to surface strains. Thus, the gage displacements could be corrected to indicate the true values of crack opening displacement without the elastic strain in the material adjacent to the crack surfaces.

The finite element program used was divided into two parts, the first using a coarse mesh of 693 joints with 560 rectangles and 132 triangles (Fig. 4a) and covering the whole specimen up to the plane of the crack: the area adjacent to the crack tip consisted of 1.587 mm square elements. The second part involved an area immediately surrounding the crack tip, being 17.46 by 9.53 mm with crack-tip elements 0.397 mm square (Fig. 4b). This surrounding area utilized the boundary conditions obtained from the coarse mesh analysis. The position of a gage placed at 0.9 mm behind the crack tip with 1.75-mm gage length is also indicated in Fig. 4b.

Applying the results of the FEM, the corrected values for the loads at which crack opening and closing are predicted on the basis of displace-

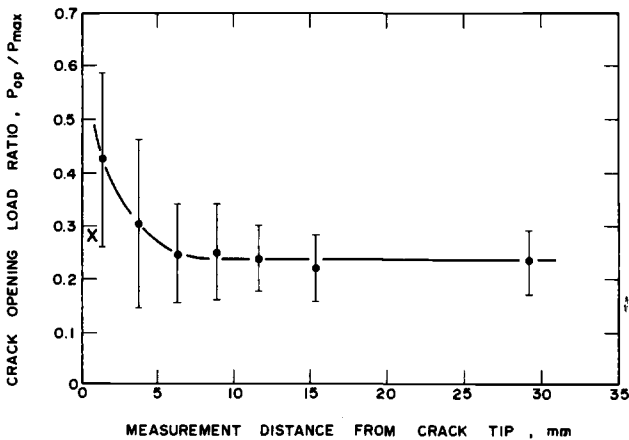


FIG. 3—Dependence of the crack opening load ratio on the distance of the crack opening displacement gage from the crack tip—average for two specimens over entire crack growth curve. The point marked X indicates the corrected value of P_{op}/P_{max} after application of the FEM to correct for surface strains.

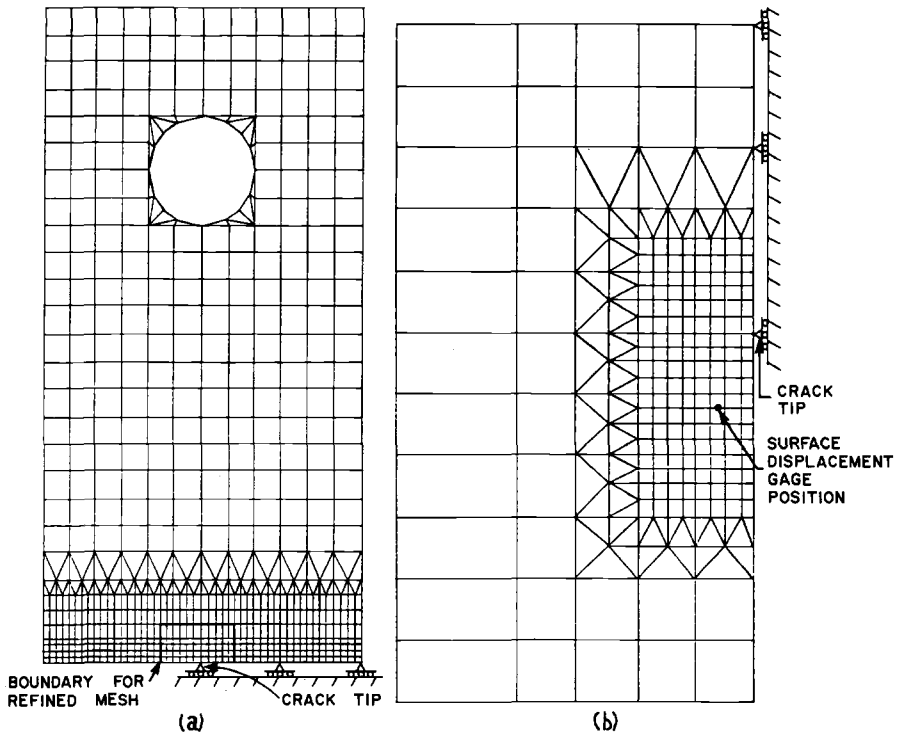


FIG. 4—Finite element grid for surface strains behind crack tip: (a) coarse grid, (b) refined grid.

ment measurements made at a distance of 0.9 mm from the crack tip are seen to be in reasonable agreement with the average values based on measurements at distances greater than 5 mm from the crack tip, as shown in Fig. 5. The FEM results indicated that the elastic strains would have an influence of about 10 percent on the measured values of crack opening displacement at a distance of up to 3 mm from the crack tip, in reasonable agreement with the value of 5 mm obtained from gage measurements as the distance above which the load ratio became constant. The corrected value of P_{op}/P_{max} at 0.9 mm from the crack tip, as obtained from FEM analysis, is also shown on Fig. 3, and is seen to compare reasonably with the values obtained some distance from the crack tip.

From the foregoing it is clear the surface strains behind the crack tip do influence the magnitude of the displacement gage readings when these are taken in close proximity to the crack tip. Thus, it is suggested that measurements used to define crack opening and crack closing should be taken at a distance from the crack tip sufficient to ensure that the local strain field does not affect them significantly.

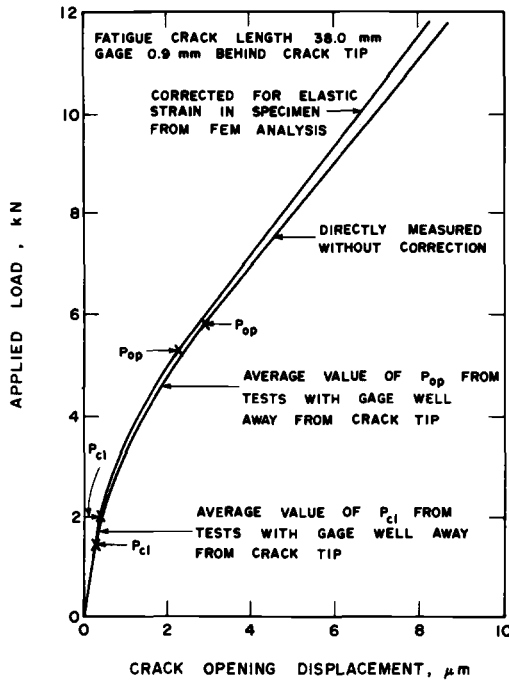


FIG. 5—Plots of applied load versus crack opening displacement showing the effect of correcting for elastic surface strains. Gage position 0.9 mm behind crack tip. The average values of crack opening and closing loads from other tests with the gage well away from the crack tip are also shown.

The opening load ratio for the two specimens is plotted against fatigue crack length in Fig. 6, being based on crack opening displacement measurements taken at a distance greater than 5 mm from the crack tip. A statistical fit yields a slope of -0.00497 , but when checked statistically at the 5 percent level of significance there is no difference between the statistically determined line and a line of slope equal to zero. In consequence, a slope equal to zero has been drawn on Fig. 6, and it is seen that the ratio can be considered independent of crack length, and hence independent of K_{max} and the plastic zone size at the crack tip. Using Elber's nomenclature [2], the effective stress range ratio, U , is defined as

$$U = (1 - P_{op}/P_{max}) / (1 - P_{min}/P_{max})$$

where P_{min} is the minimum value of the applied load, and it is seen that U is independent of crack length.

The ratio P_{cl}/P_{op} was found to be independent of the position of the displacement measurement with respect to the crack tip (Fig. 7), and as the crack opening load ratio, P_{op}/P_{max} , was independent of crack length

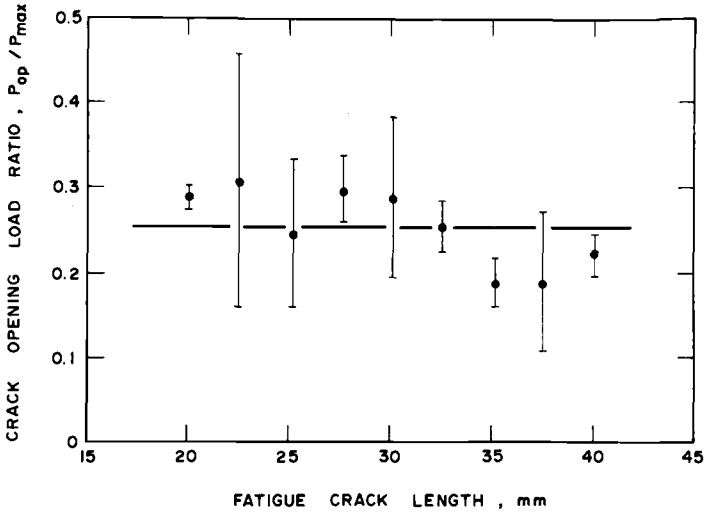


FIG. 6—Dependence of crack opening load ratio on the crack length—average for two specimens.

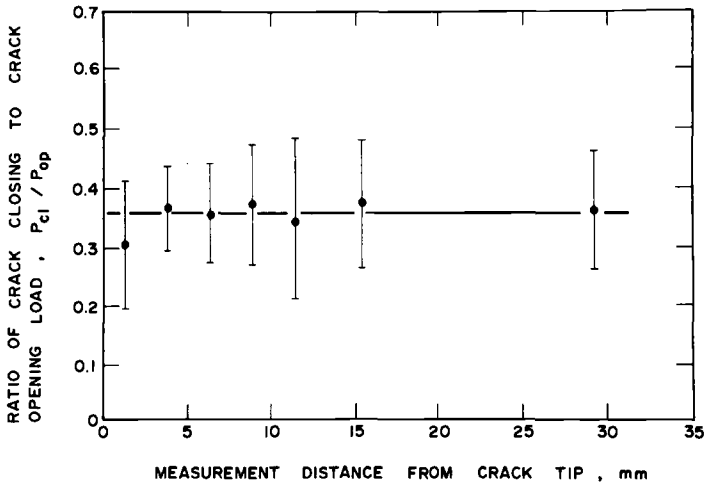


FIG. 7—Dependence of the ratio of crack closing to crack opening load on the position of the displacement gage.

(Fig. 6), it is apparent that one condition only, crack opening or crack closing, need be defined to satisfy the conditions for crack opening or crack closing for any value of crack length.

The conventional plots of fatigue crack growth rate, da/dN , versus ΔK ($= K_{max} - K_{min}$) may be modified by correcting K_{min} , the minimum value of stress intensity factor based on applied load, to either K_{op} or K_{cl} , the stress intensity factors corresponding to P_{op} and P_{cl} , respectively. The three plots of da/dN versus ΔK are given in Fig. 8, but no information is given to suggest choosing one correction over the other or over the original unmodified value of ΔK to give greater accuracy in predicting crack growth.

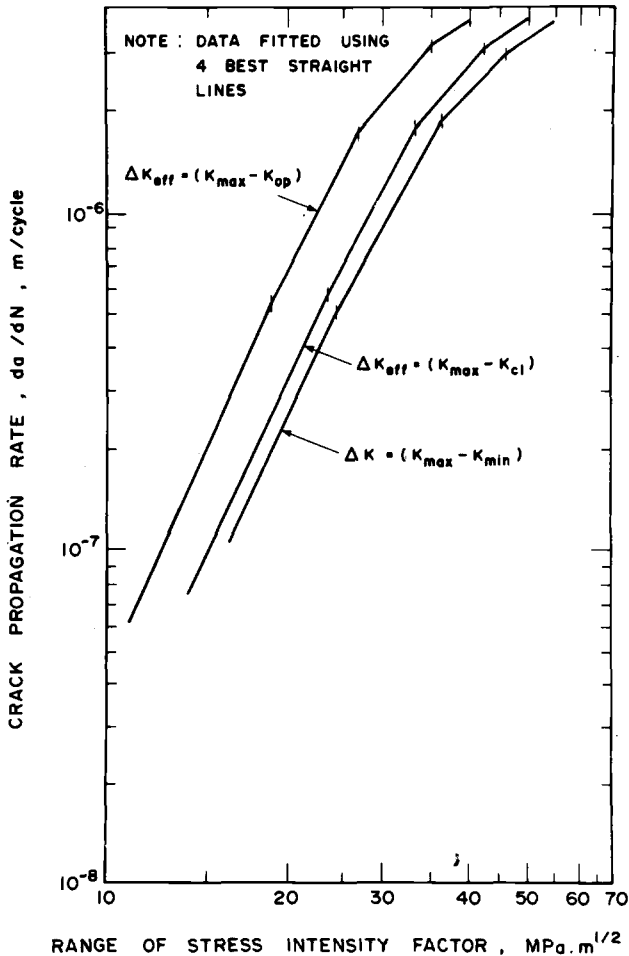


FIG. 8—Fatigue crack propagation rate as a function of range of stress intensity factor, uncorrected, corrected for crack fully open, and corrected for crack fully closed.

However, the equations corresponding to these graphs may be integrated numerically to generate a set of crack growth curves, and this has been done in Fig. 9. To obtain these, each of the four straight line segments in the graphs of Fig. 8, based on the Paris law [3], was integrated separately using 0.0254-mm increments of crack growth, and a cumulative total was used to derive the complete growth curve. It may be seen from Fig. 9 that the derived curve based on an effective ΔK incorporating the crack closure load (that is, the load at which the entire crack has normally closed) corresponds very closely to the original experimentally derived curve.

It may be noted that the comparable segments of the plots in Fig. 8 do not have the same slopes but that they vary slightly for each fit owing to the change in position of segment intercepts. The combination of changes leads to different percentages of specimen life in the various segments, resulting in alterations in the integrated growth curves. Since the data were treated statistically, including the determination of the segment intercepts, the results should be free of bias.

In further analysis of other test specimens from a group of 16, similar results were obtained. Thus, it appears that the effective range of stress intensity factor, ΔK_{eff} , in the modified Paris equation for fatigue crack propagation, should be taken at $(K_{max} - K_{cl})$.

General Discussion

The experimental results and the analysis made have demonstrated that crack opening displacements to determine the values of crack opening and

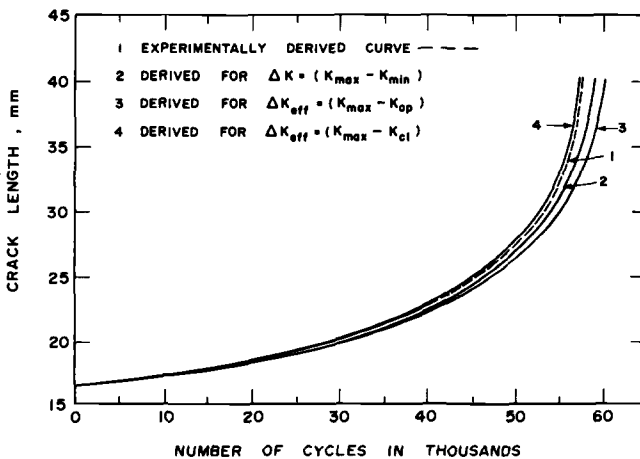


FIG. 9—Plot of crack length versus number of load cycles, showing the experimental curve, and curves derived for $\Delta K = (K_{max} - K_{min})$, $\Delta K_{eff} = (K_{max} - K_{op})$, and $\Delta K_{eff} = (K_{max} - K_{cl})$.

crack closing loads must be made at a distance from the crack tip sufficiently great to avoid errors due to the elastic strain field near to the tip. They have also indicated that correction of the range of stress intensity factor in the Paris crack growth equation, $da/dN = C(\Delta K)^n$, where C and n are constants, by substitution of K_{cl} for K_{min} gives improved prediction of crack propagation. These results were obtained for AISI 4140 steel in fatigue under essentially plane strain conditions as the extent of the slant mode at the edges constituted 0.65 percent or 0.015 mm in width on average over the length of the fatigue crack. However, it is expected that the extent of slant mode fatigue, which will be dependent on environment, specimen thickness, loading conditions, material properties and possibly frequency, will probably be a governing factor in crack closure phenomena. It should also be recognized that the distance behind the crack tip up to which the influence of surface strains is important (approximately 5 mm in this study) will also be dependent on the gage length used to measure crack opening displacements: in the present study this length was kept constant at 1.75 mm. Young's modulus will also have an effect on the extent of the strain affected region and the latter will probably be greater for aluminum and its alloys.

Obviously, additional studies are required to generalize the conclusions to cover a range of materials and, in addition, the influence of R ratio (minimum load/maximum load) requires examination. However, it is believed that the study has enabled a number of uncertainties and inconsistencies related to the crack closure phenomenon to be cleared up.

Conclusions

1. Observations of the fracture surfaces have shown that the edge or slant mode regions of the fracture surfaces close while the interior remains open, even at the crack tip.
2. Direct surface measurements using replicas have confirmed the correspondence of nonlinearity in the relationship between load and crack opening displacement to crack closure phenomena when measured by displacement gages.
3. Elastic stresses influence the measurements of crack opening obtained from displacement gages when these are placed near to the crack tip. Thus, valid measurements for a plot of load versus crack opening displacement must be taken well back from the crack tip.
4. For the specific material and test conditions employed, the crack opening or closing load ratios (P_{op}/P_{max} or P_{cl}/P_{max}) were found to be independent of fatigue crack length.
5. The ratio of crack opening to crack closing load, P_{op}/P_{cl} , was found to be constant for all positions of displacement measurement and for all values of fatigue crack length.
6. The prediction of fatigue life based on crack propagation data by

means of an equation of the form $da/dN = C(\Delta K)^n$ is improved when the range of stress intensity factor is evaluated from complete crack closure ($K_{\max} - K_c$) rather than from crack tip closure ($K_{\max} - K_{op}$) or minimum load ($K_{\max} - K_{min}$).

Acknowledgments

The authors are grateful for the financial support of these studies by the National Research Council of Canada and the Defence Research Board of Canada.

References

- [1] Elber, W., *Engineering Fracture Mechanics*, Vol. 2, 1970, pp. 37-45.
- [2] Elber, W. in *Damage Tolerance in Aircraft Structures*, ASTM STP 486, American Society for Testing and Materials, 1971, pp. 230-242.
- [3] Paris, P. C. in *Proceedings*, 10th Sagamore Conference, Syracuse University Press, 1964, p. 125.
- [4] Cheng, Y. F. and Brunner, N., *International Journal of Fracture Mechanics*, Vol. 6, 1970, pp. 431-434.
- [5] Lindley, T. C. and Richards, C. E., *Materials Science and Engineering*, Vol. 14, 1974, pp. 281-293.
- [6] Bachmann, V. and Munz, D., *International Journal of Fracture*, Vol. 11, 1975, pp. 713-715.
- [7] Katcher, M. and Kaplan, M. in *Fracture Toughness and Slow-Stable Cracking*, ASTM STP 559, American Society for Testing and Materials, 1974, pp. 264-282.
- [8] Boutle, N. F. and Dover, W. D. in *Fracture 1977*, Vol. 2, D. M. R. Taplin, Ed., University of Waterloo Press, Waterloo, Ontario, 1977, pp. 1065-1071.
- [9] Bachmann, V. and Munz, D. in *Fatigue Testing and Design*, Vol. 2, R. G. Bathgate, Ed., Society of Environmental Engineers, London, 1976, pp. 35.1-35.32.
- [10] Adams, N. J. I., *Engineering Fracture Mechanics*, Vol. 4, 1972, pp. 543-554.
- [11] Roberts, R. and Schmidt, R. A., *International Journal of Fracture Mechanics*, Vol. 8, 1972, pp. 469-471.
- [12] Schmidt, R. A. and Paris, P. C. in *Progress in Flaw Growth and Fracture Toughness Testing*, ASTM STP 536, American Society for Testing and Materials, 1973, pp. 79-94.
- [13] Buck, O., Ho, C. L., and Marcus, H. L., *Engineering Fracture Mechanics*, Vol. 5, 1973, pp. 23-34.
- [14] Nistani, H. and Kage, M. in *Fracture 1977*, Vol. 2, D. M. R. Taplin, Ed., University of Waterloo Press, Waterloo, Ontario, 1977, pp. 1065-1071.
- [15] Irving, P. E., Robinson, J. L., and Beevers, C. J., *International Journal of Fracture*, Vol. 9, 1973, pp. 105-108.
- [16] Shih, T. T. and Wei, R. P., *Engineering Fracture Mechanics*, Vol. 6, 1974, pp. 19-32.
- [17] Irving, P. E., Robinson, J. L., and Beevers, C. J., *Engineering Fracture Mechanics*, Vol. 7, 1975, pp. 619-630.
- [18] Unangst, K. D., Shih, T. T., and Wei, R. P., *Engineering Fracture Mechanics*, Vol. 19, 1977, pp. 725-734.
- [19] Kikukawa, M., Jono, M., and Tanaka, K. in *Proceedings*, 2nd International Conference on Mechanical Behavior of Materials, Federation of Materials Societies, Boston, Mass., 1976, pp. 716-720.
- [20] Hertzberg, R. W. and Von Euw, F. J., *Metallurgical Transactions*, Vol. 4, 1973, pp. 887-889.
- [21] Smith, R. A. and Miller, K. J., *International Journal of Mechanical Science*, Vol. 19, 1977, pp. 11-22.
- [22] Shaw, W. J. D. and Le May, I. in *Fatigue Testing and Design*, Vol. 2, R. G. Bathgate, Ed., Society of Environmental Engineers, London, 1976, pp. 31.1-31.24.
- [23] Shaw, W. J. D. and Le May, I. in *The Influence of Environment on Fatigue*, The Institution of Mechanical Engineers, London, 1977, pp. 93-100.

N. E. Dowling¹

Fatigue at Notches and the Local Strain and Fracture Mechanics Approaches

REFERENCE: Dowling, N. E., "Fatigue at Notches and the Local Strain and Fracture Mechanics Approaches," *Fracture Mechanics, ASTM STP 677*, C. W. Smith, Ed., American Society for Testing and Materials, 1979, pp. 247–273.

ABSTRACT: Total fatigue lives of notched members are considered to be divided into initiation and propagation phases. Notch size effects caused by crack propagation are accounted for automatically if initiation is defined as a crack size within the local notch stress field. The extent of this field may be estimated from fracture mechanics analysis, with its size being on the order of one tenth of the notch radius. Plasticity effects must be handled properly in predicting crack initiation, but linear elastic analysis is generally satisfactory for handling the propagation phase.

KEY WORDS: fatigue (materials), stresses, strains, crack propagation, fracture, plastic, cycling, mechanics, deformation, loading

Fatigue life prediction for notched members may be approached from several viewpoints. For crack initiation, the traditional approach based on nominal stresses and stress concentration factors has been supplemented recently by two more sophisticated approaches. These are the local strain approach and an approach based on the fracture mechanics parameter K/\sqrt{r} . For crack propagation, the fracture mechanics approach is now applied widely.

These various approaches are discussed in an attempt to show the bearing of each on the problem of predicting fatigue lives of notched members. The problem of defining crack initiation is considered, as are notch size effects. Local notch plasticity is discussed relative to both crack initiation and crack propagation. Near the end of the paper, a procedure is proposed for predicting fatigue lives of notched members by separating the total life into initiation and propagation phases.

¹ Fellow engineer, Westinghouse Research and Development Center, Pittsburgh, Pa. 15235.

Crack Initiation Approaches

It is useful to consider the local strain and fracture mechanics (K/\sqrt{r}) approaches to crack initiation from the viewpoint of the elastic-plastic strains occurring at the notch surface.

Elastic-Plastic Strains at Notches

The loading on a notched member may be described in terms of a nominal stress, S , which is proportional to the applied load by a geometry dependent constant. For example, for axially loaded notched members, load is usually divided by cross sectional area to obtain nominal stress. And the severity of the notch may be characterized by an elastic stress concentration factor, k_t . In particular, k_t and S are defined consistently so that the product $k_t S$ is the maximum principal stress at the notch for elastic behavior. Where plastic deformation occurs at the notch, values of $k_t S$ are fictitious stresses. Analysis that specifically considers plastic deformation must then be employed to obtain the actual notch stresses and strains.

Several workers [1-3]² have performed elastic-plastic finite element analyses that are relevant. Wilson [2] analyzed bluntly notched compact specimens as in Fig. 1a. Three different values of notch root radius, r , were used to obtain a wide range of values of elastic stress concentration factor. In this geometry, the nominal stress, S , is calculated from the applied load, P , by assuming a linear stress distribution due to tension and bending.

² The italic numbers in brackets refer to the list of references appended to this paper.

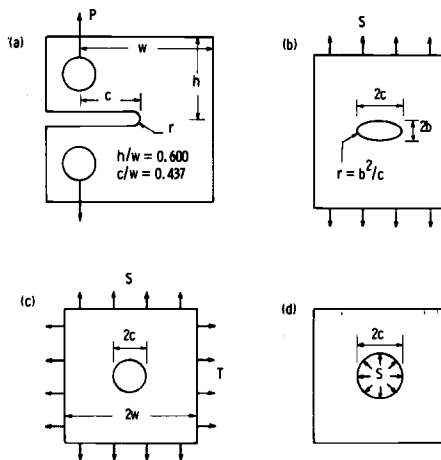


FIG. 1—Various notched members.

The results of the analysis are shown in Fig. 2, along with the uniaxial cyclic stress-strain curve [4] used as a basis for the analysis. Notch strains are plotted versus $k_t S$, thus requiring the elastic solutions to all coincide along the straight line which is shown. Beyond yielding, the strains are larger than estimated by the extrapolation of the elastic solution. This type of plot nevertheless causes an approximate normalization, despite the changes in geometry reflected in the different k_t values. Similar approximate agreement of $k_t S$ versus notch strain curves is also shown in Ref 2 for a blunt notched compact specimen and a plate with a circular hole. Hence, these analytical results imply that, for notched members of a given material, there is a reasonably unique relationship between $k_t S$ and notch strain.

Also shown in Fig. 2 is a $k_t S$ versus notch strain curve obtained from Neuber's rule [5]. Neuber's rule postulates that during plastic deformation the geometric mean of the stress and strain concentration factors remains equal to k_t

$$\sqrt{k_\sigma k_\epsilon} = k_t \tag{1}$$

If the gross deformation behavior is elastic, Eq 2 takes the form

$$\sqrt{\sigma \epsilon E} = k_t S \tag{2}$$

where σ and ϵ are local notch stress and strain. Equation 2 was combined with the cyclic stress-strain curve to obtain the relationship shown in Fig.

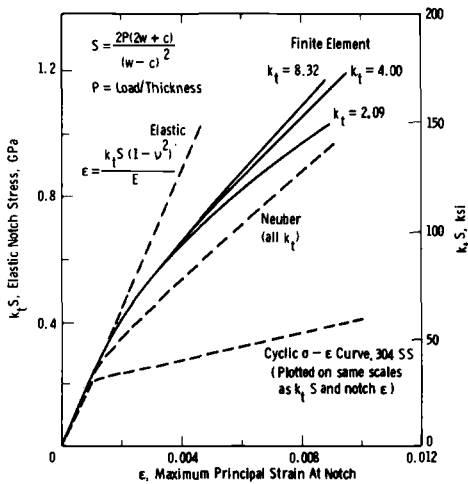


FIG. 2—Load versus notch strain curves for blunt notched compact specimens under plane strain (Wilson).

2. However, before this was done, the stress-strain curve and Eq 2 were both modified as described in detail in Ref 6 to reflect the plane strain assumption, which also was used in the finite element analysis. Note that Eq 2 provides a reasonable estimate of the strains. Also, if the stress-strain curve, hence the material and the state of stress at the notch, are unchanged, Eq 2 implies a single unique $K_t S$ versus notch strain curve for all geometries and k_t values.

There are exceptions to this approximate uniqueness of the relationship between $k_t S$ and notch strain. Figure 3 illustrates this by analytical results from Ref 1, where the $k_t S$ versus notch strain curve is altered significantly by changing the notch sharpness in circumferentially notched round bar specimens.

Additional analytical results and experimental verification thereof are needed before broad generalizations can be made concerning geometry effects on $k_t S$ versus notch strain curves. Differences can be expected where different amounts of constraint (plane stress versus plane strain) occur. Also, note that fully plastic limit load occurs at different values of $k_t S$ in various geometries. Near limit load, unusually large strains are expected, so that the $k_t S$ versus notch strain relationship will not be unique if any of the geometries involved are loaded near limit load.

Local Strain Approach

In the local strain approach, a given notch surface strain is assumed to always result in the same fatigue life. Thus, the fatigue data used are in the form of a strain versus cyclic life curve. Usually, total cycles to failure data for small unnotched axial specimens are used. Although the data are more difficult to obtain, a strain versus life curve corresponding to a specific small crack size can be used if available. Various strain versus life curves for an alloy steel are illustrated in Fig. 4. These particular data

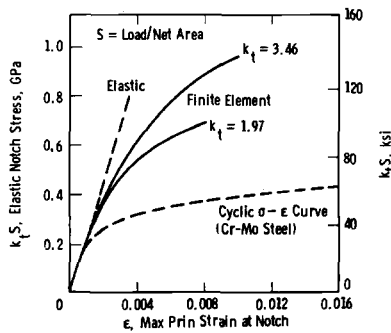


FIG. 3—Load versus notch strain curves for circumferentially notched round bar specimens loaded axially (Mowbray).

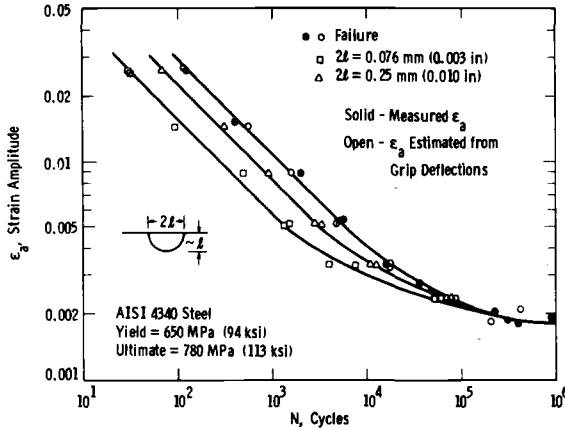


FIG. 4—Strain versus cycles to crack initiation data from unnotched axial specimens of diameter 6.3 mm (0.25 in.).

were obtained using unnotched axial specimens under controlled grip deflections as described in Ref 7.

When combined with $k_t S$ versus strain relationship such as those in Figs. 2 and 3, the strain versus life curve provides a prediction of the load versus cycles to crack initiation behavior of the notched member. Detailed analysis as by finite elements is usually unavailable, so that the $k_t S$ versus strain relationship is often estimated using Neuber's rule. Successful use of the local strain approach with Neuber's rule is demonstrated in Refs 8 and 9.

Fracture Mechanics (K/√r) Approach

At a sharp notch in an elastic body, the maximum stress is located at the notch surface and is given [10,11] approximately by

$$\sigma = \frac{2K}{\sqrt{\pi r}} \tag{3}$$

where K is the stress intensity calculated from linear elastic fracture mechanics as if the notch were a crack, and r is the notch radius. Since $\sigma = k_t S$, Eq 3 gives

$$k_t S = \frac{2K}{\sqrt{\pi r}} \tag{4}$$

and

$$k_t = \frac{2K}{S\sqrt{\pi r}} \tag{5}$$

In the fracture mechanics approach to fatigue at blunt notches [12,13], the quantity K/\sqrt{r} is plotted versus initiation life as a means of correlating the behavior of different geometric shapes. Where the estimate of k_t given by Eq 5 is accurate, Eq 4 indicates that correlating fatigue lives using K/\sqrt{r} is equivalent to using $k_t S$. Note that $\sigma = k_t S$ is a fictitious stress if local notch yielding occurs. However, from the preceding discussion relative to Fig. 2, a given value of $k_t S$ generally implies approximately equal notch strains independent of geometry. Thus, correlating initiation data for various notched geometries in terms of K/\sqrt{r} is approximately equivalent to a correlation in terms of notch strain.

However, difficulties with K/\sqrt{r} may arise due to the approximate nature of Eq 3. This can be shown by comparing k_t values from Eq 5 with more exact analytical results [2,14,15]. Table 1 makes such a comparison for various geometries illustrated in Fig. 1. For the compact specimen analyzed by Wilson [2], the fracture mechanics estimates of k_t are all within 10 percent of the values from elastic finite element analysis. However, for elliptical holes in infinite uniaxially stressed plates, the fracture mechanics estimate is accurate only for thin ellipses with major axis perpendicular to the stress direction. It is low by 33 percent for the particular case of a circular hole. Even larger errors occur for elliptical notches with major axis parallel to the stress direction, and also for various other cases involving circular holes. See Table 1.

In general, the fracture mechanics estimate of k_t will be reasonably accurate only for notches which are crack-like in form. In particular, the

TABLE 1—Stress concentration factors and notch stress field sizes for various notched members ^a

Fig.	Geometry	Case	Exact k_t	F.M. k_t	ℓ_m/r
1a	blunt notch compact specimen	$r/w = 0.005$	8.32	8.35	0.200
		$r/w = 0.0235$	4.00	3.85	0.190
		$r/w = 0.100$	2.09	1.87	0.176
1b	elliptical hole in wide plate, remote uniaxial stress	any c/b	$1 + 2c/b$	$2c/b$	varies
		$c/b = 4$	9	8	0.159
		$c/b = 2$	5	4	0.132
		$c/b = 1$	3	2	0.097
		$c/b = 0.5$	2	1	0.062
		$c/b = 0.25$	1.5	0.5	0.034
1c	circular hole in wide plate, remote stress	$T = S$	2	2	0.249
		$T = -S$	4	2	0.052
1c	circular hole in finite width plate, $T = 0$	$c/w = 0.25$	3.23	2.08	0.092
		$c/w = 0.50$	4.32	2.37	0.068
1d	pressure in circular hole	...	1	2	0.257 ^b

^a The k_t values given are equal to σ/S , where σ is the maximum principal stress at the notch, and S is nominal stress as variously defined in Figs. 1 and 2.

^b Pressure excluded from crack.

notch depth, c in Fig. 1, must be large compared to the notch radius, r . This is of course violated by circular holes and by many other types of mild notch. Where the fracture mechanics estimates of k_t are inaccurate, difficulties are expected in correlating fatigue data using K/\sqrt{r} . For example, if fatigue crack initiation data for a bluntly notched compact specimen, Fig. 1a, is compared on the basis of K/\sqrt{r} with similar data for a plate with a circular hole, such as Fig. 1c with $T = 0$ and $c/w = 0.5$, a lack of correlation is expected. Such a comparison would be a critical test of the K/\sqrt{r} approach as the data are expected to be correlated by $k_t S$ but not by K/\sqrt{r} . The published literature advocating the K/\sqrt{r} approach do not contain any such critical test.

The use of stress intensity, K , for blunt notches can be misleading as it suggests that a profoundly new approach is being used. This is not the case. Rather, fracture mechanics analysis is in effect being used simply to estimate k_t values. It is suggested that the use of plots of K/\sqrt{r} versus life should be dropped. Initiation behavior of various notched shapes should be correlated instead in terms of $k_t S$. The best available value of k_t should always be used. In some cases, fracture mechanics analysis will provide this best available value, but in others it will not.

Definition of Crack Initiation

In any approach to predicting crack initiation, some care must be used in defining this event. Linear elastic stress intensity solutions for cracks at notches [16] provide a basis for choosing a crack size for use as a definition of initiation.

Stress Intensity Solutions for Cracks at Notches

Figure 5 illustrates the stress intensity solution for the case of a circular hole in an infinite plate under uniaxial stress. The dashed line is the actual numerical solution from Ref 16, and the two solid lines are limiting cases for short and long cracks.

The short crack limiting case corresponds to a free surface crack having a length, ℓ , which is measured from the end of the notch. The stress is elevated by the stress concentration factor, $k_t = 3$, and a free surface correction factor [17] of 1.12 is needed.

$$K_s = 1.12 k_t S \sqrt{\pi \ell} \quad (6)$$

For long cracks, the stress intensity solution is the same as for a single crack of total length $2a$.

$$K_\ell = S \sqrt{\pi a} \quad (7)$$

where $a = c + \ell$, with c being the radius of the hole.

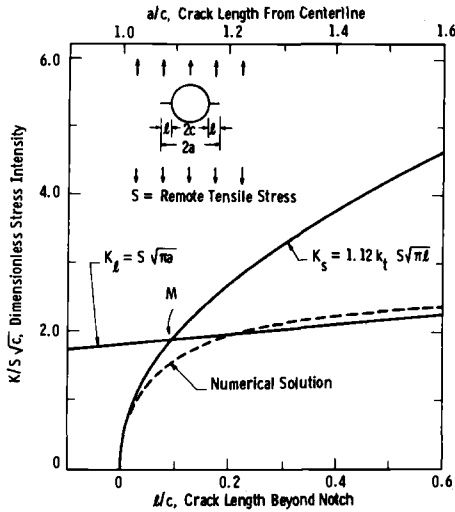


FIG. 5—Short and long crack limiting cases and numerical solution for cracks growing from a circular hole in an infinite plate (Newman).

For increasing crack length, the numerical solution first follows Eq 6, then there is a transition in behavior, followed by approximate agreement with Eq 7. Hence, there is a transition from behavior controlled by the local notch stress to behavior controlled by the bulk stress. At large crack lengths, the notch is important only in that its depth must be included in the crack length.

Consider the crack length corresponding to point *M* in Fig. 5, the intersection of the short and long crack limiting cases. This length, here called l_m , locates the transition in behavior between the short and long crack limiting cases.

Similar stress intensity solutions for cracks at notches are available [16] for the geometries of Figs. 1*b*, *c* and *d*, specifically for each case of these which is listed in Table 1. Equation 6, with the appropriate k_t value for each situation, gives the small crack limiting cases. The long crack limiting cases are given by Eq 7 except as follows: For the finite width cases of Fig. 1*c*, Eq 7 must be replaced by

$$K_l = F S \sqrt{\pi a} \tag{8}$$

where *F* is a function of a/w [16,17]. Also, the long crack limiting case [16,17] for Fig. 1*d*, assuming the pressure to be excluded from the crack, is

$$K_l = \frac{2Sc}{\sqrt{\pi a}} \tag{9}$$

For each of these situations, the short and long crack limiting cases may be combined to obtain values of ℓ_m . These are given in Table 1 as fractions of the notch radii.

For stress intensities, K , corresponding to crack lengths less than ℓ_m , ratios K/K_s were computed for each numerical analysis data point from Ref 16. And for lengths greater than ℓ_m , ratios K/K_l were computed. These are plotted in Fig. 6 versus crack lengths normalized with respect to ℓ_m . The behaviors are all qualitatively similar to that in Fig. 5. As ℓ/ℓ_m approaches unity, the stress intensities fall below the small crack limiting case, with the maximum deviation generally being 10 to 20 percent. At larger values of ℓ/ℓ_m , the numerical analysis may overshoot the long crack limiting case, in two situations by as much as 25 percent.

Size of the Local Notch Stress Field

From the behaviors of the various stress intensity solutions in Fig. 6 being similar to Fig. 5, the interpretation is made that in each case ℓ_m represents the distance within which the local notch stress field dominates the stress intensity solution. In other words, for a crack growing from a notch, ℓ_m is a measure of the extent of the local notch stress field. Even for geometries where detailed analysis as in Fig. 5 is unavailable, ℓ_m

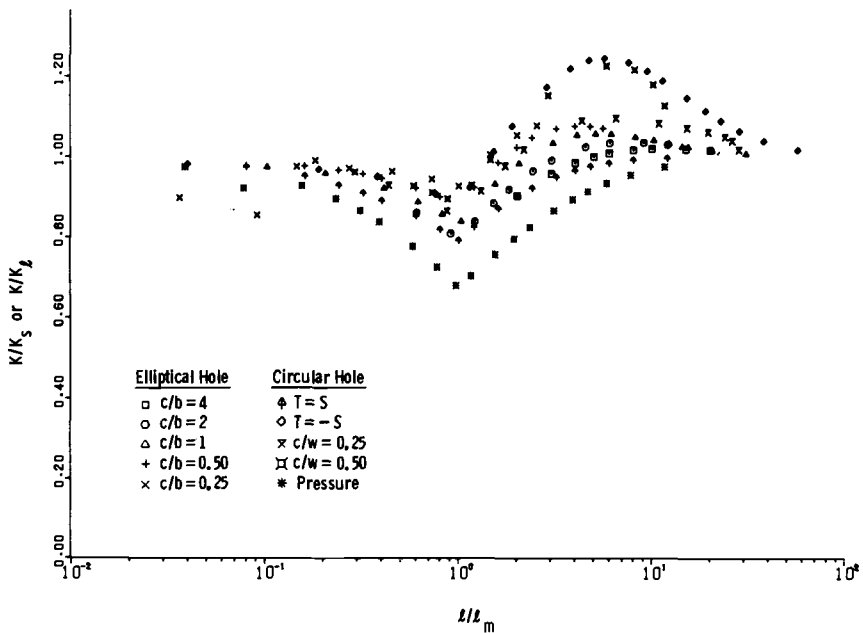


FIG. 6—Comparison of stress intensity solutions for cracks at notches with either the short crack or long crack limiting cases.

values calculated from the long and short crack limiting cases will still be assumed to have this significance. Thus, ℓ_m values are also given in Table 1 for the geometry of Fig. 1a.

For notches where the long crack limiting case is of the form of Eq 8, the following general equation for ℓ_m is obtained using Eq 6

$$\ell_m = \frac{c}{(1.12 k_t/F)^2 - 1} \quad (10)$$

where c is notch depth as variously defined in Figs. 1 or 7a. Considering deep notches, let a and c be redefined as in Fig. 7b. Equation 8 is then applicable, but Eq 10 must be modified

$$\ell_m = \frac{c}{(1.12 k_t/F)^2 + 1} \quad (11)$$

In Table 1, the various ℓ_m values range between approximately $r/30$ and $r/4$. However, values of ℓ_m for a surprising variety of relatively sharp notches fall in the narrower range of approximately $r/10$ to $r/5$. In Table 1, this is true of all the cases of Fig. 1a, and also for those of Fig. 1b except where $c/b < 1$. Values of ℓ_m for various deep hyperbolic notches [15] with $k_t > 2$ also fall within this narrower range. In general, the values increase toward $r/5$ as notch sharpness is increased. This is easily understood by combining Eqs 5 and 6, noting that K in Eq 5 is the long crack limiting case, which gives a value of $\ell_m = 0.199r$ for sharp notches.

A length parameter is also used in Ref 18 to describe the extent of the

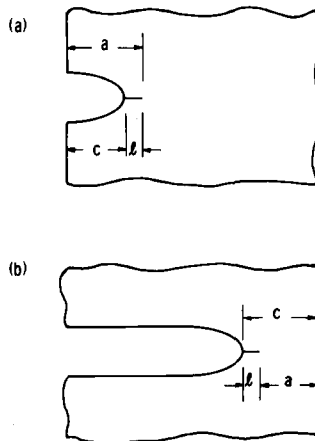


FIG. 7—Nomenclature for (a) shallow and (b) deep notches.

local notch stress field relative to cracks at notches. However, the specific estimate proposed in Ref 18 is in disagreement with the range of values $r/10$ to $r/5$ for relatively sharp notches.

Definition of Crack Initiation

Figure 8 illustrates the effect of a stress intensity solution similar to Fig. 5 on the growth of a fatigue crack. It is assumed in Fig. 8 that a very small crack of length ℓ_1 is present as a result of N_1 cycles having been applied previously. The crack length versus cycles behavior at short crack lengths will be similar to that in an edge-cracked plate having an applied nominal stress equal to $k_t S$ and an initial crack of the same size, ℓ_1 . Note that such a member has a stress intensity solution [17] identical to Eq 6, the short crack limiting case for the notched member.

With increasing crack length, as the actual stress intensity in the notched member drops below that given by Eq 6, the resulting difference in growth rates will cause the two crack length versus cycles curves to diverge. For crack lengths approximately equal to or less than ℓ_m , the behavior of the notched member is predicted reasonably by the unnotched plate under loading $k_t S$. This is illustrated by crack length, ℓ_2 in Fig. 8. Therefore, where notched member behavior is being predicted from unnotched specimen data, the choice of a crack length near or smaller than ℓ_m as a definition of initiation avoids problems with geometry dependence of the initiation life.

Assume that a crack length significantly larger than ℓ_m is used to define initiation, this being illustrated by ℓ_3 in Fig. 8. The notched member will then require a larger number of cycles than the unnotched member for propagation from ℓ_1 to ℓ_3 . If the life spent prior to length ℓ_1 is large compared to the life between ℓ_1 and ℓ_3 , then the error due to defining ℓ_3 as

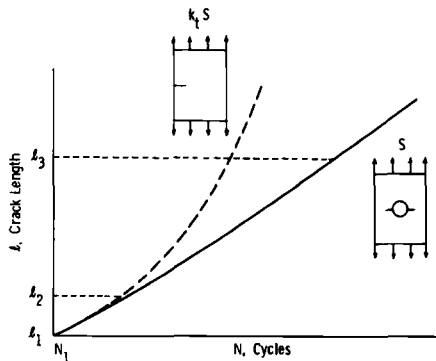


FIG. 8—Effect of propagation out of the local notch stress field on crack length versus cycles behavior.

initiation will be an unimportant fraction of the total initiation life. Hence, it is still possible in this situation for a life prediction based on an unnotched specimen under loading $k_t S$ to be accurate. However, defining initiation as a crack length equal to or less than ℓ_m is preferable as this precludes any difficulty.

Consider the situation where it is desired to use notched test specimens to simulate a notched engineering component. The lives will be independent of the geometry change as long as the crack length versus cycles behaviors, such as the solid line in Fig. 8, are similar. Where initiation is defined as a crack length equal to or less than the ℓ_m values of both the specimen and the component, Fig. 6 implies that equivalent loadings in terms of $k_t S$ will assure a reasonable simulation. Since, from the earlier discussion, equal values of $k_t S$ imply similar notch strains, local notch plasticity should not cause major problems with this approach.

However, it may be desirable to define initiation as a crack length greater than ℓ_m . In this case, the notch radius for the test specimen geometry should be chosen so that the ℓ_m values for specimen and component are equivalent. Since ℓ_m is roughly a constant fraction of the notch radius, this will result in approximately equivalent notch radii. The long crack limiting cases of the stress intensity solutions will then be the same at crack length ℓ_m , and, from Fig. 6, the actual stress intensities will be similar. By intelligent choice of the specimen geometry, it may be possible to achieve similar long crack limiting case stress intensities in specimen and component up to crack lengths considerably longer than ℓ_m . Thus, for loading at equal $k_t S$ values, and for notches with equal ℓ_m values, the principal factor limiting the defined initiation size is divergence of the long crack stress intensity solutions.

Notch Size Effects

It has been long noted that sharp notches have less effect on fatigue strength than expected based on elastic stress concentration factors, k_t , applied to unnotched specimen data. Explanations for this apparent paradox have been suggested that are based on statistical size effects or the breakdown of continuum mechanics at small size scales. Of the various relationships employed to calculate fatigue strength reduction factors for notches, the best known is probably that due to Peterson [19]

$$k_f = 1 + \frac{k_t - 1}{1 + \alpha/r} \quad (12)$$

where k_f is a reduction factor applied to unnotched specimen fatigue strengths, r is notch radius, and α is an empirical material constant having a value typically in the range 0.25 to 0.025 mm (0.01 to 0.001 in.). Except

for r large compared to α , Eq 12 implies k_f values significantly less than k_r . Test data clearly reflecting this trend are given in Ref 20.

Local notch plasticity in part explains the k_f effect. The local strain approach to crack initiation, as described earlier, accounts for this aspect of the problem. However, the effect remains even at long lives where the plasticity explanation does not apply. Hunter and Fricke [20] suggested in 1957 that the k_f effect is due primarily to crack propagation.

Notch Size Effects Due to Crack Propagation

An explanation of notch size effects based on crack propagation follows directly from the earlier discussion on the behavior of cracks at notches. Assume that both unnotched and notched members have been subjected to sufficient fatigue cycling so that they both have initial cracks of the same size, ℓ_i , which is small compared to ℓ_m for the notch. Further, define failure as a specific crack size, ℓ_f , which is larger than ℓ_m .

If the unnotched members are wide plates which develop an edge crack, the stress intensity is given [17] by Eq 8 with $F = 1.12$. Assume crack growth rate behavior of the form

$$\frac{d\ell}{dN} = AK^n \quad (13)$$

where $d\ell/dN$ is cyclic crack growth rate, and A and n are material constants. Substituting Eq 8 with $F = 1.12$ into Eq 13 and integrating yields an equation relating stress and life for propagation from ℓ_i to ℓ_f .

$$NS^n = \frac{\ell_f^{1-n/2} - \ell_i^{1-n/2}}{A(1-n/2)(1.12\sqrt{\pi})^n} \quad (14)$$

Take the notched members to be any case of an ellipse in a wide plate, Fig. 1b. Approximate the stress intensity solutions by following the small crack limiting case up to points such as M in Fig. 5, and beyond this by following the long crack limiting case. Equations 6 and 13 then give the life for propagation from ℓ_i to ℓ_m , and Eqs 7 and 13 give the life for propagation from ℓ_m to ℓ_f . Adding these two lives results in an equation relating stress and the total life for propagation from ℓ_i to ℓ_f .

$$NS^n = \frac{\ell_m^{1-n/2} - \ell_i^{1-n/2}}{A(1-n/2)(1.12k_t\sqrt{\pi})^n} + \frac{(c + \ell_f)^{1-n/2} - (c + \ell_m)^{1-n/2}}{A(1-n/2)(\sqrt{\pi})^n} \quad (15)$$

Note that the S - N curves for both smooth and notched members for propagation from ℓ_i to ℓ_f , Eqs 14 and 15, are straight lines on log-log plots with identical slopes of $-1/n$. Hence, at any given life, the notched member curve is below the unnotched member curve by a factor, k_p , which does not vary with life

$$k_p = \left[\frac{\ell_f^{1-n/2} - \ell_i^{1-n/2}}{\left[(1/k_t)^n (\ell_m^{1-n/2} - \ell_i^{1-n/2}) + (1.12)^n [(c + \ell_f)^{1-n/2} - (c + \ell_m)^{1-n/2}] \right]} \right]^{1/n} \tag{16}$$

The strength reduction factor, k_p , is a function of ℓ_i , ℓ_f , k_t , c and n . Although ℓ_m also appears in Eq 16, this is a function of k_t and c from Eq 10 with $F = 1$. It is significant that k_p depends on c as this indicates a size effect. Equation 16 is of course applicable only for the geometries assumed; however, analogous relationships can be developed for other situations.

Some values of k_p from Eq 16 are given in Table 2. A typical value of $n = 3$ is employed. The initial crack size is chosen to be quite small, and the final crack size is in an easily detectable, but not a large, size. Values are calculated for two sizes, c , for each of three shapes of elliptical hole. Note that for a given k_t value the strength reduction factor, k_p , is always larger for the larger size notch. Also, for increasing notch sharpness at a given size, c , the k_p value decreases relative to k_t . This effect is more pronounced for smaller sizes.

If the derivation above is revised for the case of the final crack size, ℓ_f , being less than ℓ_m , the simple result $k_p = k_t$ is obtained. This might be the case in practical situations where the notch radius is large. Note that $k_p = k_t$ for large notches is consistent with Eq 12 giving $k_f = k_t$ for r large compared to α .

Combined Effects of Crack Initiation and Propagation

A significant fraction of the fatigue life may be spent in initiating the crack length, ℓ_i , of Eq 16. This will reduce the importance of the propagation life in determining the overall behavior.

Figure 9 illustrates this situation. Unnotched specimen fatigue lives are divided into initiation and propagation phases defined in terms of crack lengths ℓ_i and ℓ_f . Consistent with the test data of Fig. 4 and Refs 20 and

TABLE 2—Notch fatigue strength reduction factors for crack propagation, assuming elastic behavior and various elliptical holes in wide plates.

Assume $\ell_i = 0.025 \text{ mm} = 0.001 \text{ in.}$ $\ell_f = 2.5 \text{ mm} = 0.1 \text{ in.}$ $n = 3$		k_p for Notch Size, c , of	
c/b	k_t	25 mm = 1 in.	2.5 mm = 0.1 in.
1	3	3.00	2.47
2	5	4.83	2.77
4	9	6.86	2.81

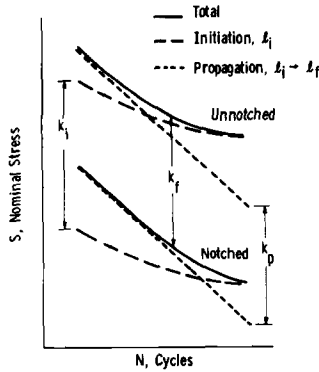


FIG. 9—Estimating notched specimen total life by first separating the life into initiation and propagation phases. Mildly notched members behave in this manner.

21, the total life is indicated to be mostly propagation at short lives, but mostly initiation at long lives. Thus, at intermediate lives there is a transition in behavior from propagation dominated to initiation dominated behavior.

These initiation and propagation phases of life are handled separately to predict the total life of the notched member. Since ℓ_i has been chosen as a sufficiently small crack size, the strength reduction factor for crack initiation, k_i , is simply equal to k_t . The strength reduction factor for the propagation life, k_p , is given by a relationship similar to Eq 16. Initiation and propagation lives can then be added to obtain total life for the notched member.

At any given life, a strength reduction factor for total life, k_f , may be defined as the ratio of the unnotched and notched member fatigue strengths. Figure 9 suggests that k_f will vary with life, always being intermediate in value between k_t and k_p . Also, based on Fig. 9, the transition from propagation dominated to initiation dominated behavior is expected to shift to longer lives for increasing notch sharpness. This is due to k_p increasing more slowly with notch sharpness than k_t . Such a trend and in general behavior similar to Fig. 9 is indeed observed for relatively mild notches [20,22].

However, an additional complexity must be added to explain the behavior of sharply notched members. Figure 10 shows long life fatigue strengths from Frost [23] for notches all of the same depth, but with a variety of different notch radii. These fatigue strengths are plotted as a function of k_t , with data being shown both for initiation and for failure. Initiation is controlled by k_t and the smooth specimen endurance limit, σ_e , as expected. However, beyond a certain sharpness of notch, these initiated cracks do not propagate to failure, the failure stress becoming independent of k_t .

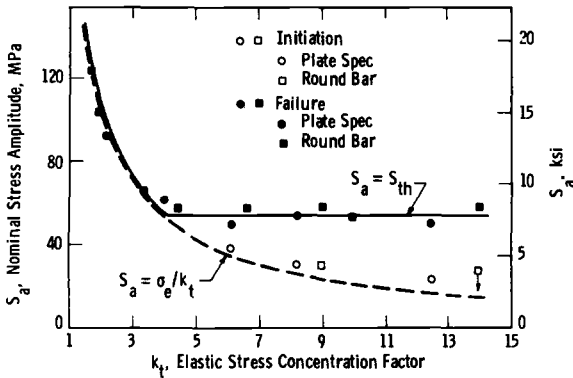


FIG. 10—Long life fatigue strengths for mild steel under completely reversed loading, for notches all of depth 5.1 mm (0.20 in.), but with various radii (Frost).

Analysis of a variety of similar data [23–25] reveals that this limiting failure stress is consistent with the fracture mechanics concept of a stress intensity threshold [26], K_{th} , below which fatigue crack growth does not occur. Considering the notch depth, c , as a crack length, and using the long crack limiting case of the stress intensity solution in the form of Eq 8, these limiting stresses are given by

$$S_{th} = \frac{K_{th}}{F \sqrt{\pi c}} \tag{17}$$

where the value of F is appropriate to each particular geometry according to Ref 17.

The intervention of such a limiting failure stress for sharply notched members modifies Fig. 9 as shown in Fig. 11. Fig. 11 suggests that, for very sharp notches, the life at all stress levels may be dominated by crack propagation. Such behavior is in fact observed [20]. From Fig. 10 and Eq 17, note that the notch sharpness necessary to cause propagation dominated behavior similar to Fig. 11, rather than behavior similar to Fig. 9, is

$$k_t > \frac{F \sigma_e \sqrt{\pi c}}{K_{th}} \tag{18}$$

In the development of Eq 16, and also in Table 2 and Figs. 9 and 11, note that linear elastic and continuum behavior are assumed. Thus, for engineering metals, these are strictly applicable only where plasticity effects are minor, that is, at relatively long lives or for highly strengthened alloys, and then only where all of the geometric dimensions of interest, such as crack length and notch radius, are large compared to the microstructure. However, the qualitative observations made are thought

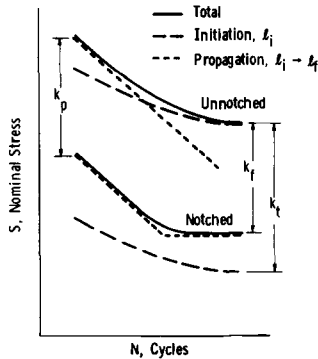


FIG. 11—Effect of crack growth threshold on relative positions of the notched and unnotched specimen S-N curves for a sharply notched member.

to be more widely applicable, as to ductile metals at short lives. In particular, crack propagation is thought generally to be the major source of size effect in notched members. As most engineering metals exhibit only slight plasticity in unnotched specimens tested at long lives, Eqs 17 and 18 are not severely limited. An exception is that neither is applicable to notches where the depth, c , is so small as not to be large compared to the microstructure of the material.

Notch Plasticity Effects

For crack initiation, local notch plasticity is accounted for by the local strain approach. Where initiation is predicted from another notched geometry by correlating lives with $k_t S$, plasticity effects are included because of similar strains occurring in both geometries at equal values of $k_t S$. If the gross behavior is elastic, notch plasticity will not affect the propagation of relatively long cracks, but its effect may be important for short cracks. It is therefore necessary to consider local notch plasticity in relation to crack propagation.

Plastic Zones at Notches

Based on the elasticity analysis of Ref 14, the stresses ahead of a notch are illustrated in Fig. 12 for one particular case of an ellipse in a wide plate, Fig 1b. Near the notch tip, the maximum and minimum principal stresses are σ_y and σ_x . This is true both for plane strain, which is illustrated, and for plane stress, where σ_z is absent.

Using the maximum shear stress criterion, the yield strength is exceeded over the distance $e/2$, where the difference $(\sigma_y - \sigma_x)$ exceeds the uniaxial yield strength, σ_y . However, equilibrium of forces requires some

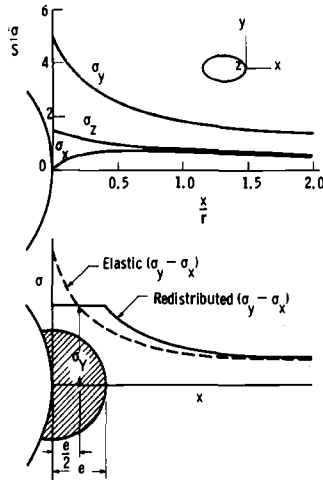


FIG. 12—Plastic zone at a notch estimated from elastic analysis.

redistribution of stresses, resulting in a plastic zone that extends roughly to a distance e from the notch tip. The preceding logic is similar to that used in estimating the plastic zone at a crack tip [27].

Applying this procedure to the stress distribution developed by Creager [11] for sharp notches gives

$$e = r[(k_t S / \sigma_Y)^{2/3} - 1] \tag{19}$$

For a given value of fictitious notch stress, $k_t S$, note that e is proportional to r , the notch radius. Equation 19 is plotted in Fig. 13, along with the results of similar estimates for various other notch geometries from Figs. 1b and 1c. Where $k_t S / \sigma_Y$ is less than unity, there is no plasticity, hence $e = 0$.

Also shown in Fig. 13 are plastic zone sizes from the plane stress finite element analysis reported in Ref 28. These particular geometries do not correspond to any of the curves, but they should approximately agree with the central group of curves for various notches under uniaxial loading. The reasonable agreement obtained supports the validity of the estimates.

Applicability of Stress Intensity Solutions for Cracks at Notches

On each curve in Fig. 13, the value of ℓ_m is indicated. The previously mentioned value of $\ell_m = 0.199r$ applies to the Creager stress distribution, and the other values are those listed in Table 1. It is significant that in each case the estimated plastic zone size exceeds ℓ_m for loads only modestly

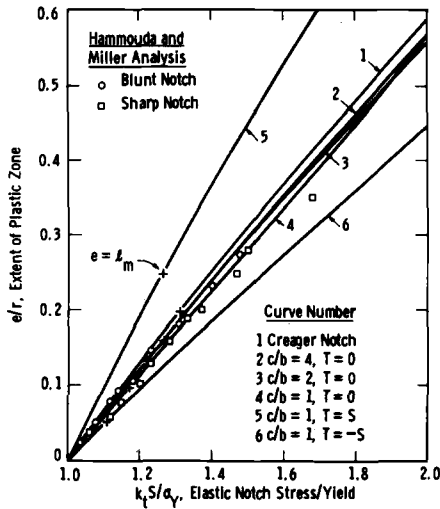


FIG. 13—Notch plastic zone size estimates for various cases of elliptical and circular holes in wide plates.

above those necessary to cause notch yielding. This occurs at values of $k_t S / \sigma_Y$ between approximately 1.1 and 1.3 for the cases illustrated, with the latter value applying to sharp notches in general. In other words, the local notch stress field, the size of which is characterized by ℓ_m , is engulfed by the plastic zone of the notch at loads just above those necessary to cause notch yielding. Note that linear elastic fracture mechanics is applicable only where the extent of plasticity is small compared to the other geometric dimensions, such as crack length. Also, note that notch plasticity usually is present in finite life fatigue, especially for ductile metals. This, it must be concluded that the small crack limiting case of the stress intensity solution, Eq 6, and also the special numerical solutions [16] for cracks at notches, as in Figs. 5 and 6, are of only limited usefulness for notch fatigue problems.

One method of overcoming this difficulty would be to employ elastic-plastic fracture mechanics for small cracks at notches. Analysis of this type is described in Ref 29 for a circular hole in a plate, where values of the J-integral [30] are computed from finite element analysis. Such an analytical result can be expressed in terms of values of stress intensity, K , which are modified, in particular, increased, to account for the effect of plasticity. For a given load causing notch yielding but not general yielding, the difference between such plasticity modified K values and the ordinary elastic solution decreases with increasing crack length [29]. Hence, the plasticity effect dies out with increasing distance from the notch.

Consider crack lengths equal to or greater than ℓ_m , and exclude loads approaching general yielding. In this case, the linear elastic stress intensity solution is given approximately by the long crack limiting case, such as Eq 8. The plastic zone size for this situation, from the expression due to Irwin [27] in the form applying to plane stress, is estimated to be

$$r_Y = \frac{1}{2\pi} \left(\frac{K}{\sigma_Y} \right)^2 \quad (20)$$

Combining Eqs 8 and 20 gives the ratio of plastic zone size to crack length, a , where $a = c + \ell$, as in Fig. 7a.

$$\frac{r_Y}{a} = \frac{1}{2} \left(\frac{FS}{\sigma_Y} \right)^2 \quad (21)$$

As F is often near unity, Eq 21 implies that the plastic zone size is small compared to the effective crack length, $a = c + \ell$, except for loads approaching general yielding. Thus, for $\ell \geq \ell_m$, plasticity modified values of K are not generally expected to differ drastically from ordinary linear elastic values of K . For the case of a circular hole in a wide plate under remote uniaxial stress, and at $\ell = \ell_m$, the analysis of Ref 29 indicates that the plasticity effect on K is 10 percent at $S/\sigma_Y \approx 0.73$, and 20 percent at $S/\sigma_Y \approx 0.85$.

Therefore, it appears to be reasonable in most situations to use linear elastic fracture mechanics to estimate crack propagation lives beyond $\ell = \ell_m$. Errors in K due to plasticity effects of the magnitude just noted will not usually have a large effect on the life calculation, especially in view of the fact that such error will decrease as the crack propagates beyond ℓ_m . Note that this situation contrasts with that for short cracks at notches, where the plasticity effect on K is generally expected to be large.

Definition of Crack Initiation Considering Plasticity and Noncontinuum Effects

In an earlier portion of this paper, it was concluded from linear elastic analysis that geometry dependence of the initiation life could be avoided only by defining initiation as a crack size within the local notch stress field, as defined by crack length ℓ_m . But in the previous discussion, it was noted that plasticity effects usually must be considered for fracture mechanics to be applied to cracks in this local notch stress field.

An additional complexity besides plasticity must be considered if short cracks at notches are to be analyzed using a fracture mechanics type of approach. Even under linear elastic conditions, short cracks may not behave as predicted from fracture mechanics data obtained using speci-

mens with long cracks [7,31,32]. This is due apparently to the lack of a continuum at small size scales, as a result of crystallographic grains or other microstructure. In another paper in this symposium [33], tentative methods are described for including in a fracture mechanics type approach both local notch plasticity and this problem with the lack of a continuum at small size scales. The approach of Ref 33 can be used to predict lives of notched members by considering the entire life to be crack propagation [34].

Another alternative is to define crack initiation as a crack length on the order of ℓ_m , using strain-life data corresponding to this same crack size to predict the number of cycles to initiation. This avoids applying fracture mechanics to very small cracks, and makes it unnecessary to analyze plasticity effects on cracks within the local notch stress field. Of course, such a definition of initiation is expected also to avoid difficulties with apparent notch size effects, as discussed earlier.

Procedure for Predicting Total Life

Based on the preceding discussion, a procedure may be assembled for the purpose of predicting total fatigue lives of notched members. The goal of this procedure is to handle notch size and plasticity effects in as simple a manner as possible while avoiding serious error. It is assumed that general yielding does not occur in the notched member.

First, estimate initiation life from either the local strain approach or from notched specimen data correlated in terms of $k_t S$. Initiation must be defined as a crack of size similar to ℓ_m , which size is of the order of one tenth of the notch radius.

Then use linear elastic fracture mechanics to calculate the propagation life from the initiation size to the size considered as failure. Use only the long crack limiting case of the stress intensity solution, and base the calculation on appropriate fatigue crack growth rate data. If desired, the minor plasticity effects which may occur outside the local notch stress field may be handled in the traditional manner [27] of increasing the crack length by the plastic zone size, as from Eq 20, before computing stress intensities, K . The initiation and propagation lives are, of course, added to obtain the total life. Failure may be assumed never to occur below the limiting stress given by Eq 17. If Eq 18 applies, it is likely that at all stress levels the initiation life will be a small fraction of the total life.

Comparison of Life Prediction Procedure with Experimental Data

Life predictions made on this basis are illustrated in Figs. 14 and 15 for bluntly and sharply notched plates under completely reversed loading. The material is the same as that in Fig. 4. Notch strains were estimated by using Neuber's rule, Eq 2, with the cyclic stress-strain curve [4] for this

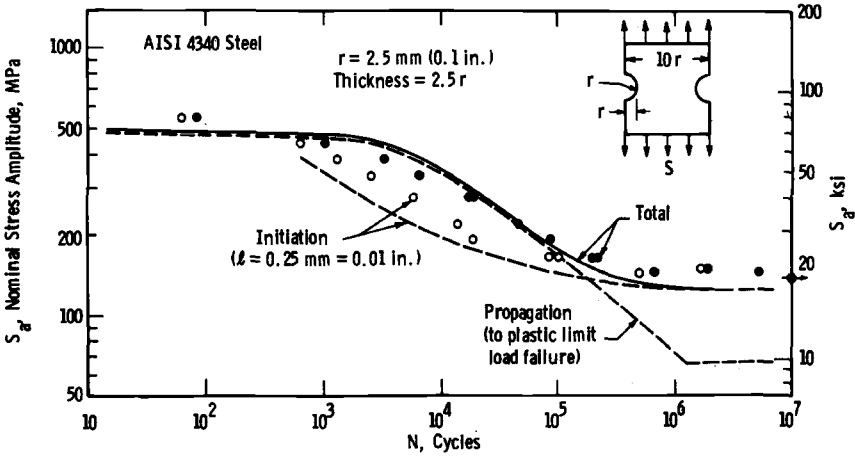


FIG. 14—Predicted behavior and test data for completely reversed loading of bluntly notched specimens.

material. These notch strains were then used with strain-life curves similar to those in Fig. 4 to obtain life estimates. From Eq 10, the ℓ_m values for blunt and sharp notches were 0.25 mm (0.01 in.) and 0.0125 mm (0.0005 in.), respectively. Strain-life data corresponding to the former, although not shown in Fig. 4, were available and were used. But the latter size is smaller than the smallest crack observations made in the strain-life tests, so that it was necessary to use the lower curve of Fig. 4.

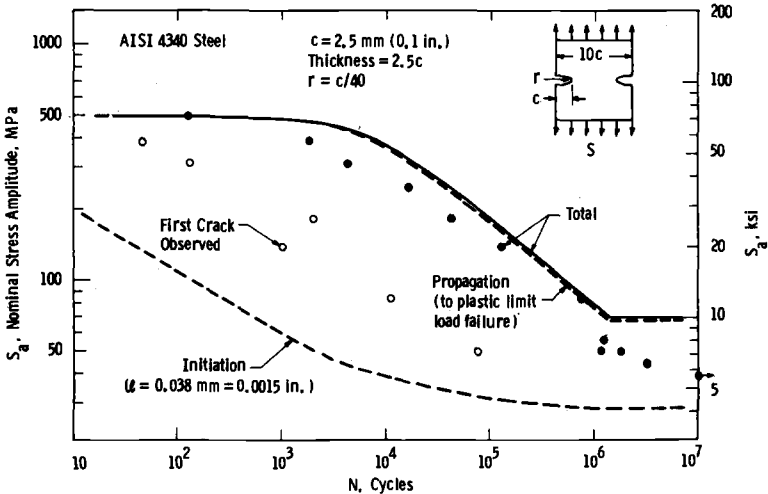


FIG. 15—Predicted behavior and test data for completely reversed loading of sharply notched specimens.

Fatigue crack growth rate data for approximately zero to tension loading ($R = 0.1$) were available for this material. These data were fitted to Eq 13 and then used with an appropriate stress intensity expression [17] to predict the propagation life curves shown in Figs. 14 and 15. The completely reversed loading in the notched specimens was handled by assuming that the compressive portion of the cycle did not contribute to crack growth. No plasticity correction was made, and propagation was predicted to terminate when the remaining uncracked ligament reached a net section stress equal to the yield strength. This latter assumption resulted in the propagation life curve approaching an upper limiting stress corresponding to net section yielding of an uncracked specimen. Appropriate test data being unavailable, Eq 17 was used with an estimated value of $K_{th} = 6.0\text{MPa}\sqrt{\text{m}}$ ($5.5\text{ksi}\sqrt{\text{in.}}$) to obtain a lower limiting stress below which failure was not expected even if initiation did occur.

Initiation and propagation lives were then added to obtain the total life curves which are shown in Figs. 14 and 15. For the blunt notch, a transition from propagation dominated to initiation dominated behavior was predicted to occur around 2×10^5 cycles. For the sharp notch, the initiation lives were always very short compared to the propagation lives, so that the life at all stresses was predicted to consist almost entirely of crack propagation. Hence, the lack of strain-life data at a crack length corresponding to the very small ℓ_m value for the sharp notch did not adversely affect prediction of the total life.

After the life prediction calculations had been made, tests were conducted, with the results being shown as data points in Figs. 14 and 15. In the bluntly notched specimens, the initiation data plotted correspond to a notch surface crack having a width equal to twice the crack depth, ℓ , defined as initiation. In the sharply notched specimens, the crack was not generally observed until its width exceeded half the specimen thickness, that is, after considerable propagation.

The test data of Figs. 14 and 15 are in reasonable agreement with the life predictions, and all major trends which were predicted were observed. In the sharply notched specimen, as expected on the basis of Eq 18, the initiation lives were a negligible fraction of the total lives. In the bluntly notched specimens, the initiation lives were longer than predicted, the nominal stresses corresponding to given values of life being on the average about 15 percent higher than predicted. At short lives, this could be due to Neuber's rule overestimating the notch strains. However, this does not apply at long lives where the behavior is elastic. It is possible that a weakest-link statistical size effect as predicted by Weibull [35] is having an influence here, the amount of highly stressed material being smaller in the notched specimen than in the unnotched specimen.

The propagation lives were somewhat shorter than predicted. It is likely that this is due principally to compressive loading contributing to crack

growth, contrary to the assumption made. At high stresses, the growth rates also may have been increased due to plastic deformation effectively increasing K above the linear elastic values used. The estimated value of K_{th} was apparently inaccurate, some of the sharply notched specimens failing below the predicted lower limiting stress.

Discussion of Life Prediction Procedure

Mean stress and variable amplitude loading effects are not considered specifically in this paper. However, the procedure just suggested provides a framework within which the various methods which have been developed for handling these effects can be applied. An exception is that correlation of initiation lives using k, S makes it difficult to account for mean stress effects, whereas the local strain approach has no such difficulty [6,8,36].

The life prediction procedure as described does not account for weakest-link size effects predicted [35] on a statistical basis due to different volumes or surface areas of highly stressed material in different geometries. This complexity applies principally to the initiation life and could be included easily. However, with reference to an earlier portion of this paper, note that the gross size effects in sharply notched members sometimes attributed to this cause can be explained in terms of problems with defining crack initiation. The problem of defining crack initiation has been dealt with, of course, and the apparent size effects arising from notch plasticity are accounted for. The actual weakest-link type size effect is thought to be minor in most applications.

One disadvantage of the procedure suggested is that it requires initiation data for specific small crack lengths, data which are difficult to obtain. It may be possible to develop methods of using total life data to estimate curves such as those in Fig. 4. Of some use here may be the hypothesis that the transition from propagation dominated to initiation dominated behavior in unnotched specimens is associated with the transition [37] from plastic deformations at short lives to elastic deformations at long lives.

Detailed initiation data are not always needed. The total life prediction in Fig. 14 is insensitive at long lives to the definition of initiation. This is due to the convergence of the various curves in Fig. 4. In Fig. 15, the definition of initiation is unimportant due to propagation dominating the behavior at all stress levels.

There is a need for additional analytical study of plasticity effects on cracks near notches. When such a study becomes available, the various inferences made in this paper on the basis of linear elastic analysis should be reexamined.

The life prediction procedure suggested for notched members is one of several that have been described recently [18,33,34,38], and others may be developed in the future. It is hoped that the extensive discussion provided will aid in comparing these various procedures and will stimulate discussion and further work. Any successful procedure must handle, either directly, or indirectly, the effects of plastic deformation, local notch fields, crack propagation, and noncontinuum behavior of very small cracks.

Conclusions

Total fatigue lives of notched members may be estimated by adding initiation and propagation lives. The initiation life prediction must account for plasticity effects, either directly or indirectly. Crack initiation must be defined as a specific small size on the order of one tenth of the notch radius. Crack propagation may generally be predicted from linear elastic fracture mechanics. Such a procedure for predicting total fatigue lives will automatically account for the major source of notch size effects, namely crack propagation out of the local notch stress field.

Acknowledgments

Westinghouse Electric Corporation sponsored the experimental work and preparation of this paper. The atmosphere and facilities which were required exist largely due to the efforts of E. T. Wessel, Manager of Structural Behavior of Materials, Westinghouse Research and Development Center.

References

- [1] Mowbray, D. F. and McConnellee, J. E., "Application of Finite Element Elastic-Plastic Stress Analysis to Notched Fatigue Specimen Behavior," 1st International Conference on Structural Mechanics in Reactor Technology, Vol. 5, West Berlin, Sept. 1971, pp. 425-441.
- [2] Wilson, W. K. in *Journal of Pressure Vessel Technology; Transactions*, American Society of Mechanical Engineers, Vol. 96, No. 4, Nov. 1974, pp. 293-298.
- [3] Kotani, S., Koibuchi, K., and Kasai, K., "The Effect of Notches on Cyclic Stress-Strain Behavior and Fatigue Crack Initiation," Mechanical Engineering Research Laboratory, Hitachi, Ltd., Kandatsu, Tsuchiura, Japan, 1977.
- [4] Landgraf, R. W., Morrow, J., and Endo, T., *Journal of Materials*, American Society for Testing and Materials, Vol. 4, No. 1, March, 1969, pp. 176-188.
- [5] Neuber, H., *Journal of Applied Mechanics; Transactions*, American Society of Mechanical Engineers, Vol. 28, Dec. 1961, pp. 544-550.
- [6] Dowling, N. E., Brose, W. R., and Wilson, W. K. in *Fatigue Under Complex Loading—Analyses and Experiments*, Advances in Engineering Series, Vol. AE-6, Society of Automotive Engineers, 1977, pp. 55-84.
- [7] Dowling, N. E. in *Cyclic Stress-Strain and Plastic Deformation Aspects of Fatigue Crack Growth*, ASTM STP 637, American Society for Testing and Materials, 1977.

- [8] Wetzel, R. M., *Journal of Materials*, American Society for Testing and Materials, Vol. 3, No. 3, Sept. 1968, pp. 646-657.
- [9] Topper, T. H., Wetzel, R. M., and Morrow, J., *Journal of Materials*, American Society for Testing and Materials, No. 1, March 1969, pp. 200-209.
- [10] Paris, P. C. and Sih, G. C. in *Fracture Toughness Testing and Its Applications*, ASTM STP 381, American Society for Testing and Materials, 1965, pp. 30-83.
- [11] Creager, M. and Paris, P. C., *International Journal of Fracture Mechanics*, Vol. 3, No. 4, Dec. 1967, pp. 247-252.
- [12] Barsom, J. M. and McNicol, R. C. in *Fracture Toughness and Slow-Stable Cracking*, ASTM STP 599, American Society for Testing and Materials, 1974, pp. 183-204.
- [13] Clark, W. G., Jr. in *Fracture Toughness and Slow-Stable Cracking*, ASTM STP 559, American Society for Testing and Materials, 1974, pp. 205-224.
- [14] Inglis, C. E., *Transactions*, Institute of Naval Architects (British), Vol. 60, 1913, pp. 219-230.
- [15] Peterson, R. E., *Stress Concentration Factors*, Wiley, New York, 1974.
- [16] Newman, J. C., Jr., "An Improved Method of Collocation for the Stress Analysis of Cracked Plates with Various Shaped Boundaries," NASA TN D-6376, National Aeronautics and Space Administration, Washington, D.C., Aug. 1971.
- [17] Tada, H., Paris, P. C., and Irwin, G. R., *The Stress Analysis of Cracks Handbook*, Del Research Corporation, Hellertown, Pa., 1973.
- [18] Smith, R. A. and Miller, K. J., *International Journal of Mechanical Engineering Science*, Vol. 19, 1977, pp. 11-22.
- [19] Peterson, R. E. in *Proceedings*, Symposium on Fatigue of Aircraft Structures; WADC Technical Report 59-507, Aug. 1959, pp. 273-299.
- [20] Hunter, M. S. and Fricke, W. G., Jr. in *Proceedings*, American Society for Testing and Materials, Vol. 57, 1957, pp. 643-654.
- [21] Manson, S. S., *Experimental Mechanics*, Society for Experimental Stress Analysis, Vol. 5, No. 7, July 1965, pp. 193-226.
- [22] Gowda, C. V. B., Leis, B. N., and Smith, K. N., *Journal of Testing and Evaluation*, American Society for Testing and Materials, Vol. 2, No. 1, Jan. 1974, pp. 57-61.
- [23] Frost, N. E., *Journal of Mechanical Engineering Science*, Vol. 2, No. 2, 1960, pp. 109-119.
- [24] Frost, N. E. and Dugdale, D. S., *Journal of the Mechanics and Physics of Solids*, Vol. 5, 1957, pp. 182-192.
- [25] Frost, N. E. in *Proceedings*, Institution of Mechanical Engineers, Vol. 173, No. 35, 1959, pp. 811-827.
- [26] Schmidt, R. A. and Paris, P. C. in *Progress in Flaw Growth and Fracture Toughness Testing*, ASTM STP 536, American Society for Testing and Materials, 1973, pp. 79-94.
- [27] McClintock, F. A. and Irwin, G. R. in *Fracture Toughness Testing and Its Applications*, ASTM STP 381, American Society for Testing and Materials, 1965, pp. 84-113.
- [28] Hammouda, M. M. and Miller, K. J., "Elastic-Plastic Fracture Mechanics Analysis of Notches," *Elastic-Plastic Fracture*, ASTM STP 668, American Society for Testing and Materials, 1979.
- [29] Sumpter, J. D. G. and Turner, C. E., "Fracture Analysis in Areas of High Nominal Strain," 2nd International Conference on Pressure Vessel Technology, San Antonio, Tex., 1973.
- [30] Rice, J. R., *Journal of Applied Mechanics; Transactions*, American Society of Mechanical Engineers, Vol. 35, June 1968, pp. 379-386.
- [31] Kitagawa, H., Takahashi, S., "Applicability of Fracture Mechanics to Very Small Cracks, or the Cracks in the Early Stage," 2nd International Conference on Mechanical Behavior of Materials, American Society for Metals, Boston, Ma., Aug. 1976, pp. 627-631.
- [32] El Haddad, M. H., Smith, K. N., and Topper, T. H., "Fatigue Crack Propagation of Short Cracks," 1978 ASME/CSME Joint Conference on Pressure Vessels and Piping, Nuclear Energy, and Materials, Montreal, Quebec, June 1978.
- [33] El Haddad, M. H., Smith, K. N., and Topper, T. H., this publication, pp. 274-289.
- [34] El Haddad, M. H., Ph.D. thesis, Department of Civil Engineering, University of Waterloo, Waterloo, Ontario, Canada, Aug. 1978.

- [35] Weibull, A., "A Statistical Theory of the Strength of Materials," *Proceedings*, Royal Swedish Institute for Engineering Research, Stockholm, Sweden, 1939.
- [36] Fuchs, H. O. in *Fatigue Under Complex Loading—Analyses and Experiments*, Advances in Engineering Series, Vol. AE-6, Society of Automotive Engineers, 1977, pp. 203–207.
- [37] Landgraf, R. W. in *Achievement of High Fatigue Resistance in Metals and Alloys*, ASTM STP 467, American Society for Testing and Materials, 1970, pp. 3–86.
- [38] Socie, D. F., Morrow, J., and Chen, W., "A Procedure for Estimating the Total Fatigue Life of Notched and Cracked Members," submitted to *Engineering Fracture Mechanics*, March 1978.

M. H. El Haddad,¹ K. N. Smith,² and T. H. Topper²

A Strain Based Intensity Factor Solution for Short Fatigue Cracks Initiating from Notches

REFERENCE: El Haddad, M. H., Smith, K. N., and Topper, T. H., "A Strain Based Intensity Factor Solution for Short Fatigue Cracks Initiating from Notches," *Fracture Mechanics, ASTM STP 677*, C. W. Smith, Ed., American Society for Testing and Materials, 1979, pp. 274–289.

ABSTRACT: A strain-based intensity factor is introduced which, while becoming equivalent to the linear elastic stress intensity factor for long elastic cracks, admits plasticity by replacing the conventional stress term with a strain term and accounts for the proximity of a short crack to a free surface by the inclusion of a length constant. Crack growth results for short cracks in both elastic and plastic strain fields of unnotched specimens, when interpreted in terms of this intensity factor, show excellent agreement with elastic long crack data. This intensity factor is then extended to plastically strained notches and the solutions obtained are tested in the correlation of short crack growth data for notches of varying severity with elastic long crack data. Constant stress amplitude tests of these notches gave crack growth rate versus crack length curves which varied from monotonically increasing for blunt notches to an initial decrease followed by an increase for sharp notches. However, all of the data fell within the long crack data when correlated by this inelastic intensity factor. Conversely, solutions for the parameter were used successfully to predict elastic and inelastic short crack growth curves for notches of various severities.

KEY WORDS: crack propagation, stresses, strains, stress and strain concentration factors, stress intensity factor, fatigue (materials).

Nomenclature

- E Modulus of elasticity
- K' Theoretical stress concentration factor, a function of crack length
- K_t Stress concentration factor of uncracked notches
- K'_σ Stress concentration factor, a function of crack length

¹ Research engineer, Ontario Hydro, 800 Kipling Ave., Toronto, Ontario, Canada M8Z 5S4.

² Associate professor and professor, respectively. Department of Civil Engineering, University of Waterloo, Waterloo, Ontario, Canada N2L 3G1.

$K'\epsilon$	Strain concentration factor, a function of crack length
N	Number of cycles
R	Ratio of minimum to maximum stress
da/dN	Crack growth rate
ℓ	Crack length measured from the edge of the notch
ℓ_0	Material constant
a	Total crack length including the depth of the notch
b	Half the plate width
c	Depth of the notch
ρ	Notch root radius
e_a	Endurance limit strain amplitude
Δe	Nominal strain range
Δs	Nominal stress range
$\Delta \epsilon$	Local strain range around crack tip in notched specimens
$\Delta \sigma$	Local stress range around crack tip in notched specimens
ΔK	Stress intensity factor
ΔK_{th}	Threshold stress intensity factor

Most of the fatigue life in many engineering structures is spent in initiating a crack at a notch root and propagating it through the region of stress concentration of the notch. However, analysis of this early stage of crack growth is not possible in terms of linear elastic fracture mechanics which is neither applicable to the plasticity generated in notches at high load levels nor accurate for very short cracks. Thus a significant portion of the fatigue life for many practical problems cannot be predicted using currently available elastic solutions. To date, investigators have obtained elastic stress intensity factors for cracks initiating from a wide range of geometries of stress raisers [1].³ Liu [2] noted that solutions given by Bowie [3] correlated well with crack propagation results for 2024-T851 aluminum circular notched plates for applied stress levels below one third of the material yield strength. Hill and Boutle [4] found that short cracks initiated from a stress concentration at high nominal stresses did not demonstrate the growth rates predicted on the basis of linear elastic fracture mechanics. Broek [5] also found that the use of elastic solutions [3] resulted in an underestimation of stress intensity in the early stages of crack growth from circular holes in 2024-T3 clad sheet specimens. Gowda, Topper, and Leis [6] modified Bowie [3] solutions to account for plasticity correlated crack propagation rates at various inelastic stress levels in circularly notched steel plates. However, they noted that the relationship between modified stress intensity factor and crack growth rate no longer followed the usual linear form on logarithmic coordinates. Crack propagation rates in the last two investigations also

³ The italic numbers in brackets refer to the list of references appended to this paper.

showed a further feature not predicted by conventional fracture mechanics, a decrease in the early stages of crack growth followed by an increase indicating that the stress intensity also should exhibit a corresponding decrease followed by an increase. An indication of a similar initial decrease in stress intensity is found in the observation of cracks that initiate but then cease to propagate [7]. The failure of existing elastic solutions for stress intensity factors to exhibit this characteristic is believed to be due to local plasticity and the inability of the aforementioned solutions to correlate the behavior of short cracks.

This paper presents an elastic plastic fracture mechanics solution for cracks initiating from notches under fatigue loading taking into consideration the effects of local plasticity around notch roots and the effect of crack size on the fatigue crack propagation process.

Fracture Mechanics Solutions for Fatigue Cracks

Smooth Specimens

Several investigators [8-12] have obtained correlations between fatigue crack growth rate and parameters expressed in terms of strain and length in inelastic crack propagation similar to the logarithmically linear stress intensity versus crack growth rate curves typical of elastic crack propagation. If a strain-based intensity factor ΔK for a crack length ℓ is taken in the form

$$\Delta K = E \Delta e \sqrt{\pi \ell} \quad (1)$$

where Δe and E are the applied strain range and modulus of elasticity of the material, respectively, the intensity factor at elastic stress levels becomes the linear elastic stress intensity ΔK

$$\Delta K = \Delta s \sqrt{\pi \ell} \quad (1a)$$

where Δs is the applied stress level. The present authors [13] have suggested that when cracks are short and the crack tip is near a free surface, Eq 1 and 1a should be modified further by increasing the effective crack length by an amount ℓ_0 where ℓ_0 is a constant characteristic of a given material and material condition to give

$$\Delta K = E \Delta e \sqrt{\pi(\ell + \ell_0)} \quad (2)$$

For elastic stress levels Eq 2 becomes

$$\Delta K = \Delta s \sqrt{\pi(\ell + \ell_0)} \quad (2a)$$

while for crack lengths much greater than ℓ_o , Eq 2 and $2a$ reduce to 1 and $1a$, respectively. Taking the usual definition of the threshold stress intensity (ΔK_{th}) as the minimum stress intensity that will give rise to crack propagation and the endurance limit strain amplitude e_a as the minimum strain amplitude at which a smooth specimen will fail by crack propagation, ℓ_o may be obtained from Eq 2 as

$$\ell_o = \frac{1}{\pi} \left(\frac{\Delta K_{th}}{2Ee_a} \right)^2 \tag{3}$$

The effectiveness of the term ℓ_o in correlating crack growth rates for short cracks with those for long cracks is demonstrated in Fig. 1 using data from Ref 9. In Fig. 1a where ΔK values are calculated using Eq 1a which deletes the ℓ_o term, growth rate trends for short and long cracks diverge sharply at low ΔK values corresponding to short crack lengths while in Fig. 1b where Eq 2a including the ℓ_o term is used in the calculation of ΔK , the long and short crack curves converge at short crack lengths. Figure 2, which reproduces data from Refs 10 and 12 with ΔK values calculated in accordance with Eq 1, shows that when defined in this manner ΔK accurately correlates data over a wide range of inelastic strain levels. Still further evidence of the efficiency of ΔK as defined by Eq 2 in correlating crack propagation data is provided in Ref 13. There, this parameter causes short crack growth rate data from a wide range of inelastic strain levels that coincides with the elastic long crack curve.

Notched Specimens

In using Eq 2 to calculate intensity factors for cracks emanating from notches, the nominal strain term Δe should be replaced by the local strain in the vicinity of the crack tip $\Delta \epsilon$. This gives

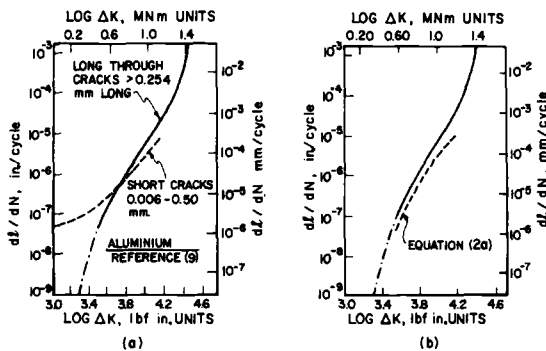


FIG. 1—Fatigue crack propagation curves for long and short cracks.

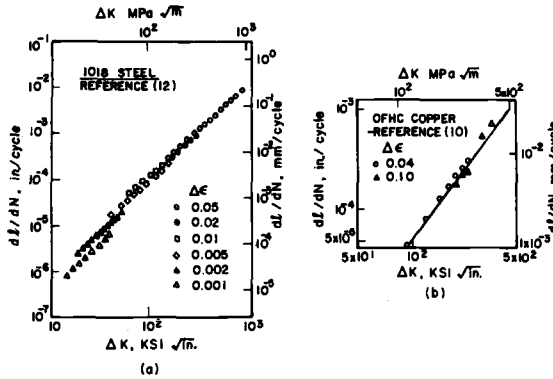


FIG. 2—Fatigue crack growth rates as a function of intensity factor ΔK .

$$\Delta K = E \Delta \epsilon \sqrt{\pi(\ell + \ell_0)} \tag{4}$$

When applied stress levels are low enough that notch strains remain elastic, solutions for the elastic stress concentration factor K' for a crack in a notch may be used to determine the local stress or strain in terms of the nominal stress or strain and Eq 4 becomes

$$\Delta K = EK' \Delta \epsilon \sqrt{\pi(\ell + \ell_0)} = K' \Delta s \sqrt{\pi(\ell + \ell_0)} \tag{4a}$$

Here the crack length is measured from the notch root and ℓ_0 is again the material constant defined by Eq 3. The stress concentration factor K' decreases as the crack length increases and approaches a value of $\sqrt{\frac{(\ell + c + \ell_0)}{(\ell + \ell_0)}}$, where c is the notch depth, as the crack passes outside the field of influence of the notch. Henceforth, the crack may be analyzed as a simple crack with a length equal to the actual crack length plus the notch depth.

At stress levels causing notch plasticity a general yielded zone develops at the notch root as shown in Fig. 3. While this zone has no influence on a long crack where the crack tip lies outside it, such as that shown in the lower half of the figure, it will for a short crack such as that shown in the upper half of the figure surround both the crack tip and its plastic zone. In the latter case the elastic solution defining the stress concentration factor K' is invalid and an inelastic solution for local strains is required. Although neither exact nor finite element plastic solutions are generally available for cracks in notches, estimates of local strains may be derived from a relationship between concentration factors proposed by Neuber [14]. He suggested that concentration factors for stress intensities would have the same form as a relationship he developed for notch root

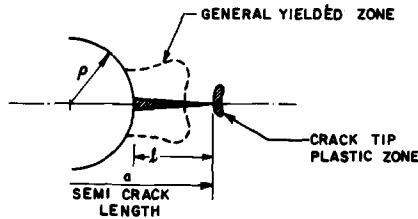
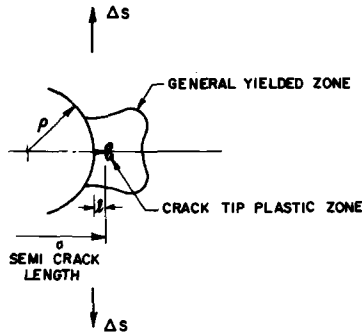


FIG. 3—General yielded zone around notch root.

stress and strain concentration factors in a shear strained member with deep longitudinal notches. The form proposed by Neuber is

$$K'^2 = K'_\epsilon \cdot K'_\sigma \tag{5}$$

where $K'_\sigma = \Delta\sigma / \Delta s$ is the stress concentration factor relating the stress range ($\Delta\sigma$) in the vicinity of the crack tip to the nominal stress, and $K'_\epsilon = \Delta\epsilon / \Delta e$ is the strain concentration factor relating local and nominal strain ranges. Rewriting Eq 5 in terms of stress and strain gives

$$K'^2 \Delta s \cdot \Delta e \cdot E = \Delta\sigma \Delta\epsilon E$$

or for the practical case of elastic nominal stress levels

$$K' \Delta s = [\Delta\sigma \Delta\epsilon E]^{1/2} \tag{6a}$$

Values of the left hand side of Eq 6a for a given crack length and nominal stress may be computed using elastic solution for K' [1]. Since terms on the right hand side involve only material stress-strain response a base curve of $(\Delta\sigma \cdot \Delta\epsilon E)^{1/2}$ versus $\Delta\epsilon \cdot E$ can be constructed from stress-strain data for a given material as shown in Fig. 4. Hence the value of $\Delta\epsilon \cdot E$ corresponding to a given value of $K' \Delta s$ can be obtained and

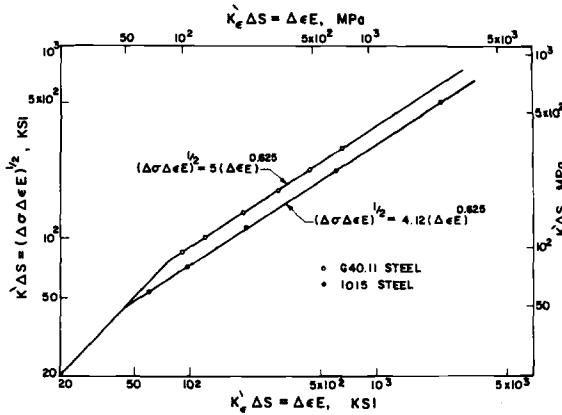


FIG. 4—Base curve of $(\Delta \sigma \Delta \epsilon E)^{1/2}$ versus $\Delta \epsilon E$.

inserted in Eq 4 to determine the stress intensity factor. If Eq 4 is recast in terms of the strain concentration factor K'_ϵ we have

$$\Delta K = EK'_\epsilon \Delta e \sqrt{\pi(\ell + \ell_0)} \tag{4b}$$

Figure 5 which compares values of K'_ϵ with those for K' in an elliptical notch at a stress level causing notch root plasticity illustrates the large differences between the Neuber solution and the elastic solution at short crack lengths. The two solutions converge at longer crack lengths, and Eq 4a then gives the same results as those obtained employing Eq 4b. It is of some interest that the distance at which $K'_\epsilon = K'$ corresponds to the size estimated for the general yielded zone in the absence of a crack [16].

Further refinements applied in the calculation of intensity factors for long cracks in this paper are the Irwin [17] correction which adds the plastic zone size to the crack length and a finite width correction [18].

Experimental Details

Constant amplitude load controlled testing at different stress levels was performed in a closed loop servocontrolled electromechanical testing machine. Three types of specimens were used fabricated from two steels CSA G40-11 and SAE 1015. The first two specimen types were plate specimens containing circular and elliptical holes. The third specimen type, a plate with two cracks grown from a small central hole to a total length equal to the size of the elliptical and circular holes, was used to obtain crack propagation data for comparison with that from the other types. Crack propagation rates were determined from traveling microscope measurements of crack lengths at various cycle numbers.

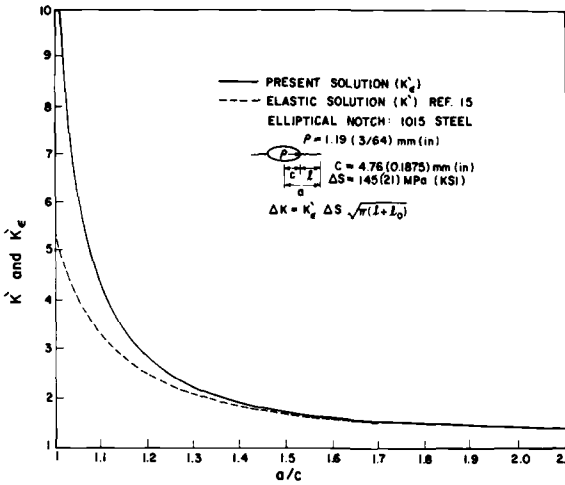


FIG. 5—Elastic and plastic solutions for K'_e .

Results and Discussion

Fatigue Crack Growth Rates

Figures 6 and 7 compare the rate of fatigue crack propagation in a G40.11 steel for five combinations of geometry and load level with that for a central crack on a da/dN versus $\Delta s \sqrt{\pi a}$ basis. Here a is taken as the semi-crack length with the notch depth being included in the crack length. In all cases fatigue crack propagation rates for notched specimens are initially higher than the rate for the central crack but this difference continually reduces and eventually disappears with increasing crack length. A further observation of interest is that while cracks in the specimens having circular notches have continuously increasing crack growth rates the cracks in the elliptically notched specimen exhibit a crack growth rate that initially decreases, reaches a minimum and thereafter increases. A similar decrease in crack growth rates is found in experimental results given by Broek [5] for cracks initiating from the end of a 0.50-mm slit cut at the edges of circular notches in 2024-T3 alclad sheet specimens. A further example of this initially decreasing crack growth rate in a specimen with a sharply decaying notch strain field is found in the results at three stress levels in an elliptically notched 1015 steel given in Fig. 8. Smith, Miller, and Hammonda [19,20] predicted this trend based on the argument that initiation and early growth of a crack is controlled by the plastic strain field of the notch which diminishes rapidly. They explained the latter increase in terms of the increasing stress intensity with crack length. Although formulated somewhat differently

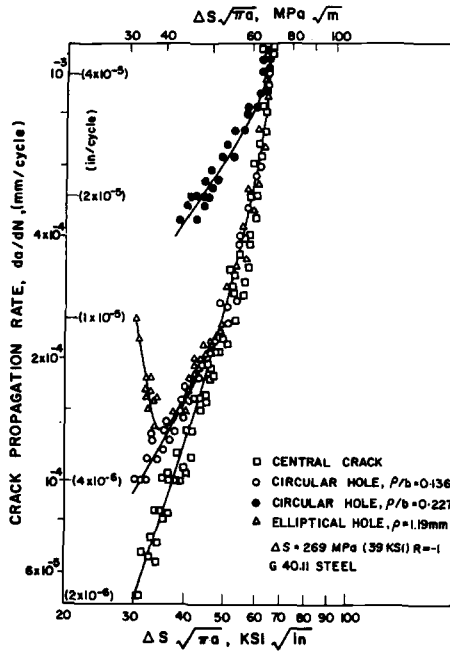


FIG. 6—Fatigue crack propagation results in case of G40.11 steel for different geometries.

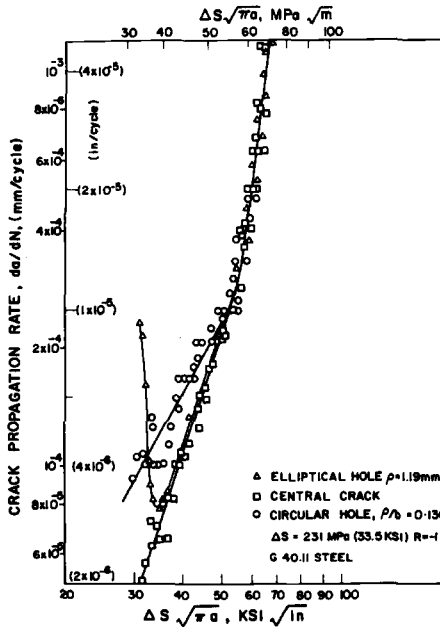


FIG. 7—Fatigue crack propagation results in case of G40.11 steel for different geometries.

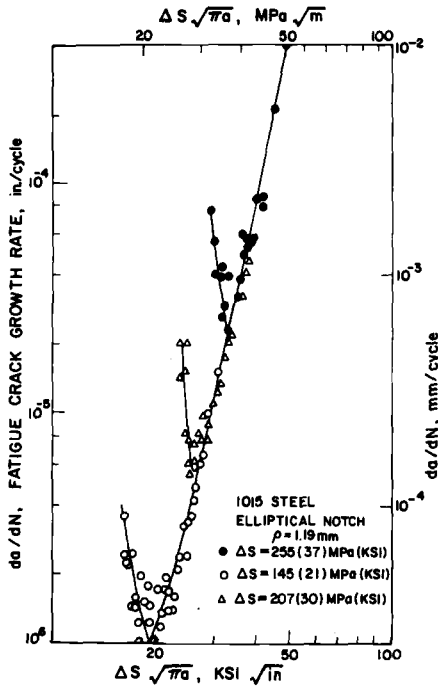


FIG. 8—Fatigue crack propagation results in case of 1015 steel for elliptical notches.

these arguments are very similar to those of the present theory. The major difference between their argument and the present approach is that in the latter the term ℓ_o specifically accounts for the effect of proximity to the surface in causing accelerated growth rates for short cracks independent of the effects of notch plasticity.

An example of the results achieved by the coupling of the short crack term ℓ_o with the Neuber approximation in calculating the plastic strain concentration factor is given in Fig. 9 for a stress range equal to 269 MPa causing plasticity around the root of an elliptical notch. In this figure experimental values of K'_ϵ are obtained by equating the unknown stress intensity at a given crack propagation rate in the notched specimen to the known stress intensity in a centrally cracked specimen having the same crack propagation rate. Note that this derivation assumes that when correctly computed equal values of ΔK give rise to equal crack growth rates in notched and centrally cracked specimens. Experimental and predicted values of K'_ϵ given in Fig. 9 show excellent agreement while estimates based on elasticity (K') would seriously underestimate the strain concentration for short cracks. As expected, at long crack lengths where the crack tip lies beyond the region of notch plasticity, elastic and inelastic solutions converge.

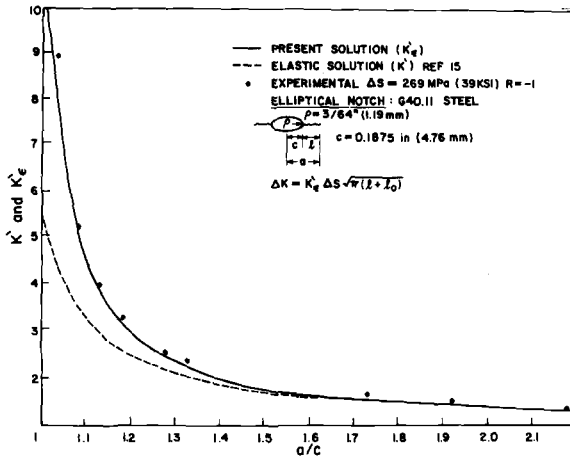


FIG. 9—Comparison between experimental and predicted results of $K'e$.

Straightforward calculations of intensity factors for the G40.11 and 1015 steel data by means of Eq 4 and the curves of Fig. 4 were performed and the results plotted versus da/dN in Figs. 10 and 11 respectively. The data show excellent agreement with the linear curve of the elastic long crack data which also are reproduced in these figures. Successful correlation also was demonstrated in Ref 21 using an approximate solution based on the J-integral method.

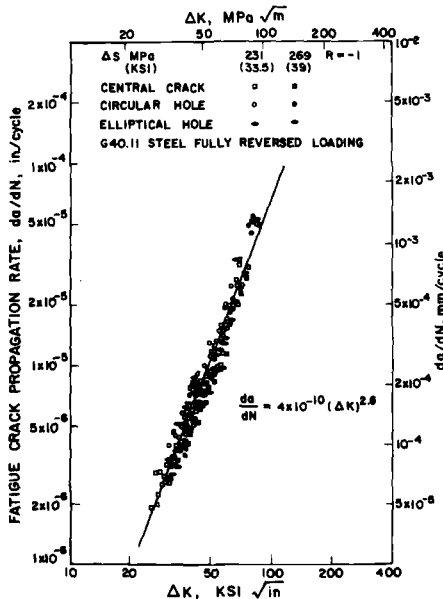


FIG. 10—Fatigue crack growth rates as a function of ΔK for G40.11 steel.

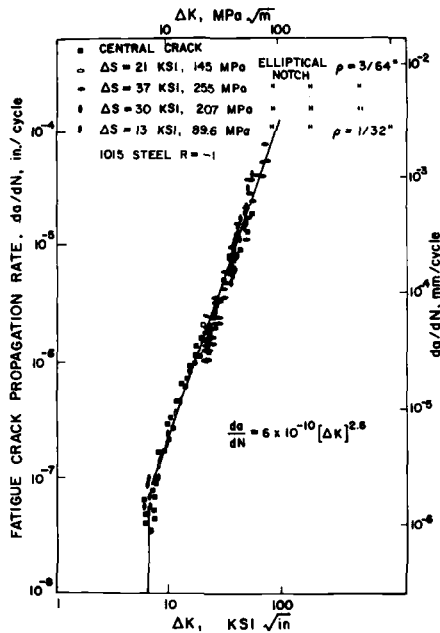


FIG. 11—Fatigue crack growth rates as a function of ΔK for 1015 steel.

Behavior of Cracks at Notches

The circular and elliptical notch data of Fig. 6 and the elliptical notch data of Fig. 8 are replotted in Figs. 12 and 13 respectively on scales of ΔK versus crack length. Crack length includes one half the depth of the notch and ΔK values are again those calculated using Eq 4 and Fig. 4. Predicted curves show excellent agreement with the data in all cases. The previously noted trends in crack growth rate reappear in Fig. 12 in the form of trends of ΔK values for both circular and elliptical notches that approach the central crack data as crack length increases. Convergence with the central crack data is more rapid for the elliptical notch data which initially decreases to minimum before increasing than for the circular notch data which continuously increases. Elliptical notch ΔK data again decrease to a minimum value and then increase as the crack extends for the load levels given in Fig. 13. This decrease moreover becomes more pronounced as the load level is increased.

Further insight into the dependence of ΔK versus crack length trends on notch geometry and size and the amount of local plasticity may be obtained if ΔK is plotted versus crack length in a nondimensional form by rearranging Eq 4b as follows:

$$\frac{\Delta K}{\Delta S \sqrt{\pi \ell_0}} = K' \epsilon \sqrt{\frac{\ell + \ell_0}{\ell_0}} \quad (7)$$

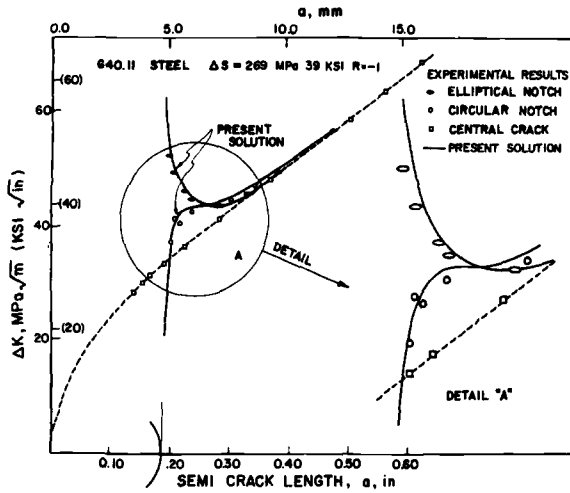


FIG. 12—Comparison between experimental and predicted results of ΔK for G40.11 steel.

Curves plotted on this basis compare the behavior of an elliptical notch, a circular notch, and a long crack for various notch diameters as shown in Fig. 14. Curves in the bottom half of the figure representing elastic notch root material response are independent of load level since K'_ϵ in Eq 7 will be equal to the elastic stress concentration factor K' . Here intensity factor values for small diameter circular and elliptical notches both initially decrease with crack length and then increase to converge with the central crack values. As the notch size is increased, this trend changes to one of continuously increasing intensity with crack length for both geometries. This change occurs at a smaller size for the circular than for

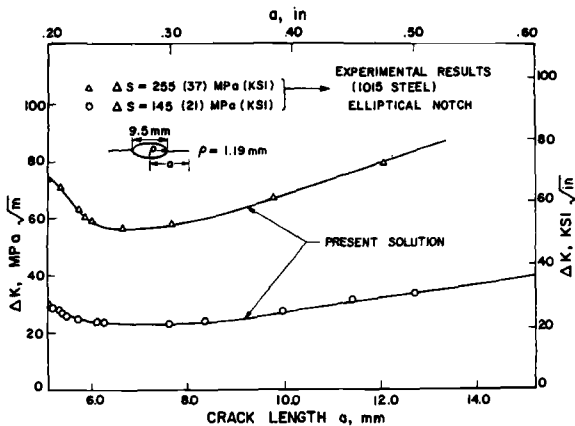


FIG. 13—Comparison between experimental and predicted results of ΔK for 1015 steel.

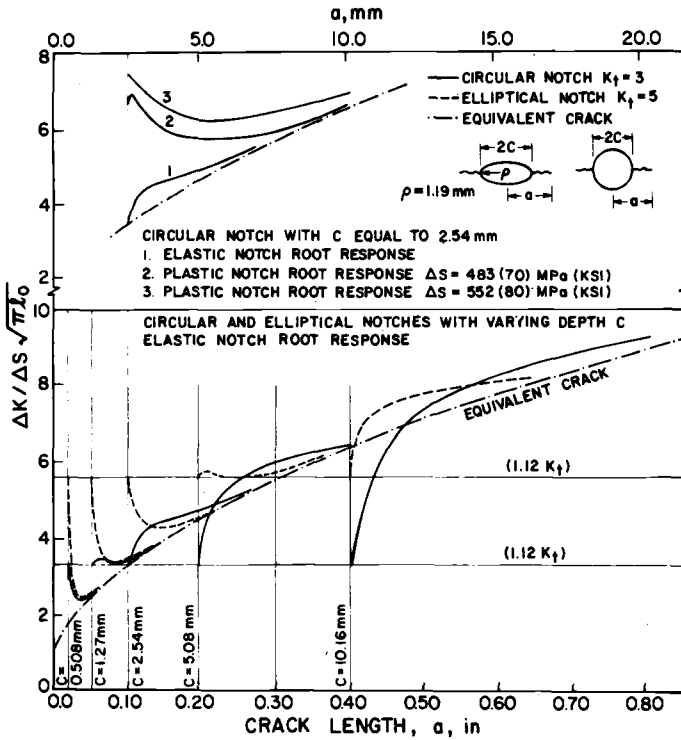


FIG. 14—Behavior of cracks at notches.

the elliptical notch with, for example, the minimum diameter for which subsequent intensities do not fall below the initial value being 2.54 mm for the former and 10.16 mm for the latter. In a recent work it is shown that this diameter is the minimum diameter for which a nonpropagating crack is possible at a constant cyclic load level [22]. At smaller diameters, if the load level applied results in an initial intensity above the threshold intensity for crack propagation but a minimum intensity below the threshold, crack growth will start and then cease when the applied intensity decreases to the threshold [22]. The upper part of Fig. 14 illustrates changes in curves of intensity versus length for a 5.08-mm diameter circular notch as the load is increased to levels causing notch plasticity. Changes in K'_ϵ , the strain concentration factor in Eq 4b at the two inelastic levels, increase intensities at the short crack lengths within the plastic zone close to the notch and raise the initial parts of the curves. However, the curves rejoin the elastic curve as the crack tip propagates beyond this inelastic region and K'_ϵ becomes equal to K' . However, the change in curve shape from continuously increasing to one having a minimum does not affect the minimum size for which nonpropagating cracks are possible in the materials considered which have an endurance

level strain at the elastic limit. Therefore, all load levels causing local metal plasticity will exceed the threshold stress intensity at any crack length.

Conclusions

1. The proposed strain-based intensity parameter accurately predicts crack growth data for short cracks and inelastic strains from elastic long crack data. It also permits a single characterization of crack growth for long and short cracks and elastic and inelastic strains and reduces to the linear elastic stress intensity factor for long cracks and elastic conditions.

2. This intensity factor when combined with plastic notch strain solutions based on an approximation suggested by Neuber also successfully correlated data for the growth of short cracks in plasticly strained notches with elastic long crack results. Conversely, short crack growth at inelastically strained notches was predicted accurately from long crack data.

3. Crack growth rate and the associated intensity factor trends for cracks in notches, that varied from an initial decrease to a minimum value followed by an increase and eventual convergence with the long crack trend for sharp notches to the blunt notch curves that continuously increased during their approach to the long crack trend, were predicted accurately.

4. Elastic solutions for intensity factor versus crack length showed that the change from these "sharp notch" to "blunt notch" trends depended both on notch geometry and notch size and delineated those notches for which nonpropagating cracks at cyclic constant load level were possible. Plastic solutions indicate that the ratio of the intensity factor within the plastic zone to that outside it progressively increases with increasing plasticity.

References

- [1] Rooke, D. P. and Cartwright, D. J., *Stress Intensity Factors*, Her Majesty's Stationery Office, London, 1976.
- [2] Liu, A. F., *Paper No. A1-1*, International Conference on Mechanical Behavior of Materials, Boston, Aug. 1976.
- [3] Bowie, O. L., *Journal of Mathematics and Physics*, Vol. 35, 1956.
- [4] Hill, S. J. and Boutle, N. F., 4th International Conference on Fracture, University of Waterloo, 1977, Vol. 2, p. 1233.
- [5] Broek, D., "The Propagation of Fatigue Cracks Emanating from Holes," NLR TR 72134 U, National Aerospace Laboratory, The Netherlands, 1972.
- [6] Gowda, C. V., Topper, T. H., and Leis, B. N., International Conference on Mechanical Behavior of Materials, Volume 2, Kyoto, Japan, 1972, pp. 187-198.
- [7] Frost, N. E., *The Aeronautical Quarterly*, Vol. 8, 1955, pp. 1.
- [8] McEvily, A. J., *Proceedings*, Air Force Conference on Fatigue and Fracture of Aircraft Structures and Materials, AFFDL-TR 70-144, pp. 451-456.
- [9] Pearson, S., *Engineering Fracture Mechanics*, Vol. 7, 1975, pp. 235-347.
- [10] Boettner, R. C., Laird, C., and McEvily, A. J., *Transactions*, Metallurgical Society of American Institute of Mechanical Engineers, Vol. 233, 1965, pp. 379-387.

- [11] Rau, C. A., Gemma, A. E., and Leverant, G. R. in *Fatigue at Elevated Temperature*, ASTM STP 520. American Society for Testing and Materials, June 1972, pp. 166–178.
- [12] Solomon, H. D., *Journal of Materials*, JMLSA, Vol. 7, No. 3, Sept. 1972, pp. 299–306.
- [13] El Haddad, M. H., Smith, K. N., and Topper, T. H., "Fatigue Crack Propagation of Short Cracks," Paper No. 78 Mat-7, 1978 ASME/CSME Joint Conference on Pressure Vessels and on Piping, Nuclear Energy, and Materials, Montreal, 25–29 June, 1978. Also in the *Journal of Engineering Materials and Technology*, Vol. 101, 1979, pp. 42–46.
- [14] Neuber, H., *Journal of Applied Mechanics*, American Society of Mechanical Engineers, Vol. 28, 1961, pp. 544–550.
- [15] Newman, J. C., "An Improved Method of Collocation for the Stress Analysis of Cracked Plates with Various Shaped Boundaries," Technical Note TN D-6376, National Aeronautics and Space Administration, Washington, D.C., Aug. 1971.
- [16] Grover, H. J., "Fatigue of Aircraft Structures," Naval Air Systems Command Department of the Navy, Washington, D.C., 1966.
- [17] Irwin, G. R., *Proceedings*, 7th Sagamore Conference, Vol. 4, 1960, p. 63.
- [18] Paris, P. C. and Sih, G. C. in *Fracture Toughness Testing and Its Applications*, ASTM STP 381, American Society for Testing and Materials, 1964, pp. 30–83.
- [19] Smith, R. A. and Miller, K. J., *International Journal of Mechanical Engineering Science*, Vol. 20, 1978, pp. 201–206.
- [20] Hammunda, H. M. and Miller, K. J. in *Elastic Plastic Fracture*, ASTM STP 668, American Society for Testing and Materials, 1979, pp. 703–719.
- [21] El Haddad, M. H., Dowling, N. E., Topper, T. H., and Smith, K. N., "J-Integral Applications for Short Fatigue Cracks at Notches," accepted for publication in the *International Journal of Fracture*, 1979.
- [22] El Haddad, M. H., Smith, K. N., and Topper, T. H., "Prediction of Nonpropagating Cracks," accepted for publication in the *Engineering Fracture Mechanics*, Vol. 11, No. 3, 1979, pp. 573–584.

B. L. Braglia,¹ R. W. Hertzberg,² and Richard Roberts³

Crack Initiation in a High-Strength Low-Alloy Steel

REFERENCE: Braglia, B. L., Hertzberg, R. W., and Roberts, Richard, "Crack Initiation in a High-Strength Low-Alloy Steel," *Fracture Mechanics, ASTM STP 677*, C. W. Smith, Ed., American Society for Testing and Materials, 1979, pp. 290-302.

ABSTRACT: The fatigue crack initiation behavior of a high-strength low-alloy steel, VAN-80, has been investigated. Crack initiation was defined, for the purposes of the study, as the existence of a 0.25-mm long crack on either surface of a modified compact tension specimen.

The parameter $\Delta K/\sqrt{\rho}$ was used in an attempt to normalize data concerning crack initiation at three finite radius notches (0.79, 1.59, and 3.18 mm). While not conclusive, a volume effect on initiation was indicated with larger radii producing shorter lives at a given $\Delta K/\sqrt{\rho}$. Similar findings have been reported by previous authors for other materials. The experimentally determined value of $(\Delta K/\sqrt{\rho})_{TH}$ for VAN-80 is 835 MPa. Samples cycled at or below this value would not be expected to initiate a crack in 10^6 cycles.

Block loading experiments were conducted in an attempt to isolate crack initiation from crack propagation processes. For all high block-low block tests, $\Sigma n/N > 1$. This result, by itself, could be interpreted as suggesting that the total fatigue process is propagation controlled. However, the situation is complicated by the fact that the VAN-80 steel is sensitive to overload induced crack propagation delay. Therefore, cracks that might initiate during the high block load cycling period would be expected to grow more slowly at a lower subsequent stress range. Since the present definition of crack initiation contains a 0.25 mm increment of crack growth, propagation related delay effects may strongly influence or overshadow the actual initiation process.

Transmission electron fractographic observations reveal that the local ΔK at short newly initiated crack fronts is much lower than that predicted by standard ΔK calibrations for the test specimen. This is consistent with elastic solutions for the stress intensity factor for small cracks growing within the sphere of influence of large geometrical notches and other specimen shape changes. Scanning electron microscope images have shown that crack initiation occurred in notched VAN-80 samples by debonding of the globular cerium sulfides from the matrix at the surface of the notch root.

KEY WORDS: fatigue crack initiation, fracture mechanics, high-strength low-alloy steel, block loading, cumulative damage, fractography, crack propagation, fatigue (materials)

¹ Experimental metallurgist, Electro-Motive Division, General Motors, La Grange, Ill. 60525.

² Professor, Department of Metallurgy and Materials Engineering, Lehigh University, Bethlehem, Pa. 18015.

³ Professor, Department of Mechanical Engineering, Lehigh University, Bethlehem, Pa. 18015.

In recent years a new category of steels has found wide acceptance where low cost, low weight, high strength, isotropic behavior, and excellent weldability are important design criteria. This group is known collectively as high-strength low-alloy (HSLA) steels and VAN-80 is a well known member of the group. High strength is achieved in the as-rolled condition by ultra-small grain size, vanadium carbonitride precipitation strengthening, and manganese solid solution strengthening. Carbon levels are kept below 0.18 percent; thus, weldability of VAN-80 is comparable to that of plain low carbon steels. Mechanical properties are further enhanced through inclusion shape control; cerium additions to the melt form cerium sulfides which retain their globular shape during hot rolling operations [1].⁴ This markedly reduces the anisotropy normally associated with ordinary hot-rolled products.

In addition to high-yield strength and isotropic behavior, a material's resistance to fatigue crack initiation is a very important design criterion. Many times, the prevention of crack initiation is the main consideration. Most components designed with this objective in mind function as intended for their entire service life without cracking. Often, however, this is achieved by overconservative design, that is, by employing lower operating stresses with the attendant penalty of increased weight.

If a crack does initiate, it will usually do so in the vicinity of locally high stress fields such as at fillets, holes, corners, and welds or at service induced scratches, nicks, wear, and corrosion pits. In many cases it is not desirable to consider these notches as sharp cracks since this would result in a very conservative design situation. Thus, it is highly advantageous to study fatigue crack initiation in the vicinity of notches.

Other investigators have addressed themselves to these same questions with regard to other materials. Jack and Price [2] studied crack initiation at notches in plain low carbon steel plates. Their studies were confined to sharp notches with radii from 0.05 to 1.25 mm. Specimens with notch root radii less than 0.25 mm showed the same initiation lives as did the 0.25 mm radius at any given applied stress level. For notches with radii from 0.25 to 1.25 mm, the applied stress required for crack initiation at a given number of cycles increased with the notch radius. They proposed that a parameter $\Delta K/\sqrt{\rho}$, where ΔK is the stress intensity range and ρ is the notch radius, be used to analyze the data. This parameter is actually a representation of the stress at the surface of the notch. Barsom and McNicol [3] then used this approach in their study of crack initiation in HY-130 steel. This parameter, $\Delta K/\sqrt{\rho}$, was found to normalize all initiation data from notches with radii from 0.20 to 9.53 mm for longer initiation lives. A slight volume effect was seen with larger radii producing shorter lives at a given $\Delta K/\sqrt{\rho}$ level at shorter initiation lives. It may be reasoned that when the notch radius is increased, a greater volume of

⁴ The italic numbers in brackets refer to the list of references appended to this paper.

material is subjected to high stress at the notch root. Therefore, fatigue life would be expected to be shorter since the probability of having a crack initiation site in the larger critical zone would be greater. It also may be argued that equal values of elastic notch surface stresses would result in higher notch surface strains for larger radii. Finally, for larger notch radii, one can argue that the effect of the notch on K will prevail for greater distances into the specimen.

Consequently, the objectives of this investigation were to develop $S-N$ type crack initiation data for notched samples of VAN-80 and to conduct additional experiments to isolate crack initiation from crack propagation processes. In addition, it was our aim to examine fracture surfaces generated during the initiation studies and the characterize fracture surface micromorphology at short crack lengths.

Materials and Experimental Procedures

The material used in this study was a HSLA steel (VAN-80) in conformance with ASTM Specification for High-Strength, Low-Alloy, Hot-Rolled, Structural Vanadium-Aluminum-Nitrogen and Titanium-Aluminum Steels (A656-75), Grade 1 requirements. The steel sheet was supplied in 1.4-m widths with a thickness of 4.62 mm. A chemical analysis of the subject material and its tensile properties are presented in Tables 1 and 2 respectively.

A modified compact tension configuration was used for crack initiation testing (Fig. 1). The normal V-notch was replaced by a finite radius notch ($\rho = 0.79, 1.59, \text{ or } 3.18 \text{ mm}$). Notches were placed such that loading would always be parallel to the rolling direction.

Notch preparation consisted of drilling and reaming the notches to size. Final polishing of the notch surface was achieved by coating wooden dowels with 6 micron diamond paste and rotating the dowel within the reamed hole. All scratches due to drilling and reaming the notch were thus

TABLE 1—VAN-80 chemical analysis.

	A-656, Grade 1 Specification	VAN-80 Supply A
Carbon	0.18 max	0.12
Manganese	1.60 max	1.43
Sulfur	0.050 max	0.007
Phosphorus	0.040 max	0.030
Silicon	0.60 max	0.48
Aluminum	0.02 min	0.02
Vanadium	0.05–0.15	0.125
Nitrogen	0.005–0.030	NA ^a

^aNA = not available.

TABLE 2—VAN-80 mechanical properties.

	A-656, Grade 1	VAN-80, Supply A	
	Specification	Longitudinal	Transverse
Yield Strength, MPa	552 min	634	655
Tensile Strength, MPa	655–793	758	758
Total Elongation, percent	12 min	25	21.5
Uniform Elongation, percent	...	14.5	13.5
Hardness (R _c)	...	22	22

removed. Surface roughness measurements, made with the aid of a Tallysurf Profilometer, yielded a surface finish of 0.13μ arithmetic average. After final polishing was completed, a jeweler's saw was used to connect the previously machined slot with the carefully prepared hole.

Fatigue crack initiation testing was conducted on 9 and 90 kN MTS electrohydraulic closed loop testing machines. All tests were run under load control at a frequency of 60 Hz with $P_{\min}/P_{\max} = 0.1$. The test system was equipped with a peak load cutoff display oscilloscope, such that only the upper and lower 0.1 percent of the load range was displayed and controlled. This allowed for very accurate control of the imposed loads.

Crack initiation throughout the study was defined to be the development of a 0.25 mm long crack, visible on either surface of the specimen. Crack formation also was detected from changes in the oscilloscope load display trace which occurs for the following reason. When a crack initiates, the compliance of the specimen increases. The MTS equipment is forced subsequently to provide a longer stroke to supply the same load as for an uncracked sample. At 60 Hz, however, this is not entirely possible due to machine response limitations. Consequently, the load drops very slightly (from 0.02 to 0.05 percent of total load). Due to the previously mentioned peak load cutoff display, this small change in

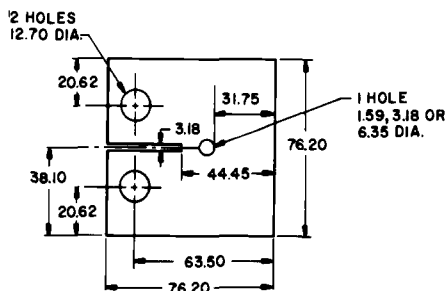


FIG. 1—Modified compact tension specimen. All units in millimetres.

loading is immediately evident. Existence of a crack is then confirmed visually with the assistance of a Gaertner $\times 50$ traveling microscope.

Block loading experiments also were conducted during this investigation. Specimens were first subjected to a block of high loads. The high block loading sequence consisted of 1500 cycles at a load range which would be expected (from prior baseline data) to cause crack initiation (that is, the development of a 0.25-mm long crack) in 3000 cycles. These overloads were applied at a frequency of 5 Hz. After overloading, loads were decreased as desired, the frequency increased to 60 Hz, and cycling allowed to continue until crack initiation was observed.

Transmission electron microscopy (TEM) was used to characterize fracture surface micromorphology in the vicinity of initiation sites. Two stage platinum-carbon replicas were taken from samples of interest for examination on a Philips 300 microscope. Scanning electron microscopy (SEM) was also used for observation of several initiation specimens. No special fracture surface preparation was necessary before examination in the Etec Auto-scan unit.

Presentation of Results

Baseline Crack Initiation Results

Results of the studies concerning crack initiation at three finite radius notches are presented in Fig. 2 as plots of applied stress intensity range (ΔK) versus crack initiation life (N_I). The definition of crack initiation used here includes both the actual initiation and subsequent propagation to a length of 0.25 mm. Therefore, the condition of $\rho \rightarrow 0$, that is, a sharp crack, was also considered; N_I for this case was determined strictly from previously obtained crack propagation data [4]. As expected, a distinct separation of the results obtained from each notch radius was observed.

As previously discussed, the parameter $\Delta K/\sqrt{\rho}$ may be used to normalize these data as shown in Fig. 3. Normalization by the use of

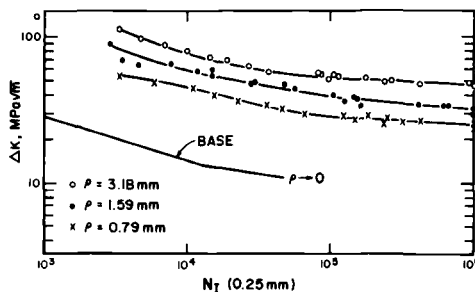


FIG. 2— ΔK versus N_I —baseline data.

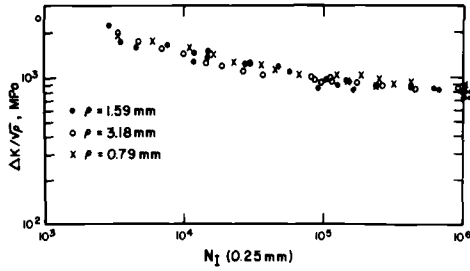


FIG. 3— $\Delta K/\sqrt{\rho}$ versus N_f —baseline data.

$\Delta K/\sqrt{\rho}$ also allows the definition of a threshold $(\Delta K/\sqrt{\rho})_{TH}$ below which crack initiation would not occur [3]. $(\Delta K/\sqrt{\rho})_{TH}$ would then be analogous to the fatigue limit in traditional $S-N$ tests. VAN-80 was found to exhibit a $(\Delta K/\sqrt{\rho})_{TH}$ of 835 MPa at 10^6 cycles as compared with values of 420 to 900 MPa found for other steel alloys [3,5,6].

It is interesting to compare the threshold value determined in this investigation with results reported previously by Rolfe and Barsom [6]. For a number of different steel alloys having yield strengths in the range from about 276 to 965 MPa, they found a correlation between $\Delta K/\sqrt{\rho}$ and yield strength with the form

$$\frac{\Delta K}{(\sigma_{ys})^{2/3} \sqrt{\rho}} = 5 \quad (1)$$

where the units are given in ksi $\sqrt{\text{in.}}$, in., and ksi. The VAN-80 results reported in this study give a ratio of 5.9 which is in good agreement with Eq 1.

It is apparent from Fig. 3 that the use of $\Delta K/\sqrt{\rho}$ does not completely normalize the experimental data. While there is scatter in the test results, it is the view of the authors that a trend exists wherein a lower value of $\Delta K/\sqrt{\rho}$ is needed to initiate a crack as ρ increases. A similar observation has been reported by others [3].

Block Loading Initiation Results

Block loading experiments were conducted in an attempt to distinguish between initiation and propagation events at the notch root. These data were then analyzed with Miner's cumulative damage law [7]. Miner's law assumes no interaction between different block loads and no sensitivity to load sequence. According to this theory, if N cycles are necessary for fatigue failure at a given stress level, it is assumed that n/N fraction of the entire life of the sample is consumed when a component experiences n cycles at that same stress level. It follows that when a series of block loads is applied to the

sample, failure is assumed to occur when $\Sigma n/N = 1$. If this relationship held true in all cases, it would greatly simplify our understanding and analysis of the fatigue process. Unfortunately, this is not found to be the case.

At times $\Sigma n/N$ is found to be greater than one and in other tests, this summation is less than one. It has been shown that notch acuity exerts a strong influence on crack initiation life under block loading conditions. Kommers [8] found that under high block-low block loading conditions in unnotched specimens, $\Sigma(n/N)$ was less than one. This would indicate that the initial high load block caused more damage than predicted by Miner's law. Crack nucleation is believed to be hastened by the high block; the following low load block would then involve propagation of this nucleated crack. Contrasted with this is the fact that Hudson and Hardrath [9] and Schijve and Broek [10] have shown that $\Sigma(n/N) > 1$ for the case of specimens containing sharp notches. The explanation for this opposite effect may be traced to crack growth rate retardation resulting from the presence of favorable residual stress or crack closure effects, or both, as reported by several authors for various materials [11,13].

Thus, if a sample containing a notch of known severity is subjected to high block-low block loading conditions, the relative importance of crack initiation versus crack propagation may be determined. That is, if such tests show $\Sigma(n/N) < 1$, then one would conclude that the fatigue process is dominated by true initiation; however, if $\Sigma n/N > 1$, then the propagation stage would appear to dominate the overall process [14].

Results of high block-low block tests on two finite radius notches ($\rho=1.59$ and 3.18 mm) are presented in Fig. 4 and 5. These figures also contain the baseline initiation data and curves which represent Miner's law expectations ($\Sigma n/N = 1$) for the high block-low block tests. Test results from a sharp crack ($\rho \rightarrow 0$) are presented in Fig. 6. This case gives the reader an indication of the susceptibility of VAN-80 to overload induced crack delay effects. Again, baseline data and Miner's law expectations are provided for comparison.

It is apparent that for all high block-low block tests, $\Sigma n/N > 1$. By the reasoning presented earlier, it would appear that for all notch radii examined, crack propagation had dominated the fatigue process. However, these data

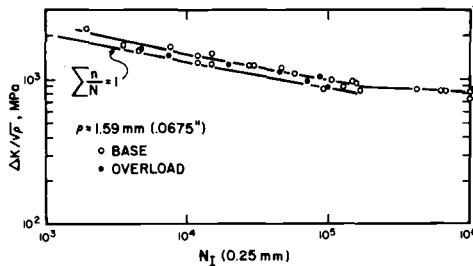


FIG. 4— $\Delta K/\sqrt{\rho}$ versus N_f —block load, $\rho = 1.59$ mm.

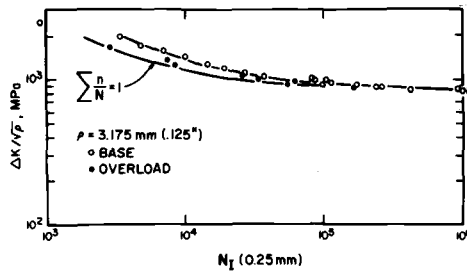


FIG. 5— $\Delta K/\sqrt{\rho}$ versus N_f —block load, $\rho = 3.175$ mm.

may be reinterpreted in a different manner, thereby leading to a different conclusion. Specifically, one should reexamine Fig. 6 which reflects the susceptibility of VAN-80 to overload induced crack retardation. Not only is $\Sigma(n/N) > 1$ for all test conditions, but under any overload more than 8 percent greater than the low block load, $\Sigma(n/N) > 1.5$; that is, the data will fall to the right of the baseline curve. When the high block was 70 percent higher than the low block, complete crack arrest occurred with no growth whatsoever observed after a quarter million cycles. Therefore, overload induced crack growth rate retardation may well exert a major influence over the block loading total fatigue process.

With this severe retardation potential in mind, a modified explanation of the high block-low block finite radius results is deemed appropriate. To begin, it is restated that the arbitrarily chosen criterion for crack initiation involves 0.25 mm of crack propagation. Consequently, it may be argued that retardation within this 0.25-mm increment of crack growth, due to compressive residual stresses or closure which was induced by the high load block, or both, may overshadow the actual damage caused by the high block. That is, the high block may still hasten initiation; however, the resultant small crack at the notch root will grow extremely slowly and consume many cycles before fulfilling our definition of initiation. For example, crack growth rates

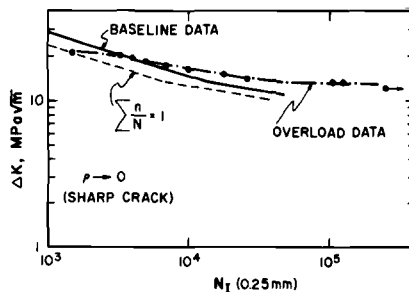


FIG. 6— ΔK versus N_f —block load, sharp crack.

within the high block affected zone were decreased by 1 to 1.5 orders of magnitude. Therefore, a revised definition of crack initiation is needed if one would wish to separate initiation and propagation stages of the fatigue process. It should be recognized that a new definition of initiation would only be advantageous if available crack detection methods could accurately detect smaller cracks.

Fracture Surface Examination

Macroscopic fracture surface examination immediately revealed one important point common to both baseline specimens and high block-low block samples. At relatively low test values of $\Delta K/\sqrt{\rho}$ (less than 1000 MPa), single initiation sites were observed. By contrast, at relatively high values of $\Delta K/\sqrt{\rho}$ (> 1000 MPa), multiple crack initiation sites were observed. This may be attributed to the fact that at high stress levels there are more potential initiation sites. This same phenomenon was not observed in high block-low block testing. That is, very small multiple cracks were *not* present at the end of the high block sequence. If small cracks had been present, some growth would be expected during the low block and multiple origins would be easily visible. Thus, it is concluded that crack initiation occurred during the low block loading.

Baseline crack initiation samples were selected for a TEM fractographic study for the purpose of relating crack initiation site fracture surface micromorphology to known fracture surface micromorphology obtained from crack propagation studies. From striation spacing data and the lack or presence of intergranular failure, local stress intensity levels could be estimated. (It has been shown that at certain intermediate ΔK levels VAN-80 fatigue fracture surfaces reveal some intergranular failure [4,15]). At short crack lengths, all specimens exhibited apparent local stress intensities much lower than the remotely applied values. For example, the striation spacings and evidence for intergranular failure along pearlite boundaries as seen in Fig. 7 imply a ΔK level of approximately $16 \text{ MPa}\sqrt{\text{m}}$ as compared with a remotely applied stress intensity of $34 \text{ MPa}\sqrt{\text{m}}$. Based on such fractographic results, it is concluded that the local effective ΔK level for very short cracks in a notched compact tension specimen is much less than one would determine from the standard CT stress intensity expression. This is consistent with elastic solutions for the stress intensity factor for small cracks growing within the sphere of influence of geometrical notches and other specimen shape changes [16].

Fracture surface examination was also conducted on the scanning electron microscope. In all cases, a series of radial markings emanated from each initiation site (Fig. 8). It was found that all initiation sites contained a single globular particle which had been separated from its

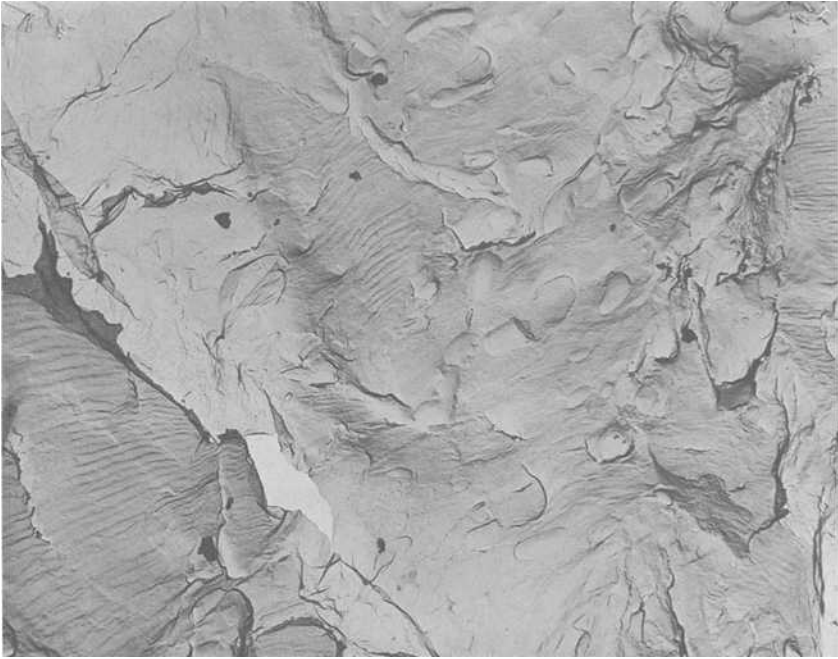


FIG. 7—Small striations (5.2×10^{-5} mm/striation) and pearlite boundary failure on sample A2-54. Applied $\Delta K = 34 \text{ MPa}\sqrt{\text{m}}$. $\times 25200$.

surrounding matrix (Fig. 9). Electron microprobe analysis of the particles at each initiation site revealed them to be cerium sulfides. This is very similar to the findings of Lankford [17] who showed that calcium aluminate inclusions served as fatigue crack initiation sites in 4340 steel.

Conclusions

The following conclusions may be drawn from this investigation:

1. Crack initiation data reported in this study were normalized by the parameter $\Delta K/\sqrt{\rho}$. This is reasonable since $\Delta K/\sqrt{\rho}$ provides an excellent measure of the maximum notch root stress levels in the specimen configuration adopted in this test program. For a one million cycle fatigue life, $(\Delta K/\sqrt{\rho})_{TH}$ is found to be 853 MPa. When this value is normalized according to the relationship suggested by Rolfe and Barsom (that is, $\Delta K/(\sigma_{ys}^{2-3}\sqrt{\rho}) = 5$) good agreement was found with results from other ferrous alloys.

2. While there is scatter in the test results, the authors conclude that a trend exists wherein a lower value of $\Delta K/\sqrt{\rho}$ is needed to initiate a crack as ρ increases.



FIG. 8—Radial markings issuing from one of the five origins on sample A2-95. $\times 300$.

3. The results of high block-low block testing where $\Sigma(n/N) > 1$ indicate that the overall fatigue process is propagation controlled even for the largest notch radius studied. It is suggested that the high block loadings hasten crack initiation but that subsequent crack propagation delay due to residual compressive stresses induced by the same initial overloads may be so pronounced that detection of the crack is postponed for very many cycles.

4. TEM fractographic observation has shown that the local effective ΔK level at the tip of a very short crack at the blunt notch root is less than the externally applied ΔK level as computed from the standard compact tension specimen K formulation. This is consistent with elastic stress intensity factor calculations for small cracks growing from notches.

5. Cerium sulfide particles present at or very near the surface of the notch root act as crack initiation sites with failure occurring along the sulfide-matrix interface.

Acknowledgment

The authors wish to acknowledge support from the Pennsylvania Science and Engineering Foundation (Agreement 352) and fellowship

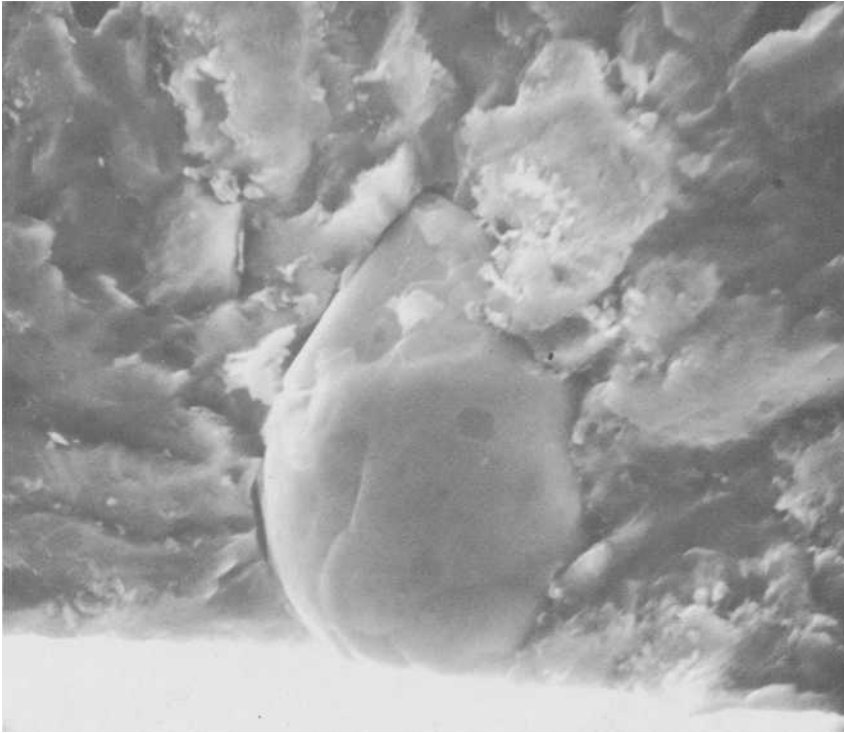


FIG. 9—Cerium sulfide at origin in A2-95 denoted by radial markings in Fig. 8. $\times 6000$.

support (for B. L. Braglia) from the Electro-Motive Division of General Motors. Jones and Laughlin Steel Company provided the VAN-80 plate and tensile properties for this material.

References

- [1] Hertzberg, R. W. and Goodenow, R. H., *Micro-Alloying 75*, Oct. 1975.
- [2] Jack, A. R. and Price, A. T., *International Journal of Fracture Mechanics*, Vol. 6, 1970, pp. 401-409.
- [3] Barsom, J. M. and McNicol, R. C. in *Fracture Toughness and Slow-Stable Cracking*, ASTM STP 559, American Society for Testing and Materials, 1974, pp. 183-204.
- [4] Braglia, B. L., "Crack Initiation and Propagation in VAN-80 Steel," M.S. thesis, Lehigh University, Bethlehem, Pa., 1978.
- [5] Clark, W. G., Jr. in *Fracture Toughness and Slow-Stable Cracking*, ASTM STP 559, American Society for Testing and Materials, 1974, pp. 205-234.
- [6] Rolfe, S. T. and Barsom, J. M., *Fracture and Fatigue Control in Structures*, Prentice-Hall, Englewood Cliffs, N. J., 1977, pp. 208-231.
- [7] Miner, M. A., *Metal Fatigue*, McGraw-Hill, 1959, p. 278.
- [8] Kommers, J. B., *Proceedings*, American Society for Testing and Materials, Vol. 45, 1945, p. 532.
- [9] Hudson, C. M. and Hardrath, H. F., Technical Note D-1803, National Aeronautics and Space Administration, 1963.
- [10] Schijve, J. and Brock, D., *Aircraft Engineering*, Vol. 34, 1962, p. 314.

- [11] von Euw, E. F. J. et al, in *Stress Analysis and Growth of Cracks*, ASTM STP 513, American Society for Testing and Materials, 1972, p. 230.
- [12] Trebules, V. W. et al, in *Progress in Flow Growth and Fracture Toughness Testing*, ASTM STP 536, American Society for Testing and Materials, 1973, p. 115.
- [13] Mills, W. J. et al, in *Cyclic Stress-Strain and Plastic Deformation Aspects of Fatigue Crack Growth*, ASTM STP 637, American Society for Testing and Materials, 1977, pp. 192-208.
- [14] Hertzberg, R. W., *Deformation and Fracture Mechanics of Engineering Materials*, Wiley, New York, 1976, p. 498.
- [15] Bretz, P. E., Braglia, B. L., and Hertzberg, R. W., manuscript in preparation.
- [16] Tada, H., Paris, P. C., and Irwin, G. R., *The Stress Analysis of Cracks Handbook*, St. Louis, Mo., 1973.

W. G. Clark, Jr.¹

Effect of Spherical Discontinuities on Fatigue Crack Growth Rate Performance

REFERENCE: Clark, W. G., Jr., "Effect of Spherical Discontinuities on Fatigue Crack Growth Rate Performance," *Fracture Mechanics, ASTM STP 677*, C. W. Smith, Ed., American Society for Testing and Materials, 1979, pp. 303-319.

ABSTRACT: Room temperature, air environment fatigue crack growth rate data were generated with 2.540 cm (1 in.) thick hot-isostatically pressed and heat-treated low carbon steel powder metal toughness specimens containing artificial defects (alumina ceramic spheres) ranging from 0.317 to 1.270 cm (0.125 in. to 0.500 in.) in diameter. The procedure used to fabricate the test material and the subsequent evaluation of the effect of the defects on the localized rate of crack growth are discussed. Results show that the effect of unbonded spherical defects on fatigue crack growth rate behavior depends upon both the effect of the defect on localized net section stresses and the crack "blunting" influence of the defect. In addition, the specific influence of the defect on the rate of crack growth depends upon the applied stress intensity level. It is also shown that relatively large isolated spherical defects are required to yield a significant effect on fatigue crack growth rate performance. A preliminary evaluation of the effect of multiple defects is also included. Recommendations for further work and additional uses for powder metal materials containing controlled artificial defects are discussed.

KEY WORDS: fatigue (materials), steels, crack growth, fracture (materials), defects, failure, structure, life, cycles, powders, crack propagation

Within the last 10 years, it has been clearly demonstrated that fracture mechanics concepts provide a unique quantitative approach to the characterization of fatigue crack growth behavior in many structural materials. Specifically, it has been shown that the rate of fatigue crack growth da/dN , is primarily dependent upon the magnitude of the alternating crack tip stresses expressed in terms of the stress intensity factor range, ΔK_I [1,2].² From knowledge of the appropriate fatigue crack growth rate properties and the inherent fracture toughness of a given

¹ Manager, fracture mechanics, Structural Behavior of Materials Department, Westinghouse Research and Development Center, Pittsburgh, Pa. 15235.

² The italic numbers in brackets refer to the list of references appended to this paper.

material, it is possible to determine accurately the number of loading cycles required for a preexisting crack to grow to the critical size for failure. This information in turn, can be used to predict the useful cyclic life of a structure and to establish realistic material acceptance and inspection criteria [1].

The advent of the fracture mechanics approach to fatigue and the practical advantages of this design concept have led to the development of an extensive amount of fatigue crack growth rate data for a wide variety of structural materials. In addition, the fracture mechanics approach to fatigue has been invaluable in developing a better understanding of the fatigue phenomenon and in identifying variables which can influence the cyclic life of a structure [3]. Among the pertinent variables which have received considerable attention to date are loading spectrum (stress range, waveform, frequency, load history, etc.), environmental effects and the associated interactions with the loading spectrum, and material variables including chemistry, strength level, and microstructure.

With regard to the effect of material variables on fatigue crack growth rate performance, one extremely important and widely recognized area of concern which has received relatively little attention is the potential effect of inherent material discontinuities on fatigue crack growth behavior. More specifically, what happens to the rate of crack growth when a growing fatigue crack intersects an area of discontinuities in an otherwise homogeneous material? This problem is of particular concern in relatively heavy section structures which are likely to contain clusters or "clouds" of small defects. The few attempts to characterize such behavior have been unsuccessful primarily because the available test material usually contained a large number of different size interacting defects which prevented a quantitative evaluation of the results [4,5]. Specifically, it was not possible to distinguish the effect of a given defect from the effect of others that were present. Consequently, the conventional approach to handling the problem of a fatigue crack growing into a region of discontinuities is to assume that the crack will essentially jump through the defective area in one cycle. Obviously, such an approach can be overly conservative and unrealistic.

In order to further pursue a practical solution to this problem, it was decided that a procedure was required which would allow the preparation of test material in which the size and location of defects could be controlled. Attempts were made to prepare such material by first using drilled holes to simulate defects and next, by casting plastic specimens containing artificial defects. Although somewhat successful, these attempts did not yield material which adequately represented the actual condition of interest. At this point, it was decided to attempt to fabricate powder metal test specimens containing artificial defects. This procedure was successful and a series of low carbon steel powder metal specimens

containing ceramic (alumina) spheres were used to simulate wrought steel containing defects. This report describes the procedure used to fabricate the test specimens and the results of a preliminary evaluation of the effect of spherical discontinuities on the rate of fatigue crack growth. Fatigue crack growth rate tests were conducted with 2.54 cm (1 in.) thick WOL-type compact toughness specimen containing artificial defects ranging from 0.317 to 1.270 cm (0.125 to 0.500 in.) in diameter and the results expressed in terms of fracture mechanics parameters.

Material and Specimen Preparation

The test material involved in this investigation consisted of hot-isostatically pressed and heat treated low carbon steel powder metal blocks 8.26 by 6.35 by 2.54 cm (3.25 by 2.50 by 1.00 in.) thick. The test blocks were fabricated with an open-ended powder metallurgy die (2.86 by 8.57 cm, 1.125 by 3.375 in. cavity) designed to produce blanks for the preparation of 2.54 cm (1 in.) thick WOL type compact toughness specimens of the geometry shown in Fig. 1. The details of the test specimen processing and subsequent heat treatment are summarized in Table 1. The powder metallurgy processing yielded material with a density essentially identical to wrought steel. The microstructure of the test material is shown in Fig. 2 and the room temperature tensile properties are given in Table 2.

Test specimens were prepared with and without artificial defects. The defects consisted of solid ceramic spheres (aluminum oxide high temperature ball bearings) 0.317, 0.635, and 1.270 cm (0.125, 0.250 and 0.500 in.) in diameter. Figure 3 shows the layout of the defects in the powder metal specimens. These specimens were made by filling the die with one half the metal powder required to make a complete specimen blank, leveling the powder, and laying the defects on the powder surface which subsequently becomes the midplane of a completed specimen. A template was used to locate the defects as shown in Fig. 3. The remaining half of the powder

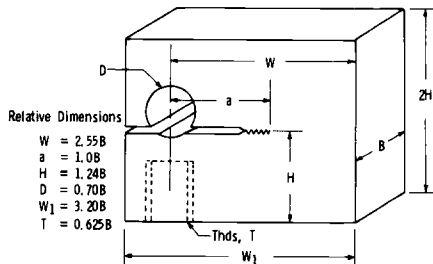


FIG. 1—WOL type compact fracture toughness specimen (relative dimensions in terms of thickness B).

TABLE 1—*Details of test specimen processing (low carbon steel).*

Powder blending
ANCOR steel 1000 powder
+ 0.5 percent microcrystal graphite
+ 0.5 percent zinc stearate (lube)
Cold pressing in 2.86 by 8.57 cm (1.125 by 3.375 in.) die press to (100 000 psi)
Dewaxing and sintering
dewax in vacuum, 275°C (530°F), 8 h
sinter in vacuum, 1121°C (2050°F), 6 h
Cold isostatic pressing
press to (100 000 psi)
Sintering
sinter in vacuum, 1121°C (2050°F), 6 h
Hot isostatic pressing
specimens canned and hot isostatic
pressed at (10 000 psi) and 1200°C (2192°F)
Heat treatment
specimens removed from can and heat treated as follows:
annealed 815°C (1500°F), 1 h
quenched in water
tempered 480°C (900°F), 0.5 h

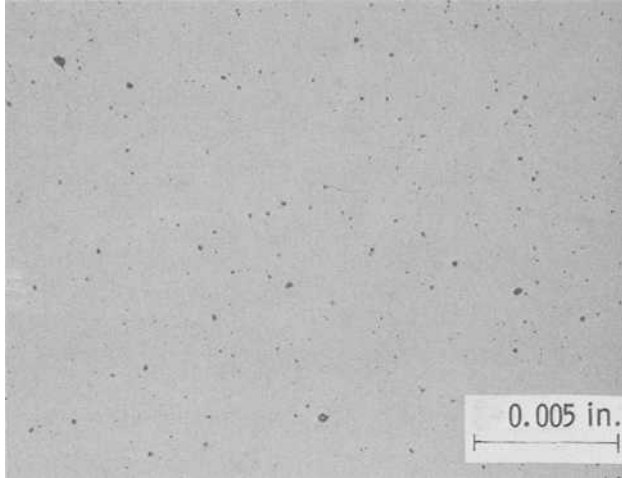
was then placed in the die (covering the defects) and the material cold pressed and sintered twice per processing steps 2 through 5 noted in Table 1. Prior to hot-isostatic pressing (Table 1, step 6), the test specimens containing artificial defects were subjected to a radiographic inspection to determine if the defects had moved in the powder during processing. Figures 4 and 5 show prints of the radiographs taken through the thickness, 2.54 cm (1 in.), and through the height, 6.35 cm (2.50 in.), of the test specimens. Note that the artificial defects remained in place during the specimen processing. Following radiographic inspection, the blanks were subjected to hot isostatic pressing and heat treated as noted in Table 1, steps 6 and 7. The heat treated blanks were then machined into 2.54 cm (1 in.) thick WOL-type compact toughness specimens (Fig. 1). Radiographs taken after final processing were used to locate the crack starter notch in the plane of the defects.

Crack Growth Rate Testing

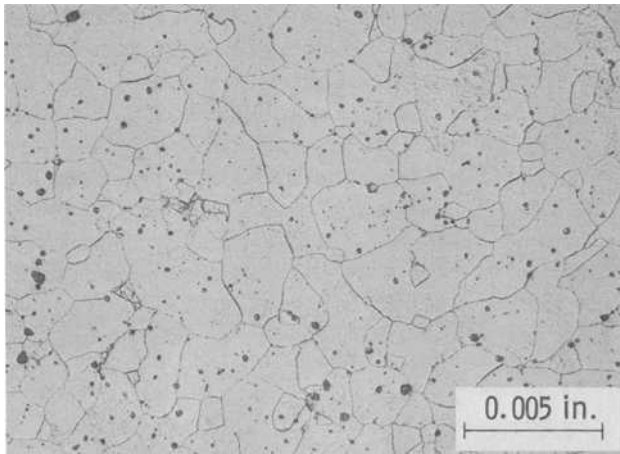
Room-temperature, laboratory air environment fatigue crack growth rate tests were conducted with the six specimens containing artificial

TABLE 2—*Tensile properties of test material.*

0.2 Percent Yield Strength, ksi	Tensile Strength, ksi	Elongation, percent	Reduction in Area, percent
78.0 (538 MPa)	111.0 (765 MPa)	18.5	52.3



Un-Etched



Etched

FIG. 2—Microstructure of powder metal test material (low carbon steel).

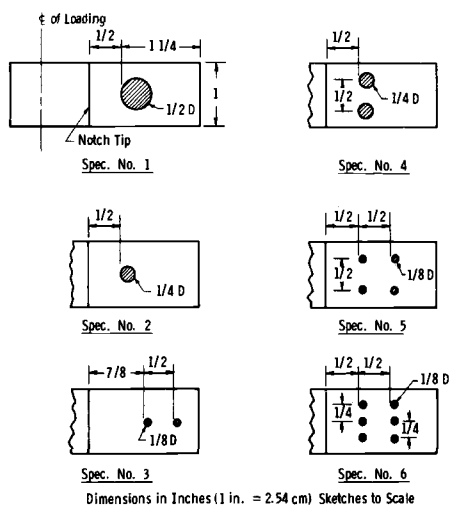


FIG. 3—Layout of defects in powder metal test specimens.

defects (Fig. 3) as well as with three identical defect-free specimens. In all cases, the test specimens were both precracked and subsequently tested to failure under essentially the same loading conditions. All tests were conducted with a servohydraulic testing machine. The applied load, P , ranged from 1.33×10^3 to 1.47×10^4 N (300 to 3300 lb) yielding a load range, ΔP , of 1.33×10^4 N (3000 lb) and a stress ratio, R , of 0.1. The specimens were precracked 0.254 cm (0.100 in.) beyond the crack starter notch tip at a test frequency of 60 Hz and tested to failure from this point at 5 Hz. The stress intensity factor range at the end of precracking was $14.85 \text{ MPa}\sqrt{\text{m}}$ ($13.5 \text{ ksi}\sqrt{\text{in.}}$). All crack length measurements were made on the surface of the specimen with a $\times 35$ binocular microscope. Crack length measurements were made at 0.051 cm (0.020 in.) increments of growth. Measurements were made on both sides of the specimen and the average values used to compute the crack growth rate.

The rate of fatigue crack growth, da/dN was determined from the crack length versus elapsed cycles data (“a” versus N) by means of the seven-point polynomial curve fitting procedure described by Clark and Hudak [6]. The corresponding stress intensity factor range, ΔK_I was computed from the expression

$$\Delta K_I = Y \frac{P_{\max} \sqrt{a}}{BW} - Y \frac{P_{\min} \sqrt{a}}{BW}$$

where

a = crack length measured from the centerline of loading,
 P_{\max} and P_{\min} = maximum and minimum loads per cycle,
 B = specimen thickness,

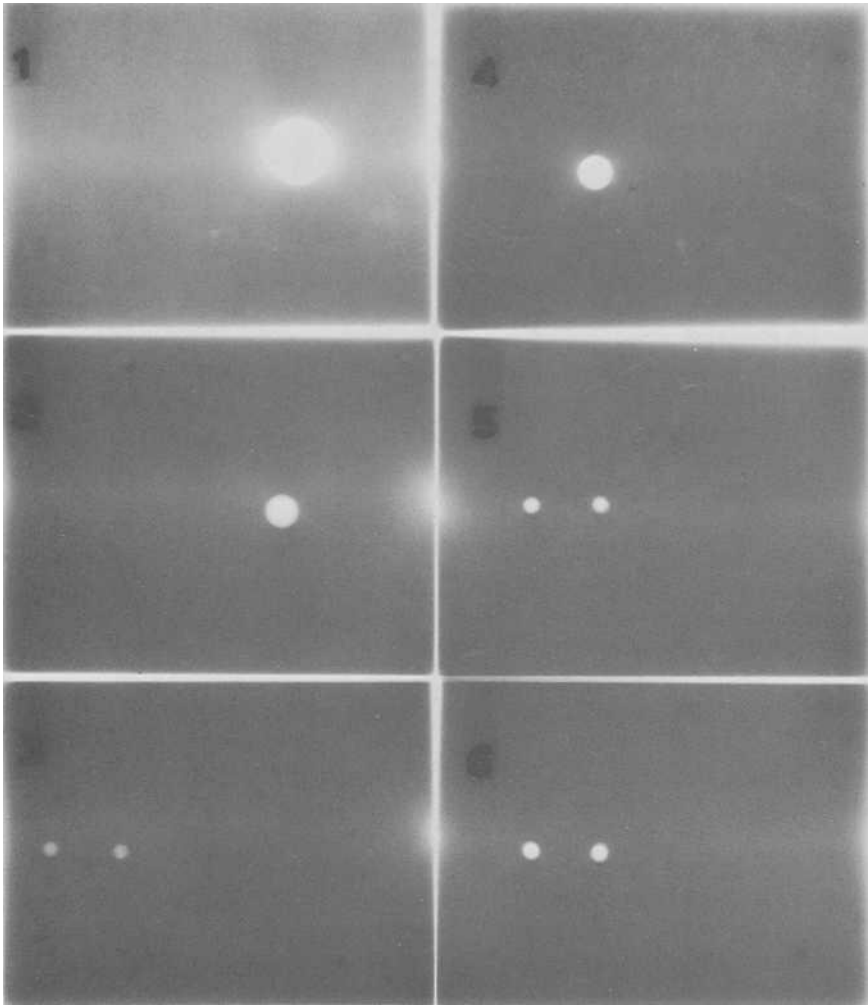


FIG. 4—X-ray of test specimens (through thickness).

W = specimen width, and
 Y = compliance factor given by

$$Y = 30.96 - 195.8 \left(\frac{a}{W} \right) + 730.6 \left(\frac{a}{W} \right)^2 - 1186.3 \left(\frac{a}{W} \right)^3 + 754.6 \left(\frac{a}{W} \right)^4$$

Test Results

Figure 6 presents the results of the fatigue crack growth rate tests conducted with the three defect-free low carbon steel powder metal

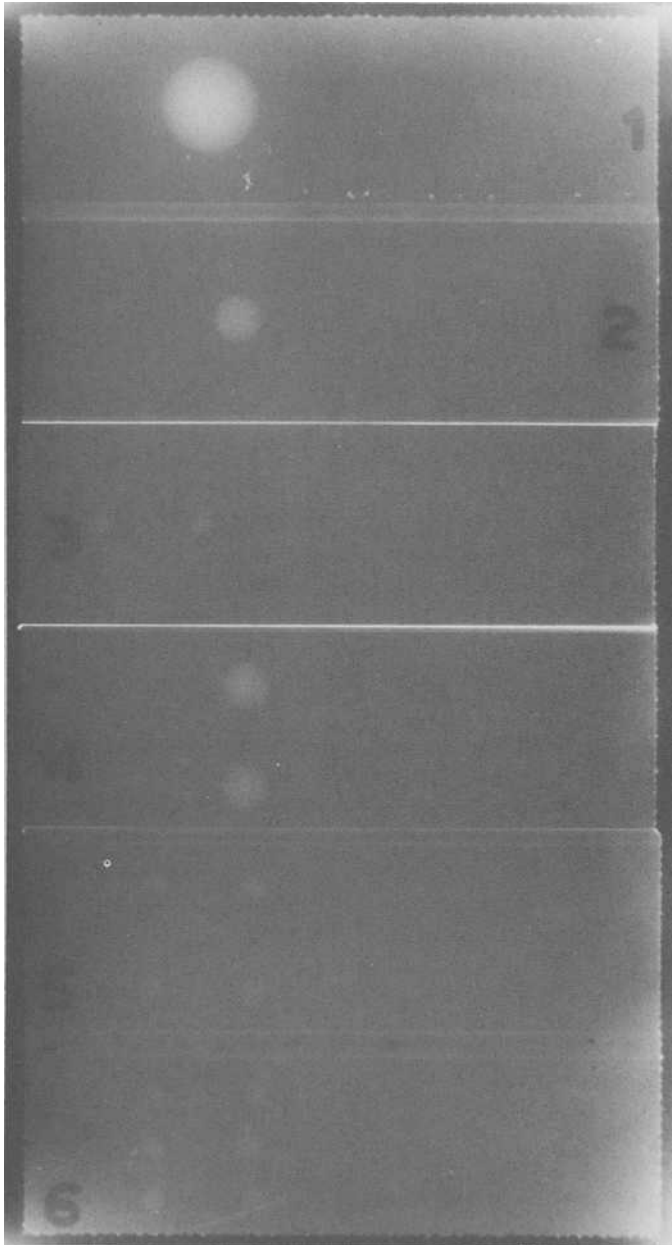


FIG. 5—X-ray of test specimens (through height).

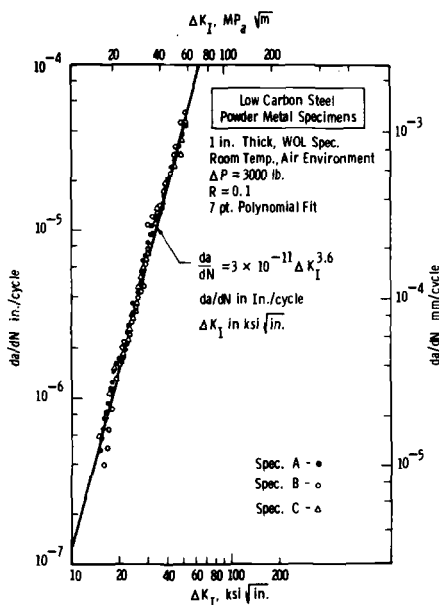


FIG. 6—Fatigue crack growth rate properties of powder metal test specimens.

specimens. The results are expressed in terms of $\log da/dN$ versus $\log \Delta K_I$, and the least squares regression line which defines the fatigue crack growth rate properties in terms of the generalized fatigue crack growth rate law, $da/dN = C_0 \Delta K_I^n$, is included [2]. Note the small amount of variability in the crack growth rate data generated with the three specimens. Such results illustrate that consistent, reproducible fatigue crack growth rate data can be developed with powder metal materials. In addition, it should be noted that the fatigue crack growth rate data developed for the powder metal steel investigated here fall within the scatterbands of room temperature, air environment fatigue crack growth rate data reported for a wide range of wrought steels [3]. The aforementioned observations clearly indicate that properly fabricated powder metal materials can be used to simulate wrought metal behavior.

Figures 7, 8, and 9 present the fatigue crack growth rate data for the six test specimens containing artificial defects. In each case, that portion of the crack growth rate data corresponding to the location of the artificial defects is noted.³ The least square regression line developed for the defect free material (Fig. 6) is also included on each plot. Note that except for that portion of the crack growth rate data affected by the presence of the artificial defects, the crack growth rate performance of test specimens 1

³ The second 0.320 cm (0.125 in.) diameter ceramic ball in specimen No. 3 (Fig. 8) was located in the fast fracture area of the specimen.

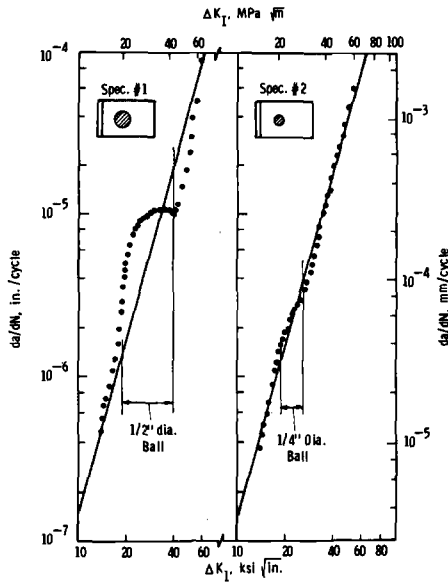


FIG. 7— da/dN versus ΔK_I for Specimens 1 and 2.

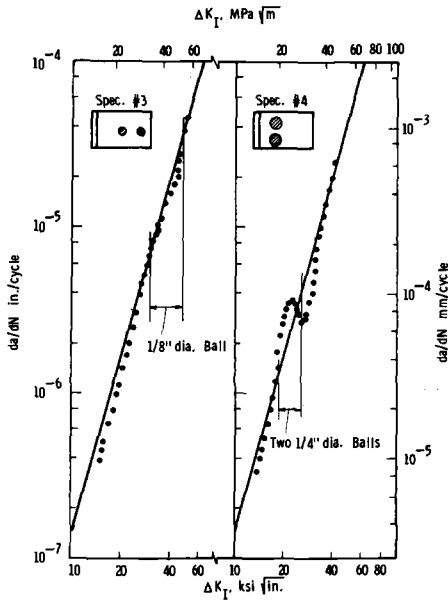


FIG. 8— da/dN versus ΔK_I for Specimens 3 and 4.

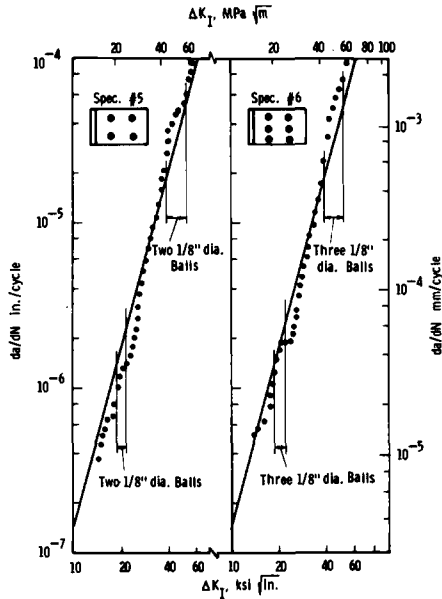


FIG. 9— da/dN versus ΔK_I for Specimens 5 and 6.

through 6 is essentially identical to that encountered with the defect free material. Note also that in general, the presence of the defects produced both an increase and a subsequent decrease in the rate of crack growth as the main fatigue crack front passes through the defect region. Consequently, the defects had a relatively small effect on the total life of each specimen. The number of loading cycles required for the 0.254 cm (0.100 in.) long precrack to grow to the critical size for failure, 3.048 cm (1.200 in.), is noted in Table 3 for each test specimen.

Although detailed crack length versus elapsed cycles (a versus N) curves were developed for each test specimen, such curves were of little value in illustrating the effect of defects on fatigue crack growth performance and as a result, these data are not included in the paper.

Figures 10 and 11 show the fracture appearance of four of the test specimens containing artificial defects. Note that in all cases, the fatigue cracks grew around the defects and none of the ceramic balls were broken. Note also that the ceramic balls did not form a bond with the steel (as indicated by the fact that many of the defects fell out of the metal upon specimen failure). Thus, we can conclude that the artificial defects evaluated here represent unbonded inclusion or void-like discontinuities.

Discussion

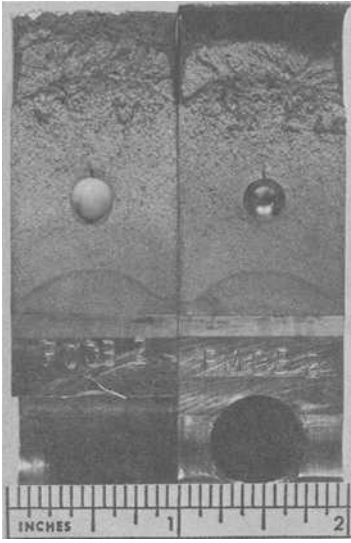
The results of this investigation reveal several pertinent observations regarding the influence of discontinuities on the rate of fatigue crack

TABLE 3—Number of loading cycles.

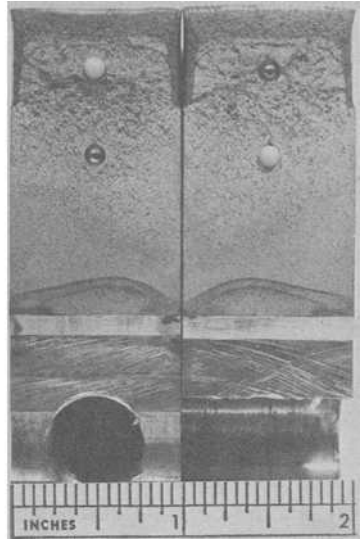
Specimen Identification	Cycles to Failure
A } no defects	903 240
B } no defects	869 250
C } no defects	881 010
	884 000 average
1 } see Fig. 3	699 290
2 } see Fig. 3	866 140
3 } see Fig. 3	1 141 000
4 } see Fig. 3	941 260
5 } see Fig. 3	1 150 000
6 } see Fig. 3	854 340

growth. Let us first consider the case of a fatigue crack intersecting a single, unbonded spherical defect; Specimens 1, 2, and 3 shown in Fig. 7 and 8. The deviation in crack growth rate from the defect-free behavior (represented by the regression line) observed for these tests and illustrated most clearly by the results for Specimen 1 (Fig. 7) provides considerable insight into the localized behavior encountered when a growing fatigue crack intersects a spherical defect. The increasing and then decreasing deviation in growth rate encountered as the crack grows through the region of the defect appears to be a direct reflection of the change in localized net section stress caused by the presence of the defect. Since the localized net section stress and the corresponding effective ΔK_I level increases and then decreases as the crack front passes through a defect of circular cross section, we would expect to see an equivalent change in the rate of crack growth. However, as the crack approaches the back side of the defect, the blunt nature of the defect tends to retard cracking, subsequently reducing the rate of crack growth. This crack blunting effect is clearly evident from the lower rate of crack growth encountered after the fatigue crack (as measured on the specimen surface) has grown beyond the defect. At this point in the test, we can easily envision a concave crack front and a corresponding reduction in crack growth rate. Crack blunting can be caused by either the need to re-initiate a fatigue crack at the back side of the defect or by the fatigue crack growing around the defect. Examination of the broken test specimens (Fig. 10 and 11) indicates that the latter situation was the case in this investigation. Specifically, the fatigue striations show evidence of two independent cracks joining together at the back of the defect.

In view of the preceding discussion it appears that at least two interacting effects control the influence of discontinuities on fatigue crack growth rate behavior—localized net section stress effects and crack blunting effects. Obviously, in order to predict accurately the effect of discontinuities on fatigue crack growth, it will be necessary to analyze the

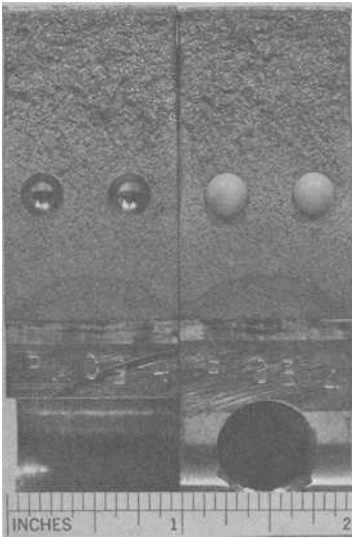


Spec. No. 2

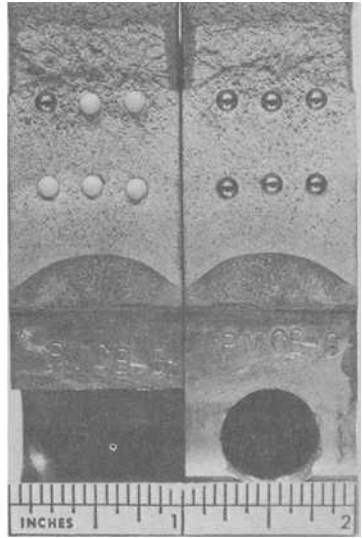


Spec. No. 3

FIG. 10—Fracture appearance of Specimens 2 and 3.



Spec. No. 4



Spec. No. 6

FIG. 11—Fracture appearance of Specimens 4 and 6.

influence of both of these factors. Although it may be possible to estimate the effect of a change in localized net section stress and the corresponding change in crack growth rate caused by the presence of a defect, it is not yet possible to predict the influence of crack blunting effects.

Comparison of the data generated with single isolated defects (Specimens 1, 2, and 3) also shows that the extent of deviation in da/dN from the defect-free behavior is directly related to the diameter of the defect. Note that the deviation both above (net section stress effect) and below (crack blunting effect) the regression line depends upon the defect size and in general, the overall effect is to reduce the influence on cyclic life. These data also clearly illustrate that relatively large isolated unbonded spherical defects are required to yield a pronounced effect on fatigue crack growth rate performance. Note that only the 1.270-cm (0.500-in.) diameter defect had a significant effect on the fatigue crack growth behavior in a 2.54-cm (1-in.) thick specimen.

The data developed for the multiple defect test specimens (Specimens 4, 5, and 6 in Figs. 8 and 9) also show both increases and decreases in the rate of crack growth as the fatigue crack passes through the defect region. Again, such behavior reflects both localized net section stress and crack blunting effects on crack growth. However, these tests also reflect the influence of multiple defect interactions on crack growth behavior. Consequently, the evaluation of these results and the comparison with the single defect data can provide at least a preliminary characterization of the effect of multiple defects on fatigue crack growth rate performance.

Among the significant observations associated with the multiple defect tests conducted here is the fact that the interaction effects between neighboring defects are relatively small. For example, note that the two 0.635-cm (0.250-in.) diameter defects (Specimen 4) had less influence on the localized rate of crack growth than the single 1.270-cm (0.500 in.) diameter defect (Specimen 1). In addition, increasing the number of 0.317-cm (0.125-in.) diameter defects from two (Specimen 5) to three (Specimen 6) had little effect on the resulting crack growth rate performance. These results imply that for the limits represented here (defects in a single plane), there is no significant magnification in localized stress due to the interaction effects of multiple spherical defects. These results are consistent with the work of Peterson regarding the interaction effects of neighboring cavities [7].

The crack growth rate data presented in Fig. 9 illustrates another very significant observation regarding the influence of discontinuities on the rate of fatigue crack growth. Note that for both test specimens (Nos. 5 and 6) the specific influence of the defects on da/dN depends upon the applied ΔK_1 level. At the low ΔK_1 level, the presence of the spherical defects produced a significant reduction in crack growth rate behavior. At the higher ΔK_1 level, the same defects produced a substantial increase in crack growth

rate. This behavior is due primarily to the fact that at the larger crack length associated with the second set of defects, the change in ΔK_I level across the defects is much larger than at the first set of defects. Thus, an equal amount of crack extension at the higher ΔK_I level both increases the rate of crack growth and reduces the effect of crack blunting by a larger amount than at the shorter crack length. Similar behavior would occur for any defects placed at various locations along the length of a compact toughness specimen. Such behavior depends upon the rate of change of ΔK_I with crack length; consequently, different loading conditions can produce different overall effects.

The results of this investigation reveal several interesting observations regarding the influence of defects on the rate of fatigue crack growth. However, it is apparent that a substantial amount of additional data are required to characterize this important behavior adequately before practical guidelines can be developed for use in the prediction of component life. The work described here was aimed primarily at developing an adequate procedure for the preparation of test material containing controlled defects and establishing the feasibility of the approach. We are currently in the process of evaluating the influence of other defect types and configurations on fatigue and fracture performance. Hopefully, these new data combined with the results presented in this investigation will provide sufficient information to allow the adequate characterization of the effect of inherent discontinuities on fracture behavior. However, the practical use of such data will still depend upon the capabilities of available nondestructive inspection techniques to identify and characterize the type of defects involved.

One of the problems associated with the quantitative evaluation of the capabilities of various nondestructive testing procedures has been the availability of test material containing controlled defects—the same problem associated with the evaluation of the effect of discontinuities on fracture behavior. In view of the success encountered with the use of powder metal material containing artificial defects as described in this paper, it would appear that similar test specimens could be used to further evaluate and characterize the capabilities of various nondestructive inspection procedures and it is strongly recommended that such techniques be given serious consideration. The radiographs shown in Figs. 4 and 5 clearly illustrate the potential use of powder metal specimens for evaluating inspection capabilities. Such techniques would also be directly applicable to the evaluation of ultrasonic inspection procedures.

Summary

This paper describes an investigation conducted to develop and substantiate a testing procedure to be used as the basis for a quantitative approach to the evaluation of the effect of inherent discontinuities on the

fatigue and fracture properties of structural metals. A powder metallurgy technique was developed to permit the preparation of test material containing controlled internal defects and preliminary fatigue crack growth rate tests were conducted to evaluate the applicability of this procedure to the characterization of wrought metal behavior.

Room-temperature, air environment fatigue crack growth rate tests were conducted with 2.540-cm (1-in.) thick hot-isostatically pressed and heat treated low carbon steel powder metal toughness specimens. Tests were conducted with specimens containing artificial defects as well as with defect-free specimens. The defects consisted of unbonded alumina ceramic spheres ranging from 0.317 to 1.270 cm (0.125 to 0.500 in.) in diameter. Both single and multiple defect configurations were evaluated. The crack growth rate data developed with the defect-free specimens were compared with wrought steel behavior and it was shown that the powder metal material could be used to simulate the behavior of wrought metal. Data generated with specimens containing defects were compared with the defect free results and the influence of the defects on the rate of crack growth evaluated. It was shown that unbonded defects of a given size produce both an increase and decrease in localized crack growth rate and the specific influence of the defect depends upon size of the defect and the applied stress intensity. Recommendations regarding additional uses for powder metal materials containing controlled defects are discussed.

Conclusions

The pertinent conclusions associated with this investigation are summarized as follows. Note that the following observations apply specifically to unbonded or void-like discontinuities.

1. Powder metallurgy techniques can be used to prepare test materials containing controlled internal defects which, in turn, can be used to simulate the effect of discontinuities on the fatigue and fracture properties of wrought materials.

2. Hot isostatically pressed and heat treated low carbon steel powder metal material yields fatigue crack growth rate properties similar to wrought steels.

3. Powder metal materials containing controlled artificial defects can be used to evaluate quantitatively the capabilities of nondestructive inspection techniques for detecting internal defects.

4. The effect of discontinuities on fatigue crack growth rate behavior depends upon both localized net section stress effects and crack "blunting" effects.

5. The specific influence of a given defect on the rate of fatigue crack growth depends upon the applied stress intensity level. The higher the stress intensity level the smaller the influence of crack "blunting."

6. Relatively large isolated spherical defects are required to yield a pronounced effect on fatigue crack growth rate performance.

7. The interaction effect of neighboring spherical defects within a single plane on fatigue crack growth rate data is relatively small.

Acknowledgments

The powder metal material used for this investigation was developed and prepared under the direction of M. W. Hagadorn of Research Metals Processing. The experimental testing was conducted by W. H. Halligan and R. C. Brown under the direction of D. R. Young of the Mechanics of Materials Laboratory. The work was sponsored by the Westinghouse Large Rotating Apparatus Division.

References

- [1] Clark, W. G., Jr., *Experimental Mechanics*, Sept. 1971, pp. 421–428.
- [2] Johnson, H. H. and Paris, P. C., *Engineering Fracture Mechanics*, Vol. 1, No. 1, 1968, pp. 3–45.
- [3] Clark, W. G., Jr., *Metals Engineering Quarterly*, Aug. 1974, pp. 16–22.
- [4] Greenberg, H. D. and Clark, W. G., Jr., *Metals Engineering Quarterly*, Aug. 1969, pp. 30–39.
- [5] Bucci, R. J., Clark, W. G., Jr., and Paris, P. C. in *Stress Analysis and Growth of Cracks*, ASTM STP 513, American Society for Testing and Materials, 1972, pp. 177–195.
- [6] Clark, W. G., Jr. and Hudak, S. J., Jr. in *Journal of Testing and Evaluation*, Vol. 3, No. 6, American Society of Testing and Materials, 1975, pp. 454–476.
- [7] Peterson, R. E., “The Interaction Effect of Neighboring Holes or Cavities,” Paper No. 64-WA/MET10, American Society of Mechanical Engineers, Aug. 1964.

Prediction of Fatigue Crack Growth Under Spectrum Loads*

REFERENCE: Gemma, A. E. and Snow, D. W., "Prediction of Fatigue Crack Growth Under Spectrum Loads," *Fracture Mechanics, ASTM STP 677*, C. W. Smith, Ed., American Society for Testing and Materials, 1979, pp. 320-338.

ABSTRACT: The reduced crack growth rate caused by each high-low load sequence of a complex load spectrum is modeled by a modified empirical constant-amplitude crack propagation relationship. The modification consists of the replacement of the crack rate term by a fractional derivative. The order of the derivative is a nondimensional parameter which is defined in terms of each high-low load sequence occurring in the spectrum. A cycle-by-cycle solution of the fractional differential equation yields the crack growth behavior for the spectrum. The approach is evaluated by comparing predictions with available experimental results for three aluminum alloys (7075-T6, 7050-T73, 2024-T3), two titanium alloys (Ti-6Al-4V, Ti-6Al-2Sn-4Zr-6Mo) and a nickel base superalloy IN-100. In all cases the method accurately predicted the general trends and estimates were well within a factor of two for 39 out of 40 tests analyzed.

KEY WORDS: crack propagation, fatigue (materials), delay cycles, overload, retarding, aluminum alloys, titanium alloys, predictions

A method is described to predict fatigue crack growth for variable amplitude fatigue. The approach is based on the results of recent studies dealing with crack retardation or the delay effect caused by a single overload [1-3].² It was found that the reduced crack growth rate following a single overload could be estimated by introducing a modification in the empirical constant amplitude crack propagation relationship. The modification consists in the replacement of the crack growth rate term by a fractional derivative; the order of the derivative being defined as the overload ratio. Then, using the condition that the increment of crack growth during the delay period is equal to the plastic zone produced by

* The authors wish to dedicate this work to the memory of Dr. Jonathon R. Osias (1945-1977).

¹ Senior assistant project engineer and analytical engineer, respectively, United Technologies Corp., Pratt and Whitney Aircraft Group, Commercial Products Division, East Hartford, Conn. 06108.

² The italic numbers in brackets refer to the list of references appended to this paper.

the overload, the solution of the fractional differential equation yields an explicit relationship for the number of delay cycles. A similar approach was developed to estimate delay caused by a single overload of varying duration at elevated temperature, that is, creep hold time effect [3]. The usefulness of this simple heuristic approach for estimating transient crack propagation behavior from the steady state (constant amplitude) crack growth relationship is encouraging. In this paper the approach is extended to variable amplitude fatigue. Predictions are compared with available experimental results for three aluminum alloys (7075-T6, 7050-T73, 2024-T3), two titanium alloys (Ti-6Al-4V, Ti-6Al-2Sn-4Zr-6Mo), and a fine-grain nickel base superalloy (IN-100). The general trends of all test results were accurately predicted and agreement was well within a factor of two. For comparative purposes and to indicate the extent of the perturbation introduced by the high-low load sequence, predictions based upon simple superposition are included.

Analysis

In order to provide a basis for comparison and to show the underlying structure of the proposed method, a simple approach is developed which permits, for an arbitrary crack geometry and mode I loading, the determination of explicit solutions of the governing crack propagation relationships for (a) the familiar constant-amplitude fatigue case, and (b) the variable amplitude fatigue case using a fractional derivative. It is hoped that this manner of presentation will provide greater insight than would a formal description. However, in the Appendix an algorithm for the practical implementation of the method is given based on the direct numerical integration of the governing fractional differential equation for crack propagation. Crack propagation for constant amplitude fatigue can be characterized by an empirical relationship of the form

$$da/dN = Af(R)(\Delta K)^n \quad (1)$$

where A and n are constants and $f(R)$ is a function which models the R-ratio dependence; ΔK is the range of the stress intensity factor. In general, the stress intensity factor is given by

$$K = \sigma\sqrt{\pi a}F \quad (2)$$

where F is a function of crack geometry and loading and has been determined for many configurations, for example [4-7].

For a specific form of F , a "piecewise" curvefit using a simple power function relation is introduced. Let

$$(\sqrt{\pi a}F)_i^n = \Phi_i a^{\beta_i} \quad i = 1, 2, 3, \dots \quad (3)$$

where the subscript refers to the specific range of crack length (crack increment) for which the curvefit parameters Φ_i , β_i are appropriate to within a desired degree of accuracy. Eq 1 can be rewritten in the convenient form

$$\begin{aligned} d(a^\alpha/dN) &= f(R)(\Delta\sigma)^n B_i & (4) \\ \alpha_i &= 1 - \beta_i & B_i = A \alpha_i \Phi_i \end{aligned}$$

Then using the initial condition $a(N_o) = a_o$, the solution of Eq 4 is

$$a = \{a_o^{\alpha_i} + f(R)(\Delta\sigma)^n B_i (N - N_o)\}^{1/\alpha_i} \quad (5)$$

Equation 5 can be used to estimate the crack growth behavior for constant amplitude fatigue. It can also be employed for the restricted class of load spectra which is characterized by a constant maximum load and variable R-ratio [8,9]. For this latter case, the load spectrum is decomposed into subspectra each consisting of a constant stress range and R-ratio. Then a set of equations similar to Eq 5 can be constructed to determine the crack growth for a single spectrum, care being taken to ensure that the load and R-ratio sequence is preserved. The repeated use of the equation-set will yield the desired crack growth estimate. The approach described will be recognized as an alternative (and equivalent) to that commonly employed: the direct numerical integration of the crack relation and the use of simple superposition. However, it is well known that the method implied by Eq 5 usually will not produce useful predictions for complex load spectra due to crack retardation. The Wheeler [10] and Willenborg [11] models are two of the better known methods which have been proposed to deal with variable amplitude fatigue. A general criticism that can be made of most models is either (a) variable amplitude crack data is required for implementation, or (b) the model gives useful predictions for a restricted class of load spectra [12]. The method proposed in this paper is subject to restriction (b); however, it will be shown that it gives useful results for a rather broad class of load spectra.

Recent studies [1-3] of delay effects due to a single overload suggest that the reduced crack growth rate following an overload can be estimated by replacing the rate term of the constant amplitude crack propagation relationship with a fractional derivative. For the single overload case, the order of the derivative is a nondimensional parameter that is defined as the overload ratio, σ_{MAX}/σ_{OL} , (Fig. 1). This simple idea is extended to variable amplitude fatigue by redefining the parameter in terms of the loads of each high-low load sequence of the spectrum.

Our choice of a definition for the parameter, λ , which is suitable for variable amplitude fatigue, is based on the observations of many investigators, for example [17-21], who have found that the ratios which play

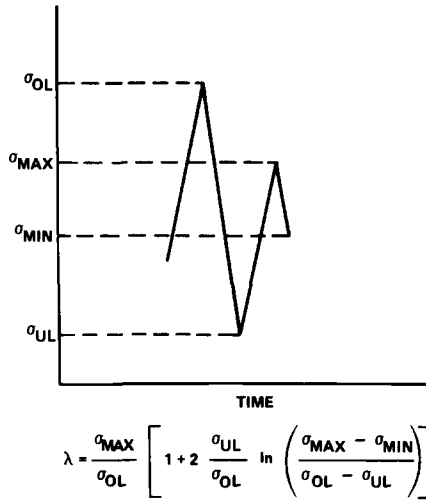


FIG. 1—Definition of high-low subspectrum parameters.

an important role in characterizing crack delay behavior are $\sigma_{\text{MAX}}/\sigma_{\text{OL}}$, $\sigma_{\text{UL}}/\sigma_{\text{OL}}$ and $\sigma_{\text{MIN}}/\sigma_{\text{MAX}}$. In addition, we require that the parameter be unity for the case of constant amplitude fatigue. Guided by these considerations, we propose the following definition for the “interaction” parameter:

For a load spectrum which consists only of tensile loading, the interaction parameter, λ_j , for the high-low sequence of the j th subspectrum is (Fig. 1)

$$\lambda_j = (\sigma_{\text{MAX}}/\sigma_{\text{OL}})\{1 + 2(\sigma_{\text{UL}}/\sigma_{\text{OL}}) \ln[(\sigma_{\text{MAX}} - \sigma_{\text{MIN}})/(\sigma_{\text{OL}} - \sigma_{\text{UL}})]\} \quad (6)$$

After replacing the differential operator of Eq 4 by a fractional differential operator, the governing equation for variable amplitude crack propagation becomes, for the j th subspectrum

$$d^{\lambda_j}(a^{\alpha_i} - a_{oj}^{\alpha_i})/[d(N - N_{oj})]^{\lambda_j} = f(R_j)(\Delta\sigma)_j^n B_i \quad (7)$$

where $(\Delta\sigma)_j = (\sigma_{\text{MAX}} - \sigma_{\text{MIN}})_j$ and a_{oj} , N_{oj} are the initial crack length and initial cycle number, respectively, of the j th subspectrum. The fractional differential operator includes the lower limits, as required. Only when the order of the differential operator is a nonnegative integer does the dependence on the lower limits vanish [12,13,14]. The solution of Eq 7 is

$$a = \{a_{oj}^{\alpha_i} + [f(R_j)(\Delta\sigma)_j^n B_i(N - N_{oj})^{\lambda_j}]/\Gamma(1 + \lambda_j)\}^{1/\alpha_i} \quad (8)$$

where $\Gamma(1 + \lambda_j)$ is the gamma function.

For the special case of constant amplitude fatigue, $f(R_j) = f(R)$, $(\Delta\sigma)_j = \Delta\sigma$, $\lambda_j = \lambda = 1$, and since $\Gamma(2) = 1$, we recover the result given by Eq 5, as required.

An examination of Eqs 5 and 8 shows that the latter will predict accelerated crack growth for the specific load subspectrum that consists of only two cycles of differing magnitudes. This can easily be shown by the following argument. If we form the ratio of the term $(a^{\alpha_i} - a_0^{\alpha_i})$ as given by Eq 8 to that given by Eq 5, we find

$$1/(\Delta N)^{1-\lambda}\Gamma(1 + \lambda)$$

where $(N - N_0) = \Delta N$. Then, for a high-low load sequence, $\lambda < 1$ and $\Gamma(1 + \lambda) < 1$, so that the preceding ratio

$$1/(\Delta N)^{1-\lambda}\Gamma(1 + \lambda) = \begin{cases} > 1 \text{ for } (\Delta N) = 1 \\ < 1 \text{ for } (\Delta N) > 1 \end{cases}$$

Furthermore, since the sign of both terms is negative, (since $\alpha_i < 1$ and therefore $B_i < 1$) we conclude that Eq 8 will predict delay or crack retardation for $(\Delta N) > 1$ and accelerated crack growth for $(\Delta N) = 1$. Unfortunately, attempts to check the predicted acceleration effect by experiment were inconclusive.

Equation 8 is the main result which embodies the proposed prediction method. Its appropriate use entails the following steps:

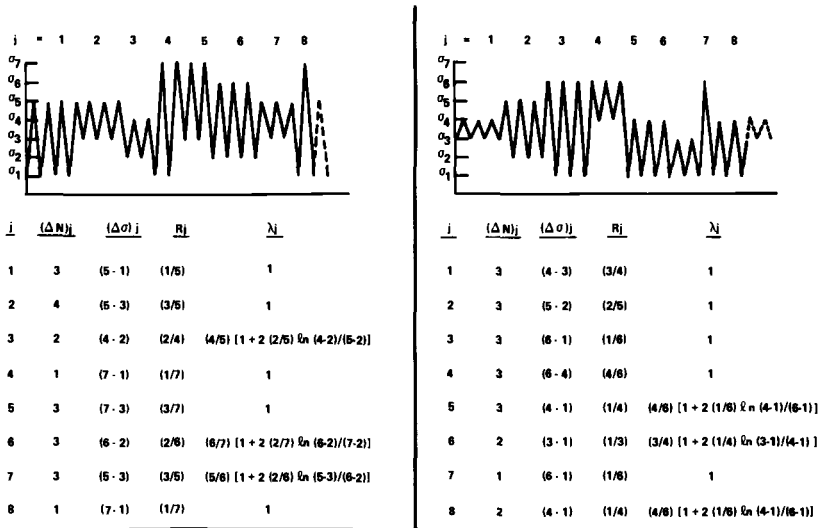
- (a) determination of the piecewise curvefit parameters, Φ_i and β_i
- (b) the decomposition of the load spectrum into a sequence of subspectra, each having fixed (constant) values for R and $\Delta\sigma$
- (c) identification of each high-low sequence of the load spectrum and the determination of the corresponding parameter λ . The parameter is to be used for the low part of each subspectrum as illustrated by Fig. 2.

The preceding steps will enable one to construct a set of equations similar to Eq 8 which must be solved sequentially, beginning with the initial crack length a_0 . The calculated (final) crack length for the first subspectrum is used for the initial crack length of the second subspectrum.

Figure 2 gives some illustrative examples of the spectrum decomposition method together with the appropriate parameters for each of the subspectra. A method that employs direct numerical integration of the basic fractional differential equation is given in the Appendix.

Evaluation

The accuracy of the prediction method was evaluated using experimental data [8,9,16,18] for three aluminum alloys (7075-T6, 7050-T73, 2024-T3), two titanium alloys (Ti-6Al-4V, Ti-6Al-2Sn-4Zr-6Mo), and a fine-



NOMENCLATURE: ALL TERMS IN PARENTHESIS INDICATE APPROPRIATE STRESS BY ITS SUBSCRIPT.

(a/b) ≡ (σ_a/σ_b) (a-b) ≡ σ_a - σ_b

FIG. 2—Examples of decomposition of a load spectrum into subspectra.

grain nickel-base superalloy (IN-100). Table 1 gives the baseline constant amplitude fatigue crack relationships used for the predictions. Figures 3 through 9 give the results of the evaluation. It can be readily seen that the method predicts the trends for all tests quite accurately and, in general, agreement is well within a factor of two except for one test (3C, Fig. 5a). The agreement is considered good in view of the variation typical of crack growth data. Predictions using simple superposition, included for comparative purposes, also provide estimates of the amount of crack retardation.

As aforementioned, it is noteworthy that the method predicts accelerated crack growth for a specific class of load spectra which consists of simply two loads with different magnitudes. Two experiments to check this prediction were carried out, Figs. 8a and 9. In order to evaluate the theoretical magnitude of the acceleration, calculations based on the proposed method were compared with simple superposition. The acceleration effect (theoretical) was found to be small and a comparison of predictions with experimental data was inconclusive.

An overview of the efficacy of the proposed method can be obtained from Table 2 and Fig. 10, where comparisons between predicted and experimental results are given. The lack of correlation of the simple superposition estimates (Fig. 10) with test results clearly indicate the highly nonlinear interaction that was present in most tests. The strong correlation found between test data and the estimates made by the

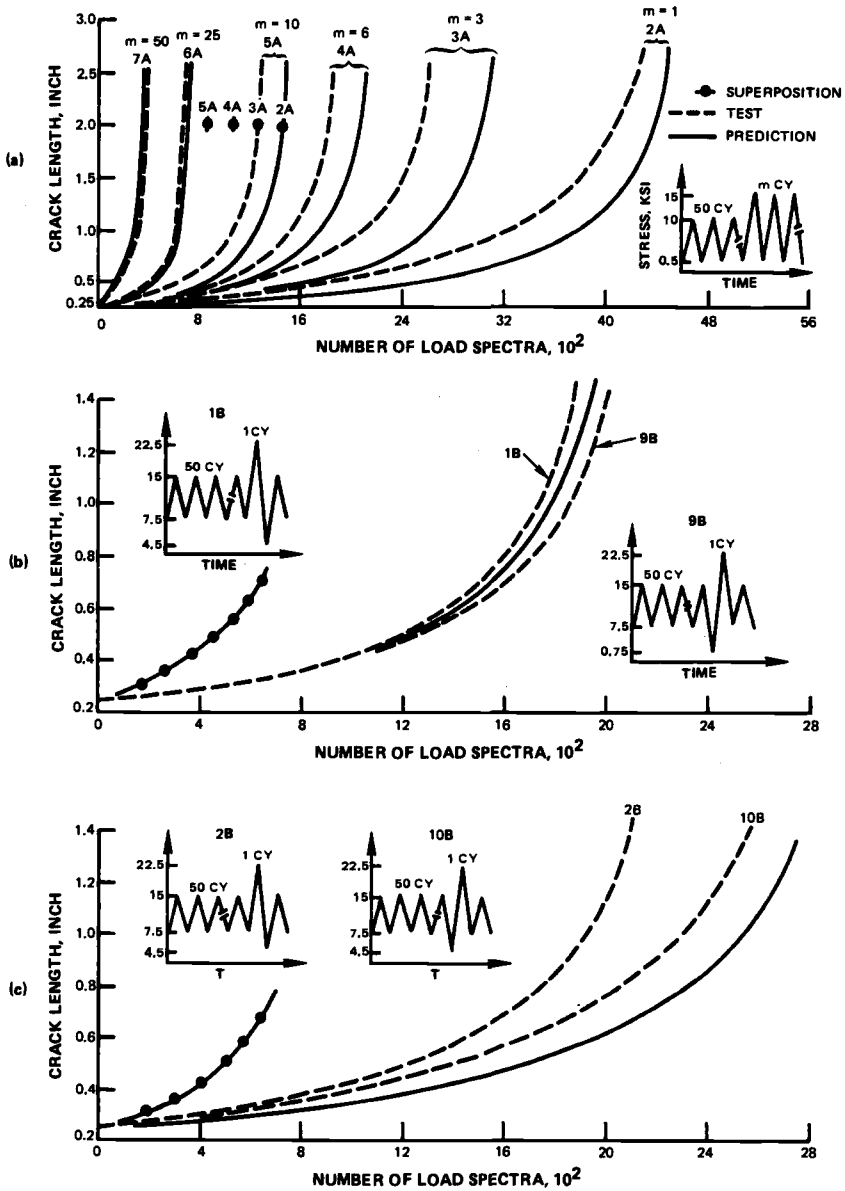


FIG. 3—Comparison of predictions with tests on 7075-T6 (Ref 8) (1 in. = 0.0254 m; 1 ksi = 1.099 MN/m²).

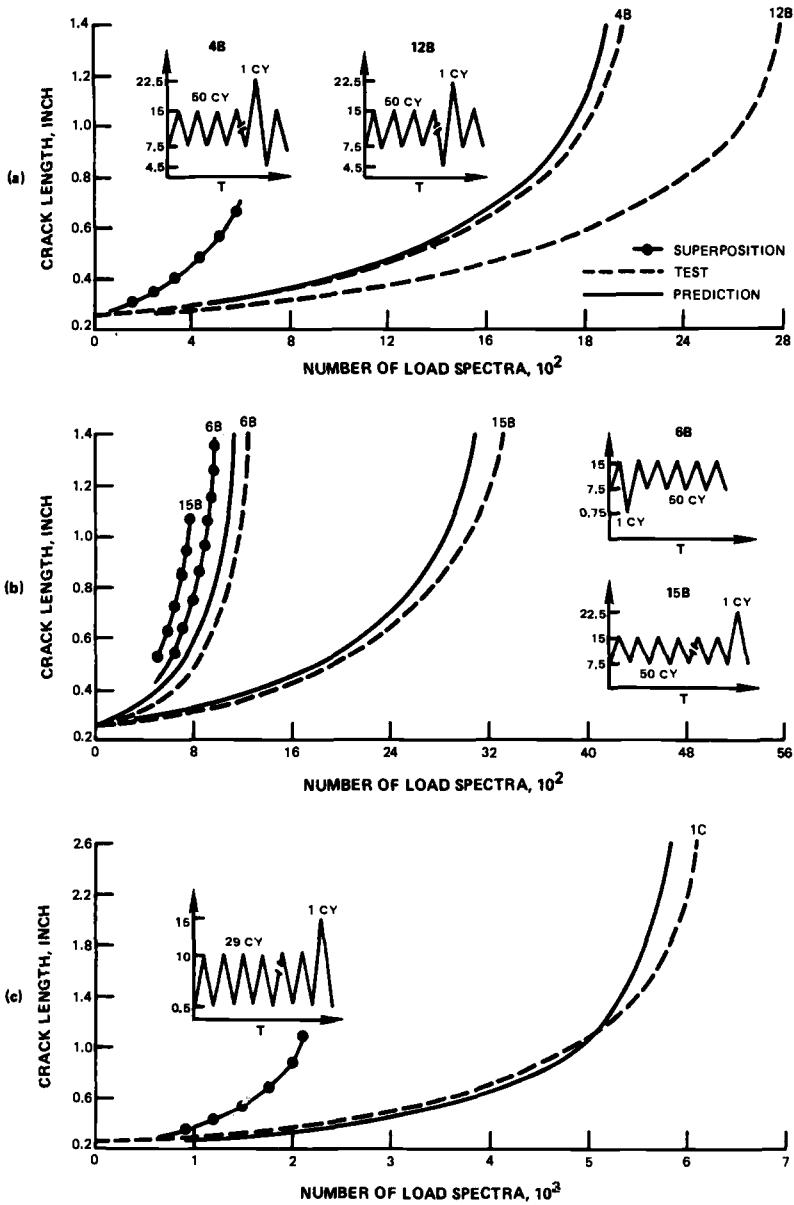


FIG. 4—Comparison of predictions with tests on 7075-T6 (Ref 8) (1 in. = 0.0254 m; 1 ksi = 1.099 MN/m²).

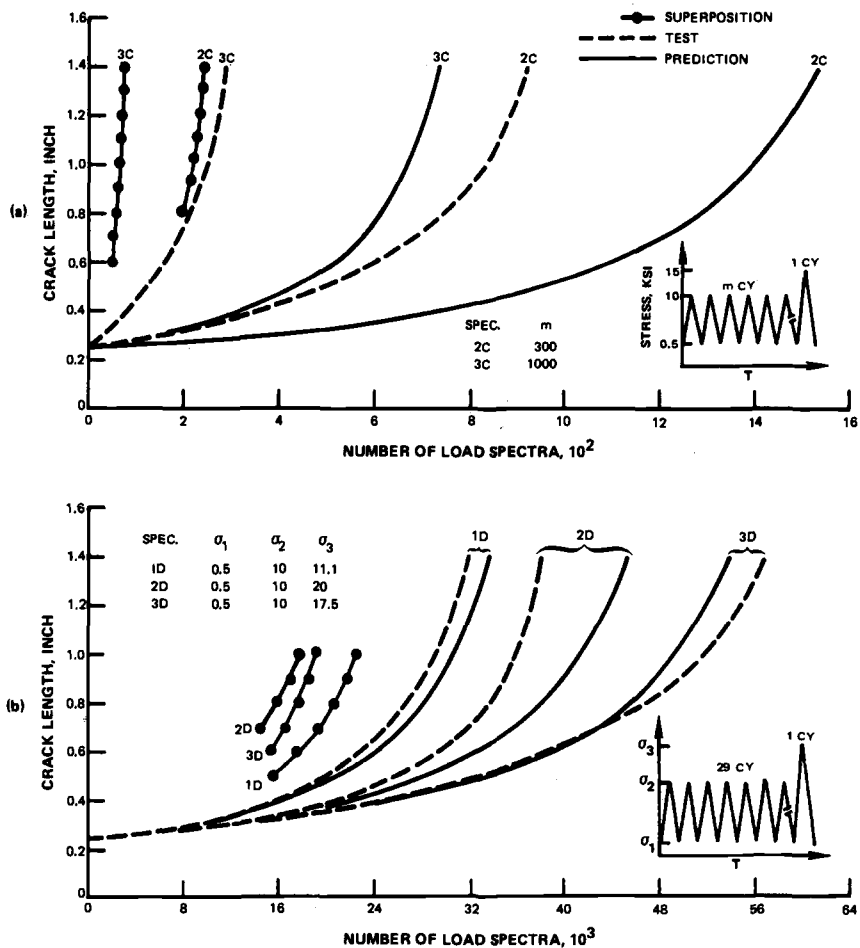


FIG. 5—Comparison of predictions with tests on 7075-T6 (Ref 8) (1 in. = 0.0254 m; 1 ksi = 1.099 MN/m²).

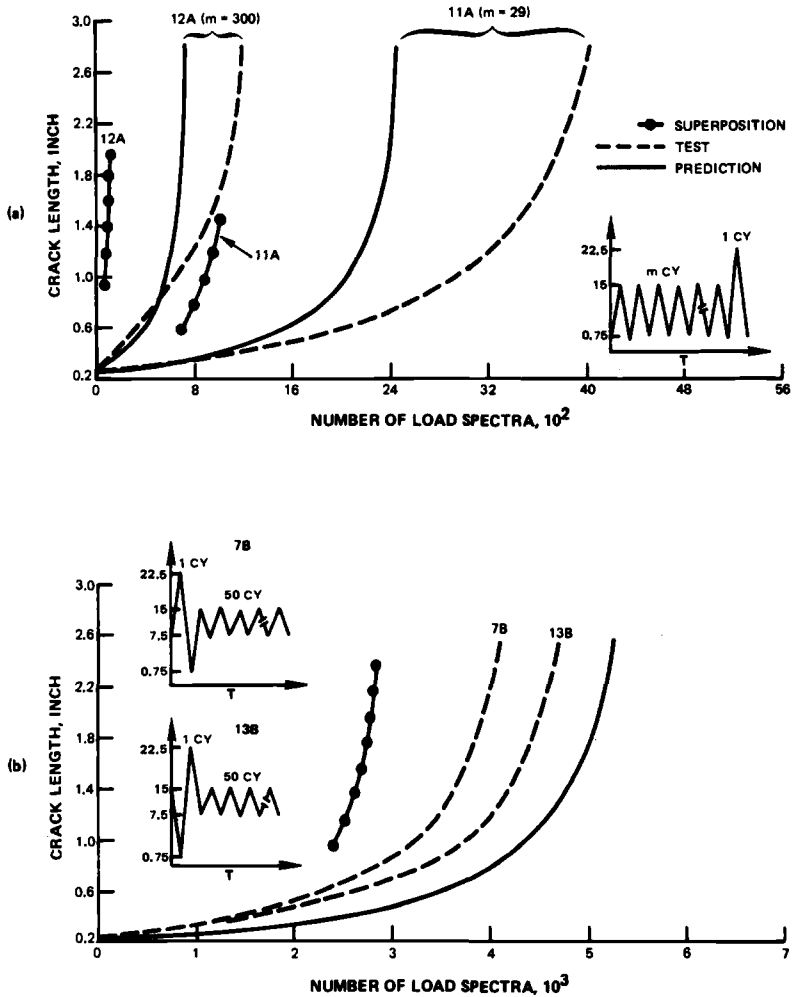
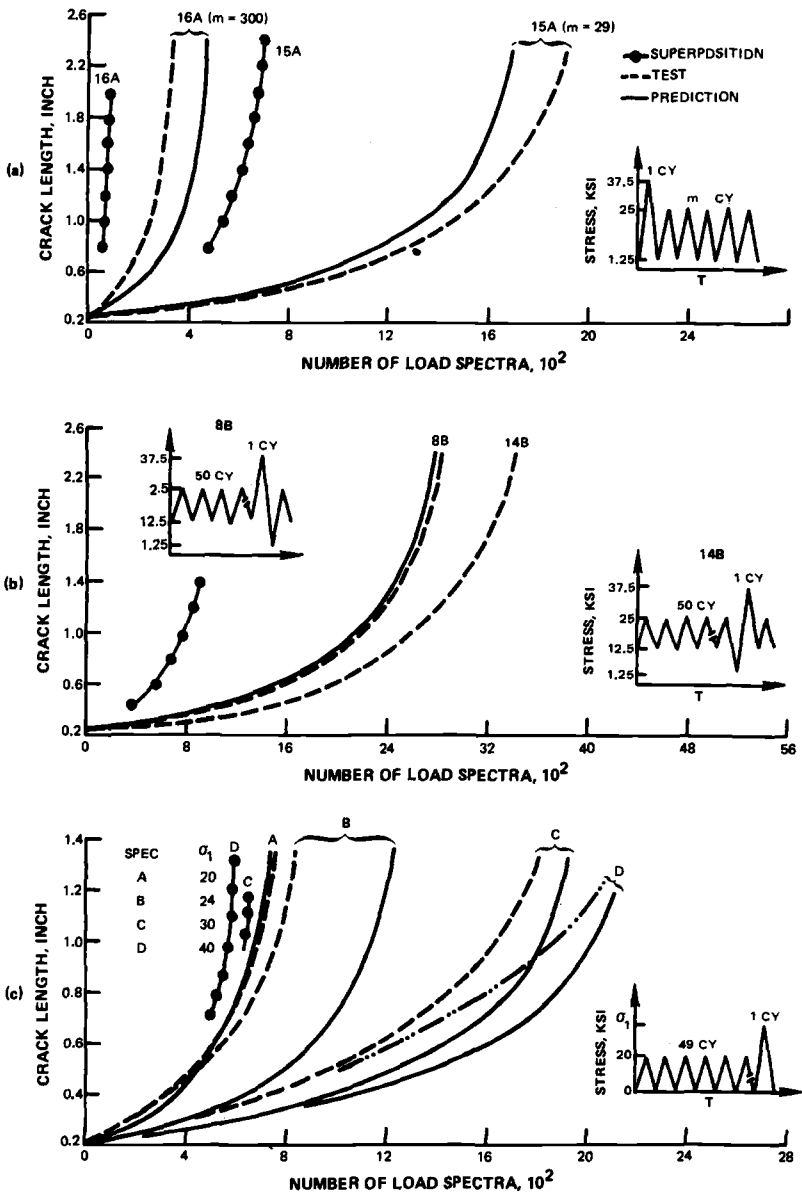
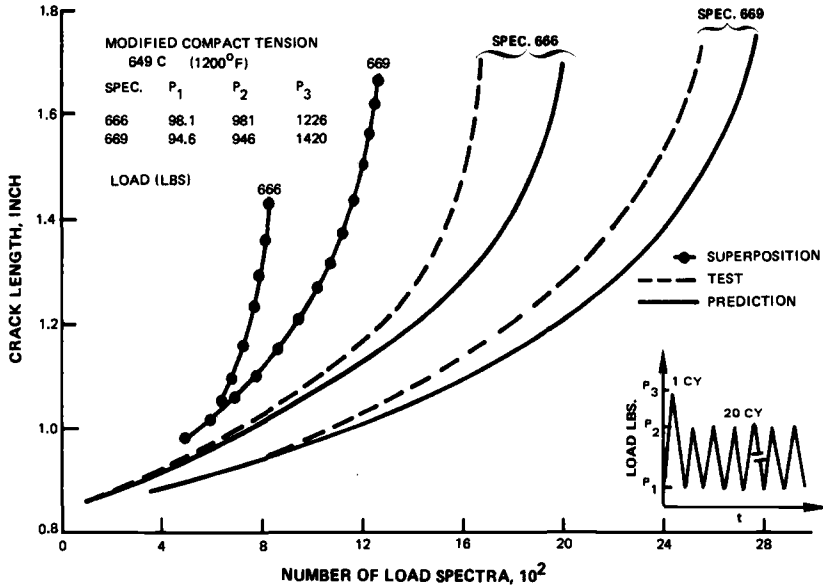
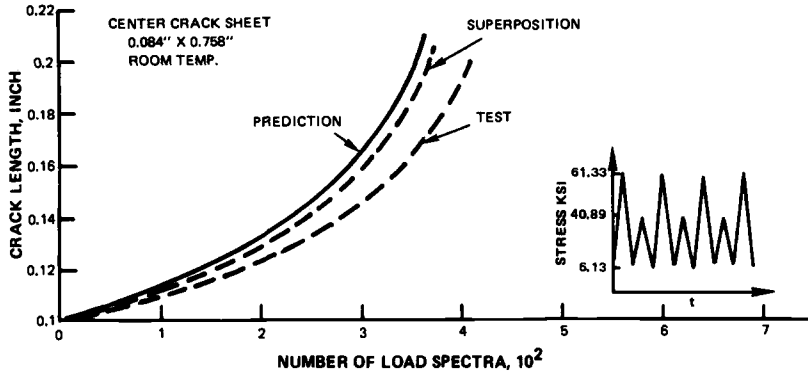


FIG. 6—Comparison of predictions with tests on 2024-T3 (Ref 8) (1 in. = 0.0254 m; 1 ksi = 1.099 MN/m²).



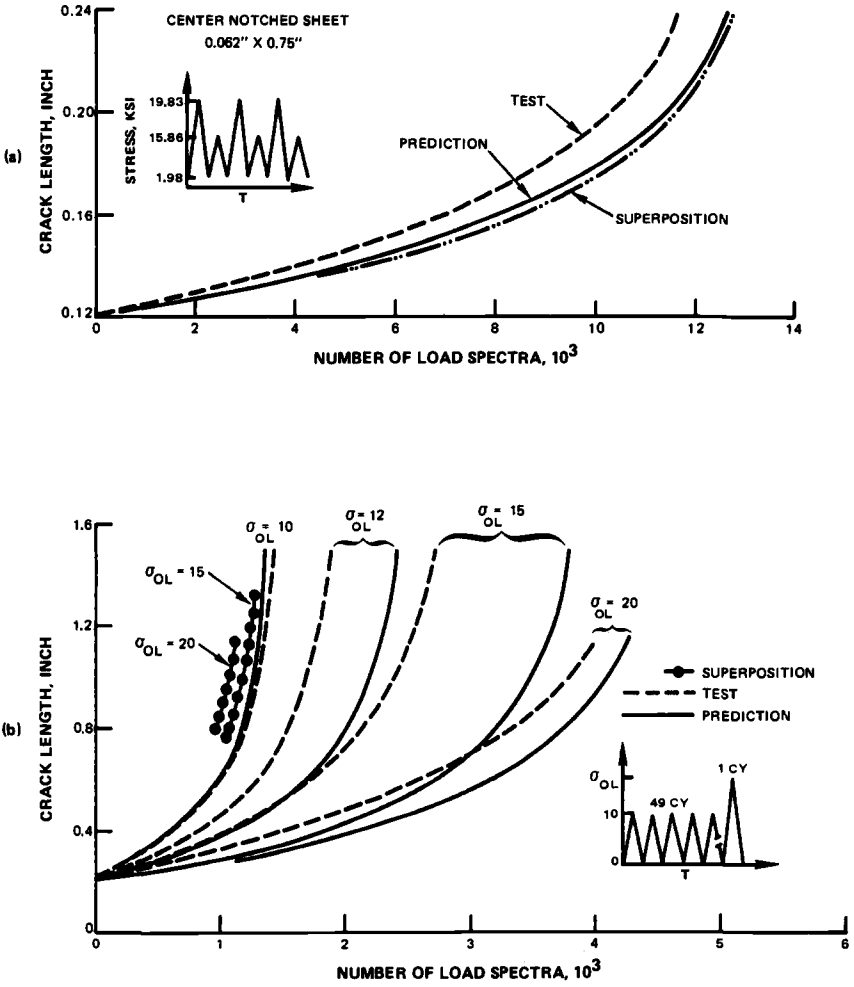
(a) and (b) Ref 8; (c) Ref 18

FIG. 7—Comparison of predictions with tests on Ti-6Al-4V (1 in. = 0.0254 m; 1 ksi = 1.099 MN/m²).



(a) Room Temperature (Ref 9)
(b) At 649°C (1200°F); (Ref 16); (1 lbf = 0.2248 N)

FIG. 8—Comparison of predictions with tests on 1N-100 (1 in. = 0.0254 m; 1 ksi = 1.099 MN/m²).



(a) Ti-6Al-2Sn-4Zr-6Mo (Ref 9)
 (b) 7050-T73 (Ref 18)
 (1 in. = 0.0254 m; 1 ksi = 1.099 MN/m²)

FIG. 9—Comparison of predictions with test.

TABLE 1—Crack propagation relationships used in predictions.

Material	n	A	$f(R)$	R	Ref
7075-T6	3.9	3.755×10^{-9}	$R^{0.373}$	$R \leq 0.5$	8
7050-T73	2.905	7.219×10^{-9}	1	$0.03 \leq R \leq 0.1$	18
2024-T3	3.86	3.25×10^{-10}	$[1 + 0.4R]^{0.86}$	$0.03 \leq R \leq 0.5$	8
Ti-6Al-4V	3.1	9.81×10^{-10}	$[1/(1-0.578R)]^{3.1}$	$-5.0 \leq R \leq 0.9$	19
Ti-6Al-2Sn-4Zr-6Mo	4.84	1.55×10^{-11}	$[1.54/(1.64 - R)]^{4.84}$	$-5.0 \leq R \leq 0.5$	9
IN-100 (R. T.)	4.27	3.325×10^{-12}	1	0.1	9
IN-100 (1200°F)	2.3	2.84×10^{-8}	1	0.1	16

$$\frac{da}{dN} = Af(R)(\Delta K)^n$$

Units: $\frac{da}{dN}$ (in./cycle) ΔK (ksi $\sqrt{\text{in.}}$)

Conversion factors: 1 in. = 0.0254 m

1 ksi = 6.895 MN/m²

1 ksi $\sqrt{\text{in.}}$ = 1.0988 MN/m^{3/2}

$C = 5/9$ (°F - 32)

TABLE 2—Comparison of experimental and theoretical results.

Figure No.	Specimen No.	aF ^a	N _{EXP} × 10 ²	N _{THEO} × 10 ²
3(a)	2A	0.0356	37.4	41.6
	3A	0.0356	24	28.3
	4A	0.0356	17.2	19.4
	5A	0.0356	12	13.8
	6A	0.0356	6.4	6.8
3(b)	7A	0.0356	3.6	3.3
	1B	0.0356	18.7	19.3
3(c)	9B	0.0356	20	19.3
	2B	0.0356	21.1	27.6
4(a)	10B	0.0356	25.7	27.6
	4B	0.0356	21.6	21
4(b)	12B	0.0356	27.9	21
	6B	0.0356	12.6	11.2
4(c)	15B	0.0356	33.5	30.9
	1C	0.0356	54.8	53
5(a)	2C	0.0356	9.2	15.4
	3C	0.0356	2.9	7.4
5(b) ^b	1D	0.0356	316	339
	2D	0.0356	384	455
	3D	0.0356	568	536
6(a)	11A	0.0356	34	22.4
	12A	0.0356	8.9	6.3
6(b)	7B	0.0356	37	48
	13B	0.0356	42	48
7(a)	15A	0.0356	16.8	15.3
	16A	0.0356	2.8	4.2
7(b)	8B	0.0356	25.3	24.4
	14B	0.0356	29.6	24.4
7(c)	A	0.0305	7.4	7.2
	B	0.0305	11.2	12.1
	C	0.0305	17.6	19
	D	0.0305	20.6	21.2
8(a) ^b		0.0051	4.1	3.6
8(b)	666	0.0356	15.4	17.9
	669	0.0356	22	24.4
9(a)		0.0061	117	128
9(b)	σ _{OL} = 10	0.0356	14	14.5
	= 12	0.0356	19	24
	= 15	0.0356	27	37.7
	= 20	0.0305	40.5	43

^a Final crack length, m.^b Not shown in Fig. 10.

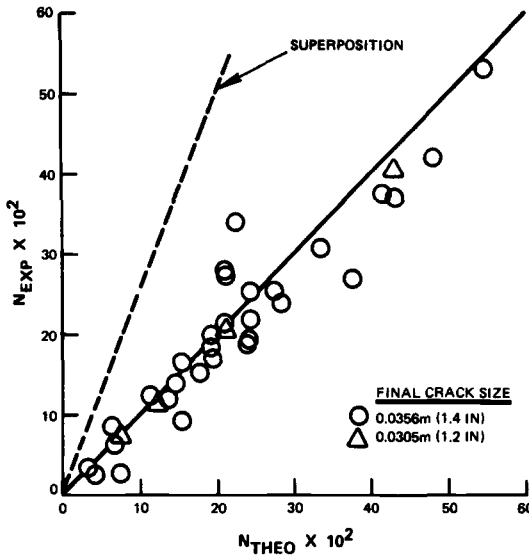


FIG. 10—Comparison of experimental results with theoretical predictions.

proposed method indicate that the approach can successfully model non-linear interaction effects.

In its present form the prediction method does not distinguish between spectra consisting of underload/overload and overload/underload sequences; similar behavior is predicted for both sequences so that only one theoretical prediction appears in some figures. Several investigators have carried out work that is relevant to this problem, including Alzos et al [17], Porter [8], and Hsu and Lassiter [18]. In future work an attempt to model these effects will be made.

Discussion

The authors clearly recognize the ad hoc nature of the model since the overload parameter is not identified with mechanisms that are known to be present, that is, residual compressive stresses, closure, etc. However, it is defined in terms of load ratios that have been found to be significant by most investigators, for example [17–22].

The load decomposition method described by Fig. 2 was chosen purely on the basis of simplicity and should be considered as a tentative approach until it has been evaluated thoroughly by comparing predictions using this method and test results for spectra that are much more complex than those considered by this work. Other approaches such as the rain flow method [23] for dealing with the cycle counting problem will receive attention in future work.

In addition, we believe that the usefulness of a fractional operator to model transient effects from steady-state behavior appears to have broader implications beyond fracture mechanics and should be explored.

Conclusion

A relatively simple method is presented and evaluated for estimating the crack growth behavior for variable amplitude fatigue. The approach requires only the constant amplitude crack propagation relationship as a function of R-ratio. The evaluation indicates that the method has merit as a practical engineering tool.

Acknowledgment

The authors wish to thank R. M. Wallace of the Government Products Division of Pratt & Whitney Aircraft Group, Florida, for test data on IN-100 and also to acknowledge the help given by J. T. Hill.

APPENDIX

The method for solving Eq 1 or Eq 7 for crack length on a cycle-by-cycle basis is not efficient for complex load spectra. The equally accurate approach of the direct numerical integration of Eq 1 is better suited for computer application, as described below.

For the most general problem with m degrees of freedom, for example, a complex crack configuration in three dimensions, Eq 1 represents a system of differential equations which may be solved for N using standard numerical techniques such as Runge-Kutta. However, the simple 1 deg of freedom problem described here may be reduced to a single step. The change in life, ΔN_i , due to an increment of crack length, Δa_i , is given by

$$\Delta N_i = \frac{1}{2} [1/(da/dN)_i + 1/(da/dN)_{i-1}] \Delta a_i \quad (9)$$

where

$$\Delta a_i = a_i - a_{i-1}$$

$$\Delta N_i = N_i - N_{i-1}$$

Therefore, the life, N , for any value of crack length may be determined by successively incrementing the crack length and calculating a new life.

In order to apply the above procedure to the general fractional derivative form of the crack growth relationship described above, consider another form of Eq 7,

$$d^\lambda a/dN^\lambda = G(\Delta K, R) \quad (10)$$

where λ is the parameter defined in terms of stress intensity factors

$$\lambda = (K_{\text{MAX}}/K_{\text{OL}}) \left\{ 1 + 2(K_{\text{UL}}/K_{\text{OL}}) \ln[(K_{\text{MAX}} - K_{\text{MIN}})/(K_{\text{OL}} - K_{\text{UL}})] \right\} \quad (11)$$

Assuming that $G(\Delta K, R)$ is independent of crack length during a given subcycle, Eq 10 may be integrated to give, for the i th subcycle

$$a_i = a_{o_i} + [G(\Delta K, R)/\Gamma(1 + \lambda_i)](N_i - N_{o_i})^{\lambda_i} \quad (12)$$

where a_{o_i} , N_{o_i} are the initial conditions. Since $\Delta N_i = 1$, the crack growth rate for the i th subcycle is given by

$$\frac{da}{dN_i} = \frac{\Delta a_i}{\Delta N_i} = \frac{G(\Delta K_i, R_i)}{\Gamma(1 + \lambda_i)} (N_i - N_{o_i})^{\lambda_i - 1} - \frac{G(\Delta K_{i-1}, R_{i-1})}{\Gamma(1 + \lambda_{i-1})} (N_{i-1} - N_{o_{i-1}})^{\lambda_{i-1} - 1} \quad (13)$$

Then Eq 13 may be used in Eq 9 and the procedure described above can be applied directly. A comparison of the results obtained by the above algorithm and by the method described in the main body of the paper showed excellent agreement; the predicted lives differing by less than 1 percent in all cases.

References

- [1] Gemma, A. E. and Allison, D. E., *International Journal of Fracture*, Vol. 12, 1976, pp. 491-494.
- [2] Gemma, A. E., Allison, D. E., and Hopkins, S. W., *Engineering Fracture Mechanics*, Vol. 9, 1977, pp. 647-654.
- [3] Gemma, A. E., "Hold-Time Effect of a Single Overload on Crack Retardation at Elevated Temperature," submitted to *Engineering Fracture Mechanics*.
- [4] Paris, P. C. and Sih, G. C. in *Fracture Toughness Testing and Its Applications*, ASTM STP 381, American Society for Testing and Materials, 1970, pp. 30-83.
- [5] Sih, G. C., *Handbook of Stress-Intensity Factors*, Institute of Fracture and Solid Mechanics, Lehigh University, Bethlehem, Pa., 1973.
- [6] Rooke, D. P. and Cartwright, D. J., *Compendium of Stress Intensity Factors*, Her Majesty's Stationery Office, London, 1976.
- [7] Tada, H., Paris, P. C., and Irwin, G. R., *The Stress Analysis of Cracks Handbook*, Del Research Corp., Hellertown, Pa. 1973.
- [8] Porter, T. R., *Engineering Fracture Mechanics*, Vol. 4, 1972, pp. 717-736.
- [9] Gemma, A. E. and Masci, R., unpublished research on Ti-6Al-2Sn-4Zr-6Mo and IN-100.
- [10] Wheeler, O. E., *Journal of Basic Engineering*, American Society of Mechanical Engineers, Vol. 94, 1972, pp. 181-186.
- [11] Willenborg, R., Engle, R. M., and Wood, H. A., "A Crack Growth Retardation Model Using an Effective Stress Concept," Technical Memo 71-1-FBR, Air Force Flight Dynamics Laboratory, Wright Patterson Air Force Base, Ohio. 1971.
- [12] Engle, R. M. and Rudd, J. L., *Journal of Aircraft*, American Institute of Aeronautics and Astronautics, Vol. 13, No. 7, 1976, pp. 462-466.
- [13] Oldham, K. B. and Spanier, J., *The Fractional Calculus*, Academic Press, New York, 1974.
- [14] Ross, B., "The Development of the Gamma Function and a Profile of Fractional Calculus," Ph.D. dissertation, New York University, 1974.
- [15] Lavoie, J. L., Osler, T. J., and Tremblay, R., *SIAM Review*, Society of Industrial and Applied Mathematics, Vol. 18, No. 2, 1976, p. 240.
- [16] Wallace, R., unpublished research on IN-100 at 1200°F.
- [17] Alzos, W. X., Skat, A. C., and Hillberry, B. M. in *Fatigue Crack Growth Under Spectrum Loads*, ASTM STP 595, American Society for Testing and Materials, 1976, pp. 41-60.
- [18] Hsu, T. M. and Lassiter, L. W., *Journal of Aircraft*, American Institute of Aeronautics and Astronautics, Vol. 12, No. 2, 1975, pp. 100-104.
- [19] Yuen, A., Hopkins, S. W., Leverant, G. R., and Rau, C. A., Jr., *Metallurgical Transactions*, Vol. 5, 1974, pp. 1833-1842.

- [20] Wei, R. P. and Shih, T. T., *International Journal of Fracture Mechanics*, Vol. 10, 1974, pp. 77–85.
- [21] Corbly, D. M. and Packman, P. F., *Engineering Fracture Mechanics*, Vol. 5, 1973, pp. 479–497.
- [22] *Fatigue Crack Growth Under Spectrum Loads*, ASTM STP 595, American Society for Testing and Materials, 1976.
- [23] Dowling, N. E., *Journal of Materials*, Vol. 7, No. 1, 1972, pp. 71–87.

Surface Flaws

Semi-Elliptical Cracks in a Cylinder Subjected to Stress Gradients

REFERENCE: Heliot, J., Labbens, R. C., and Pellissier-Tanon, A., "Semi-Elliptical Cracks in a Cylinder Subjected to Stress Gradients," *Fracture Mechanics, ASTM STP 677*, C. W. Smith, Ed., American Society for Testing and Materials, 1979, pp. 341-364.

ABSTRACT: The calculation of stress intensity factors in three-dimensional situations, under any stresses, is an engineering necessity. The authors presented at the 9th National Symposium on Fracture Mechanics, Pittsburgh, 1975, a method for calculating three-dimensional weight functions by finite elements. But the computer time was found to be too long for engineering applications.

In this study the three-dimensional problem is limited to symmetrical problems with applied stresses expressed by a polynomial in one coordinate. Calculations are performed on semi-elliptical cracks in the meridional plane of a cylinder, and the applied stress is expressed by a polynomial of the fourth degree in the coordinate in the radial direction (see nomenclature and Fig. 1). The method could be extended to other symmetrical geometries and loads.

So-called "polynomial influence functions" are defined and correspond to the terms of the polynomial. These functions depend on the radii ratio, the shape, and the depth of the crack; since these parameters are fixed, they are functions of the eccentric angle that defines a point on the crack front.

The polynomial influence functions are computed by the boundary integral equation method. The method was first tested on a penny-shaped crack for which the known weight function allowed a direct computation of the polynomial influence functions. The accuracy was found sufficient to apply the method to more difficult problems. These functions were then calculated for semi-elliptical cracks in cylinders.

The results are presented in the form of curves; they are discussed and compared with the results published by other authors.

KEY WORDS: crack propagation, fracture parameters, stress intensity factor, three-dimensional problems, semi-elliptical cracks, cylinders, boundary integral equation method, fatigue (materials)

¹ Research engineer and scientific manager, respectively, Creusot-Loire, Paris, France.

² Research consultant, Framatome, Courbevoise, France.

Nomenclature

a	Radius of a circular crack
b	Shorter semi-axis of an elliptical crack
c	Longer semi-axis of an elliptical crack
ϕ	Eccentric angle of an ellipse
k^2	$1 - c^2/a^2$
$E(k)$	Complete elliptical integral of the second kind
R_o, R_i	Outer and inner radii of a cylinder
$t = R_o - R_i$	Thickness of the wall of a cylinder
x	Abscissa from the inner face of the wall
σ_j	Applied stresses ($j = 0, 1, 2, 3, 4$)
$K(\phi)$	Stress intensity factor
$h_j(\phi)$	Polynomial influence functions
r	Short distance along a normal to the crack tip
v	Displacement of a point on the surface of the crack
E	Young's modulus
ν	Poisson's ratio
P, P'	A point on the crack surface, front
$G(P, P')$	Bueckner's weight function

The calculation of stress intensity factors in three-dimensional situations is an important engineering problem, even if it is restricted to symmetrical loads or Mode I. It is necessary to consider not only uniform tension but also stress gradients as encountered in thermal shocks, for instance. And as loads variable with time must be applied to the cracked solid, it is desirable to find a means of not repeating the complete calculation for every load.

The knowledge of three-dimensional weight functions, as defined by Bueckner [1]³ and Rice [2], would solve this problem. The authors presented at the 9th National Symposium on Fracture Mechanics an attempt for computing three-dimensional weight functions by finite elements [3]. A test was done on a penny-shaped crack in an infinite solid for which the weight function is known in closed form [4]. It was found that the computation was possible, but about 5000 s central processing unit (CPU) time were spent for this rather simple problem with a CdC 7600 computer; although improvements were possible, this was too long a time for engineering applications.

It was decided to test the possibilities of the boundary integral equation (BIE) method, as developed by Rizzo [5], Cruse [6,7], and in France by Centre Technique des Industries de la Mécanique (CETIM) [8,9]. With the BIE method the boundaries of the body are meshed, not the volume. This

³ The italic numbers in brackets refer to the list of references appended to this paper.

results in a number of nodes smaller than the number with finite elements; thus, the computing time should be shorter.

The problem to be studied was a semi-elliptical crack in the meridional plane of a cylinder subjected to a stress approximated by a polynomial in x (Fig. 1).

Previous Research on Semi-Elliptical Cracks

The problem of a semi-elliptical crack in a plate or a cylinder has been studied by several authors. To the knowledge of the authors of this paper the main studies in that domain are the following.

1. Shah and Kobayashi [10,11] derived approximate solutions for the deepest point of the crack in traction and bending from their basic work on an embedded crack [12].

2. Bueckner [13] treated analytically the problem of a surface crack in a half space, and derived stress intensity factors, crack opening displacements and weight functions; up to now no numerical calculation has been performed by this method.

3. Smith and Sorensen [14] studied a semi-elliptical crack in a plate in tension, using the iteration method. They started from the solution for the embedded crack [12], and removed tension and shear stresses on the free boundaries using solutions by Love [15] and Smith and Alavi [16].

4. Raju and Newman [17] treated the same problem by finite elements, with a special attention to accuracy and convergence.

5. Approximate values of the stress intensity factor at the deepest point of a semi-elliptical crack in a thick pressurized cylinder were published by Underwood [18].

6. Kobayashi et al [19,20] used the iteration method to calculate the stress intensity factors along the edge of a semi-elliptical crack in the

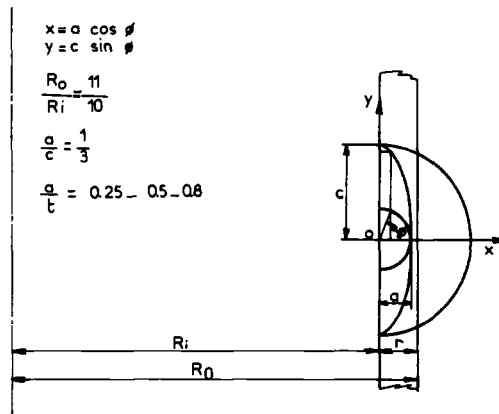


FIG. 1—Semi-elliptical crack in a cylinder.

meridional plane of a cylinder, resulting from a stress approximated by a polynomial, a hoop pressure stress, and thermal stresses. As the general solutions developed by Love [15] and Smith and Alavi [16] are only for semi-infinite solids and there exists no solution for solids limited by cylinders, they performed the iteration calculations on a plate with restrained ends simulating the cylinder and used a curvature correction factor.

7. Atluri, Kathiresan, et al [21,22] developed a hybrid-displacement method and calculated the stress intensity factors along semi-circular and semi-elliptical cracks in rather thick pressurized cylinders.

8. Finite elements were used by Blackburn and Hellen [23] for pressurized cylinders and by Reynen [24] particularly for thermally loaded cylinders.

Problems of Cracked Cylinders

All these studies yielded valuable results; however, there was a need for an engineering calculation method which would yield functions depending only upon the geometry. These functions would allow a quick calculation of stress intensity factors for any applied stress.

Assuming that the stress applied on the crack is approximated by a polynomial (Fig. 1)

$$\sigma(x) = \sigma_0 + \sigma_1 \frac{x}{t} + \sigma_2 \left(\frac{x}{t}\right)^2 + \sigma_3 \left(\frac{x}{t}\right)^3 + \sigma_4 \left(\frac{x}{t}\right)^4 \quad (1)$$

the stress intensity factor is yielded by

$$\frac{K_j(\phi)}{\sigma_j \left(\frac{a}{t}\right)^j \sqrt{\pi a}} \frac{E(k)}{\left(\cos^2 \phi + \frac{a^2}{c^2} \sin^2 \phi\right)^{1/4}} = h_j(\phi) \quad j = 0, 1, 2, 3, 4 \quad (2)$$

The $\sigma_j (a/t)^j$ are the stresses of order j at the deepest point of the crack. The functions $h_j(\phi)$, denominated "polynomial influence functions" depend only upon the geometrical parameters R_0/R_i , a/c , a/t (Fig. 1).

As it has been seen, this is also the purpose of the work of Kobayashi et al [19,20], who published results for pressure and thermal loadings, but not functions such as the $h_j(\phi)$.

The study was divided into two parts:

(a) A check of the possibilities of the program Equations Integrales Tri Dimensionnelles (EITD) developed by Centre d'Etudes Techniques des Industries Mécaniques (CETIM) according to the BIE method was accomplished by treating the problem of a penny-shaped crack in an infinite solid subjected to a stress gradient as in Eq 1; the functions $h_j(\phi)$ can be computed and calculated algebraically by integration of the weight

function of the penny-shaped crack which is known in closed form [4] and compared to the same functions computed by the BIE method.

(b) An application of the method to a semi-elliptical crack frequently met in engineering problems (Fig. 1); the following ratios were chosen for the geometrical parameters

$$\frac{R_o}{R_i} = \frac{\text{outer diameter}}{\text{inner diameter}} = \frac{11}{10} \text{ pressurized water reactor (PWR vessels)}$$

$$\frac{a}{c} = \frac{1}{3} \text{ (ASME Code, Section III, Appendix G)}$$

$$\frac{a}{t} = 0.25, 0.50, \text{ and } 0.80$$

It was felt that for engineering purposes an accuracy of 5 to 10 percent would be sufficient.

The study was limited to symmetrical problems.

It was agreed that the same work with the same data would be undertaken by McGowan and Raymund [25] who used a finite element method.

Program EITD Developed by CETIM—Test with a Penny-Shaped Crack

BIE Method

Mathematical solutions of elasticity problems by the BIE method were published a long time ago. They were resumed and applied numerically in two dimensions by Rizzo [5], and extended to three-dimensional and particularly crack problems by Cruse [6,7].

With this method any elasticity problem can be solved using two second order tensor kernels defined on the boundary, depending only upon the geometry. These two kernels allow the calculation of the displacements and tractions at the boundary by an integral equation. The displacements and stresses can be then calculated at any interior point in terms of the two kernels and the stresses and displacements at the boundary.

In this way, a three-dimensional problem is reduced to a two-dimensional problem on the boundary. In engineering computation this results in a number of elements and nodes smaller than with finite elements. Although the matrix is complete and not symmetrical, a significant reduction in computation time can be expected.

EITD Program

An important feature of this program is the introduction by Lachat and Watson [8,9] of eight nodes surface isoparametric elements. The program

allows the application of five loads and yields the displacements and stresses at the boundaries and the stresses at specified points inside the body.

Stress intensity factors can be calculated by extrapolation in a plane normal to the crack front of $\sigma \sqrt{2\pi r}$ ahead of the crack, or of

$$\sqrt{\frac{\pi}{2}} \frac{E}{2(1-\nu^2)} \frac{v}{\sqrt{r}}$$

on the crack surface.

For this study, quarter point isoparametric elements [26] which introduce a parabolic variation of the displacements were used on the crack front as they had been by several authors with finite elements; the interpolation of the stresses on the surface of the elements was parabolic.

Calculation of Polynomial Influence Functions for a Penny-Shaped Crack in an Infinite Solid

In this problem the reference length must be a , radius of the crack (Fig. 2). Equation 2 is reduced to

$$\frac{\pi}{2} \frac{K_j(\phi)}{\sigma_j \sqrt{\pi a}} = h_j(\phi) \tag{3}$$

The functions $h_j(\phi)$ are yielded by the stress intensity factors $K_j'(\phi)$ resulting from the applied stress

$$\sigma(x) = x^j$$

in which x^j is given the dimension of a stress, and σ_j is measured by a^j . Then Eq 3 yields

$$h_j(\phi) = \frac{\pi}{2} \frac{K_j'(\phi)}{a^j \sqrt{\pi a}} \tag{4}$$

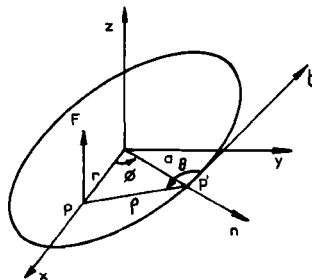


FIG. 2—A point force on a circular crack in an infinite solid.

The numerical values of the $h_j(\phi)$, dimensionless, are used in Eq 3 to calculate any stress intensity factor resulting from polynomial applied stresses.

The stress intensity factors were calculated by extrapolation of v/\sqrt{r} on the crack surface. The test on a penny-shaped crack was performed by applying stresses

$$|x|^j \quad j = 0, 1, 2, 3, 4$$

The symmetry due to the absolute value allowed the calculation to be limited to a quarter of the crack.

The CPU time for the whole set of the five functions $h_j(\phi)$ was about 80 s with a CdC 7600 computer. The $h_j(\phi)$ were also computed from the known weight function [4] (Fig. 3)

$$G(P, P') = \frac{1}{\pi\sqrt{\pi a}} \frac{\sqrt{2a\rho \sin \theta - \rho^2}}{\rho^2}$$

and with this symmetry

$$h_j(\phi) = \frac{1}{\pi^2 a} \int_s \left| \frac{x}{a} \right|^j \sqrt{\frac{2a \sin \theta}{\rho} - 1} d\rho d\theta \quad (5)$$

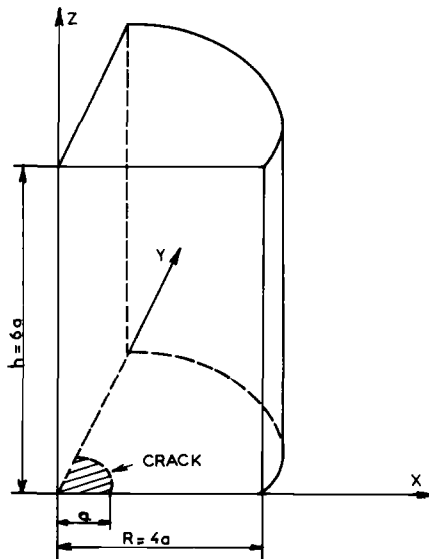


FIG. 3—Modeling a circular crack in an infinite solid.

The BIE computed values were compared to the values computed from the weight function.

An algebraic calculation is also possible for $j = 0, 2, 4$, by Eq 5 or for $j = 0, 2$ from Shah and Kobayashi's results [12]; these calculations yielded results practically equal to the computer values.

Estimation of Accuracy

The results of the BIE computation were corrected by about 1 percent to take into account the fact that the meshed solid was not infinite but a cylinder. The influence of the not perfect alignment of points v/\sqrt{r} was checked by comparing a linear and a parabolic extrapolation; the difference was always less than 1 percent. Other calculations were performed with rather coarser meshes to check the influence of the dimensions of the crack tip elements.

On Fig. 4 the angle of the crack front elements is 22.5 deg, and their width is 3.6 percent of the radius ($0.036 a$). Other tests were done with angles of 30 and 45 deg, and with width between $0.1a$ and $0.01a$. The results were found to depend very little on the length of the elements but were differently sensitive to the width; $h_0(\phi)$, uniform stress, was not sensitive; and $h_3(\phi)$ and $h_4(\phi)$ were good with a width $0.01a$ and too low by 8 to 10 percent with a width $0.1a$. Near the crack tip, at $\phi = 0$ deg the stresses $|x|^3$ and x^4 increase sharply and a narrow width is necessary; at $\phi = 90$ deg these stresses vary slowly, h_3 and h_4 are small, and relative errors of 5 percent are not of great importance.

A correlation was searched between the relative error and the relative

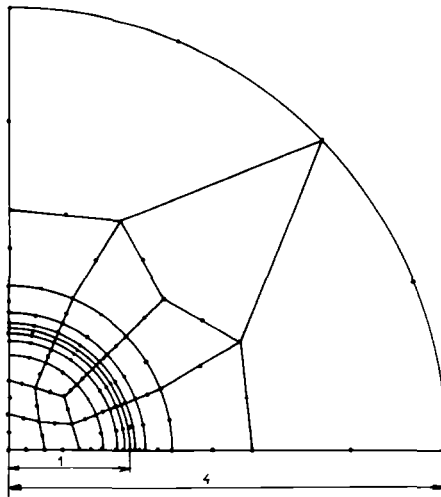


FIG. 4—Mesh in the plane of a circular crack.

load variation along the radius. With parabolic extrapolation a uniform scattering band 3 ± 1.5 percent was found; with linear extrapolation a parabolic correlation was found (Fig. 5); and the results with the mesh of Fig. 4 were found at the lower part of scattering band.

Taking into account the limited solid used for the calculation the errors may be estimated between -1.5 percent for $h_0(\phi)$ and -4 to 2 percent for $h_4(\phi)$ (see Table 1).

Semi-Elliptical Cracks in a Cylinder

As already indicated, the semi-axes ratio is one third (Fig. 1); so, the summit on the major axis is not very sharp. It was thought possible to apply the method to semi-ellipses of this eccentricity without a previous test on a complete elliptical crack embedded in an infinite solid. This test would have been necessary for sharper ellipses.

The singularity one half is questionable at the surface. Therefore, the elements near the surface are rather short, and plane stress is assumed on the surface. What is calculated by the extrapolation of v/\sqrt{r} at the surface is some average value and not the actual value of the stress intensity factor which should be zero. This inaccuracy is common to all engineering methods.

Limitation of the Meshed Structure (Fig. 6)

An elasticity calculation must be performed on a relatively thin cylinder ($R_o/R_i = 11/10$). With the BIE method computational difficulties were first met for bending nonsingular problems with center angles over 90 deg and elements limited by radii.

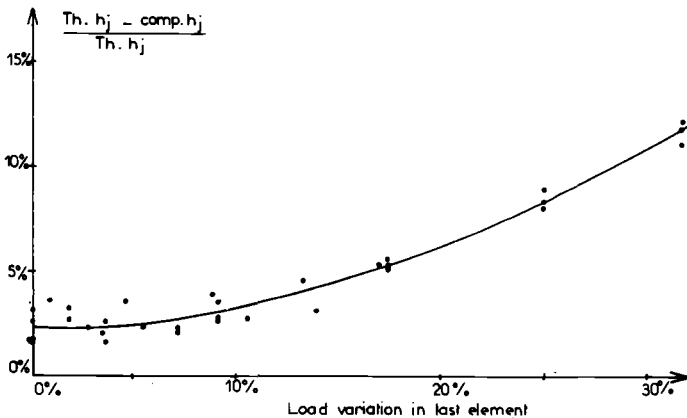


FIG. 5—Circular crack; correlation between error and stress variation in the deepest element.

TABLE 1—Penny-shaped crack—estimation of errors.

	$\phi = 0$ deg, percent	$\phi = 90$ deg, percent
$h_0(\phi)$	-1.5	-1.5
$h_1(\phi)$	-2	0.5
$h_2(\phi)$	-2.7	0.7
$h_3(\phi)$	-3.3	2.2
$h_4(\phi)$	-4	2

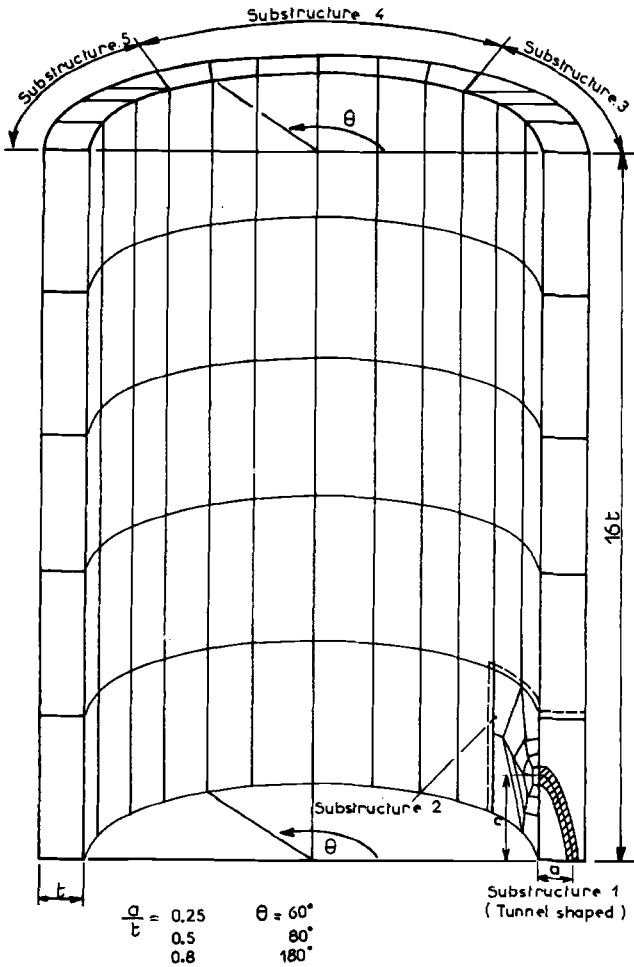


FIG. 6—Principle of the mesh of a cracked cylinder.

Therefore, the three first crack calculations were performed on portions of cylinder limited by center angles of 60 and 80 deg. It was estimated by a shell calculation that the stresses at 60 and 80 deg from the crack would not exceed 1 or 2 percent of the average stress in the ligament. These calculations were performed with a free end. It was estimated that the resulting overestimation at the free surface ($\phi = 90$ deg) for a uniform applied stress would not exceed a few percentage points for the shallow and medium cracks, 8 to 10 percent for the deep crack, and would be considerably smaller at the deepest point.

Later the use of elements of the same length on the inner and outer faces and two triangular elements yielded reliable results on a half cylinder for nonsingular bending problems. The deep crack was calculated again with no error resulting from a limited structure. The dimensions of the meshed structures are shown in Table 2.

Mesh of the Crack Surface (Fig. 7)

The calculation with a penny-shaped crack showed that rather long crack tip elements could be used but a too large width of the elements

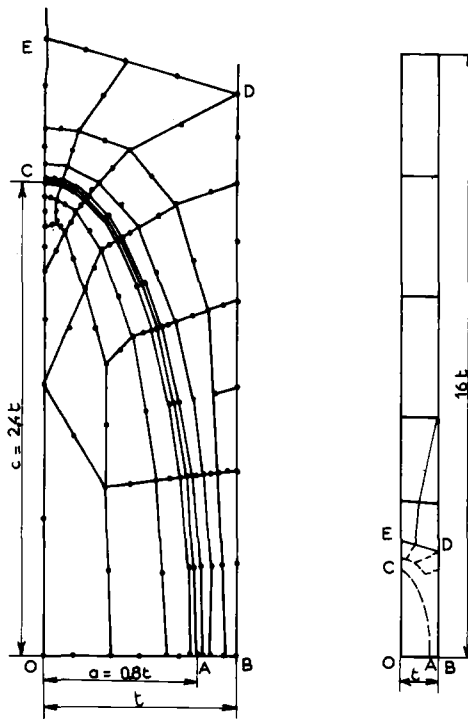


FIG. 7—Mesh in the plane of the crack.

TABLE 2—Characteristics of meshed structures.

	$\frac{R_0}{R_1} = \frac{11}{10}$ $\frac{a}{c} = \frac{1}{3}$		$\frac{a}{l} = 0,8$	
	$\frac{a}{l} = 0,25$	$\frac{a}{l} = 0,50$	First Calculation	Second Calculation
Meshed angle	60 deg	80 deg	80 deg	180 deg
Meshed length	8 <i>l</i>	12 <i>l</i>	12 <i>l</i>	16 <i>l</i>
Ends of structure	free	free	free	displacement allowed in the meridional plane
Substructure near the crack tip	intersecting	tunnel shaped	intersecting	tunnel shaped
Crack tip elements	6	6	6	6
Elements	13	13	13	13
Nodes	$\phi = 78.61$ deg	$\phi = 78.61$ deg	$\phi = 78.61$ deg	$\phi = 84.1$ deg
Nodes near the surface	84.1 deg	84.1 deg	84.1 deg	87.02 deg
Nodes on the crack surface	90 deg	90 deg	90 deg	90 deg
Total number of nodes	83	83	83	83
	507	704	697	788

could result in an underestimation of 8 to 10 percent of $h_3(\phi)$ and $h_4(\phi)$ near the deepest point where the stresses x^3 and x^4 increase quickly.

In the first calculations ($a/t = 0.25$ and 0.5) the width of the element at this point was 6 percent of the crack depth, which might result in an underestimation of 3 to 5 percent. In the last calculation ($a/t = 0.8$) this ratio was 3.5 percent, which should yield a very small underestimation. Near the surface the relative width of the elements is higher, but the stresses vary slowly and h_3 and h_4 are small.

The length of the element near the surface was determined after the angle of the normal, 30 deg for the first calculations, 15 deg for the last, which resulted in at least three nodes between $\phi = 80$ and 90 deg. On the crack front there were 6 elements and 13 nodes not equally spaced with respect to ϕ .

Substructures

The structure was divided into five substructures. In the first calculations the boundary of two substructures intersected the crack front. This resulted in oscillations for the deep crack. A tunnel-shaped substructure surrounding the crack front was used for the medium and the deep cracks. No oscillation was found.

Computer Time

The CPU time for each calculation yielding the five functions $h_j(\phi)$ at 13 points of the crack front was 650 s using a CdC 7600 computer. The time for the preparation and the presentation of the results was 100 h and could be reduced to 80 h with some practice.

Presentation of Results

Functions $h_j(\phi)$

Three sets of curves yield these functions for $a/t = 0.25$, 0.5 , and 0.8 (Figs. 8, 9, and 10).

Estimation of Errors Resulting from the Mesh and the Calculation Method

At the deepest point of the crack ($\phi = 0$) parabolic and linear extrapolation of v/\sqrt{r} were performed, and the same behavior as the penny-shaped crack was found. The difference could be reduced to 1 percent and only linear extrapolation was kept.

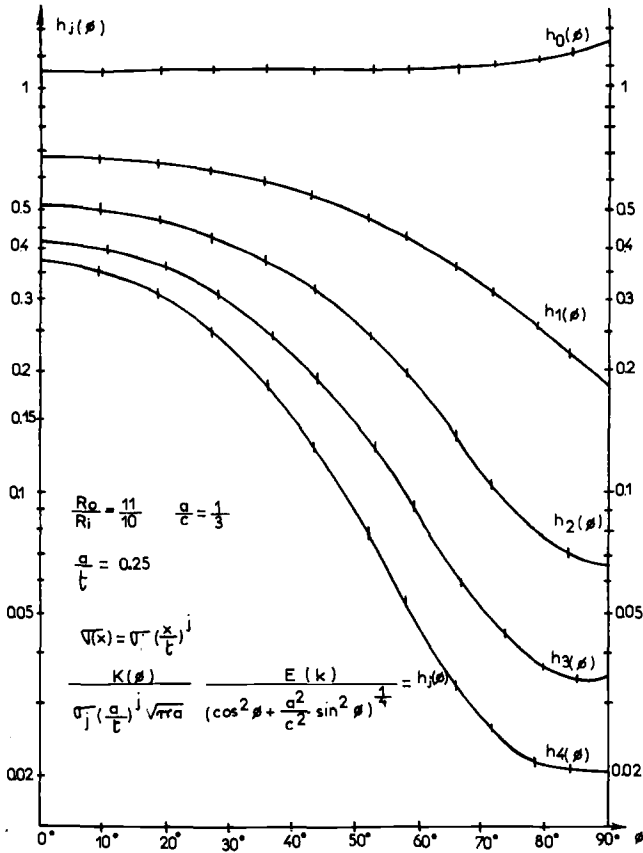


FIG. 8—Functions $h_j(\phi)$ for $a/t = 0.25$.

The underestimation at the deepest point resulting from the width of the element may vary according to Fig. 5.

for $a/t = 0.25$ and 0.5

between -2.5 ± 1 percent for $h_0(0)$ to -7.5 ± 1 percent for $h_4(0)$

for $a/t = 0.8$ (second calculation)

between -2.5 ± 1 percent for $h_0(0)$ to -4 ± 1 percent for $h_4(0)$

Near the surface ($\phi = 90$ deg) there is no reference to appreciate an error. However, the elements are short and the load variation along the normal is negligible. The errors resulting from calculation should be low, say -2 to -3 percent. On the penny-shaped crack positive errors (0 to 3

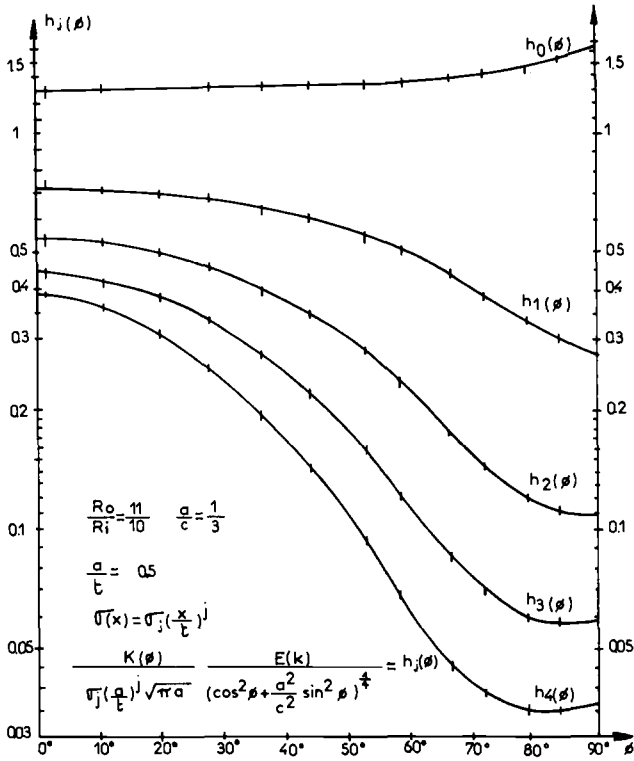


FIG. 9—Functions $h_j(\phi)$ for $a/t = 0.50$.

percent) were found for $h_2, h_3,$ and h_4 , but these functions are small on the surface and the knowledge of the error is not of great practical importance.

Errors Resulting from the Limitation of the Structure

The first calculations for the three crack depths were performed with limited angles of the cylinder and a free end; therefore, overestimations were expected. The second calculation of the deep crack was performed with an angle 180 deg, $H = 6.66c$ instead of $H = 5c$ and restrained displacements of the end. This source of overestimations disappeared this way.

From the differences between these calculations the overestimations for the other cracks might be

at the deepest point, $\phi = 0$

1 percent for all $h_j \quad a/t = 0.25$ and 0.5

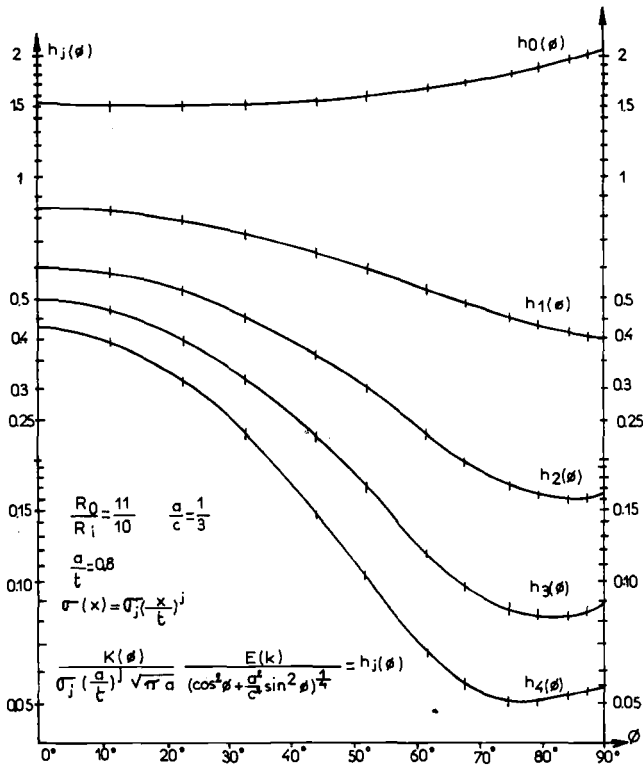


FIG. 10—Functions $h_j(\phi)$ for $a/t = 0.80$.

at the surface, $\phi = 90$

- < 2 percent for h_0, h_1 $a/t = 0.25$ and 0.5
- 2 to 3 percent for h_2, h_3, h_4 $a/t = 0.25$
- 5 to 7 percent for h_2, h_3, h_4 $a/t = 0.5$

Estimation of Total Errors

It is therefore thought that the total average errors may be estimated as shown in Table 3. A scattering band of ± 1 percent should be added. These figures do not have an absolute value. They mean that an accuracy better than 5 percent can be expected, except perhaps for the medium crack at the surface where a slightly higher overestimation is possible.

Discussion—Comparison with Other Results

Comparison with a Long Axial Crack

It has been noted by Underwood [18] that the stress intensity factor at the deepest point of a semi-elliptical crack in a thick pressurized cylinder

TABLE 3—Estimation of total errors.

	<i>a</i> / <i>l</i> = 0.25, percent	<i>a</i> / <i>l</i> = 0.5, percent	<i>a</i> / <i>l</i> = 0.8 (second calculation), percent
Deepest point $\phi = 0$ deg			
$h_0(\phi)$	-1.5	-1.5	-2.5
$h_4(\phi)$	-6.5	-5.5	-4.0
Surface $\phi = 90$ deg			
$h_0(\phi)$	-1.5	<5	-2.5
$h_4(\phi)$	a few < 0	may be >0 <5	a few < 0

is significantly smaller than the stress intensity factor of a long crack of the same depth. The stress intensity factors of long cracks in cylinders ($R_o/R_i = 11/10$) can be calculated easily by weight functions [27], and compared to $h_j(0)/E(k)$. The ratio varied according to the crack depth between 1.45 and 4.2 ($j = 0$), 1.25 and 2 ($j = 4$), which confirms Underwood's results.

Comparison Between a Cylinder and a Plate

One may wonder if the so-called cylindrical effect is important for rather thin cylinders ($R_o/R_i = 11/10$). This difference is important for deep long cracks, since the ring opposes the bending displacements of a plate [27,28]. It should be lower for elliptical cracks since even in a plate the uncracked material ahead of the ellipse between the surface and the crack depth opposes these displacements.

A comparison was attempted between the results of this study and those published by Smith and Sorensen [14] for a plate with a semi-elliptical crack subjected to a uniform tension. The differences for a uniform tension varied between 2 and 8 percent at the deepest point and between -1 and 20 percent at the surface. However, the comparison is not very significant due to the rather different methods of computation.

A comparison with Raju and Newman results [17] for semi-elliptical cracks in a plate subjected to a uniform tension is difficult since the shape of the ellipse is different ($a/c = 0.2$).

Limitation of Back Surface Effect

Using the BIE method, Cruse [28] calculated the stress intensity factors for semi-elliptical cracks of several axes ratios in a semi-infinite solid subjected to a uniform tension. Cruse's curves were interpolated for $a/c = 1/3$. The functions $h_0(\phi)$ were compared to Cruse's results. A good coincidence was found for the shallow crack.

It is also noted that for the shallow crack the results of this study are very near Kobayashi's results. Therefore it seems that the back surface effect is practically negligible for $a/t = 0.25$ but cannot be neglected for $a/t = 0.50$. With such depths the front and back surface effects cannot be separated.

Effect of Front and Back Surfaces

The influence of crack shape is approximately taken into account for a uniform tension by $[\cos^2 \phi + (c^2/a^2) \sin^2 \phi]^{1/4}$. For an embedded elliptical crack $h_0(\phi)$ would be 1.

The functions $h_0(\phi)$ exhibit a flat minimum at the deepest point and increase monotonically with ϕ . This seems rather natural, since at least for rather thin cylinders no rapid decrease of the back surface effect can be expected near $\phi = 0$, and the surface effect must be dominant beyond a certain value of ϕ . A more refined analysis [29,30] might have shown a sharp drop off very near the surface.

Comparison with Kobayashi's Results

Kobayashi et al [19,20] solved the same problem for different values of R_o/R_i , a/c and a/t . Their results are presented in the form

$$K(\phi) = M_c(\phi)M_{KS}(\phi) \frac{\sigma_0 \sqrt{\pi a}}{E(k)} \left(\cos^2 \phi + \frac{a^2}{c^2} \sin^2 \phi \right)^{1/4}$$

where σ_0 is a reference stress to be defined for every problem. Curves are yielded for $M_c(\phi)$ and $M_{KS}(\phi)$.

In Refs 19 and 20, $M_c(\phi)$ and $M_{KS}(\phi)$ for an internal pressure with no pressure in the crack were published for the following ratios

shape ratio	$a/c = 0.2$ and 0.98
radii ratio	$R_o/R_i = 10/9, 7/6, 5/4,$ and $3/2$
relative crack depth	$a/t = 0.4, 0.6,$ and 0.8

The reference stress was the hoop stress σ_0 at the inner face of the wall. In a cylinder with $R_o/R_i = 11/10$ (or $10/9$), the hoop stress resulting from an internal pressure p is approximated sufficiently by

$$\sigma_{\theta\theta}(x) = 10.52 p \left(1 - \frac{1}{10.52} \frac{x}{t} \right)$$

$$\sigma_{\theta\theta}(x) = \sigma_0 \left(1 - 0.095 \frac{x}{t} \right)$$

In this study

$$K(\phi) = \frac{\sigma_0 \sqrt{\pi a}}{E(k)} \left(\cos^2 \phi + \frac{a^2}{c^2} \sin^2 \phi \right)^{1/4} \left[h_0(\phi) - 0.095 \frac{a}{t} h_1(\phi) \right]$$

$$H(\phi) = h_0(\phi) - 0.095 \frac{a}{t} h_1(\phi)$$

must be compared to

$$M_k(\phi) = M_{KS}(\phi) M_C(\phi)$$

Calculations were performed in both studies for $a/t = 0.8$. Kobayashi's calculations were for $a/c = 0.2$ and 0.98 . A linear interpolation had been suggested in Ref 31 for such cracks in plates. In a private communication Kobayashi yielded interpolated curves for $a/c = 0.4, 0.6,$ and 0.8 .

The results for $a/c = 1/3$ and $a/t = 0.8$ are compared on Fig. 11; the curves for $M_K(\phi)$ and $H(\phi)$ are very different, and even if the curve derived from Kobayashi's results is not very accurate, a good coincidence must be noted at the deepest point with an increasing discrepancy when approaching the surface.

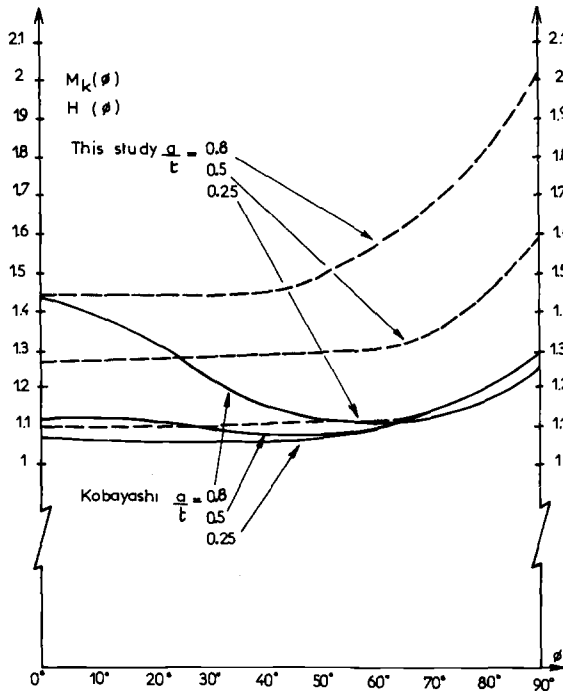


FIG. 11—Comparison with Kobayashi's results for an internal pressure.

For comparing the shallow and medium cracks ($a/t = 0.25$ and 0.5) other interpolations and extrapolations are necessary. As an indication, a good coincidence, within a few percentage points, was found for the shallow crack. For the medium crack $H(\phi)$ was found to be higher than $M_K(\phi)$ by 14 percent at the deepest point and 27 percent at the surface. This comparison is doubtful since $H(\phi)$ may have been overestimated by 5 percent, and the curve for $M_K(\phi)$ is not very certain on account of the interpolations and extrapolations.

The stress intensity factor resulting from internal pressure is always maximum at the deepest point. It seems likely that, at the surface, it increases rapidly with the depth, since the crack gets nearer and nearer a through crack.

It must be noted that, for pressurized thicker cylinders and not very large cracks, Kobayashi's calculations were in good agreement with Atluri et al [21] and Blackburn and Hellen [23]. But for rather long and deep semi-elliptical cracks ($a/c = 0.2$ and $a/t = 0.8$) in thick cylinders, Atluri and Kathiresan [22] disagreed with Kobayashi [19] at the surface.

Comparison with McGowan and Raymund's Results

These authors treated the same problem as in this study by a finite elements method [25]. The applied stress is approximated by a polynomial

$$\sigma(x) = A_0 + A_1 \frac{x}{t} + A_2 \left(\frac{x}{t}\right)^2 + A_3 \left(\frac{x}{t}\right)^3$$

The expression of $K(\phi)$ is

$$\frac{K(\phi)}{\frac{\sqrt{\pi a}}{E(k)} \left(\cos^2 \phi + \frac{a^2}{c^2} \sin^2 \phi\right)^{1/4}} = A_0 H_0(\phi) + \frac{2}{\pi} \frac{a}{t} A_1 H_1(\phi) + \frac{1}{2} \left(\frac{a}{t}\right)^2 H_2(\phi) + \frac{4}{3\pi} \left(\frac{a}{t}\right)^3 H_3(\phi)$$

The relationship between the functions $H_j(\phi)$ and $h_j(\phi)$ is (Figs. 12, 13, and 14)

$$H_0(\phi) = h_0(\phi)$$

$$H_1(\phi) = \frac{\pi}{2} h_1(\phi)$$

$$H_2(\phi) = 2 h_2(\phi)$$

$$H_3(\phi) = \frac{3\pi}{4} h_3(\phi)$$

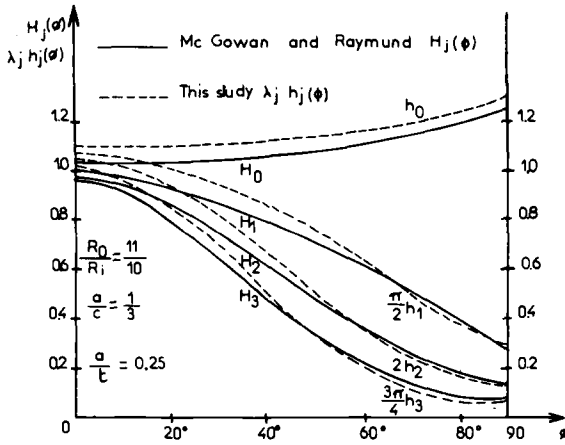


FIG. 12—Comparison with McGowan and Raymund's results for $a/t = 0.25$.

At the deepest point of the crack the results of this study are 7 to 8 percent higher than McGowan and Raymund's for $a/t = 0.25$ and 0.8 and 3 to 4 percent for $a/t = 0.5$. Near the surface they are 3 to 4 percent higher (Figs. 12, 13, 14). Therefore, the results are consistent with each other, with differences which may result from the methods and the meshes.

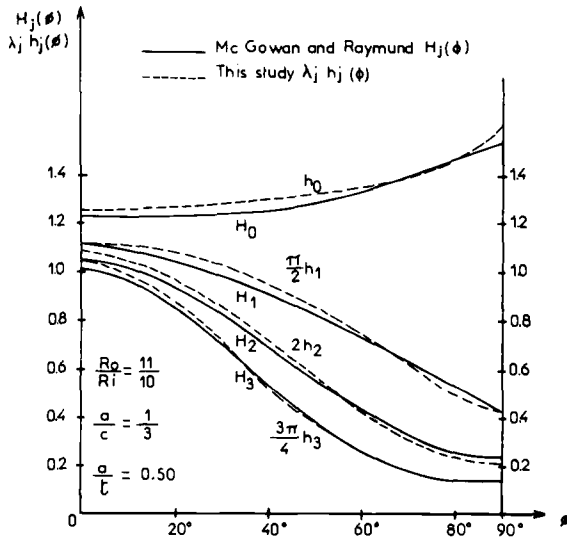


FIG. 13—Comparison with McGowan and Raymund's results for $a/t = 0.50$.

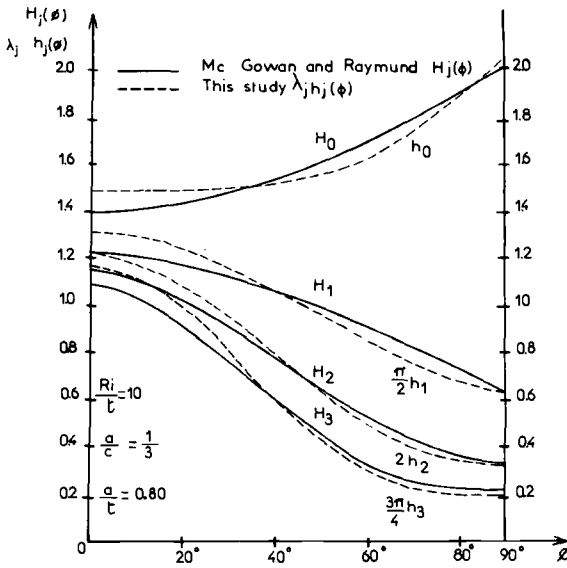


FIG. 14—Comparison with McGowan and Raymond's results for $a/c = 0.80$.

Conclusion

The purpose of this study was to develop a numerical direct method, with no approximations and correction factors, of calculating the stress intensity factor along a semi-elliptical crack in the meridional plane of a cylinder under any stress approximated by a polynomial.

A BIE program was used to calculate so-called polynomial influence functions, depending upon the geometry of the cracked cylinder which allow a simple calculation of the stress intensity factor along the crack front.

The first calculations with a limited arc of cylinder and a free end yielded overestimated results, and a correction factor would have been necessary. The last calculation with a complete half cylinder and a restrained end avoided this drawback.

As in all engineering calculations the computed stress intensity factor at the surface is an average extrapolated value, not the exact value.

The computing time for five such functions, up to x^4 , was rather short, 650 s CPU time with a CdC 7600 computer.

The accuracy was found satisfactory for engineering calculations. The most uncertain point is on the surface where it is difficult to estimate the error chiefly for higher order functions which are small at this point. An underestimation smaller than 5 percent seems possible, but an important overestimation near the surface does not seem likely.

It was confirmed that the stress intensity factor at the deepest point is always significantly smaller than that of a long axial crack of the same depth.

It is often stated that, for rather thin cylinders, the calculations of semi-elliptical cracks in a long plate with free ends is a reasonable approximation. This seems qualitatively sensible. In the absence of calculations by the same method of cracked plates with cracks having the same shape and depth as the cylinders, it was not possible to check the validity of this assumption.

Acknowledgments

The authors acknowledge the helpful discussions with the team of CETIM who wrote the program EITD; G. R. Irwin, University of Maryland; A. S. Kobayashi, University of Washington, and R. B. Wilson, Pratt and Whitney Corporation. This research was partially supported by Délégation Générale à la Recherche Scientifique et Technique, under Contract 74.7.0750.

References

- [1] Bueckner, H. F. in *Methods of Analysis and Solutions of Crack Problems*, Vol. 1, G. C. Sih; Ed., Noordhoff International Publishing, Leyden, The Netherlands, 1973.
- [2] Rice, J. R., *International Journal of Solids and Structures*, 1972, p. 751.
- [3] Labbens, R. C., Héliot, J., and Pellissier-Tanon, A. in *Cracks and Fracture, ASTM STP 601*, American Society for Testing and Materials, 1976, pp. 448–470.
- [4] Tada, H., Paris, P. C., and Irwin, G. R., *The Stress Analysis of Cracks Handbook*, Del Research Corporation, Hellertown, Pa., 1973.
- [5] Rizzo, F. J., *Quarterly of Applied Mathematics*, April 1967, pp. 83–95.
- [6] Cruse, T. A., *International Journal of Solids and Structures*, 1969, pp. 1259–1274.
- [7] Cruse, T. A., *The Surface Crack*, American Society of Mechanical Engineers, 1972, pp. 153–170.
- [8] Lachat, J. C. and Watson, J. O., Symposium on Boundary Integral Equation Method, American Society of Mechanical Engineers, June 1975.
- [9] Mémoire Technique du CETIM No. 25—CETIM, 52, Avenue Félix Louat, 60304 Senlis, France.
- [10] Shah, R. C. and Kobayashi, A. S., *International Journal of Fracture*, June 1973, pp. 133–146.
- [11] Shah, R. C. and Kobayashi, A. S. in *Stress Analysis and Growth of Cracks, ASTM STP 513*, American Society for Testing and Materials, 1971, pp. 3–21.
- [12] Shah, R. C. and Kobayashi, A. S., *Engineering Fracture Mechanics*, 1971, pp. 71–96.
- [13] Bueckner, F. H. in *Fracture Mechanics and Technology; Proceedings*, International Conference at Hong Kong, March 1977, Vol. 2, pp. 1091–1107.
- [14] Smith, F. W. and Sorensen, D. R., *International Journal of Fracture*, Feb. 1976, pp. 47–57.
- [15] Love, A. E. H., *Philosophical Transactions of the Royal Society*, Series A, Vol. 228, 1929.
- [16] Smith, F. W. and Alavi, M. J., *Journal of Engineering Fracture Mechanics*, Vol. 3, 1971, pp. 241–254.
- [17] Raju, I. S. and Newman, J. C. in *Proceedings*, Conference on Structural Mechanics in Reactor Technology, San Francisco, 1977.
- [18] Underwood, J. H. in *Stress Analysis and Growth of Cracks, ASTM STP 513*, American Society for Testing and Materials, 1972, pp. 59–70.
- [19] Kobayashi, A. S., Emery, A. F., Polvanich, N., and Love, W. J., *International Journal of Pressure Vessels and Piping*, 1977, pp. 103–122.
- [20] Kobayashi, A. S., Polvanich, N., Emery, A. F., and Love, W. J., *Journal of Pressure Vessel Technology*, Feb. 1977, pp. 83–89.
- [21] Atluri, S. N., Kathiresan, K., Kobayashi, A. S., and Nakagaki, M. in *Proceedings*, 3rd International Conference on Pressure Vessels Technology, Tokyo, 1977, pp. 527–533.
- [22] Atluri, S. N. and Kathiresan, K. in *Proceedings*, Conference on Structural Mechanics in Reactors Technology, San Francisco, 1977.

- [23] Blackburn, W. S. and Hellen, T. K., in Central Electricity Generating Board Report RD/B/N3103, Berkeley Nuclear Laboratories, 1974.
- [24] Reynen, J. in *Proceedings*, Conference on Structural Mechanics in Reactor Technology, San Francisco, 1977.
- [25] McGowan, J. J. and Raymund, M., this publication, pp. 365–380.
- [26] Henschell, R. D. and Shaw, K. G., *International Journal of Numerical Methods in Analysis*, Vol. 9, 1975, pp. 495–507.
- [27] Labbens, R. C., Pellissier-Tanon, A., and Héliot, J. in *Mechanics of Crack Growth, ASTM STP 590*, American Society for Testing and Materials, 1976, pp. 368–384.
- [28] Cruse, T. A. in *Three Dimensional Fracture Analysis*, L. E. Hulbert, Ed., Battelle Institute, Columbus, Ohio, 1976.
- [29] Hartranft, R. J. and Sih, G. C. in *Methods of Analysis Solution of Crack Problems*, Vol. 1, G. C. Sih, Ed., Noordhoff International Publishing, Leyden, The Netherlands, 1973.
- [30] Cruse, T. A. and Wilson, R. B., “Boundary Integral Equation Method for Elastic Fracture Mechanics Analysis,” Air Force Office of Scientific Research Technical Report, 1977.
- [31] Kobayashi, A. S., Polvanich, N., Emery, A. F., and Love, W. J., *Surface Flaws in Plate in Bending*.

J. J. McGowan¹ and M. Raymund¹

Stress Intensity Factor Solutions for Internal Longitudinal Semi-Elliptical Surface Flaws in a Cylinder Under Arbitrary Loadings

REFERENCE: McGowan, J. J. and Raymund, M., "Stress Intensity Factor Solutions for Internal Longitudinal Semi-Elliptical Surface Flaws in a Cylinder Under Arbitrary Loadings," *Fracture Mechanics, ASTM STP 677*, C. W. Smith, Ed., American Society for Testing and Materials, 1979, pp. 365-380.

ABSTRACT: The behavior of semi-elliptical surface flaws in cylinders is of interest in the technology of pressure vessels. The object of this study is to determine the stress intensity factor distribution around the crack front under arbitrary loading conditions for a longitudinal semi-elliptical flaw with $a/c = 1/3$ and $R_i/t = 10$; where a is the semi-minor axis of the ellipse, c is the semi-major axis, R_i is the inside radius of the cylinder, and t is the cylinder thickness. Three crack depths are studied under various loading conditions: $a/t = 0.25, 0.50, \text{ and } 0.80$.

The finite element method is used to determine the displacement solution. Parks' stiffness derivative method is used to find the stress intensity factor distribution around the semi-ellipse. The immediate crack tip geometry is modeled by use of a macroelement containing over 1600 degrees of freedom.

Four separate loadings are considered: (1) constant, (2) linear, (3) quadratic, and (4) cubic crack surface pressure. From these loadings nondimensional magnification factors are derived to represent the resulting stress intensity factors. By the method of superposition, comparisons are made with other investigators for pressure loading of a cylinder; the results agree within 8 percent of published results.

KEY WORDS: crack propagation, pressure vessels, stress intensity factors, weight functions, surface flaws, semi-elliptical flaws, structural analysis, fatigue (materials)

The semi-elliptical surface flaw is one of the most common flaw types to be found in any structure. Accurate stress intensity factor expressions are

¹ Senior engineer and senior scientist, respectively, Westinghouse Electric Corp., Nuclear Energy Systems, Pittsburgh, Pa. 15230. Dr. McGowan is now an assistant professor of Aerospace Engineering at the University of Alabama, Tuscaloosa, Ala. 35401.

necessary under all applicable loading conditions so that the structural integrity of the component can be verified. One of the geometries of particular interest in pressure vessel technology is that of a longitudinal surface flaw in a thick-walled cylinder.

Because of the difficulties of three-dimensional analysis, the first investigators studied the two-dimensional counterpart of the aforementioned geometry. Bowie and Freese [1]² studied a continuous longitudinal flaw in a cylinder under pressure. This work was generalized to both continuous longitudinal and circumferential flaws in thick cylinders under arbitrary loading by Buchalet and Bamford [2] and Labbens et al [3]. Initial attempts at approximate solutions to the full three-dimensional problem were made by Underwood [4] and Kobayashi [5]. Neither Underwood's nor Kobayashi's work included the effect of the outside surface of the cylinders. Kobayashi et al [6-8] recently have estimated stress intensity factors for longitudinal semi-elliptical surface flaws in cylinders under both pressure and thermal shock loadings. The solutions were determined from similar flaws in flat plates with appropriate hoop stress profiles. The flat plate results were modified with curvature correction factors obtained from two-dimensional analyses. Both front and back surface effects were considered, but the curvature correction factors were most appropriate for only the deepest point along the semi-ellipse.

Some direct three-dimensional solutions to the surface flaw problem in a cylinder have been made. Among these are Ayers [9], Blackburn and Hellen [10], and Atluri et al [11,12]. Ayers used a condensed quarter-point element to determine the stress intensity factor distribution of two semi-elliptical flaws in a thermally shocked cylinder with a ratio of outer to inner radius equal to 1.90. Blackburn and Hellen used a conventional three-dimensional finite element code and a virtual crack extension procedure to determine the stress intensity factor expressions for inner and outer surface flaws in cylinders under pressure with the ratio of outer to inner radius equal to 1.461. Atluri used a hybrid-displacement crack-tip element to determine the stress intensity factor distribution around the flaw border of semi-elliptical flaws in pressurized cylinders with the ratio of outer to inner radius equal to 1.5 and 2.0. For the same geometries, these direct three-dimensional approaches all give similar results (~ 10 percent variance).

As previously noted, the geometries treated in the full three-dimensional manner are only for limited loading conditions and for geometries that are widely different from commercial pressure vessels (ratio of outer radius to inner radius of 1.1). To verify the structural integrity of these pressure vessels, a considerable range of loading conditions is investigated in this study. The surface flaw shown in Fig. 1 is examined with $2c/a$ equal to 6 as recommended by the ASME Boiler and

² The italic numbers in brackets refer to the list of references appended to this paper.

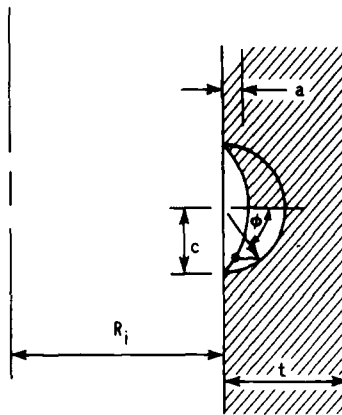


FIG. 1—Local crack-tip geometry.

Pressure Vessel Code [13]. The ratio of outer to inner radius of the cylinder is 1.1 as mentioned previously. The method of analysis uses conventional finite element methods using substructuring techniques to simplify the modeling of the crack front. The stress intensity factor distribution around the semi-ellipse is calculated using the stiffness derivative procedure as proposed by Parks [14], a method similar to that of the virtual displacement method of Blackburn and Hellen [10].

Results for 25, 50, and 80 percent crack depth are shown. These solutions are compared to that of Heliot et al [15], who solved the same series of problems independently using the boundary integral equation approach.

Finite Element Model

The immediate crack-tip region is modeled by a single macroelement as shown in Fig. 2. This macroelement is composed of 45 separate elements. The back three faces of this macroelement (those not visible in Fig. 2) are compatible with a conventional 20-node isoparametric brick element and the macroelement can be stretched in the manner of a conventional isoparametric element. The 45 subelements can have a variable number of nodes along each edge (within some minor restrictions), so that degrees of freedom can be concentrated in an area of interest. In the present form, there are 1656 degrees of freedom in the macroelement. The crack lengths in the x and y directions (as shown in Fig. 2) are variable. The advantage of this element lies primarily with the ease a semi-elliptical flaw can be introduced into an existing finite element grid.

A more complete description of the formulation of this element is given in Ref 16. After the special macroelement has been sized with the correct surface flaw geometry, the balance of the finite element model is formed out of 20-node brick elements as shown in Fig. 3. Because of two planes of

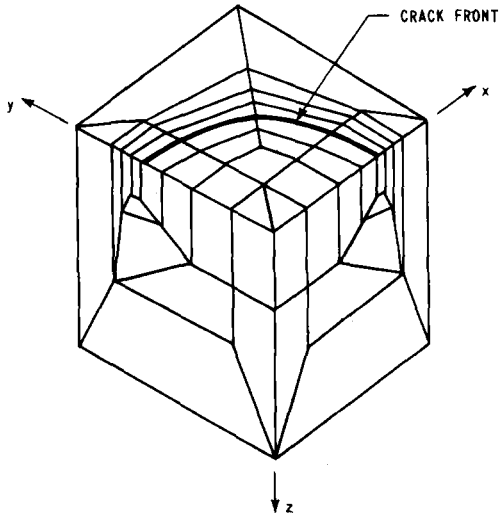


FIG. 2—Undeformed macroelement.

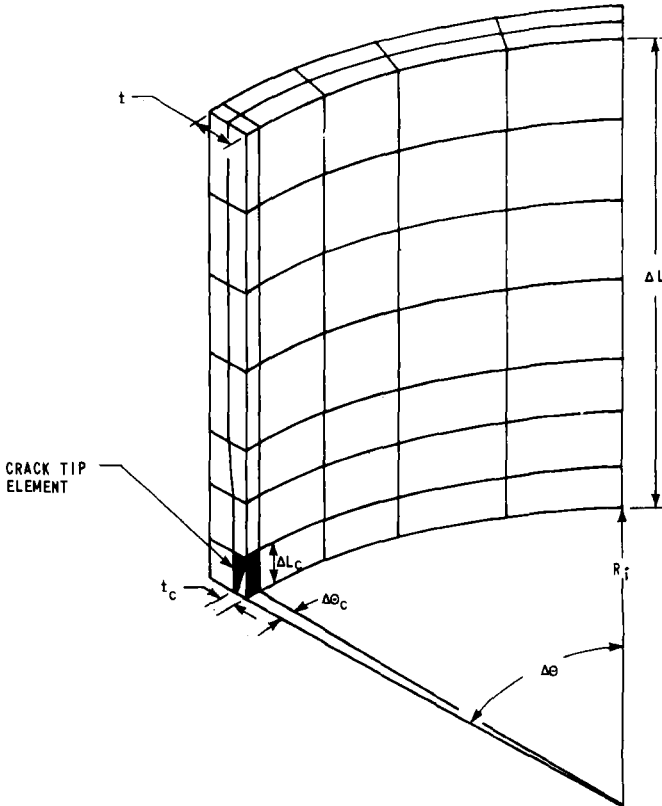


FIG. 3—Finite element model of cylinder with a longitudinal surface flaw.

symmetry only one quarter of the structure was modeled. The inside radius (R_i) of the cylinder is 1.651 m and the thickness (t) of the cylinder is 0.165 m. The aspect ratio ($2c/a$) in this study is 6. Three separate crack depths (a/t) are studied: 25, 50 and 80 percent; the details of each of these models are listed in Table 1. For the 80 percent case, two models are constructed to determine the effect of a larger finite element model with a higher number of degrees of freedom. For this study $E = 192$ GPa and $\nu = 0.3$.

Magnification Factor Solutions

Four separate loadings for each of the crack geometries are considered. These are described in Fig. 4

(1) $\sigma(x) = A_0$; (2) $\sigma(x) = A_1 x/t$; (3) $\sigma(x) = A_2 x^2/t^2$;
 and (4) $\sigma(x) = A_3 x^3/t^3$

The stress intensity factor is computed at every node point around the semi-ellipse for each loading by the Park's stiffness derivative method [14]; the implementation of this method is described more fully in Ref 16.³ Nondimensional magnification factors are determined for each of the loadings studied

$$(1) \sigma(x) = A_0; H_0(\phi) = \frac{{}^0K_1(\phi)}{A_0 \sqrt{\frac{\pi a}{Q}} (\cos^2 \phi + a^2/c^2 \sin^2 \phi)^{3/4}}$$

$$(2) \sigma(x) = A_1 x/t; H_1(\phi) = \frac{{}^1K_1(\phi) \pi/2 t/a}{A_1 \sqrt{\frac{\pi a}{Q}} (\cos^2 \phi + a^2/c^2 \sin^2 \phi)^{3/4}}$$

$$(3) \sigma(x) = A_2 x^2/t^2; H_2(\phi) = \frac{{}^2K_1(\phi) 2 t^2/a^2}{A_2 \sqrt{\frac{\pi a}{Q}} (\cos^2 \phi + a^2/c^2 \sin^2 \phi)^{3/4}}$$

$$(4) \sigma(x) = A_3 x^3/t^3; H_3(\phi) = \frac{{}^3K_1(\phi) \frac{3\pi}{4} t^3/a^3}{A_3 \sqrt{\frac{\pi a}{Q}} (\cos^2 \phi + a^2/c^2 \sin^2 \phi)^{3/4}}$$

³ It must be noted that the stiffness derivative procedure used here assumes the existence of plane strain conditions. Since it is well known that plane strain conditions are not satisfied over a finite boundary layer region near the free surface, the computed stress intensity factor by this method may not be appropriate at the free surface. The values at the free surface should be considered as only a reasonable engineering estimate.

TABLE 1—Finite element model information. ^a

	Model 1	Model 2	Model 3	Model 4
Cylinder inside radius, R_i , m	1.651	1.651	1.651	1.651
Cylinder thickness, t , m	0.165	0.165	0.165	0.165
Crack depth, a/t , percent	25	50	80	80
Aspect ratio, $2c/a$	6.0	6.0	6.0	6.0
Crack-tip element axial length, ΔL_c , mm	152	305	488	488
Crack-tip element angle, $\Delta \theta_c$, deg	1.7905	3.5810	5.7296	5.7296
Crack-tip element depth, t_c , mm	51.6	103	165	165
Mesh axial length, ΔL , m	1.753	1.753	2.438	2.438
Mesh angle, $\Delta \theta$, deg	45	45	60	90
Crack-tip element degrees of freedom	1656	1656	1656	1656
Number of standard 20-node brick elements in mesh	69	69	49	74

^a Each of the symbols listed in this table are defined in Fig. 3.

where $Q^{1/2} = \int_0^{\pi/2} (\cos^2 \phi + a^2/c^2 \sin^2 \phi)^{1/2} d\phi$ and all other symbols are

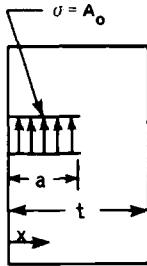
defined in Figs. 1 and 4.

The magnification factors $H_0 - H_3$ for the three crack depths studied ($a/t = 0.25, 0.50, 0.80$) are shown in Figs. 5, 6, and 7. The magnification factors for Models 3 and 4 in Table 1 do not vary from each other more than 2 percent; only the magnification factors for Model 3 are presented in Fig. 7.

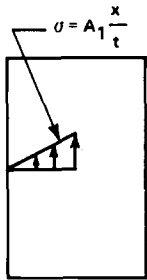
Superposition Principle

A wide variety of loadings on the surface flaw can be extracted from the four loadings considered by the method of superposition as shown in Fig. 8. The stress intensity factor K_I for the flaw in Section S of the structure, subjected to a remote loading (F, M) represented by a force F and a moment M , is equal to the stress intensity factor K_I for the same flaw in Section S of the structure with the crack surface subjected to a stress profile $\sigma(x)$. The stress profile $\sigma(x)$ is the profile developed over Section S by the remote loading (F, M).

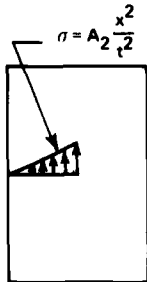
Therefore, in order to determine the K_I distribution around the flaw border under an arbitrary loading situation, the stress profile $\sigma(x)$ in



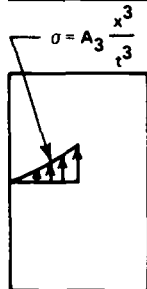
$$H_0(\phi) = \frac{{}^0K_1(\phi)}{A_0 \sqrt{\frac{\pi a}{Q} \left(\cos^2 \phi + \frac{a^2}{c^2} \sin^2 \phi \right)^{1/4}}$$



$$H_1(\phi) = \frac{{}^1K_1(\phi) \frac{\pi t}{2 a}}{A_1 \sqrt{\frac{\pi a}{Q} \left(\cos^2 \phi + \frac{a^2}{c^2} \sin^2 \phi \right)^{1/4}}$$



$$H_2(\phi) = \frac{{}^2K_1(\phi) 2 \frac{t^2}{a^2}}{A_2 \sqrt{\frac{\pi a}{Q} \left(\cos^2 \phi + \frac{a^2}{c^2} \sin^2 \phi \right)^{1/4}}$$



$$H_3(\phi) = \frac{{}^3K_1(\phi) \frac{3\pi t^3}{4 a^3}}{A_3 \sqrt{\frac{\pi a}{Q} \left(\cos^2 \phi + \frac{a^2}{c^2} \sin^2 \phi \right)^{1/4}}$$

FIG. 4—Crack surface loading cases studied.

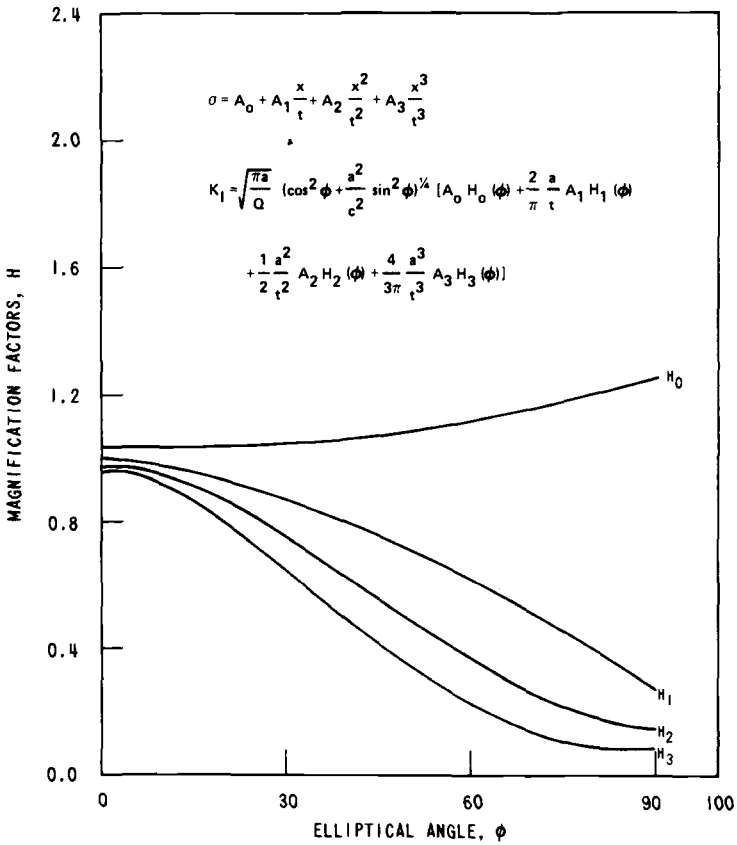


FIG. 5—Magnification factors for a longitudinal surface flaw in a cylinder where $a/t = 0.50$, $2c/a = 6$, $R/t = 10$, and $Q = 1.2426$.

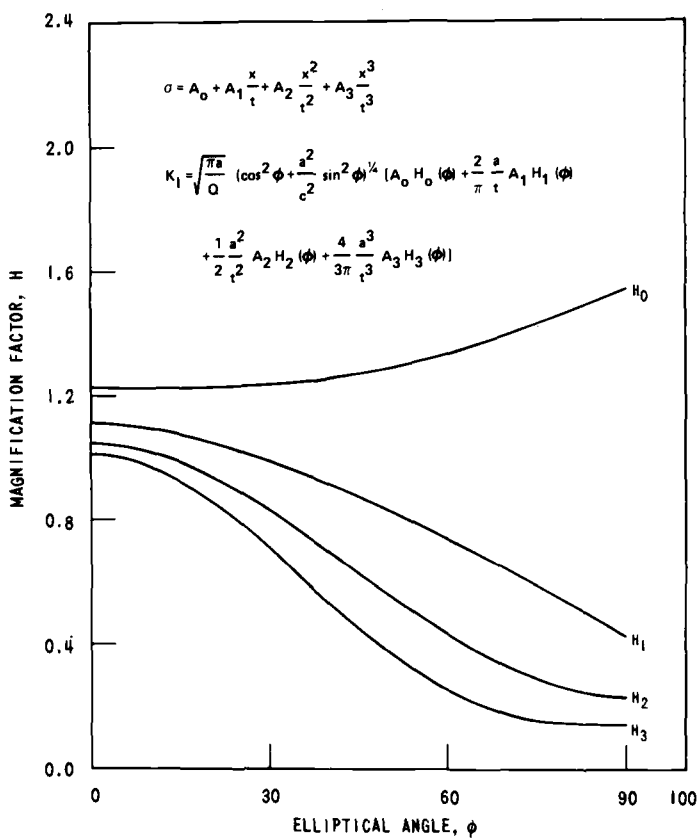


FIG. 6—Magnification factors for a longitudinal surface flaw in a cylinder where $a/t = 0.50$, $2c/a = 6$, $R_1/t = 10$, and $Q = 1.2426$.

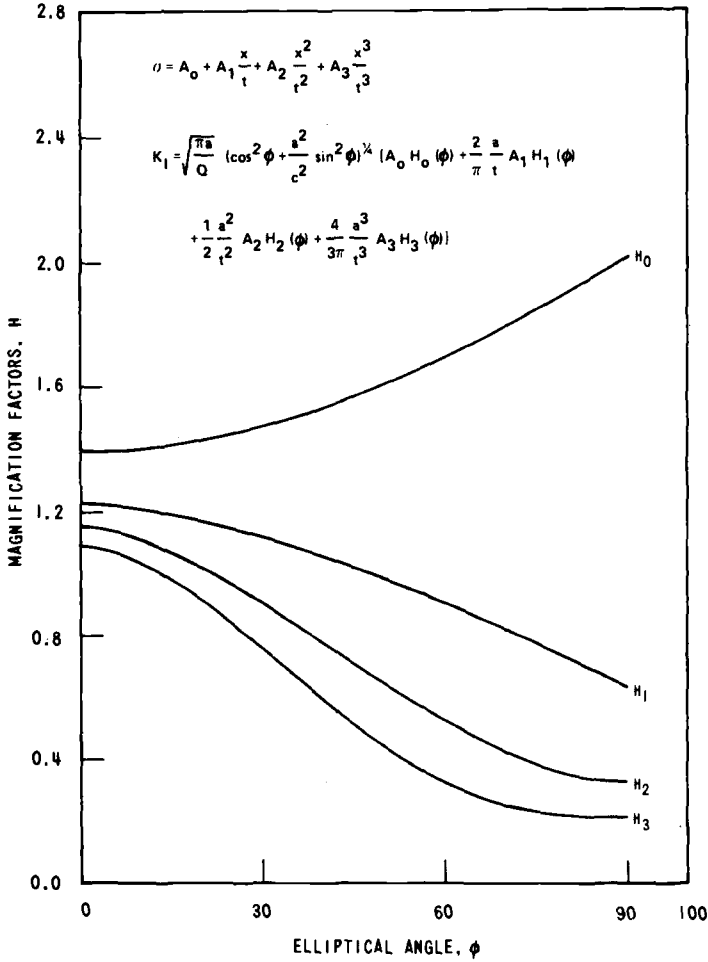


FIG. 7—Magnification factors for a longitudinal surface flaw in a cylinder where $a/t = 0.80$, $2c/a = 6$, $R_1/t = 10$, and $Q = 1.2426$.

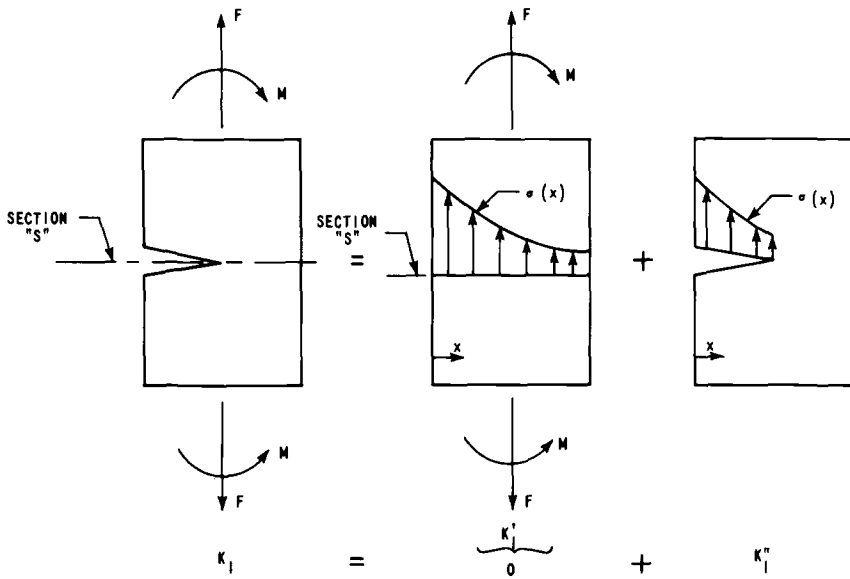


FIG. 8—Superposition principle.

Section S of the unflawed cylinder is fitted with a third-degree polynomial

$$\sigma(x) = A_0 + A_1 x/t + A_2 X^2/t^2 + A_3 x^3/t^3$$

and then the desired magnification factors would be used to determine $K_I(\phi)$

$$K_I(\phi) = \sqrt{\frac{\pi a}{Q}} (\cos^2 \phi + a^2/c^2 \sin^2 \phi)^{1/4} \left[A_0 H_0(\phi) + \frac{2}{\pi} alt A_1 H_1(\phi) + \frac{1}{2} \frac{a^2}{t^2} A_2 H_2(\phi) + \frac{4}{3\pi} a^3/t^3 A_3 H_3(\phi) \right]$$

Pressure Loading Case

Kobayashi [7] gives solutions to internal longitudinal surface flaws in cylinders under pressure loading

$$\sigma(x) = \sigma_o \frac{\left(\frac{R_o}{R_i+x}\right)^2 + 1}{\left(\frac{R_o}{R_i}\right)^2 + 1} ; \sigma_o = p \frac{\left(\frac{R_o}{R_i}\right)^2 + 1}{\left(\frac{R_o}{R_i}\right)^2 - 1}$$

where p is the internal pressure and $R_o = R_i + t$. For the case of geometries examined $R_o/R_i = 1.1$; expanding the stress distribution, $\sigma(x)$, and keeping the significant terms leads to

$$\sigma(x) = \sigma_o (1 - 0.095 x/t)$$

with $\sigma_o = 10.52 p$

For the purpose of comparison the following magnification factor, M_k is computed

$$M_k = \frac{K_I(\phi)}{\sigma_o \sqrt{\frac{\pi a}{Q}} (\cos^2 \phi + \frac{a^2}{c^2} \sin^2 \phi)^{1/4}}$$

In addition to Ref 17 and the present study, results are included from a study by Heliot et al [15] computed by the boundary integral equation method. In this analysis, K_I is determined by extrapolating displacements near the crack tip. The results from these three different approaches are shown in Figs. 9–11 for $a/t = 0.25, 0.50,$ and $0.80,$ respectively.

Discussion of Results and Conclusions

For the 25 percent crack depth all three theories agree very well, with only a 5 percent maximum difference. For the 50 percent crack depth all three solutions are very close at the maximum depth (the present study agrees within 5 percent of the other two). The present study and that of Heliot are very close over the length of the flaw; while that of Kobayashi is consistently lower than the other two, approaching 20 percent low at $\phi = 90$ deg. For the 80 percent crack depth, again all three solutions are close at the maximum depth (within 8 percent). Over the length of the flaw again this study and Heliot agree well; whereas Kobayashi's analysis is consistently lower than the other two, approaching 40 percent low at $\phi = 90$ deg. Atluri [12] has solved a similar problem with $R_i/t = 2.0, 2c/a = 10, a/t = 0.80$. For this problem the approximate analysis of Kobayashi was 45 percent low at $\phi = 90$ deg, while Kobayashi was within 5 percent at $\phi = 0$. Due to the fact that Kobayashi's curvature correction factor was taken from two-dimensional problems, it is reasonable that the best agreement would be at the point of maximum depth ($\phi = 0$ deg); and that the agreement at $\phi = 90$ deg would deteriorate as the flaw depth increases. On the other hand the agreement between this study and Heliot et al, with radically different approaches, is very good. The magnification factors presented here should provide an accurate method to ascertain the structural integrity of commercial pressure vessels under a widely varying range of loading situations.

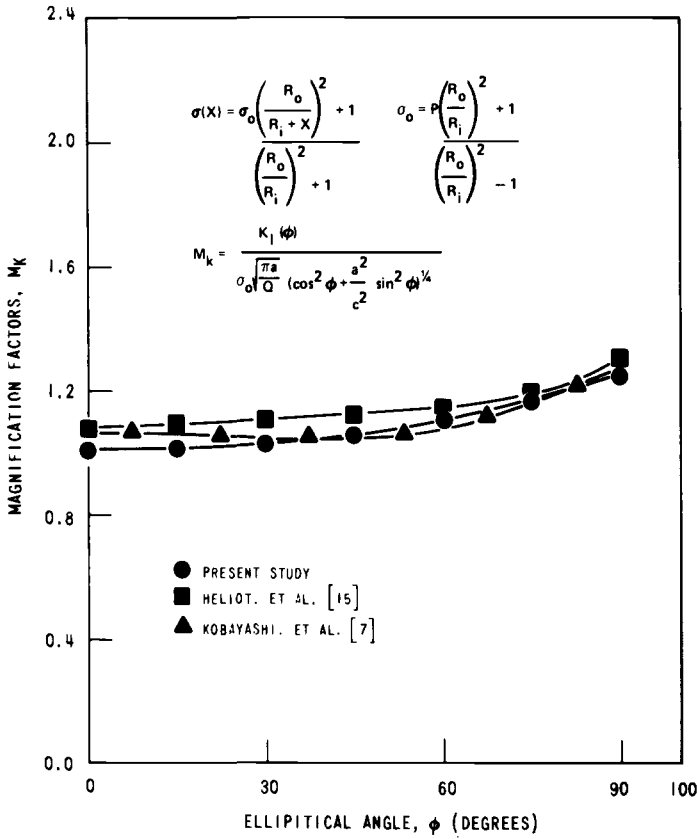


FIG. 9—Magnification factors for a longitudinal surface flaw in a cylinder with pressure loading where $a/t = 0.25$, $2c/a = 6$, and $R_i/t = 10$.

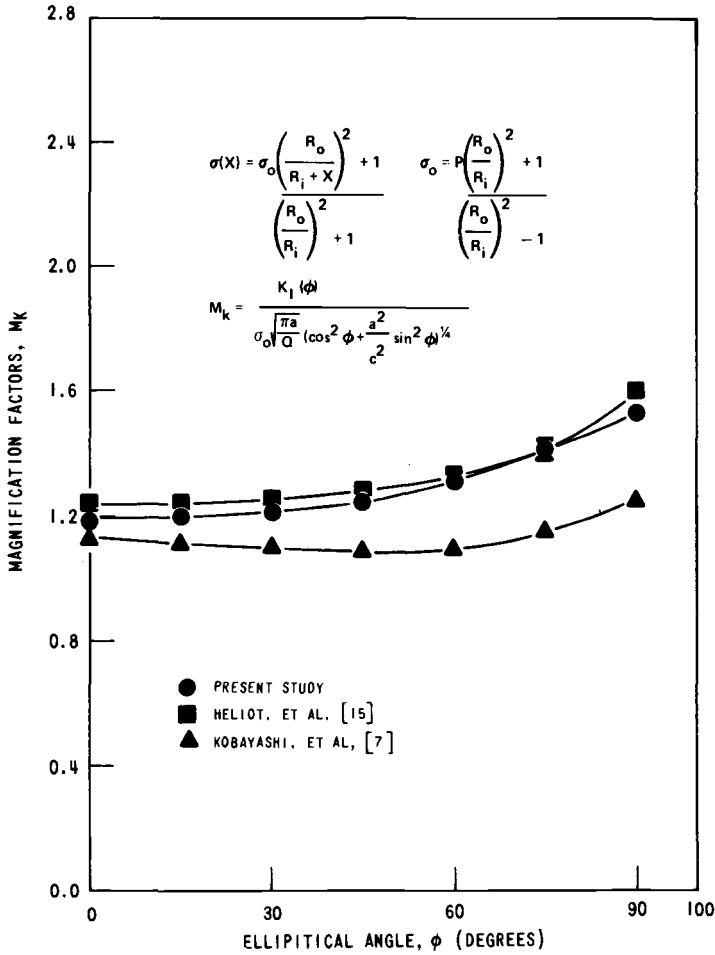


FIG. 10—Magnification factors for a longitudinal surface flaw in a cylinder with pressure loading where $a/t = 0.50$, $2c/a = 6$, and $R_i/t = 10$.

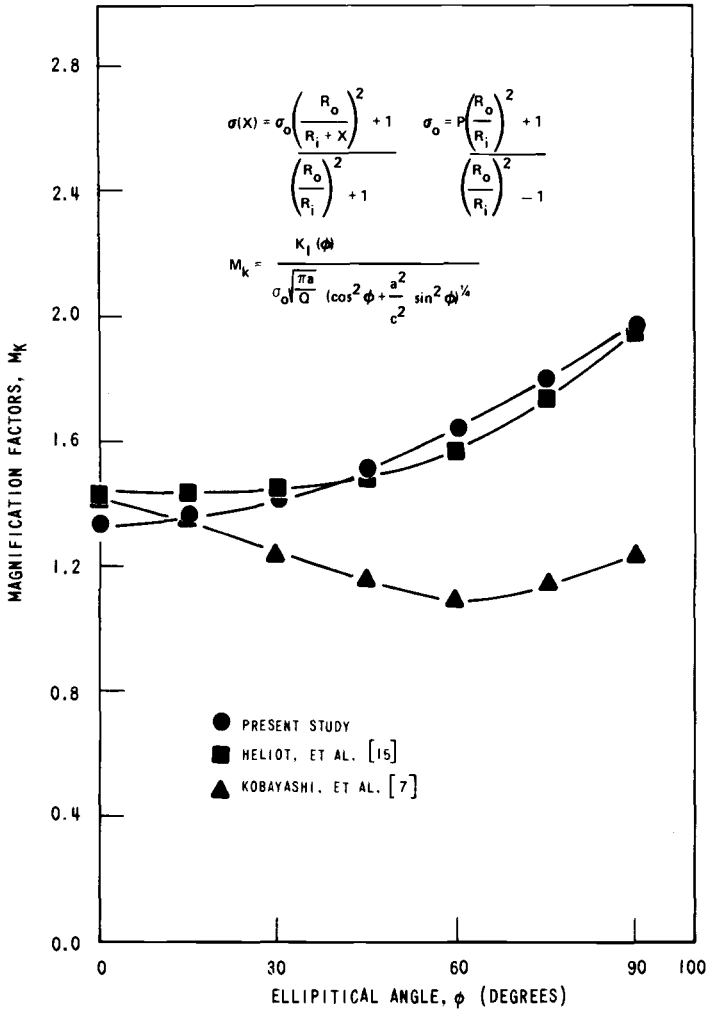


FIG. 11—Magnification factors for a longitudinal surface flaw in a cylinder with pressure loading where $a/t = 0.80$, $2c/a = 6$, and $R_i/t = 10$.

Acknowledgment

The authors wish to thank J. F. Petsche for his assistance in performing the finite element analysis, and S. Palusamy for his pioneering efforts in the pursuit of these practical problems.

References

- [1] Bowie, O. L. and Freese, C. E., *Engineering Fracture Mechanics*, Vol. 4, No. 2, June 1972, pp. 315–322.
- [2] Buchalet, C. B. and Bamford, W. H. in *Mechanics of Crack Growth, ASTM STP 590*, American Society for Testing and Materials, 1976, pp. 385–402.
- [3] Labbens, R., Pellissier-Tanon, A., and Heliot, J. in *Mechanics of Crack Growth, ASTM STP 590*, American Society for Testing and Materials, 1976, pp. 368–384.
- [4] Underwood, J. H. in *Stress Analysis and Growth of Cracks, ASTM STP 513*, American Society for Testing and Materials, 1972, pp. 59–70.
- [5] Kobayashi, A. S. in *Significance of Defects in Welded Structures*, University of Tokyo Press, Tokyo, Japan, 1974, pp. 127–143.
- [6] Kobayashi, A. S., Polvanich, N., Emery, A. F., and Love, W. J. in *Computational Fracture Mechanics*, American Society of Mechanical Engineers, 1975, pp. 121–132.
- [7] Kobayashi, A. S., Emery, A. F., Polvanich, N., and Love, W. J., *International Journal of Pressure Vessels and Piping*, Vol. 5, 1977, pp. 103–122.
- [8] Kobayashi, A. S., Emery, A. F., Polvanich, N., and Love, W. J., *Journal of Pressure Vessel Technology*, American Society of Mechanical Engineers, Feb. 1977, pp. 83–89.
- [9] Ayers, D. J. in *Computational Fracture Mechanics*, American Society of Mechanical Engineers, 1975, pp. 133–143.
- [10] Blackburn, W. S. and Hellen, T. K., "Calculation of Stress Intensity Factors for Elliptical and Semi-Elliptical Cracks in Blocks and Cylinders," Central Electricity Generating Board Report No. RD/B/N3103, July 1974.
- [11] Atluri, S. N., Kathiresan, K., Kobayashi, A. S., and Nakagaki, M. in *Proceedings of the Third International Conference on Pressure Vessel Technology* (Tokyo, Japan, 19–22, April 1977), American Society of Mechanical Engineers, pp. 527–533.
- [12] Atluri, S. H. and Kathiresan, K., "Outer and Inner Surface Flaws in Thick-Walled Pressure Vessels," paper G 5/4, *Transactions of the Fourth International Conference on Structural Mechanics in Reactor Technology*, San Francisco, Cal., 1977.
- [13] "Protection Against Nonductile Failure," ASME Boiler and Pressure Vessel Code, Section III, Appendix G, 1977 edition.
- [14] Parks, D. M., *International Journal of Fracture*, Vol. 10, 1974, pp. 487–502.
- [15] Heliot, J., Labbens, R. C., and Pellissier-Tanon, A., this publication, pp. 341–364.
- [16] Hall, C. A., Palusamy, S., and Raymund, M., "A Macroelement Approach to Computing Stress Intensity Factors for Three-Dimensional Structures," accepted for publication in the *International Journal of Fracture*, 1978.

G. Yagawa,¹ M. Ichimiya,¹ and Y. Ando¹

Theoretical and Experimental Analysis of Semi-Elliptical Surface Cracks Subject to Thermal Shock

REFERENCE: Yagawa, G., Ichimiya, M., and Ando, Y., "Theoretical and Experimental Analysis of Semi-Elliptical Surface Cracks Subject to Thermal Shock," *Fracture Mechanics, ASTM STP 677*, C. W. Smith, Ed., American Society for Testing and Materials, 1979, pp. 381-398.

ABSTRACT: This paper illustrates a procedure for estimating the stress intensity factors of a semi-elliptical surface crack in a thermally shocked thick plate.

The first step in this procedure is to calculate the time-dependent thermal stresses induced by sudden cooling of an uncracked plate by using the three-dimensional finite element codes for heat transfer and thermal stress analyses with the consideration of the space as well as time change of elastic constants. The stresses at the location of the crack surface in the uncracked plate are eliminated by the method of superposition in order to obtain a stress free crack surface.

The time-dependent distributions of the stress intensity factors along the crack front line are then determined by using the three-dimensional finite element method of crack analysis based on discretization error proposed by the present authors recently.

In order to study the effectiveness of the linear elastic fracture mechanics employed in this paper, a series of tests of brittle fracture using cracked polymethyl methacrylate (PMMA) plates is carried out by suddenly cooling the surface of plate. The measured and estimated times of fracture elapsed from the sudden cooling are found to coincide very well.

KEY WORDS: thermal shock, surface crack, fracture toughness, PMMA, finite element method, principle of superposition, stress analysis, loss-of-coolant accident fatigue (materials), crack propagation

Several kinds of structures normally operating at relatively high temperatures may be subjected to thermal shock caused by sudden cooling. For example, in case of a loss-of-coolant accident by a double-ended failure of the main coolant piping of a pressurized water reactor, cold

¹ Associate professor, graduate student, and professor, respectively, Department of Nuclear Engineering, University of Tokyo, Bunkyo-ku, Tokyo, Japan.

water is injected into the reactor vessel by operation of an emergency core cooling system. This causes a steep temperature gradient in the vessel wall which results in high thermal stresses. Such high thermal stresses are capable of inducing crack propagation in the vessel which is designed to preserve large safety margins against brittle fracture under normal operating conditions. In this context, the integrity of the reactor vessel under thermal shock conditions has been investigated analytically as well as experimentally based on linear elastic fracture mechanics [1-10]² In some of these papers, two-dimensional approaches are employed to estimate the transient stress intensity factors. These two-dimensional approaches are reasonable in most cases but sometimes expected to be too conservative. In addition, they are insufficient to treat the lateral crack extension from the three-dimensional cracks.

The objective of this paper is to present a methodology for the fracture from surface crack under thermal shock transient. Although various methods including the weight function and the finite element techniques have been published recently to compute the transient stress intensity factors under thermal fields, the present authors employ the superposition method [2-5] with the three-dimensional finite element method based on discretization error in order to solve these kinds of problems. This paper also includes the results of a series of thermal shock experiments with cracked PMMA plates. The comparison between the test results and the finite element calculations is found to be excellent.

Outline of Analysis Method

In order to economize computer time required to evaluate the three-dimensional K -values at every time interval during thermal shock transients, an approximate method based on the principle of superposition is employed here. Figure 1 schematically shows the principle, where stresses in cracked elastic body subjected to thermal load shown in Fig. 1a are equivalent to the sum of those in two elastic bodies shown in Fig. 1b and c. Figure 1b indicates the uncracked elastic body subjected to the same thermal load as that of Fig. 1a, and Fig. 1c indicates the cracked elastic body subjected to the boundary forces T_0 which cancel the stresses on the crack surface in Fig. 1b.

The first step in this procedure is to calculate the time-dependent thermal stresses in the uncracked body. The time-dependent thermal stresses on the crack surface T_0 are then approximated by the linear combination of the uniform, linear, and quadratic functions (Fig. 2). Thus, the time-dependent stress intensity factors are determined at every time step based on the approximated crack pressure loadings.

²The italic numbers in brackets refer to the list of references appended to this paper.

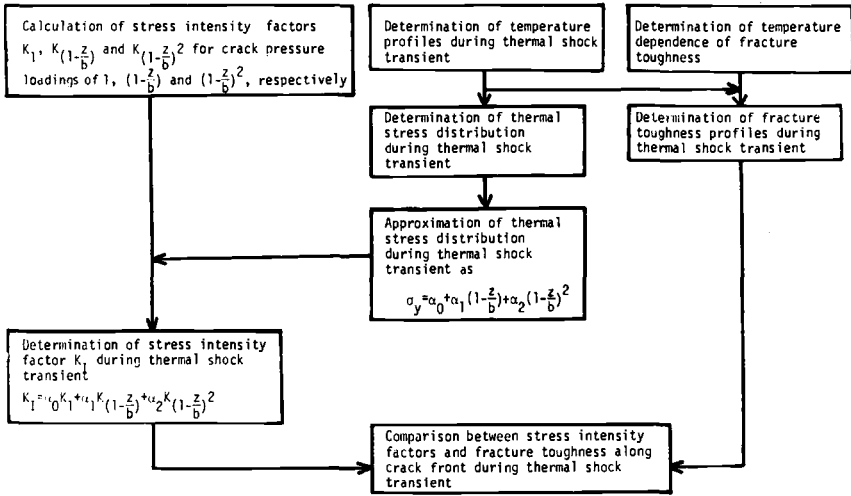


FIG. 3—Flow chart for analysis of thermal shock fracture problems.

(3) Determination of thermal stress profiles $\sigma_y(z)$ on the crack surface in the uncracked body at the same time interval as in step (2).

(4) Approximation of thermal stress $\sigma_y(z)$ on the crack surface in the uncracked body with the linear combination of the uniform, linear, and quadratic functions as follows.

$$\sigma_y(z) = \alpha_0 + \alpha_1(1 - z/b) + \alpha_2(1 - z/b)^2 \tag{1}$$

where the time-dependent constants α_0 , α_1 , and α_2 are determined with an appropriate curve fitting technique such as the least square method.

(5) Determination of stress intensity factors $K_I(z)$ at the same time interval as in steps (2) and (3), that is

$$K_I(z) = \alpha_0 K_{I1} + \alpha_1 K_{(1-z/b)} + \alpha_2 K_{(1-z/b)^2} \tag{2}$$

(6) Determination of the temperature dependence of the fracture toughness.

(7) Determination of fracture toughness profiles at the same time interval as in steps (2), (3), and (5).

(8) Comparison between K_I and K_{Ic} at each point along crack front at the same time interval as in steps (2), (3), (5), and (7). It is considered that if K_I becomes greater than or equal to K_{Ic} fracture occurs and vice versa.

The three-dimensional finite element method was used in the steps (1), (2), and (3). Especially in step (1), the method based on discretization error [11] was used. Moreover, in this paper, the procedure was applied to

the univariate and quadratic stress field $\sigma_y(z)$ on the crack surface, although it has the potential to consider more general cases.

Experiment

The test specimens used for this experiment are PMMA plates of 240 by 240 by 30 mm. The temperature dependence of Young's modulus E was measured and is depicted in Fig. 4. Poisson's ratio ν and thermal expansion coefficient α are assumed to be 0.4 and 0.0001/K, respectively. The part-circular precracks were machined with a 1-mm thick saw as shown in Fig. 5. The utilized specimens include several types of configurations; that is $2a = 50$ mm, $b = 2, 4, 6, 9, 12.5, 16, 20,$ and 24 mm. The analyzed specimens herein are three types of configurations; that is Case A of $2a = 50$ mm, $b = 4$ mm, Case B of $2a = 50$ mm, $b = 9$ mm, and Case C of $2a = 50$ mm, $b = 16$ mm. The initial temperature of all the specimens was 280 K. Then, the liquid nitrogen of the temperature 75 K was flooded suddenly in the shaded part of the upper surface of the specimens as shown in Fig. 5. The fracture time was detected by the stepwise output change of the strain gage near the crack tip caused by its breaking at the onset of rapid crack extension from the initial precrack. Figures 6 and 7 show the examples of fracture surfaces after lateral crack propagation and crack penetration through the thickness, respectively. Although it is hard to discuss the precise point of crack initiation from these sketches, it seems to begin in the neighborhood of the cooled surface. The distributions of the stresses in the thickness direction were not measured in this experiment but calculated by using three-dimensional finite element method which will be described afterwards in detail.

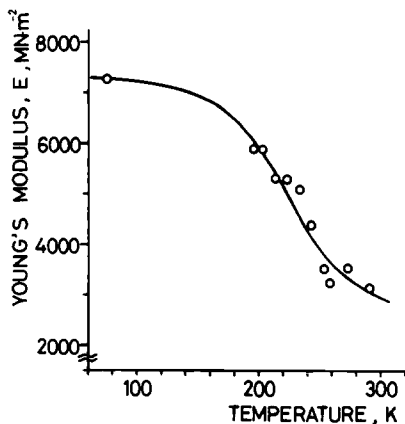


FIG. 4—Young's modulus versus temperature.

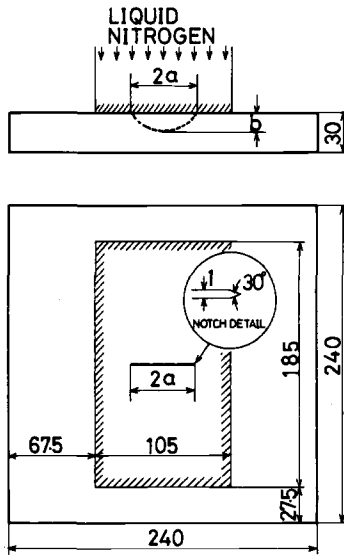


FIG. 5—Specimen geometry.

Theoretical Results and Comparison with Experiment

Determination of Stress Intensity Factors for Uniform, Linear, and Quadratic Crack Pressure Loadings

The distributions of stress intensity factors along crack fronts were determined by using the three-dimensional finite element method of crack analysis based on discretization error proposed recently by the present authors [11]. According to this method, K_{ex} , the converged value of stress intensity factor to be expected as the number of elements is increased infinitely, is expressed in the following form:

$$K_{(i)} = K_{ex} + aN_{(i)}^{-\delta}, \quad i = 1, 2, 3 \tag{3}$$

where $K_{(1)}$, $K_{(2)}$, and $K_{(3)}$ are the stress intensity factors evaluated with the numbers of meshes $N_{(1)}$, $N_{(2)}$, and $N_{(3)}$, respectively, and a , δ are unknowns to be determined together with K_{ex} by solving simultaneous Eq 3



FIG. 6—Sketch after lateral crack propagation (Specimen 11).

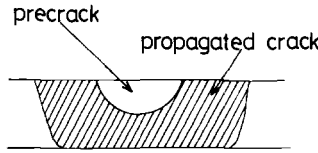
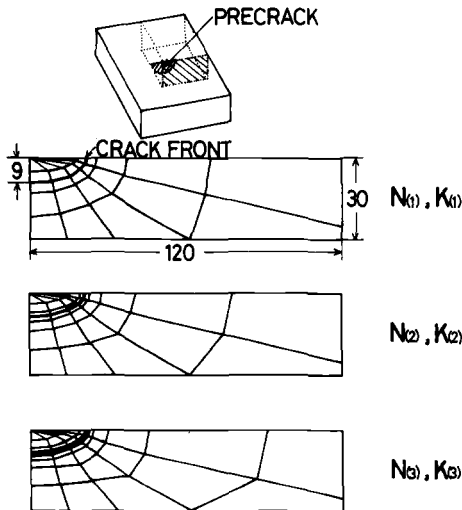


FIG. 7—Sketch after crack penetration through the thickness (Specimen 10).

The part-circular precracks are modeled as semi-elliptical surface cracks with equal depth and area as shown in Fig. 8 as an example. This figure shows three mesh discretizations of the section including crack surface for Case B. Figures 9, 10, and 11 show the calculated distributions of the stress intensity factors along crack fronts of Cases A, B, and C, respectively. In these figures, σ_y denotes the types of pressure applied on crack surface, and the dotted curves show the exact solutions for the elliptical cracks with the same crack geometries but embedded in the infinite body. It is seen from the comparison of these figures that the less the axis ratio b/a is, the more significantly the stress intensity factor for the uniform pressure decreases near the surface. This fact would be one of the reasons why a shallow crack takes a longer elapsed time to fracture than a deeper one as shown later.



$$K_{(i)} = K_{ex} + \alpha N_{(i)}^{-\delta}, \quad i=1,2,3$$

K_{ex} : CONVERGED VALUE OF K
 α, δ : UNKNOWNNS

FIG. 8—Three mesh discretizations in plane involving crack for Case B.

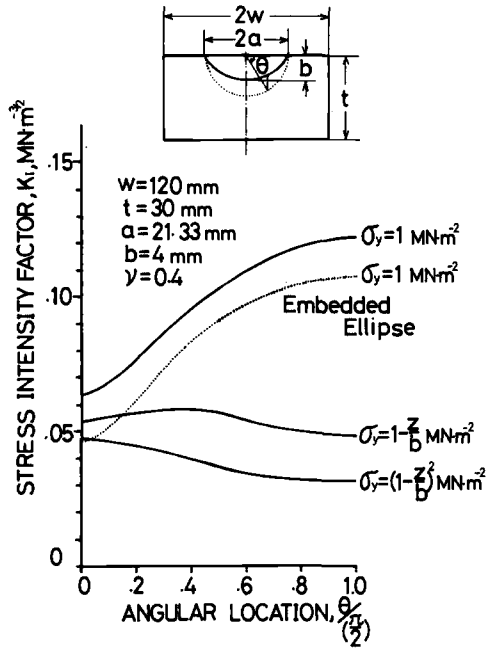


FIG. 9—Stress intensity factors of semi-elliptical surface crack for uniform, linear, and quadratic crack pressures for Case A.

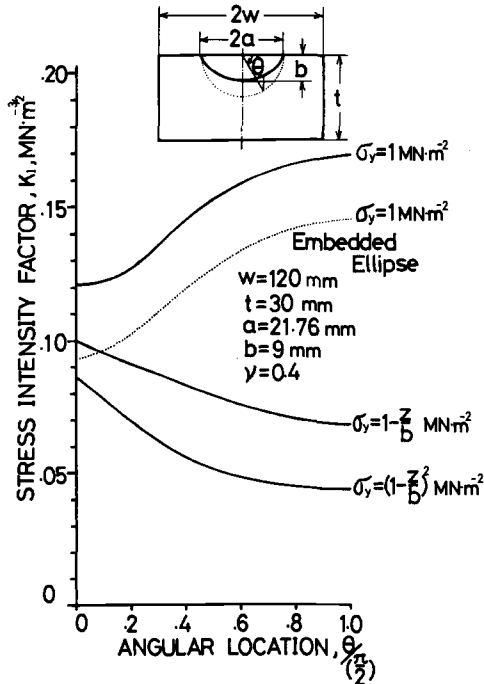


FIG. 10—Stress intensity factors of semi-elliptical surface crack for uniform, linear, and quadratic crack pressures for Case B.

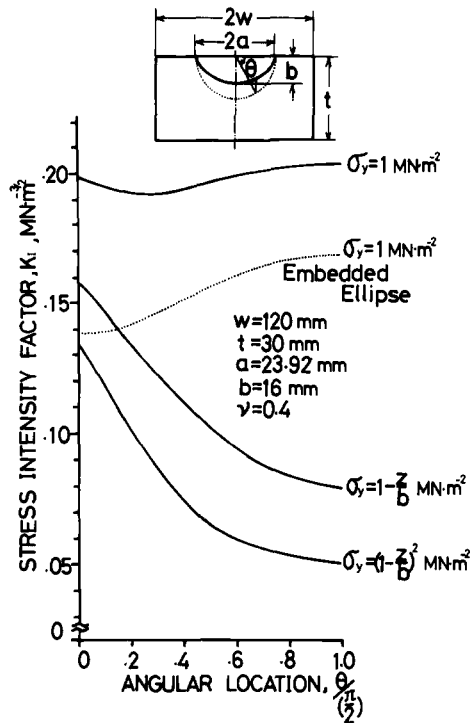


FIG. 11—Stress intensity factors of semi-elliptical surface crack for uniform, linear, and quadratic crack pressures for Case C.

Determination of Time-Dependent Temperature Distributions in Specimens Subject to Thermal Shock

Since a steep temperature gradient occurs near the cooled surface during thermal shock, it is too difficult to measure accurately the temperature variation through the thickness near the cooled surface in PMMA by thermocouple. In order to overcome this difficulty, the time-dependent temperature distributions in the specimens were determined by using the three-dimensional finite element method to adjust the heat transfer coefficient so that the calculated and the measured temperatures were coincident at the 1-mm depth from the cooled surface. The temperature distributions under thermal shock transients by this method are shown in Fig. 12. In this calculation, specific heat multiplied by density, thermal conductivity, and heat transfer coefficient are assumed to be 1.84×10^6 J/m³·K, 0.20 W/m·K and $59 \sim 147$ W/m²·K, respectively. The steep temperature gradients near the cooled surface can be seen from the figure.

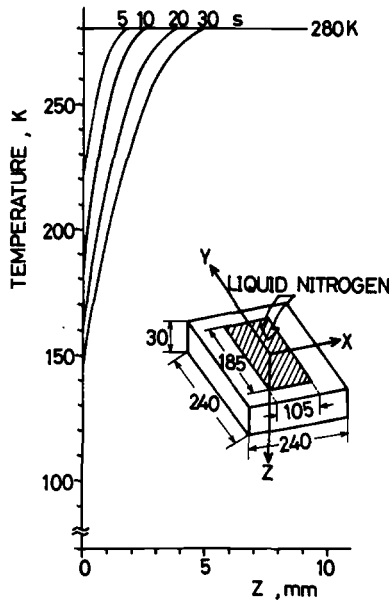


FIG. 12—Temperature profiles under thermal shock transients at $X = Y = 0$.

Determination of Time-Dependent Thermal Stresses

The time-dependent thermal stresses on the crack surface in uncracked plate were obtained by using the three-dimensional finite element method combined with the incremental method. The temperature dependence of Young's modulus is considered in this calculation according to test data as shown in Fig. 4.

Of the thermal stresses σ_y , τ_{yz} , and τ_{xy} on the crack surface, stresses τ_{yz} and τ_{xy} vanish due to the symmetry. Therefore, the stress σ_y on the crack surface as shown in Fig. 13 only was canceled in order to generate a stress free crack surface in the superposition scheme. The steep stress gradient near the cooled surface can be seen in Fig. 13.

Approximation of Crack Pressure Loads

From the geometry of the specimen and the area of cooled surface as shown in Fig. 5, the stress field $\sigma_y(x,y)$ on crack surface is considered well approximated by single parameter z only. Thus, in this paper, the combination of the uniform, linear, and quadratic functions of z was used to approximate σ_y , and the coefficients of these functions were determined at each time interval with the appropriate curve fitting techniques such as the least square method. Figure 14 shows the calculated values of coefficients α_0 , α_1 and α_2 for Cases A, B, and C. The maximum error near the surface associated with fitting the stress $\sigma_y(z)$ by the quadratic

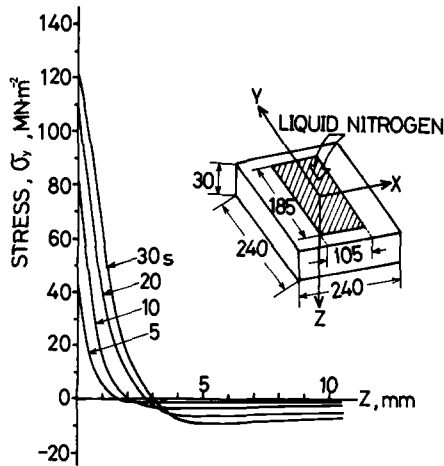


FIG. 13—Stress distributions of uncracked plate at $X = Y = 0$.

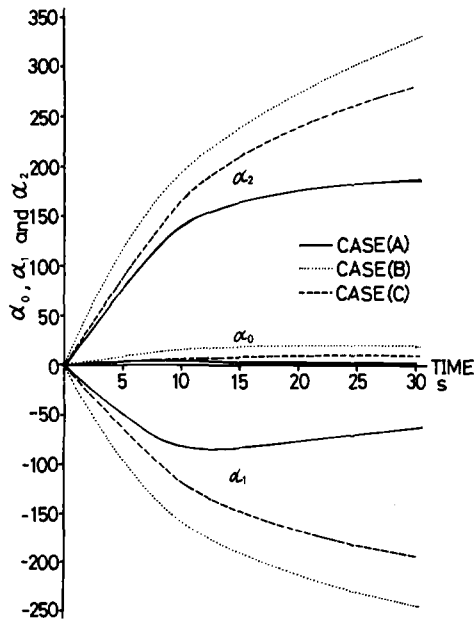


FIG. 14—Coefficients α_0 , α_1 and α_2 versus time.

polynomial representation was about 10 to 30 percent depending on the crack geometry. The deeper the crack depth is, the more accurate curve fitting seems to be necessary from the aforementioned result.

Determination of Time-Dependent Distributions of Stress Intensity Factors

The time-dependent distributions of stress intensity factors were calculated using the stress intensity factors under three kinds of loads given in Figs. 9, 10, and 11 combined with the time-dependent coefficients α_0 , α_1 , and α_2 given in Fig. 14, and the results are shown in Figs. 15, 16, and 17 for Cases A, B, and C, respectively. These figures show significant increase in the stress intensity factors approaching the cooled surface due to the front surface effect and the steep thermal stress gradient near the surface.

Determination of Temperature Dependence of Fracture Toughness

The temperature dependence of fracture toughness of PMMA was measured with the three-point bend specimens. The obtained fracture toughness curve is depicted in Fig. 18. It can be seen from this figure that K_{Ic} of PMMA decreases with increase of temperature within the temperature range of this experiment. Such a trend of toughness with temperature is characteristic of the polymer [12].

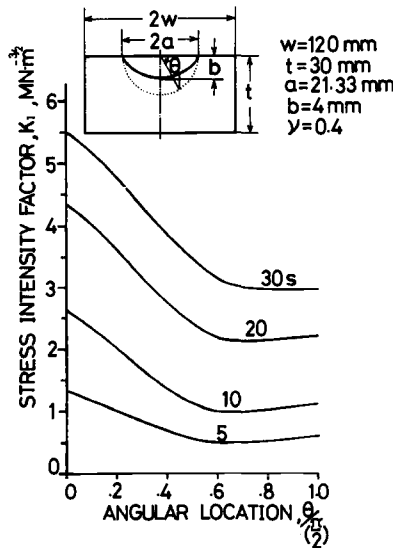


FIG. 15—Distributions of stress intensity factors under thermal shock transients for Case A.

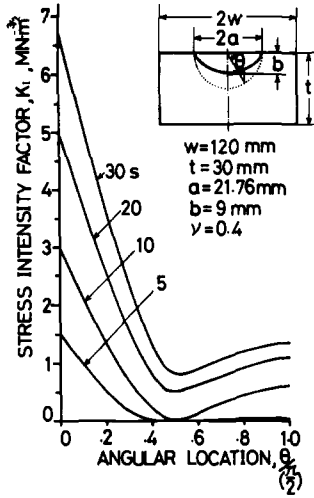


FIG. 16—Distributions of stress intensity factors under thermal shock transients for Case B.

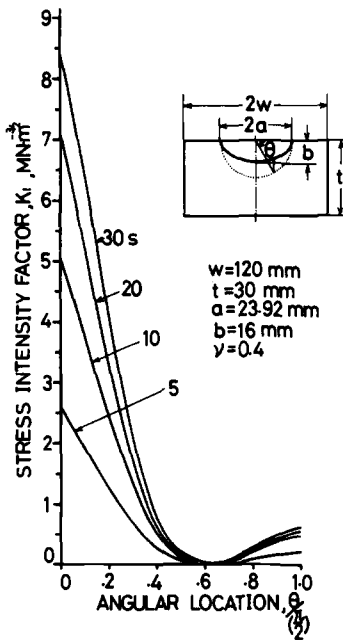


FIG. 17—Distributions of stress intensity factors under thermal shock transients for Case C.

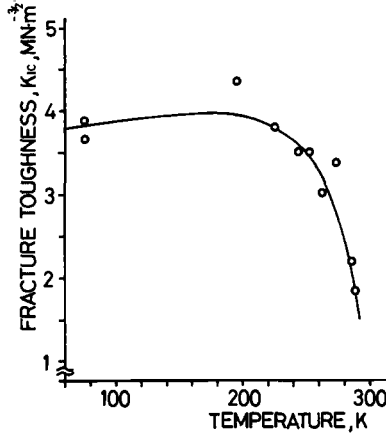


FIG. 18—Fracture toughness of PMMA versus temperature.

Determination of Time-Dependent Distributions of Fracture Toughness

The distributions of fracture toughness in the thickness direction are given in Fig. 19, which are estimated by the combination of Figs. 12 and 18.

Estimation of Time to Fracture

It is assumed in this paper that fracture occurs at the moment when K_I becomes greater than or equal to K_{Ic} at any single point along the crack front except the vicinity of the crack front-free surface intersection where the general type of singularity appears and the stress intensity factor can not be defined in a strict sense. In other words, the critical time to initiation of rapid crack propagation is determined by comparison between the stress intensity factor and fracture toughness throughout the crack front at every time interval during thermal shock transients. As can

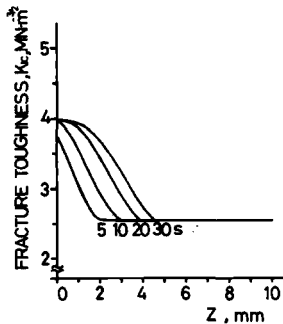


FIG. 19—Transient distributions of fracture toughness in thickness direction.

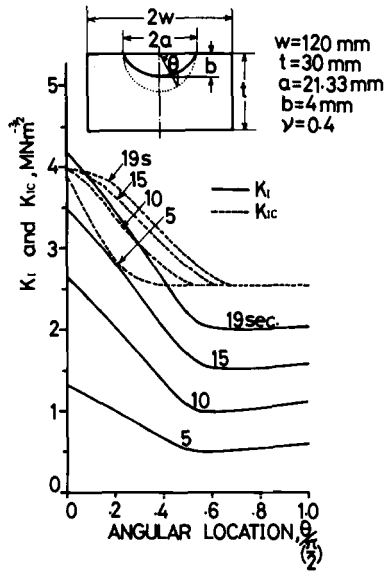


FIG. 20—Comparison between stress intensity factor and fracture toughness for Case A.

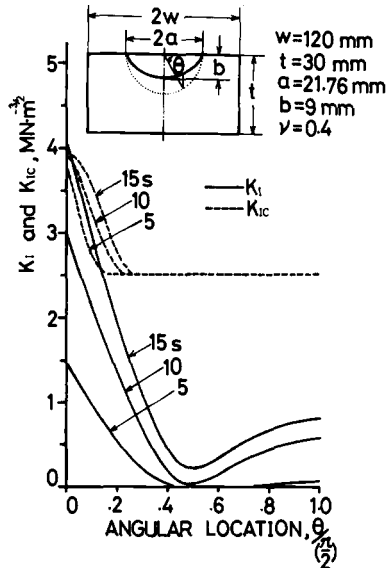


FIG. 21—Comparison between stress intensity factor and fracture toughness for Case B.

be seen from Figs. 20, 21, and 22, the times to fracture are estimated to be about 19, 15, and 9 for the Cases A, B, and C, respectively.

Comparison between Theoretical and Experimental Results

Figure 23 shows the comparison between measurement and estimation as to times to fracture elapsed from sudden cooling. In this figure, the specimen numbers are given with the pertinent experimental data. As shown in the figure, for some of the specimens fracture occurred twice consecutively in time. Specimen No. 11 is one of such examples, in which the first fracture might occur at one side of a near-surface crack front and the second at the other side (see Fig. 6).

The excellent agreement as to the fracture times between the theoretical and experimental results shown in Fig. 23 may justify the assumption that failure occurs when $K_I \geq K_{Ic}$ at any single point along crack front.

Conclusion

A procedure for treating thermal shock fracture through linear elastic fracture mechanics using the three-dimensional finite element method is described. It can be concluded that the present method may be a useful tool in investigating the thermal shock problems of practical structures such as a loss-of-coolant accident in reactor vessels.

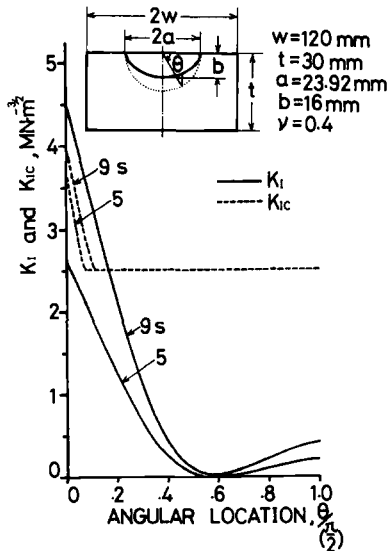


FIG. 22—Comparison between stress intensity factor and fracture toughness for Case C.

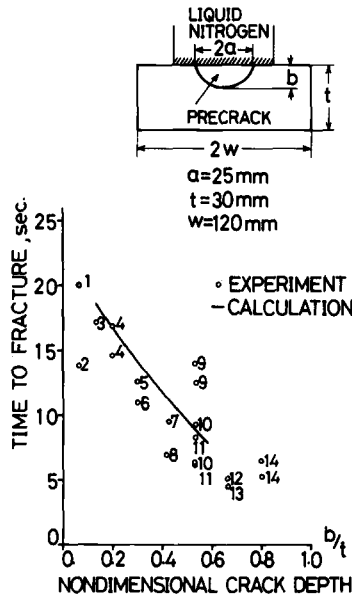


FIG. 23—Times to fracture versus normalized crack depth.

Acknowledgment

This paper was supported financially by Science and Technology Agency.

References

- [1] Ayres, D. J. in *Computational Fracture Mechanics*, E. F. Rybicki and S. E. Benzley, Eds., American Society of Mechanical Engineers, 1975, pp. 133–143.
- [2] Buchalet, C. B. and Bamford, W. H., Paper 75-WA/PVP-3, American Society of Mechanical Engineers Winter Annual Meeting, Nov. 1975.
- [3] Kobayashi, A. S., Emery, A. F., Polvanich, N., and Love, W. J., *International Journal of Pressure Vessels and Piping*, Vol. 5, 1977, pp. 103–122.
- [4] Kobayashi, A. S., Polvanich, N., Emery, A. F., and Love, W. J., *Transactions*, 4th International Conference on Structural Mechanics in Reactor Technology, Paper G 4/4, San Francisco, 1977.
- [5] Besuner, P. M., Cohen, L. M., and McLean, J. L., *Transactions*, 4th International Conference on Structural Mechanics in Reactor Technology, Paper G 4/5, San Francisco, 1977.
- [6] Reynen, J., *Transactions*, 4th International Conference on Structural Mechanics in Reactor Technology, Paper G 5/6, San Francisco, 1977.
- [7] Loss, F. J., Gray, J. R., Jr., and Hawthorne, J. R., *Transactions*, 4th International Conference on Structural Mechanics in Reactor Technology, Paper G 9/1, San Francisco, 1977.
- [8] Cheverton, R. D., Bolt, S. E., and Iskander, S. K., *Transactions*, 4th International Conference on Structural Mechanics in Reactor Technology, Paper G 9/3, San Francisco, 1977.

- [9] Ramani, D. T., *Transactions*, 4th International Conference on Structural Mechanics in Reactor Technology, Paper G 9/4, San Francisco, 1977.
- [10] Blauel, J. G., Kalthoff, J. F., and Stahn, D., *Transactions*, American Society of Mechanical Engineers, Series H, Vol. 96, Oct. 1974, pp. 299–308.
- [11] Yagawa, G., Ichimiya, M., and Ando, Y., *Proceedings*, 1st International Conference on Numerical Methods in Fracture Mechanics, A. R. Luxmoore and D. R. J. Owen, Eds., Swansea, 1978, pp. 249–267.
- [12] Tetelman, A. S. and McEvily, A. J., Jr., *Fracture of Structural Materials*, Wiley, New York, 1967.

L. Hodulak,¹ H. Kordisch,¹ S. Kunzelmann,¹
and E. Sommer¹

Growth of Part-Through Cracks

REFERENCE: Hodulak, L., Kordisch, H., Kunzelmann, S., and Sommer, E., "Growth of Part-Through Cracks," *Fracture Mechanics, ASTM STP 677*, C. W. Smith, Ed., American Society for Testing and Materials, 1979, pp. 399-410.

ABSTRACT: The growth of part-through cracks from surface notches is investigated using artificially marked fracture surfaces of both fatigued and monotonically loaded specimens. Experimental results for all specimen and crack geometries considered show that erroneous estimates of the growth of part-through cracks in thick-walled metal specimens are obtained when calculated on the basis of the stress intensity factor distribution along the crack front and on an assumed uniform response of the material throughout the specimen volume.

It is suggested that these discrepancies can be explained by a stress state dependent mechanical response of the material at the front of the loaded crack. Using this idea, qualitative models are proposed which account for the experimentally observed tendencies in the crack shape development as well as the influence of the load level on them. The effects of specimen size and bending constraint of the specimen also are discussed within the framework of the experimental results.

KEY WORDS: part-through cracks, fatigue crack growth, thick-walled metal specimens, crack shape, crack growth prediction, fatigue (materials), crack propagation

In predicting the growth of part-through cracks the linear elastic fracture mechanics (LEFM) approach is usually adopted. This approach appears convenient since the stress intensity factor distribution along the crack front has been established for various crack and specimen geometries using numerical methods [1-4]² and, also for a limited number of cases, using three-dimensional stress optical methods [5,6].

Unfortunately, the solutions obtained by different investigators disagree, in some cases considerably. This is illustrated by the example of solutions for a surface crack in a plate under uniform tension in Fig. 1 [3,4,7,8]. Despite the discrepancies in the absolute values, all curves,

¹ RNDr, Dipl.-Ing., research assistant, Dr. rer. nat. and director, respectively, Institut für Festkörpermechanik, Freiburg, West Germany.

² The italic numbers in brackets refer to the list of references appended to this paper.

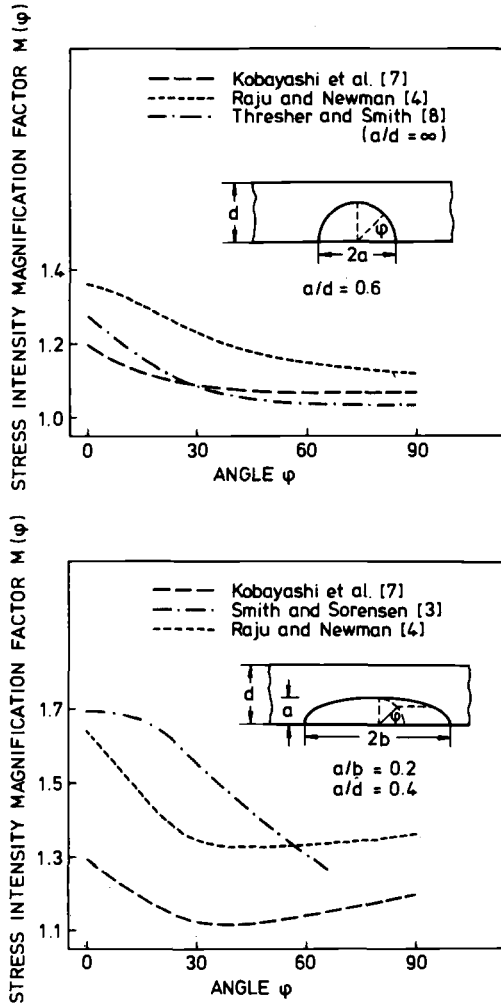


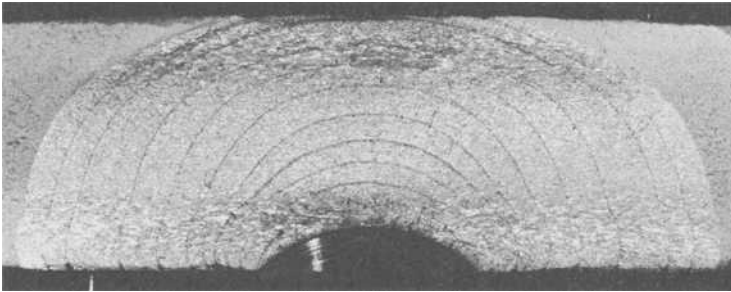
FIG. 1—Stress intensity magnification factors $M = K/\{\sigma\sqrt{\pi a}/Q \cdot [(a/b)^2 \cos^2 \varphi + \sin^2 \varphi]^{1/4}\}$ for surface crack in plates under uniform tension obtained by different investigators (Q is the crack shape factor [10]).

both for semi-circular and semi-elliptical cracks, show the same tendency. The stress intensity magnification factor at the specimen surface exceeds that at the crack apex if the crack depth does not approach the specimen thickness.

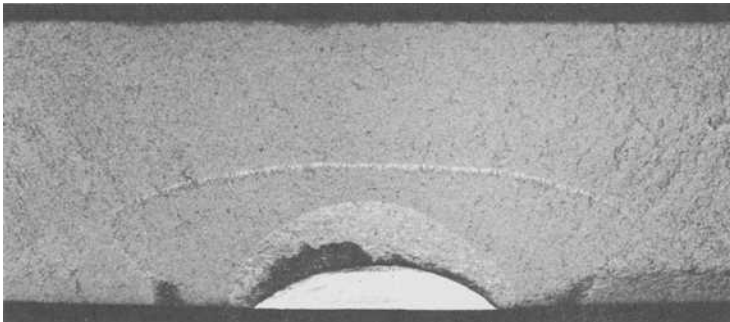
If the crack growth is estimated on the basis of any of these stress intensity distributions and under the assumption of uniform material response throughout the specimen volume, results are obtained which do not agree with the experimentally observed development of the crack shape towards a semi-circle [9]. Additionally the development of the

crack shape depends on the load level as reported in Ref 16 and demonstrated on the marked fracture surfaces developed in two identical specimens under fatigue and monotonic loading in Fig. 2.

It can be concluded that a correct prediction of the growth of part-through cracks in thick-walled metal specimens cannot be guaranteed by the aforementioned approach even if a precisely calculated stress intensity factor distribution is used. We have suggested elsewhere [9] that the discrepancies between estimated and observed crack growth can be eliminated if a locally variable crack resistance is involved in the crack growth prediction. The object of this paper is to extend our earlier model and to compare its predictions with experimental results for surface cracks in plates under uniform tension. Although the concept of LEFM is not directly applicable, the similarity of the fracture appearance in both



(a)



(b)

(a) fatigue ($\sigma_{\text{mean}} \approx 55 \text{ Nmm}^{-2}$)

(b) monotonic loading under displacement control ($\sigma \approx 300 \text{ Nmm}^{-2}$)

FIG. 2—Growth of surface cracks in the two identical aluminum alloy ($\sigma_y \approx 290 \text{ Nmm}^{-2}$) specimens under uniform loading (specimen thickness $d = 20 \text{ mm}$, gross section stress σ).

cases investigated suggests that the same conclusions may be drawn regarding general crackgrowth predictions. The results for part-through cracks in plates are more generally applicable and are not limited just to special geometrical and loading conditions.

Simple Model for the Growth of Surface Cracks in Plates Under Uniform Fatigue Load

Provided the stress intensity factor distribution $K(\varphi)$ for the initial crack is known and the crack resistance is constant throughout the specimen the crack extension distribution $\Delta l(\varphi)$ can be calculated by inserting $K(\varphi)$ in the Paris formula

$$\Delta J/\Delta N = C \cdot (\Delta K)^n \quad (1)$$

Adding $\Delta l(\varphi)$ to $l(\varphi)$ the new crack geometry is obtained. In this way the crack growth can be calculated stepwise under the condition that $K(\varphi)$ is known for all transient geometries. The development of the crack shape depends then only on the specimen and crack geometry and the loading mode (for example, ratio of tensile and bending stresses).

The development of semi-elliptical surface cracks in thick-plates can be qualitatively described by a simple model that we have proposed recently [9]. It can be shown that the shape of any surface crack in a semi-infinite medium under uniform stress will develop during growth towards a stable shape. The geometrical condition for a stable length-to-depth ratio of a surface crack of depth a and length $2b$ can be written as

$$\Delta b/\Delta a = b/a \quad (2)$$

Combining this with Eq 1 and the formula for stress intensity factor distribution of a semi-elliptical crack [3,4,7,10,11]

$$K(\varphi) = M(\varphi) \cdot \sigma \sqrt{\pi a/Q} [(a^2/b^2) \cos^2 \varphi + \sin^2 \varphi]^{1/4} \quad (3)$$

we obtain the axis ratio of the stable crack shape as

$$b/a = (M_b/M_a)^{2n/(n+2)} = \tan \alpha \quad (4)$$

where M_b , M_a are the front surface magnification factors at locations b and a , and n is the index in Eq 1, obtained by calibration tests. Experimentally care was taken that the crack growth rate $\Delta l/l \approx a/\Delta^M$ was approximately 10^{-4} mm/cycle in order to obtain the data in the linear part of the calibration curve (Eq 1). Q is the crack shape factor with correction for small scale yielding according to Ref 10. The development of the crack

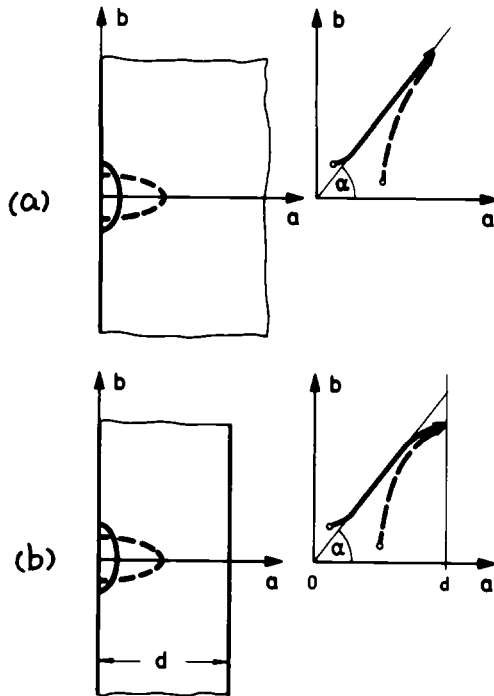
shape is shown schematically in Fig. 3a: a crack of any initial shape (b_0/a_0) should develop towards a stable shape represented by the straight line. The experimental results shown in Fig. 4 do indicate crack development towards a stable shape but the axis ratio does not correspond to that of Eq 4, being about 15 to 30 percent lower depending on which solution of $M(\varphi)$ from Fig. 1 is taken.

For deep cracks the model includes the influence of the rear surface correction factor giving rise to crack growth in the thickness direction, which increases with increasing crack depth (Fig. 3b). Also in this crack growth stage the observed crack development deviates from the predicted one with $\Delta b/\Delta a$ ([9,12,13] and Fig. 4) being higher than expected.

Improved models

Model with a Locally Variable Crack Resistance

To explain the discrepancies the model from the preceding section has been modified by postulating layers of material on the surfaces whose



(a) semi-ellipse in an semi-infinite medium, and
 (b) semi-ellipse in a plate.

FIG. 3—Expected development of idealized cracks.

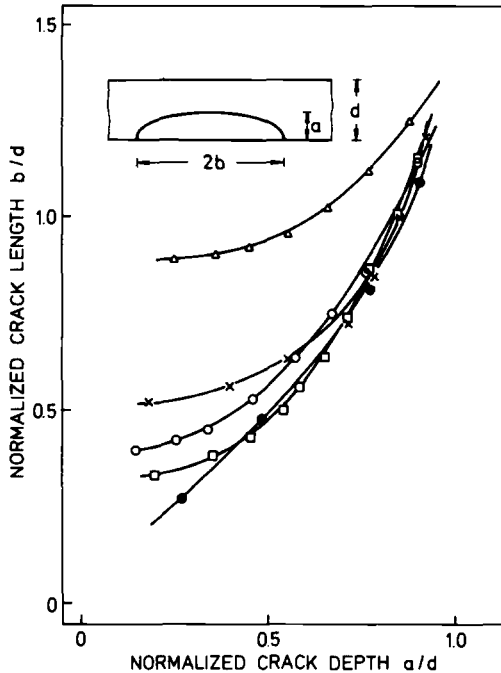


FIG. 4—Observed development of surface cracks in plates under uniform fatigue loading from various initial crack shapes. Aluminum and steel specimens, thickness $d = 10$ and 20 mm.

crack resistance is higher than that of the specimen interior. These layers represent specimen regions with lack of constraint. Their effect on crack development is shown in Fig. 5 (heavy line) compared to the previous model (dashed line). A retardation of a portion of the crack front in the front surface layer decreases the slope of $b = f(a)$ in the initial stage of crack growth. In contrast, when the crack approaches the rear surface its growth in the thickness direction is retarded in the other surface layer and the slope of $b = f(a)$ increases. The path of the heavy line corresponds to the experimental results of Fig. 4. The plausibility of the assumption of a higher crack resistance at the specimen surfaces is reinforced by the results of an examination of the growth of corner cracks under uniform tension. Although the value of the stress intensity factor of a circular corner crack is about 20 percent higher at the specimen surface than in the specimen interior ($\varphi \approx 45$ deg) [13] the growth rates at $\varphi \approx 45$ deg exceed those at the specimen surface [14] (Fig. 6).

If it is supposed that the thickness of the surface layers varies with the plane stress plastic zone size ahead of the crack front, then some dependence of the crack shape development on the load level can be expected. On the other hand the crack development should be indepen-

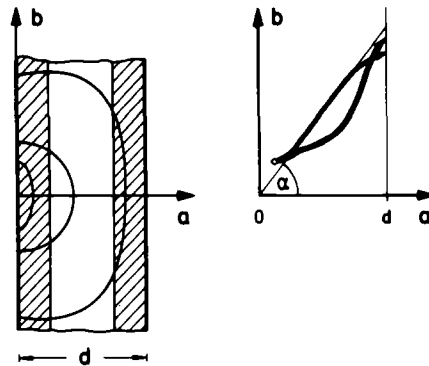


FIG. 5—Expected development of part-through cracks in plates with surface layers of higher crack resistance

dent of the specimen thickness provided all parameters are scaled correspondingly.

A comparison of crack growth in two specimens of different sizes but loaded by the same stress range $\Delta\sigma$ (Fig. 7) does appear to justify the dimensionless crack growth characteristics $b/d = f(a/d)$ used in the model [15]. Although an effect of load level on crack shape development has been observed [16], its trend (Fig. 8) appears to contradict a simple assumption of variation of the surface layer thickness with load.



FIG. 6—Fracture surface of a corner crack in an aluminum alloy plate ($\sigma_y \approx 130 \text{ Nmm}^{-2}$). Uniform fatigue markings, introduced by overloads. Notch: $a = b = 4 \text{ mm}$.

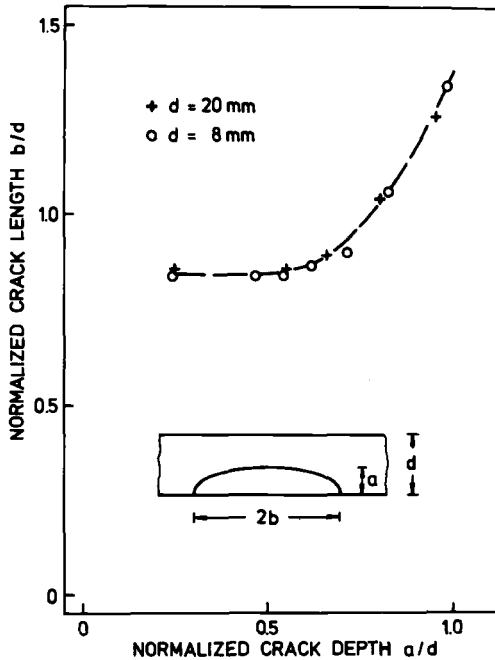


FIG. 7.—Crack development in two plate specimens of different thickness. Values of stress range $\Delta\sigma$ and of dimensionless initial crack size a/d , b/d of both specimens are equal ($\Delta\sigma \approx 50 \text{ Nmm}^{-2}$). Aluminum alloy ($\sigma_y \approx 110 \text{ Nmm}^{-2}$).

Model with a Redistribution of Stresses Due to Plastic Strains

To explain the dependence of crack shape development on load level and especially the development of cracks towards such shapes as in Fig. 2b we have recently suggested the following model [16].

The model is based on the idea that plastic deformation ahead of the crack front rearranges the distribution of stresses not only in the direction perpendicular to the crack front but also along the front since the plastic zone size varies with the stress state. The unloading ahead of the crack front at the specimen surface due to local yielding will be compensated for by some increase in load on the surrounding region. This redistribution of loading can be illustrated in terms of equivalent crack size. After adding the plane stress and plane strain plastic corrections to the actual crack front (Fig. 9a) a local maximum of the stress intensity factor appears on that portion of the effective crack front which is lagging behind. Thus crack extension will be a maximum at some depth beneath the specimen surface.

Discussion

The two models discussed in the preceding section should not be considered as alternatives but rather as two different approaches to the

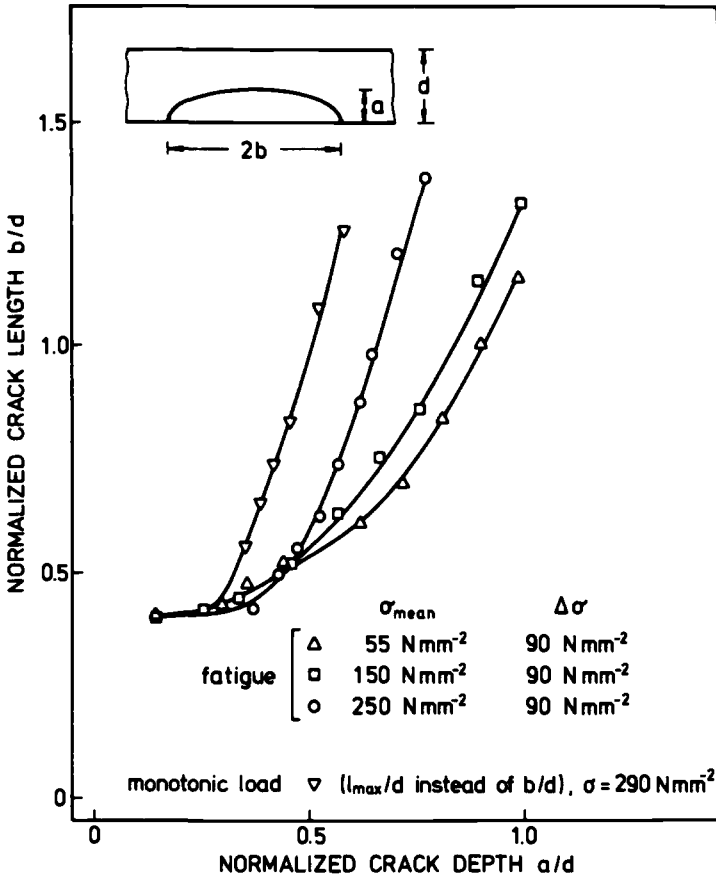


FIG. 8—Dependence of crack shape development on the load level. A surface crack in an aluminum plate ($\sigma_y \approx 290 Nmm^{-2}$) under uniform tension. Specimen size 1000 by 200 by 20 mm^3 . Initial notch: length 16 mm, depth 3.5 mm; l_{max} : absolute value of radius-vector of greatest crack extension.

same effect, namely a stress state dependent material response at the crack front of a loaded specimen. Plastic deformations ahead of cracks in metal specimens are not negligible and affect both the energy released and that absorbed on crack extension. In one of the models the effect of such plastic deformation on the absorbed energy is considered in terms of a locally variable crack resistance. In the other model the local distribution of the released energy in terms of stress intensity factor distribution is corrected to take the effect of plastic deformation into account. The first model works at the low loading levels occurring in most fatigue experiments, while the second is better for nominal mean stresses close to the yield stress.

The development of a crack towards shapes of increasing length to

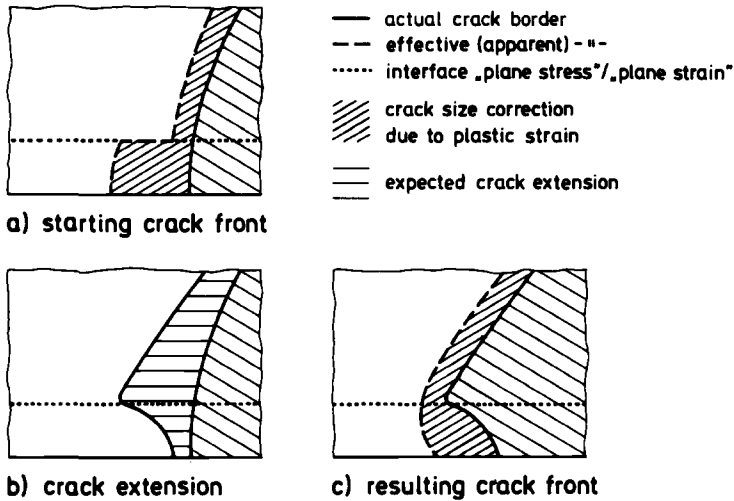


FIG. 9—A model for crack extension near the specimen surface for a high load level.

depth ratio with increasing mean stress (Fig. 8) can be understood in the following way: Since the crack size correction due to plastic strains is larger for the crack front adjacent to the specimen surface than for that at the crack apex, the effective crack shape depends on the load level. The increasing load increases the effective length-to-depth ratio of a surface crack and thus also the bending compliance of the specimen with the surface crack. The ratio of the induced bending component to the applied tensile load is then a function of the load level provided sufficient plastic deformation occurs ahead of the crack front. The bending component promotes crack growth in the length direction.

Some improvement in the prediction of the growth of deep surface cracks may be achieved also by clearing the question of the actual boundary conditions at which the stress intensity factor distributions were computed. Kobayashi [17] has recently called attention to the fact that some of the calculated stress intensity factors of surface cracks in plates were obtained under fixed grip boundary conditions, which do not correspond to experimental conditions. The bending restraint under these boundary conditions decreases the ratio K_b/K_a especially for deep cracks. Hence, using these values the crack extension ratio $\Delta b/\Delta a$ will be underestimated.

Some experimental evidence for this can be derived by comparing the development of surface cracks in specimens with different bending constraints, such as plates and tubes (Fig. 10) [18]. Both specimens, the tube with the axial surface crack, and the plate with the surface crack have identical initial geometries in the fracture plane. For an internally pressurized tube, however, the hoop stress in the wall decreases from the

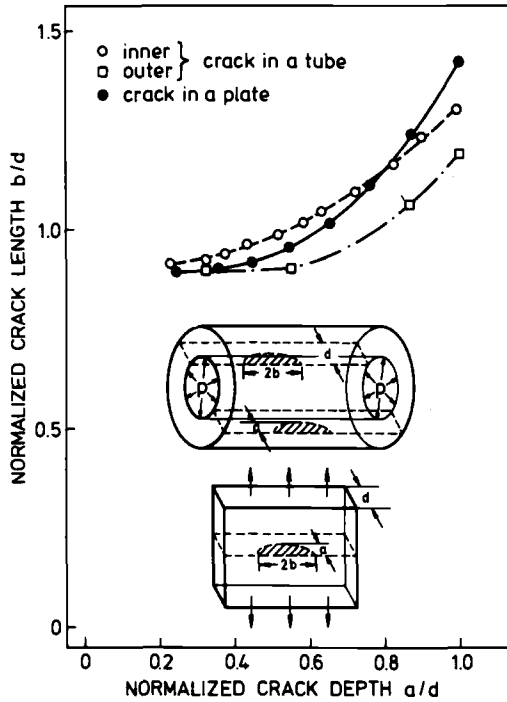


FIG. 10—Crack development in specimens with different bending constraints.

inner to the outer surface. Therefore, it may be expected that the function $b/d = f(a/d)$ for the crack in the plate specimen will lie between the corresponding functions for an outer and an inner crack in the tube. The results in Fig. 10 show that this holds for shallow cracks. The deviation for $a/d \approx 0.7$ appears then to be caused by the bending compliance of the plate.

Final Remarks

Due to the complex nature of the material response during crack growth and also due to uncertainties in the stress intensity factor results, a quantitative analysis of the proposed models was not attempted. Nevertheless the qualitative treatment may contribute to a better understanding of the growth of part-through cracks in thick-walled metal specimens.

Acknowledgment

This work is based on experimental investigations supported by the Arbeitsgemeinschaft Industrieller Forschungsvereinigungen and by the government of the Federal Republic of Germany.

References

- [1] Swedlow, J. L., *The Surface Crack: Physical Problems and Computational Solutions*, American Society of Mechanical Engineers, New York, 1972.
- [2] Kobayashi, A. S., Polvanich, N., Emery, A. F., and Love, W. J., *Journal of Pressure Vessel Technology; Transactions*, American Society of Mechanical Engineers, Vol. 99, Series, J, No. 1, 1977, pp. 83-89.
- [3] Smith, F. W. and Sorensen, D. R., *International Journal of Fracture*, Vol. 12, 1976, pp. 47-57.
- [4] Raju, I. S. and Newman, J. C., "Improved Stress-Intensity Factors for Semi-Elliptical Surface Cracks in Finite-Thickness Plates," *Transactions*, 4th International Conference on SMIRT, San Francisco, 15-19 Aug. 1977.
- [5] Smith, C. W. and Harms, A. E., *Recent Advances in Engineering Science*, Vol. 7, No. 2, 1976, pp. 59-66.
- [6] Smith, C. W., Peters, W. H., and Jolles, M. I., "Stress Intensity Factors for Reactor Vessel Nozzle Cracks," Paper No. 77.PVP-30, American Society of Mechanical Engineers, Energy Technology Conference, Houston, Sept. 1977.
- [7] Kobayashi, A. S., Emery, A. F., Polvanich, N., and Love, W. J., "Surface Flaw in a Thermally Shocked Hollow Cylinder," *Transactions*, 3rd International Conference on SMIRT, London, 1-5 Sept. 1975.
- [8] Thresher, R. W. and Smith, F. W., *Journal of Applied Mechanics*, Vol. 39, 1972, pp. 195-200.
- [9] Sommer, E., Hodulak, L., and Kordisch, H., "Growth Characteristics of Part-Through Cracks in Thick-Walled Plates and Tubes," *Journal of Pressure Vessel Technology; Transactions*, American Society of Mechanical Engineers, Vol. 99, No. 1, 1977, pp. 106-111.
- [10] Maddox, S. J., *Metal Construction*, Vol. 2, 1970, pp. 327-331.
- [11] Irwin, G. R., *Journal of Applied Mechanics*, Vol. 29, 1962, pp. 651-654.
- [12] Portch, D. J., "The Propagation of Fatigue Cracks from Surface Flaws," Report, Berkeley Nuclear Laboratories, 1976.
- [13] Nagai, A., Toyosada, M., and Okamoto, T., *Engineering Fracture Mechanics*, Vol. 7, 1975, pp. 481-490.
- [13] Kobayashi, A. S. and Enetanya, A. N., *Mechanics of Crack Growth, ASTM STP 590*; American Society for Testing and Materials, 1976, pp. 477-495.
- [14] Hodulak, L., Kordisch, H., Kunzelmann, S., and Sommer, E., "Ausbreitung von teilweise durchgehenden Rissen in einfachen Konstruktionselementen," IFKM-Bericht 76/1, Institut für Festkörpermechanik, Freiburg, 1976.
- [15] Hodulak, L., Kunzelmann, S., and Sommer, E., "Zur Entwicklung der Form von teilweise durchgehenden Rissen," IFKM-Bericht W 2/77, Institut für Festkörpermechanik, Freiburg, 1977.
- [16] Hodulak, L., Kordisch, H., Kunzelmann, S., and Sommer, E., *International Journal of Fracture*, Vol. 14, 1978, pp. R 35-R 38.
- [17] Kobayashi, A. S., "Crack Opening Displacement in a Surface Flawed Plate Subjected to Tension or Plate Bending," *Proceedings*, 2nd International Conference on Mechanical Behavior of Materials, Boston, 16-20 Aug. 1976.
- [18] Hodulak, L., Kordisch, H., and Sommer, E., "Zur Ausbreitung von teilweise durchgehenden Rissen," *Fortschritt-Berichte der VDI-Zeitschriften*, Reihe 18, No. 1, Düsseldorf, 1977.

Stress-intensity Factors for Two Symmetric Corner Cracks

REFERENCE: Raju, I. S. and Newman, J. C., Jr., "Stress-Intensity Factors for Two Symmetric Corner Cracks," *Fracture Mechanics, ASTM STP 677*, C. W. Smith, Ed., American Society for Testing and Materials, 1979, pp. 411-430.

ABSTRACT: The literature contains several analytical and experimental evaluations of Mode I stress-intensity factors for corner cracks at holes in plates subjected to remote tension, remote bending, or pin loading in the hole. Unfortunately, these solutions give very different stress-intensity factors for the same crack configuration and loading.

The purpose of this paper is to present stress-intensity factors, calculated by a three-dimensional finite-element analysis, for shallow or deep quarter-elliptical corner cracks at the edge of a hole in a finite-thickness plate. The plate was subjected to remote uniform tension, remote bending, or simulated pin loading in the hole. A wide range of configuration parameters was investigated. The crack depth-to-plate thickness ranged from 0.2 to 0.8, while the ratio of crack depth to crack length ranged from 0.2 to 2. The ratio of hole radius to plate thickness was 0.5 or 1. To verify the accuracy of the three-dimensional finite-element models employed, convergence was studied by varying the numbers of degrees of freedom (the number ranged from 4400 to 9300). The stress-intensity factor variations along the crack front are compared with solutions from the literature.

KEY WORDS: crack propagation, fatigue (materials), holes, elastic analysis, stress-intensity factors, finite elements

Nomenclature

- a* Depth of corner crack
- b* Half-width of cracked plate
- c* Length of corner crack
- F_i Stress-intensity boundary-correction factor
- h* Half-length of cracked plate
- K_I Stress-intensity factor (Mode I)
- M* Applied bending moment

¹ NRC-NASA resident research associate and research engineer, respectively, NASA Langley Research Center, Hampton, Va. 23665.

P	Applied load
Q	Shape factor for an elliptical crack
R	Radius of hole
S_b	Remote outer fiber bending stress
S_p	Hole bearing stress ($= P/2Rt$)
S_t	Remote uniform tensile stress
t	Plate thickness
x, y, z	Cartesian coordinates
θ	Angular measurement (see Fig. 5)
σ_n	Normal stress applied on hole boundary
ν	Poisson's ratio
ϕ	Parametric angle of the ellipse

Corner cracks at holes are among the most common flaws in aircraft structures. Accurate stress analyses of corner-crack configurations are needed for reliable prediction of crack-growth rates and fracture strengths. However, because of the complexities of such problems, exact solutions are not available. All investigators have used experimental or approximate analytical methods to obtain stress-intensity factors.

Engineering estimates for Mode I stress-intensity factors for some corner-crack configurations have been made by Hall and Finger [1],² Liu [2], and Newman [3]. These investigators did not consider the variation of stress-intensity factor along the crack front. Rather, their estimates gave a single value of stress-intensity factor for each crack configuration and, therefore, their estimates might be considered only as an average value of stress-intensity factor along the crack front. Shah [4] used the alternating method, along with an engineering estimate, to calculate the stress-intensity factor variation along the crack front for the corner-crack configuration subjected to either remote tension or pin loading in the hole.

McGowan and Smith [5], Smith, Jolles, and Peters [6], and Smith, Peters, and Gou [7], used three-dimensional photoelastic techniques to obtain stress-intensity factors for a variety of corner-crack configurations subjected to either remote tension or pin loading in the hole. They reported stress-intensity factors at two or three locations along the crack front.

A few three-dimensional stress analyses of the corner-crack configuration have been reported recently. To analyze a quarter-elliptical corner crack emanating from a hole in a finite-thickness plate, Smith and Kullgren [8] used a finite element-alternating method to obtain the stress-intensity factor variations along the crack front, while Kathiresan [9] and Heckmer and Bloom [10] used three-dimensional finite-element methods. Unfortunately, some of these solutions for the same configuration and loading gave different stress-intensity factors.

² The italic numbers in brackets refer to the list of references appended to this paper.

The purpose of this paper is to present Mode I stress-intensity factors, calculated by a three-dimensional finite-element analysis [11,12], for shallow or deep quarter-elliptical corner cracks at the edge of a hole in finite-thickness plates. The finite-thickness plates were subjected to remote uniform tension, remote bending, or simulated pin loading in the hole. A wide range of configuration parameters was considered. The ratio of crack depth to plate thickness ranged from 0.2 to 0.8, the ratio of crack depth to crack length ranged from 0.2 to 2, while the ratio of hole radius to plate thickness was 0.5 or 1. To study convergence, finite-element models with 4400 to 9300 deg of freedom were analyzed. The stress-intensity factors were calculated by using a nodal-force method [11]. The stress-intensity-factor variations along the crack front are presented and compared with other solutions from the literature.

Analysis

The corner-crack configuration is shown in Fig. 1. An elastic plate of thickness t , width $2b$ and length $2h$, contains a through-the-thickness circular hole of radius R . Emanating from the hole are two symmetrically placed quarter-elliptical corner cracks of length c on the front surface and of depth a on the hole surface.

Three types of loading have been considered: remote tension, remote bending, and wedge loading in the hole. The solution for wedge loading in the hole also was used in combination with the remote tension solution to obtain solutions for the case of simulated pin loading in the hole.

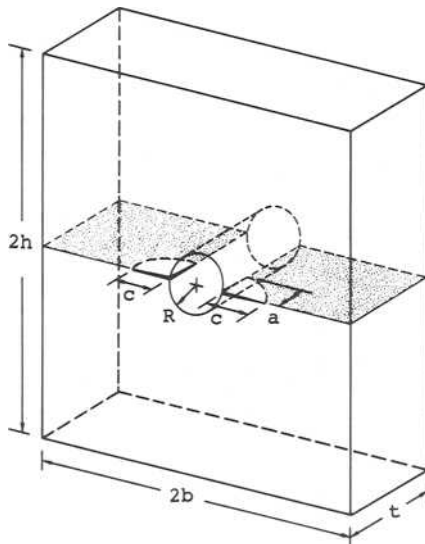


FIG. 1—Corner cracks at the edge of a hole in a finite plate.

Finite-Element Idealization

Two types of elements (isoparametric and singular [13]) were used in combination to model elastic bodies with quarter-elliptical corner cracks. Figure 2 shows a typical finite-element model for a corner crack in a large body, $b/(R+c) \geq 5$ and $h/b = 1.8$. This model idealizes one quarter of the body. Various numbers of wedges were used to form the desired crack configuration in the $y = 0$ plane. A wedge is in the region between two radial lines emanating from the point $|x| = R, z = 0$ in the $y = 0$ plane, for the circular crack model and is the region between two hyperbolas in the $y = 0$ plane for the elliptic crack model as shown in Fig. 3. For further details on modeling see Ref 12. The model shown in Fig. 2 has eight wedges, each of which is composed of elements around the crack front that are identical in pattern to that shown in the x,y plane. The isoparametric (eight-noded hexahedron) elements were used everywhere except near the crack front. Around the crack front (such as in the x,y plane) each wedge contained eight "singularity" elements in the shape of pentahedrons. The "singularity" elements produced a singular stress field at the crack front. Details of the formulation of these types of elements are given in Refs 11 and 13 and are not repeated here.

The finite-element model for the quarter-elliptical corner crack was obtained from the finite-element model for the quarter-circular crack by

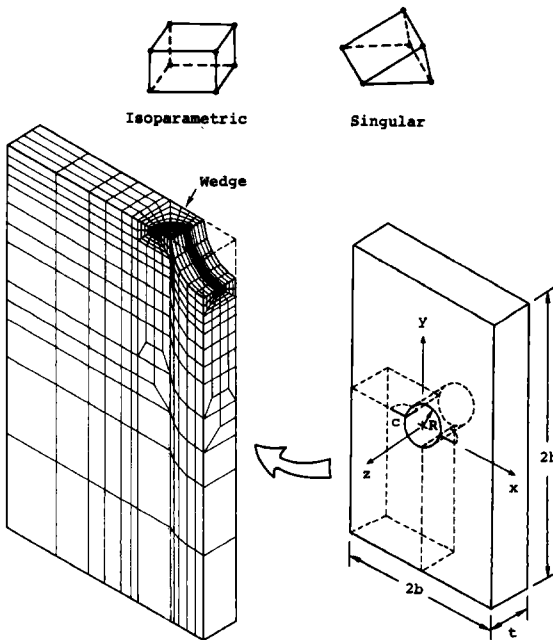


FIG. 2.—Finite-element idealization of the corner-crack configuration.

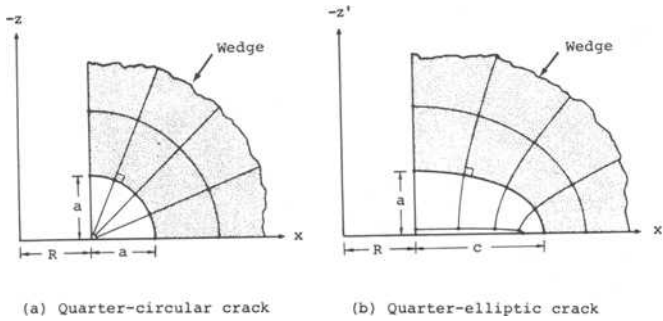


FIG. 3—Circle to ellipse transformation ($y = y' = 0$).

using an elliptic transformation only in the region of the wedges. This transformation was convenient because the nodal forces along the normals to the crack front are used to calculate the stress-intensity factors. If (x, y, z) are the Cartesian coordinates of a node in the circular-crack model and (x', y', z') are the coordinates of that same node in the elliptical-crack model, then the transformation is

$$x' = R + (x - R) \sqrt{1 + \frac{c^2 - a^2}{(x - R)^2 + z^2}}, y' = y, z' = z \text{ for } \frac{a}{c} \leq 1 \quad (1a)$$

and

$$x' = x, y' = y, z' = z \sqrt{1 + \frac{a^2 - c^2}{(x - R)^2 + z^2}} \text{ for } \frac{a}{c} > 1 \quad (1b)$$

for $x \geq R$. Figure 3 shows how circular arcs and radial lines in the x, z plane of the circular-crack model are transformed by Eqs 1a and 1b into ellipses and hyperbolas, respectively, in the x', z' plane for the elliptical-crack model. Because Eqs 1a and 1b are not valid at $x = R$ and $z = 0$, a circle of very small radius, $a/1000$, was used near $x = R$ and $z = 0$ in the circular crack model. The small circle, which maps onto a very narrow ellipse in the x', z' plane, avoids ill-shaped elements and allows the use of eight-noded elements in the elliptical-crack model. The elliptic transformation reduced the b/c ratio; therefore, to eliminate the influence of plate width, additional rectangular prism elements were added along the x' axis.

Loading

Three types of loading were applied to the finite-element models of the corner-crack configuration: (1) remote uniform tension, (2) remote bending, and (3) wedge loading in the hole. The loadings are illustrated in Fig. 4. The remote uniform tension is S_t in Fig. 4a; the remote outer fiber

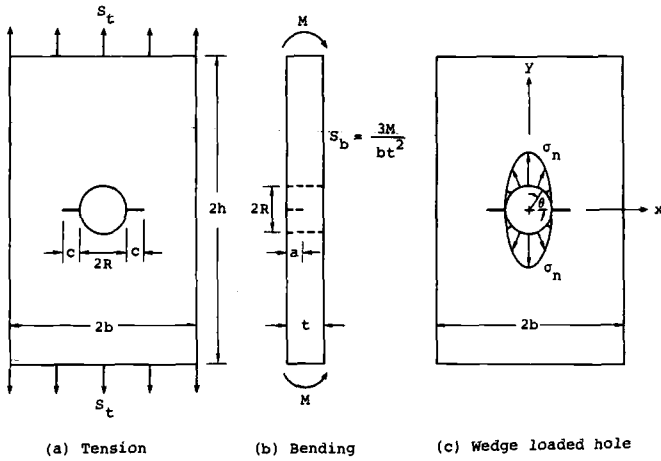


FIG. 4—Corner-crack configuration subjected to various loads.

bending stress, S_b , in Fig. 4b is calculated from the applied bending moment; and the applied normal stress on the hole boundary, σ_n , in Fig. 4c was assumed to be given by

$$\sigma_n = \frac{3P}{4Rt} \sin^2 \theta \tag{2}$$

where P is the total applied force acting in the y -direction over the arc from $\theta = 0$ to π . The particular form of σ_n was chosen to simulate pin loading (see Fig. 5). The Mode I stress-intensity factor for the case of pin loading in the hole is obtained by appropriate superposition of the results for remote uniform tension (Fig. 4a) and for wedge loading in the hole (Fig. 4c). (See Ref 3.)

Stress-Intensity Factor

Only loadings which cause Mode I (tension) deformations were analyzed. The Mode I stress-intensity factor, K_I , at any point along the quarter-elliptical corner crack in a finite-thickness plate was taken to be

$$K_I = S_i \sqrt{\pi \frac{a}{Q}} F_i \left(\frac{a}{t}, \frac{a}{c}, \frac{R}{t}, \phi \right) \tag{3}$$

where the subscript i denotes the type of applied loading (remote tension ($i=t$), remote bending ($i=b$), or wedge loading in the hole ($i=p$)); Q is the shape factor for an ellipse and is given by the square of the complete elliptic integral of the second kind [15]. The boundary-correction factor, F_i , is a function of crack depth, crack length, hole radius, plate thickness,

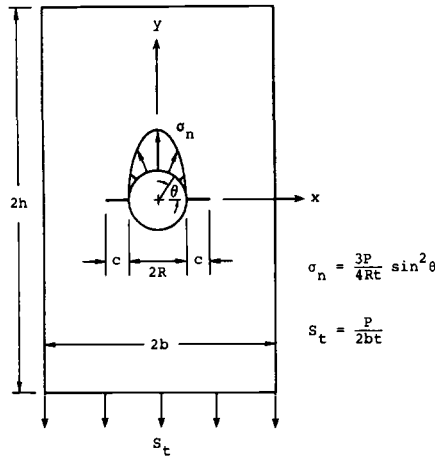


FIG. 5—Corner-crack configuration subjected to simulated pin loading.

and the parametric angle of the ellipse. Note that the length and width of the plate were chosen large enough so that they would have a negligible effect on stress intensity. Values for F_t were calculated as a function of a/t , a/c , and ϕ for $R/t = 0.5$ and 1.0 . The a/c ratios ranged from 0.2 to 2 and the a/t ratios ranged from 0.2 to 0.8 .

The stress-intensity factor (Mode I) for the simulated pin-load configuration shown in Fig. 5 was obtained by superposition of the results for the configurations shown in Figs. 4a and 4c. (Superposition of these results gives the correct normal stresses for the pin-load configuration only along the $y = 0$ plane.) For this case, the Mode I stress-intensity factor is given by

$$K_I = S_p \sqrt{\pi \frac{a}{Q}} \frac{1}{2} \left(\frac{R}{b} F_t + F_p \right) \tag{4}$$

where $S_p = P/2Rt$, and F_t and F_p are the boundary-correction factors obtained from Eq 3 for remote tension and wedge loading in the hole, respectively. (This superposition method gives no information on Mode II stress-intensity factors.)

The stress-intensity factors from the finite-element models of the quarter-elliptical corner cracks were obtained by using a nodal-force method, details of which are given in Ref 11. In this method, the nodal forces normal to the crack plane and ahead of the crack front are used to evaluate the stress-intensity factor. In contrast, the crack-opening displacement (COD) method presented in Ref 13 requires a prior assumption of either plane stress or plane strain, which is a potential source of inaccuracy. The nodal-force method requires no such assumption.

Results and Discussion

In the following sections, results for quarter-circular and quarter-elliptical corner cracks emanating from a circular hole ($R/t = 0.5$ or 1) subjected to various loadings are presented. Convergence of the stress-intensity factors for a deep quarter-elliptical corner crack were studied, by varying the number of degrees of freedom in the finite-element models from 4400 to 9300. The stress-intensity factor variations along the crack front for quarter-circular ($a/c = 1$) and quarter-elliptical ($a/c = 0.2$ and 2) corner cracks are presented as functions of a/t with $R/t = 0.5$ or 1 . (See Tables 1 and 2.) The stress-intensity factors are compared with other solutions and experimental results from the literature.

Convergence

In Ref 11, the present method was applied to the problems of embedded circular ($a/c = 1$) and embedded elliptical ($a/c = 0.2$) cracks in a large body under uniform tension. Because the results obtained for these crack shapes were generally within 1 percent of the exact solutions [15], the present method is expected to be suitable for analyses of the more complex configurations considered herein, provided that enough degrees of freedom are used to ensure convergence.

Figure 6 shows the results of the convergence study for a deep quarter-elliptical corner crack ($a/c = 0.2$, $a/t = 0.8$, $R/t = 0.5$). This configuration was chosen because proximity of the back surface to the crack front was expected to cause convergence difficulties. Four finite-element models with 4400 to 9300 degrees of freedom (DOF) were analyzed. These models used 2, 4, 8, or 10 wedges to idealize the elliptic crack front on the $y = 0$ plane. A typical eight-wedge model is shown in Fig. 2. The two-, four-, and eight-wedge models had equal wedge angles. The ten-wedge model had nonuniform wedges with smaller wedges near the intersection of the crack with the hole surface ($\phi = \pi/2$). The smaller wedges near the free surface were used to study the "boundary-layer" effect suggested by Hartranft and Sih [16]. The idealization used to model the circular hole was the same for all models (see Fig. 2). The two finest models (8454 and 9306 degrees of freedom) gave stress-intensity factors within less than one percent of each other except at the intersection of the crack front and the hole surface, where the difference was about 5 percent. The ten-wedge model with about 9300 degrees of freedom was used subsequently to obtain stress-intensity factors for all other crack configurations.

Quarter-Circular Corner Cracks

Figure 7 shows the normalized stress-intensity factors for a quarter-circular corner crack ($R/t = 0.5$) as a function of the parametric angle, ϕ ,

TABLE 1—Boundary-correction factors, F_i , for two symmetric corner cracks with $R-t = 0.5$
 $(F_i = K_{II} S_i \sqrt{\pi a l Q}; b/(R+c) \geq 5; h/b = 1.8; \nu = 0.3)$

Type of Loading	alc		1					2				
	$\frac{a}{2\phi} \frac{T}{\pi}$	0	0.2	0.5	0.8	0.2	0.5	0.8	0.2	0.5	0.8	
			0.2	0.5	0.8	0.2	0.5	0.8	0.2	0.5	0.8	
Tension	0	0.673	0.878	1.256	1.832	1.699	1.808	1.603	1.353	1.259	1.259	
	0.125	0.711	0.934	1.255	1.870	1.699	1.673	1.588	1.350	1.235	1.235	
	0.25	0.833	1.061	1.385	1.886	1.675	1.608	1.566	1.297	1.144	1.144	
	0.375	0.989	1.215	1.547	1.936	1.687	1.608	1.532	1.272	1.109	1.109	
	0.5	1.141	1.360	1.707	2.015	1.733	1.640	1.486	1.252	1.088	1.088	
	0.625	1.298	1.500	1.832	2.119	1.817	1.690	1.446	1.253	1.095	1.095	
	0.75	1.477	1.643	1.930	2.247	1.951	1.750	1.406	1.263	1.123	1.123	
	0.833	1.682	1.796	2.020	2.359	2.107	1.907	1.275	1.295	1.184	1.184	
	0.917	1.949	2.018	2.148	2.447	2.287	2.122	1.296	1.276	1.198	1.198	
	0.958	2.128	2.257	2.366	2.398	2.347	2.274	1.296	1.276	1.198	1.198	
1.0	1.885	2.276	2.554	1.985	2.072	2.164	1.053	0.977	0.824	0.824		
Bending	0	0.635	0.713	0.729	1.562	1.279	1.113	1.291	0.977	0.871	0.871	
	0.125	0.649	0.699	0.661	1.520	1.172	0.969	1.226	0.871	0.672	0.672	
	0.25	0.729	0.722	0.632	1.432	1.005	0.722	1.121	0.710	0.453	0.453	
	0.375	0.832	0.759	0.605	1.371	0.864	0.497	1.025	0.563	0.253	0.253	
	0.5	0.922	0.779	0.556	1.332	0.744	0.293	0.935	0.436	0.081	0.081	
	0.625	1.005	0.785	0.489	1.311	0.647	0.118	0.852	0.333	-0.059	-0.059	
	0.75	1.090	0.791	0.411	1.310	0.580	-0.028	0.787	0.263	-0.162	-0.162	
	0.833	1.177	0.806	0.351	1.315	0.548	-0.130	0.739	0.226	-0.221	-0.221	
	0.917	1.276	0.830	0.302	1.311	0.536	-0.205	0.704	0.209	-0.260	-0.260	
	0.958	1.310	0.846	0.262	1.247	0.518	-0.239	0.651	0.197	-0.267	-0.267	
1.0	1.084	0.770	0.219	0.984	0.417	-0.246	0.515	0.160	-0.236	-0.236		
Wedge loading	0	0.071	0.071	0.086	0.638	0.462	0.419	0.471	0.531	0.412	0.412	
	0.125	0.076	0.065	0.083	0.669	0.480	0.420	0.465	0.522	0.415	0.415	
	0.25	0.096	0.075	0.092	0.698	0.498	0.413	0.449	0.499	0.413	0.413	
	0.375	0.129	0.093	0.105	0.743	0.530	0.417	0.433	0.476	0.413	0.413	
	0.5	0.176	0.122	0.126	0.803	0.581	0.446	0.416	0.459	0.419	0.419	
	0.625	0.251	0.167	0.156	0.879	0.657	0.501	0.398	0.447	0.434	0.434	
	0.75	0.369	0.242	0.204	0.966	0.762	0.594	0.384	0.447	0.462	0.462	
	0.833	0.516	0.353	0.278	1.041	0.872	0.707	0.371	0.453	0.495	0.495	
	0.917	0.714	0.533	0.408	1.101	0.972	0.848	0.364	0.470	0.541	0.541	
	0.958	0.854	0.722	0.587	1.091	1.019	0.947	0.342	0.467	0.558	0.558	
1.0	0.797	0.818	0.759	0.917	0.978	0.927	0.277	0.401	0.497	0.497		

TABLE 2—Boundary-correction factors, F_{I_1} , for two symmetric corner cracks with $R/t = 1$.
 $(F_{I_1} = K_{1/S} \sqrt{\pi a l} Q; b/(R + c) \geq 5; h/b = 1.8; \nu = 0.3)$

Type of Loading	a/c		1					2								
	$\frac{2\phi}{\pi}$	$\frac{a}{T}$	0.2					0.2								
			0.2	0.5	0.8	0.2	0.5	0.8	0.2	0.5	0.8					
Tension	0		0.772	0.838	1.325	2.323	2.129	1.962	1.733	1.619						
	0.125		0.819	0.998	1.323	2.343	2.125	1.942	1.716	1.587						
	0.25		0.966	1.138	1.460	2.329	2.092	1.894	1.670	1.526						
	0.375		1.163	1.312	1.635	2.355	2.105	1.958	1.626	1.473						
	0.5		1.368	1.486	1.812	2.406	2.159	1.972	1.580	1.426						
	0.625		1.588	1.673	1.964	2.468	2.249	2.026	1.683	1.387						
	0.75		1.834	1.882	2.106	2.534	2.375	2.162	1.599	1.493						
	0.833		2.071	2.111	2.257	2.569	2.494	2.324	1.519	1.460						
	0.917		2.314	2.409	2.478	2.553	2.592	2.498	1.449	1.391						
	0.958		2.380	2.619	2.734	2.409	2.539	2.551	1.335	1.372						
	1.0		1.889	2.334	2.660	1.925	2.089	2.219	1.061	1.122						
	Bending	0		0.708	0.763	0.768	1.821	1.485	1.478	1.147	0.971					
		0.125		0.725	0.749	0.697	1.757	1.359	1.115	1.477	1.014					
		0.25		0.816	0.776	0.669	1.633	1.163	0.833	1.228	0.817					
		0.375		0.937	0.820	0.644	1.540	0.977	0.575	1.096	0.641					
0.5			1.046	0.847	0.595	1.467	0.854	0.340	0.976	0.490						
0.625			1.149	0.862	0.527	1.406	0.736	0.140	0.867	0.370						
0.75			1.250	0.878	0.445	1.357	0.651	-0.024	0.779	0.286						
0.833			1.336	0.902	0.378	1.312	0.604	-0.129	0.711	0.240						
0.917			1.400	0.930	0.320	1.248	0.574	-0.191	0.657	0.215						
0.958			1.360	0.927	0.282	1.137	0.537	-0.200	0.592	0.198						
1.0			1.003	0.753	0.226	0.850	0.392	-0.202	0.450	0.152						
Wedge loading		0		0.170	0.126	0.162	0.983	0.795	0.561	0.777	0.680					
		0.125		0.183	0.134	0.159	1.001	0.806	0.719	0.542	0.672					
		0.25		0.227	0.158	0.176	1.005	0.810	0.699	0.509	0.657					
		0.375		0.296	0.197	0.204	1.031	0.837	0.695	0.479	0.647					
	0.5		0.384	0.254	0.246	1.068	0.887	0.728	0.447	0.608						
	0.625		0.503	0.341	0.305	1.115	0.956	0.788	0.416	0.638						
	0.75		0.657	0.470	0.393	1.161	1.044	0.885	0.389	0.548						
	0.833		0.813	0.632	0.518	1.191	1.124	0.990	0.365	0.659						
	0.917		0.977	0.848	0.708	1.197	1.193	1.100	0.347	0.678						
	0.958		1.044	1.010	0.905	1.137	1.181	1.143	0.317	0.665						
	1.0		0.849	0.948	0.962	0.921	0.986	1.011	0.248	0.558						

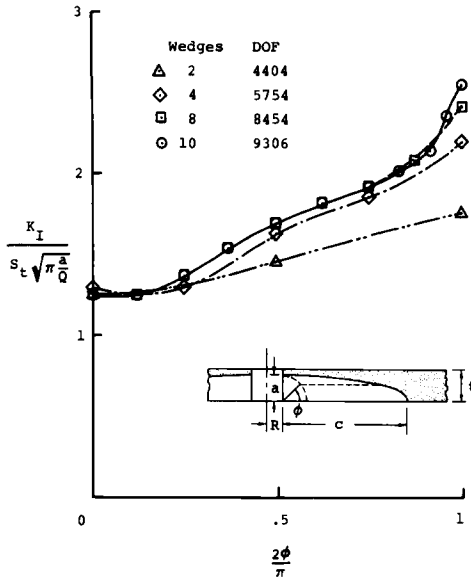


FIG. 6—Convergence of stress-intensity factors for a deep quarter-elliptic corner crack ($a/t = 0.8$; $a/c = 0.2$; $R/t = 0.5$).

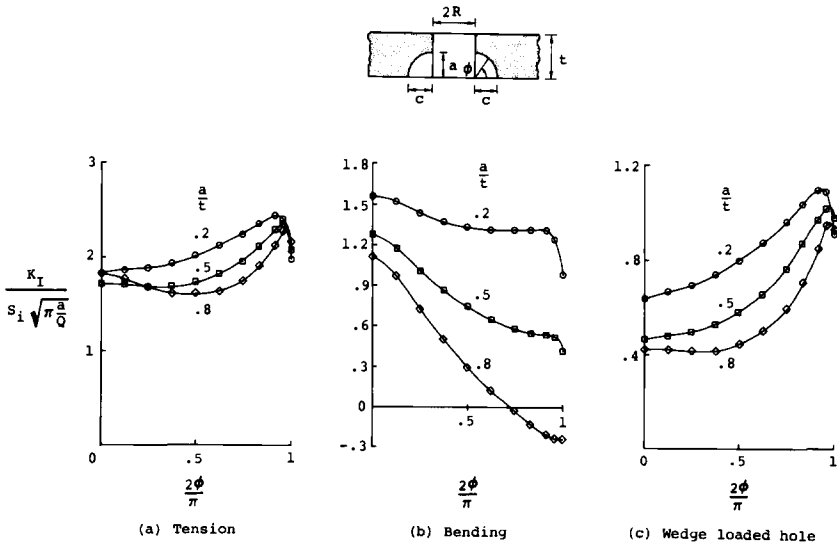


FIG. 7—Distribution of stress-intensity factors along crack front for quarter-circular corner cracks ($a/c = 1$; $R/t = 0.5$).

and the crack-depth-to-plate-thickness ratio, a/t , for remote tension, remote bending, or wedge loading in the hole. For all loading types considered, the smaller a/t ratios generally gave higher normalized stress-intensity factors. For remote tension and for wedge loading in the hole, the maximum normalized stress-intensity factor occurs near the intersection of the crack with the hole surface ($\phi = \pi/2$). For remote bending, the normalized stress-intensity factor was largest at $\phi = 0$ (front surface). The negative stress-intensity factors shown in Fig. 7b for $a/t = 0.8$ are, of course, meaningful only in the presence of sufficient tensile loading to prevent contact between crack surfaces.

The stress-intensity factors (Mode I) for quarter-circular corner cracks subjected to simulated pin loading, as shown in Fig. 5, can be obtained from the results shown in Fig. 7a and c by use of Eq 4.

Figures 8a and b show stress-intensity factors obtained by several investigators for a quarter-circular corner crack in a finite-thickness plate under remote tension. Figure 8a shows the results for a corner crack with $a/t = 0.2$ and $R/t = 0.5$. The present results are shown as solid circular symbols. Shah's estimate [4] is about 6 percent higher than the present results. The results from Heckmer and Bloom [10] are 10 to 20 percent higher than the present results near the free surfaces ($\phi = 0$ and $\pi/2$), but only about 3 percent higher in the interior. The photoelastic results [5,7], which represent the experimental stress-intensity value at the approximate midpoint of each photoelastic slice, generally agree well with the present results. However, the photoelastic results were obtained from a single-corner crack configuration. The results for a single-corner

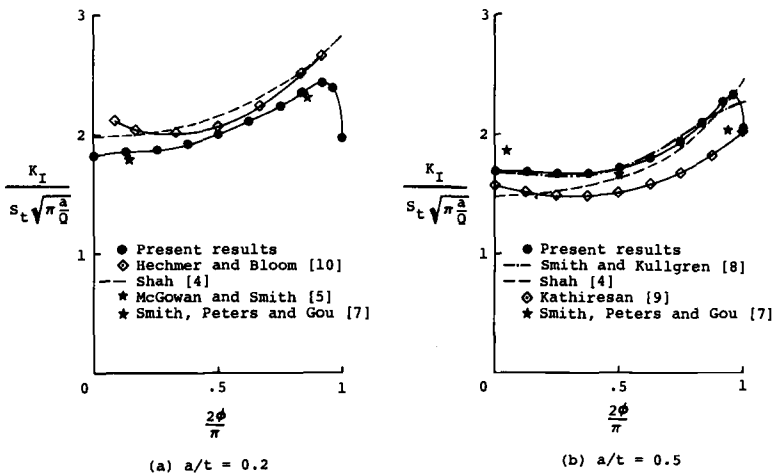


FIG. 8—Comparison of stress-intensity factors for quarter-circular corner cracks subjected to remote tension ($a/c = 1$; $R/t = 0.5$).

crack are expected to be slightly lower than those for two symmetric corner cracks [4].

The stress intensity is less near the intersection of the crack with the hole surface ($\phi = \pi/2$) than just below the surface. This behavior agrees qualitatively with that proposed by Hartranft and Sih [16]. Note that the wedge angles near $\phi = \pi/2$ are smaller than those near $\phi = 0$. Similar refinements in the wedge angles near $\phi = 0$ would probably have revealed lower stress-intensity factors in that region without changing the results in the interior [17].

Figure 8b shows the results for a deeper corner crack ($a/t = 0.5$) than that shown in Fig. 8a. Shah's estimate [4] is within 10 percent of the present results, except that Shah does not predict the lower stress intensity near $\phi = \pi/2$. Kathiresan's results [9] are 10 to 20 percent lower than the present results. This discrepancy may be attributed to the fact that the present study employed over three and one-half times as many degrees of freedom as did Kathiresan's. Smith and Kullgren's results [8] were obtained from a linear interpolation between their results for a/c of 0.75 and 1.5. Their interpolated results were in good agreement (± 5 percent) with the present solution. Again, the photoelastic results from Smith, Peters, and Gou [7] for a single-corner crack agreed to within ± 10 percent with the present results.

Some of the discrepancies between the various finite-element solutions may be attributed to the method used to extract the stress-intensity factor from the three-dimensional analyses. Figure 9 shows the stress-intensity

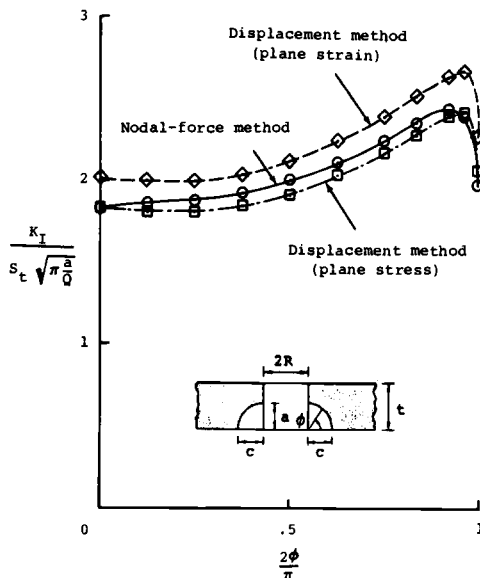


FIG. 9—Comparison of stress-intensity factors determined by displacement method (plane stress and plane strain) and nodal-force method ($a/c = 1$; $a/t = 0.2$; $R/t = 0.5$).

factor variation along the crack front for a typical corner-crack configuration as determined from the present analysis by two methods. The configuration and loading are those appropriate to Fig. 8a. The stress-intensity factors were determined from the crack-opening displacements (COD) assuming either the plane stress or plane strain and from the nodal forces ahead of the crack front [17]. The stress-intensity factors calculated from the COD method assuming plane strain were about 10 percent higher than those obtained assuming plane stress. Results from the nodal-force method fell generally between the two COD results. Because neither plane-strain nor plane-stress conditions are fully realized in a corner-cracked plate, either assumption is expected to lead to some inaccuracy in stress-intensity factors.

Quarter-Elliptical Corner Cracks

Figures 10 and 11 show the normalized stress-intensity factors for quarter-elliptical corner cracks ($a/c = 0.2$ and 2 , respectively) as a function of the parametric angle, ϕ , and the crack-depth-to-plate-thickness ratio, a/t , for remote tension, remote bending, or wedge loading in the hole.

Figure 10 ($a/c = 0.2$ and $R/t = 0.5$) shows that for remote tension, the larger a/t ratios gave higher normalized stress-intensity factors, but for remote bending or wedge loading the trend was generally reversed. For remote bending, the maximum normalized stress-intensity factor occurred near $\phi = \pi/2$ for $a/t = 0.2$ and at $\phi = 0$ for $a/t = 0.8$. The wedge-loaded hole results (Fig. 10c) showed a steep gradient in the stress-intensity factor near the hole surface.

Figure 11 ($a/c = 2$ and $R/t = 0.5$) shows that for remote tension and bending the smaller a/t ratios gave higher normalized stress-intensity factors. For remote tension and wedge loading, the stress-intensity factors varied little (about 10 to 15 percent) along the crack front compared to those for the other crack configurations ($a/c = 0.2$ and 1). For remote bending, the normalized stress-intensity factor was largest at $\phi = 0$ (front surface). Again, the negative stress-intensity factors shown in Fig. 11b for $a/t = 0.8$ are meaningful only in the presence of sufficient tensile loading to prevent crack-surface contact.

Effects of Pin Loading—The stress-intensity factors (Mode I) for quarter-elliptical corner cracks subjected to simulated pin loading, as shown in Fig. 5, can be calculated by substituting into Eq 4 the results shown in Fig. 10a and c for $a/c = 0.2$, and Fig. 11a and c and $a/c = 2$. Figure 12 shows the normalized stress-intensity factors for quarter-elliptical corner cracks ($a/c = 0.2, 1.0$, and 2.0) as a function of the parametric angle, ϕ , and the crack-depth-to-plate-thickness ratio, a/t , for simulated pin loading. The graphs are similar to those shown for the wedge-loaded case, differing mainly in magnitude. This similarity is due to

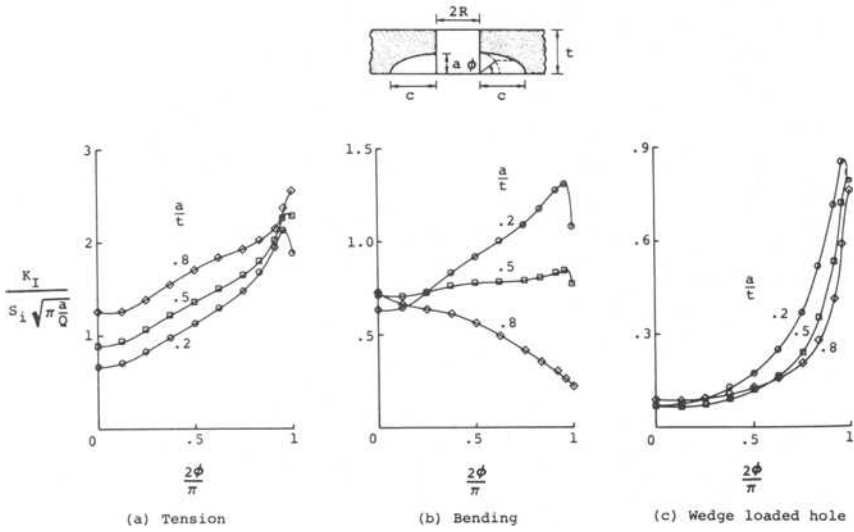


FIG. 10—Distribution of stress-intensity factors along crack front for quarter-elliptic corner cracks ($a/c = 0.2$; $R/t = 0.5$).

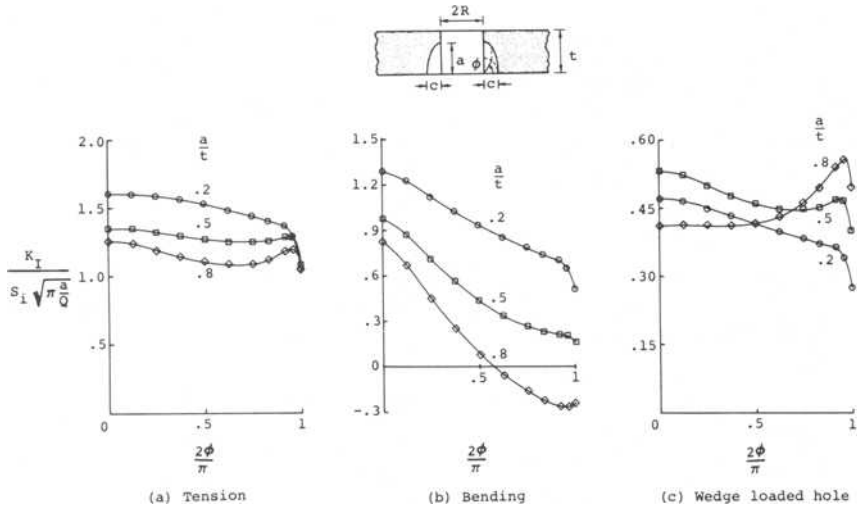


FIG. 11—Distribution of stress-intensity factors along crack front for quarter elliptic corner cracks ($a/c = 2$; $R/t = 0.5$).

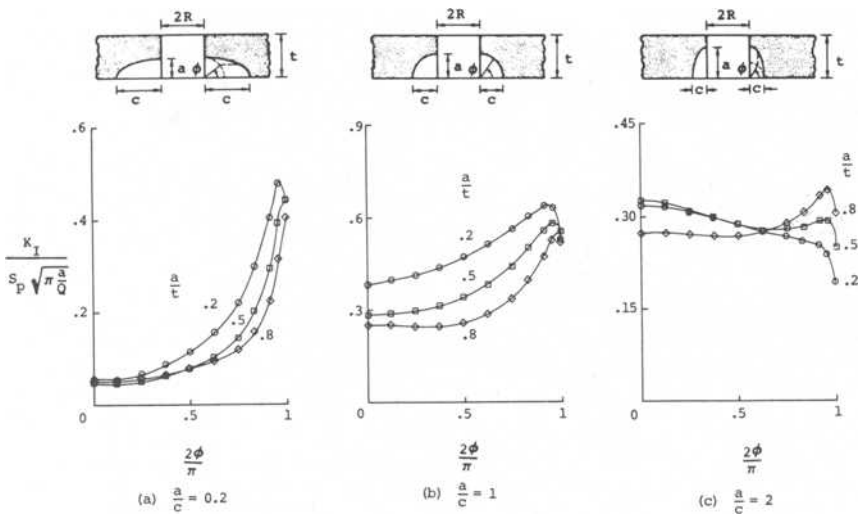


FIG. 12—Distribution of stress-intensity factors along crack front for quarter-elliptic corner cracks under simulated pin loading ($R/t = 0.5$).

the small R/b ratios considered here, which caused the contributions from the remote tension case to be small compared with those from the wedge-loaded case. As in the wedge-loaded case, the quarter-elliptic corner cracks with $a/c = 0.2$ the stress-intensity factors rise sharply with increasing ϕ near the intersection of the crack with the hole surface. For quarter-circular corner cracks, the maximum stress-intensity factor occurs near $\phi = \pi/2$. For quarter-elliptical cracks with $a/c = 2$, the stress-intensity factors are relatively constant along the crack front.

Effects of Hole Size—The effects of hole size (R/t) on the normalized stress-intensity factors for quarter-circular cracks ($a/t = 0.5$) subjected to remote tension, remote bending, and wedge-loading in the hole are shown in Fig. 13. The results in Fig. 13 and those given in Tables 1 and 2 for other crack shapes show that larger values of R/t give higher values of normalized stress-intensity factors for all types of loading considered.

Estimates for a Single-Corner Crack—The stress-intensity factors for a single-corner crack can be estimated from the results for two-symmetric corner cracks by using a conversion factor developed by Shah [4]. The relationship between one- and two-corner cracks was given by

$$(K_I)_{\text{one crack}} = \sqrt{\frac{2R + \frac{\pi ac}{4t}}{2R + \frac{\pi ac}{2t}}} (K_I)_{\text{two cracks}} \quad (5)$$

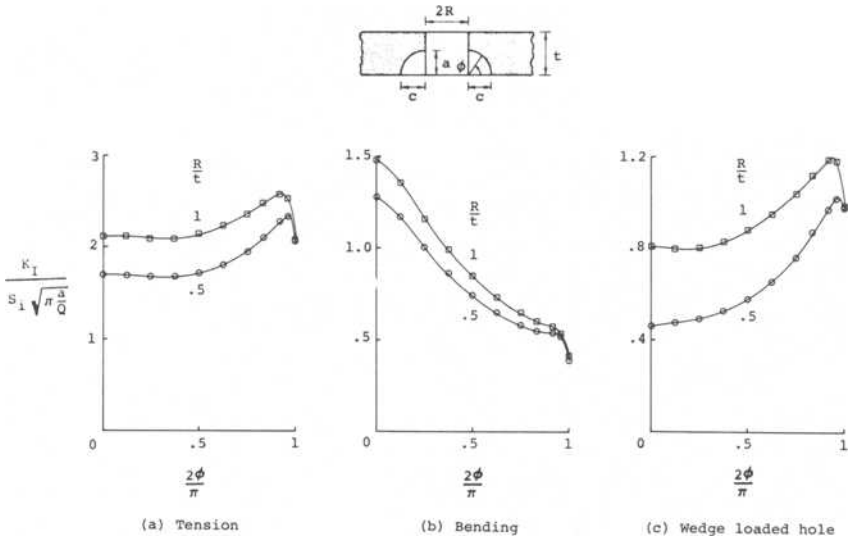


FIG. 13—Distribution of stress-intensity factors along crack front for quarter-circular corner cracks as a function of R/t ($a/c = 1$; $a/t = 0.5$).

Shah had assumed that the conversion factor was constant for all locations along the crack front; that is, independent of the parametric angle.

The normalized stress-intensity factors for a single-corner crack were computed from Eq 5 using the present results for two-corner cracks. Figure 14 shows some typical results for a single-corner crack with $a/c = 1$ or 2 for $a/t = 0.5$ and $R/t = 0.5$. The results from Smith and Kullgren [8] for a single-corner crack are shown as the dashed curves. The agreement between Smith and Kullgren's results and the present results were within about 10 percent.

Concluding Remarks

A three-dimensional finite-element elastic stress analysis was used to calculate Mode I stress-intensity factor variations along the crack front for two symmetrical quarter-elliptical corner cracks at the edge of a hole in a finite-thickness plate. The plates were subjected to remote uniform tension, remote bending, wedge loading in the hole or simulated pin loading in the hole. The ratio of crack depth to plate thickness ranged from 0.2 to 0.8, and the ratio of crack depth to crack length ranged from 0.2 to 2, while the ratio of hole radius to plate thickness was 0.5 to 1. Three-dimensional singularity elements in the shape of pentahedrons were used at the crack front; elsewhere, eight-noded hexahedrons were used. A nodal-force method which requires no prior assumption of either

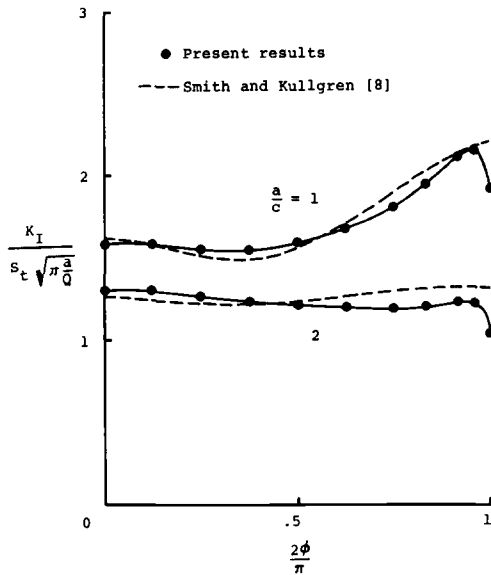


FIG. 14—Comparison of stress-intensity factors for single corner crack subjected to remote tension ($a/t = 0.5$; $R/t = 0.5$).

plane stress or plane strain was used to evaluate the stress-intensity factors.

A convergence study on stress-intensity factors for a deep quarter-elliptical corner crack in a finite-thickness plate showed satisfactory convergence. About 9300 degrees of freedom were used in calculating stress-intensity factors for all corner-crack configurations.

For quarter-circular corner cracks subjected to tension or wedge loading in the hole, the maximum stress-intensity factor occurred near the intersection of the crack with the hole surface, whereas for bending it occurred at the intersection of the crack with the front surface.

For quarter-elliptical corner cracks (crack-depth-to-crack-length ratio of 0.2) subjected to tension or wedge loading in the hole, the maximum stress-intensity factor occurred near the intersection of the crack with the hole surface for shallow cracks (crack-depth-to-plate thickness less than or equal to 0.5) but occurred at the front surface for deep cracks (crack depth-to-plate thickness ratio of 0.8).

The stress-intensity factors for quarter-elliptical corner cracks (crack depth-to-crack length ratio of two) were nearly constant (within about 10 percent) along the crack front in the cases of tension and wedge loading in the hole, though not in the case of bending, where the stress intensity factor was greatest at the intersection of the crack with the front surface.

For quarter-elliptical corner cracks subjected to simulated pin loading

in the hole (balanced by uniform tension at one end), the stress-intensity variations along the crack front were similar to those obtained for wedge loading in the hole, differing mainly in magnitude.

For all quarter-elliptical corner cracks considered, larger hole sizes (hole radius-to-plate thickness ratios) gave higher values of normalized stress-intensity factors.

The stress-intensity factors for single-corner cracks can be obtained from the stress-intensity factors for two symmetric corner cracks presented herein using Shah's conversion factor.

The stress-intensity factors obtained herein should be useful in correlating fatigue-crack-growth rates and in calculating fracture toughness for the corner-crack configurations considered.

References

- [1] Hall, L. R. and Finger, R. W., "Fracture and Fatigue Growth of Partially Embedded Flaws," AFFDL-TR-70-144, Air Force Flight Dynamics Laboratory, Dec. 1970.
- [2] Liu, A. F., *Engineering Fracture Mechanics*, Vol. 4, 1972, pp. 175-179.
- [3] Newman, J. C., Jr., "Predicting Failure of Specimens with Either Surface Cracks or Corner Cracks at Holes," NASA TND-8244, National Aeronautics and Space Administration, June 1976.
- [4] Shah, R. C. in *Mechanics of Crack Growth, ASTM STP 590*, American Society for Testing and Materials, 1976, pp. 429-459.
- [5] McGowan, J. J. and Smith, C. W. in *Mechanics of Crack Growth, ASTM STP 590*, American Society for Testing and Materials, 1976, pp. 460-476.
- [6] Smith, C. W., Jolles, M. I., and Peters, W. H., "Stress Intensity for Cracks Emanating From Pin Loaded Holes," VPI-E-76-13, Virginia Polytechnical Institute and State University, Aug. 1976.
- [7] Smith, C. W., Peters, W. H., and Gou, S. F., "Influence of Flaw Geometries on Hole-Crack Stress Intensity," presented at the 11th National Symposium on Fracture Mechanics, Blacksburg, Va., June 1978.
- [8] Smith, F. W. and Kullgren, T. E., "Theoretical and Experimental Analysis of Surface Cracks Emanating From Fastener Holes," AFFDL-TR-76-104, Air Force Flight Dynamics Laboratory, Feb. 1977.
- [9] Kathiresan, K., "Three-Dimensional Linear Elastic Fracture Mechanics Analysis by a Displacement Hybrid Finite Element," Ph.D. thesis, Georgia Institute of Technology, Atlanta, Ga., Sept. 1976.
- [10] Hechmer, J. L. and Bloom, J. M., "Determination of Stress Intensity Factors for the Corner-Cracked Hole Using the Isoparametric Singularity Element," *International Journal of Fracture*, Oct. 1977.
- [11] Raju, I. S. and Newman, J. C., Jr., "Three-Dimensional Finite-Element Analysis of Finite-Thickness Fracture Specimens," NASA TND-8414, National Aeronautics and Space Administration, May 1977.
- [12] Raju, I. S. and Newman, J. C., Jr., "Improved Stress-Intensity Factors for Semi-Elliptical Surface Cracks in Finite-Thickness Plates," NASA TMX-72825, National Aeronautics and Space Administration, Aug. 1977.
- [13] Tracey, D. M., "Finite Element for Three-Dimensional Elastic Crack Analysis," *Nuclear Engineering and Design*, Vol. 26, 1974.
- [14] Barsoum, R. S., "On the Use of Isoparametric Finite Elements in Linear Fracture Mechanics," *International Journal of Numerical Mathematics in Engineering*, Vol. 10, No. 1, Jan. 1976.

- [15] Green, A. E. and Sneddon, I. N., "The Distribution of Stress in the Neighborhood of a Flat Elliptical Crack in an Elastic Solid," *Proceedings, Cambridge Philosophical Society*, Vol. 46, 1959.
- [16] Hartranft, R. J. and Sih, G. C., "An Approximate Three-Dimensional Theory of Plates with Application to Crack Problems," *International Journal of Engineering Science*, Vol. 8, No. 8, Aug. 1970.
- [176] Raju, I. S. and Newman, J. C., Jr., "Stress Intensity Factors for a Wide Range of Semi-Elliptical Surface Cracks in Finite-Thickness Plates," to be published in *Engineering Fracture Mechanics*, Vol. 11, No. 4, 1979.

C. W. Smith,¹ W. H. Peters,¹ and S. F. Gou¹

Influence of Flaw Geometries on Hole-Crack Stress Intensities

REFERENCE: Smith, C. W., Peters, W. H., and Gou, S. F., "Influence of Flaw Geometries on Hole-Crack Stress Intensities," *Fracture Mechanics, ASTM STP 677*, C. W. Smith, Ed., American Society for Testing and Materials, 1979, pp. 431-445.

ABSTRACT: The problem geometry of a crack emanating from the intersection of a hole with a plate surface has received considerable attention in recent years. Approaches to the problem have included frozen stress photoelasticity, crack growth rate correlations, and approximate analytical studies. A comparison of results from the various approaches indicates reasonable agreement except for the case where the aspect ratio of the flaw (that is, ratio of flaw depth to length) approaches unity. Moreover, this problem and the geometries of this problem which were specified recently as benchmarks for three-dimensional cracked body analysis at a 3D fracture workshop at Battelle include this aspect ratio and also very deep flaws. For an aspect ratio ≈ 1 , the analytical solution is found to yield significantly higher results than either of the experimental methods. This paper describes a frozen stress photoelastic study of this class of flaw shapes where the ratio of hole diameter to plate thickness is approximately unity. The study utilizes a technique developed by the senior author and his associates for estimating stress intensity factor variations along the border of flaws in three-dimensional problems. Results reveal that, for deep flaws, flaw shapes are not simple and flaw growth is not self-similar. The influence of this effect and its implications are discussed.

KEY WORDS: stress intensity factors, 3D crack problems, surface flaws, stress intensity distributions, fatigue (materials), crack propagation

The problem geometry of a crack emanating from the edge of a hole in a finite thickness plate has received considerable attention [*1-9*]² in recent years due to its technological importance in a number of industrial applications. The problem geometry falls into the three dimensional (3D) cracked body category, which, except for a very few infinite body solutions such as those of Refs *10* and *11*, has resisted the efforts of analysts to achieve full field solutions, even in the purely elastic sense.

¹ Professor, assistant professor, and graduate research assistant, respectively, Department of Engineering Science and Mechanics, Virginia Polytechnic Institute and State University, Blacksburg, Va. 24061. W. H. Peters is currently on leave at Institut für Festkörpermechanik, Freiburg, West Germany.

² The italic numbers in brackets refer to the list of references appended to this paper.

However, as previously noted, a number of approximate solutions have been developed for this problem, leading to its selection [12] by workers in 3D fracture mechanics as a benchmark problem for assessing the validity of approximate 3D solution techniques.

Recently, comparisons of some of these approximate solutions have revealed a discrepancy between analytical and experimental results for crack geometries with aspect ratios of approximately unity. An experimental technique developed by the authors, utilizing the frozen stress photoelastic method to estimate stress intensity factor (SIF) distributions in three-dimensional cracked body problems, has been applied successfully to this problem geometry previously [3,4,13]; it would appear to be a suitable technique for studying the geometries in question. After reviewing concepts basic to the frozen stress photoelastic method to be employed, this paper reports results from a study of the hole-crack problem with flaw aspect ratios of approximately unity, and suggests an explanation for part of the discrepancies previously noted.

The Frozen Stress Method

In applying the frozen stress method, transparent polymeric materials which exhibit a diphase mechanical behavior are employed. At room temperature, the material responds to mechanical load in a Kelvin-like manner (Fig. 1), but, when heated to what is called the "critical" temperature, the value of the viscous or anelastic coefficient (μ) approaches zero, resulting in essentially linear elastic action. At the same time the elastic modulus drops to about one six hundredth of its room temperature value and the stress fringe value to about one twentieth of its

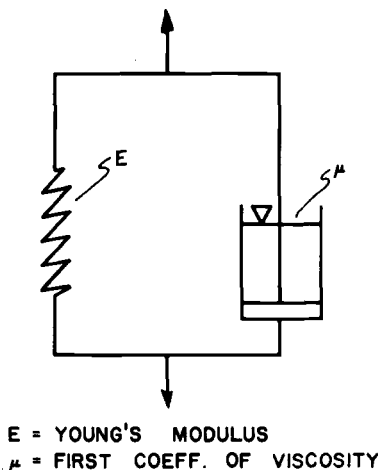


FIG. 1—Kelvin material.

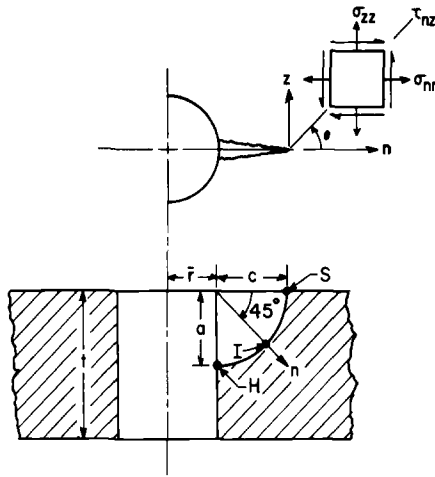


FIG. 2—Problem geometry and stress notation.

room temperature value, substantially increasing the sensitivity of the model to deformations and stress fringes when loaded above critical temperature. However, when the load is removed at room temperature after cooling under load, the recovery of the material may be neglected due to its reduced sensitivity to load at room temperature. Slices may then be removed from the body without disturbing the stress fringe or deformation fields. These slices are taken mutually orthogonal to the flaw border and the flaw surface in 3D crack body problems at intervals along the flaw border, and analyzed photoelastically. Thus, in Fig. 2, following Ref 14 the stress components are expressed in the nz plane for Mode I loading as

$$\sigma_{nn} = \frac{K_1}{(2\pi r)^{1/2}} \cos \frac{\theta}{2} \left(1 - \sin \frac{\theta}{2} \sin \frac{3\theta}{2} \right) - \sigma_{nn}^o \quad (1a)$$

$$\sigma_{zz} = \frac{K_1}{(2\pi r)^{1/2}} \cos \frac{\theta}{2} \left(1 + \sin \frac{\theta}{2} \sin \frac{3\theta}{2} \right) - \sigma_{zz}^o \quad (1b)$$

$$\tau_{nz} = \frac{K_1}{(2\pi r)^{1/2}} \sin \frac{\theta}{2} \cos \frac{\theta}{2} \cos \frac{3\theta}{2} - \tau_{nz}^o \quad (1c)$$

The first terms represent the singular part of the stress field and the σ_{ij}^o (following the Irwin approach for the plane problem) represent the contribution of the regular stress field in the form of the first terms of Taylor's series expansions of the regular stress components near the crack tip. Assuming that any flaw border can be represented as locally elliptic in shape [15], Eq 1 can be considered as applicable to such flaw-border shapes.

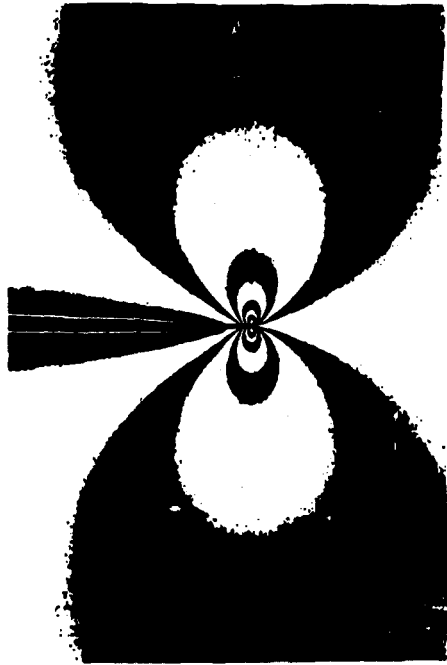


FIG. 3—Typical Mode I fringe pattern.

Observation of Mode I fringe patterns (Fig. 3) reveals that the fringes tend to spread in a direction approximately normal to the flaw surface. Thus, best fringe discrimination and accuracy is expected along $\theta = \pi/2$. By computing

$$\tau_{\max} = \frac{1}{2} [(\sigma_{nn} - \sigma_{zz})^2 + 4\tau_{nz}^2]^{1/2} \quad (2)^3$$

and truncating to the same order as Eq 1, one obtains along $\theta = \pi/2$,

$$\tau_{\max} = \frac{A}{r^{1/2}} + B \quad (3)$$

where $A = K_1/(8\pi)^{1/2}$ and $B = \text{constant containing } \sigma_{ij}^0$. Rewriting Eq 3 in a normalized form, we have

$$\frac{\tau_{\max}(8\pi r)^{1/2}}{\bar{\sigma}(\pi a)^{1/2}} = \frac{K_1}{\bar{\sigma}(\pi a)^{1/2}} + \frac{B(8\pi r)^{1/2}}{\bar{\sigma}(\pi a)^{1/2}} \quad (4)$$

³ Also, from the stress optic law $\tau_{\max} = n'f/2t'$ where n' is the stress fringe order, f is the material fringe value, and t' is the slice thickness.

or

$$\frac{K_{Ap}}{\bar{\sigma}(\pi a)^{1/2}} = \frac{K_1}{\bar{\sigma}(\pi a)^{1/2}} + \frac{B(8)^{1/2}}{\bar{\sigma}} \left(\frac{r}{a}\right)^{1/2} \quad (5)$$

where $K_{Ap} = \tau_{\max}(8\pi r)^{1/2}$ is defined as an "apparent SIF." Equation 5, when plotted as

$$\frac{K_{Ap}}{\bar{\sigma}(\pi a)^{1/2}} \text{ versus } \left(\frac{r}{a}\right)^{1/2}$$

yields a straight line which when extrapolated to the origin will yield $K_1/\bar{\sigma}(\pi a)^{1/2}$, the normalized SIF.

Since the foregoing approach utilizes a two-parameter (A, B) model and was suggested originally only for the case where the remote stress field was uniform, and where no surfaces other than the crack surfaces were present, the size of the zone dominated by Eqs 3 through 5 is expected to be constricted when such additional effects are present. However, if the linear zone of Eq 5 can be located experimentally, the two-parameter approach can still be used. If such a zone cannot be located experimentally, then additional terms leading to an equation of the form

$$\tau_{\max} = \frac{A}{r^{1/2}} + \sum_{n=0}^m B_n r^{n/2} \quad (6)$$

with suitable truncation criteria must be considered. Since such criteria are not yet established, this latter approach is avoided where possible and was not necessary in the studies described in the sequel. This approach has also been extended to Mixed Mode Analysis [16].

The Experiments

Frozen stress experiments were conducted on six stress free plates of PSM-8, a stress freezing photoelastic material manufactured by Photolastic Incorporated of Malvern, Pa. Each plate contained a hole with a starter crack produced by striking a sharp blade held against the corner of the hole (Fig. 2). Test geometries and loads are given in Table 1. The test setup is shown in Fig. 4. The test procedure was as follows:

(a) Heat model to critical temperature in test rig in a programmed electric oven.

(b) Apply small live loads to grow the natural crack to desired size, reduce loads, and cool to room temperature. In order to maintain an aspect ratio of unity, it was necessary to flex the plates before applying the live load tension.

(c) Remove loads and extract slices parallel to the nz plane (Fig. 2).

TABLE 1—Test geometries for models used in the present experiments.

Test Number		1	2	3	4	5	6
Hole radius	(\bar{r}) mm	6.35	6.35	6.35	6.35	6.35	6.35
Plate thickness	(t) mm	12.8	12.9	13.1	12.9	12.4	13.9
Crack length	(c) mm	2.36	3.30	3.81	5.89	8.13	11.3
Crack depth	(a) mm	2.54	3.30	3.81	5.92	8.00	11.1
Remote stress	($\bar{\sigma}$) kPa	49.7	70.3	43.8	70.5	61.7	55.4
alt		0.20	0.25	0.29	0.46	0.64	0.79
alc		1.07	1.00	1.00	1.00	0.98	0.98
c/\bar{r}		0.37	0.52	0.60	0.93	1.28	1.78
$2\bar{r}/t$		0.99	0.98	0.97	0.99	1.02	0.91

(d) Coat slices with matching index fluid and analyze in a crossed circular polariscope using a white light source, reading tint of passage, and employing the Tardy Method.

(e) Convert photoelastic data into SIF estimates using a least squares computer program of the two-parameter stress model.

A typical set of data with the computed line of best fit is given by Fig. 5.

Results

The crack shapes obtained are shown in Fig. 6. It was only possible to extract one slice from the smallest flaw (Test 1) and two slices from the

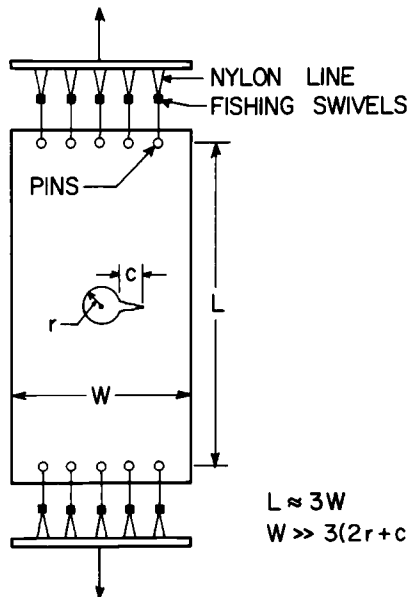


FIG. 4—Test set-up.

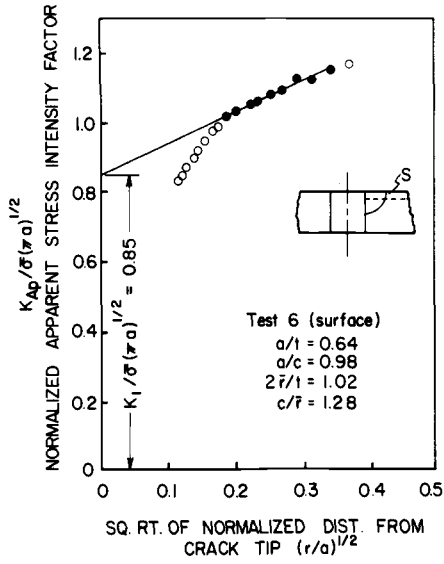


FIG. 5—Typical data and SIF estimation.

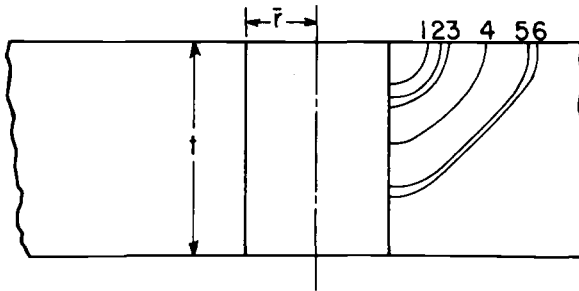


FIG. 6—Crack shapes.

two next smallest flaws (Tests 2 and 3). While the smaller flaws appear to be quarter-circular in shape as assumed in the analytical models, the flaws exhibiting $a/t > 0.40$ show significant flattening, or retarded flow growth in the central region of the flaw. This same effect has been observed in the modeling of reactor vessel nozzle corner cracks and will be cited in the next section.

The SIF distributions are shown in Fig. 7. Note that all SIF values here are normalized with respect to a common crack length so they can be compared with each other. However, when comparing these results with other studies (Tables 2 through 4), the normalized crack length is not a constant. The distributions in Fig. 7 follow the same trends as those observed in models of reactor vessel nozzle corner cracks. By comparing results of Tests 2 and 3 with results obtained for similar aspect ratios [4] (see Table 5), it may be conjectured that the curves for Tests 2 and 3 will not be symmetric but would exhibit lower values of the SIF at $\alpha = 0$ than $\alpha = 90$ deg as indicated by the dashed portions of the curves.

Discussion

This section will consist of two parts:

- (1) Comparison of present results with selected results from other analyses.
- (2) Discussion of the significance of nonself-similar flaw growth.

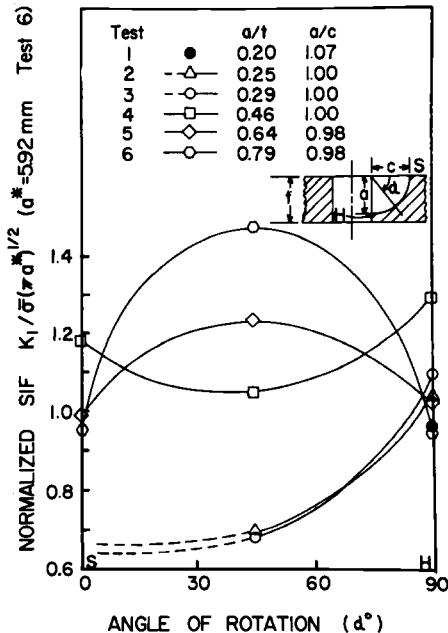


FIG. 7—SIF distributions.

TABLE 2—Comparisons of previous results for similar model geometries.

Method	<i>a/c</i>	<i>a/t</i>	$2\bar{r}/t$	$K_{IS}^a/\bar{\sigma}(\pi a)^{1/2}$	$K_{IH}^b/\bar{\sigma}(\pi a)^{1/2}$
CWS ^c	1.55	0.46	0.94	0.98	1.24
G ^d	1.60	0.46	1.07	1.11	1.30
FWS ^e	1.55	0.46	0.94	1.03	1.22
Sh ^f	1.55	0.46	0.94	1.10	1.22
CWS	1.10	0.48	0.88	0.90	1.10
G	1.20	0.60	1.00	1.24	1.11
FWS	1.10	0.48	0.89	1.03	1.36
Sh	1.10	0.48	0.88	0.97	1.38
CWS	1.98	0.74	0.95	0.95	1.08
FWS	1.98	0.74	0.95	0.95	1.06
Sh	1.98	0.74	0.95	0.95	1.00

^a K_{IS} = Mode I SIF at surface.
^b K_{IH} = Mode I SIF at hole.
^c CWS—C. W. Smith et al (photoelastic) Refs 3 and 4 and Table 5.
^d G—Grandt et al (crack growth measurements) [5].
^e FWS—F. W. Smith and Kullgren (finite element-alternating method) [9].
^f Sh—Shah (empirical relationships) [2].

TABLE 3—Comparisons between present experiments and predictions of approximate analytical methods.

Test Number	1	2	3	4	5	6
Stress Intensity Factors $K/\bar{\sigma}(\pi a)^{1/2}$ (Experimental Results)						
Surface (K_S)	1.19	0.85	0.69
Middle (K_M)	...	0.94	0.85	1.05	1.06	1.08
Hole (K_H)	1.47	1.39	1.37	1.29	0.89	0.69
$(K_S + K_H + K_M)^{1/3}$	1.47	1.17	1.11	1.18	0.93	0.82
Stress Intensity Factors $K/\bar{\sigma}(\pi a)^{1/2}$ (Analytical Results) (Difference, percent, shown in parentheses)						
G-S Hole (K_H)	1.53 (+4)	1.46 (+5)	1.44 (+5)
FWS ^a Surface (K_S)	1.03 (-15)
FWS ^a Hole (K_H)	1.36 (+6)
Sh Surface (K_S)	0.92 (-14)	0.83 (-1)	0.73 (+5)
Sh Hole (K_H)	1.75 (+19)	1.60 (+13)	1.62 (+15)	1.48 (+20)	1.39 (+36)	1.29 (+46)
Sh Middle (K_M)	...	1.20 (+21)	1.18 (+30)	1.00 (-5)	0.90 (-15)	0.81 (-25)
Newman Middle (K_M)	1.34 (-9)	1.21 (+3)	1.14 (+3)	0.99 (-16)	0.89 (-4)	0.83 (+1)
Hall Middle (K_M)	...	1.30 (+10)	1.21 (+8)	1.08 (-9)	1.05 (+12)	0.95 (+14)

^a FWS = F. W. Smith and Kullgren [9]. The geometry for this SIF is $a/c = 1.1$, $a/t = 0.5$, $2\bar{r}/t = 1.0$.

TABLE 4—Comparisons of present experimental stress intensity factors with other solutions.

Method	a/c	a/t	$2\bar{r}/t$	$K_{IS}/\bar{\sigma}(\pi a)^{1/2}$	$K_{IH}/\bar{\sigma}(\pi a)^{1/2}$
Test 4	1.00	0.46	0.99	1.19	1.29
Test 5	0.98	0.64	1.02	0.85	0.89
CWS	1.10	0.48	0.88	0.90	1.10
G	1.20	0.60	1.00	1.24	1.11
FWS	1.10	0.48	0.89	1.03	1.36
Sh	1.10	0.48	0.88	0.97	1.38

Comparison with Other Analyses

Prior studies of the hole-crack problem can be divided into two classes:

(a) Those that yield only one value of the SIF for this problem such as Refs 1 and 6.

(b) Those that yield SIF values at specific points along the flaw border such as Refs 2 through 5 and 7 through 9. We shall focus first upon the latter type results for which there are basically four approaches, two of which are experimental, and two of which are analytical.

One of the experimental approaches is described in this paper. The other, used by Grandt et al [5], involves determining the coefficients c, n in the crack growth rate equation

$$\frac{da}{dn} = c(\Delta k)^n \quad (7)$$

from a known two-dimensional solution and assuming that they apply to the 3D problem.

The analytical solution due to Shah [2] begins with a quadratic distribution of pressure loading on an embedded elliptic crack in an uncracked plate and applies empirical correction factors to account for the deviations in the problem geometry from the assumed case. A second analytical solution by F. W. Smith et al [7–9] employs a finite element-alternating method beginning with an analytical solution for an embedded elliptical flaw in an infinite solid and a finite element solution for a finite thickness plate with a hole, and performs a sequence of iterations between the two to approximate the solution for the hole crack problem.

Table 2 shows comparisons between the several methods where the independent geometric parameters a/t , a/c , $2\bar{r}/t$ are approximately the same. This table shows good correlation for cases where a/c is substantially different from unity. However, as $a/c \rightarrow 1.0$, differences of the order of 30 percent result. The two experimental studies also indicated that the cracks grew in such a manner that $a/c > 1$ for pure tensile loading. Moreover, as discussed in Ref 8, the F. W. Smith et al solution [7–9]

TABLE 5—Corrected results for Refs 3 and 4.

Ref 3, p. 466, Table 1		Stress Intensity Factors—Experimental Results								
Test Number		1	2	3	4	5	6	7	8	9
Surface K_{SEZ}	$N/mm^{3/2}$	0.327	0.446	0.308	0.311	0.383	0.382	0.373	0.305	0.239
Hole K_{HEZ}	$N/mm^{3/2}$	0.535	0.603	0.482	0.379	0.434	0.481	0.429	0.306	—
Ref 4, p. 357, Table 1 (Phase I)		Stress Intensity Factors—Experimental Results								
Test Number		1	2	3	4	5	6	7	8	
Surface $K_S/\bar{\sigma}(\pi a)^{1/2}$		1.17	0.99	0.71	0.90	0.86	0.98	0.95	0.72	
Hole $K_H/\bar{\sigma}(\pi a)^{1/2}$		1.91	1.34	1.12	1.10	0.98	1.24	1.08	0.72	
$(K_S + K_H)/2$		1.54	1.20	0.92	1.00	0.92	1.11	1.02	0.72	

tends to become unstable as $a/c \rightarrow 1$. Finally, K_H (SIF at hole) results reported in Refs 3 and 4 were significantly low for all tests in Ref 3 and all of Phase I in Ref 4 due to an error in computer programming. (Corrected values are given in Tables 2 and 5.)

Table 3 shows a comparison between the results of the present experiments with the theories noted earlier. Also included are comparisons with two additional empirical proposals due to Hall and Finger [1] and Newman [6] which incorporate experimental data into empirical models to predict average SIF values for a given hole crack. It appears that the present results show closest agreement with other results that are either experimental or are based on experimental data. On the other hand, good agreement with the F. W. Smith et al theory [7-9] has been found for aspect ratios other than $a/c \approx 1.0$ (Table 2). Moreover, the Shah theory [2] was developed for design purposes, and its conservative predictions for K_H would appear to be desirable generally.

In view of the differences between the results of the several approaches to the SIF distribution determination, it might be useful to observe (Table 3) that the Newman and Hall and Finger predictions agree to within acceptable error with the average of the experimental results shown in Fig. 7, except for the deep flaws where significant flattening occurred in the center of the flaws.

Tests 4 and 5 are compared with other results from Table 2 in Table 4. It is conjectured that the significant difference in SIF values between Tests 4 and 5 is due largely to flattening of the flaw border and redistribution in SIF values indicated in Fig. 7 and this aspect will be discussed further in the next section.

NonSelf-Similar Flaw Growth and Its Significance

The focus of this study is upon the local stress field analysis of *stably* grown flaws (as in fatigue) and, consequently, the SIF values reported, in general, are not related directly to the fracture toughness values associated with unstable flaw growth. That is, the threshold value of the SIF at a point along the flaw border required to produce stable flaw growth is not necessarily the plane strain fracture toughness of the material. It is clear from Figs. 6 and 7 that the smaller flaws exhibit self-similar flaw growth under a nonuniform SIF distribution. As the flaws grow deeper, the central part of the flaws flatten, and the SIF distribution changes from concave upward to concave downward. Subsequent flaw growth is nonself-similar. These same trends have been observed by the authors in extensive studies [17-21] on models of reactor vessel nozzle cracks, not only for cracks grown above critical temperature in photoelastic models under monotonic load, but also in fatigue tests of A508 reactor vessel steel models [22]. In fact, the authors have found that cracks grown in the photoelastic model identically duplicate those grown by fatigue in steel

models when only small scale yielding occurs. For the deeper flaws, Figs. 6 and 7 show that the slowest growth occurs near the center of the flaw borders where SIF's are greatest. This may be explained qualitatively through the simplified crack growth rate equation given by Eq 7. It suggests that the "material coefficients" c and n , as determined from flaw growth tests on "two-dimensional" specimens of known ΔK are not constants for the 3D problem. That is, for the 3D problem all of the geometric effects are not captured in ΔK . Alternatively, if one assumes that da/dN is proportional to the crack opening displacement it can be shown that [23]

$$da/dN = A'(\Delta K/E)^2 \quad (8)$$

The authors conjecture that, in the central region of the crack, a state of triaxial tension is built up creating a stiffening effect, or increase in apparent elastic modulus there, resulting in a reduced crack growth rate in accordance with Eq 8, and that this "stiffening" decreases as one approaches the points of intersection of the flaw border with the free boundaries. But if this conjecture is valid, the excellent agreement between theory and experiment noted for $a/t = 0.74$ in Table 2 must be explained. It is suggested that, since we are apparently comparing experimental SIF distributions which are concave downward (Fig. 7) with analytical SIF distributions which are concave upward [2,9] we conclude that, while this comparison indicates agreement near the boundaries, it may not do so in the central region of the flaw. Moreover, the concave downward SIF distributions exhibited by Tests 5 and 6 in Fig. 7 may explain why Hall and Finger [1] observed fracture on the interior of the flaw rather than at the hole boundary.

Two of the benchmark geometries which were selected for this problem by the Battelle Workshop on 3D Fracture [12] involved a/t values of 0.5 and 0.75, and one involved $a/c = 1.0$. The studies reported on here suggest that it may not be possible to achieve good correlation between mathematical models employing simple crack shapes and experiments along the full flaw length for these cases.

Summary

An experimental program employing the frozen stress photoelastic method to measure SIF distributions along the border of hole cracks for geometries difficult to handle analytically ($a/c \approx 1$) was described. Results were compared with various approximate analytical models. It is conjectured that, within the geometric ranges of these experiments:

- (a) Fatigue crack growth of natural flaws in pure tension tends to produce $a/c > 1.0$.
- (b) Simple flaw shapes and self-similar flaw growth adequately describe small flaw growth ($a/t < 0.3$) for this problem.

(c) Above $a/t \approx 0.4$ flaw growth is nonself-similar and SIF distributions are significantly different than predicted from mathematical models using simple flaw shapes and self-similar flaw growth constraints. This may make analytical-experimental correlation difficult along the full flaw border for such geometries.

The frozen stress method has its own constraints: it is restricted to elastic behavior of incompressible materials. However, the authors estimate that the influence of these constraints upon SIF distributions in 3D problems is of the order of the experimental error (that is, 5 to 10 percent). Moreover, because of the complex geometry of the current problem, the authors do not recommend extrapolation of the results included herein.

Acknowledgments

The authors wish to acknowledge the contributions of their colleagues J. C. Newman, F. W. Smith, L. R. Hall, R. C. Shah, and their coworkers upon whose work they have drawn heavily. They also acknowledge the staff and facilities of the Department of Engineering Science and Mechanics and the support of the National Science Foundation Research Grant No. Engr. 76-20824 and the National Aeronautics and Space Administration under Grant No. NSG1024.

References

- [1] Hall, L. R. and Finger, R. W. in *Proceedings*, Air Force Conference on Fatigue and Fracture of Aircraft Structures and Materials, AFFDL-TR-70-144, U.S. Air Force Systems Command, Wright Patterson AFB, Ohio, Sept. 1970, pp. 235-262.
- [2] Shah, R. C. in *Mechanics of Crack Growth*, ASTM STP 590, American Society for Testing and Materials, 1975, pp. 429-459.
- [3] McGowan, J. J. and Smith, C. W. in *Mechanics of Crack Growth*, ASTM STP 590, American Society for Testing and Materials, 1975, pp. 460-476.
- [4] Smith, C. W., McGowan, J. J., and Jolles, M. in *Proceedings*, 12th Annual Meeting of the Society for Engineering Science, 1975, pp. 353-362.
- [5] Snow, J. R., Grandt, A. F., and Macha, D. E., "Stress Intensity Factor Measurements for Corner Cracked Holes," SESA Paper D-36, Society for Experimental Stress Analysis, Spring Meeting, Dallas, Texas, May 1977; see also Report No. AFML-TR-74-282, U.S. Air Force Materials Laboratory, Wright-Patterson AFB, Ohio.
- [6] Newman, J. C., Jr., "Predicting Failure of Specimens with Either Surface Cracks or Corner Cracks at Holes," NASA TN D-8244, National Aeronautics and Space Administration, June 1976.
- [7] Ganong, G. P., "Quarter-Elliptical Cracks Emanating from Holes in Plates," Ph.D. thesis, Department of Mechanical Engineering, Colorado State University, July 1975 (see also Ref 9).
- [8] Kullgren, T. E., "Surface Cracks Emanating from Fastener Holes," Ph.D. thesis, Colorado State University, Department of Mechanical Engineering, Summer, 1976 (see also Ref 9).
- [9] Smith, F. W. and Kullgren, T. E., "Theoretical and Experimental Analysis of Surface Cracks Emanating from Fastener Holes," AFFDL-TR-76-104, Wright Patterson AFB, Ohio, Feb. 1977.
- [10] Sneddon, I. N., *Proceedings*, Royal Society, Series A, Vol. 187, 1946, pp. 229-260.

- [11] Green, A. E. and Sneddon, I. N., *Proceedings*, Cambridge Philosophical Society, Vol. 46, 1950, pp. 159-163.
- [12] Hulbert, L. E., *Proceedings*, Workshop on Three Dimensional Fracture Analysis, Battelle-Columbus, April 1976.
- [13] Smith, C. W., Jolles, M., and Peters, W. H., *Flaw Growth and Fracture*, ASTM STP 631, American Society for Testing and Materials, 1977, pp. 190-201.
- [14] Sih, G. C. and Kassir, M., *Journal of Applied Mechanics*, Vol. 33, No. 3, Sept. 1966, pp. 601-611; *Transactions*, American Society of Mechanical Engineers, Vol. 88, Series E, 1966.
- [15] Sih, G. C. and Liebowitz, H. L., "Mathematical Theories of Brittle Fracture," *Fracture*, Vol. 2; *Mathematical Fundamentals*, Academic Press, New York, 1968, pp. 68-188.
- [16] Smith, D. G. and Smith, C. W., *Journal of Engineering Fracture Mechanics*, Vol. 4, No. 2, June 1972, pp. 357-366.
- [17] Smith, C. W., Jolles, M., and Peters, W. H., *Developments in Mechanics*, Vol. 8; *Proceedings*, 15th Midwest Mechanics Conference, March 1977, pp. 29-31.
- [18] Smith, C. W., Jolles, M. I., and Peters, W. H., *Transactions*, 4th International Conference on Structural Mechanics in Reactor Technology, Vol. G, Structural Analysis of Steel Reactor Pressure Vessels, Paper No. G4/3.
- [19] Smith, C. W., Peters, W. H., and Jolles, M. I., "Stress Intensity Factors for Reactor Vessel Nozzle Cracks," Paper No. 77-PVP-30. American Society of Mechanical Engineers, Sept. 1977 (in press); *Journal of Pressure Vessel Technology*.
- [20] Smith, C. W., and Peters, W. H. in *Proceedings*, 12th Annual Meeting of Society for Engineering Science, Nov. 1977, pp. 991-998.
- [21] Smith, C. W., Jolles, M. I., and Peters, W. H., *Journal of Experimental Mechanics*, Vol. 17, No. 12, Dec. 1977, pp. 449-454.
- [22] Broekhoven, M. J. G., *Proceedings*, 3rd International Conference on Pressure Vessel Technology, Part 2, Materials and Fabrication, April 1977, pp. 839-852.
- [23] Hahn, G. T., Sarrate, M., and Rosenfeld, A. R. in *Proceedings*, Air Force Conference on Fatigue and Fracture of Aircraft Structures and Materials; AFFDL TR-70-144, Sept. 1970, pp. 425-450.

**Experimental Fracture Mechanics—
 K_{Ic} , J_{Ic} , Specimen Geometry Effects,
and Experimental Techniques**

A. Penelon,¹ M. N. Bassim,¹ and J. M. Dorlot¹

Variation of Fracture Toughness with Specimen Geometry and Loading Conditions in Welded Low Alloy Steels

REFERENCE: Penelon, A., Bassim, M. N., and Dorlot, J. M., "Variation of Fracture Toughness with Specimen Geometry and Loading Conditions in Welded Low Alloy Steels," *Fracture Mechanics, ASTM STP 677*, C. W. Smith, Ed., American Society for Testing and Materials, 1979, pp. 449-462.

ABSTRACT: There is an increasing demand for steels that have a good weldability and a high fracture toughness. An important example is that of the high strength low alloy (HSLA) steels used in pipeline construction in the Arctic regions. Presently, the fracture toughness of these materials is characterized primarily using Charpy impact tests which give empirical results and cannot be used in obtaining critical crack lengths at which catastrophic failure would occur.

In this work, the J-integral was determined for the heat affected zone in welds of four low alloy steels containing various concentrations of niobium and molybdenum. Various procedures for evaluation of the J-integral were used such as the deep crack method on three-point bending specimens under controlled displacement, Charpy precracked specimens under static loading and three-point bending specimens under controlled loading. In the latter case, J was determined by the method of Lanteigne, Bassim, and Hay. Results obtained show a strong dependence of J_{Ic} on geometry. A model for the plastic zone size for three-point bending specimens which is an extension of the work of Lanteigne et al was used in the calculations.

KEY WORDS: fracture toughness, J-integral, heat affected zone, welded low alloy steels

The past decade has witnessed the development of new materials which are characterized by improved mechanical properties. Among those materials are the high strength low alloy (HSLA) steels which are mainly used in construction of pipelines in the Arctic regions. Improvement of the mechanical properties of these steels is achieved by controlled hot rolling and by addition of alloying elements [1,2]² which cause grain

¹ Graduate student, senior research scientist, and associate professor, respectively, Department of Metallurgical Engineering, Ecole Polytechnique, Montreal, Quebec, Canada.

² The italic numbers in brackets refer to the list of references appended to this paper.

refinement. Several alloying elements have been investigated for this purpose, namely aluminum, vanadium, titanium, molybdenum, and niobium. Of these elements, niobium appears to be the most useful and also the cheapest. In general, HSLA steels offer an increased yield strength and a decrease in the transition temperature. However, as they are used in very severe conditions, specific properties associated with the use of these alloys become of great importance. They must show decreased susceptibility to brittle failure, higher resistance to crack propagation, and improved mechanical properties after welding.

Presently, fracture characterizations of these alloys is only obtained from qualitative methods such as Charpy and Drop Weight tests. These methods are suitable for comparative measurements, and provide a quantitative basis for material selection and design. Recently [3,4], criteria for fracture toughness, namely the stress intensity factor under dynamic loading, K_{I_d} , and the corresponding J-integral, J_{I_d} , have been obtained as a function of temperature using an instrumented Charpy test for these alloys.

In this investigation, fracture parameters of four HSLA steels containing various concentrations of niobium and molybdenum were obtained. Because of their high ductility, even at very low temperatures, the J-integral was used in order to account for their elastic-plastic behavior.

The J-integral was determined for these four steels and for the heat affected zone of welds of these steels. The objective was to characterize their fracture toughness using different specimen geometries and loading conditions and to study the effect of alloying elements on their resistance to fracture.

Methods of Evaluation of the J-Integral

Methods of evaluation of the J-integral are based on its energetic definition given by Rice [5,6]; that it is the potential energy difference between two identically loaded two-dimensional bodies having neighboring crack sizes. Begley and Landes [7] have measured J_{Ic} under controlled displacement using several specimens containing cracks of different lengths and have later proposed a systematic method for its evaluation [8]. At the same time, Rice, Paris, and Merkle [9] have proposed a simplified equation for evaluation of the J-integral using a specimen with a deep crack. Namely, the specimen should contain a crack long enough to cause fracture without subcritical crack extension; the ratio a/ω , where a is the initial crack length and ω the specimen width, as defined in ASTM Test for Plane Strain Fracture Toughness of Metallic Materials (E 399 - 74), must be at least equal to 0.5. It is then possible to obtain J_{Ic} using only one specimen, with the following equation

$$J_{Ic} = 2U/BL \quad (1)$$

where

- U = energy required to fracture the specimen (represented by the area under the load-load point displacement curve),
- B = specimen thickness, and
- L = length of the untorn ligament ahead of the crack.

Relation Between the J-Integral and K_{Ic}

The general relationship between J_{Ic} and K_{Ic} is obtained from linear elastic fracture mechanics, assuming that, at the fracture point, J_{Ic} is equal to the strain-energy release rate, G_{Ic} . Thus

$$J_{Ic} = \frac{K_{Ic}^2}{E} \tag{2}$$

where E is Young's modulus.

For ductile materials, a more accurate equation has been proposed by Lantaigne, Bassim, and Hay [10] of the form

$$J_{Ic} (K_{Ic}, E, \sigma_y) = \frac{1}{|E(a/\omega)|^2} \int_0^{K_f} \frac{\delta f(a_p/\omega)}{\delta(a_p/\omega)} \left(1 + \frac{1}{\omega} \frac{\delta \gamma_y}{\delta K_I} \frac{\delta K_I}{\delta(a/\omega)} \right) K_I d K_I \tag{3}$$

where

- σ_y = yield strength,
- K_f = stress intensity factor at the fracture load,
- K_I = stress intensity factor at any point on the load-displacement curve,
- $f(a/\omega)$ = compliance function given for a standard geometry, and
- a_p = effective crack length given as $a_p = a + \gamma_y$, where γ_y represents the plastic zone correction [11] and is given as

$$\gamma_y = (1/\alpha\pi) (K_I/\sigma_y)^2 + A_1 K_I^3 + A_2 K_I^4 + \dots \tag{4}$$

In this equation, α is a coefficient related to whether fracture is in plane stress or plane strain and was taken as six in this investigation, and A_1, A_2, \dots are given as functions of the coefficients a_1, a_2, \dots of Westergaard [12] for a crack in an infinite elastic plate.

Equations 3 and 4 can be applied to the experimental results obtained during fracture, under controlled laboratory condition, of a single specimen. γ_y is evaluated first from the load versus load point displacement. This is followed by calculation of J_{Ic} using Eq 3.

TABLE 1—Composition and mechanical properties of low-alloy steels.

COMPOSITION											
Steel	C	Mn	Si	Al	Nb	V	S	P	Mo		
A	0.095	1.27	0.175	0.038	<0.005	0.008	...		
B	0.095	1.27	0.175	0.038	0.034	...	<0.005	0.008	...		
D	0.085	1.31	0.25	0.044	0.140	...	<0.005	0.008	...		
H	0.075	1.34	0.23	0.054	0.095	...	<0.005	0.008	0.31		
MECHANICAL PROPERTIES (ROOM TEMPERATURE)											
Steel	Yield Strength, MN/m ²	Ultimate Tensile Strength, MN/m ²	Elongation, percent	Reduction in Area, percent							
A	321	443	44	75							
B	420	507	34	73							
D	486	554	36	69							
H	425	591	31	72							

Effect of Geometry

The effect of specimen geometry on the J-integral has been investigated [13,14]. J_{Ic} was measured on Charpy size specimens [15] during impact testing, and fatigue precracked Charpy specimens under slow bending conditions were recommended to rapid and inexpensive evaluation of fracture toughness [16].

Experimental Procedure

Four HSLA steels were used in this investigation. The composition and mechanical properties of these steels are given in Table 1. The difference in composition between the four alloys is essentially in the concentration of niobium and molybdenum. Steel A is a low carbon steel, without any alloying elements. Steel B has a relatively low niobium content. Steel D has a higher niobium content while Steel H has a small amount of niobium and also some molybdenum.

Coupons of these four steels were welded using the submerged arc process. The plates were butt welded in a single pass with a current of 750 A and an arc voltage of 34 V. The travel speed of the electrode was 20 cm/min. The edges of the plates were prepared with standard 60 deg bend and a back-up tape was used on the underside of the weld. All welds were examined by X-ray radiography to ensure defect-free specimens. Areas showing defects such as gas porosity or slag inclusion were rejected.

Three-point bending size specimens with the dimensions given in Fig. 1 were machined from the plates containing the weld and from another set of plates without a weld. These specimens were 10 mm thick. A preliminary polishing was performed to reveal the heat affected zone and the notch was then machined by spark erosion, with the orientation shown in Fig. 1. This technique was chosen for its great precision in obtaining a notch with the required orientation, position, and depth. Specimens were next precracked using an MTS fatigue machine such that the final stress intensity factor was lower than $15 \text{ MN} \cdot \text{m}^{-3/2}$ and to a value of a/ω at least equal to 0.6.

A set of Charpy size specimens from the base metal and with the same crack orientation as with the three-point bending specimens was also precracked on the MTS³ machine using a special loading fixture. The ratio a/ω for these specimens was also 0.6.

Because of the ductility of these steels at ambient and low temperatures, and for the purpose of comparison of the results, the specimens of all four steels were fractured at -150°C using a special MTS cold chamber. At this temperature, specimens exhibited either an entirely brittle behavior or an elastic-plastic behavior. Under controlled loading, the load rate was 1000 kg/min while in tests with controlled displacement,

³ Manufactured by Material Testing Systems, Inc., Minneapolis, Minn.

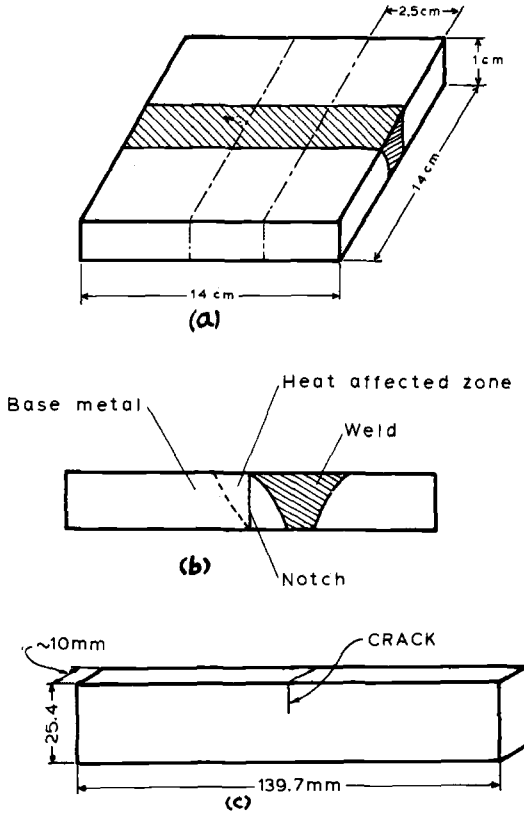


FIG. 1—Crack orientation in the heat affected zone for welded steels.

the machine was under strain control with a rate of displacement of 0.25 mm/min (Fig. 2).

The J-integral was evaluated under several loading conditions. In one series of tests, three-point bending specimens were fractured under controlled displacement and J_{Ic} was calculated using Eq 1. In another series, the load versus load-point displacement was obtained under controlled loading and J_{Ic} was estimated using Eq 3. Finally, for the base metals, J_{Ic} was obtained, using Eq 1 from load displacement curves under controlled displacement of precracked Charpy size specimens tested under static loading.

Experimental Results

Deep Crack Specimens

Figure 3 shows curves of the relation between load and load-point displacement under controlled displacement for cracks in the heat af-

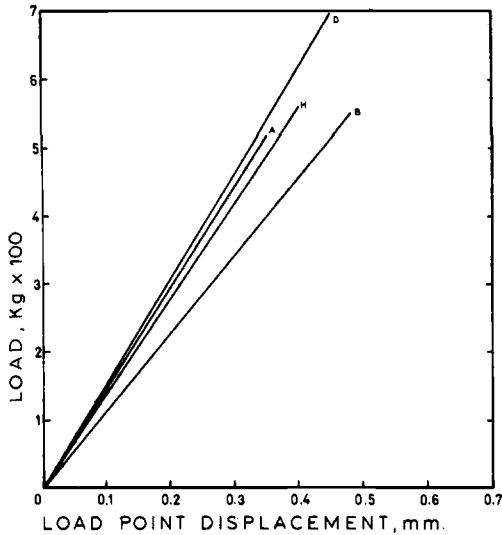


FIG. 2—Load-load point displacement curves, under controlled displacement, for three-point bending specimens of welded steels.

affected zone. First, it is noted that the specimens exhibit a completely brittle behavior with no crack extension as evident from the fracture surface. Using Eq 1, with U being the area under the curve, it was possible to calculate J_{1c} . The parameter K_{1c} was obtained using Eq 2. Young's modulus had a value of 19 000 kg/mm².

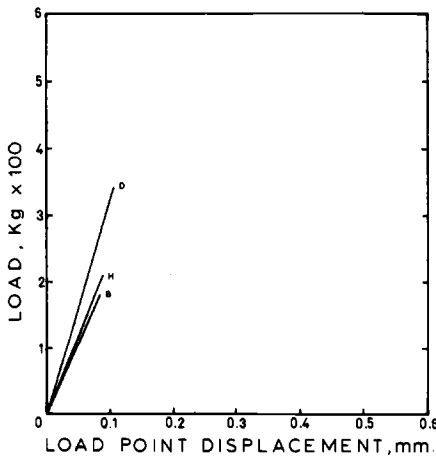


FIG. 3—Load-load point displacement curves, under controlled displacement, for Charpy size specimens of the base metal (without a weld).

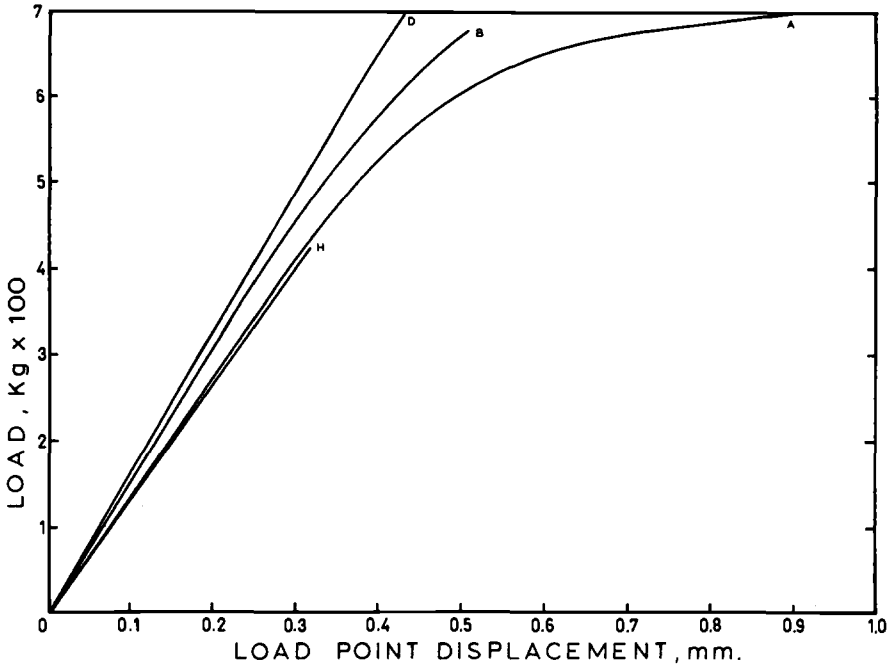


FIG. 4—Load-load point displacement curves, under controlled load, for three-point bending specimens of welded steels.

Charpy Specimens

Only specimens from the base metal were tested using this geometry. The load displacement curves obtained in this case are shown in Fig. 3. The value of J_{Ic} and, hence, K_{Ic} , were calculated exactly in the same way as for the deep crack method, using Eqs 1 and 2.

Controlled Loading Specimens

Figures 4 and 5 show the load displacement curves under controlled loading. Figure 4 is for the heat affected zone, while Fig. 5 is for the base metal. A preliminary observation indicates that, under controlled loading at the same temperature, the specimens display a greater plasticity than under controlled displacement. Taking this observation into account, the total displacement, δ_{tot} , can be written as [17]

$$\delta_{tot} = \delta_{el} + \delta_{crack} \quad (5)$$

where δ_{el} is the displacement for an uncracked elastic body and is given by Hooke's law

$$\delta_{el} = \frac{P}{BE} \{ (16 + 3(1 + \nu)) \} \quad (6)$$

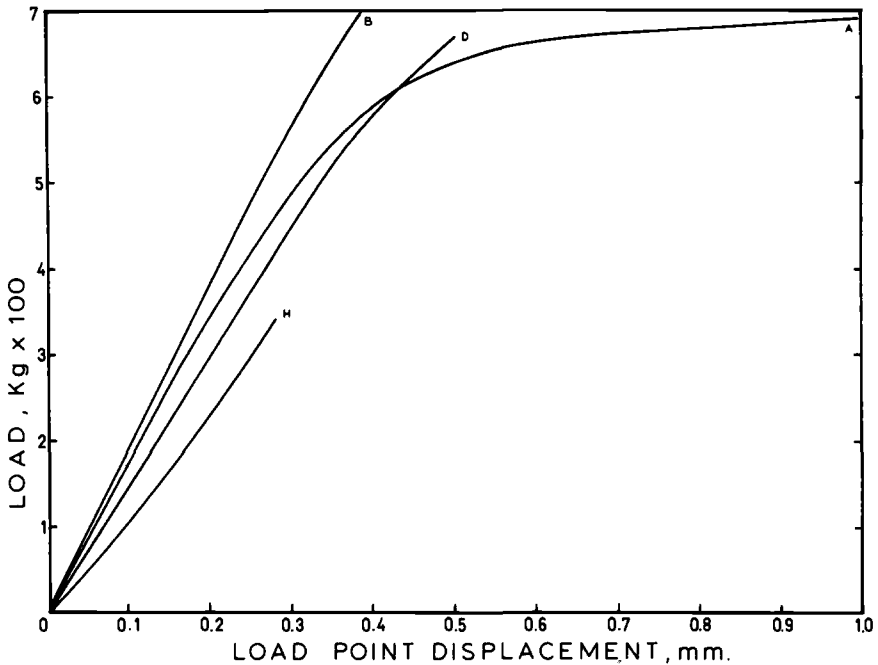


FIG. 5—Load-load point displacement curves, under controlled load, for three-point bending specimens of the base metal (without a weld).

with P being the applied load and ν Poisson's ratio, take as 0.3 for the steels. δ_{crack} is the load point displacement due to the presence of a crack and is related to the applied load and to the stress intensity factor by a relation of the form [18]

$$\delta_{\text{crack}} = \frac{2B}{PE} \int_0^a K^2 da \tag{7}$$

K_I is given by the compliance equation for a standard geometry

$$K = \frac{4P}{B\omega^{1/2}} Y(a/\omega)$$

with

$$Y(a/\omega) = 2.9(a/\omega)^{1/2} - 4.6(a/\omega)^{3/2} + 21.8(a/\omega)^{5/2} - 37.6(a/\omega)^{7/2} + 38.7(a/\omega)^{9/2}$$

for a three-point bending specimen.

After integration of Eq 7, δ_{tot} is obtained as

$$\delta_{\text{tot}} = \frac{16P}{BE} \left[1 + \frac{3}{16} (1 + \nu) + f^*(a/\omega) \right] \quad (8)$$

where $f^*(a/\omega) = 2 \int_0^a Y^2(a/\omega) da$.

Introducing $a_p = a + \gamma_y$ to account for the plasticity at the crack tip, Eq 8 becomes

$$\delta_{\text{tot}} = \frac{16P}{BE} f(a_p/\omega)$$

with

$$f(a_p/\omega) = 1 + \frac{3}{16} (1 + \nu) + f^*\left(\frac{a_p}{\omega}\right) \quad (9)$$

Using the load-displacement curve for a single specimen, it is possible to calculate $f^*(a/\omega)$ and hence $a_p \gamma_y$ is next obtained from a_p . Equation 4 is then obtained using a polynomial regression such that the coefficients A_1, A_2, \dots satisfy the conditions imposed by Westergaard. J_{1c} is then calculated using Eq 3.

Table 2 and Fig. 6 give a summary of all results obtained. In Table 2, all the calculated values of J_{1c} from the various specimen geometries and testing conditions are given. Also included are the values of K_{1c} calculated from the specimens fractured under controlled displacement directly from the load at the fracture point. These values are very close to those obtained from J_{1c} and Eq 2. Figure 6 illustrates these results as a function of the niobium content. The four steels are identified accordingly on the X axis.

Discussion

While determination of the stress intensity factor in plane strain remains the standard method for fracture characterization of materials, the J-integral is used increasingly in cases where the material exhibits elastic-plastic behavior. However, there is a great deal of uncertainty as to the validity of the methods of measurements of this J-integral and to its relation with K_{1c} as also to its independence upon specimen geometry and testing conditions.

In this work, it is shown that values of J_{1c} and hence K_{1c} , obtained from fracture of precracked Charpy size specimens are the lowest compared to those obtained from standard three-point bending specimens tested under

TABLE 2—Summary of *J*-integral measurements for different geometries and loading conditions for the four HSLA steels.

Testing Condition	Steel A	Steel B	Steel D	Steel H
Controlled displacement on three-point bending specimens of the heat affected zone, temperature -150°C	$J = 2.26$ kg/mm K (from J) = 65.53 MPa \sqrt{m} K (from P - δ curves) = 38.24 MPa \sqrt{m}	$J = 2.5$ kg/mm K (from J) = 68.92 MPa \sqrt{m} K (from P - δ curves) = 48.13 MPa \sqrt{m}	$J = 3.89$ kg/mm K (from J) = 85.97 MPa \sqrt{m} K (from P - δ curves) = 51.43 MPa \sqrt{m}	$J = 2.17$ kg/mm K (from J) = 64.21 MPa \sqrt{m} K (from P - δ curves) = 51.43 MPa \sqrt{m}
Controlled loading on three-point bending specimens of the heat affected zone, temperature -150°C	$J = 5.5$ kg/mm K (from J) = 105.60 MPa \sqrt{m} $\gamma_y = 2.77$ mm	$J = 3.658$ kg/mm K (from J) = 83.36 MPa \sqrt{m} $\gamma_y = 0.731$ mm	$J = 3.708$ kg/mm K (from J) = 83.93 MPa \sqrt{m} $\gamma_y = 0.05$ mm	$J = 0.993$ kg/mm K (from J) = 43.44 MPa \sqrt{m} $\gamma_y = r_y$
Controlled loading on three-point bending specimens of the base metal, temperature -150°C	$J = 3.823$ kg/mm K (from J) = 85.23 MPa \sqrt{m} $\gamma_y = 3.687$ mm	$J = 4.054$ kg/mm K (from J) = 87.76 MPa \sqrt{m} $\gamma_y = 0.76$ mm	$J = 3.937$ kg/mm K (from J) = 86.49 MPa \sqrt{m} $\gamma_y = 0.56$ mm	$J = 1.047$ kg/mm K (from J) = 44.59 MPa \sqrt{m} $\gamma_y = r_y$
Controlled displacement Charpy size specimens of the base metal, temperature -150°C	. . .	$J = 0.384$ kg/mm K_{ic} (from J_{ic}) = 27.01 MPa \sqrt{m} K (from P - δ curve) = 26.76 MPa \sqrt{m}	$J = 0.95$ kg/mm K_{ic} (from J_{ic}) = 42.49 MPa \sqrt{m} K (from P - δ curve) = 51.3 MPa \sqrt{m}	$J = 0.485$ kg/mm K_{ic} (from J_{ic}) = 30.36 MPa \sqrt{m} K (from P - δ curve) = 31.22 MPa \sqrt{m}

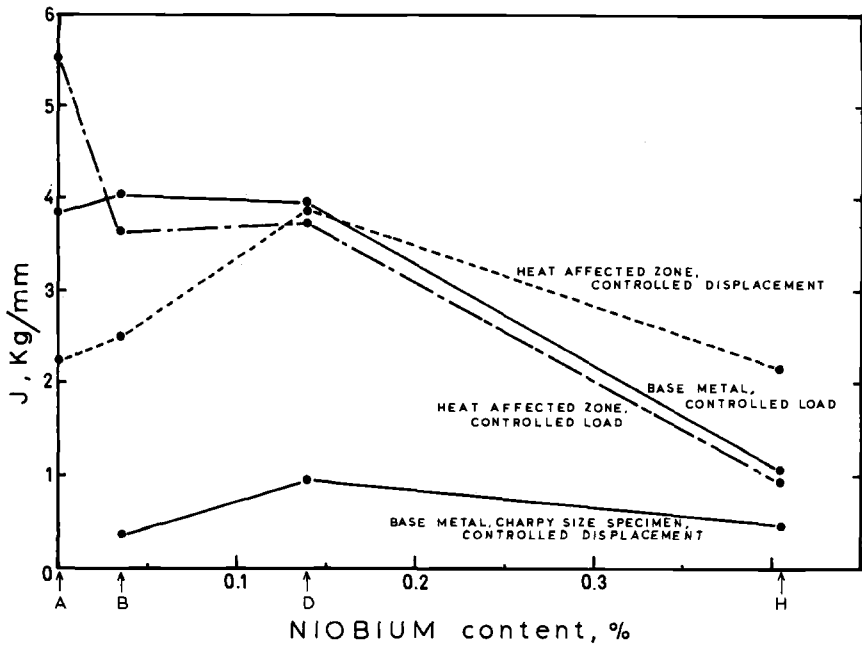


FIG. 6—The J -integral as a function of niobium content for all specimens tested under various conditions. Note that the position of Steel H, which has both niobium and molybdenum, is arbitrary.

either controlled displacement or controlled loading. The values of J_{Ic} for the specimens fractured under controlled loading are, in general, higher than those for the corresponding specimens fractured under controlled displacement. This is true both for the heat affected zone and for the base metals, and can be attributed to the deformation rate. Under controlled displacement, the deformation rate is constant while it varies continuously under controlled loading, leading to a noticeable elastic-plastic behavior, as shown in Figs. 4 and 5. Hence the plastic zone size is larger than that calculated by the Irwin equation

$$r_p = \frac{1}{\alpha \pi} \left(\frac{K_I}{\sigma_y} \right)^2$$

and Eq 4 can then be applied.

Furthermore, for the low alloy steels, the fracture toughness does not seem to vary considerably from the base metal to the heat affected zone. A minute shift in the position of the initial notch may lead to variations in the values of J_{Ic} obtained using the different geometries and loading conditions for each steel. It was observed that specimens with a higher toughness correspond to a crack path which was almost entirely in the grain refined zone. Some specimens of Steel A, particularly, exhibited

very small grain size which is thought to be responsible for the great variation in its toughness. Specimens with the same grain size as Steels B, D and H, had a lower toughness than Steels B and D.

It is shown that the addition of niobium tends to increase fracture toughness markedly, both for the base metal and for the heat affected zone. Thus, Steel D which has a higher niobium content shows an increase in toughness compared to Steel B, which in turn, has higher J_{Ic} values than Steel A which has no niobium. On the other hand, Steel H which has both niobium and molybdenum, tends to have a lower fracture toughness than steels with niobium only. It should be noted that this tendency occurs as well in the base metal as in the heat affected zone and also in the Charpy size specimens.

Summary and Conclusion

In this investigation, the J-integral was obtained for four steels characterized by their high ductility. Tests were performed in the base metal and in the heat affected zone under controlled displacement. Specimens were either standard three-point bending or Charpy specimens.

Results obtained can be summarized as follows:

1. J-integral values obtained from precracked Charpy size specimens are much lower than those from three-point bending specimens. It is thus demonstrated that an approach using precracked Charpy specimens for static fracture toughness testing yields conservative results compared to other methods of evaluation.
2. An extension of the work developed by Lantaigne et al can be formulated for three-point bending specimens under controlled loading. A formulation of plastic zone size correction, γ_p , is given, and values of J_{Ic} are obtained. The results show higher ductility than those using the deep crack method under controlled displacement.
3. The addition of niobium tends to increase fracture toughness of the base metal, and, also, of the heat affected zone. On the other hand, the simultaneous presence of niobium and molybdenum tends to decrease toughness, as compared to steels with niobium only.

Acknowledgments

The authors would like to acknowledge Dominion Bridge Company, Lachine, Quebec for supplying the material used in this investigation and for performing the required welding. The support of the National Research Council of Canada is also acknowledged and appreciated.

References

- [1] Pickering, F. B. in *Proceedings*, International Symposium on High-Strength, Low-Alloy Steels, Oct. 1975, pp. 3-24.

- [2] Gladman, I., McIvor, I. D., and Pickering, F. B., *Journal of the Iron and Steel Institute*, Vol. 210, 1972, pp. 916-930.
- [3] Bassim, M. N., Mikhail, S., and Hay, D. R., *Canadian Metallurgical Quarterly*, Nov. 1977.
- [4] Glover, A. G., McGrath, J. T., and Eaton, N. F. in *Proceedings, International Conference on Materials Engineering in the Arctic*, Sept. 1976, pp. 210-215.
- [5] Rice, J. R., *Transactions, American Society of Mechanical Engineers; Journal of Applied Mechanics*, Vol. 35, 1968, pp. 379-386.
- [6] Rice, J. R., "Mathematical Analysis in the Mechanics of Fracture," in *Fracture—An Advanced Treatise*, H. Liebowitz, Ed., Academic Press, New York, 1968.
- [7] Begley, J. A. and Landes, J. D. in *Fracture Toughness, Part 2, ASTM STP 514*, American Society for Testing and Materials, 1972, pp. 1-20.
- [8] Landes, J. P. and Begley, J. A. in *Fracture Analysis, ASTM STP 560*, American Society for Testing and Materials, 1974, pp. 170-186.
- [9] Rice, J. R., Paris, P. C., and Merkle, J. G. in *Progress in Flaw Growth and Fracture Toughness Testing, ASTM STP 536*, American Society for Testing and Materials, 1973, pp. 231-245.
- [10] Lanteigne, J., Bassim, M. N., and Hay, D. R. in *Flaw Growth and Fracture, ASTM STP 631*, American Society for Testing and Materials, 1977, pp. 202-216.
- [11] Lanteigne, J., Bassim, M. N., and Hay, D. R., *International Journal of Fracture*, Vol. 12, 1976, pp. 485-487.
- [12] Westergaard, H. M., *Transactions, American Society of Mechanical Engineers*, Vol. 61, 1939, pp. A49-A53.
- [13] Keller, H. P. and Munz, D. in *Flaw Growth and Fracture, ASTM STP 631*, American Society for Testing and Materials, 1977, pp. 217-231.
- [14] Begley, J. A. and Landes, J. D. in *Fracture Toughness, Part 2, ASTM STP 514*, American Society for Testing and Materials, 1972, pp. 24-39.
- [15] Iyer, K. R. and Miclot, R. B. in *Instrumented Impact Testing, ASTM STP 563*, American Society for Testing and Materials, 1974, pp. 146-165.
- [16] Committee on Rapid Inexpensive Tests for Determining Fracture Toughness, *International Journal of Fracture*, Vol. 13, 1977, pp. 227-230.
- [17] Penelon, A., Dorlot, J. M., and Bassim, M. N., *Engineering Fracture Mechanics*, Vol. 11, 1979, pp. 559-561.
- [18] Adams, N. J. I. and Munro, H. G., *Engineering Fracture Mechanics*, Vol. 6, 1974, pp. 119-132.
- [19] Paris, P. C. in *Flaw Growth and Fracture. ASTM STP 631*, American Society for Testing and Materials, 1977, pp. 3-27.

*J. H. Underwood*¹

J_{Ic} Results and Methods with Bend Specimens

REFERENCE: Underwood, J. H., " J_{Ic} Results and Methods with Bend Specimens," *Fracture Mechanics, ASTM STP 677*, C. W. Smith, Ed., American Society for Testing and Materials, 1979, pp. 463–473.

ABSTRACT: J_{Ic} tests were performed using 10 by 12 mm cross section bend specimens of 4335 steel with yield stress in the range of 1200 MPa. Based on analysis of the results a simple, one-specimen, J -based test procedure is proposed which can be used to obtain the J equivalent of K_{Ic} in Charpy-sized, deeply cracked specimens loaded slowly in bending.

KEY WORDS: fracture properties, test methods, toughness, bending loads, steel alloys, fatigue (materials), crack propagation

The development of the J_{Ic} method for measuring fracture toughness is described in a recent paper by Landes and Begley [1]². The basic procedures of the J_{Ic} method are used broadly now and are becoming well accepted. When there is a need to measure the fracture toughness of a material in a smaller specimen size than that required for K_{Ic} measurement, the J_{Ic} method is very useful. It provides a reliable complement to the K_{Ic} method. This does not detract at all from the more general utility of the J_{Ic} concept for characterizing fracture toughness over a wide range of specimen size and other material and test conditions. Instead, the use of the J_{Ic} method to extend the K_{Ic} approach to smaller specimen sizes is a natural progression for fracture analysts who use K_{Ic} based analyses. This, generally, is the objective of the work described here. Tests and analysis will be described which determine some conditions under which results from J_{Ic} tests can be used as an estimate of K_{Ic} . The emphasis will be to determine the extent to which the J_{Ic} method can be simplified for a given range of mechanical properties of a nickel-chromium-molybdenum steel.

¹Materials engineer, U. S. Army Armament Research and Development Command, Benet Weapons Laboratory, Watervliet, N. Y. 12189.

²The italic numbers in brackets refer to the list of references appended to this paper.

The motivation for this work is the use in a fracture-critical application of a relatively high strength, high toughness material, that is, one with yield strength and fracture toughness in the range of 1100 MPa and 160 $\text{MPa}\cdot\text{m}^{1/2}$ respectively. The application is large cannon components, which involves cyclic application of pressure to vessels using a compressible fluid. These conditions lead to the growth of fatigue cracks and the application of a large amount of stored energy, so measurement and control of fracture toughness is important. The specimen depth, W , required for K_{Ic} measurement with the material in this application is about 100 mm, based on the size criteria of ASTM Test Method for Plane Strain Fracture Toughness of Metallic Materials (E 399-78a). A specimen of this size can be obtained from only the largest of cannon components, so the J_{Ic} method is used routinely to obtain an estimate of K_{Ic} . A summary of prior results [2] has shown that the J_{Ic} method gives an accurate estimate of K_{Ic} for the material of our concern in specimen sizes as small as one quarter of the K_{Ic} requirement. The only difficulty we have with the J_{Ic} method is its complexity and related cost. In the following sections, the effect of still smaller specimen sizes and simplifications of the J_{Ic} method on the equivalence of the J_{Ic} and K_{Ic} methods will be considered.

Test Procedure

The basic procedures for the tests here were similar to those recommended by Landes and Begley [1]. The specimens were loaded in bending with load and load-point displacement recorded. The area under the load-versus-displacement curve was measured for a group of specimens, with each specimen unloaded following a different amount of crack advance, Δa , which was measured by a heat-tinting procedure. The critical value of J corresponding to the start of crack advance, J_{Ic} , was determined by a linear fit of the J -versus- Δa curve.

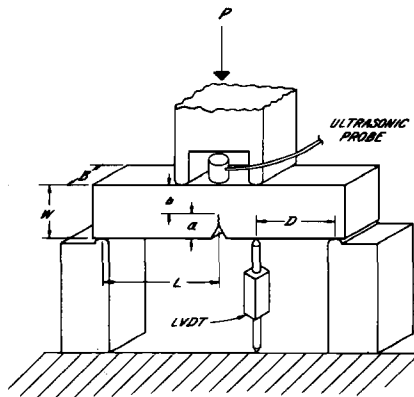


FIG. 1—Test arrangement.

A schematic description of the tests which gives details of the procedure is shown in Fig. 1. All tests were performed using the specimen geometry and the four-point bending arrangement shown in the sketch. The following dimensions were the same for all tests: specimen thickness, $B = 10.0$ mm; specimen depth, $W = 12.0$ mm; moment arm, $D = 16.5$ mm; half span, $L = 26.0$ mm. A notch and fatigue crack was produced in each specimen to a length corresponding to a/W between 0.5 and 0.7. The specimens were loaded using fixed lower supports and fixed upper load-points with space between the load-points for an ultrasonic probe. By using an end-on ultrasonic technique [2,3] continuous measurements of crack advance can be obtained during J_{Ic} and K_{Ic} tests. The displacement under one of the upper load-points was measured using a linear-varying-differential transformer.

Material and Crack Size

The two variables in the tests were material properties and crack length. Two materials were tested with different strength and toughness properties, and for each material a group of five or more specimens was tested at each of three nominal crack lengths, $a/W = 0.5, 0.6, 0.7$. Material property and crack size data for the test specimens are shown in Table 1.

The materials were obtained from two vacuum-degassed, forged cylinders with chemical compositions similar to that of 4335 steel. The specimens were in the C-R orientation. The fracture toughness listed in Table 1 for the high strength material is the mean of four tests in accordance with ASTM Method E 399 and with a range of 137 to 145 $\text{MPa} \cdot \text{m}^{1/2}$. For the low strength material it was necessary to make an estimate of K_{Ic} due to size limitations; based on experience with many similar materials [2], the estimate is believed to be accurate within the range indicated.

J_{Ic} Test Results

The results from the J_{Ic} tests are shown in Figs. 2 and 3 for the high and low strength materials respectively. In general each data point represents the J and Δa values from a separate specimen; Δa was measured from the specimen surface and J was calculated from

$$J = 2A/bB \quad (1)$$

where A is the work corresponding to the area under the load-displacement curve, b and B are specimen ligament and thickness as shown in Fig. 1. Equation 1, although not exact, can be used here, because the specimens were deeply cracked and are subjected to pure bending [1]. The data points of each plot are represented by a linear

regression line. The intersection of this line with the blunting line is J_{Ic} . The three J_{Ic} values obtained for each material are in the expected range based on K_{Ic} , and the scatter of the data points and the J_{Ic} values is not excessive. The minimum ligament, calculated for the highest J_{Ic} obtained for each material using the expression [1]

$$b_{min} = 25J_{Ic}/\sigma_{flow}$$

is generally less than one half of the actual b values. Flow stress, δ_{flow} , is the usual definition, that is, one half of the sum of yield and ultimate stresses. In all key respects the tests are believed to be proper J_{Ic} tests.

The variation in J_{Ic} with a/W shown in Figs. 2 and 3 could be interpreted as a systematic variation, particularly the high strength material data in Fig. 2. However, it is more likely that the variation in J_{Ic} is the result of the scatter which is inherent in fracture toughness results. An appropriate comparison is between the scatter of the square root of J_{Ic} and the expected scatter of K_{Ic} data. A ± 6 percent and a ± 4 percent scatter band

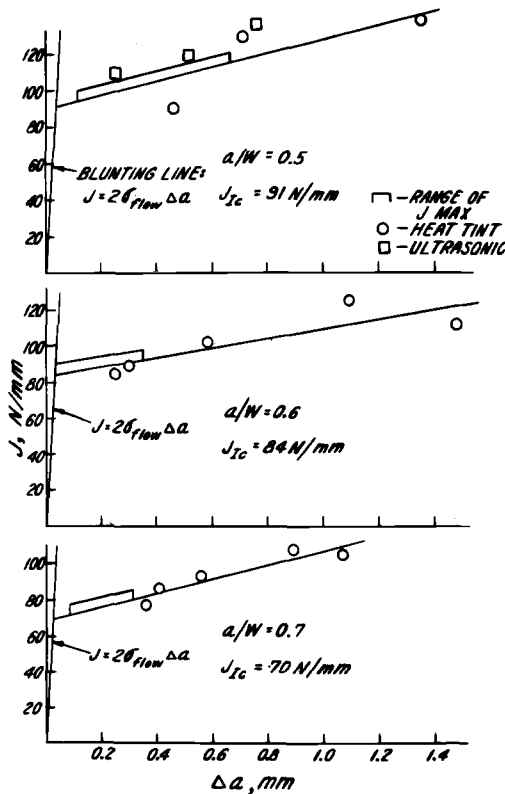


FIG. 2—J versus crack advance for high strength material.

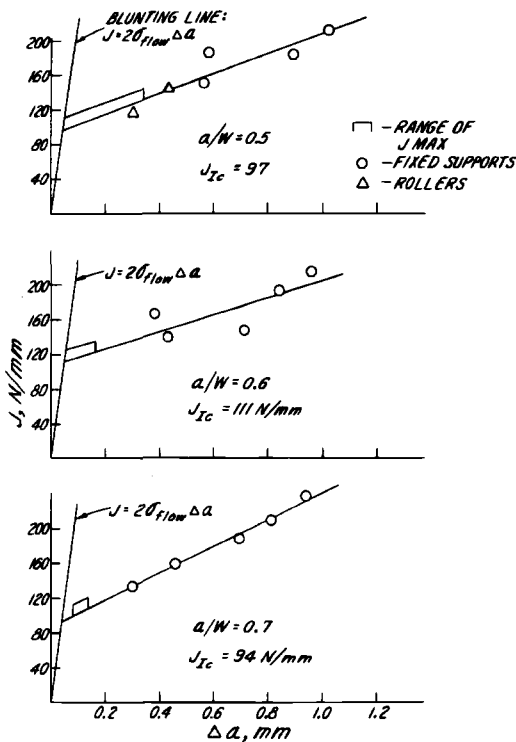


FIG. 3— J versus crack advance for low strength material.

will include the values of $\sqrt{J_{IC}}$ from the tests of Fig. 2 and Fig. 3, respectively. Scatter of this magnitude is typical of K_{IC} test results in alloy steel.

Data from two alternative test procedures are shown in Figs. 2 and 3. In the $a/W = 0.5$ plot of Fig. 2 are shown J versus Δa data for which Δa was measured using ultrasonics [3] from a single specimen. It was planned to obtain ultrasonic data from all specimens, but this was not possible because the ligament was too small. An apparent limitation of the present ultrasonic method is that b must be larger than 6 mm for reliable measurement of Δa . Three ultrasonic data points are shown, and they show the same trend as the heat-tint data. Only the intermediate point was used in linear regression, so that the one ultrasonic specimen would have the same weighting as each of the heat-tint specimens.

Data from the second alternative test procedure are shown in the $a/W = 0.5$ plot of Fig. 3. Two specimens were tested with rollers rather than fixed lower supports. The data points from the different means of support show the same trend, and both groups of data were used in linear regression. However, the results from these few specimens show only

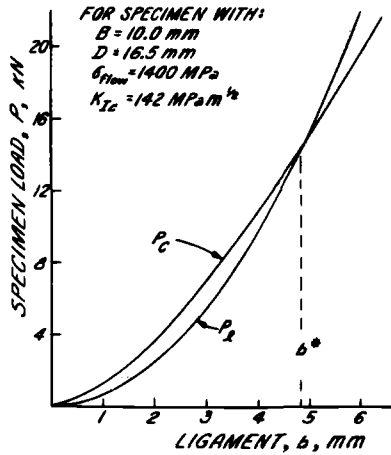


FIG. 4—Critical and limit loads as a function of ligament size.

that there was no large difference between fixed and rolling support for the specific conditions of the tests here. Any more general conclusion could be seriously in error.

One other piece of information is shown on each plot in Figs. 2 and 3, and that is the range of the J value which corresponds to maximum load for the specimens which were loaded to this extent. The range in J is shown on the J versus Δa linear regression line; this gives an indication of the Δa which corresponds to maximum load. There is a clear trend toward a smaller Δa at maximum load as both the toughness of the material and the crack depth increase. This trend is central to the ideas discussed in the following section regarding a simpler fracture toughness test.

Conditions for a Simplified J_{Ic} Test

In order to determine test conditions which will lead to a simpler, J_{Ic} -based method for measuring fracture toughness, it is helpful to consider the conditions for brittle fracture and for limit-load yielding of a bend specimen. Brittle fracture of the geometry considered here is well described by the expression [4]

$$K_{Ic} B b^{3/2} / M = 4.0$$

Defining the bending moment, M , in terms of load and specimen dimensions results in

$$P_c = 0.5 K_{Ic} B b^{3/2} / D \quad (2)$$

The limit-moment for a specimen in pure bending is [5]

$$M_l = 0.36 B b^2 \sigma_{flow}$$

the flow stress, σ_{flow} is used to account for strain hardening. Using load and specimen dimensions, the result is

$$P_l = 0.72 Bb^2\sigma_{flow}/D \tag{3}$$

Plots of Eqs 2 and 3 are shown in Fig. 4. When a specimen with a large enough value of b is loaded, a brittle fracture is expected. For a b value near the point where P_c equals P_l limit-load yielding is expected. Combining Eqs 2 and 3 gives an estimate of the b value which is the rough dividing point between brittle fracture and limit-load yielding behavior for a bend specimen

$$b^* = 0.48 (K_{Ic}/\sigma_{flow})^2 \tag{4}$$

Certainly no critical predictions of brittle or ductile behavior should be attempted with Eq 4, but it may be useful for estimating the b at which crack advance will occur at maximum load in a J_{Ic} test. For the tests here, the values of b^* are 4.9 and 10.3 mm for the high strength and low strength materials, respectively. This range of b^* overlaps the range of b in the tests, so analysis of the tests may show whether or not b^* is of any use.

The data from the tests were analyzed using a second, different approach from that of the J_{Ic} method in an attempt to arrive at a simpler but still J -based method for determining fracture toughness. The approach used and the results are outlined in Fig. 5. The J value corresponding to the point beyond maximum load at which the load has decreased by 5 percent is calculated for each specimen using Eq 1. This value, J_5 , is plotted in Fig. 5 for each specimen which was loaded to this extent; the J_5 values are shown in dimensionless form, divided by the J equivalent of K_{Ic} . The ordinate is the ratio of b measured from each specimen to b^* . The

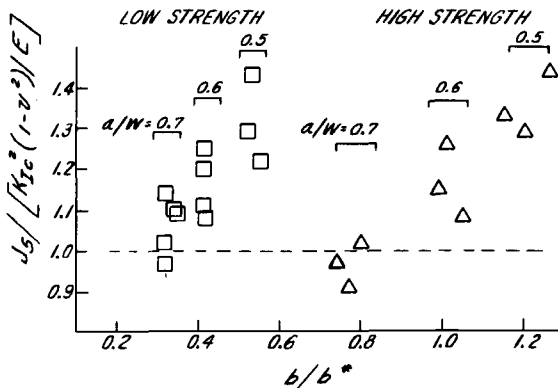


FIG. 5— J at 5 percent load drop versus ligament size.

results using this approach show quite clearly that J_5 is essentially equal to the J equivalent of K_{1c} for a/W in the range of 0.7. It is less clear just how important it is that b be equal to or less than b^* . But the results do show that b/b^* was below 1.0 for the two test situations where J_5 is equal to the J equivalent of K_{1c} . The two conditions that b/b^* be below and a/W be above certain values will be included in a suggestion for a simple, one-specimen test for fracture toughness in the following section of this report.

Conclusions—A Simple J -Based Fracture Toughness Test

Test Conditions

For the material under consideration here, J_5 , the J value for the point beyond maximum load at which the load has decreased by 5 percent, gives a good estimate of $K_{1c}^2(1-\nu^2)/E$ and is suggested as the basis of a simple, one-specimen fracture toughness test in specimen sizes of about one tenth of that required for a K_{1c} test. Deeply cracked three-point bend specimens are suggested with specimen dimensions a , b , B as follows

$$0.65 < a/W < 0.75$$

$$0.2(K_{1c}/\sigma_{flow})^2 < b < 0.4 (K_{1c}/\sigma_{flow})^2$$

$$B/W = 1.0$$

Discussion

Based on the work described here, the test conditions in the preceding paragraph will result in general, limit-load yielding as maximum load is reached, and crack advance in the specimen will occur just after maximum load and will be the cause of the drop in load. So the J value at a 5 percent decrease in load should correspond closely to the beginning of crack advance which is the main requirement of a fracture toughness test. A comparison of the J_{1c} and J_5 results with K_{1c} for the two materials is shown in Table 2. The J_{1c} values used for Table 2 are from Figs. 2 and 3; the J_5 values are the mean values of those shown in Fig. 5. As has been observed for other materials, the K equivalent of J_{1c} tends to fall below K_{1c} for the results here. The K equivalent of J_5 is above K_{1c} for tests with a/W of about 0.5, and as a/W increases and limit-load conditions are more assured the K equivalent of J_5 becomes a better estimate of K_{1c} .

The test procedure suggested here can correspond directly to a precracked, slow-bend Charpy test. Succop and Brown [6] recently reported a procedure for estimating K_{1c} from precracked, slow-bend Charpy tests.

TABLE 2—Comparison of results from J_{Ic} tests with K_{Ic} .

	a/W	$\sqrt{EJ_{Ic}/(1-\nu^2)}/K_{Ic}$	$\sqrt{EJ_5/(1-\nu^2)}/K_{Ic}$
High Strength Material	0.5	1.01	1.16
	0.6	0.97	1.08
	0.7	0.89	0.98
Low Strength Material	0.5	0.87	1.15
	0.6	0.93	1.08
	0.7	0.85	1.03

The two procedures should be compared. Succop and Brown found a good correlation between the nominal strength of a Charpy specimen and K_{Ic} in 4340 steel with a range of strength and toughness which corresponds to

$$1 \text{ mm} < (K_{Ic}/\sigma_{\text{yield}})^2 < 8 \text{ mm}$$

The properties of the material here correspond to

$$12 < (K_{Ic}/\sigma_{\text{yield}})^2 < 24 \text{ mm}$$

so there is a difference in the toughness levels of the materials used in the two procedures. In addition, the approach in the Succop and Brown work was to stay below limit load; the approach here requires that limit load be reached. So the two procedures apply to different situations.

An inherent problem with fracture tests using a single, small specimen is scatter. In the tests here much of the scatter in Fig. 5 is believed to be due to specimen size. In the case of the low strength tests with $a/W = 0.6$ for example, comparison of the load-displacement records revealed that the two specimens with higher values of J_5 showed less than one half of the drop in load for a given increment of displacement than the drop in load for the two specimens with low values of J_5 . This is attributed to the small specimen size relative to the size of areas of nonuniform properties in the material. This problem can be reduced by using as large a value of B as possible. This supports the use of a B equal to W rather than one half of W as in K_{Ic} tests.

The future plans in regard to the suggested test procedure are (a) to use deeply cracked Charpy specimens of standard outer dimensions loaded in slow bending with roller supports, (b) to test several 4335 steels in the range of 1000 to 1300 MPa yield stress, and (c) to develop an automated test procedure which includes calculation of b using compliance measurements during the elastic loading of the specimen, calculation of J_5 from load, deflection and b information, and unloading of the specimen at J_5 to allow measurement of crack advance after the test.

It must be emphasized that the use of J_5 as a measure of fracture toughness is proposed as a rapid, inexpensive screening test. It is primarily a method to obtain engineering data at low cost. It is certainly not a general method for measuring basic resistance to crack extension of materials over wide property ranges. Only when material yield stress and fracture toughness and specimen ligament are within certain narrow ranges can J_5 give a good estimate of K_{Ic} . Statistical analysis of many tests will be required to show just how useful this method will be.

References

- [1] Landes, J. D. and Begley, J. A. in *Developments in Fracture Mechanics Test Methods Standardization, ASTM STP 632*, American Society for Testing and Materials, 1977, pp. 57–81.
- [2] Underwood, J. H. in *Experimental Mechanics*, Vol. 18. No. 9, 1978, pp. 350–355.
- [3] Underwood, J. H., Winters, D. C., and Kendall, D. P. in *The Detection and Measurement of Cracks*, The Welding Institute, Cambridge, England, 1976, pp. 31–39.
- [4] Srawley, J. E. and Gross, B. in *Engineering Fracture Mechanics*, Vol. 4, 1972, pp. 587–589.
- [5] Rice, J. R., Paris, P. C., and Merkle, J. G. in *Progress in Flaw Growth and Fracture Toughness Testing, ASTM STP 536*, American Society for Testing and Materials, 1973, pp. 231–245.
- [6] Succop, G. and Brown, W. F., Jr. in *Developments in Fracture Mechanics Test Methods Standardization, ASTM STP 632*, American Society for Testing and Materials, 1977, pp. 179–192.

J. P. Gudas,¹ J. A. Joyce,² and D. A. Davis¹

Investigation of Specimen Geometry Modifications to Determine the Conservative J_I - R Curve Tearing Modulus Using the HY-130 Steel System

REFERENCE: Gudas, J. P., Joyce, J. A., and Davis, D. A., "Investigation of Specimen Geometry Modifications to Determine the Conservative J_I - R Curve Tearing Modulus Using the HY-130 Steel System," *Fracture Mechanics, ASTM STP 677*, C. W. Smith, Ed., American Society for Testing and Materials, 1979, pp. 474-485.

ABSTRACT: The objective of this work was to investigate the effects of face grooves and crack length variations of J_{Ic} and the tearing modulus of HY-130 steel. Compact specimen geometries (1TCT) with crack length ratios of 0.55, 0.65, and 0.8, and face grooves of 12.5 percent and 25 percent total cross section reduction were tested using a computer interactive unloading compliance test technique. Results of these tests showed that for this material, J_{Ic} was independent of specimen geometry for the range of geometries evaluated. The tearing modulus, however, was higher in nonface grooved specimens, in which crack tunneling occurred, and the tearing modulus was found to increase by a factor of two as crack length ratios increased from 0.55 to 0.8. In face grooved specimens, the tearing modulus was found to be constant for the various crack length ratios tested, at the lower bound of values developed with nonface grooved specimens.

KEY WORDS: elastic-plastic fracture, J_{Ic} testing, single specimen tests, tearing modulus, HY-130 steel, fracture toughness, crack propagation

The objective of this effort was to evaluate the effects of test specimen geometry on J_{Ic} and the tearing modulus of HY-130 steel. The test variables included face groove depth and crack length in 1TCT compact specimens. In previous work reported by Joyce and Gudas [1]³ a computer interactive procedure for J_I testing was developed and results of

¹ Head of Fatigue and Fracture Branch and research engineer, respectively, David W. Taylor Naval Ship Research and Development Center, Annapolis, Md. 21402.

² Assistant professor, Department of Mechanical Engineering, United States Naval Academy, Annapolis, Md. 21402.

³ The italic numbers in brackets refer to the list of references appended to this paper.

tests with various alloys were reported. It was also reported that J_I versus crack extension resistance curve slopes were elevated when crack tunneling occurred with certain alloys. With the advent of the tearing modulus concept [2], it became necessary to investigate this phenomenon with particular emphasis on developing tearing modulus measurements which are conservative and independent of specimen geometry.

Experimental Procedure

Material

HY-130 plate supplied in 25-mm thickness was used for all tests. The chemical composition of the plate is described in Table 1 and mechanical properties are presented in Table 2.

Testing

Modified compact specimens (1TCT) were produced according to Fig. 1. All cracks were placed in the T-L orientation. For testing, razor blades were attached at the load line for displacement measurement. Specimens were fatigue precracked according to ASTM Test for Plane-Strain Fracture Toughness of Metallic Materials (E 399 - 78a) criteria to crack lengths of 0.55, 0.65 and 0.8 a/w , where a is the crack length and w is the specimen width. After precracking, face grooves were machined in some specimens to total section reductions of 12.5 and 25 percent. Most specimens were face grooved with a standard Charpy cutter while several were face grooved with a 60-deg cutter with a root radius of 100 μm .

All tests were carried out at ambient temperature utilizing the computer interactive unloading compliance test facility [1] and a Tinius Olsen tensile test machine. A uniform cross head speed of 127 $\mu\text{m}/\text{min}$ was maintained throughout all tests. A schematic of the test arrangement is shown in Fig. 2. This facility allows for on-line, real-time gathering and analysis of digitized load and displacement data. J_{Ic} tests are carried out by performing a series of approximately 10 percent unloadings during the course of a normal fracture mechanics type test. From compliance measurements, instantaneous values of crack length and change in length are determined [1]. J_I is calculated according to the expression [3]

$$J_I = \frac{\beta A}{B_n (w - a)} \quad (1)$$

where

- β = multiplicative factor ≈ 2 obtained from the Merkle-Corten [4] analysis of the compact specimen,
- A = area under the load-displacement curve,

TABLE 1—Chemical composition of HY-130 steel.

Code	Components (weight percent)												
	C	Mn	P	Si	Ni	Cr	Mo	V	S	Cu	Al	Co	Ti
FKS	0.11	0.76	0.005	0.03	5.00	0.42	0.53	0.043	0.004	0.022	0.021	0.02	0.008

TABLE 2—Tensile mechanical properties of HY-130 steel.

Code	0.2 percent Yield Strength, MPa	Ultimate Tensile Strength, MPa	Elongation, percent in 2-in.	Reduction of area, percent
FKS	937	978	21	55

B_n = minimum specimen thickness,
 w = specimen width, and
 a = crack length.

The compliance formula used for these calculations was that of Hudak and Saxena [5] with a correction for plane strain.

J_{Ic} values were computed from the intersection of the crack opening stretch line ($J_I = 2\sigma_f \cdot \Delta a$) with the least squares fit of data points which fell at least 51 μm beyond the crack opening stretch line and did not exceed approximately 1.5 mm in crack growth. In this context, σ_f is the average of the material yield strength and ultimate strength and Δa is the crack extension. Paris tearing moduli were calculated as [2]

$$T = \frac{dJ_I}{da} \cdot \frac{E}{\sigma_o^2} \tag{2}$$

where

T = tearing modulus,

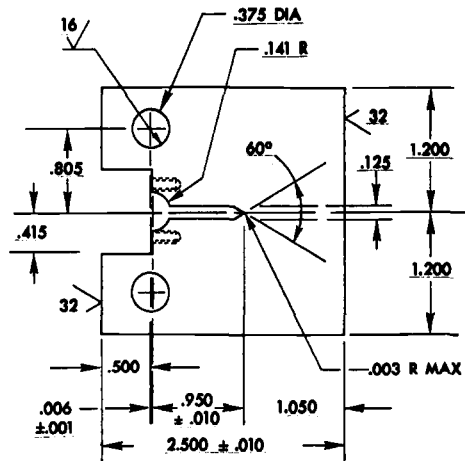


FIG. 1—Modified compact specimen (ITCT) for J_{Ic} testing (dimensions in inches).

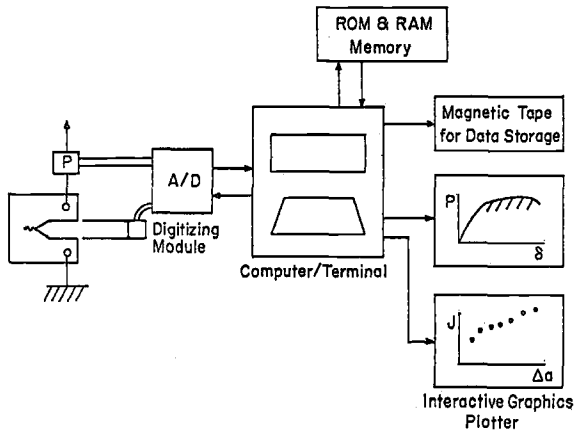


FIG. 2—Schematic of computer interactive fracture mechanics test arrangement.

dJ_I/da = slope of the J versus crack extension curve,
 E = elastic modulus, and
 σ_o = yield stress.

At the conclusion of testing, specimens were heat tinted at 370°C for 30 min. to mark the extent of crack growth. After breaking open at liquid nitrogen temperature, the crack length and crack extension were measured at nine equally spaced points across the crack front neglecting the two surface points.

Results and Discussion

The data from all tests is assembled in Table 3 which also includes results from a multispecimen test performed with this material according to the method of Landes and Begley [3]. J_{Ic} is plotted versus a/w in Fig. 3. The average J_{Ic} value obtained was 153.5 kPa·m with a scatter of +11 to -9 percent. This range of scatter is reasonable for a 25-mm plate tested in the T-L orientation. For this material, J_{Ic} appears to be independent of the face groove and crack geometries tested.

Figures 4 to 6 present the J_I versus crack extension curves for all specimens tested showing the effects of the various face groove geometries at each crack length. The results from tests with 12.5 percent face grooves for which both cutters were used showed no pattern of differences attributable to the cutter geometries. Importantly, both the 12.5 percent and 25 percent face groove geometries produced similar J_{Ic} and J_I versus crack extension curves in this material. The plots of J_I versus crack extension (Figs. 4 to 6) include solid data points which correspond to the nine-point crack length measurement plotted versus the final J_I at

TABLE 3—Results of J_{IC} tests with HY-130 steel.

a/w	Measurement	Face Groove, percent						
		0	12.5					25
0.55	specimen	T-3	T-22	T-20	T-19	T-27	T-1	
	J_{IC} kPa·m	167.2	162.1	146.2	161.3	134.1	158.0	
	dJ_I/da kPa·m/mm	110.7	119.7	109.8	71.6	85.6	86.4	
	T	24.0	26.0	23.8	15.5	18.6	18.8	
	a_0/w	0.60	0.55	0.53	0.54	0.56	0.55	
	Δa estimate mm	1.40	1.37	1.37	1.37	1.88	1.30	
	Δa measured mm	2.26	1.63	1.17	1.40	1.55	1.20	
0.65	specimen	T-4	T-23	T-12	T-8	T-21	T-9 ^a	
	J_{IC} kPa·m	174.7	161.3	142.0 ^a	163.5	160.9	147.5	
	dJ_I/da kPa·m/mm	127.4	120.5	97.7	112.6	82.8	90.8	
	T	27.8	26.2	20.5	24.5	18.0	19.5	
	a_0/w	0.69	0.67	0.70	0.68	0.67	0.68	
	Δa estimate mm	1.40	1.19	2.56	1.37	1.47	1.70	
	Δa measured mm	1.78	1.22	2.63	1.45	1.58	1.60	
0.8	specimen	T-7	T-18	T-5 ^a	T-2	T-28	T-6 ^a	
	J_{IC} kPa·m	139.6	153.7	145.7	147.3	140.4	150.6	
	dJ_I/da kPa·m/mm	189.5	196.1	104.3	84.0	106.1	115.6	
	T	41.3	42.7	22.7	18.1	23.1	24.5	
	a_0/w	0.82	0.81	0.81	0.81	0.81	0.80	
	Δa estimate mm	1.09	1.24	1.50	1.24	1.42	1.40	
	Δa measured mm	1.55	1.52	1.45	1.32	1.24	1.40	
Multiple specimen data								
	J_{IC} kPa·m	167.0						
	dJ_I/da kPa·m/mm	157.8						
	T	34.4						
	a_0/w	0.7						

^a 60 deg included angle face groove.

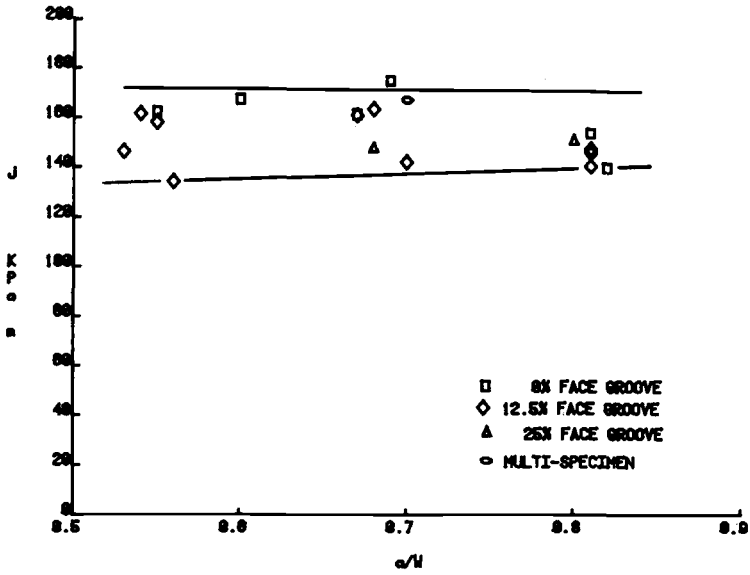


FIG. 3—Plot of J_{Ic} values versus crack length ratio for all specimens tested.

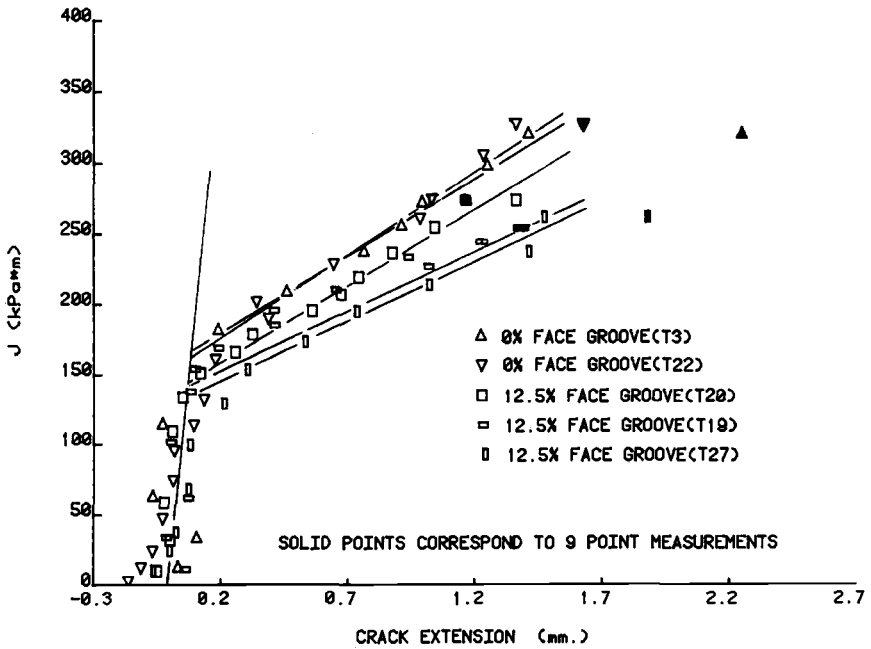


FIG. 4—Plot of J_1 versus crack extension for specimens where $a/w = 0.55$.

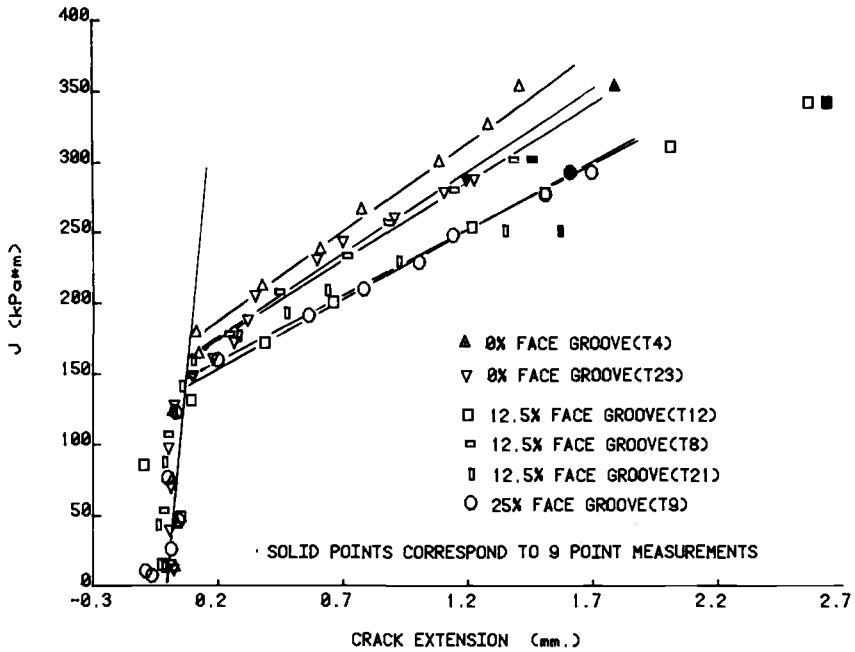


FIG. 5—Plot of J_1 versus crack extension for specimens where $a/w = 0.65$.

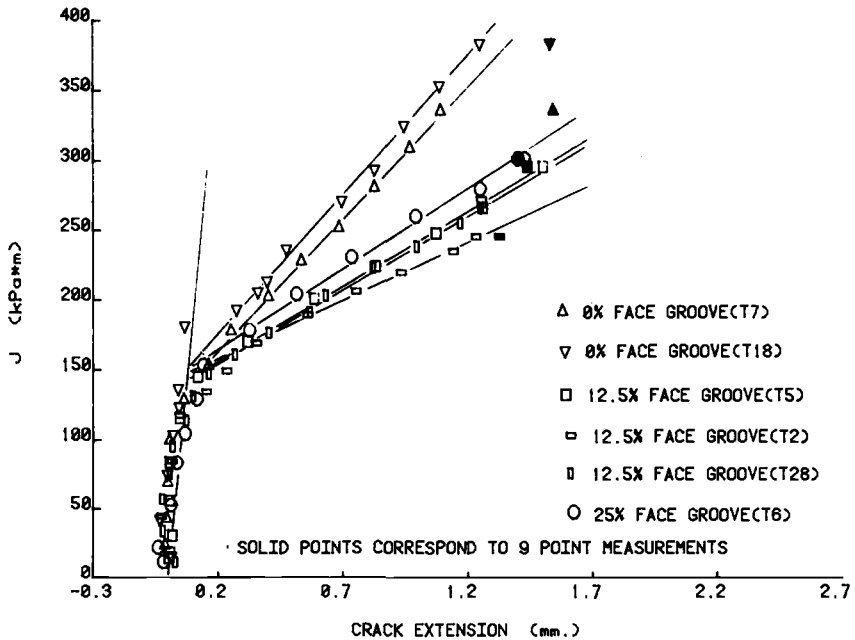


FIG. 6—Plot of J_1 versus crack extension for specimens where $a/w = 0.8$.

the completion of each test. For face grooved specimens, the nine-point measurements agree with unloading compliance estimates within $75\ \mu\text{m}$ except for two points at $a/w = 0.55$. The best agreement between the two crack length measurement techniques exists at larger a/w values where the compliance estimated crack lengths are most accurate. For nonface grooved specimens, however, nine-point measurements of crack extension are (with one exception) larger by 30 to 50 percent than the unloading compliance estimates. These results demonstrate that the crack extension estimation discrepancies reported by Joyce and Gudas [1] and observed here with the nonface grooved specimens are due to the crack tunneling effects. To support this point, Figs. 7 and 8 are photographs of specimens after test which show considerable crack tip tunneling in specimens tested without face grooves. Face grooves of 12.5 and 25 percent straightened the crack fronts by eliminating shear lip formation during crack extension.

Figure 9 is a plot of the tearing modulus (from Eq 2) for each specimen as a function of the crack length. This figure shows that for this steel, the tearing modulus for nonface grooved specimens increases markedly as a/w increases from 0.54 to 0.81. For the face grooved specimens, the tearing modulus data exist in a band at the minimum values obtained with the nonface grooved specimens, and these data are independent of crack

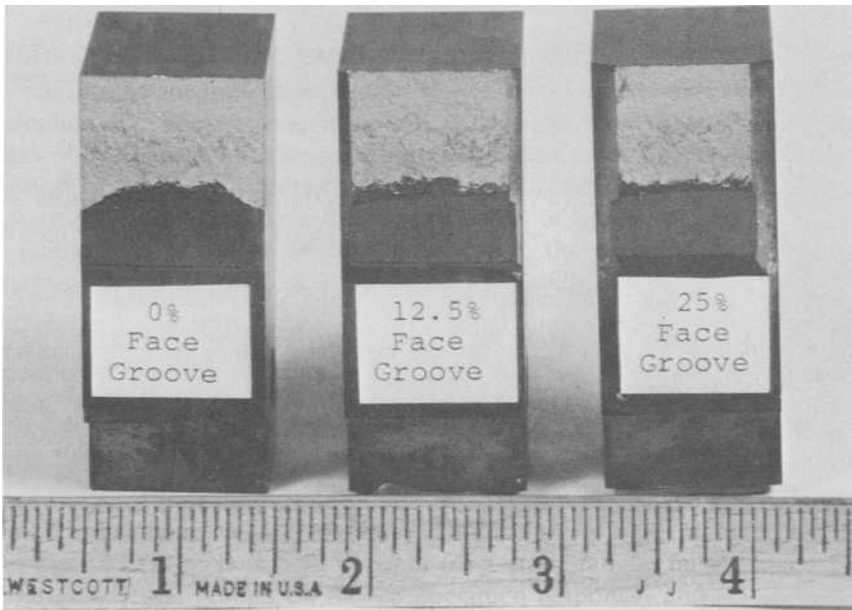


FIG. 7—Photograph of specimens ($a/w = 0.65$) after test showing type of crack extension as related to face groove depth.

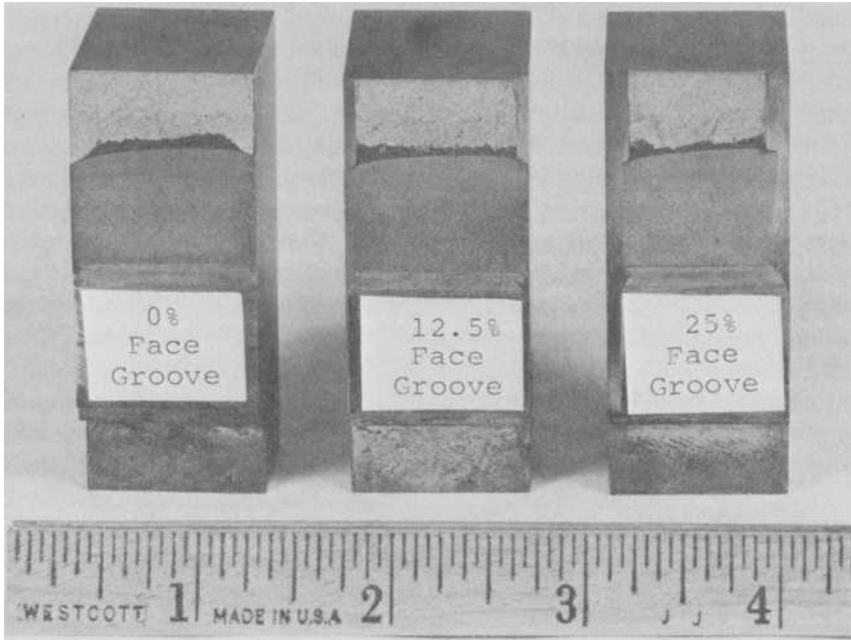


FIG. 8—Photograph of specimens ($a/w = 0.8$) after test showing type of crack extension related to face groove depth.

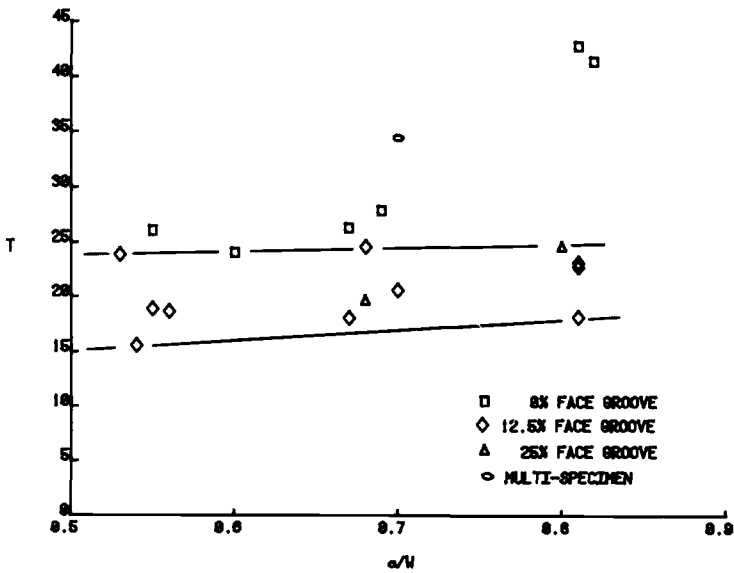


FIG. 9—Plot of tearing modulus versus crack length ratio for all specimens tested.

length. This suggests that a minimum value of the tearing modulus of HY-130 steel is reached with relatively shallow face grooves.

An interesting aspect of Fig. 10 is the position of the multispecimen data point obtained at a crack length of $0.7 a/w$. This data point falls in the band of nonface groove data showing increasing tearing modulus with crack length and is distinctly above results obtained with face grooved specimens where crack front curvature was eliminated. This suggests that the observed variation in tearing modulus results from the variation in crack front curvature and not in the different techniques of crack extension measurement. For this reason the tearing instability criteria must be related closely to the geometry of crack extension.

Conclusions

The following conclusions are drawn from the results of these tests:

1. J_{Ic} is independent of face groove geometry and crack length for the range of variables tested herein with HY-130 steel.
2. Face grooving of HY-130 steel to a total section reduction of 12.5 percent or greater produces a minimum tearing modulus when compared with other computer interactive unloading compliance test results and results from limited multispecimen tests.
3. The tearing modulus for nonface grooved specimens of this material decreases as crack length decreases apparently in response to the increase in constraint at the crack tip.
4. For 12.5 and 25 percent face grooved specimens, the tearing modulus remains constant as crack length increases at a value which coincides with the lowest value obtained with non-face grooved specimens.

The applicability of the tearing instability criterion as set out by Paris et al [2] depends in great part on the ability to extrapolate from simple laboratory specimens to a complex structure. The data presented herein suggest that the tearing modulus of a given material is dependent on the crack extension geometry when crack tunneling occurs. However, when crack tunneling is eliminated, the resulting tearing modulus is specimen geometry independent.

Acknowledgments

This task was supported by the U.S. Nuclear Regulatory Commission and the Naval Sea Systems Command.

References

- [1] Joyce, J. A. and Gudas, J. P. in *Elastic-Plastic Fracture*, ASTM STP 668, American Society for Testing and Materials, 1979, pp. 451-468.
- [2] Paris, P. C., Tada, H., Zahoor, A., and Ernst, H., "A Treatment of the Subject of

- Tearing Instability," NUREG Report No. 0311, U.S. Nuclear Regulatory Commission, Aug. 1977.
- [3] Landes, J. D. and Begley, J. A. in *Fracture Analysis*, ASTM STP 560, American Society for Testing and Materials, 1973, pp. 170-186.
 - [4] Merkle, J. G. and Corten, H. T., *Transactions*, American Society of Mechanical Engineers, Nov. 1974, pp. 286-292.
 - [5] Saxena, A. and Hudak, S. J., Jr., "Review and Extension of Compliance Information for Common Crack Growth Specimens," Paper 77-9E7-AFCGR-P1, Westinghouse Scientific, May 1973.

P. M. S. T. de Castro,¹ J. Spurrier,¹ and P. Hancock¹

An Experimental Study of the Crack Length/Specimen Width (a/W) Ratio Dependence of the Crack Opening Displacement (COD) Test Using Small-Scale Specimens

REFERENCE: de Castro, P. M. S. T., Spurrier, J., and Hancock, P., "An Experimental Study of the Crack Length/Specimen Width (a/W) Ratio Dependence of the Crack Opening Displacement (COD) Test Using Small-Scale Specimens," *Fracture Mechanics, ASTM STP 677*, C. W. Smith, Ed., American Society for Testing and Materials, 1979, pp. 486–497.

ABSTRACT: This work deals with the influence of the ratio crack length/specimen width (a/W) on crack opening displacement (COD) tests. A series of tests was performed on a weldable quality structural steel (50D, BS4360), where the ratio a/W was varied from about 0.2 to 0.8, keeping W constant. The influence of temperature was assessed by a series of tests at different temperatures over the range -90°C to room temperature.

It is concluded that critical COD, δ_c , is insensitive to a/W at low temperatures, but becomes dependent on a/W as temperatures approach the transition temperature. This behavior has been quantified and should be borne in mind in situations where the use of specimens with different a/W ratios is required.

The tests were instrumented with a clip gage at the crack mouth and a load point displacement transducer which enabled a relationship between COD and J to be determined.

KEY WORDS: mechanical properties, fracture tests, crack opening displacement (COD), J -integral, elastic plastic fracture, structural steels, fatigue (materials), crack propagation

Seventeen years ago Wells introduced crack opening displacement (COD) as a parameter to describe the capacity of material in the neighborhood of a crack tip to deform before crack growth [1].² Other

¹ Research Ph.D. student, teaching fellow, and professor of engineering metallurgy, respectively, Department of Materials, Cranfield Institute of Technology, Bedford MK43 0AL, United Kingdom.

² The italic numbers in brackets refer to the list of references appended to this paper.

concepts have been introduced meanwhile, giving alternative views on the yielding fracture problem, in particular the J-contour-integral approach introduced by Rice [2].

Both concepts have found application in engineering practice, although standard procedures for the characterization of fracture toughness by either method have still to be agreed upon. A draft for development on COD testing has been issued by the British Standards Institution [3], and the ASTM task group concerned with elastic plastic fracture is studying a recommended practice for J_{Ic} testing [4].

Specimen dimensions are important when determining fracture toughness parameters for structural steels. For a given temperature, there is, however, a value of fracture toughness, K_{Ic} , for which specimens must obey dimensional restrictions set in ASTM Test for Plane-Strain Fracture Toughness of Metallic Materials (E 399-76). For transitional and upper shelf behavior, the minimum thickness to be tested is frequently excessively large, and therefore, the use of J to obtain K_{Ic} from subsize specimens is particularly attractive. However, some geometric restrictions are also necessary for J testing [4].

Although COD measured at initiation of crack extension claims to be a material property, provided a minimum level of thickness is satisfied [5], no restrictions on specimen thickness have been agreed upon. The reason for this is that the practical usage of COD specifies that tests must be made on specimens which have the same thickness as the material of the structure under consideration.

Recently, interest has been shown in the effect of a/W ratio on fracture toughness. Different characterizing parameters have been analyzed, as for instance the nonlinear fracture toughness parameter, \tilde{G}_c , studied by Liebowitz and co-workers, which was shown to decrease with increasing a/W for two aluminum alloys [6]. Similarly, Chell et al [7] reported that both a fracture toughness analysis using a displacement curve fitting method, and J_c , showed that fracture toughness decreased with increasing crack lengths for a 1 percent CrMoV high temperature bolting steel.

As far as COD testing of structural steels is concerned, the influence of a/W ratio was studied by Ingham et al [8], who concluded that there appears to be no effect of this ratio on critical COD, but Kanazawa et al [9] found a decrease in critical COD with increase in a/W . However, their testing technique did not conform with current practice (BS DD 19), and therefore it was decided to explore this problem, carrying out on-load COD tests in three point bend specimens.

Experimental procedure

Material

The test material was obtained as a plate of 104 mm thickness to the BS4360 50D specification. The chemical composition is given in Table 1,

TABLE 1—Chemical composition of steel tested, weight percent.

Carbon	Manganese	Sulfur	Phosphorus	Silicon	Niobium	Aluminum	Titanium
0.110	1.360	<0.005	0.012	0.470	0.028	0.020	<0.010
	Vanadium	Nickel	Chromium	Molybdenum	Copper	Iron	
	<0.010	0.060	0.050	0.010	0.070	remainder	

and optical metallography indicated a fine grained, normalized structure with a low inclusion content.

Tension Tests

Tension tests of specimens cut from the rolling direction were made using Hounsfield No. 14 specimens, tested at 1.27 mm/min in a screw driven 45 kN capacity Instron testing machine, over a range of temperatures from -196°C to room temperature.

Fracture Toughness Tests

All fracture toughness tests were carried out on specimens of square cross section, $W = B = 18$ mm, which were fatigue precracked and tested in three-point bending, over a span of 72 mm.

Specimens were cut in the longitudinal direction, with a notch parallel to the plate surface and perpendicular to the rolling direction. A slit 0.15 mm wide and 3 mm deep was machined in all specimens, except those intended to have a final a/W ratio less than 0.3, where a slit depth of 2 mm was used. Fatigue precracking was carried out at stress intensity $K < 22 \text{ MNm}^{-3/2}$ up to a range of final crack lengths. Some of the specimens with higher a/W ratios were obtained by machining specimens to final size after pre-fatiguing larger specimens.

COD was monitored through a double cantilever clip gage located between knife edges screwed on the notch face of the specimen. An autographic plot of the load versus gage displacement was obtained on an XY recorder.

Specimens were also instrumented with a linear transducer mounted to measure load versus load point displacement for J measurement, following a technique similar to that introduced by Dawes [10]. This transducer measured the vertical displacement of the notch mouth relative to a reference bar which rested on pins introduced at the ends of the specimen loading span, $0.55(W-a)$ from the back face. Load versus load point displacement was recorded on a separate X-Y recorder.

The tests were carried out using an Instron testing machine at a crosshead speed of 1.27 mm/min. The specimens were cooled by total immersion in methanol maintained at the desired temperature by direct additions of liquid nitrogen. For a few tests carried out at temperatures lower than -90°C , methylated spirits were used instead of methanol.

The cooling medium was stirred constantly and temperature was monitored by a thermometer in the cooling medium, as well as by a chromel alumel thermocouple spot welded to the side of the specimen within a few millimetres of the crack tip.

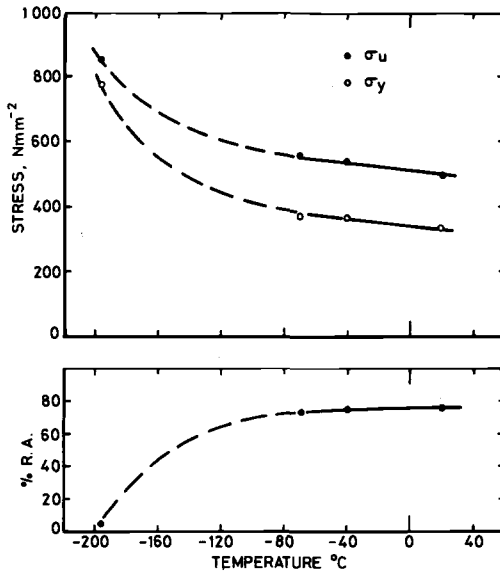


FIG. 1—Ultimate tensile strength σ_u , yield stress σ_y and percentage reduction of area for 50 D steel as function of temperature.

Results

Tension tests were made over a range of temperatures and the results are presented in Fig. 1.

Initial fracture toughness tests were made on specimens within the standard geometry following BS DD 19, that is, $0.25 < a/W < 0.35$ for square cross section specimens.

Results were calculated using the relation

$$\delta = \frac{V_g}{1 + \frac{1}{r} \left(\frac{a + z}{W - a} \right)} \tag{1}$$

where

- δ = crack opening displacement,
- V_g = clip gage measurement,
- z = knife edge height, and
- r = rotational factor,

for which the value of $r = 1/3$ was adopted, as suggested by Ingham et al [8]. Results are presented in Fig. 2. It should be noted that values plotted for temperatures below -60°C correspond to sudden unstable

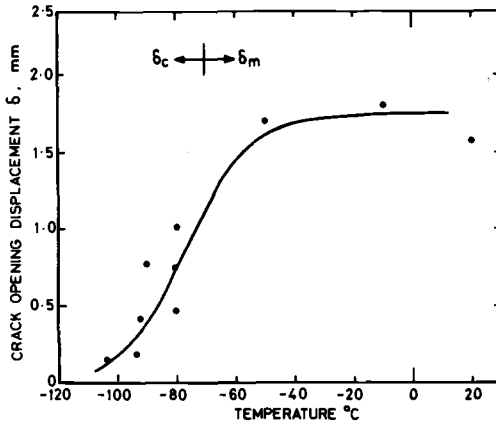


FIG. 2—Critical COD for sudden crack propagation, δ_c , and maximum load COD, δ_m , as function of temperature (specimens with $a/W = 0.3 \pm 0.05$).

fractures under rising load conditions, whereas those for higher temperatures correspond to maximum load condition, which was clearly preceded by stable crack growth. An interpretation of the significance of these last data points will be discussed later in this paper.

Subsequent tests with values of a/W ranging from approximately 0.2 to 0.8 were carried out at a temperature of -80°C , which is close to the transition temperature estimated at -75°C . A large number of tests were performed at this temperature, since it was considered that this would be necessary if any trend was to be noticed because of the scatter expected from tests in the transition region as discussed by Burdekin [11]. Results obtained using Eq 1 are presented in Fig. 3.

Results obtained at a lower temperature, -90°C , slightly above the

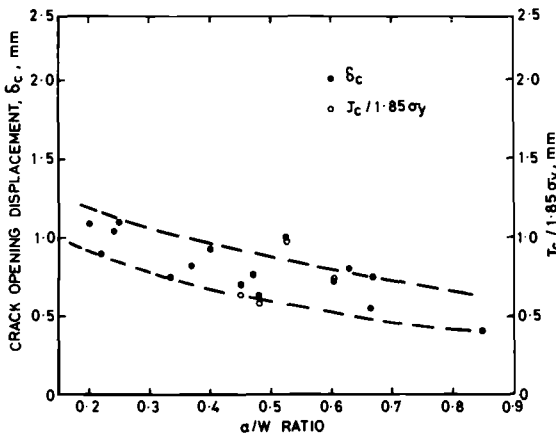


FIG. 3—Fracture toughness results at -80°C .

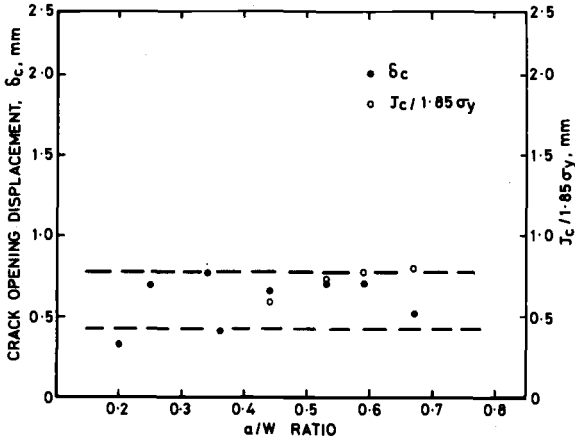


FIG. 4—Fracture toughness results at -90°C .

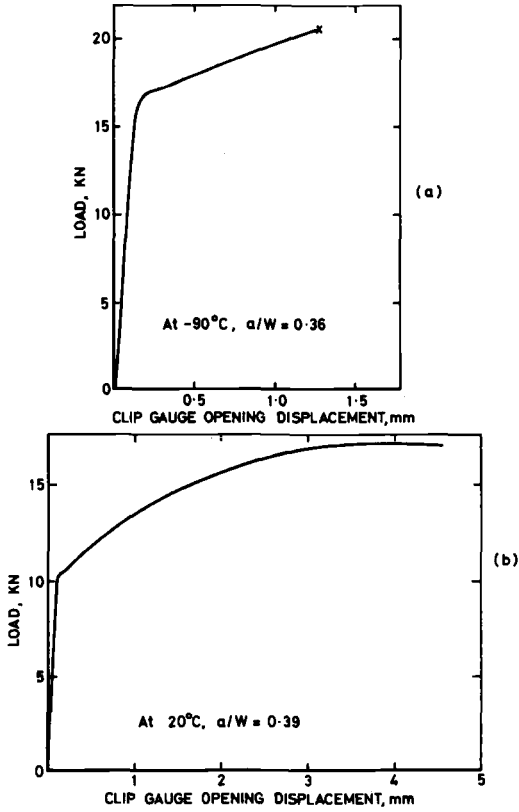


FIG. 5—Typical load versus clip gage displacement traces.

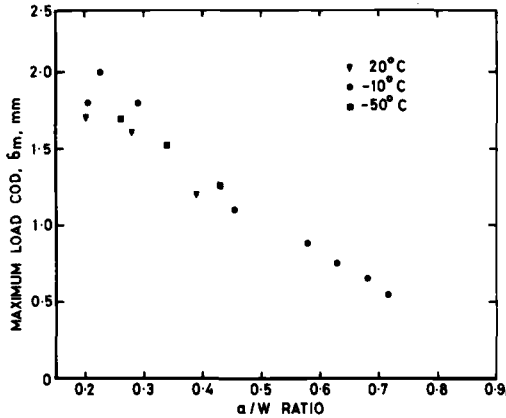


FIG. 6—Maximum load COD results.

lower shelf regime for this material, are presented in Fig. 4. All results in Figs. 3 and 4 correspond to sudden unstable crack propagation, attained under rising load. The fracture surfaces were essentially flat with small shear lips and showed no evidence of stable ductile tearing before fast fracture. A typical load versus clip gage displacement trace is shown in Fig. 5a.

Maximum load COD results for an upper shelf temperature, -10°C , with a range of a/W values are represented in Fig. 6, together with a few results obtained at -50°C and room temperature, 20°C . These followed essentially the same pattern as those for -10°C . These upper shelf results were obtained using the value of the fatigue crack length in Eq 1. A typical load versus clip gage displacement is shown in Fig. 5b.

Finally, the load versus load point displacement traces for specimens tested at -80 and -90°C , with a/W values between 0.4 and 0.7 were used to get J_c from the equation (Ref 4)

$$J = \frac{2A}{B(W - a)} \quad (2)$$

where A is the area under the load versus load point displacement curve, in units of energy. Results are presented in Table 2.

Discussion

The use of Eq 1 to calculate values of crack opening displacement is supported by findings of Ingham et al [8], whose evidence suggest that the rotational factor r is not affected by a/W , at least in the range from about 0.2 to 0.5.

Tests where failure occurred by sudden unstable crack propagation,

TABLE 2— J_c Results.

At -90°C			At -80°C		
a/W	Fracture Load	J_c	a/W	Fracture Load	J_c
	N	MNm^{-1}		N	MNm^{-1}
0.44	18 860	0.44	0.45	15 790	0.46
0.53	13 450	0.55	0.48	14 900	0.42
0.59	10 770	0.59	0.53	12 550	0.71
0.67	9 120	0.61	0.60	8 450	0.53

that is, at temperatures of -80 and -90°C , are represented in Figs. 3 and 4. This type of result is important, for recent studies of a standard fracture assessment route for weld structures by the British Standards Institution (BSI) and the Institut International de Soudure (IIS/IIW) recommend use of the COD approach for this type of fracture behavior [12,13].

There appears to be no effect of the value of a/W ratio on COD for the tests performed at -90°C . However, there is an effect for the tests performed at a higher temperature, -80°C , as shown in Fig. 3, where a decrease of COD with the increase of a/W is apparent.

Recent work by Dawes [10], using specimens with a/W ratios of 0.2 and 0.5, also shows the trend that was detected here for a larger range of a/W values. This behavior is also similar to that detected for other toughness parameters [6,7], as reviewed earlier.

J_c estimates are presented (Table 2) for some tests on specimens with a/W values between 0.4 and 0.7, where use of Eq 2 is valid, as shown by Sumpter and Turner [14]. Each value of J_c was obtained directly from one load versus load point displacement trace, without recourse to the resistance curve technique [4], since fracture was not preceded by slow crack growth in these tests.

Using the mean value of J_c for specimens tested at -90°C and at -80°C , and the corresponding standard COD results, that is, those obtained with $a/W = 0.3 \pm 0.05$, the relationship

$$J_c = m \sigma_y \delta_c \quad (3)$$

was satisfied with $m = 2.2$ at -90°C and $m = 1.5$ at -80°C , in agreement with recent results by Dawes [10], for BS4360, grade 50C steel, which fall into a scatter band bounded by 1.5 and 2.2.

Using the mean value of m (1.85), the present J_c results are plotted as $J_c/m\sigma_y$ on Figs. 3 and 4, in order to enable a direct comparison with the results obtained for crack opening displacement.

It should be noticed that although no limitations have been prescribed

for COD testing other than testing specimens of thickness equal to the structural application, restrictions have been suggested for J_{Ic} testing [4],

$$B, W - a > 25 J / [(\sigma_y + \sigma_u) / 2] \quad (4)$$

These can be expressed, using Eq 3

$$B, W - a > 25 m \delta \sigma_y / [(\sigma_y + \sigma_u) / 2] \quad (5)$$

which requires specimens of thickness greater than about 23 mm at -90°C and larger dimensions at higher temperatures. The use of thinner material is common in many structural engineering applications and therefore tests were carried out with 18 mm thickness throughout, although this does not satisfy Eq 5.

Turning to the results for upper shelf behavior, it should be noticed that all results in Fig. 6 correspond to first attainment of maximum load, and slow stable crack growth was found in all specimens.

Estimates of COD at stable crack initiation could be made but it is widely recognized that such a parameter would be unduly conservative for design purposes [10]. COD at maximum load, δ_m , may be difficult to defend from many aspects but it is used frequently for purposes of material comparison. However, great care must be taken when comparing specimens of different geometries for the present results show a marked dependence of δ_m on a/W , δ_m decreasing with the increase in a/W .

No J determination was attempted with the load versus load point displacement curves for these tests, since the usual resistance curve procedure [4] is not applicable under the present circumstances where all specimens were tested up to maximum load.

Finally, the slopes of a linear regression carried out on the data presented in Figs. 3, 4, and 6 are represented as a function of temperature in Fig. 7. It is suggested that for a given geometry, at sufficiently low temperatures, there is no effect of a/W ratio on COD; there is an

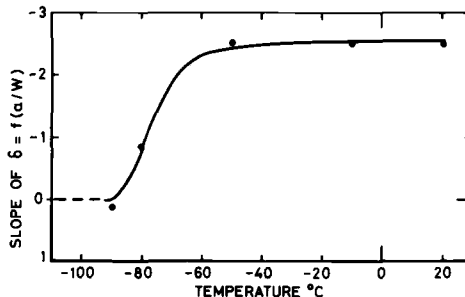


FIG. 7—Slope of COD dependence on a/W ratio.

increasing dependence of COD on a/W in the transition temperature region, and finally a constant dependence at upper shelf temperatures.

Conclusions

1. The forthcoming inclusion of the COD approach in fracture assessment standards, either in the United Kingdom (BSI) or at an international level (IIS/IIW), requires careful consideration. Specimen geometry dependence of fracture toughness is a factor that must not be overlooked.

2. It is shown that δ_c decreases with increasing a/W for temperatures near the transition temperature, and is insensitive to a/W at lower temperatures.

3. At upper shelf temperatures, where some stable crack growth occurs, δ_m presents a rather marked dependence on a/W .

4. A relationship between δ_c and J_c of the type $J_c = m\sigma_y\delta_c$ was satisfied with a mean value of $m = 1.85$ at temperatures of -80 and -90°C .

Acknowledgments

One of the authors, P. M. S. T. de Castro, wishes to acknowledge financial support received from the Calouste Gulbenkian Foundation, Lisbon, and the leave of absence for research in Cranfield granted by Faculdade de Engenharia da Universidade do Porto, Portugal.

References

- [1] Wells, A. A., "Unstable Crack Propagation in Metals—Cleavage and Fast Fracture," *Proceedings, Crack Propagation Symposium*, Vol. 1, Cranfield, 1961.
- [2] Rice, J. R., *Journal of Applied Mechanics*, 1968, p. 379.
- [3] British Standards Institution, draft for development, "Methods for Crack Opening Displacement (COD) Testing," BS DD 19, 1972.
- [4] ASTM Committee E-24 task group E 24.01.09, "Recommended Procedure for J_{Ic} Determination," task group meeting in Norfolk, Va, March 1977.
- [5] Smith, R. F. and Knott, A. F., "Crack Opening Displacement and Fibrous Fracture in Mild Steel," Conference on Practical Application of Fracture Mechanics to Pressure Vessel Technology, Institution of Mechanical Engineering, 1971, p. 65.
- [6] Liebowitz, H., Jones, D. L., and Poulouse, P. K. in *Prospects of Fracture Mechanics*, G. C. Sih et al, Eds., Noordhoff International Publishing, Leyden, The Netherlands, 1974, p. 103.
- [7] Chell, G. G. and Davidson, A., *Materials Science and Engineering*, Vol. 24, 1976, p. 45.
- [8] Ingham, T., Egan, G. R., Elliot, D., and Harrison, T. C., "The Effect of Geometry on the Interpretation of COD Test Data," Conference on Practical Application of Fracture Mechanics to Pressure Vessel Technology, Institution of Mechanical Engineering, 1971, p. 200.
- [9] Kanazawa, T., Machida, S., Momota, S., and Hagiwara, Y., "A Study of the COD Concept for Brittle Fracture Initiation," *Fracture 1969*, 2nd International Conference on Fracture, Brighton, Chapman and Hall, 1969, p. 1.
- [10] Dawes, M. G., "Elastic Plastic Fracture Toughness Based on the COD and J-Integral Concepts," presented at the ASTM Symposium on Elastic Plastic Fracture, Atlanta, Nov. 1977.
- [11] Burdekin, F. M. in *Practical Fracture Mechanics for Structural Steel*, UKAEA and Chapman and Hall, Risle, 1969, p. C1.

- [12] British Standards Institution, draft rules for the derivation of acceptance levels for defects in fusion welded joints, BSI WEE/37, Doc. 75/77081 DC, Feb. 1976.
- [13] Doc. IIS/IIW-471-74 "Proposed Assessment Methods for Flaws with Respect to Failure by Brittle Fracture," *Welding in the World*, Vol. 13, (1/2), 1975, p. 30.
- [14] Sumpter, J. D. G. and Turner, C. E. in *Cracks and Fracture*, ASTM STP 601, American Society for Testing and Materials, 1976, p. 3.

S. Mall,¹ A. S. Kobayashi,² and Y. Urabe³

Dynamic Photoelastic and Dynamic Finite Element Analyses of Polycarbonate Dynamic Tear Test Specimens

REFERENCE: Mall, S., Kobayashi, A. S., and Urabe, Y., "Dynamic Photoelastic and Dynamic Finite Element Analyses of Polycarbonate Dynamic Tear Test Specimens," *Fracture Mechanics, ASTM STP 677*, C. W. Smith, Ed., American Society for Testing and Materials, 1979, pp. 498-510.

ABSTRACT: Dynamic photoelasticity and dynamic finite element methods were used to study dynamic responses of dynamic tear test (DTT) specimens of a ductile material, that is, 3.2-mm (1/8-in.) thick polycarbonate sheets. Dynamic photoelastic patterns before and after the onset of unstable fracture showed that the dynamic fracture initiation toughness, K_{Id} , was attained during the second maximum load in the hammer load-time history and was approximately 65 percent of the fracture toughness, K_{Ic} . Also, dynamic stress intensity factors before and after crack propagation computed by dynamic finite element method using experimentally determined hammer load-time history were in reasonable agreement with those obtained from dynamic photoelasticity. The dynamic finite element analysis also showed that the dynamic fracture initiation toughness could be determined from the dynamic strain response of a strain gage located near the crack tip in conjunction with a simple static analysis.

KEY WORDS: crack propagation, dynamic fracture, dynamic photoelasticity, dynamic finite element analysis, dynamic fracture toughness, crack arrest

In a separate paper, dynamic photoelastic and dynamic finite element analyses were used to study the dynamic fracture response of dynamic tear test (DTT) specimens machined from a brittle photoelastic polymer, that is 9.5 mm (3/8 in.) thick Homalite-100 plates [1].⁴ The main objective of developing a DTT specimen is to assess the brittle fracture response of a ductile material without requiring excessive specimen thickness or side

¹ Assistant professor, Department of Mechanical Engineering, University of Maine, Orono, Me. 04473.

² Professor, Department of Mechanical Engineering, University of Washington, Seattle, Wash. 98195.

³ Research engineer, Takasago Technical Institute, Mitsubishi Heavy Industries, Takasago, Japan.

⁴ The italic numbers in brackets refer to the list of references appended to this paper.

grooving of the specimen. The DTT specimen is described in Ref 2, ASTM Test for Plane Strain Fracture Toughness of Metallic Materials (E 399-74), and Method for 5/8 In. Dynamic Tear Testing of Metallic Materials (MIL-STD-1601). It stands to reason that similar dynamic photoelastic and dynamic finite element analyses should be conducted on a ductile photoelastic material where dynamic fracture responses different from those of the brittle Homalite-100 plates could be expected.

One such photoelastic material which is suitably transparent, ductile, and relatively strain-rate insensitive is polycarbonate which has been used as a photoelastic-plastic model material by a number of investigators [3,4]. Polycarbonate flows under high stress, has a well-defined yield point of about 62 MPa (9000 psi) and exhibits a tensile instability phenomenon with accompanying Lueder's band. Although valid plane strain fracture toughness of this material is difficult to establish, it does exhibit cleavage fracture under high rate of loading and thus qualitatively models static and dynamic fracture of structural steel. As a result, polycarbonate sheets were used for dynamic photoelastic studies of DTT specimens in this investigation. In the following, the results of such dynamic photoelasticity and associated dynamic finite element analyses will be described.

Since a brief literature review on fracture toughness testing using DTT specimens as well as a review on the past dynamic photoelastic analysis of DTT specimens can be found in Ref 1, this paper will emphasize the experimental and numerical results of the polycarbonate DTT specimens. For more extensive discussion on the DTT specimen developed at the Naval Research Laboratory, see Refs 5, 6, and 7.

Polycarbonate DTT Specimen

The dynamic photoelasticity system and associated instrumentation are identical to those described in Ref 1. Figure 1 shows the drop weight tup and the four-arm strain gage bridge which was used to monitor the dynamic loading applied to the polycarbonate DTT specimen. The photoelastic model was identical in geometry to a standard 16-mm (3/8-in.) DTT specimen (MIL-STD-1601) except for its smaller thickness of 3.2 mm (7/8 in.) as shown in Fig. 1. Although a thicker polycarbonate sheet would have been preferred for simulating the plane strain state of stress in steel DTT specimens, the exceptionally high birefringence of polycarbonate resulted in crowding of isochromatic fringes in the vicinity of the crack tip and thus thinner specimens had to be used. From trial and error, the 3.2-mm (1/8-in.) thick polycarbonate was found to have the necessary optical sensitivity without buckling under the impact loading condition. Static fracture toughness tests of single-edged notch and compact tension specimens of this thin polycarbonate sheet showed significant plastic deformation and 100 percent shear lip in static fracture but a full thickness

cleavage fracture was observed in DTT specimen under dynamic loading condition.

In the as-received condition, the polycarbonate sheet exhibited considerable residual stress distribution and thus the sheets were annealed after rough cutting. This annealing caused some distortion and shrinkage and thus the rough cut was made 25 mm (1 in.) over the actual specimen size. The annealing procedure consisted of overnight heating at 160°C, followed by a gradual cooling at the rate of 5°C/h. During annealing, the polycarbonate sheet was tilted to about 5 deg over a glass sheet to prevent bubble formation between support glass and polycarbonate sheets. The starter crack consists of a 0.4 mm (0.02 in.) wide edge crack of 25 mm (1 in.) length which was sawed and fatigued at an applied stress intensity factor of approximately 10 percent of its pop-in fracture toughness, K_{Ic} .

Static and dynamic material calibration tests were carried out to determine the material stress-optic coefficient, modulus of elasticity, and Poisson's ratio at various strain rates. A split Hopkinson bar system [8] with test bars of 3.2 by 9.5 by 254 mm ($\frac{1}{8}$ by $\frac{3}{8}$ by 10 in.) and 3.2 by 9.5 by 381 mm ($\frac{1}{8}$ by $\frac{3}{8}$ by 15 in.) was used for dynamic calibration. Results of these dynamic and static material properties are given in Table 1.

A valid plane strain fracture toughness could not be obtained in this thin sheet of polycarbonate since compact tension specimens with fatigued cracks exhibited ductile failure with gross yielding and necking. A fracture toughness associated with the pop-in mode of polycarbonate was thus used following the procedure described in ASTM E 399-74 for a compact tension specimen with crack length of 19.1 mm ($\frac{3}{4}$ in.). Since the transparency of polycarbonate allowed observation of slow crack extension as well as pop-in crack extension during loading, a very small pop-in mode could be observed and the corresponding critical load was used to

TABLE 1—Average mechanical and optical properties of polycarbonate.

E_S , GPa (ksi) ^a	2.38 (345)
E_D , GPa (ksi) ^b	2.72 (395)
ν_S^c	0.36
ν_D	0.36
f_σ , MPa · mm/fringe (psi · in./fringe) ^c	6.7 (38)
$f_{\sigma D}$, MPa · mm/fringe (psi · in./fringe)	7.2 (41)
ρ kg · s ² /m ⁴ (lb · s ² /in. ⁴) ^c	22 (0.000112)
c_1 , m/s (in./s) ^d	1960 (77 000)
c_2 , m/s (in./s) ^d	910 (36 000)
c_p , m/s (in./s) ^d	1620 (63 600)
K_{Ic} , kPa \sqrt{m} (psi $\sqrt{in.}$) ^e	3430 (3 120)

^a Subscript *S* is for static properties. Average strain rate was 1.8×10^{-3} strain/s.

^b Subscript *D* is for dynamic properties. Average strain rate was 60 strain/s.

^c E , ν , f_σ , and ρ are modulus of elasticity, Poisson's ratio, material stress-optic coefficient, and density, respectively,

^d c_1 , c_2 , and c_p are dilatational, distortional, and plate wave velocity, respectively.

^e Fracture toughness associated with pop-in mode.

determine fracture toughness associated with this pop-in mode of crack extension using the expression given in ASTM Method E 399. Results of this pop-in fracture toughness are also given in Table 1. Parvin and Williams [9] reported pop-in fracture toughness of $4 \text{ MPa}\sqrt{\text{m}}$ ($3640 \text{ psi}\sqrt{\text{in.}}$) and a crack initiation fracture toughness of $2.24 \text{ MPa}\sqrt{\text{m}}$ ($2040 \text{ psi}\sqrt{\text{in.}}$) for their single-edged notch and surface notch specimens of 3 mm (0.12 in.) and 5 mm (0.2 in.) thick polycarbonate specimens. The latter initiation fracture toughness was related to the curved crack front which occurred before pop-in fracture. No such phenomenon was observed in the pop-in failure mode of the compact tension specimen used in this analysis.

Dynamic Finite Element Analysis

The dynamic finite element algorithm used in this investigation is identical to that described in Ref 10. Figure 1 also shows the finite element breakdown used in the plane stress analysis which was considered more appropriate from the theory of dynamic elasticity due to the thinness of the specimen, despite the cleavage fracture surface, which normally is associated with plane strain fracture, observed in DTT experiments.

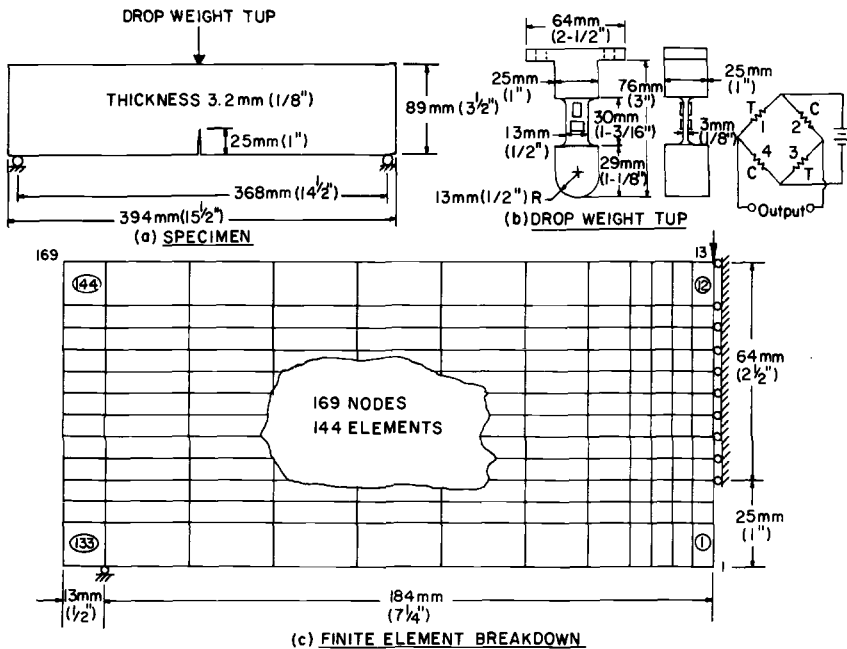


FIG. 1—Dynamic tear test (DTT) specimen.

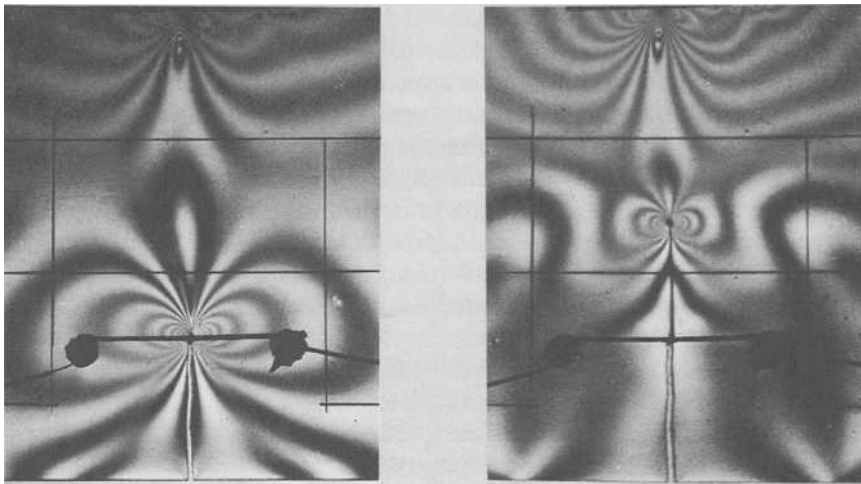
(a) 6TH FRAME 126 μ SECONDS(b) 12TH FRAME 282 μ SECONDS

FIG. 2—Typical dynamic photoelastic patterns in polycarbonate DTT specimen No. S101276-P.

Dynamic Photoelastic Results

As shown in Fig. 2, the dynamic photoelastic patterns of polycarbonate DTT specimens showed a small caustic which for this ductile polycarbonate sheet could be considered the upper bound of a plastic zone of $r_p = 0.13$ to 0.38 mm (0.005 to 0.015 in.) preceding the running crack tip. This upper bound of the plastic zone, however, was not large enough to require an elastoplastic analysis for the data reduction in the isochromatic fringe values. The small dynamic plastic zone was in contrast to the significant net section yield and shear lip formation under static loading of polycarbonate compact specimens.

The dynamic stress intensity factor was determined from the dynamic isochromatics by using Bradley's method [8]. Figure 3 shows experimental data of dynamic stress intensity factor just prior to and after crack initiation as the crack propagated in seven polycarbonate DTT specimens with initially fatigued notch. A and b in this figure as well as subsequent figures refer to the crack length and specimen height, respectively. A reasonably interpolated dynamic initiation fracture toughness, K_{I_d} , from these experimental data would be $2.3 \text{ MPa}\sqrt{\text{m}}$ ($2100 \text{ psi}\sqrt{\text{in.}}$) with time to failure of about $1000 \mu\text{s}$. This K_{I_d} value is approximately 65 percent of the pop-in static fracture toughness of $3.43 \text{ MPa}\sqrt{\text{m}}$ ($3120 \text{ psi}\sqrt{\text{in.}}$) described previously.

Figure 3 also shows that the dynamic fracture toughness (dynamic stress intensity factor), K_{I_d} , decreased as the crack propagated in

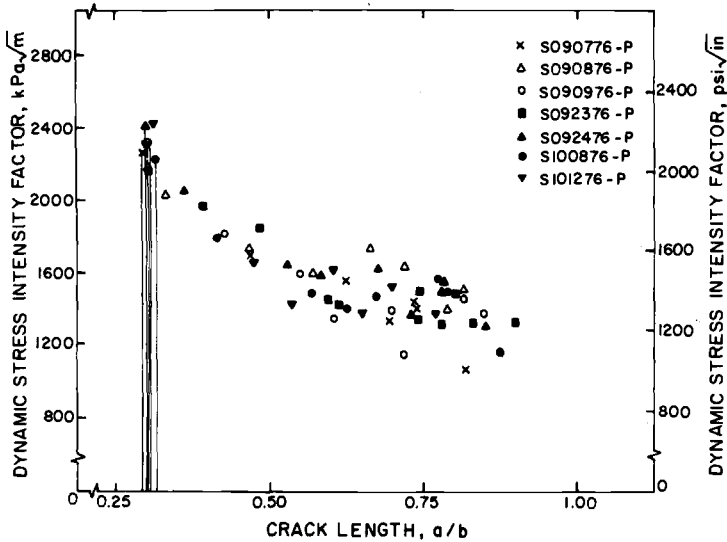


FIG. 3—Measured dynamic stress intensity factors before and after crack initiation in seven polycarbonate DTT specimens.

polycarbonate DTT specimen and is different from its counterpart of Homalite-100 DTT specimens which exhibited a maximum value in K_{Ia} after crack propagation. Furthermore, Fig. 3 shows increased fluctuations in K_{Ia} as the crack propagated deeply in the initially compressive zone where K_{Ia} decreased to about 50 percent of K_{Ia} . This result indicates that should a minimum resistance to dynamic crack propagation, K_{Im} , exist,

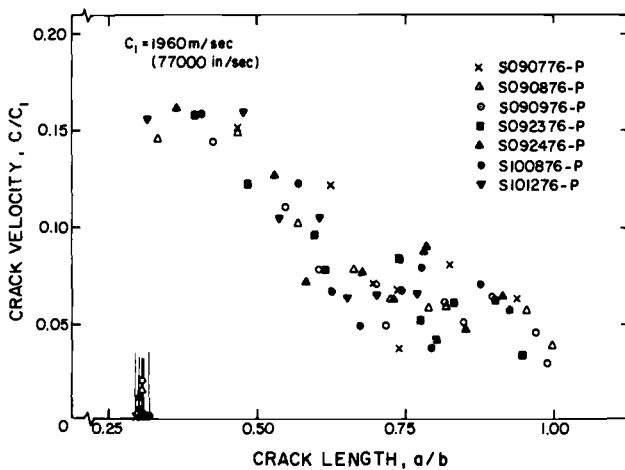


FIG. 4—Crack velocities in seven polycarbonate DTT specimens.

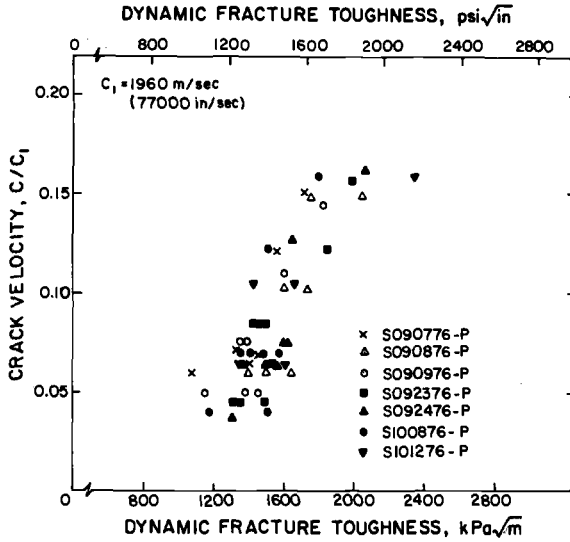


FIG. 5—Crack velocity versus dynamic fracture toughness relation of polycarbonate DTT specimens.

such K_{Im} would be considerably different from the fracture toughness, K_{Ic} , of this material.

All crack velocity data as a function of the specimen width are shown in Fig. 4. The crack velocity decreased during the first 60 percent of the specimen width and then remained nearly constant for the remaining

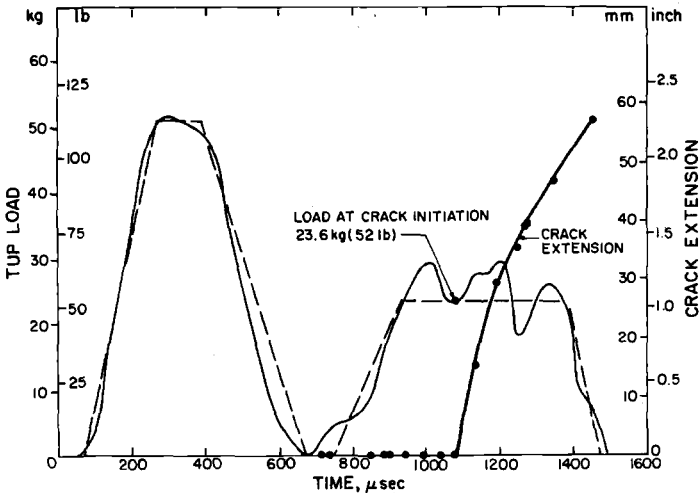


FIG. 6—Measured tup load-time history with idealized load-time curve for numerical analysis and crack extension versus time relation in DTT test No. S090776-P.

width of the specimen. This variation in crack velocity in polycarbonate DTT specimens was different from that in Homalite-100 DTT specimens, where the crack velocity precipitously dropped at about 75 percent of the DTT specimen width. Crack velocity in the initially compressive zone of the polycarbonate DTT specimen was comparatively higher than its counterpart in Homalite-100 DTT specimen and the crack curved slightly at about 50 percent of width. In contrast, sharp crack curving was observed as the crack propagated near the impact point in the Homalite-100 DTT specimens.

Figure 5 shows the dynamic fracture toughness, K_{Ic} , versus crack velocity of ductile polycarbonate specimen. The noticeable scatter in data could be due in part to the stress wave effects during dynamic loading. Although one can construct an averaged dynamic fracture toughness versus crack velocity relation of the proposed Γ -shape, such average curve was not fitted in due to large scatter of data in the present analysis even after discarding the extremely low K_{Ic} values recorded at the region's deepest crack penetration in Figs. 3 and 4.

Results of Dynamic Finite Element Analysis

Figures 6 and 7 show recorded impact load-time history for two polycarbonate specimens Nos. S090776-P and S100876-P. This impact load-time history was estimated from signals of a strain gage bridge placed 50 mm (2 in.) above the tup and should be considered only as an

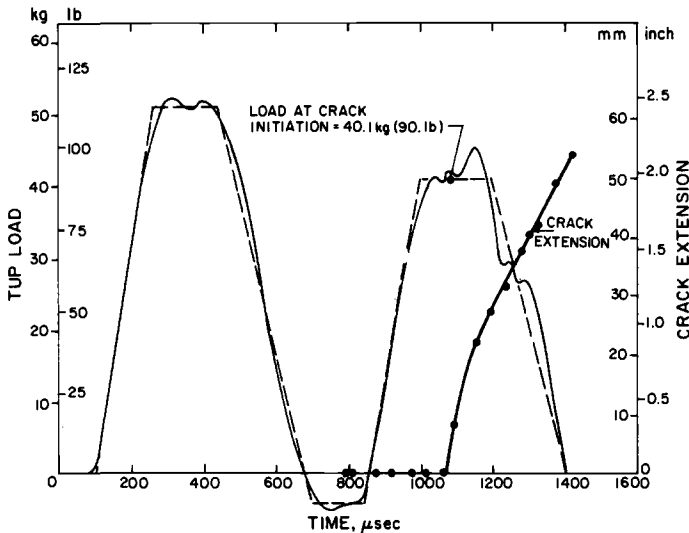


FIG. 7—Measured tup load-time history with idealized load-time curve for numerical analysis and crack extension versus time relation in DTT test No. S100876-P.

approximation of the true load-time history seen by the DTT specimen. In retrospect, a more precise measurement of the impact load could have been obtained by placing a piezo-electric transducer between the tup and the DTT specimen. For dynamic finite element analysis, the estimated load-time traces were idealized with straight line segments as shown in these two figures. In addition, the load-time trace was retarded $10 \mu\text{s}$ to account for the stress wave propagation from the average strain gage location to the tup tip. Crack-tip position as a function of time along with the interpolated crack initiation time are also shown in Figs. 6 and 7 for these two specimens.

Figures 8 and 9 show the dynamic stress intensity factor obtained from dynamic photoelasticity and dynamic finite element analysis of polycarbonate DTT specimen Nos. S090776-P and S100876-P. The large discrepancies between the measured and-calculated dynamic stress intensity factors could be attributed to the not-so-precise determination of the load-time histories as well as the unknown magnitude of viscous damping in the elastodynamic numerical analysis of polycarbonate specimens. Obviously a fine tuning of the impact load history would have reduced the discrepancies but limited computer resources precluded such additional effort.

Figures 10 and 11 show the development of numerical dynamic stress intensity factors from the start of impact to crack initiation in the two DTT specimen Nos. S090776-P and S100876-P. The experimental dynamic stress intensity factor along with computed dynamic stress intensity factor obtained at two locations in the crack tip region as per Loss' procedure [2] are also shown. Fair agreement was found between the experimental and numerical dynamic stress intensity factor.

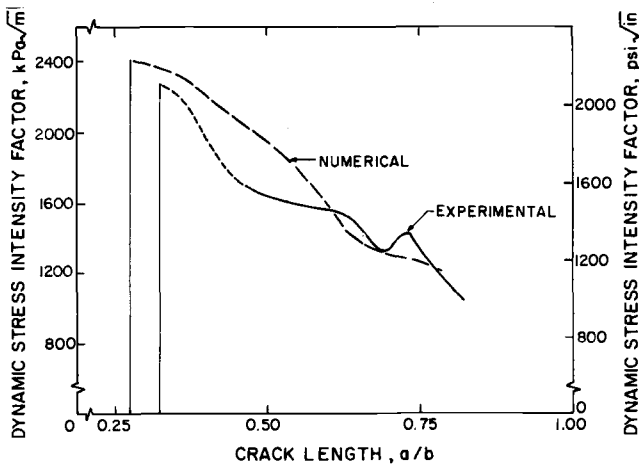


FIG. 8—Dynamic stress intensity factors in DTT test No. S090776-P.

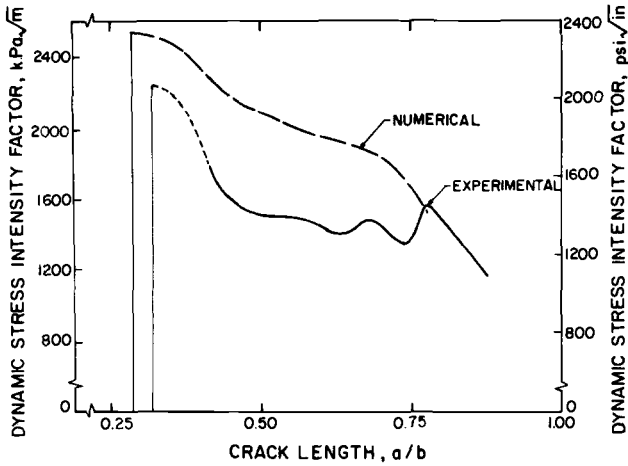


FIG. 9—Dynamic stress intensity factors in DTT test No. S100876-P.

The computed K_{Id} from the dynamic strains at two locations near the crack tip in accordance with Loss' procedure [2] is in excellent agreement with the K_{Id} obtained directly from dynamic finite element analysis. Furthermore, comparisons of Figs. 9 and 10 of polycarbonate DTT specimens with corresponding results for DTT specimens of Homalite-100 [1] show that the strain gage location near the crack tip for computing

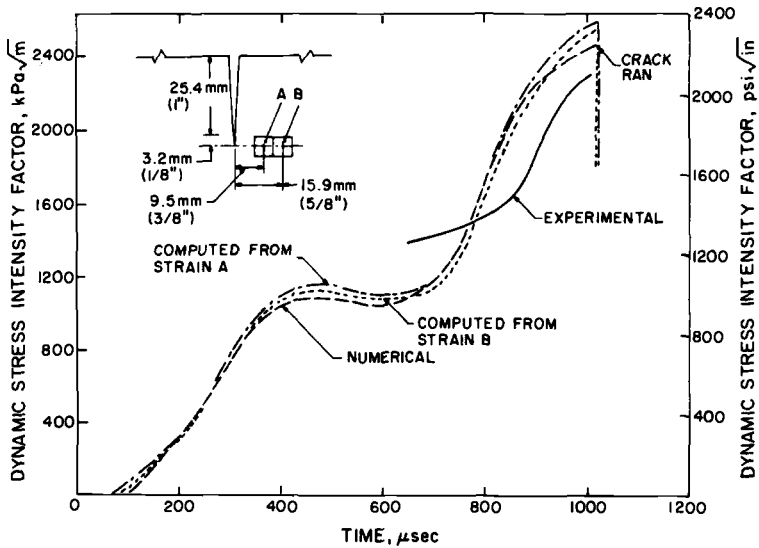


FIG. 10—Dynamic stress intensity factor from start of impact to crack initiation in DTT test No. S090776-P.

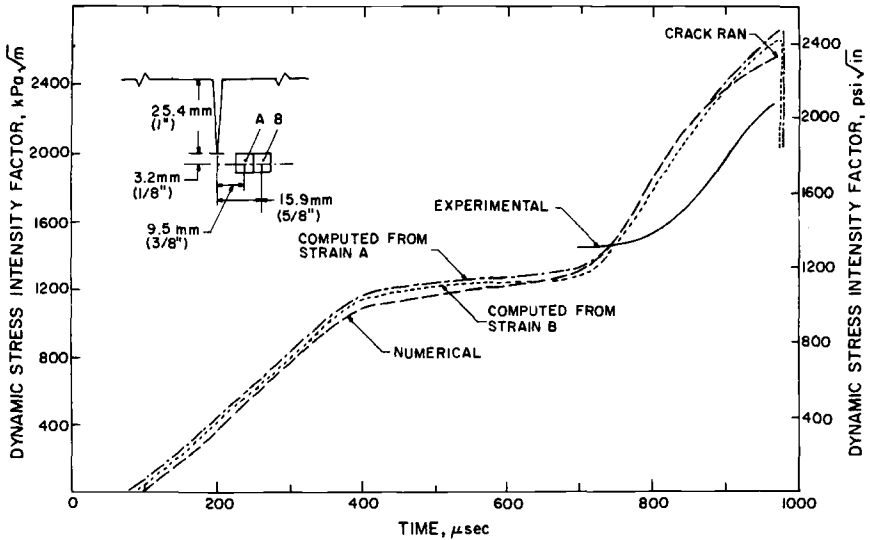


FIG. 11—Dynamic stress intensity factor from start of impact to crack initiation in DTT test No. S100876-P.

K_{Ia} by Loss' procedure would be almost the same in both the ductile polycarbonate and the brittle Homalite-100 specimen in spite of the difference in thickness, material properties, impact load-time history, and more importantly, the crack initiation time after impact.

Discussion

The primary objective of dynamic tear test (DTT) and other impact tests such as Charpy and Izod impact tests is the determination of the total energy absorbed to fracture the specimen. In the latter two impact tests, unlike the DTT results, the energy absorbed up to fracture initiation cannot be measured directly. As a result, the total work done to the specimen has been used to qualitatively characterize the fracture resistance of Charpy and Izod impact specimens. In order to provide further insight into the distribution of various energies in Charpy and Izod specimens, the computed values of external work, total strain energy, total kinetic energy, and fracture energy for the two DTT specimens Nos. S090776-P and S100876-P are plotted in Figs. 12 and 13. These figures show that kinetic and fracture energies, at times close to complete crack penetrations, of the two polycarbonate DTT specimens are 50 to 65 percent and 25 to 35 percent of the external works. The unusually high amount of total kinetic energy towards the completion of a dynamic tear test thus casts doubts on the significance of the total external work as a measure of fracture resistance of ductile material.

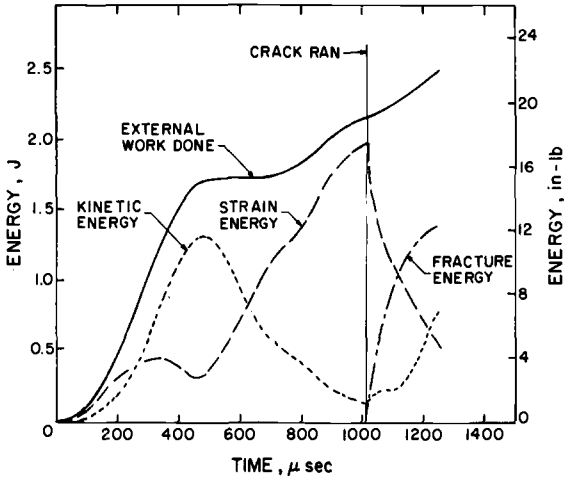


FIG. 12—Computed energies in DTT test No. S090776-P.

Conclusions

1. Dynamic fracture toughness at the onset of fracture, K_{Id} , of polycarbonate DTT specimens was about 65 percent of K_{Ic} associated with pop-in.
2. Dynamic fracture toughness, K_{ID} , during crack propagation in the polycarbonate DTT specimens decreased to about 50 percent of K_{Ic} .
3. Dynamic stress intensity factors determined from dynamic finite

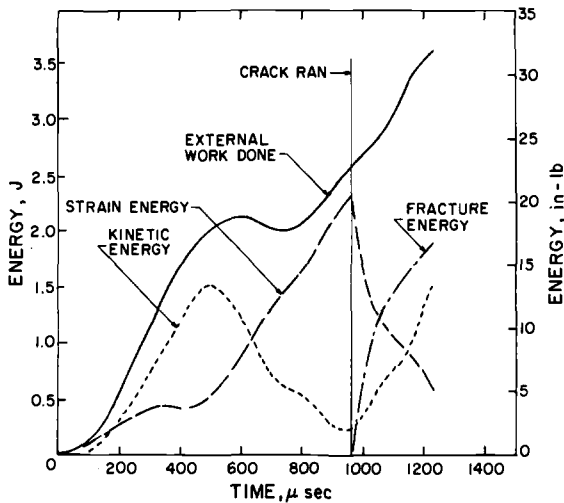


FIG. 13—Computed energies in DTT test No. S100876-P.

element agreement with each other and in reasonable agreement with the dynamic photoelasticity results.

4. The total kinetic energy represents a significant portion of the total external work at the completion of a DTT test of a ductile specimen.

Acknowledgments

The results of this investigation were obtained in a research contract funded by the Office of Naval Research (ONR) under Contract No. N00014-76-C-0600 NR064-478. The authors wish to acknowledge the support and encouragement of N. Perrone and N. Basdagas of ONR during the course of this investigation.

References

- [1] Mall, S., Kobayashi, A. S., and Urabe, Y., "Dynamic Photoelastic and Dynamic Finite Element Analyses of Dynamic Tear Test Specimens," *Experimental Mechanics*, Vol. 18, No. 12, 1978, pp. 449-456.
- [2] Loss, F. J. ed., "Structural Integrity of Water Reactor Pressure Boundary Components," Progress Report ending February 1976, Report 8006, NRL NUREG 1, Naval Research Laboratory, 26 August 1976.
- [3] Brinson, H. F., *Experimental Mechanics*, Vol. 10, No. 2, 1970, pp. 72-77.
- [4] Whitfield, J. K., "Characteristics of Polycarbonate as a Photoelastic-Plastic Material," Ph.D. thesis, Virginia Polytechnic Institute, Blacksburg, Va., 1969.
- [5] Lange, E. A., Puzak, P. P., and Cooley, L. A., "Standard Method for the $\frac{5}{8}$ Inch Dynamic Tear Test," Report No. 7159, Naval Research Laboratory, 27 August 1970.
- [6] Lange, E. A., "Fracture Toughness of Structural Metals," Report No. 7046, Naval Research Laboratory, 4 May 1970.
- [7] Lange, E. A., "Dynamic Fracture-Resistance Testing and Methods for Structural Analysis," Report No. 7979, Naval Research Laboratory, 27 April 1976.
- [8] Bradley, W. B. and Kobayashi, A. S., *Experimental Mechanics*, Vol. 10, No. 3, March 1970, pp. 106-113.
- [9] Parvin, M. and Williams, J. G., *International Journal of Fracture*, Vol. 11, No. 6, Dec. 1975, pp. 963-972.
- [10] Kobayashi, A. S., Mall, S., Urabe, Y., and Emery, A. F., "A Numerical Dynamic Fracture Analysis of Three Wedge-Loaded DCB Specimens," *Proceedings*, International Conference on Numerical Analysis in Fracture Mechanics, University College of Swansea, 9-13 January 1978.

S. J. Garwood¹

Effect of Specimen Geometry on Crack Growth Resistance

REFERENCE: Garwood, S. J., "Effect of Specimen Geometry on Crack Growth Resistance," *Fracture Mechanics, ASTM STP 677*, C. W. Smith, Ed., American Society for Testing and Materials, 1979, pp. 511–532.

ABSTRACT: The crack growth resistance of 20 mm thick (complying with American Petroleum Institute 5LX65 specifications pipeline steel) in the longitudinal orientation has been measured employing the yielding mechanics parameters J and crack opening displacement (COD) on the three-point bend and center-cracked tension specimen configurations.

The values of these parameters at the initiation of cracking for the two geometries were essentially identical. The resistance curve derived for the tension geometry, however, was appreciably steeper than its bend counterpart.

A comparison of J estimation methods is presented and a simple relationship suggested for the determination of COD resistance for the center-cracked tension geometry.

Energy balance considerations are extended to describe instability in the elastic-plastic regime and J driving force curves estimated for the three-point bend and center-cracked tension geometries.

In addition, the analysis was employed to derive the Paris instability parameter T and the results compared with the existing formulations.

KEY WORDS: fracture strength, toughness, crack resistance, crack initiation, crack propagation, geometry, instability, low alloy steels, fatigue (materials)

Nomenclature

- a Crack length
- a_0 Initial crack length
- B Specimen thickness
- CCT Center-cracked tension
- CGD Clip gage displacement
- COD Crack opening displacement
- CT Compact tension
- D Specimen height
- E, E' Young's modulus, effective E

¹ Senior research engineer, The Welding Institute, Abington, Cambridge, United Kingdom.

J	J-integral
\bar{J}	"Pseudo" J
J_o	J calculated using standard procedures
J_r	J calculated using new estimation method
J_R	J resistance
J_{TP}	J calculated using the three-parameter technique
L	Constraint factor
P	Potential energy
P_s	"Pseudo" potential energy
Q	Load
q	Displacement
R	Resistance to fracture
r	Rotational factor
S	Span
U	Energy under load-displacement record
V_g	Clip gage displacement
W	Specimen width
Z	Knife edge thickness
δ	Crack opening displacement (COD)
δ_o	COD referred to a_o
δ_r	COD resistance
Δa	Incremental crack extension
η	Multiplication factor relating J and U
$\sigma_{\text{flow}}, \sigma^*$	Flow stress
σ_u	Ultimate tensile stress
σ_Y	Yield stress

Subscripts

e	Elastic
i	Initiation
n	Current value
p	Plastic
r	Final value, that is, value after some crack extension
Y	Yield value

The need to characterize ductile crack extension in low to medium strength high toughness steels has led to the extension of yielding fracture mechanics to the measurement of crack growth resistance, R , curves [1-5].²

A number of parameters have been developed to characterize material toughness in the presence of large-scale plasticity. However, two parameters in particular have dominated the others on both theoretical and practical grounds. These are the crack opening displacement [δ] (COD)

² The italic numbers in brackets refer to the list of references appended to this paper.

and the J-contour-integral [7] criteria which have recently been reviewed extensively by Turner and Burdekin [8].

Experimental determinations to date have indicated that, provided certain size requirements are adhered to, the value of both COD and J at the initiation of tearing is geometry independent [3].

However, the growth of resistance with crack extension exhibited by many materials means that the use of toughness values associated with the initiation of crack extension can be excessively conservative when a substantial amount of stable tearing occurs before failure. Since a plot of toughness versus crack extension is used in the determination of initiation values where tearing occurs, it is an obvious extension to attempt to measure the entire resistance curve.

Linear elastic resistance curves rely, by definition, on the retention of elastic conditions. However, the growth of resistance is accompanied by an increasing plastic zone size and consequent invalidation of the elastic premise. This problem complicates the controversy over the geometry dependence of resistance curves for a given thickness. It is still not certain whether R-curves describe the growth of the plastic zone, which is geometry dependent [9], or are representative of some process zone around the advancing crack tip, which is itself surrounded by the plastic zone [10].

Recent studies [2–5] have adapted the existing yielding mechanics formulae not only in an attempt to characterize ductile crack extension in the presence of large-scale plasticity, but also to investigate the cause of the rise in resistance.

To date most resistance studies employing yielding mechanics have utilized the three-point bend and compact tension geometries. It is the purpose of this paper to investigate the extension of the current techniques to the CCT geometry and hence determine the effect that specimen configuration has on crack growth resistance and also attempt to extend linear elastic resistance curve theory to describe the stability of cracking in elastic-plastic bend and tension situations.

Theoretical Analysis

Measurement of J Resistance, J_R

The J-integral analysis [7] is strictly applicable only to nonlinear elasticity but has been extended by analogy to monotonic loading in an elastic-plastic medium [11]. Whether description of the crack tip conditions in this regime is accurate is still an open question.

For nonlinear elasticity the J-integral can be interpreted energetically as [7]

$$J = - \frac{dP}{da} \quad (1)$$

Then for the elastic-plastic case

$$\bar{J} = - \frac{dPs}{da} \quad (2)$$

where $-dPs/da$ is the "pseudo" potential energy release rate measurable as the area between monotonic load displacement diagrams of bodies of unit thickness with adjacent crack lengths.

For the situation of the propagating crack in an elastic-plastic medium, for example the material being tested herein, the monotonic loading curve at the current crack length is not available since the actual load, Q , displacement, q , record contains energy already expended in crack propagation. Unloading the test specimens only releases the stored elastic energy; the stored plastic energy is not released. The curve required for the derivation of J is the unloading curve of an equivalent nonlinear elastic material which has undergone the appropriate amount of crack extension.

In the absence of a direct means of measuring this curve a number of techniques can be used to estimate the value of J at the new crack length, J_R .

Basic Estimation Method

Estimation formulae relating the area, U , under the load-displacement record to J have been derived for certain geometries [12,13].

For the three-point bend geometry in the range $0.4 < a/W < 0.7$

$$J_o = \frac{2U}{B(W - a)} \quad (3a)$$

where B is the specimen thickness and $(W - a)$, the ligament depth. For the CCT geometry Sumpter [13] quotes

$$J_o = \frac{0.5U_p}{B(W/2 - a)} + \frac{\eta_e U_e}{B(W/2 - a)} \quad (3b)$$

Landes and Begley [14] used Eq 3a to develop an R-curve to facilitate the measurement of J_i . After the onset of tearing the overestimation of the "pseudo" energy available for further propagation from the application of total U is compensated to some extent by the use of the original ligament depth in Eq 3a. This resistance curve generally is expected to overestimate the true resistance and is designed to be accurate only before or at initiation.

Three-Parameter Technique

Another method of evaluating a J resistance curve is by the adaptation of the estimation formulae. This method, called the three-parameter technique [15], assumes a linear variation of J for a small increment of crack growth Δa . For geometries where a $J \sim U$ relationship has been derived, it is possible, by inspection of the actual load displacement diagrams from a series of tests with different amounts of crack extension, to relate the extra work required to grow the crack an amount Δa to the value of J for the growing crack. In this way a better estimate of J_R is obtained than using the basic method.

for the three-point geometry [15]

$$J_n = J_{(n-1)} \frac{W - a_n}{(W - a_{(n-1)})} + \frac{2(U_n - U_{(n-1)})}{B(W - a_{(n-1)})} \tag{4}$$

for the CCT geometry [3]

$$J_n = J_{(n-1)} + \frac{U_n - U_{(n-1)}}{B(W - a_n + a_{(n-1)})} \tag{5}$$

A Simple Estimation Method

Using similar assumptions to the three-parameter method, it is possible to estimate a value of J_R from a single specimen based on a simplified load displacement record. This allows a J resistance curve to be developed using fewer specimens and also eliminates time-consuming area measurements, as only the final load and displacement are required.

The method, which applies to specimens beyond net section yield only, is described in Ref 16. The estimation formulae are

for bend

$$J_n = \frac{Q_n q_n}{B(W - a_n)} + \frac{L\sigma_y}{S} (W - a_n) q_p \tag{6}$$

for CCT

$$J_n = \frac{Qp q m (1 - 2\eta_e) + 2\eta_e Q_n q_n}{2B(W - 2a_n)} + \frac{1.155\sigma_y q_p}{2} \tag{7}$$

Measurement of COD Resistance, δ_r

A number of possible methods of measuring COD resistance are available and have been reviewed extensively elsewhere [3]. Ductile tears would appear to propagate with a constant (for a given thickness) crack angle, the COD at the tip of the crack being $\sim 1/4$ of the COD at initiation. Using the methods for estimating δ_r , a rising resistance curve is experienced. However, since the actual COD at the tip of the crack is constant, δ_r can have no physical significance. However, it is possible to equate δ_r to a notional COD which would be attained at the tip of a blunt notch specimen of the relevant crack length deformed to the same displacement [3].

Because of the constant propagating crack angle the variation of the COD referred to the original starter crack tip, δ_o , is linear with crack extension Δa [2,3].

The most promising means of obtaining a comparative measure of crack growth resistance, δ_r , appears to be the utilization of the clip gage formulae of Wells [17] and Ingham [18] quoted in British Standard Draft DD19 [19] by assuming a constant center of rotation advancing ahead of the extending crack.

This method (fully documented in Ref 2-4) merely consists of the substitution of the final crack length ($a_o + \Delta a$) for a in the selected formula in BSI DD19.

Unfortunately, the assumption of a constant center of rotation may be accurate only for less than 4 mm of crack extension [3]. Also, care must be exercised over the selection of the value of the rotational constant (r) assumed. The Wells formula employs a value of 0.45 but Ingham quotes $1/3$. The true value appears to depend on the dimensions of the specimen [3]. In cases of uncertainty, it is best to assume the lower rotational constant as this predicts smaller CODs.

For the CCT geometry no standard clip gage relationships are available. However, as the configuration is in tension it might be expected that the COD is directly proportional to the clip gage displacement after net section yield.

Robinson [20] employed a silicone rubber infiltration technique [21] to measure the COD of mild steel CCT specimens prior to initiation and obtained the relationship

$$\text{COD} = 0.46 \text{ CGD} \quad (8)$$

for the complete range of $2a/W$. How this relationship varies with material, or after considerable amounts of tearing, is unknown.

Experimentation

Specimen Design

Full pipe thickness (20 mm), three-point bend, and CCT specimens extracted from 1 m (3-ft) diameter pipe to API 5LX65 specifications were employed. The slight curvature of the CCT specimens (~2mm deviation from linearity over the width) was insufficient to cause any experimental difficulties. All specimens were extracted in the *L-T* orientation (see Fig. 1a). The chemical and mechanical properties of the line pipe steel are given in Table 1.

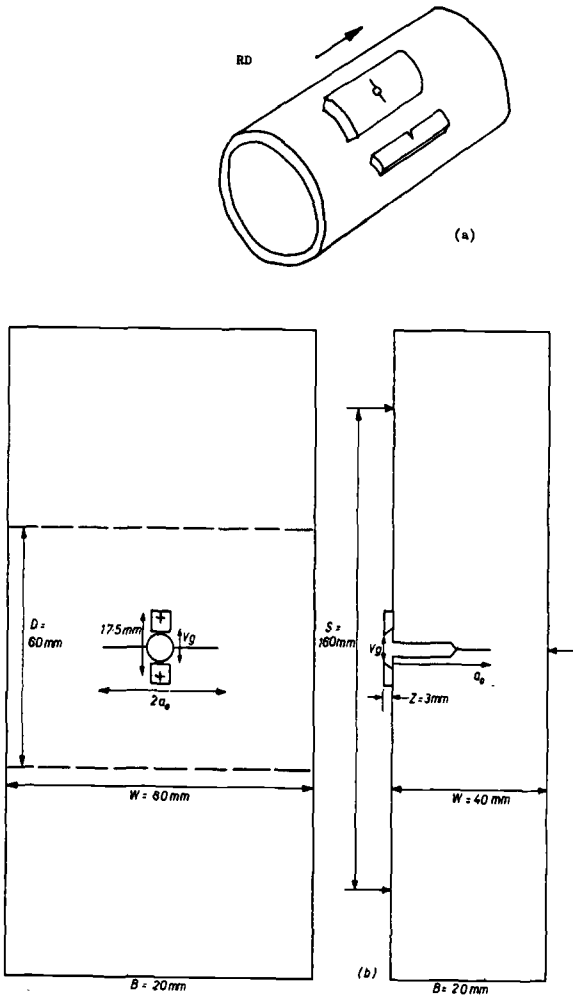


FIG. 1—(a) Specimen extraction, and (b) specimen configuration—CCT (left), three-point bend (right).

TABLE 1—Properties of API 5LX65

Chemical Compositions, weight percent										
Carbon	Sulfur	Phosphorus	Silicon	Manganese	Nitrogen	Chromium	Molybdenum	Vanadium	Niobium	Aluminum
0.06	<0.005	0.016	0.34	1.55	0.03	0.28	0.01	0.09	0.029	0.036
Mechanical Properties at Room Temperature										
Orientation	Lower yield or 0.2 percent Proof Stress, σ_y , N/mm ²	Tensile Strength, σ_u , N/mm ²	Flow Stress, $\sigma_{\text{flow}} = \frac{\sigma_y + \sigma_u}{2}$, N/mm ²		Elongation, percent	Reduction of Area, percent				
			σ_y , N/mm ²	σ_u , N/mm ²						
Longitudinal	509	595	552	30	78					
Transverse (from Ref 5)	584	607	600	27.3	72					

The bend specimens were of a BSI DD19 [19] preferred geometry with $W = 2B$, $S = 4W$ and $a_0/W \approx 0.5$. The CCT specimens used in this investigation were effectively two-bend specimens placed side by side with $W = 80$ mm and $2a/W$ in the range from 0.3 to 0.5, Fig. 1b.

Experimental Details

All tests were conducted at room temperature using a conventional hydraulic universal testing machine at a crosshead speed of 2 mm/min.

For the bend tests, load, crosshead and clip gage displacements were monitored. A correction to the crosshead readings for the extraneous displacement was determined by indenting the rollers into the broken halves of the specimens as described in Ref 22.

For the CCT geometry a clip gage was mounted across the mouth of the notch with a knife edge spacing of 17.5 mm, Fig. 1b. The displacement of this gage was monitored against load. It was unnecessary to correct for extraneous displacement in this instance because of the use of the clip gage displacement readings. Energy measurements were determined by assessment of the area under the corrected load-displacement records with a planimeter.

To obtain a crack growth resistance curve it is necessary to determine the value of toughness at different amounts of crack extension. This was achieved by loading a series of specimens to various displacements to obtain different amounts of crack extension, then unloading, heat tinting, cooling to below the transition region, and breaking open. Using this procedure the amount of stable crack extension and the stretch zone were clearly visible on the fracture surfaces, and measurements of stretch zone, initial and final crack lengths were taken as the average of nine points measured along the crack front using a traveling microscope.

Specimen Behavior

All three-point bend specimens behaved in a stable manner, initiation of tearing occurring between net section yield and maximum load. Increasing the displacement after the attainment of maximum load caused stable crack extension to continue under a falling load.

All but two of the CCT specimens comported with this behavior. The exceptions after reaching a maximum load and experiencing further crack extension under a decreasing load, failed in an unstable manner.

The unstable fracture mode in both instances was the same micro mode as the stable crack propagation, that is, ductile tear or microvoid coalescence. However, examination of the fracture surface revealed a distinct line indicative of the onset of the instability. Also, the surface of the unstable tear tended to be smoother and lighter in color than its stable counterpart. On both specimens the amount of stable tear had been

sufficient to allow complete development of the shear lips, thus final failure was entirely by a 45 deg shear mechanism.

Results

For the CCT configuration δ_o was obtained "off load" from the specimens prior to final failure using a traveling microscope. δ_r was obtained by application of Eq 8. Values of J_o and J_{TP} were derived using the area under the load-clip gage traces which should give underestimates of the J values which would obtain to the load-corrected crosshead displacement records. J_r was calculated with the appropriate η_e factor for $D/W = 0.21$ since this is the height-to-width ratio of the knife edge separation.

J initiation determination using the standard stretch zone extrapolation [23] is shown in Fig. 2a.

J_o is plotted against actual crack extension (not including the stretch zone) for both geometries in Fig. 2b and the appropriate initiation values of J read off at $\Delta a = 0$.

δ_i was obtained in a similar fashion by plotting δ_o versus Δa in Fig. 3.

J and COD resistance curves for the bend and tension configurations calculated using the parameters J_o , J_{TP} , and COD are depicted in Figs. 4 and 5.

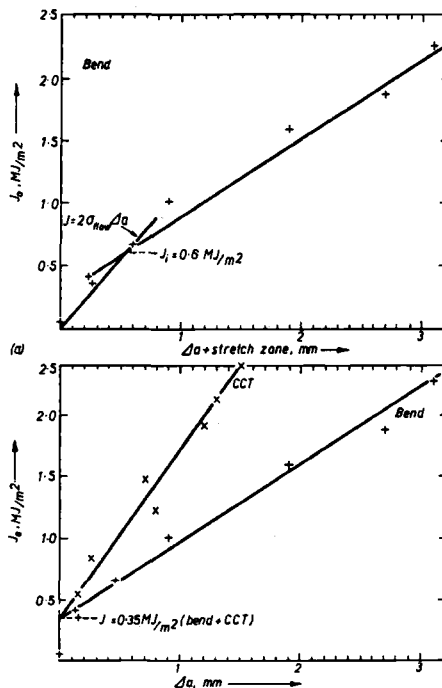


FIG. 2—Determination of initiation J .

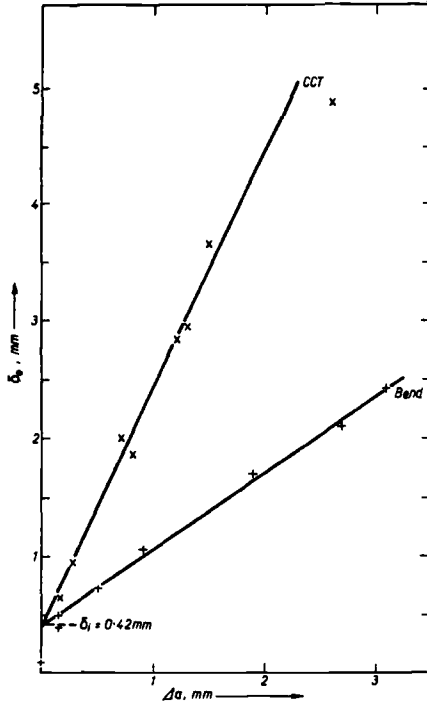


FIG. 3—Determination of COD at initiation.

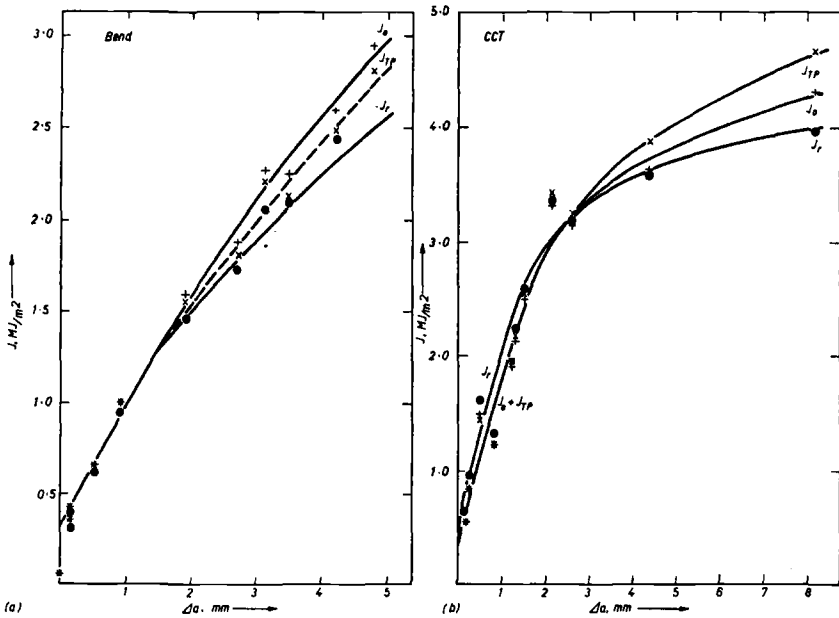


FIG. 4—J resistance curves for (a) bend specimens, and (b) CCT geometries.

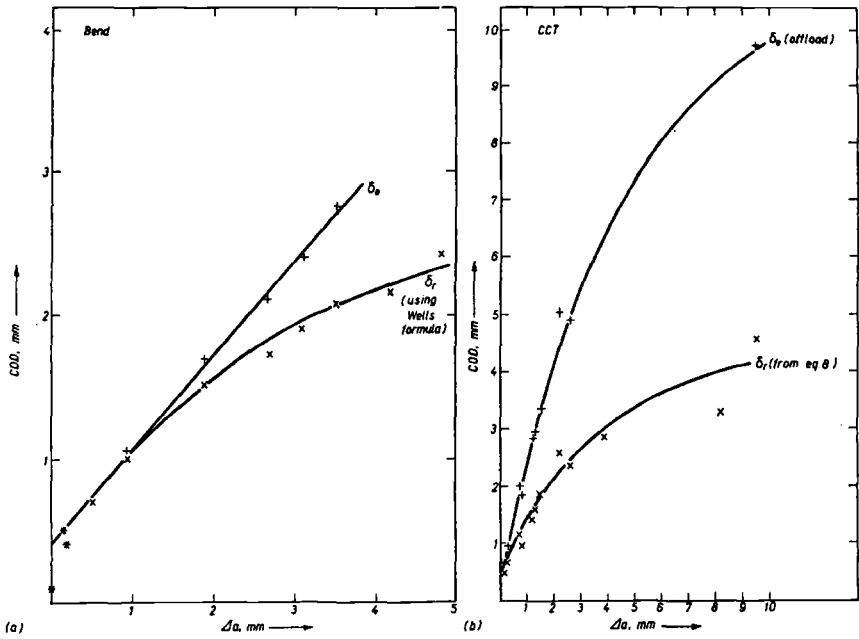


FIG. 5—COD resistance curves for (a) bend specimens, and (b) CCT geometries.

Shear lip measurements were also taken from the broken specimen halves and the variation of percentage with crack extension plotted in Fig. 6b.

Discussion

Determination of Initiation

Inspection of Fig. 2a for the bend configuration indicates the standard procedure, recommended by the ASTM Committee E 24.01.09, of extrapolating the resistance curve back to a stretch zone line given by

$$J = 2\sigma_{flow}\Delta a \tag{9}$$

This equation is derived by assuming that the stretch zone is approximately equal to COD/2, and the relationship

$$J = 1\sigma_{flow}\delta \tag{10}$$

In this particular situation the procedure gives a value of J at initiation which actually relates to a crack extension of 0.5 mm. This is due to the inaccuracies in the assumptions used to derive Eq 10.

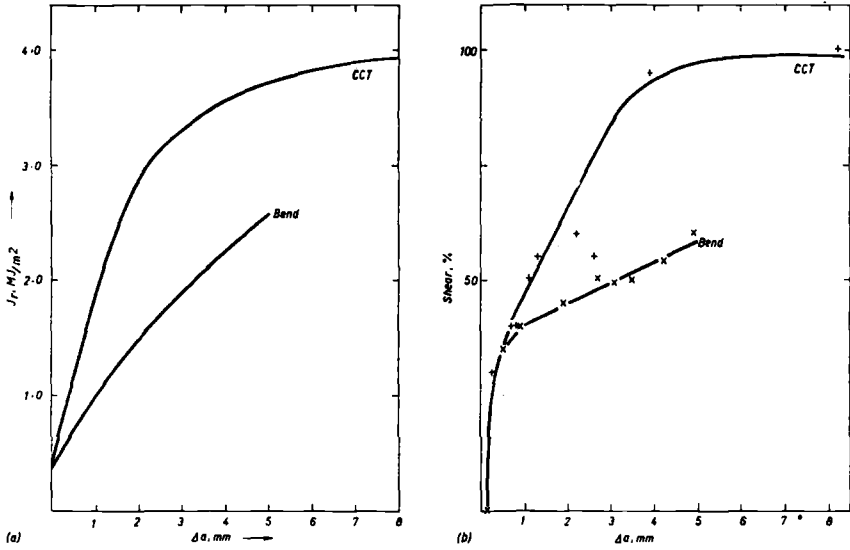


FIG. 6—Comparison of the geometric variation of (a) J_r and (b) shear lip width, with crack extensions.

By plotting J_o versus actual crack extension and extrapolating to zero crack extension, initiation values are obtained, Fig. 2b. Although the $J_o - \Delta a$ curve for the CCT geometry rises more steeply than its bend equivalent the initiation value of 0.35 MJ/m^2 is identical for both configurations.

The $\delta_o - \Delta a$ traces, Fig. 3, behave in an analogous fashion to the J_o curves. Again, an identical initiation value is obtained for the two geometries, that is, $\delta_i = 0.42$ mm.

J Resistance Curve

The three methods of estimating J resistance for the bend geometry used herein are plotted in Fig. 4a. Similar behavior to that reported in Ref 3 is exhibited: J_o being an overestimate of J_{TP} , but J_r underestimating J_{TP} . The curves for this material rise very steeply achieving almost a tenfold increase in toughness after 5 mm of crack extension.

Slightly different behavior is manifested by the CCT configuration, Fig. 4b. Here J_o underestimates J_{TP} , J_r again being the most conservative estimate for the larger crack extensions. For $\Delta a < 2.5$ mm J_r gives higher results than either J_{TP} or J_o . This occurrence is most likely to be a result of the incorporation of the correct η_e factor relevant to the initial knife edge separation in the calculation of J_r , hence allowing the evaluation of the correct amount of elastic energy in the specimen. By contrast, the area measurements employed in the J_{TP} and J_o calculations were from the load

clip gage displacement measurements, therefore the energy stored in the specimen arms is not incorporated. Thus the total energy stored in the specimen normally used in calculations of J is underestimated giving low values of J_{TP} and J_o .

COD Resistance Curve

As predicted from previous observations [2,3] the δ_o versus Δa trace for the bend specimens, Fig. 3, is linear in form. The δ_r curve exhibited in Fig. 5a was calculated using the Wells formula, Ref 17, and the final crack length measurements. As in the bend case J_R curve, a large increase in COD resistance is evident (0.4 to 2.4 mm) as the crack extends from zero to 5 mm.

The δ_o curve for the CCT geometry, Fig. 5b, was obtained from "off load" readings of the fatigue crack opening. As in the bend configuration for crack extensions of <4 mm this appears linear in form.

There is no theory to date governing the determination of COD resistance values for the CCT configuration. In the absence of any other premise the equation determined on mild steel specimens by Robinson [20], that is, Eq 8, was employed to estimate δ_r from the clip gage readings. This curve is plotted in Fig. 5b.

Effect of Specimen Configuration

As no theory has been developed allowing the evaluation of δ_r , besides the equation reported herein, it is possible to relate the two configurations tested only by comparison of the J resistance measurements, Fig. 6a.

Although starting from an identical initiation value the CCT resistance curve has a much steeper gradient than the bend, indicating a severe geometric effect.

The discrepancy between the curves is not surprising when the development of the shear lips for the two geometries is inspected, Fig. 6b. The CCT configuration is less highly constrained than its bend counterpart so the shear lips tend to form more rapidly. After ~4 mm the fracture surface of the tension pieces was entirely 45 deg shear, whereas the equivalent bend specimens were exhibiting ~50 percent normal (flat) rupture.

It has been demonstrated in Ref 3 that a rising resistance curve in bending is experienced even when failure is 100 percent normal rupture (plane strain). Inclusion of the effect of growing shear lips can then be expected to give even steeper curves according to the percentage shear present. Although the J resistance curve has been related to the amount of shear lips present, Ref 3, by extension of the Krafft hypothesis [24] it is impossible to evaluate whether the difference between the resistance curves in bend and tension stems entirely from the shear lip behavior without knowledge of the plane strain curve.

Instability Considerations

Elastic-Plastic Behavior

If no unloading occurs, that is, monotonic loading is maintained, elastic-plastic behavior can be assumed analogous to nonlinear elasticity. Hence, restating Eq 2

$$\bar{J} = - \frac{dP_s}{da}$$

where dP_s/da is the rate of change of "pseudo" potential energy. The energy is pseudo since it incorporates an irretrievable plastic energy component.

The resistance to crack extension in the elastic-plastic medium is given by J_R , so for stable crack growth

$$\bar{J} = J_R \quad (11)$$

and for instability

$$\frac{d\bar{J}}{da} \geq \frac{dJ_R}{da} \quad (12)$$

Then \bar{J} is the elastic-plastic equivalent of the crack driving force.

Elastic-Plastic Crack Driving Force Curves

To assess stability of cracking in the elastic-plastic regime it is necessary to evaluate the J resistance or J_R curve and compare this with the crack driving force \bar{J} curves.

Consider elastic-rigid plastic behavior, from Eq 2

$$\bar{J} = 2 \frac{dP_s}{da} = - \frac{1}{B} \frac{dU_{total}}{da} \quad (13)$$

Dividing U_{total} into elastic and plastic components

$$U_{total} = U_p + U_e \quad (14)$$

then for elastic-rigid plastic conditions

$$U_{total} = Q_Y q_p + \frac{Q_Y q_e}{2} \quad (15)$$

$$= Q_Y q_r - \frac{Q_Y q_e}{2} \quad (16)$$

where Q_Y is the yield load, q_r is the total displacement, and q_p and q_e are the plastic and elastic displacements.

for fixed grip conditions

$$\bar{J} = - \frac{1}{B} \frac{\partial}{\partial a} \left(Q_Y q_r - \frac{Q_Y q_e}{2} \right) \Big|_{q_r} \quad (17)$$

that is,

$$\bar{J} = \frac{q_r}{B} \frac{dQ_Y}{da} + \frac{1}{2B} \frac{d}{da} (Q_Y q_e) \quad (18)$$

Q_Y is the load at which net section yield occurs for the configurations. Hence for situations where expressions for Q_Y and q_e are known in terms of a/W the elastic-rigid plastic driving force curves can be determined. For the bend geometry slip line field analysis predicts

$$Q_Y = L \sigma_Y \frac{B}{S} (W - a)^2 \quad (19)$$

Sumpter [13] quotes $L = 1.525$, whereas Green [25] gives 1.26. The factor depends on the constraint and yield criteria assumed. For the CCT

$$Q_Y = 1.155 \sigma_Y B (W - 2a) \quad (20)$$

Then by substitution of Q_Y from Eq 20 and q_e from Ref 26 in Eq 18 the expression for the CCT geometry becomes

$$\begin{aligned} \bar{J} = & 1.155 \sigma_Y q_r + 0.667 \frac{\sigma_Y^2 W}{E'} \left(1 - \frac{2a}{W} \right) \left[- \frac{2D}{W} + 3.14 \left(\frac{2a}{W} \right) \right. \\ & - 6.28 \left(\frac{2a}{W} \right)^2 + 3.88 \left(\frac{2a}{W} \right)^3 - 5.82 \left(\frac{2a}{W} \right)^4 + 3.96 \left(\frac{2a}{W} \right)^5 \\ & \left. - 5.28 \left(\frac{2a}{W} \right)^6 + 4 \left(\frac{2a}{W} \right)^7 - 5 \left(\frac{2a}{W} \right)^8 \right] \quad (21) \end{aligned}$$

and for the bend geometry assuming $L = 1.3$ substituting for Q_Y from Eq 19

$$\begin{aligned}
\bar{J} = & 0.65\sigma_Y \left(1 - \frac{a}{W} \right) q_r - 0.211\sigma_Y^2 W \left(1 - \frac{a}{W} \right)^3 \\
& \left[\frac{0.24S^3}{EW^3} \left(1.04 + 3.28 \left(\frac{W}{S} \right)^2 (1 + \nu) \right) \right. \\
& + \frac{2S^2(1 - \nu)^2}{EW^2} \left(\frac{a}{W} \right) \left(4.21 \left(\frac{a}{W} \right) - 8.89 \left(\frac{a}{W} \right)^2 + 36.9 \left(\frac{a}{W} \right)^3 \right. \\
& - 83.6 \left(\frac{a}{W} \right)^4 + 174.3 \left(\frac{a}{W} \right)^5 - 284.8 \left(\frac{a}{W} \right)^6 + 387.6 \left(\frac{a}{W} \right)^7 \\
& \left. \left. - 322.8 \left(\frac{a}{W} \right)^8 + 149.8 \left(\frac{a}{W} \right)^9 \right) \right] \\
& + 0.058\sigma_Y^2 W \left(1 - \frac{a}{W} \right)^4 \left(\frac{2S^2}{EW^2} (1 - \nu^2) \right) \\
& \left[4.21 \times 2 \left(\frac{a}{W} \right) - 8.89 \times 3 \left(\frac{a}{W} \right)^2 \right. \\
& + 36.9 \times 4 \left(\frac{a}{W} \right)^3 - 83.6 \times 5 \left(\frac{a}{W} \right)^4 + 174.3 \times 6 \left(\frac{a}{W} \right)^5 \\
& - 284.8 \times 7 \left(\frac{a}{W} \right)^6 + 387.6 \times 8 \left(\frac{a}{W} \right)^7 \\
& \left. - 322.8 \times 9 \left(\frac{a}{W} \right)^8 + 149.8 \times 10 \left(\frac{a}{W} \right)^9 \right] \tag{22}
\end{aligned}$$

For the CCT geometry tested herein with $W = 80$ mm and using $\sigma_Y = \sigma_{flow} = 600$ N/mm² to allow for work hardening the driving force curves are obtained by application of Eq 21. These curves are, as in the elastic case, a function of D/W . With $D/W = 0.75$ flat driving force curves are achieved, Fig. 7.

For comparison purposes the linear elastic driving force curve for these specimens with $q = 1$ mm also is depicted in Fig. 7.

The resistance curve for API 5LX65 tested is also plotted in Fig. 7. This would indicate that instability will occur when the plateau value of resistance is achieved. However, the curves in Fig. 7 are for fixed grip conditions and as such do not include the effect of the machine compliance which might be expected to give the curves a slight positive slope. Instability was, in fact, achieved on this geometry when the fracture surface of the specimens exhibited 100 percent 45 deg shear which can be associated with the attainment of the plateau value.

The driving force curves for the bend geometry tested with $W = 40$ mm

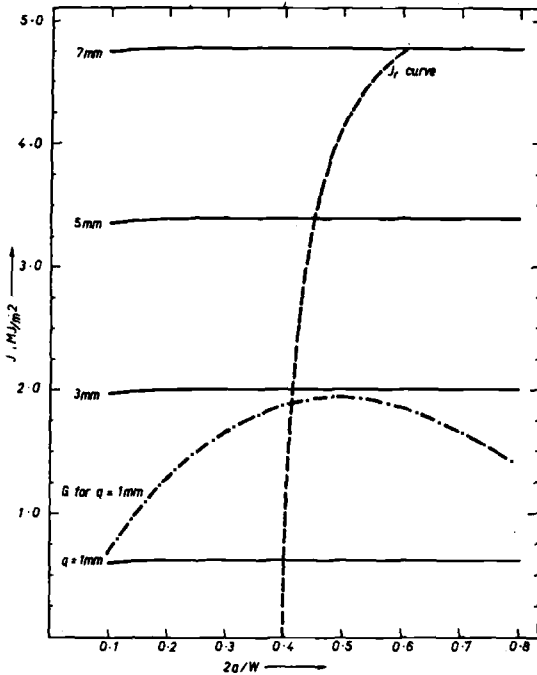


FIG. 7—Elastic-plastic driving force, fixed grip: CCT $D/W = 0.75$ for $\sigma^* = 600 \text{ N/mm}^2$, $W = 80 \text{ mm}$.

are plotted in Fig. 8. The negative slope exhibited for this geometry ensures stability even if a plateau value of resistance is attained.

Instability Parameter

Paris et al [27] have recently suggested the development of a parameter T with the intention of describing a material's stable tear properties where

$$T_{mat} = \frac{dJ_R}{da} \frac{E}{\sigma_Y^2} ; T_{app} = \frac{d\bar{J}}{da} \frac{E}{\sigma_Y^2} \tag{23}$$

dJ_R/da is the slope of the resistance curve assumed independent of configuration. Hence T_{mat} is considered to be a material parameter since E and σ_Y are material properties. T_{app} is the value of the T parameter applied and is thus a function of the rate of change driving force $d\bar{J}/da$. The simplest example to consider is the development of T_{app} for the CCT geometry. Paris [27] compared the reduction of elastic displacement with the increase of plastic displacement during crack extension using the following assumptions: (a) COD is proportional to total plastic displacement, (b) $J = \sigma_Y \text{ COD}$, and (c) that elastic-rigid plastic behavior is applicable.

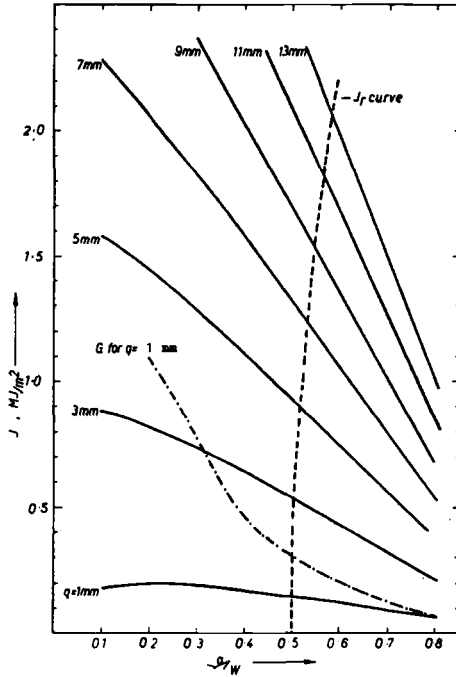


FIG. 8—Elastic-plastic driving force, fixed grip: three-point bend $S/W = 4$ for $\sigma^* = 600$ N/mm^2 , $W = 40$ mm.

The condition for instability under fixed grip conditions becomes

$$T_{mat} = \frac{dJ_R}{da} \frac{E}{\sigma_Y^2} \leq T_{app} = \frac{2D}{W} \tag{24}$$

This derivation of T_{app} can also be approached from the instability criteria given by Eq 12

$$\frac{d\bar{J}}{da} \geq \frac{dJ_R}{da}$$

For the CCT geometry \bar{J} is given by Eq 21 then

$$\begin{aligned} \frac{d\bar{J}}{da} = \frac{2L^2\sigma_Y^2}{E} & \left[\frac{D}{W} + 1.57 - 9.42 \left(\frac{2a}{W}\right) + 15.24 \left(\frac{2a}{W}\right)^2 \right. \\ & - 19.4 \left(\frac{2a}{W}\right)^3 + 24.45 \left(\frac{2a}{W}\right)^4 - 27.72 \left(\frac{2a}{W}\right)^5 \\ & \left. + 32.48 \left(\frac{2a}{W}\right)^6 - 36 \left(\frac{2a}{W}\right)^7 + 22.5 \left(\frac{2a}{W}\right)^8 \right] \tag{25} \end{aligned}$$

Hence substituting for $d\bar{J}/da$ in Eq 12 and rearranging, the instability condition becomes

$$\frac{dJ_R}{da} \frac{E}{\sigma_Y^2} \leq \frac{d\bar{J}}{da} \frac{E}{\sigma_Y^2} = 2L^2 \frac{D}{W} + f^n \left(\frac{2a}{W} \right) \quad (26)$$

The only assumptions used in this analysis are elastic-rigid plastic behavior and fixed grip conditions. Results from Eqs 24 and 26 are compared in Fig. 9.

For $D/W = 0.75$ Eq 24 gives a conservative estimate of the value of T_{app} required to cause instability within the range $0.3 < 2a/W < 0.8$. The Paris formula is optimistic outside this range for $D/W = 0.75$, but as the D/W ratio increases so the range of $2a/W$ for conservative estimates

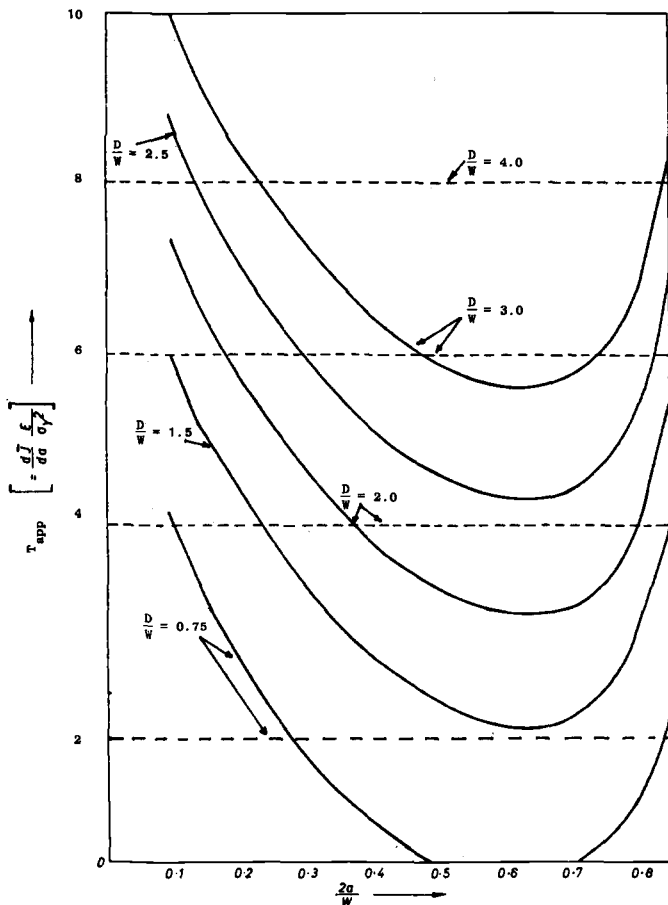


FIG. 9—CCT, fixed grip conditions, Eq 26—Paris formulations, Eq 24.

decreases for the geometry considered here. This latter phenomenon is entirely due to the constraint factor assumed. $L = 1.155$ was used in this analysis whereas Paris employed $L = 1.0$ for the derivation of Eq 24.

Paris suggests that the initial slope of the J_R curve can be utilized to ascertain the occurrence of ductile instability. This procedure will give an indication of stability immediately after the onset of crack growth but does not predict the actual instability conditions. As the crack extends so dJ_R/da can be expected to decrease and as the plateau value of resistance is attained so $dJ_R/da \rightarrow 0$. Hence to predict the actual instability point requires a comparison of the driving force and resistance curves as in Figs. 7 and 8.

Conclusions

1. The initiation values of COD and J in the bend and CCT geometries were identical.
2. Resistance curves derived for the tension specimens were appreciably steeper than their bend counterparts. The most likely cause of this effect is the larger shear lips present in the CCT specimens. However, true geometric dependence of the resistance curve is not ruled out.
3. A comparison of estimation techniques for the evaluation of J resistance on both CCT and bend configurations is presented.
4. A simple relationship suggested by Robinson [20] for the determination of COD for the CCT geometry was extended to measure the COD resistance curve.
5. For the three-point bend and CCT geometries elastic-rigid plastic driving force curves have been derived and are compared with measured resistance curves to assess the stability of tearing.
6. An energy balance approach is employed to derive the Paris et al [27] T parameter and a comparison is made between this technique and the Paris formulation for the CCT geometry.

Acknowledgments

The assistance of B. A. Wakefield and the staff of the Brittle Fracture Laboratory during the conduction of the experimental work is gratefully acknowledged. I would also like to thank O. L. Towers for providing a second opinion on the instability analyses in the report.

References

- [1] Novak, S. R., in *Resistance to Plane-Stress Fracture (R-Curve Behavior) of A572 Structural Steel*, ASTM STP 591 American Society for Testing and Materials, 1974.
- [2] Green, G. and Knott, J. F., *Journal of Mechanics and Physics of Solids*, Vol. 23, No. 3, 1975, pp. 167-183.
- [3] Garwood, S. J., "The Measurement of Crack Growth Resistance Using Yielding Fracture Mechanics," Ph.D. thesis, London, 1977.

- [4] Tanaka, K. and Harrison, J. D., "An R-Curve Approach to COD and J for an Austenitic Steel," Welding Institute Report 7/1976/E.
- [5] Kamath, M. S. and Harrison, J. D., "Ductile Crack Extension in API 5LX65 and HY130 Steels," Welding Institute Report 36/1977/E.
- [6] Wells, A. A. in *Proceedings, Crack Symposium*, Vol. 1, Cranfield, pp. 210–230.
- [7] Rice, J. R., *Journal of Applied Mechanics*, 1968, pp. 379–386.
- [8] Turner, C. E. and Burdekin, F. M., *Energy Review*, Vol. 12, 1974, pp. 439–503.
- [9] Adams, N. J. I., Munro, H. F., and Neale, B. K., "The Influence of Specimen Configuration on Yield Zone Formation and Fracture Resistance," presented at International Conference on Fracture, Waterloo, 1977.
- [10] Broberg, K. B., *Journal of Mechanics and Physics of Solids*, Vol. 23, 1975, pp. 215–237.
- [11] Begley, J. A. and Landes, J. D. in *Fracture Toughness, ASTM STP 514*, American Society for Testing and Materials, 1972, pp. 1–23.
- [12] Rice, J. R., Paris, P. C., and Merkle, J. G. in *Progress in Flow Growth and Fracture Toughness Testing, ASTM STP 536*, American Society for Testing and Materials, 1973, pp. 231–245.
- [13] Sumpter, J. D. G., "Elastic-Plastic Fracture Analysis and Design Using the Finite Element Method," Ph.D. thesis, London, 1974.
- [14] Landes, J. D. and Begley, J. A. in *Fracture Analysis, ASTM STP 560*, American Society for Testing and Materials, 1974, pp. 170–185.
- [15] Garwood, S. J., Robinson, J. N., and Turner, C. E., *International Journal of Fracture*, Vol. 11, No. 3, 1975, pp. 528–530.
- [16] Garwood, S. J., "A Method of Estimating the Value of J_R (the Value of J for a Propagating Crack) from a Single Specimen," to be published in *International Journal of Fracture*.
- [17] Wells, A. A., "The Mechanics of the Fracture Transition in Yielding Material," Queen's University, Belfast, 1970.
- [18] Ingham, T. et al, "The Effect of Geometry on the Interpretation of COD Test Data," *Proceedings, Conference on Practical Application of Fracture Mechanics to Pressure Vessel Technology*, Institute of Mechanical Engineers, London, 1971.
- [19] "Methods for crack opening displacement (COD) testing," draft for Development DD19, British Standards Institution, London, 1972.
- [20] Robinson, J. N., *International Journal of Fracture*, Vol. No. 5, 1976, pp. 723–738.
- [21] Robinson, J. N. and Tetelman, A. S. in *Fracture Toughness and Slow-Stable Cracking, ASTM STP 559*, American Society for Testing and Materials, 1974, pp. 139–158.
- [22] Dawes, M. G., "A Method of Measuring Displacements and Rotational Factors in SENB Specimens," Welding Institute Report 6/1976/E.
- [23] Draft guidelines for a recommended procedure for J_{Ic} determination, minutes of ASTM E24:01:09 Task Group, March 1977.
- [24] Krafft, J. M., Sullivan, A. M., and Boyle, R. W. in *Proceedings, Crack Symposium* Vol. 1, Cranfield, pp. 8–28.
- [25] Green, A. P., *Quarterly Journal of Mechanical Applied Mathematics*, Vol. 6, p. 223.
- [26] Bucci, R. J., Paris, P. C., Landes, J. D., and Rice, J. R. in *Fracture Toughness, ASTM STP 514*, American Society for Testing and Materials, 1972, pp. 40–69.
- [27] Paris, P. C., Tada, H., Zahoor, A., and Ernst, H., "Instability of the Tearing Mode of Elastic-Plastic Crack Growth," presented at ASTM Symposium 16–18 Nov. 1977.

Single-Edge-Cracked Crack Growth Gage

REFERENCE: Ori, J. A. and Grandt, A. F., Jr., "Single-Edge-Cracked Crack Growth Gage," *Fracture Mechanics, ASTM STP 677*, C. W. Smith, Ed., American Society for Testing and Materials, 1979, pp. 533-549.

ABSTRACT: This paper considers single-edge-cracked coupons for use with the "crack growth gage" technique for monitoring the service loading of structures that could contain preexistent cracks. Single-edge-cracked gages are bonded adhesively to larger plates which contain radially cracked holes. The bonded specimens then are subjected to various constant amplitude and one block cyclic load histories, with crack extension in both the gage and simulated structural member recorded as a function of load cycles. Cross plots of the gage and structural crack lengths at the same cyclic life are prepared and shown to agree well with predictions by a mathematical model which requires no knowledge of the actual load history.

KEY WORDS: crack propagation, fatigue (materials), fracture (materials), life (durability), stress cycle

The objective of this paper is to describe the results of some recent experiments [1]³ which are part of a continuing effort to develop the "crack growth gage" technique for monitoring service usage of potentially cracked structures. As shown schematically in Fig. 1, the approach consists of mounting a small precracked coupon (crack length = a_g) onto a load bearing structural member which is assumed to contain a flaw of length a_s . The cracked coupon receives the same load excursions as the structural member (to within a predictable scaling factor) and responds with a measurable crack extension. Previous work [2-4] has shown that it is often possible to relate the length of a_g to that of a_s during subsequent

¹ Major, USAF, formerly Air Force Institute of Technology, Wright-Patterson Air Force Base, Ohio 45433, presently San Antonio Air Logistics Center, Kelly Air Force Base, Tex. 78241.

² Materials research engineer, Air Force Materials Laboratory, Wright-Patterson Air Force Base, Ohio 45433.

³ The italic numbers in brackets refer to the list of references appended to this paper.

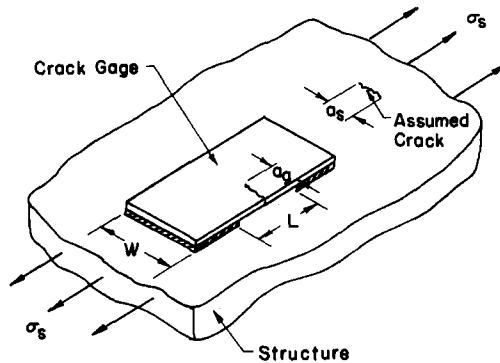


FIG. 1—Schematic view of crack gage applied to flawed structural component.

cycling. Furthermore, when fatigue crack growth can be described by a simple power law, the mathematical model developed earlier indicates that the a_s versus a_g relationship is independent of the actual loads encountered by the system. This load independence is discussed in more detail later.

It is suggested that the crack gage may provide a simpler approach to crack growth based aircraft tracking requirements [5] than present techniques such as strain recorders, pilot logs, acoustic emission, or accelerometers [6-9]. In essence, the cracked coupon can be considered as an analog computer which senses the loading applied to the structure, determines its effect on the growth of potential structural cracks, and responds with a measurable output (gage crack extension). When used with control point tracking methods [3,10-11], the crack gage output could provide the data required to assess effectively the remaining service lives of various cracked components in a given structure.

There are many potential configurations for the gage coupon, including the possibility of intentionally locating the gage crack in the structural member itself. This extreme case was considered in Refs 2 and 3, where a center crack and a radially cracked hole were located in series (with respect to the load line) in a large plate. The specimen then was subjected to a variable amplitude load history. The correlation between the two defects was predicted and shown to agree quite well with the experimental data.

To avoid placing the monitored flaw (a_g) directly in the structural member (although introducing an intentional crack at a carefully monitored and well chosen structural location may not be completely unreasonable for some applications), recent work [4,12,13] has focused on the use of adhesively bonded coupons for the crack gage. In Ref 4, for example, small center-cracked coupons were bonded to larger specimens which contained radially cracked holes. These specimens then were

subjected to various constant amplitude cyclic loading and a_s was measured as a function of the corresponding gage crack size a_g . These experimental data also agreed quite well with independent mathematical predictions made with no knowledge of the actual loading.

As reported in Refs 12 and 13, other investigators have also explored the use of adhesively bonded crack gages for fatigue load monitoring. Smith [12], for example, has described a technique for using fatigue crack growth measured in small edge cracked coupons to estimate the total cyclic life (including crack initiation) in a structural component. Johnson and Paquette [13] also have reported use of center cracked coupons for service life monitoring, and have suggested a means for remotely measuring gage crack growth by means of crack wires.

Experimental Procedures

Overview

An experimental program was conducted to evaluate single-edge-cracked coupons for use as the monitoring coupon in the crack gage technique. The structural component was simulated here by a 13.3-mm (0.525-in.) thick 2219-T851 aluminum plate which contained a radially cracked hole. The crack gages were machined from three aluminum alloys and bonded in pairs (one cracked, the other uncracked) to the structural member as shown in Fig. 2. The assembled specimens were subjected to constant amplitude load histories (and one block loading sequence) and the resulting fatigue crack growth was recorded as a function of load cycles. Eleven specimens were tested in this manner, with gage material, initial crack lengths (a_{si} and a_{gi}), and structural cyclic stress σ_s as the experimental variables. The test matrix is summarized in Table 1. A

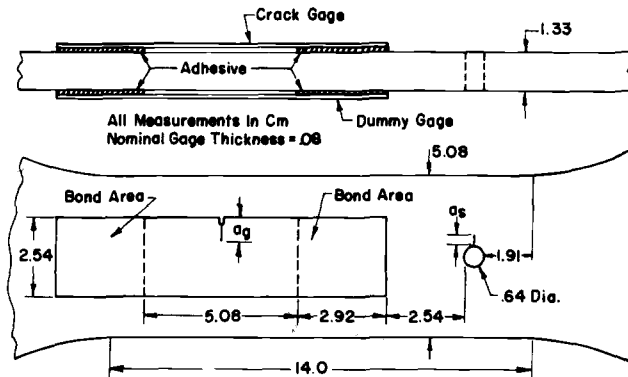


FIG. 2—Detailed view of assembled test specimen showing edge cracked gage and dummy coupon adhesively bonded to simulated structural member.

TABLE 1—*Test Matrix.*

Test Number	Gage Material	Initial Gage Crack Length a_{g1} , mm (in.)	Initial Structural Crack Length a_{s1} , mm (in.)	Structural Stress σ_s , MPa (ksi)
1	2024-T3	5.13 (0.202)	3.73 (0.147)	92 (13.3)
3	2024-T3	5.51 (0.217)	5.08 (0.200)	92 (13.3)
4	7075-T6	7.42 (0.292)	3.96 (0.156)	92 (13.3)
5	7075-T6	3.73 (0.147)	1.35 (0.053)	92 (13.3)
6	7075-T6	5.59 (0.220)	1.27 (0.050)	92 (13.3)
7	7075-T6	10.82 (0.426)	2.34 (0.092)	92 (13.3)
8	7075-T6	10.95 (0.431)	4.60 (0.181)	Block
9	7075-T6	3.84 (0.151)	1.27 (0.050)	72 (10.5)
10	2219-T851	5.11 (0.201)	1.27 (0.050)	92 (13.3)
11	2219-T851	5.08 (0.200)	1.32 (0.052)	92 (13.3)
12	2219-T851	5.05 (0.199)	1.17 (0.046)	72 (10.5)

detailed description of the experimental procedures is given in the remainder of this section.

Test Specimens

As indicated in Fig. 2, the simulated structural member was a 2219-T851 aluminum specimen with a nominal 13.3 mm (0.525 in.) thickness and a 50.8 mm (2.0 in.) width. Each specimen contained a radially cracked 6.4-mm (0.25-in.) diameter hole as the structural defect a_s . The open hole was located on the centerline and well into the uniform width section of the test specimen (see Fig. 2). Small edge-cracked coupons (nominal 0.8 mm (0.30 in) thickness) were made from three materials (2219-T851, 7075-T6 clad, and 2024-T4 aluminum), and adhesively bonded to the simulated structural member. The edge cracked coupons were 25.4 mm (1.0 in.) wide with a 50.8 mm (2.0 in.) long unbonded gage length L . The total coupon length was 109 mm (4.30 in.), allowing for a 29.2 by 25.4 mm (1.15 by 1.10 in.) bond area at each end. The 7075-T6 and 2024-T4 coupons were cut from thin rolled stock, oriented so that the edge crack propagated normal to the rolling direction in the 2024-T4 specimens, and parallel to the rolling direction in the 7075-T6 coupons. The 2219-T851 gages were machined from one of the original structural specimens with the same crack orientation as in the simulated structure.

Prior to assembly, all specimens were polished to a mirror surface to enhance crack tip resolution. The structural specimens then were precracked on a 180kN (20 ton) capacity Schenck resonate fatigue machine. First, a 0.89-mm (0.035-in.) notch was cut with a jeweler's saw in the edge of a predrilled 3.2-mm (0.125-in.) diameter hole to start the fatigue crack. Precracking loads were reduced as the crack extended until a final cyclic load of 80 percent of subsequent test load was reached. After precracking,

the hole was drilled and reamed to 6.4 mm (0.25 in.) in diameter, leaving the radial thru-the-thickness crack a_s .

The edge-cracked gages were precracked on an 18 kN (2 ton) capacity Schenck fatigue machine. A 1.3-mm (0.05-in.) notch was again centered on one edge of the gage to serve as a precracking source. Precracking loads were reduced gradually to the minimum machine capacity of 980 N (220 lb), well below the cyclic loads encountered by the gage during subsequent fatigue testing.

After surface preparation and precracking, two small coupons were bonded to the structural specimen (front and back) in the positions indicated in Fig. 2. Since the test apparatus allowed visual observation of only one gage, the second one was not precracked. This dummy gage served two useful purposes. First, the uncracked gage tended to reduce potential bending in the assembled specimen by providing a more symmetric configuration. In addition, foil strain gages mounted onto the center of the dummy coupon provided measurement of the actual load transferred into the coupon by the adhesive. The results of these load transfer measurements are discussed later.

Adhesive Bonding

Selection of the adhesive for use in these experiments involved two criteria. First, the bond had to reliably transfer load from the structural member into the small edge-cracked coupon during the entire cyclic life of the test. Second, the adhesive and associated bonding steps (surface preparation, application, curing, etc.) were to be relatively convenient for laboratory use. (No attempt was made to select an adhesive for production use or for eventual long term stability in actual structural applications.) With these two criteria in mind, preliminary cyclic tests were conducted with the following adhesives: Loctite Anerobic 610, Wrenweld, Eastman 910, and Hysol EA 1C. The two part epoxy, Hysol EA 1C, was the only adhesive which maintained bond integrity under expected test conditions, and was used for all cyclic tests reported here.

All adherend surfaces were prepared carefully to yield a serviceable bond. The bonding areas were first lightly sanded with 400 grit silicon carbide paper followed by a surface cleansing similar to that employed for strain gage application. The crack areas were masked with tape to prevent impregnation by the cleansing solution. A degreasing, etching solution was applied with a cotton tipped applicator, and the surface wiped with a clean absorbent towel to remove excess solution. A neutralizing solution was applied and wiped using the same procedure. The chemically cleaned areas of the gage were masked with a noncontaminating cellophane tape and a light film of vacuum grease was applied along the edge of the tape. Since the epoxy would not adhere to the greased area when the tape was removed, this procedure provided a straight bond line and a well

controlled gage length (length L in Fig. 2). A 0.08 mm (0.003 in.) thick TFE-fluorocarbon film was placed under the unbonded length to prevent friction between structure and gage.

Since the epoxy adhesive was refrigerated, it was allowed to reach room temperature before breaking the package seal to prevent moisture absorption. The two part epoxy was mixed and applied in a thin, even layer over the prepared gage surface. Small reference lines, scribed onto the structural specimen with the aid of a tool maker's microscope, provided a convenient means for accurately aligning the gages onto the larger specimens. Approximately 70 kPa (100 psi) of pressure was then applied to the bond area by clamps and the bond allowed to cure. Subsequent micrometer measurements of the bonds indicated that final bondline thicknesses varied from 0.05 to 0.13 mm (0.002 to 0.005 in.).

Loading Conditions

After curing, the assembled specimens were tested in cyclic tension (at approximately 30 Hz) on the large fatigue machine used for precracking. Constant amplitude cyclic stresses of $\sigma_s = 92$ and 79 MPa (13.3 and 10.5 ksi), with a stress ratio (R) near 0.1 were applied to all specimens but one. That specimen (Test 8) was subjected to a simple block loading, which consisted of the following sequence of applied stresses ($R = 0.1$): 10 000 cycles at 39 MPa (5.7 ksi), 5000 cycles at 53 MPa (7.6 ksi), 2500 cycles at 79 MPa (11.4 ksi), and 1000 cycles at 92 MPa (13.3 ksi).

Cycling was stopped periodically at a mean static load to record the crack lengths. The structural defect a_s was measured on both sides of the test specimen (front and back). Only one side of the edge-cracked gage was available for observation. All measurements were obtained by conventional techniques with the aid of low power (20 \times) microscopes. Some difficulty was encountered in obtaining uniform thru-the-thickness cracks in the relatively thick structural specimens. The a_s values presented here are based on averages of front and back crack length measurements, and, in all cases, are only reported when these two crack lengths agreed within 30 percent. In most cases, however, the front and back crack length measurements agreed well within 10 percent. In particular, specimens 5, 6, 9, 10, and 11, which had the smallest initial structural crack sizes, all met this 10 percent criteria. All a_s measurements (except tests 3 and 8) meet crack uniformity standards proposed by the American Society for Testing and Materials [14] for fatigue crack growth testing.

The nature of the resonant fatigue machine used for these tests prevented accurate load control during the approximately 150 cycles required to start, and the 100 cycles needed to stop testing. Since crack lengths were measured typically at 2500 cycle intervals, approximately 10 percent of the loading cycles were at less than full load. This feature of the

fatigue machine was not viewed as a serious limitation for the present tests, hwoever, since one of the hypotheses of the crack gage concept is that under certain conditions the a_s versus a_g curve should be nearly independent of load. Experimental evaluation of this hypothesis is discussed later.

Predictive Model

Prior to discussing the results of the fatigue tests, a model for predicting the relationship between the gage crack a_g and the structural defect a_s will be outlined. Since many of the details of the modeling procedure are presented elsewhere [2-4], only a brief description is given here.

Overview

Assume that crack growth in gage and structural materials can be described by

$$\frac{da}{dN} = F(K) \tag{1}$$

Here da/dN is the fatigue crack growth rate and $F(K)$ is an appropriate function relating the stress intensity factor K , material properties, and other significant load variables. Solving Eq 1 for the cyclic life N , and observing that both gage and structural defects see the same number of load cycle gives

$$N = \int_{a_{gs}}^{a_g} \frac{da}{F_g(K)} = \int_{a_{ss}}^{a_s} \frac{da}{F_s(K)} \tag{2}$$

Here a_g and a_s are the initial and final crack lengths, while the subscripts s and g refer to structural and gage quantities. Note that Eq 2 provides a relation between the gage and structural defects.

Equation 2 may be simplified further by specifying the function $F(K)$. An interesting special case occurs when a power type crack growth law is employed.

$$da/dN = C \bar{K}^m \tag{3}$$

Here C and m are empirical constants while \bar{K} is a measure of cyclic stress intensity. Next, relate the gage and structural stresses by

$$\sigma_g = f \sigma_s \tag{4}$$

As discussed in earlier work [2-4], f is a load-transfer function which may depend on geometry and material properties, but not on stress level. Expressing K in the form

$$K = \sigma \sqrt{\pi a} \beta \quad (5)$$

and combining Eqs 2-5 gives

$$\int_{a_n}^{a_s} \frac{da}{C_s (\sqrt{\pi a} \beta_s)^m} = \int_{a_n}^{a_g} \frac{da}{C_g (f \sqrt{\pi a} \beta_g)^m} \quad (6)$$

Here the exponent m in Eq 3 is assumed to be equal for both gage and structural materials. Note that in this specific case, Eq 6 is independent of stress level. For situations where Eq 3 is not applicable, or where the gage and structural material exponents (m in Eq 3) are not identical, the a_s versus a_g relation is not independent of load. The significance of these limitations is discussed later.

Application of Numerical Model to Present Experiments

Now consider the problem of specifying the quantities in Eq 6 for the present experiments. The material constants C_s , C_g , and m were determined from conventional constant amplitude fatigue crack growth tests. A standard closed loop electrohydraulic (MTS) test machine was used for these baseline experiments and the results are summarized in Table 2 with the measured values of C and m . (The complete data are recorded in Ref 1.) Note that the different alloys did not yield the same exponent m when least squares power laws were fit through the raw data. In order to employ the equal m assumption in Eq 6, the gage and structural exponents were averaged and new values obtained for C_s and C_g with this specified m . These modified crack growth properties, also recorded in Table 2, were found to represent the original fatigue crack growth rate behavior quite well over the range of data collected. Thus, it is felt that this modification procedure is justified for the present work.

Next, the stress intensity factor coefficients β_s and β_g must be specified. As discussed in Ref 4, a width corrected form of the well known Bowie [15] solution for radially cracked holes provides a good estimate of β_s for these experiments. For the edge cracked coupons, a recent solution [16] for displacement controlled end conditions appropriate to the present unbonded gage length ($L/W = 2$) was employed. The effective deflection applied to the edge-cracked gage was determined from the load transfer measurements obtained from foil strain gages mounted on the *uncracked* coupons described previously. If the ends of the coupon had

TABLE 2—Fatigue crack growth constants for power law equations.^a

	2219-T851 ^b	2024-T3	7075-T6
EXPERIMENTAL			
<i>C</i>	3.835×10^{-11} ($.1688 \times 10^{-18}$)	2.618×10^{-11} ($.1385 \times 10^{-18}$)	4.279×10^{-10} ($.7828 \times 10^{-16}$)
<i>m</i>	3.363	3.336	2.816
MODIFIED			
<i>C</i>	3.940×10^{-11} ($.1908 \times 10^{-18}$)	2.526×10^{-11} ($.1223 \times 10^{-18}$)	
<i>m</i>	3.349	3.349	
<i>C</i>	7.442×10^{-11} ($.2119 \times 10^{-17}$)		2.351×10^{-10} ($.6694 \times 10^{-17}$)
<i>m</i>	3.089		3.089

^a $da/dN = C\bar{K}^m$.

^b 1.33 cm (0.525 in.) thickness. Units of *C* are such that da/dN has units of m/cycle (in./cycle) and \bar{K} has units of MPa·m^{1/2} (psi·in.^{1/2}).

been attached rigidly to the structure, and if there were no bending in the system, the deflection δ over the length L would be

$$\sigma = \frac{P'_g L}{A_g E_g} = \frac{P_s L}{A_s E_s} \quad (7)$$

Here A_g , A_s , E_g , and E_s are the appropriate cross sectional areas and elastic moduli for the gage and structural members, while P'_g is the effective load in the uncracked coupon, and P_s is the remote force applied to the structure. Since the elastic moduli are approximately equal for these aluminum alloys, we have

$$P'_g = P_s \frac{A_g}{A_s} \quad (8)$$

In the actual adhesively bonded coupon, however, several factors prevent this value of P'_g from reaching the gage (adhesive strain, bending, etc.). The actual effective load P_{gact} in the uncracked coupon computed from the strain measurements is shown for three tests as a function of applied structural load P_s in Fig. 3. Note that the ratio of actual load transfer P_{gact}/P'_g had an approximate constant of 0.84 over most of the load cycle. The 5 percent variation in P_{gact}/P'_g from test to test indicated in Fig. 3 is most likely due to bondline variations. The strain gage measurements were repeated during the course of the fatigue tests, with no noticeable degradation in load transfer with cycle life. Using the

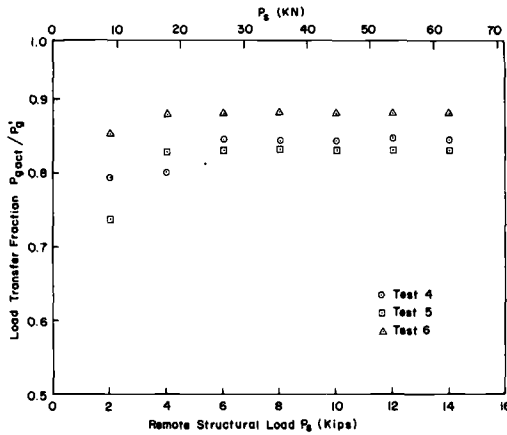


FIG. 3—Ratio of actual load transfer as a function of applied structural load obtained from strain gage measurements on uncracked coupons.

deflection due to P_{gact} computed from Eq 7 as the input displacement to the edge crack K solution [16], and letting $P_{gact} = 0.84 P'_g$ (effectively equivalent to letting $f = 0.84$ in Eq 6), specifies all of the unknown terms in Eq 6. Other numerical procedures for determining the load transfer function f are described in Refs 2-4. As described in Ref 2, Eq 6 is solved readily for a_s as a function of a_g by an iterative scheme.

Comparison of Experiment and Analysis

Now consider the experimental data and corresponding predictions obtained for the eleven specimens tested in accordance with Table 1. Recall that crack length versus elapsed cycles data were collected as indicated in Fig. 4 for tests 11 and 12 (2219-T851 gages). Next, a_s was plotted versus the value of a_g corresponding to the same cyclic life. These results are summarized in this format and compared in Figs. 5 to 8 with the numerical predictions. Examining Fig. 4, note that a_s and a_g grew much faster in specimen 11, tested at $\sigma_s = 92$ MPa (13.3 ksi), than in specimen 12 which was cycled at 72 MPa (10.5 ksi). When these data are compared in the a_s versus a_g format of Fig. 5, however, the effect of test load is much less significant. Specimen 10 is a replicate of test 11, and indicates the repeatability of results.

The two predictions shown on Fig. 5 differ only in the exponent m used in Eq 6. The curve on the left assumed the exponent ($m = 3.36$) determined for the structural thickness. (Recall that the 2219-T851 gages were machined from one of the original structural specimens.) The curve on the right assumed $m = 2.26$ as determined separately from the gage thickness. Note that both predictions agree quite satisfactorily with the

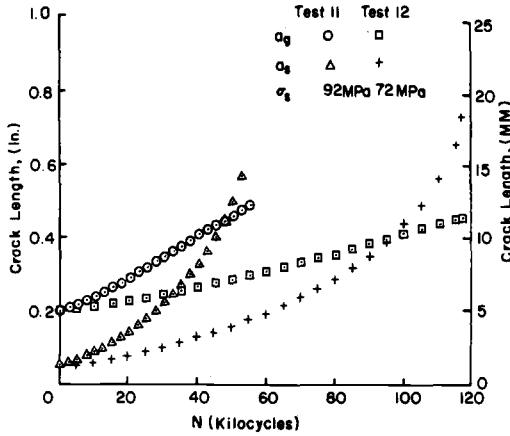


FIG. 4—Typical fatigue crack growth data for tests 11 and 12 (2219-T851 gages) showing effect of load level on crack propagation in identical specimens.

experimental results. It is significant to emphasize here that computation of Eq 6 involves no knowledge of the actual loads applied to the test specimens. In addition, the a_s versus a_g curves are fairly insensitive to the value chosen for m . (Similar results are also reported in Ref 2.)

It is useful to point out one further point with respect to Fig. 4. Note that the gage crack growth rates in both specimens 11 and 12 are

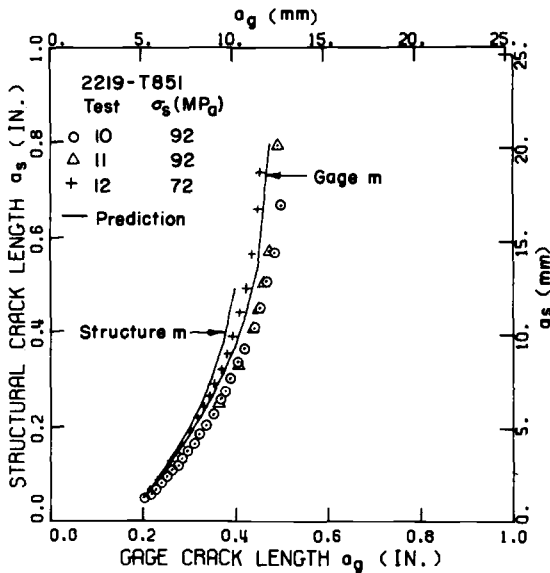


FIG. 5—Comparison of experimental data for structural crack versus gage crack with mathematical prediction for tests 10, 11, and 12 (2219-T851 aluminum gages).

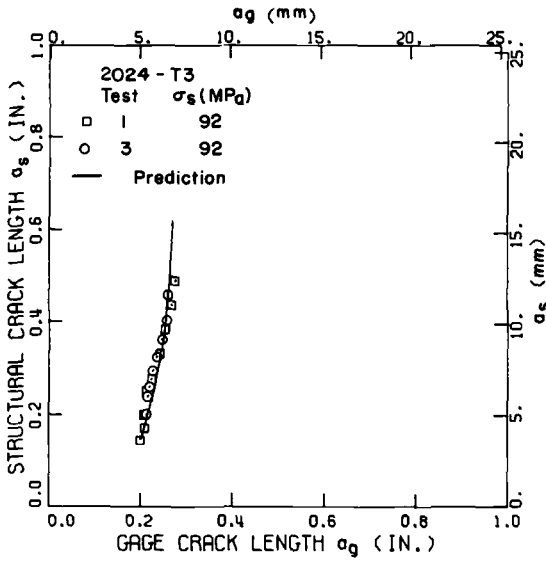


FIG. 6—Comparison of experimental data for structural crack versus gage crack with mathematical prediction for tests 1 and 3 (2024-T3 aluminum gages).

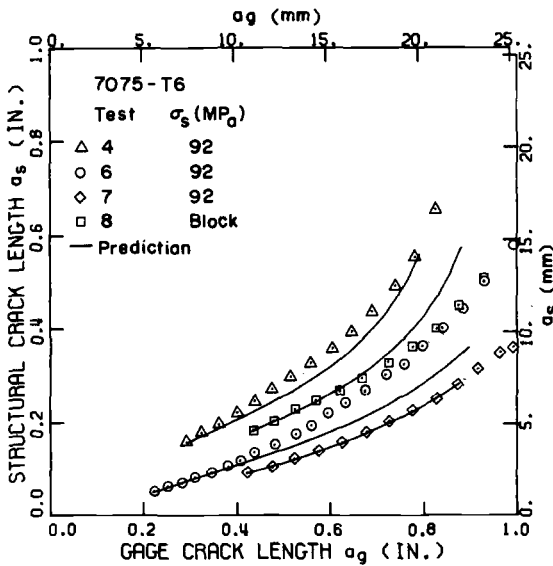


FIG. 7—Comparison of experimental data for structural crack versus gage crack with mathematical prediction for tests 4, 6, 7, and 8 (7075-T6 aluminum gages).

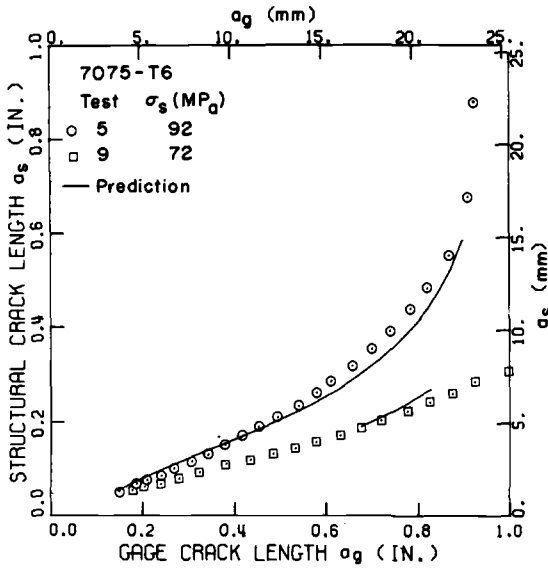


FIG. 8—Comparison of experimental data for structural crack versus gage crack with mathematical prediction for tests 5 and 9 (7075-T6 aluminum gages).

approximately constant, a fact in qualitative agreement with the stress intensity factor solution of Ref 16. That solution indicates nearly constant K over a large range of crack lengths when the edge cracked coupons are loaded with a fixed displacement. Similar periods of nearly constant gage crack growth rate were observed in the other experiments as well.

Results of the two 2024-T4 crack gages (tests 1 and 3) are shown in Fig. 6. These specimens also gave repeatable a_s versus a_g curves which agree extremely well with the numerical predictions. The steepness of these curves limits their interest from a practical standpoint, however, since the structural defect grows much faster than the gage flaw. Thus, a_s could become quite large with very little warning given by monitoring the extension of a_g . The relative steepness is not surprising, since the initial structural flaws a_{si} were much larger in tests 1 and 3 than for tests 10, 11, and 12 (the a_{gi} are similar). Thus, the ratio between structural and gage K is larger for tests 1 and 3, and the structural defect grows at a faster rate (in comparison to a_g) than in Fig. 5.

The 7075-T6 crack gage results are presented in Figs. 7 and 8. All data in Fig. 7 were obtained at a cyclic load of 92 MPa (13.3 ksi), except for specimen 8, which was subjected to the simple block loading sequence described earlier. The predictions for tests 4 and 7 agree very well with the experimental behavior, while calculations for specimens 6 and 8 initially follow the data, but then diverge slightly. Part of the deviation in test 6 (the greater of the two), may be due to changes in the test environment.

Although the test environment was not controlled, ambient laboratory temperature and relative humidity were recorded. The relative humidity for test 6 was approximately 15 to 20 percentage points lower than normal. Since the 7075-T6 aluminum alloy is particularly sensitive to environmental changes [18], this difference in test conditions could explain the slightly slower than predicted crack in gage 6.

The results of tests 5 and 9 are presented in Fig. 8. These two specimens had nearly equal initial crack lengths, but were subjected to different constant amplitude load levels. Note that the numerical prediction agrees very well with test 5, but that the data for Specimen 9 differ significantly. Although specimen 9 had a slightly larger gage flaw and a smaller defect size than specimen 5 (see Table 1), the difference is not enough to explain completely the large change in behavior. Changes in relative humidity do not appear to be the answer either. One potential explanation could lie in the stress intensity factor level of the structural defect a_s . The initial cyclic stress intensity factor ranges (ΔK) were 8.2 MPa-m^{1/2} (7.5 ksi-in.^{1/2}) for Test 9 and 11 MPa-m^{1/2} (10 ksi-in.^{1/2}) for Test 5. The original crack growth data for the 2219-T851 material given in Ref 1 indicates that below ΔK of 11 MPa-m^{1/2} (10 ksi-m^{1/2}), the slope of the da/dN versus ΔK curve is significantly steeper than indicated by the baseline constants recorded in Table 2. Such deviation from the baseline behavior at low ΔK levels could explain the slower structural crack growth in Test 9. To pursue this point further, the structural defect a_s required in Test 9 to give the same initial K of 11 MPa-m^{1/2} (10 kis-m^{1/2}) for Test 5 was determined. A prediction starting with this new crack length (and corresponding a_s) is shown in Fig. 8 as the short curve beginning in the latter portion of the specimen 9 data. This prediction agrees adequately with the remaining experimental data.

Discussion

The results of the present investigation provide encouraging support for the crack gage method for monitoring the effect of service loads on extension of possible cracks in structural components. As shown here, measurements of fatigue crack growth in small edge cracked coupons which were bonded adhesively to a larger specimen provided a convenient means for quantifying flaw extension in the parent member. The relationship between the gage and simulated structural defects was repeatable (with one explainable exception), and, in general, agreed well with predictions made by Eq 6.

The load independence suggested by Eq 6, and borne out by the experiments described here and in Refs 2-4, deserves further discussion at this point. Recall that the key assumption that allowed the loads to cancel in Eq 6 was use of Eq 3 to correlate fatigue crack growth rates. Stress level terms cannot be eliminated entirely from the general expres-

sion of Eq 2 when more complex crack growth models are employed. (See the results of calculations based on the Forman Model [18] reported in Ref 3.)

Although use of Eq 3 may seem unduly restrictive, considerable work indicates that variable amplitude loading can often be described by this simple law. It has been shown, for example, that it may be useful to interpret \bar{K} in Eq 3 as the maximum repeating stress intensity factor in a variable amplitude load history, or perhaps, as the root mean value of alternating K [10,19]. Indeed, this approach was employed in Ref 3, where growth of two cracks located in series in a long specimen subjected to a complex load spectrum were successfully related by means of Eq 6. Again, no knowledge of actual loads was required for the prediction.

However, the load independent result of Eq 6 cannot be expected to apply for all cases. It is well known, for example, that variable amplitude loading cannot always be correlated by Eq 3. For these situations, Eq 2 is still valid, but it is no longer independent of load. Since a tracking device should be as simple as possible, the requirement for another load monitoring system to reduce crack gage data could be a serious limitation of the crack gage approach for aircraft tracking requirements.

One possible solution to this problem could be to employ two independent crack gages at each tracking location. Now, returning to Eq 2, an analogous relationship can be written for the cyclic life of the two crack gages, giving

$$N = \int_{a_{1i}}^{a_1} \frac{da}{F_1(K)} = \int_{a_{2i}}^{a_2} \frac{da}{F_2(K)} \quad (9)$$

where the subscripts 1 and 2 now refer to gages 1 and 2. The functions $F_1(K)$ and $F_2(K)$, relating stress intensity level with fatigue crack growth rate, are now the appropriate expressions for the two gage materials. Although identical materials most likely would be used for both gages, giving $F_1(K) = F_2(K)$, this requirement would not appear essential. Since the crack lengths in the gages will be recorded during service, the upper limits (a_1 and a_2) on the integrals will be known, as well as the initial crack sizes a_{1i} and a_{2i} . Thus, it is possible to introduce an effective stress level as an unknown in the expressions for $F(K)$ in Eq 9. After solving Eq 9 for this stress term, one (or both) of the gages again would be matched with the assumed structural flaw as in Eq 2, and solved for the structural crack size a_s . Since this procedure allows one to choose a variety of crack growth laws to characterize crack growth, it should be possible to analyze the apparent stress level problem described in Fig. 8. Actual calculations with this algorithm remain, however, for future work.

Conclusions and Recommendations

In summary, work to date on the crack gage approach to aircraft tracking is quite encouraging. The method appears to provide promise as a simple and effective technique for monitoring the loads encountered by a structure during service, and for determining their effect on the extension of potential structural cracks. The results obtained to date lead the authors to suggest the following specific conclusions and recommendations for future research.

1. Adhesively bonded edge-cracked coupons provide an effective "gage" for monitoring loads in structural components.
2. When fatigue crack growth caused by constant amplitude or variable load histories can be correlated by a simple power law, the mathematical model employed here provides an accurate means for predicting the relation between gage and structural defects. Under these conditions, the a_s versus a_g curve is repeatable and is insensitive to load level.
3. Crack gage response for more complicated load histories should be investigated to identify possible load history dependence in the relation between gage and structural cracks.
4. The double crack gage concept outlined here should be investigated further as a means for treating potential load history effects.
5. Additional research is needed to evaluate adhesive bonding methods for ensuring long term crack gage integrity under actual service conditions.

Acknowledgments

A portion of the work discussed here was conducted by the first author (J.A.O.) in partial fulfillment of the requirements for the Degree of Master of Science at the Air Force Institute of Technology, Wright-Patterson Air Force Base, Ohio. The authors wish to thank P. J. Torvik and N. A. Ashbaugh for their helpful suggestions and discussions, and greatly appreciate the valuable assistance provided by R. F. Klinger and J. G. Paine during the experimental program.

References

- [1] Ori, J. A., "Experimental Evaluation of a Single Edge Cracked Crack Growth Gage for Monitoring Aircraft Structure," thesis, AFIT/GA/AA/770-9, Air Force Institute of Technology, Wright-Patterson Air Force Base, Ohio, Dec. 1977.
- [2] Grandt, A. F., Jr., Crane, R. L., and Gallagher, J. P. in *Fracture; Proceedings*, 4th International Conference on Fracture, Vol. 3, Waterloo, Canada, 19-24 June 1977, pp. 39-45.
- [3] Gallagher, J. P., Grandt, A. F., Jr., and Crane, R. L., *Journal of Aircraft*, Vol. 15, No. 7, July 1978, pp. 435-442.
- [4] Ashbaugh, N.E. and Grandt, A. F., Jr., in *Service Fatigue Loads Monitoring, Simulation and Analysis, ASTM STP 671*, American Society for Testing and Materials, 1979, pp. 94-117.

- [5] "Aircraft Structural Integrity Programs, Airplane Requirements," MIL-STD-1530A (11) (USAF), Dec. 11, 1975.
- [6] Morcock, D. S., "Highlights of the C-141 Service Life Monitoring Program" presented at the ASTM Symposium on Service Fatigue Loads Monitoring, Simulation and Analysis, Atlanta, Ga., 14-15 Nov. 1977.
- [7] Whitford, D. H. and Dominic, R. J. in *Proceedings*, Air Force Conference on Fatigue and Fracture of Aircraft Structures and Materials, H. A. Wood, et al, Ed., Air Force Flight Dynamics Laboratory, Wright-Patterson Air Force Base, Ohio, 1970, pp. 847-864.
- [8] Harting, D. R., *Experimental Mechanics*, Vol. 6, No. 2, Feb. 1966, pp. 19A-24A.
- [9] Spanner, J. C. and McElroy, J. W., Ed., *Monitoring Structural Integrity by Acoustic Emission*, ASTM STP 571, American Society for Testing and Materials, 1975.
- [10] Gallagher, J. P. and Stalnaker, H. D. in *Proceedings*, AIAA/ASME/SAE 17th Structures, Structural Dynamics, and Materials Conference, 5-7 May 1976, pp. 486-494.
- [11] Parker, G. S. and Pinckert, R. E., "Generalized Procedures for Tracking Crack Growth in Fighter Aircraft," presented at the ASTM Symposium on Service Fatigue Loads Monitoring, Simulation and Analysis, Atlanta, Ga., 14-15 Nov. 1977.
- [12] Smith, H. W., *Fatigue Damage Indicator*, U.S. Patent No. 3, 979, 949, assigned to The Boeing Company, Seattle, Wash., 14 Sept. 1976.
- [13] Johnson, W. S. and Paquette, S. J., "Design and Evaluation of a Cracked Gage Concept for Monitoring Potential Crack Growth in Fleet Aircraft," Report ERR-FW-1831, General Dynamics, Fort Worth, Texas, July 1977.
- [14] "Proposed Method of Test for Measurement of Fatigue Crack Growth Rates," appendix 1 to Report "Development of Standard Methods of Testing and Analyzing Fatigue Crack Growth Rate Data," Technical Report AFML-TR-78-40, Air Force Materials Laboratory, Wright-Patterson Air Force Base, Ohio, May 1978.
- [15] Bowie, O. L., *Journal of Mathematics and Physics*, Vol. 35, 1965, pp. 60-71.
- [16] Torvik, P. J., "Applications of the Extremal Principles of Elasticity to the Determination of Stress Intensity Factors," Technical Report AFIT-TR-77-3, Air Force Institute of Technology, Wright-Patterson Air Force Base, Ohio, July 1977.
- [17] Truckner, W. G., Staley, J. T., Bucci, R. J., and Thakker, A. B., "Effects of Microstructure on Fatigue Crack Growth of High Strength Aluminum Alloys," Technical Report AFML-TR-76-169, Air Force Materials Laboratory, Wright-Patterson Air Force Base, Ohio, Oct. 1976.
- [18] Forman, R. G., Kearney, B. E., and Engel, R. M., *Journal of Basic Engineering; Transactions*, American Society of Mechanical Engineers, Vol. 89, No. 3, 1967, p. 459.
- [19] Rolfe, S. T. and Barsom, J. M., *Fracture and Fatigue Control in Structures*, Prentice Hall, Englewood Cliffs, N. J., 1977.

Measurement of Crack-Tip Stress Distributions by X-Ray Diffraction*

REFERENCE: Allison, J. E., "Measurement of Crack-Tip Stress Distributions by X-Ray Diffraction," *Fracture Mechanics, ASTM STP 677*, C. W. Smith, Ed., American Society for Testing and Materials, 1979, pp. 550–562.

ABSTRACT: Crack-tip stress distributions were measured on the surface of fatigue-cracked specimens of 1045 steel using a semiautomatic X-ray diffraction technique. The influence of overload cycles and crack extension on crack-tip stress profiles was studied. These overload-influenced stress profiles were observed to follow current analytical models generally. Overload cycles were shown to have a strong effect on subsequent residual and applied stress profiles. It was deduced that overload-induced crack-tip residual stresses are tensile on the interior of the specimen, the implication being that crack growth retardation may thus be a surface related phenomenon. Crack tip applied stresses were also measured and were found to be consistent with simple models for the crack tip applied stress profile.

KEY WORDS: crack propagation, stresses, residual stresses, X-ray diffraction, crack growth retardation, fatigue (materials), steels

The accurate prediction of fatigue crack growth behavior under variable amplitude loading depends on an accurate modeling of load-interaction effects, one important load-interaction effect being the retardation of fatigue crack growth due to the application of an overload [*1*]². A number of analytical models have been developed to predict these effects, most of which are based on the inducement of compressive residual stresses either in the plastically deformed region ahead of the crack tip or in the deformed region immediately behind the propagating crack tip. These models are dependent on an understanding of the crack-tip stress profile or the crack tip plastic zone size, which are estimated generally by Rice's model [2] or variations of it, depicted in Fig. 1. More recently, finite ele-

*Original experimental data were measured in U.S. customary units.

¹ Damage tolerance and durability engineer, Air Force Flight Dynamics Laboratory, Wright-Patterson AFB, Oh. 45433. Presently at Department of Metallurgy and Materials Science, Carnegie-Mellon University, Pittsburgh, Pa. 15213.

² The italic numbers in brackets refer to the list of references appended to this paper.

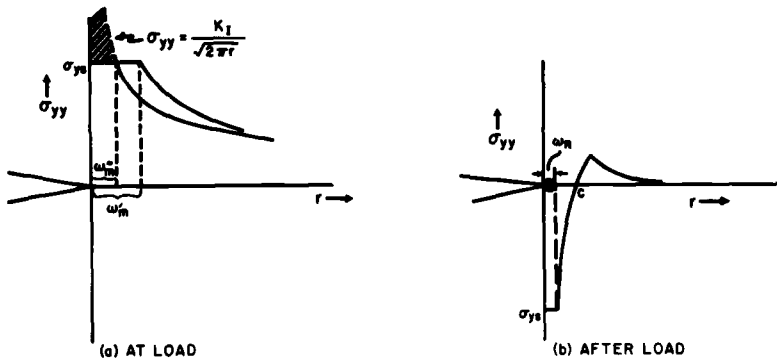


FIG.1—Schematic of crack-tip stress profiles perpendicular to crack plane.

ment analysis has been applied to the analysis of crack-tip stresses [3,4] and to model the effects of overloads and crack-tip extension on the crack-tip stress profiles [5]. While these analytical developments have been used widely to predict crack growth under variable amplitude loading, experimental determination of crack-tip stresses and how these stresses are modified by overloads and crack extension has been accomplished only in a very limited sense.

In earlier works, Taira [6] and Evans et al [7] investigated the feasibility of using X-ray diffraction to measure crack-tip stresses. In a recent study, Macherauch and Wolfsteig [8] used X-ray diffraction to measure a crack-tip residual stress profile in a steel alloy and observed the effect of this residual stress on subsequent crack-tip stress profiles while the specimen was loaded to various levels. They observed that the maximum compressive stress was approximately 40 percent of the yield strength. Since these three studies were conducted prior to the advent of the semiautomated X-ray diffraction stress analyzer, the investigations typically required 30 to 60 min per datum point. Therefore, they were quite limited in scope; however, they did establish the feasibility of investigating crack-tip stress phenomena using X-ray diffraction.

In the present investigation a semiautomatic X-ray diffraction stress analyzer was used to observe the crack-tip stress distribution. Distributions were measured prior to an overload, during the application of an overload, and after the application of an overload. Stress profiles also were determined after crack growth subsequent to the application of an overload.

Experimental Procedure

A plain carbon, 1045 steel alloy was selected for this investigation. The alloy was heat treated to produce a microstructure of fine spheroidized

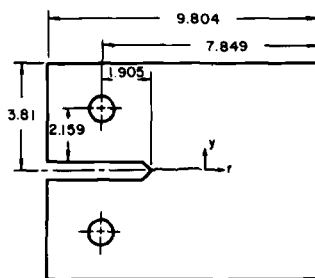


FIG. 2—Compact specimen geometry and crack-tip stress measurement coordinates (dimensions in centimetres).

carbides in a ferrite matrix with scattered proeutectoid ferrite grains. The grain size was determined to be ASTM 11 using transmission electron microscopy. The alloy exhibited a pronounced upper and lower yield point behavior, with a lower yield point of 722 MPa, an ultimate strength of 786 MPa and an elongation of 25.8 percent in a 2.54 cm gage section. The hardness was determined to be 23 on the Rockwell C Scale.

Specimen surface preparation was given careful attention to ensure a low baseline surface stress. Specimen blanks were machined and then surface ground to a thickness of 5.9 mm using a low stress grinding technique. They were then annealed in a vacuum furnace for 35 min at 540° C (1000° F) and furnace cooled. This provided a surface residual stress of ± 14 MPa. The final specimen configuration was the ASTM compact specimen shown in Fig. 2 with a height to width ratio of 0.486 and a thickness of 5.9 mm.

The stress measurements were made using a semiautomatic X-ray diffraction stress analyzer³ which is shown in Fig. 3. The X-ray diffraction equipment was designed specifically for measurements on ferritic and martensitic steels by observing the 211 reflection of the body centered cubic lattice with chromium radiation ($K\alpha$) at a diffraction angle, 2θ , of about 156 deg. The unit is equipped with two X-ray diffraction goniometers, one which measures lattice spacings normal to the surface and one which measures lattice spacings oriented at 45 deg to the surface. Each goniometer has a chromium X-ray tube and a dual Geiger tube X-ray detection device. The X-ray beam size is variable. A special collimator was used for this study which produced a 0.635 mm diameter X-ray spot on the specimen. The X-ray excitation voltage was 35 kV and the current was nominally 10 mA. The X-ray detectors automatically scan the range of 2θ values (limited to 152 to 159 deg) and search for the diffraction peak using a servomechanism.

³ The X-ray analyzer used in this investigation was the FASTRESS Stress Analyzer, manufactured by the American Analytical Corporation.

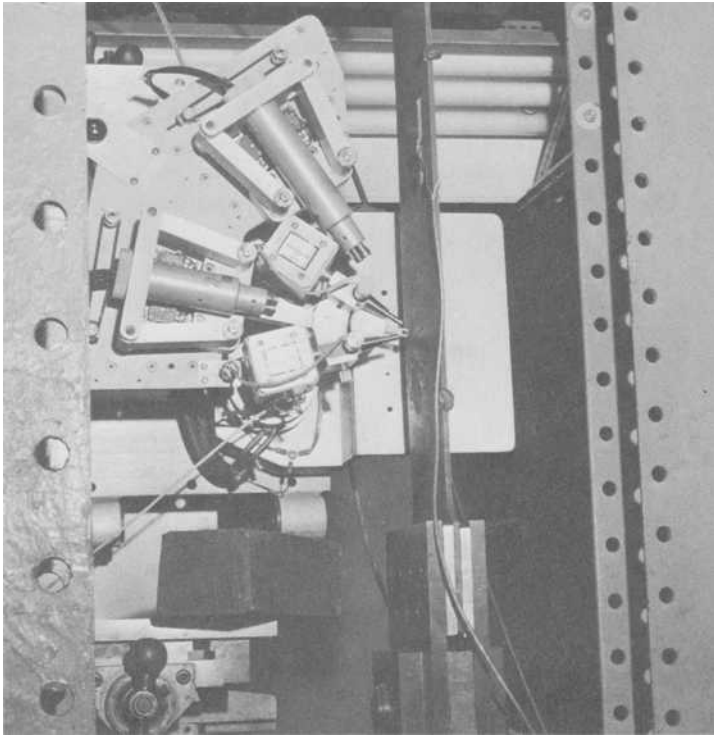


FIG. 3—X-ray diffraction stress analyzer.

The measured surface stress is given by

$$\sigma = S \cdot \Delta 2\theta \quad (1)$$

where S is a calculated or experimentally determined stress factor and $\Delta 2\theta$ is the difference between the two diffraction angles [9,10]. The difference between the diffraction angles, $\Delta 2\theta$, is registered in an electronics console and electronically multiplied by a preset stress factor, S , before being automatically plotted on the chart recorder. A stress factor of 597 MPa/deg was determined theoretically for the 1045 steel using the procedure outlined in Refs 9 and 10. This factor was verified experimentally by measuring the stress in a tensile specimen loaded to various levels and comparing these measurements with the calculated stresses. In a previous investigation [11], statistical evaluation of stress measurements using the X-ray diffraction unit on an annealed, unstressed specimen gave a mean value of +2 MPa and a standard deviation of 30 MPa. Details of the stress factor determination and the general equipment calibration are given in Ref 12.

For the purpose of this study the X-ray head was mounted on a traveling stage capable of accurately indexing 0.025 mm in the x , y , and z directions. This assemblage was located next to a hydraulic load system. Crack-tip stresses were measured normal to the crack plane, σ_{yy} as shown in Fig. 2, in specimens which had been precracked by cyclic loading. Precracking and post overload crack growth were conducted in a closed loop servohydraulic testing machine operating under load control in tension-tension loading at a load ratio (minimum load to maximum load) of 0.1 and at a frequency of 2 Hz. After precracking, the specimens then were placed in the load system with the X-ray diffraction unit and stress measurements were made in the loaded and unloaded conditions. Each stress measurement took approximately 3 min; measurement of an entire stress profile required 1 to 2 h. Repeat measurements of selected stress profiles were performed throughout the investigation. The reproducibility of individual profiles was quite good; even in the steeper parts of the curves deviations were never greater than ± 14 MPa.

Results and Discussion

Effects of Overloads and Crack Extension on Crack-Tip Stress Profiles

The results of crack-tip stress measurements before and after an overload are shown in Figs. 4 and 5. Figure 4a shows data obtained on a specimen which had been precracked under constant load producing a final maximum stress intensity, K_{\max} , of $30 \text{ MPa}\sqrt{\text{m}}$ at a crack length, a , of 25.80 mm. In the unloaded condition no appreciable crack-tip stresses were observed, due primarily to the small size of the stress gradient in comparison to the X-ray beam size. Upon loading to an intermediate level, $K = 18 \text{ MPa}\sqrt{\text{m}}$, the crack-tip stresses rose steeply behind and ahead of the crack tip. The remote load then was increased to provide the baseline stress intensity, $K = 30 \text{ MPa}\sqrt{\text{m}}$. At this load level the tensile stresses increased significantly and the tensile region extended well ahead of the crack. The fact that nonzero stresses existed behind the crack tip was attributed to the size of the X-ray beam, which was much larger than the crack opening, and thus stresses were measured in the material on both sides of the opened crack. An overload, K_{OL} , equal to $76 \text{ MPa}\sqrt{\text{m}}$ was applied to the specimen, and the resulting residual stress profile is shown in Fig. 4b. A region of compressive stresses was observed at the crack tip, with the stress decreasing smoothly to a zero stress level 2.25 mm ahead of the crack. Offsetting the high compressive stresses, low magnitude tensile stresses were observed immediately behind the crack tip; however, in general, a lack of stress balance was observed. Shaw [13] has observed that complete crack closure occurred only at the specimen surface along shear lips and that the interior crack surfaces remain open. Thus, the lack of stress balance observed here, may be indicative of

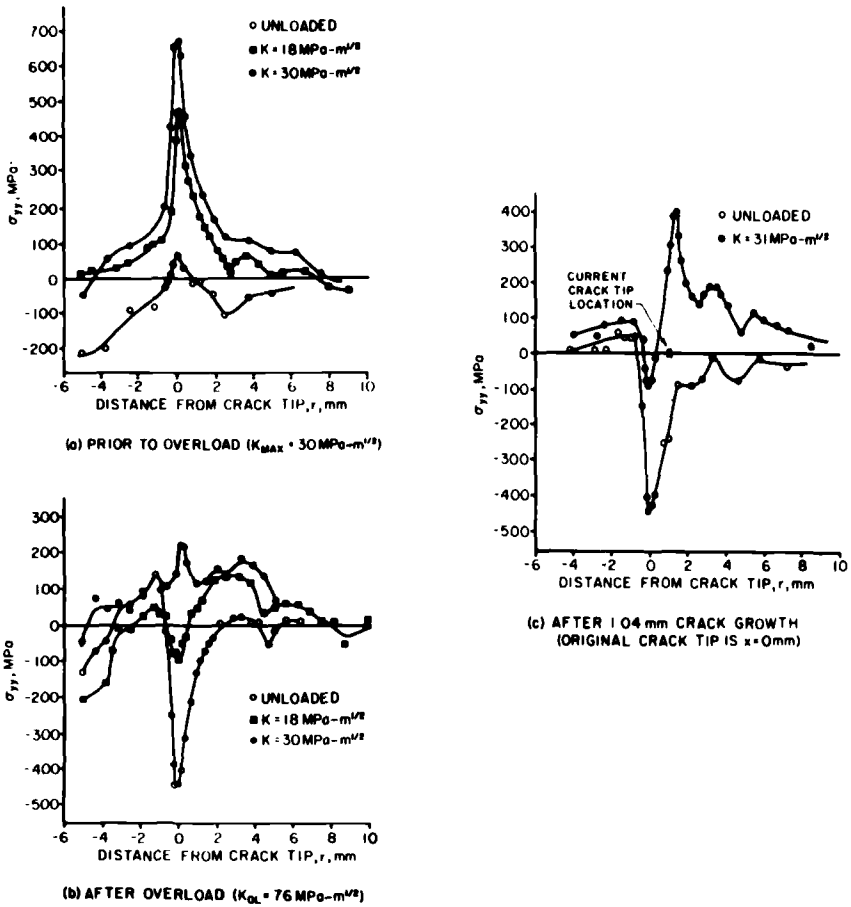


FIG. 4—Influence of $76 \text{ MPa}\sqrt{\text{m}}$ overload and 1.04 mm crack extension on crack-tip stress profile (specimen CT45-1).

subsurface tensile stresses. Upon reloading the specimen to the intermediate level, $K = 18 \text{ MPa}\sqrt{\text{m}}$ and then to the baseline stress intensity, $K = 30 \text{ MPa}\sqrt{\text{m}}$, the crack-tip stress distributions were reduced significantly compared to those measured before the $76 \text{ MPa}\sqrt{\text{m}}$ overload.

Similar measurements were made in another specimen which had been precracked under constant load to produce a final K_{max} of $44 \text{ MPa}\sqrt{\text{m}}$ at a crack length of 23.01 mm. These results are shown in Fig. 5. Figure 5a shows the preoverload stress profiles. In the unloaded condition a small region of compressive residual stresses was observed at the crack tip, due to the baseline cyclic loading. Upon loading to the maximum stress intensity ($44 \text{ MPa}\sqrt{\text{m}}$) a large tensile stressed region was observed at the crack tip, rising steeply behind and in front of the crack tip. An overload

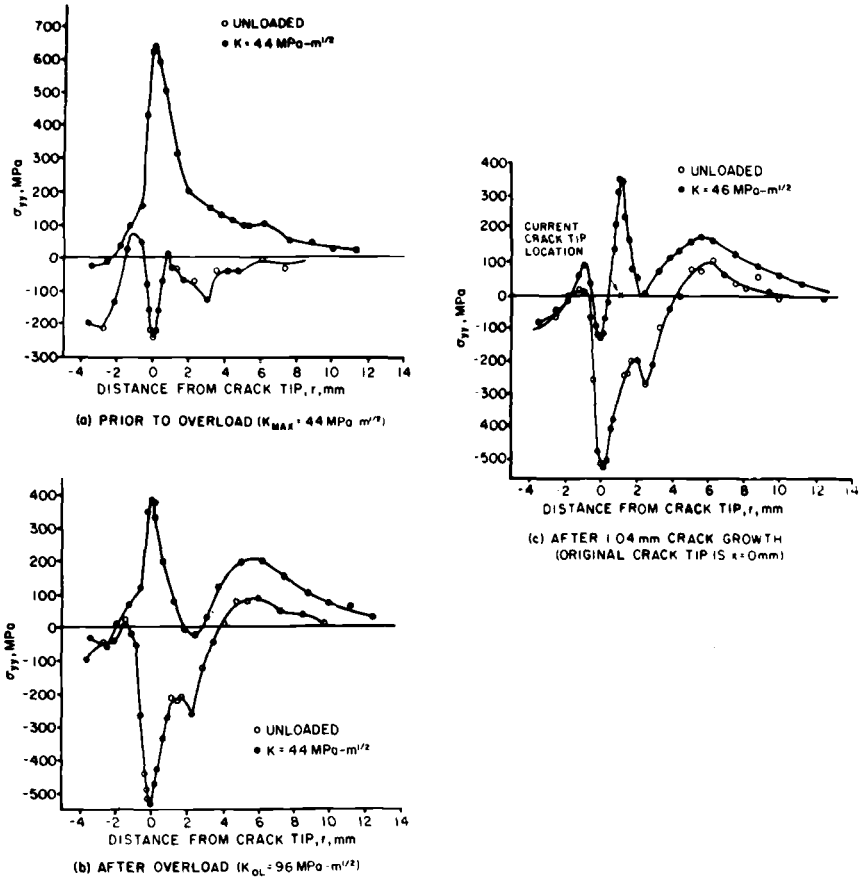


FIG. 5—Influence of $96 \text{ MPa}\sqrt{\text{m}}$ overload and 1.04 mm crack extension on crack-tip stress profiles (specimen CT45-3).

of $96 \text{ MPa}\sqrt{\text{m}}$ was applied, which produced the residual stress profile shown in Fig. 5b. The region of compressive stresses was pronounced and extended well ahead of the crack tip. Although a region of residual tensile stresses existed from 4 to 10 mm ahead of the crack, generally a lack of stress balance was observed, again indicative of subsurface residual tensile stresses. In this specimen the residual stress profile had a perturbation 2.25 mm ahead of the crack tip as can be observed in Fig. 5b. Optical observations of the specimen surface revealed that the overload had caused pronounced deformation bands at the crack tip, and thus the stress profile perturbation was possibly due to these localized slip lines. The specimen was reloaded to the baseline stress intensity ($44 \text{ MPa}\sqrt{\text{m}}$), and a region of tensile stresses was observed at the crack tip. The maximum tensile stress was reduced greatly from that at the same

load level before the overload (Fig. 5*b*). At this load level a dip in the stress profile was observed, again at 2.5 mm ahead of the crack tip, where the profile dropped rapidly to zero and then increased to produce a second region of tensile stresses well ahead of the crack. This might also be attributable to the pronounced slip lines.

After the application of the overloads both specimens were cycled at their baseline load levels to extend the cracks into their overload affected zones. Stress measurements then were taken in the unloaded and loaded conditions (Figs. 4*c*, 5*c*). Figure 4*c* shows that, except for a slight extension of the compressive stressed region at the tip of the extended crack, the residual stress profile was not affected by the crack extension of 1.04 mm. Upon loading the specimen to the baseline load level ($31 \text{ MPa}\sqrt{\text{m}}$), a tensile stress profile was observed at the crack tip which was greater than that observed immediately after the overload (Fig. 4*b*) but still significantly lower than the pre-overload stress profile shown in Fig. 4*a*. A region of compressive stresses was observed immediately behind the crack tip, which may be related to the crack closure phenomena originally observed by Elber [14].

Figure 5*c* shows similar effects for the second specimen, in which the crack was extended 1.04 mm into the overload affected zone. The overload-induced compressive residual stress region was observed to be unaffected by this crack extension. The specimen was loaded to the baseline load level ($46 \text{ MPa}\sqrt{\text{m}}$), and stress measurements showed the maximum tensile stress at the crack tip to be approximately the same as that before crack extension (Fig. 5*b*) but significantly lower than the pre-overload tensile stress. The stress profile displayed the dip at 2.25 mm ahead of the original crack tip location which was observed in Fig. 5*b*. A region of compressive stresses was observed immediately behind the crack tip similar to that observed in Fig. 4*c*.

The foregoing results are in qualitative agreement with the finite element analyses conducted by Newman [3] and Ogura and Ohji [5]. Both analyzed the plane stress (surface stress) condition, Newman for an elastic perfectly plastic material and Ogura for a strain-hardening steel. Newman demonstrated that on unloading a cracked specimen from a maximum load the maximum crack-tip stress would decrease as the load was lowered until it passed through the zero stress level and became compressive even though the remote load was tensile. A similar phenomenon was observed in the current work as shown in Fig. 4*b* for a K of $18 \text{ MPa}\sqrt{\text{m}}$ when the crack-tip stress remained in compression even though a remote tensile load was present. Ogura and Ohji studied the influence of overload level on the residual stress induced by the overload, and demonstrated that the maximum compressive residual stress at the crack tip increased with increasing overload levels. The current work showed the maximum compressive residual stress to be strongly

dependent on overload level (compare Figs. 4*b* and 5*b*). Ogura and Ohji also analyzed the effect of crack extension on the residual stress distribution around the crack tip, and observed that as the crack extended a second compressive residual stress maximum would occur at the tip of the extended crack and that the original residual stress would be reduced. Experimentally the second stress maximum was not observed nor was the overload-induced compressive stress observed to diminish with subsequent fatigue cycling. It should be noted that the crack extension was still well within the overload-induced residual stress field and further crack extension might have produced the effect described by Ogura and Ohji.

Stress analysis by X-ray diffraction measures stresses only on the specimen surface and, therefore, cannot be considered representative of the stress state internal to the specimen, that is, as the state of stress changes from plane stress to plane strain. However, due to the lack of stress balance for the post-overload residual stress distributions (Figs. 4*b* and 5*b*) an internal tensile stress distribution might be inferred. This is in agreement with experimental observations by Shaw [13], and Lindley and Richards [15] who observed that crack closure during constant amplitude loading was a surface phenomenon occurring on the shear lips with the internal fracture surfaces remaining open. Bernard, Lindley, and Richards [16] used an electric potential method to show that fatigue crack growth retardation due to the application of an overload was primarily a surface related, plane stress phenomenon. The results of this work are also supportive of this conclusion, if the lack of stress balance in the plane stress region is used to infer a tensile stress in the interior mixed-mode and plane strain regions.

Crack-Tip Stresses Due to Applied Loads

Stress profiles were determined at various intermediate levels up to the overload level. These results are shown in Figs. 6 and 7. As can be seen in both figures the stress gradients are very steep for the lower stress intensities and gradually broaden at higher stress intensities. Figure 7 shows the same dip in the stress profile 2.5 mm ahead of the crack tip which was shown in Fig. 5. It also shows that although the maximum stress at the crack tip begins to level off as load is increased, the remainder of the stress profile increases greatly as the load level is increased.

The maximum crack-tip stresses for both specimens are shown in Fig. 8 versus stress intensity. These data are compared with theoretical elastic estimates of the crack-tip stress profile with corrections made for the stress within the plastic zone. Stress analysis by X-ray diffraction measures only elastic stresses, that is, the lattice straining, and upon plastic deformation and strain hardening the stress determined by X-ray

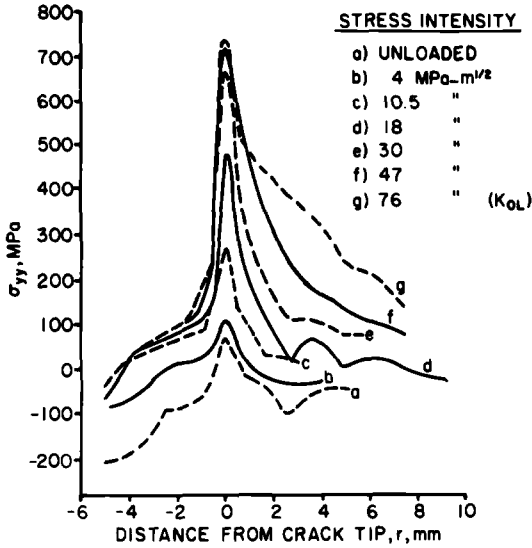


FIG. 6—Crack-tip stress profiles for various applied stress intensity levels (specimen CT 45-1).

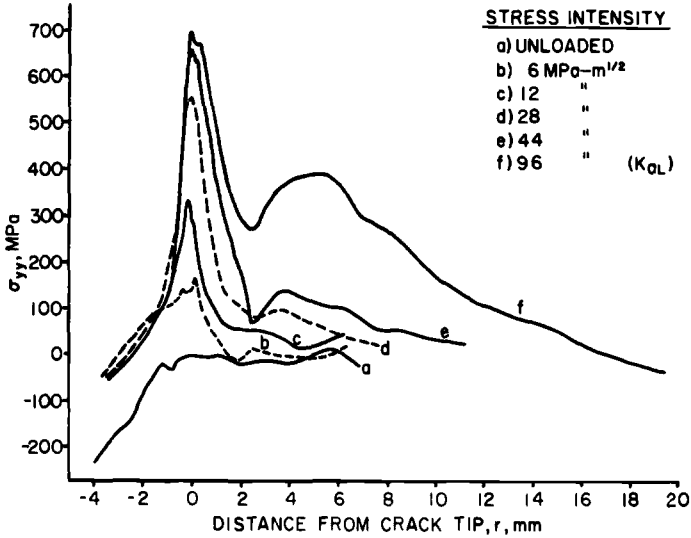


FIG. 7—Crack-tip stress profiles for various applied stress intensity levels (specimen CT45-3).

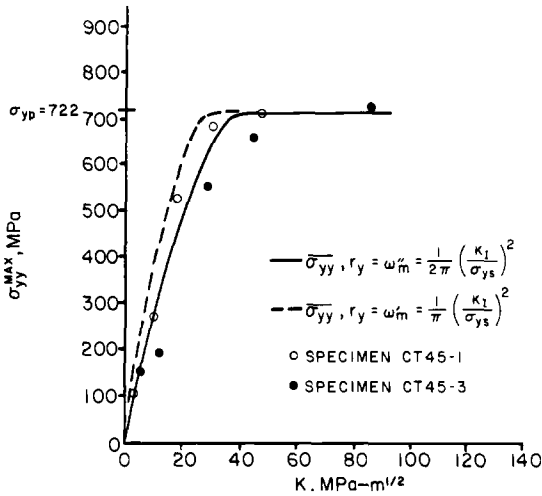


FIG. 8—Maximum measured crack-tip stress versus stress intensity compared with calculated average stress.

diffraction will increase only slightly. Thus comparing these experimentally determined stresses with models assuming elastic-perfectly plastic stress-strain behavior would appear to be a valid correlation. Additionally, the 1045 steel investigated exhibited very little strain hardening, the ultimate strength being only 786 MPa compared to a yield point of 722 MPa, and thus the experimental stresses measured are a reasonable estimate of the total stress on the specimen surface.

To account for the finite X-ray beam size (0.635 mm) it was necessary to calculate an average stress over this region. Two different corrections were made for the stress within the plastic zone, one was made according to Rice's model to account for stress redistribution, that is the plastic zone size, r_y , was equal to ω'_m shown in Fig. 1. The other plastic zone size estimate was calculated assuming no stress redistribution thus $r_y = \omega''_m$ from Fig. 1. The following relationship was used to calculate the average stress, $\bar{\sigma}_{yy}$,

$$\bar{\sigma}_{yy} = \frac{1}{0.635} \left\{ \int_0^{r_y} \sigma_{ys} dr + \int_{r_y}^{0.635} \frac{K_I}{\sqrt{2\pi r}} dr \right\} \quad (2)$$

Because strain hardening was low in this material, no attempt was made to correct the plastic zone size for strain hardening. The experimental data were observed to be generally in agreement with the calculated average stress, which indicates that for cracks which have not been subjected to overloads, the maximum stress level at the crack tip is nearly constant with respect to stress intensity.

Concluding Remarks

Stress profiles at the tip of fatigue cracks were measured using X-ray diffraction. Stress measurement using a semiautomatic X-ray diffraction device was determined to be efficient, accurate, and reliable. These stress measurements were used to study the effects of overloads and crack extension on the crack-tip stress profiles and also to evaluate simple models for crack-tip applied stress profiles.

These stress distributions were seen to be affected strongly by the application of overloads and affected only slightly by subsequent crack propagation. Evidence was found to support arguments that fatigue crack growth retardation is a surface-related plane stress phenomenon. The experimental results were quantitatively consistent with simple models for the crack-tip stress profile.

Acknowledgments

The author gratefully acknowledges the experimental assistance of H. Stalnaker, L. Bates, J. Smith and R. Kleismit. I would also like to express my appreciation for the counsel of the late J. W. Spretnak, Ohio State University, and for helpful discussions with my friends and co-workers in both the Air Force Flight Dynamics Laboratory and Materials Laboratory. This project was sponsored by the Air Force Office of Scientific Research and the Air Force Flight Dynamics Laboratory.

References

- [1] Schijve, J. in *Advances in Aeronautical Sciences*, Vol. 3; *Proceedings*, 2nd International Conference on Aeronautical Sciences, Zurich, Pergamon Press, 1960, p. 387.
- [2] Rice, J. R. in *Fatigue Crack Propagation*, ASTM STP 415, American Society for Testing and Materials, 1967, pp. 247-309.
- [3] Newman, J. C. in *Mechanics of Crack Growth*, ASTM STP 590, American Society for Testing and Materials, 1976, pp. 281-301.
- [4] Tracey, D. M., *Journal of Engineering Material and Technology; Transactions*, American Society of Mechanical Engineers, 1976, Vol. 98, pp. 146-151.
- [5] Ogura, K. and Ohji, K. in *Engineering Fracture Mechanics*, 1977, Vol. 9, pp. 471-480.
- [6] Taira, S. and Tanaka, K. in *Engineering Fracture Mechanics*, 1972, Vol. 4, pp. 925-938.
- [7] Evans, W. P., Ed., unpublished, Minutes of meeting of the X-ray Fatigue Division of the Society of Automotive Engineers Fatigue Design and Evaluation Committee, Society of Automotive Engineers, University of Iowa, Iowa City, Iowa, Sept. 1973.
- [8] Macherauch, E. and Wolfsteig, U., *Materials Science and Engineering*, 1977, Vol. 30, pp. 1-13. (also in *Z. Metallkde.*, 1974 Vol. 65, pp. 496-500).
- [9] Cullity, B. D., *Elements of X-ray Diffraction*, Addison Wesley Publishing Co., Inc., Reading, Mass. 1967.
- [10] Hilley, M. E., Ed., *Residual Stress Measurement by X-ray Diffraction*, SAE J784a, Society of Automotive Engineers, 1971.
- [11] Dietrich, G. and Potter, J. M. in *Advances in X-ray Analysis*, 1977, Vol. 20, pp. 321-328.
- [12] Allison, J. E., "Measurement of Crack Tip Stresses by X-ray Diffraction," AFFDL-TR-78-24, Air Force Flight Dynamics Laboratory, March 1978.

- [13] Shaw, W. J. D. and LeMay, I., "Crack Closure During Fatigue Crack Propagation," 11th National Symposium on Fracture Mechanics, American Society for Testing and Materials, Blacksburg, Va., 12-14 June 1978.
- [14] Elber, W. in *Damage Tolerance in Aircraft Structures, ASTM STP 486*, American Society for Testing and Materials, 1971, pp. 230-242.
- [15] Lindley, T. C. and Richards, C. E. in *Materials Science and Engineering*, 1974, Vol. 14, pp. 281-293.
- [16] Bernard, P. J., Lindley, T. C., and Richards, C. E. in *Metal Science*, Sept. 1977, pp. 390-398.

Alex Vary¹

Correlations Between Ultrasonic and Fracture Toughness Factors in Metallic Materials

REFERENCE: Vary, Alex, "Correlations Between Ultrasonic and Fracture Toughness Factors in Metallic Materials," *Fracture Mechanics, ASTM STP 677*, C. W. Smith, Ed., American Society for Testing and Materials, 1979, pp. 563–578.

ABSTRACT: A heuristic theoretical basis is proposed for the experimental correlations found between ultrasonic propagation factors and fracture toughness factors in metallic materials. A crack extension model is proposed wherein spontaneous stress (elastic) waves produced during microcracking are instrumental in promoting the onset of unstable crack extension. Material microstructural factors involved in this process are measurable by ultrasonic probing. Experimental results indicate that ultrasonic attenuation and velocity measurements will produce significant correlations with fracture toughness properties and also yield strength.

KEY WORDS: nondestructive evaluation, fracture toughness, ultrasonics, yield strength, stress waves, microstructure, crack propagation, polycrystalline materials

Nomenclature

Fundamental SI dimensions appear in parentheses.

- E Young's modulus, (N/m²)
- ξ Stress wave energy, (N/m)
- ξ_δ Stress wave emission energy, J/m², (N/m)
- f Frequency, MHz, (s⁻¹)
- G_c Critical energy release rate, (N/m)
- K_c Critical stress intensity factor, (Nm^{-3/2})
- K_{Ic} Plane strain fracture toughness, MPa√m, (Nm^{-3/2})
- ℓ Microstructural spacing distance, μm, (m)

¹ Materials technologist, National Aeronautics and Space Administration, Lewis Research Center, Cleveland, Ohio 44135.

- v_ℓ Longitudinal velocity, cm/ μ s, (m/s)
- α Attenuation coefficient, Np/cm, (m^{-1})
- β Attenuation slope, = $d\alpha/df$, (s/m)
- β_δ Attenuation slope at $f = v_\ell/\delta'$, μ s/cm, (s/m)
- β' Attenuation slope at $\alpha = 1$, μ s/cm, (s/m)
- δ Microfracture site dimension, μ m, (m)
- δ' Critical grain/subgrain size, μ m, (m)
- δ_c Critical crack opening displacement, μ m, (m)
- σ_0 Initial stress wave amplitude, (N/m²)
- σ_w Stress wave amplitude, (N/m²)
- σ_y Yield strength, (N/m²)
- $\sigma_{0.2}$ 0.2 percent elongation yield strength, MPa, (N/m²)

Strong incentives exist for developing nondestructive ultrasonic methods for evaluation of material properties such as fracture toughness [1].² First, less expensive alternatives would be available to complement and corroborate mechanical destructive tests. Second, non-destructive techniques would be available for use on structural materials or actual hardware to assess or verify mechanical strength properties. Third, from the standpoint of materials science, continued ultrasonic studies should contribute to identification and analysis of factors that determine fracture toughness and thus aid in fracture control technology.

Recent studies have yielded experimental evidence that nondestructive ultrasonic methods can be used to evaluate material fracture toughness properties [2]. The present study is based in part upon results reported in Ref 2. The previous work demonstrated that ultrasonic attenuation and velocity measurements can be used to obtain an empirical correlation with fracture toughness properties. The purpose of the present paper is to suggest a theoretical basis for the empirical relations reported in Ref 2. The material presented should encourage further investigations and more rigorous formulations of the possible relations involved.

A model (Fig. 1) is proposed for the correlations that have been found between ultrasonic propagation and fracture toughness properties of metallic materials. The model is based on stress (elastic) wave interactions during microcracking and void coalescence. (This discussion is limited to materials that fracture predominantly by void coalescence upon application of external stresses.) In the model, the formation and coalescence of microcracks are presumed to be promoted by stress wave interactions.

Equations are derived using ultrasonic quantities that are known to correlate with material fracture toughness and yield strength, that is, a material's ultrasonic attenuation coefficient and stress wave velocity. It is

² The italic numbers in brackets refer to the list of references appended to this paper.

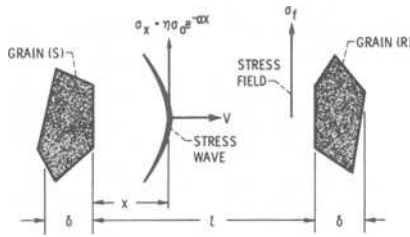


FIG. 1—Diagram of fracture model. “Grains” S and R are imbedded in a matrix subjected to a local static stress field of magnitude σ_f . A stress wave of initial amplitude σ_0 and velocity v is emitted from S. The distance between S and R is l and “grain” size is δ .

shown that the first derivative of the attenuation coefficient relative to frequency will correlate strongly with fracture toughness factors, for example, a material’s plane strain fracture toughness value. Experimental results are cited to demonstrate the mathematical correlations with 200 and 250 grade maraging steels and a titanium alloy with the composition Ti-8Mo-8V-2Fe-3Al.

Background and Approach

Fracture toughness is expressed as a critical stress intensity factor K_{Ic} . It is related to the tensile modulus and critical “strain energy release rate” G_c [1,3],

$$K_{Ic}^2 = E'G_c \tag{1}$$

The quantity E' equals E (Young’s modulus) for plane stress and $E/(1 - \nu^2)$ for plane strain conditions, where ν is Poisson’s ratio. The quantity G_c is related to yield strength σ_y [3]

$$G_c = n \delta_c \sigma_y \tag{2}$$

where δ_c is called a “critical crack opening displacement” [3] and n is a numerical coefficient. The coefficient n incorporates strain and associated factors. To determine K_{Ic} (the plane strain fracture toughness) a crack-notched specimen of suitable dimensions is loaded until the crack becomes unstable and extends abruptly.

During unstable crack growth, the stress wave propagation properties of the material are significant. Ultrasonic attenuation measurements gage factors that influence crack propagation and hence fracture toughness. A linkage among fracture toughness, ultrasonic attenuation, and wave propagation has been shown experimentally in previous studies [2,4-6].

Stress waves (that is, acoustic emissions) in metals are emitted by dislocation motions, microcracking, etc. [4,5]. Acoustic emission studies support the expectation that in high toughness materials the intensity of stress waves is reduced by the ultrasonic attenuation properties of the material [6].

Ultrasonic attenuation is given in terms of the attenuation coefficient. The total attenuation coefficient is the sum of the absorption attenuation coefficient and the scattering attenuation coefficient [7,8]. The attenuation coefficient α is a function of ultrasonic frequency. Material microstructural variations will produce corresponding variations in the slope of the $\log \alpha$ versus $\log f$ curve [2,7]. According to Ref 2, a material's fracture toughness will vary directly with β , where $\beta = d\alpha/df$. For the analytical treatment herein, the attenuation versus frequency relation will be taken as

$$\alpha = cf^m \quad (3)$$

This form assumes that scatter attenuation dominates and that m and c can be considered constants over the frequency range of interest.

The model (Fig. 1) considers a solid under external load in which the presence of a stress raiser (that is, imperfection, crack, notch, inclusion, etc.) gives rise to a highly stressed region. Let the load be just under that required to initiate unstable crack propagation in the neighborhood of the stress raiser or imperfection. Either of two events can arise upon slight increase of the load: first, microcrack nucleations will be initiated at various sites near the imperfection but these will fail to coalesce due to barrier effects. Second, microcrack coalescence will occur overcoming all barriers to rapid unstable crack extension.

It is assumed that the spontaneous stress (elastic) waves emitted by the various nucleation (microfracture) events interact with other potential nucleation sites and thus tend to promote fracturing at these sites. The energy of these waves also will be dissipated in the medium between nucleation sites. The propagation and energy losses of the waves would be influenced by scatter attenuation that occurs because of the presence of grain boundaries, inclusions, and other scattering interfaces.

The interaction and influence of ultrasonic elastic waves on crack propagation has been well documented. By using shock stressing techniques, it has been shown that sustained crack growth occurs at times when the stress wave front is at the crack tip [9]. Terminal crack speed is bounded by the stress wave's propagation velocity. Since crack speeds are less than ultrasonic wave velocities, stress wave reflections can interact with and influence the growth of a running crack [9]. It has been shown that imposition of ultrasonic waves will deflect a running crack in a predictable manner [10]. Other studies have demonstrated the effect of stress wave fronts on brittle fracture [11,12].

Model and Derivation

Consider two small bounded domains S and R in a solid. These are potential crack nucleation sites near the tip of a sharp notch or crack. They share a common dimension δ and are separated by spacing ℓ as in Fig. 1.

Let S and R represent two crystals, grains, or subgrains in a polycrystalline solid. They are imbedded in an assumed stress field, σ_i , that arises because of an externally applied load. Let S be the source of a stress wave that impinges on R as a result of a fracture in S . The stress wave emitted by S is represented in Fig. 1 by the velocity v and stress wave amplitude σ_x . The arrival of the wave at R increases the stress field locally by σ_w . The magnitude of σ_w will be determined by attenuation which in turn will depend on the number and size of (grain) boundaries encountered by the stress wave between S and R . If the wave is attenuated like any ultrasonic wave, then its amplitude at R where $x = \ell$, can be taken as

$$\sigma_w = \eta\sigma_o \exp(-\alpha\ell) \tag{4}$$

where, η is a numerical factor >0 and <1 that accounts for wave front geometry (and taken here as being about 1). The quantity σ_o is the initial stress amplitude at S and α is the attenuation coefficient characteristic of the material.

In view of the results reported in Ref 2, we first form an expression that relates the fracture toughness factor K_c^2/σ_y and the ultrasonic factor $v\beta_\delta$, where the factor $v\beta_\delta$ is based on this particular ultrasonic frequency. It will be seen that a material's grain size is an important parameter to be used in determining this ultrasonic frequency.

Let the stress wave energy required to create a microcrack of "diameter" δ in R be [13]

$$\xi = \pi\delta\sigma_w^2/E' \tag{5}$$

By fracturing S becomes the source of a broadband stress wave pulse. The wave arriving at R , σ_w , will therefore contain an energy distribution corresponding to the component frequencies [4]. The derivative of this energy with respect to wavelength λ is

$$d\xi/d\lambda = 2\pi\sigma_w^2\delta\ell v\beta/E'\lambda^2 \tag{6}$$

where Eq 6 is obtained by recalling that $\beta = d\alpha/df$ and $df/d\lambda = -v/\lambda^2$. The component wavelengths will be scattered dependong on the λ to δ

ratios. The energy loss by Rayleigh scattering of the stress wave on reaching R is

$$\xi = 2\pi\sigma_w^2\delta\ell\nu/E' \int_{\delta}^{\infty} (\beta/\lambda^2)d\lambda \quad (7a)$$

or

$$\xi_{\delta} = (2\pi\sigma_w^2\ell/E') (\nu\beta_{\delta}/m) \quad (7b)$$

The integration was performed by taking σ_w and ν as material constants. The quantity σ_w is the critical stress increment required to initiate crack nucleation in R given the static field stress σ_f . In Eq 7b β_{δ} is β evaluated at the frequency corresponding to $\lambda = \delta$. The limits of integration cover all wavelengths susceptible to Rayleigh scattering, that is, $\lambda > \delta$. The lower limit δ is the criterion for stochastic scattering. It is assumed that only wavelengths less than δ will interact strongly with the medium from S to R .

At the onset of unstable crack growth, the region around S and R is loaded with a specific strain energy represented by K_c^2/σ_y (which equals $nE'\delta_c$ by Eqs 1 and 2. This energy input is accompanied by a displacement δ_c in the loading direction in the vicinity of S and R [1,3]. It is also accompanied by acoustic emissions, that is, stress wave emissions [5]. The largest portion of the stress wave energy will be dissipated in the immediate vicinity of the sources such as S and R by stochastic scattering and absorption. Only the longer wavelengths $\lambda > \delta$ appear as stress wave emissions beyond this region.

Stress wave energy radiated away is represented by ξ_{δ} in Eq 7b. It is a small fraction of K_c^2/σ_y . Thus $N\xi_{\delta}$ is set equal to K_c^2/σ_y

$$(K_c^2/\sigma_y)^2 = N2\pi\sigma_w^2n\delta_c\ell(\nu\beta_{\delta}/m) \quad (8)$$

where $N \gg 1$ and Eq 8 is obtained by noting that E' in Eq 7b is equal to $K_c^2/n\delta_c\sigma_y$ by combining Eqs 1 and 2. Therefore, the relation between the fracture toughness factor K_c^2/σ_y and the ultrasonic factor $\nu\beta_{\delta}/m$ is

$$K_c^2/\sigma_y = \psi(\nu\beta_{\delta}/m)^{0.5} \quad (9)$$

In practice K_c is taken as the plane strain fracture toughness K_{Ic} and σ_y as the 0.2 percent yield strength $\sigma_{0.2}$. Note that $\sigma_{0.2}$ is related to K_{Ic} in that it corresponds to the onset of plastic deformation just as K_{Ic} corresponds to the onset of rapid fracturing. The longitudinal ultrasonic velocity ν_{ℓ} will be used for ν in $\nu\beta_{\delta}$. The quantities ν_{ℓ} , β_{δ} , and m are obtained by measurements such as those described in Ref 2. Equation 9 can then be

written in terms of the aforementioned quantities as

$$K_{Ic}^2/\sigma_{0.2} = \psi(v_\ell\beta_\delta/m)^{0.5} \quad (10a)$$

where

$$\psi = \sigma_w \sqrt{2\pi Nn\delta_c\ell} \quad (10b)$$

If we take σ_w as some fraction, r , of $\sigma_{0.2}$ then Eq 10 becomes,

$$(K_{Ic}/\sigma_{0.2})^2 = r\sqrt{2\pi Nn\delta_c\ell} (v_\ell\beta_\delta/m)^{0.5} \quad (11)$$

were the quantities r , N , n , δ_c , and ℓ can be estimated by specifying particular materials and test conditions. It will be seen that the relation in Eq 11 agrees with experimental data.

Discussion

Data for plotting $(K_{Ic}/\sigma_{0.2})^2$ versus $v_\ell\beta_\delta/m$ are listed in Table 1 for materials for which appropriate experimental values are available: a 200 and a 250 grade maraging steel and a titanium alloy. The quantity β_δ was calculated from $mc(v_\ell/\lambda)^{m-1}$ where λ is set equal to a critical grain size dimension δ' . This critical dimension δ' is based on measurement of grain or subgrain sizes of the various specimens by metallographic techniques. The approach adopted for determining δ' is that of finding the dimension that best characterizes the size of potential crack nucleation sites. It is assumed that this should be the average size of the most abundant grains, their boundaries, or substructures. For example, the titanium alloy specimens exhibited in an orderly grain structure (Fig. 2a). The typical grain size distribution for this material is shown in Fig. 3. In the titanium alloy the average size varied from 59 to 64 μm . The 200 and 250 grade maraging steel specimens exhibited a somewhat chaotic grain-subgrain structure (Fig. 2b). For these materials the mean subgrain boundary or lath spacing was taken as δ' giving values ranging from 8 to 15 μm . The value of δ' for each specimen is listed in Table 1. These measurements of δ' were made in accordance with the intercept method prescribed in ASTM Methods for Estimating the Average Grain Size of Metals (E 112 - 74).

It is noteworthy that the metallographic method for determining the critical grain size is not the only possible method for finding this important quantity. For the materials studied there is a correlation between velocity v_ℓ and δ' , as is shown in Fig. 4. The relations in Fig. 4 can therefore be used to confirm ultrasonically the δ' values obtained by metallographic measurements.

TABLE 1—Characteristics of fracture toughness ultrasonic specimens.^a

Specimen	Toughness Factors ^b				Ultrasonic (Stress Wave) Factors ^c				Critical grain size δ' , μm
	Yield Strength, $\sigma_{0.2}$, MPa	Fracture Toughness, K_{Ic} , $\text{MPa}\sqrt{\text{m}}$	Length Factor, $(K_{Ic}/\sigma_{0.2})^2$, mm	Elastic ^d Velocity, v_L , cm/ μs	Attenuation Curve Parameters		Attenuation Factors		
					c	m	β_1 , $\mu\text{s}/\text{cm}$	$v_L\beta_0/m$	
1-200 ^e	1320	(113)	7.33	0.564	2.22×10^{-3}	2.061	0.1063	0.787	13
2-200	1430	98.1	4.71	0.563	3.46×10^{-3}	1.896	0.0955	0.449	13
3-200	1430	92.3	4.17	0.564	5.28×10^{-3}	1.760	0.0894	0.284	14
4-200	1330	103	6.00	0.564	2.02×10^{-3}	2.024	0.0944	0.494	15
5-200	1210	(110)	8.26	0.558	7.75×10^{-4}	2.255	0.0941	0.794	14
1-250 ^f	1400	118	7.10	0.546	3.81×10^{-5}	2.595	0.0514	0.626	8.5
2-250	1400	117	6.98	0.543	2.62×10^{-5}	2.661	0.0505	0.650	8.5
3-250	1400	139	9.86	0.556	1.41×10^{-5}	2.996	0.0720	1.40	13
4-250	1400	146	10.9	0.556	1.56×10^{-5}	3.034	0.0790	1.95	13
1-Ti ^g	1075	53.7	2.50	0.576	4.38×10^{-2}	1.123	0.0693	0.0441	61
2-Ti	1370	51.0	1.39	0.590	3.98×10^{-8}	1.437	0.0307	0.0170	64
3-Ti	1230	59.9	2.37	0.591	2.27×10^{-4}	2.248	0.0538	0.0373	65
4-Ti	1085	70.0	4.16	0.586	5.63×10^{-5}	2.803	0.0854	0.117	63

^a All data is taken from Ref 2 with the exception of the last two columns. The factor $v_L\beta_0/m$ was calculated from the critical grain size δ' . The quantity δ' was determined in accordance with the discussion given in the text.

^b Yield strengths are 0.2 percent elongation values. Fracture toughness values are for plane strain conditions. Conditional (less precise) values are in parentheses.

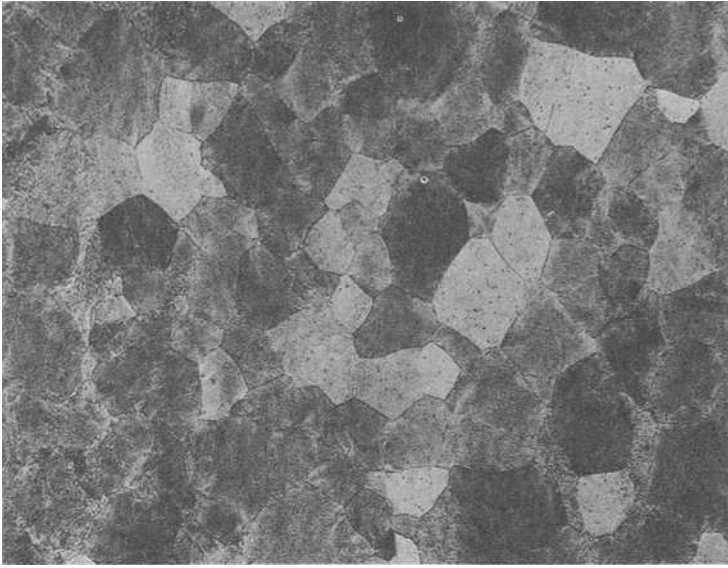
^c The attenuation versus frequency characteristic curve parameters from Ref 2 are used to calculate $\beta_1 = mc^{1/m}$ and $\beta_0 = mc(v_L/\delta')^{m-1}$, see Eq 3.

^d Longitudinal wave velocity was measured at a center frequency of approximately 30 MHz.

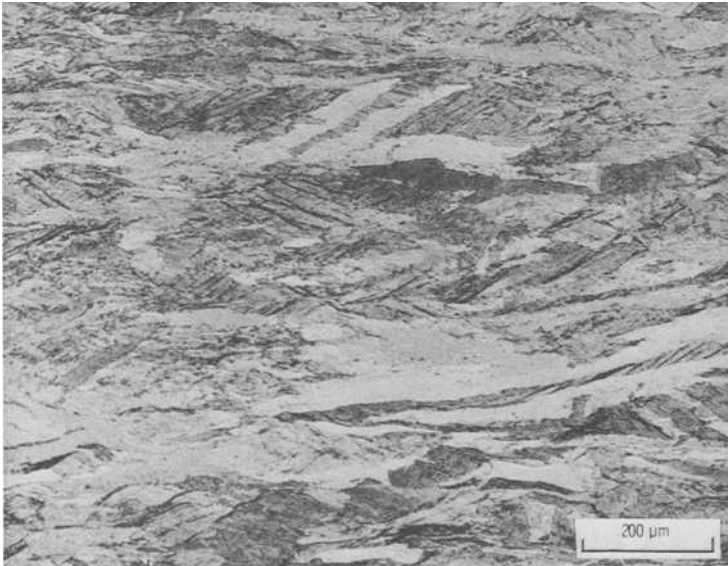
^e 200-grade maraging steel, cold rolled 50 percent and aged 8 h at temperatures ranging from 700 to 811 K.

^f 250-grade maraging steel, annealed at 1090 K, air cooled, and aged 6 h at temperatures ranging from 672 to 838 K.

^g Titanium-8Mo-8V-2Fe-3Al, solution heat treated at 1144 K for 1 h, water quenched, and aged 8 h at temperatures ranging from 700 to 867 K.



(a) TITANIUM ALLOY. ETCHANT WAS NITRIC PLUS HYDROFLUORIC.



(b) 200-GRADE MARAGING STEEL. ETCHANT WAS CALLINGS.

FIG. 2—Photomicrographs typical of two of the materials studied: a titanium alloy and a maraging steel. Original magnification was $\times 100$ for each.

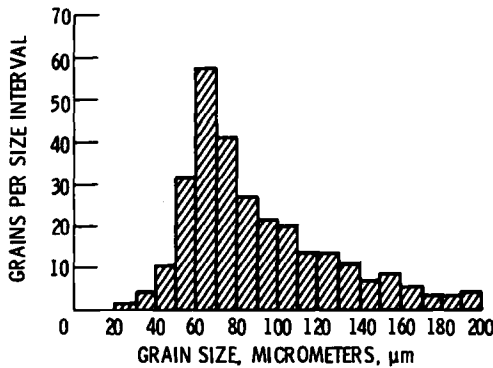


FIG. 3—Typical grain size distribution for titanium alloy Ti-8Mo-8V-2Fe-3Al. Sample population was 385.

The experimental data for $(K_{Ic}/\sigma_{0.2})^2$ versus $v_\ell \beta_\delta/m$ are plotted in Fig. 5. A curve for the 200 and 250 grade maraging steels as found by linear regression is given by

$$(K_{Ic}/\sigma_{0.2})^2 = 8.34 \times 10^{-3} (v_\ell \beta_\delta/m)^{0.522} \tag{12a}$$

while for the titanium alloy the curve is given by,

$$(K_{Ic}/\sigma_{0.2})^2 = 1.45 \times 10^{-2} (v_\ell \beta_\delta/m)^{0.564} \tag{12b}$$

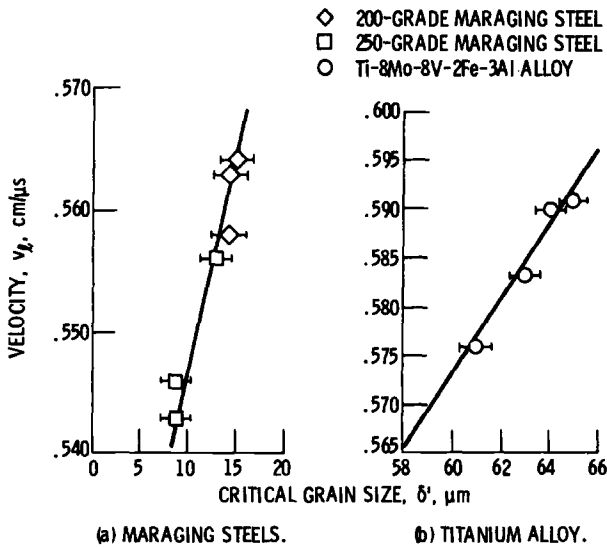


FIG. 4—Correlation of ultrasonic velocity and critical grain size for two maraging steels and a titanium alloy. Velocity measurement was at a center frequency of approximately 30 MHz.

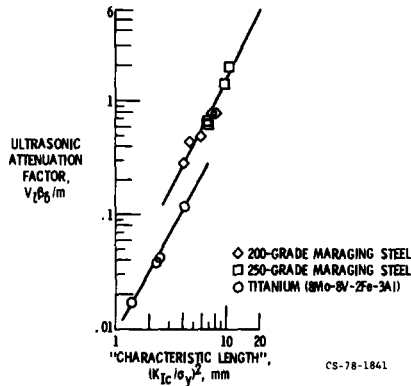


FIG. 5—Correlation of ultrasonic factor $v_l \beta_\delta / m$ and fracture toughness characteristic length factor $(K_{Ic} / \sigma_{0.2})^2$ for three metals. Linear regression curves for the experimental data are from Eqs 12a and 12b. Correlation of coefficient is > 0.9 for both curves.

The slopes of the experimental curves agree with that predicted (~ 0.05), that is, the exponents on $v_l \beta_\delta / m$ in Eqs 11 and 12 are approximately the same (within experimental error). Estimates of the coefficient of $v_l \beta_\delta / m$ also agree with the values found in Eqs 12a and 12b (see Appendix I).

Experimental results of Ref 2 also suggest the linear relation

$$\sigma_{0.2} + AK_{Ic} + B\beta_1 = C \quad (13)$$

where A , B , and C are dimensional constants. The quantities A , B , and C will assume different values according to the material involved. The ultrasonic factor β_1 is evaluated at the frequency for which $\alpha = 1$. A derivation for Eq 13 based on the model used previously is given in Appendix II.

The experimental relations given in Ref 2 are as follows:

For the 200 grade maraging steel

$$\sigma_{0.2} + 17K_{Ic} - 17 \times 10^3 \beta_1 = 1470 \pm 20 \quad (14a)$$

For the titanium alloy (Ti-8Mo-8V-2Fe-3Al)

$$\sigma_{0.2} - 8.1K_{Ic} + 8.1 \times 10^3 \beta_1 = 1200 \pm 13 \quad (14b)$$

The values of A , B , and C in Eqs 14 are based on data on Table 1. These relations also agree with the form predicted in Appendix II.

The coefficient of K_{Ic} in Eq 14 or A in Eq 13 will be positive or negative depending on the mode of fracture. (The algebraic sign of B will be opposite that of A .) According to data presented in Ref 2, if the fracture is

predominantly ductile as in the 200 grade maraging steel, then A will be positive. If brittle fracture predominates as in the titanium alloy, then A will be negative. This may depend upon the residual strain in the crack nucleation sites or whether the crack nucleation sites are energy "sources" or "sinks" during fracture.

The experimental curves of Eqs 14a and 14b are plotted at $\sigma_{0.2}$ versus a in Fig. 6a, where, the quantity $a = \beta_1 + (A/B)K_{Ic}$. The 0-intercept values of the two curves in Fig. 6a correspond to C . Figure 6b is a conventional plot of $\sigma_{0.2}$ versus K_{Ic} .

The foregoing observations indicate that nondestructive ultrasonic measurements can be used to deduce fracture toughness and yield strength values by simultaneous solution of pairs of equations, such as Eqs 11 and 13 if the ultrasonic factors β_1 and $\nu_e \beta_8/m$ are known. Other data would be needed to evaluate the latter factor, for example, the material and its critical microproperties such as the value of δ' . Ultrasonic methods such as those described in Refs 2 and 7 can produce this additional information. For the materials involved in this study it happened that the critical grain size as measured from photomicrographs results in a correlation with velocity, see Fig. 4. It thus appears that all the essential information for determining fracture toughness and yield strength can be obtained by purely ultrasonic measurements.

Current technical literature indicates the need for analytical treatments of fracture processes that are based on stress wave dynamics (9-

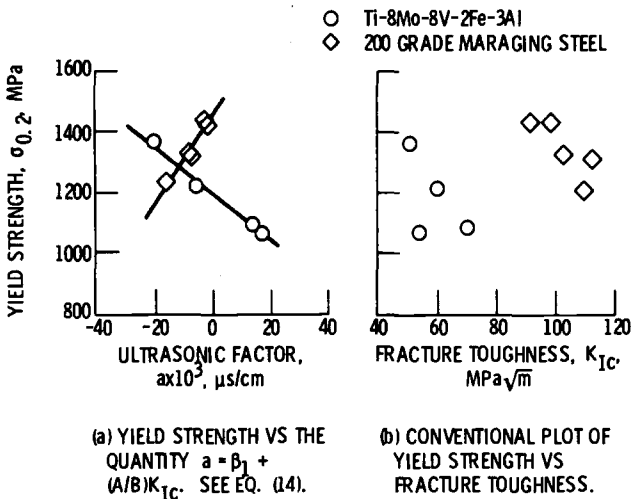


FIG. 6—Correlation of yield strength to fracture toughness for a titanium alloy and a maraging steel (from Ref 2). Refer to Table 1 for experimental data for $\sigma_{0.2}$, K_{Ic} , and β_1 .

12,14,15). More emphasis should be given to the current research in crack extension dynamics under the influence of both spontaneous (internal) and externally introduced stress waves. *In situ* ultrasonic monitoring of unstable crack initiation [16] should play a significant role in future investigations. In the past, a material's fracture toughness has been based on concepts that involve essentially static situations. It has now been demonstrated that considerably more insight can be gained by ultrasonic interrogation of materials, especially under dynamic conditions. As indicated by the results herein, key material properties such as fracture toughness and yield strength are linked closely to ultrasonic wave propagation properties.

Conclusions

It has been shown that fracture toughness and yield strength are functions of ultrasonic stress wave propagation factors in polycrystalline metallic materials. It can be inferred that spontaneous stress waves generated during crack nucleation processes play an active part in promoting the onset of rapid unstable crack extension. In the model proposed herein, the formation and coalescence of microcracks are presumed to be promoted by stress wave interactions at potential crack nucleation sites. Agreement was found between the proposed model and experimental results.

Nondestructive ultrasonic measurements can correlate with fracture properties and these measurements can aid significantly in identifying factors that influence catastrophic crack propagation in metallic materials. Fracture control technology should benefit by the use of non-destructive ultrasonic measurements of material microstructure properties that influence stress wave propagation and interactions.

The following conclusions can be drawn from the arguments in the Background section and also from the model and experimental data given herein:

1. There appears to be support for inferring that during the onset of rapid unstable crack growth, spontaneous stress waves interact with and promote crack nucleation ahead of the crack front.
2. Fracture toughness and yield strength are linked closely to the ultrasonic stress wave propagation properties of polycrystalline metals.
3. It is possible to rank material fracture toughness and yield strength by ultrasonic velocity and attenuation measurements.
4. Essential measurements for deducing fracture toughness and yield strength can be made by purely ultrasonic techniques once calibration curves have been established for a material.

APPENDIX I

Estimation of Coefficient in Eq 11

The coefficient $r\sqrt{2\pi Nn\delta_c\ell}$ in Eq 11 can be estimated as follows: First, the quantity n equals 2 for plane strain conditions [3]. The quantities r , N , δ_c , and ℓ are assigned appropriate values characteristic of the materials listed in Table 1, that is, 200 and 250 grade maraging steel and the titanium alloy Ti-8Mo-8V-2Fe-3Al. These are the materials for which appropriate experimental data are available from Ref 2.

Various measurements and estimates of stress wave energies (denoted as ξ_δ) have been made and are of the order 800 to 900 J/m² [17]. Experimental values of $K_{Ic}^2/\sigma_{0.2}$ such as those in Ref 2 indicate that the ratio of $K_{Ic}^2/\sigma_{0.2}$ to ξ_δ (that is, N) ranges from approximately 1.0×10^4 to 1.3×10^4 . The same approximate range for N also can be inferred from Eq 14: 0.81×10^4 to 1.7×10^4 . Let $N \sim 10^4$ in our estimation.

The critical crack opening displacement δ_c for the materials mentioned ranges from 9 to 25 μm . It is calculated by solving for δ_c between Eq 1 and 2 and substituting appropriate values for K_{Ic} , $\sigma_{0.2}$ and E .

The spacing dimension ℓ is of the order of the average grain boundary spacing or greater. A reasonable estimate can be based on taking $\ell = 2\delta'$ and using the critical grain sizes listed in Table 1.

The factor r depends on the ratio $\sigma_w/\sigma_{0.2}$. Based on acoustic studies [17], spontaneous stress wave emission generally rises abruptly at stresses from $0.5 \sigma_{0.2}$ to $0.9 \sigma_{0.2}$. Thereafter, a high emission rate is sustained, suggesting that corresponding values for r range from > 0.5 to 0.9 . An analysis of the relations derived in Appendix II indicates that for the materials of this study r may be taken as ~ 1 .

Values for $r\sqrt{2\pi Nn\delta_c\ell}$ based on the previous estimates are shown in Table 2. The values shown agree rather closely with the coefficients of the quantity $v\beta_\delta/m$ in Eqs 12a and 12b.

TABLE 2—Estimation of $r\sqrt{2\pi Nn\delta_c\ell}$.

Material	$r\sqrt{2\pi Nn\delta_c\ell}$	r	N	n	δ_c	ℓ
200 maraging steel	$6.8 \times 10^{-3}\text{m}$	1	10^4	2	13 μm	28 μm
250 maraging steel	$8.3 \times 10^{-3}\text{m}$	1	10^4	2	25 μm	22 μm
Ti alloy (8Mo8V2Fe3Al)	$1.2 \times 10^{-2}\text{m}$	1	10^4	2	9 μm	126 μm

APPENDIX II

Derivation of Eq 13

Consider the domain defined by the length ℓ in the model depicted in Fig. 1. The energy, ξ' , to create a crack with the major dimension ℓ can be represented by Ref 13

$$\xi' = 2\pi\ell (\sigma_f \pm \sigma_w)^2/E' \tag{15}$$

The quantity σ_w is the stress wave amplitude given by Eq 4. The \pm sign affixed to σ_w denotes that the sense of the stress wave's amplitude may be the same or opposite the sense of the static field represented by σ_f .

Taking the derivative of ξ' with respect to ℓ , and noting that $d\xi'/d\ell$ is always greater than $2\pi(\sigma_f \pm \sigma_w)^2$, we have,

$$\sigma_f \pm 2\ell\alpha\sigma_w \mp 2\ell f\sigma_w\beta > \sigma_f \tag{16}$$

The frequency, f , in the third term of Eq 16 arises because $df/d\ell = -f/\ell$. Let $\sigma_f = \sigma_y$ and $r\sigma_y = \sigma_w$ and evaluate Eq 16 for the condition where $\alpha = 1$ (that is, unit attenuation coefficient). This condition simplifies the equation so that by noting that $\sqrt{\sigma_w} = K_c\sqrt{r/E'n\delta_c}$, we can write

$$\sigma_y + AK_c + B\beta_1 > \sigma_y \tag{17a}$$

where

$$A = \pm 2\ell_1 r\sqrt{\sigma_y/E'n\delta_c} \text{ and } B = \mp 2\ell_1 kf_1 r\sigma_y \tag{17b}$$

The subscript 1 denotes unique values for ℓ_1 , f_1 , and β_1 that are associated with $\alpha = 1$. The corresponding value of f_1 is $(1/c)^{1/m}$. The quantity k takes values in accordance with wave harmonics over length ℓ_1 . With $k = 1/2$, the ratio $B/A = 1/2K_c(1/c)^{1/m}$. By using the K_{Ic} , c , and m values in Table 1 for the 200 maraging steel and the titanium alloy, it is found that $B/A \cong -10^3$ in agreement with the experimental B/A ratios in Eqs 14a and 14b. The form of Eq 17a predicts that of Eq 13. These equations suggest the energy partition

$$[\text{plastic flow}] \pm [\text{crack nucleation}] \mp [\text{stress wave}] = [\text{total energy}]$$

Note that the terms in Eqs 13 and 17a will have the dimensions of specific energy (for example, joules per square metre) if each is multiplied by a characteristic length such as δ .

References

- [1] Committee on Rapid Inexpensive Tests for Determining Fracture Toughness, National Materials Advisory Board; Commission on Sociotechnical Systems, National Research Council, "Rapid Inexpensive Tests for Determining Fracture Toughness," NMAB-328, National Academy of Sciences, 1976.
- [2] Vary, A., *Materials Evaluation*, Vol. 36, No. 7, 1978, pp. 55-64.
- [3] Hahn, G. T., Kanninen, M. F., and Rosenfeld, A. R., in *Annual Review of Materials Science*, Vol. 2, R. A. Huggins, Ed., Annual Reviews Inc., Palo Alto, Calif., 1972, pp. 381-404.
- [4] Liptai, R. G., Harris, D. O., Engle, R. B., and Tatro, C. A., *International Journal of Nondestructive Testing*, Vol. 3, Dec. 1971, pp. 215-275.
- [5] Tetelman, A. S. and Chow, R. in *Acoustic Emission, ASTM STP 505*, American Society for Testing and Materials, 1972, pp. 30-40.
- [6] Nakamura, Y., Veach, C. L., and McCauley, B. O. in *Acoustic Emission, ASTM STP 505*, American Society for Testing and Materials, 1972, pp. 164-186.
- [7] Papadakis, E. P., *Journal of the Acoustical Society of America*, Vol. 37, No. 4, April 1965, pp. 711-717.
- [8] Krautkramer, J. and Krautkramer, H., *Ultrasonic Testing of Materials*, translation of the Second Revised German Ed. by Dipl.-Ing. B. W. Zenzinger, Springer-Verlag, New York, 1969, pp. 89-121.

- [9] Kolsky, H. and Rader, D. in *Fracture—An Advanced Treatise*, Microscopic and Macroscopic Fundamentals, H. Liebowitz, Ed., Vol. 1, Academic Press, New York, 1971, pp. 533–569.
- [10] Kerkof, F., in *Dynamic Crack Propagation*, proceedings of an International Conference, G. C. Sih, Ed., Noordhoff International Publishing, Leyden, The Netherlands, 1973, pp. 3–29.
- [11] Kolsky, H. in *Dynamic Crack Propagation*, proceedings of an International Conference, G. C. Sih, Ed., Noordhoff International Publishing, Leyden, The Netherlands, 1973, pp. 399–414.
- [12] van Elst, H. C. in *Dynamic Crack Propagation*, proceedings of an International Conference, G. C. Sih, Ed., Noordhoff International Publishing, Leyden, The Netherlands, 1973, pp. 283–329.
- [13] Petch, N. J., "Metallographic Aspects of Fracture," *Fracture—An Advanced Treatise*, Microscopic and Macroscopic Fundamentals, H. Liebowitz, Ed., Vol. 1, Academic Press, New York, 1968, pp. 351–393.
- [14] Kolsky, H., *Stress Waves in Solids*, 2nd Ed., Dover, New York, 1963.
- [15] Curran, D. R., Seaman, L., and Shockey, D. A., *Physics Today*, Vol. 30, No. 1, Jan. 1977, pp. 46–55.
- [16] Klima, S. J., Fisher, D. M., and Buzzard, R. J., *Journal of Testing and Evaluation*, Vol. 4, No. 6, Nov. 1976, pp. 397–404.
- [17] Mirabile, M., *Nondestructive Testing*, Vol. 8, No. 2, April 1975, pp. 77–85.

Special Topics

Hugo Ernst,¹ P. C. Paris,¹ Mark Rossow,¹ and
J. W. Hutchinson²

Analysis of Load-Displacement Relationship to Determine J-R Curve and Tearing Instability Material Properties

REFERENCE: Ernst, Hugo, Paris, P. C., Rossow, Mark, and Hutchinson, J. W., "Analysis of Load-Displacement Relationships to Determine J-R Curve and Tearing Instability Material Properties," *Fracture Mechanics, ASTM STP 677*, C. W. Smith, Ed., American Society for Testing and Materials, 1979, pp. 581–599.

ABSTRACT: Exact methods, based on dimensional analysis of the dependence of the load on crack length and displacement using deformation theory of plasticity, are used to obtain J from a single load-displacement record for different configurations. The methods also permit the evaluation of the crack length increment Δa , and hence, complete J-R curves can be constructed. Formulae for T_{mat} and T_{app} are presented as well.

KEY WORDS: crack propagation, fatigue (materials), mechanical properties, load-displacement records, methods of analysis, J-integral, J-R curves, tearing modulus (T)

This analysis is based on recent work of Hutchinson and Paris et al [1,2],³ which suggested that load-displacement records for pure bending could be analyzed to determine J-R curve and instability related material properties. However, here the analysis will be generalized and shown to be applicable to all configurations (2-D) and especially useful for typical test configurations such as compact, three-point bend, center-cracked, etc., configurations.

Indeed, the analysis to be presented is "exact," from an analytical viewpoint, and is based on dimensional considerations in the spirit of Rice-Paris-Merkle analysis [3] based on Rice's J-integral concepts [4].

¹ Research assistant, professor of mechanics, and associate professor of civil engineering, respectively, Washington University, St. Louis, Mo. 63130.

² Professor of engineering, Harvard University, Cambridge, Mass. 02138.

³ The italic numbers in brackets refer to the list of references appended to this paper.

The strict deformation theory of plasticity interpretation of J which will be used here has been shown to be "exact" under the size restrictions described by Hutchinson and Paris [1,5] for determining J-R curves and related material properties.

Finally, the analysis will lead to the following useful results:

1. Correct (exact) methods for computing J from load-displacement records with crack growth present will be developed.
2. Methods for determining crack length change, Δa , from load-displacement records (without further instrumentation) will be developed.
3. From the results of (1) and (2), it is possible to construct J-R curves from load-displacement records alone.
4. Moreover, a material's tearing instability properties, that is, the tearing modulus, T_{mat} , may be determined from load-displacement records (without further instrumentation).
5. Similarly, a system's tendency for tearing instability, T_{appl} , may be found from further analysis and load-displacement information from the system.

Therefore, the methods to be developed here are anticipated to have extensive applicability to J-R curve methods of determining material properties controlling crack extension and stability. Moreover, since only load-displacement records are required to determine desired properties, the methods are ideally suited to certain special testing problems, such as hot cell testing of irradiated materials or dynamic testing, or both (both of which present especially difficult problems if additional instrumentation is required).

Development of a Convenient Form of the Rice J-Integral

The original familiar form of the J-integral is [4]

$$J = \oint_{\Gamma} W dy - T_i \frac{\partial u_i}{\partial x} ds \quad (1)$$

which, based on deformation theory, is path independent, when integrating around a crack tip, and can be represented equally well by the alternate forms [4]

$$J = \int_0^P \left(\frac{\partial \Delta}{\partial a} \right)_P dP = - \int_0^{\Delta} \left(\frac{\partial P}{\partial a} \right)_{\Delta} d\Delta \quad (2)$$

where, Δ is the work producing component of load point displacement for the load, P . It is noted that Eq 2 appropriately implies either $\Delta = \Delta(a, P)$ or $P = P(a, \Delta)$ as functional relationships between the variables including the crack length, a , as the third variable.

In the analysis to follow here, it is convenient to subdivide J into elastic and plastic parts, J_{eL} and J_{pL} . This is done by noting that for actual elastic-plastic situations the displacement, Δ , may always be divided into its linear-elastic and plastic parts. That is

$$\Delta = \Delta_{eL} + \Delta_{pL} \tag{3}$$

Then the first form in Eq 2 may be written

$$J = \int_0^P \left(\frac{\partial \Delta_{eL}}{\partial a} \right)_P dP + \int_0^P \left(\frac{\partial \Delta_{pL}}{\partial a} \right)_P dP \tag{4}$$

Now the first term in Eq 4 is the linear-elastic component, J_{eL} , of J , which is also the Griffith, G . That is

$$J_{eL} = \int_0^P \left(\frac{\partial \Delta_{eL}}{\partial a} \right)_P dP = G(P, a) \tag{5}$$

Moreover, the second term in Eq 4, J_{pL} , may be reinterpreted by referring to Fig. 1. This figure shows schematically load, P , versus plastic displacement, Δ_{pL} , curves for crack sizes a and $a + da$. The area between curves is noted to be $J_{pL}da$ by integrating over elements of the area by

$$J_{pL}(da) = \int_0^P \left(\frac{\partial \Delta_{pL}}{\partial a} \right)_P dP(da) \tag{6}$$

but using the alternate element it is observed that two forms are equally appropriate, that is,

$$J_{pL} = \int_0^P \left(\frac{\partial \Delta_{pL}}{\partial a} \right)_P dP = - \int_0^{\Delta_{pL}} \left(\frac{\partial P}{\partial a} \right)_{\Delta_{pL}} d\Delta_{pL} \tag{7}$$

Now substituting Eqs 5 and 7 into Eq 4, the result is

$$J = J_{eL} + J_{pL}$$

or

$$J = G(P, a) - \int_0^{\Delta_{pL}} \left(\frac{\partial P}{\partial a} \right)_{\Delta_{pL}} d\Delta_{pL} \tag{8}$$

This form, Eq 8, gives a convenient method for computing J without any

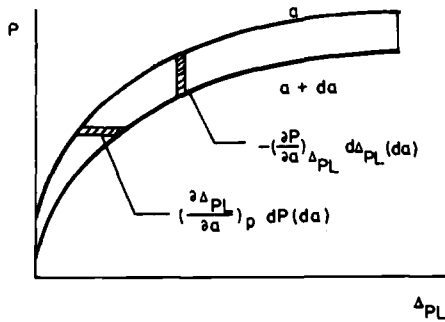


FIG. 1—Load-plastic displacement records for two neighboring crack lengths.

loss in analytical precision compared to the original forms, Eqs 1 or 2. Without ambiguity G is always to be computed using linear-elastic fracture mechanics formulas using the actual load, P , and crack length, a (without plastic zone correction). It remains to be shown here that the second term of Eq 8 may be evaluated appropriately.

Dimensional Analysis of Relationships Between Load, Crack Length, and Plastic Displacement

Normally the plasticity in a cracked member or specimen is confined to the remaining ligament at the cracked section. In order to avoid certain ambiguities requiring some modifications in the analysis, plasticity confined to the ligament region is assumed here. Under this condition, dimensional analysis leads to the following form for the relationship between load, P , crack length, a , and plastic displacement

$$\frac{\Delta_{pL}}{W} = f\left(\frac{P}{W}, \frac{a}{W}, \frac{L}{W}, \frac{B}{W}, \text{ etc}\right) \tag{9}$$

where P is taken as load per unit thickness, W is a typical characteristic (nonvarying) dimension such as width, and L, B , etc., are other characteristic dimensions. In this form a basic argument proposed by Rice [3] is that load can only appear as P/W with units, force per length squared, since f depends only on stress-strain properties having like units or nondimensional units. Furthermore, this form is correct for arbitrary monotonic stress-strain properties so that the analysis to follow will be "exact" for all stress-strain curves.

Inverting this function then

$$\frac{P}{W} = F\left(\frac{\Delta_{pL}}{W}, \frac{a}{W}, \frac{L}{W}, \frac{B}{W}, \text{ etc.}\right) \tag{10}$$

Now more appropriate forms for analysis can be modified by defining the width of the remaining uncracked ligament, b (from other dimensions, such as $W-a$). Then either b/W or $(b/W)^2$ may be factored out of $F()$ to give the special forms of Eq 10

$$P = \frac{b^2}{W} F_1 \left(\frac{\Delta_{pL}}{W}, \frac{a}{W}, \frac{L}{W}, \frac{B}{W}, \text{ etc.} \right) \tag{11a}$$

or

$$P = b F_2 \left(\frac{\Delta_{pL}}{W}, \frac{a}{W}, \frac{L}{W}, \frac{B}{W}, \text{ etc.} \right) \tag{11b}$$

Indeed, an additional form which is equally appropriate dimensionally and similar to Eq (11b) is

$$P = b F_3 \left(\frac{\Delta_{pL}}{b}, \frac{a}{W}, \frac{L}{W}, \frac{B}{W}, \text{ etc.} \right) \tag{11c}$$

Now it will be shown that these forms, in combination with Eq 8, will lead to significant results. Indeed, all of the results in Ref 3 as well as important new results will follow.

Analysis to Determine J Using First Special Functional Form, F_1

The first functional form, Eq 11a may be substituted into Eq 8, noting that $db = - da$, to give

$$J = G + \frac{2b}{W} \int_0^{\Delta_{pL}} F_1() d\Delta_{pL} - \frac{b^2}{W^2} \int_0^{\Delta_{pL}} \frac{\partial F_1}{\partial \left(\frac{a}{W} \right)} d\Delta_{pL} \tag{12}$$

Resubstituting for $F_1()$ from Eq 11a into the first integral of Eq 12 leads to

$$J = G + \underbrace{\frac{2}{b} \int_0^{\Delta_{pL}} P d\Delta_{pL}}_{\text{Rice's term}} - \underbrace{\frac{b^2}{W^2} \int_0^{\Delta_{pL}} \frac{\partial F_1}{\partial \left(\frac{a}{W} \right)} d\Delta_{pL}}_{\text{Merkle-Corten term}} \tag{13}$$

It is noted that Eq 13 is an exact form for computing J from any load displacement record but prior to the initiation of crack growth (but it could be used to compute J after crack growth provided that the final value of the crack length is used, and the load displacement record for that crack length with no crack extension is known.) Indeed, it is observed that the first integral in Eq 13 is the usual Rice [3] area under the load-displacement curve (work) with the normal $2/b$ coefficient and the second integral is a correction of the Merkle-Corten [6] type, which is "exact" in Eq 13, however.

Now Eq 13 may be used to evaluate J for any configuration, as will be discussed later. It is best applied when the correction term, the final integral, is small compared to the others, which in this case will be the situation where the uncracked ligament is subject principally to bending.

In developing J-R curves it is appropriate to extend this analysis to the situation where crack growth has commenced. This is most clearly accomplished by taking the differential of Eq 12, noting that the integral terms are functions of the independent variables, the crack size, a or b , and the plastic displacement, Δ_{pL} . The differential of Eq 12 is thus

$$\begin{aligned}
 dJ = dG + & \left[\frac{2b}{W} F_1 - \frac{b^2}{W^2} \frac{\partial F_1}{\partial \left(\frac{a}{W} \right)} \right] d\Delta_{pL} \\
 + & \left[-\frac{2}{W} \int_0^{\Delta_{pL}} F_1() d\Delta_{pL} + \frac{4b}{W^2} \int_0^{\Delta_{pL}} \frac{\partial F_1}{\partial \left(\frac{a}{W} \right)} d\Delta_{pL} \right. \\
 & \left. - \frac{b^2}{W^3} \int_0^{\Delta_{pL}} \frac{\partial^2 F_1}{\partial \left(\frac{a}{W} \right)^2} d\Delta_{pL} \right] da \quad (14)
 \end{aligned}$$

Now it is convenient for integration of Eq 14 to first define \bar{J}_{pL} as the last two terms in Eq 12, that is, it is J_{pL} computed as if no crack growth occurred, or

$$\bar{J}_{pL} = \frac{2b}{W} \int_0^{\Delta_{pL}} F_1 d\Delta_{pL} - \frac{b^2}{W^2} \int_0^{\Delta_{pL}} \frac{\partial F_1}{\partial \left(\frac{a}{W} \right)} d\Delta_{pL} \quad (15)$$

The reintegration of Eq 14 with crack growth from the initial crack size, a_0 , to a size, a , and plastic displacement 0 to Δ_{pL} is appropriate over any path, which gives

$$J = G + \bar{J}_{pL} \left[+ \int_{b=b_0}^a \frac{1}{b} \left[- \bar{J}_{pL} + \frac{3b^2}{W^2} \int_0^{\Delta_{pL}} \frac{\partial F_1}{\partial \left(\frac{a}{W} \right)} d\Delta_{pL} - \frac{b^3}{W^3} \int_0^{\Delta_{pL}} \frac{\partial^2 F_1}{\partial \left(\frac{a}{W} \right)^2} d\Delta_{pL} \right] da \right] \quad (16)$$

This result, Eq 16 in combination with Eq 15, defines an exact method of computing J in any configuration. Applied in a general way, it could be very complicated to compute in terms involving F_1 in Eqs 15 and 16. However, in applications to be cited here, the cases will be restricted to situations where the second term in Eq 15 is small compared to the first and in such cases it will be possible to ignore the terms in Eq 16 explicitly containing F_1 .

Determination of Crack Length Change and T Using the First Special Functional Form

Equation 11a, the first form, expresses the load, P , as a function of crack length a or b and plastic displacement, Δ_{pL} , and other fixed quantities. Forming the differential of P , it is

$$dP = \frac{b^2}{W^2} \frac{\partial F_1}{\partial \left(\frac{\Delta_{pL}}{W} \right)} d\Delta_{pL} + \left[\frac{b^2}{W^2} \frac{\partial F_1}{\partial \left(\frac{a}{W} \right)} - \frac{2b}{W} F_1 \right] da \quad (17)$$

Solving this expression for the crack length change, da , it is

$$da = \frac{\frac{b^2}{W^2} \frac{\partial F_1}{\partial \left(\frac{\Delta_{pL}}{W} \right)} d\Delta_{pL} - dP}{\frac{2b}{W} F_1 - \frac{b^2}{W^2} \frac{\partial F_1}{\partial \left(\frac{a}{W} \right)}} \quad (18)$$

Assuming that F_1 can be found and the initial crack size, b , is known, then the crack length change can be found during an increment along a load-displacement record, dP and $d\Delta_{pL}$.

During such an increment, dJ can also be found using Eq 14. The results from Eqs 14 and 18 are substituted into the definition of the tearing modulus, that is

$$T_{\text{mat}} = \frac{dJ}{da} \frac{E}{\sigma_0^2} \tag{19}$$

It is seen that the tearing modulus of the material, T_{mat} , can also be found for an increment of the load displacement record.

An Example—the Case of Pure Bending of a Small Remaining Ligament

For the case of a half plane with a semi-infinite crack approaching perpendicular to the free edge, leaving a remaining ligament of size, b , the load, P , may be thought of as being removed from the ligament a large distance, W , to form a pure moment, M , where

$$M = PW \tag{20}$$

Now P is regarded as tending to zero while W tends to infinity, so that M is a finite moment. Moreover, the moment will then do work through the plastic angle,

$$\theta_{\text{pL}} = \frac{\Delta_{\text{pL}}}{W} \tag{21}$$

These results, Eqs 20 and 21, may be substituted into Eq 11a leading to the form

$$M = b^2 F_1(\theta_{\text{pL}}) \tag{22}$$

where other variables disappear compared to W . Equation 13 then becomes

$$J = G + \frac{2}{b} \int_0^{\theta_{\text{pL}}} M d\theta_{\text{pL}} = \frac{2}{b} \int_0^{\theta} M d\theta \tag{23}$$

since $G = \frac{2}{b} \int_0^{\theta_{\text{eL}}} M d\theta_{\text{eL}}$ (for the semi-infinite case where $\theta = \theta_{\text{eL}} + \theta_{\text{pL}} = \theta_{\text{crack}}$) which is the familiar Rice [3] pure bending result. Moreover, Eq 14 becomes

$$dJ = dG + [2b F_1 + 0] d\theta_{\text{pL}} + \left[- \frac{2}{b^2} \int_0^{\theta_{\text{pL}}} F_1 d\theta_{\text{pL}} + 0 \right] da$$

or

$$dJ = 2bF_1d\theta - \frac{J}{b} da \tag{24}$$

Reintegrating to give a result analogous to Eq 16 leads to

$$J = 2b_0 \int_0^\theta \frac{M}{b^2} d\theta - \int_{a_0}^a \frac{J}{b} da \tag{25}$$

The analogue of Eq 18 becomes

$$da = \frac{b \frac{\partial F_1}{\partial \theta} d\theta - \frac{dM}{b}}{2F_1} \tag{26}$$

and hence Eqs 24 and 26 can be substituted into Eq 19 to give

$$T_{mat} = \frac{E}{\sigma_0^2} \frac{dJ}{da} = \frac{E}{\sigma_0^2} \left[\frac{4b^2F_1^2}{b^2 \frac{\partial F_1}{\partial \theta} - \frac{dM}{d\theta}} - \frac{J}{b} \right] \tag{27}$$

Therefore, given F_1 , it is noted that Eq 26 can be used to compute crack length changes increment by increment along a load-displacement (M versus θ) record. Then Eq 25 may be used to compute J and Eq 27 may be used to obtain T_{mat} at any point on the record. These results for pure bending were obtained in Refs 1 and 2 and in both, a simple experimental method of determining F_1 was discussed. Of course F_1 also could be determined by analytical methods, such as finite element method, using the stress-strain curve for the material to which the analysis here is applied. It is emphasized that this analysis, Eq 24 through 27, is exact, independent of material property assumptions for this example case of pure bending.

This example, pure bending, has been given because it produces the simplest results and is most likely to be familiar to the reader. However, more important is the application of these procedures to configurations which will be used for testing or the analysis of structural cracking problems. In such applications for any configuration, any one of the special forms, Eqs 11a, 11b, or 11c may be used. However, careful choice of the form, for most configurations, will lead to much more practical results. Moreover, the proper procedures for applying the results to load-displacement record analysis bears further comment here.

Additional Example—the Compact Specimen

For a compact specimen which is deeply cracked, say $a/W \geq 0.8$, the remaining ligament, $b (= W - a)$, is subjected to substantially pure bending with other planar dimensions, a, W, H , etc., being very large compared to b . In this case the analysis of pure bending in the preceding section may be applied with reasonable accuracy. However, in such applications J must be computed using analysis such as Eq 25, where the second integral is required to correct for the effects of crack growth on J . This correction has not been used throughout the previous literature except for Refs 1 and 2. Indeed, the reader is cautioned that J-R curves in the literature are only approximately correct and that their slopes, dJ/da , for the crack growth portion may be in error by 20 to 30 percent due to neglect of this correction term in previous work. Thus, it is clear that more careful analysis is warranted in even the simplest cases, especially those used in testing where material properties so evaluated will reside permanently in the published literature. It is relevant then to proceed with a general analysis of the compact specimen for all a/W values and neglect terms only where they are justifiably small compared to others.

In general the remaining ligament of a compact specimen is subjected mostly to bending but also to a moderate axial force which cannot be neglected entirely. For such cases where bending is a dominant factor, the use of the first special functional form, F_1 , as defined by Eq 11a is most appropriate. This is because in applying the analysis using that form, Eqs 12 through 19, the terms involving derivatives with respect to a/W of F_1 will be weak, that is, considerably smaller than the main terms. It will be noted here that some of these terms may then be neglected justifiably to simplify the analysis.

In reviewing the analysis, Eqs 12 through 19 will be repeated with appropriate modifications for the compact specimen. First for the determination of J prior to crack growth, Eqs 13 and 15 may be used, hence

$$J = G + \tilde{J}_{pL}$$

where

$$\tilde{J}_{pL} = \frac{2}{b_0} \int_0^{\Delta_{pL}} P d\Delta_{pL} - \frac{b_0^2}{W^2} \int_0^{\Delta_{pL}} \frac{\partial F_1}{\partial \left(\frac{a}{W} \right)} d\Delta_{pL} \quad (28)$$

$$(\text{for } \Delta a = 0)$$

Now the second term in Eq 28 involving $\partial F_1 / \partial (a/W)$ is as noted previously a Merkle-Corten type correction [6] which is known to be smaller than other terms but which disappears only at very high a/W values. Now this

term cannot be neglected in Eq 28. However, if the computation of J with growing cracks is considered using Eq 16, then note that the integral term in Eq 16 is small compared to other terms. Within this integral, the terms in the integrand explicitly involving the derivations of F_1 are small compared to \tilde{J}_{pL} , thus their effect on the overall J can be neglected. That is, with small amounts of crack growth present compared to the ligament size, b , Eq 16 may be simplified for compact specimens to give

$$J = G + \tilde{J}_{pL} - \int_{a_0}^a \frac{\tilde{J}_{pL}}{b} da$$

where (as before)

$$\tilde{J}_{pL} = \frac{2b_0}{W} \int_0^{\Delta_{pL}} F_1 d\Delta_{pL} - \frac{b_0^2}{W^2} \int_0^{\Delta_{pL}} \frac{\partial F_1}{\partial \left(\frac{a}{W}\right)} d\Delta_{pL} \tag{29}$$

(for all small Δa , $0 \leq \Delta a \ll b$)

Now the limitation of Eq 29 to small Δa is no loss in generality, since J -controlled crack growth is restricted to small crack length changes [1]. That is, for large amounts of crack growth, J -controlled crack-tip fields disappear so that J analysis itself tends to become inappropriate.

Therefore, Eq 29 is a general form which may be used to compute J accurately in compact specimens. It is noted that two types of "correction terms" exist, that is, the last terms of both parts of Eq 29. The term involving $\partial F_1 / \partial (a/W)$ is similar to the Merkle-Corten correction now in use [7], but since F_1 obviously depends on material properties and is thought to be influenced strongly by hardening, etc., the terms are definitely not identical. The conclusion here is that until demonstrated otherwise, Eq 29 is the only sure way to obtain accurate J values from compact specimen results.

In order to evaluate increments of crack length change, da , in compact specimens, Eq 18 may be used without modification. It is, again

$$da = \frac{\frac{b^2}{W^2} \frac{\partial F_1}{\partial \left(\frac{\Delta_{pL}}{W}\right)} d\Delta_{pL} - dP}{\frac{2b}{W} F_1 - \frac{b^2}{W^2} \frac{\partial F_1}{\partial \left(\frac{a}{W}\right)}} \tag{30}$$

It is likely that the term in the denominator with $\partial F_1 / \partial (a/W)$ will be

negligible, but it is carried here for further evaluation. At this point it is seen that Eqs 29 and 30 are sufficient to evaluate crack length changes, da , and J , so that J-R curves may be constructed, given F_1 and a load-displacement record. Subsequently, the means of evaluating F_1 shall be discussed. However, first it is relevant to develop the procedure to directly evaluate T_{mat} .

Adopting the usual definition of T_{mat} (see Eq 19), the remaining component required is dJ . This is obtained most directly by differentiating Eq 29 and referring to earlier expressions such as Eq 14. The simplest format neglecting terms appropriately is

$$dJ = dG + \left[\frac{2b}{W} F_1 - \frac{b^2}{W^2} \frac{\partial F_1}{\partial \left(\frac{a}{W} \right)} \right] d\Delta_{pL} - \left[\frac{2}{W} \int_0^{\Delta_{pL}} F_1 d\Delta_{pL} \right] da \quad (31)$$

Then using Eq 19, and substituting Eqs 30 and 31, T_{mat} becomes

$$T_{mat} = \frac{E}{\sigma_0^2} \left[\frac{dG}{da} + \frac{\left[\frac{2b}{W} F_1 - \frac{b^2}{W^2} \frac{\partial F_1}{\partial \left(\frac{a}{W} \right)} \right]^2}{\frac{b^2}{W^2} \frac{\partial F_1}{\partial \left(\frac{\Delta_{pL}}{W} \right)} - \frac{dP}{d\Delta_{pL}}} - \frac{2}{W} \int_0^{\Delta_{pL}} F_1 d\Delta_{pL} \right] \quad (32)$$

Therefore, for a compact specimen Eqs 29 through 32 are sufficient not only to construct a J-R curve, but also to evaluate T_{mat} directly at any point of a load-displacement record, if F_1 and its derivatives, $\partial F_1 / \partial (\Delta_{pL} / W)$ and $\partial F_1 / \partial (a / W)$, are known.

Determination of F_1 and Its Derivatives for Compact Specimens

As defined by Eq 11a, F_1 is the relationship between load and plastic displacement, for a given set of specimen proportions, including a/W , and for a given material's stress-strain curve. Then it is evident that one way to obtain the function, F_1 , is analytically through finite element method or other such methods. For example, it would be relevant to tabulate this function and its derivatives for common test configurations, such as the standard compact specimen, for Ramberg-Osgood stress-strain curves of various hardening coefficients, n .

However, it is also possible to determine F_1 and its derivatives experimentally for the actual material to be considered in a reasonably practical way. The procedure shall be described here.

More specifically it is assumed that a single load-displacement record is to be used to determine a material's crack growth properties. But in order to calibrate the method, that is, to determine F_1 and its derivatives, then assume that a few sub-size specimens of the same material are also available, where the sub-size specimens are made in exactly the same dimensional proportions as the full-size specimen, except their initial a/W values vary slightly from that of the full-size specimen to larger values. Now let all of the load-displacement records from these specimens be plotted on the basis of PW/b_0^2 versus Δ/W as shown on Fig. 2a. The elastic parts of the displacement on Fig. 2a may be noted, using initial slopes for each of the specimens, to develop Fig. 2b a plot of PW/b_0^2 versus Δ_{pL}/W in which case PW/b_0^2 is F_1 . Now the sub-sized specimens will go to larger deformations, Δ_{pL}/W , prior to having crack growth occur. Therefore, each plot of data from a sub-sized specimen is F_1 associated with its a/W value up to its own initiation of crack extension. Furthermore, the slopes of the sub-sized specimen curves give $\partial F_1/\partial(\Delta_{pL}/W)$ and the spacing of curves will give $\partial F_1/\partial(a/W)$. Therefore, all of the information on F_1 required for analysis using Eqs 29 through 32 is available. Then the full-size specimen's load displacement curve may

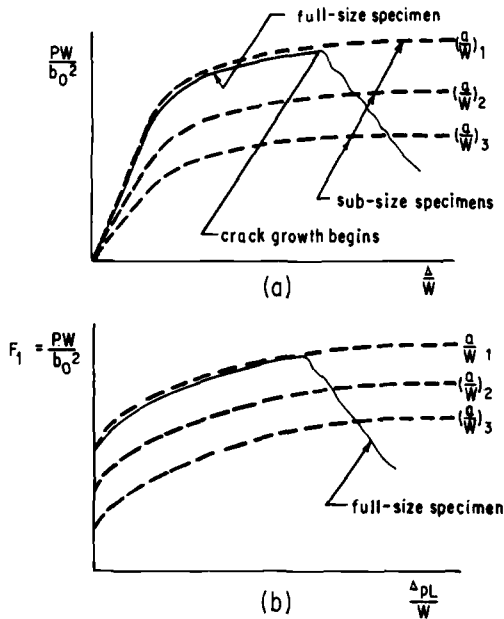


FIG. 2—Normalized load-displacement records for full and subsize specimens.

be analyzed fully using Eqs 29 through 32, integrating along this curve increment by increment as indicated by the equations to determine J , Δa , and T_{mat} which can then be used to plot a J-R curve if desired.

All of the theory behind this procedure is exact. It is calibrated for the actual material tested employing exactly the same degree of plane stress versus plane strain in the sub-size specimens of the identical proportion and material. (Indeed, after testing a full-size compact specimen, the broken halves contain enough material to make four sub-size specimens just slightly smaller than half size.) (Moreover, many reactor surveillance programs contain scaled specimen sizes of identical proportions which fortuitously turns out to be ideal for this purpose.) Finally, using this method, the terms which were neglected in developing Eqs 29 through 32 from Eqs 12 through 19 can be evaluated from the information from the sub-size specimens technique if any doubt exists.

It is noted here that other approaches, rather than direct application of Eqs 29 through 32 to the full-size specimen using sub-size specimens as passive calibrations of F_1 and its derivatives can be devised to determine J , Δa , and T_{mat} from this test information. However, each makes less than maximum use of information from the full-size specimen and therefore, is regarded as less precise. Finally, it is noted that a set of full-size specimens when tested can be used to calibrate each other, (that is, determine F_1 and derivatives without sub-size specimens), but this would be less than precise if points of beginning of crack extension, etc. were not clearly distinguishable. The practical aspects of such short cuts are to be left to experimental programs.

In summary, for evaluation of a material's cracking properties from compact specimens, the calibration method described here along with Eqs 29 through 32 forms a precise and practical basis for determining J , Δa , T_{mat} , etc. from nothing more than load-displacement records. Since other methods require costly additional instrumentation, etc., this method shows great promise.

Bending Test Specimens of the Three-Point and Four-Point Bending Type

For typical bend test specimens with a/W large enough so that plasticity is confined to the remaining ligament region, the analysis in the preceding sections on compact specimens also applies. However, all terms involving $\partial F_1/\partial(a/W)$ become very weak and can be neglected within normal accuracy requirements. Thus simply repeating Eqs 29 through 32, deleting these terms, the results are

$$J = G + \hat{J}_{\text{pL}} - \int_{a_0}^a \frac{\hat{J}_{\text{pL}}}{b} da$$

where

$$\hat{J}_{pL} = \frac{2}{b_0} \int_0^{\Delta_{pL}} P d\Delta_{pL} \tag{33}$$

and

$$da = \frac{\frac{b^2}{W^2} \frac{\partial F_1}{\partial \left(\frac{\Delta_{pL}}{W}\right)} d\Delta_{pL} - dP}{\frac{2b}{W} F_1} \tag{34}$$

and

$$T_{mat} = \frac{E}{\sigma_0^2} \left[\frac{dG}{da} + \frac{\left[\frac{2b}{W} F_1\right]^2}{\frac{b^2}{W^2} \frac{\partial F_1}{\partial \left(\frac{\Delta_{pL}}{W}\right)} - \frac{dP}{d\Delta_{pL}}} - \frac{2}{W} \int_0^{\Delta_{pL}} F_1 d\Delta_{pL} \right] \tag{35}$$

using Eqs 33 through 35 and a single sub-size specimen to determine F_1 , the evaluation procedures described in the previous section hold to determine T_{mat} , etc., from a load-displacement record of a full-size specimen. On the other hand, if doubt exists on the precision of deleting terms containing $\partial F_1/\partial(a/W)$ here, then the previous analysis, Eqs 29 through 32 can be employed in full (with further sub-size specimens required) to evaluate the effect of neglecting these terms.

It seems relevant to point out here that the final form of Eq 23 for three-point bending has been used erroneously in the past. In this connection it should be noted that the first form of Eq 23 contains G and that it must be modified for three-point bending of a finite specimen whereas the plastic term remains reasonably accurate (based on θ_{crack}). The errors were the result of the inappropriate use of linear-elastic components of the analyses. Moreover, it is also noted here that in developing J-R curves from bending tests, the final term in Eq 33, correcting for the effect of crack growth, has been neglected throughout the literature.

Applications to Predominately Tension Loading

Any of the three special functional forms, Eqs 11a, 11b, and 11c may be applied to any two-dimensional configuration. Therefore, for predomi-

nately tension, the form F_1 and its associated analysis, Eqs 12 through 19, could be employed correctly. However, in that analysis the terms involving $\partial F_1/\partial(a/W)$ and its second derivative as well, would become dominant and difficult to evaluate accurately either by experimental methods or further numerical analysis. Thus for cases where the remaining ligament is subjected principally to tension, it is equally correct but significantly more practical to apply the alternate forms F_2 or F_3 , or both. The latter form, F_3 , is only of substantial advantage whereas the remaining ligament, b , is very small compared to other dimensions, W , L , a , etc., so that F_3 is a function only of Δ_{pL}/b , and other variables disappear, as discussed originally in Ref 3. Consequently, the continuing discussion here will center on the functional form, F_2 from Eq 11b.

Substituting Eq 11b into Eq 8 gives

$$J = G + \int_0^{\Delta_{pL}} F_2 d\Delta_{pL} - \frac{b}{W} \int_0^{\Delta_{pL}} \frac{\partial F_2}{\partial \left(\frac{a}{W} \right)} d\Delta_{pL} \quad (36)$$

Resubstituting from Eq 11b for F_2 in the first integral term leads to

$$J = G + \frac{1}{b} \int_0^{\Delta_{pL}} P d\Delta_{pL} - \frac{b}{W} \int_0^{\Delta_{pL}} \frac{\partial F_2}{\partial \left(\frac{a}{W} \right)} d\Delta_{pL} \quad (37)$$

(for $\Delta a = 0$)

These results, Eqs 36 and 37 are analogous to Eqs 12 and 13 and so upon comparison we note that Rice's term in Eq 13 appears in Eq 37 but with a coefficient of one instead of two. Upon noting that the last two terms in Eqs 13 and 37 are weak (small) in bending and tension respectively, then the principal term in J_{PL} , the plastic part of J is

$$J_{PL} \cong \frac{\eta}{b} \int_0^{\Delta_{pL}} P d\Delta_{pL} \quad (38)$$

where

$\eta \rightarrow 2$ (pure bending)

$\eta \rightarrow 1$ (pure tension)

as noted by Sumpter [8], quite some time ago. Indeed, this analysis agrees with Turner's results but in addition offers Eqs 13 and 37 as exact

analysis, both being applicable to all cases if correction terms (the final terms in each) are evaluated properly.

The analysis is continued as with Eqs 14 through 19, hence

$$\begin{aligned}
 dJ = dG + \left[F_2 - \frac{b}{W} \frac{\partial F_2}{\partial \left(\frac{a}{W} \right)} \right] d\Delta_{pL} \\
 + \left[\frac{2}{W} \int_0^{\Delta_{pL}} \frac{\partial F_2}{\partial \left(\frac{a}{W} \right)} d\Delta_{pL} - \frac{b}{W^2} \int_0^{\Delta_{pL}} \frac{\partial^2 F_2}{\partial \left(\frac{a}{W} \right)^2} d\Delta_{pL} \right] da \quad (39)
 \end{aligned}$$

and

$$\begin{aligned}
 J = G + \int_0^{\Delta_{pL}} \left[F_2 - \frac{b}{W} \frac{\partial F_2}{\partial \left(\frac{a}{W} \right)} \right] d\Delta_{pL} \\
 + \int_{a_0}^a \left[\frac{2}{W} \int_0^{\Delta_{pL}} \frac{\partial F_2}{\partial \left(\frac{a}{W} \right)} d\Delta_{pL} \right. \\
 \left. - \frac{b}{W^2} \int_0^{\Delta_{pL}} \frac{\partial^2 F_2}{\partial \left(\frac{a}{W} \right)^2} d\Delta_{pL} \right] da \quad (40)
 \end{aligned}$$

$$(0 < \Delta a \ll b)$$

and

$$da = \frac{\frac{b}{W} \frac{\partial F_2}{\partial \left(\frac{\Delta_{pL}}{W} \right)} d\Delta_{pL} - dP}{F_2 - \frac{b}{W} \frac{\partial F_2}{\partial \left(\frac{a}{W} \right)}} \quad (41)$$

where

$$T_{mat} = \frac{E}{\sigma_0^2} \frac{dJ}{da} \quad (42)$$

As before, if Eqs 39 through 42 are applied to center crack or double edge notch specimens where little or no bending is present, terms containing $\partial^2 F_2 / \partial(a/W)^2$ in Eqs 39 and 40 can be neglected and the influence of the $\partial F_2 / \partial(a/W)$ term in the denominator will be small in some circumstances for certain computations. Thus a simplification of these equations for some practical cases is possible. Moreover, in such cases, experimental procedures very much like those suggested in the preceding section on determination of F_1 and its derivatives for compact specimens are appropriate. However, that analysis and subsequent experimental procedures are so similar to the preceding discussions that it is not repeated here.

A Note on Determination of T_{appl} for Analyzing the Tearing Instability

Following the analysis provided by Hutchinson [1], T_{appl} can be found from

$$T_{\text{appl}} = \frac{E}{\sigma_0^2} \left(\frac{\partial J}{\partial a} \right)_{\Delta_T} \quad (43)$$

Now $(\partial J / \partial a)_{\Delta_T}$ is the increase in J applied by a loading system per increment of crack extension with the overall system displacement, Δ_T held constant. Therefore, following Hutchinson's analysis procedures [1], the $(\partial J / \partial a)_{\Delta_T}$ may be computed making use of the forms for analyzing J herein, for example, Eqs 16, 25, 29, 33, 40, etc. Once suggested, carrying out such computations is straightforward and consequently omitted from further discussion here.

Conclusions

1. Methods of properly (exactly) computing J for various test configurations have been developed herein.
2. The methods developed correctly account for the effects of crack growth on J , which has often been in error in previous works.
3. Procedures for determining J-R curves, T_{mat} , etc. are discussed which require no more than load-displacement records from tests.

Acknowledgments

This work was sponsored by a contract from the U.S. Nuclear Regulatory Commission, Operating Reactors Division, at Washington University, St. Louis. The continued encouragement of R. Gamble and W. Hazelton of Nuclear Regulatory Commission is most gratefully acknowledged. The assistance of this work through consultation with

J. R. Rice (Brown University), and upon whose works this analysis was based, is acknowledged with thanks.

References

- [1] Hutchinson, J. W. and Paris, P. C. in *Elastic Plastic Fracture*, ASTM STP 668, American Society for Testing and Materials, 1979, pp. 37-64.
- [2] Paris, P. C., Tada, H., Zahoor, A., and Ernst, H., "A Treatment of the Subject of Tearing Instability," Report NUREG-0311, U. S. Nuclear Regulatory Commission, Aug., 1977.
- [3] Rice, J. R., Paris, P. C., and Merkle, J. G. in *Progress in Flaw Growth and Fracture Toughness Testing*, ASTM STP 536, American Society for Testing and Materials, 1973, pp. 231-235.
- [4] Rice, J. R., *Journal of Applied Mechanics*, American Society of Mechanical Engineers, 1968, pp. 379-386.
- [5] Paris, P. C., Discussion of work by J. A. Begley and J. D. Landes in *Fracture Toughness*, ASTM STP 514, American Society for Testing and Materials, 1972, pp. 1-39.
- [6] Merkle, J. and Corten, H., *Journal of Pressure Vessel Technology; Transactions*, American Society of Mechanical Engineers, 1974, pp. 286-292.
- [7] Clarke, G. A., "Tentative Recommendation Procedure for J_{Ic} Testing," American Society for Testing and Materials, Committee E-24 meeting, Norfolk, Virginia, March, 1977.
- [8] Sumpter, J. D. and Turner, C. E. in *Cracks and Fracture*, ASTM STP 601, American Society for Testing and Materials, 1976, pp. 3-18.

M. E. Karabin, Jr.,¹ and J. L. Swedlow¹

Path Dependence of J in Three Numerical Examples

REFERENCE: Karabin, M. E., Jr., and Swedlow, J. L., "Path Dependence of J in Three Numerical Examples," *Fracture Mechanics, ASTM STP 677*, C. W. Smith, Ed., American Society for Testing and Materials, 1979, pp. 600–613.

ABSTRACT: Three cracked geometries are studied with the aid of a new finite element model. The procedure employs a variable singularity at the crack tip that tracks changes in the material response during the loading process. Two of the problems are tension-loaded center-crack panels and the other is a three-point bend specimen. Results usually agree quite well with other numerical and analytical analyses. An exception is the finding that J is path dependent as a substantial plastic zone develops. Credible J values are obtained near the crack tip and J shows a significant increase as the radius of J path increases over two orders of magnitude. Far field J exhibits agreement with analyses whose method implements the deformation theory of plasticity. However, this particular model employs incremental theory. Incremental and deformation theories are identical provided the stresses exhibit proportionality. This proportionality is found in the far field stresses but not near the tip. Consistent with the concept of nonproportionality, the path dependence of J is linked to the relative resharpening of the crack flank near the tip in center-crack specimens.

KEY WORDS: crack propagation, deformation, plasticity, J-integral

Recently a new finite element model has been used to study two-dimensional stationary crack problems. The distinguishing feature of the model is a special element at the crack tip that possesses a variable singularity. Thus, changes and their rates can be detected as the material response goes from an elastic to an elasto-plastic characterization. It has been found that most of the results agree well with other analyses. The J-integral, however, has been found to exhibit path dependence as a significant amount of plasticity develops. Trends are systematic and two factors are suggested as causes for the J behavior.

¹ Graduate assistant and professor, respectively, Department of Mechanical Engineering, Carnegie Institute of Technology, Carnegie-Mellon University, Pittsburgh, Pa. 15213. Dr. Karabin is now affiliated with Advanced Reactors Division, Westinghouse Electric Corporation, Madison, Pa. 15663.

Model Description

Before discussing the results, a brief description of the model is presented. Displacements within the special element for a given increment of load are of the form

$$\begin{aligned}\delta u_r &= A_1(\theta) + A_2(\theta)r + A_3(\theta)r^P \\ \delta u_\theta &= B_1(\theta) + B_2(\theta)r + B_3(\theta)r^P\end{aligned}\quad (1)$$

where δu_r , δu_θ are the incremental cylindrical displacements associated with the r, θ coordinate system centered at the crack tip. P represents a variable incremental exponent. Surrounding the special element are conventional constant strain elements. There is a small displacement incompatibility between the two element types; we have ascertained that this is not serious until very high loads are applied.

The exponent P and the conventional nodal degrees of freedom are found through the minimization of an energy-like functional Π , which is precisely the analogue to potential energy used in classical elasticity. Minimization assures equilibrium within the increment in the same manner that minimum potential energy operates in the linear elastic case. The requirement is

$$d\Pi = (\partial\Pi/\partial\{\delta u\})d\{\delta u\} + (\partial\Pi/\partial P)dP = 0 \quad (2)$$

where $\{\delta u\}$ represents the vector array of all the nodal degrees of freedom, including the regular elements. In order to avoid solution of a large number of nonlinear equations, each component of Eq 2 is set equal to zero

$$\partial\Pi/\partial\{\delta u\} = [K]\{\delta u\} - \{\delta T\} = 0 \quad (3)$$

$$\Pi = \text{minimum (w.r.t.)}P$$

where the first expression represents the usual stiffness equations and, in the second, the correct value of P is determined. These two equations are solved simultaneously but iteratively to determine the minimum of Π , in accordance with Eq 2. A fuller description of the method employed by the computer program, SPECCEL, is given by Swedlow [1,2],² but it may be noted that convergence usually is achieved in two or three cycles. By having a variable exponent it is possible to follow changes in material response as it goes from elastic to elastoplastic, thereby modeling local response accurately. Note that previous numerical analyses employing special elements embed the singularity associated with linear elas-

² The italic numbers in brackets refer to the list of references appended to this paper.

ticity [3], or with a value for a material possessing a strict power hardening stress-strain curve [4] as characterized by the HRR theory [5,6].

J-Integral

In determining the fully plastic singularity, the HRR theory uses the deformation theory of plasticity. SPECEL implements the incremental theory of plasticity. The distinction between deformation and incremental theories is critical in the J-integral development. J is defined as

$$J = \int_{\Gamma} W dy - t_k \frac{\partial u_k}{\partial x} ds \quad (4)$$

where

- Γ = counterclockwise path encircling the crack tip,
- W = strain energy density,
- t_k and u_k = traction and displacement components on Γ , respectively,
- x, y = usual cartesian coordinate directions with the origin at the crack tip, x being in the direction of crack prolongation, and
- s = variable of integration along the path Γ .

Rice [7] shows that J is path independent, using small strain theory and requiring the strain energy density to be defined as $W = W(\epsilon) = \int_0^\epsilon \sigma_{ij} d\epsilon_{ij}$ which admits materials characterized as either linear elastic or power hardening within the context of deformation theory of plasticity. No such proof exists for materials following the more realistic incremental theory. SPECEL also uses small strain theory, and the results have been checked so that the criterion [8] ensuring their validity has been met.

Previous finite element results [4,9] do not raise the question of J path dependence. But these analyses embed the HRR singularity as a constant throughout the loading process. A more recent work by Atluri et al [10] reports evidence of a path dependent J . This analysis also embeds the HRR singularity as a constant and uses small strain theory. Atluri argues that the reason for the path dependence he observes is the breakdown in small strain theory as applied to the definition of J . When using a more appropriate definition of J based on finite deformations [11], Atluri's J regains its path independence. As mentioned earlier the small strain theory is appropriate to SPECEL's results. Yet, there is J path dependence in all of the elasto-plastic problems solved by SPECEL and this is in some way tied to the variable singularity.

Problem Description

Specifically, this work studies three specimens—two center-crack and one three-point bend. All are solved as plane strain problems with a special element size of $1/64$ of the crack length (half crack length in center-crack problems). The first problem (designated PH) is a tension loaded center-crack panel with a length-to-width ratio of three and a width-to-crack length ratio of two. The stress-strain curve is a power hardening relationship of the form

$$(\epsilon_o/\epsilon_L) = (\tau_o/\tau_L)^3; \tau_o/\tau_L > 1 \quad (5)$$

where ϵ_o and τ_o are the octahedral strain and shear stress, respectively. ϵ_L and τ_L are the corresponding yield point quantities, 1.3×10^{-4} and 6.9 MN/m^2 ($1 \times 10^3 \text{ lb/in.}^2$).

Previous work by Riccardella and Swedlow [12] provide the basis for the second center-crack specimen, designated RS. An A533, grade B, class 1 low-alloy steel is analyzed. The length-to-width ratio is $7/6$ and the width-to-crack length ratio is three. Loading is achieved by uniform displacements that produce a net tensile load. The only difference between the procedure used in Ref 12 and this report is the finite element formulation and map.

ASTM Committee E-24 on Fracture Testing [13] has set the guidelines for the final problem, denoted as BEND. This is the three-point bend specimen comprised of a low work hardening material.

$$\epsilon_e = \frac{\sigma_e}{E} + \left(\frac{\sigma_e}{B_o} \right)^{10}, \sigma_e/\sigma_y > 1 \quad (6)$$

E is 0.2177 TN/m^2 ($31.58 \times 10^6 \text{ lb/in.}^2$); B_o is 827 MN/m^2 ($120 \times 10^3 \text{ lb/in.}^2$); the effective yield stress is 207 MN/m^2 ($30 \times 10^3 \text{ lb/in.}^2$), and Poisson's ratio is 0.3. The specimen width-to-crack length ratio is two and the length-to-width is four. This set of problems thus involves two basic geometries and three materials—one actual, two constructed. Owing to the elastic strains, deformation is never fully incompressible.

Results

Credibility of the method has been verified [14]. Nearly all of the results agree well with theory or other numerical results. Focus here is directed towards evidence of J -integral path dependence. J results are given in terms of Y , defined as

$$Y = \frac{\sqrt{EJ/(1-\nu^2)}}{\bar{\sigma}\sqrt{a}} \quad (7)$$

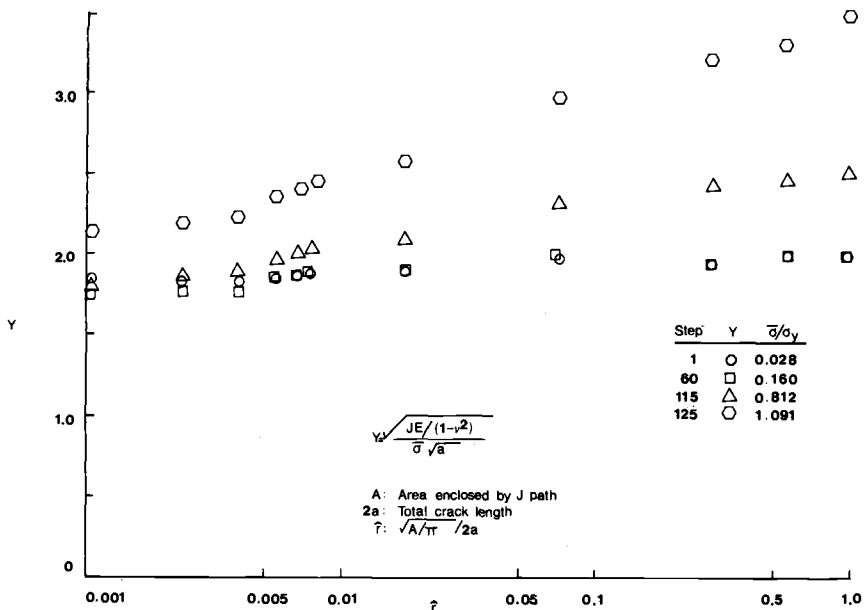


FIG. 1—Normalized *J* versus effective path radius \hat{r} (PH case).

where $\bar{\sigma}$ is the (net) applied stress and a is the crack length (half crack length in center-crack specimens). First note in Fig. 1 the result of Y plotted against the effective radius \hat{r} of the J path for the power hardening center-crack problem. Data at four load levels are shown: elastic, yield first detected beyond the special element, net section yield, and gross section yield. Eleven J paths are shown spanning three orders of magnitude in path radius. For the elastic step the normalized J value reflects a reasonable degree of path independence, as it should from analytical considerations. At net section yield far field Y values are increasing noticeably faster than the near field counterparts. This trend continues with further loading.

In Fig. 2, near and far field Y values are plotted as a function of applied load. Each value represents an average of three paths. Also shown are the numerical results for the elastic case, Tada et al [15], and a fully plastic case, Goldman and Hutchinson [9]. Good agreement exists between SPECCEL and Tada for the elastic step. Subsequent loading shows a decrease (7 percent) in the near field Y for low loads ($\bar{\sigma}/\sigma_y < 0.6$). The far field value follows the small scale yielding (elastic) prediction until roughly $\bar{\sigma}/\sigma_y = 0.8$ at which point it follows the Goldman and Hutchinson results, showing agreement to within 15 percent. Near field Y shows quite a different result.

One possible explanation for the path dependence may be tied to the

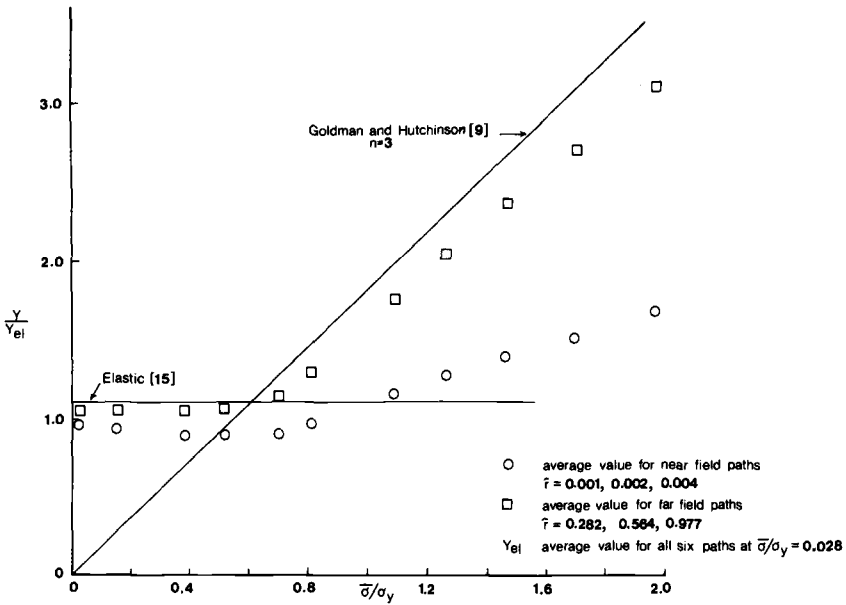


FIG. 2— Y/Y_{el} versus $\bar{\sigma}/\sigma_y$ for near and far field paths (PH case).

relationship between the incremental and deformation theories of plasticity. Ilyushin [16] has shown that the two theories lead to identical results provided that the tensor of similitude is constant as a function of load at every point within the body. The tensor of similitude is defined as

$$\pi_{ij} = s_{ij}/\tau_0 \tag{8}$$

where s_{ij} is the stress deviator. A corollary of this statement is that deformation and incremental theories are identical if proportional loading exists. That is, the stresses remain in fixed proportion to one another throughout the loading process at every point in the body.

Figure 3 shows the in-plane components of the tensor of similitude ahead of the crack tip as a function of load for near and far field values. It is evident that the near field values are not constant with load whereas the far field values are nearly so. This indicates that in the far field region, where the tensor of similitude is nearly constant, the incremental and deformation theories of plasticity are equivalent. This would explain the close agreement between the Goldman and Hutchinson J results (deformation) and the far field J values of SPECEL (incremental). SPECEL's near field J values are obtained in a region where the tensor of similitude is nonconstant and, hence, no agreement is to be expected with the deformation theory results. Proportional loading was checked around the entire J path for a number of load steps in both the near and far field. The

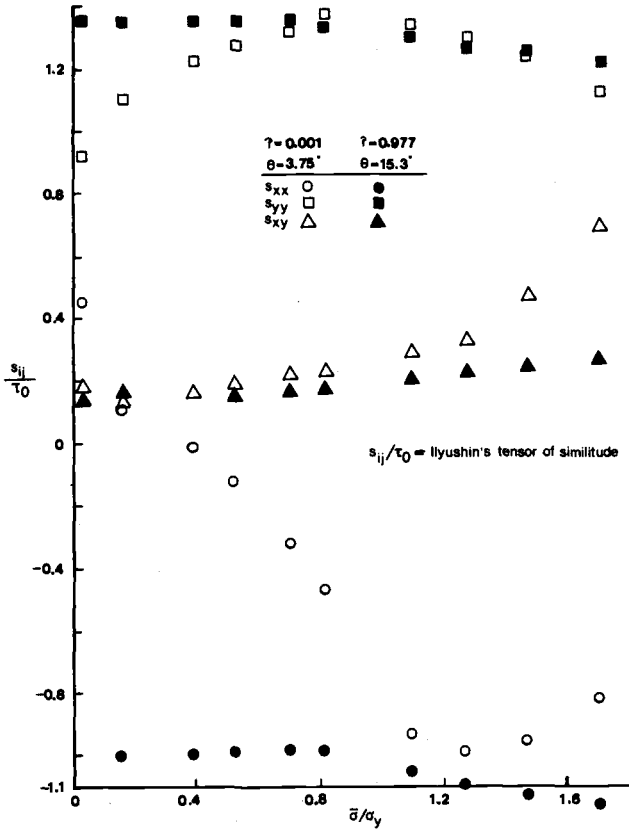


FIG. 3— s_{ij}/τ_0 versus $\bar{\sigma}/\sigma_y$ ahead of crack tip (PH case).

findings are in line with the preceding argument—proportional loading exists in the far field but not in the region close to the tip. Near field stresses change from a pattern given by the first two terms of the elastic Williams solution [17] to the one term plastic Hutchinson solution for a material with a cubic power hardening relationship [5]. Redistribution of these near field stresses siphons off some of the energy input used to drive the crack (that is, increase J). Far field J values do not sense the redistribution and yield higher J values.

Similar J results for the second center-crack panel can be seen in the next two figures. In Fig. 4, J is nearly constant as a function of path radius for low loads. But beginning at net section yield ($\bar{\sigma}/\sigma_y = 0.87$), J is definitely path dependent.

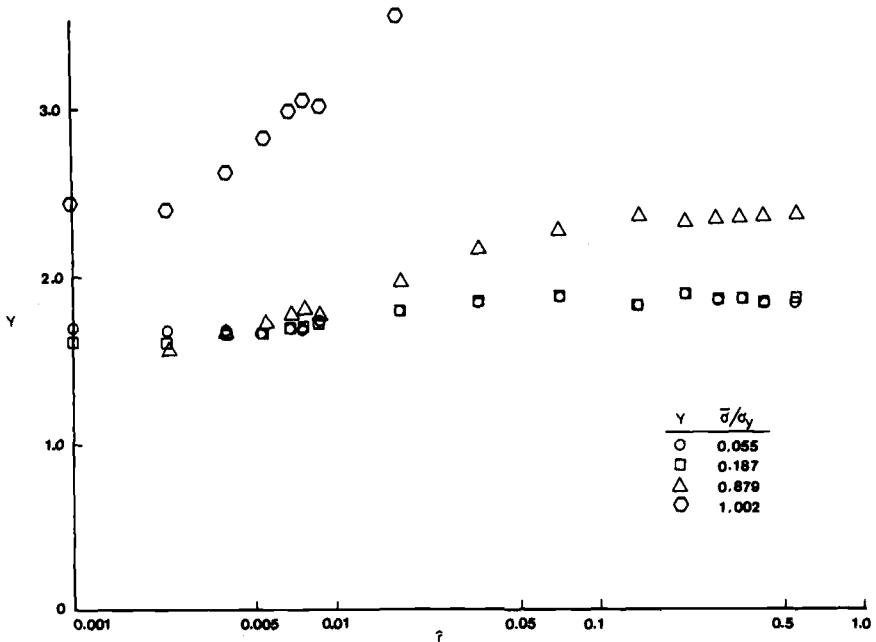


FIG. 4—Normalized J versus effective path radius \hat{r} (RS case).

The stress-strain curve in this problem represents a real material. Two power hardening approximations to this curve are, beyond yield.

$$(1) \quad \epsilon/\epsilon_L = 3.11(\tau/\tau_L)^{7.74}$$

$$(2) \quad \epsilon_e/\epsilon_L = \sigma_e/E + 0.514(\sigma_e/\sigma_y)^{10} \quad (9)$$

where the two curves are in octahedral and effective quantities, respectively. Figure 5 shows the Goldman and Hutchinson results for center-crack panels using these two curves as well as the near and far field Y values from SPECEL using the real material curve. The tendencies are similar to the first problem. Far field Y values follow the small scale yielding (elastic) prediction for low load levels and then SPECEL's results increase sharply. Although SPECEL's far field Y agrees with neither of the Goldman and Hutchinson predictions, it does have the same shape and relative magnitude after net section yield. The near field shows a slight decrease from the small scale yielding value before net section yield at which point it increases but at a considerably slower rate than the far field value. Again the answer can be found in the tensor of similitude. Although not shown here, near field stresses show a considerable amount

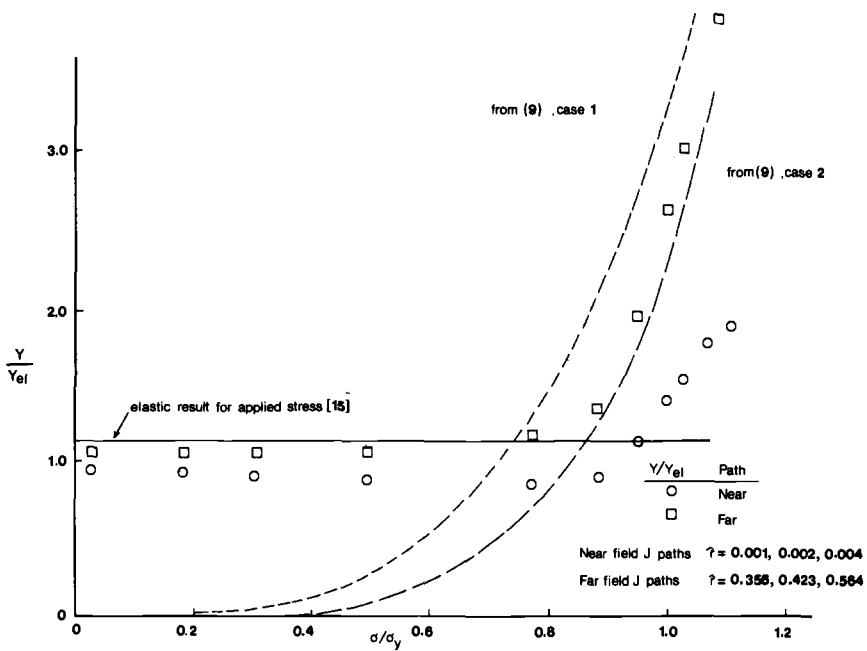


FIG. 5—Near and far field J values versus applied load (RS case), numerical data and Goldman-Hutchinson prediction [9].

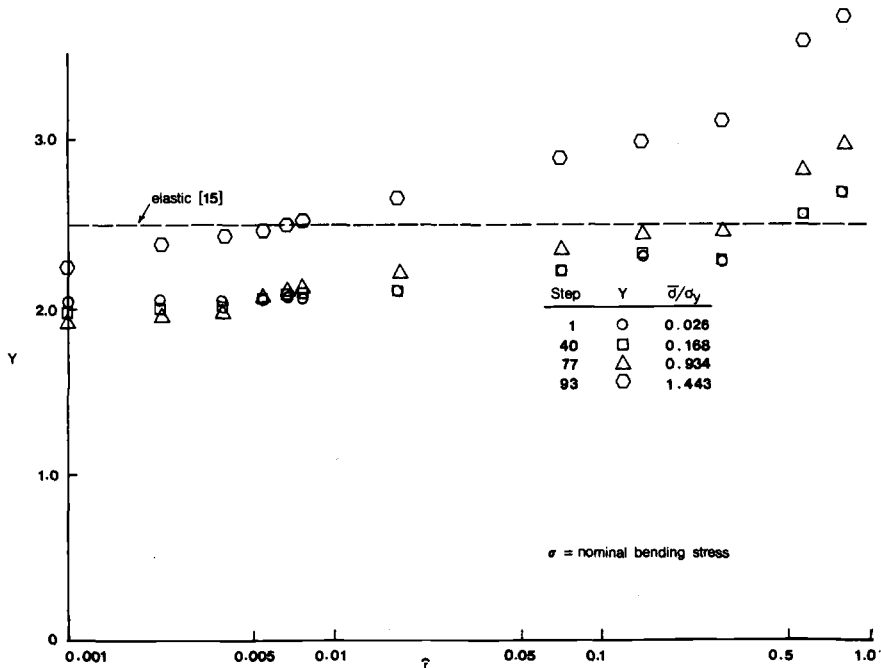


FIG. 6—Normalized J versus effective path radius \hat{r} (BEND case).

TABLE 1—Coefficient of variation in J values over nine paths, $0.0010 \leq \hat{r} \leq 0.2821$, center crack problem using material in Eq 5 and bend problem for material in Eq 6. Elastic response, net section yield, and gross section yield.

	BEND	PH
elastic	0.09	0.06
NSY	0.17	0.21
GSY	0.22	0.31

of redistribution whereas far field stresses exhibit proportionality throughout the loading process.

The final example is the three-point bend specimen. Y as a function of path radius is shown for a few load levels in Fig. 6. The load levels are given in terms of applied displacement: elastic, yield extending just beyond the special element, net section yield, and a higher load level, roughly twice the applied displacement at net section yield. Small scale yielding results do not portray J as being very constant. This is due to the fact that the constant strain elements used in SPECCEL do not do a good job of handling bending. However, the scatter in Y is not that great at net section yield as for the center-crack cases.

Table 1 compares the J scatter for the bend and power hardening center crack problems. Shown in the table is the coefficient of variation (standard deviation divided by the mean) for nine identical J paths with $0.0010 \leq \hat{r} \leq 0.2821$. Three load levels are given: elastic, net section yield, and gross section yield. For the bend problem the applied displacement at gross yield is 2.03 times the displacement at net section yield; for the center-crack problem the ratio of the two displacements is only 1.63. Although the bend problem shows much more J scatter for the elastic step, it is evident that the coefficient of variation in J grows more quickly for the center-crack specimen. This leads to a second possible explanation of J path dependence.

J has been linked to crack opening displacement (COD) in other analyses [18,19]. At the least, a direct proportionality exists between J and COD. Although no attempt will be made here to define a workable COD for these three problems, it is evident that COD must be related to the transverse displacements of the crack flank near the tip. In Figs. 7, 8, and 9, this transverse displacement is plotted against the crack mouth opening for all three problems. Where a linear relationship exists between the mouth opening and transverse displacement, this portion of the crack flank is increasing in constant proportion to the mouth. For the case of the bend specimen, Fig. 7, displacements along the entire length of the crack are increasing in proportion to the mouth opening (by virtue of the linear relationships at all

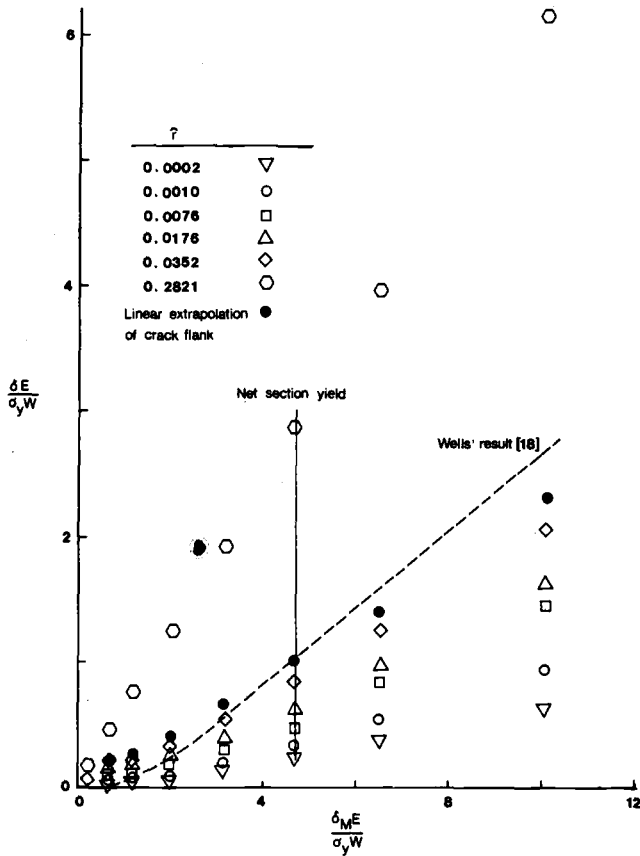


FIG. 7—Crack flank opening δ versus mouth opening δ_M (BEND case).

the positions along the crack flank). Hence, displacements near the tip could be found by extrapolation of displacements far from the tip along the flank. But in both center crack problems, the result is quite different. After net section yield the linear relationship between mouth opening and transverse displacements breaks down near the tip. ($\hat{r} < 0.07$). This breakdown becomes more severe closer to the tip. Hence, using more than 85 percent of the crack length ($\hat{r} > 0.07$) to extrapolate near tip transverse displacements would lead to an overestimation. The sense of this relative resharping would be missed outside of a small zone around the tip. Assuming J is in some way related to this near tip transverse displacement, J measured near the tip would feel the effect of the relative resharping. Far field J , not sensing the relative resharping in its transverse displacements, would overpredict the near field values. Since

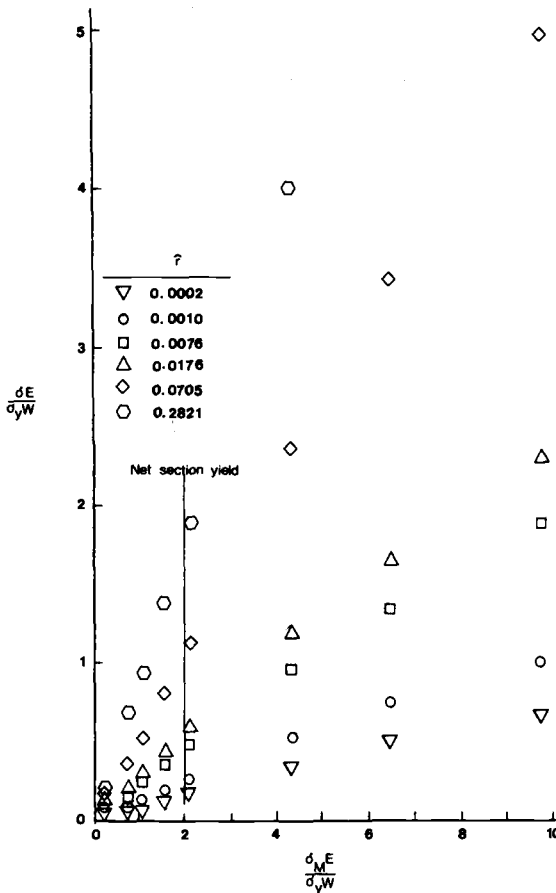


FIG. 8—Crack flank opening δ versus crack mouth opening δ_M (PH case).

the relative resharping is absent in the bend problems it gives more constant J at higher loads.

Concluding Remarks

Two reasons have thus been identified as possible sources of J 's path dependence: nonproportionality of the stress field local to the crack tip, and a relative resharping of the crack in a manner peculiar to the overall specimen geometry. Certainly these results are dependent upon the numerics in SPECEL; they are also dependent upon the particular material and its modeling, and upon the specimen geometry involved. One can easily conceive of an experiment to test the present findings. Computation of J and test values of J_{Ic} would be compared for various

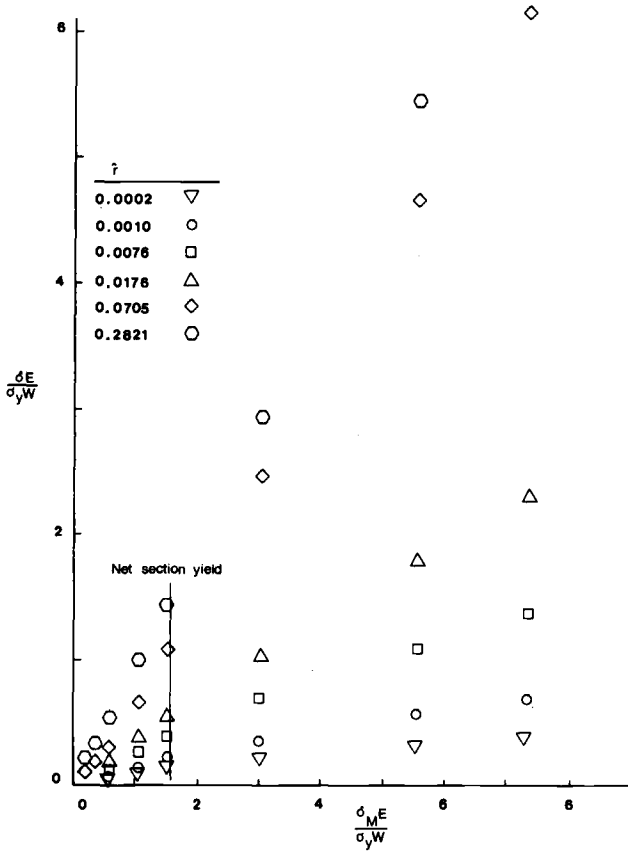


FIG. 9—Crack flank opening δ versus crack mouth opening δ_M (RS case).

specimen geometries, using selected materials. Additionally, data for quantities such as COD might be examined. Our present purpose is not so much to detail an experimental program as it is to provide the results of careful computation. The indication is, however, that physical testing of these results is the next logical step in carrying the research forward.

Acknowledgment

The authors wish to express their thanks to the National Aeronautical and Space Administration for their support towards the work in this report sponsored by NASA Research Grant NGR-39-087-053.

References

[1] Swedlow, J. L., Report SM 74-10, Department of Mechanical Engineering, Carnegie-Mellon University, 1974. See also Swedlow, J. L., *International Journal for Numerical Methods in Engineering*, Vol. 12, 1978, pp. 1779-1798.

- [2] Swedlow, J. L. and Karabin, M. E., Jr., in *Fracture 1977*, University of Waterloo, Vol. 1, 1977, pp. 117–131.
- [3] Wilson, W. K. in *Stress Analysis and Growth of Cracks*, ASTM STP 513, American Society for Testing and Materials, 1972, pp. 90–105.
- [4] Hilton, P. D. and Hutchinson, J. W., *Engineering Fracture Mechanics*, Vol. 3, 1971, pp. 435–451.
- [5] Hutchinson, J. W., *Journal of the Mechanics and Physics of Solids*, Vol. 16, 1968, pp. 13–31.
- [6] Rice, J. R. and Rosengren, G. F., *Journal of the Mechanics and Physics of Solids*, Vol. 16, 1968, pp. 1–12.
- [7] Rice, J. R., *Journal of Applied Mechanics*, Vol. 35, 1968, pp. 379–386.
- [8] McMeeking, R. M. and Rice, J. R., *International Journal of Solids and Structures*, Vol. 11, 1975, pp. 601–616.
- [9] Goldman, N. L. and Hutchinson, J. W., *International Journal of Solids and Structures*, Vol. 11, 1975, pp. 575–591.
- [10] Aturi, S. N., Nakagaki, M., and Chen, W. in *Flaw Growth and Fracture*, ASTM STP 631, American Society for Testing and Materials, 1977, pp. 42–61.
- [11] Knowles, J. K. and Sternberg, E., Technical Report No. 27, Division of Engineering and Applied Science, California Institute of Technology, 1973.
- [12] Riccardella, P. C. and Swedlow, J. L. in *Fracture Analysis*, ASTM STP 560, American Society for Testing and Materials, 1974, pp. 134–154.
- [13] Wilson, W. L. and Osias, J. R., *International Journal of Fracture*, Vol. 14, 1978, pp. R95–R108.
- [14] Karabin, M. E., “Elasto-Plastic Flow in Cracked Bodies Using a New Special Element,” Ph.D. thesis, Report SM 77-11, Department of Mechanical Engineering, Carnegie-Mellon University, 1977.
- [15] Tada, H., Paris, P. C., and Irwin, G. C., *The Stress Analysis of Cracks Handbook*, Del Research Corporation, Hellertown, Pa., 1973.
- [16] Ilyushin, A. A., *Prikladnaya Matematika i Mekhanika*, Vol. 10, 1946, pp. 347–356.
- [17] Williams, M. L., *Journal of Applied Mechanics*, Vol. 24, 1957, pp. 109–114.
- [18] Wells, H. H. in *Proceedings*, 3rd Canadian Congress of Applied Mechanics, Calgary, Canada, 1971, pp. 59–77.
- [19] Hayes, D. J. and Turner, C. E., *International Journal of Fracture*, Vol. 10, 1974, pp. 17–32.

C. E. Turner¹

Description of Stable and Unstable Crack Growth in the Elastic Plastic Regime in Terms of J_r Resistance Curves

REFERENCE: Turner, C. E., "Description of Stable and Unstable Crack Growth in the Elastic Plastic Regime in Terms of J_r Resistance Curves," *Fracture Mechanics, ASTM STP 677*, C. W. Smith, Ed., American Society for Testing and Materials, 1979, pp. 614-628.

ABSTRACT: A simple estimate is made of the elastic energy release rate, I , available from an elastic-plastic cracked component in terms of G and collapse load. I may be significantly greater than G from linear elastic behavior. A crack growth resistance curve is measured in terms of a J -like quantity, J_r , that is related to the plastic work absorbed by a geometry dependent factor, η . The increment of elastic energy is compared to the increment of plastic work at constant displacement to predict the possibility of stable or unstable crack growth. Effects of machine compliance are included. Some recent results on instability, test piece size restrictions, and conventional J crack growth curves are recovered as a special case. Illustrative examples are given based on estimates of I and J_r curves measured on a low-strength structural steel for mixed mode or flat fracture with ductile micro-mechanism.

KEY WORDS: resistance curves, instability, J-contour-integral, slow crack growth, mechanical test methods, fatigue (materials), crack propagation

If w_{av} is work available, which may or may not contain external sources, and w_{pab} is plastic work absorbed in the fracture process, then a balance of energy rate with respect to crack length, a , gives

$$\frac{dw_{av}}{da} = \frac{dw_{pab}}{da} + \gamma + \text{kinetic energy rate, etc.} \quad (1)$$

where γ is surface energy.

Differentiating with respect to a at constant displacement q

$$\frac{\partial^2 w_{av}}{\partial a^2} = \frac{\partial^2 w_{pab}}{\partial a^2} + \frac{\partial}{\partial a} (\gamma + \text{dissipative terms}) \quad (2a)$$

¹ Professor, materials in mechanical engineering, Imperial College, London, United Kingdom.

If the second term on the right is zero or essentially positive, then for the possibility of unstable behavior

$$\partial^2 w_{av} / \partial a^2 \geq \partial^2 w_{ab} / \partial a^2 \quad (2b)$$

a result discussed in other terms by Orowan for ductile instability. If for crack growth in the elastic-plastic case the energy rate available is expressed as a G -like term, G_{ep} , and by extension of the usage of the J -contour integral (evaluated as $J = -\partial w / \partial a$ prior to initiation) a J -like term, J_R , is envisaged for the dissipation rate, than Eq 2b becomes

$$\frac{\partial G_{ep}}{\partial a} \geq \frac{\partial J_R}{\partial a} \quad (3)$$

A suitable measure of J_R and the evaluation of G_{ep} is discussed as follows, and leads to a statement of unstable crack growth in terms of an inequality of energy rates.

As a different approach Paris et al [1]² equate plastic and elastic changes in length which, multiplied by suitable load functions, would imply an energy balance. Because plastic change in length is derived from crack opening displacement (COD), the result may apply only where the yield does not spread to the ends of the component, that is, for deep notch or nonhardening pieces, since for shallow notches with hardening, plasticity spreads to the ends remote from the notches. However, there is a drawback to an energy balance approach that may be fundamental. Rice [2] has stated that in material with finite hardening the elastic and plastic energy rates always balance as the crack growth increment $\Delta a \rightarrow 0$. There has been little comment on this in the literature until recently [3-7]. If this view is correct, can Eqs 1 and 2 be satisfied in a useful way for $\Delta a \rightarrow 0$? Computations [3,4] may deliberately or fortuitously avoid the limit by making Δa finite, but analytical methods usually rely on forming a derivative as $\Delta a \rightarrow 0$. It is assumed here that, provided the remote plastic work and the local surface energy are not separated, a useful inequality can be struck between the elastic and total dissipative terms. This implies that they will not converge asymptotically so that small errors in estimation will not lead to gross errors in prediction. Note that computation and experiment do show differences between the monotonically loaded cut-longer crack and the crack growing under load. Therefore, it may be questioned whether simple solutions (for example, slip line fields and collapse loads) that are not history dependent are of any use for estimates of the required terms.

In the following, the foregoing uncertainties are ignored. Estimates are made of the left side of Eq 1 and the right side is determined experimen-

² The italic numbers in brackets refer to the list of references appended to this paper.

tally without separating the plasticity and surface energy terms, so that $((dw_{pab}/da) + \gamma)$ is replaced by the total dissipative rate dw_{ab} .

Estimation of Energy Rate Available

An estimate of the elastic energy available on crack growth from a plastic load deformation curve can be made by a direct extension of the well-known method for calculating G from compliance in linear elastic fracture mechanics (LEFM). Referring to Fig. 1, for unloading with no crack growth BC would be parallel to the loading line OA , ignoring the effects of hysteresis and reversed plasticity. If crack growth occurs at constant displacement, in elasticity the net reduction in load is BD' , due to a reduction of area $(-\sigma_n da)$ causing BD and an increase in net stress $((W-a)d\sigma_n)$ causing $D'D$. This latter term cannot arise in the case of plasticity if the net stress σ_n is restricted to σ_Y . The compliance line, DE , is parallel to the lefm case, $D'C$. The difference is that the unloading line from D does not pass through the transposed origin C as would have been the case for a purely elastic event. The area corresponding to $GBda$ in the lefm case is $BD'C$. The extra energy release $D'DEC$ is available in the elastic-plastic case. After extensive yielding a good estimate of the decreases in load, BD , is the change in plastic limit load, Q_L , with crack length, and the area $D'DEC$ can be written either $q_{el}(DQ_L - dQ_{el})$ where dQ_{el} is the elastic term BD' , or as $Q_L dq_{el}$. The energy release rate, I , with plasticity near the limit condition is

$$BI = \left. \frac{\partial w_{el}}{\partial a} \right|_q \tag{4a}$$

$$= BG - Q_L dq_{el}/da \tag{4b}$$

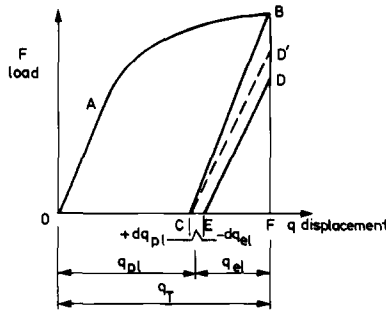


FIG. 1—Estimation of elastic energy release rate for a crack growing in an elastic-plastic component.

$$\text{or} \quad = BG - q_{el} (dQ_L - dQ_{el})/da \quad (4c)$$

Using the notation $\eta = \frac{W - a}{Q} \frac{\partial Q}{\partial a}$ as detailed in the Appendix, then

$$BI = BG - q_{el} \left(1 - \frac{\eta_{el}}{\eta_{pl}} \right) \frac{\partial Q_L}{\partial a} \quad (4d)$$

Note dq_{el} , dQ_L , dQ_{el} are inherently negative and $\eta_{el}/\eta_{pl} \leq 1$. This estimate is probably adequate to cover a mild degree of work hardening, if the yield stress is replaced by a flow stress. The expressions may not be adequate for a large degree of hardening or near the "elbow" of the load deflection curve where the net section stress is not approximately equal to yield stress, since in either case some part of the term DD' can exist. Nevertheless $G < G_{ep} < I$ so that G and I provide bounds between which the true energy release rate G_{ep} will lie. The excess of I over G is of course geometry dependent and for some configuration (where $\eta_{el} \approx \eta_{pl}$) is quite small.

This estimation is made at fixed total displacement, q_T , and is thus the minimum energy rate available. If external forces of a known compliance are acting an effective total length of structure, ${}_eD$, can be estimated and q_{el} replaced by an effective displacement, ${}_e q_{el}$, Eq 4. If the true length of the component is D , clearly ${}_eD > D$, perhaps by a large amount. For fixed load, ${}_eD \rightarrow \infty$ and an unlimited rate of energy available is implied for the present static treatment. In reality, kinetic energy effects and stress wave phenomena would dominate the behavior. In bending problems, the external compliance can clearly be treated as an effective span ${}_eS$.

Evaluation of Energy Absorption Rate

The absorption rate is $B\gamma_{eff} + \frac{\partial w_{pl}}{\partial a}$, where B is thickness. γ_{eff} includes the local Irwin-Orowen plastic dissipation and $\partial w_{pl}/\partial a$ the "remote" plasticity with a somewhat arbitrary division between the two. If J_i is identified with γ_{eff} (begging the issue of whether J_i is indeed the appropriate energetic measure of initiation), then a J -like dissipative term

$$BJ_R = BJ_i + \partial w_{pl}/\partial a \quad (5a)$$

might be formulated to define a resistance (R) curve. In fact, a different J -like term, here called J_r , was defined [8-10] for this purpose from the relationship between J and work

$$J = \eta w/B(W - a) \quad (5b)$$

rather than J and work rate

$$J = \eta \partial w / B \partial a \quad (5c)$$

thus

$$\Delta J_r = \eta \Delta W_T / B (W - a) + J_r (1 - \eta) \Delta a / (W - a) \quad (6a)$$

$$= (\eta_{pl} \Delta w_{pl} + \eta_{el} \Delta w_{el}) / B (W - a) + J_r (1 - \eta) \Delta a / (W - a) \quad (6b)$$

Δw_T is the increase in total work done, elastic, plastic, and surface, in growing a crack by a small increment Δa . In this interpretation Δw_{pl} includes the surface work term. It is implied that the meaning of the resistance curve, when expressed in terms of J_r versus Δa , is indeed just the increase in plastic work done (including shear lip formation if full thickness fracture), and not an increase in microtoughness per se. It also is implied that a measure of the plastic work under increasing load is relevant to a crack that may grow to find instability at constant displacement. Clearly the elastic contribution to the two cases is quite different but it is assumed that, at least for small amounts of crack growth Δa , the plastic and surface absorptions are the same, irrespective of the loading conditions.

The initial slope of the R-curve expressed in terms of J_r will be the same as that found during the extrapolation procedure in conventional J toughness testing that is here called dJ_{or}/da . It should also be noted that on this definition of resistance curve the steady state propagation of a contained plastic zone and the ensuing tearing is represented by $dJ_r/da = \text{constant}$, not by $dJ_r/da = 0$ since there is a continuous absorption of plastic work.

Measurements of J_r can be made in full thickness (Fig. 2, SGR-O) or in flat fracture (Fig. 3) by use of deep side grooves. The object of this distinction is twofold, though not strictly relevant to the present argument. First, it allows a J-R curve to be estimated that should be relevant to part-through cracks that do not generate shear lips, and second, it demonstrates that the increase in crack growth resistance is only partly due to shear lip with a significant portion due to plasticity effects ahead of the growing crack even in flat fracture.

It should be noted that although the exposition of J_r in Ref 8 and its use in Ref 10 were for three-point bend, the derivation [9] allows for other configurations by virtue of a different value for the geometry dependent constant, η_{pl} , in the J -work done relationship (see Appendix). The J_r curve should thus be geometry independent (a point that is still unproven experimentally) as for other fracture mechanics concepts. If the material response is such that the tearing or cracking behavior is sensitive to

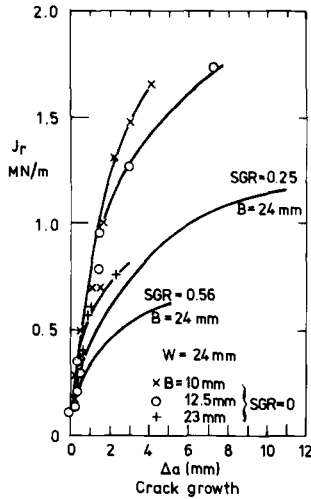


FIG. 2—Crack growth resistance curves expressed in terms of J_r ; three-point bending, $a_0/W = 0.5$, for various thicknesses and degrees of side grooving (side groove ratio (SGR) = $(B - B_{net})/B$; En32 structural steel 0.17 carbon, 0.74 manganese, 0.23 silicon, normalized; $\sigma_y = 285 \text{ Mn/m}^2$ (from Ref 10).

individual principal or shear stress values, then it is unlikely that a single parameter can be useful. A one-parameter fracture mechanics approach implies that the stress system at the tip of the advancing crack will be dominated by unique events there and not influenced by differences in biaxiality somewhat removed from the tip. These more remote terms will of course be geometry dependent but are already accounted for by the η_{pl} term. The existence or otherwise of a substantially unique response to an advancing crack may depend on the micromechanism in question.

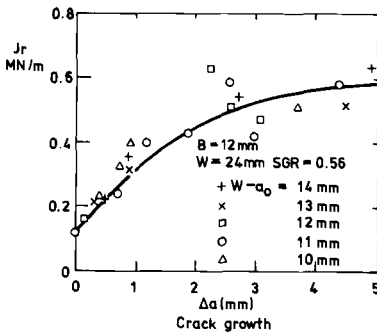


FIG. 3—Crack growth resistance curve for flat fracture expressed in terms of J_r ; three-point bending, deep side grooves, various initial crack lengths a_0 ; material as Fig. 2 (from Ref 10.)

Instability

For unstable growth Eqs 2b or 3 should be satisfied. For stable growth Eq 1 is sufficient. In the present picture Eq 1 is interpreted at constant overall displacement so that the work available, w_{av} , is restricted to sources internal to the system, although the system can include part of the immediate structure or testing machine, if so desired. Neglecting kinetic energy etc., Eq 1 is written, using Eqs 4 and 6, as

$$BI = - \left. \frac{\partial w_{el}}{\partial a} \right|_q = \left[\frac{dJ_r}{da} - \frac{J_r(1-\eta)}{(W-a)} - \frac{\eta_{el}}{B(W-a)} \frac{dw_{el}}{da} \right] \frac{B(W-a)}{\eta_{pl}} \quad (7)$$

When expressed as an inequality, this restatement of Eq 1 at constant displacement is taken as the practical statement of unstable crack growth in the absence of dissipations other than the test piece plasticity included in J_r . Thus, assuming (as discussed later) that the first term of Eq 6, ΔJ_r , dominates over $J_r \Delta a$, the condition for unstable crack growth becomes

$$I \geq \frac{(W-a)}{\eta_{pl}} \frac{dJ_r}{da} - \frac{\eta_{el}}{\eta_{pl}} G \quad (8)$$

where $\eta_{el} G/B(W-a)$ is the (increase) in elastic strain energy that occurred during measurement of the J_r curve at substantially constant (slightly increasing) load and which therefore has to be subtracted if a measure of dw_{pl} alone is required.

Final instability would occur according to Eq 2 when

$$B \frac{\partial I}{\partial a} \geq \frac{\partial^2 w_{pl}}{\partial a^2} \quad (9)$$

This equation is not further discussed here beyond noting that for a convex $J_r - \Delta a$ curve, $\partial^2 w_{pl}/\partial a^2$ is inherently negative while $\partial I/\partial a \big|_q$ may be either positive or negative according to the geometry of the configuration.

Applications

Applying Eq 8 to single edge notch tension with I from Eq 4d $q_{el} = (\sigma D/E) (\phi_n/\phi_o)$ where D is gage length, ϕ_n the notched compliance, and ϕ_o the unnotched compliance, D/EBW ; $Q_L = L\sigma_Y B(W-a)$ where L is the constraint factor. For simplicity dL/da is here neglected (see Appendix). The gross section stress, σ , in forming q_{el} must be re-expressed as $\sigma = L\sigma_Y(W-a)/W$ since net section yield is implied. Thus

$$\frac{(\eta_{pl} + \eta_{el})}{(W-a)} G + \frac{\sigma_Y^2 D}{EW} L^2 \frac{\phi_n}{\phi_o} (\eta_{pl} - \eta_{el}) \geq \frac{dJ_r}{da} \quad (10a)$$

In deep notches $\eta_{pl} \approx 1$; $L \triangleq 1$; η_{el} is a function of gage length. For typical test pieces it might be about one half, so that approximately

$$\frac{3G}{2(W-a)} + \frac{\sigma_Y^2 D}{2EW} \frac{\phi_n}{\phi_o} \approx \frac{dJ_r}{da} \tag{10b}$$

The major group $\sigma_Y^2 D/EW \propto dJ_r/da$ is similar to that in Ref 1 except in so far as dJ_r is used here instead of dJ_{or} and the former decreases more rapidly with Δa than does the latter. The compliance ratio ϕ_n/ϕ_o is omitted [1] for simplicity. A factor of two exists [1] (that is, $2\sigma_Y^2 D/EW$) from a treatment of a double-ended crack there and would arise in the present formulation as dQ_L is introduced into the evaluation of I (Eq 4b). The remaining differences ($(\eta_{pl} - \eta_{el}) \triangleq 1/2$; and the extra term $(\eta_{pl} + \eta_{el})G/(W - a)$ approximately equal to $3G/2(W - a)$) do not appear to have a counterpart in Ref 1. To the extent that they tend to cancel, the final difference may not be great. The source is the inclusion of ‘‘inherently’’ elastic terms in the evaluation of I and J_r as well as the ‘‘extra’’ elastic changes introduced to cancel out the plasticity effects and thus maintain constant length.

In three-point bending, $q_{el} = (\sigma S^2/6EW) (\phi_n/\phi_o)$ where S is span. $Q_L = 1.5Q_Y = B\sigma_Y L(W - a)^2/S$ for a rectangular cross section. Again neglecting dL/da and expressing the gross section bending stress, σ , in terms of the limit load for the ligament and inserting in Eq 8, using Eq 4d for I

$$\frac{(\eta_{pl} + \eta_{el})}{(W - a)} G + \frac{\sigma_Y^2 S}{EW} \left(\frac{W-a}{W}\right)^2 \frac{L^2 \phi_n}{2 \phi_o} (\eta_{pl} - \eta_{el}) \approx \frac{dJ_r}{da} \tag{11}$$

if slow growth is to occur at constant overall displacement. The major group is again the same as Ref 1 and the comments made in connection with the extra terms in Eq 10 apply here. In addition, it may be noted that for deep notch bending $\eta_{pl} \approx \eta_{el} \triangleq 2$, so that the term in G dominates the left hand side and the second term is nearly zero, implying that DD' , Fig. 1, is very small. Eqs 10 and 11 can be reduced further using $G = Y^2 \sigma^2 a/E$ where Y is the LEFM shape factor. Relating σ to σ_Y and net to gross area again (since σ is restricted by the ligament stress being σ_Y); noting the elastic compliance ratio ϕ_n/ϕ_o can be written in terms of η_{el} as

$$\phi_n/\phi_o = \frac{2Y^2 x (1 - x)}{z \eta_{el}} \tag{12}$$

where

$x = a/W$; $z = S/9W$ for bending or D/W for tension; then for tension, Eq 10 reduces to

$$Y^2 L^2 \times (1 - x) \left[\eta_{pl} \left(1 + \frac{2}{\eta_{el}} \right) + \eta_{el} - 2 \right] \approx \frac{E}{\sigma_Y^2} \frac{dJ_r}{da} \tag{13a}$$

and for bending, Eq 11 reduces to

$$Y^2 L^2 \times (1 - x)^3 \left[\eta_{pl} \left(1 + \frac{9}{\eta_{el}} \right) + \eta_{el} - 9 \right] \geq \frac{E}{\sigma_Y^2} \frac{dJ}{da} \quad (13b)$$

(the constraint factor L has been retained though terms in dL/da and d^2L/da^2 neglected. For some configurations, notably shallow notches, this is not permissible since L varies rapidly with crack length). In Ref 1 the term $(E/\sigma_Y^2) (dJ/da)$ is termed the tearing modulus. It is based on the initial tangent J_{or} which may be larger than the steady state value of dJ_r/da . Values typical of single edge notch tension, with ends held parallel, and three-point bending give (approximately)

Values of the left side of Eq 13

a/W	0.4	0.5	0.6	
$D/W = 4$	4	5	6	tension
$D/W = 8$	9	10	11	tension
$S/W = 4$	25	25	25	bending

while on the right side $(E/\sigma_Y^2) (dJ_r/da)$ gives, for initiation in flat fracture and quasi steady state respectively, about 800 and 80 for low-strength structural steel or about 200 and 20 for a high-yield steel (with the same J_r curve; this may not be realistic). Clearly a long gage length tension piece may approach a steady-state tear, for a material with a low tearing modulus. The tabulated values ignore machine compliance.

A typical machine compliance might be $\phi_m = 1/40$ to $1/400$ m/MN so the effective tensile gage length ratio $D/W \approx BE\phi_m$ (in addition to the actual test piece) gives η_{el} of perhaps about 0.02 and a number such as 50 or 200 for the left side of Eq 13a. This is quite compatible with a machine-induced rapid crack growth in steel for the dJ_r data quoted, although a closer estimate of the several very rough approximations is clearly desirable.

Discussion

It is not proven, and may be deemed unlikely, that toughness of a growing crack is independent of geometry, despite the incorporation of a geometric factor, η_{pl} into the analysis that relates J_r to the work done. It is also not demonstrated that J_r , although derived from work done, is indeed the required measure of toughness in two respects. First, it is not established in the literature that the plastic work (including shear lip effect if appropriate) is the cause of the crack growth resistance that is being

sought, and second, that J_r , when corrected for the elastic component³ is unequivocally the exact description of the plastic work.

The overall argument is that J_r is a more realistic measure of the feature being sought than other definitions of resistance curves. This statement is supported in part by the experimental evidence [9,11]. The cause of the growth of resistance does not appear to be metallurgical in the sense that there is no evidence of "extra toughness" from examination of the surface and local COD (Fig. 4) is constant at the advancing tip after a small initiation distance [11]. Yet even without shear lip effect, there is a large increase in J_r that directly reflects the extra work done during the rising load-stable growth process. The effects of shear lip can be added [9,10] if the proportion of shear lip is known, but this cannot as yet be predicted.

A relation between J_{or} and J_r can be demonstrated easily. The well-known relationship between J and work done, w , can be generalized (Appendix) as

$$J = \eta w / B(W - a) \quad (14a)$$

where

$$\frac{dJ}{da} = \frac{J}{\eta} \frac{\partial \eta}{\partial a} + \frac{J}{w} \frac{\partial w}{\partial a} + \frac{J}{W - a} \quad (14b)$$

If $\partial \eta / \partial a \ll (\eta / J) (dJ / da)$ then the first term can be omitted. Clearly this is acceptable for deep notches where η varies but little with crack length. If $J / W - a \ll dJ / da$ then

$$\frac{dJ}{da} \triangleq \frac{J}{w} \frac{dw}{da} \approx \frac{\eta(dw/da)}{B(W - a)} \approx \frac{dJ_r}{da} \quad (14c)$$

This expression is the leading term in Eq 6 so that $dJ_r \triangleq dJ_{or}$ when $((W - a) / J) (dJ / da) \gg 1$. This inequality is seen to be the same as the ω factor proposed in relation to Ref 1 as a necessary restriction on J-R curve testing [12]. However, it appears to limit the use of J_{or} as an approximation to J_r , not as a limitation of J_r itself. If it is argued that the well-known restriction on J testing (for determining J_i at initiation) is $(W - a) > 25$ or $50 J_i / \sigma_Y$, which is interpreted as $25 \delta_i$, then it could be argued that the similar restriction for J_r testing is $25 \delta_a$, where δ_a is the characteristic COD of the advancing tip, several times (here fourfold) smaller than δ_i , Fig. 4. The present data are valid according to $(W - a_o) > 25 \delta_i$ at initiation

³ The elastic term in J_r could be eliminated experimentally by taking only the plastic component $\eta_p w_{pl}$. It has been eliminated here algebraically by subtracting a term $\eta_e G / \eta_{pl}$ from Δw_T .

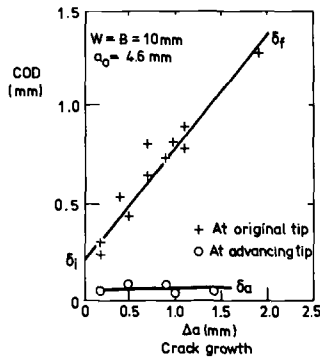


FIG. 4—Infiltration COD at the original (fatigue) and advancing crack tip during slow growth; three-point bending, no side grooves, material as Fig. 2 (from Ref 11.)

(where a_0 is original crack length) and to $(W - a) > 25 \delta_a$ during slow growth although violating the condition $J/(W - a) \ll dJ/da$ during growth. Brief discussion of the slow growth crack profiles in terms of Rice [13] is offered [11] and a relationship to Wnuk [14] and Broberg [15] will be discussed elsewhere.

There must also be some doubt as to whether I based on change in collapse load is suitable at the "elbow" of the load curve when collapse has not been reached but no simple treatment of that regime has yet been seen. It must also be noted that the treatment here is based on Eq 8 for slow growth at constant displacement (including the effects of compliance in a simulated effective length of component if need be), but no use has here been made of the more rigorous statement of unstable growth, Eq 9.

The J_r curves studied so far relate to near plane strain with fracture in microvoid coalescence. In principle the method seems applicable to plane stress if the appropriate collapse loads are used and plane stress (or mixed mode) J_r curves are found. Further study of the invariance of J_r with geometry is clearly necessary. The effect of temperature and strain rate on J_r has not been studied. For structural steels cleavage is likely at lower temperatures. The author's view of this is that a criterion such as a critical tensile stress has to be met over a small process zone ahead of the tip. It is accepted generally and argued easily on grounds of dimensional analysis that if below-gross yield cleavage obeys LFM then the ductility transition (that is, from below to above gross yield) will be size dependent. It does not seem easy to show that the micromode transition from cleavage to shear is also size dependent. If a postulated cleavage criterion was not quite reached before gross yield, four factors come into play as yield spreads: partial loss of in-plane constraint, partial loss of out-of-plane constraint, increase of flow stress with work hardening and perhaps strain rate, and possible alteration with deformation and local strain rate of the criterion that has to be met. The writer sees no immediate prospect of

assessing whether the balance of these factors would increase or decrease the likelihood of post-yield cleavage occurring after a certain amount of slow stable growth in or just above the temperature transition regime. However, there has been a recent attempt in this direction [16]. If it were to occur the resistance curve generated in micro-void coalescence would not appear to be relevant, a transition to another lower toughness mode presumably “cutting off” the J_r curve as the alternative criteria are met.

Conclusions

A simple evaluation has been made of the energy release rates I for an elastic plastic cracked body in two dimensions. For LEFM $I = G$ but with extensive plasticity $G < I$. An R-curve has already been proposed in terms of a J -like measure J_r , in which dJ_r/da describes the rate of absorption of energy as the crack spreads and an experimental technique proposed for finding it [8]. For slow growth, stable but with no external work, the two energy rates are equated. For unstable growth their next derivatives with respect to length should be equated. The former step gives a relationship similar to that proposed on somewhat different arguments by Paris et al [1] with the addition of an elastic energy term, and other geometry dependent modifications. An example of the use of the criterion is given for $\omega \gg 1$ but comparison with experiments has not yet been made. The method suggests a redefinition of G_R curves that will be discussed elsewhere.

Acknowledgments

The analysis is consequent upon the work of S. Garwood [9,17] for the SRC project Macro-micro Aspects of Fracture at Imperial College. The subject matter in the Appendix was developed as part of a study of shallow notches following a re-analysis of the computations of J. D. G. Sumpter and more recent data produced by C. Noad also for the SRC project.

APPENDIX

The η Factor

For rigid-plastic material

$$J_{pl} = \frac{-1}{B} \frac{\partial w}{\partial a} \Big|_q ; w = Q_L q \tag{15}$$

$$= \frac{-q}{B} \frac{\partial Q_L}{\partial a} \tag{16}$$

Write the collapse load as

$$Q_L = L\sigma_Y B(W - A)^N/S_N^{-1} \tag{17}$$

where

$N = 1$ for tension,

$N = 2$ for bending, and

$S =$ span or gage length where L is the constraint factor here taken as a geometric variable though also containing the plane strain effect 1.155 if von Mises criterion is used.

$$\partial Q_L/\partial a = -\eta_{pl} Q_L/(W - a) \tag{18}$$

where

$$\eta_{pl} = \frac{-(W - a)}{W} \frac{1}{Q_L} \frac{\partial Q_L}{\partial a/W} \tag{19}$$

$$= N - \frac{(W - a)}{W} \frac{1}{L} \frac{\partial L}{\partial a/W} \tag{20}$$

This formulation is used since the same term is required in the well-known statements

$$J_{pl} = \eta_{pl} w_{pl}/B(W - a) \tag{21}$$

and also for the well-known linear slope of the J_{pl}/q_{pl} graph

$$J_{pl}/q_{pl} = \eta_{pl} L(W - a)_N^{-1} \sigma_Y/S_N^{-1} \tag{22}$$

From Eq 20 if the constraint factor L is known, η_{pl} can be evaluated. For deep notch tension SEN, CCP, $\eta_{pl} \hat{=} 1$ and for deep notch bending $\eta_{pl} \approx 2$ since $\partial L/\partial a$ is small once the notch is deep enough for constraint to be developed fully. For DEN [18] used the constraint factor [19]

$$L \hat{=} 1 + 1n(W - a)/(W - 2a) \tag{23}$$

in an evaluation of the slope J_{pl}/q_{pl} and found good agreement with computed results for deep notches. The wider implications of the term η_{pl} and the identity between η_{pl} (Eqs 18, 20, 21, and 22) was not discussed. The effect of work hardening on the slope J/q_{pl} for shallow notch tension was noted [18,20] but again not related specifically to η_{pl} . In the estimates of J_{pl} and J_{pl}/q_{pl} using Eq 21 and 22 there are further complications if, as in shallow notch work hardening tension or pure bending plasticity spreads beyond the slip line region of the notch to the remote ends and estimates of η for use with shallow notches will be made elsewhere.

The elastic η factor was defined [21] as

$$G = \frac{\eta_{el} w_{el}}{B(W - a)} \tag{24}$$

where $w_{el} = \frac{1}{2}Qq$ for a "triangular" loading diagram. η_{el} can be evaluated from known expressions for K or experimental values of compliance, or load

$$-\frac{W-a}{W} \frac{1}{Q_{el}} \left. \frac{\partial Q_{el}}{\partial a/W} \right|_q = \eta_{el} \quad (25)$$

Eq 25 and 18 have been used in moving from Eq 4c to 4d in the evaluation of I .

For deep notch bending, $\eta_{el} \triangleq 2$, rather closely so, for $S/W = 4$. For longer spans and less deep notches η_{el} decreases, reaching quite small value (for example, 0.2) for some shallow notches. In tension the effect of gage length dominates. Typical values might be $\eta_{el} \triangleq 0.25$ for $D/W = 4$; $2a/w = 0.5$, reducing as D/W increase and as a/W decreases again reaching small values, of the order of $2\pi a/D$ for shallow notches in center-cracked plates.

The use of elastic, plastic, or total estimates of work done and the corresponding values of η were discussed [22] but again, the wider application of the same term to the various uses described here was not pointed out.

References

- [1] Paris, P. C. et al., "A Treatment of the Subject of Tearing Instability," Report NUREG 0311, Washington University, St. Louis, Aug. 1977; also *Elastic-Plastic Fracture, ASTM STP 668*, American Society for Testing and Materials, 1979, pp. 251-265.
- [2] Rice, J. R., "An Examination of the Fracture Mechanics Energy Balance from the Point of View of Continuum Mechanics," International Conference on Fracture, Vol. 1, Sendai, 1965, p. 269.
- [3] Kfoury, A. P. and Miller, K. J. in *Proceedings*, Institute of Mechanical Engineering, Vol. 190, No. 48, London, 1976, p. 57.
- [4] Kfoury, A. P. and Rice, J. A. in *Fracture 1977*, 4th International Conference on Fracture, Vol. 1, University of Waterloo, p. 43.
- [5] Luxmoore, A. R. and Morgan, K., *International Journal of Fracture*, Vol. 13, No. 4, 1977, p. 553.
- [6] Rice, J. R., in *The Mechanics of Fracture*, American Society of Mechanical Engineers, New York, 1976, p. 23.
- [7] Discussion Group contribution to *Numerical Methods in Fracture Mechanics*, Luxmoore and Owen, Eds., University College, Swansea, 1978.
- [8] Garwood, S. J., Robinson, J. N., and Turner, C. E. in *International Journal of Fracture*, Vol. 11, No. 3, 1975, p. 528.
- [9] Garwood, S. J., "The Measurement of Crack Growth Resistance Using Yielding Fracture Mechanics," Ph.D. thesis, University of London, 1977.
- [10] Garwood, S. J. and Turner, C. E. in *Fracture 1977*, 4th International Conference on Fracture, Vol. 3, University of Waterloo, p. 279.
- [11] Garwood, S. J. and Turner, C. E., "Crack Opening Measurements in Slow Stable Crack Growth," *International Journal of Fracture*, Vol. 14, 1978, pp. R195-R198.
- [12] Hutchinson, J. N. and Paris, P. C., *Elastic-Plastic Fracture, ASTM STP 668*, American Society for Testing and Materials, 1979, pp. 37-64.
- [13] Rice, J. R. in *Numerical Methods in Fracture Mechanics*, Luxmoore and Owen, Eds., University College, Swansea, 1978, p. 434.
- [14] Wnuk, M. P. in *Fracture 1977*, 4th International Conference on Fracture, Vol. 3, University of Waterloo, p. 59.
- [15] Broberg, K. B. in *Prospects of Fracture Mechanics*, Sih et al, Eds., Noordhoff International Publishing, Leyden, The Netherlands, 1974, p. 125.
- [16] Milne, I. and Chell, G. G. in *Elastic-Plastic Fracture, ASTM STP 668*, American Society for Testing and Materials, 1979, pp. 358-377.
- [17] Garwood, S. J., Pratt, P. L., and Turner, C. E., "Measurement of Slow Stable Crack Growth in Structural Steels and Prediction of Unstable Fracture," OECD-NEA Specialists meeting on elastoplastic fracture mechanics UKAEA, Daresbury, May 1978.

- [18] Sumpter, J. D. G., "Elastic Plastic Fracture Analysis and Design Using the Finite Element Method," Ph.D. thesis, University of London, 1973.
- [19] Ewing, D. J. F. and Hill, R. J., *Journal of Mechanics and Physics of Solids*, Vol. 15, 1967, p. 115.
- [20] Sumpter, J. D. G. and Turner, C. E., *International Journal of Fracture*, Vol. 12, No. 6, 1976, p. 861.
- [21] Turner, C. E., *Material Science and Engineering*, Vol. 11, 1973, p. 225.
- [22] Srawley, J., *International Journal of Fracture*, Vol. 12, 1976, p. 470.

Strain Energy Release Rate Method for Predicting Failure Modes in Composite Materials

REFERENCE: Williams, R. S. and Reifsnider, K. L., "Strain Energy Release Rate Method for Predicting Failure Modes in Composite Materials," *Fracture Mechanics, ASTM STP 677*, C. W. Smith, Ed., American Society for Testing and Materials, 1979, pp. 629-650.

ABSTRACT: One of the oldest and most firmly established concepts associated with the fracture of uniform homogeneous materials is the idea that strain energy release rate can be used to characterize the "driving force" for flaw growth, that is, the tendency for propagation. For linear elastic treatments of self-similar crack propagation the concept can be shown to be equivalent to the single parameter field stress intensity representation. The inhomogeneity and nonuniformity of composite materials and the consequent complexity of damage makes a direct extension of that concept to damage development in those materials difficult, if not impossible. Progress in that direction has been hampered by difficulty in defining the stress state in a damaged composite, and by inadequate laboratory information concerning the precise physical nature of the damage state.

In the present work these two difficulties were approached, respectively, by using a three-dimensional finite element scheme to generate internal stress field information and by making extensive scanning electron microscope studies of damage in two composite laminates. The paper reports the calculation of energy release rates for debonding, delamination and fiber breakage, and subsequent predictions of damage modes for two material systems. Correlation with experimental observations is good. The results also identify the influence of such parameters as fiber-matrix stiffness ratio on fracture mode, and the prediction of most probable debond sites.

KEY WORDS: composite materials, failure modes, strain energy, fracture mechanics, fatigue (materials), crack propagation

The fatigue and fracture damage mechanisms involved in the failure of fiber reinforced composite materials are many, complex, and interdependent. There have been several efforts to utilize linear elastic fracture

¹ Senior Research Engineer, Babcock and Wilcox, Lynchburg Research Center, Lynchburg, Va. 24505.

² Chairman, materials engineering group, Virginia Polytechnic Institute and State University, Engineering Science and Mechanics Department, Blacksburg, Va. 24061.

mechanics (LEFM) [1-5]³ in describing the fracture behavior of composites. In most cases the material is treated as a flawed anisotropic plate. This flaw is usually a crack, which is induced artificially by means of a saw-cut or sharp notch. Then, using conventional methods, critical values of the stress intensity factor (K_{Ic}) or the strain energy release rate (G_{Ic}), or both, are determined, using the change in length of this induced crack as the damage parameter. The basic premise of this type of analysis is the assumption that the failure of these materials can be characterized by the propagation of a single crack to failure.

The results of a large number of fatigue and static tests of boron/epoxy (B/Ep) and boron/aluminum (B/Al) flawed angle-ply coupons [6,7] have indicated that damage propagation consists more nearly of an advancement of a damage affected zone rather than the propagation of a single crack. Within this zone there exists some combination of fiber breakage, debonding, delamination, and matrix cracking. Since closed form analysis of each of these damage mechanisms proves quite cumbersome [8], a more general approach is desired. One possible approach has its origin in the fracture energy release concept postulated by Griffith and further expanded by Orowan, Irwin, and Kies [9,10].

Theory

The concept of crack instability in a solid as first postulated by Griffith [11] is that the crack will begin to propagate when the elastic energy released by its growth is greater than the energy required to create the new fracture surfaces. The Griffith concept assumes self-similar propagation. In an effort to account for the direction of propagation, Sih [11] has proposed the concept of strain energy density. Sih's theory has two fundamental hypotheses: the crack will spread in the direction of maximum potential energy density and the critical intensity of this potential field governs the onset of crack propagation.

In light of the two previous concepts, it seems reasonable that the potential for strain energy release is the driving force for crack propagation. Extending this line of reasoning to include the various damage mechanisms observed in composite material failure; then, each individual mechanism has a distinct driving force or potential for strain energy release. As stated by the Second Law of Thermodynamics, a system subjected to irreversible processes must experience an increase in entropy. Since the processes involved in each damage mechanism are, by nature, irreversible, and for an isothermal system an increase in entropy is directly proportional to a decrease in internal energy, damage propagation

³ The italic numbers in brackets refer to the list of references appended to this paper.

can be thought of as a process directly governed by the Second Law. (It is assumed that no work is done on or by the system during the damage events, or if it is, that it does not influence the internal choice of damage mechanism.) It therefore follows that an event that causes the greatest decrease in internal energy will be the most likely to occur, given an otherwise equal probability of occurrence for all possible events. This assumption is made in the spirit of the proportionality between entropy and probability assumed by Boltzman [12]. Applying this directly to a composite material system, if all other factors affecting the probability of occurrence of several damage mechanisms are the same, then the mechanisms most likely to occur first will have the highest potential for release of strain energy (since the prime contributor to a decrease in internal energy is a release in strain energy). Therefore, for total damage development in a composite material, given an otherwise equal probability of occurrence of all possible damage mechanisms, the total driving force will be related to a summation of the potential for strain energy release of all mechanisms, with those mechanisms having the highest value dominating or most likely to occur.

In the following sections, three predominant damage mechanisms, debonding, delamination, and fiber breakage, will be considered. By suitable analytical methods an expression for the potential for strain energy release for each will be developed and compared.

A. Fiber Debonding

In this section an expression for the stored strain energy of a simple fiber/sheath model is presented. The strain energy release caused by debonding will then be taken to be the difference in strain energy of the coupled fiber/sheath system and that for the fiber and sheath considered separately. The analysis is a plane strain, axisymmetric, elastic solution (although for the B/Al case the secant modulus was used to account partially for plasticity) first formulated by Ebert and Gadd [13].

Using the model shown in Fig. 1, it can be shown that

$$U = \frac{1}{2}(\sigma_{rr}\epsilon_{rr} + \sigma_{\theta\theta}\epsilon_{\theta\theta} + \sigma_{zz}\epsilon_{zz}) \quad (1)$$

$$U' = \frac{1}{2}(\sigma'_{rr}\epsilon'_{rr} + \sigma'_{\theta\theta}\epsilon'_{\theta\theta} + \sigma'_{zz}\epsilon'_{zz}) \quad (2)$$

and

$$U_{total} = U + U' \quad (3)$$

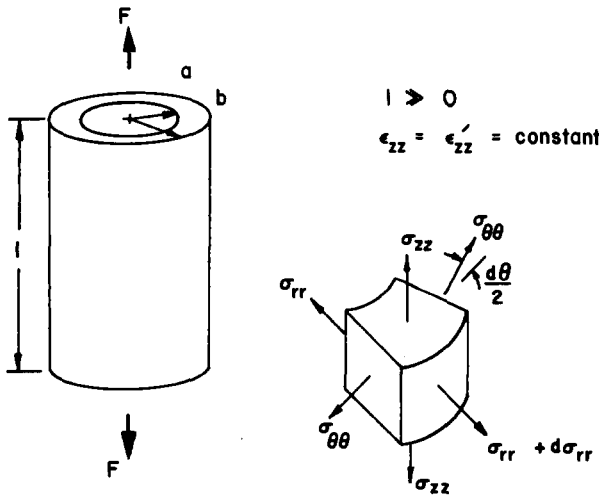


FIG. 1—Fiber/sheath model.

where U is the strain energy, the primed quantities refer to the fiber, and the unprimed ones to the matrix. Further, the expressions for stress are

$$\begin{aligned} \sigma_{rr} &= a^2 \epsilon_{zz} (1 - 2\nu) (1 - b^2/r^2) (K/\beta) \\ \sigma_{\theta\theta} &= a^2 \epsilon_{zz} (1 - 2\nu) (1 - b^2/r^2) (K/\beta) \\ \sigma_{zz} &= E \epsilon_{zz} + a^2 \nu \epsilon_{zz} (1 - 2\nu) (K/\beta) \\ \sigma_{r\theta} &= \sigma_{rz} = \sigma_{\theta z} = 0 \end{aligned} \tag{4}$$

and

$$\begin{aligned} \sigma_{rr}' &= \sigma_{\theta\theta}' = \epsilon_{zz} K' \left\{ \left[\frac{a^2(1 - 2\nu) + b^2}{\beta} \right] - (\nu - \nu') \right\} \\ \sigma_{zz}' &= E' \epsilon_{zz} + 2\nu' \epsilon_{zz} K' \left\{ \left[\frac{a^2(1 - 2\nu) + b^2}{\beta} \right] - (\nu - \nu') \right\} \\ \sigma_{zr}' &= \sigma_{r\theta}' = \sigma_{\theta z}' = 0 \end{aligned} \tag{5}$$

and those for strain are

$$\begin{aligned} \epsilon_{rr} &= \frac{d\theta}{dr} = \frac{a^2}{\beta} \epsilon_{zz} [(1 - 2\nu) - (2b^2/r^2)] - \nu \epsilon_{zz} \\ \epsilon_{\theta\theta} &= \theta/r = \frac{a^2}{\beta} \epsilon_{zz} [(1 - 2\nu) + (2b^2/r^2)] - \nu \epsilon_{zz} \\ \epsilon_{r\theta} &= \epsilon_{rz} = \epsilon_{\theta z} = 0 \end{aligned} \tag{6}$$

and

$$\epsilon_{rr}' = \epsilon_{\theta\theta}' = \theta'/r = \epsilon_{zz} \left\{ \left[\frac{a^2(1-2\nu) + b^2}{\beta} \right] - \nu \right\} \quad (7)$$

$$\epsilon'_{r\theta} = \epsilon'_{rz} = \epsilon'_{\theta z} = 0$$

where

$$\beta = [1/(\nu - \nu')] [a^2(1 - 2\nu)(1 - K/K') + b^2(1 + (1 - 2\nu)K/K')] \quad (8)$$

To evaluate the total strain energy, the expressions for stress and strain are substituted into Eqs 1 and 2 and the results integrated over the matrix and fiber, respectively.

For the case where the matrix and the fiber are separated, there exists a simple state of uniaxial tension. Therefore, the strain energy is simply

$$U_0 = \frac{1}{2} \sigma_{zz} \epsilon_{zz} = \frac{1}{2} E \epsilon_{zz}^2 \quad (9)$$

and

$$U_0' = \frac{1}{2} E' \epsilon_{zz}^2 \quad (10)$$

for the matrix and the fiber, respectively. And the total unbonded strain energy is

$$U_{0\text{total}} = U_0 + U_0' \quad (11)$$

This, then, results in the strain energy release for debonding to be

$$G_{DB} = U_{\text{total}} - U_{0\text{total}} \quad (12)$$

It should be noted that no mention of units was made in the previous derivation. For the time being, these quantities will be left as densities (energy/volume). In a later section this matter will be developed more completely.

B. Delamination

The calculation of the strain energy release caused by delamination was accomplished using a three-dimensional, finite element program developed by Barkler, Lin, Dana, and Pryor [14,15].

The program is an isoparametric finite element, minimum potential energy formulation for the problem of a rectangular laminated plate with a hole; several hole shapes can be handled (diamond, square, and circular).

The curved element has 72 degrees of freedom with the degrees of freedom preserved at the interfaces so that connections between lamina may be made. Cubical planeform and linear through-the-thickness displacement response functions are used. A conjugate gradient method selects a set of displacements that minimize the total potential energy of the system. According to variational principles, then, this set of displacements is the unique solution to the problem. A listing and complete program user's guide can be found in Ref. 16.

For these calculations a circular hole modeled by the mesh configuration as shown in Fig. 2 was used. All of the anisotropic characteristics of the actual specimens were simulated by the program. To simulate delamination a very thin lamina was sandwiched between the two lamina to be uncoupled. For the coupled case this lamina was assumed to have the material properties of the matrix. To simulate delamination the stiffness of this lamina was allowed to approach unity. The concept of using stiffness reduction to simulate damage is similar to the Unimod scheme originated by Reifsnider and used with good results by Reifsnider and Nair [17]. Since the finite element program could only accommodate up to twelve axisymmetric lamina, in order that the model correspond to available test coupons, only four delamination simulation layers were possible. These were situated symmetrically between the 0/+45 deg plies, since, from experimental evidence, delamination occurred there most

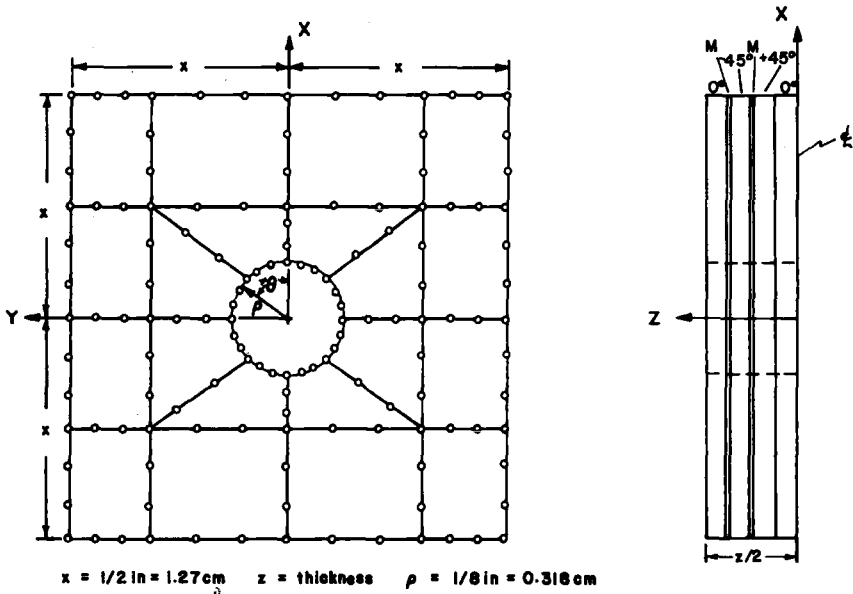


FIG. 2—Element and node structure of finite element model.

frequently. Since the computer program could only consider a symmetric configuration, the simulated delaminations were also symmetric.

All possible combinations of delaminations were run and the strain energy release was calculated by taking the difference in stored strain energy before and after simulated delamination.

C. Fiber Breakage

Two factors that must be considered when calculating the strain energy released when a constrained fiber fractures are the effective gage length over which the fiber fails (the length of the fiber over which the strain energy release occurs), and the stress distribution in this region before and after fracture. Since most of the literature in this area stops one step short of actual application, the approach for this section will be first to examine representative work and then extend it by means of a suitable rationale to arrive at an expression for strain energy release.

Olster and Jones [18] considered the case of a crack in the matrix approaching the interface perpendicular to the fiber for both ductile and brittle matrix materials. For the case of the brittle matrix, they assumed that debonding would occur and that the debonded region would represent the effective gage length. Within this region, they assumed the stress in the fiber to be constant and equal to the ultimate stress at failure. For the case of the ductile matrix, the effective gage length was determined by the extent of the plastic zone associated with fracture point and decreasing linearly to some remote value outside the plastic zone.

Several finite element studies have been made of the stress distribution in the fiber and the matrix caused by the fracture of a single fiber. Barker and MacLaughlin [19] used a linear elastic analysis to examine axially loaded unidirectional composites with a single discontinuous fiber surrounded by unbroken fibers. They varied fiber volume fraction, end-gap sizes and fiber/matrix modulus ratios, and plotted fiber and matrix stresses versus distance along the fracture fiber. As the end-gap decreased or the modulus ratio increased, or both, the distribution of stresses moving away from the fracture, along the fiber, tended to drop off more sharply.

Iremonger and Wood [20] performed a similar study, but also included the case where the end-gap was void of matrix material. They found that, for the case of the void end-gap, the stress drop off was sharper than when it was filled with matrix. In other respects, the results agreed quite well with those of Barker and MacLaughlin.

To account for the effect of plastic deformation in the matrix, Iremonger and Wood [21] determined the stress distribution along the fibers for a discontinuous fiber composite with elastic fibers and elastoplastic matrix material. Using material parameters similar to those of boron/aluminum (B/Al), they determined the stress distribution in the

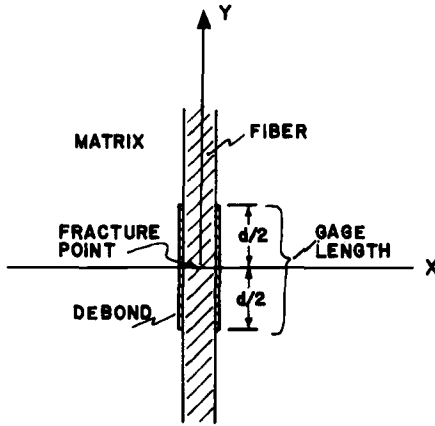


FIG. 3—Brittle matrix fiber break model, showing gage length.

fiber and the matrix, before and after fracture, for an end-gap size of 0.5 fiber diameters. They also concluded that once the matrix was yielded fully, the modulus ratio had little effect and most of the load was carried by the fiber. The axial stress distribution in a fiber adjacent to a discontinuous fiber was also determined.

As evidenced by the previous discussion, there is a considerable variation in what might be considered as the effective gage length and in what manner the stresses are distributed in this region, depending upon such variables as a ductile or brittle matrix, the end-gap size, the aspect ratio, the modulus ratio, or the fiber volume fraction, or all of these. Therefore, to restrict this discussion to the present class of structural engineering materials, only two cases will be considered. The first case

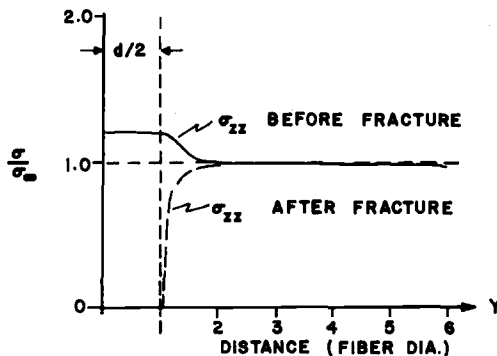


FIG. 4—Stress distribution in fiber for a brittle matrix composite.

will assume a low strength, brittle matrix with a high modulus ratio, similar to a boron/epoxy (B/Ep) composite. The second case will assume a high strength, elastoplastic matrix and a somewhat low modulus ratio, similar to a B/Al composite. Both cases will consider small void end-gaps and about a 50 percent fiber volume fraction.

For the brittle matrix case, the effective gage length will be assumed to be the length of the debond region (Fig. 3). In this region the fiber will be assumed to have a constant stress value equal to its failure stress. The assumed fiber and matrix stresses, before and after fracture (based on the trends discussed in Refs 19 and 20), are shown in Figs. 4 and 5. Realizing that much greater amounts of energy are stored within the fiber ($E_f/E_m \approx 120$) than in the matrix, it is feasible to assume that the bulk of the energy is released by the fiber over the debonded region, and the energy lost by the fiber outside the debonded region is gained by the matrix as shown in Fig. 5. Therefore, the expression for the strain energy release, with units of energy, will be

$$G_f = \frac{\sigma_f^2}{2E'} (d^2 \pi a^2) \quad (13)$$

where

- σ_f = fiber failure stress,
- E' = fiber modulus,
- d = debond length, and
- a = fiber radius.

Now, for the ductile matrix case, the determination of the effective gage length is considerably more difficult. Since the fiber can withstand stresses of the order of 2757 to 3447 MPa, and the matrix has yielded at 103 MPa, the majority of the strain energy is stored in the fiber. Figure 6 is a plot from Iremonger and Wood [21] of the axial stress in the fiber caused

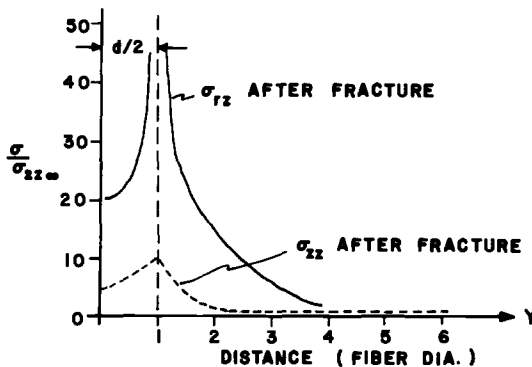


FIG. 5—Stress distribution in matrix for a brittle matrix composite.

by a broken adjacent fiber. Also shown is the stress distribution in that fiber after fracture. Since the end-gap size is large (about one half a fiber diameter) and filled with matrix material for the distributions shown in Fig. 6, it is quite likely that the drop off or rise is sharper than shown for the present smaller void end-gap case.

Since the contribution to the strain energy release of the matrix is small by comparison to that of the fiber, only that of the fiber will be considered. Also, due to the smaller end-gap, it is reasonable to assume that the probable gage length is closer to four fiber diameters than six, as shown in Fig. 6. Therefore, the strain energy release can be expressed as

$$G_f = 2 \int_0^{4a} \frac{1}{2E'} \sigma_1^2(x) dx - 2 \int_0^{4a} \frac{1}{2E'} \sigma_2^2(x) dx, \quad (14)$$

where $\sigma_1(x)$ and $\sigma_2(x)$ are the stress distributions before and after fracture. It is assumed that the maximum stress before fracture at $x = 0$ is the

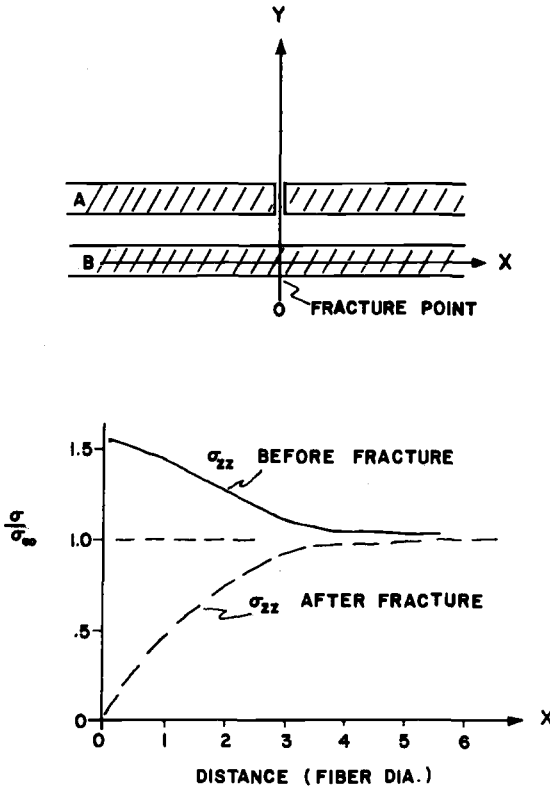


FIG. 6—Axial stress distribution in fiber for ductile matrix composite.

failure stress (σ_f) and the stress at $x = 4a$ is $2/3\sigma_f$. It is further assumed that the stress behaves linearly between these two points. If these substitutions are made in Eq 14 and the result is integrated, and then simplified, the strain energy release (with units of energy per unit area) is

$$G_f = \frac{20}{9} \frac{\sigma_f^2 a}{E'} \quad (15)$$

where

σ_f = failure stress in fiber,
 E' = fiber modulus, and
 a = fiber radius.

Now that either an expression for or a means of calculating the strain energy release has been presented for all major damage mechanisms, there remains the problem of expressing each in consistent units. Recalling Griffith's original formulation of his energy criterion, he considered the energy released by the crack in forming a new fracture surface. In the present case the different damage mechanisms are all markedly different in manner of occurrence, but in all situations there is a creation of a new fracture surface. Therefore, to allow the necessary comparison between the strain energy released by each damage mechanism, in the subsequent calculations they will be expressed in terms of energy released per newly created fracture area (inch pounds per square inch).

Results

The energy released per newly created fracture area was calculated for the cases of B/Ep and B/Al composites. A large, well documented set of data of static and fatigue tests exists for these materials [6,7] making experimental correlation possible.

Using the material properties in Table 1 and the expressions developed in Part A of the previous section, the average values of the stresses and integrated values of the strain energies for the matrix and the fiber are shown in Table 2. The primed quantities denote the fiber and the unprimed ones represent the matrix. For this table, strain energy is expressed in terms of energy per unit length along the fiber.

The computed strain energies, associated with delamination using the properties given in Table 1, are listed in Table 3. The ply configuration was (0 deg; M; -45 deg; M; +45 deg; 0 deg)_{sym}, where M designates the matrix layer. The symbol D was used to indicate delamination simulation using the modified Unimod scheme. The strain energy values listed have units of energy.

TABLE 1—Material parameters used in calculating strain energy.

Material Parameter	B/Ep	B/AI
Used in fiber/sheath model		
E_{secant} (matrix) GPa (msi)	...	25.8 (3.75)
E (matrix) GPa (msi)	3.4 (.49)	68.9 (10.0)
E' (fiber) GPa (msi)	400 (58.0)	400 (58.0)
ν (matrix)	0.31	0.33
ν' (fiber)	0.20	0.20
Fiber volume fraction	55 percent	50 percent
a cm (in.)	0.005 (.002)	0.007 (0.0028)
b cm (in.)	0.006 (.0024)	0.009 (0.00351)
$\epsilon_{zz} = \epsilon_{zz}'$	0.006	0.004
σ_f' (fiber) MPa (ksi)	3102 (450)	3102 (450)
σ_{yield} (matrix) MPa (ksi)	...	103 (15)
Used in computer program		
ϵ_{11}	0.006	0.004
0-deg laminate: E_{11} GPa (msi)	186 (27.0)	214 (31.0)
E_{22} GPa (msi)	176 (25.5)	138 (20.0)
E_{33} GPa (msi)	176 (25.5)	138 (20.0)
ν_{12}	0.23	0.25
ν_{13}	0.23	0.27
ν_{23}	0.35	0.27
G_{12} GPa (msi)	6.89 (1.0)	48.2 (7.0)
G_{13} GPa (msi)	6.89 (1.0)	48.2 (7.0)
G_{23} GPa (msi)	6.2 (0.9)	46.8 (6.8)
Matrix layer: $E_{11} = E_{22} = E_{33}$ GPa (msi)	3.4 (.49)	70.3 (10.2)
$\nu_{12} = \nu_{13} = \nu_{23}$	0.31	0.33
$G_{12} = G_{13} = G_{23}$ GPa (msi)	1.3 (.19)	26.5 (3.84)
Debond layer: $E_{11} = E_{22} = E_{33}$ kPa (psi)	6.89 (1.0)	6.89 (1.0)
$\nu_{12} = \nu_{13} = \nu_{23}$	0.31	0.33
$G_{12} = G_{13} = G_{23}$ kPa (psi)	2.63 (0.382)	2.6 (0.376)

TABLE 2—Average stress values and strain energy values calculated using fiber/sheath model.

Parameter	B/Ep	B/AI
Stresses before debonding in Mpa (ksi)		
$\sigma_{\theta\theta}' = \sigma_{rr}'$	-0.41 (-60)	-7.58 (-1100)
σ_{zz}'	2392 (347)	2206 (320)
$\sigma_{\theta\theta}$	4770 (692)	21.4 (3.1)
σ_{rr}	-4770 (-692)	5.1 (0.740)
σ_{zz}	20.5 (2.982)	103.4 (15)
Stresses after debonding in MPa (ksi)		
$\sigma_{\theta\theta}' = \sigma_{rr}'$	0	0
σ_{zz}'	2392 (347)	1599 (232)
$\sigma_{\theta\theta} = \sigma_{rr}$	0	0
σ_{zz}	20.3 (2.940)	103.4 (15)
Strain energy before debonding in Nm/m (in.-#/in.)		
U'	0.058 (0.01311)	0.062 (0.0139)
U	0.148 (0.0333)	0.005 (0.001144)
Strain energy after debonding in Nm/m (in.-#/in.)		
U'	0.058 (0.01311)	0.051 (0.0114)
U	0.00022 (0.00005)	0.0051 (0.001148)

TABLE 3—Computed strain energy values associated with delamination using computer program and composite configuration of (0 deg;M; -45 deg; M; +45 deg; 0 deg)_{sym.}

Configuration	B/Ep	B/Al
<i>U</i> in Nm (in.·lb) for <i>M,M</i> ^a	0.571 (5.0597)	0.577 (5.110)
<i>M,D</i>	0.56 (4.9555)	0.547 (4.8438)
<i>D,M</i>	0.554 (4.8998)	0.562 (4.9750)
<i>D,D</i>	0.544 (4.8153)	0.523 (4.6325)

^a where *M* = matrix in tact, and *D* = delamination at the *M* matrix position.

Using the results of Tables 2 and 3 and equations developed in the previous section (Part C), the strain energy released per newly created fracture area is listed in Table 4. Since the strain energy released when a fiber breaks in a brittle matrix is dependent upon the debond length, the value is expressed in terms of energy/newly created fracture surface/unit debond length. The strain energy released for the case of delamination is expressed in terms of going from state one to state two (that is, *MM* to *MD* or *MD* to *DD*, etc.).

Discussion

The Strain Energy Release-Potential Theory (SERPT), previously postulated, can be summarized as follows: if the probability of occurrence of several damage mechanisms is otherwise the same, then the mechanism most likely to occur first will be the one which has the highest potential for release of stored strain energy. The purpose of this section will be to compare the predictions of this theory, based on the strain energy release values tabulated in Table 4, with observations (made both visually and utilizing scanning electron microscopy) of the damage

TABLE 4—Strain energy released for different damage mechanisms.

Damage Mechanism	<i>G</i> for B/Ep	<i>G</i> for B/Al
	Nm/m ² ($\frac{\text{in.}\cdot\text{lb}}{\text{in.}^2}$)	Nm/m ² ($\frac{\text{in.}\cdot\text{lb}}{\text{in.}^2}$)
Fiber/matrix debonding	463 (2.6445)	24.45 (0.1396)
Delamination: <i>MM</i> to <i>MD</i>	22.7 (0.1296)	58 (0.3312)
<i>MM</i> to <i>DM</i>	34.8 (0.1989)	29.4 (0.1680)
<i>MM</i> to <i>DD</i>	26.6 (0.1520)	52 (0.2970)
<i>MD</i> to <i>DD</i>	30.54 (0.1744)	46 (0.2628)
<i>DM</i> to <i>DD</i>	18.4 (0.1051)	74.6 (0.4260)
Fiber breakage:		
—in terms of debond length	7.2 × 10 ⁸ (d(m)) (1043.9 (d)(in.))	...
—approximation based on Eq 16	...	3803 (21.72)

propagation and the resulting fracture of B/Ep and B/Al composite specimens. Finally, on the basis of these comparisons, a model will be proposed for each composite system.

First, considering B/Ep, the SERPT predicts that, initially, the fiber/matrix will debond. Since fiber breakage is related to the debond length for a given fiber, it is possible to predict the debond length prior to fracture in the following manner. Initially when the debond length is small, the potential strain energy release for fiber fracture is also small (this assumes that there is sufficient stress within the fiber for fracture). But as the debond length increases, the potential strain energy release for fiber fracture increases, while the potential strain energy release for debonding remains constant. Therefore, when the potential strain energy release for fiber fracture exceeds that for debonding, at some critical debond length, the fiber will fracture. This is expressed as

$$G_{\text{fiber}} \left(\frac{\text{in.} \cdot \text{lb}}{\text{in.}^3} \right) \times d_{\text{critical}} (\text{in.}) \geq G_{\text{debond}} \left(\frac{\text{in.} \cdot \text{lb}}{\text{in.}^2} \right). \quad (16)$$

Using a fiber failure stress of 3102 MPa (450 ksi) for B/Ep, the critical debond length is approximately one half of a fiber diameter. This is somewhat low. A typical scanning electron micrograph of a fracture surface such as that shown in Fig. 7 indicates values ranging from one to two fiber diameters. The assumed failure stress of 3102 MPa (450 ksi) is quite high. Since the material is quite notch sensitive, the value is more likely close to 2413 MPa (350 ksi) due to damage during fabrication. Also, the scanning electron microscope observations were of angle-ply composites, subjecting the fiber to a combined stress state, which could have the effect of further lowering the effective failure stress. Accounting for these factors, in calculating the critical debond length, gives a somewhat higher value (1.0 to 1.5 fiber diameters), therefore showing better correlation between theory and observation.

Now examining the strain energy release values for delamination in B/Ep the most probable delamination site would be the outside 0 to 45 deg interface, followed by the ± 45 deg interface. Comparing this with experimental observations (Fig. 8), this is consistently the case. During the fatigue tests, after a significant amount of vertical damage (this appears as an *H* around the hole in the specimen, with the sides of the *H* parallel to the loading direction) has occurred, 0/45 deg delamination usually is noted both above and below the hole. This is evident in Fig. 8 which shows the 0/-45 deg interface to be delaminated the most consistently and severely. It should be pointed out that there is some delamination present between all plies. This is to be expected since, as evidenced by Table 1, there are extremely high stresses in the matrix. Generally, these stresses are higher than the matrix material can withstand. There-

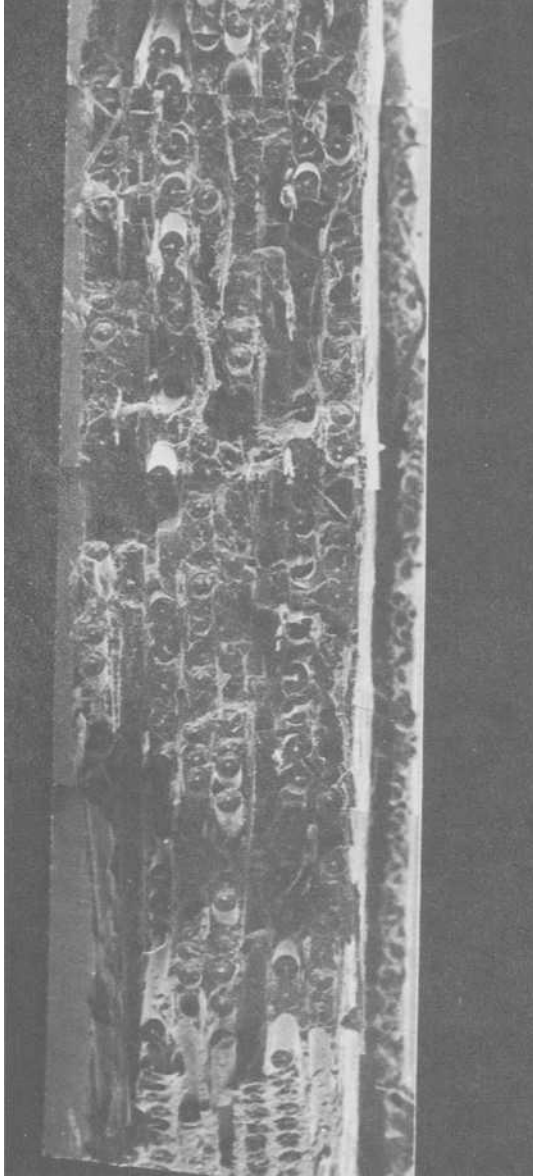


FIG. 7—*B/Ep II static fracture surface.*

fore, there is a substantial amount of intramatrix cracking and crazing. This matrix damage serves to provide initiation sites for future damage, which leads to delamination of all interfaces with the exception of the 0/0 deg case. Also, since the analysis, both closed form and finite element, is elastic and does not account for the presence of damage, the values in Table 4 can be compared to each other only before large amounts of damage have occurred. However, it is postulated that the relative values of the strain energy release may be compared between the cases of debonding and fiber breakage and also between the possible delamination sites. Therefore, for the case of B/E_p , although debonding and fiber breakage may increase the potential for strain energy release due to delamination, the initial preferential ordering may not be altered.

Based on the previous discussion, the failure model for a brittle matrix composite with a high fiber/matrix modulus ratio is as follows. Initially, caused by very high matrix stress, there is much small scale matrix cracking. This cracking initiates fiber/matrix debonding, which grows to a critical length until the fiber fractures. Debonding is then further initiated in the surrounding fibers and proceeds until fiber breakage occurs. These processes tend to increase the potential for strain energy release due to delamination, and delamination would subsequently occur. The ordering, as indicated by the strain energy release values shown in Table 4, would remain the same. The delamination occurs first and is most severe at the 0/-45 deg interface, followed by the ± 45 deg position and then the +45/0 deg position (least severe). Delamination at the 0/0 deg interface is highly unlikely. Caused by large amounts of debonding and delamination, the matrix is degraded severely and in high damage zones (such as around the H pattern) crumbles and "falls out" of the composite system. Finally, the previously mentioned mechanisms propagate and coalesce to cause specimen separation. Examination of fractographs in Figs. 7 and 8 appear to confirm this.

Next we consider B/A_l , a ductile matrix, low fiber/matrix modulus ratio composite. For this material the damage mode preference and the mechanisms of damage propagation are quite different from B/E_p . Due to the extremely low potential for strain energy release due to debonding, especially as compared to B/E_p , debonding is predicted to be highly unlikely. This is the case, as shown in Fig. 9 which shows no presence of fiber/matrix debonding. Also, once there is significant plastic deformation of the matrix material and a sufficient stress concentration develops to cause fiber stresses to rise near the critical value, fiber breakage is very likely due to the high value of potential strain energy release. It should be noted that the value listed in Table 2 is somewhat high because of several approximations made in its calculation, but it is quite apparent that it should be, by far, the most probable initial damage mechanism.

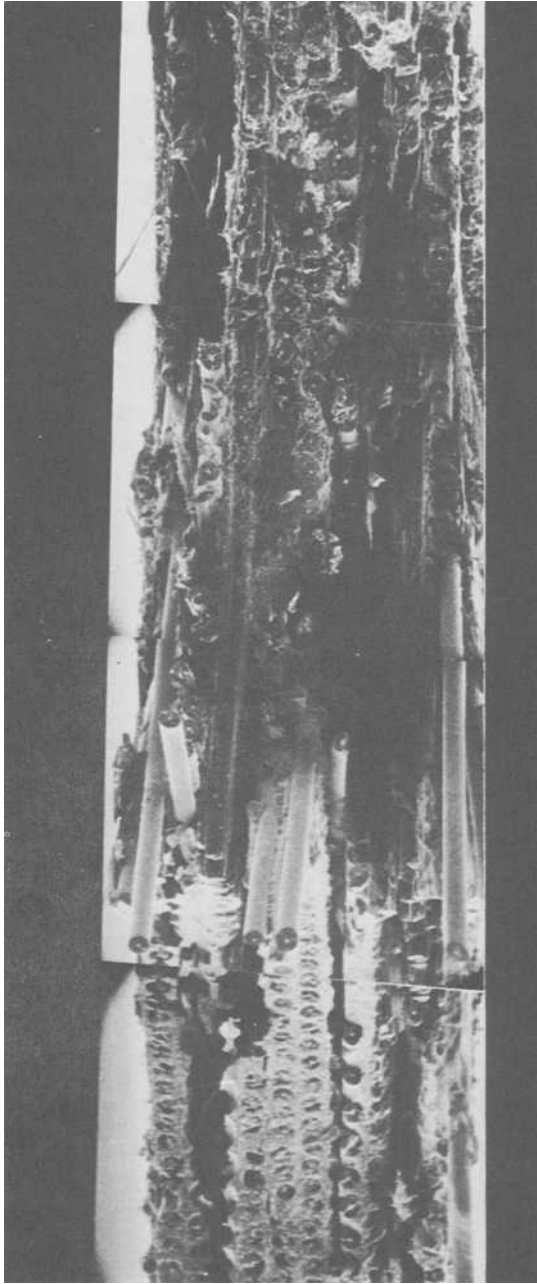


FIG. 8—B/Ep II 30 Hz fatigue fracture surface.

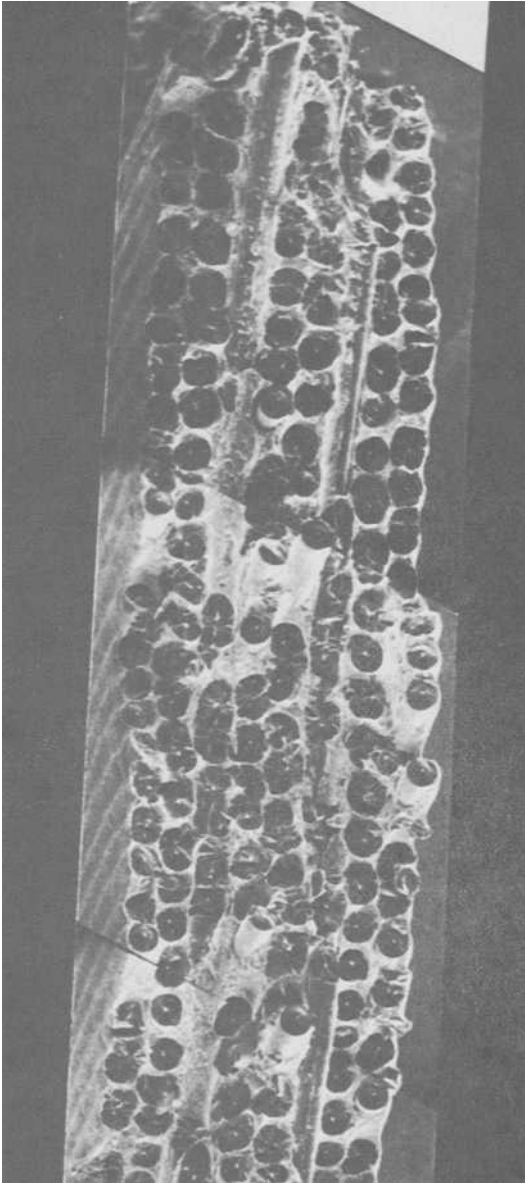


FIG. 9—B/A1 Ib static fracture surface.

Delamination should occur in a different sequence for B/AI than B/Ep. As shown in Table 4; the ± 45 deg site is the most probable, with the 0/-45 deg site a poor second. And again, as in the previous cases, experimental observation and scanning electron microscopy (Fig. 10) show this to be the case. All interfaces, with the exception of the 0/0 deg and sometimes the +45/0 deg sites, show some delamination, but the ± 45 deg site is found to be the most severe.

Now in constructing a possible failure model for B/AI, a necessary consideration is what causes the initial stress concentration sufficient to induce close-to-failure level stresses in the fiber. Scanning electron microscopy has revealed the presence of line-voids (separations of the aluminum/aluminum diffusion bond between the fibers). When the matrix is deformed plastically, there is some opening of these line-voids, causing a stress riser that quite possibly initiates fiber breakage. This would further increase stress concentrations in surrounding fibers, which then continue to fracture. These fiber fractures, then, increase the potential strain energy release for delamination, and delamination takes place controlled by the maximum potential for strain energy release. These damage mechanisms then coalesce and form an irregular fracture surface that is nonuniform in direction and in its plane of propagation, causing failure.

Conclusions

As evidenced by the previous sections, there is substantial agreement between the Strain Energy Release-Potential Theory (SERPT) and experimental findings. In summary, several conclusions are drawn.

1. An explanation of situations wherein the fiber or the matrix controls composite material damage development can be put forth. For the case where there is substantial (elastic) property mismatch, as indicated by a high modulus ratio, there is higher tendency for the fiber and matrix to separate. This leads to debonding and eventual matrix degradation, which causes failure; this may be characterized as matrix-controlled damage development. When the modulus ratio is low, this tendency for separation is less and debonding is much less likely to occur. In that case, fiber breakage is much more likely, initiating and dominating failure; this may be characterized as fiber-controlled damage development. An important conclusion is, then, that the fiber/matrix modulus ratio plays a substantial role in composite material fatigue response.

2. Using the Strain Energy Release-Potential Theory, debond probability and length can be predicted. Also, the most probable delamination sites can be determined. The initial inter-relationship between the occurrence of different damage mechanisms can be explained in terms of relative probabilities of occurrence based on relative potential for strain energy release.

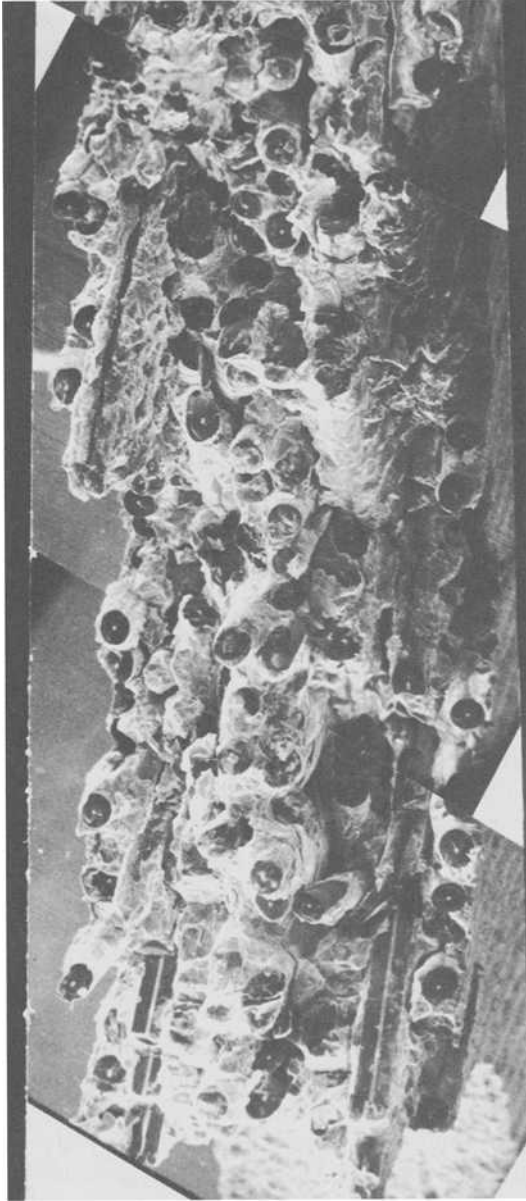


FIG. 10—*B/Al 1b 15 Hz fatigue fracture surface.*

By addition of the probability of occurrence (not including the previously discussed energy considerations) to the Strain Energy Release-Potential Theory, it would be possible to provide the foundation for a theoretical estimation of a critical strain energy release rate for a composite material system. This possibility provides a basis for future work.

Acknowledgments

The authors wish to acknowledge the support of the Air Force Office of Scientific Research under contract number AFOSR-72-2358 monitored by W. Walker.

Our thanks, also, to P. Schmidt for typing the manuscript.

References

- [1] Beaumont, P. R. and Tetelman, A. S., "The Fracture Strength and Toughness of Fibrous Composites," UCLA-ENG-7269, Livermore, Calif., Aug. 1972.
- [2] Konish, H. T., Cruse, T. A., and Swedlow, J. L. in *Analysis of the Test Methods for High Modulus Fibers and Composites*, ASTM STP 521, American Society for Testing and Materials, 1973, pp. 133-142.
- [3] Zweben, C., *Analysis of the Test Methods for High Modulus Fibers and Composites*, ASTM STP 521, American Society for Testing and Materials, 1973, pp. 65-97.
- [4] Waddoups, M. E., Eisenmann, J. R., and Kaminski, B. E., *Journal of Composite Materials*, Vol. 5, Oct. 1971, pp. 102-117.
- [5] Mandell, J. F. and Meier, U., "Fatigue Crack Propagation in 0°/90° E-Glass/Epoxy Composites," presented at the ASTM Fall Symposium, Bal Harbor, Fla., Dec. 1973.
- [6] Williams, R. A., Reifsnider, K. L., Stinchcomb, W. W., and Turgay, H. T., "The Effect of Frequency on the Fatigue Damage of Boron/Aluminum Fiber Reinforced Composite Materials," Contract No. AFOSR-72-2358, AFOSR Technical Report, Oct. 1974.
- [7] Williams, R. S., Reifsnider, K. L., Stinchcomb, W. W., and Turgay, H. T., "The Effect of Frequency and Strain Amplitude on the Fatigue Damage of Boron/Epoxy Fiber Reinforced Composite Materials," Contract No. AFOSR-72-2358, AFOSR Technical Report, Oct. 1974.
- [8] Corten, H. T., "Fracture Mechanics of Composites," *Fracture*, Vol. 7, Academic Press Inc., N. Y., 1972.
- [9] Orowan, E., *Welding Research Supplement*, March 1955, pp. 157S-160S.
- [10] Irwin, G. R. and Kies, J. A., *Welding Research Supplement*, April 1954, pp. 193S-198S.
- [11] Sih, G. C., "Introductory Chapter: A Special Theory of Crack Propagation," *Mechanics of Fracture I*, G. C. Sih Ed., Noordhoff International Press, Leyden, 1973, pp. XII-XLV.
- [12] Grossman, L. M., *Thermodynamics and Statistical Mechanics*, McGraw-Hill, New York, 1969.
- [13] Ebert, L. J. and Gadd, J. D., "A Mathematical Model for the Mechanical Behavior of Interfaces in Composite Materials," *Fiber Composite Materials*, American Society for Metals, 1964.
- [14] Dana, J. R., "Three Dimensional Finite Element Analysis of Thick Laminated Composites—Including Interlaminar and Boundary Effects Near Circular Holes," Ph.D. dissertation, Department of Engineering Science and Mechanics, Virginia Polytechnic Institute and State University, Blacksburg, Va., 1973.
- [15] Barker, R. M., Dana, J. R., and Pryor, C. W., "Three Dimensional Analysis of Stress Concentrations Near Holes in Laminated Composites," Technical Report No. VPI-E-72-27, Virginia Polytechnic Institute and State University, Blacksburg, Va., Dec. 1972.

- [16] Dana, J. R. and Barker, R. M., "Three Dimensional Finite Element Program: User's Guide," Technical Report No. VPI-E-74-19, Virginia Polytechnic Institute and State University, Blacksburg, Va., Aug. 1974.
- [17] Nair, P. and Reifsnider, K. L., *Fracture Analysis*, ASTM STP 560, American Society for Testing and Materials, 1974, pp. 211-225.
- [18] Olster, E. F. and Jones, R. C., *Composite Materials: Testing and Design (Second Conference)*, ASTM STP 497, American Society for Testing and Materials, 1972, pp. 189-205.
- [19] Barker, R. M. and MacLaughlin, T. P., *Journal of Composite Materials*, Vol. 5, Oct. 1971, pp. 282-291.
- [20] Iremonger, M. J. and Wood, W. G., *Journal of Strain Analysis*, Vol. 2, No. 3, 1967, pp. 81-89.
- [21] Iremonger, M. J. and Wood, W. G., *Journal of Strain Analysis*, Vol. 5, No. 3, 1970, pp. 88-96.

S. S. Wang¹

An Analysis of Tapered Double-Cantilever-Beam Fracture Toughness Test for Adhesive Joints

REFERENCE: Wang, S. S., "An Analysis of Tapered Double-Cantilever-Beam Fracture Toughness Test for Adhesive Joints," *Fracture Mechanics, ASTM STP 677*, C. W. Smith, Ed., American Society for Testing and Materials, 1979, pp. 651-667.

ABSTRACT: This paper presents an analytical study of the tapered double-cantilever-beam (DCB) fracture mechanics test of polymeric adhesives and joints. The test specimen consists of high modulus metal adherends bonded together by a thin layer, low modulus adhesive. The fracture of the joint is modeled by the growth of a cohesive crack in the adhesive bond. The analysis employs an advanced hybrid-stress finite element method based on the formulation of Muskhelishvili's complex stress functions through a modified complementary energy principle. Numerically exact solutions are obtained for the joints with various geometries and material parameters. The crack-tip stress field, the associated stress intensity factor, and the energy release rate are determined quantitatively for each case. Characteristics of the specimen response and fundamental differences in the crack-tip behavior between a monolithic material and the joint are revealed. Effects of the adherend/adhesive modulus ratio, adhesive layer thickness, specimen geometry, and crack length on the tests are studied. Approximations involved in test results due to the specimen design by a simple beam theory are determined also.

KEY WORDS: adhesive, adherend, joints, tapered DCB specimen, fracture mechanics, hybrid-stress finite element method, crack-tip stress field, stress intensity factor, energy release rate, crack propagation, fatigue (materials).

Flaw resistance is of great importance in the design and analysis of adhesive joints, since it is directly responsible for the reliability and integrity of adhesively bonded structures, which are used increasingly in many advanced engineering applications such as aircraft constructions. Fracture mechanics tests are employed currently to evaluate the flaw

¹ Assistant professor, Department of Theoretical and Applied Mechanics, University of Illinois, Urbana, Ill. 61801.

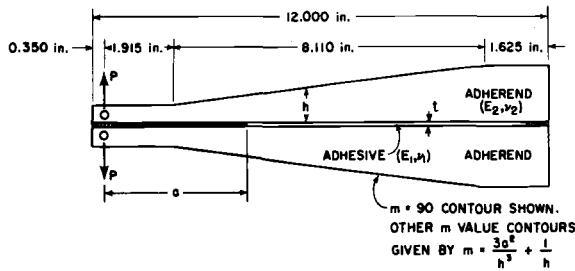


FIG. 1—Tapered DCB specimen.

tolerance of the polymeric adhesives and joints. These tests, which have been used to determine fracture toughness of monolithic materials, employ a tapered double cantilever beam (TDCB) specimen consisting of contoured metal adherends bonded together by a thin layer adhesive (Fig. 1). A cohesive crack is introduced in the low modulus adhesive layer of the joint as shown in Fig. 2, and the associated energy release rate is evaluated in the fracture test. The shape of the adherend is designed by a simple one-dimensional beam theory to give an approximately linear compliance [1-3]² during the course of crack growth. It has been shown [4-6] that deformation and fracture are extremely localized within the thin adhesive layer, which the simple beam approximation fails to consider. Thus, the direct application of this test to study the adhesive joint fracture has been of great concern, since the fracture behavior of the joint may be different from a monolithic case.

This problem is very complicated in nature and involves many difficulties such as the inherent crack-tip singular behavior, the modeling of the vanishingly thin, but critically important, adhesive layer, the compatibility of the multiphase material system, and the complex geometry of the adhesive joint. Furthermore, large differences in moduli and in linear dimensions between the adherend and the adhesive may cause serious rounding errors in computational schemes. The very localized nature of the embedded crack-tip singularity and of the adhesive bond was shown to introduce the adhesive layer thickness as a characteristic dimension [4,6] in this problem. Thus it is unwise to make any simplifications which fail to consider the existence and the general behavior of the thin adhesive layer.

This paper presents a rigorous study on the fracture mechanics test of the tapered DCB adhesive joints in which the adhesive layer is fully taken into account as a two-dimensional continuum. The current approach, based on an advanced hybrid-stress finite element method, has the capacity to overcome these complexities and difficulties. It gives rapid

² The italic numbers in brackets refer to the list of references appended to this paper.

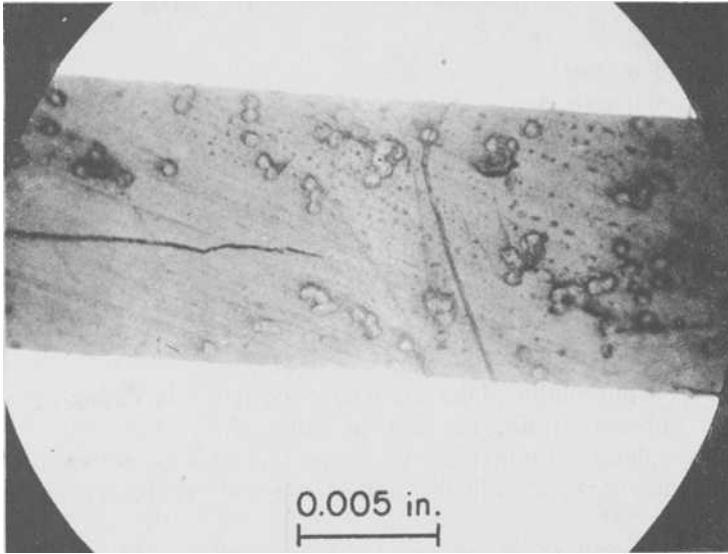


FIG. 2—Sharp cohesive crack in 0.0254 cm (0.010 in.) thick adhesive with carrier cloth, tapered DCB specimen, $m = 35.43 \text{ cm}^{-1}$ (90 in.^{-1}).

rates of convergence of solutions and enables an accurate description of the high stress gradient in the thin adhesive layer. More importantly, the singularity and higher order terms of the crack-tip stress field can be incorporated conveniently into the formulation, leading to a capability of solving the adhesive joint fracture problem with complexities in geometries, material parameters, and loading conditions.

Fracture Mechanics Test of TDCB Adhesive Joint

The stress distribution in the vicinity of a sharp crack in an elastic monolithic material has been available for many years [7,8]. In general, stresses near the crack tip in an infinite sheet under opening-mode loading take the form

$$\sigma_{ij} = \frac{K_I}{\sqrt{2\pi r}} f_{ij}(\theta) + O(\sqrt{r}) \quad (1)$$

where r and θ are polar coordinates with their origin at the crack tip. The stress intensity factor K_I is defined as

$$K_I = \sigma_\infty Y \sqrt{a} \quad (2)$$

where

- σ_∞ = applied stress,
- a = crack length, and
- Y = a function of the specimen geometry.

Values of Y for a wide range of geometries have been obtained by various analytical and experimental methods [9]. The associated strain energy release rate, \mathcal{G}_I , is related to K_I by

$$\mathcal{G}_I = \frac{K_I^2}{E} (1 - \nu^2) \quad (3)$$

for isotropic, monolithic plane strain cases, where E is Young's modulus, and ν is Poisson's ratio. The critical value of K_I or \mathcal{G}_I , denoting the fracture toughness of a material by K_{Ic} or \mathcal{G}_{Ic} , may be determined if the proper value of Y is available and if the test meets certain validity requirements [9].

The direct applicability of Eqs 1-3 to multiphase adhesive joints has been assumed and used to measure the \mathcal{G}_c [10-13], but these fundamental relationships and the validity of using this toughness testing technique for the fracture design of the joints have not been fully addressed. It is not quite clear as to what extent the crack-tip field follows the classical fracture mechanics requirements and whether the \mathcal{G} - K relationship in Eq 3 is implied in the adhesive joint fracture. While an exact analysis of the fracture of the adhesive joints is absent at the present time, efforts toward understanding the fundamental behavior of this kind of fracture problem have led to the establishment of some useful analytical expressions for the commonly used specimens. The earliest and most widely employed analysis for the DCB specimen was based on a simple one-dimensional monolithic beam theory [1,2]. Solutions for the monolithic beams have been assumed to hold for general cases, and \mathcal{G}_I for the test is related to the specimen compliance λ by

$$\mathcal{G}_I = \frac{P^2}{2} \frac{\partial \lambda}{\partial a} \quad (4)$$

where P is the applied force. Assuming that each crack flank behaves as a cantilever beam and that the compliance is not affected significantly by the presence of the thin adhesive, \mathcal{G}_I may be approximated by

$$\mathcal{G}_I = \frac{4P^2}{E_2} \left[\frac{3a^2}{h^3} + \frac{1}{h} \right] \quad (5)$$

where E_2 is the adherend modulus, and h , the height of the beam.

This relationship is employed in the design of the approximately linear compliance test specimen. To construct a specimen in which the crack would propagate at a constant load, the shape of the adherend (variation of h with a) is designed so that $\partial\lambda/\partial a$ has a constant value, that is

$$m = \frac{3a^2}{h^3} + \frac{1}{h} = \text{constant} \tag{6}$$

where m is called the shape factor and has a dimension of cm^{-1} (inch^{-1}). Within the accuracy of the simple beam theory used to derive Eq 5, such a specimen should display a constant crack propagation force, P , regardless of the crack length. Thus the crack length does not need to be measured during the test. The specimen with a specific m of 35.43 cm^{-1} (90 in^{-1}) pictured in Fig. 1 has been proposed as a standard fracture test of adhesives and adhesive joints (ASTM Recommended Practice for Fracture Strength in Cleavage of Adhesives in Bonded Joints (D 3433 – 75)). Substituting Eq 6 into Eq 5 gives \mathcal{G}_I for the TDCB specimen as

$$\mathcal{G}_I = \frac{P^2}{2} \frac{8}{E_2} m \tag{7}$$

The associated value of K_I may be determined from Eq 3 whose validity in the adhesive joint fracture has been proved in Ref 6, giving

$$K_I = 2P \left[\frac{m}{1 - \nu^2} \right]^{1/2} \left[\frac{E_2}{E_1} \right]^{-1/2} \tag{8}$$

It is clear that the knowledge of an accurate near field behavior, including the fundamental nature of the crack-tip singular response, is essential to provide a better understanding of the complex problem. A meaningful assessment of the application of the monolithic fracture mechanics test to the adhesive fracture problem requires a sound theoretical foundation as do similar studies of monolithic materials.

Method of Analysis

The hybrid-stress finite element method, pioneered by Pian [14], is considered particularly suitable for studying the current plane crack problem by the introduction of a crack-tip superelement, in which the stress singularity is properly considered by an appropriately incorporated stress field. The stress hybrid model for crack problems was first introduced by Pian et al [15] and later refined by Tong et al [16] using the complex variable formulation of the Muskhelishvili's stress functions. Formulations for the crack-tip element and its surrounding hybrid ele-

ments have been described in detail elsewhere [6,16]. The advantages and superiority of using this method for studying fracture problems of adhesives and adhesive joints were discussed in Refs 6, 17, and 18. Only a brief outline is given in this section.

Crack-Tip Superelement Formulation

The conventional displacement model and nonsingular hybrid element approach have great difficulty in handling crack problems even in a monolithic material, since the use of high order polynomials as interpolation functions does not improve the rate of solution convergence. The reason for this is that the convergence rate of the numerical solution is controlled by the singular nature of the crack-tip region [19]. However, the advanced hybrid element formulation permits a proper incorporation of the stress singularity and higher order terms, which leads to more accurate results with very rapid rates of solution convergence.

Considering a plane elasticity problem with a prescribed boundary traction \bar{T}_i over the boundary s_σ and a prescribed displacement \bar{u}_i over the boundary s_u , the functional π_m to be varied in the minimization procedure is

$$\pi_m = \int_{\partial A_m} (\bar{u}_i - u_i) T_i ds - \int_{(s_\sigma)_m} \bar{u}_i \bar{T}_i ds + \frac{1}{2} \iint_{A_m} [\sigma_{ij}(u_{i,j} + u_{j,i}) - S_{ijkl} \sigma_{ij} \sigma_{kl}] dA \quad (9)$$

where u_i and T_i are the displacement and traction over an element boundary ∂A_m , and u_i , σ_{ij} , and S_{ijkl} are the displacement vector, the stress compliance tensors within an element A_m . In this superelement formulation, the stress and displacement fields within A_m and the boundary displacements along ∂A_m are assumed independently [6,16]. All Euler equations in the theory of elasticity are satisfied.

Following Muskhelishvili's formulation [20], the stress and displacement fields can be expressed in terms of two stress functions $\phi(z)$ and $\psi(z)$ of a complex variable z as

$$\sigma_{yy} + \sigma_{xx} = 2 [\phi'(z) + \overline{\phi'(z)}] \quad (10a)$$

$$\sigma_{yy} - \sigma_{xx} + 2i \sigma_{xy} = 2 [\bar{z} \phi''(z) + \psi'(z)] \quad (10b)$$

and

$$2\mu(u + iv) = \eta \phi(z) - z \overline{\phi'(z)} - \overline{\psi(z)} \quad (10c)$$

in which μ is the shear modulus, η is equal to $3 - 4\nu$ for plane strain or $(3 - 4\nu)/(1 + \nu)$ for plane stress condition, and ν is Poisson's ratio. The traction-free boundary condition along crack surfaces may be established as

$$i \int_{s_m} (T_x + iT_y) ds = \phi(z) + z \overline{\phi'(z)} + \psi(z) = 0 \tag{11}$$

Introducing a mapping function $z = w(\zeta) = \zeta^2$ with $-\pi/2 \leq \arg \zeta \leq \pi/2$, $\psi(\zeta)$ may be related to $\phi(\zeta)$ by Eq 11 as

$$\psi(\zeta) = -\overline{\phi(-\bar{\zeta})} - \overline{w(-\bar{\zeta})} \frac{\phi'(\zeta)}{w'(\zeta)} \tag{12}$$

In constructing the crack element stiffness matrix, $\phi(\zeta)$ is assumed to have the form

$$\phi(\zeta) = \sum_{j=1}^N b_j \zeta^j \tag{13}$$

Thus, we may have

$$\psi(\zeta) = -\sum_{j=1}^N \left[\bar{b}_j (-1)^j + \frac{j}{2} b_j \right] \zeta^j \tag{14}$$

with $b_j = \beta_j + i \beta_{N+j}$ and β_s being real constants.

Using the stresses and the displacements derived from the functions $\phi(\zeta)$ and $\psi(\zeta)$, the boundary traction \underline{T} and the interior displacement \underline{u} in A_m may be expressed in terms of β_s by

$$\underline{T} = \underline{R} \underline{\beta} \tag{15a}$$

$$\underline{u} = \underline{U} \underline{\beta} \tag{15b}$$

The boundary displacement $\tilde{\underline{u}}$ may be interpolated by nodal displacements \underline{q} as

$$\tilde{\underline{u}} = \underline{L} \underline{q} \tag{16}$$

where \underline{L} is an interpolation function.

Substituting Eqs 15 and 16 into Eq 9 and taking variations of the

functional π_m with respect to $\underline{\beta}$, the stiffness matrix \underline{k}_m of the crack element may be obtained as

$$\underline{k}_m = \underline{G}^T \underline{H}^{-1} \underline{G} \quad (17)$$

where

$$\underline{H} = \frac{1}{2} \int_{\partial A_m} (\underline{U}^T \underline{R} + \underline{R}^T \underline{U}) ds \quad (18a)$$

$$\underline{G} = \frac{1}{2} \int_{\partial A_m} \underline{R}^T \underline{L} ds \quad (18b)$$

Regular Hybrid Element

The complementary energy functional to be varied for the surrounding nonsingular elements is given by [14]

$$\pi_r = \iint_{A_r} \frac{1}{2} \underline{\sigma}^T \underline{S} \underline{\sigma} dA - \int_{(s_u)_r} \underline{\bar{u}}^T \underline{T} ds \quad (19)$$

Along the boundary of an element, the displacement vector $\underline{\bar{u}}$ is expressed in terms of nodal displacements \underline{q} by

$$\underline{\bar{u}} = \underline{L} \underline{q} \quad (20)$$

The stresses in the interior of the element are expressed by the stress parameters $\underline{\beta}$ as

$$\underline{\sigma} = \underline{P} \underline{\beta} \quad (21)$$

where \underline{P} is chosen to satisfy the homogeneous equilibrium equations. Substituting Eqs 20 and 21 into Eq 19 and minimizing the functional π_r with respect to $\underline{\beta}$ s, the element stiffness matrix \underline{k}_r can be obtained as

$$\underline{k}_r = \underline{G}^T \underline{H}^{-1} \underline{G} \quad (22)$$

where

$$\underline{H} = \iint_{A_r} \underline{P}^T \underline{S} \underline{P} dA \quad (23a)$$

$$\underline{G} = \int_{s_r} \underline{R}^T \underline{L} ds \quad (23b)$$

Solutions of the Problem

The assembled linear equations for the whole system may be written as

$$\underline{K}q = \underline{Q} \quad (24)$$

where \underline{K} is the global stiffness matrix, and \underline{Q} , the consistent loading vector.

After solving q from Eq 24 by an appropriate solution scheme, the stress field and $\underline{\beta}$ can be determined. Stress intensity factors K_I and K_{II} corresponding to an applied stress level and a crack length may be found from the following relationships

$$K_I = \sqrt{2\pi} \beta_1$$

and (25)

$$K_{II} = \sqrt{2\pi} \beta_{n+1}$$

The associated elastic energy release rates, \underline{G}_I and \underline{G}_{II} , can be obtained accurately by a standard numerical method.

Solution Convergence and Accuracy

The accuracy and convergence assessments of solutions are complicated by several unusual features of the problem and of the method of analysis due to the singular nature of the crack and the vanishingly small dimension of the adhesive layer. A study of the accuracy and convergence of the analysis and solution stability was conducted by testing cases for which independent solutions are available. Details of the study were reported elsewhere [6] and are not repeated here. Excellent agreements with existing closed-form solutions were observed. The results indicated that accuracy within approximately 1 percent of the converged solutions of K 's and \underline{G} 's can be obtained for the optimum mesh arrangements used in the current study.

Results and Discussion

The cohesive crack observed in Fig. 2 was assumed to be at the center of the adhesive layer for simplicity without losing generality. Thus, only a half of the specimen needs to be considered in the analysis due to symmetry. The TDCB test specimen for studying adhesive joint fracture was modeled by an optimum mesh configuration, as shown in Fig. 3. The adherend/adhesive modulus ratio, E_2/E_1 , was chosen within a broad range of three decades. An E_2/E_1 of approximately 20 is typical for

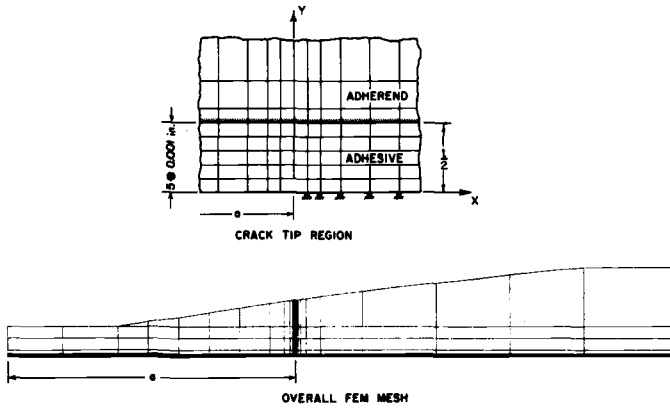


FIG. 3—FEM mesh for tapered DCB specimen, $m = 35.43 \text{ cm}^{-1}$ (90 in.^{-1}), $a = 12.7 \text{ cm}$ (5.0 in.), $t = 0.0254 \text{ cm}$ (0.010 in.).

structural aluminum joined by an epoxy adhesive. The shape factor, m , was considered to have values varying from 4 to 1000 (in.^{-1}) in this study.

Crack-Tip Stress Field

The crack-tip stress field and its associated stress intensity factor, which characterize the adhesive joint fracture behavior, were determined for the cases of various modulus ratios and adhesive thicknesses. Figure 4 gives the distributions of the most dominant stress, σ_{yy} , ahead of the crack tip. The stress distributions shown in the figure follow a classical fracture mechanics solution, that is, a $1/\sqrt{r}$ singularity, in the near field. The monolithic fracture case (that is, $E_2/E_1 = 1$) approximates the singular behavior farther from the crack tip. This reveals the more localized nature of the singularity in brittle adhesive joint systems as compared to monolithic materials. The result also indicates that stresses in the adhesive level off quickly away from the crack-tip region and reach a uniform distribution in the far field. This is especially true for the cases of larger E_2/E_1 ratios. At a greater distance of x beyond 0.25 cm (0.1 in.) not shown in the figure, the stresses rapidly decrease and become compressive; details of this are given in Refs 6 and 17. While this result was calculated for the TDCB specimen with a crack length of 7.62 cm (3.0 in.) and a shape factor of 35.43 cm^{-1} (90 in.^{-1}), it gives common features of opening mode adhesive joint fracture in the specimens of different m s and a s. Changing the adherend shape or the crack length only alters the intensity of the crack-tip stresses, but not the essential character of the near field. Effects of the specimen configuration and the crack length on the crack tip response will be discussed later.

The localized singular crack-tip domain embedded in the adhesive layer

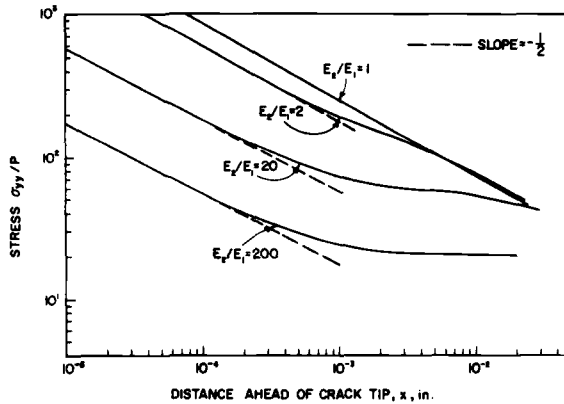


FIG. 4—Effect of elastic modulus ratio on σ_{yy} ahead of crack tip, TDCB specimen, $m = 35.43 \text{ cm}^{-1}$ (90 in.^{-1}), $a = 7.62 \text{ cm}$ (3.0 in.), $t = 0.0254 \text{ cm}$ (0.010 in.).

provides basic insight into the application of the classical (monolithic) fracture mechanics concept to the adhesive joint fracture problem. The use of fracture mechanics tests to evaluate the fracture toughness and failure behavior of adhesive joints can be justified easily for cases with small scale crack-tip yielding so that the plastic zone is contained well within the singular domain; thus, the elastic crack-tip field is not disturbed significantly. Based on the result in Fig. 4 and the arguments in Ref 6, it appears that the allowable yield zone size for the appropriate use of the fracture mechanics test may be smaller in a typical adhesive joint system than that in a monolithic material. For the adhesive joints in which gross yielding is developed over the entire bond line, fracture energy release rates may be measured, but brittle fracture involving flaw criticality may not occur in many cases [4,6,21].

Effects of Modulus Ratio and Adhesive Thickness

The modulus ratio of the adherend to the adhesive is an important factor affecting the failure behavior of the joint. Figure 5 gives the values of K_I as a function of E_2/E_1 for the adhesive joints with various m s, indicating a linear relationship over a broad range of three decades on the log-log plot. Although an approximately constant \mathcal{G}_I may be obtained from the tests using different adhesives, K_I varies with the modulus ratio by an inverse power law relationship of $1/2$. This implies that significant differences in local deformation and fracture may occur within the bond line when different adhesives are used.

Effects of the adhesive layer thickness on the fracture of the joints are examined also. In the TDCB fracture specimens with adhesive thicknesses ranging from 0.0127 to 0.0635 cm. (5 to 25 mils), a constant crack-tip

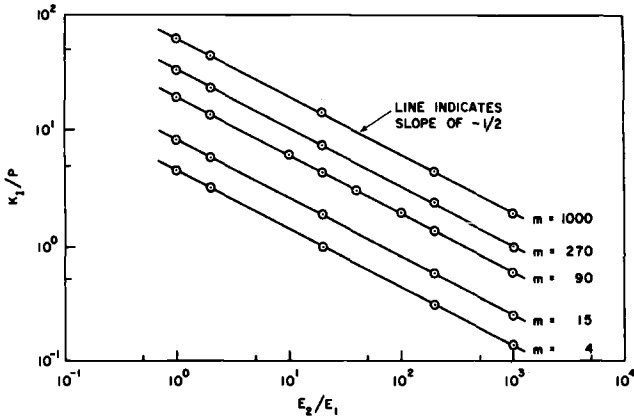


FIG. 5— K_I versus E_2/E_1 for TDCB specimens, various m 's, $a = 7.62$ cm (3.0 in.), $t = 0.0254$ cm (10 mils).

stress intensity factor, K_I , is obtained for a given m and a , as shown in Fig. 6. Therefore, the near field stresses are identical as a result of the very localized and embedded singular stress domain. It should be mentioned that the constraint on resin deformation by high modulus adherends may vary with different adhesive layer thicknesses, which could introduce distinct yield zone sizes within the bond line if a ductile adhesive is employed. This phenomenon has been observed in the experiments by Bascom et al [4].

Beam Approximation in TDCB Specimen Design

One of the characteristics of the TDCB adhesive joint is the linear compliance of the specimen determined from the simple one-dimensional beam theory as previously mentioned. In reality, the specimen may behave very differently from a simple one-dimensional beam, especially in the cases of small m values. Thus, it is worthwhile to assess the approximation involved using the current accurate analysis so that a more precise K -calibration for the test specimen may be established. A parameter α , denoting the ratio of the Q_I obtained from the beam theory to that from the singular finite element method, is used for this purpose.

$$\alpha = \frac{(Q_I)_{\text{beam}}}{(Q_I)_{\text{FEM}}} \quad (26)$$

Using Eqs 3 and 7, it yields

$$\alpha = \frac{4P^2m}{(1-v^2)} \frac{1}{(K_I^2)_{\text{FEM}}} \left(\frac{E_2}{E_1} \right)^{-1} \quad (27)$$

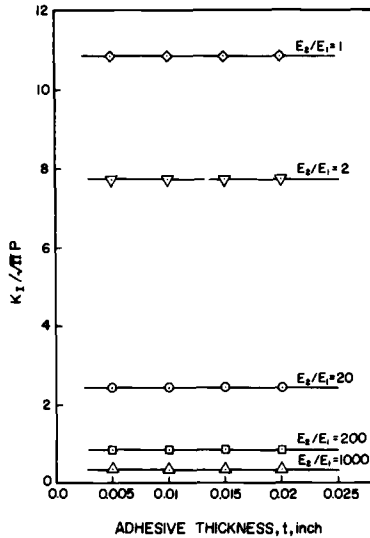


FIG. 6—Effect of adhesive thickness on stress intensity factor for tapered DCB specimen ($m = 35.43 \text{ cm}^{-1}$ (90 in.⁻¹), $a = 7.62 \text{ cm}$ (3 in.)).

In general, α may be a function of E_2/E_1 , m , and a . However, solutions obtained from the current analysis indicate that α is insensitive to the modulus ratio, and Fig. 7 confirms this. Thus, the approximation introduced by the simple beam theory is not in any way attributable to the adhesive layer, but is due to the geometric simplification, as is the case for the monolithic material.

Figure 8 indicates that α is indeed a function of both m and a . The value of α may range from 0.64 to 1.11 for the various geometry parameters

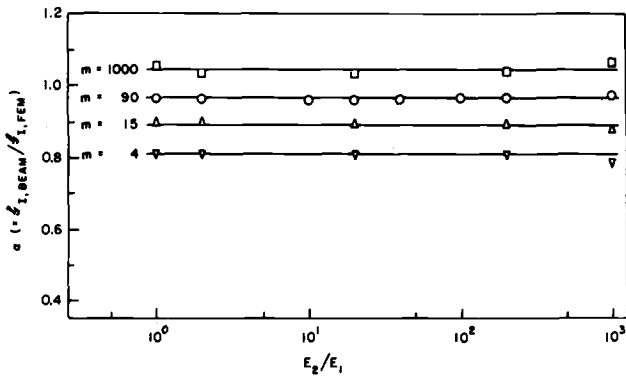


FIG. 7— α versus E_2/E_1 for various m 's in TDCB specimens, $a = 7.62 \text{ cm}$ (3.0 in.), $t = 0.0254 \text{ cm}$ (10 mils).

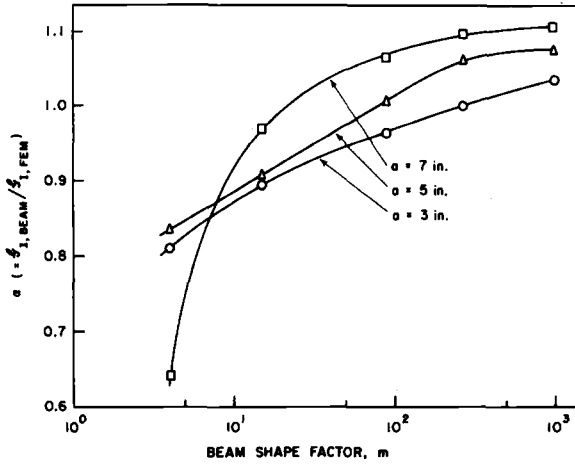


FIG. 8— α versus m , TDCB specimen, various a 's, $E_2/E_1 = 20$, $t = 0.0254$ cm (10 mils).

studied. For the specific case of $m = 35.43 \text{ cm}^{-1}$ (90 in^{-1}) shown in Fig. 9, α varies approximately from 0.95 to 1.06, depending upon the crack length. The corresponding value of K_I , predicted by the beam theory to be constant with crack length variation, actually decreases by 5 to 6 percent as the crack extends, as shown in Fig. 10. These results are in general agreement with the experimental data reported in Ref 10, which suggested a value of α in the range of 1.0 for $m = 35.43 \text{ cm}^{-1}$ (90 in^{-1}) and 0.73 for $m = 1.575 \text{ cm}^{-1}$ (4 in^{-1}). It is expected that carefully conducted compliance calibrations would yield a similar variation of α with a to that given in Figs. 8–10, but such data are not presently available.

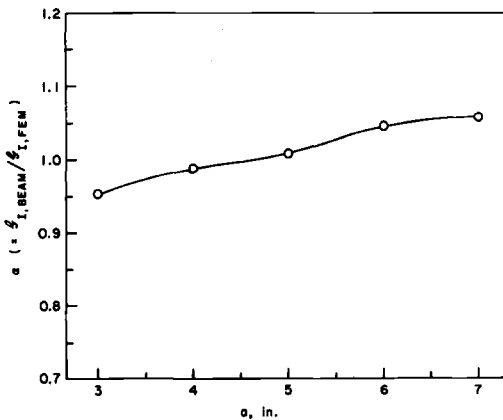


FIG. 9— α versus crack length for $m = 35.43 \text{ cm}^{-1}$ (90 in^{-1}), $E_2/E_1 = 20$, $t = 0.0254$ cm (10 mils).

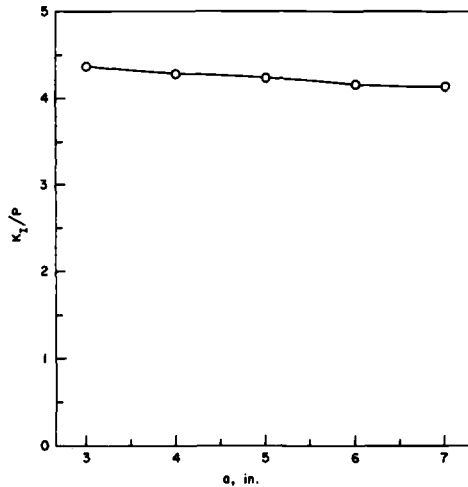


FIG. 10— K_I versus crack length for $m = 35.43 \text{ cm}^{-1}$ (90 in.^{-1}), $E_2/E_1 = 20$, $t = 0.0254 \text{ cm}$ (10 mils).

The results in this section suggest that the values of \mathcal{G}_I predicted by the beam theory are approximations which may contain systematic errors related to the specimen geometry. The advanced hybrid-stress FEM provides a very accurate calibration for the test specimen, which could be used to determine \mathcal{G}_I and K_I . These approximations may result, at least, from the following reasons:

1. The specimen shape does not correspond to m for the first 5 cm. (2 in.) of the crack, but follows a DCB shape instead.
2. Beam theory is one-dimensional and cannot examine accurately the specimen with a complex geometry, particularly the cases with lower m 's.

This situation is common in any simple approximation used for calibration of a fracture specimen. It is fortunate that the case of greatest interest, that is, $m = 35.43 \text{ cm.}^{-1}$ (90 in.^{-1}), involves the least amount of error based on the simple beam approximation.

Summary and Conclusions

A study on the fracture mechanics test of polymeric adhesives and joints using a tapered DCB specimen has been conducted. An advanced singular hybrid-stress finite element method has been successfully developed to analyze the adhesive joint fracture. The local crack-tip stress field, the associated stress intensity factor and the energy release rate were determined precisely for the joints with various adherend/adhesive modulus ratios and shape factors. Characteristics of the specimen response and fundamental differences in the crack-tip behavior between a

monolithic material and an adhesive joint were revealed. The localized singular domain in the adhesive layer coupled with the predicted large plastic yield zone size provides unique features of the joint fracture behavior and the application of the classical (monolithic) fracture mechanics concept to adhesive fracture tests. Effects of the adhesive layer thickness and the adherend/adhesive modulus ratio on the test were also elucidated. Systematic approximations involved in the test results due to the specimen design based on a simple one-dimensional beam theory were found to be significant in many cases. A more accurate K -calibration obtained by the current analysis may be used as a reference in optimizing the contour shape of test specimens.

Acknowledgment

The author is indebted to F. J. McGarry and J. F. Mandell of the Massachusetts Institute of Technology for their helpful discussions during the course of this study.

References

- [1] Gilman, J. J., *Fracture*, B. L. Averbach et al, Eds., Massachusetts Institute of Technology Press, Cambridge, Mass., 1959, pp. 193-224.
- [2] Ripling, E. J., Mostovoy, S., and Corten, H. T., *Journal of Adhesion*, Vol. 3, 1971, pp. 107-123.
- [3] Mostovoy, S., Ripling, E. J., and Berch, C. F., *Journal of Adhesion*, Vol. 3, 1971, pp. 125-144.
- [4] Bascom, W. D., Cottingham, R. L., Jones, R. L., and Peyser, P., *Journal of Polymer Science*, Vol. 19, 1975, pp. 2545-2562.
- [5] Farhad, F., Muki, R., and Westman, R. A., *International Journal of Solids and Structures*, Vol. 13, No. 6, 1977, pp. 561-570.
- [6] Wang, S. S., Mandell, J. F., and McGarry, F. J., *International Journal of Fracture*, Vol. 14, No. 1, Feb. 1978, pp. 39-58.
- [7] Williams, M. L., *Journal of Applied Mechanics*, Transactions of the American Society of Mechanical Engineers, Vol. 24, 1957, pp. 109-114.
- [8] Paris, P. C. and Sih, G. C. in *Fracture Toughness Testing and Its Applications*, ASTM STP 381, American Society for Testing and Materials, 1965, pp. 51-84.
- [9] Brown, W. F., Jr. and Srawley, J. F., *Plane Strain Crack Toughness Testing of High Strength Materials*, ASTM STP 410, American Society for Testing and Materials, 1966.
- [10] Ripling, E. J., Mostovoy, S., and Patrick, R. L., *Materials Research and Standards*, Vol. 4, No. 3, 1964, pp. 129-138.
- [11] Irwin, G. R., *Treatise on Adhesion and Adhesives*, Vol. 1, R. L. Patrick, Ed., Marcel Dekker, Inc., 1967, pp. 223-268.
- [12] Mostovoy, S. and Ripling, E. J., *Polymer Science and Technology*, Vol. 9B, 1975, pp. 513-561.
- [13] Trantina, G. G., *Journal of Composite Materials*, Vol. 6, 1972, pp. 371-385.
- [14] Pian, T. H. H., *AIAA Journal*, American Institute of Aeronautics and Astronautics, Vol. 2, 1964, pp. 1333-1336.
- [15] Pian, T. H. H., Tong, P., and Luk, C. H. in *Proceedings of the 3rd Conference on Matrix Methods in Structural Mechanics*, Wright-Patterson Air Force Base, Ohio, 1971, pp. 661-682.
- [16] Tong, P., Pian, T. H. H., and Lasry, S. J., *International Journal of Numerical Methods in Engineering*, Vol. 7, 1973, pp. 297-308.

- [17] Wang, S. S., Mandell, J. F., and McGarry, F. J., "Fracture of Adhesive Joints," Research Report R76-1, Department of Materials Science and Engineering, Massachusetts Institute of Technology, Cambridge, Mass., 1976.
- [18] Wang, S. S., Mandell, J. F., Christesen, T. H., and McGarry, F. J., "Analysis of Lap Shear Adhesive Joints With and Without Short Edge Cracks," Research Report R76-2, Department of Materials Science and Engineering, Massachusetts Institute of Technology, Cambridge, Mass., 1976.
- [19] Tong, P. and Pian, T. H. H., *International Journal of Solids and Structures*, Vol. 9, 1973, pp. 313-321.
- [20] Muskhelishvili, N. I., *Some Basic Problems in the Mathematical Theory of Elasticity*, Nordhoff, Gronigen, Holland, 1953.
- [21] Williams, M. L., *Journal of Adhesion*, Vol. 4, 1972, pp. 381-421.

R. L. Ramkumar,¹ S. V. Kulkarni,² R. B. Pipes,³
and S. N. Chatterjee¹

Analytical Modeling and ND Monitoring of Interlaminar Defects in Fiber-Reinforced Composites

REFERENCE: Ramkumar, R. L., Kulkarni, S. V., Pipes, R. B., and Chatterjee, S. N., "Analytical Modeling and ND Monitoring of Interlaminar Defects in Fiber-Reinforced Composites," *Fracture Mechanics, ASTM STP 677*, C. W. Smith, Ed., American Society for Testing and Materials, 1979, pp. 668–684.

ABSTRACT: Interlaminar defects in laminated structural components made of fiber-reinforced composites originate during fabrication or service, or both. Fabrication defects occur during the preparation of the prepreg, laminate layup and cure, or assembly. Service damage may be precipitated by a fatigue load spectrum, impact, or environmental effects. An analytical evaluation of the critical flaw size as a function of the applied stress levels, fatigue cycles, and environment helps quantify the severity of such flaws. A methodology is developed to use nondestructive measurements of the flaw size, after a given period of service, to establish new bounds for fail-safe applications. The analysis considers delaminations in a cantilevered, laminated beam at arbitrary locations along the length of the beam and through its thickness. For an initial flaw size, the critical load at which the debond tends to propagate is estimated through the Griffith energy balance criterion. The beam is modeled as a Timoshenko beam and the individual laminae are graphite fiber-reinforced epoxy matrix composites. A wearout concept is used to account for property degradation with service and the resultant change in the criticality of the flaw. A family of plots for different loading cycles is used to establish bounds on the service life and the maximum growth of the flaw, for a given loading and any initial flaw size. In addition, a catastrophic debond growth boundary is also established. An ND monitoring of the defect size, in liaison with the above, will enhance the fail-safe design of the structural component by a nondestructive evaluation (NDE) analyst.

KEY WORDS: composite materials, delaminations, nondestructive evaluation, Griffith criterion, wearout concept, crack propagation, fatigue (materials)

Defects in fiber-reinforced composite laminated structural components originate during fabrication and during service. Fabrication or "birth

¹ Senior engineers, Materials Sciences Corp., Blue Bell Office Campus, Blue Bell, Pa. 19422.

² Consulting engineer, Lansdale, Pa., 19446.

³ Associate professor, University of Delaware, Newark, Del. 19711.

defects” may occur during the preparation of the prepreg (improper yarn spacing, broken filaments), laminate layup and cure (matrix voids, resin-rich regions, interlaminar damage), and structural component assembly (improper drilling, machining, and potential flaw growth regions such as bolted joints, etc.). Service damage will occur due to a fatigue load spectrum (which is random in nature), impact or FOD (foreign object damage), and environment (ultraviolet, moisture, corrosion, lightning, etc.). Various types of flaws may originate and propagate during the service phase of a structural component. This paper focuses on interlaminar defects.

Until recently, there was no formal quantitative criterion for inspection of advanced composite materials. With the introduction of the Aircraft Structural Integrity Program (MIL-STD-1530A), the need for a quantitative approach for inspection and damage tolerance has been identified. Allowable flaw limits and damage growth rates must be determined to establish inspection intervals and the flaw characteristics which make repair mandatory. The technology to assess the effects of defects should address the following: (a) critical flaw identification and detection, (b) analysis and ND monitoring of flaw growth, and (c) establishment of critical flaw size as a function of stress levels, fatigue cycles, and environment. Thus, in order to develop the nondestructive evaluation technology for fiber-reinforced composite materials, it is necessary that the development of detection capabilities be coupled with development of the technology that is capable of assessing the influence of flaw geometry upon strength and stiffness.

Static Failure Analysis

The usefulness of the methodology is demonstrated⁴ through a simple example since the response of fiber-reinforced composites is influenced, in general, by material heterogeneity, statistical variability, microstructural crack growth, and the three-dimensional state of the stress field. Considering aircraft applications, a flawed wing is modeled as a cantilevered layered beam. A simplified static analysis is presented in the Appendix to estimate the criticality of an interlaminar delamination in a laminated beam. The delamination, through the width, is assumed to exist at any axial location along the length of the beam, and between any two laminae through the thickness (Fig. 1). To reduce the problem to a tractable form and to gain an initial knowledge of the behavior of delaminated beams, it is assumed that the debond propagates along the interface in a collinear fashion.

The static failure model analyzes the debonded beam as four separate

⁴ Ramkumar, R. L., Kulkarni, S. V., and Pipes, R. B., “Definition and Modeling of Critical Flaws in Graphite Fiber Reinforced Epoxy Resin Matrix Composite Materials,” Technical Report, Naval Air Development Center, Warminster, Pa., Jan. 1978.

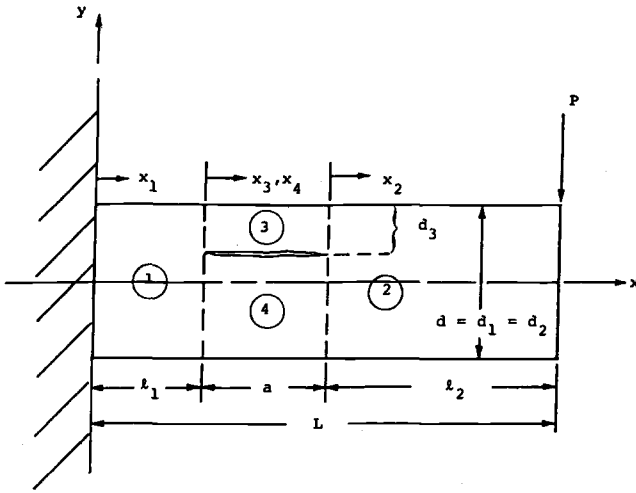


FIG. 1—Tip-loaded, layered, cantilevered beam with an interlaminar delamination.

beam elements joined together at the crack tips with the proper boundary and matching conditions (Figs. 1, 2). Each beam element is treated as a Timoshenko beam to incorporate shear deformation effects. The corresponding equations, boundary conditions, and the displacement solutions for the four elements are presented in the Appendix. The total strain energy in the tip-loaded, cantilevered, debonded beam is obtained using Clapeyron's theorem. The strain energy is dependent on the location and the length of the delamination, the magnitude of the applied load, and the material and geometric properties of the laminated beam.

The criticality of the delamination is determined through Griffith's energy balance criterion. This classical fracture mechanics approach states that the loss in the total strain energy due to an incremental change

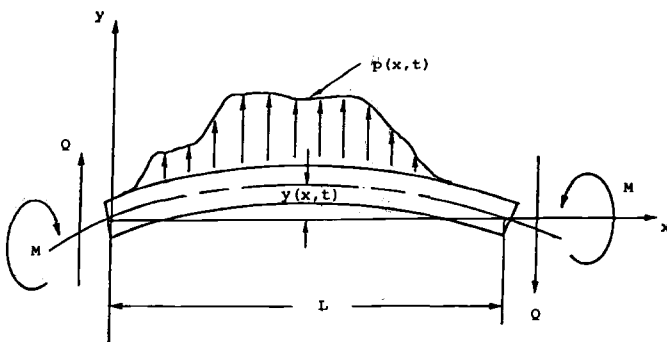


FIG. 2—Beam element and sign conventions.

in the crack length is equal to the surface fracture energy that is necessary to create the corresponding surface area. Inherent in the application of this criterion is the knowledge of the measure of γ_a , which is the specific adhesive surface fracture energy required to create unit surface area through the propagation of the delamination.

The application of Griffith's energy balance criterion leads to a closed-form solution for $P_{cr}/\sqrt{\gamma_a}$ as a function of the beam data (Appendix). P_{cr} is the magnitude of the tip load at which propagation of the delamination is imminent. An experimental data point, in liaison with this solution, will suffice to estimate the magnitude of γ_a .

It is seen from the appendix that the critical value of the tip load is a function of the location and length of delamination, the material and geometric properties of the beam, and the specific adhesive surface fracture energy for the given adherend-adhesive combination. The propagation of the delamination, along the interface, may take place in any of the following directions depending on the material and geometric data: (a) propagation of the delamination into element 1, (b) propagation of the delamination into element 2, and (c) propagation of the delamination into elements 1 and 2 simultaneously. The critical load for each mode is obtained and the direction in which the delamination propagates is governed by the least of the three P_{cr} values.

Figure 3 shows the effect of the location of the delamination on the critical load. It is seen that a debond in the midplane tends to propagate at a lower P_{cr} value compared to a delamination elsewhere. Table 1

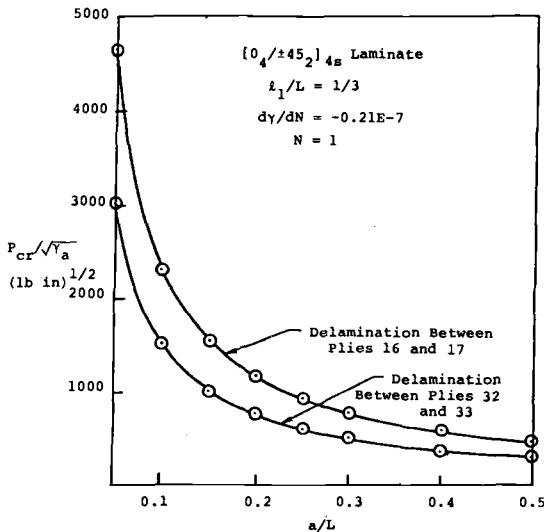


FIG. 3—Effect of crack location on the critical delamination load for a $[0_4/\pm 45_2]_4s$ laminate.

TABLE 1—Computed γ_a values for two delamination sizes.

Specimen ^a	a/L	P_{cr} , lb ^b	$P_{cr}/\sqrt{\gamma_a}$ From Analysis, lb·in ^{1/2}	γ_a , lb/in
1-1	1/3	716.5	456.4	2.46
1-2	1/3	760.5	456.4	2.78
1-3	1/3	518.0	456.4	1.29
1-4	1/3	584.0	456.4	1.64
				Average
1/2-1	1/6	1047.0	912.8	1.32
1/2-2	1/6	1014.0	912.8	1.23
1/2-3	1/6	1075.0	912.8	1.39
				Average
				1.31

^a Debond is in the midplane and is centered in the test section of length = 3 in.

^b 1 lb = 4.4482 N and 1 in. = 2.54 cm.

presents the γ_a values computed from two sets of experimental results for different initial debond sizes. The two γ_a values show good agreement even though a simplified beam analysis was used.

Fatigue Analysis

On fatigue loading a notched or debonded laminate, high axial and shear stresses near the crack tip cause the material in the vicinity of the crack to be degraded much more rapidly than the rest of the laminate. This spatial variation of the property degradation in the laminate is a result of the different stress states in the individual laminae, and the large stress concentration at the crack tips in the neighboring laminae. An analytical prediction of the three-dimensional stress state in a flawed laminate is a formidable task, and a simplified numerical solution is used as the alternative.

The parameters that influence the three-dimensional stress state in a flawed laminate, and hence, the property degradations, are: the number of cycles of loading, N ; the ratio, S , of the maximum fatigue load to the static failure load of the virgin (unnotched and without delaminations) laminated beam; the stress ratio, R , that is, the ratio of the minimum to the maximum fatigue load; the frequency of cyclic loading, ω ; and the ratio, η , of the static failure load of a flawed beam of known flaw size to the static failure load of the virgin, unflawed laminated beam. For a debonded beam, η is a function of the initial debond size, a/L , and can be obtained from the static failure analysis (Fig. 3).

The general fatigue philosophy is based on using unflawed lamina fatigue data to predict the local property changes in flawed laminates.^{4,5}

⁵ McLaughlin, P. V., Jr., Kulkarni, S. V., Huang, S. N., and Rosen, B. W., "Fatigue of Notched Fiber Composite Laminates, Part I: Analytical Model," NASA CR-132747, National Aeronautics and Space Administration, Langley Research Center, Hampton, Va., March 1975.

Fatigue tests are to be conducted on unflawed coupons to span a wide range of stress states and the desired property degradations measured.

A simplified fatigue philosophy^{4,5} is used here to model the property degradation mathematically in an empirical manner. The spatial stress variation in each lamina is approximated by an average stress state throughout the lamina. This approximates the spatial variation in the lamina S value by an average S value for each lamina in the flawed laminate. The spatial variation of the property degradations in each ply is thus approximated by average degraded ply properties to simplify the analysis. The fatigue degradation in each ply in a flawed beam can then be assumed to be a function of N and the laminate S/η value which is the ratio of the maximum applied fatigue load to the static failure load of the flawed beam of known initial flaw size.

The fatigue analysis is carried out by computing the laminate property degradations from the lamina fatigue data using laminated plate theory. This is done for the four beam elements in the present analysis. The lamina fatigue data are obtained from experiments on flawed, perfectly bonded unidirectional specimens. These tests are carried out at different S levels. When the lamina fatigue data are used in the fatigue failure analysis of a flawed beam, the η value corresponding to the measured flaw size is computed from the static failure analysis; the lamina fatigue data corresponding to the laminate S/η value are used in the laminate analysis to obtain average degradations in the four beam elements. Hence, for different initial flaw sizes, different levels of degradations result depending on the ratio of the maximum fatigue load to the static failure load of the flawed beam. As a further simplification in this example, the rates of property degradation in this beam are assumed to be constant in all plies. Thus the effect of the differences in property degradation resulting from different stress levels in the various plies is disregarded to simplify the example. Different rates of degradation are used, however, for the different moduli of the plies (that is, E_1 , E_2 , G_{12}). These rates are the rates of degradation corresponding to the initial laminate S/η value. The effect of the change in laminate S/η on the degradation rates is ignored.

The static failure analysis for a flawed laminate under a given set of loading conditions requires the stiffness and strength properties as input data. Fatigue failure analysis is carried out by considering a finite number of load cycle intervals, and using the degraded properties for each interval in the static failure analysis.

Figure 4 shows the variation in the critical load with the number of cycles and the debond size for a $[0_4/\pm 45_2]_{48}$ beam under cyclic loading. The debond is located at $\ell_1/L = 1/3$ and it is at the laminate middle surface. The effects of crack growth will be discussed subsequently. The assumed property degradation rates are stated on the figure. These rates correspond to a laminate S/η value of two thirds for an initial debond size of $a/L = 0.2$. If the initial debond size is different, different curves (for

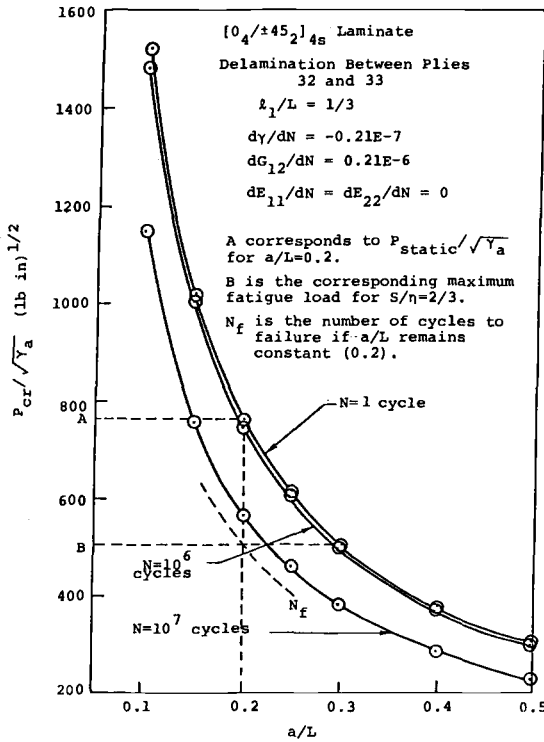


FIG. 4—Effect of fatigue cycles on the critical delamination load for a $[0_4/\pm 45_2]_{4s}$ laminate.

the new laminate S/η value) result for $N = 10^6$ cycles and $N = 10^7$ cycles in Fig. 4.

NDE Methodology to Predict Flaw Criticality

In evaluating the integrity of structural elements, nondestructive inspection focuses upon detection of flaws and the determination of their sizes, while nondestructive evaluation techniques translate these into a measure of the criticality of the flaws. Allowable limits for flaw size and damage growth rates must be determined to establish inspection intervals for in-service flawed structural elements, and to determine flaw characteristics that make repair mandatory. To this end, an NDE methodology is developed herein. It is built around: (a) a static/fatigue failure analysis, (b) experimental results on flawed specimen response, and (c) an NDE methodology to assess the criticality of a flaw using NDT.

The analytical results predicted by the static/fatigue failure model (Figs. 3, 4) form the basis of the NDE methodology. For a defect of a

known initial size and location, a family of curves describes the variation of the critical load with the defect size for different values of N (Fig. 4). As the number of cycles (N) of known loading conditions increases, the spatial degradation of the material properties causes a lowering of the critical load at which the propagation of a delamination of known size is imminent (Fig. 4). The crack growth is stable if additional load is required to increase the crack size, and unstable if an increase in a/L results in a reduction of the critical load. The present model for an interlaminar defect in a beam yields values of critical load at which the imminent propagation of the debond is unstable by nature. Unstable crack growth is represented in Figs. 3 and 4, where the critical load decreases with a growth in the delamination. If an applied load reaches the critical value for the existent length of debond, the debond tends to grow indefinitely. Hence, the afore-mentioned family of curves describes the catastrophic debond growth for each value of N . This is of major importance to the NDE analyst.

For a known size and location of a debond in a delaminated beam, curves of $P_{cr}/\sqrt{\gamma a}$ versus a/L can be drawn for various values of N as shown in Fig. 4. As discussed earlier, these curves are all calculated based upon the assumption that property degradation occurs throughout the laminate at constant rates (as shown in Fig. 4). In actuality, the degradation rates depend upon the crack size and the stress ratio S/η . For these calculations, the degradation rates used were those for $a/L = 0.2$ and $S/\eta = 2/3$. From curves of this type, the static failure load, P_{static} , for any initial debond size can be obtained from the $N = 1$ curve. For illustrative purposes, $P_{static}/\sqrt{\gamma a}$ for an a/L value of 0.2 is selected in Fig. 4. If the laminate S level for fatigue loading is chosen, the maximum cyclic load, $P_{fatigue}$, can be determined as $S \times P_{static}^{unflawed}$. $P_{fatigue}$ for the chosen laminate S value corresponds to a particular laminate S/η value for the known debond size. $P_{fatigue}$ for $S/\eta = 2/3$ is shown in Fig. 4. The line $P_{cr}/\sqrt{\gamma a} = P_{fatigue}/\sqrt{\gamma a}$ intersects the family of failure curves at various points. The points of intersection of $P_{fatigue}$ with the family of curves can be plotted as an a/L versus $\log N$ curve (Fig. 5). The lower solid curve in Fig. 5 defines the lifetime to catastrophic propagation of an initial debond of the specified size. The upper solid curve differs from this only in the assumption that the surface energy remains constant while the stiffnesses degrade.

All of these calculations result in unstable crack propagation. Experimentally, however, a stable crack propagation is observed. Figure 6 shows the ultrasonic "C" scans of a debonded specimen at intervals of 10 000 cycles under known fatigue loading conditions. The growth of the delamination with N is measured from this figure and plotted in Fig. 7. Strictly speaking, once the debond grows, the η value (and hence the laminate S/η) changes. Thus, different fatigue data are required and a new

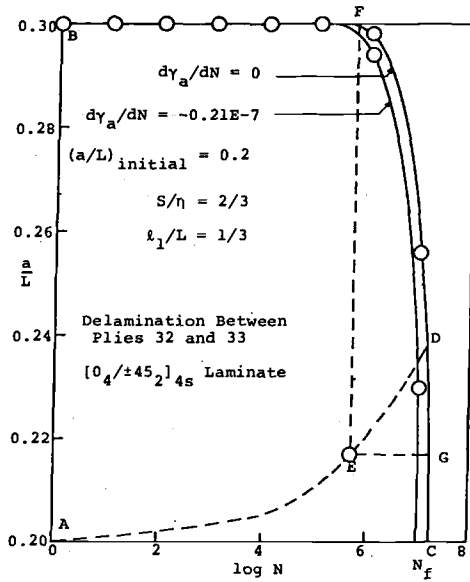


FIG. 5—Catastrophic crack growth boundary for an initial $a/L = 0.2$ and $S/\eta = 2/3$ for a $[0_4/\pm 45_2]_{4s}$ laminate.

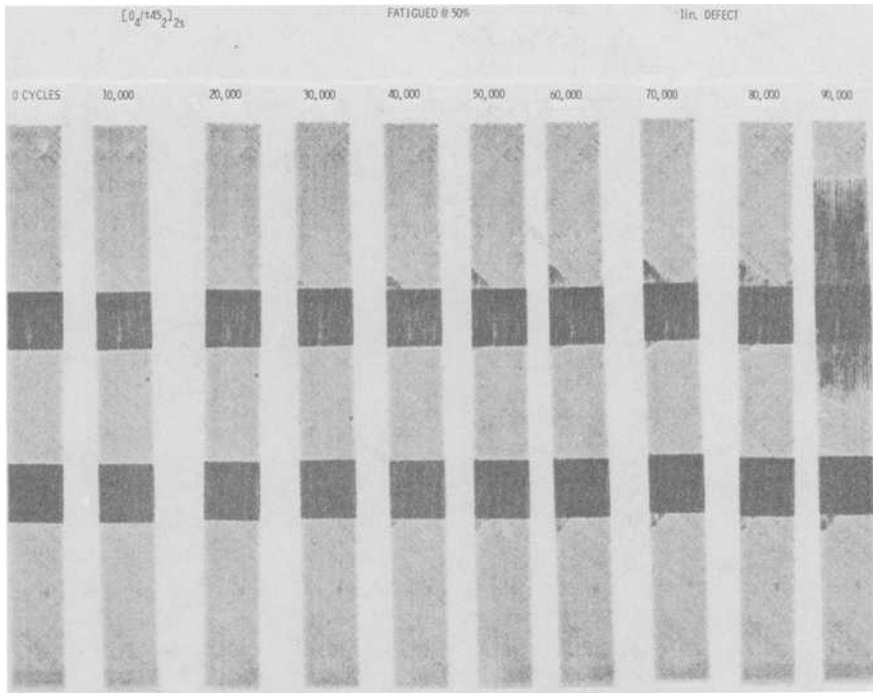


FIG. 6—Growth of interlaminar damage with N in a $[0_4/\pm 45_2]_{2s}$ specimen at $S = 0.5$ (initial defect size = 2.54 cm).

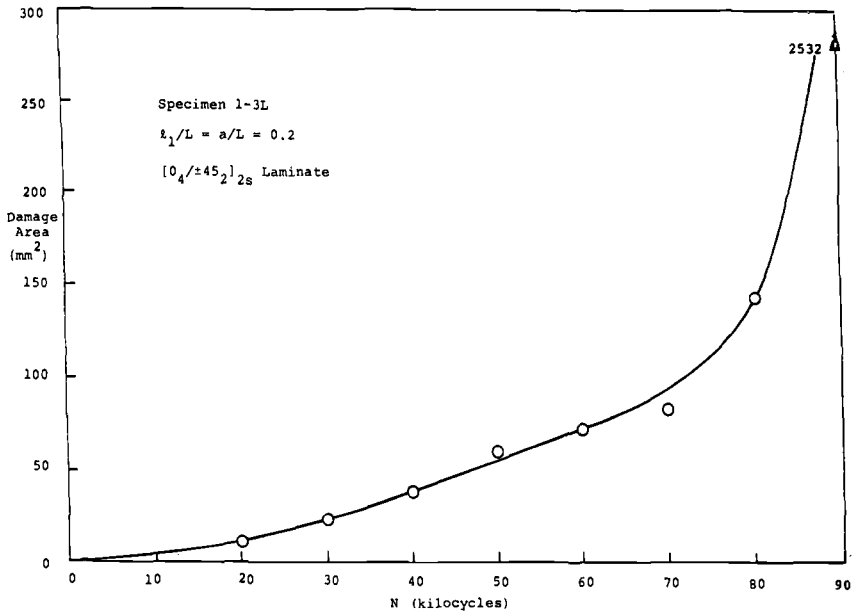


FIG. 7—Growth of damage area at the failure site with N for a $[0_4/\pm 45_2]_{2s}$ laminate with a 2.54 cm debond.

family of $P_{cr}/\sqrt{\gamma a}$ versus a/L for various N curves should be used. This is not done in Fig. 5 for reasons explained earlier. The initial debond size of $a/L = 0.2$ is the lower bound on the a/L value. N_f (see Fig. 5) is the number of cycles after which an initial debond of size $a/L = 0.2$ will propagate catastrophically without any intermediate growth. N_f is a hypothetical upper bound on N , since in reality, the damage may grow with N , thus shortening lifetime. Point B corresponds to that debond size at which a static load of magnitude equal to $P_{fatigue}$ precipitates a catastrophic failure ($N = 1$). On fatigue loading, the debond in a laminated beam appears to grow in a stable manner, as shown by curve AED in Fig. 5, until the $(a/L, N)$ combination corresponds to a catastrophic situation. If the property degradation rate is insensitive to debond size, then the solid curves will still represent a failure curve. Point D in Fig. 5 then represents a typical $(a/L, N)$ combination at which catastrophic debond growth precipitates after stable crack growth.

Knowing the location and initial size of the debond, and the chosen cyclic maximum load, the boundary for catastrophic propagation of the delamination is obtained. This boundary is drawn on an a/L versus N plot for every value of initial debond size. The procedure for this follows the steps outlined below:

1. Determine the initial debond size (a/L and its location).
2. From the static failure analysis, obtain a $P_{cr}/\sqrt{\gamma a}$ versus a/L curve for the debonded beam.

3. Given the maximum applied cyclic load and the static failure load of the unflawed, virgin beam, determine the laminate S/η value for the initial debond size from the static failure analysis results.

4. Using lamina degradation data corresponding to the initial laminate S/η value, obtain a family of curves defining catastrophic growth of defect for different values of N .

5. Corresponding to the maximum cyclic load, obtain the critical values of a/L (greater than or equal to the initial value) for different values of N .

6. Plot these points on an a/L versus N plot, and draw a curve through them to define the catastrophic debond growth boundary.

Figure 5 presents the instability boundary for a $[0_4/\pm 45_2]_{48}$ laminated beam with a debond in the midplane. *BFDGC* is the curve that defines unstable debond growth or failure. While the outer curve assumes no degradation in the specific adhesive surface energy, the inner one assumes a degradation in γ_a that is of the same order as the shear modulus degradation, based on the reasoning that the surface energy is affected directly by a deterioration in the shear resistance at the adherend-adhesive interface. The initial defect size ($a/L = 0.2$) is labeled *A*, and the critical defect size for static failure at the maximum cyclic load is labeled *B*. Point *C* denotes the hypothetical number of cycles the beam can go through until failure without any growth of the defect. This is not a physically realizable state since the damage generally grows when the flawed specimen is subjected to cyclic loading.

The actual growth of the damage, which can be monitored ultrasonically, may follow a path similar to that shown by the discontinuous line *AED*. From an NDE point of view, if the specimen is inspected after a few cycles and the defect has grown to the extent shown by *E*, the residual strength and lifetime of the specimen have to be determined to decide on the need for mandatory repair. If the initial debond ($a/L = 0.2$) has grown to state *E* after about 5.75×10^6 cycles, *FDG* becomes the new envelope that bounds stable crack growth. At *E*, if the fatigued beam specimen were tested statically, from the measure of *EF* and the static failure analysis (Fig. 3), the residual strength in the beam may be computed. Also, an overestimation of the residual lifetime of the beam may be obtained from the measure of *EG*. *EG* is an overestimation of the residual lifetime since it assumes the debond size at *E* to remain constant when cyclic loading on the delaminated beam is assumed to be applied for an additional number of cycles (given by *EG*). Hence, from Fig. 5, it is seen that *EF* is a measure of the residual strength in the specimen and *EG* is an overestimation of its residual lifetime. These then could be compared with a quantified criterion for mandatory repair and serve as an assessment of the criticality of the flaw.

APPENDIX

Static Analysis to Determine the Criticality of Interlaminar Delaminations in Laminated Beams

The Euler equations for a tip-loaded, uniform, cantilevered Timoshenko beam are⁶

$$EI \frac{d^2\psi}{dx^2} + k \left(\frac{dy}{dx} - \psi \right) = 0 \tag{1}$$

$$\frac{d}{dx} \left[k \left(\frac{dy}{dx} - \psi \right) \right] = 0 \tag{2}$$

The deflected beam geometry, its coordinates, the loading, and transverse shear force conventions are shown in Fig. 2. ψ is the slope of the deflection curve neglecting shear deformation and β is the angle of shear at the neutral axis. The total slope is

$$\frac{\partial y}{\partial x} = \psi + \beta \tag{3}$$

E is the Young's modulus of the beam material, and I is the cross-sectional moment of inertia.

$$k = k'AG \tag{4}$$

where A is the cross-sectional area of the beam, G is the shear modulus of elasticity, and k' is a numerical constant depending on the geometry of the cross-section. For a rectangular cross section, $k' = 2/3$. The bending moment, M , and the transverse shear force, Q , at any section of the beam are given by

$$M = EI \frac{d\psi}{dx}, \tag{5}$$

and

$$Q = -k \left(\frac{dy}{dx} - \psi \right) \tag{6}$$

The deflections, slopes, and material properties of the four different beams are identified by the use of proper subscripts. The axial coordinate x_i for the i th beam has its origin at the left end of that beam (Fig. 1). Equations 1 and 2 may be combined to give a third order, ordinary differential equation for $y_i(x)$. This results in twelve constants of integration when all of the four beam elements are considered. In addition, the transverse shear force division elements above and below the crack of length a lead to an extra unknown to be solved for. If the applied tip load is P and the beam element above the crack ($i = 3$) carries a transverse shear force for \bar{P} , the element below the crack ($i = 4$) carries a shear force of $(P - \bar{P})$.

⁶ Fung, Y. C., *Foundations of Solid Mechanics*, Prentice-Hall of India, New Delhi, 1968.

The 13 boundary and matching conditions used in obtaining the deflection solution at any axial location of the debonded beam are

$$y_1(x_1 = 0) = 0, \text{ or, } y_1 = 0 \text{ at } x_1 = 0 \quad (7)$$

$$\psi_1(x_1 = 0) = 0 \quad (8)$$

$$M_2(x_2 = \ell_2) = 0 \quad (9)$$

$$M_1(x_1 = \ell_1) = -P(\ell_2 + a) \quad (10)$$

$$\psi_3(x_3 = 0) = \psi_1(x_1 = \ell_1) \quad (11)$$

$$\psi_3(x_3 = 0) = \psi_4(x_4 = 0) \quad (12)$$

$$y_3(x_3 = 0) = y_1(x_1 = \ell_1) \quad (13)$$

$$y_3(x_3 = 0) = y_4(x_4 = 0) \quad (14)$$

$$y_2(x_2 = 0) = y_3(x_3 = a) \quad (15)$$

$$y_2(x_2 = 0) = y_4(x_4 = a) \quad (16)$$

$$\psi_2(x_2 = 0) = \psi_3(x_3 = a) \quad (17)$$

$$\psi_2(x_2 = 0) = \psi_4(x_4 = a) \quad (18)$$

$$M_1(x_1 = \ell_1) = M_3(x_3 = 0) + M_4(x_4 = 0) + M_{\text{axial}} \quad (19)$$

M_{axial} is the bending moment due to the couple created by the horizontal or axial force reactions H_3 and H_4 in beam elements 3 and 4, respectively. The axial forces are a result of an elongation of element 3 and a corresponding contraction of element 4 in order to ensure compatibility of displacements and slopes. The axial elongation in element 3 (u_3) is given by

$$u_3 = -\Delta\psi \frac{d_4}{2} + u_0 \quad (20)$$

where

$$\Delta\psi = \psi_2(x_2 = 0) - \psi_1(x_1 = \ell_1) \quad (21)$$

$$d_4/2 = d/2 - d_3/2 \quad (22)$$

and u_0 is the axial rigid body displacement in elements 3 and 4. $d = d_1 = d_2$ is the total thickness of the debonded beam, and d_3 and d_4 are the thicknesses of elements 3 and 4, respectively. It follows that the axial contraction, u_4 , in element 4 is

$$u_4 = u_0 + \Delta\psi \frac{d_3}{2} \quad (23)$$

Since

$$u_3 = \frac{H_3 a}{A_3 E_3} \text{ and } u_4 = \frac{H_4 a}{A_4 E_4} \tag{24}$$

the axial force equilibrium equation at the crack tip locations,

$$H_3 + H_4 = 0 \tag{25}$$

yields a solution for the rigid body displacement

$$u_0 = \frac{\Delta\psi}{2(A_3 E_3 + A_4 E_4)} (A_3 E_3 d_4 - A_4 E_4 d_3) \tag{26}$$

if b is the width of the beam, $A_3 = b d_3$ and $A_4 = b d_4$. This simplifies Eq 26 to

$$u_0 = \frac{d_3 d_4 (E_3 - E_4)}{2(d_3 E_3 + d_4 E_4)} \Delta\psi \tag{27}$$

An interesting inference from Eq 27 is that a rigid body translation takes place only when E_3 is not equal to E_4 . If the beam material is isotropic, or if the delamination in a midplane-symmetric, laminated, anisotropic beam is in the midplane, there will be no rigid body axial displacements. When the debond occurs between two layers such that E_3 and E_4 have different magnitudes, a rigid body translation in elements 3 and 4 is essential for displacement and slope compatibility.

With the preceding expressions for the axial forces in elements 3 and 4, half the total beam thickness apart, M_{axial} may be written as

$$M_{axial} = -H_3 d/2 = -A_3 E_3 u_3 d/2a \tag{28}$$

Using the boundary and matching conditions, Eqs 7 through 19, in the general solutions to the beam Eqs 1 and 2, for all the four elements, the deflection function for the tip-loaded delaminated beam is obtained. Computing the tip deflection from this solution, Clapeyron's theorem is used to obtain the total strain energy, U , in the beam

$$U = -\frac{1}{2} P y_2(x_2 = \ell_2) \tag{29}$$

or

$$2U/P^2 = -\frac{y_2(x_2 = \ell_2)}{P} \tag{30}$$

Carrying out the aforementioned substitutions, one obtains

$$\frac{2U}{P^2} = \frac{\ell_2^3}{3(EI)_2} - \frac{C_2}{P} \ell_2 - \frac{C_3}{P} + \frac{\ell_2}{k_2} \tag{31}$$

where

$$\frac{C_2}{P} = \frac{C_8}{P} - \frac{a(\ell_2 + 0.5a)}{\phi_2} \tag{32}$$

$$\frac{C_3}{P} = \left[\frac{a^3}{6(EI)_3} - \frac{a}{K_3} \right] \frac{\tilde{P}}{P} + \frac{C_7}{P} \frac{a^2}{2} + \frac{C_8}{P} a + \frac{C_9}{P} \tag{33}$$

$$\frac{C_7}{P} = - \frac{a}{2(EI)_3} \frac{\tilde{P}}{P} - \frac{(\ell_2 + 0.5a)}{\phi_2} \tag{34}$$

$$\frac{C_8}{P} = \frac{\ell_1(\ell_1 - 2L)}{2(EI)_1} \tag{35}$$

$$\frac{C_9}{P} = \frac{\ell_1^2(\ell_1 - 3L)}{6(EI)_1} - \frac{\ell_1}{k_1} \tag{36}$$

$$\frac{\tilde{P}}{P} = \frac{a_1}{a_1 + a_2} \tag{37}$$

$$a_1 = \frac{a^2}{12(EI)_4} + \frac{1}{K_4} \tag{38}$$

$$a_2 = \frac{a^2}{12(EI)_3} + \frac{1}{k_3} \tag{39}$$

$$\phi_2 = \phi_1 + (EI)_3 + (EI)_4 \tag{40}$$

$$\phi_1 = \frac{A_3 E_3 E_4 d_4 d^2}{4(d_3 E_3 + d_4 E_4)} = \frac{a M_{axial}}{\Delta \psi} \tag{41}$$

The Griffith energy balance criterion is used to determine the criticality of the delamination. Let γ_a be the specific adhesive surface fracture energy that is required to create unit surface area through the propagation of the delamination. The energy balance criterion states that the loss in the total strain energy due to an incremental change in the crack length is equal to the surface fracture energy that is necessary to create the corresponding surface area. Expressed mathematically, the Griffith energy balance criterion is

$$\frac{\partial U}{\partial a} = 2b\gamma_a \tag{42}$$

Substituting Eq 31 into Eq 42

$$\frac{2(\partial U/da)}{P_{cr}^2} = \frac{4b\gamma_a}{P_{cr}^2} = \frac{\ell_2^2}{(EI)_2} \frac{d\ell_2}{da} - \frac{C_2}{P} \frac{d\ell_2}{da} - \ell_2 \frac{d(C_2/P)}{da} - \frac{d(C_3/P)}{da} + \frac{1}{k_2} \frac{d\ell_2}{da} = \phi_3 \quad (43)$$

or

$$P_{cr}/\sqrt{\gamma_a} = 2\sqrt{b/\phi_3} \quad (44)$$

P_{cr} is the magnitude of the critical load at which propagation of delamination is imminent. The derivatives that appear in the expression for ϕ_3 , Eq 43, are

$$\frac{d(C_2/P)}{da} = \frac{a}{(EI)_3} \frac{\tilde{P}}{P} + \frac{a^2}{2(EI)_3} \frac{d(\tilde{P}/P)}{da} + \frac{C_7}{P} + a \frac{d(C_7/P)}{da} + \frac{d(C_8/P)}{da} \quad (45)$$

$$\begin{aligned} \frac{d(C_3/P)}{da} = & -\frac{1}{k_3} \frac{\tilde{P}}{P} - \frac{a}{k_3} \frac{d(\tilde{P}/P)}{da} + \frac{a^2}{2(EI)_3} \frac{\tilde{P}}{P} + \frac{a^3}{6(EI)_3} \frac{d(\tilde{P}/P)}{da} \\ & + a \frac{C_7}{P} + \frac{a^2}{2} \frac{d(C_7/P)}{da} + \frac{C_8}{P} + a \frac{d(C_8/P)}{da} + \frac{d(C_9/P)}{da} \end{aligned} \quad (46)$$

$$\frac{d(C_7/P)}{da} = -\frac{[d\ell_2/da + 0.5]}{\phi_2} - \frac{1}{2(EI)_3} \left[\tilde{P}/P + a \frac{d(\tilde{P}/P)}{da} \right] \quad (47)$$

$$\frac{d(C_8/P)}{da} = -\frac{(L - \ell_1)}{(EI)_1} \frac{d\ell_1}{da} \quad (48)$$

$$\frac{d(C_9/P)}{da} = -\frac{(L - 0.5\ell_1)}{(EI)_1} \ell_1 \frac{d\ell_1}{da} - \frac{1}{k_1} \frac{d\ell_1}{da} \quad (49)$$

$$\frac{d(\tilde{P}/P)}{da} = \frac{a}{6(EI)_4(a_1 + a_2)} \left[1 - \frac{\tilde{P}}{P} \left\{ 1 + \frac{(EI)_4}{(EI)_3} \right\} \right] \quad (50)$$

It is seen from Eq 44 that the critical value of the tip load is a function of the location and length of delamination, the material and geometric properties of the beam, and the specific adhesive surface fracture energy for the given adherend-adhesive combination. The propagation of the delamination, along the interface, may take place in any of the following ways depending on the material and geometric data:

- propagation of the delamination into element 1; in this case, $d\ell_1 = -da$ and $d\ell_2 = 0$;
- propagation of the delamination into element 2; in this case, $d\ell_2 = -da$ and $d\ell_1 = 0$;
- propagation of the delamination into elements 1 and 2 simultaneously; in this case, $d\ell_1 = d\ell_2 = -da/2$.

The critical load for each case is obtained by substituting the appropriate values of $d\ell_1/da$ and $d\ell_2/da$ into Eq 44. The direction in which the delamination propagates is governed by the least of the three P_{cr} values.

The variation of $P_{cr}/\sqrt{\gamma_a}$ with the crack length a may be plotted for different sets of beam data. One experimental data point on this curve would suffice to evaluate γ_a .

Acknowledgments

This effort was supported by NADC Contract N62269-77-C-0092 to Materials Sciences Corporation. The authors would like to thank R. Blake for his efforts in the experimental program and H. Goodman and L. Husted for typing the manuscript.

Stress Intensity Factors for a Circular Ring with Uniform Array of Radial Cracks Using Cubic Isoparametric Singular Elements

REFERENCE: Pu, S. L. and Hussain, M. A., "Stress Intensity Factors for a Circular Ring with Uniform Array of Radial Cracks Using Cubic Isoparametric Singular Elements," *Fracture Mechanics, ASTM STP 677*, C. W. Smith, Ed., American Society for Testing and Materials, 1979, pp. 685-699.

ABSTRACT: The plane problem of a uniform array of equal depth radial cracks originating at the internal boundary of a pressurized circular ring is considered. The finite element method using 12-node quadrilateral, isoparametric elements is adopted. The collapsed singular elements recently developed by the authors are used around the crack tip. The stress intensity factors at a crack tip can be obtained for any finite number of radial cracks and for a large variety of diameter ratios and crack-depth to wall-thickness ratios.

For the special case of a single radial crack and two diametrically opposed radial cracks, stress intensity factors have been obtained by Bowie and Freese using modified mapping-collocation method and by Shannon using a very large number of constant-strain triangular elements. Results of these two different approaches agree quite well except for shallow cracks relative to the cylinder wall thickness. The present finite element results using a maximum of seventeen elements are in better agreement with those of Bowie and Freese, including the results for shallow cracks.

For the case of 40 radial cracks in a cylinder of diameter ratio 2.0, Goldthorpe obtained an empirical formula for the stress intensity factor based on an approximate procedure applied to data of Tweed and Rooke for 40 radial cracks from a hole in an infinite plate. The present results agree with Goldthorpe's results for shallow cracks. For large crack-depth to wall-thickness ratios, Goldthorpe's formula tends to be too low for the stress intensity factors.

The current study has shown that the ring with two diametrically opposed cracks is in general the weakest configuration (highest value in K_I). In the range of diameter ratio 1.5 to 2.5, the ring with three radial cracks is also weaker than that with only one radial crack. For more than three cracks, the denser the radial cracks are the more stable the ring will be.

KEY WORDS: fracture properties, stress intensity factors, multiple cracks, cylinders, isoparametric elements, crack-tip elements, fatigue (materials), crack propagation

¹ Mathematician and mechanical engineer, respectively, Armament Research and Development Command, Benet Weapons Laboratory, Watervliet Arsenal, Watervliet, N. Y. 12189.

The plane problem of radial cracks, equal and finite in length, originating at a circular hole in an infinite plate under uniaxial or biaxial tension has been solved by Bowie [1].² His solution is based on the complex variable method. He obtained numerical results for a single crack and two diametrically opposite cracks. Using this analysis, Kutter [2] computed the stress distribution for a maximum of 16 radial cracks. A special case when the radius of the circular hole is zero was considered by Westmann [3]. His solution is obtained utilizing Mellin transforms. The crack-tip stress intensity factors are evaluated numerically for any number of radial cracks. Using Mellin transforms, Tweed and Rooke [4–6] reconsidered Bowie's and Westmann's problems. They obtained stress intensity factors for various crack numbers and lengths. A problem of this nature is of particular interest in the field of rock mechanics such as underground cavities under hydraulic pressure or blasting. It is also useful for circular cutouts in sheet material. The application of this problem to axial cracks in a circular hollow cylinder is of limited practical value because the solution is only valid for very large diameter ratios.

Various approximate techniques have been developed for the stress intensity factor of radial cracks radiating at the bore of a circular ring. Winnie and Wundt [7] used Bowie's infinite plate solution and a mean-stress concept to obtain strain-energy release rate for a bored and notched rotating disk of large diameter ratios. Williams and Isherwood [8] presented an approximate method for the calculation of the strain-energy release rate for finite plates. They obtained numerical results for rotating disks with diameter ratios less than that required in Ref 7. In the study of cracked gun barrels, Goldthorpe [9] computed the stress intensity factor for a pressurized cylinder of diameter ratio 2.0 with 40 radial cracks based on an approximate procedure by Cartright and Rooke [10] and the results of radial cracks in an infinite plate by Tweed and Rooke [6]. The modified mapping-collocation technique which combines modified versions of conformal mapping and boundary collocation methods was presented originally by Bowie and Neal [11] as a procedure for the analysis of an internal crack in a finite geometry. This technique was employed by Bowie and Freese [12] to evaluate stress intensity factors for a circular ring with a single radial crack at the inner hole under axisymmetric tension on the outer boundary. Numerical results for the circular ring with two diametrically opposed cracks were supplied by Freese and Bowie in a private communication with Underwood [13]. The concept of load relief factor, first used by Neuber [14], was applied by Baratta [15] to determine approximately the stress intensity factors for a multiple-cracked circular ring. A weight function technique proposed by Rice [16] was employed by

² The italic numbers in brackets refer to the list of references appended to this paper.

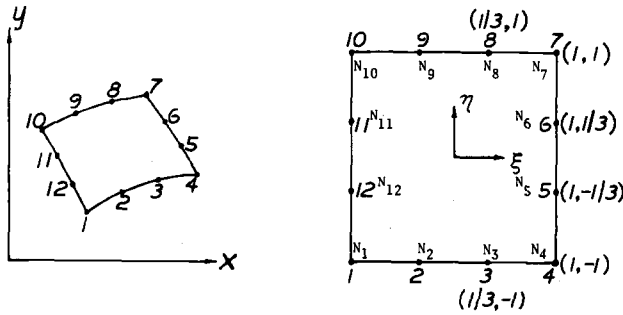
Grandt [17] to obtain stress intensity factors for one and two radially cracked rings.

The finite element technique has become an important numerical method for practical problems in structural mechanics because of its ability to treat very general geometric configurations and loading conditions. Shannon [18] using the constant strain triangular elements, obtained stress intensity factors for a thick-walled cylinder with one or two radial cracks. Because of the large strain gradients in the vicinity of a crack tip, an extremely fine element grid was used near the crack tip. His results were compared with Bowie and Freese's mapping-collocation results in Ref 13. Many refinements in finite element approach to crack problems have been developed in the past decade. Wilson [19] introduced the embedded singularity. Special crack-tip elements were used by Tracey [20], Blackburn [21], Benzley and Beisinger [22]. Using quadratic isoparametric elements, Henshell and Shaw [23] and Barsoum [24] found independently that the inverse square root singularity at a crack tip was obtained by placing the mid-side nodes at quarter points in the vicinity of the crack tip. These elements are implemented in NASTRAN as dummy elements by Hussain et al [25]. A 12-node, isoparametric element is used by Gifford [26], where two special crack-tip elements are implemented in his computer program APES [26] for fracture mechanics problems. The concept of shifting the mid-side nodes to quarter points in an 8-node isoparametric element is extended by the authors to 12-node isoparametric elements [27]. The inverse square root singularity of the strain field at the crack tip is obtained by collapsing the quadrilateral elements into triangular elements around the crack tip and placing the two side nodes on each of the straight line segments passing through the tip at 1/9 and 4/9 of the length of the segment from the tip. With these collapsed 12-node triangular elements as singular elements and around a crack tip, APES is used in this paper to compute the stress intensity factor for a radially multiple-cracked circular ring. The results are compared with previous results obtained by other investigators.

12-Node Quadrilateral Isoparametric Element

A typical 12-node, quadrilateral element, in Cartesian coordinates (x,y) which is mapped to a square in the curvilinear space (ξ,η) with vertexes at $(\pm 1, \pm 1)$, is shown in Fig. 1. The assumption for displacement components takes the form

$$\begin{aligned}
 u &= \sum_{i=1}^{12} N_i(\xi,\eta)u_i \\
 v &= \sum_{i=1}^{12} N_i(\xi,\eta)v_i
 \end{aligned}
 \tag{1}$$



$$\begin{aligned}
 N_1 &= \frac{1}{32} (1-n) (1-\xi) [-10+9(\xi^2+\eta^2)] & N_7 &= \frac{1}{32} (1+n) (1+\xi) [-10+9(\xi^2+\eta^2)] \\
 N_2 &= \frac{9}{32} (1-n) (1-\xi^2) (1-3\xi) & N_8 &= \frac{9}{32} (1+n) (1-\xi^2) (1+3\xi) \\
 N_3 &= \frac{9}{32} (1-n) (1-\xi^2) (1+3\xi) & N_9 &= \frac{9}{32} (1+n) (1-\xi^2) (1-3\xi) \\
 N_4 &= \frac{1}{32} (1-n) (1+\xi) [-10+9(\xi^2+\eta^2)] & N_{10} &= \frac{1}{32} (1+n) (1-\xi) [-10+9(\xi^2+\eta^2)] \\
 N_5 &= \frac{9}{32} (1+\xi) (1-\eta^2) (1-3\eta) & N_{11} &= \frac{9}{32} (1-\xi) (1-\eta^2) (1+3\eta) \\
 N_6 &= \frac{9}{32} (1+\xi) (1-\eta^2) (1+3\eta) & N_{12} &= \frac{9}{32} (1-\xi) (1-\eta^2) (1-3\eta)
 \end{aligned}$$

FIG. 1—Shape functions and numbering sequence for a 12-node quadrilateral element.

where u, v are x, y components of displacement of a point whose natural coordinates are ξ, η ; u_i, v_i are displacement components of node i , and $N_i(\xi, \eta)$ is the shape function given in Ref 28 which can be written as

$$\begin{aligned}
 N_i(\xi, \eta) &= \frac{1}{256} (1 + \xi\xi_i)(1 + \eta\eta_i)[-10 + 9(\xi^2 + \eta^2)][-10 + 9(\xi_i^2 + \eta_i^2)] \\
 &+ \frac{81}{256}(1 + \xi\xi_i)(1 + 9\eta\eta_i)(1 - \eta^2)(1 - \eta_i^2) \\
 &+ \frac{81}{256}(1 + \eta\eta_i)(1 + 9\xi\xi_i)(1 - \xi^2)(1 - \xi_i^2) \quad (2)
 \end{aligned}$$

for node i whose Cartesian and curvilinear coordinates are (x_i, y_i) and (ξ_i, η_i) respectively. The element is isoparametric, hence the same shape function is used for coordinate transformation

$$\begin{aligned}
 x &= \sum_{i=1}^{12} N_i(\xi, \eta)x_i \\
 y &= \sum_{i=1}^{12} N_i(\xi, \eta)y_i \quad (3)
 \end{aligned}$$

The element stiffness matrix is found in the usual way and is given by [24,25]

$$[K] = \int_{-1}^1 \int_{-1}^1 [B]^T [D] [B] \det |J| d\xi d\eta \tag{4}$$

where $[B]$ is a matrix relating joint displacements to the strain field $\{\epsilon\}$

$$\{\epsilon\} = [B] \begin{Bmatrix} \vdots \\ u_i \\ v_i \\ \vdots \end{Bmatrix}$$

and $[D]$ is the material stiff matrix given by

$$[D] = \frac{E}{1 - \nu^2} \begin{bmatrix} 1 & \nu & 0 \\ \nu & 1 & 0 \\ 0 & 0 & (1 - \nu)/2 \end{bmatrix} \text{ and } [D] = \frac{E}{(1 + \nu)(1 - 2\nu)} \begin{bmatrix} 1 - \nu & \nu & 0 \\ \nu & 1 - \nu & 0 \\ 0 & 0 & (1 - 2\nu)/2 \end{bmatrix} \tag{5}$$

for the case of plane stress and plane strain respectively. In Eq 5, E is the modulus of elasticity and ν is Poisson's ratio of the material. The Jacobian matrix $[J]$ is given by

$$[J] = \begin{bmatrix} \frac{\partial x}{\partial \xi} & \frac{\partial y}{\partial \xi} \\ \frac{\partial x}{\partial \eta} & \frac{\partial y}{\partial \eta} \end{bmatrix} = \begin{bmatrix} \dots & \frac{\partial N_i}{\partial \xi} & \dots \\ \dots & \frac{\partial N_i}{\partial \eta} & \dots \end{bmatrix} \begin{bmatrix} \dots \\ x_i y_i \\ \dots \end{bmatrix} \tag{6}$$

whenever the determinant of $[J]$ is zero, the stresses and strains become singular [23-25]. (This is due to the fact the computation of $\{\epsilon\}$ requires inverse of $[J]$.)

Crack-Tip Element

The inverse square root singularity of the elastic strain field at a crack tip can be obtained by a simple technique of collapsing the quadrilateral elements into triangular elements around the crack tip as shown in Fig. 2. The side nodes 2,3 of the line segment 1-4 of length ℓ are moved to $\ell/9$ and $4\ell/9$ positions measured from the tip, node 1. Similarly, nodes 9 and 8 of the line segment 7-10 of length ℓ (we choose to use isosceles triangles

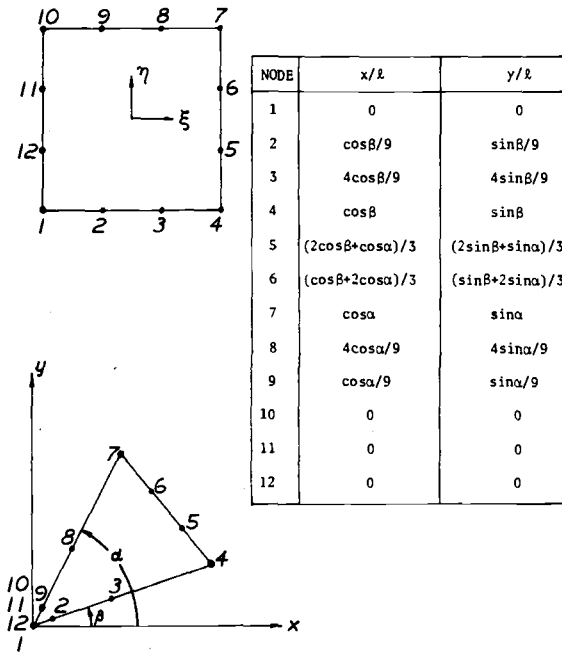


FIG. 2—A normalized square in (ξ, η) plane mapped into a collapsed triangular element in (x, y) plane with the side $\xi = -1$ degenerated into a point at the crack tip.

around a crack tip, but any scalene triangles may be used) are moved to $\ell/9$ and $4\ell/9$ from node 10 which coincides with nodes 11, 12, and 1. The line segment 4-7 must be straight and the nodes 5 and 6 must divide the line segment into equal segments. Otherwise numerical results may become unstable [27,29]. From Eq 3 the Cartesian coordinates of any point (ξ, η) , $-1 \leq \xi \leq 1$ and $-1 \leq \eta \leq 1$, are

$$\begin{aligned}
 x &= (\ell/8)(1 + \xi)^2[(1 - \eta) \cos \beta + (1 + \eta) \cos \alpha] \\
 y &= (\ell/8)(1 + \xi)^2[(1 - \eta) \sin \beta + (1 + \eta) \sin \alpha]
 \end{aligned}
 \tag{7}$$

The Jacobian then becomes

$$|J| = (\ell/4)^2(1 + \xi)^3 \sin(\alpha - \beta)
 \tag{8}$$

This shows the strain is singular at $x = 0$ ($\xi = -1$) along any ray from $x = 0$ since $|J| = 0$ at $\xi = -1$ for all η . It has been shown in Ref 27 that the singularity of the strain field at $r = 0$ is of the order of $(1/\sqrt{r})$ if the nodes 1, 10, 11, and 12 are tied together during deformation, that is

$$\begin{aligned}
 u_1 &= u_{10} = u_{11} = u_{12} \\
 v_1 &= v_{10} = v_{11} = v_{12}
 \end{aligned}
 \tag{9}$$

If nodes, 1, 10, 11, and 12 are not tied together, then the strain singularity is of the order of $(1/r)$, the perfect plastic singularity. This is analogous to the findings in Ref 30 for quadratic, isoparametric elements. However, the authors have found that the multipoint constraint has little effect on numerical results for the elastic plane problem of a circular ring with multiple cracks.

Determination of Stress Intensity Factors

If displacements of a node near the crack tip obtained from the finite element method are substituted into the well-known near crack-tip displacement formula [31], the stress intensity factor can be computed simply. There are a number of ways to estimate the stress intensity factors [32] from the nodal displacements. A simple, yet accurate way for a Mode I crack is the use of vertical component of the relative displacement of node 14 in reference to node 10, Fig. 3.

$$K_I = \left(\frac{2\pi}{\ell} \right)^{1/2} \frac{3E(v_{14} - v_{10})}{(1 + \nu)(\kappa + 1)} \quad (10)$$

where

$$\begin{aligned} \kappa &= (3 - \nu)/(1 + \nu), \text{ for plane stress, and} \\ \kappa &= 3 - 4\nu, \text{ for plane strain.} \end{aligned}$$

This simple formula gives good results if 1 to 2 percent of the crack length is used for $(\ell/9)$, the distance between the crack tip and the nearest node.

Idealization of a Ring Sector

The internal pressure p applied on the internal bore leads to stress boundary conditions on the boundary of radial cracks. Since the stress intensity factor K_I associated with radial cracks in an internally pressurized cylinder is the same as that produced by uniform axisymmetric tension of equal magnitude applied on the external boundary we consider this external loading in the present finite element method.

A great advantage of using cubic isoparametric elements is that only a few elements are needed to model an elastic structure containing cracks. Let the number of radial cracks be n and let the cracks be of equal depth and equally spaced. The central angle between two adjacent cracks is $2\pi/n$. Let R_1 and R_2 be inner and outer radii of the ring; the diameter ratio R_2/R_1 is denoted by W . The wall thickness of the ring, $t = R_2 - R_1 = R_1(W - 1)$, is used to normalize the crack depth a . The crack-depth to wall-thickness ratio a/t is called the dimensionless crack length, an important parameter used in this analysis. For the axisymmetric problem,

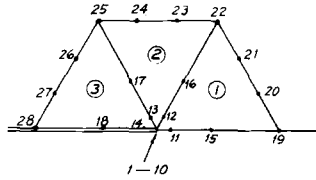
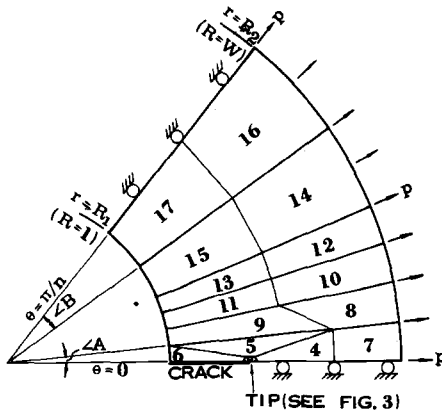


FIG 3—Three collapsed triangular elements surrounding a Mode I crack tip.

the region of interest is confined by $1 \leq R \leq W$ and $0 \leq \theta \leq \theta_0$, where $\theta_0 = \pi/n$ and $R = r/R_1$, Fig. 4. The pair (r, θ) are polar coordinates with the center of the cylinder as the pole and the line on which lies the only crack in the region of interest as the polar axis. The region of interest is subdivided into several sectors. The maximum number of sectors (NS) used is 6 and the maximum number of elements (NE) is 17. The number of nodes (NN) for 17 elements is 119. The sector containing the crack has seven elements. The remaining sectors have only two elements in each sector. A reduction of two elements and thirteen nodes will result from a reduction of one sector. The sector containing the crack has a central



n	1	2	3	4	5	6	8	9	10	12	15	18	20	30	40
NE				17						15	13	11	9		
NN				119						106	93	80	67		
NS				6						5	4	3	2		
NA	1	1	2	4	6	4	3	5	6	5	4	2	3	2	1
NB	5	5	4	2	0	2	3	1	0	0	0	1	0	0	1
∠A	7.5		6.0		4.5					3.0					
∠B	34.5	16.5	12.5	10.5	0	6.0	4.5	5.0	0	0	0	4.0	0	0	1.5

FIG. 4—The region of interest for a ring with n radial cracks and the finite-element idealization.

angle $\angle A$. The central angle of the remaining sectors may be either $\angle A$ or $\angle B$. Let N_A and N_B be the number of sectors having central angle $\angle A$ and $\angle B$, respectively. The sum of N_A and N_B is the total number of sectors used for that particular geometry. A table in Fig. 4 gives the actual values of N_E , N_N , N_S , N_A , N_B , $\angle A$, $\angle B$ used in our numerical computation for $n = 1$ to 40.

Figure 5 gives the actual idealization for a cylinder with two diametrically opposed cracks. The region of interest is a quarter of the cylinder. We have used $N_E = 17$, $N_N = 119$, $N_S = 6$, $N_A = 1$, $N_B = 5$, $\angle A = 7.5$ deg, and $\angle B = 16.5$ deg. The numbering sequence of the seven elements and their nodes varies slightly depending on the dimensionless crack length. For crack length $a/t \leq 0.6$ the elements are numbered as shown in Fig. 5a. For $a/t > 0.6$, the change is shown in Fig. 5b.

Computer Programs NASTRAN and APES

The NASTRAN implementation of the 12-node quadrilateral follows that of the 8-node quadrilateral as described in Ref 25. The dummy user element facility of NASTRAN is used. This requires coding routines to calculate element stiffness matrixes and stress recovery computations. Modifications to existing NASTRAN source code are made to provide

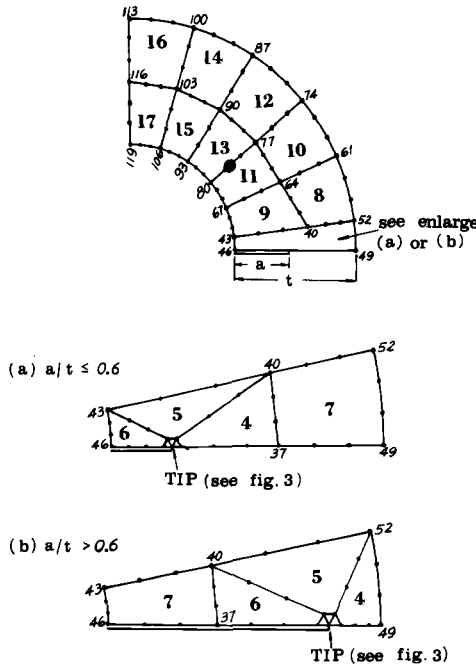


FIG. 5—The idealization of a ring with two radial cracks and the numbering sequence for (a) $a/t \leq 0.6$ and (b) $a/t > 0.6$.

proper output formats for the element. Stress intensity factors for Mode I cracks are calculated using Eq 10 and using the multipoint constraint, Eq 9. Three-point (four-point as optional) Gaussian quadrature normally is used to evaluate each partial integrations of the double integral in Eq 4. All stiffness computations are performed in double precision while stress recovery is performed in single precision.

The finite element computer program APES [26], an acronym for Axisymmetric/Planar Elastic Structures, is a special program, using 12-node quadrilateral elements. It automatically generates coordinates of nodes intermediate to element corner nodes for a straightline element edge. The work-equivalent loads are computed automatically for arbitrarily distributed stresses along any element edge. The result of these features greatly reduces both the effort of input data preparation and the probability of error. Because of the convenience, APES is chosen in the present computation of stress intensity factors for multiple cracks.

For linear elastic fracture mechanics applications, APES has two special crack-tip elements for users to choose. The first of these is a circular core element [19] centered on the crack tip in which the leading terms of the elastic singular solution are taken to dominate. The second is simply an enrichment of the 12-node isoparametric element [22]. We believe the collapsed 12-node triangular elements are more convenient to use for crack problems than either of the two special crack tip elements originally used in APES. We modified the program slightly to avoid the use of special crack-tip elements. A collapsed triangular element around a crack tip is defined as an ordinary quadrilateral element with four nodes having the same coordinates and four intermediate nodes shifted to $\ell/9$ and $4\ell/9$ positions. The multipoint constraint conditions, Eq 9, are not available in APES. Since the effect in the elastic range is negligibly small, the stress intensity factors are computed by Eq 10 with nodes 1 to 10 not tied together in the direction of crack. In the direction perpendicular to the crack conditions $v_1 = v_2 = \dots = v_{10} = 0$ are used.

Numerical Results

The computer program APES, incorporated with collapsed 12-node triangular elements as singular elements around a crack tip, is used to evaluate stress intensity factors for a thick-walled cylinder with one and two radial cracks. Comparing with Bowie and Freese's results, the present finite element results are in better agreement than those of Shannon's finite element results. Table 1 lists values of $K_I/p\sqrt{a}$ for the case of single radial crack for various values at a/t and for $W = 1.6$ and 2.5 . The values in Columns 1 and 2 of the table are either calculated from Table 1 of Underwood [13] or from Fig. 7-6 of Shannon [33]. The difference between our finite element results and those of Bowie and Freese

TABLE 1—Values of $K_I/p\sqrt{a}$ for pressurized cylinders with one crack.

W	a/t	(1) Bowie and Freese	(2) Shannon	(3) Pu and Hussain	(3)/(1)
1.6	0.1	6.39	5.80	6.34	0.992
	0.2	6.58	6.32	6.70	1.018
	0.3	7.10	6.85	7.01	0.987
	0.4	7.82	7.50	7.92	1.013
	0.5	8.60	8.20	8.53	0.992
	0.6	9.38	8.95	9.22	0.983
	0.7	10.16	9.90	10.26	1.010
	0.8	11.01	11.07	11.29	1.025
2.5	0.1	4.16	3.85	4.26	1.024
	0.2	3.97	3.80	4.05	1.020
	0.3	3.92	3.80	3.84	0.980
	0.4	3.97	3.90	3.99	1.005
	0.5	4.06	4.00	4.09	1.007
	0.6	4.25	4.20	4.28	1.007
	0.7	4.58	4.50	4.59	1.002
	0.8	5.10	5.00	5.04	0.988

are, in general, within a 2 percent range. Similar agreement is found for cylinders with two radial cracks.

The weight function method employed by Grandt [17] also gives accurate results for one and two radial cracks. For $W = 2.0$, the graphs of $K_I/p\sqrt{a}$ versus a/t based on values obtained from either the weight function method or the present finite element method could not be distinguished from those labeled with $n = 1$ and 2 shown in Fig. 6 obtained by Bowie and Freese using the mapping collocation method.

With the confidence thus gained, the computer program APES is used to calculate stress intensity factors of cylinders with many radial cracks. Using the idealization given in Fig. 4, stress intensity factors are obtained for $n = 1$ to 40, $a/t = 0.1$ to 0.6 and for $W = 1.5, 2.0$ and 2.5. Results are shown in Figs. 6 through 9. There are very few reliable numerical results available in the literature for stress intensity factors of finite ring with more than two radial cracks. We found only Goldthorpe's results for 40 cracks [9] and Baratta's results for 36 and 48 cracks [15] for $W = 2.0$. For the purpose of comparison, we obtained $K_I/p\sqrt{a}$ for 20 cracks for a ring of $W = 2.0$ using a load relief factors method [15] and the data for multiple cracks at a circular hole in an infinite solid by Tweed and Rooke [6]. The results and Baratta's results for 36 cracks, those of Goldthorpe's 40 cracks together with the current finite element results for 20 and 40 cracks are plotted in Fig. 6. It can be seen that stress intensity factors estimated by Goldthorpe are too low while those by Baratta are too high when compared with results obtained by our finite element method.

In Figs. 7 through 9, we plotted $K_I/p\sqrt{R_1}$ instead of $K_I/p\sqrt{a}$ versus n for three different values of W . The quantity $K_I/p\sqrt{R_1}$ gives the actual value of

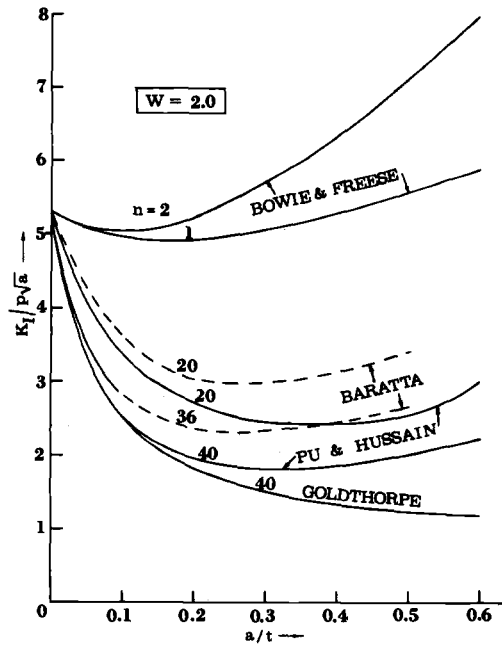


FIG. 6—Comparison of stress intensity factors by different methods for a ring with n radial cracks.

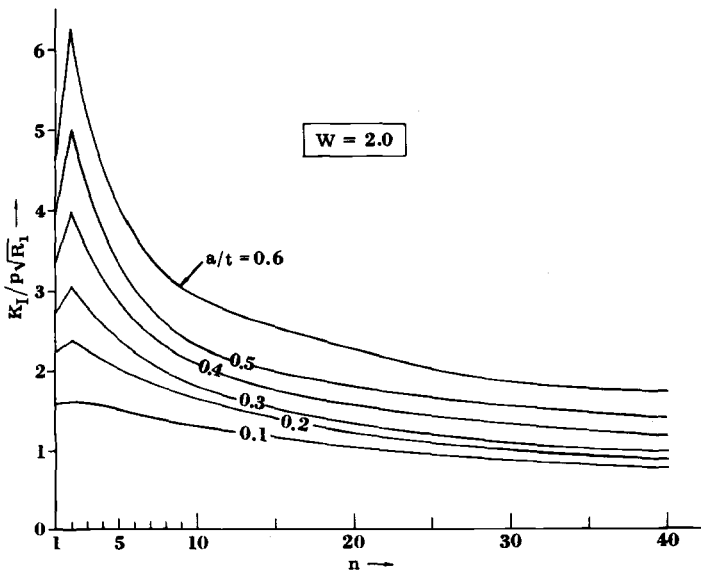


FIG. 7— $K_I / p\sqrt{R_1}$ versus n for various values of a/t for $W = 2.0$.

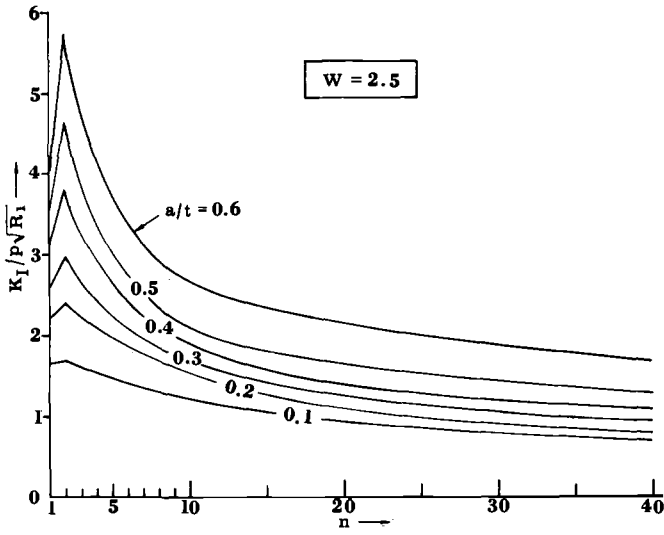


FIG. 8— $K_I/p \sqrt{R_1}$ versus n for various values of a/t for $W = 2.5$.

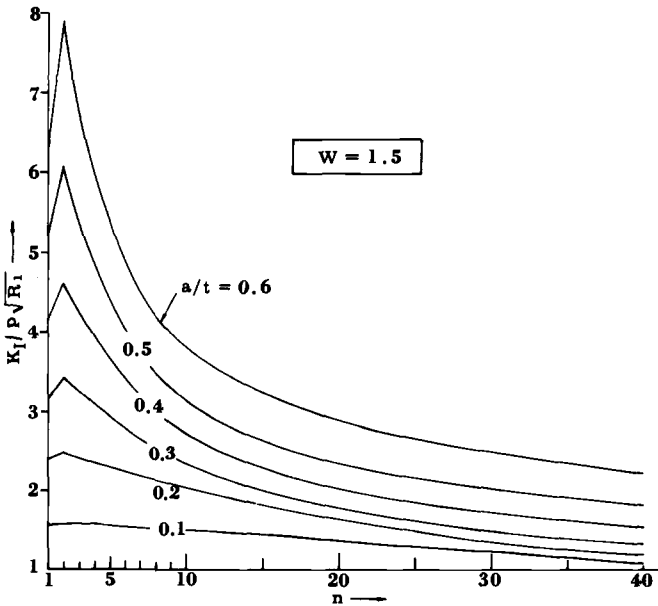


FIG. 9— $K_I/p \sqrt{R_1}$ versus n for various values of a/t for $W = 1.5$.

K_I for $p = 1$ and $R_1 = 1$. An obvious maximum of $K_I/p\sqrt{R_1}$ is seen at $n = 2$ for $a/t > 0.1$. The value of $K_I/p\sqrt{R_1}$ decreases rather fast as the number of cracks increases from $n = 2$. The drop in $K_I/p\sqrt{R_1}$ levels off for $n > 20$. For $a/t > 0.1$, it is safe to conclude that the two-crack situation represents the worst case of multiple cracking. The case of three-crack situation is the next worst situation. The single-crack situation is usually worse than the case of four cracks. For $a/t = 0.1$ variation in $K_I/p\sqrt{R_1}$ is so small that the difference between the maximum and the next highest value is within the limit of accuracy of the finite element method. Further numerical results must be obtained to give definite conclusion whether the maximum of $K_I/p\sqrt{R_1}$ always occurs at $n = 2$ even for very shallow cracks. However it becomes less important whether the worst situation is still the two crack case since the stress intensity factors remain nearly a constant for small values of n for very shallow cracks. In other words, in the initial stage of multiple cracking, each crack has little effects on the growth of other cracks.

Conclusions

The use of collapsed 12-node triangular elements as singular crack tip elements has been shown to give excellent results for a thick-walled cylinder with multiple radial cracks. The numerical results show that the two-crack case is in general the worst situation in multiple cracking. For large crack depths, the stress intensity factor for the worst situation may be as high as 150 percent of that of the corresponding single crack case. For a very shallow crack, the stress intensity factor of a cracked cylinder will not be affected significantly by the presence of other shallow cracks in a relatively large crack spacing. Hence the single crack case may be used to represent the multiple crack situation when the relative crack depth to crack spacing ratio is small. The effect of interaction of cracks on the stress intensity factor of a cracked cylinder in terms of the dimensionless crack length, the diameter ratio, and the relative ratio of crack depth to crack spacing can be studied by the present method using unequal crack depths and unequal spacing of radial cracks.

Acknowledgment

The authors wish to thank L. N. Gifford, Jr. of Naval Ship Research and Development Center for providing the computer program APES for our use.

References

- [1] Bowie, O. L., *Journal of Mathematics and Physics*, Vol. 35, pp. 60–71.
- [2] Westmann, R. A., *Journal of Mathematics and Physics*, Vol. 43, pp. 191–198.
- [3] Kutter, H. K., *International Journal of Fracture Mechanics*, Vol. 6, 1970, pp. 233–247.
- [4] Tweed, J. and Rooke, D. P., *International Journal of Engineering Science*, Vol. 11, 1973, p. 1185.

- [5] Tweed, J. and Rooke, D. P., *International Journal of Engineering Science*, Vol. 12, 1974, p. 423.
- [6] Tweed, J. and Rooke, D. P., *International Journal of Engineering Science*, Vol. 13, 1975, pp. 653–661.
- [7] Winne, D. H. and Wundt, B. M., *Transactions*, American Society of Mechanical Engineers, Vol. 80, 1958, pp. 1643–1658.
- [8] Williams, J. G. and Isherwood, D. P., *Journal of Strain Analysis*, Vol. 3, 1968, pp. 17–22.
- [9] Goldthorpe, B. D., "Fatigue and Fracture of Thick Walled Cylinders and Gun Barrels," *Case Studies In Fracture Mechanics*, T. P. Rich and D. J. Cartright, Eds., Army Materials and Mechanics Research Center, Technical Report MS 77–5, 1977.
- [10] Cartright, D. J. and Rooke, D. P., *Engineering Fracture Mechanics*, Vol. 6, 1974, p. 563.
- [11] Bowie, O. L. and Neal, D. M., *International Journal of Fracture Mechanics*, Vol. 6, 1970, p. 199.
- [12] Bowie, O. L. and Freese, C. E., *Journal of Engineering Mechanics*, Vol. 4, 1972, pp. 315–321.
- [13] Underwood, J. H., *International Journal of Pressure Vessels and Piping*, Vol. 3, 1975, p. 229.
- [14] Neuber, H., "Theory of Notch Stresses," AEC TR 4547, 1958.
- [15] Baratta, F. I., "Stress Intensity Factors For Internal Multiple Cracks in Thick-Walled Cylinders Stressed by Internal Pressure Using Load Relief Factors," *Engineering Fracture Mechanics* (in press).
- [16] Rice, J. R., *International Journal of Solids and Structures*, Vol. 8, 1972, pp. 751–758.
- [17] Grandt, A. F., Jr., "Two Dimensional Stress Intensity Factor Solutions for Radially Cracked Rings," AMFL-TR-75-121, Air Force Materials Laboratory, 1975.
- [18] Shannon, R. W. E., *International Journal of Pressure Vessels and Piping*, Vol. 2, 1974, p. 19.
- [19] Wilson, W. K., "Combined Mode Fracture Mechanics," Ph.D. dissertation, University of Pittsburgh, 1969.
- [20] Tracey, D. M., *Engineering Fracture Mechanics*, Vol. 3, 1971, pp. 255–265.
- [21] Blackburn, W. S., "Calculation of Stress Intensity Factors at Crack Tips Using Special Finite Elements," *The Mathematics of Finite Elements and Applications*, Brunel University, 1973.
- [22] Benzley, S. E. and Beisinger, A. E., "Chiles—A Finite Element Computer Program that Calculates the Intensities of Linear Elastic Singularities," Technical Report SLA-73-0894, Sandia Laboratories, 1973.
- [23] Henshell, R. D. and Shaw, K. G., *International Journal of Numerical Methods in Engineering*, Vol. 9, 1975, pp. 495–507.
- [24] Barsoum, R. S., *International Journal of Numerical Methods in Engineering*, Vol. 10, 1976, pp. 25–37.
- [25] Hussain, M. A., Lorensen, W. E., and Pflegl, G., NASA TM-X-3428, National Aeronautics and Space Administration, 1976, p. 419.
- [26] Gifford, L. N., Jr., Report 4799, Naval Ship Research and Development Center, 1975.
- [27] Pu, S. L. and Hussain, M. A., "The Collapsed Cubic Isoparametric Element as a Singular Element for Crack Problems," *International Journal of Numerical Methods in Engineering*, Vol. 12, 1978, pp. 1727–1742.
- [28] Zienkiewicz, O. O., *The Finite Element in Engineering Science*, McGraw Hill, London, 1971.
- [29] Hussain, M. A. and Lorensen, W. E. in *Proceedings*, 15th Midwest Mechanics Conference, March 1977, p. 40.
- [30] Barsoum, R. S., *International Journal of Numerical Methods in Engineering*, Vol. 11, 1977.
- [31] Williams, M. L., *Journal of Applied Mechanics*, Vol. 24, 1957, pp. 109–114.
- [32] Pu, S. L., Hussain, M. A., and Lorensen, W. E., "Collapsed 12-Node Triangular Elements As Crack Tip Elements For Elastic Fracture," Report AR-LCB-TR-77047, Watervliet Arsenal, 1977.
- [33] Shannon, R. W. E., "The Application of Linear Elastic Fracture Mechanics to the Internally Pressurized Thick-Walled Cylinder," Ph.D. dissertation, The Queen's University of Belfast, 1970.

E. M. Smoley¹

Interpretations of Crack Surface Topologies for Poly(Vinyl Chloride)

REFERENCE: Smoley, E. M., "Interpretations of Crack Surface Topologies for Poly(Vinyl Chloride)," *Fracture Mechanics, ASTM STP 677*, C. W. Smith, Ed., American Society for Testing and Materials, 1979, pp. 700–716.

ABSTRACT: Craze and crack growth were described on Mode I subcritical crack surface topologies formed in unplasticized and plasticized poly(vinyl chloride) (PVC). Types of deformations and material separations were noted. Topologies also were examined for the effects of suppressing the secondary β relaxation process, which is a molecular motion in the PVC polymer chain. A crack surface feature formed by catastrophic crack velocities was discussed.

KEY WORDS: poly(vinyl chloride), craze, crack, subcritical velocity, fractography, crack surface topology, β -relaxation, crack nucleation, ductile-brittle transition, microvoid coalescence, plastic instability, fatigue (materials), crack propagation

The objective is to identify and interpret, using the microscopic techniques of fractography, some characteristic crack surface topologies formed in poly(vinyl chloride) (PVC) by cracks propagating at subcritical and catastrophic velocities.

Crack surface topologies examined by microscopic fractography [1]² are important since they reflect rather strongly on the mechanics of deformation and fracture that participate in crack nucleation, propagation, and arrest. The topologies frequently reveal something about the type of mechanical bulk properties that might be related to the material separation process occurring at a crack tip. Moreover, ductile-brittle transitions are identified by crack surface topologies, for example, from plane strain to plane stress, from one form of microstructure to another, and from small scale to large scale yielding. Topologies are evidence of

¹ Senior research scientist, Armstrong Cork Co. Research and Development Center, Lancaster, Pa. 17604.

² The italic numbers in brackets refer to the list of references appended to this paper.

deformations; consequently, they frequently can be interpreted in terms of the corresponding stresses. They are a significant factor in identifying the dissipative mechanisms that inhibit crack growth. Even crack nucleation and growth can be described from observations of crack surface features. Finally, the use of such topologies in application or engineering failure analysis is well documented in fracture mechanics literature.

Experimental

Material Composition

Material ingredients consist of a PVC resin, Firestone's FPC 9282; a plasticizer, di-2-ethyl hexyl phthalate (DOP); and a dibutyltin thermal stabilizer. The amounts of plasticizer were 40, 17.5, 15, and 5 parts by weight per 100 parts (phr). At each plasticizer level there were 2 phr of thermal stabilizer. The \bar{M}_w for the PVC resin is 5.51×10^4 , and the \bar{M}_n is 2.91×10^4 .

Material-Process Conditions

Ingredients were mixed, using dry-blending techniques, in a Henschel mixer. Consolidation and fusion of the mix were carried out in a cavity mold. Six minutes were allowed for the mold containing the mix to preheat from room temperature to 177°C. The mold then was pressurized and maintained at 177°C for an additional 6 min. At the end of this time, the heat was discontinued and a final 6-min period was allowed for the mold to cool to room temperature while the cavity pressure was maintained.

Material was fabricated in sheets 23 by 23 by 0.32 cm. Only fully consolidated material was selected for test. Full consolidation was indicated by equality between the theoretical and experimentally measured density. The density was calculated from the weighted sum of specific volumes for the ingredients.

Apparatus

Crack surface topologies were obtained from a dog-bone tensile specimen (type I) as described in ASTM Test for Tensile Properties of Plastics (D 638 - 76). Specimens were fabricated from the material in sheet form. Gage length and width of the uniform section was 5.7 and 1.3 cm, respectively. There were no preformed cracks in the specimens; the cracks nucleated because of bulk or surface heterogeneities in the material.

Specimens were installed and loaded at a constant extension rate in an Instron tensile machine to produce Mode I crack-propagation conditions. The crosshead speed was 8.5×10^{-3} cm/s; the test temperature was 23

$\pm 1.0^{\circ}\text{C}$; and the relative humidity was 50 ± 2 percent. Tests also were performed at -196°C .

A wedge-loaded double-cantilever-beam (WLDCB) specimen, described by Rosenfield et al [2] was used to observe craze development at a crack tip as well as crack propagation through the craze material.

Microscopy was carried out using a Jeolco JSM-U3 scanning electron microscope and a Leitz Ortholux-Pol research microscope. The latter was used to view crack-tip dynamics in the WLDCB geometry.

Discussion of Results

Effects of Molecular Motions on Crack Surface Topology

Figures 1, 2, and 3 are top views of a Mode I crack surface formed in a rigid PVC tensile specimen loaded in an Instron tensile tester at a slow rate at room temperature. In Fig. 1 the dark, featureless circular area includes both nucleation and subcritical topologies, however, because the topology attributed to nucleation activity is difficult to identify, the dark area is primarily subcritical. The circular boundary is where the crack tip terminated subcritical propagation and began to accelerate. Crack movement within the subcritical area was probably radially outward from the center.

A more magnified view, Fig. 2, shows the subcritical topology to consist mainly of equiaxed dimples about $2\ \mu\text{m}$ in diameter. Lips, ridges, or rims in the dimples reflect a shear mode of deformation which characterizes a ductile plastic material separation process. Dimples appear uniform in depth and exhibit some form of microsurface roughness, difficult to define because of the lack of resolution on the micrograph.

More magnification on the dimple topology can be seen in Fig. 3. The dimple features just mentioned point up that crack nucleation in rigid PVC at room temperature begins with the development of microvoids and crack propagation at subcritical velocity is attributable to the coalescence of these microvoids. The material separation process underlying the coalescence involves shear deformations and a plastic instability condition in the thinned down walls between the expanding microvoids.

The microvoids nucleate in a form of plastic deformation called a craze. Crazeing is the precursor to crack nucleation and propagation in thermoplastic polymers such as rigid PVC at room temperature; in fact, it may be the precursor to crack growth in a wide variety of other polymer structures.

The craze and crack are interrelated as shown in Fig. 4 which is a side view of a crack that propagated at subcritical velocity in a WLDCB [2] specimen fabricated from rigid PVC. Here the craze is seen as a Dugdale plastic zone which forms and propagates at the crack tip. In Fig. 4, fragments of the craze after the crack has passed through it are revealed

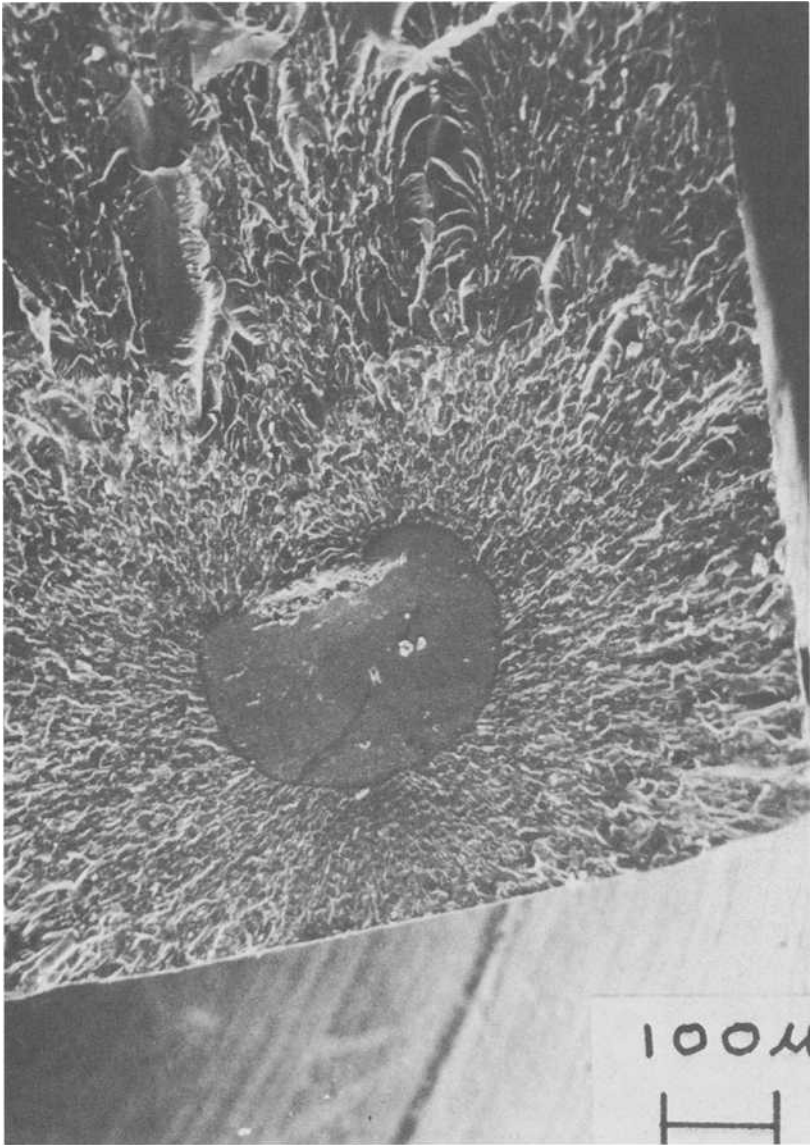


FIG. 1—The flat circular area is the subcritical-growth topology.

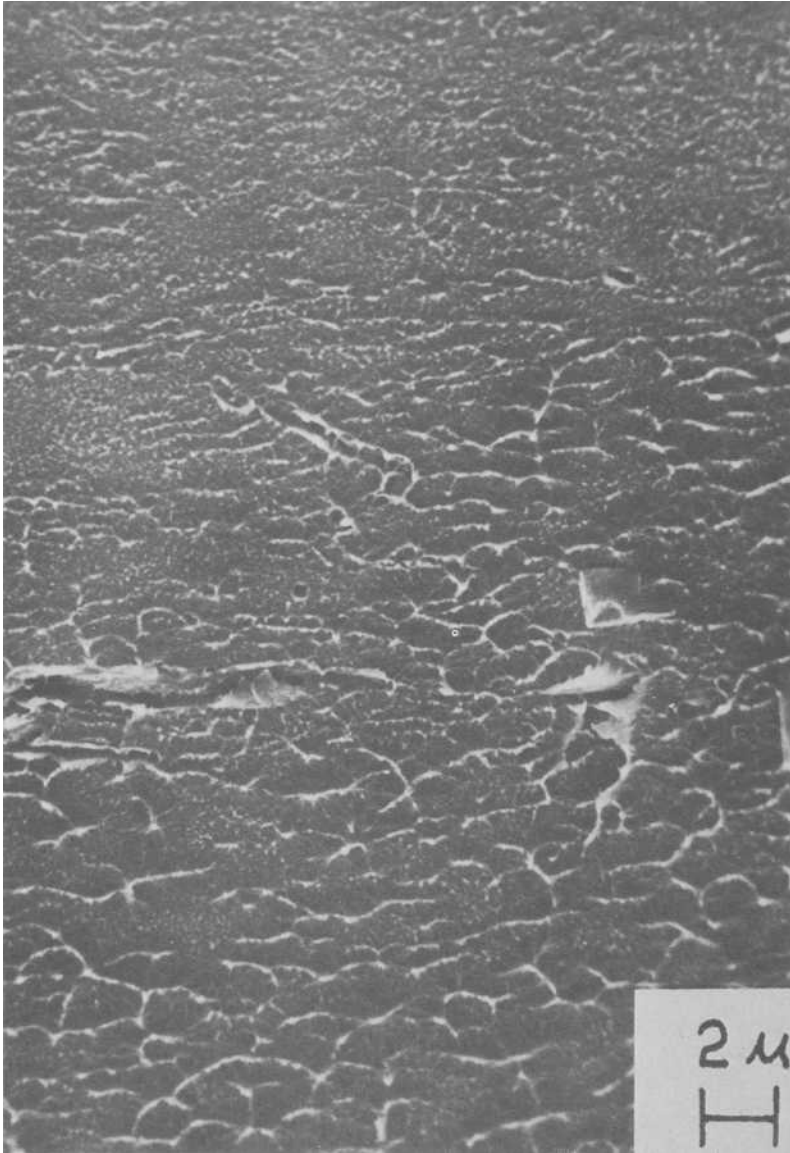


FIG. 2—A more-magnified view of the subcritical-growth area. Most of the area was formed by the coalescence of microvoids. Ridges or tips of the ruptured microvoids are outlined in white.

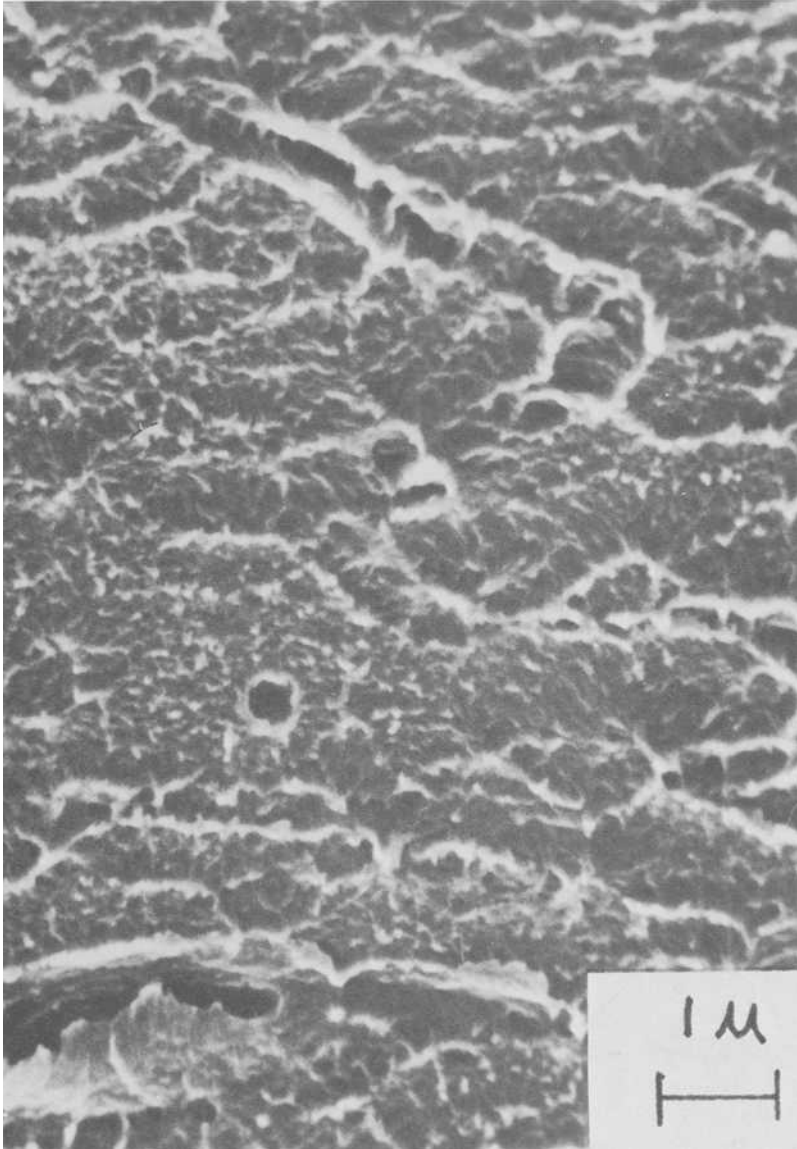


FIG. 3—At $\times 10\ 000$ the ridges on the ruptured microvoid are more discernible and the microvoid walls may be roughened by ruptured craze material.

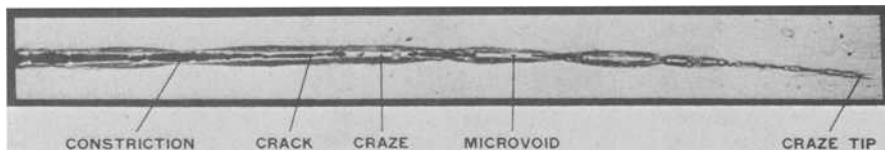


FIG. 4—A side view of a crack propagating in a wedge-loaded double-cantilever-beam geometry. At the tip one can see the double primary crazes which are just beginning to diverge.

by strips of stress-whitened material which is bounded on the top and bottom by rather wide dark bands, roughly the craze polymer boundaries.

Actually the craze itself consists of long elongated microvoids about 100 to 200 Å in diameter interconnected by oriented polymer material [3]. It is a porous structure in which the initial phases of mechanical breakdown constitute crack nucleation activity. However, the microvoids or dimples shown in the surface topology in Fig. 3 are not to be viewed as nucleation activity. Actually they form beyond the nucleation phase when the crack tip is fully developed in the craze. But the undefined microsurface roughness which has been pointed out on the surface of the dimples or microvoids in Fig. 3 could very well be a reflection of the actual craze structure consisting of even smaller microvoids on the 100 to 200 Å level.

Crack propagation through the craze is along at least three possible paths [4]. First, is microvoid coalescence where the crack tip propagates along a median plane midway between the top and bottom of the craze as shown in Fig. 4? This is the mode of propagation that gives rise to the surface topologies already described in reference to Figs. 1, 2, and 3. Second, the crack may propagate, not by microvoid coalescence, but by a viscous material separation process which leaves the crack surface topology smooth and featureless at least at the microscopy resolutions employed in the present study. Third, the crack tip may diverge from the median plane and be reflected from the craze-polymer boundaries which define the top and bottom of a craze in a Mode I stress field. In other words the crack tip oscillates between the top and bottom of the craze forming the topology shown in Fig. 5 which is a top view of a Mode I crack surface in rigid PVC. The featureless areas are where the crack tip went through the craze and the rough areas formed as concentric rings are where the crack tip spalled off uncrazed polymer as the tip was reflected from the craze-polymer boundary. Actually, the topology in Fig. 5 forms during the initial stages of crack-tip acceleration while the microvoid coalescence and the viscous modes of material separation accompanying crack-tip movement usually are associated with subcritical velocities.

Crazing is an important dissipative mechanism inhibiting crack growth not only in thermoplastic polymers but in other polymer structures as well. So it is of interest to observe the manner in which molecular motions in

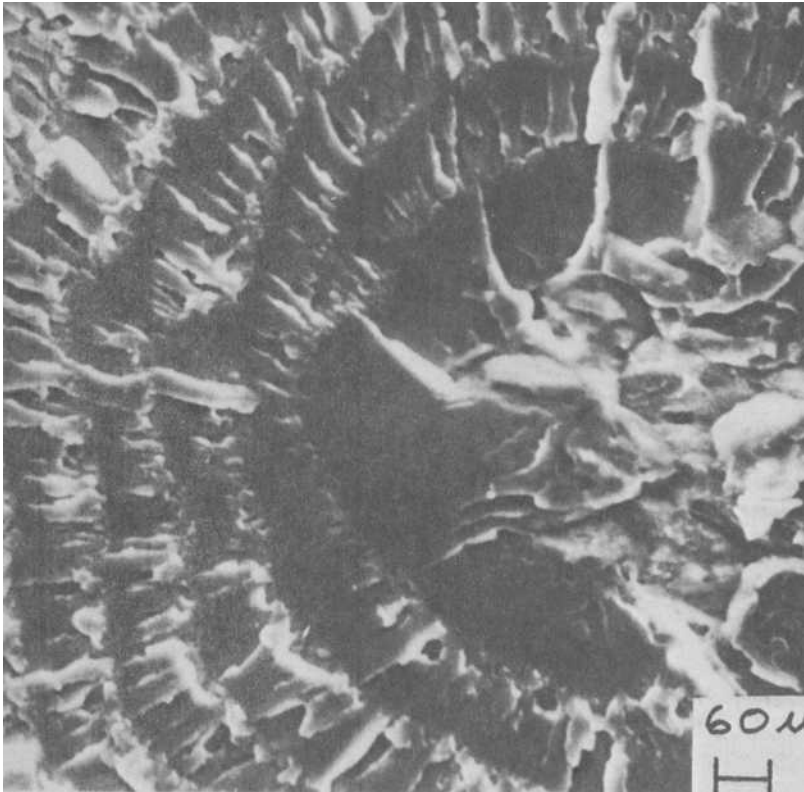


FIG. 5—Crack-propagation direction is normal to the concentric rings formed by the crack tip propagating through the craze-polymer boundary. The concentric rings were probably formed during crack-tip acceleration.

PVC affect the craze formation in terms of the crack surface topologies already described.

The PVC molecule can be viewed as a long molecular chain which near absolute zero is relatively rigid and immobile. As the temperature increases, however, certain segments of the polymer chain will begin to rotate around the chain axis with the overall shape of the molecule remaining somewhat unchanged. In PVC this mode of molecular motion or deformation occurs at about -30 to -50°C ; it is called a secondary or beta mode of relaxation. At 82°C the entire chain loses its rigidity and its center of gravity begins translatory motion. This is the glass transition temperature. In general, at any temperature the mode of deformation exhibited by a polymer chain is sometimes viewed as the superposition of all the primitive modes of deformation available at the lower temperatures. It is common knowledge that the secondary β -mode in rigid PVC at

room temperature, say 23°C, can be suppressed or impeded by the addition of 5 percent weight fraction DOP plasticizer, a processing aid. The question is what does this do to the crack surface topology.

Part of the answer is seen in Fig. 6 which is a top view of a Mode I crack surface topology. A dramatic change is indicated. Evidence of subcritical growth by microvoid coalescence, which was so prominent on the micrographs in Figs. 1, 2, and 3, has been practically eliminated, the crack apparently going directly into the accelerative phase of propagation. The rough areas probably resulted from the crack tip spalling off material from the craze-polymer boundary, with the craze itself having undergone very little extension or deformation. Thus suppression of the β process causes an abrupt ductile to brittle transition in rigid PVC at room temperature. This also is manifested by changes in certain bulk mechanical properties such as tensile strength, impact strength [6], fracture toughness, degree of nonlinearity in the stress strain curve, yield [5], and draw characteristics. Consequently, in order for the craze to be an effective dissipative mechanism inhibiting crack growth it must extend or deform and the extension is critically dependent on the β secondary deformation process in the molecular chain.

High Crack Tip Velocity Effects on Crack Surface Topology

Figure 7 is a view of a rigid PVC tensile specimen loaded to fracture in an Instron tensile machine at a slow rate at room temperature, 23°C. A crack propagated transversely across the specimen through partially drawn material while another crack propagated longitudinally in the direction of the applied tensile load. This mode of ultimate failure has been noted by other investigators, for instance, Peterlin [7] in the case of drawn polyethylene and nylon. Cross et al [8] also noted an alternation in transverse and longitudinal crack propagations in drawn rigid PVC. The longitudinal crack in Fig. 7 propagated at catastrophic velocity before being arrested; an examination of the crack surface topology revealed an interesting effect due to a high crack-tip velocity.

Figure 8 is a view looking downward onto the longitudinal crack surface; nothing unusual can be observed except for some irregular river topologies formed by cracks propagating in the same direction but on slightly different planes. However, in Fig. 9 at a higher magnification one can see the formation of long highly extended filaments. At still higher magnification in Fig. 10, more detail on the filaments is revealed. It appears that they are uniform in diameter and are highly extended, indicating the existence of plastic stability which is necessary in a material for drawability. Filaments appear to rupture in a ductile manner, that is, completely necked down and separated by shear deformations. Figure 11 is an additional example of filament formation. These are on Mode I crack



FIG. 6—Surface topology for the slightly plasticized PVC composition. The spall pattern appears random and somewhat shallow. Crack propagation was from the top to bottom of the micrograph.

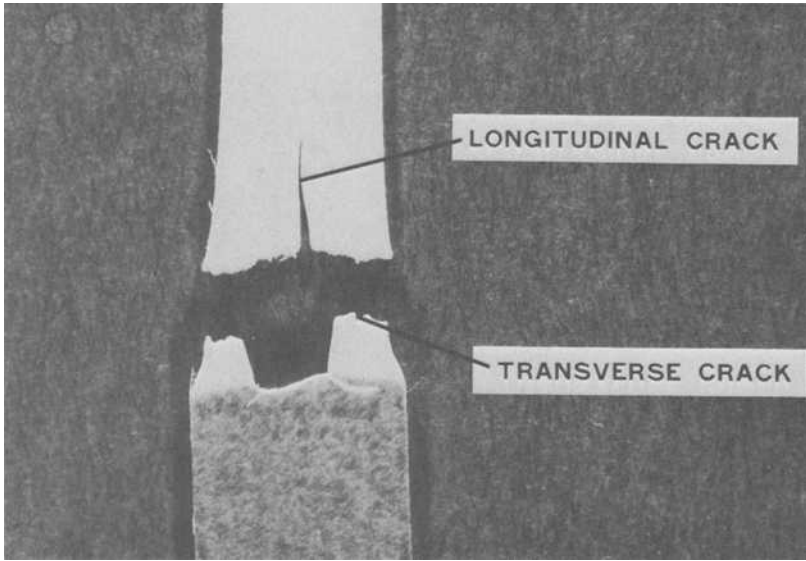


FIG. 7—Transverse and longitudinal cracks in drawn, rigid PVC.

surface formed in a highly plasticized PVC specimen exposed to an impact test having a time scale of about 3 ms.

Other investigators have observed ligament formations on crack surface topologies resulting from crack tip velocities greater than those associated with the subcritical regime. Bird et al [9] noted them on the fracture surface topology for polystyrene and attributed their formation to plastic deformation of a thin sheet of material remaining between the main crack and a secondary crack when they overtake each other on slightly different planes. Cross et al [8] also noted ligaments on the transverse crack surface topology in rigid PVC and pointed out that they resulted from an adiabatic thermal condition arising from high internal strain energies in a tensile specimen when exposed to a tensile load. Actual heat developed by a propagating crack is still a controversial matter. Kambour [10] calculated no appreciable temperature rise in poly(methyl methacrylate) for crack velocities less than 1.0 cm/s. At this low velocity, apparently heat conduction is sufficient to maintain thermal equilibrium. Marshall et al [11] correlates the onset of catastrophic crack propagation with a transition from isothermal to adiabatic conditions at the crack tip. The transition is characterized by a plastic instability induced by a thermal softening when the crack-tip changes from low to high velocity. Finally, Werchert et al [12] calculated from a theoretical model that crack-tip temperatures can attain high values at high crack velocities and points out experimental results that confirm model predictions.

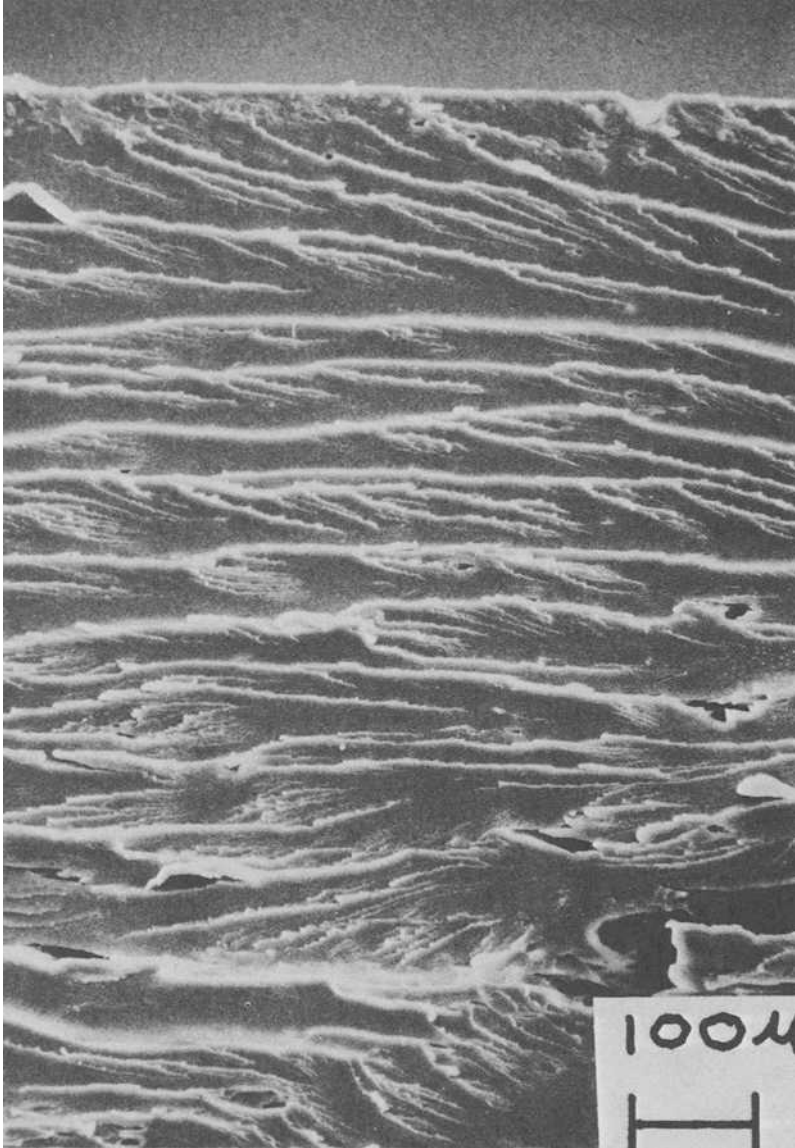


FIG. 8—*Top view of the longitudinal-crack surface.*

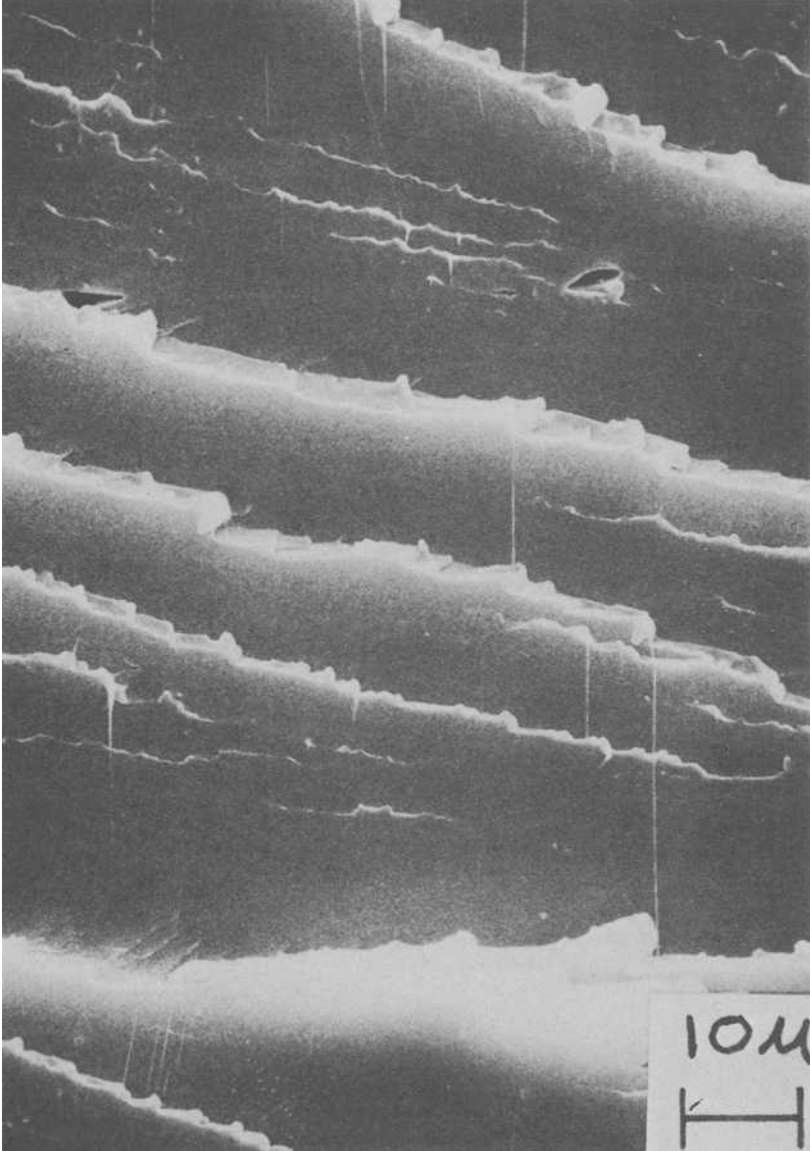


FIG. 9—A more magnified view of Fig. 8. Note the ligaments or filaments.

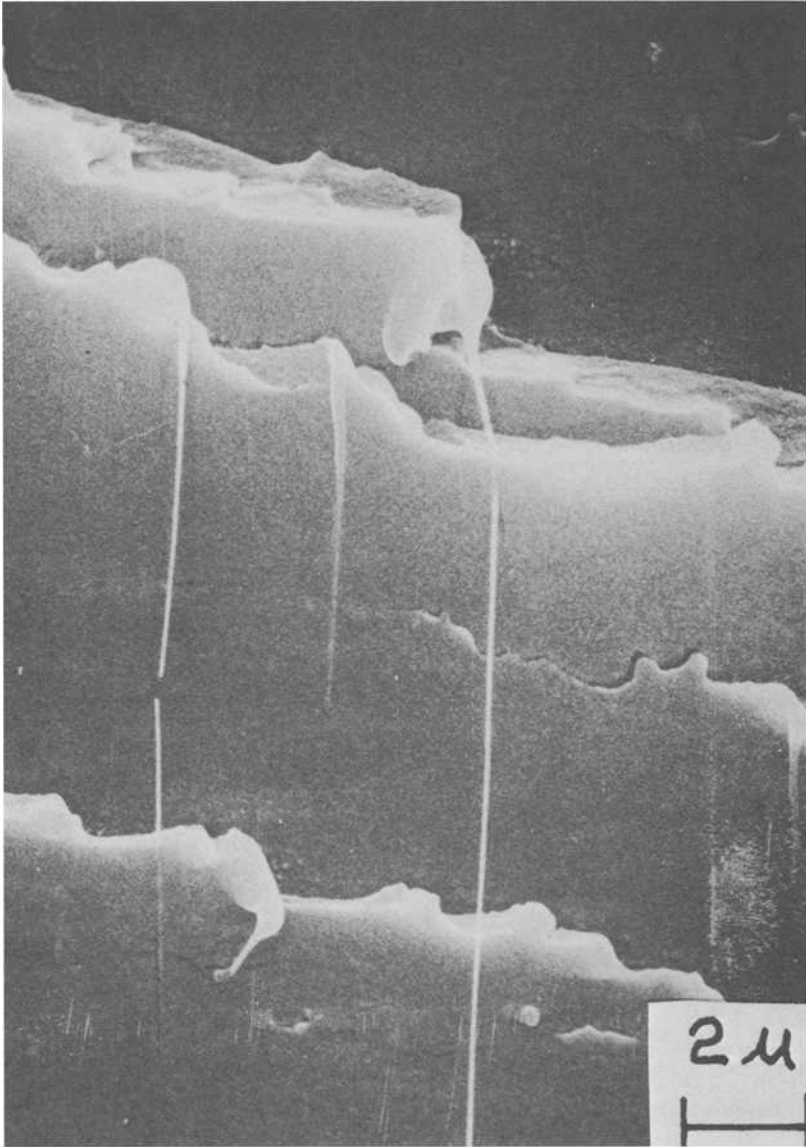


FIG. 10—Crack propagation in Figs. 8, 9, and 10 was from right to left on the micrograph. On this micrograph the tapered base of the filament can be seen.

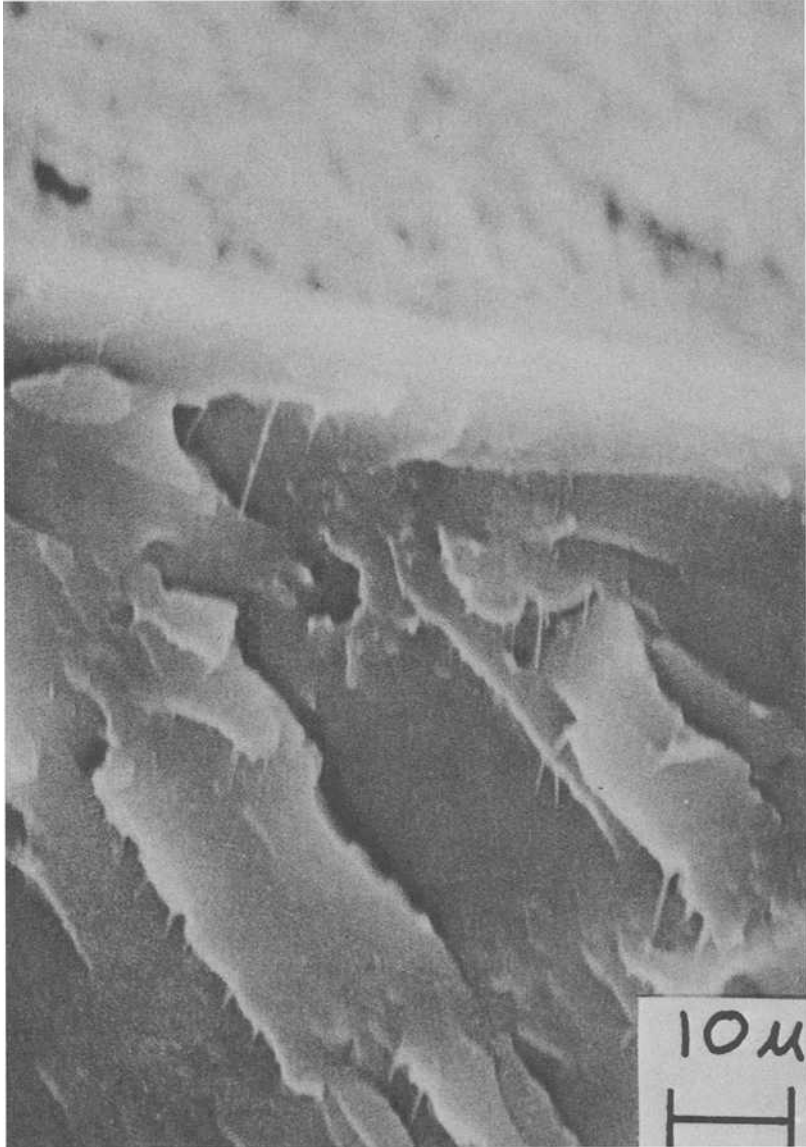


FIG. 11—*Filaments or ligaments on the crack surface topology for a highly plasticized PVC composition. Propagation direction was from the top to the bottom of the micrograph.*

Within this framework of literature background, the extension of the filaments or ligaments shown in Figs. 8, 9, 10, and 11 was possible because of a plastic stability condition local to the propagating crack tip. Also there is evidence of the shearing condition noted by Bird et al [9] and of the adiabatic thermal condition noted by Cross et al [8]. This evidence is most obvious in Fig. 10 where the ligaments appear to originate and extend from the side of a step in a river pattern. However, whatever their nature, origin, and formation, the filaments are important because they are probably germane to the technology of drawing. There is evidence [13] for speculating that the β deformation process in the PVC molecular chain may also have a role in the formation of the filament topology.

Summary

Mode I crack nucleation in rigid unplasticized PVC originates in crazing. One mechanism of subcritical crack propagation involves the process of microvoid growth and coalescence in the median craze plane. The material separation process in the coalescence appears to be a plastic instability developing in the walls between microvoids. Addition of a small level of di-2-ethyl hexyl phthalate (DOP) in PVC to suppress the secondary β -process in the molecular chain, practically eliminates the subcritical surface topology. Consequently, β molecular motions are involved in the ability of the polymer chain to make long-range cooperative configurational changes essential for craze extension which is a factor in inhibiting crack growth.

Long, highly extended ligaments or filaments have been noted on catastrophic crack surfaces for both rigid and highly plasticized PVC. They appear to stem from an adiabatic thermal condition and a shear deformation condition formed when multiple cracks intersect or join up on a common crack front. Ligaments may be evidence of the materials ability to undergo extensive localized drawing.

References

- [1] Wolock, I., and Newman, S. B. in *Fracture Processes in Polymer Solids*, B. Rosen, Ed., Interscience, New York, 1964, p. 235.
- [2] Rosenfield, A. R. and Mincer, P. M., *Journal of Polymer Science*, No. 32, 1971, p. 283.
- [3] Kambour, R. P., *Journal of Polymer Science*, Vol. 7, 1973, p. 1.
- [4] Doyle, M. J., *Journal of Polymer Science*, Vol. 13, 1975, p. 127.
- [5] Baumens-Cromet, C., Baumens, J. C., and Homes, G., *Journal of Polymer Science*, Vol. 7, 1969, p. 235.
- [6] Boyer, R. F., *Polymer Engineering and Science*, Vol. 8, No. 3, 1968, p. 161.
- [7] Peterlin, A., *Journal of Macromolecular Science—Physics*, B8 (1-2), 1973, p. 83.
- [8] Cross, A. and Howard, R. N., *Journal of Polymer Science*, Vol. 11, 1973, p. 2423.
- [9] Bird, R. J., Mann, J., Pogany, G., and Rooney, G., *Polymer*, Vol. 7, No. 7, 1966, p. 307.

- [10] Kambour, R. P. and Barker, R. E., Jr., *Journal of Polymer Science*, Vol. 4, 1966, p. 359.
- [11] Marshall, G. P., Coutts, L. H., and Williams, J.G., *Journal of Material Science*, Vol. 9, 1974, p. 1409.
- [12] Werchert, R. and Schonert, K., *Journal of Mechanics and Physics of Solids*, Vol. 22, 1974, p. 127.
- [13] Smoley, E. M., *Journal of Applied Polymer Science*, Vol. 20, 1976, p. 217.

Engineering Applications

M. E. McDermott¹ and R. I. Stephens¹

Experimental Determination of K_I for Hollow Rectangular Tubes Containing Corner Cracks

REFERENCE: McDermott, M. E. and Stephens, R. I., "Experimental Determination of K_I for Hollow Rectangular Tubes Containing Corner Cracks," *Fracture Mechanics, ASTM STP 677*, C. W. Smith, Ed., American Society for Testing and Materials, 1979, pp. 719-733.

ABSTRACT: This research used the fatigue crack growth rate experimental method to obtain K_I for an initial circular corner crack in a hollow rectangular tube subjected to pure bending. Reference crack growth rate data were obtained using compact tension (CT), single edge notch (SEN) and four-point (4-pt) bend specimens. Three mild steel tube height-to-width ratios, h/w (2/3, 1, and 3/2) were tested. K_I was obtained for both top face and side face cracks within 30 percent experimental deviation for the three h/w ratios. Least square conservative upper bound equations were obtained. The conservative upper bound results are proposed as general K_I expressions applicable to design situations.

KEY WORDS: fracture mechanics, stress intensity, cracks, crack growth, fatigue (materials), tubes, steel, design

Fracture mechanics principles are being used to analyze and predict fatigue crack growth life of many structural components. To apply these principles, the engineer must have an expression for the stress intensity factor for the crack geometry and component of concern. Approximate stress intensities for complex crack geometries and components can often be obtained through a combination of known correction factors, numerical, analytical, or experimental methods. The purpose of this research was to determine experimentally the opening mode stress intensity factor, K_I , for a hollow rectangular tube, subjected to pure bending, which initially contains an external circular corner crack. The beam and basic geometry of the corner crack are shown in Fig. 1. The crack lies in the plane of the

¹ Research assistant and professor, respectively, Materials Engineering Division, University of Iowa, Iowa City, Iowa 52242.

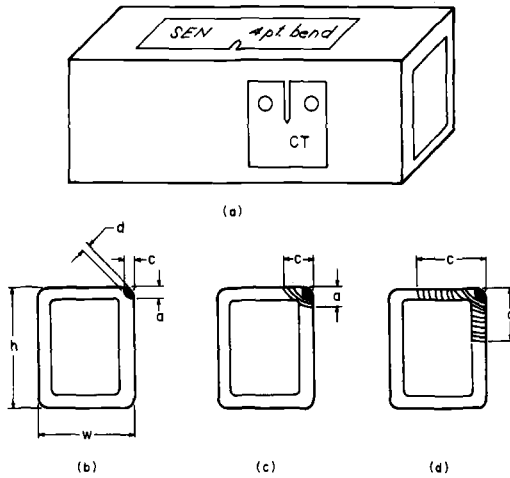


FIG. 1—Reference specimen positions and tube corner crack geometry.

cross section. K_I was desired at all external surface positions from the initial corner crack position, Fig. 1*b*, to where the crack intersects the inner corner, Fig. 1*c* and to where the crack propagates along both the top and side faces, Fig. 1*d*. K_I was developed for crack positions as measured by lengths c and a on the top and side surfaces respectively as shown in Figs. 1*b* to 1*d*. Independent data analysis on each face of the tube resulted in two distinct dependent functional expressions for K_I .

The experimental method utilized the log-linear portion of the sigmoidal curve of crack growth rate versus stress intensity range as given by

$$\frac{da}{dN} = A (\Delta K)^n \quad (1)$$

This method has been used to obtain K_I for various complex shapes and also to verify numerical K_I solutions [1-8].² It is based on the rationale that at any instant da/dN is associated with a unique value of ΔK . If A and n are known for a given material and R ratio, these values, along with crack growth rates and crack lengths for a complex crack geometry, may be used to find instantaneous values of ΔK for the complex shape [1]. Using a general expression for stress intensity

$$\Delta K = \Delta \sigma \sqrt{\pi} f(a, \text{geometric parameters}) \quad (2)$$

the known instantaneous values of ΔK , $\Delta \sigma$, and a can be inserted to generate the calibration function f , for specific crack lengths.

² The italic numbers in brackets refer to the list of references appended to this paper.

Test Procedures

Material used to determine K_I was mild steel obtained in the form of 51 by 51 mm (2 by 2 in.) and 51 by 76 mm (2 by 3 in.) hollow rectangular tubing with 6.4 mm (1/4 in.) wall thickness. Specimens were taken from one 6.1 m (20 ft) length of each size tubing. The 51 by 76 mm (2 by 3 in.) tube had been cold-formed and was thus normalized at 900°C for 1 h and aircooled to minimize microstructural differences with the hot-formed 51 by 51 mm (2 by 2 in.) tube.

To obtain the relationship between crack growth rate, da/dN , and stress intensity range ΔK , reference specimens from each material type were machined and tested. Reference specimens included compact tension (CT), single edge notch (SEN), and four-point bend (4-pt bend). Specimens were machined from the tubes as shown in Fig. 1a such that crack growth directions were the same as in the actual test tubes. All reference specimens contained chevron starter notches. Table 1 summarizes the reference tests performed and the specimen dimensions, where h is the specimen height or length, w is the width and a_0 is the initial fatigue crack length. All reference specimens were pre-fatigue cracked and then tested at frequencies between 15 and 30 Hz with the stress ratio R equal to 0.1. An 88.96 kN (20 kip) closed-loop electrohydraulic test system was used for reference tests. Crack lengths were measured with a least reading 0.25 mm (0.01 in.) scale, a $\times 45$ optical microscope and stroboscopic lighting. The proposed ASTM Tentative Test for Constant-Load-Amplitude Fatigue Crack Growth Rates Above 10^{-8} m/cycle (E 647-78T) was followed in all reference testing. Crack length versus applied cycles was reduced to Eq 1 using a least square second order sequential polynomial. Stress intensities for the three reference specimens were

CT Specimen

$$K_I = \frac{P\sqrt{a}}{Bw} \left[30.96 - 195.8 \left(\frac{a}{w}\right) + 730.6 \left(\frac{a}{w}\right)^2 - 1186.3 \left(\frac{a}{w}\right)^3 + 754.6 \left(\frac{a}{w}\right)^4 \right] \quad (3)$$

4-pt bend [9]

$$K_I = \frac{6M\sqrt{a}}{Bw^2} \left[1.99 - 2.47 \left(\frac{a}{w}\right) + 12.97 \left(\frac{a}{w}\right)^2 - 23.17 \left(\frac{a}{w}\right)^3 + 24.8 \left(\frac{a}{w}\right)^4 \right] \quad (4)$$

TABLE 1—Reference specimen dimensions.

Tube, mm (in.)	Specimen ^a	<i>h</i> , mm (in.)	<i>w</i> , mm (in.)	<i>a</i> ₀ , mm (in.)
51 by 51 (2 by 2)	CT	17.1 (0.672)	28.4 (1.12)	7.1 (0.28)
	SEN	142 (5.6)	35.6 (1.4)	6.4 (0.25)
51 by 76 (2 by 3)	CT	57.2 (2.25)	45.7 (1.8)	8.9 (0.35)
	SEN	229 (9.0)	57.2 (2.25)	9.5 (0.37)
	4 pt bend	229 (9.0)	57.2 (2.25)	9.5 (0.37)

^a Nominal thickness was 6.4 mm (0.25 in.) and stress ratio $R = 0.1$.

SEN [9]

$$K_1 = \frac{P\sqrt{a}}{Bw} \left[1.99 - 0.41 \left(\frac{a}{w} \right) + 18.7 \left(\frac{a}{w} \right)^2 - 38.48 \left(\frac{a}{w} \right)^3 + 53.85 \left(\frac{a}{w} \right)^4 \right] \quad (5)$$

The hollow tubes were cut to 61-cm (24-in.) lengths. A starter notch was machined in the corner of each tube using a 47.6-mm (1 7/8-in.) diameter 0.6-mm (0.025-in.) thick circular saw. The last 0.25-mm (0.01-in.) depth was cut with a 0.15-mm (0.0006-in.) thick saw. Initial notch depth, d , shown in Fig. 1*b* ranged from 1.9 to 5.1 mm (0.075 to 0.200 in.). The tubes were tested under 4 pt bend conditions in the closed-loop electrohydraulic test system as shown in Fig. 2. The testing fixture was patterned after that suggested by Brown and Srawley [9]. Three height-to-width (h/w) ratios (2/3, 1, and 3/2) were tested with duplicate tests for each h/w ratio. All tests were run with $R = 0.1$ at 8.5 Hz. This frequency is between two and three times lower than that used with the reference specimens and should not be a significant influencing factor. Crack length measurements were made on both the top and side polished faces using a 0.25-mm (0.01-in.) least reading scale and a $\times 45$ optical microscope. Tests were stopped and the tube removed from the test fixture while measuring crack lengths. Between 19 and 29 crack length and applied cycles data points were taken for each crack side. Both top and side cracks were allowed to grow 1 mm (0.04 in.) out of the machine notch in the fatigue precrack period prior to recording data for analysis. Final precracking was accomplished with the same loads used in the actual testing. Numerical differentiation using the sequential second order polynomial was employed to develop crack growth rates, da/dN or dc/dN , versus crack length, a or c . Nominal stress range, $\Delta\sigma$, was obtained from

$$\Delta\sigma = \frac{(\Delta M)y}{I} \quad (6)$$

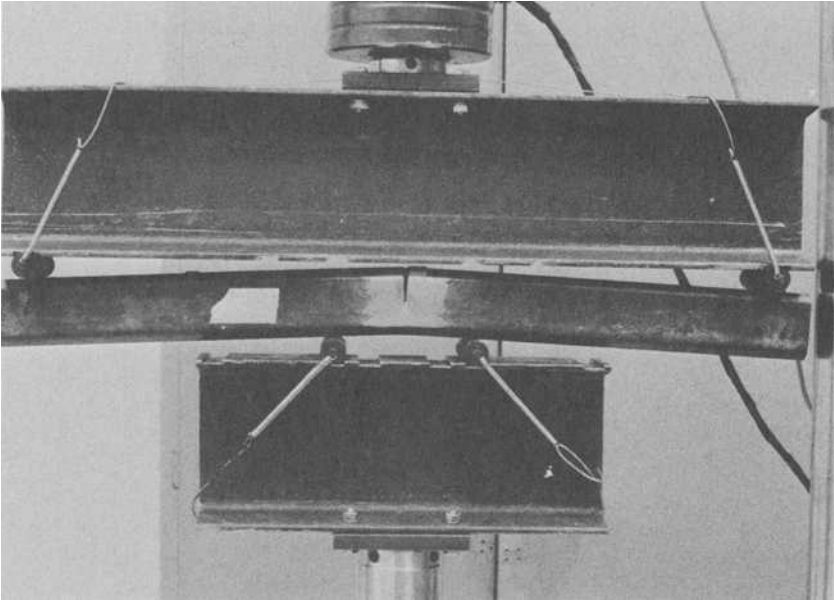


FIG. 2—Steel tube in 4-pt bend test apparatus at failure.

where

- ΔM = constant amplitude bending moment range,
- y = distance from the centroidal axis to the top fiber, and
- I = moment of inertia

I was obtained by dividing each tube into four straight and four quarter arcs. The nominal stress range for the three h/w ratios was between 124 and 143 MPa (18 and 28 ksi).

Beach marks were intermittently formed on the surface of some tubes during testing to ascertain crack front shapes. They were formed by applying several thousand reduced load cycles.

Results and Discussion

The reference constant amplitude crack growth rate versus stress intensity range data for specimens taken from the 51 by 76 mm (2 by 3 in.) tubes are shown in Fig. 3. Data for the CT, SEN, and 4-pt bend specimens are superimposed. Scatter for duplicate specimens was within 20 percent for the majority of the data with the CT specimen having the lowest crack growth rates. Scatter for the three different specimens superimposed in Fig. 3 was within a factor of two for all ΔK values. This is quite

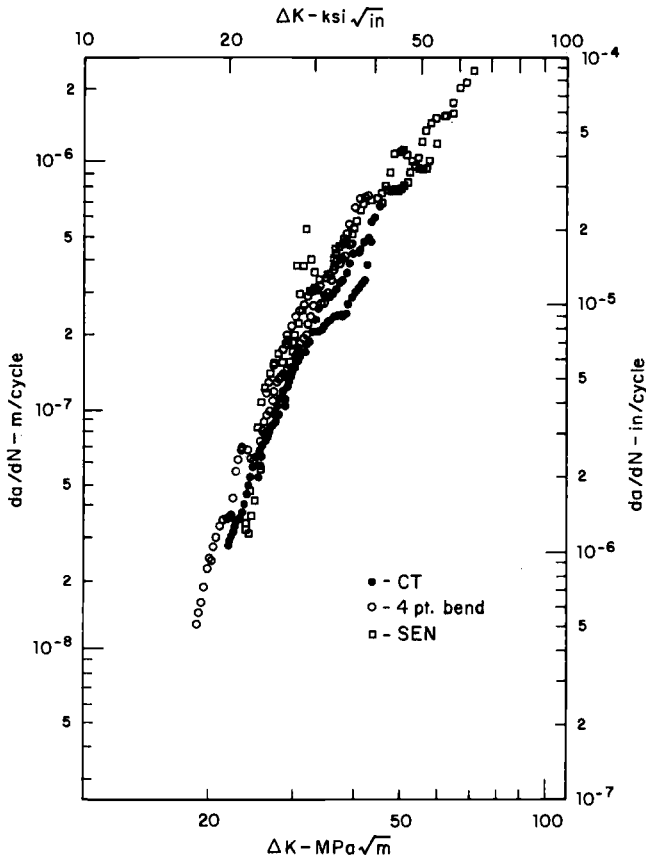


FIG. 3—Crack growth rate reference data 51 by 76 mm (2 by 3 in.) steel tubes.

reasonable considering that duplication of identical specimens can have this same level of scatter. A log-linear least square regression analysis was performed on all of the data in Fig. 3 to ascertain the most representative parameters A and n to be used with the tube tests in order to minimize error in the K_I calculations. The same procedure was used with the 51 by 51 mm (2 by 2 in.) tube material. The tube crack growth rates were within the extremes of the reference specimen rates. The following crack growth characteristic reference equations were determined:

$$\begin{aligned}
 & \text{51 by 76 mm} \\
 & \text{(2 by 3 in.)} \\
 & \text{tubes} \quad \left\{ \begin{aligned}
 \frac{da}{dN} \text{ (m/cycle)} &= 3.22 \times 10^{-13} (\Delta K \text{ MPa}\sqrt{\text{m}})^{3.824} \\
 \frac{da}{dN} \text{ (in./cycle)} &= 1.819 \times 10^{-11} (\Delta K \text{ ksi}\sqrt{\text{in.}})^{3.824}
 \end{aligned} \right. \quad (7)
 \end{aligned}$$

$$\begin{aligned}
 & \left. \begin{array}{l} 51 \text{ by } 51 \text{ mm} \\ (2 \text{ by } 2 \text{ in.}) \\ \text{tubes} \end{array} \right\} \begin{cases} \frac{da}{dN} \text{ (m/cycle)} = 6.5 \times 10^{-13} (\Delta K \text{ MPa}\sqrt{\text{m}})^{3.436} \\ \frac{da}{dN} \text{ (in./cycle)} = 3.548 \times 10^{-11} (\Delta K \text{ ksi}\sqrt{\text{in.}})^{3.436} \end{cases} \quad (8)
 \end{aligned}$$

Typical crack growth data for the hollow tubular specimens are shown in Fig. 4. The initial crack lengths on the top and side faces are not equal due to the higher crack growth rates that occurred on the top face during precracking and test cycling. Figure 5 is a plot of the top crack length, c , versus the side crack length, a , for all three h/w values. Data for the duplicate h/w ratios fall together and have a slope greater than 1. As the h/w ratio increases from 2/3 to 3/2 the slope decreases which indicates an

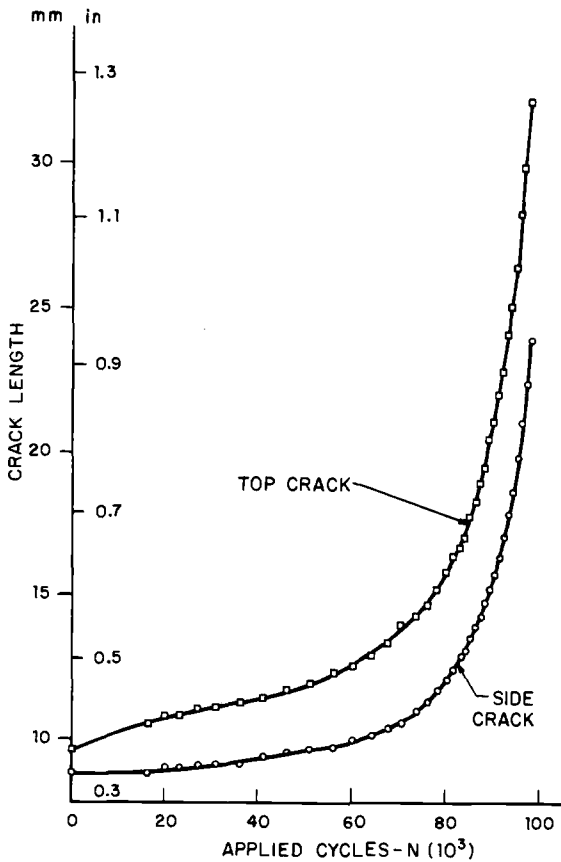


FIG. 4—Crack length versus applied cycles for $h/w = 2/3$, steel tubes, $\Delta\sigma = 165 \text{ MPa}$ (23 ksi).

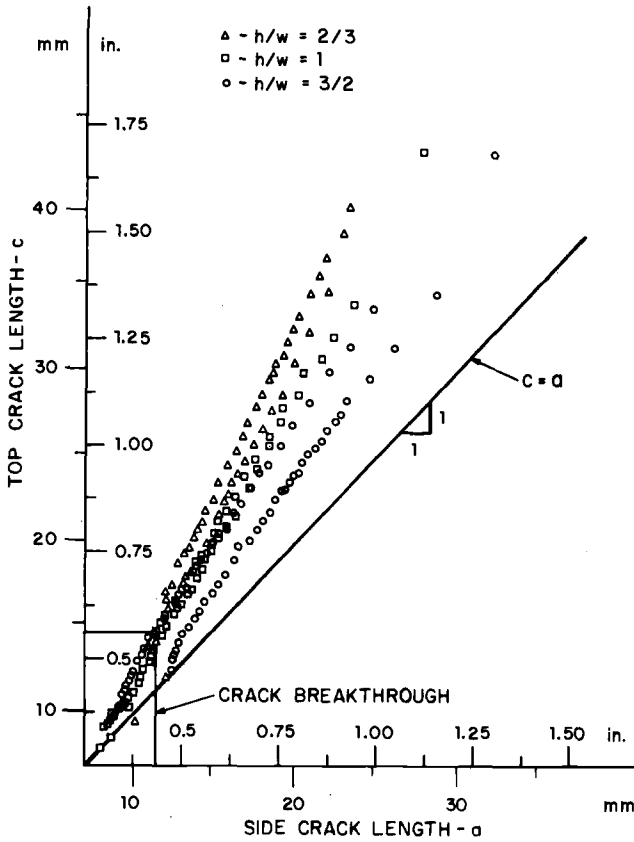


FIG. 5—Top crack length versus side crack length in steel tubes.

h/w effect is present in the crack length relationships. The crack breakthrough to the inner corner is labeled in Fig. 5. Essentially no change in crack growth rates occurred as the crack broke through the inner corner.

Figure 6 shows typical fracture surface for all three h/w ratios. Beach marks for $h/w = 3/2$ indicate that the top face crack tips do not grow perpendicular to the tube face and that the crack-tip external surface position leads. However, the side crack tips are more nearly perpendicular to the side face. This difference in behavior can be attributed to the bending stress gradient along the top ligament crack tip.

Calibration of the top face crack stress intensity was made using

$$K_I = \sigma \sqrt{\pi w} f(c/w) \quad (9)$$

Stress intensity K_I or ΔK_I was calculated using crack growth parameters obtained from reference specimens, tube crack growth data, and Eq 1.

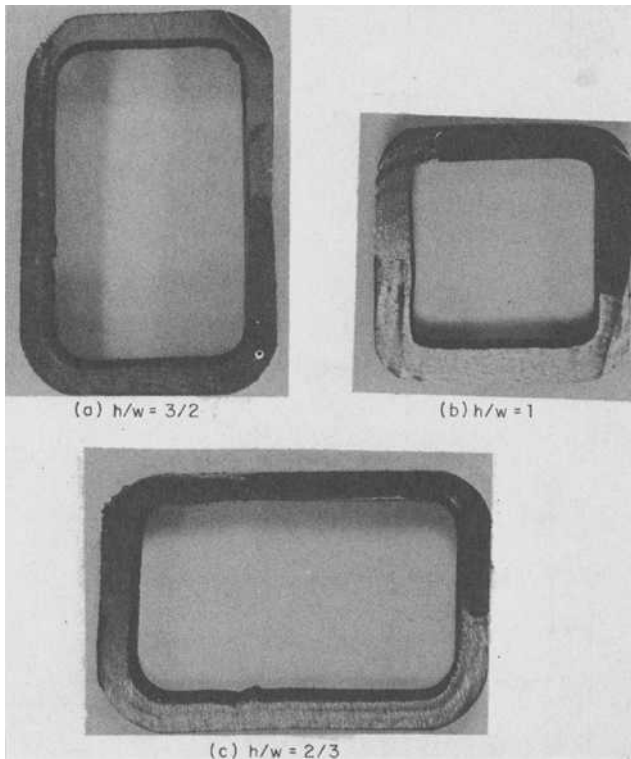


FIG. 6—Steel tube fracture surfaces.

Nominal stress σ and $\Delta\sigma$ was obtained from experimental loading conditions using Eq 6. Discrete values of $f(c/w)$ were calculated from Eq 9. Figure 7 is a plot of these functional values, $f(c/w)$, versus c/w for all six tubes for c/w varying from 0.18 to 0.55. Experimental values of $f(c/w)$ were analyzed to determine the scatter present. For each h/w ratio, values of $f(c/w)$ for corresponding c/w ratios (approximately 15 data points for each h/w ratio) were compared to determine variations. For each h/w ratio average variations between duplicate tests ranged between 10 and 20 percent. No specific banding trends existed for the three different h/w ratios. Variation in $f(c/w)$ for all six tubes averaged slightly less than 30 percent for different c/w ratios. This variation was considered small enough to justify describing all three h/w ratio data with a least square and upper bound function. A least square and upper bound fourth order polynomial was fit through the data. The upper bound function can be considered a conservative expression. The following expressions define $f(c/w)$ for the top cracks with c/w ranging from 0.18 to 0.55.

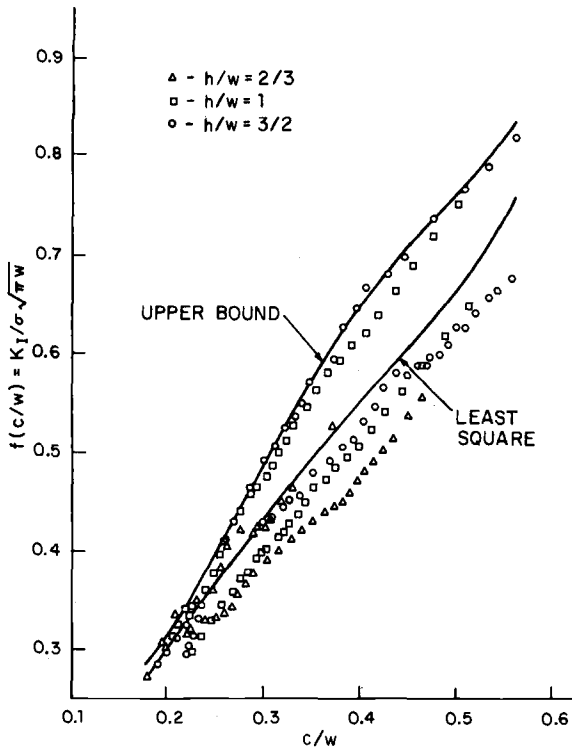


FIG. 7—Stress intensity dimensionless functions, $f(c/w)$, for top cracks.

least square

$$f(c/w) = 0.207 - 1.231 (c/w) + 13.416 (c/w)^2 - 29.478 (c/w)^3 + 22.453 (c/w)^4 \quad (10)$$

conservative upper bound

$$f(c/w) = 0.615 - 6.410 (c/w) + 36.256 (c/w)^2 - 67.662 (c/w)^3 + 43.915 (c/w)^4 \quad (11)$$

A similar analysis was made on the side face crack. Values of $f(a/h)$ obtained from

$$K_I = \sigma \sqrt{\pi h} f(a/h) \quad (12)$$

are plotted in Fig. 8 for all three h/w ratios. Average deviation between duplicate tests for each h/w were similar to the top crack deviations.

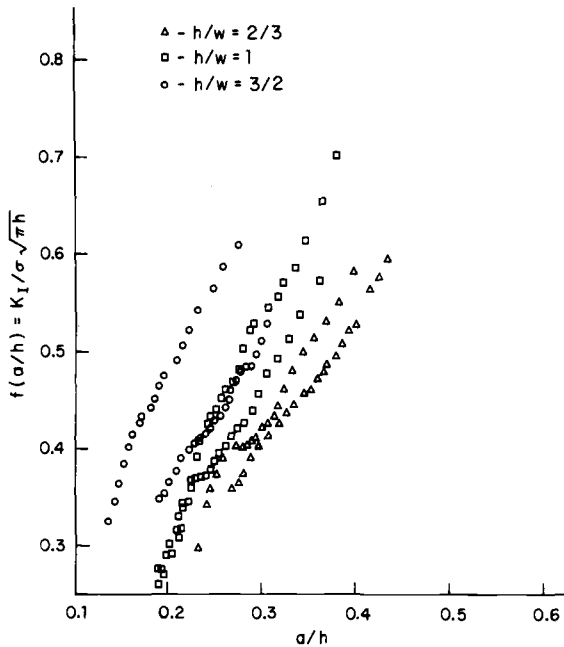


FIG. 8—Stress intensity dimensionless function, $f(a/h)$, for side cracks.

However, the total scatter band for all three h/w ratios includes deviations of over 70 percent for a given a/h . Thus, the h/w ratio influences $f(a/h)$ and thus influences K_I for the side crack. Referring to Fig. 5, the h/w ratio demonstrated an influence on the c/a ratio. As h/w increased, which reduces the bending stress gradient, the difference between the top and side crack growth rates decreased. Analysis of the top crack data indicated no influence by the h/w ratio for a given nominal bending stress σ . Figure 5, then, implies that side crack growth rate and hence K_I for the side crack increases with h/w for a given nominal stress. This h/w influence is also shown in Fig. 8 by the banding tendency of the three different h/w values.

In order to generalize K_I for side cracks, Eq 11 was modified by $\sqrt{h/w}$ to yield:

$$K_I = \sigma \sqrt{\pi h^2/w} f^*(a/h) \tag{13}$$

$f^*(a/h)$ versus a/h is shown in Fig. 9 for all three h/w values. Introduction of $\sqrt{h/w}$ reduces the scatter band to the same order of deviation as that observed in $f(c/w)$ for the top cracks. Variation in $f^*(a/h)$ for all six tubes ranged from approximately 10 to 35 percent, averaging less than 20 percent for the complete a/h span. A least square and upper bound fourth

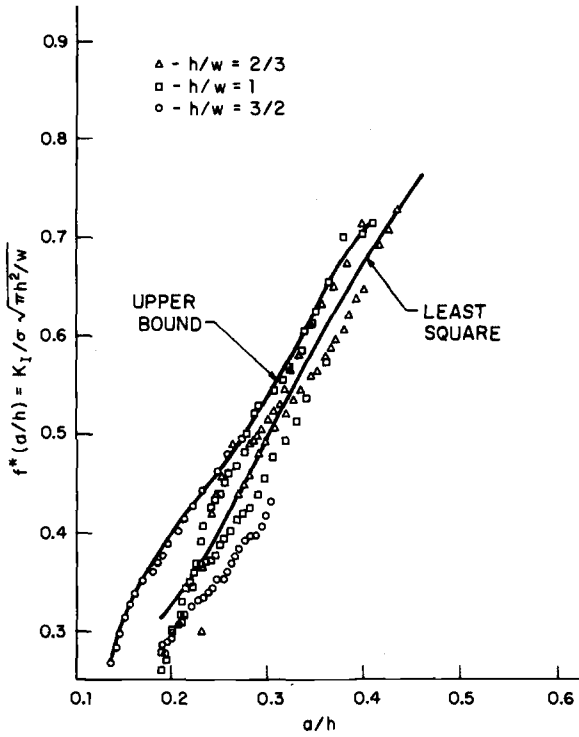


FIG. 9—Stress intensity dimensionless function, $f^*(a/h)$, for side cracks.

order polynomial was obtained for $f^*(a/h)$ in the same manner as for $f(c/w)$ for the top cracks. The following expressions define $f^*(a/h)$ for the side cracks with a/h ranging from 0.15 to 0.45

least square

$$f^*(a/h) = 0.959 - 10.394 (a/h) + 53.541 (a/h)^2 - 100.787 (a/h)^3 + 68.492 (a/h)^4 \quad (14)$$

conservative upper bound

$$f^*(a/h) = -1.008 + 19.06 (a/h) + 101.05 (a/h)^2 + 247.75 (a/h)^3 - 218.89 (a/h)^4 \quad (15)$$

Thus the stress intensity for the top face crack can be calculated using

$$K_I = \sigma \sqrt{\pi w} f(c/w) \quad (9)$$

and stress intensity for the side face crack can be calculated using

$$K_I = \sigma \sqrt{\pi h^2/w} f^*(a/h) \tag{13}$$

The two equations are not independent since crack length c and a are linearly related for specific h/w ratios as shown in Fig. 5. For a given beam, K_I was always greater at the top crack than at the side crack.

The above least square K_I values were compared with available expressions for different but similar geometries and configurations [10]. The circular corner crack in the hollow rectangular tube resembles the plane quarter-circular corner crack in a tensile bar. This resemblance is best when the tube corner crack is small, that is, has not broken through to the inner corner. As the cracks grow past the inner corner the top crack begins to resemble that of a through single edge crack (SEN) in a semi-infinite plate subjected to uniaxial tension, or perhaps that of an infinite or finite width center cracked panel in tension (CCT). The longer side cracks also resemble that of a finite or semi-infinite uniaxial SEN specimen and a 4-pt bend specimen. Comparison of these models with K_I least square values obtained experimentally in the research are shown in Fig. 10. The horizontal line with $K_{model}/K_{exp} = 1.0$ represents complete

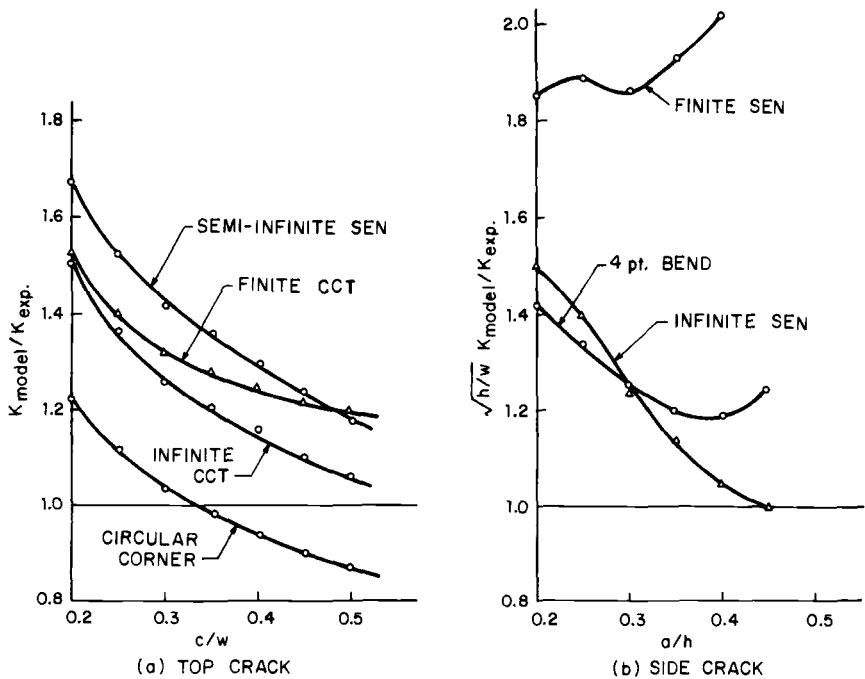


FIG. 10—Comparison of modeled K_I values with experimental K_I .

agreement between the model and the experimental Eqs 9 and 10 (top cracks) or 13 and 14 (side cracks). Models in Fig. 10 are for uniaxial tension except for the 4-pt bend specimens. In most cases the models predict a K_I value higher than the least square Eqs 10 and 14. Differences range from zero to factors of 2.5. Thus the experimentally determined stress intensities, despite their inherent scatter and experimental errors, appear to be the best current estimation of K_I for the total corner crack in a hollow thin-walled tube subjected to bending.

Summary and Conclusions

1. Stress intensities K_I were obtained for corner cracks in rectangular tubes subjected to pure bending for h/w of 2/3, 1 and 3/2 using the experimental fatigue crack growth method. For top cracks

$$K_I = \sigma \sqrt{\pi w} f(c/w)$$

while for side cracks

$$K_I = \sigma \sqrt{\pi h^2/w} f^*(a/w)$$

Both least square and conservative upper bound fourth order polynomials were determined for $f(c/w)$ and $f^*(a/w)$. The conservative upper bound curves are proposed as general K_I expressions applicable to design with hollow tubes containing corner cracks subjected to bending.

2. Average variation in $f(c/w)$ or $f^*(a/h)$ for all tests was within 30 percent which is considered very reasonable. Variation in duplicate baseline fatigue crack growth data alone can be greater than 30 percent.

3. Crack growth rates were higher for top face cracks than for side face cracks. Thus K_I is higher for the top face cracks.

4. The relationships between the top face and side face cracks were dependent upon h/w and hence stress gradient. The smaller h/w values provided the greatest crack growth difference.

5. Surface crack growth rates were not influenced as the corner crack broke through the inner corner.

6. Reference constant amplitude fatigue crack growth rate data using CT, SEN, and 4-pt bend specimens were within a factor of two for all specimen configurations for a given tube material.

7. The experimentally determined K_I values were compared with other known reasonably similar configurations such as the quarter-circular corner crack, SEN, CCT, and 4-pt bend specimen. Differences from zero to factors of 2.5 existed. No one model adequately compared with the experimental values of K_I found in this research. Thus K_I obtained in this

research is considered as the current best estimation of K_I for corner cracks in hollow tubes subjected to bending.

Acknowledgment

The authors would like to thank H. Berns and D. Galiart for their interesting discussions and Deere and Co. Technical Center, Moline, Illinois for sponsoring this research.

References

- [1] James, L. A. and Anderson, W. E., *Engineering Fracture Mechanics*, Vol. 1, April 1969, p. 565.
- [2] Hubbard, R. P., *Journal of Basic Engineering*, Vol. 91, Dec. 1969, p. 625.
- [3] Poe, C. C., Jr., in *Damage Tolerance in Aircraft Structures, ASTM STP 486*, American Society for Testing and Materials, 1971, p. 79.
- [4] Adams, N. J. in *Damage Tolerance in Aircraft Structures, ASTM STP 486*, American Society for Testing and Materials, 1971, p. 39.
- [5] Grandt, A. F., Jr., and Sinclair, G. M. in *Stress Analysis and Growth of Cracks, ASTM STP 513*, American Society for Testing and Materials, 1972, p. 37.
- [6] Grandt, A. F., Jr., and Hinnerichs, T. D. in *Proceedings, Army Symposium on Solid Mechanics 1974: The Role of Mechanics in Design of Structural Joints, AMMRC MS 74-8*, Sept. 1974.
- [7] Snow, J. R., "A Stress Intensity Factor Calibration for Corner Flaws at an Open Hole," AFML-TR-74-282, Wright-Patterson Air Force Base, May 1975.
- [8] Seidl, W. in *Fracture 1977*, Vol. 3; *Proceedings*, 4th International Conference on Fracture, Waterloo, Canada, June 1977, p. 601.
- [9] Brown, W. F., Jr., and Srawley, J. E., *Plane Strain Crack Toughness Testing of High Strength Metallic Materials, ASTM STP 410*, American Society for Testing and Materials, 1966.
- [10] Rooke, D. P. and Cartwright, D. J., *Compendium of Stress Intensity Factors*, Her Majesty's Stationery Office, London, 1976.

B. W. Christ,¹ J. H. Smith,¹ and G. E. Hicho¹

Fracture Analysis of a Pneumatically Burst Seamless-Steel Compressed Gas Container

REFERENCE: Christ, B. W., Smith, J. H., and Hicho, G. E., "Fracture Analysis of a Pneumatically Burst Seamless-Steel Compressed Gas Container," *Fracture Mechanics, ASTM STP 677*, C. W. Smith, Ed., America Society for Testing and Materials, 1979, pp. 734-745.

ABSTRACT: This paper describes the fracture analysis of a seamless steel compressed gas container which burst at a reported pressure of 17.3 MPa (2500 psi) during filling. Design burst pressure was about 35.2 MPa (5100 psi). The container was made of a quenched and tempered carbon-manganese steel with yield and tensile strengths of 517 and 687 MPa (75 000 and 99 800 psi), respectively. The vessel had been in service for about 6 months and had been filled perhaps twice before it burst. The fracture origin was a pair of part-through cracks in a gouged region on the outside surface. Fracture at the origin was ductile and the fast fracture was also ductile. The empirical methodology developed at Battelle-Columbus for analyzing the burst of line pipe was utilized to analyze the ductile fracture initiation of this compressed gas container. K_c , J_{Ic} and K_{Ic} were estimated for this carbon-manganese pressure vessel steel.

KEY WORDS: pressure vessel, pneumatic burst, steel, ductile fracture, fracture toughness, fatigue (materials), crack propagation

Description of Container That Burst

This paper describes the fracture analysis of a seamless steel compressed gas container that burst at a reported pressure of about 17.3 MPa (2500 psi) during filling. Design burst pressure was about 35.2 MPa (5100 psi). Temperature at the time of filling was estimated to be between 26.6 and 54.4°C (80 and 130°F). The burst pressure vessel, shown in Fig. 1, was a 217-mm diameter (8 9/15-in.) oxygen cylinder of the type frequently found in the laboratory or welding shop. It was made of a quenched and

¹ Deputy chief and project leaders, Fracture and Deformation Division, National Bureau of Standards, Washington, D. C. 20234.

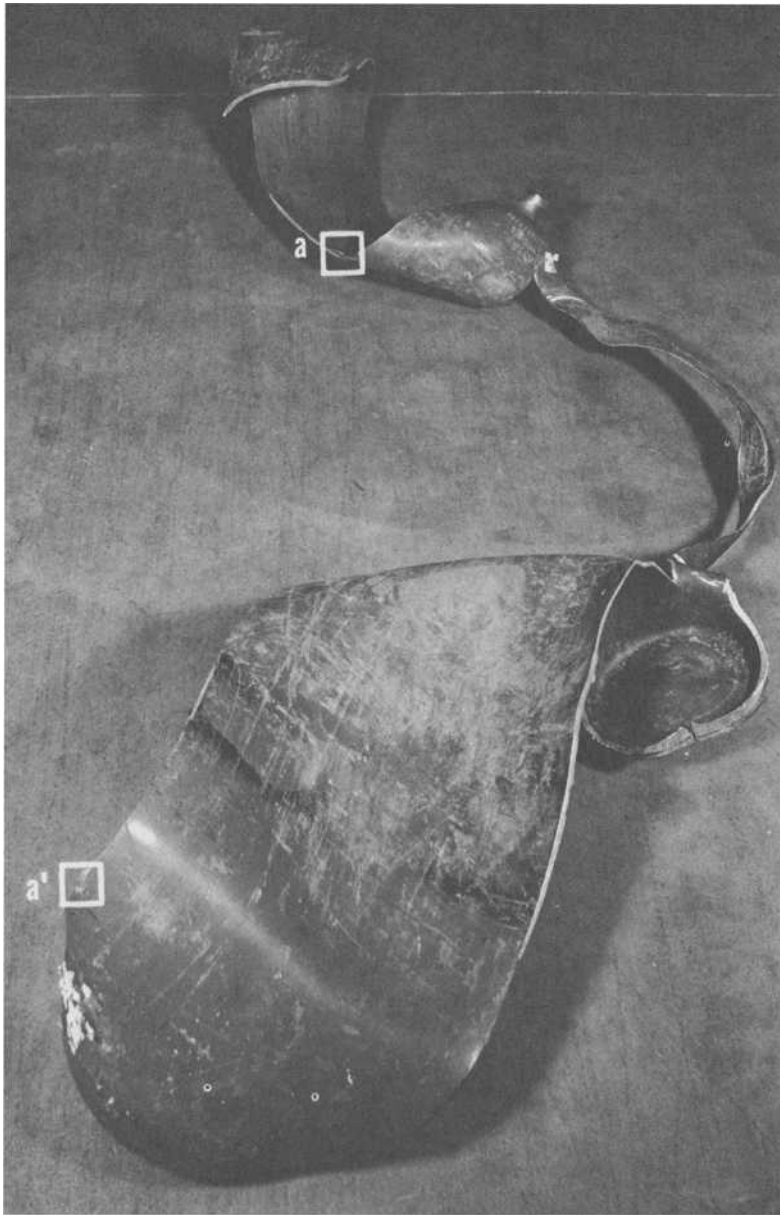


FIG. 1—Overall view of pneumatically burst gas cylinder, showing the bottom and one half of the neck. Regions a and a' indicate the fracture origin.

tempered carbon-manganese steel. Yield and tensile strength were 517 and 687 MPa (75 000 and 99 800 psi), respectively. Sidewall thickness was about 6.4 mm (0.25 in.). The vessel had been in service for about 6 months and had been filled perhaps twice before it burst. The bursting vessel grazed the operator's ankle, but caused no other significant damage. This container was manufactured according to U.S. Department of Transportation Specification 3AA of the Code of Federal Regulations, Title 49.

The fracture resulted in three longitudinal tears which arrested in the head and bottom of the vessel, so that the burst vessel consisted of three ribbon-like sections that remained connected (Fig. 1). No fragmentation occurred. The fracture surface appeared fibrous, and 45 deg shear lips were evident along most of the fracture surface. Hence, the fracture was ductile.

The fracture origin was a pair of part-through axial cracks in a gouged region on the outside surface about 22.8 cm (9 in.) below the neck (Fig. 2). The fracture surface of these cracks appeared fibrous and ductile. These cracks appeared to have resulted from external mechanical forces which led to the gouging, and associated flow lines and strain hardening. No fractographic evidence was found to suggest that the cracks were enlarged by fatigue or stress corrosion prior to the burst. Analysis by means of an empirical method developed for line pipe [1]² indicated that the part-through cracks became full-through cracks during the early stages of filling, and that filling continued while leaking until unstable shear fracture initiated. For purposes of stress analysis by means of fracture mechanics, plane stress fracture toughness, K_{Ic} , was estimated from an established correlation [1-3] between Dynamic Charpy upper shelf energy and K_{Ic} . Static J-integral tests [4] were carried out to estimate J_{Ic} , and the plane strain fracture toughness, K_{Ic} , for this pressure vessel steel.

Hoop Stress at Fracture

The application of fracture mechanics to pressure vessels facilitates the prediction of stability, leaking, or catastrophic fracture in terms of fracture toughness, crack size, and applied stress. Analysis of thin-walled cylindrical shells made of ductile metals by means of fracture mechanics is in the early stages of development [1-3,5,6]. The following fracture mechanics analysis of the pneumatically-burst compressed gas container is based on the empirical methodology reported by Maxey [1-3]. This methodology was formulated to predict the onset of ductile fracture of line pipe steels having yield strengths in the range 276 to 483 MPa (40 000 to 70 000 psi). It seems reasonable to apply this methodology to a steel gas container of 517 MPa (75 000 psi) yield strength which ruptured in a

² The italic numbers in brackets refer to the list of references appended to this paper.

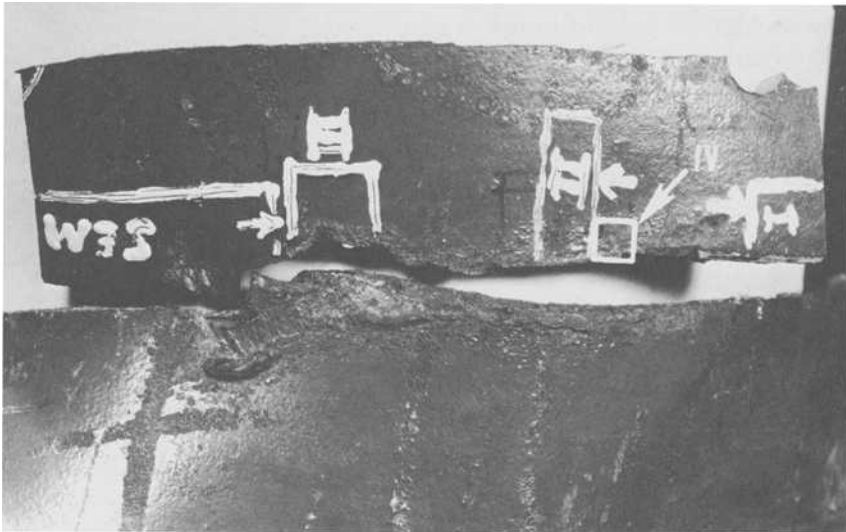
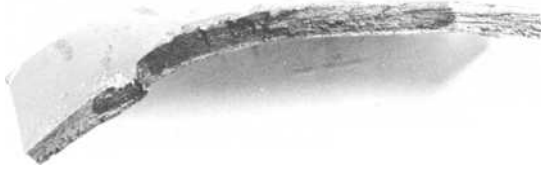
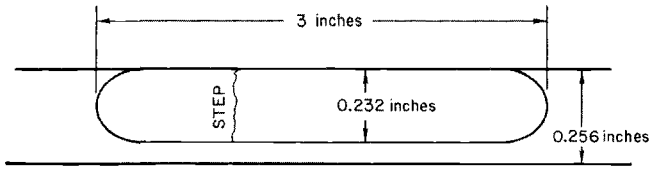


FIG. 2—(a) View of the side of the fracture origin labeled a in Figure 1, with a schematic diagram showing dimensions, and (b) mating halves of the fracture origin placed together to give an approximate picture of the configuration before burst. 1 in = 25.4 mm.

ductile manner. As a starting point, Maxey [1—3] (and others [5,6]) point out that stress magnification will occur at the ends of a crack. Consequently, plastic flow and fracture can occur at nominal applied wall stresses lower than the yield strength. In the case of a longitudinal crack in the sidewall of a cylindrical pressure vessel, stress magnification is due to redistribution of the hoop stress around the crack and to bending moments caused by bulging near the crack.

The stress magnification factor due to bulging of tubular products containing a through-wall, axial defect, M_T , was developed by Folias [7] and is given by

$$M_T = \left(1 + 1.255 \frac{c^2}{RT} - 0.0135 \frac{c^4}{R^2 t^2} \right)^{1/2} \quad (1a)$$

For the case of a part-through axial crack, the stress magnification factor, M_P , is estimated by Maxey [2] as

$$M_P = \frac{1 - d/t}{1 - d/M_T t} \quad (1b)$$

where

- d = depth of a part-through crack,
- $2c$ = length of a through-wall crack,
- R = cylinder radius,
- t = wall thickness,
- $2c'$ = equivalent crack length in the case of a part-through crack with non-rectangular ends ($2c' = A/d$, where A = actual area of surface flaw along its length), and

M'_T is calculated using c' instead of c in Eq 1a.

The stress magnification factor shows up in the equations used to calculate the hoop stress at failure. Equations have been defined by Maxey [1-3] for two types of fractures, classified as "flow stress controlled" (plastic behavior) and "toughness controlled" (elastic-plastic behavior). Equations for both types of behavior appear below.

In the case of a through-wall, axial crack, the equation for the hoop stress at failure for toughness-controlled behavior, σ_T , is

$$\ell n \secant \frac{\pi}{2} (M_T \sigma_T / \sigma_f) = K_c^2 \pi / (8c \sigma_f^2) = 12E \pi (C_v / A_c) / (8c \sigma_f^2) \quad (2a)$$

For a through-wall defect, the equation for the hoop stress at failure for flow stress controlled behavior, σ_T^* , is

$$\sigma_T^* = \sigma_f / M_T \quad (2b)$$

In the case of a part-through axial crack, the hoop stress at failure for toughness-controlled behavior, σ_P , is given by

$$\ell n \secant \frac{\pi}{2} (M_P \sigma_P / \sigma_f) = K_c^2 \pi / (8c' \sigma_f^2) = 12E \pi (C_v / A_c) / (8c' \sigma_f^2) \quad (3a)$$

whereas for flow stress controlled behavior, the equation is

$$\sigma_p^* = \sigma_f/M_p \quad (3b)$$

where

- σ_T, σ_p = hoop stress at failure for toughness controlled behavior,
- σ_T^*, σ_p^* = hoop stress at failure for flow stress controlled behavior,
- σ_f = the flow stress of the steel (assumed by Maxey and others to be yield strength plus 10 000 psi),
- K_c = plane stress fracture toughness of material,
- C_V/A_c = impact energy per unit area of a Charpy test specimen in foot-pounds (half size or full size),
- E = Young's modulus (30×10^6 psi),
- $2c$ or $2c'$ = the length of the crack,
- M_T = stress magnification factor given by Eq 1a, and
- M_p = stress magnification factor given by Eq 1b

Stress analysis cannot be carried out easily for the case of the two closely spaced, but separate cracks shown in Fig. 2. Hence, to estimate upper and lower bounds for the hoop stress at failure, calculations were made for the actual 6.3-cm (2 1/2-in.) long crack and for an assumed 7.6-cm (3-in.) long crack. Because of the depth of the part-through crack, 91 percent of the wall thickness, determination of c' rather than c for calculating M_p was considered an unnecessary refinement. Results appear in Table 1, where the first column shows that the stress magnification factor is larger for the part-through crack than for the full through crack. The second column shows a factor based on the Charpy test results which is used to classify the fracture as toughness controlled or flow stress controlled. Maxey indicates that values of this factor less than four, as appearing in the table, mean that the fracture is toughness controlled. Thus, Eqs 2a and 3a were used to calculate the hoop stresses at failure. Results appear in the third column. Values of the parameter, $M\sigma/\sigma_f$, which appear in the fourth column, also show that the fracture was slightly toughness controlled. A data point representing these results falls in the toughness-controlled regime of a plot by Maxey which shows the empirical relationship between full-scale burst test results and toughness inferred from Charpy upper shelf energy (Fig. 3).

In the case of the part-through crack, failure means that the ligament beneath the part-through crack ruptured, and a full-through crack formed. At this point, results in Table 1 suggest that the cylinder simply leaked, because the ligament ruptured at a hoop stress of 84.1 to 139.4 MPa (12 200 to 20 200 psi), which is less than the stress required for the full-through crack to run catastrophically, namely, 263.9 to 374.7 MPa (38 100 to 54 300 psi). Continued filling of the leaking cylinder to the allowable filling pressure would have developed hoop stresses in this

TABLE 1—Results of stress analysis for axial, part-through and full-through cracks.

Type and Length of Crack, $2c$	Stress Magnification Factor	$K_c^2 \pi / 8c \sigma_f^2 = [12E\pi(C_v/A_c)] / 8c \sigma_f^2$	Hoop Stress At Failure Toughness Controlled		$M \sigma / \sigma_f$
			MPa	psi	
Part through, cm (in.)	$M_p = 3.74$	1.41	139.4	20 200	0.84
	$M_p = 5.88$	1.18	84.1	12 200	0.80
Full through cm (in.)	$M_T = 1.39$	1.41	374.7	54 300	0.84
	$M_T = 1.88$	1.18	263.9	38 100	0.80

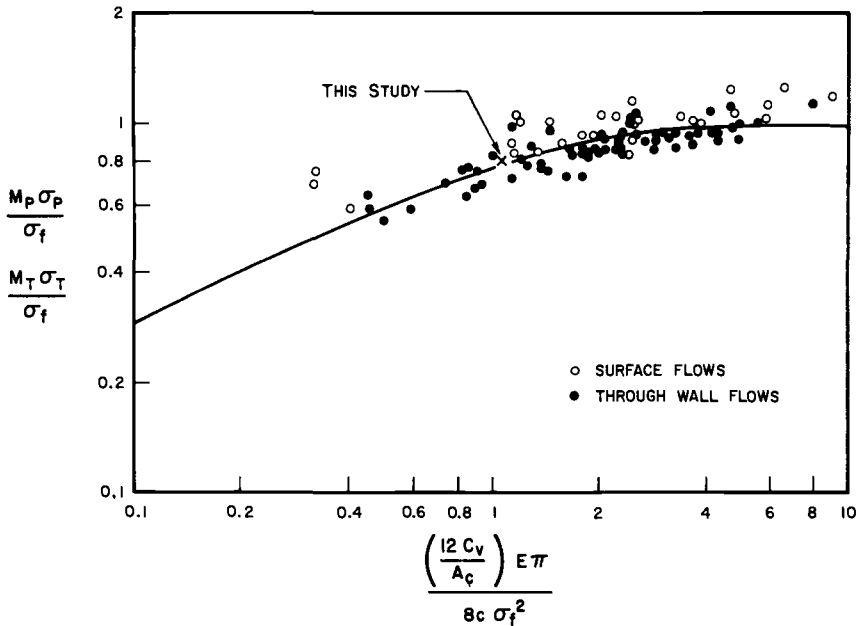


FIG. 3—Correlation between burst test results and Charpy test results. (Data reported by Maxey [4] with point representing present cylinder added.)

range. For example, the hoop stress estimated from the reported gas pressure at burst

$$\sigma_B = PR/t = 17.25 \times 4.28/0.256 = 288.4 \text{ MPa (41 800 psi)}$$

falls in this stress range.

Estimation of Fracture Toughness

K_c from Charpy Tests

Dynamic Charpy V-notch tests were carried out according to ASTM Notched Bar Impact Testing of Metallic Materials (E 23-72) for standard half-size longitudinal (L-C) and circumferential (C-L) specimens. Some flattening of the steel was necessary to produce straight test specimens. Results appear in Fig. 4, where it is evident that the upper shelf energy for longitudinal fracture is about one fourth that for transverse fracture. This effect is due to nonmetallic inclusions drawn out in the longitudinal direction during fabrication [8]. Filling of the compressed gas container took place at a temperature above the observed transition temperature, thus accounting for the observed ductile fracture at the time of burst.

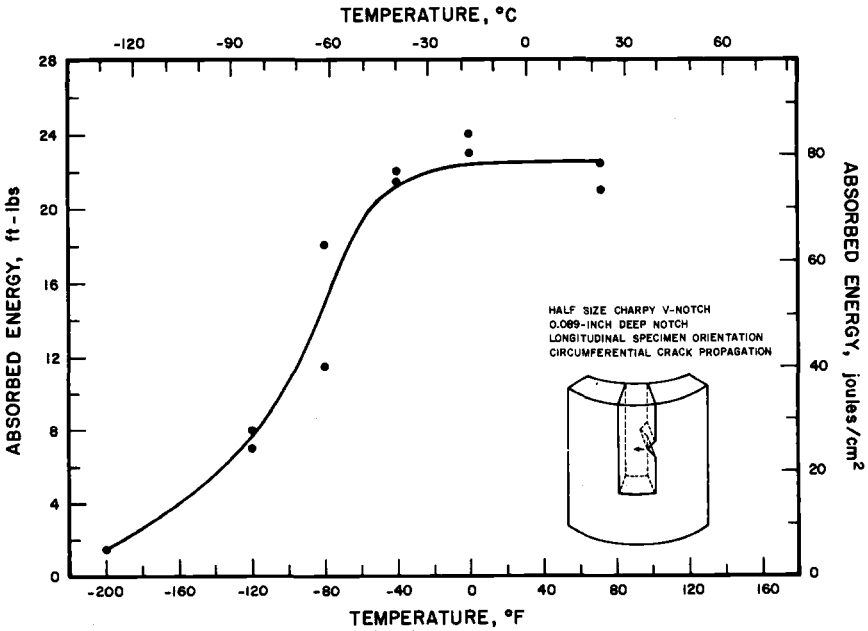
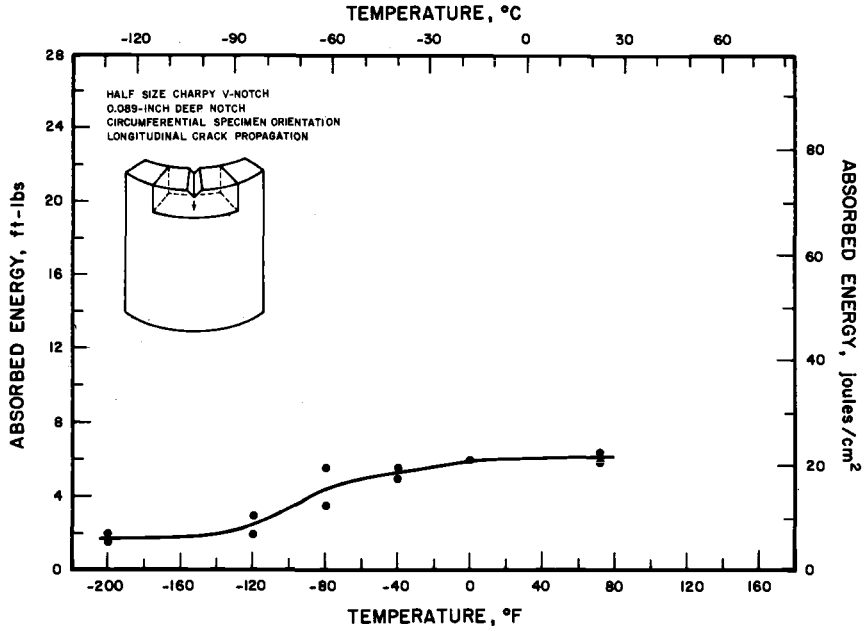


FIG. 4—(a) Absorbed energy versus temperature for longitudinal crack propagation, and (b) absorbed energy versus temperature for circumferential crack propagation.

Plane stress fracture toughness was estimated from the empirical correlation reported by Maxey [1-3]

$$K_c = \sqrt{12 E C_v / A_c} \quad (4)$$

where the terms have the meanings defined in the preceding section. The Charpy energy per unit area for longitudinal cracking was 21.8 J/cm^2 ($100 \text{ ft}\cdot\text{lb/in.}^2$), and K_c was $209 \text{ MPa}\sqrt{\text{m}}$ ($190 \text{ ksi}\sqrt{\text{in.}}$). This value of K_c compares favorably with other plane stress values reported for quenched and tempered steels of similar yield strength [9].

K_{Ic} from J -Integral Tests

Static J -integral tests were carried out according to the test procedure recommended by the Steering Committee of the E 24.01.09 Task Group on Elastic-Plastic Fracture, "Recommended Practices for the Determination of J_{Ic} Point from the J versus a R-curve." Compact tension specimens (1-T) were machined from flattened steel pieces, then fatigue precracked and tested at room temperature. Specimens were taken in the C-L orientation so that cracking occurred longitudinally. The clip gage was fastened at the load line in such a fashion that the gage could move freely during the test. Test results appear in Fig. 5, where it is evident that $J_{Ic} = 13.7 \text{ kJ/m}^2$ ($78.3 \text{ in.}\cdot\text{lb/in.}^2$). From the relationship,

$$K_{Ic}^2 = J_{Ic} E / (1 - \nu^2) \quad (5)$$

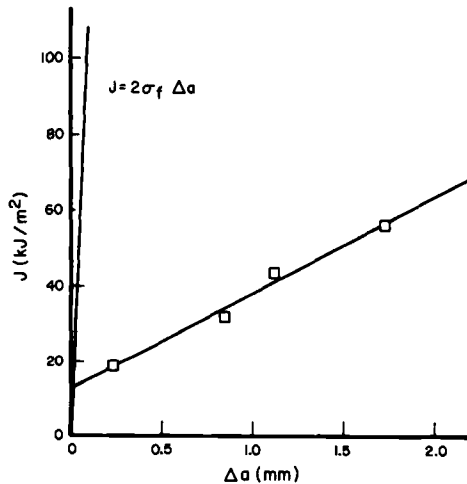


FIG. 5—Static J -integral test results for compact tension specimens oriented for longitudinal crack propagation.

where

E = Young's modulus,
 ν = Poisson's ratio, and

K_{Ic} is estimated to be $50.6 \text{ MPa } \sqrt{\text{m}}$ ($46 \text{ ksi } - \sqrt{\text{in.}}$).

A single specimen was tested using the unloading compliance method. In this method, load was increased successively to higher values, and crack growth was estimated from the compliance measured during each unloading. J_{Ic} was determined from the resulting plot of J versus Δa to be 21.3 kJ/m^2 , and K_{Ic} equaled $62.9 \text{ ksi } \sqrt{\text{in.}}$. These results agree well with the results obtained by means of the direct measurement of crack growth.

Comparison of Estimated K_c and K_{Ic} .

K_c estimated from the upper shelf Charpy values, $209 \text{ MPa } \sqrt{\text{m}}$ ($190 \text{ ksi } \sqrt{\text{in.}}$), is substantially greater than K_{Ic} estimated from results of the J_{Ic} test, $50.6 \text{ MPa } \sqrt{\text{m}}$ ($46 \text{ ksi } \sqrt{\text{in.}}$). Apparently this difference arises from the two different physical situations under consideration. The value of K_c represents the plane stress fracture toughness for ductile crack initiation estimated from a full scale test on a thin walled cylindrical shell using

$$K_c^2 \pi / (8c \sigma_f^2) = \ell n \secant \frac{\pi}{2} (M_T \sigma_T / \sigma_f) \quad (6)$$

where the terms are defined in the preceding section. On the other hand, the value of K_{Ic} represents the plane strain fracture toughness for brittle crack initiation which would be estimated from a valid size specimen tested according to ASTM Test for Plane-Strain Fracture Toughness of Metallic Materials (E 399 - 76).

Discussion

Evidence accumulated in this investigation suggests that the pair of part-through cracks shown in Fig. 2 popped in by means of ductile propagation to about 91 percent of the sidewall thickness in a steel having a K_c of $209 \text{ MPa } \sqrt{\text{m}}$ ($190 \text{ ksi } \sqrt{\text{in.}}$). At first glance, this is unexpectedly deep pop-in for what appears to be such tough material. However, flow lines associated with the gouges suggest that stresses well in excess of the yield stress, 517 MPa ($75\,000 \text{ psi}$), were applied during the gouging process. Furthermore, it might be that the gouges developed from an impact loading, which would suggest a K_d less than the K_c of $209 \text{ MPa } \sqrt{\text{m}}$ ($190 \text{ ksi } \sqrt{\text{in.}}$). In support of this speculation, Fig. 2a shows regions where features of the fracture surface topography in the darkened origin and fast propagation region are continuous. This observation is taken as evidence that ductile fracture at the origin occurred at a fast

propagation rate. The strain hardening accompanying gouging might also have a tendency to reduce the fracture toughness. In view of the foregoing observations, it may be that the deep part-through cracks resulted from a very high-stress impact. Results of the fracture analysis suggest that the gas pressure in the cylinder at the time of gouging was less than about 6.89 MPa (1000 psi).

The topography of the fracture surface at the origin was uniform. There was no fractographic evidence for different crack growth processes, as determined using the scanning electron microscope and the optical microscope. In particular, no evidence for fatigue or stress corrosion cracking was found.

With regard to the safety objectives of the Code of Federal Regulations, it is observed that this compressed gas container steel is sufficiently tough that the critical crack size for a leak-before-break criterion at allowable filling pressure is about 5.08 cm (2 in.). Hence, improved inspection rather than increased toughness seems to be a reasonable approach for minimizing the occurrence of catastrophic pneumatic burst in the future.

Acknowledgment

The investigation reported herein was supported in part by the Materials Transportation Bureau, U.S. Department of Transportation, Washington, D.C., 20590. J. P. Gudas of the Naval Ship Research and Development Center, Annapolis, Md., determined J_{IC} by means of the unloading compliance method.

References

- [1] Maxey, W. A., Kiefner, J. F., Eiber, R. J., and Duffy, A. R. in *Fracture Toughness, ASTM STP 514*, American Society for Testing and Materials, 1972, pp. 70–81.
- [2] Kiefner, J. F., Maxey, W. A., Eiber, R. J., and Duffy, A. R. in *Progress in Flaw Growth and Fracture Toughness Testing, ASTM STP 536*, American Society for Testing and Materials, 1973, pp. 461–481.
- [3] Maxey, W. A., "Fracture Initiation, Propagation and Arrest," 5th Symposium On Line Pipe Research, Pipeline Research Committee of American Gas Association, Houston, Tx., Nov. 1974, pp. J-1–J-31.
- [4] Steering Committee of the ASTM E 24.01.09 Task Group on Elastic-Plastic Fracture, "Recommended Practices for the Determination of J_{IC} Point from the J versus an R-Curve," American Society for Testing and Materials, March 1977.
- [5] Broek, D. in *Elementary Engineering Fracture Mechanics*, Chapter 15.2, Noordhoff International Publishing, Leyden, The Netherlands, 1974.
- [6] Erdogan, F., *International Journal of Pressure Vessels and Piping*, Vol. 4, Oct. 1976, pp. 253–283.
- [7] Folias, E. S., "The Stresses in a Cylindrical Shell Containing an Axial Crack," Report No. 64-174, Aerospace Research Laboratories, El Segundo, Calif., 1964.
- [8] Christ, B. W. and Smith, J. H., "Metallurgical Evaluation and Fracture Analysis of a Pneumatically-Burst Seamless Steel Compressed Gas Cylinder," NBSIR 76-118, National Bureau of Standards, Washington D.C., April 1977.
- [9] Sullivan, A. M. and Stoop, J., "Some Fracture Mechanics Relationships for Thin Sheet Materials," NRL Report 7650, Strength of Materials Branch, Metallurgy Division, Naval Research Laboratory, Washington, D.C., 21 Dec. 1973.

Crack Growth in Externally Flawed, Autofrettaged Thick-Walled Cylinders and Rings

REFERENCE: Kapp, J. A. and Eisenstadt, R., "Crack Growth in Externally Flawed, Autofrettaged Thick-Walled Cylinders and Rings," *Fracture Mechanics, ASTM STP 677*, C. W. Smith, Ed., American Society for Testing and Materials, 1979, pp. 746-756.

ABSTRACT: A study has been made to investigate the effect of autofrettage on crack growth in externally flawed, thick-walled cylinders and rings. With the use of singular finite elements, stress intensity factors were determined for cylinders containing a single, external crack oriented in the radial direction, subjected to either internal pressure or to a diametrical compression load normal to the crack plane. Fatigue crack growth rate experiments were conducted using several rings cut from cylinders which had been autofrettaged different amounts. The rings were fatigue cycled using the aforementioned compressive loading, which produced a properly oriented external crack. The results of these experiments show that fatigue crack growth rates can be increased by as much as an order of magnitude in cylinders which have been fully autofrettaged over those which contain no residual stresses. There is not sufficient data to model this increase in crack growth rate empirically; however, some comments are given on the effect of autofrettage residual stress on fatigue crack growth rate.

KEY WORDS: autofrettage, fatigue, finite elements, fracture mechanics, pressure vessels, fatigue (materials), crack propagation

A common vessel used to contain very high pressures such as those encountered during the firing of cannons is the thick walled cylinder. The stresses developed in thick-walled cylinders subjected to internal pressure were determined by Lamé. Tensile stresses occur through the wall thickness of the cylinder with the largest occurring at the inside radius (bore). Several techniques have been developed to reduce the operating bore stress by inducing compressive residual stresses at that surface.

¹ Mechanical engineer, U. S. Army Armament Research and Development Command, Benet Weapons Laboratory, LCWSL, Watervliet Arsenal, Watervliet, N.Y. 12189.

² Professor, Department of Mechanical Engineering, Union College, Schenectady, N.Y. 12309.

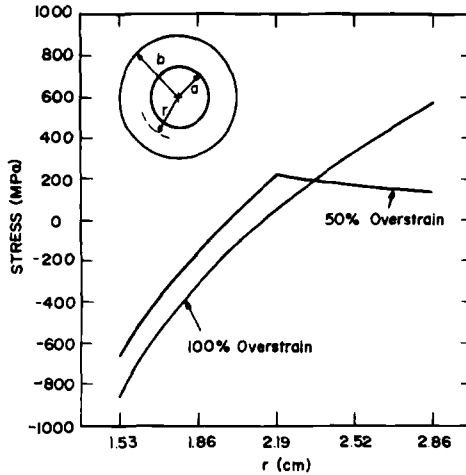


FIG. 1—Autofrettage residual stress distributions, calculated from Ref 1, for 50 percent overstrain and 100 percent overstrain in a cylinder where $a = 1.53$ cm, $b = 2.86$ cm, with a yield strength of 1144 MPa.

Autofrettage is a very effective method of developing compressive residual stresses at the bore and is used extensively on cannon.

Autofrettage is an overstraining process which produces the desired residual stresses when a thick-walled cylinder is subjected to sufficient pressure to cause plastic deformation to some extent through the wall thickness of the cylinder. Under the application of the autofrettage pressure, the bore undergoes plastic deformation, and will try to remain deformed when the pressure is released. The outside portion of the cylinder deforms little under the autofrettage pressure, and attempts to recover to nearly its original position upon removal of the pressure. This nonuniform recovery results in compressive residual stresses at the bore and tensile residual stresses at the outside radius. Two autofrettage residual stress distributions are shown in Fig. 1.

The optimum autofrettage condition traditionally has been considered that which will allow for the maximum internal pressure to be contained elastically. For most cylinders of practical interest, the optimization occurs when the autofrettage pressure causes plastic flow throughout the entire cylinder wall thickness [1]³. This is called the 100 percent overstrain condition.⁴ The 100 percent overstrain condition also results in the maximum fatigue life for smooth cylinders [1-3] where the failure initiates at the bore surface. Should an autofrettaged cylinder have structural discontinuities at the outside radius, the combination of tensile residual

³ The italic numbers in brackets refer to the list of references appended to this paper.

⁴ Percent overstrain is defined as the percentage of wall thickness subjected to plastic strain under the application of the autofrettage pressure.

stresses and tensile operating stresses plus stress concentration could result in fatigue cracks initiating at this surface. This report presents the results of an investigation of the growth of cracks initiated at the outside radius of a cylinder.

Procedure

The study involved both experiment and analysis. Experiments were conducted to measure fatigue crack growth in cylinders which had been autofrettaged various amounts using a ring specimen. The design of the specimen used was suggested by Underwood [4]. The specimen is merely a thin ring, loaded in compression in its diametrical plane normal to the starter notch as pictured in Fig. 2, producing tensile stresses at the notch. This specimen can be cycled easily in a high cycle fatigue machine, is manufactured easily, and retains the autofrettage residual stresses.

The actual specimens were obtained from three cylinders. Two of these cylinders were autofrettaged, one to 50 percent overstrain, the other to 100 percent overstrain. The third cylinder was not autofrettaged; the specimens obtained from this cylinder are referred to as the 0 percent overstrain specimens. After autofrettage, the cylinders were sectioned to obtain two ring specimens from each cylinder. Each specimen was notched subsequently and fatigue cycled.

The analysis performed was to develop the stress intensity factor, K , for an externally flawed thick-walled cylinder subjected to the aforementioned compression load. K also was determined for the same cylinder subjected to internal pressure.

The K solutions were developed through the use of eight-node isoparametric quadrilateral finite elements in the NASTRAN program. These elements very accurately model the near field of a crack tip when

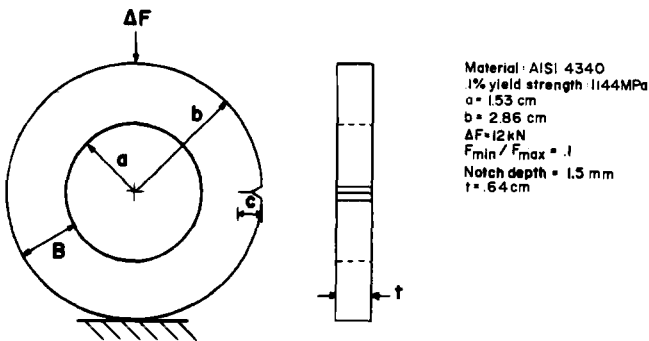


FIG. 2—Schematic representation of the ring experiment.

their geometry is uniquely specified [5]. When one of the sides of the quadrilateral is collapsed to a point, by making the three nodes that connect it coincident, and the adjacent mid-side nodes are placed exactly one quarter of the distance between the collapsed side and the remaining corner nodes, the resulting numerical approximation for the displacement of the element is proportional to the square root of the distance from the collapsed side [5,6]. This results in inverse square root singular strains, exactly the singularity occurring at a crack tip [7]. These elements have yielded excellent results when used to model radial cracks in cylindrical structures [8,9].

Most cannons are thick-walled cylinders which have radius ratios falling in the relatively small range of about 1.8 to 2.2. For the purpose of this initial study, we decided to develop K solutions for a cylinder with a nominal radius ratio of 2.0, assuming these solutions apply approximately over the entire radius ratio range of interest.

Due to symmetry with respect to the plane of the crack only one half of a cylinder is required in the analysis. The finite element mesh consisted of 92 elements, including six singular elements, connected by 325 nodes (Fig. 3). In all, nine different meshes were analyzed, one each for nine equally spaced values of c/B from 0.17 to 0.83. Figure 3 is the mesh used for $c/B = 0.5$. All computer runs were made on an IBM 360/44. The total time per run, including both the internal pressure and the diametrical line loading conditions, was about 20 min.

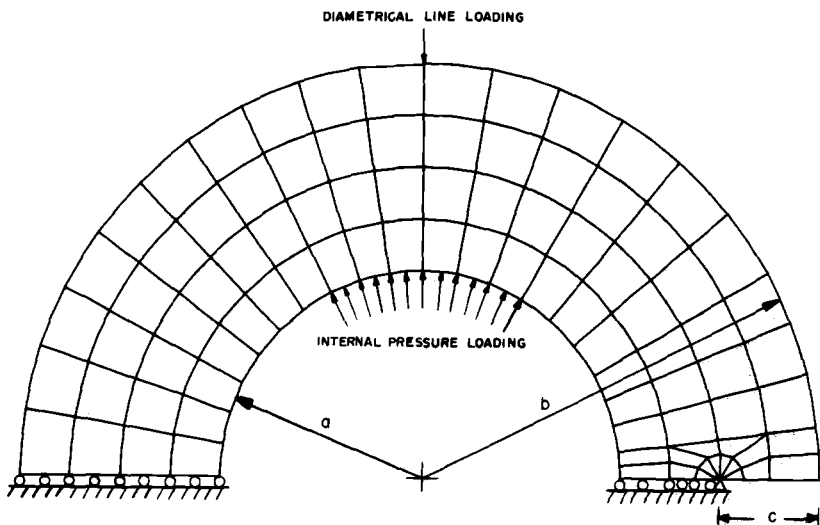


FIG. 3—The finite element mesh used to analyze a thick-walled cylinder with a radius ratio of two and a crack which is one half of the wall thickness deep, indicating the two different loading conditions and the boundary conditions.

Numerical Results

Internal Pressure Loading

Several investigators have previously addressed the problem of external cracks in thin-walled cylinders using various methods [10-13]. Emery and Segedin [13] developed a finite difference scheme, and applied it to thick-walled as well as thin-walled cylinders. These finite difference solutions for radius ratios of 1.67 and 2.86 are compared to our finite element results for a radius ratio of 2.0 in Table 1. The disagreement could be attributed to either an inaccurate or an inappropriate finite difference method. Most recently, Tracey [14] also has solved this problem for a cylinder with a radius ratio of 2.0 using boundary value collocation. His results also are shown in Table 1, and show excellent agreement with the finite element results developed here.

An expression of the following type was used to fit the finite element data

$$K = \sigma\sqrt{\pi c} Y(c/B) \quad (1)$$

where σ is an arbitrarily chosen stress to ensure the proper dimensions, and Y is a function of nondimensional crack depth. In this case, σ was chosen as the Lamé tangential stress in an uncracked cylinder at the outside radius. This results in

$$K = \frac{2P_i a^2}{b^2 - a^2} \sqrt{\pi c} Y(c/B)$$

where P_i is the internal pressure.

The best fit for Y is

$$Y(c/B) = 1.12 + 0.31(c/B) + 6.85(c/B)^2 - 12.12(c/B)^3 + 10.02(c/B)^4 \quad (2)$$

This expression was determined using multi-variable linear regression, and is accurate to ± 2 percent over the range of c/B from 0 to 0.83. Equation 2 is plotted in Fig. 4.

Diametrical Line Loading

The finite element K results for the diametrical line loading are also presented in Table 1. The stress intensity factor increases with increasing crack depth until the crack is about 30 percent through the wall thickness, levels off and decreases, until closure is predicted for very deep cracks. This behavior is explained with the aid of the solution for the stresses

TABLE 1—Stress intensity factor solutions for cylinders with a single external crack oriented in the radial direction.

This Study $a/b = 2.0$		Traey [14] $a/b = 2.0$		Emery and Segedin [13] $a/b = 1.67$		Emery and Segedin [13] $a/b = 2.0$	
c/B	$K/\sigma\sqrt{\pi c}$	c/B	$K/\sigma\sqrt{\pi c}$	c/B	$K/\sigma\sqrt{\pi c}$	c/B	$K/\sigma\sqrt{\pi c}$
0.167	1.341	0.1	1.20	0.1	1.12	0.13	1.14
0.250	1.465	0.2	1.37	0.22	1.29	0.27	1.34
0.333	1.635	0.3	1.56	0.34	1.40	0.39	1.48
0.417	1.883	0.4	1.80	0.45	1.54	0.51	1.60
0.500	2.102	0.5	2.10	0.55	1.69	0.61	1.74
0.583	2.404	0.6	2.49	0.65	1.87	0.70	1.93
0.667	2.753						
0.750	3.247						
0.833	3.958						

This Study $a/b = 2.0$	
c/B	$K/\sigma\sqrt{\pi c}$
0.167	0.953
0.250	0.881
0.333	0.793
0.417	0.693
0.500	0.582
0.583	0.441
0.667	0.251

Diametrical Line Loading $\left(\sigma = \frac{5.88F}{\pi b t} \right)$	
This Study $a/b = 2.0$	
c/B	$K/\sigma\sqrt{\pi c}$
0.167	0.953
0.250	0.881
0.333	0.793
0.417	0.693
0.500	0.582
0.583	0.441
0.667	0.251

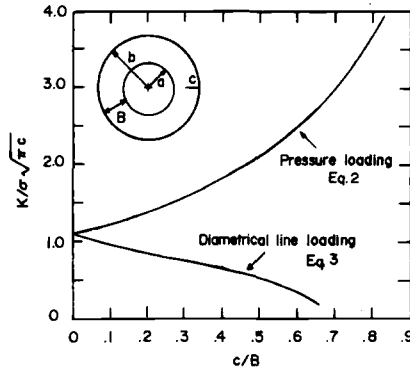


FIG. 4—The stress intensity factor solutions for a thick-walled cylinder with a radius ratio of two. For the pressure loading, σ is $2P_0 a^2 / (b^2 - a^2)$. For the diametrical line loading σ is $5.88F/\pi bt$.

in cylinders under diametrical loading given in Timoshenko and Goodier [15]. This solution reveals that the plane where we have introduced the crack is subjected to relatively low tension at the outside radius and much greater compression at the inside radius with a hyperbolic distribution through the wall thickness. Thus, as the crack depth increases, the crack tip enters a compressive stress field resulting in low K for deep cracks.

Again an expression of the form of Eq 1 was developed to fit the finite element results. In this case σ was taken as the stress at the outside radius for a cylinder with a radius ratio of 2.0, subjected to a total diametrical force F as given in [15]

$$K = \frac{5.88F}{\pi bt} \sqrt{\pi c} Y(c/B)$$

The value of the outside radius b , used in the determination of Y from the numerical data was 4, since the finite element mesh used has an outside radius of 4 units. The best fit for Y was found to be

$$Y(c/B) = 1.12 - 1.14(c/B) + 1.23(c/B)^2 - 2.20(c/B)^3 \quad (3)$$

This expression was also determined using regression, and is accurate to ± 1 percent over c/B from 0 to .67. Equation 3 is also plotted in Fig. 4. Note that both Equations 2 and 3 converge to 1.12 for short cracks.

Experimental Results

Crack growth data were gathered from a total of five specimens (one 100 percent overstrain specimen failed before any data were gathered

from it); all these data are plotted in Fig. 5. This plot shows that difficulty was encountered when attempting to initiate and grow cracks in the 0 percent overstrain specimens. No cracks developed in a 0 percent overstrain specimen with a starter notch 1.5 mm deep. Two new 0 percent specimens were prepared with 3.5-mm starter notches in which fatigue cracks were initiated. The apparent nonreproducibility of crack initiation between the two 0 percent specimens is due to the fact that these specimens were cycled very close to the fatigue threshold value, ΔK_{th} , at the root of the notch.

All of the c versus N curves in Fig. 5 tend to verify the finite element prediction of closure for deep cracks under the diametrical loading. In all cases, the fatigue cracks grew initially at an ever increasing rate, attained a maximum growth rate, then propagated at a slower rate until eventually the cracks stopped growing. This behavior indicates a loading history of first increasing ΔK , then decreasing ΔK , which is predicted by the finite element solution developed here.

The data were fitted by the curves shown in Fig. 5. The slopes of these curves were measured graphically to determine the crack growth rates (dc/dN). The first slope measurements are made at $c = 3.5$ mm and at each 0.5-mm increment in c up to $c = 7.0$ mm for the data from the autofrettage specimens. Because of the deeper starter notches, the first slope measurement of the data from the 0 percent specimens are at $c = 4.5$ mm. The crack growth rate is plotted against crack depth in Fig. 6.

The stress intensity factor range (ΔK) was determined for the 0 percent specimens at the same c values where dc/dN was measured, using the finite element K solution for the diametrical line loading. These calculations show that all the observed crack growth occurred over a very

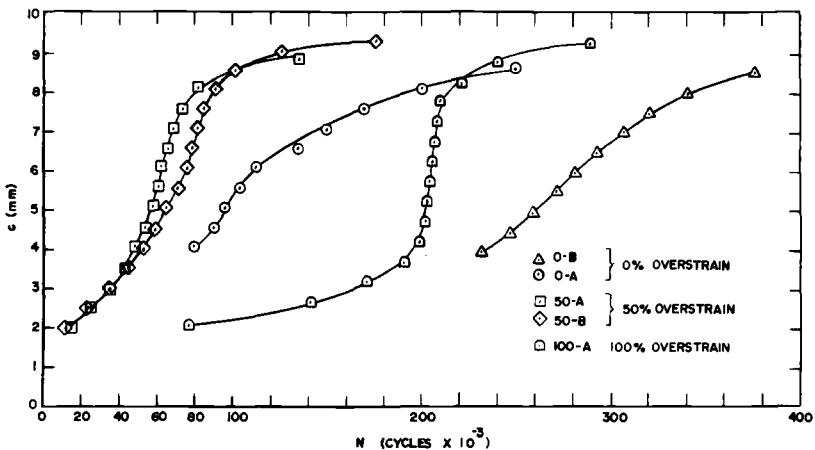


FIG. 5—The observed crack depth versus fatigue cycles from the ring experiment.

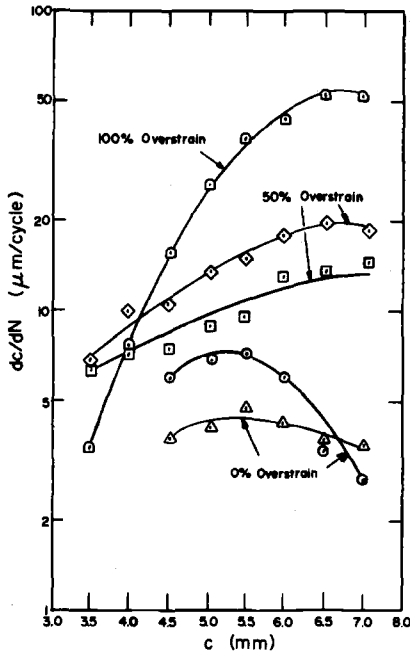


FIG. 6—Crack growth rate versus crack depth measured from the ring experiment.

narrow band of ΔK ($\sim 11.1 \text{ MPa}\cdot\text{m}^{1/2} < \Delta K < \sim 16.6 \text{ MPa}\cdot\text{m}^{1/2}$), which is close to the threshold value of ΔK of the material tested. Because of this small range of data, no attempt was made to model the effects of autofrettage using these test results.

Discussion

Although there are insufficient data to develop a mathematical model of the effect of autofrettage on crack growth, there are ample results to make some initial comments on these effects. In examining Fig. 6, it is readily observed that crack growth rate generally increases with increasing amounts of overstrain. At a crack depth of 5.5 cm, where the fastest crack growth rates were measured on both 0 percent specimens, cracks propagated about twice as fast in the 50 percent overstrain specimens, and nearly an order of magnitude faster in the 100 percent overstrain specimen.

The increase in growth rate may be attributed to the increase in the R ratio ($R = K_{\text{min}}/K_{\text{max}}$) during fatigue loading due to the tensile residual stresses from autofrettage. Two investigators recently have measured the effect of R on crack growth rates in several materials [16,17]. Both of these studies show that increasing R normally increases dc/dN , in all of the

materials that they tested. The amount of increase depends on the value of R and the applied ΔK , with the maximum increase occurring at ΔK close to the threshold of ΔK .

Using the stress solution for rings under diametrical loading from [15], we find that the maximum applied stress near the starter notch is about 125 MPa. A value of R for shallow crack depths for the 50 percent overstrain and 100 percent overstrain specimens can be found using the calculated residual stresses at the outside radius from Fig. 1. These calculations reveal R increasing from 0.1 in the 0 percent overstrain specimens to 0.56 and 0.82 respectively for the 50 and 100 percent overstrain specimens. Because of the gradients of the residual stresses as shown in Fig. 1, these R values will change as the crack advances. The aforementioned values are reported only to show that R could be affected substantially by the autofrettage residual stresses. It would be unwise to compare an R value for the nonlinear residual and applied stresses in the ring specimens to the R value associated with uniformly stressed laboratory specimens.

Conclusions

The crack growth measurements conducted reveal that autofrettage increases by as much as an order of magnitude fatigue crack growth rate in thick-walled cylinders containing a single external crack oriented in the radial direction. This large increase in crack growth rate is the result of effectively increasing the R ratio due to the autofrettage tensile residual stresses at the outside radius of the cylinders. Since the applied ΔK is close to the threshold value of ΔK , where crack growth rate is most sensitive to R , the large increase that was measured is probably the greatest that will occur. More testing is required to be able to model the changes in crack growth rate with autofrettage over a larger range of ΔK .

Acknowledgment

The authors would like to acknowledge the help of W. Mortimer for his assistance in conducting these experiments, J. Bak for obtaining the specimens, M. Hussain, W. Lorensen, and G. Pflagl, for their suggestions and assistance in the use of the program NASTRAN, and J. Underwood for his many suggestions, guidance, and assistance in analyzing the data.

References

- [1] Davidson, T. E. and Kendall, D. P., "The Design of Pressure Vessels for Very High Pressure Operation," Technical Report WVT-6917, Watervliet Arsenal, Watervliet, N.Y., 1969.
- [2] Davidson, T. E., Eisenstadt, R., and Reiner, A. N., *Journal of Basic Engineering*, Dec. 1963, pp. 555-565.

- [3] Davidson, T. E. and Throop, J. F., "Practical Fracture Mechanics Applications to Design of High Pressure Vessels," Technical Report WVT-TR-76047, Benet Weapons Laboratory, Watervliet, N. Y., 1976.
- [4] Underwood, J. H., private communication, July 1976.
- [5] Barsoum, R. S., *International Journal for Numerical Methods in Engineering*, Vol. 10, 1976, pp. 25-37.
- [6] Henshell, R. D., *International Journal for Numerical Methods in Engineering*, Vol. 9, 1975, pp. 495-507.
- [7] Irwin, G. R., *Journal of Applied Mechanics*, Vol. 24, 1957, pp. 361-364.
- [8] Hussain, M. A., Lorensen, W. E., and Pflegl, G. A., "The Quarter-Point Quadratic Isoparametric Element as a Singular Element for Crack Problems," NASA Technical Memorandum, NASTRAN: Users Experience 1976.
- [9] Kapp, J. A., Pflegl, G. A., and Underwood, J. H., *International Journal of Fracture*, Vol. 13, 1977, pp. 721-724.
- [10] Kobayashi, A. S., "A Simple Procedure for Estimating Stress Intensity Factors in the Region of a High Stress Gradient," Interim Report No. 1, U.S. Army Research Grant No. DA-ARO-D-31-124-73-638, 1973.
- [11] Chopra, P. S., *Nuclear Engineering Design*, Vol. 29, 1974, pp. 7-21.
- [12] Kobayashi, A. S., Maiden, D. E., and Simon, B. J., "Application of Finite Element Analysis Method to Two-Dimensional Problems in Fracture Mechanics," Paper No. 69-WA/PVP-12, American Society of Mechanical Engineers, 1969.
- [13] Emery, A. F. and Segedin, *Journal of Basic Engineering*, June 1972, pp. 387-393.
- [14] Tracy, P. G., "Elastic Analysis of Radial Cracks Emanating from the Outer and Inner Surfaces of a Circular Ring," submitted to *Engineering Fracture Mechanics*.
- [15] Timoshenko, S. P., and Goodier, J. N., *Theory of Elasticity*, 3rd Ed., McGraw Hill, N. Y., 1970, pp. 136-138.
- [16] Marci, G., this publication, pp. 168-186.
- [17] Vasquez, J. A., Morrone, A., and Gasco, J. C., this publication, pp. 187-197.

D. R. Galliard¹

Estimating Fatigue Crack Propagation Lives at the Test Site

REFERENCE: Galliard, D. R., "Estimating Fatigue Crack Propagation Lives at the Test Site," *Fracture Mechanics, ASTM STP 677*, C. W. Smith, Ed., American Society for Testing and Materials, 1979, pp. 757-769.

ABSTRACT: The durability of prototypical machines often is evaluated in the ground vehicle industry by field testing the machine. This field test usually consists of a representative sample of the customer's operation. From this sample, a forecast of the crack propagation fatigue life can be made.

A portable computer installation with interactive programs has been developed. Timeliness of data reduction has improved drastically the impact that test results have on the design and development process.

A brief description of the data acquisition system is presented. Major emphasis is given to the procedures that reduce these data and to the methods of cataloging intermediate data. Examples are given for typical output and, finally, verification of the analysis and computer program is made by comparing the life estimates with results of actual component test results.

KEY WORDS: fatigue (materials), crack propagation, computer program, field test

Nomenclature

- a Crack length, mm
- a_i Crack length at one of the discrete levels between the initial and final crack length, mm
- a_o Initial crack length as established in the material properties file, mm
- a_f Final crack length as specified by the test engineer in a data file or as calculated from the highest strain and the fracture toughness, mm
- B Blocks of a sample variable amplitude history
- B_f Number of blocks to grow a crack from an initial crack size to final fracture
- δa Crack growth per cycle, mm

¹ Staff engineer, engineering mechanics, The Technical Center, Deere and Co., Moline, Ill. 61265.

- da_i Incremental growth from one block of sample history at the crack length a_i , mm
- dB_i Incremental segment of a block of sample history at the crack length a_i
- m Exponent of the Paris equation, $da/dN = (\Delta K)^m$
- C Coefficient of the Paris equation with units of $\text{mm}/(\text{Nmm}^{-3/2})^m$
- e Value of strain measured by a strain gage and is assumed to be proportional to remote stress
- e_{\max} Maximum value of strain found in the sample strain-time history
- Δe_{eff} Effective strain range as determined by rainflow counting with a constant closure strain
- E Modulus of elasticity, N/mm^2
- t Test time; that is, the real time of the sample history.
- T Predicted time to grow the crack from the initial crack size to final crack size, h
- W Dimension that characterizes the component geometry, usually the width, mm

This paper describes a procedure used by one manufacturer to extend its fatigue prediction ability. The failure of machines due to fatigue continues to be one of the most difficult failure modes to evaluate. Its consequences are often costly and sometimes tragic. Therefore, a considerable amount of effort is expended by product designers and developers [1,2]² to improve their methods of determining the machine's structural integrity related to fatigue. A brief review of the needs of the test engineer as well as the procedures used previously for fatigue evaluation is helpful in understanding the reasons for use of some of the methods described in this paper.

Test engineer's needs vary with the type of machine that is being developed. Nonetheless, he usually is given the assignment of evaluating the structural integrity of the design. A common practice is to locate potential fatigue failure regions by use of brittle lacquer [3]. This permits him to locate a strain gage to record a "nominal" strain-time history. Once the transducer is located, he generally will simulate a customer's operation [4] such as "digging in clay soil." Quite often it is *not* convenient to simulate all of a customer's operations as a continuous time history. So a series of samples called "runs" is collected. These samples are usually relatively short, less than 10 min of real time. Finally, the data analysis must be completed at the test site for the results to have maximum impact on the design.

Traditional methods of calculating fatigue life are to use rotating beam stress-life or smooth polished axial specimen strain-life material

² The italic numbers in brackets refer to the list of references appended to this paper.

properties to calculate "crack initiation life" [5,6]. However, there are applications where the probability of a crack existing from manufacturing processing or fatigue requires an analysis procedure that can estimate crack growth [7,8].

Therefore, the following computer program was developed to match the needs of designers and test engineers and provide an extension of their contemporary procedures.

Data Collection

The data collection equipment is housed in a trailer for transport to the test site. Once the equipment is located at a convenient distance from the field, radio telemetry is used to transfer the signal from the test vehicle to the trailer. Most of the systems at present are limited to 31 independent channels of data transmission. Also, most systems use a computer that has 32 K words of core storage with 2.6 million words of disk storage and a cathode ray tube (CRT) as an input/output (I/O) device [9].

Real Time Data Analysis

Data reduction for fatigue related analysis during the test consists of: (1) sampling the data, (2) using a simplified digital filtering scheme to eliminate "small strain excursions," (3) determining the maximum and minimum value of each channel, and (4) storing the data in 100 word blocks on a 1.3 million word removable disk.

The data then consists of "peaks" and "valleys" in a time sequence for each channel. Also, the maximum and minimum for each channel with its computer disk storage location is stored at the beginning of each data test run.

Verification of Test Data

Test data are verified by a post-processing program that displays the maximum and minimum for each channel, plots a pseudo-time history of the peaks and valleys, or displays the 100 values for a given data block. A pseudo-time history is a strain-time plot formed by connecting the peaks and valleys that are stored. Since some of the small excursions have been edited, the frequency of these data is false. However, the amplitude of the plot gives the test engineer a visual indication that closely resembles his experience with oscillograph strain-time histories. In this last mode, it is also possible to edit individual values of data.

The collection of data up to this point is common to most of the fatigue programs. Further details of this real time portion of data collection and data reduction are documented in Refs 6 and 9.

Preliminary Data Files

Several data files must be made available before post-processing of the peak-valley data begins. One of these files is a material properties file. This file is structured as a menu of materials that are identified by an integer. For example, Fig. 1 is a display of material number 38 with the common name of MAN-TEN. The first four properties help define the material and are included only for that purpose. Properties five through ten are used in crack initiation programs. Properties eleven through fourteen are used in the crack propagation program. The coefficient of the Paris equation [10] is shown as property number eleven with units of $\text{mm}/(\text{Nmm}^{-3/2})^m$ where m is the exponent of the Paris equation. Although initial crack length, property number thirteen, is not a material property, it is included for the convenience of the test engineer. Initial crack length is selected by the test engineer, who must rely on his experience with the manufacturing process pertinent to that location. He will often analyze the data twice to obtain upper and lower bound life predictions. This approach also will determine the sensitivity of the life prediction to initial crack size. Property number fourteen is the fracture toughness of the material and has units of $\text{Nmm}^{-3/2}$. The confidence of the materials properties is displayed in line number fifteen by a three-digit integer. Each digit refers to the level of confidence for monotonic, cyclic, and crack growth properties, respectively.

MATERIAL NO. 38	MAN-TEN
1 (BHN) BRINNEL HARDNESS NUMBER	215.00
2 (SU) ULTIMATE STRENGTH	565.00
3 (SY) MONOTONIC YIELD STRENGTH	324.00
4 (SYP) CYCLIC YIELD STRENGTH	0.00000
5 (B) FATIGUE STRENGTH EXPONENT	-0.95000E-01
6 (SFP) FATIGUE STRENGTH COEFFICIENT	930.00
7 (E) MODULUS OF ELASTICITY	0.20600E+06
8 (ND) CYCLIC STRAIN HARDENING EXPONENT	0.20200
9 (EFP) FATIGUE DUCTILITY COEFFICIENT	0.26000
10 (C) FATIGUE DUCTILITY EXPONENT	-0.47000
11 (D) COEFFICIENT OF DA/DN	0.38470E-13
12 (EX) EXPONENT OF DA/DN	3.4300
13 (ICL) INITIAL CRACK LENGTH	28.000
14 (CSI) CRITICAL STRESS INTENSITY	4000.0
15 (CON) CONFIDENCE OF DATA	123.00

FIG. 1—Material properties.

Individual digits range from “1” to “5” where “1” refers to the highest level of confidence and “5” refers to the lowest level. For material properties to rate a “1” would require many laboratory tests with complete statistical sampling of the material. A rating of “5” typically would represent estimates derived from other material properties. For example, the number “113” would indicate the highest level of confidence in the monotonic and cyclic properties with median level confidence in the crack growth properties.

A second data file is a menu of stress intensity relationships. The test engineer can select the appropriate stress intensity for each channel by choosing an integer that is associated with a particular loading, crack shape, and component shape. These stress intensity relationships were selected from several references [11-14]. An example, geometry code number 17, is shown in Fig. 2. The function is stored as 96 values in equal increments of a/W between 0 and 0.95.

A third set of data provides test information such as test location, date, etc. This set of data files also provides channel dependent information, such as transducer name and calibration. An example of these kinds of data are shown in Fig. 3. These data are entered by an interactive program as are the other data file programs. The program user enters the column title, then the channel number. He then enters the value in question. For example, if the critical crack length of channel 4 was changed to zero, the user would first enter LE and a carriage return. The cursor of the CRT would then move to the right of “CHANNEL?” He would then enter 4 with a carriage return. The cursor would then move to the right of 54.0 under the column of LENGTH. He would then enter zero with a carriage return. If a value of zero is entered in this column, the analysis program will calculate the critical crack length using the maximum value of the data for that channel and the stress intensity relationship specified by the geometry code. Other pertinent data such as transducer calibration, material code, transducer name, and dimension (W) are entered in a similar manner.

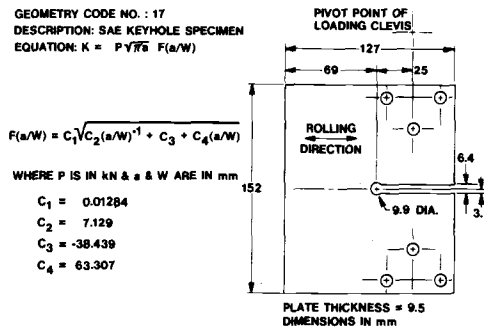


FIG. 2—Geometry code data.

CH#	GEO CODE	LENGTH	CLOSURE	DIMEN	D2
1	17	39.0	0.0	94.0	0.0
2	17	43.0	0.0	94.0	0.0
3	17	50.0	0.0	94.0	0.0
4	17	54.0	0.0	94.0	0.0
5	17	63.0	0.0	94.0	0.0

ENTER COLUMN TITLE

CHANNEL?

FIG. 3—Channel dependent data.

Analysis of the Data

The crack propagation prediction program is written also as an interactive conversational type of program. So upon execution of the program, several questions are printed such as "ENTER THE RUN NUMBER," "ENTER THE CHANNEL NUMBERS," and "MATERIAL PROPERTIES LISTING?" A flow chart of the procedures is shown in Fig. 4. If the response to the question "MATERIAL PROPERTIES LISTING?" is "YES," then an output similar to Fig. 5 is printed. The heading on this figure is a standard subroutine that is included with all output pages. Only the materials that are used in this analysis are printed. The program is halted at this point waiting for a carriage return before continuing the analysis. This pause provides time for the test engineer to make a hard copy of the output if needed.

After printing the material properties, the program will analyze the first requested channel. The procedures used for this analysis are as follows:

1. Read the data from a disk starting at the maximum value. Also read materials properties including the initial crack length.

2. Determine the final crack length for fracture. If a positive value was given for LENGTH as shown in Fig. 3, then that value will be used for the final crack length. If zero was specified in this data file, then the program will calculate the final crack length. This calculation is done by searching the geometry code file until the following equation is satisfied

$$K_c = e_{\max} \cdot E \sqrt{\pi a} \cdot F(a/W) \quad (1)$$

3. After the initial and final crack lengths have been determined, the difference is divided into 100 equally spaced crack intervals, according to

$$a_{i+1} - a_i = (a_f - a_0)/100 \quad (2)$$

4. A crack growth increment due to an effective strain range can be written as

$$\delta a = C(E \cdot \Delta e_{\text{eff}})^m \cdot [\sqrt{\pi a} \cdot F(a, W)]^m \quad (3)$$

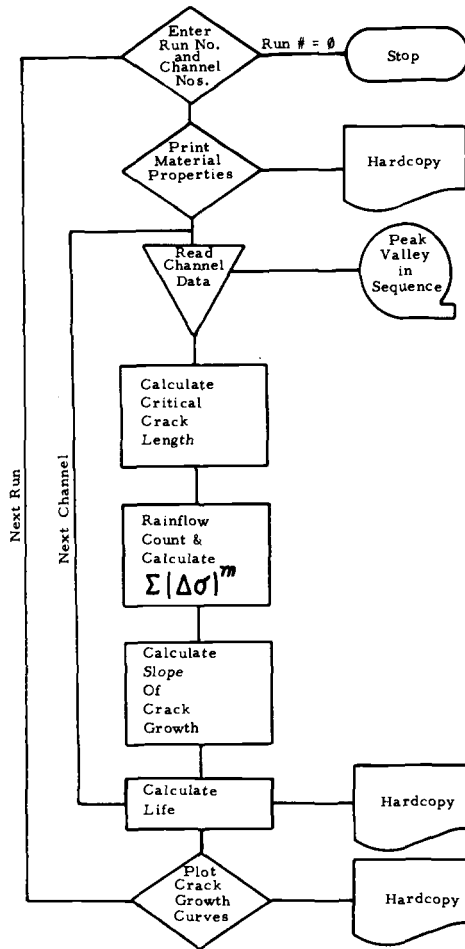


FIG. 4—Flow chart of analysis procedures.

MACHINE: SAE SPECIMEN
 LOCATION: MOLINE, ILL
 TEST ENGINEER: GALLIART
 CONDITIONS: SAE COMPLIANCE DELTA K
 OPERATION: SAE TRANSMISSION(DEERE) HISTORY

DATE: 12OCT77
 TEST TIME: 60 MIN 0 SEC
 RUN NUMBER: 1

MATERIAL	BHN	MODULUS OF ELAST. (GPA)	ULTIM. STRNG. (MPA)	MONOT. YIELD STRNG. (MPA)	CRACK GROWTH COEFF.	CRACK GROWTH EXPON.	FRACT TOUGH (MPA SR/MM)	INIT CRACK LENGTH (MM)
MAN-TEN	215	206.0	565.0	324.0	0.38E-13	3.4	4000.	28.0

FIG. 5—Material properties used in analysis.

Then the growth rate at the i^{th} crack length a_i due to a sample history can be expressed as [15]

$$\frac{da_i}{dB} = \Sigma \phi a_i = C \cdot [\sqrt{\pi a} \cdot F(a_i, W)]^m \cdot \Sigma (E \cdot \Delta e_{eff})^m \quad (4)$$

Since the last factor in Eq 4, $[\Sigma (E \cdot \Delta e_{eff})^m]$, is independent of crack length the sum can be calculated over the entire sample history. The effective strain range is formed by rainflow counting [16] the peaks and valleys and by including a constant closure strain [8,17]. Rainflow counting was chosen since this counting procedure was used on crack initiation procedures and several researchers [8,18] have used the method to make good crack propagation predictions.

In simplest terms, rainflow counting is to treat small events as interruptions of larger overall events. The method matches the highest peak and the lowest valley, then the next largest and smallest, etc., until peaks and valleys have all been paired.

The use of an effective strain range follows the assumption that fatigue cracks grow only during that portion of the load cycle where the crack tip is open [17]. The use of a constant closure strain is based on the assumption that the sample history is classified as a "short" spectra [8,15]. The data begin with the maximum strain, so the ranges are determined by the simple relationship

$$\Delta e_{eff} = |e_{i-2} - e_{i-1}| \text{ if } |e_{i-2} - e_{i-1}| \leq |e_{i-1} - e_i| \quad (5)$$

where $e_i = e_i$ if $e_i \geq \text{closure}$ and $e_i = \text{closure}$ if $e_i < \text{closure}$.

The factorization of this summation in Eq 4 is an important concept since the data have to be read and rainflow counted only once. The slope of the crack growth, (da/dB) , shown graphically in Fig. 6, is then calculated for the 100 equally spaced crack lengths.

5. The number of blocks of sample history to grow the crack from the initial crack length to final crack length is then calculated according to Ref 18, that is

$$B_f = \int_{a_0}^{a_f} \frac{dB}{da_i} \cdot da_i \quad (6)$$

which can be approximated by

$$B_f = \sum_{i=2}^{100} \frac{\frac{dB}{da_i} + \frac{dB}{da_{i-1}}}{2} \cdot [a_i - a_{i-1}] \quad (7)$$

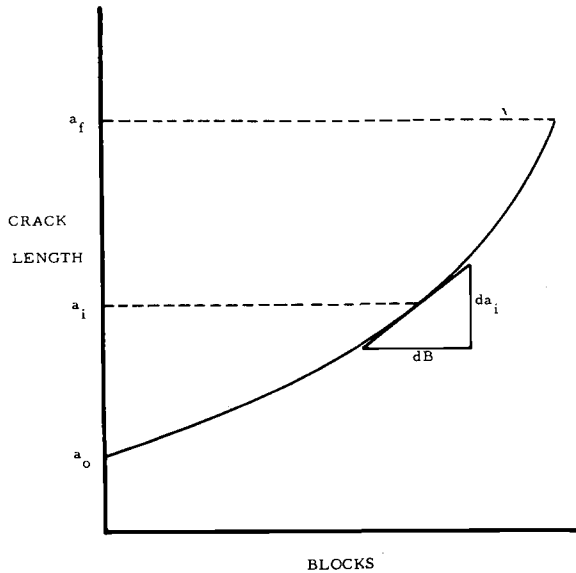


FIG. 6—Crack length versus blocks of a sample time history.

The inverse slope is shown graphically in Fig. 7.

6. The final result then is simply to multiply the number of blocks, B_f , by the time of each block; that is, the real time of the sample history

$$T = B_f \cdot t \quad (8)$$

7. The time in hours, T , to grow the crack from initial to final crack length is written to a data file for later processing. The results are also written to the CRT with a standard heading as shown in Fig. 8.

8. The aforementioned steps are repeated until all of the channels that were requested for a given run are analyzed.

Data Output

In addition to the output mentioned above, Figs. 5 and 8, an optional plotting routine is available. After all requested channels have been analyzed, the user can input a carriage return which will cause the message to be printed: "DO YOU WANT CRACK GROWTH CURVES?" If the response is "YES," the message "WHICH CHANNEL?" will be printed. A response of a channel number that has been analyzed will provide a plot similar to Fig. 9. Ordered pairs of B_f and a_i were stored in temporary arrays during the summation of Eq 7. The plot then is simply a connection of the 100 ordered pairs of $B_f \cdot t$ and a_i . Automatic scaling of the plot is provided to give growth curves. The

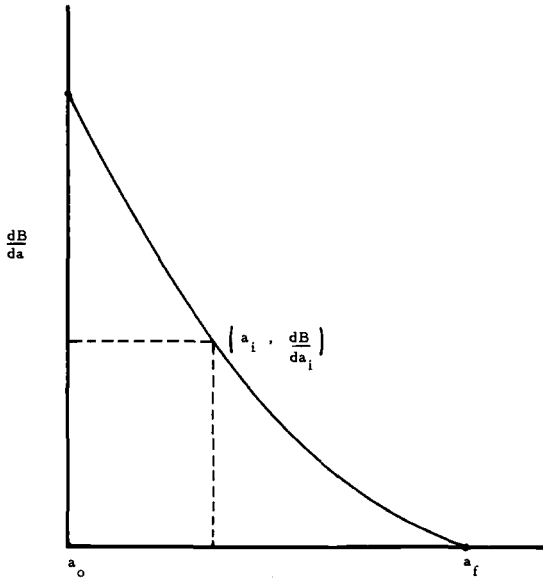


FIG. 7—Crack growth slope reciprocal versus crack length.

program will repeat the plotting loop until a null response is given to the question “WHICH CHANNEL?”

The program then returns to the first question “ENTER THE RUN NUMBER.” At this time, the user may choose to analyze a different run or he may choose to exit the program by a null response with a carriage return.

Limitations

Although the accuracy of the procedures diminishes at short lives, it is of small consequence to the designer. These failures will appear in routine

```

MACHINE: SAE SPECIMEN          DATE: 12OCT77
LOCATION:  MOBILE,  ILL.        TEST TIME:  60 MIN  0 SEC
TEST ENGINEER: GALLIART      RUN NUMBER:  1
CONDITIONS: SAE COMPLIANCE DELTA K
OPERATION: SAE TRANSMISSION(DEERE) HISTORY
    
```

CHANNEL	GAGE MATERIAL	GEO. TYPE	INIT. CRACK LENGTH (MM)	FINAL CRACK LENGTH (MM)	PROPAGATION LIFE (HOURS)
1	71.2 MAN-TEN	17	28.0	39.0	0.167E+01
2	71.2 MAN-TEN	17	28.0	43.0	0.194E+01
3	35.6 MAN-TEN	17	28.0	50.0	0.419E+02
4	35.6 MAN-TEN	17	28.0	54.0	0.433E+02
5	15.6 MAN-TEN	17	28.0	63.0	0.204E+04

DO YOU WANT CRACK GROWTH CURVES?
Y

FIG. 8—Predicted propagation lives.

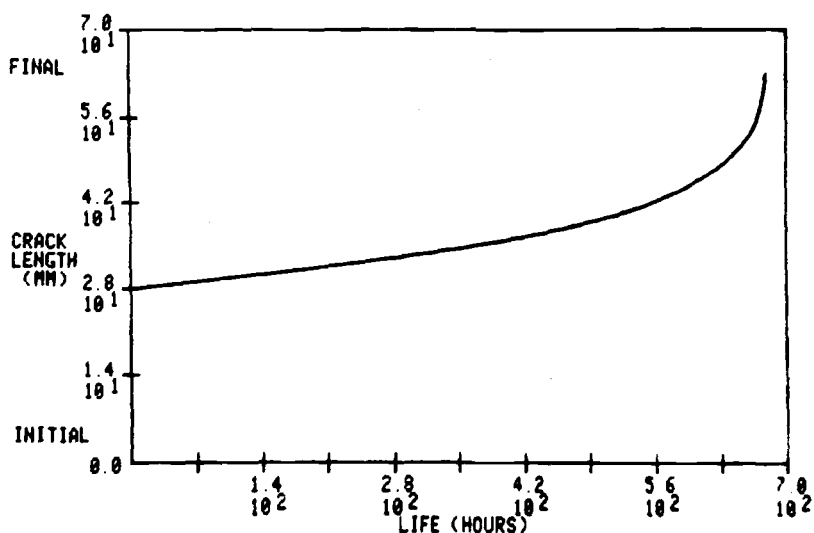


FIG. 9—Crack growth plot.

“shake down” tests. Also, the method of calculating propagation life is dependent upon the sample history repeating itself many times during the life. However, this is consistent with the basic data collection scheme and is representative of many real service histories.

Program Verification

A test plan [19] to “debug” a computer program is an important part of its development. The data provided by the SAE round robin test program [20] proved to be invaluable as a bench mark for the program and the analysis procedures. Likewise, the research provided by several sources [8,21,22] proved to be helpful for the development of several basic concepts.

A plot of laboratory test data versus the predicted results by this program are shown in Fig. 10. An “ideal” prediction would be one in which the data are centered over the diagonal line. For reference, lines were drawn at factors of three greater or less than the ideal prediction. The scatter of the laboratory data is often as large as these reference lines.

Conclusions

The crack propagation program that is described in this paper is a significant extension to the traditional fatigue prediction procedures used by this and other manufacturers. Since the program was not written to replace the traditional procedures, but was written to complement the

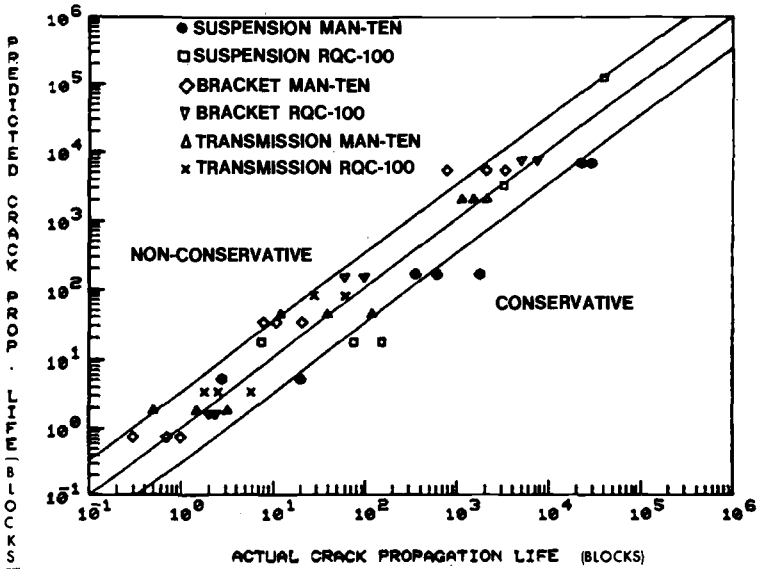


FIG. 10—Computer program verification summary.

procedures, it was important to use the same fundamental data collected in real time. Hence, a field test need not be repeated for each analysis.

The fact that the procedure does not account for load sequence effects such as crack growth delay due to an overload, tends to make the predictions conservative. However, this is consistent with many manufacturers' design philosophy.

Although future improvements will be made on the procedures described in this paper, the needs of the designer and test engineer for quick and relatively easy-to-use procedures must not be sacrificed.

Acknowledgments

The author wishes to acknowledge the counsel and research efforts of Darrell Socie and Drew Nelson and the many participants in the SAE Cumulative Fatigue Damage Round-Robin test program that provided much valuable data for checking program procedures. And finally, the author wishes to thank John Epplin for providing most of the programming expertise to develop the computer programs.

References

- [1] Graham, J. A., Ed., *Fatigue Design Handbook*, Society of Automotive Engineers, Vol. 4, 1968.
- [2] Berns, H. D., "Field Service History Analysis for Ground Vehicles," Paper No. 750553, Society of Automotive Engineers, April 1975.

- [3] Kuehl, R. A. and Berns, D. K., "Field Techniques for Brittle Coatings," presented at SESA Annual Meeting, Society for Experimental Stress Analysis, Cleveland, Oct. 1964.
- [4] Galliard, D. R., "Field Test Data Vs. Customer Loads," Paper No. 730140, Society of Automotive Engineers, presented at the International Automotive Engineering Congress, Detroit, Jan. 1973.
- [5] Galliard, D. R. and Tucker, L. E., "Data Acquisition and Fatigue Life Predictions," ASAE Paper No. 72-622, presented at the American Society of Agricultural Engineers, Chicago, Dec. 1972.
- [6] Downing, S. D., Galliard, D. R., and Berenyi, T. A., "A Neuber's Rule Fatigue Analysis Procedure for Use with a Mobile Computer," Paper No. 760317, Society of Automotive Engineers, presented at SAE Automotive Engineering Congress and Exposition, Detroit, Feb. 1976.
- [7] Schijve, J. in *Fatigue Crack Growth Under Spectrum Loads*, ASTM STP 595, American Society for Testing and Materials, 1976, p. 3.
- [8] Socie, D. R., "Estimating Fatigue Crack Initiation and Propagation Lives in Notched Plates Under Variable Loading Histories," Report No. 417, Department of Theoretical and Applied Mechanics, University of Illinois, June 1977.
- [9] Galliard, D. R. et al, "On-Line Data Acquisition and Reduction in the field," Report No. SP-410, Society of Automotive Engineers, presented at Earthmoving Conference, Milwaukee, Sept. 1976.
- [10] Paris, P. C. and Erdogan, F., *Journal of Basic Engineering; Transactions*, American Society of Mechanical Engineers, Series D, Vol. 85, No. 3, 1963, p. 528.
- [11] Tada, H., Paris, P., and Irwin, G., *The Stress Analysis of Cracks Handbook*, Del Research Corporation, Hellertown, Pa., 1973.
- [12] Sih, G. C., *Handbook of Stress-Intensity Factors*, Institute of Fracture and Solid Mechanics, Lehigh University, Bethlehem, Pa., 1973.
- [13] Rooke, D. P. and Cartwright, D. J., "Stress Intensity Factors," Her Majesty's Stationery Office, London, The Hillington Press, Uxbridge, Middlesex, 1976.
- [14] McDermott, M. E. and Stephens, R. I., this publication, pp. 719-733.
- [15] Elber, W. in *Fatigue Crack Growth Under Spectrum Loads*, ASTM STP 595, American Society for Testing and Materials, 1975, pp. 236-247.
- [16] Matsuisaki, M. and Endo T., "Fatigue of Metals Subjected to Varying Stress," presented at Kyushu District Meeting, Japan Society of Mechanical Engineers, Kitakyushu-Shi, March 1968.
- [17] Elber W. in *Damage Tolerance in Aircraft Structures*, ASTM STP 486, American Society for Testing and Materials, 1971, pp. 230-242.
- [18] Nelson, D. V. and Fuchs, H. O. in *Fatigue Crack Growth Under Spectrum Loads*, ASTM STP 595, American Society for Testing and Materials, 1975, pp. 267-287.
- [19] Metzger, P. W., *Managing a Programming Project*, Prentice Hall, Edgewood Cliffs, N.J., 1973, pp. 113-156.
- [20] Bussa, S. and Tucker, L., "The SAE Cumulative Fatigue Damage Test Program," Paper No. 750038, Society of Automotive Engineers, presented at SAE Automotive Engineering Congress, Detroit, Feb. 1975.
- [21] Nelson, D. V. and Fuchs, H. O., "Prediction of Cumulative Fatigue Damage Using Condensed Load Histories," Paper No. 750045, Society of Automotive Engineers, presented at the Automotive Engineering Congress, Detroit, Feb. 1975.
- [22] Stephens, R. I., Mauritzson, G., Benner, P. H., and Galliard, D. R., "Fatigue and Fracture Toughness of SAE 0030 Cast Steel and Comparison with SAE 1020 Wrought Steel," *Journal of Steel Castings Research*, No. 83, July 1978.

B. Kong¹ and P. C. Paris¹

On the Cup and Cone Fracture of Tensile Bars

REFERENCE: Kong, B. and Paris, P. C., "On the Cup and Cone Fracture of Tensile Bars," *Fracture Mechanics, ASTM STP 677*, C. W. Smith, Ed., American Society for Testing and Materials, 1979, pp. 770-780.

ABSTRACT: This paper attempts to apply the recently developed concepts of tearing instability for cracks under fully plastic conditions to tensile bar fracture. Presuming that the transition from flat fracture to the shear wall of a cup and cone fracture is triggered by the onset of tearing instability is supported by experimental data. Moreover, additional experimental evidence indicates that the initial flat part of the fracture precedes instability for cup and cone behavior. Therefore, this work suggests that the tearing instability theory may indeed be applicable to at least some situations involving extensive plastic deformation prior to cracking failure.

KEY WORDS: tension tests, fracture (materials), fracture mechanics, tearing instability, fatigue (materials), plastic deformation

Nomenclature

- a Crack size
- A Cross sectional area
- C_M Testing machine compliance
- d Diameter of flat crack region
- D Tensile bar diameter
- E Modulus of elasticity
- J Rice's J-integral [2]
- J_{1c} Value of J at commencement of crack growth
- L Tensile bar length
- L_{eff} Equivalent length of a tensile bar adjusting for gripping and compliance of the testing machine
- P_L Limit load
- T Tearing modulus (applied by the system *or* material's resistance)

¹ Undergraduate research assistant and professor of mechanics, respectively, Washington University, St. Louis, Mo. 63130.

- dJ/da Tearing slope of a J-integral R-curve [1]
 σ_o Flow stress (average of yield and ultimate)
 σ_f Fracture stress of a tensile bar
 σ_{tip} Fracture stress adjusted for an internal crack in a tensile bar
 Δ_{EL} Elastic system displacement
 Δ_{PL} Plastic system displacement
 δ_T Crack tip opening displacement

The round-bar tension test is the test commonly used to determine the global deformation properties of materials. However, little understanding has been developed on the mechanism of the final cup-cone fracture of ductile tensile bars. Recently, an analysis of this instability based upon the mechanics of progressive fracturing was suggested [1].²

This research was initiated on the observation that the familiar cup and cone fracture surface of tensile bars suggests a size dependent shift in the fracture mechanism during crack growth and separation. Since with large plastic deformation and necking the stress condition of tensile bars is most severe at the center, it is probable that the flat region in the cup and cone fracture surface corresponds to the early stable tearing which later changes to unstable tearing as the crack reaches a critical size.

Therefore, it seems appropriate here to attempt to apply the newly developed tearing instability theory, that is, the so-called tearing modulus, T , concept, developed by the fracture research group at Washington University [1]. The approach will be to attempt to use this theory to predict the switch from stable crack growth to unstable growth as the fracture mode changes from flat to oblique-shear during a cup and cone failure.

Theory Development

As fracture instability is approached, the specimen is fully plastic in the necked region around the crack, and the flow stress on the remaining ligament is approximately constant. Crack propagation decreases the area of remaining uncracked ligament and thus lowers the plastic limit load. Assuming fixed grips, this results in some amount of elastic shortening of the unnecked portions of the specimen. During the instant of unstable fracture, the movement of testing machine grips is nearly zero, and thus the total length of the specimen remains nearly constant. Therefore, with an increment of crack growth, if the amount of elastic shortening is greater than the amount of plastic elongation associated with crack growth, then instability results or vice versa. As will be seen a specific

² The italic numbers in brackets refer to the list of references appended to this paper.

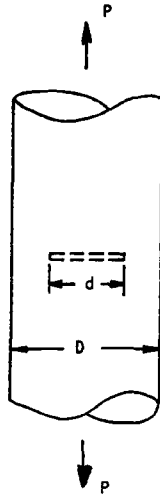


FIG. 1—Circular center-cracked round tensile bar, $d = 2a$.

amount of plastic elongation is associated with an increment of crack growth.

Subsequently, when the amount of plastic elongation and elastic shortening are equated, then all intrinsic material properties, as distinguished from properties of geometric configuration of the specimen, can be separated to different sides of an equation. The side of material properties is termed T_{material} , while the side of geometric configuration is termed T_{applied} [1]. For all cases [1] that have been explored

$$T_{\text{material}} = \frac{dJ}{da} \frac{E}{\sigma_0^2} \quad (1)$$

which becomes the definition of T_{material} , the tearing modulus.

The configuration of a round tensile bar with a circular center crack is shown in Fig. 1.

Following the analysis in Ref 1, the limit load, P_L , is given by

$$P_L = \frac{\pi}{4} (D^2 - d^2) \sigma_f \quad (2)$$

By first approximation σ_f is assumed to be independent of r and θ . Differentiating, the load drop due to crack extension is obtained.

$$dP_L = -\sigma_f \pi d da \quad (3)$$

The elastic shortening due to load drop is therefore

$$d\Delta_{EL} = \frac{dP_L L}{AE} = \frac{-\sigma_f \pi d da L}{\frac{\pi D^2}{4} E} = -4\sigma_f \frac{Ld}{D^2 E} da \quad (4)$$

From the appropriate slip field, the plastic lengthening is nearly equal to crack opening stretch δ_T , hence, we assume

$$d\Delta_{PL} \approx d\delta_T \quad (5)$$

From Refs 2,3,4 it has been shown that

$$dJ = \sigma_o d\delta_T \quad (6)$$

where dJ is an incremental increase in Rice's J-integral, therefore

$$d\Delta_{PL} = \frac{dJ}{\sigma_o} \quad (7)$$

Comparing $|d\Delta_{EL}| \geq |d\Delta_{PL}|$, and manipulating terms the instability condition is

$$T_{\text{material}} = \frac{dJ}{da} \frac{E}{\sigma_o^2} \leq \frac{4Ld}{D^2} = T_{\text{applied}} \quad (8)$$

because $\sigma_f \approx \sigma_o$.

Similar to the development of tearing instability of a single microflaw ahead of a crack tip [1], the tearing instability of a single microflaw in uniform plastic stress field can be obtained

$$T_{\text{material}} = \frac{dJ}{da} \frac{E}{\sigma_o^2} \leq 2.6 = T_{\text{applied}} \quad (9)$$

Notice that an assumption in this derivation is that the flaw is so small that it has negligible influence on the gross flow field, and thus none of the geometric dimensions are involved in the T_{applied} expression.

Equations 8 and 9, the cracking instability criteria, suggest the following behavior patterns. After some amount of deformation a micro flaw in the center of a tensile bar might begin to grow. (In particular the beginning of growth might be associated with J_{1c} [1,2] or a similar parameter). If growth begins and T_{material} is less than 2.6, then Eq 9 implies instability from the beginning of growth and perhaps sudden completely flat fracture occurs, a so-called star fracture. However, if T_{material} is greater than 2.6,

TABLE 1—Chemical composition of ASTM A471.

Material	C	P	S	Si	Mn	Ni	Cr	Mo	V
ASTM A471 (NiCrMoV)	0.26	0.01	0.007	0.026	0.31	3.34	1.67	0.44	0.13

Eq 9 implies that microflow growth will at first be stable. But as the crack grows, its diameter, d , increases and Eq 8 implies that at some point, T_{applied} , may correspondingly increase to exceed T_{material} and instability should ensue. Since the slip field associated with Eq 8 is 45 deg slip from the crack tip to the outside of the bar, this instability mechanism accounts for the change from flat stable growth to oblique-shear, forming the cup and cone.

Material for Initial Tests

ASTM A471 rotor steel was chosen for initial tests. Its chemical compositions are listed in Table 1.

T_{material} for ASTM A471 at 200°C was obtained by Paris et al in their bend bar tests [1]. The average value for 15 tests was $T_{\text{material}} = 36.1$ (nondimensional). However, prior to crack growth and instability in a tensile bar large plastic deformations take place, especially at the neck, and so for T as defined in Eq 1, the T_{material} value just given should be adjusted for changes in flow stress, σ_o , and the tearing slope, dJ/da , of the J-integral R-curve. Herein, adjustment will be made only for the flow stress, σ_o , as computed from load and area at the moment of unstable fracture.

Testing Procedures

ASTM 0.505-in. standard tensile bars heated to 200°C by an electric tape were pulled slowly to fracture under displacement control in an MTS servo hydraulic test machine, or load control (slightly cracked valve) in a Baldwin machine. Diameters, and areas of flat portion in the cup and cone fracture surfaces were measured and recorded in Table 2.

In addition a few additional tests were interrupted just before fracture failure. Two of these necked specimens were then fatigued in an MTS machine by appropriate reduction of the mean load, and amplitude as visible cracks enlarged. After fracturing in fatigue, surfaces were examined to see if sizable cracks had developed prior to the fatigue process. Further, X-ray photographs of two other necked but unfractured specimens were taken at an angle perpendicular to the longitudinal axis to attempt to determine whether microcracks had grown prior to fracture instability. The fatigued specimens showed moderate growth of micro-

TABLE 2—Test results for ASTM A471.

Specimen Number	Machine	P_{fracture} , kips	D_{neck} , in.	A_{lip} , in. ²	σ_{lip} , kips/in. ²	D_o , in.	d , in.	L_{eff} , in.	Temperature, °C	T_{material}	T_{applied}
3	Baldwin	20.4	0.352	0.070	294	0.493	0.190	4.0	200	6.8	12.0
5	Baldwin	20.5	0.341	0.060	330	0.490	0.180	4.0	75	5.4	12.0
6	Baldwin	20.5	0.360	0.72	285	0.488	0.178	4.0	75	7.3	11.7
8	MTS	21.6	0.359	0.066	328	0.490	0.178	4.5	200	7.4	13.4
9	MTS	20.8	0.381	0.090	232	0.505	0.176	5.4	200	11.0	14.9
11	MTS	24.3	0.365	0.085	241	0.503	0.125	4.9	200	10.2	9.7
12	MTS	20.5	0.366	0.079	260	0.505	0.180	4.5	200	8.8	12.8

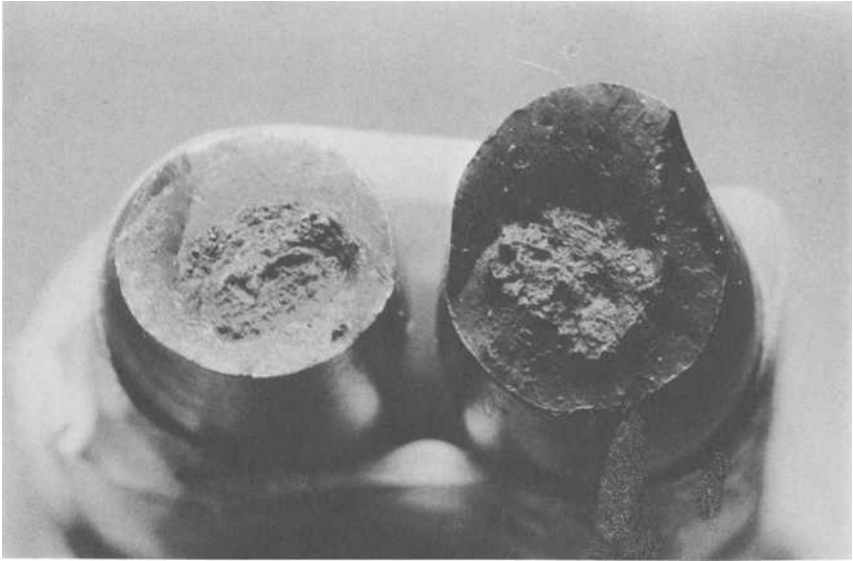


FIG. 2—*Typical cup and cone fractures of ASTM A471.*

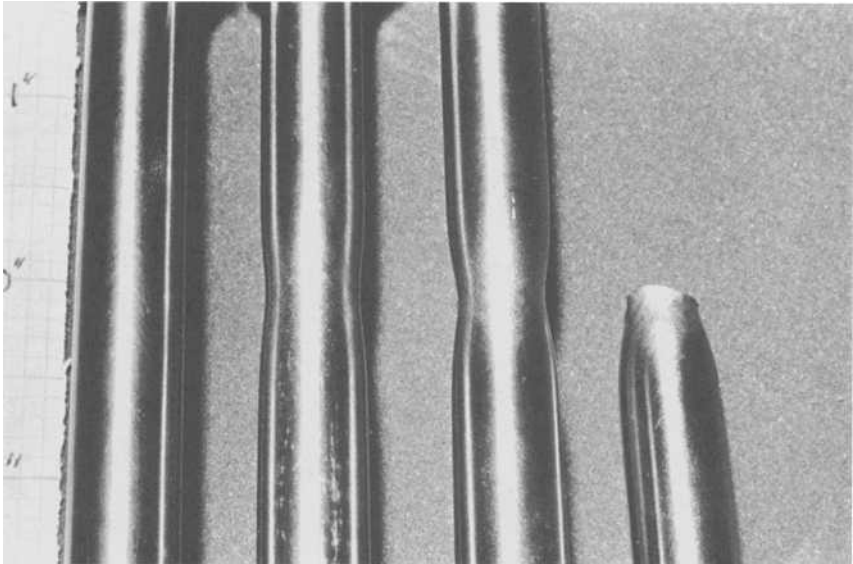


FIG. 3—*Interrupted tests of necked tensile bars (two center bars) compared to unstretched and fractured bars.*

flaws prior to fatiguing, but the X-ray method did not lead to any observations of cracks.

Figure 2 shows typical cup and cone fractures of the bars tested to failure. Figure 3 shows two interrupted necked bars between an untested bar and a fractured bar.

Results and Calculations for Tests-To-Fracture Failure

Compliances of the test machines were estimated by considering only the bending of the crosshead, the most compliant part. The results are

$$C_M = \frac{v}{P} = \frac{1}{24} \frac{L^3}{EI}$$

$$C_{MTS} \sim 2.3 \times 10^{-8} \text{ in. lb}^{-1}$$

$$C_{Bald} \sim 2.9 \times 10^{-8} \text{ in. lb}^{-1}$$

For incorporation into computations using Eq 8, L , is replaced by an effective length, L_{eff} , which is adjusted for testing machine compliance and the bar ends of enlarged diameter.

$$L_{eff} = L_{specimen} \times \frac{C_{specimen} + C_M}{C_{specimen}}$$

where

$$L_{specimen} = L_{gage} + L_{grip} \times \left(\frac{D_{gage}}{D_{grip}} \right)^2$$

where dimensions are illustrated in Fig. 4.

In addition the slant fracture surface area, A_{lip} , of the cup and cone fracture was estimated from the diameters of the flat area, d , and the neck, D_{neck} . From this result and the fracture load, $P_{fracture}$, the adjusted flow stress, σ_{lip} , was computed. Results of these measurements and computations are given in Table 2.

Results for Interrupted Tests

At the necked section of interrupted tests surface flaws up to 1/20 in. long and 1/40 in. wide were observed with the unaided eye. The X-ray photographs (have low resolving power) showed no clear indication of the visible surface flaws nor interior flaws for these same tests. Therefore the X-ray technique led to doubtful results.

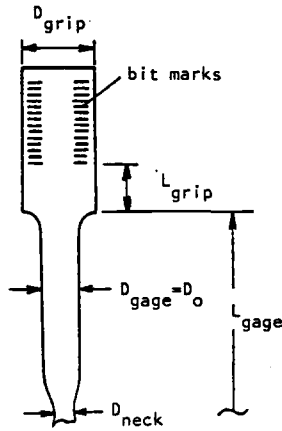


FIG. 4—Test bar dimensions.

On the other hand the fracture surface of one of the two specimens subject to fatigue subsequent to necking revealed that substantial cracks developed prior to fatiguing. Thus stable growth of flaws preceded instability.

Discussion

The previous analysis for fracture instability of a microflaw, Eq 9, gives $T_{applied}$ approximately equal to 2.6 which is lower than all $T_{material}$ values given in Table 2. This agrees with the hypothesis that the ductile fracture of tensile bar initiates with stable development of interior microflaws. Interrupted tests also support this contention. Comparison of $T_{material}$ and $T_{applied}$ values based on Eq 8 shown in Table 2 also supports the hypothesis as well, since instability is predicted only for substantial cracks.

Fatiguing to fracture after interrupting a test only revealed one plane, and the location of this plane was determined by a small surface flaw which dominated fatigue cracking. Thus, that plane may be some longitudinal distance away from the center flaw which would have dominated static fracture. Therefore, the fatigued plane does not necessarily expose the interior flaw of interest. A better X-ray technique or longitudinal sectioning are suggested for future studies. Nevertheless one of the fatigued surfaces showed both interior and exterior flaws, verifying the possibility of interior flaw development prior to unstable fracture.

This project was a preliminary study of applying the tearing instability theory [1] to ductile tensile bar fracture. Therefore for simplification some assumptions and approximations were included; such as assuming dJ/da does not change with large plastic deformation; σ_f is uniform throughout

the cross section, the interior crack is unique, circular, and symmetric with respect to the longitudinal axis, etc. Consequently, it is quite surprising to find that the T_{material} and T_{applied} values for each test agree within a factor of 2 in Table 2. Since the values are quite independently obtained, this is regarded as excellent agreement. In future studies it will be appropriate to further investigate the theory by varying parameters such as temperature, gage length, gage diameter, and materials, as well as exploring the assumptions of the theory discussed here.

However, while this preliminary study has left many questions unanswered, it did indeed show the distinct possibility that the theory of tearing instability may explain ductile cup and cone fractures.

Following completion of the current work some additional results were obtained which add further to the credibility of this work. A resume of these results is given in the Appendix.

Conclusions

1. Tearing instability theory [1] has been applied to cup and cone fractures of A471 steel tensile bars with quantitatively consistent results.

2. Interrupting tests upon necking but prior to fracture and then fatiguing to failure leads to concluding that microflaws grew in a stable manner prior to instability.

3. The application of tearing instability to these tests of A471 predicted, as observed, that microflaw growth would be stable.

4. Presuming that stable microflaw growth generated the flat center of the cup and cone fracture, then instability occurred with the being of formation of the shear wall.

5. The application of tearing instability theory with the flat center, as the final stable flaw size leads to quantitative prediction of instability (within a factor of 2 for T_{material} versus T_{applied}) and implies a switch to the shear wall as observed.

6. Additional studies should be performed to explore further the variables involved in cup and cone fractures.

Acknowledgment

The partial support of this and previous [1] work under contract with the Division of Operating Reactors, The U.S. Nuclear Regulatory Commission at Washington University, is acknowledged. The encouragement of W. Hazelton and R. Gamble of the National Research Council has been instrumental to these studies. The continued support of this study under National Science Foundation Grant ENG 77-20937 is also gratefully acknowledged. Moreover, material and data supplied by Westinghouse Research, through the cooperation of E. T. Wessel is noted with thanks.

APPENDIX

Additional Results on A453 Steel

Tension test results of ASTM A453 stainless steel were made available by Westinghouse Research Laboratories for tests at different temperatures according to the ASTM Standard Methods of Tension Testing of Metallic Materials (E 8-69). They also provided J-R curve results. The chemical composition of the material is listed in Table 3. The tension test results and the J-R curves, together with the assumption that the load at fracture is 80 percent of the maximum load, and the compliance of the test machine is zero, T_{material} and T_{applied} are calculated as in Eq 8 and shown in Table 4.

TABLE 3—Chemical composition of ASTM A453.

Material	C	P	S	Si	Mn	Ni	Cr	Mo	V
ASTM A453 (A286)	0.036	0.017	0.0025	0.57	1.72	25.8	14.9	1.31	0.31

TABLE 4—Test results for ASTM A453.

Specimen Number	Temperature, °F	dJ/da , lb·in. ⁻²	T_{material}	T_{applied}
T_{23}	75	18800	9.7	8
T_{31}	75	18800	14.4	6
T_{24}	400	10500	7.3	8
T_{32}	400	10500	3.7	9
T_{25}	800	7140	8.7	5
T_{34}	800	7140	8.1	5

References

- [1] Paris, P. C., Tada, H., Zahoor, A., and Ernst, H. in *Elastic-Plastic Fracture*, ASTM STP 668, American Society for Testing and Materials, 1979, pp. 5-36.
- [2] Rice, J. R., *The Mechanics of Fracture*, F. Erdogan, Ed., American Society of Mechanical Engineers, 1976.
- [3] Paris, P. C. in *Flow Growth and Fracture*, ASTM STP 631, Proceedings of the 10th National Symposium on Fracture Mechanics, American Society for Testing and Materials, 1977, pp. 3-27.
- [4] Rice, J. R., "Elastic-Plastic Models for Stable Crack Growth," *Mechanics and Mechanisms of Crack Growth*, British Steel Corp., 1973.
- [5] Polakowski, N. H., and Ripling, E. J., *Strength and Structure of Engineering Materials*, Prentice-Hall, Englewood Cliffs, N. J., 1964.

Summary

Summary

Approximately half of this volume has been devoted to the general subject of fatigue crack growth, including effects of combined stress, non-periodic load spectra, temperature, crack closure and residual stress, notches and material discontinuities. Other topics treated include the analytical and experimental analysis of surface flaws, K_{Ic} - J_{Ic} determination, elasto-plastic analysis, specimen geometry effects, experimental techniques for measuring fracture toughness and crack growth parameters, crack initiation, and a group of papers describing the application of fracture mechanics to engineering problems of current technological importance involving cracked bodies of complex geometry.

The influence of combined fields in fatigue crack growth studies was investigated. From experiments on aluminum alloys, Liu, Allison, Dittmer, and Yamane concluded that the transverse stress exerted no influence upon crack growth when constant stress ratios were applied cyclicly. In another study, Pook and Greenan found that the fatigue crack growth threshold depended upon the ΔK_I of the branch crack in some cases and upon the ΔK_I of the original crack in others where Mode II loads were combined with Mode I loads on the original crack.

Several papers focused on load spectrum effects. Based upon a comparison of experimental results with a continuum model, Nowack, Trautmann, Schulte, and Lütjering found that mechanical processes exert a strong influence upon load sequence effects on the fatigue crack growth in aluminum alloys, but that microstructural changes could produce significant deviations from the continuum mechanical analysis. In another study, Artley, Gallagher, and Stalnaker concluded, from an analysis of experimental data on aluminum alloy, that both overload magnitude and frequency exert significant effects upon crack growth rate. Gemma and Snow developed a mechanical model which used constant amplitude fatigue crack growth data at various stress ratios to predict reduced crack growth rates caused by high-low load sequences and showed that correct trends were predicted when compared with test results on several alloys.

The influence of temperature on fatigue crack growth was investigated. Douglas and Plumtree utilized a unified life prediction theory based upon damage accumulation in order to predict crack growth rates at elevated temperature. Tobler, Mikesell, and Reed recorded variations in K_{Ic} with temperature over a wide range of temperatures including the transitional

range for low-carbon steels. On the basis of experiments on aluminum alloys at low temperatures, Pettit and VanOrden concluded that service temperature R-curves should be used in ranking materials for use in the cryogenic temperature region. Shih and Clark found that the influence of temperature on fatigue crack growth rates in rotor steel was frequency dependent, primarily at low frequencies. However, at all frequencies studied, the fatigue crack growth rate decreased initially with increasing temperature and then increased with continued temperature increase.

Several investigations were conducted which focused upon the influence of crack tip plasticity upon fatigue crack growth. Fühning and Seeger developed a continuum mathematical model for describing load history induced residual stress effects upon crack-tip plasticity and fatigue crack growth. In another analytical study, Marci quantified the concentration of crack closure effects near specimen surfaces. Vazquez, Morrone, and Gasco conducted an experimental study of fatigue crack closure in steel from which they identified K_{\max} as the most suitable parameter for correlating fatigue crack closure behavior. Glinka showed how the influence of residual stresses in cracked steel weldments on fatigue crack growth could be predicted qualitatively from existing models. On the basis of observations of experiments on aluminum alloys and steel, Saxena and Hudak explained the dependence of load ratio effects on crack growth rates through mean stress relaxation. Based upon experimental observations, Shaw and LeMay concluded that crack growth curves could be predicted accurately provided the proper crack closure load was used.

Several studies were reported upon which dealt with the initiation and growth of fatigue cracks from notches, where the use of Linear Elastic-Fracture Mechanics may be questionable. Dowling described a general approach to notch size effects based upon the growth of small cracks. El Haddad, Smith, and Topper presented an approach to the short fatigue crack emanating from a notch based upon a strain intensity factor. Braglia, Hertzberg, and Roberts identified the micromechanisms responsible for crack initiation in notched high-strength low-alloy steel.

Finally, an investigation by Clark is included which studies the influence of macroscopic spherical discontinuities upon the fatigue crack growth rate in powder metal steel specimens.

Several papers, both analytical and experimental, addressed three dimensional cracked body problems involving surface flaws. Using a boundary integral-influence function approach, Heliot, Labbens, and Pellissier-Tanon computed stress intensities for semi-elliptic cracks in meridional planes of thin-walled cylinders under internal pressure. McGowan and Raymund addressed the same problem utilizing a finite-element approach and their results correlated well with those of the previously mentioned study. Yagawa, Ichimiya, and Ando used the finite element method to compute the time dependent thermal stresses induced by the sudden cooling of a thick plate containing a surface crack. The

results predicted by the model were compared with test results on plexiglas plates and estimated times to fracture agreed fairly well. Hodulak, Kordisch, Kunzelmann, and Sommer, in an experimental study of the fatigue crack growth of surface flaws in plates found evidence of nonuniform material behavior along the flaw border which they suggest may be due to a stress state dependent mechanical response. Raju and Newman, using a finite element model, computed stress intensities for the technologically important problem of a crack emanating from the intersection edge of a hole with a plate. In a frozen stress photoelastic study of the same problem, Smith, Peters, and Gou found that nonself-similar flaw growth appeared to produce changes in the stress intensity distribution during flaw growth and suggested that the cause may be due to an effect such as suggested by Hodulak et al.

Several papers were devoted to K_{Ic} - J_{Ic} evaluations for different materials, some of which included tear modulus measurements. Penelon, Bassim, and Dorlot, in evaluating J-integrals for material in the heat affected zone of steel alloys, observed a strong dependence of J_{Ic} upon geometry. Underwood measured J_{Ic} in steel using a bend test and presented a correction procedure for computing J_{Ic} values from C-shaped specimens.

Several papers presented studies which were directed towards the analysis and measurement of specimen geometry effects upon test results. Gudas, Joyce, and Davis studied such an influence upon the J_{Ic} curve Tear Modulus in HY130 steel and found that face-grooving effects were significant. deCastro, Spurrier, and Hancock quantified the influence of the crack length to specimen width ratio upon the crack opening displacement for structural steels in the cryogenic to room-temperature region. Mall, Kobayashi and Urabe conducted dynamic photoelastic studies on dynamic tear test specimens in order to measure the variation of the dynamic stress intensity factor with time. A finite element model was constructed which correlated with the experimental results. Garwood showed that the values of J and the crack opening displacements were essentially the same for both three-point bend and center-cracked tension specimens of pipeline steel. The corresponding resistance curves, however, were different, and analytical explanations were offered.

Several papers utilized particular experimental techniques for obtaining information on fracture parameters. Ori and Grandt evaluated the use of cracked coupons bonded to structures with expected preexistent cracks so that the coupons experienced load histories similar to the structure for predicting crack growth. Allison used X-ray stress analysis to measure both residual and applied stresses near a crack tip. Results confirmed the presence of crack closure type stress fields. Vary described a mechanical model which is based upon the assumption that microcracking is promoted by elastic wave interactions, and relations between ultrasonic and fracture parameters were obtained.

Reflecting the continued effort to adapt fracture concepts to plastic cracking, several papers focused upon the analysis of such cases. Ernst, Paris, Rossow, and Hutchinson developed analytical methods for computing J from load displacement test records which take into account the influence of the extension of the crack. Karabin and Swedlow, in a finite element analysis, found a path dependence in J when the plastic zone size is not small. They suggest that this effect is related to a resharpener of the crack flank near the tip in center-cracked specimens. Turner provided a description of stable and unstable crack growth for elastic-plastic behavior in terms of J_r resistance curves.

Three papers addressed the general topic of composite fracture. Williams and Reifsnider presented a strain energy release based finite element model for predicting failure modes in composite laminates which was correlated with experimental observations. Wang described a hybrid stress finite element analysis of the tapered double cantilever beam fracture toughness specimen which revealed a number of important features. Ramkumar, Kulkarni, Pipes, and Chatterjee presented an analysis of delaminations in a laminated cantilever beam of various locations in the beam. The model suggests mechanisms for progressive cracking in laminates.

A number of interesting papers were contributed which addressed special topics in fracture mechanics. Kong and Paris used a model of ductile fracture in tensile bars to suggest that tearing instability theory might apply to some cases of fracture in the presence of extensive plastic deformation. Pu and Hussain estimated stress intensity factors for a uniform array of radial cracks around a circular ring using a finite element approach. Smoley studied crack surface topologies in poly(vinyl chloride) for nucleation, subcritical and critical flaw growth for both plasticized and unplasticized material. Both craze and crack growth regimes were observed.

The preceding contributions to the developmental aspects of fracture mechanics were augmented by several papers which focused upon the utilization of fracture mechanics in specific engineering applications. McDermott and Stephens conducted tests on hollow rectangular tubes containing corner cracks and described a procedure for predicting K_{Ic} values and crack growth based upon existing solutions. Christ, Smith, and Hicho described the post failure analysis of a pneumatically burst seamless steel compressed gas cylinder which led to recommendations for minimizing the occurrence of such failures. Kapp and Eisenstadt described a procedure for modeling flaw growth in autofrettaged cylinders for use in design. Finally, Galliard described a design technique which utilized test data from a field test of a prototype as input data to a computerized program for designing against failure from fatigue crack growth in the ground vehicle industry.

The papers included in this volume show that fatigue crack growth

continues to occupy an important position in fracture mechanics. Moreover, while crack initiation appears to be controlled mechanically, crack growth is shown to be sensitive to many other side effects as well, a number of which are quantified herein.

Another area of substantial activity involves the extension of the basic concepts of fracture mechanics to the prediction of fracture in the presence of substantial amounts of plasticity.

New results, both analytical and experimental, suggest that more complex models will be necessary in order to provide an acceptably accurate description of crack growth and fracture in problems involving complex three-dimensional geometries. It is encouraging to note that, as the problems under study become more complex, new analyses and experimental techniques are being developed for use in dealing with such problems.

Taken collectively, this volume records advances in the development and application of fracture mechanics along a broad front. It would seem to portend a trend which will extend the use of fracture mechanics to a wider range of environments and to more complex problems in the future.

C. W. Smith

Department of Engineering and Mechanics, Virginia Polytechnic Institute and State University, Blacksburg, Va. 24061; symposium chairman and editor.

Index

- A**
- Adherend, 651
 - Adhesive, 651
 - Aluminum alloys, 5, 36, 54, 106, 168, 187, 215, 320
 - Autofrettage, 746
- B**
- Bending loads, 463
 - Biaxial loading, 5
 - Block loading, 290
 - Boundary integral equation method, 341
- C**
- Combined loading, 23
 - Complex stress functions, 651
 - Composite materials, 629, 668
 - Crack closure, 144, 168
 - Crack growth
 - Gage, 533
 - Prediction, 399
 - Retardation, 550
 - Cracks, 700, 719
 - Arrest, 498
 - Closure, 36, 215, 233
 - Initiation, 23, 247, 511
 - Nucleation, 700
 - Opening displacement, 106, 486
 - Resistance, 511
 - Retardation, 198
 - Shape, 399
 - Surface topology, 700
 - Tip stress field, 651
 - Craze, 700
 - Cumulative damage, 290
 - Cyclic loads, 144, 247, 303
 - Delay cycles, 320
 - Cylinders, 341, 685
- D**
- Damage accumulation, 68
 - Defects, 303
 - Deformation, 247, 600
 - Delaminations, 668
 - Design, 719
 - Displacements (deformations), 36
 - Ductile-brittle transition, 700
 - Ductile fracture, 734
 - Dynamic
 - Fracture toughness, 498
 - Photoelasticity, 498
- E**
- Elastic analysis, 411, 651
 - Elastic-plastic
 - Analysis, 614
 - Fracture, 474, 486

F

Failure, 303
 Failure modes, 629
 Fatigue crack initiation, 290
 Crack closure, 187
 Fatigue crack growth, 5, 23, 36, 54,
 68, 85, 106, 125, 144, 168,
 187, 198, 215, 233, 247, 274,
 290, 303, 320, 533, 550, 614,
 629, 700, 719, 746, 757
 Fiber-reinforced epoxy, 668
 Field test, 757
 Finite elements, 381, 411, 498, 600,
 629, 651, 746
 Fractographic results, 106, 290, 700
 Fracture parameters, 341
 Properties, 463, 685
 Strength, 511
 Tests, 486
 Toughness, 85, 106, 381, 449,
 463, 474, 511, 563, 734
 Frequency, 125

G

Geometry effects, 486, 511

H

Heat affected zone, 449
 High temperature fatigue, 68
 Hole-cracks, 411, 431
 Hollow rectangular tube, 719

I

Influence functions, 341
 Instability, 511, 614
 Iron-nickel-chromium alloys, 68

J

J_{Ic} tests, 463, 474
 J_r , 614
 J-R curves, 580
 J-integral, 68, 449, 486, 580, 600,
 614
 Joints, 651

L

Loss-of-coolant accident, 381

M

Materials
 Aluminum alloys, 5, 36, 54, 106,
 168, 187, 215, 320
 Composites, 629, 668
 Nickel alloys, 67, 85
 Plastics, 381, 498, 700
 Powdered metal, 303
 Steel alloys, 23, 68, 85, 125, 187,
 198, 215, 233, 290, 303, 449,
 463, 474, 486, 550, 719, 734
 Titanium alloys, 320
 Material memory, 144
 Mathematical methods (*see* Elastic
 analysis, Elastic-plastic
 analysis, Boundary inte-
 grals, Finite element,
 Weight functions, Stiffness
 derivative
 Mechanical properties, 85, 486, 580
 Microstructural crack propagation
 mechanism, 36
 Microstructure, 563
 Microvoid coalescence, 700
 Mode II, 23
 Multiple cracks, 685

- N**
- Nickel alloys, 68, 85
 Nondestructive evaluation, 550, 563, 668
 Notch size effects, 247
- O**
- Overload, 144, 320
- P**
- Photoelastic analysis, 431, 498
 Plastic instability, 700
 Plasticity effects, 144, 247, 600
 PMMA, 381
 Pneumatic burst test, 734
 Polycarbonate, 498
 Poly(vinyl chloride), 700
 Pressure vessels, 365, 734, 746
- R**
- R-curve, 106, 614
 Residual stress, 144, 198, 550
 Retardation, 320
- S**
- Scanning electron microscope studies, 629
 Spot-welded joints, 23
 Stage II fatigue (materials), 168
 Statistical methods, 54
 Steel alloys, 23, 85, 125, 187, 198, 215, 233, 290, 303, 449, 463, 474, 486, 550, 719, 734
 Stiffness derivative method, 365
- Strain
 Concentration, 144
 Energy, 629
 Intensity factor, 274, 365, 411, 431
 Stress, 247, 274, 550
 Analysis, 381
 Cycling, 23, 533
 Intensity distributions, 341, 365, 381, 411, 431
 Intensity factor, 54, 233, 341, 651, 685
 Relaxation, 215
 Waves, 563
 Stress and strain concentration factors, 274
 Structural memory, 144
 Subcritical velocity, 700
 Surface flaws, 341, 365, 381, 399, 411, 431
- T**
- Tapered DCB specimen, 651
 Tearing modulus, 474, 511, 580, 770
 Temperature, 85, 106, 125
 Thermal shock, 381
 Three-dimensional problems, 341, 431
 Titanium alloys, 320
 Tubes, 719
- U**
- Ultrasonics, 563
 Underload, 144
- V**
- Variable amplitude loading, 36, 54

W

Wearout concept, 668
Weight functions, 365
Welding residual stresses, 198

X

X-ray diffraction, 550